IFMBE Proceedings

Lenka Lhotska · Lucie Sukupova
Igor Lacković · Geoffrey S. Ibbott (Eds.)

Volume 68/2

World Congress on Medical Physics and Biomedical Engineering 2018

June 3–8, 2018, Prague, Czech Republic (Vol. 2)

IUPESM
PRAGUE 2018

Springer

IFMBE Proceedings

Volume 68/2

Series editor

Ratko Magjarevic

Deputy Editors

Fatimah Ibrahim
Igor Lacković
Piotr Ładyżyński
Emilio Sacristan Rock

The International Federation for Medical and Biological Engineering, IFMBE, is a federation of national and transnational organizations representing internationally the interests of medical and biological engineering and sciences. The IFMBE is a non-profit organization fostering the creation, dissemination and application of medical and biological engineering knowledge and the management of technology for improved health and quality of life. Its activities include participation in the formulation of public policy and the dissemination of information through publications and forums. Within the field of medical, clinical, and biological engineering, IFMBE's aims are to encourage research and the application of knowledge, and to disseminate information and promote collaboration. The objectives of the IFMBE are scientific, technological, literary, and educational.

The IFMBE is a WHO accredited NGO covering the full range of biomedical and clinical engineering, healthcare, healthcare technology and management. It is representing through its 60 member societies some 120.000 professionals involved in the various issues of improved health and health care delivery.

IFMBE Officers
President: James Goh, Vice-President: Shankhar M. Krishnan
Past President: Ratko Magjarevic
Treasurer: Marc Nyssen, Secretary-General: Kang Ping LIN
http://www.ifmbe.org

Lenka Lhotska · Lucie Sukupova
Igor Lacković · Geoffrey S. Ibbott
Editors

World Congress on Medical Physics and Biomedical Engineering 2018

June 3–8, 2018, Prague, Czech Republic
(Vol. 2)

IUPESM
PRAGUE 2018

Springer

Editors
Lenka Lhotska
CIIRC
Czech Technical University in Prague
Prague
Czech Republic

Lucie Sukupova
Institute of Clinical and Experimental
    Medicine
Prague
Czech Republic

Igor Lacković
Faculty of Electrical Engineering
    and Computing
University of Zagreb
Zagreb
Croatia

Geoffrey S. Ibbott
Department of Radiation Physics
The University of Texas MD Anderson
    Cancer Center
Houston, TX
USA

Printed on acid-free paper

Preface

This book presents the proceedings of the IUPESM World Congress on Biomedical Engineering and Medical Physics, a triennially organized joint meeting of medical physicists, biomedical engineers, and adjoining healthcare professionals. Besides the purely scientific and technological topics, the 2018 Congress will also focus on other aspects of professional involvement in health care, such as education and training, accreditation and certification, health technology assessment, and patient safety. The IUPESM meeting is an important forum for medical physicists and biomedical engineers in medicine and healthcare to learn and share knowledge, and to discuss the latest research outcomes and technological advancements as well as new ideas in both medical physics and biomedical engineering field.

Biomedical engineering and medical physics represent challenging and rapidly growing areas. Building on the success of the previous World Congresses, the aim of the World Congress 2018 is to continue in bringing together scientists, researchers, and practitioners from different disciplines, namely from mathematics, computer science, bioinformatics, biomedical engineering, medical physics, medicine, biology, and different fields of life sciences, so that they can present and discuss their research results. We hope that the World Congress 2018 will serve as a platform for fruitful discussions between all attendees, where participants can exchange their recent results, identify future directions and challenges, initiate possible collaborative research, and develop common languages for solving problems in the realm of biomedical engineering and medical physics.

Following a thorough peer-reviewed process, we have finally selected 498 papers. The Scientific Committee would like to thank the reviewers for their excellent job. The articles can be found in the proceedings and are divided into the main tracks and special sessions. The papers show how broad the spectrum of topics in biomedical engineering and medical physics is.

The editors would like to thank all the participants for their high-quality contributions and Springer for publishing the proceedings of the World Congress.

Prague, Czech Republic	Lenka Lhotska
Prague, Czech Republic	Lucie Sukupova
Zagreb, Croatia	Igor Lacković
Houston, USA	Geoffrey S. Ibbott
March 2018	

Organizing Committees

Congress Coordinating Committee

Chair

Kin Yin Cheung, Chair, IOMP, Hong Kong

Members

Howell Round, IOMP, New Zealand
Slavik Tabakov, IOMP, UK
Virginia Tsapaki, IOMP, Greece
James Goh, IFMBE, Singapore
Kang Ping Lin, IFMBE, Chinese Taipei
Herb Voigt, co-opted, IFMBE, USA †
Monique Frize, co-opted, IFMBE, Canada

Congress Organizing Committee

Co-chairs

Jaromir Cmiral, Czech Republic, BME
Libor Judas, Czech Republic, MedPhys

Secretaries

Frantisek Lopot, Czech Republic, BME
Karel Nechvil, Czech Republic, MedPhys

Members

Financial Committee Co-chairs

Martin Mayer, Czech Republic, BME
Vít Richter, Czech Republic, MedPhys

Scientific Committee Co-chairs

Lenka Lhotska, Czech Republic, BME
Lucie Sukupova, Czech Republic, MedPhys

Publicity Committee Chair

Martina Novakova, Czech Republic, BME, MedPhys

Education Committee Co-chairs

Jiri Hozman, Czech Republic, BME
Irena Koniarova, Czech Republic, MedPhys

Financial Committee

Co-chairs

Martin Mayer, Czech Republic, BME
Vit Richter, Czech Republic, MedPhys

Members

Jan Hanousek, Czech Republic, BME
Anchali Krisanachinda, IOMP
Mark Nyssen, IUPESM, IFMBE
Vaclav Poljak, Czech Republic, MedPhys

Scientific Committee

Co-chairs

Geofrey Ibbott, IOMP
Lenka Lhotska, Czech Republic, BME
Igor Lackovic, IFMBE
Lucie Sukupova, Czech Republic, MedPhys

Members

Magdalena Bazalova-Carter, Canada
Carmel Caruana, Malta
Tomas Cechak, Czech Republic
Paul Chang, Singapore
Kin Yin Cheung, Hong Kong, China
Jiri Chvojka, Czech Republic
Matej Daniel, Czech Republic
Marie Davidkova, Czech Republic
Harry Delis, IAEA
Pavel Dvorak, Czech Republic
Ludovic Ferrer, France
Martin Falk, Czech Republic
Christian Gasser, Sweden
Csilla Gergely, France
Susanna Guatelli, Australia
Jens Haueisen, Germany
Jan Havlik, Czech Republic
Jiří Hozman, Czech Republic
Marjan Hummel, The Netherlands
Leonidas D. Iassemidis, USA
Tom Judd, USA
Peter Knoll, Austria
Radim Kolar, Czech Republic
Jana Kolarova, Czech Republic
Christian Kollmann, Austria
Irena Koniarova, Czech Republic
David Korpas, Czech Republic
Vladimir Krajca, Czech Republic
Jan Kremlacek, Czech Republic
Petr Marsalek, Czech Republic
Deborah Van Der Merwe, IAEA
Karel Nechvil, Czech Republic

Chris Nuggent, UK
Pirkko Nykänen, Finland
Hakan Nystrom, Sweden
Pawel Olko, Poland
Maria Perez, WHO
Vaclav Porod, Czech Republic
Kevin Prise, UK
Ivo Provaznik, Czech Republic
Jaroslav Ptáček, Czech Republic
Vladimir Rogalewicz, Czech Republic
Simo Saarakkala, Finland
Ioannis Sechopoulos, The Netherlands
Milan Sonka, USA
Olga Stepankova, Czech Republic
Lucie Sukupova, Czech Republic
Krystina Tack, USA
Annalisa Trianni, Italy
Jiri Trnka, Czech Republic
Virginia Tsapaki, Greece
Adriana Velazquez, WHO
Frantisek Vlcek, Czech Republic
Jan Vrba, Czech Republic
Kevin Warwick, UK
Martha Zequera Diaz, Columbia

Program Committee

Co-chairs

Jaromir Cmiral, Czech Republic, BME
Libor Judas, Czech Republic, MedPhys

Members

Lenka Lhotska, Czech Republic, BME
Frantisek Lopot, Czech Republic, BME
Karel Nechvil, Czech Republic, MedPhys
Martina Novakova, Czech Republic, BME
Lucie Sukupova, Czech Republic, MedPhys

Publicity Committee

Chair

Martina Novakova, Czech Republic

Members

Pavla Buricova, Czech Republic
Michele Hilts, Canada
Jeannie Hsiu Ding Wong, Malaysia
Akos Jobbagy, Hungary
Luiz Kun, USA
Pavla Novakova, Czech Republic
Magdalena Stoeva, Bulgaria
Tae-Suk Suh, Republic of Korea
Jaw-lin Wang, Chinese Taipei

Education Committee

Co-chairs

Jiri Hozman, Czech Republic, BME
Irena Koniarova, Czech Republic, MedPhys

Members

Jiri Kofranek, Czech Republic, BME
Vladimír Krajca, Czech Republic, BME
Simo Saarakkala, Finland, BME
Ioannis Sechopoulos, The Netherlands, MedPhys

Professional Standards Committee

Co-chairs

David Korpas, Czech Republic, BME
Libor Judas, Czech Republic, MedPhys

Members

John Damilakis, Greece, MedPhys
Michele Hilts, Canada
Jeannie Hsiu Ding Wong, Malaysia
Tomas Kron, Australia, MedPhys
Siew Lok Toh, Singapore, BME
Yakov Pipman, USA, MedPhys
Kang Ping Lin, Chinese Taipei, BME
Jaroslav Ptacek, Czech Republic, MedPhys
Christoph Trauernicht, South Africa, MedPhys

Publication Committee

Chair

Vladimir Marik, Czech Republic

Co-chair

Igor Lacković, Croatia

International Advisory Board (BME)

Co-chairs

James Goh, Singapore
Ratko Magjarevic, Croatia

Members

Guillermo Avendano C., Chile
Paulo De Carvalho, Portugal
Jaromir Cmiral, Czech Republic
Fong Chin Su, Chinese Taipei
David Elad, Israel
Yubo Fan, China

Mário Forjaz Secca, Portugal
Monique Frize, Canada
Birgit Glasmacher, Germany
Peter Hunter, New Zealand
Ernesto Iadanza, Italy
Fatimah Ibrahim, Malaysia
Timo Jämsä, Finland
Akos Jobbagy, Hungary
Eleni Kaldoudi, TBA
Peter Kneppo, Czech Republic
Shankar Krishnan, USA
Eric Laciar Leber, Argentina
Igor Lackovic, Croatia
Piotr Ladyzynski, Poland
Lenka Lhotska, Czech Republic
Nigel Lovell, Australia
Alan Murray, UK
Marc Nyssen, Belgium
Leandro Pecchia, UK
Kang Ping Lin, Chinese Taipei
Ichiro Sakuma, Japan
Maria Siebes, The Netherlands
Nitish Thakor, Singapore
Herbert F. Voigt, USA
Min Wang, Hong Kong

International Advisory Board (MP)

Co-chairs

Kin Yin Cheung, Hong Kong, China
Slavik Tabakov, UK

Members

Laila Al Balooshi, UAE
Abdullah Al Hajj, KSA
Huda Al Naemi, Qatar
Rodolfo Alfonso Laguardia, Cuba
Supriyanto Ardjo Pawiro, Indonesia
Eva Bezak, Australia
Marco Brambila, Italy
David Brettle, UK
Arun Chougule, India
John Damilakis, Greece
Catherine Dejean, France
Ludovic Ferrer, France
Michelle Hilts, Canada
Jeannie Hsiu Ding Wong, Malaysia
Amaury Hornbeck, France
Geoffrey Ibbott, USA
Ahmed Ibn Seddik, Morocco
Taofeeq Ige, Nigeria
Petro Julkunen, Finland
Simone Kodlulovich, Brazil

Acknowledgements

Organizing Societies

International Societies

Collaborating Institution

Sponsors

varian

RaySearch
Laboratories

Elekta

About IFMBE

The International Federation for Medical and Biological Engineering (IFMBE) is primarily a federation of national and transnational societies. These professional organizations represent interests in medical and biological engineering. IFMBE is also a non-governmental organization (NGO) for the United Nations and the World Health Organization (WHO), where we are uniquely positioned to influence the delivery of health care to the world through biomedical and clinical engineering.

The IFMBE's objectives are scientific and technological as well as educational and literary. Within the field of medical, biological, and clinical engineering, IFMBE's aims are to encourage research and application of knowledge and to disseminate information and promote collaboration. The ways in which we disseminate information include the following: organizing World Congresses and Regional Conferences, publishing our flagship journal Medical and Biological Engineering and Computing (MBEC), our Web-based newsletter—IFMBE News, our Congress and Conference Proceedings, and books. The ways in which we promote collaborations are through networking programs, workshops, and partnerships with other professional groups, e.g., Engineering World Health.

Mission

The mission of IFMBE is to encourage, support, represent, and unify the worldwide medical and biological engineering community in order to promote health and quality of life through the advancement of research, development, application, and management of technology.

Objectives

The objectives of the International Federation for Medical and Biological Engineering shall be scientific, technological, literary, and educational. Within the field of medical, clinical, and biological engineering, its aims shall be to encourage research and the application of knowledge and to disseminate information and promote collaboration.

In pursuit of these aims, the Federation may, in relation to its specific field of interest, engage in any of the following activities: sponsorship of national and international meetings, publication of official journals, cooperation with other societies and organizations, appointment of commissions on special problems, awarding of prizes and distinctions, establishment of professional standards and ethics within the field, or in any other activities which in the opinion of the General Assembly or the Administrative Council would further the cause of medical, clinical, or biological engineering. It may promote the formation of regional, national, international, or specialized societies, groups or boards, the coordination of bibliographic or informational services, and the improvement of standards in terminology, equipment, methods and safety practices, and the delivery of health care.

In general, the Federation shall work to promote improved communication and understanding in the world community of engineering, medicine, and biology.

Contents

Off-label Use of Medical Devices in Cardiovascular Medicine—When the Final Decision About the Safety and Effectiveness Is Needed

David Macku

Abstract

The use of a medical device in cardiovascular medicine according to the instructions provides maximum quality and safety, which has been clinically tested and then clinically evaluated. When you use a medical device and do not follow the instructions for use, you use a medical device off-label. Off-label use of a medical device can be seen not as an extension of the clinical use of a medical device, but also as a way of expanding scientific knowledge. Some off-label uses of a medical device provide positive health effects, and some do not. Two examples of off-label use in cardiovascular medicine are presented. While the off-label use of drug-eluting stents is commonly accepted, the off-label use of continuous left ventricular assist devices as continuous flow total artificial hearts provide very poor clinical results. Medical doctors and their patients should know which off-label use method works and which does not.

Keywords

Off-label use • Ventricular assist device • Continuous flow total artificial heart • Safety • Effectiveness

1 Introduction

1.1 Off-label Use

The use of a medical device in the way indicated in the instructions is called "on-label use of a medical device." When you buy any medical device, a manufacturer invites you to read the instructions for use and to use it as instructed. It is convenient for you. When you use a medical device in this authorized way, you achieve the desired effect and safety of the medical device. Additionally, when you make a warrant claim to the manufacturer, they always ask you whether you followed the instructions for use when you used the medical device. If your answer is no, the warranty claim will not be accepted. The use of a medical device as directed in the instructions provides maximum quality and safety, which has been clinically tested and then clinically evaluated. When you use a medical device and do not follow the instructions for use, you use the medical device 'off-label'. Some off-label uses of medical devices work and such uses of off-label methods can be used by doctors to treat their patients. In our article, we label them as 'bright off-label methods'. However there are also new technologies using medical devices off-label, which do not provide satisfactory results. Such new medical technologies should not be supported. For the purpose of our article, we call them and 'dark off-label methods'.

1.2 Bright Off-label Use

As an example of a successful application of medical devices in off-label use in clinical practice and as an example of a bright off-label method it is noteworthy to mention the use of drug-eluting stents in application beyond that included in the device manufacturer's information for use and the FDA indications [1]. In this study, the frequency and outcomes of off-label or untested use of drug-eluting stents compared with standard use were evaluated from the large multicenter prospective PCI registry. They observed that approximately half of all use of drug-eluting stents occurs in off-label or untested settings. Compared with standard use, short-term outcomes appear to be worse with off-label and untested use. However, even with off-label or untested use of drug-eluting stents, overall absolute events' rates both in-hospital and at 12 months following PCI remains relatively low. The FDA had convened the Circulatory system Devices Advisory Panel to review the broader use of drug eluting stents in real-world clinical use and the implication of DES outside of

D. Macku (✉)
Czech Technical University in Prague, Technicka 2,
16627 Prague, Czech Republic
e-mail: davidmacku@yahoo.com

their approved indications. The panel concluded that there is a need for a comprehensive assessment of the safety and efficiency of off-label use of DES. The Circulatory system Devices Advisory Panel has not put any bans or restrictions on the off-label or untested use of drug-eluting stents [2]. The use of drug eluting stents continues in on-label, off-label and untested settings.

1.3 Dark Off-label Use

As an example of a dark off-label method, we present a medical device in cardiac surgery. Specifically, the use of two units of a continuous left ventricular assist device (LVAD) as a total artificial heart (TAH) [3]. If the use of continuous LVADs as TAH prove safe and effective, it would mean a breakthrough in the field of mechanical circulatory support. The main principle of this method is to replace very complex pulsatile flow with a continuous one. Axial or centrifugal pumps are very small and safe, and they can generate such type of flow. Cardiac surgeons have a lot of experience with these types of pumps, but so far only as LVAD. The extension in the use of these reliable pumps (the extension in use as TAH) would be good news for manufacturers who currently recommend these pumps only for LVAD use. Some doctors see a great future in the use of centrifugal and axial pumps as TAH, but at the same time, they are calling for more research in the area of microcirculatory alterations in the presence of non-pulsatile circulation [4]. All existing animals studies, all experiments with continuous pumps implanted as TAH have been carried out only with constant pump rates. The blood flows coming out from pumps in this setting up cause blood pressure flat line. There is also a way to generate pulsatile flow by using continuous pumps, i.e. when we periodically change their pump rates [5]. If we could live with continuous blood flow, and the continuous flow would be equal to pulsatile flow we could regard this as a scientific stunner. Many doctors and researchers still believe that pulsatile flow is superior to the continuous one; pulsatile flow causes better circulation than continuous flow [3]. Cardiac surgeons who have performed off-label cardiac procedures with continuous pumps and have established continuous blood flow in human bodies, have their biggest problem being a lack of evidence, i.e. chronic continuous flow had been sufficient for organs' perfusion in their patients. The use of two units of continuous LVAD and their implantation as TAH has also been called as a 'continuous flow total artificial heart (CFTAH)'. Many animal studies with axial pumps implanted as CFTAH have been presented as proof of success and have given us hope that mammalians can take benefit from pulseless circulation and could survive for weeks or months [6–9]. The survival of patients with CFTAH has not been so smooth.

All three patients have had difficult postoperative courses. Neither of them has survived. The first patient survived one week [10], the second patient survived five weeks [11], and the third one died after six months in 2012 [12, 13].

Since the last surgeries, several years have passed. No articles about patients with CFTAH have occurred in scientific journals or public media since that time. If any cardiac departments worldwide have performed this off-label method since then, they were performed silently without the publishing of the results of their work.

2 Methods

Based on the example of the bright off-label method it is obvious that the off-label use has its worth, but the process of the implementation of an off-label medical device should be planned and should follow some rules. I recommend this algorithm for this process. At the end of this process, the decision safety and effectiveness should be known (Fig. 1).

3 Discussion

When the off-label method assessment shows significant positive health effects in patients, a medical device can be exploited in new use and can be assessed as safe and effective. Otherwise, off-label use with significant negative health effects in patients can be seen as not safe and not efficient. Clinical data about the off-label method and its assessment should be published with commentary. There is a question of who would make the decision on the low effectiveness and safety of off-label technology when it causes apparently an poor clinical outcome. The decision may be made by any Cardiology, or Cardiac surgery societies or the FDA advisory panel can decide about the problematic off-label issue in specific cases. The last off-label surgery with CFTAH took place five years ago. It has been a long time. During this period no successful or unsuccessful surgeries with CFTAH with constant pumps rate have been recorded. The time has come to make an assessment and a decision on the safety and effectiveness of this new off-label use method. The patient-physician relationship is a covenant that obliges the physician to act in the patient's best interest and put the needs and welfare of the patient first; it is the duty of the physician to synthesize anecdotal experiences, available data and society guidelines, and apply them to the particular patients that he or she is treating [14]. If physicians use a product for an indication, not in the approved labeling, they have the responsibility to be well informed about the product, to base its use on firm scientific rationale and on sound medical evidence [15].
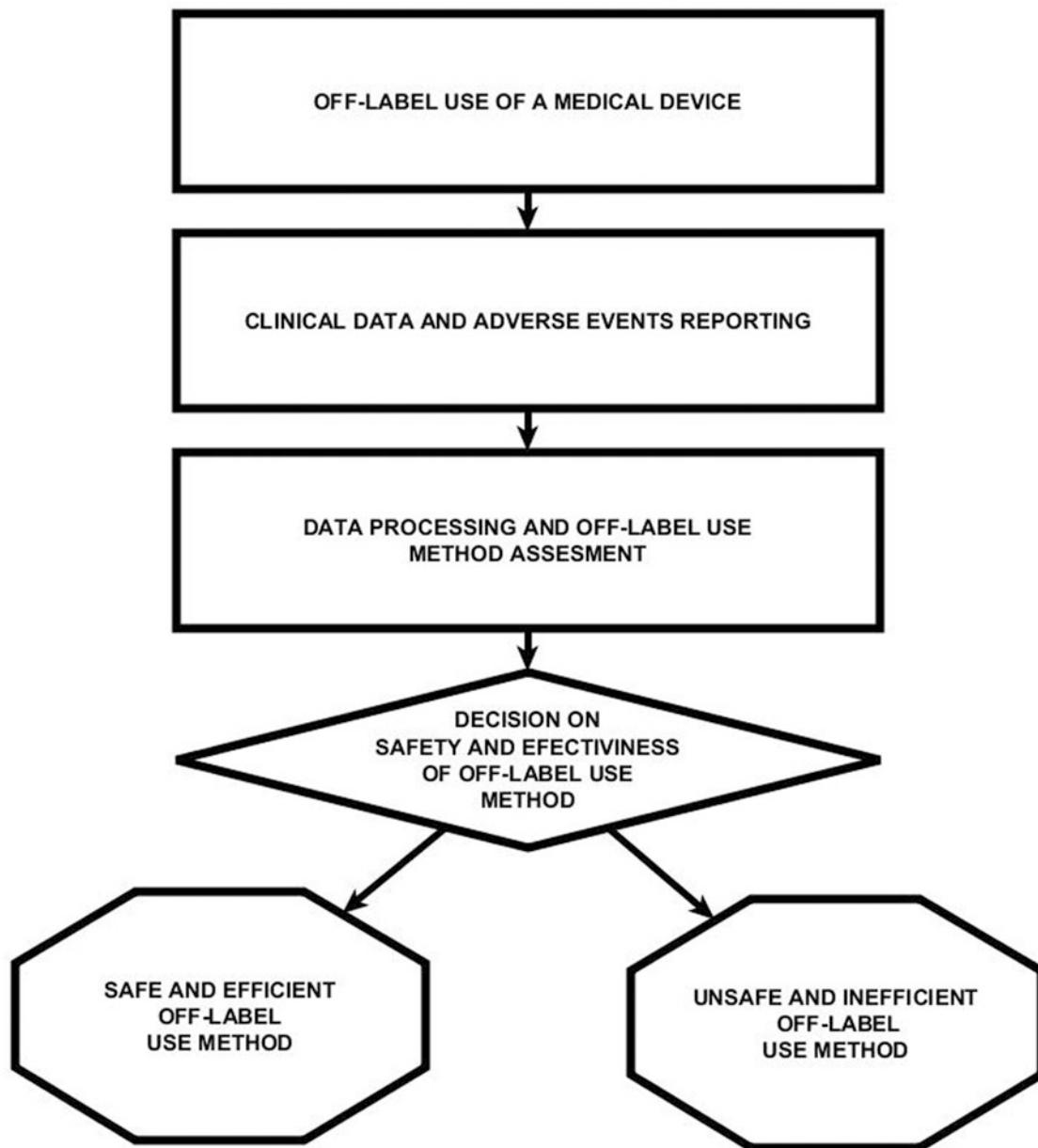
Fig. 1 The process of the implementation of an off-label medical device in clinical practice

I provide the available scientific data and articles, which are cited in References, as the input for the decision and the result. The flow-chart algorithm describes the decision tree used in medical device trials and evaluation. Examples of the unapproved use of approved medical devices from clinical practice can be seen as the added value of the article.

4 Conclusion

The author of the article state that the use of chronic non-pulsatile flow is not based on firm scientific rationale and on sound medical evidence. The off-label use of CFTAH

without pulsatile augmentation can be considered to an off-label method with a dark future.

Statements The author declares that he has no conflict of interest.

References

1. Beohar N, Davidson CJ, Kip KE, Goodreau L, Vlachos HA, Meyers SN, Benzuly KH, Flaherty JD, Ricciardi MJ, Bennett CL, Williams DO. Outcomes and complications associated with off-label and untested use of drug-eluting stents. Jama 297(18), 1992–2000 (2007).
2. FDA. Summary from the Circulatory system Devices Panel Meeting – December 7 & 8, 2006. https://www.fda.gov/ohrms/dockets/ac/06/minutes/2006-4253m2-%20Final%201208summ.pdf, last assessed 2017/12/12.
3. Macku D. The Continuous Flow Total Artificial Heart in Clinical Practice. In: World Congress on Medical Physics and Biomedical Engineering, June 7–12, 2015, Toronto, Canada. Springer International Publishing, 2015. p. 318–321.
4. Shekar K, Gregory SD, Fraser JF. Mechanical circulatory support in the new era: an overview. Critical Care. 2016;20(1):66.
5. Cohn WE, Timms DL, Frazier OH. Total artificial hearts: past, present, and future. Nature Reviews Cardiology. 2015;12(10):609–617.
6. Cohn WE, Handy KM, Parnis SM, Conger JL, Winkler JA, Frazier OH. Eight-year experience with a continuous-flow total artificial heart in calves. ASAIO Journal. 2014;60(1):25–30.
7. Cohn WE, Winkler JA, Parnis S, Costas GG, Beathard S, Conger J, Frazier OH. Ninety-day survival of a calf implanted with a continuous-flow total artificial heart. ASAIO Journal. 2014;60(1):15–18.
8. Frazier OH, Cohn WE, Tuzun E, Winkler JA, Gregoric ID. Continuous-flow total artificial heart supports long-term survival of a calf. Texas Heart Institute Journal. 2009;36(6):568–574.
9. Karimov JH, Fukamachi K, Moazami N, Kobayashi M, Sale S, Mielke N, Sunagawa G, Horvath D, Gao S, Golding LA. In vivo evaluation of the Cleveland Clinic continuous-flow total artificial heart in calves. The Journal of Heart and Lung Transplantation. 2014;33(4):S165–S166.
10. Loebe M, Bruckner B, Reardon MJ, van Doorn E, Estep J, Gregoric, I, Masud F, Cohn W, Motomure T, Tore-Amione G, Frazier OH. Initial clinical experience of total cardiac replacement with Dual Heartmate-II® Axial Flow Pumps for severe biventricular heart failure. Methodist DeBakey cardiovascular journal. 2011;7(1):40–44.
11. Frazier OH, Cohn WE. Continuous-Flow Total Heart Replacement Device. Texas Heart Institute Journal. 2012; 39(4):542–546.
12. Pirk J, Maly J, Szarszoi O, Urban M, Kotulak T, Riha H, Neuzil P, Netuka I. Total artificial heart support with two continuous-flow ventricular assist devices in a patient with an infiltrating cardiac sarcoma. ASAIO Journal. 2013;59(2):178–180.
13. Czech man with no heart dies after six months. BBC news. BBC Homepage [online]. Retrieved 28.3.2017. From: http://www.bbc.com/news/world-europe-19977958.
14. Price MJ, Teirstein PS. The off-versus on-label use of medical devices in interventional cardiovascular medicine: Clarifying the ambiguity between regulatory labeling and clinical decision-making, Part 1: PCI. Catheterization and Cardiovascular Interventions. 2008;72(4):500–504.
15. FDA. "Off-Label" and Investigational Use Of Marketed Drugs, Biologics, and Medical Devices - Information Sheet. https://www.fda.gov/RegulatoryInformation/Guidances/ucm126486.htm.

One Pulsatile Heart Pump Size Does Not Fit All Patients

David Macku and Iva Novotna

Abstract

One of the main principles of personalized medicine is to adapt health care to the specific needs of our patients. Based on this principle, medical devices should be tailored to the specific characteristics of the patients and doctors should choose medical devices for patients according to their size. Both pulsatile and continuous flow ventricular assist device help patients with heart failure. Every left ventricular assist device usually contains a pump that a cardiac surgeon connects to the apex of the heart. Pulsatile ventricular assist device systems using volume displacement pulsatile pumps are designed and mainly used for children patients. The first generation ventricular assist devices systems for adult patients relied on volume displacement pumps with one constant stroke volume for all sizes of patients. The concept of one size of the medical device for all patients goes against the principle of personalized medicine. A cardiovascular model in Modelica has confirmed that a pump with one constant pump stroke volume of 65 ml can generate uncontrolled flow and pressure curves oscillating over the normotensive zone for small patients and under the normotensive zone for large patients. The one pulsatile pump size for all patients may cause harm due to non-physiological flow and pressure condition in circulations.

D. Macku (✉) · I. Novotna
Czech Technical University in Prague, Technicka 2, 16627
Prague, Czech Republic
e-mail: davidmacku@yahoo.com

1 Introduction

1.1 Mismatch

The term of personalized medicine is broadly understood. Institutions, Associations, councils, and coalition explain this term different ways [1]. President's Council of Advisors on Science and Technology describes the term as "the tailoring of medical treatment to the individual characteristics of each patient". When treating patients with drugs, the drug effectiveness depends on the drug dosage that doctors administer according to the size of the patient. The size of a patient can be expressed as BSA (body surface area) or as weight. Pharmacology prefers to express the size of the patients in weight. Small doses are administered for small-sized patients, medium doses are administered for middle-sized patients, and large doses are administered for large-sized patients. Those who get a lower dose of the drug do not benefit from the treatment, conversely patients who get a higher dose than they need, can be harmed due to the toxic effect of the drug. When treating patients with implantable medical devices, the situation is similar. The size of the patient should play a crucial role in the appropriate selection of a device. When we implant a small mechanical aortal valve in a large patient, we cause him harm. A properly functioning small mechanical valve in a large-sized patient is insufficient, and the clinical view of such a patient will mitigate the patient with a stenotic native aortal valve. Cardiac surgeons always have to calculate the size of a mechanical valve according to the size of the patient. The inappropriate ratio is called a mismatch. The large mechanical aortic valve cannot be inserted in the small patient because of the small diameter of the aorta and their aortic root. This cardiac operation cannot be physically performed. Therefore, all manufacturers produce aortic mechanical valves in several sizes to meet the needs of cardiac surgeons and their patients. In everyday life, we purchase shoes according to their size. The mismatch is

when a shoe s tight—the shoe is smaller than your foot or when your foot is loose—the shoe is bigger than your foot.

1.2 Volume Displacement Pulsatile Pumps

Left ventricular assist device (LVAD) contains a mechanical blood pump that is used to support heart function and blood flow in people who have diseased hearts. It helps the left ventricle pumps blood to the aorta. The aorta is the main artery that carries oxygen-rich blood from your heart to your body. Continuous blood pumps are the most used type of pumps that are now implanted in adult patients worldwide. That is primarily for safety reasons which has been verified by clinical studies [2]. The first generation of blood pumps for adult patients were the so called volume displacement pumps; they contained an elastomer sack with valves able to produce pulsatile blood flow. Pressure and vacuum between the hard shell of the pump and the sack cause sucking and expelling of blood out of the chamber of the pump. The Thoratec Company produced VAD pumps with only one size of the pump's chamber for an adult patient (65 ml) [3] (Fig. 1).

The Berlin Heart company produced and still produces pumps with different sizes of pumps' chambers, which are available for pediatric patients. The appropriate size of the pump is chosen according to the weight of a child patient [3]. The key question remains as to whether it is appropriate to use the one-size of pump chamber for all adult patients with their different sizes. For a volume displacement pump (used as a left VAD) with one constant chamber and thus with one stroke volume, the manufacturer recommends in its instructions to operate the pump in automatic mode. That means the mode of complete filling and complete emptying of the pump chamber. For instance, when the pump chamber has a volume of 65 ml and the blood in it should be expelled in the time of 300 ms, such pump creates the same average blood flow in all sized patients and namely 13 l/min. Each healthy person is unique, each with different weight and

length, with various parameters for their aortas (length and width), having a different stroke heart volume. The average blood flow per ejection must also vary. We know that different sizes of vascular beds are dimensioned for different sizes of stroke volumes, and produce the same characteristic pressure curve shape with a pressure maximum of 120 mm Hg and a pressure minimum of 80 mm Hg.

1.3 Hypothesis

We state the hypothesis, in which different sizes of vascular beds can react differently when native human hearts are replaced by one artificial pulsatile pump with a one size of the pump chamber (Fig. 2).

1.4 Modeling

In the diploma thesis [4] and in the article [5], we wanted to show how the unadapted circulation would react to an installation of different sized pumps. We created three sizes of human circulations in the model. The first one was a small-sized patient, for which a stroke volume of 30 ml was used in his circulation. The second one was normal-sized patient, for which a stroke volume of 65 ml was used in his circulation, and the third one was large-sized patient, which a stroke volume of 100 ml was used in his circulation. Three artificial pumps with different sized chambers were tested in the model. The first pump ejected a stroke volume of 30 ml, the second one ejected a stroke volume of 65 ml, and the third one ejected a stroke volume of 100 ml. In the article [5], we present the experiment for a patient for which a stroke volume of 65 was used with hypothetic volume displacement pump with the stroke volume of 100 ml. In this experiment we have observed how the pressure and flow patterns change when employing pump with the maximal stroke volume of 100 ml, which is fully filled and emptied in each cycle. As the pressure curve exceeds the limit of

Fig. 1 Volume displacement pumps for children and adults
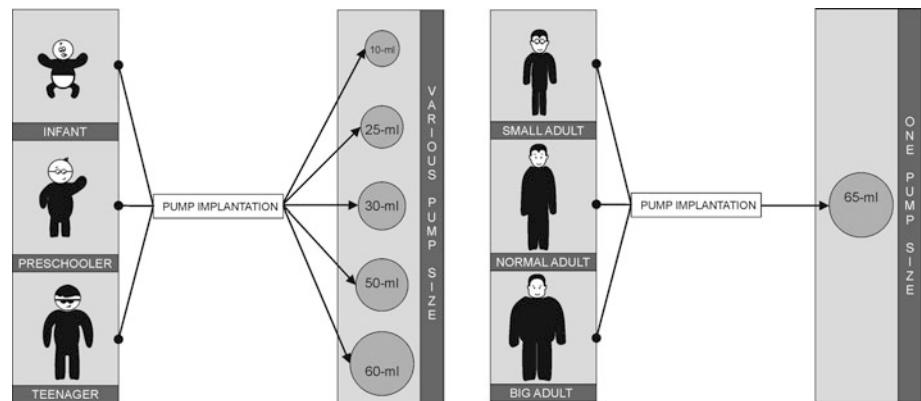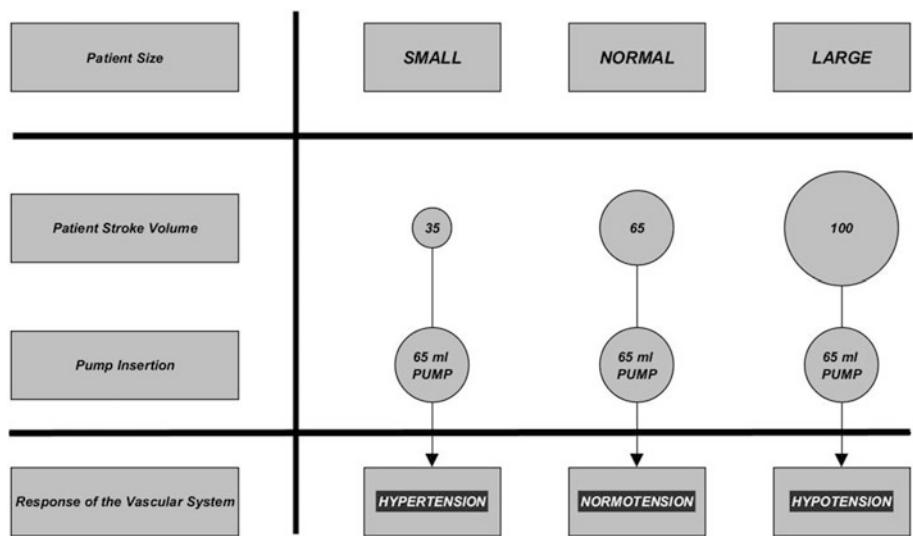
Fig. 2 Hypothesis of the volume displacement pump-patient mismatch in small and large-sized patients: the insertion of 65 ml pump in small-sized patients causes hypertension, the insertion of 65 ml pump in large-sized patients causes hypotension

hypertension (140 mm Hg), the experiment proves that using a pulsatile pump with full-fill/full-eject mode could be highly non-physiological for patients with the body size which is used to lower stroke volumes. We use the model implemented in Modelica language.

2 Discussion

The VAD pulsatile pumps belong to the implantable medical devices. The PMC principles speaks of "the tailoring of medical treatment to the individual characteristics of each patient". The size of the patient as well as their genome is unique. Therefore, therapy with medical devices should also be tailored to their individual needs—to their size. We know a good number of implantable medical devices, which respect the PMC principles: the mechanical valves are selected according to the diameter of the annulus, coronary stents are selected according to the diameter of vessels, and pulsatile Berlin Heart pumps are selected according to the weight of the child patient. This article aims to highlight the possibility of different behavior when using single size of the pulsatile pump for different sizes of human bodies. We submit evidence, in the first stage of the experimentation—modeling and simulation, the occurrence of atypical pressure behavior in the various sizes of the human blood stream. Our results very clearly show that after model calibration on specific stroke volumes, the model depicts an atypical pressure waveform in the hypertensive zone for small sized patients and the hypotension zone for large-sized patients. Long-term utilization of a relatively large VAD pump in small sized patients and having them in the hypertensive zone, as well as the long-term utilization of a relatively small VAD pump in large-sized patients and having them in the hypotensive zone, can cause VAD functioning with lower

safety for patients. We can conclude that having just one type of pump with one stroke volume cannot generate the same pressure response in different sized patients.

The correlation between the body size of children patients and the incidence of adverse complications is mentioned in the journal [6]. The relationship between the incidence of adverse events and possible systemic hypertension and hypotension caused by LVAD cannot be confirmed due to the absence of clinical trials. We are fully aware that the dominant type of VAD pump used in cardiac centers for adult patients is now continuous non-pulse pumps. However, the issue of volume displacement VAD pumps with a single constant stroke volume has not yet been dealt with in depth. It appears that pulsatility in the human body is necessary. Reflecting this fact, manufacturers have started to design and produce continuous pumps that can generate an artificial pulse wave by changing the pump speed rate (for example Heartmate III—Thoratec Corporation, St Jude Medical). We assume that the demand for pumps making artificial and controlled pulse waves in our patients will be permanent, so the development of innovative VAD pumps can again be in line with the "volume displacement pumps." These VAD pumps would regulate their stroke volumes according to the patient's size, to the extent of heart failure, to the actual patients' needs. Such assistance systems would react to changes in blood pressure and flow in systemic circulation based on the data gained from pressure and flow sensors placed into patients' vascular beds. Applying one constant pump chamber in different sized patients, the physician should always be aware of possible unexpected events. Inserting a VAD pump with one constant stroke volume in small or large patients is very similar to replacing an unfitting artificial heart valve prosthesis in the patient. We can call it "pump—patient mismatch." For confirmation that the hypothesis about the correlation between pump-patients

mismatch and the extent of adverse events is right, it is necessary to access the clinical information data basis of patients supported by an LVAD pump with a single constant stroke volume.

We are aware that our article is lacking a detailed description of one model for each of three patient sizes of circulation. The real data gained from the simulation is also not mentioned in this article. But modeling and simulation is not the main goal of this article. The article is about patient safety. The model description and results of the simulation were published in our previous work.

3 Conclusion

Each of the patients coming to the cardiac center is unique, which means having various weights and lengths, in various stages of heart failure, having a different extent of vascular impairment. Our model confirmed that a volume displacement pulsatile LVAD pump with one constant pump stroke volume (65 ml) could generate uncontrolled pressure curves oscillating in the hypotensive zone for large patients and the hypertensive zone for small patients. Such a non-physiological status might be associated with a higher incidence of adverse complications in these patients. It is good to perceive principles of personalized medicine as tools for proper selection of the sizes of medical devices for our patients and prevent adverse events in these patients. The clinical practice and recommendations for how to treat different patients with different pulsatile pumps have been very well developed for children. The first generation of pulsatile pumps for adults had not taken into account the size of

patient, and thus a mismatch between the patient's size and the pump's size might occur in patients.

References

1. US food and drug administration. Paving the Way for Personalized Medicine, http://www.fda.gov/downloads/scienceresearch/specialtopics/personalizedmedicine/ucm372421.pdf, last accessed 2017/12/12.
2. Slaughter, M. S., Rogers, J. G., Milano, C. A., Russell, S. D., Conte, J. V., Feldman, D., Sun, B, Tatooles, T.C., Degado, R.M., Long, J. W., Wozniak, T. C., Ghummna, W., Farrar, D.J., Frazie, O.H. Advanced heart failure treated with continuous-flow left ventricular assist device. New England Journal of Medicine, 361(23), 2241–2251 (2009).
3. Fuhrman, B. P., Zimmerman, J. J: Pediatric critical care. Elsevier Health Sciences, 315 (2011).
4. Ježek, F.: Simulation of flow and pressure pattern in patients with different body size supported by pulsatle ventricular assist device. Master's thesis. CTU in Prague, http://cyberold.felk.cvut.cz/research/theses/papers/117.pdf, last accessed 2017/12/12.
5. Ježek, F., Privitzer, P., Mateják, M., Macků,,D.: Demonstration of the Risk of Fixed Ejection Volume in Ventricular Assist Devices in Small Patients Using Web Simulator. In 5th European Conference of the International Federation for Medical and Biological Engineering, pp. 489–49. Springer Berlin Heidelberg (2011).
6. Miera, O., Schmitt, K. R., Delmo-Walter, E., Ovroutski, S., Hetzer, R., Berger, F.: Pump size of Berlin Heart EXCOR pediatric device influences clinical outcome in children. The Journal of Heart and Lung Transplantation, 33(8), 816–821 (2014).

Effect of Weight Input in Magnetic Resonance Imaging System on Radio-Frequency-Induced Heating of Metallic Implants

Atsushi Ono, Shinichi Arao, Satoru Takata, Tatsuhiro Gotanda, Rumi Gotanda, and Akihiko Tabuchi

Abstract

Radio-frequency-(RF)-induced heating in clinical magnetic resonance imaging (MRI) may pose risks to patients with metallic implants. The specific absorption rate (SAR), a representative index for the estimation of a temperature increase, may be influenced by the weight input in the MR system. We investigate the RF-induced heating of implants as a function of the weight input in the MRI system. The employed measurement method for the implant heating conformed to the American Society for Testing and Materials (ASTM) F2182-11a criteria. Two different implants (titanium-alloy humeral nail and stainless-steel shaft) were analyzed. All experiments were performed using a clinical 1.5-T MR system. MRI was performed using a transmit/receive radio-frequency body coil at a whole-body average SAR of 2.0 W/kg for 15 min. The weight input in the system was in the range of 10–200 kg. Temperature measurements of the implant tip were performed using a fiber optic thermometer system. For a weight of 60 kg, the highest temperature changes for the humeral nail and stainless-steel shaft were 3.9 °C and 5.9 °C, respectively, while for a weight of 200 kg, the highest temperature changes were 9.9 °C and 12.4 °C, respectively. The highest temperature change increased with the weight in the range of 10–140 kg. These findings suggest that even at a permissible SAR level, there are potential risks of RF heating on patients with implants, owing to the large input weight in the MRI system.

1 Introduction

In magnetic resonance imaging (MRI), the heating caused by absorbed radio-frequency (RF) energy poses risks to the imaged biologic tissues. In particular, the concerns related to the RF-induced heating increase when conductive implants are present in the body [1]. Specific absorption rate (SAR) is a representative index employed to estimate the temperature increase, defined as the power absorbed per unit mass of tissue; it is expressed in watts per kilogram (W/kg). For patient safety, the international safety standards defined by the International Electrotechnical Commission (IEC) strictly limit the SAR [2]. The MR imager estimates the SAR when pulse sequences are prescribed to patients. The SAR predictions may be based on previously acquired measurement data [3]. Depending on the SAR, the weight input in an MR device could have a significant influence on the heating of the implant. We investigate the RF-induced heating of implants, as a function of the weight input in the MRI system.

2 Materials and Methods

In vitro implant heating measurements were performed according to the American Society for Testing and Materials (ASTM) F2182-11a criteria [4]. A plastic phantom container was employed, with a depth of 12 cm, length of 60 cm, and width of 36 cm. The phantom was filled with saline and gelling agent [hydroxyethyl cellulose (HEC)] to simulate the electrical and thermal properties of tissues in the body (Fig. 1).

A. Ono (✉) · T. Gotanda · R. Gotanda
Kawasaki University of Medical Welfare, Kurashiki, Okayama, Japan
e-mail: a_ono@mw.kawasaki-m.ac.jp

S. Arao · A. Tabuchi
Kawasaki College of Allied Health Professions, Kurashiki, Okayama, Japan

S. Takata
Kousei Hospital, Okayama, Okayama, Japan

Fig. 1 Dimensions of the phantom material (gelled saline) placed in a plastic phantom container. **a** Top and **b** side views
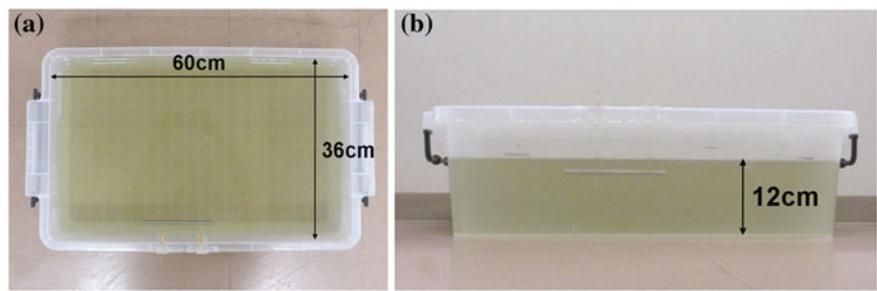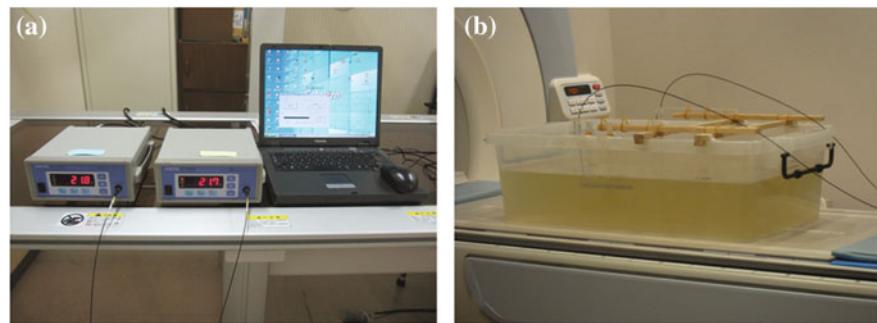
Fig. 2 RF-induced heating test system. **a** Two fiber-optic thermometers. **b** Positions of the phantom and temperature probes

A shaft implant (length: 15 cm, diameter: 8 mm) made of SUS316L stainless-steel and 24-cm humeral nail implant made of Ti-6Al-4V titanium-alloy were selected for testing. The implant was mounted on a plastic frame parallel to the static magnetic field, and placed 2 cm away from the gel surface and wall of the container. All experiments were performed using a clinical 1.5-T MR system (EXCELART Vantage powered by Atlas; Toshiba, Tokyo, Japan). MRI was performed using a transmit/receive RF body coil at a whole-body average SAR of 2.0 W/kg for 15 min. In order to achieve a relatively high exposure to the RF power, the fast spin echo sequence was employed. The other scan parameters were: scan plane: coronal, echo time: 80 ms, repetition time: 1,204–12,723 ms, field of view: 42 cm, slice thickness: 3.2 mm, matrix: 256 × 256, number of excitations: 20–30, number of slices: 22, number of echoes: 160, echo train space: 5 ms, and bandwidth: 651 Hz. For the assessment of the RF-induced heating of the stainless-steel implant, the value of the weight entered in the system was varied in the range of 10–200 kg. In each scan, the RF power and repetition time of the sequence, which depended on the input weight, were recorded. For the assessment with the titanium-alloy humeral nail, the weight inputs in the system were 60 and 200 kg. Two fiber-optic thermometers (FL-2000; Anritsu Keiki Inc, Tokyo, Japan) were employed for the temperature measurements (Fig. 2a), composed of optical fibers with a length of 10 m, which do not exhibit a considerable influence from the magnetic field and RF irradiation. The fiber-optic system had a resolution of 0.1 °C, and it was set to operate at a rate of one sample per second. The background noise was ±0.1 °C. The phantom was placed at the center of the static magnetic field, and the tip of the implant was placed at the center of B_0 (Fig. 2b).

In order to record representative temperatures, the terminal portion of the temperature probe was positioned on the tip of the implant. In addition, the fiber-optic thermometer probe was placed in the gel at the opposite side of the phantom to record a reference temperature. The highest temperature changes recorded by the fiber-optic thermometer probes are reported.

3 Results

For the assessment of the RF-induced heating of the stainless-steel implant, the temperature changes of the implant's tip during the 15-min RF irradiation were recorded, as shown in Fig. 3a, for weight values of 30, 60, and 200 kg entered in the system. The highest measured temperature changes of the implant were 3.0, 6.0, and 12.4 °C, respectively. Under the same conditions, the changes in the reference temperature during the 15-min RF irradiation are shown in Fig. 3b. The highest reference temperature changes at the input weights of 30, 60, and 200 kg were 0.6, 1.2, and 2.5 °C, respectively.

For the measurements with input weight values in the range of 10–200 kg, the maximum temperature increase of the implant's tip and reference position are shown in Fig. 4. The highest temperature change of the implant's tip increased from 1.3 to 12.4 °C with the increase of the weight from 10 to 140 kg. On the other hand, in the weight range of 140–200 kg, the highest temperature change was constant.

Fig. 3 Temperature changes of the implant (**a**) and reference position (**b**) during the 15-min RF irradiation for input weights of 30, 60, and 200 kg
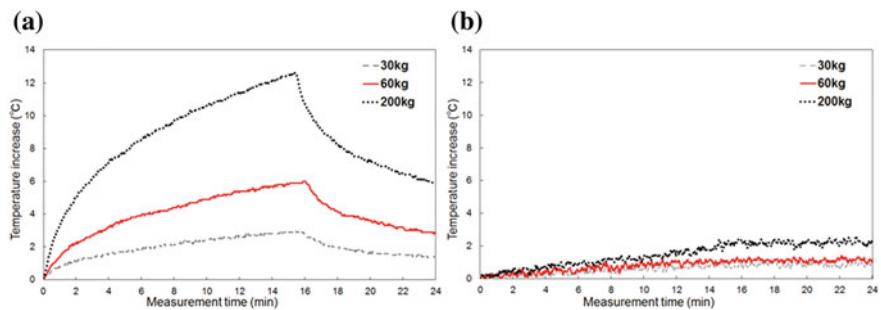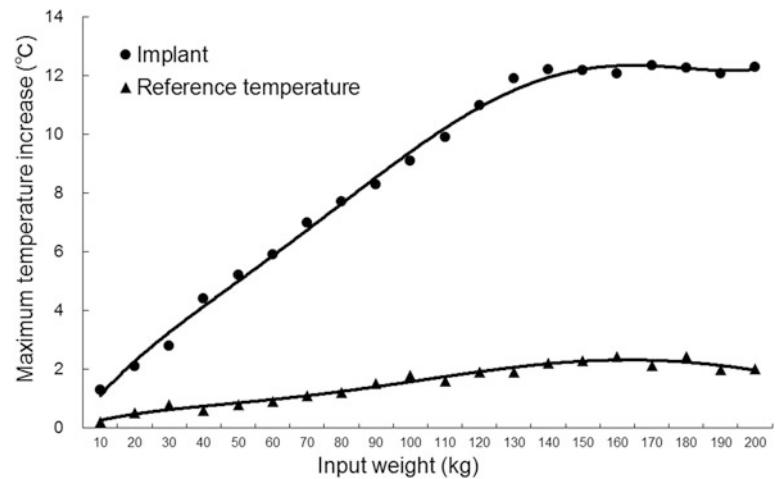
Fig. 4 Dependence of the highest temperature change of the implant as a function of the input weight in the range of 10–200 kg

The values of the RF power and repetition time of the sequence, depended on the input weight. With the increase of the input weight from 10 to 140 kg, the repetition time of the sequence decreased, whereas the RF power was stable. In the input weight range of 140–200 kg, both repetition time and RF power were stable.

In the assessment of the titanium-alloy humeral nail, the temperature changes of the implant's tip during the 15-min RF irradiation were 3.9 °C and 9.9 °C for input weights of 60 kg and 200 kg, respectively (Fig. 5).
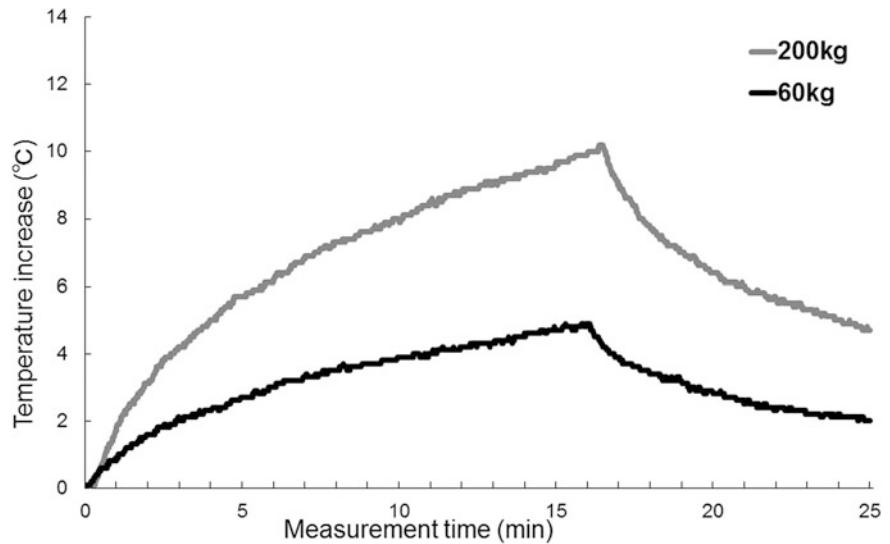
4 Discussion

Using a whole-body SAR of 2.0 W/kg at 1.5 T, when the stainless-steel implant was placed in the "worst-case" position in the phantom filled with gelled saline, a good linear relationship was observed between the highest temperature change and input weight in the range of 10–140 kg. The increase in the highest temperature change of the implant with the input weight corresponded to a decrease in the repetition time of the scan sequence. In contrast, the RF power was constant, unaffected by the changes in the input weight. The small repetition time of the scan sequence

allows to increase the duty cycle of the RF pulses, which leads to mass eddy currents on the surface of the conductive implant. For input weights larger than 140 kg, the lower limit of the repetition time of the scan sequence led to the constant temperature increase. However, this limitation may be influenced by the variations of the scan sequence and/or parameters. The algorithm employed to estimate the whole-body SAR, displayed on the MR console, depends on the body modelling and combination of hardware- and software-related factors [5]; it is not accessible to the user. The SAR could be estimated using calorimetric and pulse energy methods. In general, the MR scanner's computer adds up the energies of all RF pulses in the sequence, divides by the pulse repetition time to obtain the value of the power and divides by the patient weight to obtain the whole-body SAR [4]. Therefore, a large input weight could allow a decrease of the repetition time, leading to a large energy of the RF pulse.

Several factors affect the level of the RF-induced heating of the implant, including the SAR rate, patient position in the coil, type of scan sequence, patient characteristics, duration of scan procedure, type and position of the transmit coil, implant design, implant orientation in the patient, degree of perfusion near the device, temperature measurement

Fig. 5 Temperature changes of the tip of the titanium-alloy humeral nail during the 15-min RF irradiation, for input weights of 60 and 200 kg

procedure, etc. [6, 7]. However, the weight input in the MR system has not been recognized as a factor for the RF-induced heating of a conductive device.

It is worth noting that the whole-body SAR of 2.0 W/kg, considered in this study, is the upper limit of the normal operation mode defined by the IEC [2]. Moreover, the two tested implants were different in terms of material and shape; neither of the implants had an elongated shape such as those of leads and wires. The IEC guidelines for RF exposure recommend local temperature increase limits of 1–2 °C in any 10 g of tissue. Even at the weight value of 60 kg, the temperature increases of the humeral nail and stainless-steel shaft implants after 15 min of MRI could exceed the above permitted limit. In addition, our results indicate that the increase of the input weight may lead to a local temperature increase, and possibility of thermal damage (worst-case) in clinical MRI. Further investigations including laboratory animals are required to clarify clinical applicability of our findings.

5   Conclusion

This study demonstrated that even if SAR is within the limit of the normal operation mode defined by the IEC, patients with active and device implants are exposed to a potential risk of RF-induced heating, which depends on the weight input in the MRI. For larger weights in the MR system, the risks of RF-induced heating of the implants should be carefully considered.

References

1. Shellock, F. G., Shellock V. J.: Cardiovascular catheters and accessories: ex vivo testing of ferromagnetism, heating, and artifacts associated with MRI. Journal of Magnetic Resonance Imaging 8(6), 1338–42 (1998).
2. International Electrotechnical Commission.: International standard, medical equipment - IEC 60601-2-33: Particular requirements for the safety of magnetic resonance equipment for medical diagnosis. 3rd ed. International Electrotechnical Commission, Geneva, Switzerland (2010).
3. National Electrical Manufacturers Association.: NEMA Standards Publication MS 8 – 2016: Characterization of the Specific Absorption Rate for Magnetic Resonance Imaging Systems. National Electrical Manufacturers Association, Rosslyn, Virginia, USA (2016).
4. American Society for Testing and Materials (ASTM) International.: ASTM F2182-11a: standard test method for measurement of radio frequency induced heating near passive implants during magnetic resonance imaging. ASTM International, West Conshohocken, Pennsylvania, USA (2011).
5. Baker, K. B., Tkach, J. A., Nyenhuis, J. A., Phillips, M., Shellock, F.G., Gonzalez-Martinez, J., Rezai, A. R.: Evaluation of specific absorption rate as a dosimeter of MRI-related implant heating. Journal of Magnetic Resonance Imaging 20(2), 315–20 (2004).
6. Muranaka, H., Horiguchi, T., Usui, S., Ueda, Y., Nakamura, O., Ikeda, F., Iwakura, K., Nakaya, G.: Evaluation of RF heating on humerus implant in phantoms during 1.5T MR imaging and comparisons with electromagnetic simulation. Magnetic Resonance in Medical Sciences 5(2), 79–88 (2006).
7. Mattei, E., Triventi, M., Calcagnini, G., Censi, F., Kainz, W., Mendoza, G., Bassen, H. I., Bartolini, P.: Complexity of MRI induced heating on metallic leads: experimental measurements of 374 configurations. BioMedical Engineering OnLine 7(11) (2008).

An Ergonomic Evaluation of Physical and Mental Loads in Standing-up Motion from Forward-Sloping Toilet Seats

Shuichi Ino, Manabu Chikai, Emi Ozawa, and Hiroshi Endo

Abstract

We aim to develop a new in-home assistance system to aid in the standing-up motion from toilet seats in assisted bathrooms. The underlying design concept for accessible toilet facilities is to use a novel compact actuation device —a metal hydride actuator with several unique properties such as softness, noiselessness, and being lightweight— for tilting a toilet seat when required, thus helping elderly or frail people to stand-up after excretion. This ergonomic study evaluates the easiness of the standing-up motion using both objective and subjective data from healthy participants, as a prior step before developing the envisaged toilet seat tilting system. In the experiment, the participants were monitored to obtain simultaneous objective data concerning muscle activity, 3D body motion, center of pressure, and seat pressure distribution. Additionally, all participants were requested to provide subjective data (comfort scores) while standing up from a toilet seat under four different conditions—four different forward-tilting angles ($0°$, $5°$, $10°$, and $15°$). All participants repeated the motion 25 times for each tilting angle, and provided feedback regarding their standing-up experience and feelings under each condition. According to the collected subjective data, a toilet seat tilt angle of approximately $10°$ increased the easiness and comfort of the standing-up motion. However, according to the measured objective data, the standing-up motion has individual variations in the electromyogram magnitude, center of pressure excursion, and seat pressure pattern, implying that to analyze the standing-up motion both the measured objective data and the perceived subjective data must be considered.

1 Introduction

In recent years, the number of slip and fall accidents during walking or movement of elderly people has been increasing [1, 2]. Slip and fall during bathroom use accounted for over 40% of the total number of accidents; these accidents occur not only during walking and transfer, but also when attempting standing-up motions—for example, standing-up from a bathtub or a toilet seat. Consequently, it is necessary to develop assistance systems to support the standing-up motion from toilet seats.

In previous work, we discussed the development of a new assistance system to aid in the standing-up motion from toilet seats. The concept underlying the assistance system for accessible toilet facilities presented in relies on the use of an active toilet seat whose forward-sloping seat angle can be changed to aid the standing-up motion after excretion; the rear part of the toilet seat is vertically lifted by a soft metal hydride (MH) actuator [3], as shown in Fig. 1, thus helping to mitigate the physical and mental loads for physically vulnerable people when standing up.

As a prior step before developing a toilet seat tilting system for accessible toilet facilities, this pilot study collected ergonomic data from healthy participants to analyze the relationship between the collected objective and subjective data, and the effect of the toilet seat angle on the standing-up motion performance.

S. Ino (✉) · M. Chikai · E. Ozawa · H. Endo
National Institute of Advanced Industrial Science and Technology
(AIST), Tsukuba, Japan
e-mail: s-ino@aist.go.jp

E. Ozawa
Showa-Inan General Hospital, Komagane, Japan
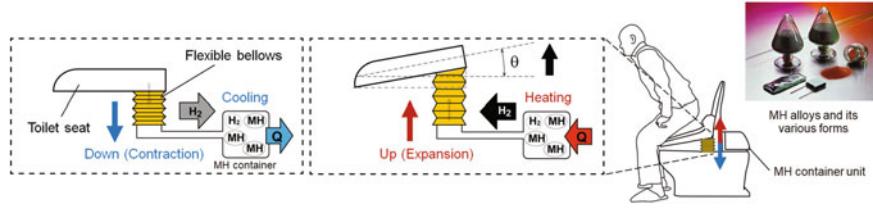
Fig. 1 Concept of a toilet seat tilting system using a soft metal hydride (MH) actuator

2 Materials and Methods

2.1 Participants

Five healthy participants (three men and two women) with an age distribution of 46.6 ± 11.5 year were monitored while using a portable toilet with a variable slope angle seat, as shown in Fig. 2. The body height and weight distributions of the participants were 165.4 ± 7.0 cm and 58.0 ± 6.7 kg, respectively. The protocol was approved by the Institutional Review Board of the National Institute of Advanced Industrial Science and Technology, and all participants provided informed consent.

2.2 Measuring System
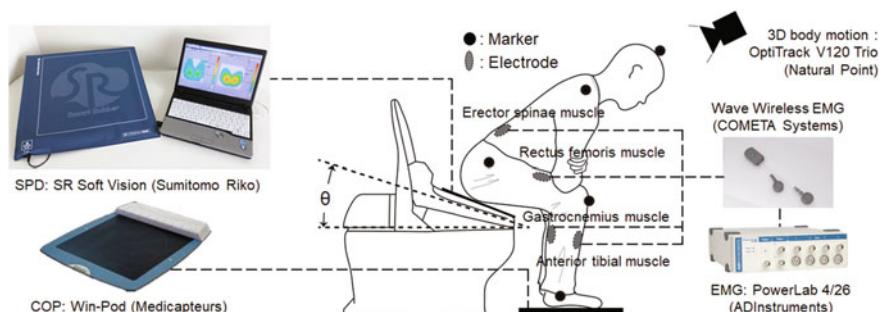
The muscle activity of each participant was measured using a portable wireless Electromyogram (EMG) device and an analog to digital converter with disposable electrodes attached to the skin above the erector spinae muscle, rectus femoris muscle, anterior tibial muscle, and gastrocnemius muscle on the right half of the body, as shown in Fig. 2. The EMG device collected data at 1,000 Hz. The body motion was measured using a 3D optical motion capture system. Five markers were attached to the skin above the head, acromion, iliac crest, caput fibulae, and lateral malleolus on the right half of the body, as shown in Fig. 2. The motion capture system collected data at 120 Hz. The center of pressure (COP) and the foot pressure distribution were measured using a pressure sensor platform. The COP data were collected at 100 Hz. The seat pressure distribution (SPD) was measured using a flexible pressure sensor seat. The sensor seat collected data at 5 Hz. Finally, after these experiments, all participants recalled concerning the comfort score (perceived easiness or difficulty) of the motion for each seat angle, in a five-point scale questionnaire.

2.3 Procedure

A portable toilet was used in this study; the toilet seat angle θ was changed from 0° to 15°, in 5° steps. In the experiments, the height from the floor to the top of the toilet seat was individually established for each participant, to reduce the bias of the body habitus and sitting position characteristics. This height was determined by the individual lower leg length to obtain a similar sitting leg position: for a seat angle of 0°, the angles between the thigh and lower leg, and between the lower leg and foot were set to 90°. During this experiment, the foot placement for the 0° seat angle was used as the reference for all participants. The standing-up motion procedure was outlined in a guide to all participants. They sat on the toilet seat with their hands crossed over their chest—which means that they could not use their hands while standing-up—and then performed the standing-up motion until they reached a standing position. They repeated the motion 25 times for each toilet seat angle. The statistical significance was determined by one-way ANOVA. A Tukey–Kramer test was used in the multiple comparison of the differences between the results at different toilet seat angles.

Fig. 2 Schematic diagram of the experimental setup for tilting a toilet seat
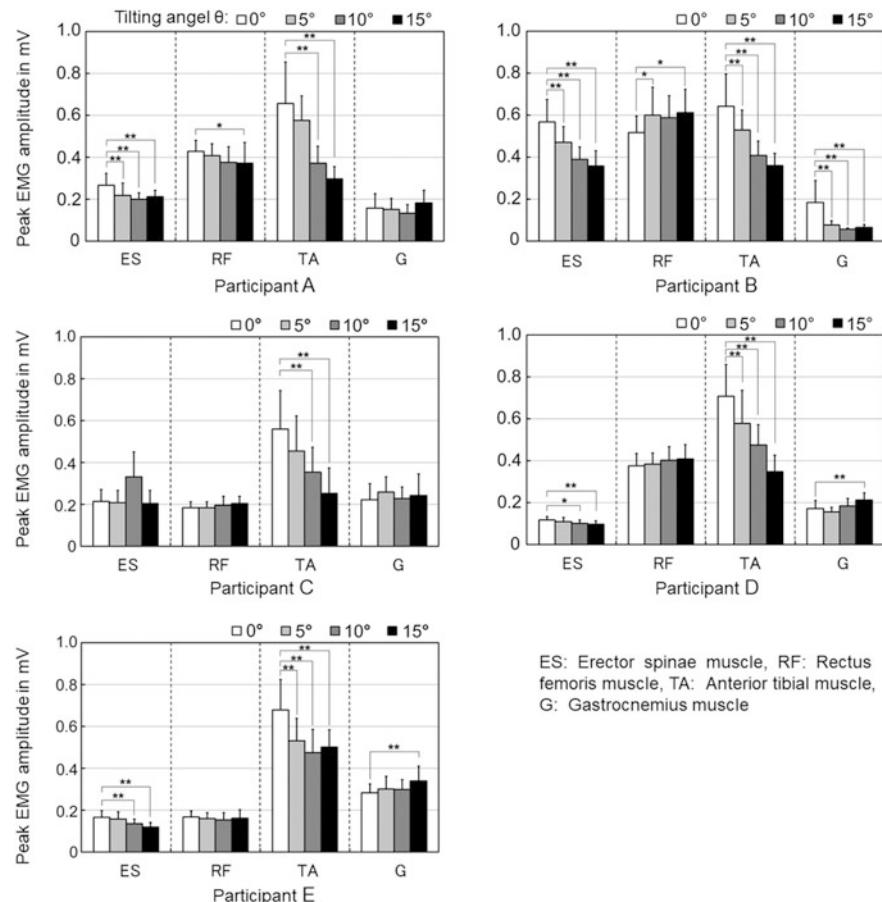
3   Results

3.1   EMG

The average peak EMG amplitude during the standing-up motion can be seen in Fig. 3. The ANOVA results statistically indicate that the muscle activity was indeed affected by the toilet seat angle, for all participants. The anterior tibial muscle activity decreased with higher seat angles, with statistically significant differences being observed between the 0° and higher (10° and 15°) seat angles ($p < 0.05$). For participants A, B, D, and E, the elector spinae muscle activity decreased with higher seat angles, with statistically significant differences observed between the 0° and 15° seat angles ($p < 0.01$). For participant A, the rectus femoris muscle activity decreased with a seat angle of 15°, and there were statistically significant differences between the 0° and 15° seat angles ($p < 0.05$). For participant B, however, the rectus femoris muscle activity increased with the 15° seat angle, with statistically significant differences between the 0° and 15° seat angles ($p < 0.0$). For the other participants (C, D, and E), the rectus femoris muscle activity remained unchanged.

3.2   COP

The average peak-to-peak COP displacement (Ds) in the sagittal plane during the standing motion can be seen in Fig. 4. The COP displacement tended to decrease for higher toilet seat angles for most participants, except for participant E. There were statistically significant differences between the 0° and higher (10° and 15°) seat angles for participants A and D ($p < 0.05$).

3.3   SPD

The area of SPD cells with seat pressure over 200 mm Hg (26.7 kPa), which is related with the risk of pressure ulcer formation, is shown in Fig. 5. The seat pressure at the position of the gluteus maximus muscle and/or the biceps femoris muscle increased for higher toilet seat angles. The high SPD cells (over 200 mm Hg) increased for higher toilet seat angles in the case of participants B, C, D, and E. Statistically significant differences were found between the 0° and 15° cases, and between the 5° and 15° cases ($p < 0.05$). In contrast, the high SPD cells decreased with higher toilet

Fig. 3 Peak EMG amplitude during the standing-up motion for the different toilet seat angles. Significant differences from the 0° seat angle are indicated by **$p < 0.01$; *$p < 0.05$

ES: Erector spinae muscle, RF: Rectus femoris muscle, TA: Anterior tibial muscle, G: Gastrocnemius muscle
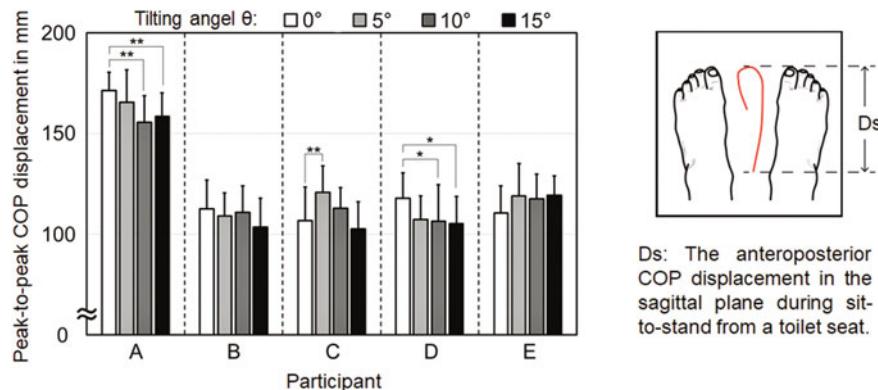
Fig. 4 Peak-to-peak COP displacement (Ds) during the standing-up motion from the toilet seat in sagittal plane. Significant differences from the 0° seat angle are indicated by $**p < 0.01$; $*p < 0.05$
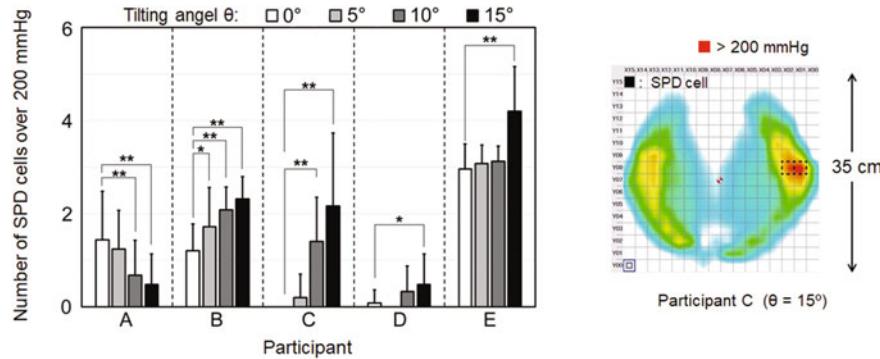
Fig. 5 The number of SPD cells with seat pressures over 200 mm Hg (left) and an example of SPD images observed for a 15° forward-sloping toilet seat in participant C (right). Significant differences from the 0° seat angle are indicated by $**p < 0.01$; $*p < 0.05$

seat angles for participant A; there were significant differences between the 0° and higher (10° and 15°) seat angles ($p < 0.05$).

3.4 Comfort Score

The data of comfort score regarding the standing-up motion were assessed at all tested angles of the toilet seat. All participants found that standing up was easy when the seat angle was 10°. Participants A, C, D, and E found it easier to stand with the 5° and 10° angles, whereas participant B preferred to stand with a toilet seat angle of 15°.

4 Discussion

The experimental results indicate that almost the subjects could stand-up easier, experiencing smaller physical loads, when the toilet seat was tilted at approximately 10° from the usual horizontal condition. The subjective data regarding the most comfortable seat angle was fairly stable in all subjects, the measured objective data showed some individual differences in EMG, COP, or SPD. Therefore, in the design of forward-sloping toilet seats for assisted bathrooms, it will be important to be prudent and not only estimate the objective data concerning physical loads through kinematic measurements, but also consider subjective data concerning the perceived mental and physical loads on various physically vulnerable people during the standing-up motion.

In future works, the easiness of the standing-up motion will be discussed in depth, considering the various involved characteristics such as the differences in ankle dorsiflexion and the body size. As a next step, we plan to measure the standing-up motion with elderly people; according to the obtained motion characteristics, the assistance system will then need to consider each individual and suggest the most suitable toilet seat angle for each case.

References

1. Hignett, S., Wolf, L.: Reducing inpatient falls: Human Factors & Ergonomics offers a novel solution by designing safety from the patients' perspective. International Journal of Nursing Studies, 59, A1–A3 (2016).

2. Ozawa, E., Chikai, M., Kobayashi, H., Miyazawa, H., Koizumi, N., Miyajima, T., Kitano, A., Ino, S.: Experimental Study on Physical Burden of Transfer Assistance for Excretion. Journal of Advanced Computational Intelligence and Intelligent Informatics, 21(2), 363–370 (2017).

3. Ino, S., Sato, M., Hosono, M., Izumi, T.: Development of a soft metal hydride actuator using a laminate bellows for rehabilitation systems. Sensors and Actuators B: Chemical, 136(1), 86–91 (2009).

Optimal Variable Refocus Flip Angle Control Method and Echo Train Length for Suppressing Exposure to Radio Frequency

Akihiko Tabuchi, Shinichi Arao, Toshizo Katsuda, Atsushi Ono, Tatsuhiro Gotanda, and Rumi Gotanda

Abstract

The popularization of 3-Tesla magnetic resonance imaging (MRI) has improved the quality of images and shortened typical examination times. However, a side effect of this is increased exposure to radio frequency (RF) radiation. The amount of RF exposure can be controlled using a technique called variable refocus flip angle (vRFA). Controlling vRFA is also an important for improving the signal to noise ratio (SNR) and for reducing blurring on MRI images. In this study, we examined the influence of controlling vRFA and echo train length (ETL) on SNR. To do this, we used a device that can arbitrarily control three angles—the fifth RFA, the RFA centered in k-space, and the final RFA. Using a phantom, T1 and T2 values were made equal to gray- and white-matter, respectively. The repetition time was 5000 ms and echo time 90 ms. By setting the fifth RFA to 40° and using an ETL of 11–15, the signal shifted smoothly to a pseudo steady-state (PSS), and a stable signal was obtained. Further, we were able to suppress blurring by gently changing the k-space-centered RFA. In the final echo, we were able to maintain PSS by increasing the final RFA up to 180°, resulting in a high SNR. Results of this study showed the changes reduced RF exposure. Using an ETL of 30, blurring was reduced, though RFA control was similar to that used with ETLs of 11–15; although slightly higher RF exposure was required to obtain a high SNR, the fifth RFA was required to be 60°–90°.

Keywords

Variable refocus flip angle • Pseudo steady-state Blurring

1 Introduction

In recent years, magnetic resonance (MR) imaging devices have emerged that can achieve a high signal to noise ratio (SNR) as the static field intensity becomes higher in the magnetic field. In addition, with the introduction of high-performance gradient magnetic field systems and high-speed imaging sequences, it has become possible to acquire images with high levels of spatial resolution. However, owing to MR systems that use high-intensity magnetic fields to perform high-speed imaging, exposure to radio frequency (RF) has become a problem [1]. In particular, 3D turbo spin echo imaging, which uses many refocusing flip angles, is associated with higher exposure to RF. In order to reduce patient's RF exposure, recently, a method using variable refocus flip angles (vRFA) and low-refocusing flip angles was developed [2, 3]. However, to date, there have been few studies testing vRFA for multi-slice two-dimensional turbo spin echo (2D TSE) imaging. The purpose of this study is to suppress RF exposure while maintaining T2 contrast and SNR equivalent to the conventional method by using vRFA in the brain image using the 2D-TSE method.

A. Tabuchi (✉)
Kawasaki Medical School General Medical Center, Okayama, Okayama, Japan
e-mail: a.tabuchi@hp.kawasaki-m.ac.jp

S. Arao
Kawasaki College of Allied Health Professions, Kurashiki, Okayama, Japan

T. Katsuda
Faculty of Health Sciences, Butsuryo College of Osaka, Sakai, Osaka, Japan

A. Tabuchi · A. Ono · T. Gotanda · R. Gotanda
Kawasaki University of Medical Welfare, Kurashiki, Okayama, Japan

2 Materials and Methods

2.1 MR System, Phantom and Sequence Parameter

All images shown in this article were obtained with a 3T MR scanner ('Ingenia 3.0CX'; Philips Medical Systems, Netherlands). In this system, the vRFA was controlled for with the following three points: (1) the 5th RFA, (2) the RFA of k-space center (center RFA), and (3) the final RFA. A 90-401 phantom made by Nikko Fines was used. Section with T1 and T2 values equivalent to white matter (WM) and gray matter (GM) (respectively) were used. The T1 · T2 values of WM and GM section were 930.4 ms · 78.0 ms, 1213.6 ms, 133.1 ms respectively. The parameters for the T2-weighted 2D turbo spin-echo were as follows: repetition time of 5,000 ms, equivalent echo time of 90 ms for one axial 5-mm thick slice with a 256-mm × 256-mm field of view. The matrix was 256 × 256.

2.2 Image Acquisition and Analysis

RF exposure, signal intensity change, contrast to noise ratio and blurring in each sweep pattern using ETL 15. First, phantom images were obtained using sweep patterns illustrated in Fig. 1 with an echo train length (ETL) of 15. The RF exposure was obtained from the B1+RMS values on the console in each pattern. SNR was calculated in WM section. B1+RMS, SNR was normalized using values obtained by setting the conventional RFA to 1. Finally, a profile curve was created for the edge portion of the phantom, and blurring was evaluated.

Signal intensity change by each sweep pattern when ETL was changed
Next, using the three sweep patterns (5th RFA—center RFA—final RFA: 40°–60°–180°, 60°–80°–180°, 90°–110°–180°) that had no blurring and the highest SNR values, we varied ETL between 11, 15, 19, 23, and 27, and acquired a corresponding image. From these images, the SNR of WM was calculated for each ETL. The SNR was normalized to a value of 1 using conventional RFA and compared with SNR of each ETL.

Change in signal intensity within k-space
One-dimensional imaging was acquired changes in signal intensity in the k-space in each of the patterns A, B, C when 5th RFA was set to 40°. Finally, one-dimensional imaging was acquired in each ETL, for discuss the signal intensity changes within the k-space in the pattern.

3 Results

RF exposure, signal intensity change and blurring in each sweep pattern using ETL 15.

Sweep pattern	a	b	c	a'	b'	c'
5th - K=0 - Final (RFA) (degree)	40° - 60° - 180°	40° - 110° - 180°	40° - 160° - 180°	40° - 60° - 140°	40° - 90° - 140°	40° - 120° - 140°
	60° - 80° - 180°	60° - 120° - 180°	60° - 160° - 180°	60° - 80° - 140°	60° - 100° - 140°	60° - 120° - 140°
	90° - 110° - 180°	90° - 135° - 180°	90° - 160° - 180°	90° - 100° - 140°	90° - 115° - 140°	90° - 130° - 140°
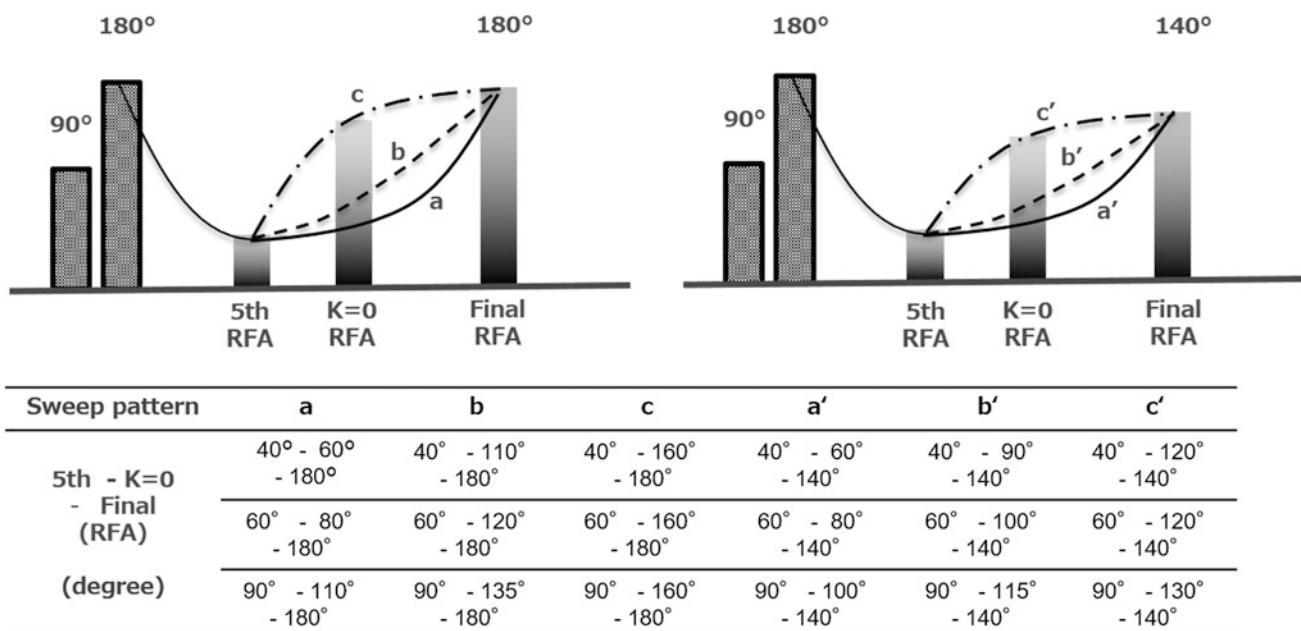
Fig. 1 Images were acquired by increasing RFA with the following three patterns with respect to the final RFA of 140° and 180°. Type A, A′: Slowly raised the 5th RFA—center RFA intervals, and steeply raised the center RFA—final RFA intervals. Type B, B′: slowly raised the 5th RFA—center RFA—final RFA intervals. Type C, C′: Steeply raised the 5th RFA—center RFA intervals, and slowly raised the center RFA—final RFA intervals
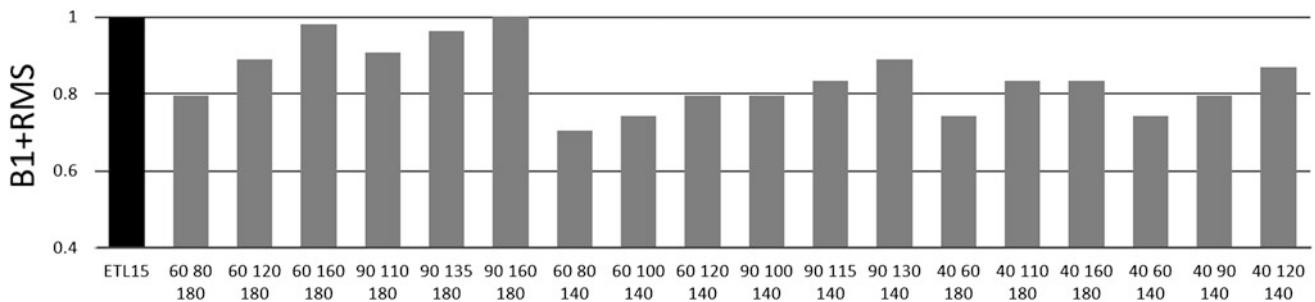
Fig. 2 The ratio of B1+RMS for each sweep pattern compared to conventional RFA
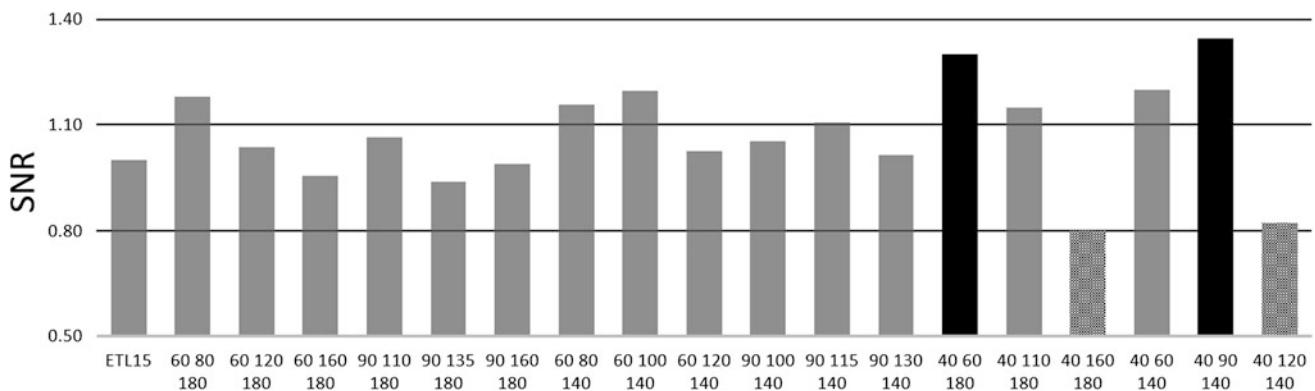
Fig. 3 SNRs for white matter for each sweep pattern compared to conventional RFA

Figure 2 shows value obtained by normalizing B1+RMS in each sweep pattern so that it was equal to 1 in conventional RFA. Results show that the smaller the RFA of the 5th and 7th (center of k-space) becomes, the smaller the value of B1+RMS becomes. In particular, we found that we were able to suppress B1+RMS the most using the 40°–60°–140°, 40°–60°–180°, 60°–80°–140° combinations.

Figure 3 shows the SNR of WM in each of the three sweep patterns normalized so that the SNR became 1 in the conventional RFA. In the B, B′ pattern, the combination of 40°–90°–140° provided the best SNR. By contrast, in C, C′ pattern, the 40°–160°–180° and 40°–120°–140° combinations showed the poorest SNR.

Figure 4 shows profiling curves for the edge portion of phantoms for each sweep pattern. In the A, A′, B and B′

patterns, edge portions overlap with all profile curves, meaning that there was no blurring. However, in C and C′ patterns, the edge portion was shifted away from the curve, indicating that there was blurring.

Signal intensity change by each sweep pattern when ETL was changed

Figure 5 shows values obtained by normalizing the SNR of WM in each ETL and sweep pattern so that the SNR of WM was equal to 1 in the conventional RFA. For ETL between 11 and 15, the SNR was significantly lower in all patterns than in conventional RFA. However, in ETL between 19 and 27, SNR was worse only when 5th RFA was set to 40°, and setting the 5th RFA 60° and 90° produced SNR equal to conventional RFA.
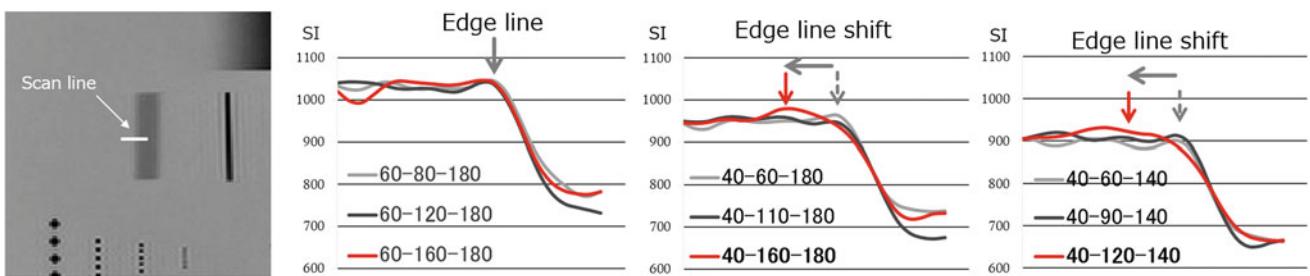
Fig. 4 The profiling curve of the edge portion of phantom of each sweep pattern
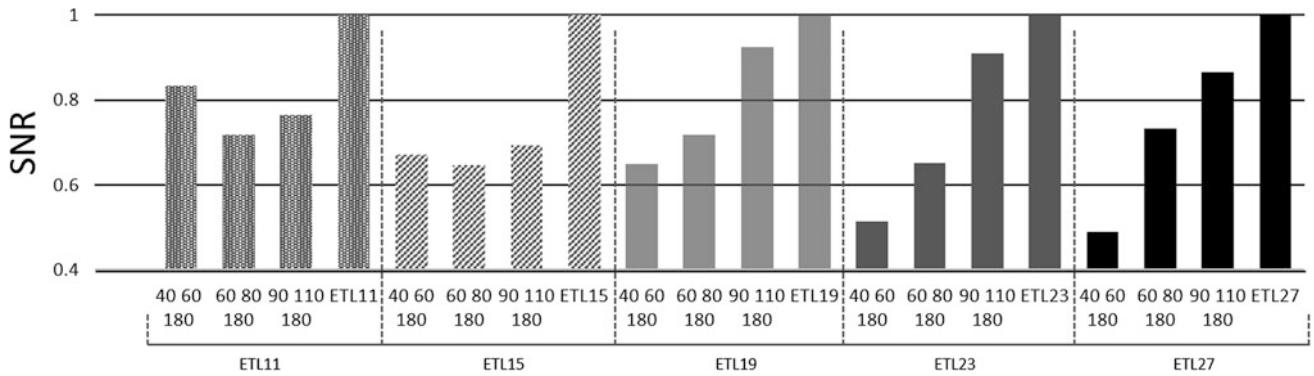
Fig. 5 SNRs of WM for each sweep pattern in each ETL compared to conventional RFA
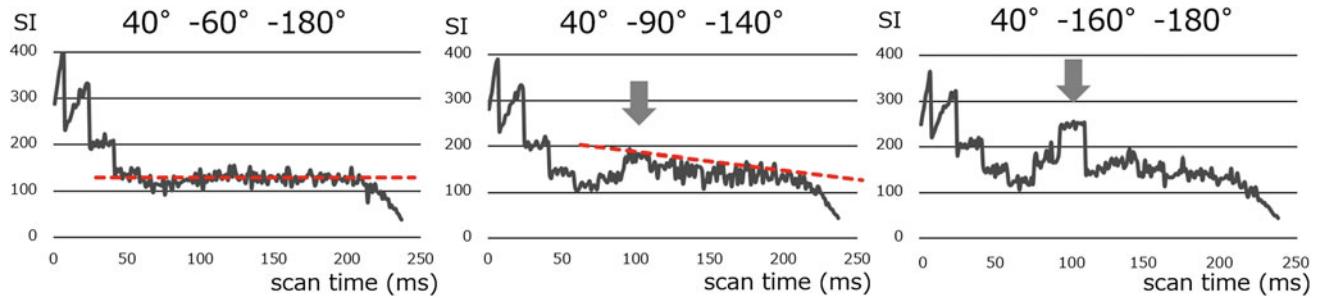
Fig. 6 1D imaging due to the difference in pattern of vRFA

Figure 6 shows 1D imaging due to a pattern of vRFA (A: 40°–60°–180°, B: 40°–90°–140°, C: 40°–160°–180°) when the 5th RFA is set to 40°. In sweep pattern A, the signal intensity did not decrease until the final echo. In sweep pattern B, a small increase in signal intensity was observed around the center of k-space, but intensity of the signal decreased at the final echo. In the sweep pattern for C, significant changes in signal intensity were observed around the center of k-space, although signal intensity fell at the final echo.

Figure 7 illustrates 1D imaging due to the difference in pattern of vRFA in ETL11 and 27. When the 5th RFA was set to 40° and the ETL was 11, results found that the signal intensity of the final echo increased. However, in ETL 27, the signal intensity at final echo decreased. By contrast, when the 5th RFA was 90°, the signal intensity of the final echo decreases with both ETL 11 and ETL 27, but overall, the signal intensity at ETL 27 tended to be higher.

4 Discussion

When the 5th RFA was set to 40° and the last RFA was set to 180°, it was possible to obtain a high SNR when sweep pattern A center RFA was 60°. In addition, when the 5th RFA was set to 40° and the last RFA was set to 140°, it was

possible to obtain a high SNR when sweep pattern B, center RFA was 90°.

In this study, the SNR for sweep patterns A (40°–60°–180°) and B (40°–90°–140°) were comparable. When 40°–90°–140°, the signal intensity in low frequency showed a slight increase, although the signal intensity of the final echoes was somewhat decreased. On the other hand, with 40°–60°–180°, we were able to maintain the signal intensity from low frequency until the last RFA (Fig. 6). The former suggests that the signal intensity increased in whole k-space, when the signal intensity becomes large in the low frequency. On the other hand, the latter suggests that raising the signal intensity during final echoes not only demonstrates conventional T2 relaxation, and maintains PSS [4], but by reducing residual transverse magnetization, we were able to significantly increase the signal intensity.

We observed considerable blurring in the C, C′ sweep pattern, when 40° was used for 5th RFA. This was especially true with the 40°–160°–180°, 40°–110°–180°, 40°–120°–140° configurations (Fig. 6). One explanation for this may have been that the change in signal intensity in the low frequency was large, and the signal was not able to maintain to high frequency, causing blurring [5].

We also found that in ETL 11, even if the 5th RFA was reduced to 40°, by setting the final RFA to 180°, we were able to raise the intensity of the final signal and maintain the
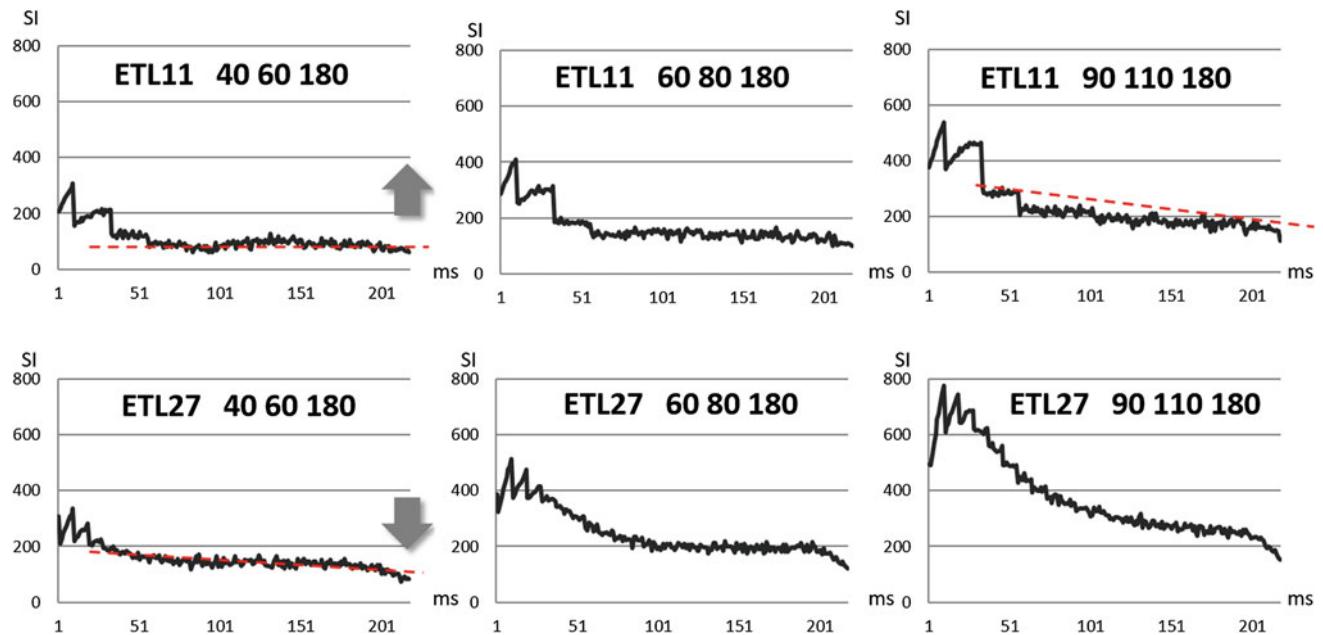
Fig. 7 1D imaging due to the difference in pattern of vRFA in ETL11 and 27

PSS. As a result, we were able to achieve a high SNR image and reduce RF exposure. However, it is considered that when ETL is 19 or more, T2 relaxation occurs between 5th RFA and center RFA (ETL9), which makes it difficult to maintain PSS. Therefore, although doing this does increase RF exposure slightly, our results indicate that a high SNR image can be obtained by setting the 5th RFA to 90°.

5 Conclusion

The purpose of this study was to optimize vRFA to reduce subject's exposure to RF on the premise of T2 contrast, SNR similar to TSE method in brain imaging using 2D TSE method. For ETL from 11 to 15, by lowering the 5th RFA to 40°, gradually raising to the center of k-space, and raising the final echo to 180°, we were able to achieve a high SNR and prevent blurring on images. On the other hand, when we increased the ETL to 19 and decreased the 5th RFA, the final echo was not improved and the SNR was worse. Therefore,

in order to acquire images with high SNR, we suggest setting the 5th RFA to approximately 90°, although some compromise in RF exposure will be necessary.

References

1. Zhu Y.: Parallel excitation with an array of transmit coils. Magn Reson Med 51 (4) 775–784 (2004).
2. Busse RF.: Fast spin echo sequences with very long echo trains: design of variable refocusing flip angle schedules and generation of clinical T2 contrast. Magn Reson Med 55, 1030–1037 (2006).
3. Hargreaves BA.: Variable-rate selective excitation for rapid MRI sequences. Magn Reson Med 52 (3) 590–597 (2004).
4. Juergen, H.: Multiecho Sequences with Variable Refocusing Flip Angle: Optimization of Signal Behavior Using Smooth Transitions Between Pseudo Steady States (TRAPS). Magn Reson Med 49, 527–538 (2003).
5. Yamashita Y.: Gd-EOB-DTPA Enhanced Dynamic MR Imaging: Optimization of Arterial Phase Imaging. NICHIDOKU-IHO vol.55 (2), 15–26 (2010).

Fault Identification in a Blood Pump Using Neural Networks

Jan Kühn, Mateusz Buglowski, André Stollenwerk, Stefan Kowalewski, Marian Walter, Steffen Leonhardt, Jan Petran, Rüdger Kopp, Rolf Rossaint, and Thorsten Janisch

Abstract

This paper compares two fault identification implementations based on a neural network and a model based approach. Our worked example is the detection of gas bubbles in the pump head of a centrifugal blood pump. We focus on algorithms applicable on minimal sensor data with a reasonable implementation effort. The approaches were restricted to the desired blood flow and the measured rotational speed of the pump. We evaluated both implementations with data from an ECMO system.

Keywords

Fault identification • Blood pump • Neural network
ECMO • Hazard • Clinical assistance

1 Introduction

Complex therapies suffering from a high probability of complications need reliable identification methods. Desirable is an approach which works on a minimal set of sensor data with sufficient efficiency. This motivates the application of machine learning approaches. Such an approach allows to work with less knowledge of the system structure but results in other requirements.

J. Kühn (✉) · M. Buglowski · A. Stollenwerk · S. Kowalewski
Informatik 11 - Embedded Software, RWTH Aachen University, 52056 Aachen, Germany
e-mail: kuehn@embedded.rwth-aachen.de

M. Walter · S. Leonhardt
Philips Chair for Medical Information Technology, RWTH Aachen University, 52056 Aachen, Germany

J. Petran · R. Kopp · T. Janisch
Department of Intensive Care and Intermediate Care, RWTH Aachen University Hospital, 52056 Aachen, Germany

R. Rossaint
Clinic for Anesthesiology, RWTH Aachen University Hospital, 52056 Aachen, Germany

Our work tries to quantify the usefulness of such an algorithm for a worked example from the field of intensive care.

The validation data is taken from an experimental setup for the treatment of acute respiratory distress syndrome (ARDS). As explained in [2], ARDS is a life threatening disease caused by traumas or non-cardic diseases (e.g. H1N1 pandemic in 2009). A therapy for serious cases can include extracorporeal membrane oxygenation (ECMO). An ECMO system is also part of the research setup which is described in [3].

The range of medical applications using centrifugal blood pumps is increasing [5]. A centrifugal blood pump generates a pressure difference and thus a flow by rotary acceleration of the blood.

1.1 Intrusion of Gas Bubbles

The intrusion of gas bubbles in an ECMO setup can lead to fatal embolisms. Clinical reports mention that of all complications during ECMO therapy more than 4% were air embolisms [1, 9]. Such faults are more likely to appear in the initial application phase and critical for a successful startup phase. Reasons for such a gas intrusion can be insufficient priming, stop-cocks in a wrong position, leaks at connections and defects of the oxygenator membrane. Some applications like cardiopulmonary bypasses use an active detection with a bubble trap to prevent bubbles from entering the patient's body. However, continuous supervision is not commonly used in ECMO applications [7].

The supervision of the pump head covers many critical positions for intrusion because the negative pressure ahead of the pump caused by suction of the blood might lead to an intrusion even at small leaks. The extracorporeal circuit behind the pump head benefits from the positive pressure preventing an intrusion of gas. A bubble detection is often part of an ultrasound flow sensor and installed at the venous return. The resolution is usually depending on the tube
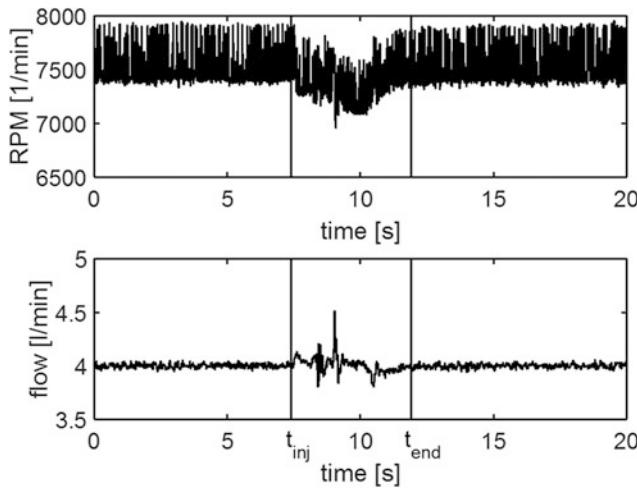
Fig. 1 Sensor data of an injection of 20 ml saline solution

diameter. In case of the ABD05 (SONOTECH GmbH, Halle, Germany) is the specified minimal bubble size one third of the tube diameter, which is a diameter of 3/8″ and a bubble size greater than 0.017 ml in case of the worked example. In case of a leakage in the circuit before the oxygenator, it will fill until bubbles pass the oxygenator and enter the patient's body. Pump supervision allows a redundant and early reaction regarding such a gas intrusion.

The deviation of a well known behavior is usually prioritized as fault detection method and rather often applied since it includes a wide range of known and perhaps unknown faults. Substantial prerequisite for an automated advice regarding a hazardous state of the system is an exact identification of the problem. Observing data of a single sensor in presence of disturbances shows that incidents can be distinguished but need a unique algorithm for each type of fault. An example is the injection of saline solution in
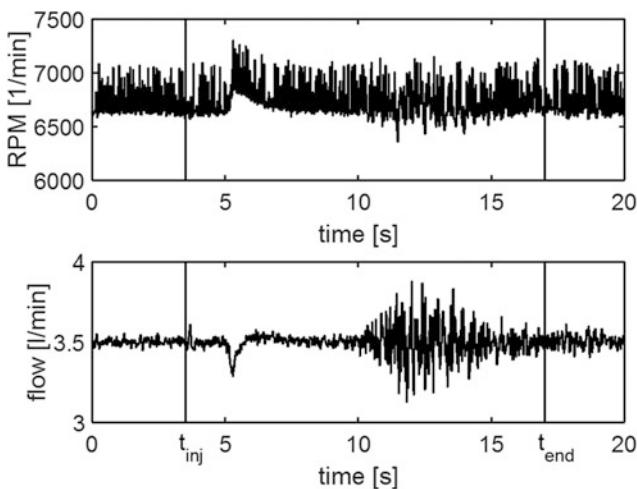
Fig. 2 Sensor data of a bubble of 0.2 ml size

Fig. 1 which has different characteristics compared to the bubble in Fig. 2. The intrusion of a gas bubble into the pump head causes a loss in momentum which results in a disturbance of the flow and causes a reaction of the flow controller. A detailed fluid dynamic modeling is usually an unreasonable effort for every possible hazard in the development process of a medical device. These challenges motivate the use of generalized approaches based on machine learning or system models with strong approximations instead of detailed modeling.

1.2 Test Setup

An exemplary setup like the ECMO setup providing the validation data is rather complex. It will not be covered here in detail, because all the crucial effects can be reproduced in a simplified setup. A more detailed description of the clinical context and the ECMO therapy setup is given in [3].

Our validation data is taken from a research project focusing on ECMO therapy supervision and control. We realized an artificial gas intrusion by injection of air bubbles at the venous outlet before the pump. These bubbles enter the pump head, pass the oxygenator and usually get caught in its bubble trap.

We used a simplified mock loop consisting of a reservoir, a flow sensor and a DP2 blood pump (MEDOS AG, Heilbronn, Germany) to generate an adequate amount of data, which is necessary to train a neural network. Bubbles were generated using a small cannula and a fast switching valve of the type MHE2 (FESTO AG, Esslingen, Germany) which is pressurized with around 0.4 bar. We choose the switching time of the valve to reproduce the observed effect in the RPM signal. This allowed the fast generation of training data.

2 Methods

2.1 Identification Using Neural Networks

The machine learning approach used in this paper is based on a Convolutional Neural Network (CNN).

Structure of the Neural Network The chosen structure of the CNN, as shown in Fig. 3, consists of two convolutional and two fully-connected layers.

Training of the Neural Network The speed of the pump head was chosen as the sole sensor to be decisive of the observed phenomenon. Only the set value for the bloodflow was added as a second feature vector. Although no excessive filtering was conducted, the data was interpolated to fit a fixed timestep of 0.02 s and the RPM signals per time frame

were subtracted by the minimum of the RPM signal in that time frame.

Further alteration of the original data was achieved by adding white-noise. The dataset for learning consists of 1095 datasets of bubbles, all generated in the mock loop, and 17,857 datasets of non-bubble data of combined mock data and actual therapy setup data. This total of 18,952 datasets was augmented by 15 different white-noise sets resulting in 303,232 training datasets.

2.2 Model Based Approach

Model The system has nonlinear components, like the viscosity of the blood in the pump head. As described in detail in [4, 8] the overall model can be simplified. In case of this scenario, it includes the behavior of a PID flow controller. We use a second order model with one zero point for linearization. Input is the target blood flow $Q(s)$ and output is the rotational frequency of the pump $W(s)$ (RPM). The nonlinearity is handled by using a set of n systems, identified for the operation range of interest.

$$W_i(s) = Q_i(s) \frac{a_{i1}s + a_{i0}}{b_{i2}s^2 + b_{i1}s + b_{i0}}$$

The incident of a bubble is modeled as a discrete change of the model parameters. This change was identified for the smallest bubble in the mock loop and scaled for the other operation points. The algorithm is applied to intervals covering most of the effects of a bubble.

Fault Identification The fault is identified by matching the root mean square error (RMSE) against an empirical error limit ε_l for each window of observed data $w_m(t)$ over an interval with the length t_w and a discretization stepsize t_s.

$$\mathrm{Min}\left(\mathrm{RMSE}(w_i', w_m')\right) < \varepsilon_l$$
$$\forall i = 1, 2, \ldots n$$

3 Results

In the following, we present the results using the smallest bubbles which showed an identifiable reaction in the RPM signal. This allows us to test the usability of both approaches in a challenging range of operation. The bubble size is between 0.1 and 0.5 ml. Smaller bubbles did not have any visible effect on the RPM signal.

Data from the physical setup has been acquired in several trials between 2014 and 2017. *set0*, which is a small evaluation set from a trial in January 2017, consists of 212 datasets and contains 10 bubbles. It was used to determine the learning progress (see Fig. 4). *set1* from November 2014 comprises of 12 bubbles and consists of 5032 datasets in total, including around 85 min of data. *set2* from October 2016 contains 43 bubbles and a total of 4628 datasets (77 min). *set3* is from April 2017 and consists of 12 bubbles and a total of 5088 datasets (85 min). The most recent dataset *set4* was recorded in November 2017 with a total of 4875 datasets (81 min) including 22 bubbles. Hence there are 89 bubbles in sets *set1*– *set4* with nearly 5.5 h of trial data.

The execution time of the CNN for 60,000 learning cycles was approximately 16 min. This results in roughly 16 s per 1000 cycles, which also is the number of cycles after which the learning process was monitored by running the *set0*. As seen in Fig. 4, the accuracy of the CNN converges after 20,000 cycles at around 0.9430 before dropping again after 80,000 cycles. The evaluation of all sets together executed in about 15 s. The execution of the model needs on average 0.56 s per run on a personal computer, depending on the overall payload of the CPU and its capacity. Hence the average runtime of the model over all datasets is accumulated at 3.05 h.

3.1 Identification Results

As seen in Table 1 the CNN has a better performance on *set1* with 8 out of 12 (66.7%) correctly identified bubbles and only two false positives out of the remaining 5020
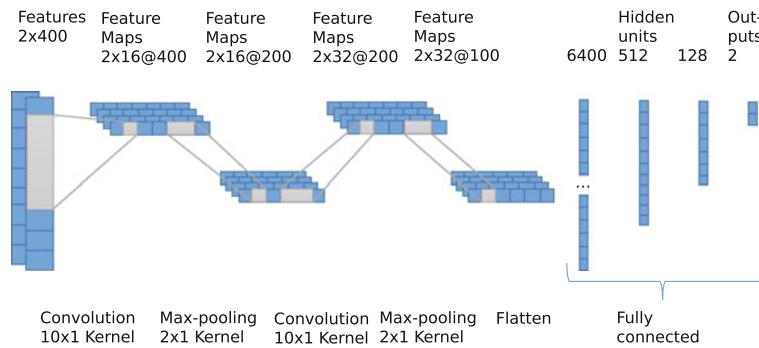
Fig. 3 Structure of the used convolutional neural network

(0.04%) non-bubble data points. Whereas the model only identified 4 out of 12 (33.3%) bubbles and also had with 822 (16.4%) false positives on the non-bubble data the highest false positive rate. On *set2*, the CNN was able to determine all 43 (100.0%) of the 43 bubbles, while 24 (55.8%) were correctly identified with the model approach. The model performed on that set with 25 (0.55%) of false positives better than the CNN with 33 (0.71%) of false positives. The CNN approach classified 6 (50.0%) out of 12 bubbles in *set3* correctly, whereas the model could only identify 2 (16.7%) bubbles correctly. The 2 (0.04%) false positives the model produced were the lowest on any set together with the results of the CNN on *set1*. The CNN had its most false positives with 98 (1.92%) on *set3*. On *set4* the CNN detected only 2 (9.09%) of the bubbles, while the model could identify 5 (22.7%) of the bubbles. Although the CNN had problems identifying the bubbles, there were only 6 (0.12%) of false positives. In contrast the model classified 107 (2.20%) datasets wrongly as bubbles. Overall the CNN identified 59 (66.3%) of the 89 bubbles correctly and misidentified 139 (0.71%) datasets as bubbles. The model approach classified 35 (38.9%) bubbles correctly and had 956 (4.89%) false positives.

3.2 Reliability and Disturbances

The machine learning approach has a success rate of detecting bubbles of 66.3%. Considering that the data for the evaluation datasets is obtained manually, one can argue that the exact point in time when the RPM increases due to the bubble is crucial for detection. See the characteristic increase in Fig. 5 *set1*—bubble 8 at time 3 s. This bubble was detected by both algorithms. Whereas *set4*—bubble 3 was not identified by both approaches. The amplitude of the noise on the RPM signal in this example is visibly higher. Hence a simple error calculation as the model uses, will
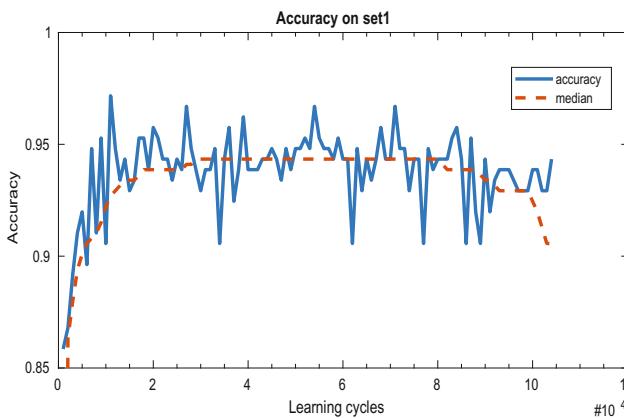
increase the error faster resulting in an undetected bubble. The noise on the data in *set4* can be explained by the usage of a roller pump during the trials which was not present or turned on during other trials.

In Fig. 5 the *set4*—bubble 4 is recognised by the CNN, but not by the model. Again the amplitude of the noise adds to the error in the model based approach and it is hard to distinguish the bubble by a human. The CNN successfully classified it as a bubble due to the generalising behaviour of ANNs.

All three exemplary bubbles were of size 0.3 ml. The created training data was aimed at replicating bubbles of that size. *set1* contains bubbles of sizes of 0.5, 0.4, 0.3, and 0.2 ml. The missed bubbles by the CNN were of sizes 0.3 and 0.2 ml. The model recognized two bubbles of size 0.5 ml and one each of size 0.4 and 0.3 ml. *set2* contains bubbles of sizes 0.15, 0.2, 0.3, and 0.5 ml. While the CNN was able to identify all 43 bubbles correctly, the model identified all 12 bubbles of size 0.15 ml correctly, 7 out of 17 0.3 ml bubbles, and 5 out of 6 0.2 ml bubbles. But none of the 8 bubbles of size 0.5 ml. *set3* is composed of bubbles of size 0.3 ml. Hence, the CNN identified 6 bubbles and the model 2 out of the 12 bubbles in the set. *set4* consists of bubbles of sizes 0.3, 0.2, and 0.1 ml. The CNN approach was able to identify only two 0.3 ml bubbles. The model identified 3 bubbles of size 0.3 ml and two of size 0.2 ml.

Our approaches detected several false positives, which is not very surprising, since both were applied to characteristics hard to detect. Their sensitivity can be traded for robustness. However, the number of false positives can be easily reduced in combination with a more general fault detection approach (see [6]).

3.3 Effort and Usability
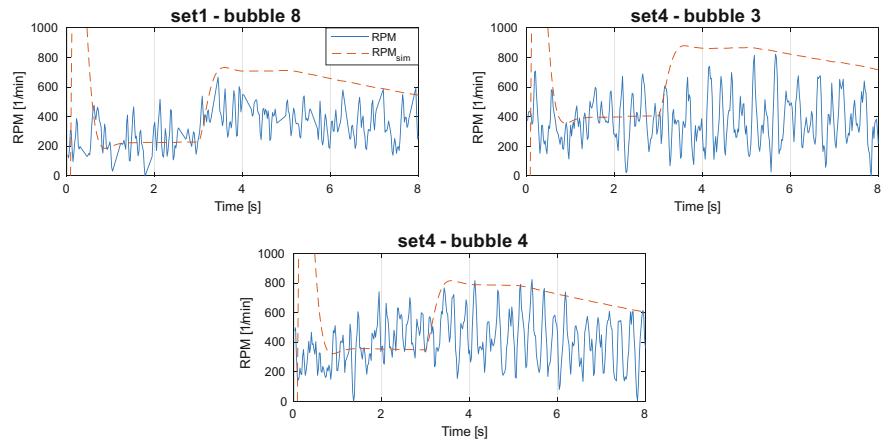
The neural network approach does not require knowledge about the system. However, the chosen model-based approach cannot be realized without knowledge of system theory. Despite the fact, that our model based approach might achieve an improved detection rate after further refining, the overall testing effort to estimate the impact of design decisions is rather time consuming. The initial effort of implementation needed for the machine learning approach has a higher reuseability or adaptability for similar problems but suffers from the computational effort necessary for each training.

The model based approach requires only a set of step answers for the identification of the linearized system. Hence, the most significant trade-off in favor of the model based approach is the amount of data needed for the training of a neural network, which restricts the application to faults reproducible without extensive effort. The model based

Fig. 4 Accuracy of the CNN on *set0*

Table 1 Identification results of CNN and model M. n is the number of datasets per set, n_b is the number of bubbles, p_t the number of true positives (percentage of bubbles) and p_f the number of false positives (percentage of non-bubble data)

		n	n_b	p_t	p_f
set1	CNN	5032	12	8 (66.7%)	2 (0.04%)
	M			4 (33.3%)	822 (16.4%)
set2	CNN	4628	43	43 (100%)	33 (0.71%)
	M			24 (55.8%)	25 (0.55%)
set3	CNN	5112	12	6 (50.0%)	98 (1.92%)
	M			2 (16.7%)	2 (0.04%)
set4	CNN	4875	22	2 (9.09%)	6 (0.12%)
	M			5 (22.7%)	107 (2.20%)
Total	CNN	19647	89	59 (66.3%)	139 (0.71%)
	M			35 (39.3%)	956 (4.89%)

Fig. 5 *RPM* signals after preprocessing and one of the corresponding model-outputs RPM_{sim} of bubble 8 in *set1* and bubbles 3 and 4 in *set4*. The error-detection considered only data after a runtime of 1 s due to the override of the model before that

approach does not need the mock-loop and could be developed using the observed data examples of the clinical setup.

4 Conclusion

We evaluated the performance of two different fault detection approaches. The presented approaches support existing detection methods because a gas intrusion can be detected earlier. These approaches are also valuable in case of setups without dedicated bubble detection. Both approaches do not rely on detailed system modeling and were applied to test data from different settings to show their effectiveness in a realistic clinical scenario, including the problem of varying conditions. The neural network performed well and had a higher detection rate compared to the model-based approach,

even though the variation of training data was mostly achieved by augmentation methods. However, the application is reduced on systems where a sufficient amount data is available.

References

1. Allen, S., Holena, D., McCunn, M., Kohl, B., Sarani, B.: A review of the fundamental principles and evidence base in the use of extracorporeal membrane oxygenation (ECMO) in critically ill adult patients. Journal of intensive care medicine **26**(1), 13–26 (2011)

2. Bishop, J.F., Murnane, M.P., Owen, R.: Australia's winter with the 2009 pandemic influenza A (H1N1) virus. New England Journal of Medicine **361**(27), 2591–2594 (2009)

3. Brendle, C., Mülders, T., Kühn, J., Janisch, T., Kopp, R., Rossaint, R., Stollenwerk, A., Kowalewski, S., Misgeld, B., Leonhardt, S., Walter, M.: Physiological closed-loop control of mechanical ventilation and extracorporeal membrane oxygenation. Biomedical Engineering/Biomedizinische Technik (2017). To appear

4. Choi, S., Boston, J.R., Thomas, D., Antaki, J.F.: Modeling and identification of an axial flow blood pump. In: 1997 American Control Conference, Proceedings of the, vol. 6, pp. 3714–3715. IEEE (1997)

5. Halaweish, I., Cole, A., Cooley, E., Lynch, W.R., Haft, J.W.: Roller and centrifugal pumps: a retrospective comparison of bleeding complications in extracorporeal membrane oxygenation. ASAIO Journal **61**(5), 496–501 (2015)

6. Kühn, J., Brendle, C., Stollenwerk, A., Schweigler, M., Kowalewski, S., Janisch, T., Rossaint, R., Leonhardt, S., Walter, M., Kopp, R.: Decentralized safety concept for closed-loop controlled intensive care. Biomedical Engineering/Biomedizinische Technik **62**, 213–223 (2017)

7. Lawson, D.S., Lawson, A.F., Walczak, R., McRobb, C., McDermott, P., Shearer, I.R., Lodge, A., Jaggers, J.: North American neonatal extracorporeal membrane oxygenation (ECMO) devices and team roles: 2008 survey results of Extracorporeal Life Support Organization (ELSO) centers. Journal of ExtraCorporeal Technology **40**(3), 166 (2008)

8. Misgeld, B.J.: Automatic control of the heart-lung machine. Ruhr-Universität Bochum, Diss (2006)

9. Turner, D.A., Cheifetz, I.M.: Extracorporeal membrane oxygenation for adult respiratory failure. Respiratory care **58**(6), 1038–1052 (2013)

Elaboration of New NDRLs as Part of Third National Patient Dose Survey in Diagnostic Radiology in Bulgaria

Asen Dimov, Ivan Tsanev, Desislava Ivanova, and Filip Simeonov

Abstract

Purpose: The aim of this research is to elaborate an update of National Diagnostic Reference Levels (NDRLs) in Bulgaria, as required by National and International legislation. Methods and Materials: Special questionnaires and methodology instructions for submission of required data were distributed to all hospitals in the country. Patient dose records and corresponding technical data were delivered from medical institutions via following three methods: by e-mail, by specialized on-line system, or by paper. A national patient dose database build on MS Access was elaborated and employed for storing, processing and analysing of the collected data. Results: More than 10,500 patient dose records on more than 190 X-ray systems from over 90 health establishments have been collected and analysed. New national DRLs were elaborated and proposed for: Chest PA, Pelvis AP, Abdomen AP, Thoracic Spine AP, Thoracic Spine Lat, Lumbar Spine AP, Lumbar Spine Lat, Skull AP, Scull Lat, Barium meal, Barium enema, Coronary Angiography and Percutaneous Coronary Intervention—in terms of KAP; for Computed Tomography (CT) of Head, Abdomen and Lumbar Spine—in terms of CTDIw and DLP; for Mammography—in terms of ESAK and AGD. Conclusion: The new DRL values obtained are proposed as NDRLs for the country. Most are comparable with other European NDRLs with a few exceptions only. Those exceptions are most probably related to actual optimization in existing radiology practices.

Keywords

NDRLs • Patient dose • Diagnostic radiology

1 Introduction

Establishment, regular review and use of diagnostic reference levels (DRLs) for medical radiodiagnostic examination is required and recommended by international organizations and by local national legislation [1–4]. Two national patient dose surveys for establishing and updating National Diagnostic Reference Levels (NDRLs) have been performed in Bulgaria so far [5, 6]. Third National Patient Dose Survey (TNS) started by National Centre of Radiobiology and Radiation Protection (NCRRP) in 2016 with non-financial support from Ministry of Health (MoH) and regional Departments of Radiation Hygiene (DRH) to the Regional Health Inspectorates (RHI) under the umbrella of MoH, based in 5 of the main cities in the country. In fulfilment of this task, NCRRP has developed web-based platform and a set of standard paper forms and instructions for data collection [5–7].

2 Materials and Methods

Methods for elaboration of NDRLs for different anatomic locations and measurements of patient doses during TNS are based on the "Recommendations and Guidance for use of Diagnostic Reference Levels in Radiology" and "National protocol for measurement methods of patient doses in X-ray Diagnostics" respectively [8, 9]. Some of the available International recommendations for elaboration of NDRLs were taken into account also [1–3]. According to the chosen methodology patient dose data from at least 20 X-ray systems should be used for each projection or examination for establishing a DRL. A sample of at least 20 standard sized adult patients should be collected for each standard projection or examination on each X-ray system. The personal patient weight should lie in interval of 50–90 kg with an average of 70 ± 3 kg. The Typical Dose (TD) for each standard projection is being calculated as an arithmetic mean

A. Dimov (✉) · I. Tsanev · D. Ivanova · F. Simeonov
National Centre of Radiobiology and Radiation Protection, 3, Sv. Georgi Sofiyski Street, 1606 Sofia, Bulgaria
e-mail: adimov_sl@yahoo.com;
a.dimov@ncrrp.org; a.dimov07@gmail.com

of the relevant dosimetric quantity for the sample of patients. This approach was chosen, since TNS was designed and started in 2016 prior to the official publication of new recommendations of International Commission of Radiological Protection (ICRP), as well as for purposes of easier comparison with previous national and international studies performed so far [1, 10–12]. For children slightly different approach based on median value of dosimetric quantity for the sample of patients is employed for elaboration of typical dose on each X-ray system in accordance with European Guideline [13].

Bulgarian guidance as well as foreign protocols recommends that for adult patients NDRL shell be defined closer to the third quartile of distribution of the typical doses estimated for each projection, examination or procedure.

A national patient dose database build on MS Access was elaborated and employed for storing, processing and analysing of collected data [14].

2.1 Organization and Data Collection During Third National Survey

Four methods of data collection have been employed:

A. Using internet based platform for automatic sending: www.drl-bg.com [6];
B. Via electronic tables sent by e-mail to the electronic address of the survey: rzmo@ncrrp.org;
C. Via paper hard copy by post mail;
D. Via information on local typical doses defined in Health Establishments.

All information including terms and conditions for data collection and submission was made available on web page of the TNS [7]. On this web page following information is available for download on both MS Excel and Adobe Acrobat format files: a Short and a Full Instruction for data collection; all necessary forms for registering of X-ray systems properties and patient dose registration forms for all types of Diagnostic Radiology Examinations. These forms include patient's anthropomorphic data; main exposure parameters; dosimetric quantities recommended by IAEA TRS 457 and ICRP: measured Kerma Area Product (*KAP*); displayed dose index in case of Computed Tomography (CT): $CTDI_w$, $CTDI_{vol}$ or DLP [1, 15]. The web page has also a link to the on-line platform for registering of patient doses for those sites, which do prefer to use this method of data submission to NCRRP [6]. Calls to the Health Institutions to participate in TNS were published on the web page of TNS as Circular Letters of the Director of NCRRP and the Minister of Healthcare [5, 7].

For mammography the reported parameters are: tube potential (kVp); target/filter combination; exposure tube current and time product (mAs); half value layer (HVL); tube output (µGy/mAs); optical density (OD for film-screen systems); source to breast support distance (mm) and patient data. In the mammo quality control tests measurements of incident air kerma (IAK) was also implemented. Incident air kerma is the air kerma from the incident beam on the central x-ray beam axis at the focal-spot-to surface distance at the skin entrance plane. The average absorbed dose in the glandular tissue in a uniformly compressed breast (AGD) can be determined by first getting the IAK measurements on the standardized 45 mm PPMA phantom and standard breast. In TNS AGD is calculated according to the method recommended by the EUREF European guidelines for quality assurance in mammography screening [16].

AGD is derived by calculation using the following formula:

$$AGD = IAK\,g\,c\,s, \tag{1}$$

recommended by European protocols and IAEA TRS 457 Code of Practice [15]. Mammography dose survey included 33 X-ray systems: 17 in hospitals and 16 in Ambulances or in smaller Medical Centres. Different systems were equipped with different detectors: 20 X-ray units with Film Screen Combinations (FSC); 5 with Computed Radiography (CR) plates and 6 with a Direct Digital Radiography (DDR) detector.

3 Results

A total number of 10,565 patient dose records from 91 Health Establishments were collected at NCRRP, as corresponding numbers per modality were as follows: 5731; 1793; 1100; 1237; 704, for: Radiography; Computed Tomography (CT); Mammography; Interventional Cardiology and Fluoroscopy respectively. Those data comprised 195 X-ray systems distributed as follows: 81% in Hospitals and 19% in Ambulances and smaller Medical Centres. 58 of the X-ray units were situated in the Capital—Sofia, 41 in bigger cities and 96 in middle and small size cities. About 67% of patient dose data were submitted via e-mail and about 22% by post mail on paper—via above mentioned methods B and C respectively. Submission of data via input in the web based system (Method A) appeared to be not a popular choice for Health establishments participated in TNS, although it was highly recommended by MoH and NCRRP as the primary submission choice. Submission of information on local typical doses elaborated in Health Establishments (Method D) appeared to be not a preferred choice either. Such dosimetric data were collected mainly for

Table 1 NDRLs values from TNS and SNS given in KAP (μGy m^2) for radiography projections and fluoroscopy Ba examinations

	Chest PA	Abd AP	LS AP	LS Lat	Pelv AP	TS AP	TS Lat	Skull AP	Skull Lat	Ba enema	Ba meal
TNS	45	300	240	360	230	110	220	80	75	1840	1570
SNS	40	–	300	400	400	–	–			4000	1800

Table 2 NDRLs values from TNS, SNS and other NDRLs for ca and PCI given in KAP (μGy m^2)

Survey	TNS	SNS	EU	IE, 2009	AU, 2014	UK, 2010
CA	4600	4000	6000	5310	5865	3600
PCI	13400	14000	–	8400	12900	4000

Table 3 NDRLs values from TNS, SNS and EU for CT of head, chest, abdomen and lumbar spine given in DLP (mGy cm), C_w (mGy) and C_{vol} (mGy)

	Head			Chest			Abdomen			Lumbar spine		
	DLP	C_{vol}	C_w	DLP	C_{vol}	C_w	DLP	C_{vol}	C_w	DLP	C_{vol}	C_w
TNS	1000	60	80	500	16	18	470	18	17	580	20	19
SNS	1000	–	60	550	–	25	600	–	30	–	–	–
EU	1000	60	–	400	10	–	800	25	–	500	35	–

Table 4 Third quartile values for AGD and ESAK obtained at phantom and patients studies at TNS and NDRLs obtained from SNS

	Patients	Phantom	Phantom
	AGD (mGy)		ESAK (mGy)
3-rd quartile	2.4	2.3	12
SNS NDRL		2.3	12

Table 5 Preliminary NDRLs from TNS for paediatric radiography of chest

	0–1 years old	1–5 years old	5–10 years old	10–15 years old
	KAP (μGy m^2)			
TNS	6	8	10	16

mammography units with assistance and input from an external medical physics group providing quality control (QC) service to most of mammography systems participated in TNS.

NDRLs obtained from TNS and SNS for Anterior-Posterior (AP), Posterior-Anterior (PA), or Lateral (Lat) Radiography projections of: Chest; Abdomen (Abd); Lumbar Spine (LS); Pelvis (Pelv); Thoracic Spine (TS); Skull (SK); as well as Fluoroscopy Barium (Ba) Contrast studies are shown in Table 1 [6]. Respective data for Coronary Angiography (CA) and Percutaneous Coronary Intervention (PCI) obtained from TNS, SNS, European (EU) and some foreign surveys are shown in Table 2 [6, 10]. NDRLs for CT given in DLP (mGy cm), CTDI$_w$ (C_w) (mGy) and CTDI$_{vol}$ (C_{vol}) obtained from TNS, SNS and EU study are shown in Table 3 [6, 10].

Table 4 shows calculated AGD and *ESAK* from Phantom and AGD from Patient mammography exposure data. Last are recommended as NDRLs for mammography.

Preliminary NDRLs for paediatrics in frame of TNS are obtained for Chest X-ray radiography projection only. Their values are displayed at Table 5.

A more complete set of tables with detailed statistics can be obtained from the author.

4 Discussions

Most values of Bulgarian NDRLs determined during TNS for Radiography projections and Fluoroscopy Barium Contrast studies are closer to other European countries NDRLs with exception for Chest PA [12]. Higher NDRL for

Chest PA is mainly due to commonly used non-optimal "soft" technique with potential of the tube significantly lower than recommended along with anti-scatter grid put always in place which is a commonly observed practice [17].

Differences in SNS and TNS results are due mainly to change in equipment technology of X-ray imaging systems in place. Decrease in NDRLs is observed in all examinations with an exceptions for CA. Increase in NDRL value for this examination is explained with smaller and not so representative patient samples in SNS in comparison with TNS. For PCI for example, this trend is not valid and during TNS we obtained lower then SNS value as a NDRL [11].

Difference in NDRL values for AGD obtained from phantom and patient exposure data is related probably to lack of precise information for Anode-Filter combinations on some of X-ray systems in study, which decreased the number of systems included in Phantom based AGD assessment.

The smaller proportion of patient data submitted by the health establishments using the "on-line data collection platform" (Method A.) might be related to its present user interface design and a need for its further development, improvement and promotion.

5 Conclusions

Third national patient dose survey collected significantly bigger amount of data than first and second national surveys and hence appeared to be more representative for the country. NDRLs are determined for more Diagnostic Radiology Examinations. Successful realization of TNS became possible due to joint efforts of NCRRP staff, active involvement of Radiation control departments of Regional Health Inspectorates (RHI), medical physicist and other responsible staff in the health establishments in the country and principal support from Management of NCRRP and the Ministry of Health.

Conflict of Interest The authors declare that they have no conflict of interest.

Statement of Informed Consent Informed consent was obtained from all individual participants included in the study.

Protection of Human Subjects and Animals in Research All procedures performed in studies involving human participants were in accordance with the ethical standards of the institutional and/or national research committee and with the 1964 Helsinki declaration and its later amendments or comparable ethical standards.

References

1. Diagnostic reference levels in medical imaging. ICRP Publication 135. Ann. ICRP 46(1) (2017).
2. Radiation protection and safety of radiation sources: International basic safety standards. IAEA safety standards series No. GSR Part 3. IAEA, Vienna (2014).
3. Council Directive 2013/59/Euratom of 5 December 2013 laying down basic safety standards for protection against the dangers arising from exposure to ionising radiation, and repealing Directives 89/618/Euratom, 90/641/Euratom, 96/29/Euratom, 97/43/Euratom and 2003/122/Euratom. Official Journal of the European Union, L 13, 17 January 2014, 1–73 (2013). ISSN 1977-0677.
4. Ordinance N.o30 of the Ministry of Health for protection of individuals at medical exposure, promulgated in State Gazette № 91 of November 15 (2005) (in Bulgarian).
5. Vassileva J, Dimov A, at el. Bulgarian experience in the establishment of reference dose levels and implementation of a quality control system in diagnostic radiology. Radiation Protection Dosimetry, Vol. 117, No. 1–3, 131–134 (2005).
6. Vassileva J., Ingilizova K. Dimov A., et al. National survey of patient doses in diagnostic and interventional radiology and nuclear medicine 2002–2013. NCRRP, Sofia (2013), ISBN: 978-619-90135-4-0.
7. Karadjov, A. Dimov, A. Vassileva, J. Anatschkowa, E. Recommendations and guidance for the use of the diagnostic reference levels in radiology. EC Phare Project: Radiation protection and safety in medical use of ionising radiation, Reference Number: BG/2000/IB/EN 01–05, National Centre of Radiobiology and Radiation Protection, Bulgaria (2003).
8. Karadjov, A. Dimov, A. Vassileva, J. Anatschkowa, E. Protocol on the methods for patient dose measurements in x-ray diagnostics. EC Phare Project: Radiation protection and safety in medical use of ionising radiation, Reference Number: BG/2000/IB/EN 01–05, National Centre of Radiobiology and Radiation Protection, Bulgaria (2003).
9. European Guidelines on DRLs for Paediatric Imaging. Final complete draft (2016) (in press), available online at: http://www.eurosafeimaging.org/wp/wp-content/uploads/2014/02/European-Guidelines-on-DRLs-for-Paediatric-Imaging_Revised_18-July-2016_clean.pdf, last accessed: 2017/09/02.
10. European Commission. Radiation Protection N 180. Diagnostic Reference Levels in Thirty-six European Countries: Part 2/2. Directorate-General for Energy, Directorate D - Nuclear Safety & Fuel Cycle, Unit D3 — Radiation Protection (2014).
11. Dimov A, Ivanova D, at el. Design, methodology and purposes of the third national patient dose survey in diagnostic radiology. Scientific works of the union of scientists in Bulgaria – Plovdiv. Series G. Medicine, Pharmacy and Dental Medicine, Vol. XIX, House of Scientists, Plovdiv (2016). ISSN 1311 – 9427.
12. Vassileva J., Simeonov F., at el. On-line data collection platform for national dose surveys in diagnostic and interventional radiology Radiation Protection Dosimetry 165 (1–4): 121–124 (2015).
13. National Centre for Radiobiology and Radiation Protection. Web page of National Survey DRL2016. URL: http://www.ncrrp.org/new/bg/DRL2016-c437, last accessed on 2017/11/25.
14. European Communities. European guidelines for quality assurance in breast cancer screening and diagnosis. Fourth edition Supplements. Luxembourg: Office for Official Publications of the European Communities (2013).

15. TECHNICAL REPORTS SERIES No. 457. Dosimetry in diagnostic radiology: an international code of practice. International Atomic Energy Agency, Vienna (2007), ISBN 92–0–115406–2.

16. Dimov A., Simeonov F., Tsanev I., at al. National patient dose surveys of chest radiography: 2002–2017. Is radiology practice in the country optimized? Roentgenologia & Radiologia (in manuscript).

17. Tsanev IM, Dimov AA. (2016) National database for patient dose registration and analysis in diagnostic radiology. In: Proceedings of 12-th National medical physics and biomedical engineering conference-NMPEC, pp. 51–60. Sofia (2016).

Development of Identification System for Surgical Instruments Using UHF Band RFID and Low-Intensity Antennae

Ryosuke Hosaka

Abstract

Post-op vestigial remnant of surgical instruments in the body is a very serious problem. The current two-dimensional symbol system is being used to help manage this problem. However, the two-dimensional symbols have to be identified one at a time, since the symbols are a sort of printed matter. An HF band passive RFID system was also proposed. This system also had problems in identifying the signals of a large number of surgical instruments in bulk, since the scope of its identification area was relatively small. To improve the deficiencies of this system, a UHF band passive RFID system was developed. The authors have also proposed a new low-intensity antennae for the UHF band passive RFID system. This new system cannot radiate an electrical field strong enough to interfere with medical equipment and should not pose a problem to any electronic equipment in the operating room. From our experimental results using 50 surgical instruments, all the instruments were identified in less than one second with this new RFID system, even when the instruments were covered with water residue. These results are very promising and indicate that the proposed RFID system will be an improvement to the surgical instrument management systems currently being used. This new system will also undoubtedly reduce the workload of surgical nurses, while reducing human error in the operating room.

R. Hosaka (✉)
Shonan Institute of Technology, Fujisawa, Kanagawa 251-8511, Japan
e-mail: hosaka@info.shonan-it.ac.jp

1 Introduction

Vestigial remnant of surgical instruments is serious problem in medical scene. Various technologies are proposed to solve the problem. One of them is two-dimensional symbol. The system is useful to manage the instruments. However, the system have to be identified one at a time, since the symbols are a sort of printed matter. In Japan, HF band RFID system is also proposed. This system also had problems in identifying the signals of a large number of surgical instruments in bulk, since its identification area as a detection area is small in principle. To improve the deficiencies of this system, UHF band passive RFID system was proposed by author to identify the all the surgical instruments. Author proposed automatic tracking system for medical engineering devices and patients using UHF (920 MHz) band passive RFID tag system [1–3]. Author also proposed management system for surgical instruments using UHF band passive RFID tag system [4]. Compact UHF band RFID tag is used in the system. From the experimental results, 100 instruments were identified in 15 s. However, It is difficult to control radiated field intensity outside of identification box. In this paper, new system for identification of surgical instruments is reported. From experimental results, 50 instruments were identified in less than one second. Radiated field intensity was kept safety level. It is considered that the proposed system is effective for management of surgical instruments in operation room.

2 Identification of Surgical Instruments

Surgical instruments should be identified in before and after of operation to reduce the vestigial remnant and to manage their history of usage. In the present, two-dimensional symbol system is being used for identification in Japan. In this method, hand-operation is necessary to identify the symbol on the instruments, since the symbol is a sort of

printed matter. By the way, hand-operation gives rise to the human error. Automatic identification system for surgical instrument is hoped to eliminate the human error.

Wireless identification is useful to manage the surgical instruments without human error, since the hand-operation is unnecessary. In this paper, new type of compact UHF band passive RFID tag is proposed to identify the surgical instruments. The new compact RFID tag is shown in Fig. 1. The tag is sized 5.5 mm × 2.5 mm × 3.5 mm in typical. Its weight is approx. 0.1 g. It is light enough to mount on the surgical instruments. Balance of the instrument can be controlled suitable, since the weight of the tag is too light.

3 New Identification System

New identification system is also proposed in this paper. New low-intensity antennae are used in the system. The antennae situation is shown in Fig. 2.

The low-intensity antennae RECOPIC are found in identification box. RECOPIC is developed by TEIJIN LIMITED. This antennae cannot radiate an electrical field strong enough to interfere with medical equipment in principle. Two RECOPIC antennae are set to ceiling of the identification box. Another two antennae are set to bottom of the box. Vertical interval between ceiling antennae and bottom antennae is set to 30 mm. Horizontal Intervals of two antennae on the ceiling and the bottom are set to 10 mm, from view point of optimization of field intensity distribution in the identification box. The antennae are connected to UHF band passive RFID reader. Impinj speedway is used as reader of the system. Its maximum output power is 1 W.
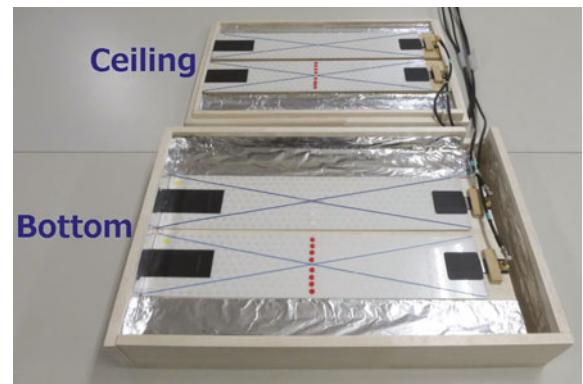
Fig. 2 New low-intensity antennae system

Electrical field intensity level is estimated. The field intensity is measured by spectrum analyzer NEC SpeCat2. Measurement points are set on the center of the identification box. The points are set 10 and 100 mm from top of the box. The output power of RFID reader is set to 1 W. Result of the experiment is shown in Fig. 3. In the Fig. 3, all the data are indicated in lower level less than 3 V/m. The value is safe enough for all type of the medical equipment. The electrical field intensity is managed within safety level using this antennae.

It is considered that the electrical field intensity is kept within safe level, maintaining the working integrity of any electronic device in the operating room.

Post-op surgical instruments are identified in the identification box. In the post-op identification, The instruments can be put on the tray in bulk. Maximum amount of instruments is designed 50. Appearance of 50 surgical instruments on identification tray is shown in Fig. 4.
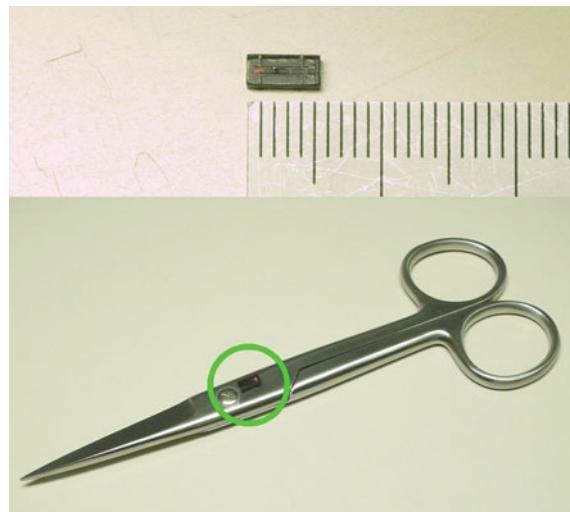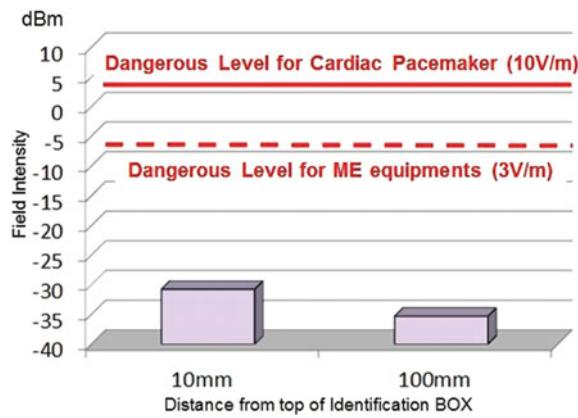
Fig. 1 New compact UHF band tag for surgical instruments

Fig. 3 Measured field intensity on antennae system

Fig. 4 50 instruments on identification tray

4 Identification Experiment

4.1 Method

50 instruments put on the tray in bulk. All of the instruments are constructed by forceps, surgical scissors, some types of tweezers and so on. New compact tag are attached on each instruments.

The identification tray with instruments is put into the identification box. The tray set on to the center of the low-intensity antennae. The experimental situation is shown in Fig. 5. The instruments were identified by the proposed system in 20 times. Output power of the RFID reader is set to 1 W.

Amount of identified tag and required time length were measured in each trial. Experimental condition is monitored in system screen.

Fig. 5 Instruments tray on antennae system

4.2 Result

An example of monitor screen for identification system is shown in Fig. 6. Amount of the identified tag and the identification time length were indicated in the monitor screen.

In the experimental results of 100 times identification, 50 instruments are identified perfectly. All instruments are identified in all trials in less than one second. It is enough to reduce the work load of surgical nurse for management of the surgical instruments.

5 Water Resistant Experiment

5.1 Method

UHF band wireless communication is often disturbed by water. There are various water like a water drops, water residue, blood and so on. Water resistant of the proposed system is estimated in the experiment.

50 instruments with new compact tag are set on identification tray (Fig. 4). Moisture contents are sprayed over the instruments. Moisture contents are water and physiological saline solution in this experiment. physiological saline solution is substitution of the blood. Sprayed amount are defined 8.5 and 17 ml from actual operating room condition. Sprayed condition is shown in Fig. 7. In this case, 8.5 ml water is sprayed. Sprayed instruments are identified 20 times each. Identification ratio and required time length were measured in the experiment. Output power of reader is set to 1 W.
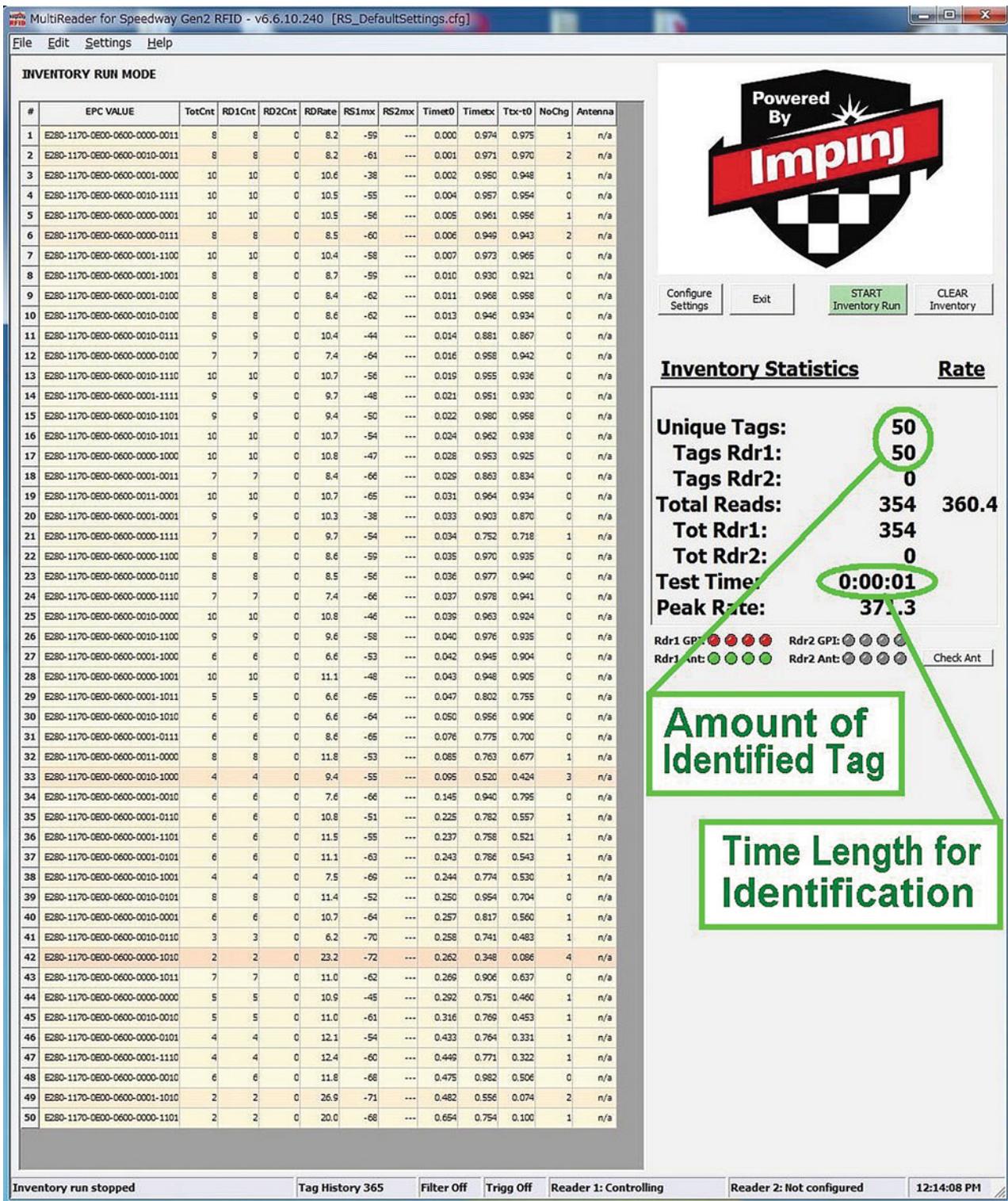
Fig. 6 An example of experimental result

Fig. 7 Water residue on the instruments

5.2 Result

In the case of water 8.5, 17 ml and physiological saline solution 8.5 ml, identification is completed within one second. All of instruments were identified. In the case of physiological saline solution 17 ml, identification ratio is 92%. In the case of physiological saline solution 17 ml, the identification ratio decreased.

6 Discussion

In the proposed system, 50 surgical instruments could be identified in less than one second. Post operation identification of the instruments is completed in short time length.

High frequency loss occurs in nearby the water. Small output power wireless communication like the RFID system is often disturbed by moisture contents. However, proposed system can be operated under actual operating room condition.

It is going to reduce the workload of nurse to use the system for instruments management. The identification is effective to reduce the human error, since the instruments are identified automatically. It is considered that the patient safety is kept by the system in post operation.

The price of the new UHF band passive compact RFID tag in the study is approx. 0.1€. The measured electrical field intensity outside of identification box is kept safety level for medical scene. It is described that the proposed UHF band passive RFID system is useful for identification of surgical instruments in the operating room.

7 Conclusions

In the proposed system, measured electrical field intensity is kept within safety level in operating room. 50 surgical instruments are identified in less than 1 s. These experimental results are promising and indicate that the proposed RFID system will be an improvement to the surgical instrument management systems currently being used. The proposed system will also undoubtedly reduce the workload of surgical nurses, while reducing human error in the operating room.

References

1. R. Hosaka and T. Akahane: Evaluation of 950 MHz RFID tag system as a marker for patient tracking at ward in hospital, In: Proc. IFMBE 5th. European Congress of the International Federation for Medical and Biological Engineering 2011, volume 37, Springer, pp. 1136–1139. Budapest (2011)
2. R. Hosaka et. al.: Experimental Trial to Detect Medical Engineering Equipments in Hospital by Passive UHF RFID Tag, In: Proc. 2013 7th International Symposium on Medical Information and Communication Technology, pp. 81–84, Tokyo (2013)
3. R. Hosaka: Possibility Evaluation of Automatic Tracking for Medical Devices and Patients using UHF band Passive RFID Tag in Hospital, In: Proc. of 37th. Annual International Conference of the IEEE Engineering in Medicine and Biology Society, 4pages in DVD, Milano (2015)
4. R. Hosaka and R. Noji: Automatic identification for surgical instruments using UHF band passive RFID, In: IFMBE Proceedings, EMBEC & NBC 2017, vol. 65, Springer, pp. 1061–1064, Tampere (2017)

Establishing Traceability Chain of Infusion and Perfusor Pumps Using Legal Metrology Procedures in Bosnia and Herzegovina

Lejla Gurbeta, Zijad Džemic, and Almir Badnjevic

Abstract

Establishing the traceability chain of measurements for medical devices (MDs) commonly used in everyday patient treatment was the main objective of this paper. This should directly ensure that through periodical calibrations of etalons and independent inspection procedure of MDs according to international standards, safe and accurate diagnosis and treatment can be created. This study is designed to cover 850 perfusors and 700 infusion pumps used in public and private healthcare institutions, during a period of one year. Testing procedures were carried out according to international standards and legal metrology legislative procedures in Bosnia and Herzegovina. The results show that the average measurement uncertainty of infusion pump is 0.9 ml, while for perfusor pump is 0.7 ml. These obtained results combined with other relevant documents, references and competences create the traceability chain. Additionally, as consequence cost benefits analysis proved yearly savings of 50% if healthcare institutions follow legal metrology procedures compared with unnecessary manufactures attests. Research emphasizes importance of establishing traceability chain in protection of public health. Results offered also implications for adequacy of etalon calibration and preventive maintenance performed on MDs. Based on collected measurement data, web-based application with database of infusion and perfusor pumps used in healthcare institutions in Bosnia and Herzegovina was created.

1 Introduction

MDs are classified as products of special importance for retaining the health of many people [1], and as such are subject to numerous regulatory investigations that determine the entire life-cycle of the devices, from production, sales, use and disposal. Around the world they are regulated by specific directives, with the goal of setting up the essential requirements for these devices from the aspects of health, safety, and use. For example, all member countries of EU must comply with various Medical Devices Directives (MDD) [2–4], but only few of them, along with United States, and Canada carry out the procedure for proper post-market surveillance. Nowadays, post-market surveillance is done mainly by manufacturers and distributors. Post-market surveillance is done through establishment of databases for reporting incidents involving MDs [5, 6]. Information from these databases are used by manufacturers to enhance characteristics of device and ensure that similar events do not happen again, but MD safety and performance

L. Gurbeta (✉) · A. Badnjevic
Faculty of Engineering and Natural Sciences, Genetics and Bioengineering Department, International Burch University, Sarajevo, Bosnia and Herzegovina
e-mail: lejla@verlab.ba; gurbetalejla@gmail.com; gurbeta.lejla@ibu.edu.ba

A. Badnjevic
e-mail: almir@verlab.ba

L. Gurbeta · A. Badnjevic
Medical Device Inspection Laboratory Verlab Ltd., Sarajevo, Bosnia and Herzegovina

Z. Džemic
Institute of Metrology of Bosnia and Herzegovina, Sarajevo, Bosnia and Herzegovina
e-mail: zijad.dzemic@met.gov.ba

L. Gurbeta
Technical Faculty, University of Bihac, Bihac, Bosnia and Herzegovina

A. Badnjevic
Faculty of Engineering, University of Sarajevo, Sarajevo, Bosnia and Herzegovina

management is still left at the levels of healthcare institution management level or by MD distributors and authorized resellers. Numerous international guidelines define how healthcare institutions should perform these health technology assessments [7], but there are some countries where these guidelines are not adopted and MD management and safety insurance is done ad-hoc. In those countries, it is necessary to implement directives of new approach MDs, like it is proposed in EU countries, Canada and USA, but in other countries this problem remains, i.e. MD post-market surveillance in terms of safety and performance is still not defined.

Measurements in other areas such as military, food, drugs and other, are regulated and controlled by country to ensure consumer confidence to provided services, fair trade and standardization of the processes. Measurement confidence is achieved by through definition of internationally accepted units of measurement, realization of units of measurement in practice, and the application of chains of traceability (linking measurements to reference standards) [8]. Ensuring traceability chain to SI unit is part of scientific metrology [9], but ensuring confidence of measurement for the purpose of fair trade, safety and performance of process is part of legal metrology [10]. Therefore, to ensure safety and performance of MDs, legal metrology framework can be created to define legal requirements regarding measurement, units of measurement, measuring devices and methods of measurement to satisfy the needs for protection of health, safety of treatment and accuracy of diagnosis [11]. Internationally, legal metrology is harmonized by the International Organization of Legal Metrology (OIML) [12]. OIML have developed a number of guidelines to assist members, particularly developing nations, to draw up appropriate legislation concerning metrology across all facets of society and guidelines where such measurements have legal impact. The organization has no legal authority to impose solutions on its members, but its recommendations are often used by member states as part of their own domestic law, so any application of metrology may fall under the scope of legal metrology if regulations are applicable to all measuring methods and instruments, and in particular if quality control is supervised by the state [12]. Therefore, competence in establishing of legal metrology framework is entrusted to relevant national authorities of the state.

The key components that are used to form Legal Metrology Framework (LMF) for MDs are MDs, metrology and international standards [11, 13–16]. As defined by International Bureau of Weights and Measures (BIPM) [9], measurement is a process of assigning numerical value to certain physical parameter and it is always an approximation of true value, therefore it is always given with stated certainty of measurement result. Unfortunately, a large gap in understanding these basic metrological concepts in healthcare is recognized [17]. Better understanding of these terms would help healthcare professionals in interpretation results and recognizing possible misleading outputs of devices. As MDs can be classified as device with function, all metrological regulations can be applied to ensure safety and accuracy of performance for devices that are already being used in real-time settings. Therefore, traceability chain for MD measurements can be established. Traceability chain [18] is established through unbroken chain of comparisons to SI unit which is achieved through calculation of measurement uncertainty for each stage in that process for certain parameter. Each stage of this process needs to be documented, and to ensure interchangeability and interoperability of the results international standards need to be adopted. In this way, all key components of legal metrology framework are connected and comprise of several stakeholders such as healthcare institutions, laboratories for inspection of safety and performance of MDs, National Metrology Institutes, regulatory bodies with primary standards for defined measurements and regulatory bodies withhold of reference standards. By establishing this traceability chain for medical measurement, final diagnosis for patient will be made based on reliable measurements and there won't be any differences in diagnosis, from medical measurement point, if diagnosis was established in different healthcare institutions using different technology [11]. On the other hand, this legal metrology system presents another approach to health technology assessment methods [12].

This paper presents results of a study conducted on MDs introduced into legal metrology framework for MDs implemented in Bosnia and Herzegovina healthcare institutions [11, 19]. The hypothesis investigated through this research is that introduced legal metrology procedures increase safety and performance characteristics of MDs and that this way of health technology assessment results in cost benefits for healthcare institutions. The hypothesis was investigated on case study of infusion pumps and perfusor used in healthcare institutions in Bosnia and Herzegovina.

2 Methods

This study covers specific data collected during three years, from January 2015 to December 2017. It was collected (measured) in healthcare institutions in Bosnia and

Herzegovina, more specifically clinical centers, hospitals and several primary healthcare institutions in Bosnia and Herzegovina. All measurements during the research were conducted by appointed laboratory. For measurement of output parameters of devices, procedures in accordance with ISO 17020 [20] Conformity assessment—Requirements for the operation of various types of bodies performing inspection were used. The study covered 850 perfusors and 700 infusion pumps. All measurements were performed using etalon Fluke Biomedical IDA 5 which was calibrated in accredited laboratory according to ISO 17025 [21] standard to ensure the measurement traceability. The inspection procedure was adopted. It consisted of visual inspection, electrical safety inspection and performance inspection. Electrical safety inspection was conducted according to IEC 60601 Medical electrical equipment [22] was used, as described in [23, 24]. For measurement of device output, all devices were inspected by output parameter—flow, and six measuring points were defined. When all parameters were measured, measurement error was calculated and referred to valid international standards and national regulative. The inspected devices were divided into two groups: accurate (A) and faulty (F). Accurate devices had acceptable output parameter error limits. Faulty devices either failed the electrical safety inspection or had output parameter error higher than acceptable. Failed visual inspection, failed electrical safety inspection or nonconformity of one output parameter were criteria to label infusion pumps as faulty. All measurement results and conformity assessments were analyzed using statistical analysis [25].

3 Results and Conclusion

Table 1 shows total number of infusion and perfusors pumps inspected through period of three years. Significant increase of number of inspected devices is recorded in the third year of the study showing that the users (healthcare institutions) have understood the benefits of independent inspection of MDs.

Also, increasing positive trend of accurate devices can be seen. These results are indication that periodical inspections of performance of MDs, in this case of perfusors and infusion pumps, are useful for detecting performance deviations. As for the traceability, it is achieved to SI unit liter, based on uncertainties of inspected device, working etalon, reference etalon, combined uncertainty for perfusor pumps is 0.7 ml, and for infusion pumps is 0.9 ml. This value was calculated following standard procedures of combining uncertainties gained through each step of calibration and taking into account device accuracy specified by the manufacturer [26]. Table 2 shows the average relative and absolute annual growth in the number of examined MDs (accurate and faulty). As it can be seen, the number of accurate MDs is growing at high rate. Based on collected data, and previous studies in the area [19, 23, 24, 26–28], a linear estimation to 2018 year can be made, Table 2. This data is extremely important, proving good indication that the legal metrology system for MD has introduced improvement in terms of safety and performance of devices that already in use in everyday healthcare activities and in very demanding environment. These periodical inspections can also serve as a good indication on whether devices are being operated in prescribed manner.

Additionally, as consequence cost benefits analysis, presented in Table 3, proved yearly savings of 50% if healthcare institutions follow legal metrology procedures compared with self-prescribed manufactures maintenance [29].

Results offer implications for adequacy of etalon calibration and preventive maintenance performed on MDs. Based on collected measurement data, web-based application with database of infusion and perfusor pumps used in healthcare institutions in Bosnia and Herzegovina was created [30].

The hypothesis introduced in this research can be confirmed since all the above presented results indicate increase of safety and accuracy of performance of these devices introduced into legal metrology framework. Yearly inspections were found to be a good indication of device handling as well since majority of malfunctions and break-downs

Table 1 Performance of inspected MDs (2015–2017)

Year	2015			2016			2017
No. of device inspected	191			350			1009
Total number 1550	Accurate			Faulty			
Year	2015	2016	2017	2015	2016	2017	
No. of devices	103	267	853	88	83	156	
Percentage (%)	*54*	*76*	*85*	*46*	*24*	*15*	

Table 2 The number of accurate devices according to the linear trend equation

	Predicted no. of inspected devices in 2018	Coefficient of determination	Representatives of the linear trend
Accurate	1189	0.923	Excellent
Faulty	102	0.715	Weaker

Source Author's calculations

Table 3 Cost analysis based on performed inspections

	No. of devices	Cost of manufacturer attest[a]	Periodical inspection[b]
Total	**1009**	201,800.00 EUR	100,900.00 EUR
Accurate	**853**	**170,600.00 EUR**	**85,300.00 EUR**
Faulty	**156**	31,200.00 EUR	15,600.00 EUR
	Savings	100,900.00 EUR	**50%**

[a]The costs of average manufacturer attest (calculated as personnel/time)
[b]The cost of periodical inspection according to prescribed minimal prices

comes from bad handling and usage of equipment which affects device performance.

Conflict of Interests Authors report no conflict of interests.

References

1. World Health Organization available at www.who.int.
2. Directive 2014/32/EU of the European Parliament and of the Council of 26 February 2014.
3. European Commission. Directive 90/385/EEC. Active implantable medical devices.
4. Directive 90/358/EEC Decision of the European Parliament of 3 April 1990.
5. MAUDE – Manufacturer and User Facility Device Experience.
6. MHRA Adverse incident reporting.
7. Herndon JH, Hwang R, Bozic KH. Healthcare technology and technology assessment. European Spine Journal. 2007;16 (8):1293–1302. https://doi.org/10.1007/s00586-007-0369-z.
8. Chappel, Sam, Opportunities and future trends in legal metrology control of measuring instruments. Organisation Internationale de Métrologie Légale (OIML) Bulletin, (2004).
9. International Bureau of Weights and Measures BIPM, Available at: http://www.bipm.org.
10. Czichos, Horst; Smith, Leslie, eds. (2011). Springer Handbook of Metrology and Testing (2nd ed.). 1.2.2 Categories of Metrology. ISBN 978-3-642-16640-2.
11. Badnjević A., Cifrek M., Magjarević R., Džemić Z. (eds) Inspection of Medical Devices for regulatory purposes. Series in Biomedical Engineering. Springer, Singapore.
12. Organisation Internationale de Métrologie Légale/International Organization of Legal Metrology Collège français de métrologie [French College of Metrology] (2006). Placko, Dominique, ed. Metrology in Industry – The Key for Quality (PDF). ISTE. 2.4.1 Scope of legal metrology. ISBN 978-1-905209-51-4.
13. Badnjevic A, Gurbeta L, Boskovic D, Dzemic Z. "Measurement in medicine – Past, present, future", Folia Medica Facultatis Medicinae Universitatis Saraeviensis Journal (2015).
14. Badnjevic A, Gurbeta L, Boskovic D, Dzemic Z. "Medical devices in legal metrology", IEEE 4th Mediterranean Conference on Embedded Computing (MECO), pp: 365–367, 14–18 June 2015, Budva, Montenegro.
15. Badnjević A., Cifrek M., Magjarević R., Džemić Z. (2018) Introduction. In: Badnjević A., Cifrek M., Magjarević R., Džemić Z. (eds) Inspection of Medical Devices. Series in Biomedical Engineering. Springer, Singapore.
16. Bošnjaković A., Badnjević A., Džemić Z. (2018) Legal Metrology System—Past, Present, Future. In: Badnjević A., Cifrek M., Magjarević R., Džemić Z. (eds) Inspection of Medical Devices. Series in Biomedical Engineering. Springer, Singapore.
17. Do Céu Ferreira, M. (2011). The role of metrology in the field of medical devices. International Journal of Metrology and Quality Engineering, 2(2), 135–140.
18. BIMP – Metrological traceability definition. Available at: https://www.bipm.org/en/bipm-services/calibrations/traceability.html.
19. E. Iadanza. Chapter: Inspection and Testing of Infusion Pumps in the book Badnjević A., Cifrek M., Magjarević R., Džemić Z. (eds) Inspection of Medical Devices for regulatory purposes. Series in Biomedical Engineering. Springer, Singapore.
20. ISO/IEC 17020:2012 Preview Conformity assessment – Requirements for the operation of various types of bodies performing inspection, Available at: www.iso.org.
21. ISO/IEC 17025:2012 Preview Conformity assessment – Requirements for the operation of various types of bodies performing calibration, Available at: www.iso.org.
22. EC 60601-1:2005 +A1:2012 Medical electrical equipment - Part 1: General requirements for basic safety and essential performance, 3rd Ed., Geneva, IEC 2012 - Medical electrical equipment – Part 2-24: Particular requirements for the safety of infusion pumps and controllers.
23. Gurbeta L., Alic B., Dzemic Z., Badnjevic A. (2017) Testing of infusion pumps in healthcare institutions in Bosnia and Herzegovina. In: Eskola H., Väisänen O., Viik J.,

Hyttinen J. (eds) EMBEC & NBC 2017. EMBEC 2017, NBC 2017. IFMBE Proceedings, 65. Springer, Singapore.

24. Gurbeta L., Alic B., Dzemic Z., Badnjevic A. (2017) Testing of dialysis machines in healthcare institutions in Bosnia and Herzegovina. In: Eskola H., Väisänen O., Viik J., Hyttinen J. (eds) EMBEC & NBC 2017. EMBEC 2017, NBC 2017. IFMBE Proceedings, 65. Springer, Singapore.

25. Eva Goldwater, Biostatistics Consulting Center, University of Massachusetts School of Public Health - Using Excel for Statistical Data Analysis – Caveats, Microsoft Excel Tool.

26. Gurbeta, L., Dzemic, Z., Bego, T., Sejdic, E., Badnjevic, A. "Testing of Anesthesia Machines and Defibrillators in Healthcare Institutions", J Med Syst (2017) 41: 133.

27. Badnjevic A, Gurbeta L, Jimenez E.R., Iadanza E. "Testing of mechanical ventilators and infant incubators in healthcare institutions" Technology and Health Care (2017). 25. 2.

28. Gurbeta L, Badnjevic A, Dzemic Z, Jimenez E.R, Jakupovic A, "Testing of therapeutic ultrasound in healthcare institutions in Bosnia and Herzegovina", 2nd EAI International Conference on Future Access Enablers of Ubiquitous and Intelligent Infrastructures.

29. Vuković D., Badnjević A., Omanović – Mikličanin E. (2018) Cost Effectiveness and Increasing of Accuracy of Medical Devices In Legal Metrology System: Case Study Bosnia and Herzegovina. In: Badnjević A., Cifrek M., Magjarević R., Džemić Z. (eds) Inspection of Medical Devices. Series in Biomedical Engineering. Springer, Singapore.

30. Gurbeta L, Badnjević A., "Inspection process of medical devices in healthcare institutions: software solution," Health Technol. (2017) Volume 7, Issue 1, pp 109–117.

31. International Organization of Legal Metrology. Available at: https://www.oiml.org/en.

Medical Devices Safety Enhancement and Performance Improvement Through a Periodic Calibration Program

A. Tavakoli Golpaygani, M. M. Movahedi, and H. Hafezi

Abstract

Today's have been seen more than 10,000 different types of medical devices in medical centers and hospitals. Physicians need better accurate medical measurements to better diagnosing diseases, monitoring patients and delivering treatments. The lack of correct and appropriate measurements will certainly have diverse effects in diagnostic and treatment procedures. In 1999, Institute of Medicine reported more than 44,000 medical error deaths annually in medical centers. Safety and performance testing of medical devices in the medical sector is a one of the key factor in improving public health. Acquiring results of some investigations demonstrate a need for new and severe regulations on periodic performance verifications especially in high-risk equipment. The metrological reliability of four high risk medical devices, Electrosurgical unit, Defibrillator, Syringe pump and Infant incubator in use some medical centers and hospitals (privates and publics) according to international and national standards were evaluated. Quantitative analysis of some parameters that impact the safety and performance represented the amount of the obtained results in some equipment are in critical range with higher values than standard limitations. Acquiring results represent a need for severe regulations on periodic performance verifications and quality control program especially in high-risk equipment. Also it is necessary to provide training courses for operating staff in the field of meterology in medicine. One of the main aim of these training courses is to present what's the critical operation parameters and how the operators can get good accuracy results on each medical devices.

1 Introduction

Nowadays, electrical devices are being employed in a wide variety of fields in medical sciences with different effects. According to importance of this matter in relation to human health, periodic verification, safety and performance testing of medical devices in the form of quality control tests and calibration are necessary. This issue has started and noticed seriously in the past decade for medical devices.

Even the best medical measuring instruments and equipment are affected by wear and tear, environmental changes and other factors, losing accuracy over time. According to importance to human health, systematic and periodic checking of test and measuring instruments according to national and international standards on a regular schedule is very essential for reliable measurements. This process has many advantages such as maximizing effectiveness and minimizing risk for patient and operator.

Safety and performance testing is required to ensure the results and reports are accurate and with the optimum level of reliability and safety of delivering treatment and diagnosis process. Accuracy of the instrument readings provides how the medical devices can generate test results which are very close to the true value. For example in many illnesses such as hypertension symptom; diagnostic process starts with only one physiological parameter (blood pressure) measurement. In the other side in many situations, initial stage of disease diagnosis starts with laboratory testing of different samples from patients (such as blood, urine, …) and finally the laboratory output is only some analytical data. These

A. Tavakoli Golpaygani
Department of Biomedical Engineering, Standard Research Institute, Karaj, Iran

M. M. Movahedi
Department of Medical Physics, Shiraz University of Medical Sciences, Shiraz, Iran

H. Hafezi (✉)
Department of Biomedical Engineering, Islamic Azad University, Tehran, Iran
e-mail: homa.h200@gmail.com

data are used in determining whether a patient has a disease or not. We expect high quality service from every clinical laboratories, which that all test results produced by all laboratories at all times should be accurate and clinically meaningful. Medical error measurements by the medical devices tend to shift the test results from the true value, so an error can cause under-detection or over-detection of diseases. Physicians decided based on the clinical results obtained from the different measurements, if the results are not correct and accurate, it might cause the physician to under-dose or over-dose the patient with incorrect prescription [1, 2].

2   Methods and Case Studies

Hospitals and medical centers must ensure that their critical medical devices are safe, accurate, reliable and operating at the required level of performance. Below, for instance the results of four investigations of electrical safety and metrological reliability for four important medical devices with a high applicability in treatment process are presented. In each of these studies more than twenty equipment with different models were used at some publics and privates hospitals were tested. A schematic of each device is presented in Fig. 1.

2.1   A Case Study on Electrosurgical Equipment

Electrosurgical units (ESU) are the most common type of electrical equipment in the operating room. Electrosurgical unit is one of the most effective surgical instruments, through better control and management of complications
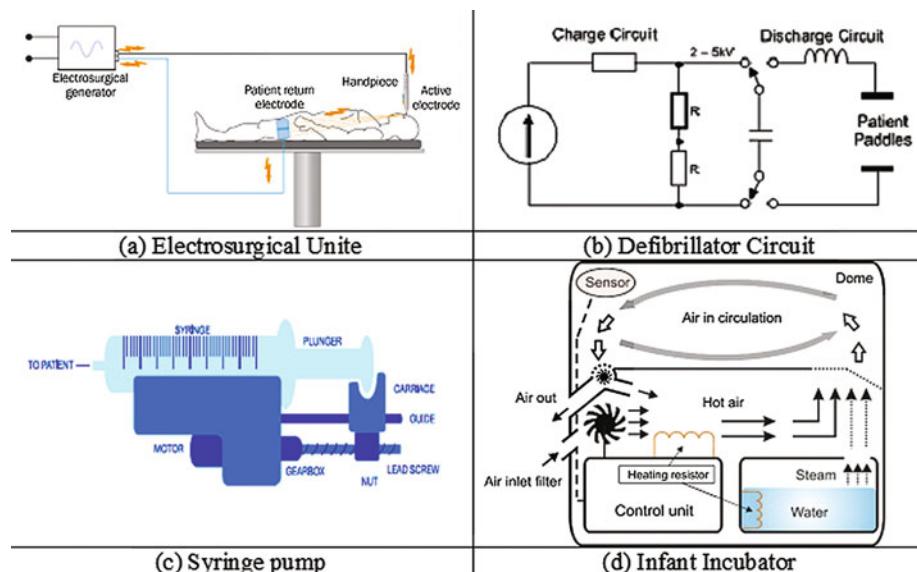
during surgery, it is improved patient safety. The principle of electrosurgery is inducing heat by high frequency electrical current. Coagulation, cutting, desiccation and fulguration of biological tissue are different effect of electrosurgery function. The correct operation of electrosurgical unit is essential to ensure patient safety. In this case study, quantitative analysis of HF leakage current measurements, showed the amount of the obtained results in many units are in critical range and have higher values than standard limitations especially in ground referenced generators.

The amount of earth resistance of hospital or medical centers has important effect on HF leakage currents of electrosurgical equipment. High earth resistance causes high HF leakage current, so the quality of earth system of medical centers has a key role in safety performance of an electrosurgical unit. The achieved results in this case study represent that HF leakage current of ground referenced generators are more than isolated generators. Therefore, the use of isolated generators in order to reach to high level of patients' safety is preferred in medical centers [3].

2.2   A Case Study on Defibrillators Equipment

Medical research and statistical analysis all over the world show generally over 135,000 people die annually following acute myocardial infarction as ventricular fibrillation (VF) or ventricular tachycardia (VT), and the only effective treatment for which is early defibrillation. Defibrillation is the application of a predefine electrical current through the myocardium, this phenomenon causes synchronous depolarization of the cardiac muscle. This action terminates the arrhythmia, and allows normal sinus rhythm to be reestablished.

Fig. 1 A schematic of medical devices in case studies

(a) Electrosurgical Unite

(b) Defibrillator Circuit

(c) Syringe pump

(d) Infant Incubator

In this case study the performance and safety testing of frequent use, manual defibrillators equipment in use at some hospitals were evaluated. Quantitative analysis of accuracy of delivered energy measurements, represented the amount of the obtained results in many units are critical and have less value over the standard limitations, especially in devices with poor quality battery. The delivered energy of defibrillators especially in frequent discharge are dependent seriously on the power battery condition. Only some devices delivered acceptable output accuracy of delivered energy and the accuracy in poor quality battery condition, after activation of discharge alarm were low.

General electrical safety evaluations for measuring the patient leakage current and patient auxiliary leakage current carried out for all of the under test devices. In some cases the amount of leakage currents were over the standard limitations. As a technical investigation, it is shown that the earth system quality of hospital has a role key in electrical safety test and it is necessary to evaluate the quality of hospital earth system [4].

2.3   A Case Study on Infusion Pumps Equipment

Infusion devices are used extensively in clinical settings and patients' homes as an essential tool for providing critical care, perioperative care and management of pain. It is estimated that 80% of hospitalised patients receive intravenous (IV) therapy. Infusion devices are used extensively in clinical settings and patients' homes as an essential tool for providing critical care and perioperative care. Because infusion pumps are frequently used to administer critical fluids, including high-risk medications, pump failures can have significant implications for patient safety. So, the reliability of infusion pumps is extremely important. In the third study, quantitative analysis of flow rate accuracy measurements, represented the amount of the obtained results in some units are critical and have inaccurate values, especially in equipment with inappropriate IV set. For example, it has been seen, the usage of a wrong or nonstandard syringe or tubing set, which is not made based on the approved technical specifications, increases the occurred error percent and the inaccuracy 10–20%. The position of drip detector is an important factor in infusion pumps. If the detector is installed near the injection location, then the error percent can increase up to 25%. The reduction of battery power is one of the effective factors on the performance of the infusion pumps. It has been seen that the low quality batteries and the batteries which are sensitive to the improper voltage could reduce the outflow rate between 10 and 30%.

The obtained results showed due to design and manufacturing technology development of the pumps, it is required to consider supplementary professional training courses for the users to enable them to use all available pump options and reduce the human errors [5].

2.4   A Case Study on Infant Incubators Equipment

Most of the neonatal or newborn babies were put in infant incubators for overcoming the distress during the post-natal care. These incubators can be defined as an optimal cabin environment with electronic equipment supplying the premature or babies with illness problems to be able to continue their vital functions. It shows more than 80% of neonatal babies are hospitalized in infant incubators and are treated there over a period of 3 days to 7 months. In the fourth study, quantitative analysis of temperature and humidity accuracy measurements and stability of temperature, represented the amount of the obtained results in some units are critical and are not in standard limitations. Stability of temperature is very important factor, some incident such as apnea can result from variations in an incubator temperature. In some devices with repairment history have been seen that selected and replaced temperature sensor didn't have required accuracy as defined specification in manufacture's documents or manual.

General electrical safety evaluations for measuring the patient leakage currents and patient auxiliary currents carried out for all of the under test devices. In some cases the amount of patient leakage currents were over the standard limitations, especially in two under test devices with recoiling of motor's fan, the patient leakage current and the noise level of fan were more than limited amounts [6].

3   Discussion

Safety and performance testing of medical devices in the medical sector is a one of the key factor in improving public health. For the best confidence in their functioning and operation, the medical devices used in medical centers and hospitals for monitoring and treatment of patients require periodic safety and performance checking. Physicians need better accurate medical measurements in order to better diagnose diseases, monitor patients and deliver treatments.

Even an error in a simple medical device such as clinical thermometers for measuring body temperature, sphygmomanometers for measuring blood pressure, weighing scales for measuring body weight etc. can cause medical decision making to shift from the normal decision. In some condition, medical errors might cause patients pain bearing permanent or temporary disability and in some state even cause death. In another view, this matter can cause increasing health costs. Increasing the number of follow-up tests, medication

and treatment for a patient who has been incorrectly diagnosed to have a certain disease will be incurred health costs.

4 Conclusion

Today's for the importance of medical measurement accuracy in diagnosis and effectiveness in treatment, calibration of medical devices to ensure quality control of them are becoming increase significantly. Testing and calibration of medical devices ensures accuracy, effectiveness and long life of them, which ultimately enables medical centers to achieve the highest degree of quality control. Acquiring results in four discussed case studies indicate a need for new and severe regulations on periodic performance verifications and medical equipment quality control and calibration. This matter is more significant in high-risks medical devices. For some electro medical devices have been seen they were imported without permission, license or any restriction and there is no product-approvals of their origin. In many hospitals, there are some deficiencies related to the operator and users of medical devices, some of them are noticed below.

1. They thought that a calibrated device works without any error for a long time and no need recalibration in defined interval.
2. The calibration certificates are kept in outside of the operating area and difficult to access for operators and users.

3. The benefits of a calibration service is unknown and in many situation is regarded as a purchased documents.

So, it is also necessary provide training courses on the fundamental of operation and performance parameters for medical staff in the field of metrology in medicine and how they can get good accuracy results especially in high risk medical devices.

Finally, it is obvious, responsibility, education, commitment, management support and sufficient resources are the strongest drivers for developing a successful culture of maintenance and calibration in technical medical management.

References

1. Khandpour R. S. "Handbook of Biomedical Instrumentation". McGraw Hill; (2014).
2. Street L. "Introduction to Biomedical Engineering technology". CRC Press; (2008).
3. Tavakoli Golpaygani A., Movahedi M.M. and Reza M. "A Study on Performance and Safety Tests of Electrosurgical Equipment". Journal of Biomedical Physics and Engineering; (2016).
4. Tavakoli Golpaygani A., Movahedi M.M., Reza M. "A Study on Performance and Safety Tests of Defibrillators Equipment" Journal of Biomedical Physics and Engineering; (2016).
5. Tavakoli Golpaygani A., Movahedi M.M., Reza Mand Hassani K. "A study on performance and safety test of infusion pump devices" Journal of Biomedical Research; (2017).
6. Tavakoli Golpaygani A., Movahedi M.M. and Reza M. "A study on performance and safety test of infant incubators devices" Journal of Biomedical Research; (2018).

Legal Metrology Procedures for Increasing Safety and Performance Characteristics with Cost Benefits Analysis: Case Study Dialysis Machines

Lejla Gurbeta, Dijana Vukovic, Zijad Džemic, and Almir Badnjevic

Abstract

The objective of this paper was to increase safety and performance characteristics with cost benefits of medical devices (MDs) by introducing legal metrology procedures. This should directly improve the quality of patient safety and re-liability of treatment. This study is designed to cover 1100 dialysis machines used in public and private healthcare institutions, during a period of three years. Testing procedures were carried out according to international standards and legal metrology legislative procedures in Bosnia and Herzegovina. The results show that the average rate of faulty devices during three years testing period is 36.33% and should either have its results be verified, or the device removed from use or scheduled for corrective maintenance. Additionally, cost benefits analysis shows yearly savings of 30% if healthcare institutions follow legal metrology procedures compared with unnecessary manufactures attests. Research emphasizes importance of independent safety and performance inspections and gives recommendations for the frequency of inspection based on measurements. Results offer implications for adequacy of preventive and corrective maintenance performed in healthcare institutions. Based on collected measurement data, web-based application with database of dialysis machines used in healthcare institutions in Bosnia and Herzegovina is created. Thus, legal metrology procedures enabled establishing traceability chain for this type of MDs.

L. Gurbeta (✉) · A. Badnjevic
Faculty of Engineering and Natural Sciences, Genetics and Bioengineering Department, International Burch University, Sarajevo, Bosnia and Herzegovina
e-mail: lejla@verlab.ba; gurbetalejla@gmail.com; gurbeta.lejla@ibu.edu.ba

A. Badnjevic
e-mail: almir@verlab.ba

L. Gurbeta · A. Badnjevic
Medical Device Inspection Laboratory Verlab Ltd., Sarajevo, Bosnia and Herzegovina

L. Gurbeta
Technical Faculty, University of Bihac, Bihac, Bosnia and Herzegovina

D. Vukovic
Faculty of Economics, University of Bihac, Bihac, Bosnia and Herzegovina

Z. Džemic
Institute of Metrology of Bosnia and Herzegovina, Sarajevo, Bosnia and Herzegovina
e-mail: zijad.dzemic@met.gov.ba

A. Badnjevic
Faculty of Engineering, University of Sarajevo, Sarajevo, Bosnia and Herzegovina

1 Introduction

A health technology is defined as an intervention that may be used to promote health, prevent, diagnose or treat acute or chronic disease, or for rehabilitation [1]. Because of its complexity, in the past years, healthcare has become a subject of interest for regulatory bodies resulting in many policies. Despite the complexity, each healthcare system relies on basic principles—measurement of physical parameters needed for medical diagnosis and treatment. Measurements are acquired using various health technology, i.e. medical devices (MDs), so because of their widespread used, MDs present huge liability in healthcare system. Every measurement acquired with these devices represents an evidence in the overall path leading to final diagnosis and treatment of patients. Because of the variety of MDs available on the market nowadays and given the fact that these devices are classified as products of special importance for retaining the health of many people, special attention should be given to evaluation of safety and performance [2].

Therefore, common polices that regulate patient safety, clinical diagnosis interpretability and reliability have been investigated. The purpose of these policies is to ensure that appropriate and effective health technology is being used during the diagnosis and treatment of patient. These policies are applied through different health technology assessment (HTA) methods.

As it is defined by World Health Organization (WHO), HTA is a multidisciplinary process to evaluate the social, economic, organizational and ethical issues of a health intervention or health technology [2]. Also, it represents a way to strengthen evidence regarding clinical effectiveness, safety, cost-effectiveness and, and when broadly applied, includes social, ethical, and legal aspects of the use of health technologies [3]. HTA brings together all stakeholder in healthcare system, from patients and their families, healthcare professionals, management boards, manufacturers and others. This topic is very active internationally and it is continuously evolving by the need to support management, clinical, and policy decisions. There are several international agencies supporting the advancement of HTA on the global stage. Health Technology Assessment international (HTAi) [4] and the International Network of Agencies in Health Technology Assessment (INAHTA) [1] have demonstrated commitment to advance and collaborate on health technology assessment with WHO and any country or community that is interested. Under the HTA, different aspects can be defined according to life-cycle of MD. The clinical effectiveness of the device, already in use in everyday activities can be ensured by safe and accurate performance of MD. Numerous international guidelines define how healthcare institutions should perform health technology assessments [5, 6], but there are still countries where HTA has not been adopted and MD management and safety insurance are done ad hoc. In those countries, it is necessary to implement methods to ensure that HTA is done periodically. This periodical assessment of performance of MDs that are already in the use will create the internationally reliable, effective and safe healthcare system.

This paper presents the effects of introducing health technology method in healthcare institutions in Bosnia and Herzegovina. The mentioned health technology assessment method is implemented through legal metrology framework and ensures safety and performance of MDs used in healthcare institutions in Bosnia and Herzegovina. The social and economical impact of introducing these methods in healthcare is presented through dialysis machine case study.

2 Methods

2.1 Legal Metrology Procedure

The key component of the health technology assessment method introduced into healthcare system in Bosnia and Herzegovina through legal metrology system are MDs, metrology and international standards [7–10]. This framework is introduced for the purpose of health technology assessment. Since MDs can be observed as electrical systems with measuring function, metrological concepts can be applied, so MD assessment can be done periodically observing its safety and performance indicators. As performance indicators, patient related parameters need to be taken as relevant. The assessment of safety and performance of MD is done through unbroken chain of comparisons. The hierarchy of stakeholders involved in the process is shown in the Fig. 1.

According to the presented figure, to ensure safety and effectiveness of performance of MDs an independent inspection body is needed. This regulatory body is equipped with sophisticated equipment needed to measure patient related parameters defined based on the group of MDs. Since this is inspection body it needs to be accredited by the ISO 17020 [11]. Any application of metrology in one country is regulated by National Institute of Metrology (NMI). The safety and performance effectiveness are established through traceability chain comprising of testing of MD performance with working etalons, calibrations of working etalons, documentation and laboratory competence. The calibration of working etalons needs to be conducted by ISO 17025 [12] accredited laboratories, and through this re-calibration, traceability to primary standards, SI units is achieved [13].

For the performance inspection during this research, measurement points of conductivity and temperature. All measurements are performed using etalon, Messa Labs 90 XL [14] with appropriate module for conductivity and temperature that is calibrated in laboratory according to ISO 17025 to ensure the traceability chain. When all parameters are measured, measurement error were calculated and assessment was done [15]. Devices were classified into two groups: accurate (A) and faulty (F), based on the measured data. By establishing this traceability chain for medical measurement, final diagnosis for patient is made based on reliable measurements and there isn't any differences in diagnosis, from medical measurement point, if diagnosis is established in different healthcare institutions using different technology.
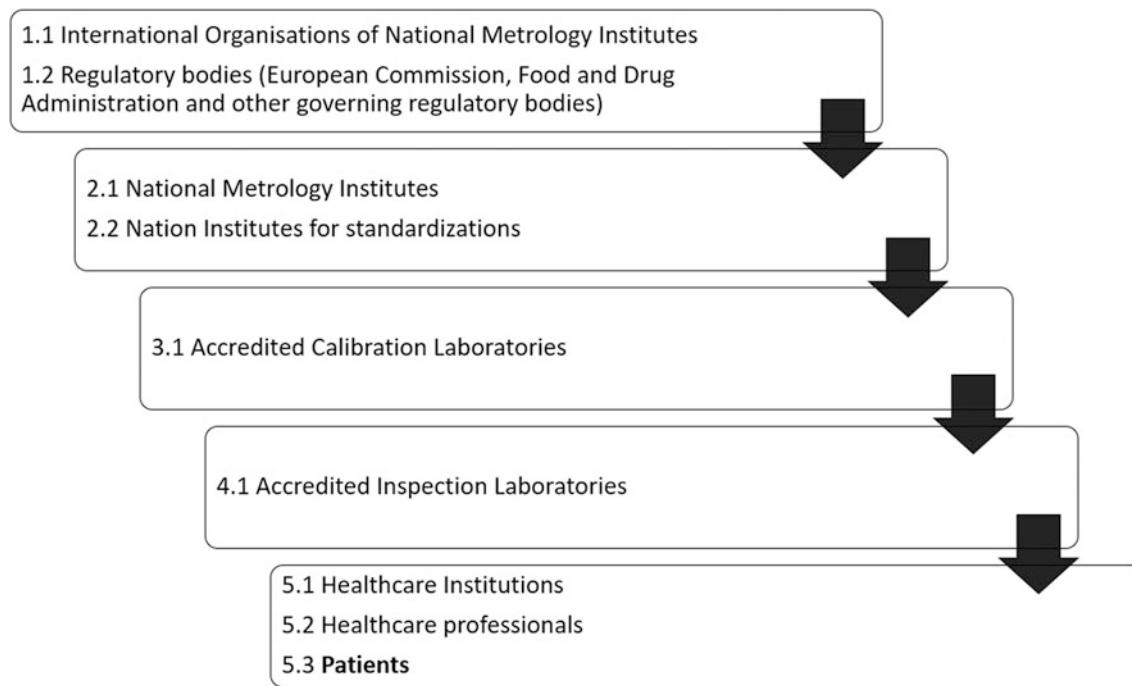
Fig. 1 Hierarchy chain for adopted HTA method

2.2 Dataset

This study presents the result of analysis of specific data collected during three years, from January 2015 to December 2017. The data was collected in healthcare institutions in Bosnia and Herzegovina, more specifically dialysis centers in Bosnia and Herzegovina. Overall data was acquired by appointed regulatory body in Bosnia and Herzegovina, MD inspection laboratory and stored in database [16–18]. All data were processed using basic statistical tools [19]. As mentioned before, data consisted of device identification and measurement parameters of temperature and conductivity.

The inspection procedure consists of (a) visual inspection and (b) electrical safety inspection and (c) performance inspection—inspection of measurement error. The inspected devices were classified to accurate (A) or faulty (F) based on the measurement results. Accurate devices satisfy electrical safety inspection and comply with acceptable error limits. Faulty devices either do not pass electrical safety inspection or have output error higher than the referent values defined in applicable regulatory documents [20, 21]. Safety inspection is conducted according to IEC 60601 [20]. For electrical safety inspection working etalon Fluke Biomedical ESA 620 was used.

3 Results and Conclusion

Table 1 shows total number of dialysis machines inspected through period of three years. Significant increase of number of inspected devices is recorded in the third year of the study showing that the users (healthcare institutions) have understood the benefits of independent inspection of MDs. The results show that the average rate of faulty devices during three years testing period is 36.33% and should either have its results be tested, or the device removed from use or scheduled for corrective maintenance.

Increasing positive trend of accurate devices can be seen. The grow rate of accurate devices in the period 2015–2016 is 15%, while during 2016–2017 the rate of accurate dialysis machines has been continuous with reported increase of 2%. These results are indication that adopted health technology assessment, in this case of dialysis machines, are useful for detecting performance deviations.

Table 2 shows the average relative and absolute annual growth in the number of examined MDs (accurate and faulty). Based on collected data, and previous studies in the area [22–27], linear estimation to 2018 year can be made, Table 2. As it can be seen, the number of accurate MDs is growing at high rate. This data is extremely important,

Table 1 Performance of inspected MDs (2015–2017)

Year	**2015**			**2016**			**2017**	
No. of device inspected	264			389			447	
Total number of devices 1100	Accurate				Faulty			
Year	**2015**	**2016**	**2017**	**2015**	**2016**	**2017**		
No. of devices inspected	139	266	314	125	123	133		
Percentage (%)	*53*	*68*	*70*	*47*	*32*	*30*		

Table 2 The number of accurate and faulty devices according to the linear trend equation prediction

	2018	Coefficient of determination	Representatives of the linear trend
Accurate	940	0.917	Excellent
Faulty	440	0.628	Weak
Total	1380	Increase of 25% in respect to 3-year period	

Source Author's calculations

Table 3 Cost analysis based on performed inspections

	No. of devices	Cost of manufacturer attest[a]	Periodical inspection[b]
Total	**1100**	253,000.00 EUR	176,000.00 EUR
Accurate	**719**	**163,990.00 EUR**	**115,040.00 EUR**
Faulty	381	87,630.00 EUR	60,960.00 EUR
Savings			**30%**

[a]The costs of average manufacturer attest (calculated as personnel/time)
[b]The cost of periodical inspection according to prescribed minimal prices

serving as indication that the legal metrology system for MD is contributing to improvement of safety and performance of devices that are already in use in healthcare environment.

Additionally, as consequence cost benefits analysis, presented in Table 3, proved yearly savings of 30% if healthcare institutions follow legal metrology procedures compared with self-prescribed manufactures maintenance [27].

Also, the goal of analysis was to determine whether the proportions of the accurate MDs by the observed years and the proportion of faulty MDs by the observed years differ by accident or statistically significant. For that purpose, hi-square test was used. Results show that although there is a favorable trend of increasing the proportion of the accurate devices the differences between the indicated proportions are not statistically significant while differences between faulty devices over years are statistically significant. Results offer implications for adequacy of preventive and corrective maintenance performed in healthcare institutions and also indication about the conditions that devices are used in (appropriate usage of device or not).

Conflict of Interests Authors report no conflict of interests.

References

1. International Network of Agencies in Health Technology Assessment - INAHTA World Health Organization available at www.who.int
2. Luce BR, et al. (2010). "EBM, HTA, and CER: clearing the confusion". Milbank Q. 88
3. Health Technology Assessment international, Available at: https://www.htai.org/
4. Herndon JH, Hwang R, Bozic KH. Healthcare technology and technology assessment. European Spine Journal. 2007;16 (8):1293–1302. https://doi.org/10.1007/s00586-007-0369-z.
5. Badnjević A., Cifrek M., Magjarević R., Džemić Z. (eds) Inspection of medical devices for regulatory purposes. Series in Biomedical Engineering. Springer, Singapore
6. E. Iadanza., Y. Diro. Clinical Engineering Handbook - Biomedical Engineering, 2004.
7. Badnjevic A, Gurbeta L, Boskovic D, Dzemic Z. "Measurement in medicine – Past, present, future", Folia Medica Facultatis Medicinae Universitatis Saraeviensis Journal (2015)
8. Badnjevic A, Gurbeta L, Boskovic D, Dzemic Z. "Medical devices in legal metrology", IEEE 4th Mediterranean Conference on Embedded Computing (MECO), pp: 365–367
9. Badnjević A., Cifrek M., Magjarević R., Džemić Z. (2018) Introduction. In: Badnjević A., Cifrek M., Magjarević R., Džemić Z. (eds) Inspection of medical devices for regulatory purposes. Series in Biomedical Engineering. Springer, Singapore

10. ISO/IEC 17020:2012 Preview Conformity assessment – Requirements for the operation of various types of bodies performing inspection, Available at: www.iso.org
11. ISO/IEC 17025:2012 Preview Conformity assessment – Requirements for the operation of various types of bodies performing calibration, Available at: www.iso.org
12. Chappel, Sam, Opportunities and future trends in legal metrology control of measuring instruments. Organisation Internationale de Métrologie Légale (OIML) Bulletin, (2004).
13. XL™ Meter, User's Guide at www.mesalabs.com
14. D. Boskovic. Chapter: Dialysis machines in the book: Inspection of medical devices for regulatory purposes. Series in Biomedical Engineering. Springer, Singapore
15. Gurbeta L, Badnjević A., "Inspection process of medical devices in healthcare institutions: software solution," Health Technol. (2017) Volume 7, Issue 1, pp 109–117
16. Gurbeta L, Badnjevic A, Pinjo N, Ljumic F, "Software Package for Tracking Status of Inspection Dates and Reports of Medical Devices in Healthcare Institutions of Bosnia and Herzegovina", XXV International Conference on Information, Communication and Automation Technologies (IEEE ICAT), pp:1–5, 29–31 October 2015
17. Gurbeta L, Badnjevic A, Sejdinovic D, Alic B, Abd El-Ilah L, Zunic E, "Software Solution for Tracking Inspection Processes of Medical Devices from Legal Metrology System", XIV Mediterranean Conference on Medical and Biological Engineering and Computing
18. Eva Goldwater, Biostatistics Consulting Center, University of Massachusetts School of Public Health - Using Excel for Statistical Data Analysis – Caveats, Microsoft Excel Tool.
19. Official Gazette of Bosnia and Herzegovina No. 75/14
20. IEC 60601-1:2005 +A1:2012 Medical electrical equipment - Part 1: General requirements for basic safety and essential performance, 3rd Ed., Geneva, IEC 2012 and IEC 60601-2-16 Medical electrical equipment - Part 2–16: Particular requirements for basic safety and essential performance of haemodialysis, haemodiafiltration and haemofiltration equipment
21. L. Gurbeta, S. Izetbegović, A. Badnjević-Čengić, Neonatal and Peadiatric Incubators in the book: Inspection of medical devices for regulatory purposes., A. Badnjevic, M. Cifrek, R. Magjarevic, Z. Dzemic
22. Gurbeta L., Alic B., Dzemic Z., Badnjevic A. (2017) Testing of infusion pumps in healthcare institutions in Bosnia and Herzegovina. In: Eskola H., Väisänen O., Viik J., Hyttinen J. (eds) EMBEC & NBC 2017. EMBEC 2017, NBC 2017. IFMBE Proceedings, 65. Springer
23. Gurbeta L., Alic B., Dzemic Z., Badnjevic A. (2017) Testing of dialysis machines in healthcare institutions in Bosnia and Herzegovina. In: Eskola H., Väisänen O., Viik J., Hyttinen J. (eds) EMBEC & NBC 2017. EMBEC 2017, NBC 2017. IFMBE Proceedings, 65.
24. Badnjevic A, Gurbeta L, Jimenez E.R., Iadanza E. „Testing of mechanical ventilators and infant incubators in healthcare institutions "Technology and Health Care (2017). 25. 2,
25. Gurbeta, L., Dzemic, Z., Bego, T., Sejdic, E., Badnjevic, A. "Testing of Anesthesia Machines and Defibrillators in Healthcare Institutions", J Med Syst (2017) 41: 133
26. Gurbeta L, Badnjevic A, Dzemic Z, Jimenez E.R, Jakupovic A, "Testing of therapeutic ultrasound in healthcare institutions in Bosnia and Herzegovina", 2nd EAI International Conference on Future Access Enablers of Ubiquitous and Intelligent Infrastructures
27. Vuković D., Badnjević A., Omanović – Mikličanin E. (2018) Cost Effectiveness and Increasing of Accuracy of Medical Devices in Legal Metrology System: Case Study Bosnia and Herzegovina. In: Badnjević A., Cifrek M., Magjarević R., Džemić Z. (eds Inspection of medical devices for regulatory purposes. Series in Biomedical Engineering. Springer, Singapore

In Vivo Dosimetry in Total Body Irradiation

Eilen Llanes Veiga, Rodolfo Alfonso Laguardia,
and Roberto Caballero Pinelo

Abstract

Total Body Irradiation (TBI) is a radiotherapy technique that consists of irradiating homogeneously the whole patients body and it is characterized by extended source to surface distances and the use of large irradiation fields. The limitations of the available input data and inherent problems with the calculation procedures make it very difficult to accurately determine the dose distributions in TBI. For these reasons, it is highly recommended to use In Vivo Dosimetry (IVD), to guarantee the quality of TBI treatments as a direct measurement of the delivered dose. An IVD QA system was implemented based on semiconductor diodes and radiochromic films. For the commissioning of the system, both detector types were calibrated independently. This guarantees the traceability of the measurements. An assessment was made on the sources of uncertainties. A tolerance level of $\pm 10\%$ was established for the combined contribution of both computational and experimental uncertainties. An experiment to a phantom was carried out to simulate a clinical TBI procedure. In this way, the calibration of the dosimetry system was corroborated. Finally, the IVD system was applied in TBI of three real patients. The discrepancies obtained between the prescribed and measured doses were below the established tolerance level of $\pm 10\%$.

E. Llanes Veiga (✉)
Institute of Oncology and Radiobiology, La Habana, Cuba
e-mail: ellanes2307@gmail.com

R. A. Laguardia
Superior Institute of Technologies and Applied Sciences,
La Habana, Cuba

R. C. Pinelo
"Hermanos Ameijeiras" Hospital, La Habana, Cuba

1 Introduction

Total Body Irradiation (TBI) is a radiotherapeutic treatment that consists of irradiating the patient's body volume in a homogeneous way. The conditions for total body irradiation are distinguished by large source to surface distance (SSD) and large fields of irradiation [1]. The limitations of the available input data and problems inherent to the calculation procedures make it difficult to accurately determine the distribution of doses in TBI when using the majority of the planning systems available in radiotherapy services. In addition, variations in the patient's set-up can modify the dose distributions dramatically. For these reasons, it is necessary to implement an in vivo dosimetry (DIV) technique for the verification of the dose.

In vivo dosimetry is a widely recognized method for patient-specific quality control of the absolute doses administered in radiotherapy treatments. The IVD allows a comprehensive verification of the planning process, from the calculation of the dose, the set-up of the patient and the treatment delivery. This procedure redundantly guarantees that the absolute doses calculated by the treatment plan are correct, and simultaneously that the parameters of the fields have been properly adopted by the unit.

2 Materials and Methods

At the moment, the "Hermanos Ameijeiras" hospital is the only center in Cuba where TBI is carried out. This traditional technique is adapted to the conditions available in the hospital. A photon beam generated by a Cobalt-60 unit, model Theratron Elite 80, at an SSD of 350 cm is used to irradiate the patient. To ensure a horizontal beam, the gantry of the unit is set to 90°. The collimator is set 45°, for a diagonal arrangement. This configuration allows a radiation field size at the patient's distance of up to 2 m.

Ten grays (10 Gy) is prescribed to the patient's midline and the dose to the lungs is restricted to 6 Gy. The dose is fractionated into two sections. In the first section, the lungs are protected with lead blocks to ensure that the dose is reduced to the tolerance levels specified by the radiation oncologist; these blocks are previously customized to the specific patient. Two AP and PA fields are delivered each section with and without the blocks.

A feasibility study conducted at the department, concluded that diodes (VivoLog semiconductor probes designed for Co-60 beams) and radiochromic films are suitable for the purpose of this work.

Four E5 diode probes were attached to a PTW MULTIDOS electrometer by a junction box. The PTW "VivoSoft" software was used to process the measurements. Due to the fact that the diodes had been in use for more than ten years and were integrated into a different measurement system, it was necessary to carry out acceptance tests that would ensure the reproducibility of the measurements. As part of the acceptance process, the stability of the post-irradiation signal, the linearity of the dose response and the intrinsic accuracy were analyzed.

Two calibrations coefficients under TBI conditions for both, entrance and exit dose measurement, were determine for each diode. In addition, due to the energetic dependence of the diodes [2, 3], it was necessary to calculate a correction factor for the presence of blocking. It was not necessary to calculate other factors since the other conditions such as field size and surface source distance remain constant.

The radiochromic films used are of EBT 3 type. Small pieces of 2 cm × 2.5 cm were cut, where the largest dimension of the piece coincides with the vertical direction of the film. A support made of PMMA slabs was designed to hold the EBT3 films (Fig. 1), this holder ensures the electronic equilibrium for Co-60, and allows to adequately accommodate the films on the patient, without damaging or contaminating them. In this way, adequate reproducibility in the dosimetric response of the films is ensured.

To simulate the patient's body, 3 different phantoms were coupled as shown in Fig. 2. The head region was represented by a fixed depth IBA acrylic phantom; the thorax was simulated by RW3 (water equivalent) slabs and the pelvis was imitated by an in-house wax phantom.

2.1 Test Case

Before applying the in vivo dosimetry system in real patients, an end-to-end test was designed to check the reliability of the system proposed in order to assess in practice all the factors involved in the dosimetry process, excluding the intrinsic aspects.

A TBI treatment with typical doses was planned for the proposed phantom and the treatment was delivered under normal conditions. The diodes and films were placed as shown in Fig. 2 to measure the entrance dose. To measure the exit dose, a similar set of detectors were placed in the same points, but on the back of the phantom.
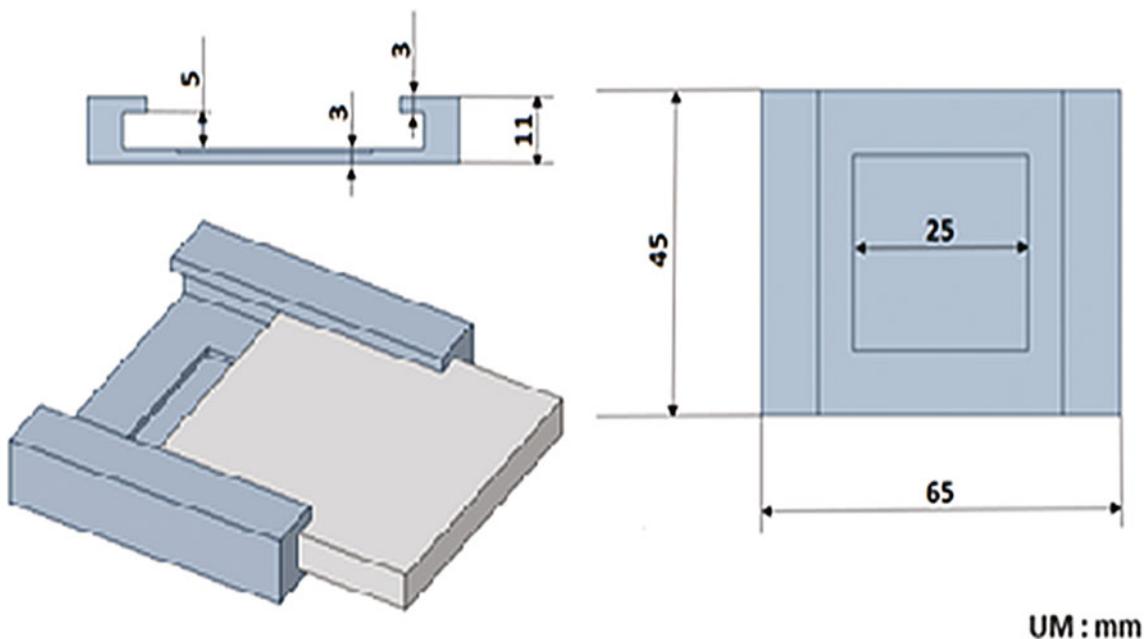
Fig. 1 Support for film used in IVD
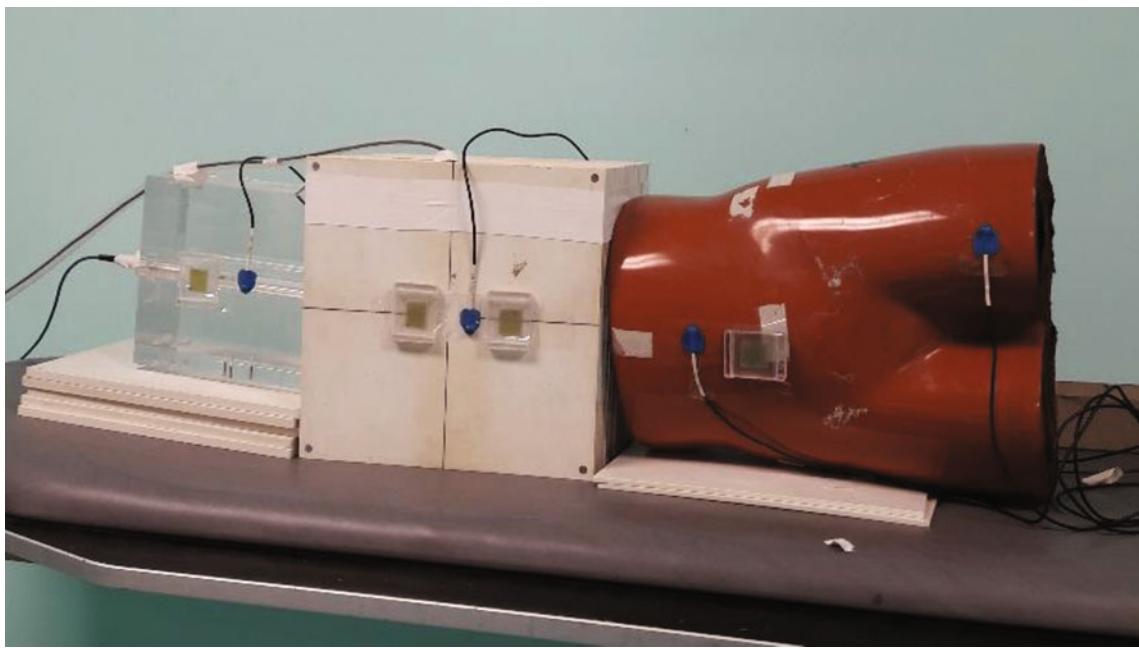
Fig. 2 TBI Phantom and detectors used in the IVD end-to-end test case for the TBI procedure. (1) Fixed depth IBA acrylic phantom, the thorax was mimic with (2) RW3 (water equivalent) slabs and the pelvis was simulated using (3) an in-house wax phantom

2.2 Measurements in Patients

Once the IVD system was verified through the test case, it was applied to direct measurements in real TBI patients. The first two cases were verified using only the diodes and in the third patient, the EBT films were added. This was due to the fact that, at the time of the first cases, the calibration of the films was not yet available.

The points selected to measure the entrance and the exit dose with diodes were: behind the lung block and the pelvic region.

The films were added with the aim of measuring other points of interest such as the head, the pelvis, and extremities.

3 Results

As a result of the acceptance tests of the diodes, it was obtained that the highest variation of the post-irradiation signal for the diode was 0.09%, below the 0.1% recommended by the European Society of Therapeutic Radiology and Oncology [1].

In order to demonstrate the linearity of the diodes response with the dose, a series of irradiation was performed. The linear regression coefficient obtained for the 4 diodes was equal to 1.0. The repeatability of the signal for all diode was within a standard deviation of 0.07%, well below the 1% tolerance recommended by the ESTRO [2, 4].

In general, the semiconductor probes responded in real patients accordingly to the acceptance tests carried out, demonstrating that they are in perfect conditions for their use.

As for the calibration process, the coefficients are between -9×10^6 and -5×10^6 Gy/c, which shows the consistency of their response. The correction factor for the doses measured behind the block was found to be 0.538, this indicates that the response is overestimated by around 50%, due to the energy response dependence.

The entrance dose calibration curve for the EBT3 films was established. No correction was considered for film measurements, since its tissue equivalent composition [6].

3.1 Test Case

The results showed that the doses measured by the EBT3 films along the central axis are in agreement with those measured by the diodes, the average discrepancy value is around -2.7%. A better match between planned and measured doses were obtained with the films, but the differences are within the standard uncertainties of the measuring systems; therefore, one cannot infer an advantage of one detector type over the other for this application.

The greatest discrepancies of the planned doses with the measured ones are found in the most extreme points of the phantom, with an average value of 5.5% which can be associated to the smaller scatter contribution in these areas.

In general, the discrepancies of the measured doses with respect to the prescribed dose are less than 10%. In the case of TBI, it is very difficult to deliver a homogeneous dose for all the body due to human anatomy irregularities and the acceptance is recommended within this limit.

Based on the analysis of the results, it may be recommended to use the diodes for the measurements of the entrance and exit doses at the points of greatest risk and to use the films only for entrance doses as a way to monitor the homogeneity of the dose distribution. An action level of 10% was established as the acceptance criterion of the weighted average discrepancy between prescribed and measured dose to the midline.

3.2 Measurements in Patients

As mentioned before, the first patients were only measured with diodes, the discrepancies obtained are found in Table 1. It is considered that the main reason of dose discrepancies is associated to patient set up. Due to the irregular anatomy of the patient one cannot guarantee a source to surface distance (SSD) of 350 cm for all measuring points, which is assumed in the planning system.

In the treatment planning system, the irradiation time for the blocked field depends on the thickness of the lung. This value is calculated by the planning system as function of the AP diameter of the patient. In real patients any deviation of the anatomy from this assumed proportionality could lead to a relatively high discrepancy as shown in Table 1.

The discrepancy between the weighted average dose and the prescribed dose is within the tolerance level stated above.

As an example, a case that combines measurements with both types of detectors and the resulting discrepancies are shown in Table 2.

It can be observed that the discrepancies vary depending on the location. The main sources of uncertainties are associated with the set up and variation of the anterior-posterior diameter in the different measurement points, since a weighted average of this dimension is used by the planning system for the calculation.

As mentioned before, the action level is established by comparison with the weighted average of discrepancies. By increasing the number of measurement points, better statistics are affordable, reducing random uncertainties. For this example, a weighted average of the discrepancies of 2.2% was obtained, that is within the established tolerance level of $\pm 10\%$.

4 Conclusions

In the present work, a IVD system based on silicon diodes and radiochromic films was implemented for the TBI treatments carried out in a Theratron Elite 80 cobalt therapy unit, as a tool for quality assurance patient-specific.

Based on the results of the end-to-end test case and the patients evaluated, it could be concluded that the developed and implemented IVD system is an effective tool for the detection of gross errors or inaccuracies greater than 10% in the dose calculations for TBI. For the moment, with the calibration coefficients and correction factors established in this work, it is advisable to implement the TBI IVD on the basis of entrance and exit doses only with diodes, while film measurements should be used for evaluating uniformity of the dose.

It can be concluded, therefore, that an action level of $\pm 10\%$ discrepancy between the doses calculated by the computerized planning system and the measurements during IVD can be a realistic value for practical purposes in the clinical routine. The systematization of the IVD in the patients to be treated with the TBI will make it possible to determine if it is necessary to relax or make this proposed action level more rigorous.

It is worth noting that the average discrepancies obtained in all the patients evaluated were within the established

Table 1 Discrepancies in % between the measured dose with diodes and the prescribed midline dose in the patients

Patient	Pelvis	Lung	Average
A	−15.04	5.36	−2.8
B	−13.5	2.4	−3.9

Table 2 Discrepancies in % between the measured dose with diodes and EBT and the prescribed midline dose in the patient

Patient C	Heads	Thorax	Lung	Abdomen	Pelvis	Thigh	Leg	Average
Diode			−8.4		−3.2			
EST3	3.9	−0.4		16.3		14.0	9.8	
Average								2.2

tolerance levels, demonstrating the good dosimetry quality of the total body irradiation treatments offered at the "Hermanos Ameijeiras" hospital.

Conflict of Interests The authors declare that they have no conflict of interest.

References

1. D. Beltrán, «Irradiacion Corporal Total (TBI),» de Fundación Grupo IMO, Murcia, 2015.

2. E. Y. (Chair), «DIODE IN VIVO DOSIMETRY FOR PATIENTS RECEIVING EXTERNAL BEAM RADIATION THERAPY,» American Association of Physicists in Medicine by Medical Physics, 2005.

3. D. Huyskens, «Practical Guidelines for the Implementation of in vivo Dosimetry with Diodes in External radiotherapy with Photon Beams,» Booklet, nº 5, 2011.

4. AAPM, «Diode In Vivo Dosimetry For patients receiving external beam radiation therapy,» United States of America, February 2005.

5. J. Van Dan y G. Marinello, «METHODS FOR IN VIVO DOSIMETRY IN EXTERNAL RADIOTHERAPY,» ESTRO, Brussels, 2006.

6. R. Arráns, H. Miras, M. Ortiz-Seidel y J. Terrón, Dosimetría con películas radiocrómicas, Sevilla: Servicio de Radiofísica. Hospital Virgen Macarena, 2009.

Part II
Accreditation and Certification

Documentation Template for the Usability Engineering Process for Medical Devices

Daniel Scherer and Francisco Ferreira Gouveia Filho

Abstract

Introduction: Medical device regulatory processes are currently based on technical (ISO IEC 62366:2015) and regulatory standards (IEC ISO 60601-1-6:2015), which provide an international standard to be applied in evaluating devices and their documentation. However, the lack of standardization in the usability engineering processes used by the manufacturers, and the absence of pre-established metrics for such processes are constant problems in the medical device universe, particularly hindering the evaluation processes. It was verified that the current norms are insufficient to guarantee good usability engineering processes, even with the existence of good usability practices in the literature. Objective: This paper presents an analysis of the requirements contained in current standards and proposes a documentation model for usability engineering of medical devices, from the presentation of some techniques that are used in the process of device development. Method: This work is based on literature reviews to identify the state of the art in usability engineering; analysis of current standards, to verify what the regulatory requirements are, and how to comply with them; comparative studies with existing documentation to identify strengths and weaknesses in documentation processes; and elaboration of documentation prototypes. Results: From these results, it was possible to prepare a template document with all the points required by the current norms. Appropriate techniques were also listed for the accomplishment of some stages of the process, creating greater rigidity in the definition of the parameters of the documentation.

1 Introduction

In medical practices, there is a growing use of health devices for both observation and treatment of patients. As a result, there is a growing concern about errors in use caused by inadequate usability of devices, since many of them are developed without the application of appropriate usability engineering processes, which makes them difficult to learn, non-intuitive, and complex. The fact that less-qualified users (including patients themselves) are becoming users only exacerbates these concerns.

The current technical standard for usability in medical devices is NBR 62366:2015 [9], which deals with usability engineering processes. However, although it is the norm to be followed regarding the application of Usability Engineering for medical devices, it does not detail all the procedures required for the execution of the tasks. However, this one also does not detail the required procedures completely, which opens the door to different interpretations of the requirements contained in the standards and allows possible failures in usability engineering processes.

The development of a usability engineering process for a health device requires a lot of effort; although many organizations deal with it by treating it as "common sense". In such a process, what is intended is a reasonable usability, which minimizes usage errors and minimizes the risks associated with use.

Given this, this work aims to develop a usability engineering documentation template for medical devices that meets the minimum requirements of current standards, providing a common standard that can be used by pharmacists and regulatory bodies.

D. Scherer (✉) · F. F. Gouveia Filho
Nucleus of Strategic Technologies in Health, State University of Paraiba, Campina Grande, PB 58429-500, Brazil
e-mail: professorscherer@gmail.com

2   Methodology

A bibliographical review of similar works was carried out to verify which works are relevant to this research, to check positive and negative points of them, and to obtain a knowledge of the current scenario of Usability Engineering for medical devices. We did research in two publications databases: PubMed and JIMR, where the key words used were: usability engineering, usability, and medical device.

Study of current standards was made based on the current norms of usability for medical devices: NBR 62366, essential norm for the development of a good usability engineering [9]; ISO 14971, once NBR 62366 refers to ISO 14971 for performing some stages of its process [1, 9]; and ISO 9241, which does not specifically deal with health devices, but has principles that prove effective in evaluating system usability [7].

Comparative study of examples of documentation of two examples of usability documentation was carried out: an example of NBR 62366 (digital thermometer [9]), and the documentation of the Generic Infusion Pump (GIP) [5]. Based on this, a comparative study was carried out to verify the coverage of each example according to the normative requirements, which aspects were not yet reached, and which aspects should be added at work.

Based on the studies carried out, a proposal for a documentation model was prepared, which meets the specifications of the standard.

3   Literature Review

With the searches, the following points were identified:

- There are techniques of usability evaluation already validated by previous work, which may be considered good usability engineering practices [2, 3, 6, 8, 12];
- The same type of medical device may have its usability validated by different techniques [2, 3, 6, 8, 12];
- There are proposals to standardize using techniques previously seen and incorporates m others, proposing the creation of frameworks [6, 12], and there are proposals that are based on international standards to establish acceptance criteria [8];
- By using techniques already validated and considered as good practices, but focusing on medical devices, it is possible to circumvent some problems already known in the use of such techniques [2, 3];

Through reading these materials [4, 10, 11], we have identified several usability engineering techniques that can be used in development processes.

With the revision and analysis of the current norms, it was possible to identify the following points: (i) the standards contain requirements that are necessary for the compliance of the process with the regulatory bodies, but do not contain parameters or acceptance criteria for the fulfillment of such requirements [1, 9]; (ii) standards do not define which techniques to use, nor does it define metrics for the evaluation and acceptance of device components [9]; (iii) each manufacturer defines what is or is not acceptable in the development of usability [9].

With the study of the examples of usability engineering documentation, it was possible to identify the following points: (i) the example presented in the standard does not meet some of the requirements contained in the standard itself [9]; (ii) the GIP documentation presents a more complete material, but the usability information is not concentrated in a single document [5].

4   Proposal

With the analysis of the points contained in the standards, together with the studies carried out for this work, a combination and refinement of the elements described in the current regulations was done, resulting in the creation of a documentation structure that absorbs the normative elements while offering structure. In Fig. 1 it is possible to see the relationship between the NBR 62366 elements and the structure.

Application Specification

No new items were added to this step, since the items contained in the standard are considered sufficient for the documentation of the usability specification. The artifact generated by this step is a brief Specification Report, containing all the information pointed out above.

Use Contexts

The standard does not require the definition of concepts, but suggests six contextual factors to be addressed. For this work, these same contextual factors are defined as mandatory, and are composed of:

- Context Space;
- Social Context;
- Technological Context;
- Hygienic context;
- Physical Context;
- Activity Context.

NBR 62366 structure

- Application specification
- Frequently used functions
- Identification of usability-related dangers and dangerous situations
- Primary operation functions
- Usability specification
- Usability validation plan
- User interface project
- Usability verification
- Usability validation

Proposed structure

- Application Specification
- Use Contexts
- User Profiles
- User Interface Requirements Listing
- Use Scenarios
- Risk Analysis and Management
- User Interface Project
- Verification and Validation
- Versioning

Fig. 1 Current documentation structure x Proposed structure

The artifact generated by this step will be the Use Context Report, where the manufacturer should show that it considered all the points listed above.

User Profiles

For this stage, the normative requirements are composed by:

- Identifier;
- Genre;
- Age;
- Minimum language comprehension;
- Minimal cultural context;
- Minimum experience;
- Minimum level of education;
- Professional competence;
- For this work, in addition to these points, Potential deficiencies of intended users should also be considered. The artifact generated in this step should be the User Profiles intended for the device.

User Interface Requirements Listing

For this work, the requirements will be defined in the following categories:

- Task Requirements—this category lists the requirements of characteristics considered "desirable" in the interface of the device;
- Operating Requirements—in this category are:
  - Requirements related to primary operation functions;
  - Requirements to determine if functions are easily recognized by the user;
  - Requirements for most frequently used scenarios.

- Security Requirements—this category lists requirements coming from the usage scenarios that are security related.

Therefore, each requirement must contain at least the following information:

- A unique identifier;
- The description of the requirement;
- The risks associated with the requisite;
- The use cases associated with the requirement.

The artifact generated by this step will be the Project Requirements Document, which will be composed of the compilation of all generated requirements.

Use Scenarios

For this work, the usage scenarios are divided into five groups, which together span the device lifecycle. They are:

- Installation (scenarios involving the initial preparation of the device);
- Operation (standard device operating scenarios);
- Maintenance (repair and calibration scenarios of the device);
- Storage (packaging and storage scenarios);
- Transport.

Each scenario should list all its Primary Operation Functions, which are the primary operations of the device for health throughout its use cycle, as well as its Safety Related Functions, which are functions that require inherent safety features to role, including functions used in emergency situations.

From the functions listed in the previous section, use cases will be generated that should contain the following information:

- The reason for task execution (context);
- The state of the pre-task device (pre-conditions);
- The final result of the task (post-conditions);
- The common task execution routine (success scenario).

In addition, each use case should have at least one use case diagram and one activity diagram, following the UML language.

The artifacts generated by this step will be the usage scenarios, the listing of the primary operation functions, and the use cases, gathered in a Usage Scenarios Report.

Risk Analysis and Management

Initially we have:

- Risk assessment and analysis;
- Risk assessment;
- Implementation and verification of risk control measures;
- Evaluation of acceptability of residual risks.

For this work, it was defined that all the above points should be considered. In addition, the manufacturer must present at least a Preliminary Risk Analysis. The analysis should be a high-level survey of possible risk situations, and should contain the following information [4]:

- The task/function associated with risk;
- A unique identifier for each risk;
- The description of the risk;
- The cause of the risk;
- The effects of risk;
- The initial probability of the risk occurs;
- The initial severity of the risk;
- Recommended actions for risk mitigation;
- The final probability and severity;
- Comments.

In addition, a questionnaire was prepared based on the questionnaire used in ISO 9241, which deals with usability for traditional software [7], but with questions from NBR 62366 and ISO 14971 [1, 9].

User Interface Project

For this work, in order to take into account the requirement of the standard, the manufacturer must develop: (i) a visual prototype of the device interface; and (ii) a chart demonstrates how it works.

In this step, the manufacturer must consider all the requirements generated in the previous phases, as well as considering all usage scenarios. These elements will compose the artifact called Interface Initial Project.

Verification and Validation

For this work, the manufacturer must carry out at least one questionnaire for each user profile identified in the previous steps. The questionnaire should address topics such as user satisfaction and ease of use of the device. In this section of the usability document, the following should be included: (i) the questions used in the questionnaire; (ii) the responses of each user profile; (iii) a comparison between each of the questions.

In addition, the manufacturer shall verify that one or more techniques are required for this step (depending on the type of device) and shall use more than one validation method, such as: Audits; Heuristic analysis; Interviews; Blind tests; Expert Reviews; Prototyping; Participatory project.

All the documentation generated by the validation process must be attached to the questionnaires carried out initially to compose the Validation Report.

Versioning

For this work the manufacturer must include a Version History Documentation, where each line must contain at least the following information:

- The date the modifications were made;
- The current version of the document;
- What modifications have been made;
- The name of the responsible person.

5   Final Considerations

This work aimed to identify the state of the art in usability engineering for medical devices, to verify the requirements of the current regulatory standards for these devices, to analyze examples of documentation, and to propose a standard of documentation for usability engineering in medical devices.

With the bibliographic review, it was possible to verify that there are techniques that are already defined as good practices in the universe of usability engineering, but the regulatory norm does not mention them directly.

With the study of the documentation examples, several points of the documentation were identified that can be better defined, and with the proposed solutions, it was verified that the information contained therein tends to be better structured and easier to understand. Based on this, the elaboration of the document model was developed with a focus on the organization of information and the definition of acceptable minimum parameters, and it is expected to achieve satisfactory results, once validated.

For the validation of this work, it will be necessary to apply the documentation model in a project.

References

1. ANSI/AAMI/ISO 14971: 2007. Medical devices - Application of risk management to medical devices.
2. ARMIJO, D.; MCDONNELL, C.; WERNER, K. Electronic Health Record Usability: Evaluation and Use Case Framework. AHRQ Publication, Rockville, n. 9, October 2009.
3. DOBRE, J., et al. Rapid Heuristic Evaluation: Ensuring Fast and Reliable Usability Support. Proceedings of the Human Factors and Ergonomics Society Annual Meeting, v. 61, n. 1, p. 610–614, September 2017.
4. ERICSON, CA Hazard Analysis Techniques for System Safety. Hoboken: John Wiley & Sons, 2005.
5. GIP. Generic Infusion Pump Research Project. Available at: <https://rtg.cis.upenn.edu/gip/>. Accessed on: August 10, 2017.
6. HARRINGTON, C. et al. Using a Unified Usability Framework to Dramatically Improve the Usability of an EMR Module. AMIA Annual Symposium Proceedings, p. 549–558, 2011.
7. ISO 9241: 1998. Ergonomic requirements for office work with visual display terminals (VDTs).
8. MEEHAN, RA et al. Increasing EHR system usability through standards: Conformance criteria in the HL7 EHR-system functional model. Journal of Biomedical Informatics 63, August 11, 2016.
9. NBR IEC 62366: 2010. Products for health - Application of usability engineering to health products.
10. WIKLUND, M.; KENDLER, J.; STROCHLIC, A. Usability Testing of Medical Devices. 2ª. ed. Boca Raton: CRC Press, 2015.
11. WILSON, JR; SHARPLES, S. Evaluation of Human Work. 4ª. ed. Boca Raton: CRC Press, 2015.
12. ZHANG, J.; WALJI, MF TURF: Toward a unified framework of EHR usability. Journal of Biomedical Informatics, August 16, 2011.

Part III
Health Technology Assessment

Cost-Effectiveness of Minimally Invasive Total Hip Endoprosthesis Implantation as Compared with the Conventional Approach

Tereza Lísalová and Ondřej Gajdoš

Abstract

Objectives: The total hip endoprosthesis implantation is one of the most common surgical procedures of the present day, and surgeons can choose different approaches. The aim of this study is to compare two surgical approaches—the conventional approach and the minimally invasive approach. Methods: Clinical outcomes have been obtained through a literature review of clinical trials. Value engineering methods and multiple-criteria decision methods—namely Saaty's matrix, the Technique for Order of Preference by Similarity to Ideal Solution (TOPSIS) and the Analytic Hierarchy Process (AHP)—were used for setting the scales of criteria and effects, respectively. The total direct costs per patient were carried out by a systematic cost analysis from the healthcare provider's perspective. The cost-effectiveness analysis compared the conventional and the minimally invasive approaches. The calculations were completed by a sensitivity analysis. Results: A total of 180 patients were enrolled in the study. The total costs per patient were CZK 57 084 ($\sim$EUR 2 243) for the conventional approach, and CZK 54 321 ($\sim$EUR 2 134) for the minimally invasive approach. Applying the TOPSIS method, the cost-effectiveness ratio is CZK 125 157 ($\sim$EUR 4 917) for the conventional approach, and CZK 88 586 ($\sim$EUR 3 480) for the minimally invasive approach. These results were also confirmed using the AHP method, when the C/E ratio is CZK 112 859 ($\sim$EUR 4 434) for the conventional approach, and CZK 106 116 ($\sim$EUR 4 169) for the minimally invasive approach. Conclusions: The results based on the cost-effectiveness analysis show that the minimally invasive approach to the total hip endoprosthesis implantation is more cost-effective than the conventional approach.

1 Introduction

The total hip endoprosthesis implantation is one of the most common surgical procedures of the present day. Therefore, the reliability of the process has a great socio-economic importance [1, 2]. It is also one of the most successful procedures for improving the quality of life of patients suffering from degenerative joint disease [3]. In the field of hip joint endoprosthetics, surgeons can choose from various surgical approaches that can be divided according to the location of the cut and its method in terms of the degree of invasiveness and the patient position during the operation. The choice may affect the early postoperative phase [4, 5].

Due to limited resources and a relatively rapid implementation of new technologies, emphasis should be placed on the justification and value decision of new practices in terms of clinical and economic benefits arising from their use.

The main motivation for this study is a small amount of information concerning differences in resource utilization and in the length of stay between the minimally invasive and the generally applied approaches of total hip endoprosthesis implantation in the Czech Republic. The aim of this study is to carry out a cost-effectiveness analysis and to compare two selected surgical approaches—a conventional one (Watson-Jones) and a minimally invasive (the anterolateral approach—cut to 10 cm) representing the current trend in endoprosthetics.

T. Lísalová · O. Gajdoš (✉)
Faculty of Biomedical Engineering, Czech Technical University in Prague, Kladno, Czech Republic
e-mail: ondrej.gajdos@fbmi.cvut.cz; og.gajdo@gmail.com

T. Lísalová
e-mail: tereza.lisalova@fbmi.cvut.cz

2 Methods

The cost-effectiveness analysis considering costs together with effects was chosen from the Health Technology Assessment area to compare the two operational approaches. Value engineering methods and multiple-criteria decision making were used to quantify the effects. The total cost per patient with the total hip endoprosthesis implantation was estimated from the healthcare provider's perspective based on data collected in 2016. At the end of the study, the cost-effectiveness analysis and a sensitivity analysis were performed.

2.1 Economic-Clinical Outcomes

The values were obtained by a literary research of clinical trials, and then the total outcomes were quantified and statistically processed. The literary research for appropriate studies was carried out between March 2016 and May 2017 using the following databases: Springer Link, Web of Science, PubMed, Science Direct, Medvik, and Summon meta-browsers. The time period was chosen from 2006 to 2016. The following keywords were searched for: hip replacement, hip arthroplasty or THR, surgical approach, cost effectiveness, cost analysis or economics, mini-invasive surgery, minimally invasive and MIS. Meta-analyzes, literature reviews of randomized controlled trials and randomized controlled trials themselves were the main sources of data.

Clinicians from the field were addressed to select the clinical outcomes to be considered. Based on the expert judgment, the following outcomes were selected for the overall effect: time of surgery, complication rate, blood loss, hospitalization time, Harris score, C-reactive protein, hemoglobin level, pain.

2.2 Determining the Weights of the Economic-Clinical Outcomes

The weights of the individual economic-clinical effects were determined based on a discussion of an expert group and a subsequent application of Saaty's matrix. The expert group was comprised of surgeons dealing with both total hip endoprosthesis approaches and one rehabilitation physician.

2.3 Multiple-Criteria Decision Making

Two multiple-criteria decision making (MCDM) methods were used to determine the total effect. Primarily the TOPSIS method was applied, followed by a verification by means of the Analytic Hierarchy Process (AHP).

2.4 Cost Analysis

The study presents calculations of total costs associated with the intervention followed by a cost analysis. The costs were collected from one of the principal hospitals in Prague. The total number of beds at its orthopedic clinic is 148, of which 25 beds are available for total hip endoprosthesis patients. The Intensive Care Unit (ICU) of the orthopedic clinic, where patients spend some time after the surgery, has 8 beds.

Patient data were provided for 180 patients (64 of the minimally invasive approach and 116 in the control groups). This was a randomized patient selection and the study was limited to the single-sided cemented endoprostheses.

Only the direct medical costs for total hip endoprosthesis implantation using the minimally invasive approach and the conventional approach were included in the calculation. The total costs of the interventions were calculated summing the following items. Their source is mainly the economic department of the hospital.

Cost of hospitalization. In order to calculate the cost of hospitalization, it was necessary to determine the length of the hospitalization prior to the surgery, after the surgery at the ICU and in the standard clinical ward. The cost of a hospitalization day was found out as a share of the total costs of the orthopedic department and the ICU orthopedic ward, resp., and the total number of treatment days in the same period. The costs of hospitalization were calculated for each patient as the product of the length of hospitalization and the costs per a treatment day.

Salary costs. The salary cost calculations can be labelled as bottom-up. It was necessary to make a list of all professions involved including the number of individual health workers participating in each profession. The information were collected during the consultations with the surgeons and nurses based on the analysis of the current state of art, the hospital's clinical information system, the average earnings information system and operative reports. The intervention process was divided into preoperative examinations, the surgery, hospitalization, and postoperative examinations. The salary costs were calculated separately for each phase and subsequently summed.

Consumables during the surgery. Operative reports, invoices, data provided by the Beznoska company (see below), the code list of the General Health Insurance Company, reimbursement data, observed consumption during the surgery, and consultations with the surgical nurse were used to determine consumables during the surgery [6–8]. The most expensive item was the implant (86.1% of

the cost of consumables). In both approaches, the same Beznoska replacement (cemented both the femoral and the acetabular components) was used; Beznoska is a Czech producer of implants, tools, and surgical utensils for orthopedic surgery and traumatology.

Overhead costs. Total overhead costs consist of the sum of overhead costs of the operating theatre and the overhead costs of the entire hospital. The overhead costs of the operating theatre were determined using the profit and loss statement, where the costs items representing overheads were selected. The costs per minute were calculated based on total overheads and the production time. The total overhead costs for the operating theatre were determined for both approaches based on costs per minute and the surgery time. The calculation of overhead costs for the entire hospital was carried out using the cost matrix (allocation matrix) divided by the cost centers.

2.5 Cost-Effectiveness Analysis

The overall economic-clinical effects calculated on the basis of the multiple-criteria decision making methods and the total costs of interventions (the minimally invasive approach and the conventional approach) were used in the cost-effectiveness analysis (CEA). The CEA itself was calculated according to the formula [9, 10]

$$\frac{C_A}{E_A} < \frac{C_B}{E_B}. \tag{1}$$

2.6 Sensitivity Analysis

The sensitivity analysis is used to examine the degree of influence of selected factors on the cost-effectiveness ratio. A one-way sensitivity analysis was applied. The selected effects include the influence of using mean values in the TOPSIS method, the influence of the length of hospitalization, the influence of complications, and the influence of the increase in the total costs of the minimally invasive techniques [11].

3 Results

3.1 Determination of Weights for the Economic-Clinical Outcomes

Based on the expert opinion, the highest weight among outcomes was assigned to the complication rate (i.e. this outcome is considered the most important), and the lowest weight to the hospitalization time. The determined weights of individual criteria were used in the TOPSIS and the AHP

methods. Table 1 shows all the weights for economic-clinical outcomes determined by the experts.

3.2 Multiple-Criteria Decision Making

The medians of the individual outcomes were used in the TOPSIS method to determine the overall economic-clinical effect. The AHP method was subsequently used to verify the results obtained by the TOPSIS method. Table 2 shows the results of both methods. The overall economic-clinical effect according to AHP is slightly higher for the minimally invasive approach, and thus the result of TOPSIS is confirmed.

3.3 Cost Analysis

Total costs per one patient were figured out for the conventional approach and for the minimally invasive approach, resp., when higher costs were shown for the conventional approach. However, the difference between the approaches is only CZK 2 763. Table 3 shows the total costs.

3.4 Cost-Effectiveness Analysis

The cost-effectiveness analysis is based on the results of the cost analysis and the multiple-criteria decision making. The minimally invasive approach is more cost-effective from the

Table 1 Weights of economic-clinical outcomes

Economic-clinical outcomes	Outcome weight
Time of surgery	0.0332
Complication rate	0.3396
Blood loss	0.2298
Hospitalization time	0.0218
Harris score	0.1129
C-reactive protein	0.0560
Hemoglobin level	0.0983
Pain	0.1083

Table 2 Multiple-criteria decision making

	Conventional approach	Minimally invasive approach
TOPSIS	0.4561	0.6132
AHP	0.5058	0.5119
Final order	Second	First

Table 3 Total costs

Cost item	Conventional approach	Minimally invasive approach
Cost of hospitalization (CZK)	12 348	11 319
Salary costs (CZK)	13 504	12 435
Consumables (CZK)	17 895	17 585
Overhead costs (CZK)	13 337	12 981
Total costs (CZK)	57 084	54 321

healthcare provider's perspective. This result was confirmed by the effects of both the TOPIS and the AHP methods. All results are listed in Table 4.

3.5   Sensitivity Analysis

When using the average values instead of the medians in the TOPSIS method, the sequence of the approaches is affected mainly by the clinical outcome of the complication rate due to the highest weight of this criterion. In this case, the sequence of approaches in the cost-effectiveness analysis was turned to the conventional approach.

In the sensitivity analysis, we also studied the effect of the percentage decrease and increase in the complication rate in the minimally invasive techniques. Increasing the complication rate by 20% in the minimally invasive techniques leads to a change in the order of approaches. From this point of view, the cost-effectiveness ratio is higher for the minimally invasive approaches.

By reducing the hospitalization time in the sensitivity analysis, both interventions lead to a slight increase in the cost-effectiveness.

The CEA value was also obtained higher for the minimally invasive approach when increasing the total cost of the minimally invasive approach by 50%.

4   Discussion

The use of minimally invasive approaches in endoprosthetics is not very frequent, and clinician's opinions are often sceptical about these techniques. Many surgeons have expressed their mistrust in finding economic (in some cases also clinical) benefits. The absence of records of a part of data required for the evaluation confirms that hospitals pay little emphasis on the effectiveness of the use of resources. In the Czech Republic, there is a stronger focus on improving the clinical outcomes of surgeries, when the surgeons consider the complication rate for the most important parameter. This clinical effect was given the highest weight by the expert group; thus it affected the results of the multi-criteria decision most of all. Another important aspect is the endoprosthesis life prolongation [12–14].

According to some authors, shorter approaches provide benefits such as lower blood loss (lower need for blood transfusion), less pain, shorter hospitalization, or a better cosmetic effect. The disadvantage of shorter incisions is, for example, the impossibility of using them in obese patients, which can be a great constraint due to the increasing incidence of this phenomenon [2, 15–18].

In the Czech Republic, the length of hospitalization is not a factor influencing the minimally invasive approaches expansion. Only a few authors are concerned with influencing the length of stay of the patient in the hospital. There is no pressure to shorten the length of hospitalization. Hospitals are often used as social facilities by patients awaiting admission to a rehabilitation facility. The length of hospitalization was relatively long in the hospital collaborating in this study, which confirmed a small incentive to shorten the length of hospitalization. It is also influenced by the motivation of the patient to heal. Currently, the length of stay in the hospital is prolonged by the necessary prevention of thromboembolic disease, one of the postoperative complications. Hospitalization is largely influenced by the hospital policy, too. Accelerated discharge may cause neglecting some complications, reducing patient comfort, increasing the amount of side effects caused by, for example, premature limb loading, or insufficient education for physiotherapy, in the case of non-rehabilitative care, at the expense of possible savings [12, 13, 19].

According to some studies, the mini-invasive approaches influence the early postoperative phase, while there are no differences in the results in the two groups during a long-term observation. Mini-invasive approaches could decrease the number of necessary revisions in the future, which would have a positive impact on the use of additional resources. However, cost effectiveness should be monitored due to a high number of total hip endoprosthesis

Table 4 Cost-effective analysis

	Surgical approach	Effect	Total costs (CZK)	CEA	Final order
TOPSIS	Conventional	0.4561	57 084	125 157	Second
	Minimally invasive	0.6132	54 321	88 586	First
AHP	Conventional	0.5058	57 084	112 859	Second
	Minimally invasive	0.5119	54 321	106 116	First

implantations performed, and an increase in the incidence of osteoarthritis [12–15, 20].

5 Conclusions

Differences in both approaches are insignificant, yet the minimally invasive approaches are not more expensive than the conventional methods and provide slightly better clinical results. The cost-effectiveness analysis resulted in favour of the minimally invasive techniques; hence they have been identified as the more cost-effective ones.

Conflict of Interests The authors declare no conflict of interests.

References

1. HIGASHI, Hideki a Jan J. BARENDREGT. Cost-effectiveness of total hip and knee replacements for the Australian population with osteoarthritis: Discrete-event simulation model. PLoS ONE 6(9), (2011).
2. XU, Chang-Peng, Xue LI, Jin-Qi SONG, Zhuang CUI a Bin YU. Mini-Incision versus Standard Incision Total Hip Arthroplasty Regarding Surgical Outcomes: A Systematic Review and Meta-Analysis of Randomized Controlled Trials. PLoS ONE 8 (11), e80021 (2013).
3. MAZOOCHIAN, Farhad, Patrick WEBER, Sara SCHRAMM, Sandra UTZSCHNEIDER, Andreas FOTTNER a Volkmar JANSSON. Minimally invasive total hip arthroplasty: a randomized controlled prospective trial. Archives of Orthopaedic and Trauma Surgery, vol. 129, 1633–1639 (2009).
4. DUNGL, Pavel. Ortopedie. 2nd edn. Grada, Praha (2014). ISBN 80-247-4357-8.
5. HERNÁNDEZ-VAQUERO, D., M. FERNÁNDEZ-FAIREN, A. TORRES-PEREZ a A. SANTAMARÍA. Minimally invasive surgery versus conventional surgery. A review of the scientific evidence. Revista Española de Cirugía Ortopédica y Traumatología (English Edition) 56(6), 444–458 (2012).
6. MINISTERSTVO ZDRAVOTNICTVÍ ČESKÉ REPUBLIKY. Seznam zdravotních výkonů, https://szv.mzcr.cz/Vykon/Detail/66612, last accessed 2017/12/28.
7. BEZNOSKA S.R.O. Cementovaný dřík TEP kyčelního kloubu – typ Poldi, http://www.beznoska.cz/product/cementovany-drik-tep-kycelniho-kloubu-typ-poldi/, last accessed 2017/12/28.
8. VŠEOBECNÁ ZDRAVOTNÍ POJIŠŤOVNA. Číselník VZP – ZP (ZUM) verze 981, https://webevzp.blob.core.windows.net/media/Default/dokumenty/ciselniky/ostatni/pzt_981_m.pdf, last accessed 2017/12/28.
9. MCCARRON, Jesse A., Clark BAUMBUSCH, James D. MICHELSON a Paul A. MANNER. Economic evaluation of perioperative admissions for direct lateral versus two-incision minimally Invasive total hip arthroplasty. Seminars in Arthroplasty 19(2), 180–185 (2008).
10. KNEPPO, Peter, Vladimír ROGALEWICZ, Ilya IVLEV, Ivana JUŘIČKOVÁ a Gleb DONIN. Hodnocení zdravotnických přístrojů. Vybrané kapitoly pro praxi. Česká technika - nakladatelství ČVUT, Praha (2013). ISBN 978-80-01-05430-7.
11. BOZIC, Kevin J, Khaled J SALEH, Aaron G ROSENBERG a Harry E RUBASH. Economic evaluation in total hip arthroplasty: analysis and review of the literature. The Journal of Arthroplasty 19(2), 180–189 (2004).
12. MUSIL, David. Přínos miniinvazivní MIS-AL techniky při implantaci totální náhrady kyčelního kloubu, zdravotně sociální aspekty MIS-AL přístupu. Doctoral thesis. Jihočeská univerzita v Českých Budějovicích (2011).
13. KUBEŠ, J., I. LANDOR, A. PODŠKUBKA, M. MAJERNÍČEK a J. VČELÁK. Total Hip Replacement from a MIS-AL Approach (Comparison with a Standard Anterolateral Approach. Acta chirurgiae orthopaedicae et traumatologiae Cechoslovaca, vol. 76, 288–294 (2009).
14. GEISSLER, Alexander, David SCHELLER-KREINSEN a Wilm QUENTIN. Do DRGs appropriately explain variations in costs and length of stay of hip replacement? A comparative assessment of DRG systems across ten European countries. Health economics 21(2), 103–115 (2012).
15. KUBEŠ, Radovan. Mini-invazivní implantace endoprotéz kyčelního kloubu. Doctoral thesis. Univerzita Karlova, Plzeň (2009).
16. VARELA EGOCHEAGA, José Ramón, Miguel Ángel SUÁREZ-SUÁREZ, María FERNÁNDEZ-VILLÁN, Vanessa GONZÁLEZ-SASTRE, José Ramón VARELA-GÓMEZ a Antonio MURCIA-MAZÓN. Minimally invasive posterior approach in total hip arthroplasty: a prospective randomised trial. Anales del sistema sanitario de Navarra 33(1), 133–143 (2010).
17. NAVARRO ESPIGARES, J.L., E. HERNANDEZ TORRES a J.L. RUIZ ARRANZ. Minimally Invasive Surgery in Total Hip Arthroplasty: A Cost-Effectiveness Analysis. Value in Health 14 (7), A263 (2011).
18. TOMÁŠ, Tomáš, Luboš NACHTNEBL, Lukáš PAZOUREK, Milan JURICA a David NÁHLÍK. Srovnání miniinvazivního předního a laterálního přístupu se standardním přístupem dle Watson-Jonese při endoprotéze kyčelního kloubu. Ortopedie 1(6), 259–263 (2007).
19. STEHLÍK, Jiří. Nový typ miniinvazivní TEP kyčle. Sestra. 2005, vol. 5.
20. BOZIC, Kevin a Don BERINGER. Economic considerations in minimally invasive total joint arthroplasty. Clinical orthopaedics and related research, vol. 463, 20–25 (2007).

The Robustness of TOPSIS Results Using Sensitivity Analysis Based on Weight Tuning

Millek Jiří

Abstract

Multiple-criteria decision analysis (MCDA) is one of the support techniques for Health Technology Assessment (HTA). A typical method is the Technique for Order of Preference by Similarity to Ideal Solution (TOPSIS). The output of TOPSIS presents an order of alternatives. A significant risk may be posed by an inappropriate setup of the weights of the criteria such that a very small deviation from the proper value could substantially change the final result. Sensitivity analysis is a method for testing changes of the final order by a modification of the original input data or by small deviation of the original weights of the criteria. This original approach is very slow and computationally demanding in the case of a change of the value of any attribute. The newly proposed method is significantly faster, making it possible to change of the values of the weights by only a few computations within TOPSIS. In the first stage, TOPSIS is used to compute the values of the Positive and Negative Ideal Solutions (PIS and NIS), and sensitivity analysis is only performed for the changed weights in the next stage. In the proposed method, a weight is adjusted (and the other weights recalculated) in order to find a range where the order of the alternatives remains unchanged for the modified weights. The weight adjustment can have the form of a fixed change or of an iterative process approximating the stability range for the weight. The new method is fast and simple to implement, providing a robust output of TOPSIS and pointing out a possible wrong setup of the initial weight(s).

Keywords

Sensitivity analysis • MCDA • TOPSIS • HTA

M. Jiří (✉)
Faculty of Biomedical Engineering, Czech Technical University,
Kladno, Czech Republic
e-mail: jiri.millek@fbmi.cvut.cz

1 Introduction

Multiple-criteria decision analysis (MCDA) is a decision making support technique in Health Technology Assessment (HTA) [1]. A typical method used is the Technique for Order of Preference by Similarity to Ideal Solution (TOPSIS).

Sometimes it is very difficult to define adequate weights of all criteria and the scales of some attributes are dissimilar, which leads to a considerably different output order of the alternatives. The potential risk cannot be detected without sensitivity analysis. There are many various methods for sensitivity analysis, which typically test the link between the initial setup of the input parameters and the final results.

1.1 TOPSIS

The output of TOPSIS presents an order of alternatives. A significant risk may be posed by an inappropriate setup of the weights of the criteria such that a very small deviation from the proper value could substantially change the final result.

1.2 Five Steps of TOPSIS

The basic concept of TOPSIS was introduced by Hwang 1981 [2]. TOPSIS is a compromise method which compares the distances of each alternative from the Positive Ideal Position (PIS) and the Negative Ideal Position (NIS). Although numerous modifications of Hwang's version have been proposed, the original version is still functioning and very popular. The traditional procedure is designed in the following five steps.

The first step is a transformation of each cost criterion to a benefit criterion. The next step is normalization, i.e. rescaling

the values of the criterion to the {0; 1} scale. Many methods can be used for normalization [3], including Jüttler-Millek method (my modification of Jüttler-Körth method). The output of normalization is a decision-making matrix of all the criteria and alternatives. In my modification, the criteria are in the rows and the alternatives in the columns of the matrix. The next operation is weighting of the decision-making matrix. Each row is multiplied by the weight of the corresponding criterion. Two values (the PIS and the NIS) are computed for each alternative, representing the distance of the attribute (the value of the alternative in the criterion) from the maximum and minimum values in the criterion. The final ranking is determined by the values of the ratios of the summed distances from the NIS and the PIS for each alternative.

1.3 Sensitivity Analysis

Sensitivity analysis is a method for testing changes of the final order by a modification of the original input data or by a small deviation of the original weights of the criteria. This original approach is very slow and computationally demanding in the case of a change of the value of any attribute.

Many methods have been developed for determining the weights of the criteria. TOPSIS does not test the effect of the weight settings, however. Sensitivity analysis is one of the ways to test the impact of weight adjustments.

2 Proposed Method

The proposed method uses sensitivity analysis with weight adjustment. The aim is to minimize the computational demands of TOPSIS sensitivity analysis and offer a universal weight testing method. The basic element of the method is an adjustment of all weight values when changing one particular weight.

2.1 Computation of the Weighted Matrix

The first three steps of TOPSIS are unchanged in the proposed sensitivity analysis method. Weights with normalized values are used in the third step following formula (1).

$$v_{ij} = r_{ij}w_j; i, j \in \mathbb{N} \tag{1}$$

where v_{ij} are the weighted values, r_{ij} are the normalized values of a criterion and w_j is the weight of the criterion. This equation creates a weighted matrix (2).

$$V = R\overrightarrow{W}; \overrightarrow{W} = w_j; j \in \mathbb{N} \tag{2}$$

where V is a weighted matrix, R is a normalized matrix and $\overrightarrow{W}$ is a vector of weights.

2.2 Matrixes of Distances

The matrixes of distances are computed in the fourth step of TOPSIS out of the weighted matrix and the PIS and NIS values which identify the maximum and minimum values in each row (criterion) (3, 4). The vectors of the PIS and NIS values are created over the whole weighted matrix (5, 6).

$$v_j^+ = MAX(v_{ij}); i, j \in \mathbb{N} \tag{3}$$

$$v_j^- = MIN(v_{ij}); i, j \in \mathbb{N} \tag{4}$$

$$\overrightarrow{V^+} = v_j^+; j \in \mathbb{N} \tag{5}$$

$$\overrightarrow{V^-} = v_j^-; j \in \mathbb{N} \tag{6}$$

The following equations are applied to the PIS and NIS values (7, 8) or whole vectors (9, 10).

$$d_j^+ = \left\{ \sum_j \left(v_{ij} - v_j^+ \right)^2 \right\}^{\frac{1}{2}} \tag{7}$$

$$d_j^- = \left\{ \sum_j \left(v_{ij} - v_j^- \right)^2 \right\}^{\frac{1}{2}} \tag{8}$$

$$d_j^+ = \left\{ \sum_j \left(\overrightarrow{v_j} - \overrightarrow{V^+} \right)^2 \right\}^{\frac{1}{2}} \tag{9}$$

$$d_j^- = \left\{ \sum_j \left(\overrightarrow{v_j} - \overrightarrow{V^-} \right)^2 \right\}^{\frac{1}{2}} \tag{10}$$

Using the distribution property of the weight vector from the inner brackets, we receive:

$$d_j^+ = \left\{ \sum_j \left(\overrightarrow{v_j} - \overrightarrow{V^+} \right)^2 \right\}^{\frac{1}{2}} = \left\{ \sum_j \left(\overrightarrow{RW_j} - \overrightarrow{RW^+} \right)^2 \right\}^{\frac{1}{2}}$$
$$= \left\{ \sum_j \left(\overrightarrow{W^2} \left(\overrightarrow{R_j} - \overrightarrow{R^+} \right)^2 \right) \right\}^{\frac{1}{2}} \tag{11}$$

$$d_j^- = \left\{ \sum_j \left(\overrightarrow{v_j} - \overrightarrow{V^-} \right)^2 \right\}^{\frac{1}{2}} = \left\{ \sum_j \left(\overrightarrow{RW_j} - \overrightarrow{RW^-} \right)^2 \right\}^{\frac{1}{2}}$$
$$= \left\{ \sum_j \left(\overrightarrow{W^2} \left(\overrightarrow{R_j} - \overrightarrow{R^-} \right)^2 \right) \right\}^{\frac{1}{2}} \tag{12}$$

This is an important point of the new approach, because the modified vector $\overrightarrow{W^2}$ for sensitivity analysis remains stable for all the alternatives (13, 14).

$$\overrightarrow{R_*^+} = \left(\overrightarrow{R_j} - \overrightarrow{R^+} \right)^2; j \in \mathbb{N} \tag{13}$$

$$\overrightarrow{R_*^-} = \left(\overrightarrow{R_j} - \overrightarrow{R^-} \right)^2; j \in \mathbb{N} \tag{14}$$

where $\overrightarrow{R_*^+}$ and $\overrightarrow{R_*^-}$ are two vectors of the distances of unweighted criteria, which are calculated for each alternative for future use.

2.3　New Weights

This is a very interesting approach to testing the sensitivity of the resulting order to the weights in TOPSIS [4]. An important condition is that the sum of the weights w_p equals 1 (15). If a single original weight is changed, w_p is recalculated to a new weight w_p' using (16), where Δ is the change (positive or negative), and the equality to 1 no longer holds (17).

$$\sum_{p=1}^{k} w_p = 1; k, p \in \mathbb{N} \tag{15}$$

$$w_p' = w_p + \Delta_p; p \in \mathbb{N}, \Delta \in \mathbb{R}, \ w_p' > 1 \tag{16}$$

$$\sum_{p=1}^{k} w_p' \neq 1; k, p \in \mathbb{N} \tag{17}$$

The proposed sensitivity analysis method accepts a targeted change of only one weight, and the other weights must be recalculated (18)

$$w_j' = \frac{1 - \Delta_p - w_p}{1 - w_p} w_j; j, p \in \mathbb{N} \cup j \neq p \tag{18}$$

$$w_j' = \frac{1 - w_p'}{1 - w_p} w_j; j, p \in \mathbb{N} \cup j \neq p \tag{19}$$

$$\gamma = \frac{1 - w_p'}{1 - w_p}; p \in \mathbb{Z} \tag{20}$$

$$\overrightarrow{W'} = \gamma \overrightarrow{W} \tag{21}$$

where γ is a coefficient of the correction all other weights except for the tested weight.

$$d_j^{+'} = \left\{ \sum \left(\overrightarrow{W^2} \overrightarrow{R_*^+} \right) \right\}^{\frac{1}{2}} - \left\{ \left(w_p \left(\overrightarrow{R_j} - \overrightarrow{R^+} \right) \right)^2 \right\}^{\frac{1}{2}} \tag{22}$$

$$d_j^{-'} = \left\{ \sum \left(\overrightarrow{W^2} \overrightarrow{R_*^-} \right) \right\}^{\frac{1}{2}} - \left\{ \left(w_p \left(\overrightarrow{R_j} - \overrightarrow{R^-} \right) \right)^2 \right\}^{\frac{1}{2}} \tag{23}$$

where $d_j^{+'}$ and $d_j^{-'}$ are the recalculated new distances from the PIS and NIS (22, 23).

3　Proposed Approach

The newly proposed method uses the Eqs. (18, 19, 20, 21) in cycles for sensitivity testing of each weight, while gradually adjusting the vector $\overrightarrow{W}$.

Sensitivity analysis is proposed in the following steps:

1. Perform standard TOPSIS while saving the matrixes $\overrightarrow{R_*^+}$, $\overrightarrow{R_*^-}$, $\overrightarrow{W}$ and the resulting order of the alternatives for further use.
2. Change one weight w_p and adjust the other weights using the coefficient γ (20). Construct $\overrightarrow{W'}$ out of the changed values (21).
3. Calculate the new distances from the saved vectors (22, 23).
4. Calculate the new relative closeness using the standard TOPSIS procedure.
5. Evaluate the new order of alternatives and check if it equals the original, saved order.

3.1　Setup of the Weight of the Tested Criterion

There are two different approaches to testing using the proposed sensitivity analysis method: the tested value of the weight w_p could be defined as a fixed value or iteratively using the bisection method (a binary search tree).

Fixed-change weight test

This is a quick and simple weight testing solution. The basic test applies a fixed change to the tested weight, e.g. by adding or subtracting a percentage (e.g., $\pm 5\%$ or 10%) or an absolute value to/from the weight. This test checks the potential change of the results of the TOPSIS method (the order of the alternatives) related to the change of weight

(arbitrarily set up by the tester at the beginning of the testing process).

Tuned weight test

More accurate results can be obtained when the change is performed step by step using the bisection method. The accuracy depends on the number of the iterations and on the initial value of the tested weight. Unlike the previous approach, this procedure can be used to find the range of values of the weight within which the order of the alternatives remains unchanged.

4 Results

The proposed method reduces the computational demands of sensitivity analysis for TOPSIS. The main benefit lies in a reduction of the repeatedly computed steps 1–4 of TOPSIS.

The fixed-change weight SA tests one or two values of the weight of the criterion—an upper one, a lower one or both. It is fast and provides an indicative value of the weights. The output is the information on whether the resulting order will be different when the weight is changed by a specific step. This is a quick test of the stability of the final order of alternatives.

The tuned weight test approximates the stability range for the tested weight of a criterion, regardless of whether it is smaller or larger than the step change chosen for the fixed-range approach, at the cost of somewhat higher computation demands.

5 Discussion

Although this sensitivity analysis has been developed for use in HTA, it is a universal method usable across the fields of application of MCDA.

The new fast and simple to implement method provides a robust output of the TOPSIS method. The tuned-weight approach allows to create an overview of the positions of the initial weights within their respective stability ranges, thus pointing out a possible wrong setup of some weight(s).

The newly proposed sensitivity analysis method is not designed for the testing of the statistical distribution of values in a criterion, although it might be very interesting to observe the effect of the distribution on the final ranking of the alternatives.

Other possibilities for future research are to apply the proposed method to fuzzy TOPSIS [5–7] or to compare it with the VIKOR method [8–11].

References

1. EUnetHTA JA2; Joint Action on HTA 2012–2015 Methodological Standards and Procedures (MSP) for Full core HTA content development. (2015)
2. Hwang, C.-L., Yoon, K.: Multiple Attribute Decision Making. Springer Berlin Heidelberg, Berlin, Heidelberg (1981)
3. Vafaei, N., Ribeiro, R.A., Camarinha-Matos, L.M.: Normalization Techniques for Multi-Criteria Decision Making. In: Liu, S., Delibašić, B., Linden, I., and Oderanti, F.O. (eds.) THE EWG-DSS 2016 Int. Conference On Decision Support System Technology (ICDSST 2016): Decision Support Systems Addressing Sustainability & Societal Challenges. pp. 23–25, Plymouth, (2016)
4. Alinezhad, A., Amini, A.: Sensitivity Analysis of TOPSIS Technique : The Results of Change in the Weight of One Attribute on the Final Ranking of Alternatives. J. Optim. Ind. Eng. 7, 23–28 (2011)
5. Li, D.-F., Nan, J.-X.: Extension of the TOPSIS for Multi-Attribute Group Decision Making under Atanassov IFS Environments. Int. J. Fuzzy Syst. Appl. 1, 47–61 (2011). https://doi.org/10.4018/ijfsa.2011100104
6. Abou-el-enien, T.H.M., Abo-sinna, M.A.: Interactive TOPSIS Algorithm for Fuzzy Large Scale Two-Level Linear Multiple Objective Programming Problems. 869, 152–163 (2015)
7. Igoulalene, I., Benyoucef, L., Tiwari, M.K.: Novel fuzzy hybrid multi-criteria group decision making approaches for the strategic supplier selection problem. Expert Syst. Appl. 42, 3342–3346 (2015). https://doi.org/10.1016/j.eswa.2014.12.014
8. Duckstein, L., Opricovic, S.: Multiobjective optimization in river basin development. Water Resour. Res. 16, 14–20 (1980). https://doi.org/10.1029/wr016i001p00014
9. Opricovic, S., Tzeng, G.H.: Compromise solution by MCDM methods: A comparative analysis of VIKOR and TOPSIS. Eur. J. Oper. Res. 156, 445–455 (2004). https://doi.org/10.1016/s0377-2217(03)00020-1
10. Opricovic, S., Tzeng, G.H.: Extended VIKOR method in comparison with outranking methods. Eur. J. Oper. Res. 178, 514–529 (2007). https://doi.org/10.1016/j.ejor.2006.01.020
11. Afful-Dadzie, E., Nabareseh, S., Oplatková, Z.K., Klímek, P.: Model for Assessing Quality of Online Health Information: A Fuzzy VIKOR Based Method. J. Multi-Criteria Decis. Anal. 23, 49–62 (2016). https://doi.org/10.1002/mcda.1558
12. Millek, J.: Draft analytical tools for multi-criteria decision-making in HTA, (2017)

Application of HTA in Optometry

Miroslav Selčan and Ivana Kubátová

Abstract

The main objective was to evaluate possible options for refractive error correction for three categories of clients (children from 6 years with light myopia, teenagers from 15 with astigmatism, adults with starting presbyopia) considering the available correction methods (glasses, contact lenses, refractive surgery). The evaluation was performed through data on the amount and frequency of orders in an optical shop and eye clinic. The data were gradually processed and the calculation of the cost of correction was performed from the perspective of a client. FMEA was done for individual methods of correction, and multiple-criteria evaluation applying the TOPSIS method was figured out. The TOPSIS method alone showed the glasses correction to be the best. The CEA, i.e. after considering the economic view, prioritized the contact lens correction. The best possible combination of correction methods for the refractive errors is, due to possible health risks, the combination of correction with glasses and contact lenses.

Keywords

Refractive correction • HTA • Cost effectiveness

1 Introduction

One of the key decision makers, for clients, is the cost of correction aid. There are both glasses and contact lenses at all price levels and many methods of refractive surgery.

The aim of the thesis is to evaluate and compare methods of refractive errors correction. The result is a determination of the best options for correcting refractive errors from the client's perspective.

Individual senses do not function fully immediately after birth, but they develop at a different pace, with the eye maturing out of all senses as the last [1, 2]. For good image vision, not only good lighting conditions are desired, but these stimuli must be focused as much as possible on the retina. The main condition is the correct ratio between the fracture of the areas of the optical environment of all parts of the eye and the anterior-posterior length of the eye [2].

The cornea and lenses also alter during the growth. With the growing eye, the diameter of the cornea increases. With the diameter increasing, however, the cornea becomes thinner and at the same time flashes, thereby changing its frailty [2].

Presbyopia usually begins after the 40th year of age, but due to various reasons, it may appear before the 38th year or vice versa after the 48th year of life [2, 3]. Among the three most important factors in the development of presbyopia are the drop-in elasticity of the capsule, the lens substance and the constant lens growth [2].

Two thirds of the population carry or use some of the different modalities of a refractive error correction: glasses, contact lenses and/or refractive surgery [4]. Let's summarize pros and cons for individual modalities.

One of the drawbacks of glasses can be the prize. Some people are dissatisfied to such an extent that they either consider or have undergone surgical interventions in the hope of long-term savings. Glasses may not be easy to wear during sporting moments or specific work, which can be a psychological problem [4].

More than half of the contact lens users wear them all the time. Other users wear contact lenses only for certain occasions.

A large number of people may deem the application and the aftercare of contact lenses difficult. Contact lenses may not be suitable for a particular type of refractive errors, and their wear may also cause side effects. In addition, as a combination with glasses, the customer can pose additional financial burdens [5].

M. Selčan (✉) · I. Kubátová
Faculty of Biomedical Engineering, CTU, Nám. Sítná 3105, 272 01 Kladno, Czech Republic
e-mail: miroslav.selcan@fbmi.cvut.cz

Refractive surgery can eliminate or minimize the value of ocular dioptric errors. However, it is necessary to think and anticipate the potential impacts this option poses. The most common technique is LASIK (laser-assisted in situ keratomileusis).

Refractive surgery is a fairly expensive matter and is not covered by a health insurance company; therefore, it is viewed by some people as a luxury service for rich clients. Clients feel comfortable and find their own personality and freedom again. This option also speaks for a profitable investment that, in a long run, makes it possible to save money [6].

Growing population, including its aging, is generally recognized as an important factor when estimating the size of the market for refractory error corrections worldwide.

Total economic costs (from the state's point of view) spent on the group of people with eye problems amounted to $16.6 billion in Australia in 2009, accounting for approximately $29,905 per person. The largest share of the cost for a specific diagnosis of cataract occupies 18%, followed closely with 16% of those allocated to refractive errors [7].

Belgians correct refractive errors mostly by glasses or contact lenses. The refractive surgery is limited mainly to more serious cases. In addition, surgery for correction of refractive errors do not fall under the mandatory health insurance system [4, 8]. Figure 1 shows the total 15-year cost and its composition for each correction method for a 30-year-old patient, i.e. of the age of a probable onset of presbyopia from Belgium.

Estimated total cost of ophthalmic disease in the USA was $139 billion (refraction errors $16.1 billion) in 2013. The amount includes both direct costs of $66.8 billion, including health care costs for diagnostics, medical aids, a special training program, etc., as well as $72.2 billion of indirect costs that include productivity loss, long-term care and more. If we were billing the total costs to the patients, it would be $450 per person [9, 10].

In the Czech Republic, glasses as one of the possible correction methods are borne by 44% of the population over
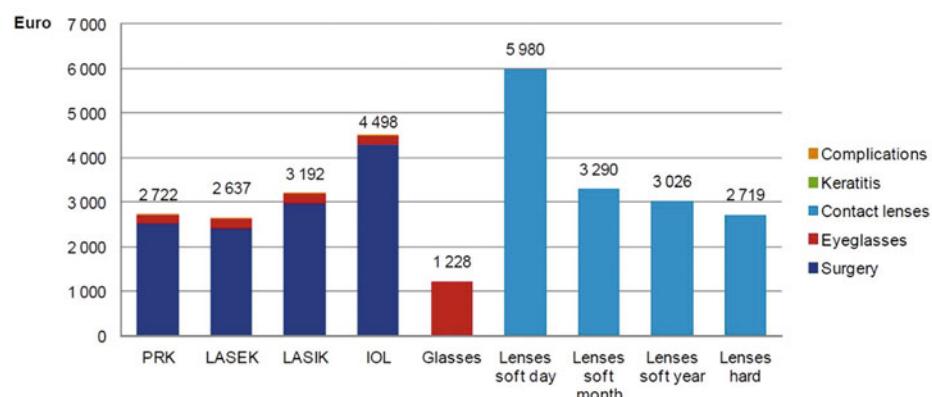
15. An unfavorable finding is that more than 13% of people who are aware of their worsening vision, do not wear eyeglasses nor contact lenses [11]. With the growing trend of a healthy lifestyle, the number of people who resolve their correction through refractive surgery is also rising. Between 2012 and 2013, the number of an eye clinic clients in the 21–40 age group increased by 25% [12].

2 Methods

Three groups of clients with different initial parameters were formed: (i) myopia in children from the age of 6; (ii) myopia, common astigmatism in adolescence (from 15 years of age); (iii) presbyopia after the 40th–45th year of age. The time horizon of the analysis was set to 80 years. In each group, the client could use different correction tools. Data were obtained from an optical shop (measurement archive, contact lens archive and customer club) and an eye clinic (archive of cataract surgery). A record of 5,000 records of refractive measurements was searched in the optical shop, where 133 records of clients with three or more continuous refraction measurements were selected. They established their profile in the customer club and simultaneously met the parameters of the three assigned groups. From the list of active contact lens carriers, 239 bearer records were searched, for which a suitable type of contact lenses had already been established. The combinations were made by decision to choose the correction at 15 years of age, next from 20 to 40 for 5 years, 45 until 80. In the first group (i) was made 56 combinations, in the second group (ii) was made 56 combinations, too and in the third group was made 4 combinations. Costs for every combination was calculated. A discount rate wasn't use for customer and his better image of the costs of the refractive correction.

A group of eight professional optometrists was formed. For each correction method, the potential risks associated with the use of the particular type of correction aid were identified. All members of all groups of experts were asked

Fig. 1 Total cost of refraction error corrections in a 30-year-old patient [4]

to evaluate individual methods independently on the other members of the group, where the individual analyzes were subsequently processed and a FMEA created taking into account the values of all group members like other assessment.

For each of the three client groups, combinations of options for the use of all three types of correction aids were created separately. Modeling begins with the first glasses purchase at the age of six. At the age of 15, the first splitting occurs, either using of glasses or alternatively wearing of glasses together with contact (daily or monthly) lenses. At the age of 20, choices can be made between glasses, contact lenses, or refractive surgery. The same options are available in the age of 25, 30 and 35. In the refractive surgery, a successful operation is planned when the need for glasses will occur with the onset of presbyopia. The potential failure of the operation can be included in the possibility of a later decision on the operation. Between the age of 40 and 45, the above-mentioned manifestation of presbyopia is beginning to appear. When switching from glasses or day contact lenses, it is possible to continue with your usual glasses or choose multifocal glasses or multifocal contact lenses.

The cost effectiveness analysis (CEA) was selected for this study. In order to complete the HTA (Health Technology Assessment) study, the risk analysis, namely FMEA (Failure mode and effect analysis), and the sensitivity analysis were used. The TOPSIS method was used to quantify the non-financial effects, when ten criteria were employed—weighted (the resulting comfort—0.2; the field of vision—0.01; the average purchase price—0.15; the consequent costs for an adult until the onset of presbyopia—0.1; the

development of pathological changes—0.15; hygiene susceptibility—0.05; the risk of loss of corrective aid—0.05; reversibility—0.15; user problems—0.09; difficulties for the wearer—0.05). The weights of individual criteria were created with the help of professional staff.

3 Results

3.1 Glasses for Vision Correction

Out of 133 records, there were 13 children, 26 teenagers and 94 adult customers. From the analysis of the customer club records, it was possible to determine the amount of money the customer paid for each contract, and the time of the order. The period of the orders was 1.25 years for children, 1.67 for teenagers and 2.87 for adults (Fig. 2).

Figure 3 shows the average annual costs of eyeglass correction acquisition for each of the assigned groups and their growing tendency to increase costs. The difference in the cost level for each category proves different specific needs of each group.

3.2 Contact Lenses

The highest frequency of annual costs of acquiring contact lenses resulting from regular optic purchases is around €200 (Fig. 4). This amount corresponds to a purchase of two packs (each for one eye) of monthly contact lenses for €49 per box, which is sufficient for 6 months. However, the

Fig. 2 Frequency of eye correction in all groups
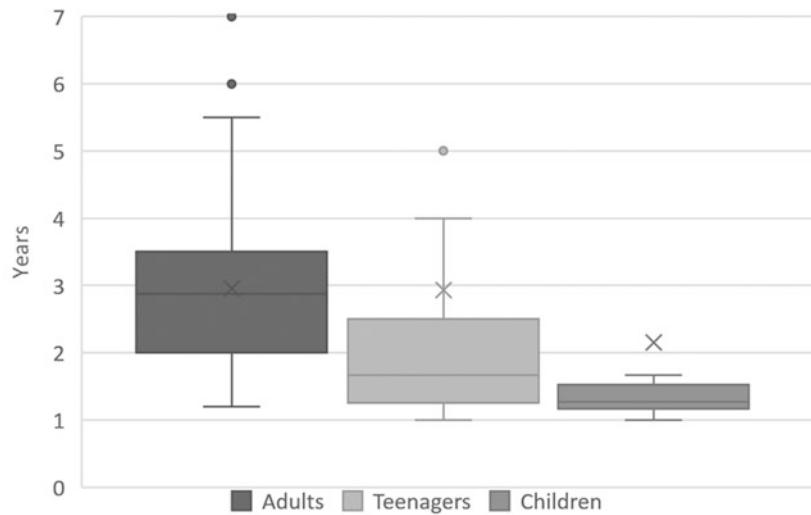
Fig. 3 Average costs of eyeglass correction for all categories
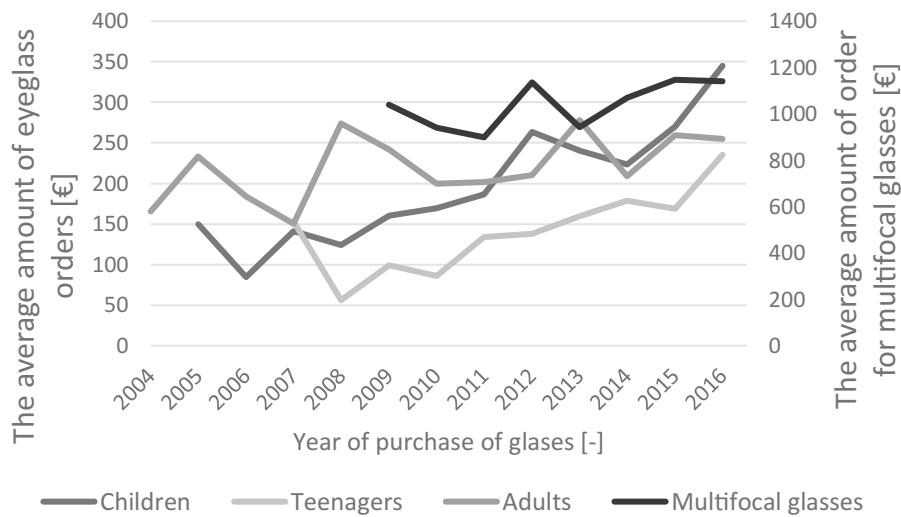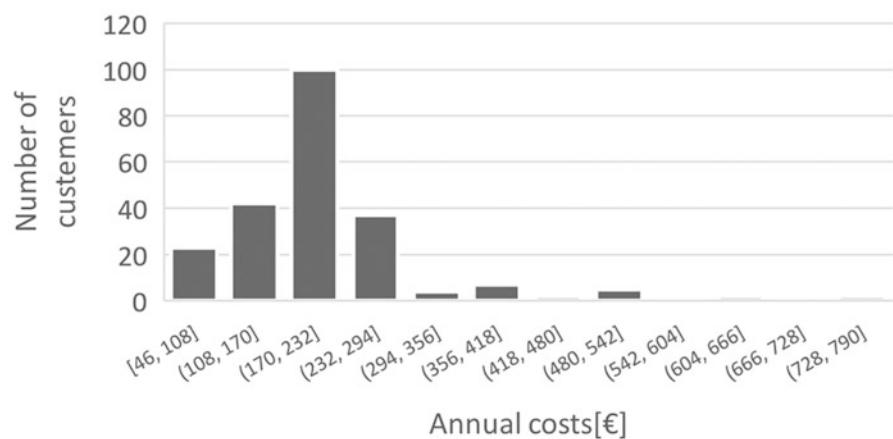
Fig. 4 Numer of customers according to annual amount of money spent for contact lenses

contact lens solution necessary for cleaning and hygiene of the contact lenses must be added to this type of lenses (€22 for 4 months).

3.3 Refractive Surgery

In the case of laser surgery, the price is between €400 and €800 per eye. In particular, €400 is charged per eye for the LASIK surgery.

3.4 Cataract

A total of 199 operations were obtained from the cataract surgery archive. The age range of clients ranged between 41

and 100 years, with the highest frequency of operations occurring in the age between 60 and 77.

3.5 Calculation of Correction Combinations and Their Modeling

Combinations (i) with the lowest cash costs include wearing monofocal glasses, undergoing the LASIK surgery in the age of 20, and again wearing monofocal glasses only when presbyopia begins to manifest (€5,296 totally).

The difference between (i) and (ii) was at the beginning of the model, which started in the age of 15. Costs of glasses and contact lenses, due to the presence of astigmatism, was approx. by 10% higher reflecting the price difference of toric lenses from spherical ones, both for contact lenses and lenses

Table 1 Results of evaluation by the TOPSIS method

Parameter	Rating	Order
Glasses	0.5818	1
Contact lenses	0.5426	2
Refractive surgery	0.3672	3

Table 2 Results of the CEA

Parameter	C/E	E/C·1000
Glasses	10,313	0.0970
Contact lenses	2303	0.4341
Refractive surgery	54,466	0.0184

for glasses. The result was similar to the first group: wearing monofocal glasses, LASIK in the age of 20, and again wearing monofocal glasses when presbyopia begins to manifest (€4,427).

The third group (iii) contains the lowest number of correction combinations due to the beginning of modeling with the occurrence of presbyopic difficulties in the age above 40–45. The lowest cost of correction is wearing only monofocal glasses (€2,467).

3.6 FMEA

There is a low risk for the eyeglasses used for vision correction. There are no potential risks to be included in the high-risk group. There are only risks ranging from a low to medium degree (breakage of glasses, insufficient adaptation to the shape and client's needs, inability to get used to multifocal glasses, etc.).

In the case of contact lenses, a higher number of possible risks may occur. The most serious threat posed to the wearers of contact lenses by using the lenses longer than recommended. This is one of the reasons that may cause other possible health risks. Other threats include improper use of the solution for contact lenses, selection of bad type, etc. Such problems can occur with an inappropriate application of contact lenses.

Refractive surgery brings a high number of potential, mainly health, risks. The highest risk of this modality is the fact that there are no freely available independent evaluations of the clinics and other health care facilities that perform the surgery. The success factor of the surgery is one of the main elements in preventing potential risks. Despite the fact that several measures have been designed reducing the impact of possible risks, there are still risks with a high severity of possible consequences.

3.7 CEA

The effects of individual methods of correction required for the CEA were found by the TOPSIS method (Table 1).

From the point of view of the effectiveness per output unit, the best cost-effectiveness ratio is for contact lenses (Table 2). The same order of the correction methods was found also in the case of costs per unit.

ICER selected contact lenses as the most appropriate correction method (Fig. 5), from the perspective of effectiveness and the effect on the monetary cost unit, too.

3.8 Sensitivity Analysis

The sensitivity was measured in two ways, namely by decreasing or increasing prices. The price reduction or increase was considered only for contact lenses, or just for glasses, or for glasses and contact lenses at the same time. The price of refractive surgery was altered. The change in purchase price has an impact on the cost criterion for adults until the onset of presbyopia and the resulting comfort from the correction method.

Reduce contact lens prices was presented by prices from optics to drug. The price of glasses was reduced by lowering the purchase price to one third of the current price (Table 3). The order of decision-making of the correction methods, however, remains the same.

The increase in the price of contact lenses was made by including the price of daily lenses instead of monthly lenses. In the case of glasses, the value of the order was doubled (Table 4). With a higher price for contact lenses, decisions in favor of glasses and refractive surgery are slightly elevated. In the case of price increases for both glasses and contact lenses, their decision value falls a bit.

Fig. 5 Comparison of refractive methods by ICER

contact lenses - glasses	refractive surgery- glasses	refractive surgery- contact lenses
4722	-2618	-4264

Compared methods [-]
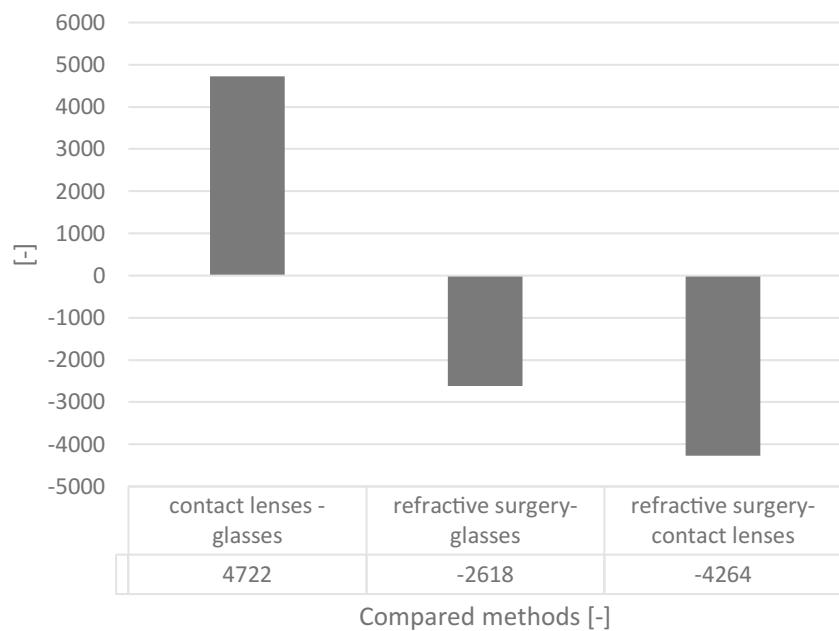
Table 3 Sensitivity analysis: lowering purchase prices

Parameter	Lower price rating	Glasses order	Lower price rating	Lenses order	Lower price rating	Glasses and lenses order
Glasses	0.6002	1	0.5370	1	0.5575	1
Contact lenses	0.5404	2	0.5107	2	0.4890	2
Refractive surgery	0.3739	3	0.4414	3	0.4179	3

Table 4 Sensitivity analysis: increased purchase prices

Parameter	Higher price rating	Glasses order	Higher price rating	Lenses order	Higher price rating	Glasses and lenses order
Glasses	0.5386	2	0.6048	1	0.5615	1
Contact lenses	0.5443	1	0.5285	2	0.5360	2
Refractive surgery	0.3538	3	0.3823	3	0.3721	3

4 Discussion

Outside the Czech Republic, studies have been carried out to try to calculate the costs associated with a refractive error from client's perspective. However, the results are not easily transferable from one country to other country. Apart from different healthcare systems, the methodology of how the results are obtained (calculated) is of great importance. In the USA, the costs associated with eye disease and eye damage are $450 per person [9]. The figure was obtained by dividing the total amount by the total number of inhabitants. A more detailed study was conducted in Australia, where the resulting costs were $29,905 per person. However, the study was performed only in patients of the age of 40 (Vision 2020, 2010). The Belgian study shows the total costs and their composition for each correction method for a 30-year-old patient for the period of 15 years, i.e. until the age of presbyopia onset [4, 8]. There have been no such studies for the Czech Republic.

The choice and influence of the type of refractive aid depends on the age of the client, from using only glasses

lifelong, to changing glasses and contact lenses with a subsequent refractive surgery and return to the glasses and lenses alternation in the presbyopic age and above.

5 Conclusion

In the study, we collected and evaluated data on glasses, contact lenses, refractive surgery costs from the perspective of a client. When modeling possible age-related combinations of correction aids, 116 combinations were found. The least costly for (i) myopia in children from the age of 6 is to wear monofocal glasses, and once again wearing the monofocal glasses, undergoing the LASIK surgery in the age of 20, and again wearing monofocal glasses only when presbyopia begins to manifest (€5,296). For (ii) myopia and common astigmatism in adolescence (from 15 years of age), the cheapest option was to start with glasses, undergo LASIK at the age of 20, and again wearing monofocal glasses when presbyopia begins to manifest (€4,427). For presbyopia after the 40th–45th year of age the best option are monofocal glasses (€2,467).

FMEA processed for individual corrections showed no high risk for the glasses correction. In the case of contact lenses, there are certain health hazards that can be minimized by following the instructions from the producer and clinic. Refractive surgery carries risks that have little chance to be changed.

The cost-effectiveness analysis was calculated applying a multiple-criteria analysis (the TOPSIS method). It resulted in preferring eyeglasses followed by contact lenses and refractive surgery in the third place.

Conflict of Interests The authors declare no conflict of interests.

References

1. Anton, M. Refrakční vady a jejich vyšetřovací metody. 3rd edn., Brno: Národní centrum ošetřovatelství a nelékařských zdravotnických oborů, 2004.
2. Anton, M. Vývoj refrakce oka: úvodní část. Česká oční optika. 2005, vol. 46, č. 1, str. 8.
3. Skrbek, M. Přínos korekce malých refrakčních vad. Brno, 2009.
4. Christiaens W, Kohn L, Obyn C, De Winter L, Gussé S, Defourny N, De Laet C, Paulus D. Correction of refractive errors of the eye in adults – Synthesis. Health Services Research (HSR) Brussels: Belgian Health Care Knowledge Centre (KCE). 2013. KCE Reports 202Cs.
5. Efron, N., ed. Contact lens practice. 3rd ed. Oxford: Elsevier, 2017.
6. Barták, M.; Masopustová, I.; Lamblová, K.; Rogalewicz, V. Cost of senile cataract surgery in 65 + population in the Czech Republic In: Central European Conference in Finance and Economics (CEFE2017). Košice: Technická univerzita v Košiciach, Ekonomická fakulta, 2017. pp. 70–79.
7. The Economic Impact of Vision Loss in Australia in 2009. Melbourne, Australia: Vision 2020 Australia, 2010.
8. Obyn C, Smit Y, Post P, Kohn L, Defourny N, Christiaens W, Paulus D. Correction of refractive errors of the eye in adults – Part 2: laser surgery and intraocular lenses. Health Technology Assessment (HTA) Brussels: Belgian Health Care Knowledge Centre (KCE). 2013. KCE Reports 215. D/2013/10.273/105.
9. Wittenborn, J., Rein, D., The Economic Burden of Vision Loss and Eye Disorders in the United States. Chicago, 2013.
10. Frick KD, Gower EW, Kempen JH, Wolff JL. Economic impact of visual impairment and blindness in the United States. Arch Ophthalmol 2007 Apr;125(4).
11. Bad vision? Denik, https://www.denik.cz/zdravi/spatny_zrak_pruzkum.html, last accessed 2018/01/25.
12. Refractive surgery like answer on vision errors Lexum, https://www.lexum.cz/o-ocni-klinice-lexum/news/laserova-operace-je-vyhodnym-resenim-ocnich-problemu, last accessed 2018/01/25.
13. Eyewear Market Size By Product, 2015–2022, https://www.gminsights.com/industry-analysis/eyewear-market, last accessed 2017/05/17.

A Preliminary Cost/Efficacy Analysis of MIRUS™ System for Sedation of Critical Patients

E. Ciagli, F. Frosini, D. Cocchi, P. Tortoli, S. Romagnoli, C. Quarti, A. R. De Gaudio, and A. Belardinelli

Abstract

Introduction Side effects of traditional analgo-sedative agents call the attention to alternative strategies of sedation for critically ill patients; volatile anaesthetics (VAs) are considered potential substitutes in selected categories of patients. MIRUS™ (Pall Corporation and TIM Germany) is an innovative system for the administration of VAs to these patients admitted in intensive care unit (ICU). **Methods** The aim of this study was to analyse the clinical and economical characteristics of MIRUS™, following the Health Technology Assessment principles (HTA); in particular, the study was focused on defining a cost/efficacy ratio of the use of MIRUS™ in an ICU with 8 beds and 80 procedures/year. HTA allows predicting the system impact in the clinical pathway before material introduction. **Results** The assessment showed that MIRUS™ could be innovative, safe and efficient, especially when applied to critically ill patients with compromised organ function. For the purposes of assessment, three classes of ICU treatments have been defined: short- (6–24 h), medium- (24–96 h) and long-term (>96 h) sedation (SS, MS, LS). Based on the technical characteristics of system, MIRUS™ could be considered unfit for LS. Considering clinical charac-

teristics, effects on patients, sedation times and costs, the HTA shows how the procedure costs are different for each class. **Conclusions** In conclusion, the use of MIRUS™ could be useful and effective for critically ill patients, in which standard sedation may be associated with drug hangover. This assessment seems economically advantageous for SS, where cost/efficacy ratios are positive performing 400 procedures/year, while for MS the cost of drugs impacts on the procedure cost. Therefore, looking at the potential clinical benefits on all potential treatable patients, the best addition strategy of the system in the hospital should be evaluated to optimize the cost/efficacy ratio.

1 Introduction

Critically ill patients usually receive sedative drugs with the aim to increase the tolerability to invasive procedures and mechanical ventilation, avoid agitation and promoting sleep. Different sedation strategies are applied in intensive care units (ICUs) [1, 2].

Side effects of traditional analgo-sedative agents (benzodiazepines, propofol, and ketamine) call the attention to alternative strategies of sedation; in particular, volatile anaesthetics (VAs) are potential substitutions to the standard agents in selected categories of patients including those with reduced hepatic and renal function, those with status epilepticus and those with status asthmaticus [3–5]. Recognized and hypothesized benefits attributed to VAs in comparison with benzodiazepines or propofol are shorter wake up and extubation times, faster sedation and return to

E. Ciagli (✉) · F. Frosini · D. Cocchi · P. Tortoli
Department of Information Engineering, University of Florence, Florence, Italy
e-mail: elena.ciagli@unifi.it

S. Romagnoli · A. R. De Gaudio
Department of Anesthesia and Critical Care, Azienda Ospedaliero-Universitaria Careggi, Florence, Italy

C. Quarti
Pall Italy, Milan, Italy

A. Belardinelli
Department of Innovation, Quality and Control, Azienda Ospedaliero-Universitaria Careggi, Florence, Italy

spontaneous breathing, fewer delirium, distal organs protection (lungs, liver, kidney) and improve in mortality [6, 7]. VAs are safe and efficient for the sedation, are well tolerated and easily predictable effects; in general, they could be considered as ideal sedative agents especially in selected populations [8].

MIRUS™ (Pall Corporation and TIM Germany) is an innovative system for the administration of VAs to patients admitted in ICU. It is a fully automated and closed system that can be used for the administration of Sevoflurane, Desflurane and Isoflurane [9–11].

The aim of this study was to analyse the clinical and economical characteristics of MIRUS™, following the Health Technology Assessment principles (HTA).

2 Method

Health Technology Assessment is a support method for technology purchases that assess their quality, safety, efficacy and efficiency. HTA is considered a bridge that links hospital decision maker with scientific evidence by useful reporting system, and it allows predicting the system impact in the clinical pathway before material introduction. After the analysis of system's scientific evidences, reference clinical pathway and characteristics of new technology, it is possible to create the HTA report about economic aspects, performances and possible benefits of the technology.

In this study, it has been developed a HTA report about MIRUS™ system; the analysis was focused on defining a cost/efficacy ratio of the use of system in an ICU with 8 beds and 80 procedures/year. For the aim, it was necessary to analyse and itemize some different elements about system appropriateness and benefits in relation with the current situation. The appropriateness elements are: staff requirements, structural impact, impact on the process, procedure cost, economic analysis and financial commitment. The benefits elements are: safety, clinical efficacy, impact on the patient, cost/effectiveness, reliability and innovativeness [12, 13].

HTA report consists to assign to each elements a score of improvement, deterioration or stability in relation with the actual situation, so as to highlights system characteristics and appropriateness/benefits ratio. Scores of each characteristic, combined with his weight, define the radar of appropriateness and benefits, as shown in Fig. 1 for MIRUS™ system. Subsequently each feature will be explained in detail.

3 Results

The traditional sedation method of reference is intravenous administration of propofol.

The examined system MIRUS™ does not require any particular staff requirement, its learning curve is very short and the interface user friendly.

Its installation and employment do not provide any structural impact compared to the traditional method of sedation.

MIRUS™ does not foresee changes in terms of operative times or days of recovery; therefore, changes in terms of impact on the process, health organization and management of clinical pathways are not foreseen, with its implementation replacing the traditional method.

Regarding staff requirements, structural impact and impact on the process, MIRUS™ does not require any particular precaution.

The assessment shows that MIRUS™ is more innovative, safe and efficient in relation with the traditional method of sedation, especially when applied to critically ill patients with compromised organ function.

His closed-circuit architecture ensures that the entire drug supplied to patients is assimilated by it, increasing the efficiency of sedation, and that the surrounding environment is not contaminated by VAs, rising safety even for health workers. MIRUS™ has also an automatic end-expiratory control system, which allows to inject the anesthetics in moment with higher inspiratory flow. In fact, providing the anesthetic in the initial phases of the inhalation, it is prevented that this remains in the trachea or upper airways and it is expelled immediately with the subsequent expiration, increasing the perfusion of the gas and the effectiveness of the treatment. MIRUS™ allows to precisely establish the best moment of VAs injection through its control unit; this unit measures also gas concentration and respiratory parameters, and allows rapid variation of sedation level, according to the patient's pathophysiological conditions and according to clinical needs.

Besides the use of VAs has less disabling impact on the critical ill patients with particularly compromised organs, such as patients treated in ICUs. In fact, sevoflurane, desflurane and isoflurane are not prone to accumulate in patients with impaired clearance function than standard anesthetics; they are not metabolized by kidneys and liver and totally removed by the lungs. Accumulation of sedatives eventually leads to prolonged mechanical ventilation, ICU and hospital stay, mortality and costs. The induction of anesthesia and the awakening from it are much faster in the case of use of VAs; they guarantee lower post-traumatic stress and the practically total absence of post-awakening delirium. Safety, clinical efficacy and impact on the patient improve compared to the traditional method.

For the purposes of economic assessment of system, three classes of ICU treatments have been defined: short- (6–24 h), medium- (24–96 h) and long-term (>96 h) sedation (SS, MS, LS). Patients fit for SS could be those who underwent
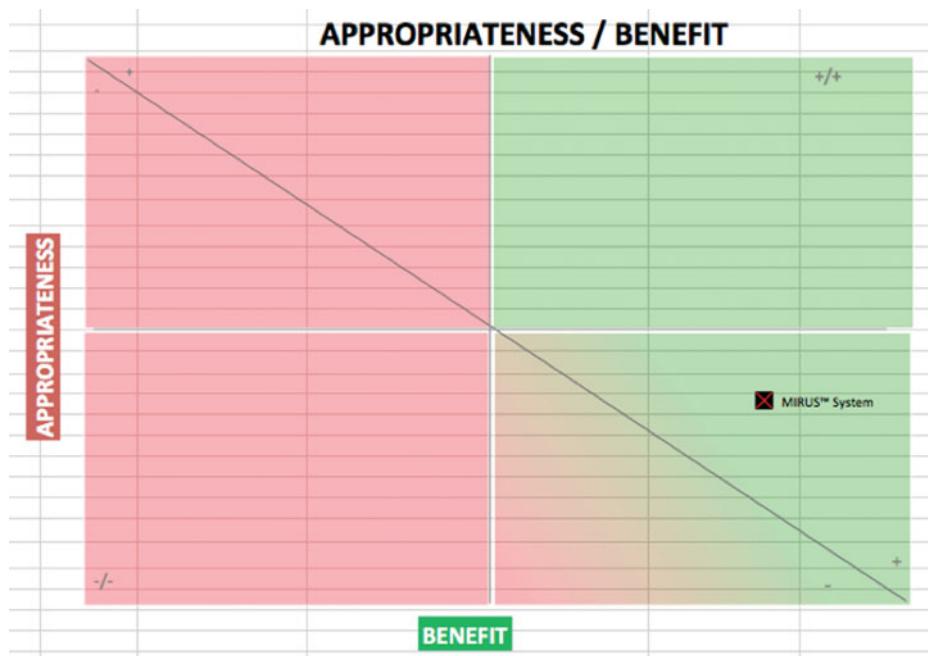
Fig. 1 Radar appropriateness/benefit of MIRUS™

Table 1 Characterization of consumable materials

Classes of ICU treatments	Number of patients treatable with a reflector	Number of patients treatable with a filter
Short sedation (SS)	32	8
Medium sedation (MS)	8	2

Fig. 2 MIRUS^{TM} procedure cost for SS

Procedure cost - Medium Sedation (MS)

Fig. 3 MIRUS™ procedure cost for MS

surgery, MS could be optimal for trauma patients while LS for oncological patients. Looking at the technical characteristics of system, MIRUS™ could not be used for very LS, especially due to the impossibility to apply humidification to the airway circuit.

The economic assessment includes in HTA model shows how the procedure costs are different for each class. The cost elements that contribute to calculate the procedure cost are: the size of necessary investment for the creation of anesthesiology station (I), costs of consumable materials (C), costs of drugs (D), time of sedation (S), average hourly consumption of agents (H) (10 ml/h of propofol and 7.89 ml/h of sevoflurane [14, 15]), cost of maintenance (M), expected system years of life (Y) and number of annual treatments (T) [16]. The formula used in the model to calculate the procedure cost (P) is:

$$P = (I/Y)/T + M/T + C + (H * S * D) \qquad (1)$$

Consumable materials of system are a reflector and a filter; the technical characteristics provide that a reflector, once activated, can be used for a prolonged anesthetic administration of up to 8 days, while a filter can be used for a maximum of 48 continuous hours. Based on the clinical indications of anesthetic administration, more patients may be treated with the same consumable material, such as showed in Table 1.

This aspect is the most important reason why the procedure costs are different between classes of treatment; in fact, reflector and filter could be used for a different number of patients in relation with the time of treatment and their cost could be assign differently (see Figs. 2 and 3).

How the figures shown, the procedure cost, considering 80 procedures/years, is 85.41 € for SS and 154.13 € for MS. The procedure costs for traditional method are 2.59 € for SS and 7.09 € for MS; these derive only from cost of consumables and cost of propofol used in the traditional procedure. From the figures it is possible to highlight how the procedure cost steadies and approaches traditional cost by carrying out at least 400 annual treatments; in this case the procedure costs are 35.41 € for SS and 104.13 € for MS.

4 Conclusions

In conclusion, the use of MIRUS™ could be safe, useful and effective for critically ill patients, in which standard sedation may be associated with drug hangover.

Regarding economic aspects, the traditional method of sedation results in general the most convenient, assumed the consumables used and the type of drug administered. Looking the clinical aspects and economic characteristics of MIRUS™ system, this assessment shows how the system

could be economically advantageous for SS, where cost/efficacy ratios are positive and the procedure cost close with the traditional method performing at least 400 procedures/year. On the contrary, for the treatments in MS, the cost of volatile agents impact on the procedure cost, and consequently on general economic analysis.

Therefore, looking at the potential clinical benefits of MIRUS™ system on all potential treatable patients, the best addition strategy of the system in the hospital should be evaluated to optimize the cost/efficacy ratio and to implement the clinical pathways of ICUs.

Conflict of Interest The authors declare that they have no conflict of interest.

References

1. Barr J., et al.: Clinical practice guidelines for the management of pain, agitation, and delirium in adult patients in the intensive care unit. Critical care medicine 41.1 (2013): 263–306.
2. Reade M. C., and Simon F.: Sedation and delirium in the intensive care unit. New England Journal of Medicine 370.5 (2014): 444–454.
3. Baron R., et al.: Evidence and consensus-based guideline for the management of delirium, analgesia, and sedation in intensive care medicine. Revision 2015 (DAS-Guideline 2015)–short version. GMS German Medical Science 13 (2015).
4. Soukup J., et al.: State of the art: sedation concepts with volatile anesthetics in critically ill patients. Journal of critical care 24.4 (2009): 535–544.
5. Jerath A., et al.: Volatile Anesthetics. Is a New Player Emerging in Critical Care Sedation?. American journal of respiratory and critical care medicine 193.11 (2016): 1202–1212.
6. Grabitz S. D., et al.: Dose-dependent protective effect of inhalational anesthetics against postoperative respiratory complications: a prospective analysis of data on file from three hospitals in New England. Critical care medicine 45.1 (2017): e30–e39.
7. O'Gara B., and Daniel T.: Lung protective properties of the volatile anesthetics. Intensive care medicine 42.9 (2016): 1487–1489.
8. Bellgardt M., et al.: Inhalative Anästhetika in der Intensivmedizin. Intensivmedizin up2date 9.03 (2013): 185–204.
9. Bomberg H., et al.: Evaluating the efficiency of desflurane reflection in two commercially available reflectors. Journal of clinical monitoring and computing (2016): 1–10.
10. Vinnikov V., et al.: Automated control of end-tidal volatile anaesthetic concentration using the MIRUS™ system: a comparison of isoflurane, sevoflurane and desflurane in anaesthesia. Critical Care 19.1 (2015): P495.
11. Bomberg H., et al.: A novel device for target controlled administration and reflection of desflurane–the Mirus™. Anaesthesia 69.11 (2014): 1241–1250.
12. Miniati R., et al.: Development of sustainable models for technology evaluation in hospital. Technology and Health Care 22.5 (2014): 729–739.
13. Frosini F., et al.: Integrated HTA-FMEA/FMECA methodology for the evaluation of robotic system in urology and general surgery. Technology and Health Care 24.6 (2016): 873–887.
14. Romagnoli S., et al.: The New MIRUS System for Short-Term Sedation in Postsurgical ICU Patients. Critical care medicine 45.9 (2017): e925–e931.
15. Mancinelli P., et al.: MIRUS™, a new system for sedation with halogenates in the ICU: a preliminary study of feasibility in postsurgical patients. Critical Care 19.1 (2015): P492.
16. Drummond, M. F., et al.: Methods for the economic evaluation of health care programmes. Oxford university press, 2015.

HTA in the Czech Republic: Still Behind

Vladimír Rogalewicz, Ivana Kubátová, Gleb Donin, Tomáš Doležal,
Klára Lamblová, Jana Bartáková, and Peter Kneppo

Abstract

The paper analyses the current state of HTA implementation and organisational initiatives in the Czech Republic. Although there have been some substantial elements of HTA applied in the decision process of pharmaceutical reimbursement since 2008, HTA methods are rather disregarded in other technologies. Since there is practically no demand for HTA studies from payers and state representatives, HTA has been cultivated above all by interested individuals and small academic research groups around them. These groups have succeeded in keeping pace with the global development both in theoretical and practical issues (among others in HTA methods for medical devices), however, the practical production of country specific HTA studies is rather rare. The main problem is non-existence of a national commonly accepted methodology and a legal framework. At least two attempts to establish a regular HTA process initiated by the Ministry of Health were destined to fail due to frequent personal changes in the Ministry. We discuss topical issues to be solved on the way to a national HTA system, and present our vision of a possible solution.

Keywords

HTA • Czech Republic • Current state

1 Introduction

Health Technology Assessment (HTA) was suggested in 1970s to cope with the problem of a conflict between sources and demands in healthcare. It comprises a number of methods for assessing safety, effectiveness, appropriateness and costs of health technologies, i.e. pharmaceuticals, devices, materials, diagnostic and therapeutic procedures, preventive measures, and/or organizational and managerial measures. Next to that, it addresses also unintended consequences of technologies on social, ethical, legal, political and organizational issues. Latest since the 1990s, HTA has been used as a decision-supporting tool in most of the developed countries.

In the Czech environment, first information about HTA appeared relatively late. Two articles in the journal *Praktický lékař* in 2002 and 2003 [1, 2] were probably the first information about HTA in the Czech Republic, while the paper by Žaloudník et al. [3] can be considered the first serious attempt to introduce HTA to the country. In 2008, Dlouhý et al. published a review paper [4] expressing their opinion that "The neglect of HTA in the past might be excused by the fact that the main issue was a jump to catch up with the West in the fields we had been lagging behind. (…) At present, many national [healthcare] facilities are top level. (…) Hence, the slow development of HTA in the Czech Republic cannot be excused any more." Ten years later the situation does not seem to have changed much. The only exception is the drug reimbursement regulation. This paper will address the current state of HTA in the Czech Republic and try to name the reasons for its unsatisfactory situation, giving some accent to medical devices.

2 Drug Pricing and Reimbursement

A concentrated effort of some HTA popularizers including one of the authors (T.D.) mirrored in the 2008 amendment to the Act No. 48/1997 Coll. on Public Health Insurance that prescribes some fragments of HTA for drug pricing and reimbursement proceedings. In order a (new) drug was listed for reimbursement from the public health insurance (that covers about 80% of all healthcare payments in the country), the applicant (typically a pharma company) has to present a

V. Rogalewicz (✉) · I. Kubátová · G. Donin · P. Kneppo
CzechHTA, Faculty of Biomedical Engineering, Czech Technical
University in Prague, Prague, Czech Republic
e-mail: rogalewicz@fbmi.cvut.cz

T. Doležal · K. Lamblová · J. Bartáková
iHETA, Prague, Czech Republic

cost utility analysis and a budget impact analysis to the State Institute of Drug Control (SÚKL) that is the responsible state authority. However, at the beginning there was no generally accepted methodology for preparation of these analyses as well as for their content.

The situation was reflected by the Czech Pharmacoeconomic Society that drafted and published guidelines for health-economic evaluations [5]. However, the Society does not represent the whole Czech HTA community, and their guidelines serve as an optional tool. Despite of some effort to cover all technologies, it is modeled above all for pharmaceuticals. The SÚKL also produced their recommendations for cost-effectiveness analyses (published in 2013 and amended in 2017) [6]. The rules implemented by the SÚKL have been changing over the years; at present, the required documents and the transparency of the procedure approach a true HTA process, at least as concerns its economic side. However, organizational, social and other issues considered by multidisciplinary HTA analyses are not taken into account by the Institute. There is no separation of the appraisal, approval and decision phases within the SÚKL, at least in their organizational structure. Since the SÚKL is a governmental body with decision-making powers, acting as a HTA agency would bring them into a conflict of interests.

While the process is at least partly covered by the SÚKL for drugs, there is no formal HTA procedure for any other technologies incl. medical devices, diagnostic and therapeutic interventions, preventive measures, or organizational measures.

3   Attempts to Implement HTA Processes and Establish an Agency

In the time of the above described legislative activity, there definitely was a community of experts (above all in the academic sphere) in the Czech Republic, who had an interest in promoting and disseminating methods and findings of evidence-based medicine and HTA. Such a group and their common belief is probably the decisive factor in reaching their political goals [7]. Löblová suggests that "One of the crucial beliefs of an HTA community would be healthcare technologies that offer an unfavorable cost-benefit ratio should not be reimbursed (unless there are overriding concerns), and that this ratio should be established by a thorough scientific multidisciplinary analysis" [7]. Nobody of that community expected that the legal requirements incorporated in the Act No. 48/1997 Coll. in 2007 would be their last success for a long time.

It has not been a period without any HTA initiative. The health ministers Jurásková, Heger, Holcát and Němeček were interested in HTA and started some initiatives. However, due to different reasons their time in the office was limited to fulfil the whole process of HTA institutionalization, while also each of them had a different inkling of what HTA is. The most promising project was started by the Ministry of Health in 2012. EU pressure was one of the impulses: Article 15 of the EU Cross-Border Healthcare Directive (2011/24/EU) set up a network of national HTA bodies, which meant the Czech Republic needed to decide on an institution to represent it in the new network. Several organizational setups were considered throughout 2012–3, and some formal materials were drafted by an external group supported by a ministerial grant [8–10]. However, the government fell in June 2013, no finished materials were published, and the successors in the office preferred other solutions. There were two other smaller ministerial initiatives in 2010 and 2015. The result of that of 2010 was a research grant focused on HTA for medical devices [11]. In 2015, a tender for HTA implementation was managed by the Ministry; although the winning consortium was announced, the funding was actually never provided. Thus, all attempts to establish a regular HTA process initiated by the Ministry of Health were destined to fail due to frequent personal changes in the Ministry.

4   Medical Devices

Application of HTA methods for medical devices appeared to be a real challenge. While some therapeutic devices can be assessed within the whole intervention, diagnostic devices have posed many problems [12–14]. These are usually relatively expensive technologies with multiple applications, and thus they require the perspective of a hospital or a region as a whole. The CzechHTA group backed by biomedical engineers from the Czech Technical University in Prague have focused on HTA methods for devices for last 10 years. The main goal of HTA studies for devices is not to optimize the cost-effectiveness ratio, but to support the decision-making process about procurement and/or incorporation of the device. The clinical benefit is not expressed in terms of life expectancy and/or quality of life, but rather in the rate of diagnostic yield. This requires application of multiple-criteria decision analysis (MCDA), often in a combination with value engineering methods [11, 15, 16]. Despite of partial results, some problems have not been decided yet, including the choice of a suitable MCDA method [16], or the selection of the expert group [17].

Next to that, the group studied general conditions for device assessment [13, 18], pricing and procurement problems [11, 18–20], and assessment of devices in a hospital [14, 21, 22]. Thus, the Czech HTA community has succeeded in keeping pace with the European development in HTA for medical devices that appeared in the spotlight of the cost-effectiveness and HTA research [23–29].

5 Discussion

Despite of the effort of some individuals, the institutionalization of HTA stays behind the global (and European) development. What is missing is a legal framework and a generally respected authority that would coordinate activities, issue guidelines, as well as approve HTA studies so that they could not be called in question without evidence. The capacity problem that has been often mentioned in this context is probably not relevant any more. HTA methods are taught within study programs at the Faculty of Biomedical Engineering of Czech Technical University in Kladno (several hundred master level graduates), and also to some extent at the Pharmaceutical Faculty of Charles University and the Medical Faculty of Masaryk University in Brno. Although requiring some more training and international experience, these graduates are able to work in the HTA field immediately.

Löblová [30] recently studied the history of HTA institutionalization in the Czech Republic and showed that the Czech academic (she calls it epistemic) community was prepared to influence establishing a HTA agency and processes in the same (or even higher) measure as in Poland, where they were successful. She proposes a hypothesis that the result was affected above all by external random events like economic crises, geopolitical developments or political scandals, in the Czech case primarily by the frequent changes in the government (government fall, changes in the position of the minister).

In our opinion, HTA has never been supported enough by the stakeholders, and the academic community has not been strong enough to put it through. In another paper, Löblová [9] studied the roles of individual actors. Even if her results are interesting, we would like to complete them with our observations. Although many complain, the Czech healthcare system is more or less working with respect to the delivery of accessible care. Any change (and an introduction of HTA would be a rather heavy change) represents a danger for many actors. The bureaucracy would lose a part of their power, the public health insurance companies (belonging to the bureaucracy) would at least have more responsibility and hence more work (at present they redistribute the premium, while the rules are decided by the Ministry of Health). Healthcare providers (hospitals) are afraid of a violation of a fragile financial balance, being accommodated to the status quo. Also clinicians are interested above all in reimbursement, when the older ones do not believe in economic methods. However, some of the younger generation (especially from university hospitals and other facilities involved in research) are interested in economic consequences of the methods they propose. Patient organizations are weak in the Czech Republic, and the existing ones are afraid of a worse access of patients to expensive healthcare. The general public has been frightened that any new administrative barrier would make the current extremely liberal healthcare system less patient-friendly putting obstacles to the accessibility of some care. The current adoptive system with a low level of transparency might also become less open to new technologies. In reality, we have a two-tier system, hardly permissive for new drugs on the one hand, and open but orderless and static for non-pharmaceutical technologies on the other. As concerns industry, the situation differs in the pharma industry and the medical device industry. The former support the institutionalization of HTA as a way to equalizing the conditions, the later consider HTA for another administrative barrier, and mostly oppose it. Thus, the political consensus to introduce HTA methods into the Czech healthcare system at the national level is missing (except for the existing requirements in drug reimbursement proceedings). Let us remark that a quite different situation is at the hospital level. The interest in the hospital-based HTA has been growing, especially in the area of medical device procurement and in hospital process adjustment.

On the other hand, the academic (epistemic) community is prepared for an establishment of a national HTA system. In our opinion, what is most important is the legal framework and a general agreement on common guidelines supported by a kind of their official acknowledgement. No new super-office is necessary; Czech Republic can follow the model of one or more small ("light") HTA bodies. Until the health insurance offices manage the healthcare (and not only distribute the collected premium money), the government should support the newly established HTA bodies by commissioning some studies and by encouraging other authorities to order some analyses for their own purposes. On the other hand, it may be some disappointment that HTA studies do not bring final solutions, but only provide decision-makers with further evidence; decisions are a purely political issue and should take into account all dimensions of the problem (which is contained in a good HTA study, though).

6 Conclusion

The HTA landscape is not a tabula rasa in the Czech Republic. There is a visible (academic) community supporting it, and most healthcare actors are generally informed, although they have sometimes unrealistic believes and expectations. What is missing is a demand for HTA studies to support decisions at the national level. Completed Czech HTA studies have been rare if any until now; nevertheless, there are numerous results of partial studies available (and sometimes even applied in practice). The

institutionalization will probably depend on the political will of future governments. The Czech Republic is not alone disregarding HTA methods or results. The situation is similar in most European post-communist countries [7]. An introduction of a transparent HTA process would not probably bring any decrease in costs, but would support the quality of the healthcare and its adaptation to up-to-date medicine.

Conflict of Interests The authors declare no conflict of interests.

References

1. Grundová, D., Malina, A., Šimek, J., Křížová, E.: Co je hodnocení technologií (Technology Assessment-TA). Praktický lékař 82, 83–88 (2002)
2. Křížová, E., Šimek, J., Malina, A., Grundová, D., Trčková, M.: Zdravotnické technologie v empirickém šetření. Hodnocení dostupnosti a dalších etických aspektů u vybraných technologií v čekém prostředí. Praktický lékař 83, 690–694 (2003)
3. Žaloudík, J., Dušek, L., Vyzula, R.: Koncepce HTA pro onkologii. Klinická onkologie 17, 5–10 (2004)
4. Dlouhý, M., Barták, M., Hlaváček, A., Kokavec, P., Malina, A.: Zdravotnické technologie v ČR [A need for health technology assessment in the Czech Republic]. Zdravotnictví v České republice 11, 136–138 (2008)
5. ČFES: Doporučené postupy České farmakoekonomické společnosti (ČFES) pro zdravotně-ekonomická hodnocení v ČR. Česká farmakoekonomická společnost, Praha (October 2016)
6. SÚKL: Postup pro posuzování analýzy nákladové efektivity. SP-CAU-028. Státní úřad pro kontrolu léčiv, Praha (2017)
7. Loblova, O.: Three worlds of health technology assessment: explaining patterns of diffusion of HTA agencies in Europe. Health Economics Policy and Law 11, 253–273 (2016)
8. Dáme HTA zelenou? (http://sdruzeniobcan.cz/files/obcanvsiti2012_10.pdf). Sdružení Občan z.s., Praha (2012)
9. Löblová, O.: Who's afraid of institutionalizing health technology assessment (HTA)?: Interests and policy positions on HTA in the Czech Republic. Health Economics, Policy and Law 1–25 (2017)
10. Gulacsi, L., Rotar, A., Niewada, M., Loblova, O., Rencz, F., Petrova, G., Boncz, I., Klazinga, N.: Health technology assessment in Poland, the Czech Republic, Hungary, Romania and Bulgaria. European Journal of Health Economics 15, S13–S25 (2014)
11. Rosina, J., Rogalewicz, V., Ivlev, I., Juřičková, I., Donin, G., Jantosová, N., Vacek, J., Otawová, R., Kneppo, P.: Health Technology Assessment for Medical Devices. Lekar a technika - Clinician and Technology 44, 23–36 (2014)
12. Drummond, M., Griffin, A., Tarricone, R.: Economic evaluation for devices and drugs, same or different? Value in Health 12, 402–404 (2009)
13. Rogalewicz, V., Jurickova, I.: Specificities of Medical Devices Affecting Health Technology Assessment Methodology. Proceedings IWBBIO2014: International Work-Conference on Bioinformatics and Biomedical Engineering, Vols 1 and 2, 1229–1234 (2014)
14. Rogalewicz, V.: Health technology assessment as a tool for medical devices management in hospitals. 2015 E-Health and Bioengineering Conference (EHB) (2015)
15. Ivlev, I., Kneppo, P., Bartak, M.: Multicriteria decision analysis: a multifaceted approach to medical equipment management. Technological and Economic Development of Economy 20, 576–589 (2014)
16. Kubátová, I.: Application of value engineering and multiple-criteria decision making in medical devices assessment [Využití hodnotového inženýrství a multikriteriálního rozhodování při hodnocení zdravotnické techniky]. PhD Thesis, Faculty of Biomedical Engineering, pp. 120. Czech Technical University in Prague, Kladno (2015)
17. Ivlev, I., Kneppo, P., Bartak, M.: Method for selecting expert groups and determining the importance of expert' judgments for the purpose of managerial decision-making tasks in health system. E & M Ekonomie a Management 18, 57–72 (2015)
18. Rogalewicz, V., Ujhelyiova, A., Pousek, L., Sinkorova, V., Kneppo, P.: Health Technology Assessment and Medical Devices. 2011 E-Health and Bioengineering Conference (EHB) (2011)
19. Donin, G., Kneppo, P.: Medical Device Procurement Tracking System: Concept and Methods. In: Lacković, I., Vasic, D. (eds.) 6th European Conference of the International Federation for Medical and Biological Engineering, IFMBE Proceedings vol. 45, pp. 629–632. Springer International Publishing (2015)
20. Donin, G., Barták, M., Kneppo, P.: Estimation of medical equipment prices – a case study of tomotherapy equipment in the Czech Republic. Journal of Business Economics and Management 18, 1193–1211 (2017)
21. Királyová, E., Steklá, M., Donin, G.: Selection of a PET/CT scanner for the department of nuclear medicine. 6th IEEE International Conference on E-Health and Bioengineering, EHB 2017, pp. 329–332. Grigore T. Popa University of Medicine and Pharmacy, Sinaia; Romania (2017)
22. Rogalewicz, V., Matuskova, K., Zavadil, M., Vaclavikova, A., Kamensky, V.: POCT cost effectiveness case study on the way to a HB-HTA unit. Value in Health 20, A600-A600 (2017)
23. Ciani, O., Federici, C., Tarricone, R.: Current and Future Trends in the HTA of Medical Devices. XIV Mediterranean Conference on Medical and Biological Engineering and Computing MEDICON 2016, IFMBE Proceedings, vol 57, pp. 1345–1348. Springer International Publishing, Cham (2016)
24. Rothery, C., Claxton, K., Palmer, S., Epstein, D., Tarricone, R., Sculpher, M.: Characterising Uncertainty in the Assessment of Medical Devices and Determining Future Research Needs. Health Economics 26, 109–123 (2017)
25. Fuchs, S., Olberg, B., Panteli, D., Perleth, M., Busse, R.: HTA of medical devices: Challenges and ideas for the future from a European perspective. Health Policy 121, 215–229 (2017)
26. Fuchs, S., Olberg, B., Panteli, D., Busse, R.: Health Technology Assessment of medical devices in Europe: processes, practices, and methods. International Journal of Technology Assessment in Health Care 32, 246–255 (2016)
27. Broekhuizen, H., Groothuis-Oudshoorn, C.G.M., van Til, J.A., Hummel, J.M., IJzerman, M.J.: A Review and Classification of Approaches for Dealing with Uncertainty in Multi-Criteria Decision Analysis for Healthcare Decisions. Pharmacoeconomics 33, 445–455 (2015)
28. Pecchia, L., Mirarchi, L., Doniacovo, R., Marsico, V., Bracale, M.: Health Technology Assessment for a Service Contract: a new method for decisional tools. 11th International Congress of the IUPESM/World Congress on Medical Physics and Biomedical Engineering, IFMBE Proceedings vol. 25, pp. 105–108. Springer, Berlin, Heidelberg (2009)
29. Schnell-Inderst, P., Mayer, J., Lauterberg, J., Hunger, T., Arvandi, M., Conrads-Frank, A., Nachtnebel, A., Wild, C., Siebert, U.:

Health technology assessment of medical devices: What is different? An overview of three European projects. Zeitschrift für Evidenz, Fortbildung und Qualität im Gesundheitswesen 109, 309–318 (2015)

30. Löblová, O.: When Epistemic Communities Fail: Exploring the Mechanism of Policy Influence. Policy Studies Journal https://doi.org/10.1111/psj.12213 (2017)

Cost-Effectiveness Analysis of Intrabeam System Introduction to the Czech Healthcare System Environment

Vojtěch Kamenský, Gleb Donin, Veronika Burianová, Ondřej Gajdoš,
Vladimír Rogalewicz, Ivana Kubátová, Silvie Jeřábková,
and Peter Kneppo

Abstract

Backround: Intrabeam system is a technology used in oncology for intraoperative radiotherapy (IORT), a technique of partial delivery of radiation therapy to the tumour bed during surgery. The aim of this study is to evaluate cost effectiveness of the Intrabeam system compared to the standard treatment with external beam radiotherapy (EBRT) in early stage breast cancer treatment in order to reach a decision on a possible introduction of the technology to the Czech healthcare system. Methods: In order to determine the clinical effects, a worldwide literature review was conducted. The cost of the Intrabeam system was estimated based on available information about acquisitions of the system worldwide in the last 5 years. The cost of treatment was calculated from the perspective of a healthcare payer, and all the information gathered was summarized in a Markov model to finalize the cost-effectiveness calculation. A sensitivity analysis was performed. Results: The input of the model was based on the TARGIT-A pragmatic randomized controlled trial—the largest and most comprehensive study among 26 selected studies from the literature review. The estimated purchase cost of the system for the Czech Republic was determined in the range of CZK 16–20 million without VAT. Based on the findings, three versions (baseline, optimistic, pessimistic) of the calculation for IORT interventions using Intrabeam were determined. In the baseline scenario, the cost of the Intrabeam system intervention was CZK 38 559, the ICER value was CZK 53 483 saved per 1 QALY lost. The results of the sensitivity analysis are consistent with the results of the baseline scenario. The ICER value is not above the cost-effectiveness threshold (currently a little above CZK 1.2 million), which is required to consider the technology cost effective. Conclusion: According to the results of the cost-effectiveness analysis, we do not currently recommend the Intrabeam system to be introduced into the Czech healthcare system.

V. Kamenský (✉) · G. Donin · V. Burianová · O. Gajdoš
V. Rogalewicz · I. Kubátová · S. Jeřábková · P. Kneppo
Faculty of Biomedical Engineering, Czech Technical University in Prague, Kladno, Czech Republic
e-mail: vojtech.kamensky@fbmi.cvut.cz; kamenvoj@gmail.com

G. Donin
e-mail: gleb.donin@fbmi.cvut.cz

V. Burianová
e-mail: veronika.burianova@fbmi.cvut.cz

O. Gajdoš
e-mail: ondrej.gajdos@fbmi.cvut.cz

V. Rogalewicz
e-mail: rogalewicz@fbmi.cvut.cz

I. Kubátová
e-mail: ivana.kubatova@fbmi.cvut.cz

S. Jeřábková
e-mail: silvie.jerabkova@vzp.cz

P. Kneppo
e-mail: kneppo@fbmi.cvut.cz

1 Introduction

Modern medicine tries to go toward less radical, less invasive and patient-friendly techniques. Intraoperative radiotherapy (intraoperative radiation therapy, IORT) is the modality that aimed to provide the radiation therapy of malignant tumours during surgery [1].

CARL ZEISS Intrabeam system is one of the devices used for IORT [2, 3]. The main component of the Intrabeam system is a miniature accelerator that emits and accelerates electrons. The electron beam is guided through the tube into an applicator. Applicator emitted low energy X-ray radiation. Different shapes and sizes of applicators allows to be used Intrabeam system in various parts of the patient's body.

Due to limited resources and a relatively rapid implementation of new technologies, emphasis should be placed on the justification and value decision of new practices in terms of clinical and economic benefits arising from their use.

Breast cancer is the second most common cancer in the population of Czech woman. It is a malignant tumour with the highest mortality; in 2014 there was 36.22 deaths per 100 000 women and incidence rate was 130.85 cases per 100 000 women. Mortality showed a slight decline in the last years, which can be caused by a more effective treatment [4] on the other hand incidence decreased in the last years. The current standard treatment of breast cancer is breast conserving surgery (BCS, e.g. lumpectomy) followed by postoperative irradiation of the entire breast [5]. "Intraoperative radiotherapy of breast cancer" is a partial delivery of radiation to the tumour bed during the surgery, immediately after breast conserving surgery. IORT can be also used as a "boost-therapy" for a common application of external breast irradiation.

The aim of this study is to evaluate cost effectiveness of the Intrabeam system compared to EBRT in early stage breast cancer treatment in order to reach a decision on a possible introduction of the technology to the Czech healthcare system.

2 Methods

2.1 Clinical Effectiveness

In order to determine the clinical effects, a worldwide literature review was conducted. The review was limited to the time period of January 2001 to December 2016, These data base systems were used for literature review: Web of Science, ScienceDirect (Elsevier), SpringerLink, Wiley Online Library, Medline, The Cochrane Library, Google Scholar. Searches were not limited with respect to the study design. Only studies written fully in English were included.

Inclusion criteria: the study focus is on women with early operable tumours; the study contains at least one of the following outputs: local recurrence, overall survival, disease-free survival, adverse effects of treatment, complications, health related quality of life (HRQoL), progression-free survival; it may or may not be a randomized controlled trial; the study is aimed at: IORT using the Intrabeam system compared with EBRT, or IORT using the Intrabeam system followed by external irradiation compared with EBRT.

2.2 Cost of Therapy

Cost of therapy were calculated from the perspective of the healthcare payer. The costs were calculated in three scenarios: realistic, pessimistic, and optimistic (scenarios vary in the purchase price, service costs, and the number of operation per year). The costs of the Intrabeam IORT were estimated based on these cost elements: purchase price of the Intrabeam system, service costs, personnel requirements, materials and medicines consumed directly in the performance. Cost of EBRT was calculated on the basis of publicly accessible data, particularly the Decree No. 324/2014 Coll. [6]. Cost of therapy used in the calculation are in the Table 1.

2.3 Cost Effectiveness Model

For evaluation of cost-effectiveness of early breast cancer therapy was selected model suggested by Picot et al. [7]. The model was adapted for the conditions of the Czech healthcare system and was used for estimation the costs, the benefits and the cost-effectiveness ratio of the IORT using Intrabeam system compared to EBRT for early operable breast tumours.

The structure of the Markov model [7] contains six different patient states: recurrence free, local recurrence, disease free after local recurrence, any other recurrence, death from breast cancer, deaths from other causes. Table 2 contains estimated transition probabilities and Fig. 1 shows

Table 1 Costs of the considered procedures
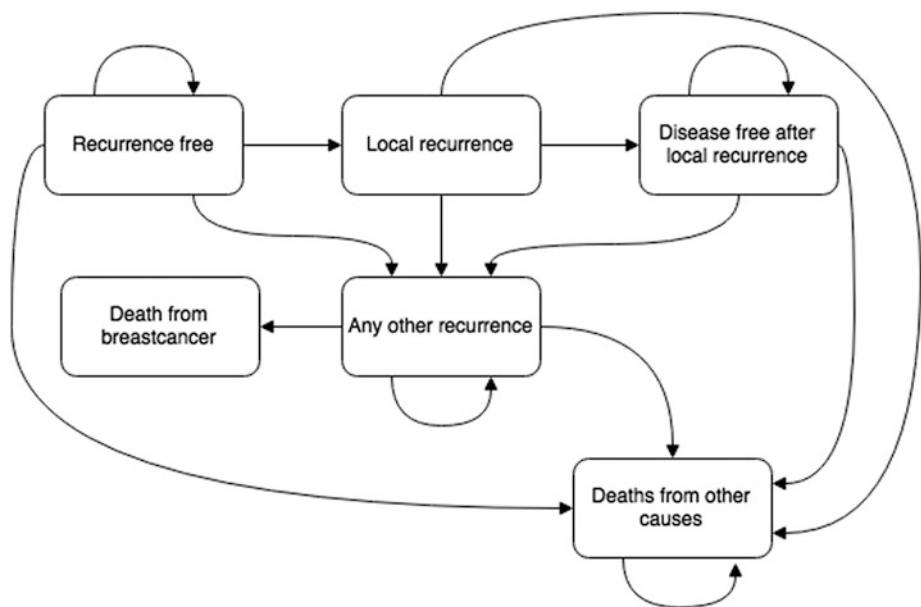
Medical procedure	Average costs; CZK
5-week long EBRT treatment	42 866
6.5-week long EBRT treatment	59 993
Intrabeam basic scenario	38 559
Intrabeam pessimistic scenario	59 076
Intrabeam optimistic scenario	29 328
Mastectomy	8 029
Lumpectomy	5 343
Breast reconstruction	5 992

Table 2 Transition probabilities

State	IORT	EBRT
Any other recurrence → no recurrence	0.0098	0.0096
Any other recurrence → local recurrence	0.0514	0.0514
Death from breast cancer	0.0067	0.0055
Any other recurrence → death from breast cancer	0.6832	0.5698
Recurrence free → local recurrence [7]	Change in time	Change in time
Deaths from other causes [8]	Change in time	Change in time

Fig. 1 Markov model transition [7]

possible transitions between the states. The model is based on the following assumptions: cycle length is 1 year; time horizon of model is 40 years; patients start in recurrence-free state; repeated local recurrence is not modelled.

In the Czech Republic is not officially set a threshold for ICER; however, we consider the threshold of three times the GDP per capita recommended by the World Health Organisation [9] (1.213 million CZK in the Czech Republic as for 2014). We used 3.5% discount rate on costs.

2.4 Quality of Life

The data from study of Picot et al. [7] was used for evaluation of quality of life. The values for five independent medical conditions were: recurrence-free in the first year (0.7728); recurrence-free after first year (0.8112); local recurrence (0.8112); disease-free after local recurrence (0.8112); any other recurrence (0.6850). We used 3.5% discount rate on quality of life.

2.5 Sensitivity Analysis

In our study we performed several one-way sensitivity analyses. In the sensitivity analysis the cost-effectiveness ratio was calculated using the values of pessimistic and optimistic scenarios of the Intrabeam system cost calculation. In the baseline scenario model, all patients with local recurrence undergo mastectomy and breast reconstruction is performed in 50% of patients. In the sensitivity analysis we changed the parameters [7]: (1) the number of patients with mastectomy that undergo IORT was raised to 80%, while the remaining 20% undergo a lumpectomy; (2) the share of women that undergo breast reconstruction was decreased to only 31%. The effect of variations in the transitional probabilities to ICER was also investigated.

Table 3 Results of basic scenario

Intervention	Total costs (CZK)	QALY	Incremental cost (CZK)	Incremental QALY	ICER
Results without discounted results					
EBRT	62 784	14.553	N/a	N/a	N/a
IORT	47 585	14.269	−15 199	−0.284	53 483
Results with 3.5% 3.5% discounting rate					
EBRT	61 923	10.106	N/a	N/a	N/a
IORT	47 275	9.960	−14 649	−0.146	100 443

3 Results

3.1 Clinical Effectiveness

The literature review provided 960 papers. Based on the inclusion criteria, 107 papers were selected for detailed reviews and their full texts were read by two researchers. Finally, 26 studies were included in the clinical effectiveness assessment. The largest and most comprehensive study among those 26 selected is the pragmatic randomized controlled trial TARGIT-A [1, 10]. Some further studies included in the analysis were partial results from the individual centres involved in the TARGIT-A study [11–18]. From the point of view of the design and scope of the studies, TARGIT-A was the only reliable one.

3.2 Cost of Therapy

Cost calculations for the therapy using the Intrabeam IORT device were based on cost data from the Czech healthcare system. Purchase costs and service prices of Itrabeam were calculated from published data [7, 19–25].

Three versions of the calculation sheet for IORT using Intrabeam were calculated based on these findings: the baseline scenario, and a pessimistic and a optimistic scenarios that were later used in the sensitivity analysis. In the baseline scenario, the cost of the Intrabeam system intervention was CZK 38 559 CZK, in the optimistic 29 328 CZK, and in the pessimistic 59 076 CZK.

3.3 Cost-Effectiveness

To create a complex cost-effectiveness model we used Markov model designed by Picot et al. [7] and its assumptions, results of the TARGIT-A trial, and data from the Czech healthcare system.

In the basic scenario the new intervention (IORT using Intrabeam) is cheaper, but less effective than the standard treatment (EBRT). In that situation the ICER value must be above the cost-effectiveness threshold in order the new intervention was accepted. ICER value in basic scenario was 53 483 CZK saved per 1 QALY lost. The ICER ratio of the Intrabeam system is below this threshold, and therefore does not meet the criteria for adoption of the new technology. Results of cost-effectiveness are shown in Table 3.

3.4 Sensitivity Analysis

For the optimistic scenario (85 965 and 163 738 with 3.5% discounting rate) and pessimistic scenario (−18 712 and −40 237 with 3.5% discounting rate) was the ICER value also below the recommended limit for adoption of interventions. Parameters changed in the sensitivity analysis were: the share of patients to undergo mastectomy after the IORT (53 935 and 101 324 with 3.5% discounting rate) and share of patient with a breast reconstruction performed after mastectomy did not affect the ICER value (53 594 and 100 614 with 3.5% discounting rate). For results variations in the transitional probabilities see Table 4.

4 Discussion

Within the search of clinical studies, only one multicentre RCT study was identified—TARGIT-A [1, 10]. This study was criticizing by some authors [26, 27] for the conclusions that the recurrence often occurs much later and short median follow up of the TARGIT-A study (29 month). The results of the ELIOT study [27] and the study by Kreike et al. [28] examining rate of local recurrence for similar therapy indicated that the risk of local recurrence does not decrease over time. In our model we applied values of local recurrence extrapolated from TARGIT-A [9] by Picot et al. [7].

According to the baseline scenario, IORT using Intrabeam is a less expensive option, but provides less effect. However, ICER of IORT using Intrabeam versus EBRT is below the threshold recommended by WHO (three times GDP per capita—1.213 million CZK in the Czech Republic as for 2014). The ICER values of basic scenario of IORT using Intrabeam versus EBRT are 53 483 CZK/QALY

Table 4 Sensitivity analysis

Parameters	Lower limit	Upper limit	Lower limit ICER	Upper limit ICER	Span
Five-year probability of any other recurrence EBRT	0.029	0.071	17 905	−46 990	64 895
Five-year probability of any other recurrence IORT	0.028	0.071	−54 928	18 004	72 932
Five-year probability of death from breast cancer EBRT	0.014	0.045	24 684	103 224	78 540
Five-year probability of death from breast cancer IORT	0.016	0.055	−307 500	38 945	346 445
The age of the patients at the entry into the model (years)	55	72	32 196	146 207	114 011

(without discounting) or 93 753 CZK/QALY (considering 3.5% discounting).

These results are in agreement with Picot et al. [7] and Shah et al. [29], but differ from Alvarado et al. [30]. In the Alvarado et al. model—five-state Markov chain model for the economic evaluation—IORT intervention dominates EBRT (provides more QALYs with less cost). Alvarado et al. [30] and Grobmayer et al. [31] concluded that the treatment using the Intrabeam system is associated with lower costs and with outcomes comparable to those of EBRT.

In our study the results of the sensitivity analysis are consistent with the results of the baseline scenario. The ICER value does not exceed the cost-effectiveness threshold. In the case of the pessimistic scenario the EBRT treatment is dominant—IORT with Intrabeam system is more expensive and provides less QALYs.

IORT must be applied only in properly selected patients. If his restrictive limitations are not applied, there is a reduction in the proportion of IORT patients that can undergo repeated lumpectomy that reduces the expected amount of gained QALYs and increases the total costs. In their opinion, an early integration of IORT into clinical practice could reduce the financial burden of breast cancer therapy, while allowing patients to undergo a less stressful treatment. An advantage of the Intrabeam system is that it may not only be only used in breast cancer therapy, but could also be used in treatment of other tumours [32]. If we use a device to treat patients with other indications than breast cancer, we can reduce the cost of the device (cost per patient). This may affect CEA calculations in favour of IORT.

5   Conclusions

According to the results of the cost-effectiveness assessment we do not currently recommend the Intrabeam system to be introduced into the environment of the Czech healthcare system. It is advisable to repeat the economic evaluation after completing clinical data from future clinical studies tackling long-term results.

References

1. Vaidya JS, Joseph DJ, Tobias JS, Bulsara M, Wenz F, Saunders C, et al. Targeted intraoperative radiotherapy versus whole breast radiotherapy for breast cancer (TARGIT-A trial): an international, prospective, randomised, non-inferiority phase 3 trial. Lancet (London, England). 2010 Jul 10; 376(9735):91–102.
2. Park CC, Yom SS, Podgorsak MB, Harris E, Price RA Jr, Bevan A, et al. American Society for Therapeutic Radiology and Oncology (ASTRO) Emerging Technology Committee report on electronic brachytherapy. Int J Radiat Oncol Biol Phys. 2010 Mar 15; 76(4):963–72.
3. Carl Zeiss Meditec Inc. INTRABEAM Radiotherapy System Uniquely Flexible Radiotherapy [Internet]. [cited 2015 Sep 30]. Available from: http://www.zeiss.com/meditec/en_de/products—solutions/intraoperative-radiotherapy/intrabeam-for-breast-cancer/intrabeam.html.
4. Dušek L, Mužík J, Kubásek M, Koptíková J, Žaloudík J, Vyzula R, et al. Epidemiology of malignant tumors in the Czech Republic (Epidemiologie zhoubných nádorů v České republice) [Internet web page; cited 2016 Dec 30]. Version 7.0. Available from: http://www.svod.cz.
5. Deneve JL, Hoefer RA, Harris EER, Laronga C. Accelerated partial breast irradiation: a review and description of an early North American surgical experience with the intrabeam delivery system. Cancer Control. 2012 Oct; 19(4):295–308.
6. The Czech Republic. Act No. 324/2014 Coll. defining point value and health care expenses paid by public health care insurance and regulatory limits (Vyhláška č. 324/2014 Sb. hodnoty bodu, úhrady zdravotní péče hrazené z pojištění pro r. 2015). 2014. Available from: https://portal.gov.cz/app/zakony/zakon.jsp?page=0&nr=324~2F2014&rpp=15#seznam.
7. Picot J, Copley V, Colquitt JL, Kalita N, Hartwell D, Bryant J. The INTRABEAM® Photon Radiotherapy System for the adjuvant treatment of early breast cancer: a systematic review and economic evaluation. Health Technol Assess (Rockv). 2015; 19(69):1–190.
8. Czech Statistical Office (Český statistický úřad). Life tables (Úmrtnostní tabulky) [Internet; cited 2015 Oct 26]. Available from: https://www.czso.cz/csu/czso/umrtnostni_tabulky.
9. WHO. The world health report 2002 - Reducing Risks, Promoting Healthy Life. 2002; Available from: http://www.who.int/whr/2002/en/.
10. Vaidya JS, Wenz F, Bulsara M, Tobias JS, Joseph DJ, Keshtgar M, et al. Risk-adapted targeted intraoperative radiotherapy versus

whole-breast radiotherapy for breast cancer: 5-year results for local control and overall survival from the TARGIT-A randomised trial. Lancet (London, England). 2014 Feb 15; 383(9917):603–13.

11. Engel D, Schnitzer A, Brade J, Blank E, Wenz F, Suetterlin M, et al. Are Mammographic Changes in the Tumor Bed More Pronounced After Intraoperative Radiotherapy for Breast Cancer? Subgroup Analysis from a Randomized Trial. Breast J. 2013 Jan; 19(1):92–5.

12. Elsberger B, Romsauerova A, Vinnicombe S, Whelehan P, Brown DC, Dewar JA, et al. Comparison of mammographic findings after intraoperative radiotherapy or external beam whole breast radiotherapy. Eur J Surg Oncol. 2014 Feb; 40(2):163–7.

13. Keshtgar MRS, Vaidya JS, Tobias JS, Wenz F, Joseph D, Stacey C, et al. Targeted Intraoperative Radiotherapy for Breast Cancer in Patients in Whom External Beam Radiation Is Not Possible. Int J Radiat Oncol. 2011 May; 80(1):31–8.

14. Keshtgar MMRS, Williams NRN, Bulsara M, Saunders C, Flyger H, Cardoso JS, et al. Objective assessment of cosmetic outcome after targeted intraoperative radiotherapy in breast cancer: results from a randomised controlled trial. Breast cancer Res. 2013 Aug; 140(3):519–25.

15. Sperk E, Welzel G, Keller A, Kraus-Tiefenbacher U, Gerhardt A, Sütterlin M, et al. Late radiation toxicity after intraoperative radiotherapy (IORT) for breast cancer: results from the randomized phase III trial TARGIT A. Breast Cancer Res Treat. 2012 Aug; 135(1):253–60.

16. Tuschy B, Berlit S, Romero S, Sperk E, Wenz F, Kehl S, et al. Clinical aspects of intraoperative radiotherapy in early breast cancer: short-term complications after IORT in women treated with low energy x-rays. Radiat Oncol. 2013 Jan; 8:95.

17. Welzel G, Hofmann F, Blank E, Kraus-Tiefenbacher U, Hermann B, Sütterlin M, et al. Health-related quality of life after breast-conserving surgery and intraoperative radiotherapy for breast cancer using low-kilovoltage X-rays. Ann Surg Oncol. 2010 Oct; 17 Suppl 3:359–67.

18. Welzel G, Boch A, Sperk E, Hofmann F, Kraus-Tiefenbacher U, Gerhardt A, et al. Radiation-related quality of life parameters after targeted intraoperative radiotherapy versus whole breast radiotherapy in patients with breast cancer: results from the randomized phase III trial TARGIT-A. Radiat Oncol. 2013 Jan; 8:9.

19. Xie X, Dendukuri N, McGregor M. Single-dose Intraoperative Radiotherapy Using Intrabeam® for Early-stage Breast cancer: A Health Technology Assessment [Internet]. Montreal (Canada); 2012. [cited 2015 Oct 26]. Available from: https://www.mcgill.ca/tau/sites/mcgill.ca.tau/files/muhc_tau_2012_63_intrabeam.pdf.

20. Swedish Agency for Health Technology Assessment and Assessment of Social Services. Intraoperativ strålbehandling med Intrabeam vid primär operation för bröstcancer [Internet]. 2013. Available from: http://plus.lj.se/info_files/infosida40495/Intraoperativ_stralbehandling_brostkirurgi.pdf.

21. National Health Committee. Intraoperative Radiotherapy (IORT): An Overview [Internet]. Wellington: National Health Committee; 2015. Available from: http://www.moh.govt.nz/notebook/nbbooks.nsf/0/47935E07292B2EEFCC257F7F0007A1F0/$file/iort-t2-update-post-consultation.pdf.

22. TED Tenders electronic daily. AT-Feldkirch: The equipment and accessories for radiotherapy 2010/S 77-114201 Contract award notice [Internet]. [cited 2015 Oct 21]. Available from: http://ted.europa.eu/udl?uri=TED:NOTICE:114201-2010:TEXT:CS:HTML.

23. TED Tenders electronic daily. Poland-Wałbrzych: medical equipments 2014/S 249-441526 Contract award notice [Internet]. [cited 2015 Oct 21]. Available from: http://ted.europa.eu/udl?uri=TED:NOTICE:441526-2014:TEXT:CS:HTML.

24. TED Tenders electronic daily. Poland-Wałbrzych: medical equipments 2015/S 179-325006 Contract award notice [Internet]. [cited 2015 Oct 21]. Available from: http://ted.europa.eu/udl?uri=TED:NOTICE:325006-2015:TEXT:CS:HTML.

25. TED Tenders electronic daily. France-Caen: X-ray therapy devices 2015/S 191-345605 Contract award notice [Internet]. [cited 2015 Oct 21]. Available from: http://ted.europa.eu/udl?uri=TED:NOTICE:345605-2015:TEXT:CS:HTML.

26. Bartelink H. Intraoperative radiotherapy for breast cancer: tail wagging the dog? Lancet Oncol. 2004 Apr; 5(4):207–8.

27. Veronesi U, Orecchia R, Maisonneuve P, Viale G, Rotmensz N, Sangalli C, et al. Intraoperative radiotherapy versus external radiotherapy for early breast cancer (ELIOT): a randomised controlled equivalence trial. Lancet Oncol. 2013 Dec;14 (13):1269–77.

28. Kreike B, Hart AAM, van de Velde T, Borger J, Peterse H, Rutgers E, et al. Continuing Risk of Ipsilateral Breast Relapse After Breast-Conserving Therapy at Long-Term Follow-up. Int J Radiat Oncol. 2008; 71(4):1014–21.

29. Shah C, Lanni TB, Saini H, Nanavati A, Wilkinson J Ben, Badiyan S, et al. Cost-efficacy of acceleration partial-breast irradiation compared with whole-breast irradiation. Breast Cancer Res Treat. 2013 Feb; 138(1):127–35.

30. Alvarado MD, Mohan AJ, Esserman LJ, Park CC, Harrison BL, Howe RJ, et al. Cost-effectiveness analysis of intraoperative radiation therapy for early-stage breast cancer. Ann Surg Oncol. 2013 Sep; 20(9):2873–80.

31. Grobmyer SR, Lightsey JL, Bryant CM, Shaw C, Yeung A, Bhandare N, et al. Low-kilovoltage, single-dose intraoperative radiation therapy for breast cancer: results and impact on a multidisciplinary breast cancer program. J Am Coll Surg. 2013 Apr; 216(4):617-23-4.

32. Williams NR, Pigott KH, Brew-Graves C, Keshtgar MRS. Intraoperative radiotherapy for breast cancer. Gland Surg. 2014 May; 3 (2):109–19.

Economic Evaluation of Robotic Radiosurgery System for Prostate Cancer Treatments in the Czech Republic

Denisa Horáková and Gleb Donin

Abstract

The purpose of this study was to carry out the economic evaluation of robotic stereotactic body radiation therapy (rSBRT) in comparison with conventional intensity-modulated radiation therapy (IMRT) for the treatment of localized prostate cancer in the Czech Republic. Cost-utility analysis was used for the economic evaluation of both technologies based on their costs and the number of quality-adjusted life years gained (QALYs). Utilities of both technologies were identified in literature. An estimation of treatment costs was obtained from publicly available secondary sources for the Czech Republic. The cost-utility analysis was conducted from provider's perspective for three scenarios (optimistic, realistic, and pessimistic). According to the results of cost-utility analysis, in every scenario concerned IMRT was both more effective and less costly than rSBRT. Namely, in realistic scenario, IMRT and rSBRT accrued 9.96 QALY/53,198 CZK and 9.93 QALY/79,956 CZK, respectively. rSBRT reached the same or lower values of the cost-utility ratio than IMRT in situation, when the acquisition price of rSBRT equipment was lower than CZK 58 million in the realistic scenario. Under the conditions of the Czech healthcare system, IMRT was more cost-effective than rSBRT for localized prostate cancer treatment in all the analyzed scenarios.

D. Horáková · G. Donin (✉)
Department of Biomedical Technology, Czech Technical University in Prague, Nám. Sítná 3105, 272 01 Kladno, Czech Republic
e-mail: gleb.donin@fbmi.cvut.cz

1 Background

Prostate cancer is the most common cancer (excl. non-melanoma skin cancer) in men in the Czech Republic. In 2015, 7,049 cases of prostate cancer were reported [1], with a ratio of 136.1 cases per 100,000 men. Radiotherapy as the primary alternative to prostate cancer treatment has seen a sharp rise over the last two decades. New trends in external radiotherapy include proton therapy and stereotactic radiotherapy. Intensity-modulated radiation therapy (IMRT) is a standard radiotherapy treatment nowadays.

Stereotactic body radiation therapy (SBRT) offers several advantages over conventional IMRT fractionation. SBRT is commonly delivered either using a gantry-based linear accelerator or a robotic arm-mounted linear accelerator (rSBRT). CyberKnife is the only commercially available rSBRT system and it delivers larger doses of radiation to a tumor tissue in 4–5 fractions. This appears to be a big advantage over conventional IMRT, which employs approximately 40 fractions of smaller radiation doses. Many studies indicate that prostate cancer is more sensitive to higher doses of radiation [2, 3]. It was also noted that there is a potential for treatment cost reduction [4].

Several studies from abroad compared IMRT and SBRT (in general) in terms of treatment costs per patient with prostate cancer [5–11]. According to these studies, it is clear that SBRT is less expensive and brings greater or comparable benefits than IMRT. The first and only rSBRT system in the Czech Republic is the one operating since 2010 at the University Hospital in Ostrava (UH Ostrava). Other hospitals consider purchasing this technology, however no study on economic efficiency of rSBRT in comparison with IMRT has been conducted for the Czech Republic so far.

The objective of this study was to carry out the economic evaluation of rSBRT in comparison with conventional IMRT for the localized prostate cancer treatment in the Czech Republic.

2   Methods

2.1   Treatment Process

The process of the radiotherapy for the prostate cancer treatment by rSBRT and IMRT was analyzed based on literature, publicly available information, the Czech legislation and consultations with radiation oncologist.

Both types of radiotherapy start with a 30-min examination by radiation oncologist. In the case of rSBRT then 3–5 golden seeds are placed into the prostate, usually by a urologist. This step takes about 15 min [12]. IMRT requires localization of the target volume on the simulator. Localization is performed by a radiation oncologist and a radiological assistant or physicist (about 60 min).

Both types of radiotherapy are followed by CT scanning in the small pelvis area. This examination is performed by a radiation oncologist and a radiological assistant for a total of about 30 min [12]. The rSBRT treatment is typically followed by MRI for therapy planning (about 60 min), which is performed by a radiologist and a radiation physicist [12–14]. In some rare cases, MRI is also indicated for planning IMRT treatment [15].

Subsequently, treatment planning is performed for both types of radiotherapy. The rSBRT treatment planning is performed by two radiation oncologists (120 min) and the radiation physicist (about 200 min) [12, 16]. The IMRT planning is performed by the radiotherapist and the radiation physicist (about 90 min) [12]. After radiotherapy planning and prior to therapy, a simulation of the radiation plan is performed on the simulator in the case of IMRT. Simulation is performed by the radiotherapist for about 60 min [12].

Before each fraction, the patient's position is checked according to the treatment plan. Position verification is performed by a radiotherapist and radiological assistant for approximately 10 min before each irradiation [12]. The rSBRT treatment is performed by a radiation oncologist along with a radiologist assistant (about 120 min). In case of rSBRT, the total dose is usually divided into 5 fractions. IMRT is delivered by radiotherapist and radiological assistant (about 12 min) typically in 37 fractions.

For both rSBRT and IMRT, an output check is performed at the end of the entire irradiation cycle. This check takes about 30 min and is performed by a radiation oncologist [12]. In case of IMRT, the patient undergoes continuous monitoring during the irradiation cycle. In most cases, treatment lasts for seven weeks, so the patient usually goes through a check at the end of each week. This check-up is carried out by the radiation oncologist and takes about 15 min [12].

2.2   Costs and Economic Evaluation

The cost analysis was conducted from provider perspective. The cost of treatment per patient was calculated according to the literature, public contracts and other sources. The considered cost items included the acquisition costs of radiotherapy equipment, personnel costs, material costs, the maintenance and servicing costs of the devices, CT scanning, X-ray and MRI costs, and overhead costs. The time horizon considered was 10 years due to the average lifespan of linear accelerators and other radiotherapy devices [17].

In order to estimate the provider's expenditures on treatment under distinct conditions (wages, equipment prices, price of consumables etc.), a scenario analysis was used. The costs were set for three scenarios: optimistic (best case), realistic (best guess) and pessimistic (worst case). The scenarios represented the set of assumptions on both the health services utilization and cost items. The main differences between parameters and costs used in scenarios are represented in Table 1.

The acquisition price of rSBRT system was estimated based on prices abroad, because only one piece of the device was purchased in the Czech Republic at the time. Previous local acquisitions were used for the estimation of IMRT price. Consistent with the medical device assessment literature, maintenance costs were calculated as a percentage of acquisition costs. The calculation presumed that rSBRT and IMRT was used for the similar number of patients per year. The annual number of patients was estimated at 600 and resulted from the information of the UH Ostrava official website as well as of Institute of Health Information and Statistics of the Czech Republic [28].

Personnel costs were determined according to the duration of the individual procedures in the treatment process, type of occupation and the Czech Average Earnings Information System (ISPV) [27]. Subsequently, the total personnel costs for optimistic, realistic and pessimistic scenarios were calculated including all the contributions paid by the employer.

Consumable costs were calculated based on current market prices and public contracts. The costs of MRI, CT and X-ray simulator was also considered during calculation. These costs were calculated based on publicly available acquisition prices for these devices and the percentage of annual maintenance costs. Consistently with the previous studies, overhead costs were calculated as 20% of the total cost [18].

Total costs for treatment per patient were calculated according to the equation:

$$Costs = \frac{P_o + C_s}{n \cdot l} + C_m + C_p + C_{CT} + C_{SIM} + C_{MRI} + C_R,$$

(1)

Table 1 Parameters and costs used in this study

Parameters	Scenario			Source
	Optimistic	Realistic	Pessimistic	
Acquisition cost, mil. CZK				
rSBRT	110	150	200	Assumption based on [18–22]
IMRT	71	88	100	[23, 24]
Maintenance cost, % of the acquisition cost				
rSBRT	4	6	8	Assumption based on [18, 19, 21, 22]
IMRT	4	7	10	Assumption based on local service contacts and [18, 25, 26]
Personnel wages				
Selected statistical characteristic from ISPV	Median	Q3	D9	[27]
Consumables, per patient, CZK				
rSBRT	6,370	8,470	12,722	
IMRT	15	15	2,167	
Diagnostic/simulation equipment, costs allocation per patient, CZK				
X-ray simulator	2,842	3,193	3,481	
MRI	1,842	2,968	4,912	
CT	348	719	1,173	

where P_o is the acquisition cost for radiotherapy equipment (rSBRT or IMRT), C_s is the annual maintenance cost, n is the annual number of patients, l is the lifespan of the radiotherapy equipment, C_m—consumables costs, C_p—personnel costs, C_{CT}—CT scanning costs, C_{SIM}—costs of treatment planning with a simulation machine, C_{MRI}—costs of MRI and C_R—overhead costs.

For the cost-utility analysis, the number of QALY gained by each technology was taken from the study on cost-effectiveness comparison of rSBRT and IMRT.

One of the main goals of this study was to determine the cost-effectiveness boundary for rSBRT acquisition price in comparison with IMRT. Specifically, at what rSBRT acquisition price the cost-utility of rSBRT is equal to the cost-utility of IMRT. The cost-effectiveness boundaries for rSBRT acquisition price were calculated for the optimistic, realistic and pessimistic scenarios.

3 Results

The total costs of treatment of one patient with the localized prostate cancer by both rSBRT and IMRT for realistic scenario are presented in the Table 2. In realistic scenario, rSBRT was more costly than IMRT (79,956 CZK vs. 54,372 CZK per patient) primarily because of the higher acquisition and maintenance costs of rSBRT. The personnel costs for both technologies were comparable. In other considered scenarios, rSBRT was also more expensive than IMRT (52,927 CZK vs. 41,699 CZK for optimistic and 114,339 CZK vs. 76,320 CZK for pessimistic scenarios).

In literature, several studies on utility comparison of IMRT and stereotactic radiotherapy for the treatment of prostate cancer were identified [5–11]. However only Sher's study distinguished rSBRT from general stereotactic radiotherapy [9]. According to this study, patients treated with rSBRT gained 9.93 QALY and with IMRT 9.96 QALY.

The results of the cost-utility analysis are presented in the Table 3. In the realistic scenario case, IMRT and rSBRT accrued 9.96 QALY/53,198 CZK and 9.93 QALY/79,956 CZK, respectively. rSBRT is less effective than IMRT, and also more expensive. Analysis of ICERs demonstrate that rSBRT is dominated by IMRT in all scenarios concerned.

The cost-effectiveness boundary for rSBRT acquisition price for realistic scenario is represented on Fig. 1. The solid line illustrates dependence of the cost-utility for rSBRT on its acquisition price for realistic scenario. The horizontal dashed line shows the cost-utility ratio of IMRT for realistic scenario. The vertical dotted line expresses the initial purchase price of rSBRT (150 million CZK) according to a realistic scenario. The diamond on intersection of solid and dashed lines demonstrates the cost-effectiveness boundary for the acquisition price of rSBRT. In other words, if rSBRT is to be more cost-effective than IMRT, it will have to cost no more than 58 million CZK.

The price boundaries for all scenarios are indicated in the Table 4. The acquisition price of rSBRT used in the scenarios was always significantly higher than the cost-effectiveness boundary.

Table 2 Total costs per patient—realistic scenario

Costs	rSBRT	IMRT
Acquisition cost	25,000 CZK	14,686 CZK
Maintenance cost	12,000 CZK	8,224 CZK
Consumables	8,470 CZK	15 CZK
Personnel cost	17,473 CZK	17,299 CZK
Simulation	N/a	3,193 CZK
CT	719 CZK	719 CZK
MRI	2,968 CZK	N/a
Overhead	13,326 CZK	9,062 CZK
Total	79,956 CZK	53,198 CZK

Table 3 The results of cost-utility analysis for rSBRT and IMRT

Technology	Scenario		
	Optimistic	Realistic	Pessimistic
rSBRT			
Cost per patient, CZK	52,927	79,956	114,339
Effect, QALY	9.930		
Cost-utility, CZK/QALY	5,330	8,052	11,515
IMRT			
Cost per patient, CZK	41,699	53,198	76,320
Effect, QALY	9.960		
Cost-utility, CZK/QALY	3,959	5,342	7,663
Incremental			
Cost per patient, CZK	−11,228	−26,758	−38,019
Effect, QALY	0.03		
ICER, CZK/QALY	IMRT is dominant over rSBRT		
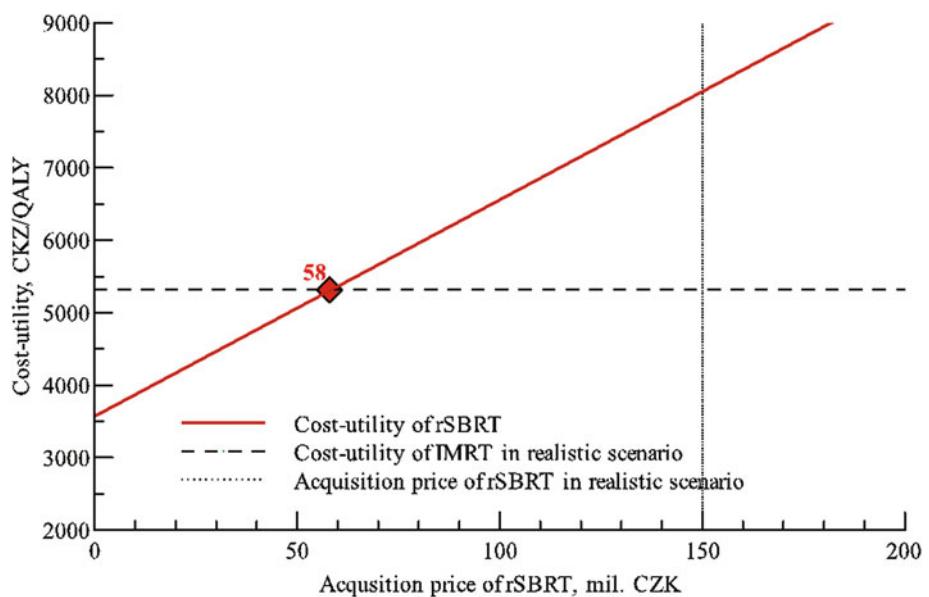
Fig. 1 The cost-utility of rSBRT versus its acquisition price (realistic scenario)

Table 4 Acquisition prices of rSBRT used in scenarios and cost-effectiveness boundaries

	Scenario		
	Optimistic	Realistic	Pessimistic
Acquisition price in scenario, million CZK	110	150	200
Cost-effectiveness boundary, million CZK	58	58	83

4 Discussion

The total cost of treatment per patient for the optimistic, realistic and pessimistic scenario was estimated at 52,927 CZK, 79,956 CZK and 114,339 CZK for CK and 41,699 CZK, 53,198 CZK and 76,320 CZK, for IMRT assuming 600 patients per year are treated. These results are consistent with other studies. In the Italian study from 2013 (500 patients for rSBRT and 400 patients for IMRT per year), the treatment costs from payer's perspective were estimated at 4,099.81 EUR for rSBRT and 3,318.41 EUR for IMRT (approx. 108,952 CZK for CK and 88,187 CZK for IMRT) [18]. The Spanish study from 2005 (600 patients/year) indicates that the cost of the rSBRT treatment was 5,321 EUR (approx. 141,406 CZK) [22]. The costs were calculated from provider perspective. In the second Spanish study from 2014, the IMRT treatment costs (310 patients/year) were estimated at 3,911.91 EUR (approx. 103,959 CZK) [25]. Based on the results of current study and the studies abroad it can be noted that IMRT treatment in the most cases is less expensive than rSBRT treatment.

According to this study, IMRT was in all cases more cost-effective than rSBRT. No study focused on comparison of the cost-effectiveness of IMRT and rSBRT from provider's perspective was identified in the literature reviewed. Most studies evaluated cost-effectiveness from payer's perspective. Another problem is that all the studies, apart from one exception, evaluated the cost-effectiveness of SBRT in general and not particularly the cost-effectiveness of the rSBRT. The only study that evaluated rSBRT separately was the study by Sher et al. [9]. This study demonstrated that cost-utility of rSBRT was 9.93 QALY/$25,561 and 9.96 QALY/$34,127 for IMRT. According to these results, rSBRT was more cost-effective than IMRT from payer's perspective. A different perspective and a different approach to the determination of treatment costs could probably explain difference in cost-effectiveness with current study. Besides the perspective used in the analysis, the cost-effectiveness ratio of technology depends greatly on the utilization of the radiotherapy equipment, its acquisition price and personnel costs. These costs could significantly differ in various countries.

The scenario analysis could overvalue the uncertainty associated with the results of economic evaluation [29].

However, the results of different considered scenarios are consistent in terms of treatment costs for both technologies. IMRT was less expensive than rSBRT in all scenarios.

It is noticeable, that the results of cost-utility analysis in this study are strongly determined by transferred utility values. Except the Sher's study [9], no other studies were identified that investigated the utility of IMRT and rSBRT. The study was conducted in USA and evaluated effects of both technologies using Markov model in population of 65-year-old men with a lifetime time horizon. Discounting rate in Sher's study was 3% which is commonly used discount rate in the Czech healthcare environment [30]. Disease, treatment, and toxicity data were extracted from the literature. Although health state valuations are not commonly generalizable [31], it was assumed, that health care modeling results (calculated on the basis of treatment effects and utilities in different health states) could be transferred due to limited information available. The uncertainty associated with utility was not addressed and it could be considered as a limitation of this study. Future studies could overcome this limitation by using health economics modelling in combination with probabilistic sensitivity analysis to delineate the health states after treatment with IMRT and rSBRT.

No randomized controlled study focused on a comparison of the clinical effects of IMRT and rSBRT was identified in the literature. The existence of such a study would certainly be beneficial for the assessment of cost effectiveness of these technologies.

5 Conclusion

The cost-utility ratio of rSBRT was higher than that of IMRT and rSBRT was dominated by IMRT in all scenarios concerned. rSBRT reached the same or lower values of the cost-utility ratio as the IMRT in situations, when the acquisition price of the rSBRT equipment was significantly lower than price used in the scenarios. Under the conditions of the Czech healthcare system, the IMRT is more cost-effective than the rSBRT for localized prostate cancer treatment from provider's perspective.

The results of this work can be used by medical management as a decision-making tool for strategic investment by other Czech healthcare facilities planning to purchase rSBRT technology.

Conflict of Interests   The authors declare no conflict of interests.

References

1. IHIS: Cancer Incidence in the Czech Republic, 2015. Institute of Health Information and Statistics of the Czech Republic, Prague (2017).

2. Brenner, D.J., Martinez, A.A., Edmundson, G.K., Mitchell, C., Thames, H.D., Armour, E.P.: Direct evidence that prostate tumors show high sensitivity to fractionation (low α/β ratio), similar to late-responding normal tissue. Int. J. Radiat. Oncol. 52, 6–13 (2002).

3. Fowler, J., Chappell, R., Ritter, M.: Is α/β for prostate tumors really low? International Journal of Radiation Oncology Biology Physics. 50(4), 1021–1031 (2001).

4. Moon, D.H., Efstathiou, J.A., Chen, R.C.: What is the best way to radiate the prostate in 2016? Urologic oncology. 35(2), 59–68 (2017).

5. Avkshtol, V., Dong, Y., Hayes, S.B., Hallman, M.A., Price, R.A., Sobczak, M.L., Horwitz, E.M., Zaorsky, N.G.: A comparison of robotic arm versus gantry linear accelerator stereotactic body radiation therapy for prostate cancer. Research and reports in urology. 8, 145–158 (2016).

6. Parthan, A., Pruttivarasin, N., Davies, D., Taylor, D.C.A., Pawar, V., Bijlani, A., Lich, K.H., Chen, R.C.: Comparative cost-effectiveness of stereotactic body radiation therapy versus intensity-modulated and proton radiation therapy for localized prostate cancer. Frontiers in oncology. 2, 81 (2012).

7. Hodges, J.C., Lotan, Y., Boike, T.P., Benton, R., Barrier, A., Timmerman, R.D.: Costeffectiveness analysis of stereotactic body radiation therapy versus intensity-modulated radiation therapy: an emerging initial radiation treatment option for organ-confined prostate cancer. Journal of oncology practice. 8(3S), e31 s–7 s (2012).

8. Yu, J.B., Cramer, L.D., Herrin, J., Soulos, P.R., Potosky, A.L., Gross, C.P.: Stereotactic Body Radiation Therapy Versus Intensity-Modulated Radiation Therapy for Prostate Cancer: Comparison of Toxicity. Journal of clinical oncology: official journal of the American Society of Clinical Oncology. 32(12), 1195–1201 (2014).

9. Sher, D.J., Parikh, R.B., Mays-Jackson, S., Punglia, R.S.: Cost-effectiveness analysis of SBRT versus IMRT for low-risk prostate cancer. American journal of clinical oncology. 37(3), 215–221 (2014).

10. Laviana, A.A., Ilg, A.M., Veruttipong, D., Tan, H.-J., Burke, M.A., Niedzwiecki, D.R., Kupelian, P.A., King, C.R., Steinberg, M.L., Kundavaram, C.R., Kamrava, M., Kaplan, A.L., Moriarity, A.K., Hsu, W., Margolis, D.J.A., Hu, J.C., Saigal, C.S.: Utilizing time-driven activity-based costing to understand the short- and long-term costs of treating localized, low-risk prostate cancer. Cancer. 122, 447–455 (2016).

11. Halpern, J.A., Sedrakyan, A., Hsu, W.-C., Mao, J., Daskivich, T.J., Nguyen, P.L., Golden, E.B., Kang, J., Hu, J.C.: Use, complications, and costs of stereotactic body radiotherapy for localized prostate cancer. Cancer. 122, 2496–2504 (2016).

12. Ministry of Health of the Czech Republic: Seznam zdravotních výkonů, https://szv.mzcr.cz/Vykon, last accessed 2018/01/30.

13. Sharieff, W., Greenspoon, J.N., Dayes, I., Chow, T., Wright, J., Lukka, H.: The Technique, Resources and Costs of Stereotactic Body Radiotherapy of Prostate Cancer: A Comparison of Dose Regimens and Delivery Systems. Technology in cancer research & treatment. 15(1), 171–178 (2016).

14. Ministerstvo zdravotnictví ČR: Národní radiologické standardy - radiační onkologie. Věstník Ministerstva zdravotnictví. 2, 62–202 (2016).

15. Krupa, P., Šlampa, P.: Moderní radikální radioterapie karcinomu prostaty a její možná rizika. Postgraduální medicína. 2, 65–69 (2016).

16. Cvek, J., Knybel, L., Otáhal, B., Feltl, D.: Možnosti stereotaktického ozáření páteře a míchy přístrojem CyberKnife. Onkologie. 5(2), 83–86 (2011).

17. James, S.: A guide to modern radiotherapy. Society of Radiographers, London (2013).

18. Branchi, M., Goglio, S., Sottocorno, M.: Innovazione Nei Trattamenti Radioterapici. (2014), http://docplayer.it/11882083-Innovazione-nei-trattamenti-radioterapici.html, last accessed 2018/01/30.

19. U.S. Securities and Exchange Commission: Accuray CyberKnife® Shared Ownership Agreement. (2017).

20. Věstník veřejných zakázek. Evidenční číslo zakázky: 60033765, https://old.vestnikverejnychzakazek.cz/cs/Form/Display/96699, last accessed 2018/03/15.

21. Ohinmaa, A.: Cost estimation of stereotactic radiosurgery: application to Alberta. Edmonton, Canada (2003).

22. Calcerrada, N., Sabés, R.: Efectividad, seguridad y estimación de costes del sistema de radiocirugía CyberKnife. Unidad de Evaluación de Tecnologías Sanitarias (UETS), Agencia Laín Entralgo, Madrid (2005).

23. Zukalová, V.: Klasifikace a oceňování radioterapeutických zdravotnických přístrojů, Master Thesis, Faculty of Biomedical Engineering, Czech Technical University in Prague, Kladno (2017).

24. IHIS: Kategorizace zdravotnické techniky a zdravotnických prostředků, http://uzis.cz/katalog/klasifikace/kategorizace-zdravotnicke-techniky-zdravotnickych-prostredku, last accessed 2018/03/15.

25. Gutiérrez-Ibarluzea, I., Gutiérrez Iglesias, A., Galnares Cordero, L., Shengelia Shapiro, L., Boveda Carro, E., Celeiro González, J., Bilbao Zulaica, P., Bayon Yusta, J.: Evaluación de radioterapia conformada con haces de intesidad modulada. IMRT. Ministerio de Sanidad, Servicios Sociales e Igualdad. Servicio de Evaluación de Tecnologías Sanitarias del País Vasco, Vitoria-Gasteiz (2014).

26. Yong, J.H.E., McGowan, T., Redmond-Misner, R., Beca, J., Warde, P., Gutierrez, E., Hoch, J.S.: Estimating the costs of intensity-modulated and 3-dimensional conformal radiotherapy in Ontario. Current Oncology. 23(3), e228–e238 (2016).

27. Average Earnings Information System Homepage, http://www.ispv.cz/en/homepage.aspx, last accessed 2018/01/30.

28. IHIS: Zdravotnická ročenka České republiky 2015. Institute of Health Information and Statistics of the Czech Republic, Prague (2017).

29. Briggs, A.H., Gray, A.M.: Handling uncertainty in economic evaluations of healthcare interventions. BMJ. 319, 635–8 (1999).

30. Skoupá, J., Annemans, L., Hájek, P.: Health Economic Data Requirements and Availability in the European Union: Results of a Survey Among 10 European Countries. Value in Health Regional Issues. 4(7), 53–57 (2014).

31. Drummond, M., Barbieri, M., Cook, J., Glick, H.A., Lis, J., Malik, F., Reed, S.D., Rutten, F., Sculpher, M., Severens, J.: Transferability of economic evaluations across jurisdictions: ISPOR good research practices task force report. Value in Health. 12 (4), 409–418 (2009).

Usability of Volume Pulse Wave Biosignal

D. Korpas and J. Haluzikova

Abstract

The aim of this study is to show the usability of volume pulse wave measurement on superficial arteries, using a method as close as possible to manual palpation. The parameters evaluated can be generally assessed from the time domain, derivations, velocity, or frequency domain. In the time domain, a number of wave proportions can be measured. In this study, the parameters were derived from time and amplitude measurement of the pulse wave run. The mean coefficients of variation in (%) of parameters in one pulse waveform were: crest time 11.8; systolic amplitude 8.45; relative crest time 11.38; interwave distance 12.97; relative dicrotic amplitude 23.1; relative dicrotic time 7.15; augmentation index 13.23; PWV 6.76. The mean coefficients of variation in (%) of parameters in the long-term measurement were: crest time 9.17; systolic amplitude 10.79; relative crest time 6.91; interwave distance 3.77; relative dicrotic amplitude 11.37; relative dicrotic time 1.87; augmentation index 4.58; PWV 5.87. The variations measured are very large. As a result, it is not possible to accurately and quantitatively evaluate the pulse wave measured by palpation. The results show that the coefficients of variation for the parameters of the volume pulse wave biosignal can increase up to double-digit values.

D. Korpas (✉) · J. Haluzikova
Faculty of Public Policies, Institute of Nursing, Silesian
University, Opava, Czech Republic
e-mail: david.korpas@fvp.slu.cz

1 Introduction

The pulse wave (PW) is a complex physiological phenomenon occurring in an arterial system during blood circulation. In every site through which the pulse waveform passes, pressure changes, blood flow velocity changes, and profile changes can be observed. The resulting pulse waveform is determined by the phase sum of forward and reflected waves. The temporal differences of reflected pulse waves in each part of the circulation are responsible for waveform differences of the central and peripheral pulse waves. This explains the differences between the peripheral and central pressure waveforms, which may be as high as 20 mm Hg [1]. The central pressure waveform is important in determining left ventricular workload, which is relatively independent of the brachial pressure [2].

Suitable palpation sites are at the radial, ulnar, brachial, femoral, popliteal, posterior tibial, dorsalis pedis, and superficial temporal arteries. Naturally, the PW contour varies in these different parts of the circulation. It also depends on physiological or pathophysiological conditions of the body. Pathological events such as arteriosclerosis or diabetes have a major impact, particularly on artery elasticity [3]. With age, a combination of increased reflective capacity at peripheral sites and faster pulse wave velocity (PWV) within stiffened vessels causes premature augmentation of the systolic waveform [1]. As arteries lose their elasticity, both the PWV and the amplitude of the reflected wave increase. This leads to changes in the pulse waveform, especially in the diastolic, dicrotic part. The PWV is also influenced by hypertension or certain heart diseases.

There continue to emerge scientific papers dealing with various measurement techniques [4, 5] and with innovative evaluation of physiology [6] or disease [7]. The available studies often focus on PWV evaluation and modeling of central carotid waveform [8–10]. Our method aims to be as close as possible to simple manual palpation, but much more sensitive. Our objective is to determine the characteristics of

the measured volume pulse wave as a physiological biosignal as well as to evaluate the usability of this biosignal.

2   Materials and Methods
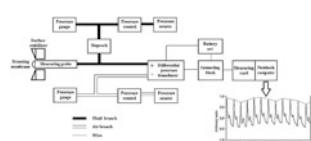
There are several methods of pulse wave measurement based on different principles and depending on the type of pulse wave to be measured. For a rapid and safe measurement, however, non-invasive methods are used only.

Pulse wave is a real biosignal and can be evaluated using analytical and mathematical methods. However, an essential limitation is that this signal is not stationary. The use of classic FFT is therefore not appropriate. In this paper, only the evaluation of parameters of the waveform time course is used. As a matter of fact, the variability between individual pulses occurs due to physiological effects, primarily due to respiratory arrhythmia. The purpose of the following procedure is to quantify the variability.

2.1   Measurement Technique

The original measuring device consists of a scanning membrane on a probe, a surface stabilizer, a probe, a liquid and air part for pressure transmission, and a differential pressure transducer. Further, there is a connecting block, a measuring card, and a PC with software for the analysis and storage of pulse waveforms. The artery volume changes are measured with an adhesive, very thin membrane which is fixed to the palpation spot near the superficial artery. For our evaluation, the radial artery was used because of easy accessibility. The volume changes caused by a spreading pulse wave during heart systole are scanned with a probe. These volume changes affect the uncompressed fluid behind the membrane on the probe, transfer themselves into pressure changes, and move through a system of tiny hoses towards the positive input of a sensitive differential pressure transducer (Fig. 1). The probe membrane has a convex shape because of internal pressure of the fluid media. This internal pressure is created by the fluid pressure source and regulated with pressure control and gauge. The differential pressure transmitter converts the pressure differences into electrical voltage. The output of the transducer is connected to the measuring PC with analyzing software.

2.2   Pulse Wave Parameters

The evaluated PW parameters were: crest time, systolic amplitude, relative crest time, interwave distance, relative dicrotic amplitude, relative dicrotic time, augmentation index, and PWV. By means of Fig. 1, these parameters are defined as follows: crest time = TP1; systolic amplitude = AP1; relative crest time = TP1/TPT; interwave distance = IWT/TPT; relative dicrotic amplitude = AP2/AP1; relative dicrotic time = TP2/TPT; augmentation index = (AP1 − AP2)/AP1 (Fig. 2).
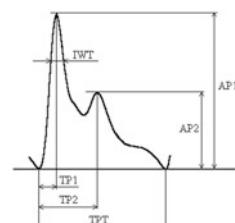
PVW is the temporal difference between the R wave of the QRS complex on surface ECG and the beginning of systole in the pulse waveform palpation spot, divided by the distance of this spot from the heart. This of course must not be confused with blood flow velocity which is much slower and has a different physiological meaning.

2.3   Subjects and Measurement Procedure

The study evaluated this single pulse waveform in thirty-seven subjects (8 males and 29 females), aged (mean ± SD) 21.2 ± 3.2 years, systolic blood pressure 116.3 ± 17.7 mm Hg, diastolic blood pressure 68.2 ± 13.2 mm Hg, heart rate 78.1 ± 14.5 min^{-1}, BMI 24.6 ± 4.1 kg/m^2, recruited among the university staff and students. They had no previous cardiovascular (or other serious) disease and were taking no cardiovascular medication. Each subject had lain in the supine position for 5 min in a quiet room before the pulse wave and blood pressure recordings were taken. The measurement probe was placed on the radial artery palpation spot and positioned carefully until the signal was strongest. The breathing was synchronized to 15 min^{-1} using an acoustic signal. Following that, the computer recorded the PW signal for 30 s. As a valid value for each measurement, a mean and standard deviation of twenty-five consecutive pulses was used. This value of twenty-five pulses was chosen as long enough to arch over several breathing circulatory waves. The aim was to determine the parameter's variation during one pulse waveform.

In the long-term measurement study, one measurement was taken in only one subject for 36 consecutive days. The measurement procedure was the same as above. The reason

Fig. 1 Block diagram of the device and the resulting curve

Fig. 2 Description of pulse wave parameters: (TP1) time to systolic peak; (TP2) time to dicrotic peak; (TPT) total pulse time; (IWT) interwave time in 2/3 of the peak height; (AP1) amplitude of systolic peak; (AP2) amplitude of dicrotic peak

for using just one subject for the long-term study is that the pulse wave parameters seem to be characteristic for individuals and depend on common physiological conditions, e.g. body height.

2.4 Data Analysis

In the study evaluating one pulse waveform, the mean coefficient of variation was calculated from the coefficients of variation of all subjects for each parameter. The coefficient of variation for a single subject was the ratio of the standard deviation to the mean value of the parameter.

In the long-term study, the mean coefficient of variation was calculated from all daily measurements for each parameter. The values of each parameter were again calculated as the mean from twenty-five consecutive pulses in the pulse waveform.

3 Results

3.1 One Pulse Waveform

The resultant coefficients of variation for parameters in one pulse waveform are shown in Table 1.

3.2 Long-Term Measurement

The resultant coefficients of variation for parameters in the long-term measurement are shown below in Table 2.

4 Discussion

The study evaluated the variability of the parameters from two aspects. On the one hand, it evaluated the variability of the parameters within a single pulse wave sequence and their sensitivity to respiratory arrhythmia. Furthermore, it looked at the stability of the parameters in repeated measurements, i.e. their capacity to characterize the properties of the arterial system of the individual evaluated.

In the first part, the results showed the coefficients of variation to be most often above 10% and even higher. Some of these variations are physiological due to respiratory arrhythmia, but some parameters are apparently not usable for further evaluation. The best variation was for PWV with a value of 6.76%.

The second part of the study aimed at determining the most stable parameters which can be used to quantify the arterial system of an individual. Although the measurement was done on a single subject, it is obvious that the most stable parameters are those derived from the temporal

Table 1 Mean coefficient of variation of parameters in one pulse waveform

Parameter	Mean coefficient of variation (%)
Crest time	11.8
Systolic amplitude	8.45
Relative crest time	11.38
Interwave distance	12.97
Relative dicrotic amplitude	23.1
Relative dicrotic time	7.15
Augmentation index	13.23
PWV	6.76

Table 2 Mean coefficient of variation of parameters in the long-term measurement

Parameter	Mean coefficient of variation (%)
Crest time	9.17
Systolic amplitude	10.79
Relative crest time	6.91
Interwave distance	3.77
Relative dicrotic amplitude	11.37
Relative dicrotic time	1.87
Augmentation index	4.58
PWV	5.87

characteristics of the pulse wave. In particular, the relative dicrotic time parameter showed a mean variability of 1.87%, which was the best value obtained.

However, the variations measured are generally very high. As a result, it is not possible to accurately and quantitatively evaluate the pulse wave measured by palpation. Obviously, there is only a possibility of qualitative assessment based on the presence or absence of characteristic patterns of a time course, as with ECG assessments.

Conflict of Interests The authors declare that they have no conflict of interest.

References

1. Pauca AL, Wallenhaupt SL, Kon ND, Tucker WY. Does radial artery pressure accurately reflect aortic pressure? Chest 1992;102 (4):1193–8.
2. Lane HA, Smith JC, Davies JS. Noninvasive assessment of preclinical atherosclerosis. Vasc Health Risk Manag 2006;2(1):19–30. https://doi.org/10.2147/vhrm.2006.2.1.19.
3. O'Rourke FM, Pauca A, Xiong-Jing J. Pulse Wave Analysis. British Journal of Clinical Pharmacology, 51, 2001, s.507–522.
4. Leitão C, Antunes P, André P, Pinto JL, Bastos JM. Central arterial pulse waveform acquisition with a portable pen-like optical fiber sensor. Blood Press Monit. 2015 Feb;20(1):43–6.
5. Kamshilin AA, Sidorov IS, Babayan L, Volynsky MA, Giniatullin R, Mamontov OV. Accurate measurement of the pulse wave delay with imaging photoplethysmography. Biomed Opt Express. 2016 Nov 16;7(12):5138–5147.
6. Xu L, Yao Y, Wang H, He D, Wang L, Jiang Y. Morphology variability of radial pulse wave during exercise. Biomed Mater Eng. 2014;24(6):3605–11.
7. Wentland AL, Grist TM, Wieben O. Review of MRI-based measurements of pulse wave velocity: a biomarker of arterial stiffness. Cardiovasc Diagn Ther. 2014 Apr;4(2):193–206.
8. Chai R, Xu LS, Yao Y, Hao LL, Qi L. Comparison of Regression Analysis and Transfer Function in Estimating the Parameters of Central Pulse Waves from Brachial Pulse Wave. Stud Health Technol Inform. 2017;245:573–577.
9. Bargiotas I, Mousseaux E, Yu WC, Venkatesh BA, Bollache E, de Cesare A, Lima JA, Redheuil A, Kachenoura N. Estimation of aortic pulse wave transit time in cardiovascular magnetic resonance using complex wavelet cross-spectrum analysis. J Cardiovasc Magn Reson. 2015 Jul 30;17:65.
10. Fushimi Y, Okada T, Yamamoto A, Kanagaki M, Imai H, Togashi K. Estimation of the timing of carotid artery flow using peripheral pulse wave-gated MRI. J Magn Reson Imaging. 2012 Aug;36(2):454–8.

Stable EEG Spatiospectral Sources Using Relative Power as Group-ICA Input

René Labounek, David A. Bridwell, Radek Mareček, Martin Lamoš,
Michal Mikl, Milan Brázdil, Jiří Jan, and Petr Hluštík

Abstract

Within the last decade, various blind source separation algorithms (BSS) isolating distinct EEG oscillations were derived and implemented. Group Independent Component Analysis (group-ICA) is a promising tool for decomposing spatiospectral EEG maps across multiple subjects. However, researchers are faced with many preprocessing options prior to performing group-ICA, which potentially influences the results. To examine the influence of preprocessing steps, within this article we compare results derived from group-ICA using the absolute power of spatiospectral maps and the relative power of spatiospectral maps. Within a previous study, we used K-means clustering to demonstrate group-ICA of absolute power spatiospectral maps generates sources which are stable across different paradigms (i.e. resting-state, semantic decision, visual oddball) Within the current study, we compare these maps with those obtained using relative power of spatiospectral maps as input to group-ICA. We find that relative EEG power contains 10 stable spatiospectral patterns which were similar to those observed using absolute power as inputs. Interestingly, relative power revealed two γ-band (20–40 Hz) patterns which were present across 3 paradigms, but not present using absolute power. This finding suggests that relative power potentially emphasizes low energy signals which are obscured by the high energy low frequency which dominates absolute power measures.

1 Introduction

The EEG signal is considered a stochastic process comprised of a mixture of distinct electrophysiological brain processes, where different frequencies become dominant during different cognitive states [1]. Within the last decade, multisubject blind source separation (BSS) techniques of EEG spectra have been developed and implemented for isolating these distinct EEG oscillations [2]. One multisubject technique gaining in popularity is spatiospectral group-ICA, conducted on the absolute power of spectral densities computed across multiple epochs [3]. We have recently identified spatiospectral sources derived using this method which appear (i.e. are stable) across different paradigms (i.e. resting state, semantic decision, visual oddball) [4].

Different EEG preprocessing steps could potentially influence the results of spatiospectral group-ICA. In order to explore this further, we compare the spatiospectral maps derived in our previous study using absolute power with those derived using relative power maps as inputs (i.e. the spatiospectral heuristic model [5]). This preprocessing step is particularly interesting based upon previous studies reporting that relative power fluctuations correspond more with the experimental task than absolute power fluctuations [6–8]. Within the current study we compute spatiospectral sources using relative power as input, and compare these sources to those derived in our previous study [4] using absolute power. In addition, we examine the degree in which the fluctuations of sources derived from relative or absolute power better correspond with the timecourse of experimental stimuli.

R. Labounek (✉) · P. Hluštík
University Hospital Olomouc, I. P. Pavlova 6, 779 00 Olomouc, Czech Republic
e-mail: rene.labounek@gmail.com; rene.labounek@fnol.cz

R. Labounek · P. Hluštík
Palacký University Olomouc, Křížkovského 511/8, 771 47 Olomouc, Czech Republic

D. A. Bridwell
Mind Research Network, Albuquerque, NM 87106, USA

R. Mareček · M. Lamoš · M. Mikl · M. Brázdil
Central European Institute of Technology, Kamenice 753/5, 625 00 Brno, Czech Republic

J. Jan
Brno University of Technology, Antonínská 548/1, 601 90 Brno, Czech Republic

2   Materials and Methods

2.1   EEG Data Acquisition

The scalp EEG data was acquired simultaneously with fMRI using an MR compatible 32-channel 10/20 EEG system (*BrainProducts, Germany*) with a 5 kHz sampling frequency. Two channels were used for ECG and EOG. Simultaneous fMRI data was acquired using a 1.5T Siemens Symphony Numaris. Informed consent was obtained from all subjects after the procedures were fully explained, and the study was approved by the local ethics committee. The equipment was identical during acquisitions of the three paradigms described below. For more detailed description of the paradigms, and acquisition parameters, see [4].

Resting-state paradigm: Fifty healthy subjects participated in a 15 min "resting-state" experiment (RST, 30 right handed men, 20 right-handed women; age 25 ± 5 years). Subjects were instructed to lie still within the fMRI scanner with their eyes closed, not to think of anything specific, and not to fall asleep.

Semantic decision paradigm: A block design semantic decision task (SDT) was performed by 42 healthy subjects (22 right-handed men, 2 left-handed men, 18 right-handed women; age 25 ± 5 years). The block stimulation design was implemented in order to elicit robust language network activation.

Visual oddball paradigm: An event-related visual oddball task (VOT) was performed by 21 healthy subjects measured in 4 inter-leaved sessions (13 right-handed men, 1 left-handed man, 7 right-handed women; age 23 ± 2 years).

2.2   EEG Data Preprocessing

EEG data were preprocessed using BrainVision Analyzer 2.02 (*BrainProducts, Germany*). Gradient artifacts were removed using template subtraction [9] and signals were resampled to 250 Hz (antialiasing filter included), and filtered with a Butterworth zero phase 1–40 Hz band-pass filter. Cardiobalistogram artifacts were removed by subtracting the average pulse artifact waveform from each channel [10] and signals were re-referenced to the average. For visual oddball EEG data, eye-blinking artifacts were removed by conducting a temporal ICA decomposition and removing eye-blink artifacts from the back-reconstructed time course [4].

2.3   Spatiospectral Group-ICA, Clustering of the Sources and Regression of the Timecourses

The preprocessed EEG signal from each lead was normalized such that the time course was normally distributed $N(0, 1)$, and divided into 1.66 s epochs (i.e. the shortest repetition time of simultaneous fMRI acquisition [4]) without overlap. Each epoch was transformed to the spectral domain with fast Fourier transform (FFT), generating a vector (length = 67) of complex valued spectral coefficients between 0 and 40 Hz. Complex values were converted to relative power by taking the absolute value, squaring and dividing by the absolute power of the whole epoch. The output vector of 67 real relative power values comprised a 3D matrix E with dimensions n_t EEG epochs, n_c electrodes and n_ω spectral coefficients. The 3D matrix $E(n_t, n_c, n_\omega)$ was transformed into a 2D matrix $E(n_t, n_c * n_\omega)$ and used as input into spatiospectral group-ICA (Eq. 1) [3], returning a group mixing matrix W with dimensions $W(n_t, m)$ and a group source matrix S with dimensions $S(m, n_c * n_\omega)$. The dimension m is the number of decomposed ICs ($m = 20$).

$$E = WS \qquad (1)$$

As described in [4], group-ICA was conducted followed by K-means clustering [11] (40 clusters) of the back-reconstructed individual spatiospectral maps for each paradigm. Forty output clusters were selected based on the elbow of residual variance and predictive residual variance curves for 2–250 output clusters (see Fig. S4 of our previous study [4]). Multiple linear regression was conducted between the timecourses of stable spatiospectral patterns in W and stimulus vectors, and statistically significant relationships were identified using one-sample t-tests computed on the regression coefficients.

3   Results

Twenty-one of the 40 output clusters were organized into 16 final K-means clusters (Fig. 1) whose spatiospectral patterns appear to be of physiological origin. Thirteen clusters were not included since their patterns consisted of single-frequency peak which appeared artefactual, and which was not present over the 3 paradigms. The remaining 6 excluded clusters contained less than 5% of single-subject patterns of at least one paradigm and are thus considered noise. Twelve of the sixteen patterns derived from relative EEG power were stable over all three paradigms (Fig. 1a, b). Of these twelve stable sources, ten appeared visually similar to patterns that were observed for absolute EEG power (Fig. 1a) [4]. Two stable γ-band patterns (Fig. 1b) were present with relative power but not with absolute power [4]. One cluster representing β-band activity (~ 20 Hz) was present for SDT and VOT data but not RST (Fig. 1c). For the cluster number (cl. n.) 29, the spatial distribution of the pattern looks identical over paradigms, but the frequency peak within relative power maps appears to differ across paradigms (Fig. 2a). Three clusters contained maps (one θ-band and two γ-band patterns) which were present during RST but not SDT or VOT (Fig. 1d).

(a) sources stable over paradigms and observed also in absolute EEG power

(b) sources stable over paradimgs and observed only in relative EEG power

(c) source stable over SDT and VOT

(d) sources unique for the resting-state paradigm
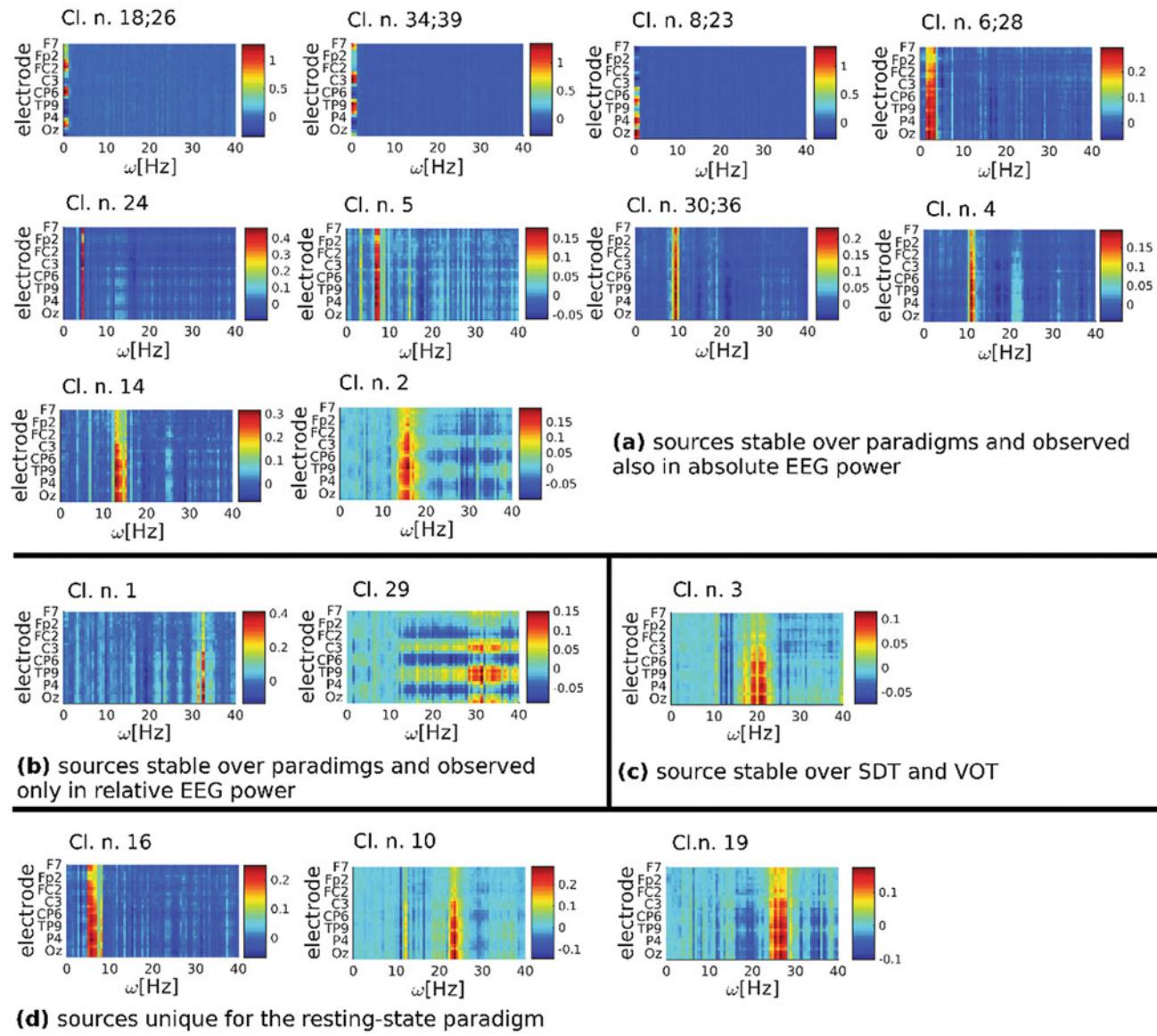
Fig. 1 Spatiospectral sources using relative EEG power as input to group-ICA
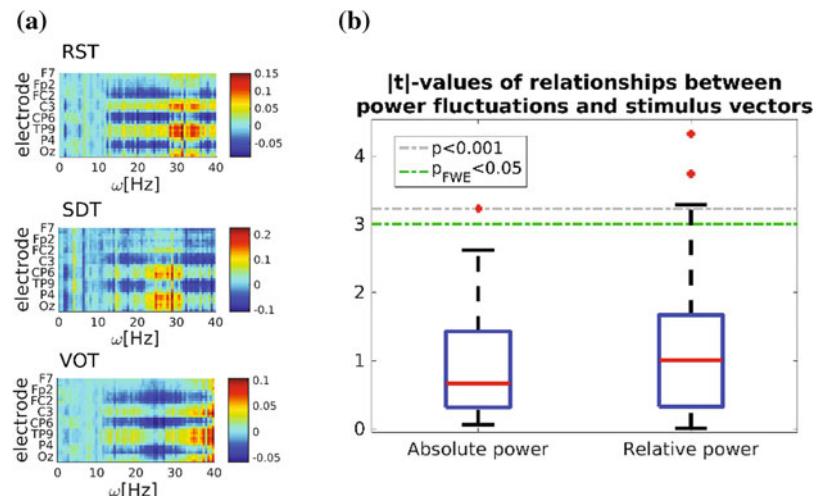
Fig. 2 a Similar spatial pattern and variable peaks in aggregated relative power of the cl. n. 29 over paradigms **b** relationships between timecourses of stable spatiospectral sources and stimulus vectors using absolute and relative EEG power as input to group-ICA

Although significant relationships with stimulus vectors were found for both power types, there appears to be no statistically significant difference in the distribution of |T|-values computed between the two (Fig. 2b). The difference between absolute or relative power relationships with the stimuli (Fig. 2b) is p < 0.162 based on two-sample t-test between distributions or p < 0.150 based on a 10 000 sample bootstrap test. |T|-values are not normally distributed, since the p-values of one-sample Kolmogorov-Smirnov tests are p < $6.1 * 10^{-14}$ for the absolute power and p < $1.8 * 10^{-12}$ for the relative power. Further research should be conducted to examine the potential influences of relative and absolute power map timecourses and stimulus timecourses.

4 Discussion

4.1 Novelty

The current study extends our recent study [4], by demonstrating that group ICA spatiospectral sources derived from relative power are stable across paradigms, and, we highlight the similarities and differences among relative and absolute power sources.

4.2 Absolute or Relative Power for Spatiospectral Group-ICA?

As previously shown for the absolute EEG power, we demonstrate here that relative EEG power also consists of stable spatiospectral patterns over paradigms. Although lower reproducibility of spatiospectral group-ICA estimates (using ICASSO [12]) has been observed and reported for sources derived from relative EEG power [4]. Ten stable sources were present within maps derived from absolute and relative EEG power, while two stable γ-band patterns (Fig. 1b) and 3 possibly physiological γ-band patterns (cl. n. 3, cl. n. 10 and cl. n. 19; Fig. 1c, d) were present with relative power but not absolute power. Relative power potentially emphasizes low energy signals which are obscured by the high energy low frequency which dominates absolute power measures.

We found significant relationships between stimuli and timecourses for both types of power values, with slightly higher t-values for relative power (although not statistically significant). This finding motivates further examination of task-related changes in EEG power fluctuations with relative and absolute power.

4.3 Limits and Possible Future Work

The spatiotemporal resolution (e.g. 30 electrodes and an epoch window time 1.66 s) can influence the group-ICA results and ultimately influence the relationship between the task and spatiospectral timecourses. Currently, we are capturing high-density (256-electrodes) EEG data where we will be able to decrease the epoch window time to durations that better capture evoked potential timing without undersampling. These findings can be compared with the present findings to better understand the influence of spatiotemporal resolution on group-ICA and the relationship between source timecourses and stimulus timing.

References

1. Buzsaki, G.: Rhythms of the Brain. Oxford University Press, (2006).
2. Huster, R. J., Raud, L.: A Tutorial Review on Multi-subject Decomposition of EEG. Brain Topogr. 31(1), 3–16, (2018). https://doi.org/10.1007/s10548-017-0603-x.
3. Bridwell, D. A., Wu, L., Eichele, T., Calhoun, V. D.: The spatiospectral characterization of brain networks: fusing concurrent EEG spectra and fMRI maps. Neuroimage 69, 101–11, (2013). https://doi.org/10.1016/j.neuroimage.2012.12.024.
4. Labounek, R., Bridwell, D. A., Mareček, R., et al.: Stable scalp EEG spatiospectral patterns across paradigms estimated by group ICA. Brain Topogr. 31(1), 76–89 (2018). https://doi.org/10.1007/s10548-017-0585-8.
5. Labounek, R., Janeček, D., Mareček, R., et al.: Generalized EEG-fMRI spectral and spatiospectral heuristic models. In: 13th International Symposium on Biomedical Imaging: From Nano to Macro, IEEE, Prague, pp. 767–770, (2016). https://doi.org/10.1109/isbi.2016.7493379.
6. Klimesch, W.: EEG alpha and theta oscillations reflect cognitive and memory performance: a review and analysis. Brain Res Rev 29, 169–95, (1999). https://doi.org/10.1016/s0165-0173(98)00056-3.
7. Kilner, J. M., Mattout, J., Henson, R., Friston, K. J.: Hemodynamic correlates of EEG: a heuristic. Neuroimage 28, 280–286, (2005). https://doi.org/10.1016/j.neuroimage.2005.06.008.
8. Labounek, R., Lamoš, M., Mareček, R., et al.: Exploring task-related variability in fMRI data using fluctuations in power spectrum of simultaneously acquired EEG. Journal of Neuroscience Methods 245, 125–136, (2015). https://doi.org/10.1016/j.jneumeth.2015.02.016.
9. Allen, P. J., Josephs, O., Turner, R.: A method for removing imaging artifact from continuous EEG recorded during functional MRI. Neuroimage 12,230–239, (2000). https://doi.org/10.1006/nimg.2000.0599.
10. Allen, P. J., Polizzi, G., Krakow, K., et al.: Identification of EEG events in the MR scanner: the problem of pulse artifact and a method for its subtraction. Neuroimage 8, 229–239, (1998). https://doi.org/10.1006/nimg.1998.0361.
11. Pascual-Marqui, R. D., Michel, C. M., Lehmann, D.: Segmentation of brain electrical activity into microstates: model estimation and validation. Trans Biomed Eng IEEE 42, 658–665, (1995). https://doi.org/10.1109/10.391164.
12. Himberg, J., Hyvärinen, A., Esposito, F.: Validating the independent components of neuroimaging time series via clustering and visualization. Neuroimage 22, 1214–1222, (2004). https://doi.org/10.1016/j.neuroimage.2004.03.027.

Simulation of Required CPAP Usage to Normalize AHI in Obstructive Sleep Apnea Patients

Antti Kulkas, Sami Nikkonen, Juha Töyräs, Esa Mervaala, and Timo Leppänen

Abstract

Obstructive sleep apnea (OSA) is a highly prevalent disease with severe health consequences. The severity of OSA is estimated with apnea-hypopnea-index (AHI). OSA is often treated with continuous positive airway pressure (CPAP). The aim of the current work was to create a numerical simulator showing benefits of different levels of usage of CPAP treatment. 226 male OSA patients were evaluated. CPAP treatment was simulated in 5 min intervals starting from the beginning of the night and continuing until the end. The cutoff point where AHI reached normal level of <5 events/h were determined for mild, moderate and severe OSA categories. We found a trend of increasing AHI towards the end of the night. The median values of required simulated CPAP usage times to normalize the AHI values (AHI < 5 events/h) were 3.9 h, 5.3 h and 6.2 h in the mild, moderate and severe OSA severity categories, respectively. CPAP treatment adherence can be limited in OSA patients due to several reasons. The presented CPAP treatment simulation tool could aid the clinicians to give patient specific recommendation to the OSA patients for required CPAP treatment times and to motivate the patients to higher adherence levels of the treatment. This could possibly better prevent the harmful health consequences related to OSA.

A. Kulkas (✉)
Department of Clinical Neurophysiology, Seinäjoki Central Hospital, Seinäjoki, Finland
e-mail: antti.kulkas@epshp.fi

A. Kulkas · S. Nikkonen · J. Töyräs
Department of Applied Physics, University of Eastern Finland, Kuopio, Finland

S. Nikkonen · J. Töyräs · E. Mervaala · T. Leppänen
Department of Clinical Neurophysiology, Diagnostic Imaging Center, Kuopio University Hospital, Kuopio, Finland

E. Mervaala
Faculty of Health Sciences, Department of Clinical Neurophysiology, Institute of Clinical Medicine, University of Eastern Finland, Kuopio, Finland

1 Introduction

Obstructive sleep apnea (OSA) is a highly prevalent severe nocturnal disease characterized by partial (hypopnea) and total (apnea) breathing cessations during sleep, which are known to have severe health consequences [1, 2]. The severity estimation of OSA is based on the average frequency of these breathing cessation events during sleep i.e. apnea-hypopnea-index (AHI) [3].

OSA is often treated with continuous positive airway pressure (CPAP) device to eliminate obstructive breathing cessations. At sufficient pressure level CPAP treatment keeps the upper airways open and prevents the breathing cessation events. CPAP treatment is effective when applied but unfortunately, the adherence to CPAP treatment is often limited. The average CPAP usage per night normally varies between 3 and 4 h [4]. It has been shown that the adherence diminishes with lengthening of the treatment period [4]. Due to the limited use of the CPAP treatment, the treatment results are not always optimal [5]. It has been shown that limited CPAP use, around 3 h per night, does not eliminate the risk of severe cardiovascular health consequences in moderate to severe OSA patients [5].

The aim of the present research was to create a numerical simulator for CPAP treatment to indicate how the CPAP usage affects the total AHI. It was hypothesized that the effect of CPAP usage on AHI is not uniform in different parts of the night. At the same time we aimed to find the cutoff point for the treatment time required to normalize AHI values to level of <5 events/h in different OSA severity categories. This could aid the clinicians to give recommendations on the required treatment levels and to motivate the

patients to use CPAP sufficient amount to prevent the harmful health consequences of OSA.

2 Patients and Methods

Ambulatory polygraphies of 226 male patients with suspected OSA recorded at the Kuopio University Hospital region were analyzed. The local ethical committee gave a favorable statement to conduct the study (decision numbers 127/2004 and 24/2013). The patient material has been previously used in our earlier study [6]. The ambulatory polygraphies were analyzed based on the standard American Academy of Sleep Medicine (AASM) rules [7]. The recommended hypopnea rule 4A [7] was used based on the AASM recommendations and clinical practice at the Kuopio University Hospital at the time of the analysis. Apneas and hypopneas were automatically scored (Remlogic, version 3.2, and Somnologica, version 3.2 softwares, Embla Co., Broomsfield, CO, USA) and the scorings manually verified and corrected when necessary. AHI was determined based on the breathing cessation events and patients were divided into four different OSA severity categories based on the total AHI; normal AHI < 5, mild $5 \leq$ AHI < 15, moderate $15 \leq$ AHI < 30, and severe AHI $\geq$ 30 events/h.

The scored breathing cessation events were imported into Matlab (Mathworks, Natick, MA, USA) software. Custom-made CPAP treatment simulator was then programmed with Matlab. The custom-made Matlab script utilizes the information of the analyzed breathing cessation events. The simulation of CPAP usage was started from the beginning of the recording as it was assumed that the typical CPAP adherence is focused at the beginning of the night. The simulated CPAP treatment time was increased with 5 min intervals until it reached the end of the recording in each patient. The events inside the simulated CPAP treatment periods were considered to be prevented by the treatment and AHI during the simulated CPAP usage was considered to be 0 events/h. Simulated AHI was then calculated based on the remaining breathing cessation events after the simulated CPAP use. In the simulation, the cutoff point where AHI reached normal level of <5 events/h were also determined for each patient.

3 Results

There were 88, 68, 46 and 24 patients in normal, mild, moderate and severe OSA severity categories. The patient demographics are presented in Table 1. The median AHI values inside the different severity categories are presented as a function of simulated CPAP usage time (h) and percentage (%) of usage from the total analyzed time (Fig. 1). It can be seen that the reduction in AHI after simulated CPAP treatment is not linear. In the early hours of simulated CPAP treatment the reduction of AHI has less steep slope than later on during the night. The median values of the required simulated CPAP usage times to normalize the AHI values (AHI < 5 events/h) were 3.9 h, 5.3 h and 6.2 h in the mild, moderate and severe OSA severity categories, respectively (Table 1). The corresponding percentages of the required simulated CPAP use from the total analyzed time were 52.8%, 78.9%, 90.2%, respectively (Table 1).

4 Discussion

In the current study, a simulation of CPAP usage was performed for 226 suspected OSA patients. The simulation showed that the reduction of AHI during the simulated CPAP treatment is not linear during the night. This indicates that AHI varies hour by hour during the night, generally increasing towards morning. Therefore, there is a trend of increasing simulated treatment response towards the end of the night.

Obstructive sleep apnea is a highly prevalent disease with severe health consequences [2]. Breathing cessation events during the night are typically treated with CPAP where the

Table 1 Patient demographics and simulated CPAP usage results in different OSA severity categories, median (interquartile range)

	Normal	Mild	Moderate	Severe
Number of patients	88	68	46	24
Age (years)	51.4 (45.9–57.6)	57.3 (47.2–62.5)	50.2 (42.2–59.3)	54.2 (48.2–62.7)
BMI (kg/m^2)	27.7 (25.6–29.4)	28.1 (25.1–32.6)	31.8 (28.4–34.7)	29.6 (26.3–36.0)
AHI (1/h)	2.5 (0.8–3.7)	8.8 (7.0–10.7)	19.6 (17.5–24.6)	47.3 (37.5–57.2)
Total analyzed time (min)	415.0 (371.2–454.4)	415.6 (373.1–450.5)	415.3 (376.1–454.8)	407.3 (375.4–437.8)
CPAP usage to AHI < 5 (%)	–	52.8 (45.3–69.0)	78.9 (63.7–84.5)	90.2 (82.7–91.8)
CPAP usage to AHI < 5 (h)	–	3.9 (2.9–4.8)	5.3 (4.3–6.1)	6.2 (5.8–6.8)

CPAP usage to AHI < 5 (%) denotes the median percentage from total analyzed time and *CPAP usage to AHI < 5 (h)* median time of CPAP usage required to achieve normal AHI level (AHI < 5 events/h)
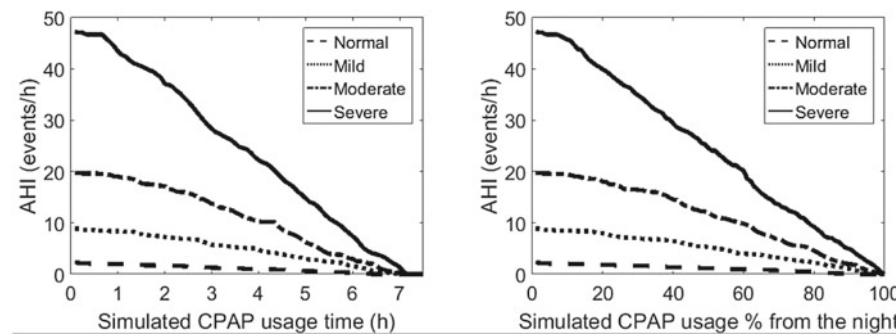
Fig. 1 Effect of simulated CPAP usage time (left panel) and percentage (right panel) on median AHI in different OSA severity categories. The reduction in the median AHI is not linear in any of the OSA severity categories. There is a trend of increasing effect of the CPAP usage (larger decrease in the median AHI) towards the end of the night. In more severe categories longer usage is required to achieve AHI < 5 events/h

continuous pressure keeps the airways open and flowing air prevents the obstruction of breathing. Unfortunately, the adherence to CPAP treatment is limited due to several factors including e.g. dry mouth, nasal symptoms, eye problems, claustrophobia, noise problems, soreness or skin irritation and mask fit and leak problems [4]. The average CPAP adherence after 1, 6 and 12 months of treatment was reported to be 4.4, 3.8 and 3.3 h in moderate to severe OSA patients [4]. In the current study, the CPAP treatment simulation showed that to normalize the AHI values (AHI < 5 events/h) would require 3.9 h, 5.3 h and 6.2 h of CPAP usage in mild, moderate and severe OSA categories, respectively. These values could aid the clinicians to give recommendation of the CPAP treatment levels required to the patients. This could increase the benefits of the treatment as it has been shown that the risk of adverse cardiovascular events cannot be prevented with limited nightly CPAP treatment times [5].

Our study also showed that the response to simulated CPAP treatment is not linear. The AHI values vary hour by hour during the night and there is a trend of increasing AHI towards the end of the night. It has been suggested that fluid shift from the legs to the neck during the night is linked with AHI in nonobese men; stronger shift leading into higher AHI [8]. This could be one possible reason behind the fact that AHI increased towards the end of the night. As the CPAP treatment is assumed to be focused into the beginning of the night the treatment results might not be optimal. The reduction on the total AHI is smaller when the simulated CPAP treatment is focused to the beginning of the night compared to the simulate CPAP treatment at the end of the night. Therefore, if the adherence is limited, focusing the CPAP treatment to the worst hours during the night would presumably improve the treatment results.

It is acknowledged that the present study is not without limitations. The current study was performed on a single night polygraphies. There is known internight variability in the AHI values that could affect the current results [9]. Also sleeping position, gender, age and BMI are known factors that can influence AHI [10–14] and these factors were not controlled in the current study. There are also uncertainties in the ambulatory polygraphies related to onset and offset of sleep. Also the sleep quality and sleep stages can be associated with OSA severity and they were not controlled in the study.

The presented CPAP treatment simulation tool could be applied to single night polygraphies to show the patient the effect of CPAP treatment at different levels of adherence. At the same time the level of needed adherence to normalize AHI could be determined and this could aid the clinicians to give patient specific recommendation of the minimum CPAP use required. Therefore, the CPAP treatment simulation tool could be useful to motivate the patients to use CPAP and to show the level of required CPAP usage to decrease the risk of severe health consequences related to OSA.

References

1. Marin J, Carrizo SJ, Vicente L, Agusti A. Long-term cardiovascular outcomes in men with obstructive sleep apnea-hypopnoea with or without treatment with continuous positive air pressure: an observational study. Lancet. 365, 1046–1053 (2005).
2. Somers V, White D, Amin R, Abraham WT, Costa F, Culebras A, Daniels S, Floras JS, Hunt CE, Pickering TG, Russel R, Woo M,

Young T. Sleep Apnea and Cardiovascular Disease: An American Heart Association/American College of Cardiology Foundation Scientific Statement From the American Heart Association Council for High Blood Pressure Research Professional Education Committee, Council on. Circulation. 118(14), 1497–1518 (2008).

3. American Academy of Sleep Medicine Task Force. Sleep – Related Breathing Disorders in Adults: Recommendations for Syndrome Definition and Measurement Techniques in Clinical Research. Sleep. 22(5), 667–689 (1999).

4. Chai-Coetzer CL, Luo Y-M, Antic NA, Zhang XL, Chen BY, He QY, Heeley E, Huang SG, Anderson C, Zhong NS, McEvoy RD. Predictors of Long-Term Adherence to Continuous Positive Airway Pressure Therapy in Patients with Obstructive Sleep Apnea and Cardiovascular Disease in the SAVE Study. Sleep. 36(12), 1929–1937 (2013).

5. McEvoy RD, Antic NA, Heeley E, Luo Y, Ou Q, Zhang X, Mediano O, Chen R, Drager LF, Liu Z, Chen G, Du B, McArdle N, Mukherjee S, Tripathi M, Billot L, Li Q, Lorenzi-Filho G, Barbe F, Redline S, Wang J, Arima H, Neal B, White DP, Grunstein RR, Zhong N, Anderson CS. CPAP for Prevention of Cardiovascular Events in Obstructive Sleep Apnea. N Engl J Med. 375(10), 919–931 (2016).

6. Muraja-Murro A, Kulkas A, Hiltunen M, Kupari S, Hukkanen T, Tiihonen P, Mervaala E, Töyräs J. The severity of individual obstruction events is related to increased mortality rate in severe obstructive sleep apnea. J Sleep Res. 22(6), 663–669 (2013).

7. Iber C, Ancoli-Israel S, Chesson AL, Quan SF. AASM Manual for the Scoring of Sleep and Associated Events: Rules, Terminology and Technical Specifications. 1st ed. Westchester, IL: American Academy of Sleep Medicine; 2007.

8. Redolfi S, Yumino D, Ruttanaumpawan P, Yau B, Su MC, Lam J, Bradley T. Relationship between Overnight Rostal Fluid Shift and Obstructive Sleep Apnea in Nonobese Men. Am J Respir Crit Care Med. 179(3), 241–246 (2009).

9. Bittencourt LR, Suchecki D, Tufik S, Peres C, Togeiro SM, Bagnato MC, Nery LE. The variability of the apnoea-hypopnoea index. J Sleep Res. 10(3), 245–251 (2001).

10. Leppänen T, Töyräs J, Muraja-Murro A, Kupari S, Tiihonen P, Mervaala E, Kulkas A. Length of Individual Apnea Events Is Increased by Supine Position and Modulated by Severity of Obstructive Sleep Apnea. Sleep Disord. 2016, 1–13 (2016).

11. Leppänen T, Kulkas A, Mervaala E, Töyräs J. Severity of individual obstruction events is gender dependent in sleep apnea. Sleep Breath. 21(2), 397–404 (2017).

12. Kulkas A, Leppänen T, Sahlman J, Tiihonen P, Mervaala E, Kokkarinen J, Randell J, Seppä J, Tuomilehto H, Töyräs J. Novel parameters reflect changes in morphology of respiratory events during weight loss. Physiol Meas. 34(9), 1013–1026 (2013).

13. Kulkas A, Leppänen T, Sahlman J, Tiihonen P, Mervaala E, Kokkarinen J, Randell J, Seppä J, Töyräs J, Tuomilehto H. Weight loss alters severity of individual nocturnal respiratory events depending on sleeping position. Physiol Meas. 35(10), 2037–2052 (2014).

14. Kulkas A, Leppänen T, Sahlman J, Tiihonen P, Mervaala E, Kokkarinen J, Randell J, Seppä J, Töyräs J, Tuomilehto H. Amount of weight loss or gain influences the severity of respiratory events in sleep apnea. Med Biol Eng Comput. 53(10), 975–988 (2015).

SAHS Patients' Classification Based on Oximetry and Respiratory Effort Signal: An Alternative Method

C. Dell'Aquila, L. Correa, R. Correa, G. Cañadas, and E. Laciar

Abstract

The "Gold Standard" for Sleep Apnea/Hypopnea Syndrome (SAHS) diagnosis is the study of Polysomnography (PSG) in a sleep laboratory. It consists of connect to patient's body several sensors. The standards are the oronasal airflow (OAS) and pulse oximeter (SpO_2) sensors while Respiratory Inductance Plethysmography sensor (RIP) is alternative. The airflow signal can be estimated from RIP signal (RIPFlow). Hypopneas are detected in $\%SpO_2$ desaturation events through baseline. However, there isn't a consensus about this value's definition. The signals sent by such sensors are analyzed by an expert to get the Apnea/Hypopnea Index (AHI) and to classify the patients into four groups: Normal, Mild, Moderate and Severe. In this study, an alternative method for scoring apnea/hypopnea events based on thorax and abdomen RIP sensor and for analyzing the $\%SpO_2$ values variations using Median Absolute Deviation (MAD) is proposed. For time domain comparison, the Pearson's correlation coefficient was computed on the RIPFlow with the respiratory flow signal. Also, the automatic algorithms from standard and proposed method were implemented to obtain AHI. In order to test the proposed method's performance, PSG recordings acquired in 23 adult patients are used. The Sensitivity (Sen), Specificity (Sp) and Accuracy (Acc) values were calculated considering patients classification for the standard method and well as the one proposed. Results indicate a high correlation (p-value < 0.05) in flow estimation and an improvement in patient classification using the model based on the RIPflow and the MAD-SpO_2.

Keywords

SAHS • Respiratory inductance plethysmography
SpO_2 variability

1 Introduction

The Sleep Apnea/Hypopnea Syndrome (SAHS) is a common respiratory disorder that affects severely 1 of 15 adults in general population [1]. The implications of SAHS are its impact in cardiovascular system, such as, hypertension, arrhythmia, and coronary artery disease. Also, it has effect on daytime functioning by causing irritability, inattention and somnolence, increasing accident level [2].

SAHS is mainly characterized by the recurrence of both total breathing cessation (apnea events) and significant airflow reduction (hypopnea events) during sleep time [3]. It can be produced by upper airway collapse during sleep (obstructive) or when brain temporarily stops sending signals to the muscles that control breathing (central).

The "Gold Standard" for SAHS diagnosis is the Polysomnography (PSG) study and it consists of connects several sensors on patient's body in sleep laboratory. The portable sleep home monitors (PM) have been introduced to diagnose sleep apnea/hypopnea with the goal of reducing the inconvenience and expense associated with PSG's laboratory [4].

The American Academy of Sleep Medicine (AASM) has recommended rules for scoring apnea/hypopnea events [5]. Apnea in adults is scored when there is a drop in the peak respiratory flow by $\geq 90\%$ of pre-event baseline for ≥ 10 s. Hypopnea in adults is scored when the peak of respiratory

C. Dell'Aquila · L. Correa · R. Correa · G. Cañadas
E. Laciar (✉)
Facultad de Ingeniería, Gabinete de Tecnología Médica,
Universidad Nacional de San Juan, San Juan, Argentina
e-mail: laciar@gateme.unsj.edu.ar

C. Dell'Aquila
e-mail: carlos.dellaquila@unsj.edu.ar

C. Dell'Aquila · R. Correa · G. Cañadas · E. Laciar
Consejo Nacional de Investigaciones Científicas y Técnicas,
Ministerio de Ciencia, Tecnología e Innovación Productiva de la
Nación, Buenos Aires, Argentina

airflow drop by $\geq 30\%$ of pre-event baseline for ≥ 10 s in association with either $\geq 3\%$ arterial oxygen desaturation or an arousal. The pre-event baseline is defined for stable and unstable patient's breathings patterns [3]. The AHI index is the rate of Apnea/Hypopnea events per hour and it is used to classify the patient in four groups: **Normal** (<5), **Mild** (between 5 and 15), **Moderate** (between 15 and 30) and **Severe** (>30), according with AASM [3].

Currently, the recommended sensors for SAHS diagnosis are OAS and SpO_2 sensors. The respiratory effort is measured with RIP and it is considered as alternative sensor by AASM's task force [3]. This include the RIPSum which is the sum of the thorax and abdomen RIP belt signals. The RIPFlow (the time derivative of the RIPSum), an estimation of respiratory airflow signal (RespFlow).

The detection of blood oxygen desaturation event associated with SAHS is defined as a drop from a baseline preceding the event. However, there isn't consensus about "baseline SpO_2". The AASM Task Force reproduces the same definition for stable pattern breathing's baseline, but also considered that SpO_2 is a no linear signal: the same drop percentage in the SpO_2 implies different variations in the arterial oxygen saturation depending on the baseline considered [3].

Studies have evaluated the accuracy of RIPSum and RIPFlow to detect apneas and hypopneas. The work of Thurnheer et al. showed good agreement in the measured with these signal with the pneumotachograph [6]. Another study proposed a method based on ensemble learning to estimate the respiratory flow, the thoracic respiratory effort and the abdominal respiratory effort from acceleration of suprasternal notch, the thorax and the abdomen, respectively [7].

In a recent research, Kogan et al. showed that an improvement in sensitivity and specificity could be obtained when scoring hypopneas by RIPSum channel when compared with both the recommended and acceptable criteria of the American Academy of Sleep Medicine [8].

In a previous work of this group, different models were studied based on the measurement of SpO_2's variability to detect arterial's oxygenation desaturation event and respiratory flow signal estimation from respiratory effort signal [9]. In this work, this study is extended and two tests were performed. The first one, the Pearson's correlation coefficient was computed on the RIPFlow with RespFlow, for time domain comparison. The second, the performance in SAHS patient's classification of the proposed and standard method is evaluated using a special method to compute *Sen*, *Sp* and *Acc* for 4 classification groups.

2 Materials and Methods

2.1 Database

The database used is freely available in Physionet's web site [10]. It contains 25 full overnight PSG recordings of patients (age: 50 ± 18 years, 21M and 4F) with suspected sleep disordered-breathing. The recording lasts from 5.9 to 7.7 h. It also includes sleep stages and respiratory annotations done by experts with the respiratory event start and last; and event classification (Central Apnea/Hypopnea, Obstructive Apnea/Hypopnea and Mixed events).

In this study, the RespFlow, RIPSum and $\%SpO_2$ signals, sampled at 128 Hz, were used. RespFlow is calibrated signal expressed in liters/seconds and SpO_2 is the percentage of blood oxygen saturation. The RIPSum signal is the sum of Thorax and Abdomen respiratory effort, which is a non-calibrated signal.

The recordings UCDDB006 and UCDDB011 were not used because they have problems in the recording of the signals of interest for our purpose.

2.2 Signal Pre-processing

A digital filter is applied to RespFlow and RIPSum signals, to obtain the spectral range that defines the respiratory process, which comes up to 0.5 Hz [11]. The bidirectional 4th order Butterworth low-pass filter has been selected with cut-off frequency in 0.5 Hz. It has the zero-phase distortion advantage.

In order to obtain the RIPFlow, a five points Differentiator-Integrator filter is applied to RIPSum. It derives the input signal and has a low pass frequency response to attenuate the amplified noise in the differentiator process. The filtered RespFlow and RIPSum signals are show in Fig. 1 for Obstructive and central Hypopneas events as example.

In order to evaluate the similarity between RespFlow and RIPFlow signal the cross correlation was computed. The Pearson correlation coefficient obtained was r = 0.7414 (p = 0.001) and indicated a high correlation as show in Fig. 2 for UCDDB003as example, but the results are same for all used recordings.

The $\%SpO_2$ signal is resampled to 32 Hz to decrease the computational cost, according to AASM—Manual Scoring of Sleep and Associated Events that recommends a minimum of 25 Hz [5].
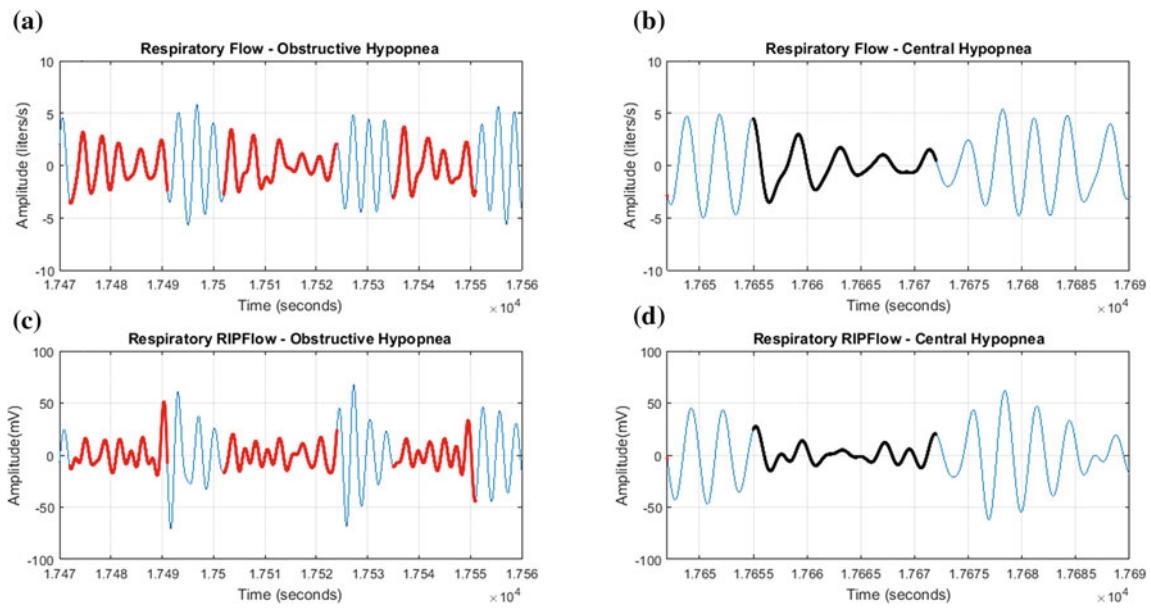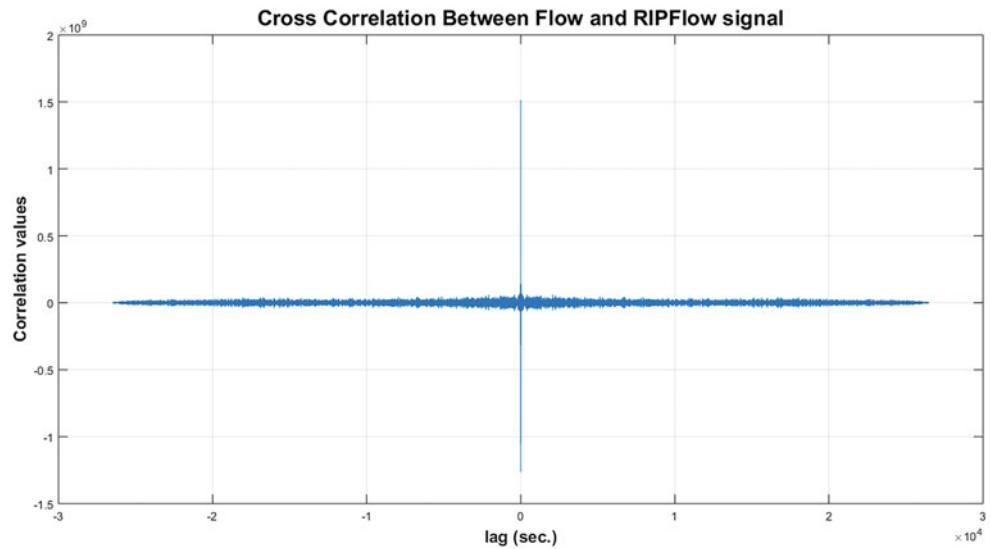
Fig. 1 (**a**) and (**b**) Obstructive Hypopnea (in red) in RespFlow and RIPFlow signals, respectively. (**c**) and (**d**) Central Hypopnea (in black) in RespFlow and RIPFlow signals, respectively (Color figure online)

Fig. 2 Cross correlation RIPFlow and flow for UCDDB003 recording

2.3 Patients' Classification

The Breathing Baseline (BB) is defined as 3 largest breaths in the 2 min preceding onset of the event, in individuals without a stable breathing pattern, and it valid for RespFlow and RIPFlow signals [6]. In the present work, BB is estimated to determine Threshold (*Th*) that is used to convert a Respiratory Signal (RS) in square signals.

The RS is divided into 1 min duration segments and each one is associated with a *Th*. In order to compute it for a present segment, the 2 min previous are analyzed. If RS was lower than 10% of *Th* by 10 s, the event is scored as an

apnea. In the other hand, if RS was lower than 70% by 10 s the event is scored as a possible hypopnea and $\%SpO_2$ is analyzed. The Median Absolute Deviation (MAD) is used to measure their variations. Then, if variations are greater than a fixed set value, the event is scored as hypopnea. The completed process is detailed in a previous work [9]. Finally, patient is classified base on AHI value (1).

$$AHI = \frac{Respiratory\,Event\,(apnea/hypopnea)}{Total\,Sleep\,Time\,(hours)} \cdot 60 \qquad (1)$$

In this work, amount of True Positive (TP), True Negative (TN), False Positive (FP) and False Negative (FN) were

Table 1 Confusion matrix for two methods

PSG	Standard: Flow 3%-SpO$_2$				Proposed: RIPFlow MAD-SpO$_2$				Total
Data base	Normal	Mild	Moderate	Severe	Normal	Mild	Moderate	Severe	
Normal	1	3	0	0	3	1	0	0	4
Mild	0	5	3	0	0	8	0	0	8
Moderate	0	1	2	3	0	1	4	1	6
Severe	0	0	0	5	0	0	0	5	5

computed for each group (Normal, Mild, Moderate and Severe) based on, AHI value. The *Sen*, *Sp*, *Acc* values were computed with Eqs. (2), (3) and (4), respectively.

$$Sen = \frac{TP}{TP + \sum FN} \tag{2}$$

$$Sp = \frac{\sum TN}{\sum FP + \sum TN} \tag{3}$$

$$Acc = \frac{\sum TP + \sum TN}{\sum FP + \sum TN + \sum FN + \sum TP} \tag{4}$$

These values are obtained for each group. For each one, the summations are considering the other two groups as one. For example, to compute the *Sen* for *Normal* group the FN is considering the group *Mild + Moderate + Severe*.

3 Results

Two algorithms were implemented, the standard and the proposed here, which use alternative sensors. For each one, the AHI was computed for all patients, and also obtained from database's information as reference. Then, based on each these values the patient was classified as Normal, Mild, Moderate and Severe.

Table 1 shows the confusion matrix and Table 2 show a statistical results for patients' classification from standard algorithm (Flow and SpO$_2$ drop by >3% of pre-event baseline) and from the proposed (RIPFlow and %SpO$_2$ variations measurement using MAD).

4 Discussion and Conclusions

In this work, the performance of the algorithms for apnea and hypopnea detection was evaluated and the resulting AHI value. The proposed method uses alternative sensors that are recommended by AASM, such as, RIP. The method was compared with the "Gold standard" that uses AOS for apnea detection. Furthermore, both methods use the %SpO$_2$ to detect hypopneas events with different analyses. The first one was the standard recommend by AASM and the other base on MAD.

Two performance tests were applied in order to evaluate the proposed method. The first one, the values of *Sen*, *Sp* and *Acc* were obtained from confusion matrix with three patients' group based on AHI value for each patient (Table 1). This classification criterion is recommended by AASM. The results show an improvement with the proposed method. Is important to mention, there aren't other works that apply this criteria.

The results show an improvement in event detection when the method based on RIPFlow and MAD-SpO$_2$. These results are in accordance with the work of Kogan et al. [8].

It is important to mention, the AASM recommend the criteria of %SpO$_2$ drop by >3% oxygen saturation analyses although could there are resaturation events at the event's end. For this reason, a measurement of SpO$_2$'s variability (such as, MAD) causes better results.

Another important advantage of the proposed methodology is the simplicity in the signal acquisition; it also is no invasive and does not affect patient comfort, as opposite to

Table 2 Statistics results for two methods

(%)	Standard: Flow 3%-SpO$_2$				Proposed: RIPFlow MAD-SpO$_2$			
	Normal (%)	Mild (%)	Moderate (%)	Severe (%)	Normal (%)	Mild (%)	Moderate (%)	Severe (%)
Sen	25	62.5	33.33	100	75	100	66.67	100
Sp	63.16	72.73	64.71	44.44	89.47	92.31	94.12	83.33
Acc	56.52	56.52	56.52	56.52	86.96	86.96	86.96	86.96

the AOS, which comfortless produce a lower quality in the PSG study.

Besides, the threshold analysis of the RIPflow and the variability SpO_2 measurements implies a low computational cost, are easily computed and may be implemented in any processor. These qualities make it suitable for wireless applications.

Conflict of Interest The authors declare that they have no conflict of interest.

References

1. L. Ma, J. Zhang, and Y. Liu, "Roles and Mechanisms of Obstructive Sleep Apnea-Hypopnea Syndrome and Chronic Intermittent Hypoxia in Atherosclerosis: Evidence and Prospective," *Oxid. Med. Cell. Longev.*, vol. 2016, 2016.
2. P. de Chazal, N. Sadr, and M. Jayawardhana, "An ECG oximetry system for identifying obstructive and central apnoea events," in *2015 37th Annual International Conference of the IEEE Engineering in Medicine and Biology Society (EMBC)*, 2015, pp. 7671–7674.
3. R. B. Berry *et al.*, "Rules for Scoring Respiratory Events in Sleep: Update of the 2007 AASM Manual for the Scoring of Sleep and Associated Events: Deliberations of the Sleep Apnea Definitions Task Force of the American Academy of Sleep Medicine," *J. Clin. Sleep Med.*, vol. 8, no. 5, pp. 597–619, Oct. 2012.
4. N. A. Collop and W. M. Anderson, "Clinical Guidelines for the Use of Unattended Portable Monitors in the Diagnosis of Obstructive Sleep Apnea in Adult Patients," *Jcsm*, vol. 3, no. 7, 2007.
5. C. Iber, S. Ancoli-Israel, A. L. Chesson, and S. F. Quan, "Manual for the Scoring of Sleep and Associated Events, 1st ed," Westchester, Illinois, 2007.
6. R. Thurnheer, X. Xie, and K. E. Bloch, "Accuracy of nasal cannula pressure recordings for assessment of ventilation during sleep," *Am. J. Respir. Crit. Care Med.*, vol. 164, no. 10, pp. 1914–1919, 2001.
7. P. Dehkordi, M. Marzencki, K. Tavakolian, M. Kaminska, and B. Kaminska, "Monitoring torso acceleration for estimating the respiratory flow and efforts for sleep apnea detection," in *2012 Annual International Conference of the IEEE Engineering in Medicine and Biology Society*, 2012, pp. 6345–6348.
8. D. Kogan, A. Jain, S. Kimbro, G. Gutierrez, and V. Jain, "Respiratory Inductance Plethysmography Improved Diagnostic Sensitivity and Specificity of Obstructive Sleep Apnea," *Respir. Care*, vol. 61, no. 8, pp. 1033–1037, 2016.
9. C. R. Dell'Aquila, L. S. Correa, R. Correa, G. E. Cañadas, and E. Laciar, "New insights into the scoring of respiratory events based on alternative sensors: A comparative effectiveness study," in *VII Latin American Congress on Biomedical Engineering CLAIB 2016, Bucaramanga, Santander, Colombia, October 26th–28th, 2016*, I. Torres, J. Bustamante, and D. A. Sierra, Eds. Singapore: Springer Singapore, 2017, pp. 605–608.
10. Physionet, "St. Vincent's University Hospital/University College Dublin Sleep ApneaDatabase," 2008. [Online]. Available: St. Vincent's University Hospital/University College Dublin Sleep ApneaDatabase.
11. S. J. Redmond and C. Heneghan, "Cardiorespiratory-based sleep staging in subjects with obstructive sleep apnea," *IEEE Trans. Biomed. Eng.*, vol. 53, no. 3, pp. 485–496, 2006.

Electrical Right and Left Cardiac Atrioventricular and Left Atrial Delay in Cardiac Resynchronization Therapy Responder and Non-responder with Sinus Rhythm

Matthias Heinke, Gudrun Dannberg, Tobias Heinke, and Helmut Kühnert

Abstract

Cardiac resynchronization therapy (CRT) with hemodynamic optimized biventricular pacing is an established therapy for heart failure patients with sinus rhythm, reduced left ventricular ejection fraction and wide QRS complex. The aim of the study was to evaluate electrical right and left cardiac atrioventricular delay and left atrial delay in CRT responder and non-responder with sinus rhythm. **Methods**: Heart failure patients with New York Heart Association class 3.0 ± 0.3, sinus rhythm and $27.7 \pm 6.1\%$ left ventricular ejection fraction were measured by surface ECG and transesophageal bipolar left atrial and left ventricular ECG before implantation of CRT devices. Electrical right cardiac atrioventricular delay was measured between onset of P wave and onset of QRS complex in the surface ECG, left cardiac atrioventricular delay between onset of left atrial signal and onset of left ventricular signal in the transesophageal ECG and left atrial delay between onset and offset of left atrial signal in the transesophageal ECG. **Results**: Electrical atrioventricular and left atrial delay were 196.9 ± 38.7 ms right and 194.5 ± 44.9 ms left cardiac atrioventricular delay, and 47.7 ± 13.9 ms left atrial delay. There were positive correlation between right and left cardiac atrioventricular delay ($r = 0.803$ $P < 0.001$) and negative correlation between left atrial delay and left ventricular ejection fraction ($r = -0.694$ $P = 0.026$) with 67% CRT responder. **Conclusions**: Transesophageal electrical left cardiac atrioventricular delay and left atrial delay may be useful preoperative atrial desynchronization parameters to improve CRT optimization.

1 Introduction

Cardiac resynchronization therapy (CRT) with hemodynamic optimized atrial sensed biventricular pacing is an established therapy for heart failure patients with sinus rhythm, reduced left ventricular ejection fraction and wide QRS complex with electrical interventricular desynchronization, but many CRT patients are clinically CRT non-responders or CRT low-responders [1–3]. Sinner and Co-workers found in up to 50% of the CRT patients with empiric CRT parameters echocardiographic optimal atrioventricular delay [4].

Transesophageal focused electrocardiography allows heart rhythm analysis with local left atrial signals and left ventricular signals [5]. The aim of the study was to evaluate electrical right and left cardiac atrioventricular delay and left atrial delay in CRT responder, CRT low-responder and CRT non-responder with sinus rhythm.

2 Methods

Fifteen heart failure patients with sinus rhythm, New York Heart Association class 3.0 ± 0.3, $27.7 \pm 6.1\%$ left ventricular ejection fraction, 160.1 ± 27.2 ms QRS duration and 196.9 ± 38.7 ms right cardiac atrioventricular delay were measured by surface ECG and transesophageal bipolar

M. Heinke (✉)

Department of Electrical Engineering and Information Technology, Biomedical Engineering of University of Applied Sciences Offenburg, Badstrasse 24, 77652 Offenburg, Germany
e-mail: matthias.heinke@hs-offenburg.de

G. Dannberg · H. Kühnert
Department of Internal Medicine I, University of Jena, Am Klinikum 1, 07747 Jena, Germany

T. Heinke
Siemens Healthcare GmbH, Röntgenstrasse 2, 07407 Rudolstadt, Germany
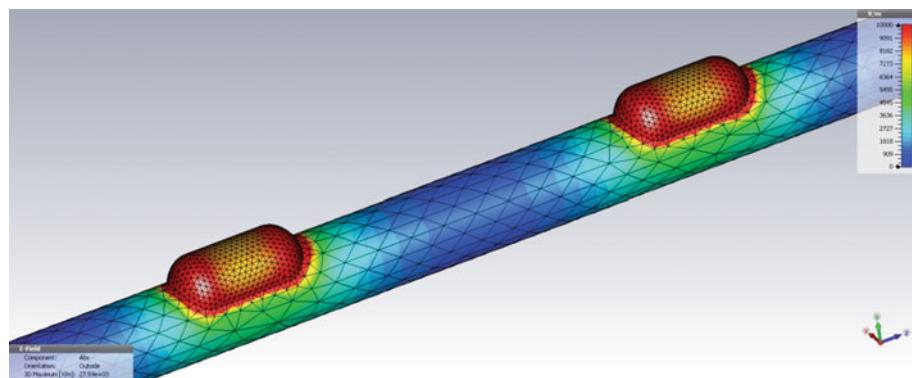
Fig. 1 Simulation of transesophageal bipolar hemispherical electrodes and bipolar electrical pacing field for transesophageal bipolar left atrial pacing and bipolar left atrial electrocardiography, V/m—electrical pacing field, E-Field—electrical field

left atrial and left ventricular ECG with hemispherical electrodes before implantation of CRT devices (see Fig. 1).

Electrical right atrioventricular delay was measured between onset of P wave and onset of QRS complex in the surface ECG. Electrical left cardiac atrioventricular delay was analysed between onset of left atrial signal and onset of left ventricular signal in the transesophageal ECG. Electrical left atrial delay was measured between onset and offset of left atrial signal in the transesophageal ECG.

Statistical analysis was performed by Origin® 2017 software (OriginLab Corporation, Northampon, MA, USA) with a statistical significance of p < 0.05 and with Pearson correlation coefficients. Electromagnetic simulation was

performed with CST STUDIO SUITE® (CST—Computer Simulation Technology, Darmstadt).

3 Results

Electrical atrioventricular and left atrial delay in fifteen CRT patients were 196.9 ± 38.7 ms right and 194.5 ± 44.9 ms left cardiac atrioventricular delay, and 47.7 ± 13.9 ms left atrial delay. There were positive correlation between right and left cardiac atrioventricular delay (r = 0.803 P < 0.001) (see Fig. 2), negative correlation between left atrial delay and left ventricular ejection fraction (r = −0.694 P = 0.026).
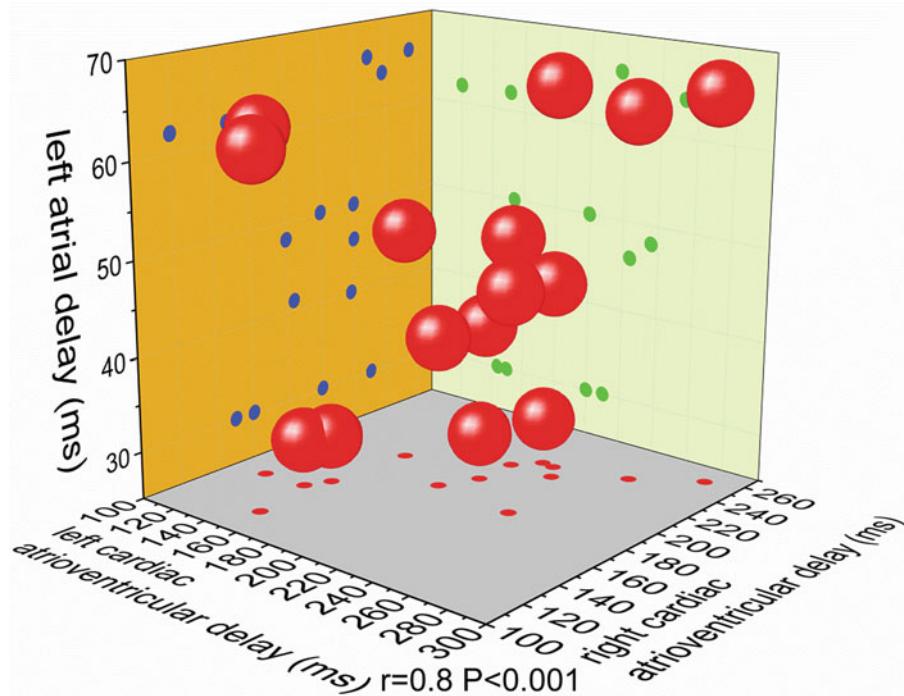
Fig. 2 Electrical left atrial delay, right cardiac atrioventricular delay and left cardiac atrioventricular delay in cardiac resynchronization therapy patients with sinus rhythm, r, P—Pearson correlation coefficients
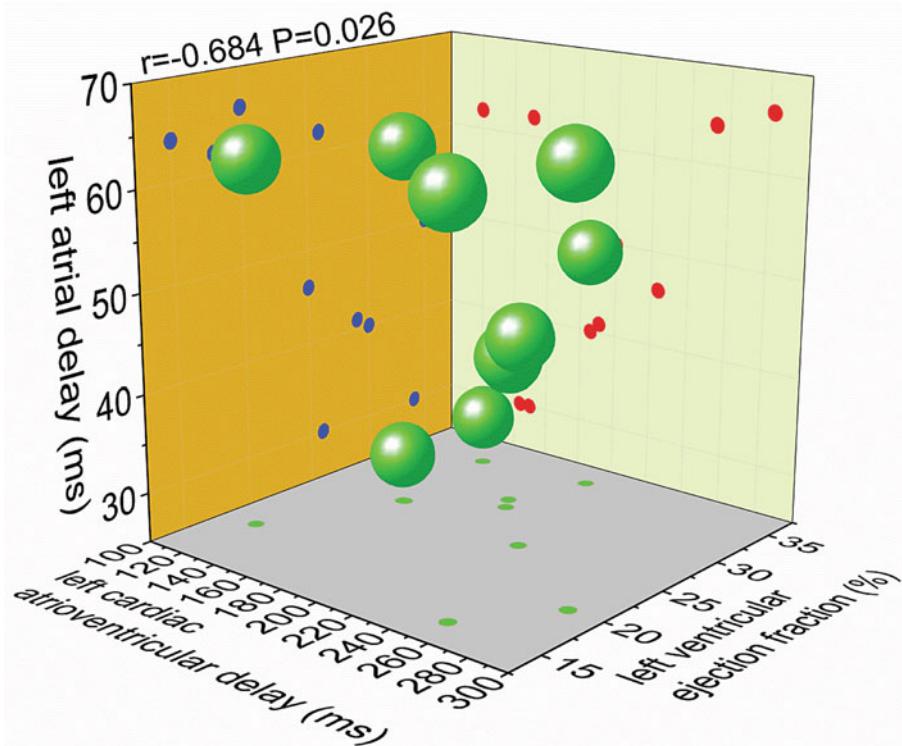
Fig. 3 Electrical left atrial delay, left cardiac atrioventricular delay and left ventricular ejection fraction in cardiac resynchronization therapy responder with sinus rhythm, r, P—Pearson correlation coefficients

Electrical atrioventricular and left atrial delay in ten CRT responders were 191.4 ± 45.0 ms right and 190.1 ± 51.5 ms left cardiac atrioventricular delay, and 49.1 ± 13.9 ms left atrial delay. Left ventricular ejection fraction was $25.8 \pm 6.6\%$ in CRT responder. There were positive correlation between right and left cardiac atrioventricular delay $(r = 0.904 \ P < 0.001)$, and negative correlation between left atrial delay and left ventricular ejection fraction $(r = -0.693 \ P = 0.026)$ (see Fig. 3). During 6.3 ± 2.8 month CRT responder follow-up, the New York Heart Association class improved from 3.1 ± 0.3 to 2.0 ± 0.2.

Electrical atrioventricular and left atrial delay in two CRT non-responder and three CRT low-responder were 207.8 ± 21.4 ms right and 214.6 ± 13.4 ms left cardiac atrioventricular delay and 44.8 ± 15.2 ms left atrial delay. Left ventricular ejection fraction was $31.6 \pm 1.8\%$ in CRT non-responders and low-responder. During 5.0 ± 4.7 month CRT non-responder follow-up, the New York Heart Association class not improved from class 3 to class 3. During 9.3 ± 1.5 month CRT low-responder follow-up, the New York Heart Association class improved only from 2.8 ± 0.3 to 2.3 ± 0.5.

4 Discussion

CRT non-response and the electrical cardiac conduction delays in CRT responder and non-responder are unsolved problems in CRT. Engels and Co-worker evaluated the optimal and individual CRT atrioventricular delay with electrocardiograms from CRT pacing electrodes and found an optimal atrial sensed biventricular pacing delay for left ventricular fusion pacing [6]. Lee and Co-workers evaluated significant hemodynamic differences of 49 endocardial left ventricular pacing sites, atrioventricular and interventricular delays in CRT patients with differences between postimplant pacing and 6 months CRT [7].

We evaluated transesophageal electrical cardiac conduction delays and left ventricular ejection fraction in CRT and found a positive correlation between right and left cardiac atrioventricular delay and negative correlation between left atrial delay and left ventricular ejection fraction in CRT responders. Left ventricular ejection fraction was lower in CRT responder than in CRT non-responder and CRT low-responder. Electrical right and left atrioventricular delay were longer in CRT non-responder and CRT low-responder than in CRT responder.

Transesophageal electrical left cardiac atrioventricular delay and left atrial delay may be useful preoperative atrial conduction delay parameters to improve CRT optimization with optimal atrial sensed biventricular pacing or left ventricular fusion pacing.

Author's Statement Authors state no conflict of interest. The research related to human use has been complied with all the relevant national regulations, institutional policies and in accordance the tenets of the Helsinki Declaration, and has been approved by the authors' institutional review board or equivalent committee.

References

1. Steinberg, B.A., Wehrenberg, S., Jackson, K.P., Hayes, D.L., Varma, N., Powell, B.D., Day, J.D., Frazier-Mills, C.G., Stein, K. M., Jones, P.W., Piccini, J.P.: Atrioventricular and ventricular-to-ventricular programming in patients with cardiac resynchronization therapy: results from ALTITUDE. J Interv Card Electrophysiol. 44(3), 279–87 (2015).

2. Gold, M.R., Birgersdotter-Green, U., Singh, J.P., Ellenbogen, K.A., Yu, Y., Meyer, T.E., Seth, M., Tchou, P.J.: The relationship between ventricular electrical delay and left ventricular remodeling with cardiac resynchronization therapy. European Heart Journal 32, 2516–2524 (2011).

3. Heinke, M., Kühnert, H., Heinke, T., Tumampos, J., Dannberg, G.: Left cardiac atrioventricular delay and interventricular delay in cardiac resynchronization therapy responder and non-responder. Current Directions in Biomedical Engineering. 2(1): 247–250 (2016).

4. Sinner GJ1, Gupta VA2, Seratnahaei A2, Charnigo RJ3, Darrat YH2, Elayi SC2, Leung SW2, Sorrell VL: Atrioventricular dyssynchrony from empiric device settings is common in cardiac resynchronization therapy and adversely impacts left ventricular morphology and function. Echocardiography, 34(4): 496–503 (2017).

5. Heinke, M., Ismer, B., Kühnert, H., Figulla, H.R.: Transesophageal left ventricular electrogramm-recording and temporary pacing to improve patient selection for cardiac resynchronization. Med Biol Eng Comput 49: 851–858 (2011).

6. Engels, E.B., Mafi-Rad, M., Hermans, B.J.M., Aranda, A., van Stipdonk, A.M.W., Rienstra, M., Scheerder, C.O.S., Maass, A.H., Prinzen, F.W., Vernooy, K.: Tailoring device settings in cardiac resynchronization therapy using electrograms from pacing electrodes. Europace https://doi.org/10.1093/europace/eux208. [Epub ahead of print] (2017).

7. Lee, A.W., Crozier, A., Hyde, E.R., Lamata, P., Truong, M., Sohal, M., Jackson, T., Behar, J.M., Claridge, S., Shetty, A., Sammut, E., Plank, G., Rinaldi, C.A., Niederer. S.: Biophysical Modeling to Determine the Optimization of Left Ventricular Pacing Site and AV/VV Delays in the Acute and Chronic Phase of Cardiac Resynchronization Therapy. J Cardiovasc Electrophysiol. 28 (2):208–215. https://doi.org/10.1111/jce.13134. (2017).

Spectral Analysis of Signal Averaging Electrocardiography in Atrial and Ventricular Tachycardia Arrhythmias

Jonas Tumampos and Matthias Heinke

Abstract

Targeting complex fractionated atrial electrocardiograms detected by automated algorithms during ablation of persistent atrial fibrillation has produced conflicting outcomes in previous electrophysiological studies and catheter ablation of atrial fibrillation and ventricular tachycardia. The aim of the investigation was to evaluate atrial and ventricular high frequency fractionated electrical signals with signal averaging technique. **Methods**: Signal averaging electrocardigraphy allows high resolution ECG technique to eliminate interference noise signals in the recorded ECG. The algorithm use automatic ECG trigger function for signal averaged transthoracic, transesophageal and intra-cardiac ECG signals with novel LabVIEW software. **Results**: The analysis in the time domain evaluated fractionated atrial signals at the end of the signal averaged P-wave and fractionated ventricular signals at the end of the QRS complex. We evaluated atrial flutter in the time domain with two-to-one atrioventricular conduction, 212.0 ± 4.1 ms atrial cycle length, 426.0 ± 8.2 ms ventricular cycle length, 58.2 ± 1.8 ms P-wave duration, 119.6 ± 6.4 ms PQ duration, 103.0 ± 2.4 ms QRS duration and 296.4 ± 6.8 ms QT duration. The analysis in the frequency domain evaluated high frequency fractionated atrial signals during the P-wave and high frequency fractionated ventricular signals during QRS complex. **Conclusions**: Spectral analysis of signal averaging electrocardiography with novel LabVIEW software can be utilized to evaluate atrial and ventricular conduction delays in patients with atrial fibrillation and ventricular tachycardia. Complex fractionated atrial and ventricular electrocardiograms may be useful parameters to evaluate electrical cardiac bradycardia and tachycardia signals in atrial fibrillation and ventricular tachycardia ablation.

1 Introduction

Targeting complex fractionated atrial electrocardiograms detected by automated algorithms during ablation of persistent atrial fibrillation has produced conflicting outcomes in previous electrophysiological studies. Transesophageal focused bipolar left atrial and left ventricular ECG can evaluate interatrial delay, left atrial delay, interventricular delay, left ventricular delay and left cardiac atrioventricular delay in patients with heart failure and heart rhythm disturbances [1–3].

The aim of the investigation was to evaluate atrial and ventricular high frequency fractionated electrical signals with signal averaging technique.

2 Methods

Signal averaging electrocardigraphy (ECG) allows high resolution ECG technique to eliminate interference noise signals in the recorded ECG. The algorithm uses automatic ECG trigger function for signal averaged transthoracic, transesophageal and intra-cardiac ECG signals with novel Lab-VIEW software (National Instruments, Austin, Texas, USA).

For spectral analysis we used fast Fourier transformation in combination with spectral-temporal mapping and wavelet transformation for evaluation of detailed information about the frequency and intensity of high frequency atrial and ventricular signals (see Fig. 1). Signals of 60 s were averaged with a sampling rate of 1 kHz.

J. Tumampos · M. Heinke (✉)
Department of Electrical Engineering and Information
Technology, Biomedical Engineering of University of Applied
Sciences Offenburg, Badstrasse 24, 77652 Offenburg, Germany
e-mail: matthias.heinke@hs-offenburg.de

J. Tumampos
e-mail: jonas.tumampos@yahoo.de
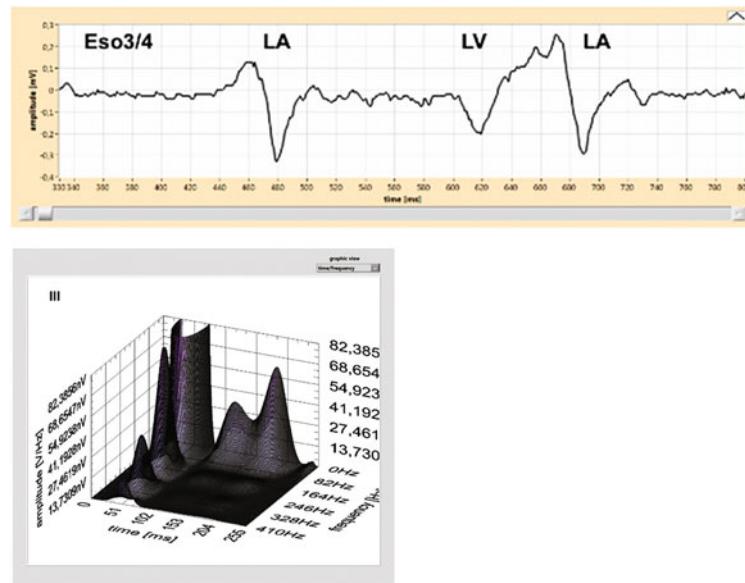
Fig. 1 Transesophageal bipolar left atrial and left ventricular ECG Eso3/4 and spectral-temporal mapping of surface ECG III after signal averaging of 74 heartbeats over a time of 60 s with a sampling rate of 1 kHz. The patient shows atrial flutter with a two-to-one atrioventricular conduction and superposition of atrial and ventricular signals. LA—left atrial signal, LV—left ventricular signal, Eso3/4—transesophageal bipolar ECG, III—surface ECG
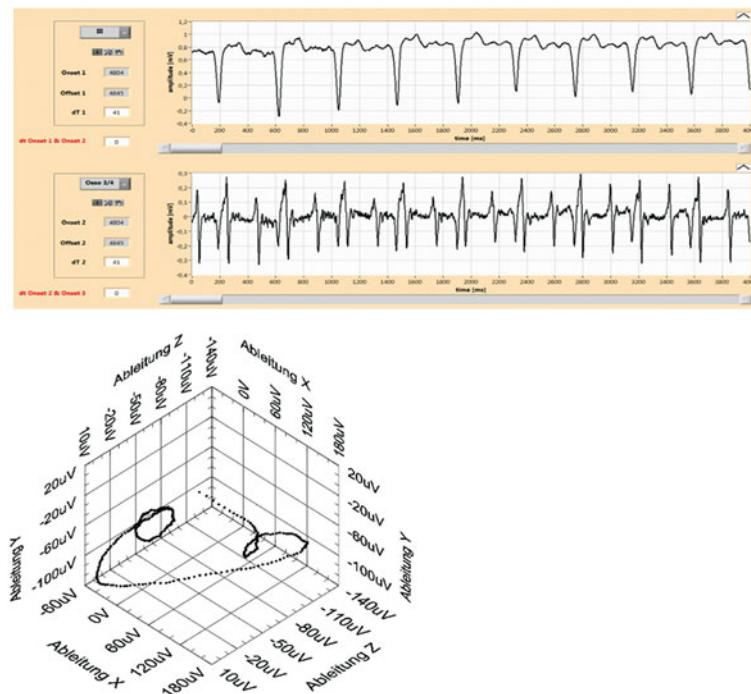
Fig. 2 Atrial flutter with two-to-one atrioventricular conduction, surface ECG III, transesophageal bipolar left atrial and left ventricular ECG Eso3/4, vector loop of the vector ECG and superposition of atrial and ventricular signals. Eso3/4—transesophageal bipolar ECG, III—surface ECG
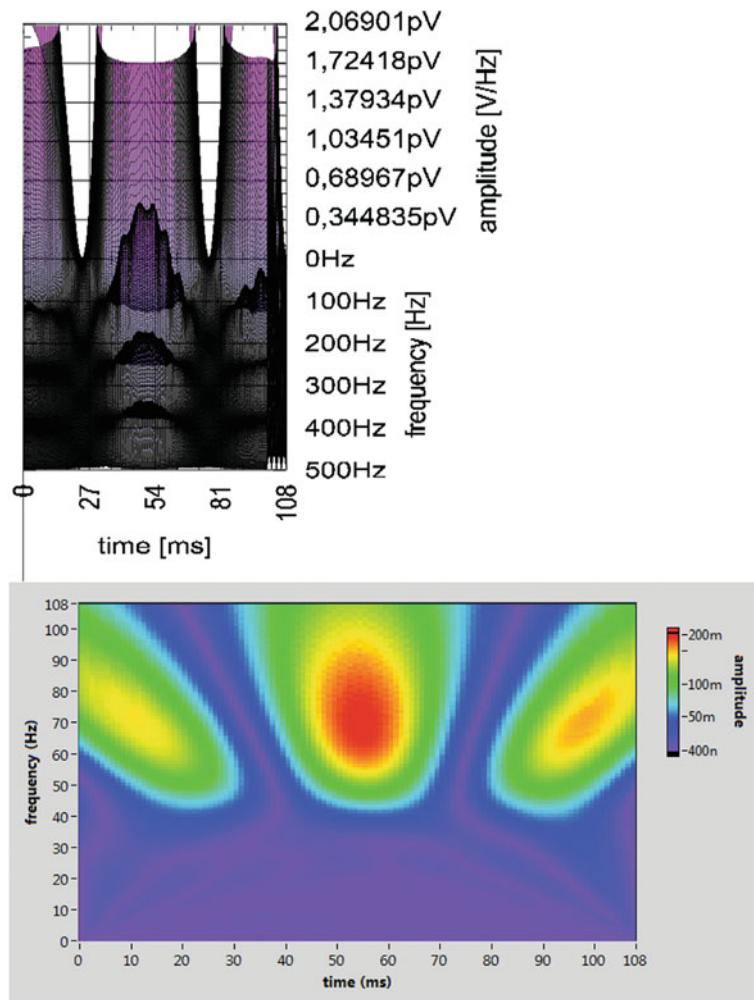
Fig. 3 Spectral analysis of atrial flutter with two-to-one atrioventricular conduction with spectral-temporal mapping and wavelet transformation

3   Results

Spectral-temporal mapping and wavelet transformation of the signal averaged ECG allows the evaluation of high frequency fractionated atrial signals in patients with atrial fibrillation and high frequency ventricular signals in patients with ventricular tachycardia.

3.1   Atrial Tachycardia Arrhythmias

The analysis in the time domain evaluated fractionated atrial signals at the end of the signal averaged P-wave and fractionated ventricular signals at the end of the QRS complex. We evaluated atrial flutter in the time domain with two-to-one atrioventricular conduction, 212.0 ± 4.1 ms atrial cycle length, 426.0 ± 8.2 ms ventricular cycle length,

$58.2 \pm 1,8$ ms P-wave duration, 119.6 ± 6.4 ms PQ duration, 103.0 ± 2.4 ms QRS duration, 296.4 ± 6.8 ms QT duration, 42.3 ± 2.7 ms left atrial delay, 9.1 ± 3.6 ms interatrial delay, 61.0 ± 3.8 ms left ventricular delay, 12.4 ± 4.7 ms interventricular delay and 130.2 ± 7.3 ms left cardiac atrioventricular delay (see Fig. 2).

The analysis in the frequency domain evaluated high frequency fractionated atrial signals during the P-wave and high frequency fractionated ventricular signals during QRS complex (see Fig. 3).

3.2   Ventricular Tachycardia Arrhythmias

The combination of analysis in the time and frequency domain allowed the evaluation of fractionated signals during atrial and ventricular conduction, ventricular premature beats (see Fig. 4) and supraventricular premature beats.
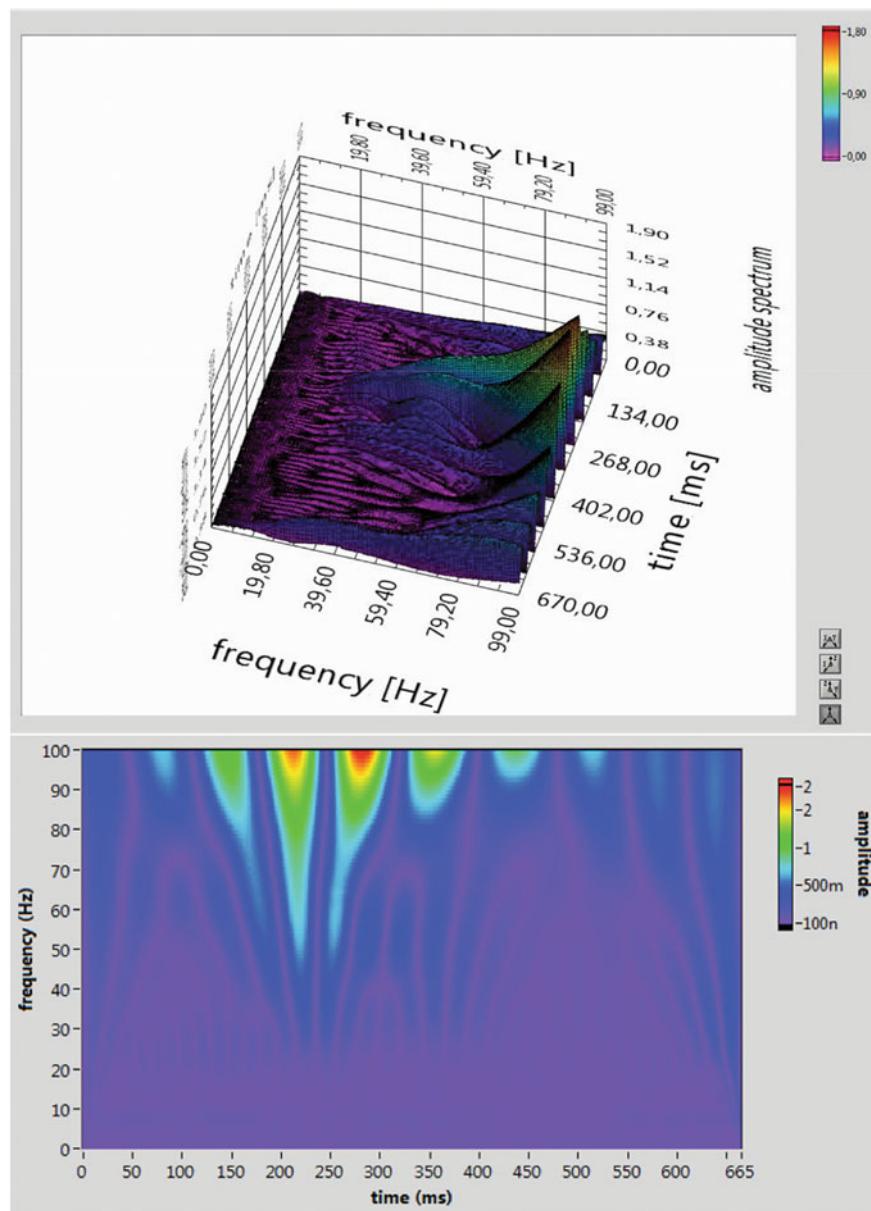
Fig. 4 Spectral analysis of ventricular premature beat with wavelet transformation

4   Discussion

Almeida and co-workers evaluated complex fractionated atrial electrocardiograms (CFAEs) in patients with atrial fibrillation and/or ventricular tachycardia with NavX versus CARTO algorithms and different results of CFAEs detection [4]. Spectral analysis of signal averaging electrocardiography with novel LabVIEW software can be utilized to evaluate atrial and ventricular conduction delays in patients with atrial fibrillation and ventricular tachycardia. Complex fractionated atrial electrocardiograms may be useful parameters to evaluate electrical cardiac bradycardia and tachycardia signals in atrial fibrillation ablation.

Author's Statement   Authors state no conflict of interest. The research related to human use has been complied with all the relevant national regulations, institutional policies and in accordance the tenets of the Helsinki Declaration, and has been approved by the authors' institutional review board or equivalent committee.

References

1. Heinke, M., Ismer. B., Kühnert, H., Figulla, H.R.: Transesophageal left ventricular electrogramm-recording and temporary pacing to improve patient selection for cardiac resynchronization. Med Biol Eng Comput 49: 851–858 (2011).

2. Heinke, M., Surber, R., Kühnert, H., Dannberg, G., Prochnau D., Figulla, H.R.: Transesophageal left ventricular posterior wall potential in heart failure patients with biventricular pacing. Biomed. Techn. 52: 173–179 (2007).

3. Heinke, M., Kühnert, H., Heinke, T., Tumampos, J., Dannberg, G.: Left cardiac atrioventricular delay and interventricular delay in cardiac resynchronization therapy responder and non-responder. Current Directions in Biomedical Engineering. 2(1): 247–250 (2016).

4. Almeida, T.P., Chu, G.S., Salinet, J.L., Vanheusden, F.J., Li, X., Tuan, J.H., Stafford, P.J., Ng, G.A., Schlindwein, F.S.: Minimizing discordances in automated classification of fractionated electrograms in human persistent atrial fibrillation. Med Biol Eng Comput 54:1695–1706 (2016).

A Clinico-Statistical Analysis of Writer's Cramp Signals: Study with Indigenously Developed Multi-channel Intramuscular EMG

Venkateshwarla Rama Raju

Abstract

We investigated the hand muscles of Dystonia Writer's cramp (WC) subjects affected due to DYT1 gene mutations in the brain. In clinical environments WC is done subjectively and lacking the objective. Therefore, the aim of the study is to determine if there is a quantifiable EMG difference in Writer's Cramp (WC) patients with concordant mirror movements (MMs) from those with discordant MMs. For this, the five innocuous intramuscular microelectrodes (100 μ) are passed through five-muscles of intrinsic right-hand (RH). The EMG signals are acquired parallelly from five-muscles using indigenously built multi-channel EMG while subject writing with right-hand (RH), and with intrinsic left-hand. A canonical correlation-analysis between right-hand writing signal (RHWS) and left hand writing signals (LHWS) for each subject was carried out; giving squared canonical correlations. Correlations, for each subject between the signals when inscribing firstly with RH and then with LH are specified. Though, correlations are mostly negligible, albeit, some correlations are quite significant and distinctly high. These are presented as a Table of significant-correlations, i.e., correlations which are greater than 0.50 in absolute-value. It is found that often, the same muscle pairs will have significant correlation with same sign, in both 'hand signals' (i.e., RHWS, LHWS). In our computation, the scatter plot showed first two principal component (PC) scores explaining about 80% of variation. However, these findings are to be cross—validated with clinical findings on the same subjects.

Nomenclature

ECR	Extensor-Carpi-Radialis
ECU	Extensor-Carpi-Ulnaris
FCR	Flexor-Carpi-Radialis
FCU	Flexor-Carpi-Ulnaris
EDC	(ED2)Extensor-Digitorum-Communis-2nd digit fascicle
EPL and EPB	Extensor-Pollicis-Longus and Brevis
EIP	Extensor-Indicis-Proprius
EIL	Extensor-Indicis-Longus
FPL	Flexor-Pollicis-Longus
FPB	Flexor Pollicis Brevis
ADP	Adductor-Pollicis
APB and APL	Abductor-Pollicis-Brevis and Longus

V. Rama Raju (✉)
Department of Computer Science & Engineering, CMR College of Engineering & Technology (UGC Autonomous), Kandlakoya, Medchal Rd, Hyderabad, 501401, India
e-mail: drvrr@cmrcet.org; system@ou.ernet.in; idcoucea@hd1.vsnl.net.in

V. Rama Raju
Jawaharlal Nehru Technological University Hyderabad JNTUH, Hyderabad, India

V. Rama Raju
Biomedical, Neurology & Neurosurgery, Nizam's Institute of Medical Sciences, Hyderabad, India

V. Rama Raju
Biomedical Engineering Department, Osmania University College of Engineering (Autonomous), Hyderabad, OU, India

1 Introduction

1.1 Electromyography

Electromyography (EMG) is a complex signal arising during muscle contraction. Its characteristics are affected by many factors including diseases, such as Limb girdle dystrophy, repetitive strain injury syndrome, Writer's cramp's, Musicians Cramp, etc. [1, 2]. The EMG signal looks very noisy with complex interference patterns (immersed) but indeed is highly structured. In neurology, EMG is performed for nerve

conduction studies and muscle testing. It is a electro-neuro medical diagnostic technique applied to muscle systems and peripheral nerves in particular to nerve injuries and muscle damages. However, the search for advancing its machinery is on for the past two and quarter centuries which were first discovered by Luigi Galvin a way back in 1791.

Recent studies have demonstrated the potential of providing multichannel recordings of intramuscular EMG Writer's cramp [1–5]. Intramuscular microrecording has the ability to record from deep muscles without cross talk. Such approaches have included conventional EMG methods [6, 7] and multivariate statistical multiscaling methods for multi-dimensionality [1–10]. Remarkably, intramuscular EMG obtained from Implantable myoelectric Sensors (IMES) in the flexor aspect of forearm were used simultaneously to control dexterous hand muscles. In this study, we performed multivariate statistical signal processing techniques. Five electrodes are implanted into the right-hand (RH) and subject instructed to inscribe with left-hand (LH) this has mainly to see the mirror objects (mirror movements) of right hand while writing with LH.

1.2 Writer's Cramp

Writer's cramp (WC) is a task-specific commonest focal dystonia of the hand was explained 200 years prior to primary torsion-dystonia [11]. It is a disorder caused by muscle spasms of the flexor aspect of forearms occurring during performing fine motor tasks, such as writing and playing instrumental music (WC, Musician's cramp, etc.) [12]. It is also referred to as scrivener's palsy and mogigraphia.

1.3 Dystonia

Dystonia is a disorder causing variable muscle tone and frequent dexterous hand muscle quiver [11], defined as a neurological syndrome characterized by involuntary, continued, patterned, and frequently repetitive muscle contractions of differing muscles, causing caricature movements or irregular postures [12].

1.4 EMG in Writer's Cramp

Typically, EMG is used for guiding botulinum-toxin (BonNT/Botox) injections into muscles once muscle selection is over. Use of custom-built EMG in selecting muscles for injecting Botox is useful, but is limited by the fact that limited causal EMG sampling may yield limited unrepresentative information. Further EMG findings may be confounded by compensatory movements and local discomfort caused by EMG wires. Therefore, to overcome these issues, microelectrodes are implanted into multiple muscles which can record the EMG during the activation of the dystonia and can provide substantial information on the involvement of deeper or not palpable-muscles. With the, advent of sophisticated imaging signal modalities the organic nature of writer's-cramp is no more in doubt.

1.5 Clinical Features

Occasional subjects may report a history of trauma or strain to the affected limb. Most subjects initially complain of feelings of tension in the fingers or forearms that interfere with the fluency of writing; a minority may also experience pain. Then the pen is held forcefully with anomalous excessive contraction (dystonia) of the hand and/or forearm muscles, causing different patterns of deviation from the normal or premorbid pen grip and hand-posture, Writing may begin normally with dystonic posturing occurring after drawing few spirals, a few alphabets or words; In some subject develops dystonia of hand even before commencement of writing, as soon as they reach up to pick the pen. A common pattern of writer's cramp involves excessive flexion of the thumb and index finger, with pronation of the hand and ulnar deviation of the wrist.

2 Methods

A set of five miniature sterilized microelectrodes (100 μ, from California Fine Wire Company, USA), were used in each subject. Each subject with Writer's cramp was seated comfortably in a specially designed revolving chair for sitting and writing. The electrode sites were found by palpating the muscle during a voluntary contraction and electrodes were inserted into specific-target muscles on identification of the traces on Oscilloscope and neurologist opinion. The skin was always cleaned thoroughly with spirit before the electrode placement. The placements were tested for accuracy, 'cross-talk', bad connections, etc. by requesting the subject to perform several test movements (i.e., putting the particular muscle into action) and test writing (Figs. 1 and 2).
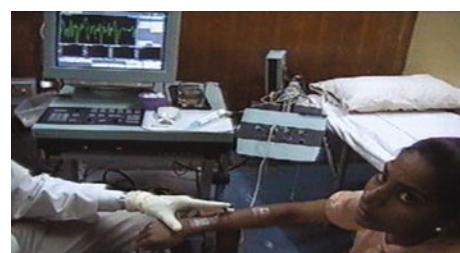
Fig. 1 Insertion of fine wire electrode in extensor carpi radialis (ECR)
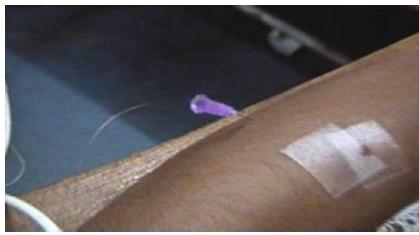
Fig. 2 Checking accuracy of the fine wire electrode placement by active muscle contraction

Fig. 3 Subject writing after insertion of micro wire electrodes with indigenous EMG prototype
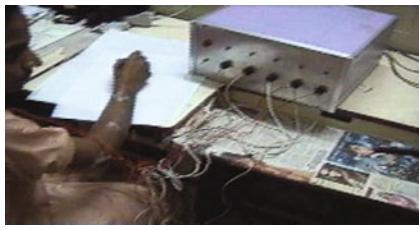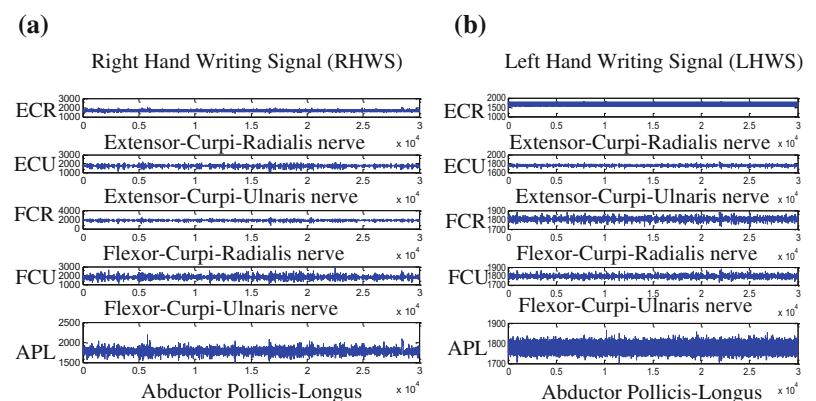
Fig. 4 A close up of writing during signal recording with indigenously developed EMG prototype

Later, the electrodes were connected to our indigenously developed 5 channel 'prototype' machine (Figs. 3 and 4) interfaced to the Pentium-III computer. The amplifiers have an input impedance of >200 MΩ and common mode rejection ratio of 58 dB. Each output channel was filtered to remove motion artifact and high-frequency noise using notch

band pass filters with cut-off frequencies 0.5 Hz (Lower) and 10 kHz (Upper). A sampling frequency 3 kz/channel was used.

As most discordant muscle movements are those of wrist, 4 muscles causing flexion and extension of wrist viz, ECR, ECU, FCR, FCU were analyzed in all patients and one more muscle (as decided by the Neurologist, for example, ADP, APL, etc. which showed the maximum discordance of mirror dystonia) on the right hand was included. EMG signals were simultaneously recorded from all five muscles while the patients inscribed with RHWS and LHWS (Fig. 5a, b).

2.1 Multivariate Techniques

For a given population of size ($N = 12$ *subjects*), the σ^2 (called variance is the average of the squared deviation of each data point from the mean-value) is mathematically expressed and computed as

$$\sigma^2 = \frac{1}{N}\left[\sum_{i=1}^{N}(x_i - \mu)^2\right] \quad (1)$$

where $(\boldsymbol{x_i} - \boldsymbol{\mu})$ is the deviation of each data point from the mean. By squaring the deviations, more weight is placed on points that those points lie away from the mean, further. The $\boldsymbol{\sigma^2}$ is the population parameter and quantifies the dispersion in the entire population of size N. therefore, the variance for a sample is designated by s^2 which can be computed differently

$$s^2 = \frac{1}{n-1}\left[\sum_{i=1}^{n}(x_i - X)^2\right] \quad (2)$$

The covariance was performed. For solving the Eigen vectors, in our computation, we adopted the Jacobi method is a method of solving a tridiagonal matrix equation with largest absolute values in each row and column dominated by the diagonal element. Each diagonal element is solved

Fig. 5 **a** LH muscle signals of patient 1 D group. **b** RH muscle signals of patient 1D group

Table 1 Fifth muscle right hand writing signal (RHWS) > left hand writing signal (>2 times larger)

Group	R > L	L ≥ R	
D	4	0	4
C	3	5	8
	7	5	12

Table 2 Analysis of variance (*anova*) for means

Source	SS/10^5	df	MS/10^5	F-ratio	[a]df of F-ratio	*p*-Value
Patients	0.1978	11	0.0180	1.9270	11.99	0.0466
Muscles	1.5134	9	0.1682	18.0226	9.99	0.0000
Error	0.9237	99	0.0093			
Total	2.6349	119	–	–	–	–

[a]degree of freedom

for, and an approximate value plugged in. The process is then iterated until it converges. The algorithm reviewed from numerical algorithms group (NAG) routines and from the numerical recipes in C/C++ text (Cambridge University press [13]), Bath Information and Data Services (BIDS), University of Bath, UK. Principal component analysis (PCA) requires that the Eigen-values and the covariance matrix be formed. The Eigen-values obtained are unique for the entire set. In fact, it turns out that the Eigen-vector with the highest Eigen-value is the principle component of the data set. The Eigen-vector with the largest Eigen-value is the one that will point down the middle of the data. It is the most significant relationship between the data dimensions.

3 Results and Discussion

In analyzing the standard deviation (SD) of the 5th muscle (selected because of active MM's)—the D group always showed significantly larger SD's with the right hand as compared to the left hand (around 2–10 times larger). The following Table 1 gives the statistical significance.

$\chi^2 \cong 4.2857$ for 1 df, which is significant at 5% with p = 0.0383 significant.

In the C group the right was larger (>2 times) in 3 out of 8 only and in 1 patient the left was greater than right (>5

times). This would be consistent with the hypothesis that larger variances occur in the D group because a larger compensatory force is needed to overcome the dystonic force. In the C group the absence of this difference in a majority would suggest that here the difference between the two is absent or minimal. The 12 patients both LHWS and RHWS means (12 × 10 means) are analyzed, using them as primary data (i.e., ignoring the variations within the signals). The purpose is to see whether, on the whole, patients differ in their averages and whether, across patients muscle averages differ, as compared to inherent variability: The computational results of this analysis, is given in the Table 2.

As expected, there is not much evidence of differences between patient averages but there is highly significant difference in the averages for the 10 muscles of 12 patients. A similar analysis of variance (ANOVA), carried out on the corresponding standard deviations (i.e., on 12 patients LHWS and RHWS (12 × 10) standard deviations, see Table 4) of signal strength is given in Table 3.

Here, we clearly see that there is large variability among the patients while the variations observed in different muscles are not significant. In other words, more useful information [in the sense of throwing light on the 'behavior' of patients with Writer's cramp (WC)] can be expected by a probe into variation patterns (AC-component) of the signals than the mean levels (DC-components). Perhaps a study of

Table 3 Analysis of variance (*anova*) for standard deviation

Source	SS/10^5	df	MS/10^5	F-ratio	[a]df of F-ratio	p-Value
Patients	0.5033	11	0.0458	3.09	11.99	0.0013
Muscles	0.0915	9	0.0102	0.69	9.99	0.2836
Error	1.4649	99	0.0148			
Total	2.0597	119	–	–	–	–

[a]degree of freedom
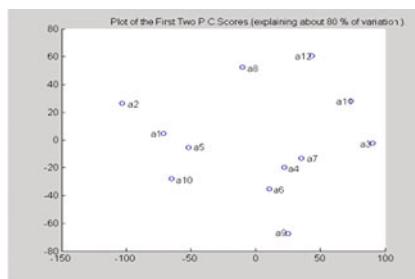
Fig. 6 Scatter plot of the first two P.C. scores (80% of variation)

'normal' peoples' data as a control can clarify the matter. In order to see how far the overall information on the Means and SD's of patients can be summarized by a smaller number of 'scores', singular value decomposition [SVD, essentially equivalent to the principal component analysis (PCA—a latent variate factorial or factor mathematical analysis technique)] was carried out on each of the two matrices, i.e., the means and the standard deviations. Correlation between signals from different muscles in the same hand: The correlations, for each patient, between the signals when writing with the right hand and when writing with the left hand though mostly the correlations are negligible, some correlations are quite significant and markedly high. These are significant correlations (i.e., correlations which are greater than (>) 0.50 in absolute value. A further attempt at clustering the 12 WC subjects by using the principal component (PC) scores of their "differences" in counts of signals was made, with the following results: The total sum of squares is 89,260 while the first two components account for 68,836 = 50,219 + 18,617 i.e., accounts for about 75% ($\sim$80%) of the variation in the data. This pair of coordinates give a good enough summary representation of the information conveyed by the distance matrix. The two (centered) principal component scores for the 12 subjects are given in the Table 4.

A scatter plot of these scores is shown in the Fig. 6. Their distances are summarized in the Euclidean space, which

subject is nearer to and which are the subjects farthest to each other.

From this plot of the first two PC scores of the 12 subjects, the following conclusions are drawn. The points are well scattered out, without clear pattern except for the case of subjects $\{a_6, a_4, a_7\}$. These three are near enough to one another as compared to the remaining nine subjects. Indeed, these three seem to form a lineal ordered set (and thus forming ellipsoidal curves or resembling clouds in the space) with a_4 coming between a_6 and a_7. It is also suggestive that $\{a_3, a_{11}, a_{12}\}$, $\{a_{10}, a_5\}$ may form two similar lineal ordered sets, though the distances are much larger than in the case of the first set. Subjects $\{a8, a9\}$ are isolated and are very farthest to each other and thus explaining circa $\sim$80% variance.

4 Conclusions

Our study showed significant quantifiable EMG-differences in the signals seen while writing with the right and left-hands between those WC's patients with C group versus those with D group. The canonical-variates defined for 2 sets-of-variates observed on the same "individuals" are pairs of linear-combinations of the two-sets, which are maximally correlated with each other, but uncorrelated with other such sets. In the present case one can construct a combination of RH and LH signals, which have a maximum possible correlation. If the correlation is high-enough, it would mean that two-signal-sets are somehow interrelated possibly the same causal-mechanism being responsible for the signal-patterns in the right and left-hand-signals. Otherwise, the two sets of signals appear to be independent of each other on the whole. The data analyses made in this direction showed some significant findings which led to attempts at more sophisticated analyses multivariate techniques leading to effective data summarization and measures of dissimilarity between patients as reflected in the signals recorded and consequent

Table 4 Principal component scores of 12 subjects

$$
Pa_2 = \begin{pmatrix}
-100.7286 & 4.9914 \\
-135.4948 & 18.6261 \\
58.9665 & 31.6554 \\
-4.4131 & 0.9095 \\
-80.9136 & 1.0355 \\
-12.1537 & -18.3320 \\
7.9185 & 8.2583 \\
-49.9930 & 63.3184 \\
9.2109 & -46.9489 \\
-86.4117 & -27.6721 \\
37.5296 & 55.9556 \\
0.8076 & 82.0194
\end{pmatrix}
$$

possible clustering among them. However, these did not lead to any meaningful clinical conclusions. These analyses could possibly be applied to longitudinal follow-ups and correlations with a normal control population in future to better comprehend the phenomenon of Writer's cramp.

References

1. V, Rama. Raju.: A Study of Advanced Multi-Channel EMG in Writer's Cramp. MD/PhD Thesis submitted to Nizam's Institute of Medical Sciences, Hyderabad, India, Aug (2009).
2. V. Rama Raju, A Study of Multi-Channel EMG in Writer's Cramp Signals. PhD Thesis submitted to Nizam's Institute of Medical Sciences, Hyderabad, India, Dec (2003).
3. Lauren, H. Smith., Todd, A. Kuiken., Levi, J. Hargrove.: Evaluation of Linear Regression Simultaneous Myoelectric Control Using Intramuscular EMG. IEEE Transactions on Biomedical Engineering, 63 (4), 737–746 (2016).
4. Francesco, Felici., Valentina, Quaresima., Luigi, Fattorini.: Biceps brachii myoelectric and oxygenation changes during static and sinusoidal isometric exercises. Journal of Electromyography and Kinesiology ELSEVIER Publi. 92, e1–e11 (2009).
5. Carlo Codivari, Andrew J. Lees, V. Peter Misra, and Peter Brown.: EMG-EMG Coherence in Writer's Cramp. Journal of Movement Disorders 17(5), 1011–1016 (2002).
6. Pascal, Grosse., M, Edwards., M A J, Tijssen., A, Schrag., Andrew, J. lees., K P, Bhatia., and Peter, Brown.: Patterns of EMG-EMG Coherence in Limb Dystonia. Journal of Movement Disorders 19 (7), 758–769(2004).
7. Carlo, Codivari., Andrew, J. Lees., Peter, v. Misra, and Peter, Brown.: EMG-EMG Coherence in Writer's Cramp, Journal of Movement Disorders 17 (5), 1011–1016 (2002).
8. L, H. Smith.: Real-time simultaneous and proportional myoelectric control using intramuscular EMG. J. Neural Eng 11, 00613 (2014).
9. P, F. Pasquina.: First in man demonstration of fully implantable myoelectric sensors to control an advanced prosthetic wrist and hand in Proc. Myoelectric Controls Symp. Fredericton, NB, Canada, 170–173 (2014).
10. E, N. Kamavuako.: Wrist torque estimation during simultaneous and continuously changing movements: Surface versus untargeted intramuscular EMG. J. Neurophysiol. 109, 2658–2665 (2013).
11. Grundmann, K.: Primary torsion dystonia. Arch Neurol 62, 682–685 (2005).
12. Jancovic J.: A text book movement disorders. 5th Edition 2007.
13. William, H Press, Saul A. Teukolsky, William T. Vetterling, and Brian P. Flannery, Numerical Recipes in C++, Cambridge University Press, 2002.

Classification of Myopotentials of Hand's Motions to Control Applications

Lukas Peter, Filip Maryncak, Antonino Proto, and Martin Cerny

Abstract

Realization of the system for classification of hand's gestures is described in this paper. The first goal was to create hardware that would be able to measure signal of myopotentials for computer analysis without external noise and with right amplification. The second goal was to program an algorithm which could classify specific gestures of hand. Hardware prototype of four measuring channels was created by combination of 2nd order filters and right amount amplification. The user is isolated from the power source using galvanic isolation because of usage of active electrodes. For digitizing the data, the Arduino Nano microcontroller was selected and programmed using defined communication protocol. The computer software is programmed in C# programming language. Signal processing and drawing to user interface is in real time. The one of five possible gestures that user made is chosen using fuzzy logic and designed system of scaling.

Keywords

Electromyography • Fuzzy • Classification of myopotentials • Hands gestures

1 Introduction

Nowadays the wearable technologies are trying to simplify everyday activities of their users or trying to collect data during the day and night. Under the continuous collection of data, you can imagine a smart watch, that measure your hearth rate, count your steps and based on that data evaluates your daily activity. But what you could control applications in your computer or mobile phone just by making a gesture by your hand? This is exactly the subject matter of this paper.

First of all, the genesis of myopotentials must be understood. It is a complex system that includes both neural and muscular system. The theoretical schematic for measuring myopotentials was designed based on this knowledge. The design was then used for creating PCB to measure myopotentials. Also the galvanic isolation between user and power source must be created because of usage of active reference electrode [1].

With fully functional prototype for measuring myopotentials, it could now be possible to create algorithm for gesture classification. The communication protocol was created between Arduino Nano, that used for digitizing the signal and octet stuffing, and computer. That the algorithm for adaptive segmentation was designed. Adaptive segmentation allows to detect differences in both amplitude and frequency in real time for multiple channels. After the right gesture segmentation, the two phase gesture classification is used to determine correct gesture.

2 Hardware Prototype

The first major goal was to create prototype with which it could be possible to measure myopotentials without noise and with right amplification [2].

The myopotentials are measured from four channels. Each channel consists of two electrodes in differential mode, one instrumental amplifier, one high-pass filter, one low-pass filter, one notch filter with adjustable quality and one operational amplifier for final amplification.

L. Peter (✉) · F. Maryncak · A. Proto · M. Cerny
Department of Cyebrnetics and Biomedical Engineering,
VSB-Technical University of Ostrava, Ostrava, 70800, Czech
Republic
e-mail: lukas.peter@vsb.cz

2.1 Power Source

The whole prototype board is powered from Arduino Nano. Therefore the supply voltage is USB 5 V. Because of the symmetrical power supply was needed a simple circuit was designed to create ±2.5 V and virtual ground.

2.2 Galvanic Isolation

The reference electrode is connected to the virtual ground therefore the galvanic isolation must be preset while using the device. It is for safety of the user and also to meet the requirements by IEC 60601-1 [3]. The most convenient way is to isolate the whole USB on its way from computer (power source) to Arduino. The isolator ADuM4160 was used for data lines D+ and D−. Because the ADuM4160 did not provide enough power to supply the rest of the board, the DC-DC converter was used to isolate the power lines. The DC-DC converter provides isolated 1 W power to supply the prototype board and Arduino while the ADuM4160 isolates the data lines.

2.3 The Instrumental Amplifier

The INA126 from Texas Instruments was used as instrumental amplifier. It acts as a differential amplifier and has easily adjustable amplification.

The amplification was set on 9. Effect of polarization of electrodes was appearing with higher value of amplification.

2.4 Filtration

The myopotentials have frequency spectrum between 20 and 500 Hz so filtering the unneeded frequencies is in place. The topology of second order Sallen-Key was used for high-pass filter as well as for the low-pas filter.

The cut-off frequency was calculated thanks to equation.

As mentioned before, the second order Sallen-Key topology was used for low-pass filter as well.

The cut-off frequency was set close to 500 Hz (495 Hz). The difference is caused because of values of electric components [4].

The notch filter for 50 Hz must be used to reduce noise from electrical network and surroundings. Notch filter with very narrow frequency characteristic was used to preserve the most of the precious biological signal. It is a combination of two operational amplifier and twin T connection. It has also adjustable quality (Q) with trimmer.

2.5 End Amplification

The final amplification was used to amplify to signal to get most of the resolution from A/D converter. It was used a classic non-inverting wiring. The amplification was set to $A = 341$. So the total amplification is 350 with combination with instrumental amplifier.

The amplified biological signal goes to Arduino Nano where is converted to digital signal and sent to computer via galvanic isolation [5].

3 Software

The software part consists of communication protocol between Arduino Nano and computer, plotting the measured signal, adaptive segmentation of the gestures, calculating the features and finally two phase classification of the gestures.

3.1 Communication Protocol

The signal is digitized by 10-bit A/D converter which is included in Arduino Nano. The values are continually read from analogue pins, checked for unique values and then put into packet. Three forbidden values are used in packet to determine where packet starts, where packet ends and to mark the octet stuffing (Fig. 1).

The unique values can be only present at designated place in the packet. Based on this knowledge it is possible to determine the start of the packet and the end of the packet when processed in computer. When the COM port is successfully opened, the incoming measured data starts streaming into PC. The octet stuffing is removed in the first place. Then the values are divided into four channel as per
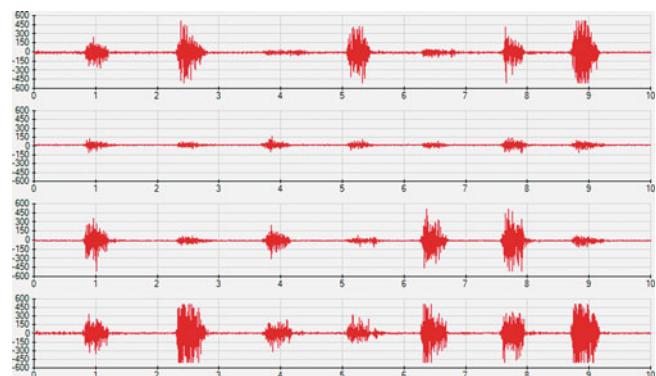
Fig. 1 Plotted signal from four channels of EMG measurement. Myopotencials were measured from four muscles. It can be seen that each movement of the hand activates different muscles
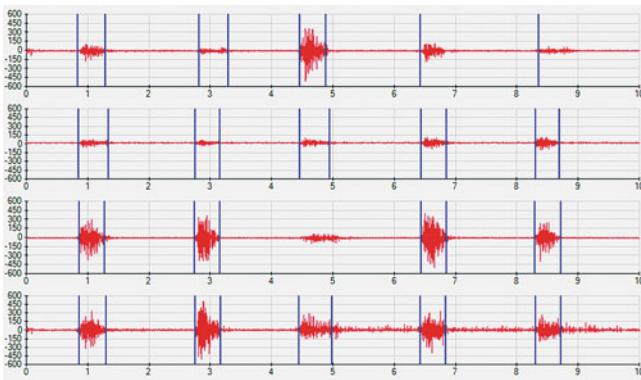
Fig. 2 Plotted segmented signal. For the third gesture there is missing one of evaluated segment in third channel. In this case it is used algorithm based on comparison all of rest segments in same time to evaluate the beginning and the end of missing segment

connection on the prototype board. The measured signal is plotted in real time as shown in Fig. 2.

3.2 Adaptive Segmentation

One of the most crucial part was to know when and where did the gesture occurred in the signal. This was what adaptive segmentation was used for.

Method of adaptive segmentation was dividing the signal into quasi-stationarity segments of variable length, depending on the occurrence of non-stationarities in the signal (diagram of the segmentation of signal can be seen on the Fig. 2). The key factors for choosing the right method of adaptive segmentation were:

- Fast algorithm
- High precision
- Multiple channel segmentation

Based on the key factors, the algorithm using two connected windows and detecting differences of amplitude and frequency was used. Two windows are mowing along the signal in each channel. In each window the differences are computed. Amplitude and frequency difference computing was based on Eq. 1 for Amplitude difference and on Eq. 2.

$$ADIF = \sum_{i=1}^{WL} |x_i| \quad (1)$$

$$FDIF = \sum_{i=1}^{WL} |x_i - x_{i-1}| \quad (2)$$

where WL is window length and it was set to 400 samples. Combining Eqs. 1 and 2 the total difference was calculated:

$$DIF = 1 \cdot |ADIF_1 - ADIF_2| + 7 \cdot |FDIF_1 - FDIF_2| \quad (3)$$

If the difference is higher than the calculated threshold, the segment border is marked on the place of local maximum of the difference.

$$THR = \frac{1}{BL}(1 \cdot |ADIF_1 - ADIF_2| + 7 \cdot |FDIF_1 - FDIF_2|) \quad (4)$$

where BL is size of incoming data or the number of values in current sample.

4 Conclusion

The adaptive segmentation and plotting the graph runs smoothly as well as the classification when it comes to computing memory. It uses only small amount of processor and RAM.

Segment borders are plotted in real time directly on the measures signal. The classification is also done and shown in real time, right after the gesture is done. There is an option to save the raw values in.csv format for further analysis. There is also an option to save just to features from found segments.

Algorithm was tested by counting the successful classification for each gesture. Each gesture was performed 40 times.

The results shown, that the Fist have 100% successful rate of classification. Next most successful gesture is Left with 85% rate. Other gestures are around 60%. This can be caused by too much overlap in fuzzy sets. Over all successful rate 73% is sufficient at this first experimental stage.

This project proved, that gesture classification can be done just by using good algorithm for adaptive segmentation and fuzzy logic based classification. There are some considerable options that can improve further successful rate of classification.

References

1. MERLETTI, Roberto; PARKER, Philip A. (ed.). Electromyography: physiology, engineering, and non-invasive applications. John Wiley & Sons, 2004.
2. CHEN, Xiang, et al. Multiple hand gesture recognition based on surface EMG signal. In: Bioinformatics and Biomedical Engineering, 2007. ICBBE 2007. The 1st International Conference on. IEEE, 2007. p. 506–509.
3. BOYALI, Ali; HASHIMOTO, Naohisa; MATSUMOTO, Osamu. Hand posture and gesture recognition using MYO armband and spectral collaborative representation based classification. In:

Consumer Electronics (GCCE), 2015 IEEE 4th Global Conference on. IEEE, 2015. p. 200–201.

4. PHINYOMARK, Angkoon, et al. The usefulness of mean and median frequencies in electromyography analysis. In: Computational intelligence in electromyography analysis-A perspective on current applications and future challenges. InTech, 2012.

5. TOMCZYSKI, Jakub; KACZMAREK, Piotr; MAKOWSKI, Tomasz. Hand gesture-based interface with multichannel sEMG band enabling unknown gesture discrimination. In: Robot Motion and Control (RoMoCo), 2015 10th International Workshop on. IEEE, 2015. p. 52–57.

Quantitative EEG in Mild Cognitive Impairment and Alzheimer's Disease by AR-Spectral and Multi-scale Entropy Analysis

Xiaoke Chai, Xiaohong Weng, Zhimin Zhang, Yangting Lu, Guitong Liu, and Haijun Niu

Abstract

To assist effective and precise diagnosis for mild cognitive impairment (MCI) and Alzheimer's disease (AD), Electroencephalograph (EEG) has been widely used in clinical research of patients with AD at MCI state. To study the linear and nonlinear abnormality of EEG in AD and MCI patients, multiple characteristics was applied to distinguish AD and MCI patients from the normal controls (NC). EEG signals was recorded from 28 subjects, including 10 AD patients, 8 MCI subjects and 10 healthy elderly people. EEG signals in all channels was computed by auto-regressive model and multi scale entropy (MSE) to obtain relative power spectral density (PSD) value of each frequency band and entropy value in different time scales. Area under Receiver operating characteristic curve (AUC) was used to compare the classification ability of the two method. The ratio Alpha/theta of MCI group in left frontal area can distinguish MCI from NC subjects. Also the long scale entropy value in left frontal-central area manifests a better accuracy in distinguish AD and MCI from NC group. In addition, the combined feature from alpha/theta and long scale entropy in the left frontal central area can discriminate AD from NC group with higher AUC reaching 0.89. This indicated that combined PSD and MSE can be taken as a potential measure to detect AD in early state.

X. Chai (✉) · X. Weng · Z. Zhang · Y. Lu · G. Liu · H. Niu
School of Biological Science and Medical Engineering, Beihang University, Beijing, China
e-mail: chaixiaoke@buaa.edu.cn

H. Niu (✉)
Beijing Advanced Innovation Center for Biomedical Engineering, Beihang University, Beijing, China
e-mail: hjniu@buaa.edu.cn

1 Introduction

Alzheimer's disease is a degenerative diseases of the central nervous increasingly affects the elderly people, causing loss in cognition, memory, even language function [1]. About 10–15% of MCI elderly people each year developed into AD, effective diagnosis and treatment for MCI is very important [2]. The clinical detection of MCI and AD is mainly based on subjective neuropsychological test [3]. The imaging method was used to study the brain structure changes of MCI and AD, but its specificity is not high in the early stage of AD [4]. Also the detection based on biomarkers is invasive [5]. EEG can reflect the physiological activities of the brain, and because of its low-cost, non-invasive and high time resolution, it has been widely used in clinical research of patients with AD at the MCI stage [6].

Quantitative EEG recordings in rest state provide an ideal methodology of the rapid detection in MCI and AD [7]. Babiloni et al. [8] presented the hippocampus volume is related to the loss of alpha rhythms in AD. Moretti et al. [9] found the alpha relative power of MCI in the frontal area was decreased, and power in theta band was increased. Compared with traditional spectrum estimation, the parameter estimation based on AR model performs better, it has been used to calculate PSD of EEG in MCI studies [10].

Although linear analysis is important to quantify the abnormal EEG rhythm of patients with MCI or AD, considering the non-stationarity and randomicity of EEG signal, complexity measures such as entropy were widely used to analysis EEG in AD patients. Abasolo et al. [11] showed the entropy of AD patients in the parietal area is lower than health elderly. Hogan et al. [12] found that the entropy of MCI subjects was reduced. MSE analysis base on entropy

can measure the probability of producing new information for sequences under different scales size, it has been used in cognitive neuroscience. Mizuno et al. [13] found large scale entropy of AD patients in whole brain areas was higher than healthy elderly. Previous studies suggested the complexity changing of EEG signals related to cognitive impairment may be inconsistent in different time scales.

In this work to further quantify both linear and nonlinear comprehensive abnormality of EEG in MCI and AD patients, the PSD and MSE method was adopted to analysis the MCI, AD and normal elderly. Then we compared the accuracy of PSD value, MSE value and combined index in distinguishing AD and MCI from healthy elderly.

2 Subject and Experiment

2.1 Participants

Ten hospitalized AD patients from the department of neurology, JiangBin Hospital in NanNing, GuangXi province (China), and 18 volunteers over 60 years old were recruited. All subjects were right-handness, after clinical evaluation and neurological examinations, eight subjects whose MMSE score were ranged from 24 to 27 composed to be MCI group, other subjects composed to be NC group. Table 1 gives the information of subjects. '*' means difference of MMSE in three groups was significant. The difference in age, gender and education level are not significant.

2.2 EEG Recording

The data collected by the NicoletOne EEG acquisition instrument with 16 channels, sampling rate is 250 Hz. During the experiment the electrode impedance was kept under in 5 KΩ, acquisition channel concludes Fp1, Fp2, F3, F4, C3, C4, P3, P4, O1, O2, F7, F8, T3, T4, T5, T6. Five minutes EEG signal was collected in rest state with eyes closed. Five segment of 5 s which has no obvious interference in all channels was selected for subsequent processing. EEG signal was preprocessed by 0.05–40 Hz band pass filter, all data was processed in MATLAB (R2012a).

3 Method

3.1 Power Spectrum Density (PSD)

PSD analysis for each segment is estimated using AR Burg method, which is one of the most frequently used parametric method. AR model is based on modeling the data sequence as the output of a causal and discrete filter whose input is white noise. Thus the AR model of order p is expressed by the difference equation. AR parameters was estimated by the Burg algorithm, and the optimal order of AR model was estimated by the final prediction error criterion (FPE). The PSD in each frequency band was normalized to obtain the relative PSD, where the sub-band was selected as delta band in 0.5–4 Hz, theta band in 4–8 Hz, alpha band in 8–13 Hz and beta band in 13–30 Hz. And alpha/theta which shows the ratio of PSD in alpha band versus theta band was computed.

3.2 Multi-scale Entropy (MSE)

MSE is a method which measure the complexity of a finite length time series to quantify the probability of generating new information on different time scales. MSE method based on sample entropy of different scales was calculated as the following steps [13]: Firstly, for EEG time series X, construct a coarse-grained time series Y according to a scale factor, the length of reconstruction time series is M, in this work set m = 2 to get the new time series Y_m. Secondly, quantify the sample entropy of each coarse-grained time series, the distance between each Y_m was computed. Set a threshold, r = 0.25, the number of the distance less than r was calculated as B, then obtain the average ratio of this number to the total number of vectors. Lastly, for the next number of dimensions m + 1, repeat the above steps to obtain the sample entropy of each scale from 1 to 20.

3.3 Statistical Analysis

Comparison between groups (NC and MCI, MCI and AD, NC and AD) was made using the independent samples

Table 1 Information of subjects

Heading level	NC (N = 10)	MCI (N = 8)	AD (N = 10)	ANOVA P
Sex (female/male)	6/4	4/4	4/6	0.38
Age (years)	74.4 ± 9.6	79.1 ± 8.7	80.6 ± 6.7	0.25
Education (years)	8.5 ± 2.1	8.5 ± 1.4	8.0 ± 0.1	0.69
MMSE	28.9 ± 1.2	24.6 ± 0.7	16.9 ± 1.5	0.00*

T-test. ROC curves was used to estimate the discriminating ability of PSD and MSE. Area under curve (AUC) of ROC near the upper left corner indicate diagnostic capabilities. Statistical procedures was performed using SPSS 19.0.

4 Results

4.1 MSE in Different Scales

The sample entropy value on 1–20 scales in each channel of AD, MCI and NC group was shown in "Fig. 1". For each scale we compared the difference between AD and NC group. The red box indicated that within this range of scales, differences was statistically significant between AD and NC group. The long scale entropy of AD group was greater than MCI group, and the value of MCI group was greater than NC group, especially for scales more than 12, there was significant differences in each channel of the left side brain areas.

The average entropy from 13 to 20 were computed as the long scale entropy value. "Figure 2" shows the long scale entropy in left frontal, left occipital, left parietal occipital, left temporal, right frontal, right occipital, right occipital area and right temporal areas, differences between AD and NC group were analyzed by t test. The long scale entropy value of AD group was greater than MCI group, and the value of MCI was greater than NC group. Especially the difference between AD

and NC group in the left frontal, left frontal-central and left parietal-occipital areas was significant.

4.2 PSD in Different Band

The average PSD value of different frequency band in each channel of the three group was shown Table 2, '*' means difference between AD and NC group was significant, and '+' means difference between AD and MCI group was significant.

For Alpha/Theta, difference between groups on left and right side of four brain areas were also analyzed by t test. As shown in "Fig. 3", the line means $p < 0.05$, the difference was significant. There was significant difference of the alpha/theta value in left frontal, left temporal, right temporal and right parietal occipital areas. There was significant difference of the alpha/theta value in left frontal area of MCI and NC group. And there was significant difference of the alpha/theta value in right parietal occipital area of MCI and AD group.

4.3 ROC Analysis

AUC was used to assess the ability of index in discriminating AD and MCI from NC group, the AUC of alpha/theta and long scale entropy in eight areas was computed, as Table 3 shows, '*' means AUC is more than 0.7. The results
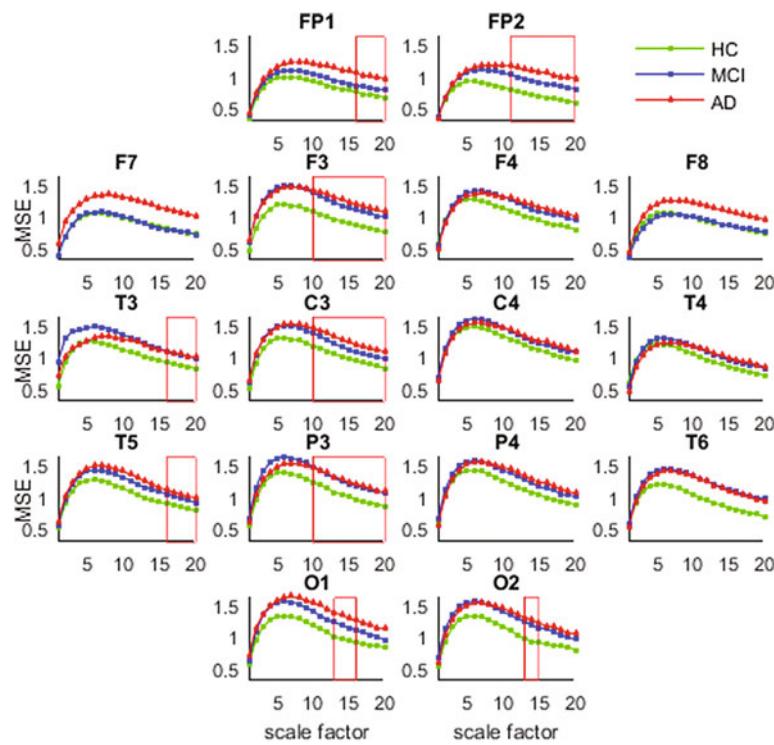
Fig. 1 MSE in different scales of different channel
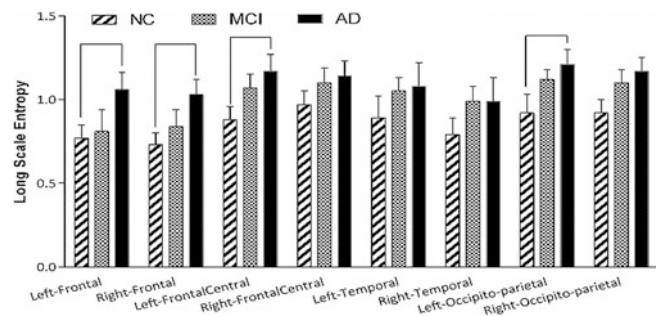
Fig. 2 Alpha/theta in different areas

Table 2 PSD index of different frequency band

	β	α	θ	δ	(β + α)/(θ + δ)	α/θ
NC	0.18 ± 0.03	0.41 ± 0.05	0.24 ± 0.02	0.16 ± 0.04	0.72 ± 0.34	2.91 ± 0.33
MCI	0.15 ± 0.02*	0.40 ± 0.06	0.28 ± 0.02*	0.16 ± 0.05	0.60 ± 0.33*	2.13 ± 0.31*
AD	0.12 ± 0.01*,+	0.33 ± 0.05*,+	0.37 ± 0.02*,+	0.19 ± 0.06*,+	0.28 ± 0.16*,+	0.95 ± 0.12*,+
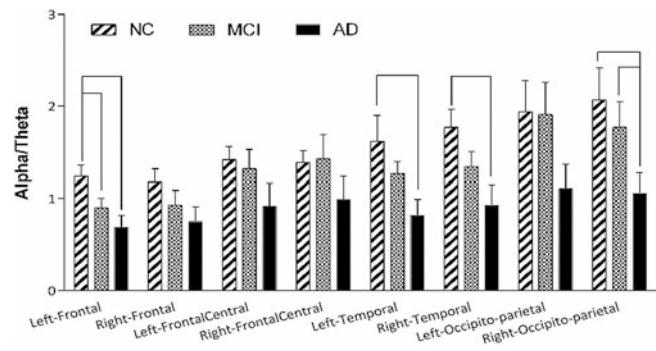
Fig. 3 Long-scale entropy in different areas

Table 3 AUC of alpha/theta and long scale entropy

Brain areas	AUC of alpha/theta		AUC of long scale entropy	
	AD and NC	MCI and NC	AD and NC	MCI and NC
L-Frontal	0.61	0.76*	0.77*	0.55
R-Frontal	0.68	0.56	0.80	0.54
L-FrontalCentral	0.75*	0.48	0.81*	0.73*
R-FrontalCentral	0.59	0.58	0.68	0.61
L-Temporal	0.56	0.69	0.65	0.58
R-Temporal	0.65	0.58	0.63	0.65
L Occipitoparietal	0.86*	0.55	0.74*	0.69
R Occipitoparietal	0.79*	0.74*	0.67	0.69

indicated that the two indexes in left frontal-central and occipito-parietal areas has certain accuracy in discriminating AD from NC group. AUC of linear and nonlinear index in the Left Frontal-Central area was all more than 0.7, with 0.75 and 0.81. We further combined those two value in left frontal-central area to distinguish AD from NC group, the AUC of combined index reached 0.89, which is higher than AUC from any single feature.

5 Discussion

In this study, linear and non-linear method, PSD and MSE analysis was employed to distinguish MCI and AD patients from normal elderly. Cognitive impairment is related to the spontaneous EEG activity rhythm, the abnormality of all the PSD index in MCI and AD patient was consistent with the

prior studies. The significant declined power of alpha band in AD patients was indicated, and these values of MCI subjects also has a downward trend compared with normal elderly. The alpha/theta ratio in left frontal and right occipito-parietal areas can be a typical feature of cognitive decline, which discriminated MCI from normal elderly significantly.

For MSE analysis, we determined the appropriate range of scale to obtain long scale entropy value, the complexity abnormality of MCI patients was consistent with prior studies. The long scale entropy in left frontal-central and ccipito-parietal areas provided better classification performance between AD patient and normal elderly. And in left frontal-central area it also provided good classification performance between the MCI and NC. This manifests EEG abnormality in dominant side brain areas of AD patients is more notable. The complexity of EEG from MSE analysis can provide more information which may benefit our understanding of cognitive impairment.

Since the brain is a complex system showing both linear and nonlinear features, combining PSD and MSE which can reflect the rhythmicity as well as complexity, to obtain effective multiple quantitative EEG index in rest state, can be taken as a potential measure in early screen of AD.

Conflict of Interest The authors declare that they have no conflict of interest.

References

1. Oulhaj A, Wilcock G K, Smith A D, et al. Predicting the time of conversion to MCI in the elderly: Role of verbal expression and learning [J]. Neurology, 73(73), 1436–42 (2009).

2. Levey A, Lah J: Mild cognitive impairment: An opportunity to identify patients at high risk for progression to Alzheimer's disease. Clin Ther, 28(7), 991–1001 (2006).

3. Serrao V T, Brucki S M D, Campanholo K R, et al. Performance of a sample of patients with Mild Cognitive Impairment (MCI), Alzheimer's Disease (AD) and healthy elderly on a lexical decision test (LDT) as a measure of pre-morbid intelligence [J]. Dementia E Neuropsychologia, 9(3), 265–269 (2015).

4. Hua X, Leow A D, Parikshak N, et al. Tensor-based morphometry as a neuroimaging biomarker for Alzheimer's disease: an MRI study of 676 AD, MCI, and normal subjects [J]. Neuroimage, 43 (3), 458–469 (2011).

5. Cabral C, Morgado P M, Campos C D, et al. Predicting conversion from MCI to AD with FDG-PET brain images at different prodromal stages [J]. Computers in Biology & Medicine, 58, 101–109 (2015).

6. Poil SS, De HW, Wm V D F, et al. Integrative EEG biomarkers predict progression to Alzheimer's disease at the MCI stage [J]. Frontiers in Aging Neuroscience, 5(2), 99–103 (2013).

7. Jeong J: EEG dynamics in patients with Alzheimer's disease. Clinical neurophysiology, 115(7), 1490–1505 (2004).

8. Babiloni C, Frisoni GB, Pievani M, et al: Hippocampal volume and cortical sources of EEG alpha rhythms in mild cognitive impairment and Alzheimer disease.[J]. NeuroImage, 44(1), 123–135 (2009).

9. Moretti D V, Miniussi C, Frisoni G B, et al. Hippocampal atrophy and EEG markers in subjects with mild cognitive impairment.[J]. Clinical Neurophysiology, 118(12), 2716–29 (2007).

10. Liu X, Zhang C, Ji Z, et al. Multiple characteristics analysis of Alzheimer's electroencephalogram by power spectral density and Lempel-Ziv complexity [J]. Cognitive Neurodynamics, 10(2), 1–13 (2016).

11. Abasolo D, Hornero R, Espino P, et al.: Analysis of regularity in the EEG background activity of Alzheimer's disease patients with Approximate Entropy. Clinical Neurophysiology, 116(8):1826–1834 (2005).

12. Hogan MJ, Kilmartin L, Keane M, et al.: Electrophysiological entropy in younger adults, older controls and older cognitively declined adults. Brain research, 1445, 1–10 (2012).

13. Mizuno T, Takahashi T, Cho RY, et al.: Assessment of EEG dynamical complexity in Alzheimer's disease using multiscale entropy. Clinical Neurophysiology, 121(9), 1438–1446 (2010).

Analysis of Electroencephalographic Dynamic Functional Connectivity in Alzheimer's Disease

Pablo Núñez, Jesús Poza, Carlos Gómez, Saúl J. Ruiz-Gómez, Víctor Rodríguez-González, Miguel Ángel Tola-Arribas, Mónica Cano, and Roberto Hornero

Abstract

The aim of this study was to characterize the dynamic functional connectivity of resting-state electroencephalographic (EEG) activity in Alzheimer's disease (AD). The magnitude squared coherence (*MSCOH*) of 50 patients with dementia due to AD and 28 cognitively healthy controls was computed. *MSCOH* was estimated in epochs of 60 s subdivided in overlapping windows of different lengths (1, 2, 3, 5 and 10 s; 50% overlap). The effect of epoch length was tested on *MSCOH* and it was found that *MSCOH* stabilized at a window length of 3 s. We tested whether the *MSCOH* fluctuations observed reflected actual changes in functional connectivity by means of surrogate data testing, with the standard deviation of *MSCOH* chosen as the test statistic. The results showed that the variability of the measure could be due to dynamic functional connectivity. Furthermore, a significant reduction in the dynamic *MSCOH* connectivity of AD patients compared to controls was found in the delta (0–4 Hz) and beta-1 (13–30 Hz) bands. This indicated that AD patients show lesser variation in neural connectivity during resting state. Finally, a correlation between relative power and standard deviation was found, suggesting that an increase/peak in power spectrum could be a pre-requisite for dynamic functional connectivity in a specific frequency band.

Keywords

Alzheimer's disease • Dynamic functional connectivity
Electroencephalogram • Neural dynamics
Coherence • Relative power

1 Introduction

Alzheimer's disease (AD) neurodegeneration has an effect on the temporally coordinated brain networks, which underlie cognitive functions. These networks become more abnormal with the progression of AD, as alterations in the processing and transmission of information begin to appear [1]. The aberrant brain networks associated to AD can be reflected in the alterations of the synchronization patterns and brain connectivity observed in resting-state electroencephalographic (EEG) recordings [1].

The majority of studies focusing on brain synchronization and connectivity during resting state assume that functional connectivity (FC) remains temporally stationary. However, it is important to take the spontaneous fluctuations of brain activity into account, as it has been suggested that resting-state activity is not stationary [2]. Thus, the quantification of dynamic changes in FC metrics could provide relevant information regarding the stability of brain networks [3].

Most dynamic functional connectivity (dFC) studies in the literature have been performed with functional magnetic resonance imaging (fMRI) recordings [3]. Therefore, the study of dFC on electroencephalographic (EEG) recordings is of great interest. In the specific case of AD, only a small number of studies have addressed the characterization of FC variability patterns [3].

This paper presents a novel methodology, aimed at obtaining a first approximation to the dynamics of FC in AD. Specifically, this study addresses the following research questions: (i) what epoch length is needed to obtain stable connectivity measures?; (ii) can dFC be found in AD

P. Núñez (✉) · J. Poza · C. Gómez · S. J. Ruiz-Gómez · V. Rodríguez-González · R. Hornero
Biomedical Engineering Group, University of Valladolid, Valladolid, Spain
e-mail: pablo.nunez@gib.tel.uva.es

M. Á. Tola-Arribas
Neurology Service, Río Hortega University Hospital, Valladolid, Spain

M. Cano
Clinical Neurophysiology Service, Río Hortega University Hospital, Valladolid, Spain

patients and healthy controls?; (iii) do dFC patterns differ between both groups?

2 Materials

2.1 Subjects

A population of 28 healthy control subjects (C) and 50 patients with AD was analyzed. The subjects were matched by age. Patients were diagnosed according to the criteria of the National Institute on Aging and Alzheimer's Association (NIA-AA) [4]. The controls were elderly people without cognitive impairment, or history of neurological or psychiatric diseases. None of the participants took medications that could influence EEG records.

The socio-demographic characteristics of each group are specified in Table 1. All participants and caregivers were informed about the research and study protocol and gave their written and informed consent. The Ethical Committee of the "Río Hortega" University Hospital (Valladolid, Spain) approved the study according to the Code of Ethics of the World Medical Association (Declaration of Helsinki).

2.2 Electroencephalographic Recordings

EEG signals were recorded using a 19-channel EEG system (XLTEK®, Natus Medical) at the Department of Clinical Neurophysiology of the "Río Hortega" University Hospital. EEG activity was acquired from Fp1, Fp2, Fz, F3, F4, F7, F8, Cz, C3, C4, T3, T4, T5, T6, Pz, P3, P4, O1 y O2, at a sampling frequency of 200 Hz. Subjects were asked to remain with eyes closed, awake, and still during EEG acquisition. Five minutes of EEG activity were recorded for each subject. After a preliminary independent component analysis to remove artifacted components, the EEG recordings were then preprocessed in three steps: (i) filtering using a notch filter (50 Hz) and a Hamming window bandpass filter ([1 70] Hz); (ii) segmentation into 5 s epochs; and (iii) visual rejection of artifacts, selecting the first 60 consecutive seconds without artifacts for each subject.

3 Methods

3.1 Estimation of Variability

Coherency (COH) is a measure that analyzes the consistency between the EEG activity of different pairs of electrodes in order to characterize the connectivity between brain regions. COH is the standardized cross-spectrum of signals X and Y across trials, divided by the product of their power spectrum. Magnitude squared COH (MSCOH) combines sensitivity to both phase and magnitude synchrony and is defined as [5]:

$$MSCOH_{xy}(f,t) = \left|COH_{xy}(f,t)\right|^2 = \frac{|S_{XY}(f,t)|^2}{P_X(f,t)P_y(f,t)} \quad (1)$$

where S_{XY} is the cross-spectrum of X and Y, and P_X and P_Y are the power spectral density (PSD) of X and Y, respectively. The relative power (RP) was computed from the PSD in the conventional frequency bands: delta (δ, 1–4 Hz), theta (θ, 4–8 Hz), alpha (α, 8–13 Hz), beta-1 ($\beta1$, 13–19 Hz), beta-2 ($\beta2$, 19–30 Hz) and gamma (γ, 30–70 Hz).

3.2 Protocol

In order to study the dynamic properties of functional connectivity coupling patterns, MSCOH was computed between each pair of electrodes over the 60 s epochs by means of sliding windows with 50% overlap. Afterwards, the mean value of MSCOH (μ_{MSCOH}) and the standard deviation (κ_{MSCOH}) were obtained. κ_{MSCOH} was used as the test statistic in order to detect the existence of dFC [6]. The connectivity matrixes for each frequency band were grouped into five regions (frontal, left-temporal, right-temporal, central and parieto-occipital) and inter-regional and intra-regional μ_{MSCOH} and κ_{MSCOH} values were averaged among the electrodes within each region pair. After this procedure, the connectivity matrix was reduced to a 5×5 size (5 regions). All subsequent analyses were performed on these matrixes. This procedure was performed on windows of 1, 2, 3, 5 and 10 s, in the aforementioned 6 conventional frequency bands.

Table 1 Socio-demographic and clinical data. Mean values ± standard deviation. A: primary education or below; B: secondary education or above; MMSE: Mini-Mental State Examination

Data	Alzheimer's disease	Controls
Number of subjects	50	28
Age (years)	79.9 ± 5.8	76.1 ± 34.0
Gender (male:female)	21:28	8:20
Education level (A:B)	37:13	9:19
MMSE	21.2 ± 4.0	28.9 ± 1.1

3.3 Statistical Analysis

Shapiro-Wilk and Levene tests showed that μ_{MSCOH} and κ_{MSCOH} values did not meet parametric test conditions. Then, the Mann-Whitney U-test was used to evaluate the differences between groups across each frequency band and region. An FDR correction was performed in order to correct for multiple comparisons. Furthermore, a Spearman correlation analysis was performed between the RP values and the average κ_{MSCOH} values of each channel.

3.4 Analysis of Window Stability

The Friedman test was used on the μ_{MSCOH} values to detect the effects of window length on the MSCOH measures. In case the Friedman test showed a significant effect, Dunn's multiple comparison test was applied to determine the window in which the MSCOH measurements became stable, defined as the shortest window length that does not show significant differences with longer window sizes [7].

3.5 Detection of Dynamic Functional Connectivity

It is important to take into account the fact that the mere presence of fluctuations in connectivity measures is not

sufficient proof of the existence of dFC. Due to the noisy nature of the recordings, the fact that the observed connectivity values are estimates of the true FC values cannot be ignored [6]. Therefore, in order to determine whether the observed fluctuations reflect real FC changes, an adequate statistical test must be carried out [6]. We followed the statistical test described by Prichard and Theiler [8], which has been previously used by Hindriks et al. [6]. In our case, 1000 surrogate versions of each EEG segment were constructed from the original signals.

4 Results and Discussion

First, we determined the window size in which the MSCOH measurements became stable. It was found that for both groups this size was 3 s. All further tests were thus performed on values obtained with a 3 s sliding window. We then assessed whether the κ_{MSCOH} values were statistically significant [6]. For each, inter-regional and intra-regional pair we performed an FDR correction on the p-values associated with the z-scores of all the connections within each pair. After this, we determined that a regional pair had dFC if at least one of the connections within it had a statistically significant κ_{MSCOH} value after the FDR correction.

Figure 1a shows the number of subjects that showed statistically significant μ_{MSCOH} in each regional pair. The beta-1 band showed the highest number of regional pairs
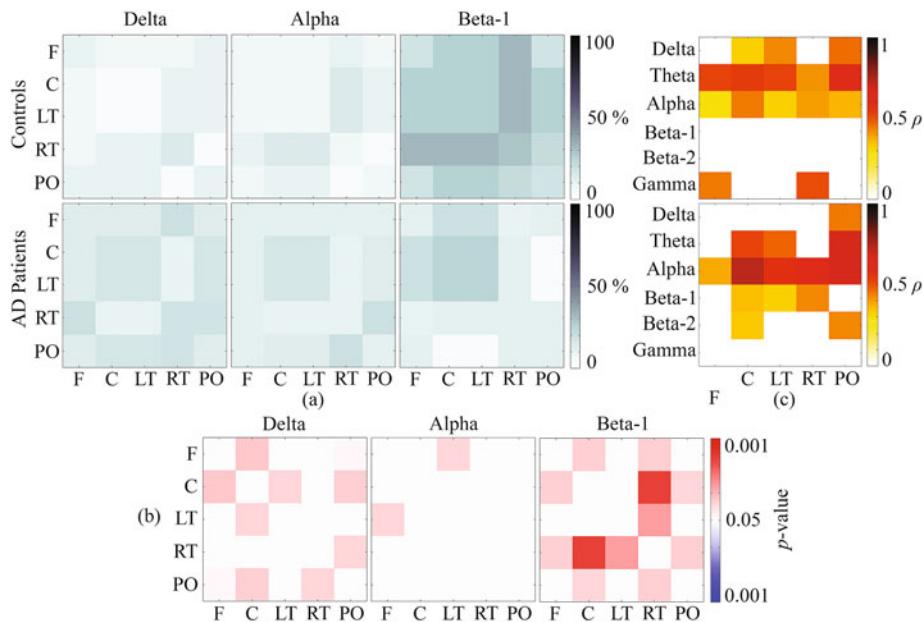
Fig. 1 MSCOH dFC analysis for a 3-s sliding window. **a** Percentage of subjects that showed statistically significant μ_{MSCOH} in each regional pair for each group. **b** Statistically significant p-values for the κ_{MSCOH} comparisons between groups. Red values indicate greater κ_{MSCOH} for C than AD patients, while blue values indicate greater κ_{MSCOH} for AD patients than C. **c** Correlation between RP values and κ_{MSCOH} for each group. Only the bands with significant between-group differences are shown. Correspondence with regions F: frontal, C: central, LT: left-temporal, RT: right-temporal, PO: parieto-occipital (Color figure online)

with dFC, especially for controls, nearing 50% of subjects in some cases. The statistical differences in μ_{MSCOH} between groups are also shown in Fig. 1b. The most statistically significant differences were located in the beta-1 band, especially in the connections between the right-temporal region and the remaining ones. These results are consistent with previous findings that support the role of the right hemisphere in brain disconnection related to AD [9]. Less statistically significant differences were also found in the delta band. Controls showed more variation in connectivity than AD patients, which is in agreement with other studies that found a loss of irregularity and variability in AD neural activity [9].

The correlation analysis between RP and the average κ_{MSCOH} values of each EEG channel in each band, displayed in Fig. 1c, showed statistically significant positive correlation in the delta, theta and alpha band for most regions in controls. AD patients, on the other hand, showed weaker positive correlation in the beta-1 band as well, suggesting that spectral power is a pre-requisite for dFC.

This study has some limitations. Firstly, more controls should be included in the database in order to balance the number of AD patients and controls. Furthermore, a third group of mild cognitive impairment (MCI) patients should be included in future studies, given its importance as a prodromal form of AD [9].

5   Conclusion

The results suggest that MSCOH variability could be due to dFC. Moreover, AD patients show lesser variation in neural connectivity than controls, which suggests a loss of variability in AD. Finally, the correlation between relative power and κ_{MSCOH} hints that a peak in power spectrum in a frequency band could be a pre-requisite for dFC.

References

1. Babiloni C, et al.: Brain neural synchronization and functional coupling in Alzheimer's disease as revealed by resting state EEG rhythms. Int J Psychophysiol 103, 88–102 (2015).
2. Hansen ECA, et al.: Functional connectivity dynamics: Modeling the switching behavior of the resting state. Neuroimage 105, 525–535 (2015).
3. Hutchison RM, et al.: Dynamic functional connectivity: Promise, issues, and interpretations. Neuroimage 80, 360–378 (2013).
4. McKhann G, et al.: The diagnosis of dementia due to Alzheimer's disease: Recommendations from the National Institute on Aging-Alzheimer's Association workgroups on diagnostic guidelines for Alzheimer's disease. Alzheimers Dement 7(3), 263–26 (2011).
5. Roach BJ, Mathalon DH.: Event-related EEG time-frequency analysis: An overview of measures and an analysis of early gamma band phase locking in schizophrenia. Schizophr Bull 34(5), 907–926 (2008).
6. Hindriks R, et al.: Can sliding-window correlations reveal dynamic functional connectivity in resting-state fMRI? Neuroimage 127, 242–256 (2016).
7. Fraschini M, et al.: The effect of epoch length on estimated EEG functional connectivity and brain network organisation. J Neural Eng 13(3), 36015 (2016).
8. Prichard D, Theiler J.: Generating surrogate data for time series with several simultaneously measured variables. Phys Rev Lett 73(7), 951–954 (1994).
9. Poza J, et al.: Spatio-Temporal fluctuations of neural dynamics in mild cognitive impairment and Alzheimer's disease. Curr Alzheimer Res 14(9), 924–936 (2017).

Assessment of ECG Signal Quality After Compression

Andrea Němcová⬤, Martin Vítek⬤, Lucie Maršánová⬤,
Radovan Smíšek⬤, and Lukáš Smital⬤

Abstract

Highly efficient lossy compression algorithms for ECG signals are connected with distortion of the signals; lossy compression is a compromise between compression efficiency and signal quality. It is recommended to express this relation using rate-distortion curve. To decide whether the signal is suitable for further analysis, it is necessary to assess its quality after reconstruction. Although there exist many methods for quality assessment, neither of them is standardized or unified. The methods usually do not offer any information about their acceptable values. This paper introduces 10 new methods for signal quality assessment and their limits. Four methods are simple (entropy, mean, median, spectra similarity), two are based on delineation of ECG (SiP, SiPA), and four combine dynamic time warping, delineation, and calculation of distance (DTWdist, DTWpmf-p1, DTWpmfp2, pmfp). These methods are tested on the whole standard CSE database using compression algorithm based on wavelet transform and set partitioning in hierarchical trees. The signals were compressed with various efficiency expressed by average value length (avL). Two ECG experts divided the compressed signals into three quality groups: perfect quality, good quality, not evaluable ECG. Owing to the experts' ECG classification, we set the range of avL for each quality group. Based on this, we determined corresponding ranges of new methods' values. Based on the trend of rate-distortion curve, its sensitivity, variability, their ratio at important boundary avL = 0.8 bps, and computational demand of the methods, we recommend four methods for further use.

1 Introduction

The evaluation of signal quality after compression is tightly connected with compression (and reconstruction) itself. Lossy compression always brings distortion of the signal and we have to decide whether the signal is still suitable for further analysis or not and how detail the analysis can be. For evaluation of the signal quality, it is advantageous to use more methods all at one. It is favourable to use methods based on principles with various trends to look at the signal from different points of view. This proceeding paper introduces 10 new methods for ECG quality assessment, which are based on different principles—statistics, dynamic time warping (DTW), and delineation. More than 40 methods exist for evaluation of signal quality after compression, but here is not enough space to mention or compare them. Thus, the new methods are compared with subjective assessment provided by experts.

Popular combination of wavelet transform (WT) and set partitioning in hierarchical trees (SPIHT) was used for compression [1, 2]. We compressed 1,875 signals (125 records, 15 leads) from The Common Standards in Cardiography (CSE) database [3]—the second most cited standard ECG database [4]. In all signals, the DC component was subtracted to reach the highest objectivity. The signals were compressed with various efficiency expressed by average value length (avL)—33 values from 0.1 bits per sample (bps) to 9 bps. avL expresses how many bits are needed to code one sample of signal.

A. Němcová (✉) · M. Vítek · L. Maršánová
R. Smíšek · L. Smital
Faculty of Electrical Engineering and Communication, Department of Biomedical Engineering, Brno University of Technology, Technická 12, 616 00 Brno, Czech Republic
e-mail: nemcovaa@feec.vutbr.cz

R. Smíšek
Institute of Scientific Instruments, The Czech Academy of Sciences, Královopolská 147, 612 64 Brno, Czech Republic

2 Methods

2.1 Simple Methods

In telemedicine, the emphasis is put on fast transmission. Therefore, the simpler the method for ECG signal quality evaluation is, the better. At first we focused on simple methods which have low computational demand (CD): entropy, mean, median, spectra similarity. To the best of our knowledge, these methods were not used for ECG quality assessment anywhere. The principle of these methods is to compute entropy, mean, and median of the original and the reconstructed signal, and calculate the absolute value of their difference. In case of spectra similarity, at first the spectrum for each signal is computed and then the sum of absolute values of difference between the spectra is calculated. If the original signal is equal or very similar to the reconstructed signal, the values of simple methods will be zero or low, respectively. Simple methods can be categorized into the group of objective methods without diagnostic information.

2.2 Similarity—Positions (SiP), Positions and Amplitudes (SiPA)

SiP and SiPA methods were inspired by similarity method in [5], where the original method is described very briefly and calculates rather dissimilarity only for one significant point. The SiP(A) method is based on delineation, therefore it belongs to the group of objective methods with diagnostic information based on delineation. We used delineation algorithm based on WT [6] that detects 8 ECG significant points (Ponset, P, Poffset, QRSonset, QRS, QRSoffset, T, and Toffset). The range of SiP(A) was normalized to 0–100% (0% = two signals are not similar at all, 100% = signals are equal).

SiP algorithm works with positions of significant points before and after compression. For each significant point, the difference in original $D0$ and reconstructed signal D is computed. If the difference is smaller than the tolerance tol predefined by the user, the error ERS_{SiP} which is directly proportional to the difference value is calculated according to Eq. (1). The range of ERS_{SiP} is [0; 1). If the difference is greater than tol, the error $ERS_{SiP} = 1$. If some significant point is missing or is in excess, the error is also equal to 1. In Eqs. (1) and (2) i stands for index of significant point in ECG; ERS_{SiP} is a vector. SiPA is a modification of SiP, which takes into consideration both positions and amplitudes of ECG significant points. $A0$ and A are the amplitudes in original and reconstructed signal, respectively. Numerator of the Eq. (2) is the Euclidean distance between the significant point of original and reconstructed signal. ERS_{SiP} and

ERS_{SiPA} are calculated for each type of significant points. According to Eq. (3), the similarity SiP (or SiPA) is calculated using the error ERS for each type of 8 significant points and for each signal. Finally, the SiP or SiPA values are averaged to obtain only one number for each avL.

$$ERS_{SiP}(i) = \frac{|D0(i) - D(i)|}{tol} \tag{1}$$

$$ERS_{SiPA}(i) = \frac{\sqrt{(D0(i) - D(i))^2 + (A0(i) - A(i))^2}}{tol} \tag{2}$$

$$SiP = 100 - \frac{100}{length(D0)} \cdot \sum ERS \tag{3}$$

2.3 Dynamic Time Warping—Fiducial Points and Distance

DTW for the purpose of signal quality evaluation is briefly described in [7, 8]. However, there were not enough details in these original works, so in this paper the DTW method was adjusted and extended. According to [8], the method provides similar information about the signal quality as the cardiologist. In this work, we introduce one method, which evaluates percentage match of fiducial points (pmfp) without the use of DTW and 3 methods which use DTW (DTWdist, DTWpmfp1, and DTWpmfp2).

In pmfp method, (1a) the original signal as well as the reconstructed one are delineated using algorithm [6]; (1b) the positions of fiducial points in both signals are compared without any tolerance; (1c) the pmfp is calculated. The algorithm of DTWdist is as follows: (2a) DTW is applied on the original and the reconstructed signal; (2b) the smallest possible Euclidean distance (DTWdist) between the warped signals is calculated. DTWpmfp1 combines previous methods this way: (3a) is the same as (1a); (3b) is the same as (2a); (3c) finding the positions of fiducial points in warped signals; (3d) the positions of fiducial points in warped signals are compared without any tolerance; (3e) DTWpmfp1 is calculated. DTWpmfp2 is very similar to DTWpmfp1: (4a) only the original signal is delineated; (4b) is the same as (2a); (4c) the fiducial points are found in both warped signals; (4d) is the same as (3d); (4e) DTWpmfp2 is calculated.

3 Results

Before any objective ECG signal quality evaluation, two ECG experts evaluated the signal quality subjectively. Based on the signal quality, they set two boundaries of avL (the second row of Table 2) for each of 250 signals from leads I

and V1 compressed with different efficiency (33 values of avL), which naturally causes some distortion. ECG signal can be classified into one of three quality groups (separated by the two avL boundaries): (a) perfect quality, evaluable without any restrictions, (b) good quality, some parts of ECG (such as P wave, ST segment) are distorted due to compression; potential of analysis is reduced, and (c) not evaluable ECG, significant distortion; in this group only the rhythm can be approximately evaluated. The overall avL boundaries (for all 250 signals) can be set as strict (max case in Table 2—maximum of the 250 boundary values of avL between perfect and good quality groups and maximum between good and not evaluable groups); it means that none of the signals with avL higher than 0.8 and 0.25 bps belongs to the lower quality group. The boundaries can be set as mild (min case in Table 2); it means that some signals can belong to the better quality group. In Table 2, there is also shown the median case, which is compromise between max and min case. In cooperation with experts we selected avL = 0.8 bps as the most important limit, which separates signals with and without any visible diagnostic distortion.

All new objective quality methods were tested on the whole CSE database. In Fig. 1, there are shown average trends of each method for all 1,875 signals. For each method, sensitivity—derivative of the curve at avL = 0.8 bps, variability (standard deviation) of 15 mean lead curves at avL = 0.8 bps and sensitivity-variability ratio (SVR) were calculated. Methods, which are suitable for ECG quality assessment should have monotonous trend, maximal sensitivity and SVR, minimal variability at avL = 0.8 bps, and low CD. Final combination of methods should be as much diverse as possible.

The results of methods based on entropy, spectrum, mean, and median are shown in Fig. 1a–d. Methods based on entropy and mean have non-monotonous trend, therefore they cannot be recommended for further use. Mean has very low values and differs from median because the DC component was subtracted before compression and assessment of signal quality after compression. Trends of methods based on spectrum and median are monotonous. Their sensitivity, variability, and SVR are shown in Table 1. From these two methods, the spectrum based method is the better one. Compared to the methods based on different principles, it has quite low SVR but also low CD.

Figure 1e shows trends of SiP and SiPA methods for three values of *tol* = {10, 50, 100} samples. All the curves have similar trend. The sensitivity of methods differs with avL. It is also influenced by set of *tol*; lower *tol* means higher sensitivity but also higher variability. SiP10 and SiPA10 have the highest SVRs from all tested SiP and SiPA settings, respectively.

Figure 1f shows the results of algorithms based on DTW and/or pmfp. Methods pmfp, DTWpmfp1, DTWpmfp2 have similar trend. DTWdist has different trend; it decreases with increasing avL. According to Table 1, DTWpmfp2 has the highest sensitivity and one of the lowest variability for avL = 0.8 bps; it leads to the best SVR. This method is considered as the best one from this criterion point of view. Conversely, its CD is high.

In Table 2, there are limits of aforementioned methods used for evaluation of ECG signal quality after compression. Methods based on entropy and mean of the ECG signal are excluded, because of their non-monotonous trends. These methods are not suitable for ECG quality assessment. Each

Fig. 1 Results of ECG quality methods evaluation **a** entropy, **b** spectrum, **c** mean, **d** median, **e** SiP and SiPA, **f** DTWdist (right y-axis), pmfp, DTWpmfp1, DTWpmfp2 (left y-axis)
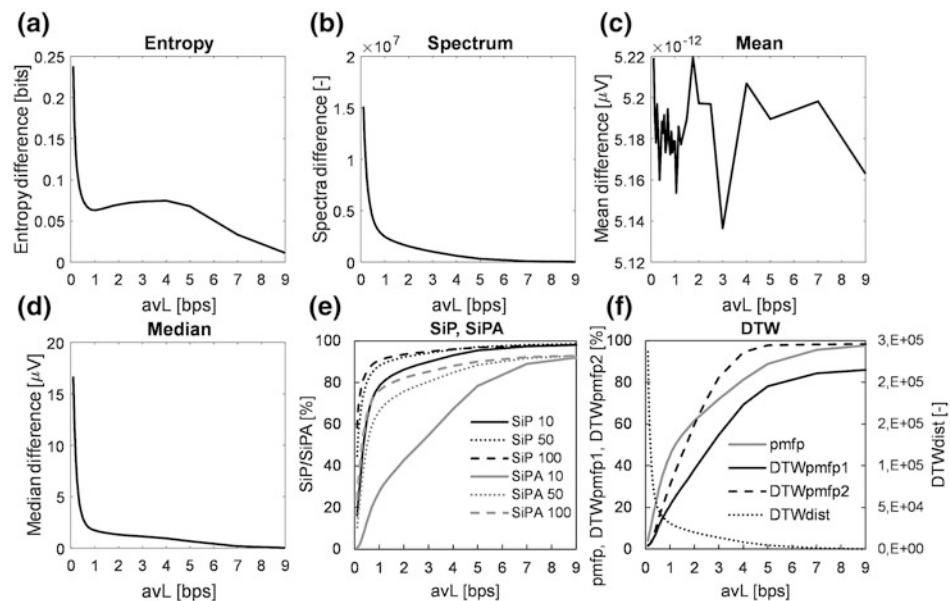
Table 1 Sensitivity, variability, and SVR of all methods with monotonous trend at avL = 0.8 bps. The best values are in bold type. CD can be either 1 low, 2 medium, 3 high

	Spectrum	Median	SiP 10	SiP 50	SiP 100	SiPA 10	SiPA 50	SiPA 100	pmfp	DTW dist	DTW pmfp1	DTW pmfp2
Sensitivity	0.0905	0.0797	0.0336	0.0150	0.0096	0.1118	0.0421	0.0243	0.0856	0.0765	0.1217	**0.1375**
Variability	0.1510	0.1479	0.0524	**0.0284**	0.0316	0.1499	0.0581	0.0375	0.1096	0.1824	0.1037	0.0442
SVR	0.5990	0.5387	0.6412	0.5263	0.3036	0.7459	0.7238	0.6491	0.7808	0.4193	1.1736	**3.1101**
CD	1	1	3	3	3	3	3	3	3	2	3	3

Table 2 The recommendations for compression. The most appropriate methods for signal quality evaluation are in bold type. Each group of methods is separated by one shade of grey

	the min case		the max case		the median case	
	avL = 0.15 bps	avL = 0.1 bps	avL = 0.8 bps	avL = 0.25 bps	avL = 0.4 bps	avL = 0.15 bps
Spectrum	**12091857.5115**	**15133378.8312**	**2887228.9266**	**8112696.3762**	**5232712.7220**	**12091857.5115**
Median	11.9473	16.6801	1.9352	6.8538	3.8431	11.9473
SiP (*tol* = 10)	**23.8865**	**16.1937**	**74.3863**	**36.9844**	**54.2201**	**23.8865**
SiP (*tol* = 50)	55.2404	44.8439	86.0896	66.4660	76.2224	55.2404
SiP (*tol* = 100)	68.1514	58.3583	89.3209	76.5162	82.8409	68.1514
SiPA (*tol* = 10)	**1.3450**	**0.6691**	**22.9493**	**3.6061**	**9.1245**	**1.3450**
SiPA (*tol* = 50)	16.4922	10.5426	62.2647	27.6299	42.2802	16.4922
SiPA (*tol* = 100)	32.6525	24.0233	73.4674	45.1699	58.5243	32.6525
DTWdist	163401.9399	236292.7518	35573.1051	96567.9761	59781.1229	163401.9399
pmfp	6.9803	4.1680	38.8426	12.7424	20.8510	6.9803
DTWpmfp1	2.1313	1.8104	17.0338	3.4858	6.9504	2.1313
DTWpmfp2	**2.0985**	**1.5452**	**23.9714**	**3.9844**	**9.0792**	**2.0985**

group of methods is separated by one shade of grey. The most appropriate methods are in bold type.

4 Discussion

The lossy compression is always a compromise between the amount of data and their quality. It is important to decide for what purpose the ECG signal will be used. According to this, we can set the minimum avL or maximum error of the compressed signal before compression. If we cannot set the parameters of compression ahead, we can at least verify whether the output signal is suitable for particular analysis. The methods for evaluation of ECG signal quality after compression should be selected according to their performance. To evaluate the signal quality correctly, we recommend to subtract the DC component. We also recommend to use combination of methods based on different principles. It enables to look at the signal from different points of view.

From simple methods, the best one is based on spectra similarity. Its advantage is low CD. From the methods based on similarity of fiducial points, both SiP and SiPA can be used. From the tested tolerance, 10 samples seem the best.

According to the highest sensitivity, low variability, and overall highest SVR, the best method—DTWpmfp2—is from the group based on DTW and delineation. The methods from the last two groups inform about diagnostic distortion. On the other hand, they have high CD and they are also dependent on quality of delineation algorithm. ECG quality evaluation methods with diagnostic information using delineation have great potential; they inform about distortion in important parts of ECG. Their disadvantage is the necessity of the delineation algorithm use, which flawless version does not exist. These algorithms can introduce an artificial error into ECG quality assessment.

5 Conclusion

We present 10 new algorithms for assessment of ECG signal quality after compression. These algorithms were tested in terms of their suitability for further use. As a compression algorithm we used well known combination of WT and SPIHT. Testing signals come from the standard CSE database. Suitable algorithms should have monotonous trend, low CD, maximal sensitivity and SVR, and minimal

variability in the area of avL = 0.8 bps (which is the strict bound between signals of perfect quality, evaluable without restrictions and signals with some distortion). The combination of selected methods should be as much diverse as possible. Therefore, we recommend four methods: method based on spectrum, SiP10, SiPA10, and DTW pmfp2.

Conflict of Interest The authors declare that they have no conflict of interest.

References

1. Lu, Z., Kim, D.Y., Pearlman, W.A.: Wavelet compression of ECG signals by the set partitioning in hierarchical trees algorithm. IEEE T BIO-MED ENG 47(7), 849–856 (2000).
2. Hrubeš J., Vítek, M., Kozumplík J.: Possibilities of Wavelet Decomposition for SPIHT Compression of ECG Signals. Analysis of Biomedical Signals and Images. Biosignal, 451–454 (2008).
3. The CSE Working Party: Common standards for quantitative electrocardiography. CD-ROM version of the CSE database (1990).
4. Smíšek, R., Maršánová, L., Němcová, A., Vítek, M., Kozumplík, J., Nováková, M.: CSE Database: Extended Annotations and New Recommendations for ECG Software Testing. MED BIOL ENG COMPUT 55(8), 1473–1482 (2017).
5. Twomey, N., Walsh, N., Doyle, O., McGinley, B., Glavin, M., Jones, E., Marnane, W.P.: The effect of lossy ECG compression on QRS and HRV feature extraction. 32nd Annual International Conference of the IEEE EMBS, Buenos Aires, Argentina. (2010).
6. Vítek, M., Hrubeš J., Kozumplík J.: A Wavelet-Based ECG Delineation with Improved P Wave Offset Detection Accuracy. Analysis of Biomedical Signals and Images. Biosignal, 160–165 (2010).
7. Shorten, G.P., Burke, M.J.: A novel approach in testing the accuracy of ECG compression using partial percentage RMS difference and dynamic time warping. Recent Researches in Communications, Automation, Signal Processing, Nanotechnology, Austronomy & Nuclear Physics 2011, Athens. WSEAS, 89–94 (2011).
8. Shorten, G.P., Burke, M.J.: The application of dynamic time warping to measure the accuracy of ECG compression. CIRC SYST SIGNAL PR 5(3), 305–313 (2011).

Event-Related Synchronization/Desynchronization in Neural Oscillatory Changes Caused by Implicit Biases of Spatial Frequency in Electroencephalography

K. Kato, H. Kadokura, T. Kuroki, and A. Ishikawa

Abstract

Spatial frequency may elicit characteristic mental and neural activity in humans, exhibiting a 1/f fluctuation. However, a visual pattern with only spatial frequency information will not necessarily explicitly affect any reaction, but may do so implicitly. We adopted an implicit association test (IAT), which is widely used in the research of implicit biases, to answer that question. At the same time, we attempted to characterize the neural activities associated with implicit spatial frequency biases by using electroencephalography (EEG). We used two types of checkered-pattern stimuli, high and low density, as targets. The high and low densities correspond to high and low spatial frequencies. There were two evaluative categories, with associated nouns and adjectives carrying a range of positive and negative meanings. EEG data were recorded, and the event-related synchronization (ERS) or desynchronization (ERD) for each event was analyzed based on the intertrial variances for the theta (4–7 Hz), alpha (8–13 Hz), low beta (13–20 Hz), high beta (20–30 Hz), and gamma (30–80 Hz) bands for each strong and weak associative strength comparison between targets. The category (e.g., high spatial frequency–positive or low spatial frequency–negative) was then obtained from the reaction times of the IAT for each subject. The ERS characteristics differed between strong and weak associative strengths, measured at the central areas at around 400–500 ms. This difference suggests that spatial frequency characteristics affect neural oscillatory activity associated with implicit biases of spatial frequency.

1 Introduction

Spatial frequency may elicit characteristic mental and neural activity in humans, exhibiting a 1/f fluctuation. We have previously found that neural activities associated with cognitive neural processes are affected by spatial frequency [1] and the visual search of images is influenced by spatial frequency [2]. However, a visual pattern that consists only of spatial frequency information (e.g., a checkerboard pattern) will not necessarily affect any reaction explicitly, but it may do so implicitly. We adopted an implicit association test (IAT), which is widely used in the research of implicit biases, to answer that question. IAT is a categorization task that measures the differential association of two target concepts with an attribute based on reaction time [3]. In addition to psychophysical evidence such as reaction time, it is also interesting to investigate the neural basis of judgments in the IAT. Studies have evaluated the event-related potential (ERP) associated with implicit biases [for example, 4,−5]; however, neural oscillatory activity in terms of event-related synchronization/desynchronization (ERS/ERD) has not yet been characterized. Thus, we attempted to characterize the neural activities associated with implicit biases of spatial frequency by using ERS and ERD.

2 Methods

In this study, the strength of the association between the target category, high or low spatial frequency, and the evaluative category, positive or negative meanings as a result of individual implicit biases was investigated.

K. Kato (✉) · H. Kadokura
Tohoku Gakuin University, 1-13-1, Chuo, Tagajyo, Japan
e-mail: k_kato@mail.tohoku-gakuin.ac.jp

T. Kuroki · A. Ishikawa
Takenaka Research and Development Institute, 1-5-1, Ohtsuka, Inzai, Japan

In this present study, we used two types of checkered-pattern image stimulus, high and low density, as targets. Figure 1 shows examples of the image stimuli and the high and low densities correspond to high and low spatial frequencies, respectively. Five images with high and low spatial frequency that had slightly different densities were used. In two evaluative categories, word stimuli, namely those associated nouns and adjectives carrying a range of positive and negative meanings such as "Scary," "Dirty," "Hateful," "Peace," "Happy," and "Tender" among others, were used.

The experimental set-up consisted of seven blocks. Figure 2 shows an experimental paradigm used in the 3rd and 4th blocks. The term of the target and evaluative category, and word stimulus were presented in Japanese. The translations are shown in the square area in Fig. 2. In first trial, a fixation cue was presented for 1000 ms and was followed by the word stimulus for 1500 ms. Next, the cue and image stimulus in the second trial were presented for 1000 and 1500 ms, respectively. Word and image stimuli were presented alternately. The 3rd and 4th blocks consisted of blocks of 20 and 50 trials, respectively. In these blocks, the reaction time and EEG signal were measured with associations of high spatial frequency and positive category (or low frequency and negative), as well as low spatial frequency and positive category (or high frequency and negative) in the 6th and 7th blocks of 20 and 50 trials, respectively. The remaining blocks were practice blocks.

Subjects were asked to sort the image and word stimuli into categories (e.g., high spatial frequency–positive or low spatial frequency–negative) by pressing a button on the computer controlling the task. The reaction times were measured for each trial and the IAT score was calculated for each subject as described [3]. Briefly, the difference in the mean reaction time between the 6th and 3rd blocks, and 7th and 4th blocks was calculated, and divided by the standard deviation of all trials in the 6th and 3rd blocks, and 7th and 4th blocks, respectively. The two quotients were then averaged. A positive IAT score suggests strong associative strength for high frequency and positive category (or low/negative), and weak strength for low frequency and positive category (or high/negative). In contract, a negative IAT score suggests strong associative strength for low frequency and positive category (or high/negative) and weak strength for high frequency and positive category (or low/negative).
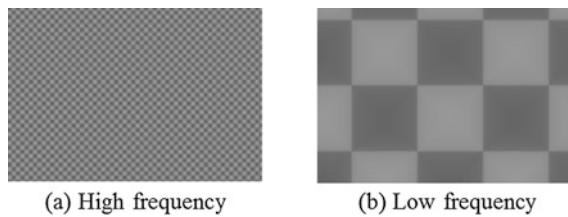
The EEG signal was recorded from F_{p1}, F_{p2}, F_7, F_3, F_z, F_4, F_8, T_3, C_3, C_z, C_4, T_4, T_5, P_3, P_z, P_4, T_6, O_1, and O_2 electrodes based on the international 10–20 system. Reference electrodes were linked electrodes placed on both ears. Data were collected between a 100-ms prestimulus and a 1500-ms poststimulus period in reference to a trigger signal presented at stimulus onset after executing independent component analysis to reject eye movement artifacts. For comparison of ERS and ERD, a continuous wavelet transform using Morlet's mother function was conducted for each EEG epoch from 1 to 80 Hz per 0.1 Hz, except for those that included artifacts exceeding 100 μV at the F_{p1} and F_{p2} electrodes. Intertrial variances of the wavelet coefficients for each frequency per 0.1 Hz were calculated using Eq. (1). The band-averaged variances in the theta (4–7 Hz), alpha (8–13 Hz), low beta (13–20 Hz), high beta (20–30 Hz), and gamma (40–80 Hz) frequency ranges were then calculated for each strong and weak associative strength comparison using Eq. (1):

$$Variance = \frac{1}{N-1} \sum_{i=1}^{N} \left\{ x_{f(i,j)} - \overline{X}_{f(j)} \right\}^2 \qquad (1)$$

where $N = 20$ or 50 indicating the total number of trials, $x_{f(i,j)}$ denotes the j-th sample (wavelet coefficients) of the i-th trial, and $\overline{X}_{f(j)}$ represents the mean of data at the j-th sample. The 100-ms prestimulus period served as the value for baseline normalization. The band-averaged variances were filtered through a low-pass digital filter with a cutoff frequency of 8 Hz for wave-smoothing.

Five healthy men (age, 21–22 years) participated in the experiments. All the participants were native Japanese speakers and provided written, informed consent. The study design was approved by the Ethics Committee of Tohoku Gakuin University.

3 Results

The IAT scores were as follows: subject A, 1.03; subject B, 0.54; subject C, 0.53; subject D, 0.46, and subject E, −0.02. All subjects except subject E, exhibited a strong associative strength for high frequency and positive category. Therefore, the ERS/ERD for strong and weak associative strength was calculated to use block EEG data selectively for each subject depending on the IAT score (subject A–D: 3rd and 4th block data for strong strength, and 6th and 7th for weak strength,

(a) High frequency   (b) Low frequency

Fig. 1 Example of image stimuli with **a** high and **b** low spatial frequency

Fig. 2 Experimental paradigm used in 3rd and 4th blocks
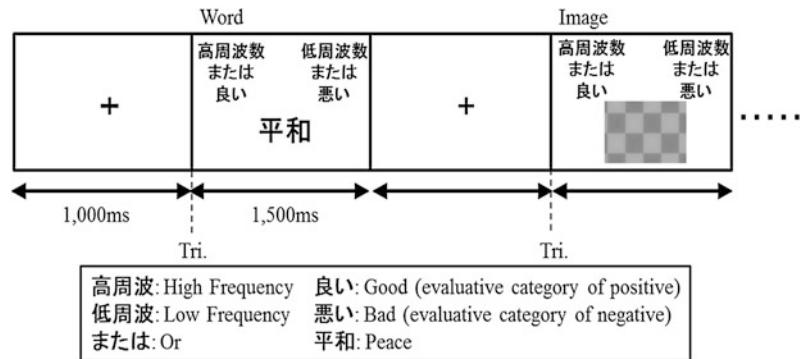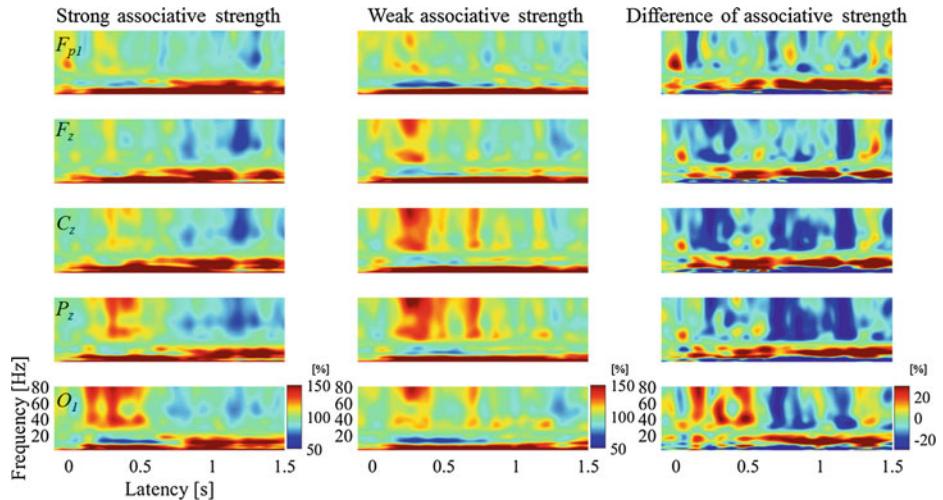
Fig. 3 Intertrial variance from 1 to 80 Hz at F_{p1}, F_z, C_z, P_z, and O_1 in the strong (left) and weak (middle) associative strength and the difference (right panel) averaged over all subjects. Red and blue colors indicate ERS and ERD, respectively (Color figure online)

subject E: 6th and 7th block data for strong and 3rd and 4th for weak strength.). The reaction times averaged over all subjects were 600.6 ± 79.98 ms and 723.9 ± 65.0 ms for the strong and weak associations, respectively.

Figure 3 shows the time-frequency characteristics at the midline area (F_{p1}, F_z, C_z, P_z, and O_1) for normalized intertrial variances from 1 to 80 Hz for both associative strength (left and middle) and the difference (right). The intertrial variances were averaged over all subjects to evaluate the ERD (represented with a decrease in variance as blue) and ERS (represented with an increase in variance as red). For strong strength associations, the ERS was measured from 1 to 20 Hz corresponding to the theta, alpha, and beta bands at latencies of 0–1500 ms and compared with the weak strength associations.

Figure 4 shows the time course of the band-averaged variances for the theta (4–7 Hz), alpha (8–13 Hz), and low beta bands (13–20 Hz). The peak ERS for the theta band was around 500–600 ms for the strong association and 900–1,000 ms for the weak association, as observed in the frontal and central areas (F_z and C_z). The ERD for the alpha band was observed around 300 ms in the parietal and occipital areas (P_z and O_z) for both associations. However, the

following peak ERS around 400–500 ms in frontal and central areas (F_z and C_z), and broad ERS starting from 600 ms, was larger for the strong association than the weak one. The ERD for the low-beta band exhibited fluctuations similar to the alpha band, except for the 400–500 ms ERS peak.

In these components, the averaged variances between 480 ± 125 ms of the alpha-ERS, corresponding to the 400–500 ms component were calculated. All subjects exhibited a higher value in the strong association than in the weak one at T_3, C_z and C_3 as shown in Table 1. The high-beta and gamma bands showed no characteristic responses.

4   Discussion and Conclusion

The reaction times were estimated at around 500 and 600 ms for the strong and weak associations, respectively, while considering that the motor response of the button press as 110 ms [4]. In the present study, we focused on the alpha-ERS component around 400–500 ms that suggested a relationship with the neural activity of implicit biases of spatial frequency because the latency of the component was

Fig. 4 Time course of band-averaged variances for theta (4–7 Hz, left), alpha (8–13 Hz, middle), and low-beta (13–20 Hz, right) band for strong (red) and weak (green) associative strength averaged over all subjects at F_{p1}, F_z, C_z, P_z, and O_1 (Color figure online)
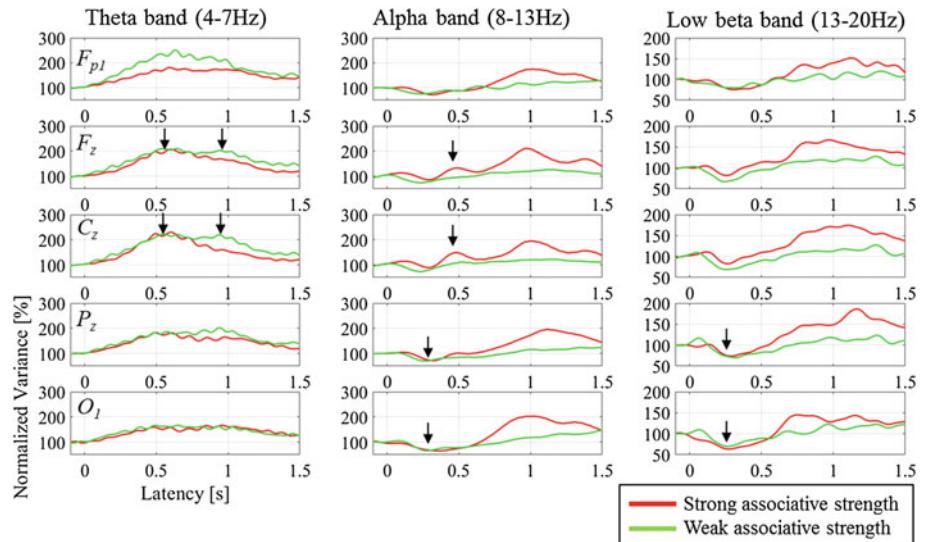
Table 1 Averaged variance of the alpha-ERS

		Sub. A	Sub. B	Sub. C	Sub. D	Sub. E
T_3	Strong (%)	81.6	97.4	115.9	97.8	130.8
	Weak	58.9	79.9	109.3	74.6	88.6
C_3	Strong	66.1	77.9	130.3	103.8	150.2
	Weak	46.1	59.5	126.7	82.7	103.6
C_z	Strong	88.8	74.7	145.5	157.7	199.3
	Weak	46.4	55.9	130.4	140.6	148.8

prior to the decision time for sorting the word or image. The alpha-ERS was higher for the strong associations than for the weak ones around at the central area. Healy et al. [5] showed that the reaction time for the strong association was more affected by implicit biases (IAT score) than for weak associations. Therefore, little ERS response for weak associations may be reasonable. However, further discussion concerning this point is necessary. The neural activities in alpha-ERS suggested an association with cognitive control and top-down attention related to implicit biases [5].

In conclusion, ERS/ERD could reveal other aspects of neural activity of implicit associations compared with those revealed by ERP alone. In brief, the alpha-ERS suggests that spatial frequency characteristics affect neural oscillatory activity associated with implicit spatial frequency biases.

Conflict of Interest The authors declare that they have no conflict of interest.

References

1. Kato, K., Miura, O.: Oscillatory neural activity associated with cognitive processes affected by spatial frequency. IEEJ Trans, 9, 288–293 (2014).
2. Kato, K., Tashiro, K., Kuroki, T., Ishikawa, A.: Visual search controlled by spatial frequency without salient features in an image. IEEJ Trans, 10(s1), S91–S95 (2015).
3. Greenwald, AG., Nosek, BA., Banaji, MR.: Understanding and using the implicit association test: 1. An improved scoring algorithm. J Pers Soc Psychol, 85(2), 197–216 (2003).
4. Kato, K., Kobayashi, T., Kuriki, S.: Event-related potentials elicited by the alternation of perceived images in binocular rivalry. Japanese Journal of Medical Electronics and Biological Engineering, 36(2), 111–118 (1998) (in Japanese).
5. Healy, GF., Boran, L., Smeaton, AF.: Neural patterns of the implicit association test. Front Hum Neurosci, 9, 1–16 (2015).
6. He, Y., Johnson, MK., Dovidio, JF., McCathy, G.: The relation between race-related implicit associations and scalp-recorded neural activity evoked by faces from different races, Soc Neurosci, 4(5), 426–442 (2009).

Design and Development of Advanced Multi-channel EMG Micro Electrode Recording System

Venkateshwarla Rama Raju

Abstract

A new multi-channel EMG system with innocuous microelectrode recoding in the digitized form having a high sampling frequency going up to 6 kHz, maximum conversion of A/D converter 40 k samples/s was indigenously developed and installed at our NIMS tertiary care center in neurosciences millennium block (Hyderabad, India) with the department of neurology. Because of the limited computer system bus capacity of the interface, the sampling frequency of 6 kHz was provided for each channel. All 5 channels sampled simultaneously at 3 kHz. The continuous analogue signals while displayed on the 15 MHz frequency Oscilloscope (Philips maker dual tracer) were parallelly recorded online and stored digitally (using a 12 bit A/DC card (Dantec Dynamics maker, Denmark), embedded in Pentium computer. The EMG signals are acquired—recorded with a special reference to Writer's cramp. The number of signal units in other words motor neurons in dominant intrinsic right hand is more than in the non dominant intrinsic left hand, and we found that there is a quantifiable difference between the two groups (concordant and discordant).

V. Rama Raju (✉)
Department of Computer Science & Engineering, CMR College of Engineering & Technology (UGC Autonomous), Kandlakoya, Medchal Rd, Hyderabad, 501401, India
e-mail: drvrr@cmrcet.org; system@ou.ernet.in; idcoucea@hd1.vsnl.net.in

V. Rama Raju
Jawaharlal Nehru Technological University Hyderabad JNTUH, Hyderabad, India

V. Rama Raju
Biomedical, Neurology & Neurosurgery, Nizam's Institute of Medical Sciences, Hyderabad, India

V. Rama Raju
Biomedical Engineering Department, Osmania University College of Engineering (Autonomous), Hyderabad, India

1 Introduction

In biomedical systems, the technical specifications—configuration and performance of the instrumentation highly influence the accuracy of measurement so that meaningful recording of electrical activity can only be performed with properly designed equipment [1–3].

The range of voltage and frequency encountered in electromyography (EMG) is much greater than that observed in electroencephalography (EEG), Electrocardiography (ECG), and electro-cochleao-gram [2, 3]. The objective of any signal-recording system is to obtain a faithful reproduction of the physiological event; i.e., signals picked up by the electrodes should be amplified and presented to the examiner/user–observer without noise and distortion and free from any interference which may obscure the signal [1–12]. The work in the present study provides the hardware development of the multi-channel EMG and the ability to record from a deeper target muscles of Writer's cramp syndrome without any crosstalk.

1.1 The Amplifier

As per De Luca, Weitkunat and others [1–3], the input impedance of the EMG amplifier should be well over 10 MΩ to ensure noise and distortion free recording. Impedance is the combination of electrical resistance® and capacitance©. All devices should have input-impedance to prevent loading of the input signal. If loading occurs the signal strength is reduced. Amplifiers with more than 10 Giga Ω need no skin preparation. However, palpation is required.

1.2 Differential Input

When an electrode is inserted into a muscle it pickups action potentials (due fluctuations occurring in the membranes);

however, it may also pickup 50 Hz—hum potentials (vibration noise etc.) from power supplies or poor grounding or other sources. To overcome this difficulty, filters can be employed. The ability of a differential amplifier to reject identical signals is called common mode rejection (CMR), for instance, a differential amplifier that produces a 0.001 V output when driven by a 1 V signal common to both inputs has a CMRR of 1/0.001 or 1000/1, and hence, high CMRR is necessary condition for eliminating interference from recording.

2 Methods

This study was approved from the Nizam's Institute of Medical Sciences (Telangana State University) NIMS tertiary care hospital Hyderabad (India) and Indian council for medical research (ICMR) India and FDA approval from USA.

In this study, we have constructed an EMG amplifier setup for multi channel capturing of EMG signal with special reference to Writer's cramp from the subject having input impedance greater than 200 MΩ. An input-impedance of at least >100 MΩs is required for amplification system, CMRR of 65 dB and variable gain 1000–10,000. Ag electrodes used. Good differential amplifiers' with CMRR should have rejection ratio close to 100,000. In other words, the signals are amplified 100,000 times more than unwanted potentials appearing as a common mode voltage. The input impedances of the most amplifiers range from 100 kΩ to hundreds of MΩs.

2.1 EMG Amplifiers Technical Specifications

Instrumentation Amplifier Gain = 10, CMRR = 65 dB, Gain select amplifier: Gain = 30; Low-pass filter: Upper cut-off-frequency = 10 kHz; Gain = 2; High-pass filter: Lower cut-off frequency = 0.05 Hz, Gain = 2; Input impedance: >200 MΩs., (CMRR = 65 dB); Number of channels: 5, expandable as per the user requirement.; Sampling rate: 8-kHz per channel; user choices available; Notch/Band-pass Filter: 50 Hz.

2.2 Computer System Configuration

Computer: IBM certified Intel Pentium III Processor: (Intel chipset); Memory: 64 MB RAM; Clock speed: 500 MHz; 1.44 MB FDD; 10 GB HDD; SVGA Card with 1 MB RAM, 2 serial, 1 parallel-port, keyboard, mouse and mouse pad. Multimedia sound card, the Windows and Microsoft Disc (MS-DOS) environment operating systems. The
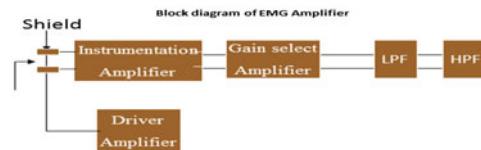
Fig. 1 Block diagram of MG amplifier with driver mechanism amplifier bandwidth: 0.5–10 kHz

hardware design methods are explained below. The EMG circuitry envisages mainly four stages: 1. Instrumentation amplifier with a driver circuit, 2 Gain-set amplifier, 3. Low-pass filter, 4. High-pass filter. The EMG signals are acquired with fine innocuous intramuscular wire 50 μm diameter and flat surface electrodes placed on the skin of the muscle under investigation. The signals picked up by the electrodes are applied to the body of the subject are passed to the amplifier circuitry through coaxial cables. Different stages of the circuitry are described below and the block diagram of the EMG amplifier can be seen in Fig. 1.

2.3 Instrumentation Amplifier

The input impedance offered by one Op-Amp differential amplifier is far too less for high resistance sources like the human-body. Here it is essential that the body does not source any kind of current because it is required to drive the circuit. The requirement is of an amplifier-circuit that has high-end input-impedance so-as-to faithfully effectively reproduce the signal fed to it. This kind of requirement is perfectly provided by the Three-Op-Amp instrumentation amplifier. In addition to high input impedance, the amplifier configuration also has a very high common-mode rejection ratio (CMRR), which effectively removes the 50 Hz line frequency inherent in most of the signals. The circuit diagram can be seen in Fig. 2 (for this circuit, $R_1 = R_3 = R_4 = R_5 = R_6 = R_7 = 10$ kΩs; $R_2 = 2.2$ kΩs.

Gain-set amplifier: The second stage of the amplification is done by, Gain-set amplifier. The EMG signal captured typically is 100 mV. After the instrumentation amplifier stage, the voltage is amplified to 1 mV range. Now the noise inherent in the filters and other signal conditioning
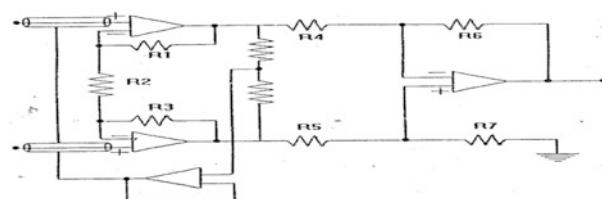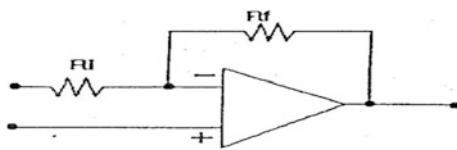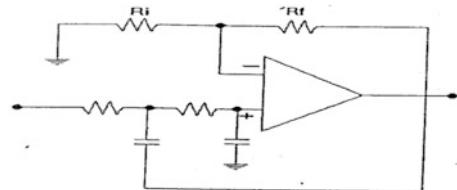
Fig. 2 Circuit diagram of instrumentation Op-Amp; R1 = R3 = R4 = R5 = R6 = R7 = 10 kΩ; R2 = 2.2 kΩ

Fig. 3 Circuit diagram of gain-set amplifier

Fig. 4 Circuit diagram of low-pass filter

Fig. 5 Circuit diagram of high-pass filter

processes is of the same order and thus the signal fed to these circuits will not be accurate. To eliminate this we have employed another stage of the—amplification which amplifies the signal only. A single Op-Amp with gain adjusted by the resistors is adequate to the serve purpose. For EMG, a gain of 30 is set at this stage. The circuit diagram can be seen in Fig. 3 (The gain for this circuit is given by: $G = (R_f + R_i)/(R_i)$).

The two resistors of non-inverting amplifiers are hooked together and ground connection is eliminated. This circuit can be analyzed as follows:
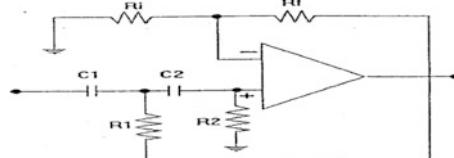
Common mode: If $V_1 = V_2$ as in the common mode, the current through the resistor R_1 is zero. Since no cur-rent flows through the inputs of the Op-Amps, current through R_2 is also a zero. Hence at both the outputs the voltage appearing is V_1 and the common mode gain $G_c = 1$. Differential mode: If $V_1 \neq V_2$ as in the differential mode, the voltage across R_1 is $V_1 - V_2$. This causes a current to flow through R_1 that also flows through resistor string R_2, R_1, R_2. Hence, the output voltage becomes:

$$V_3 - V_4 = i(\text{since} : R_2 + R_1 + R_2). \text{Where} - \text{as}, V_1 - V_2$$
$$= i * R_1.$$

Therefore, differential gain $G = (V_3 - V_4)/(V_1 - V_2) = (2R_2 + R_1)/(R_1)$.

Since, the G_c is 1, the CMRR is equal to the G_d, which is usually greater than unity. The instrumentation amplifier has high input impedance, a high CMRR, and a gain that can be changed by adjusting R_1.

Low-pass filter: A second order low-pass filter is obtained, by cascading two RC (resistor capacitor) net-works. The input signal will undergo two-step attenuation first by R_1C_1 stage and then by R_2C_2 stage. To improve the sharpness of amplitude response within the vicinity of the cut-off frequency an Op-Amp is introduced in the circuit

as shown in Fig. 4 (This is in non-inverting mode where positive feedback is employed through capacitor©).

High-pass filter: To improve the sharpness of amplitude response within the vicinity of the cut-off frequency an Op-Amp is introduced in the circuit as shown in Fig. 5 (this is in non-inverting model where feedback is employed through C).

The capacitor is lifted from the ground and connected to Op-Amp output. This connection provides positive feedback path and is effective only within the vicinity of cut-off where sharp-ness is needed.

Microelectrodes: A set of five miniature microelectrodes each 50 μm, from California Fine Wire Company, USA, were used in each patient. Since the electrodes are inserted into specific target muscles, unlike in the case of surface EMG, flexor electrode amplifiers contributed only to flexor con-traction muscles (i.e., FCR, FCU, during writing during mirror movements), extensor electrode amplifiers con-tributed only to extensor contraction muscles (i.e., ECR, FCR, during writing and during mirror movements) and 5th electrode amplifier contributed only to 5th muscle contraction (i.e., ADP/APB, etc.) during writing and during mirror movements.

Recording technique: In most EMG recording systems, frequency responses of amplifier recording should match frequency spectrum of the EMG waveform—signal. Since relative movements of electrodes cause low frequency noises, and hence high pass filtering is must (lower-cutoff 0.5 Hz and upper 20 kHz maximum for a typical lower cutoff). Because, surface EMG frequencies as high as 0.5 kHz, therefore, band-pass filters be used.

Signals acquired and noise suppressed: The next step carried our study is suppressing the noise blocks from signals and computing the number of signal units from each muscle. From each signal (of 30,000 sample points) 300 blocks of length 100 each are constructed and their means are computed. Also the standard deviations (SDs) of these are calculated, after 'centering' the signal (i.e., subtracting the DC components). The signal amplitude values within 1 standard deviation are treated as 'noise' and the means of blocks whose mean values are within 1 SD are taken as zero i.e., containing only 'noise'; only those blocks whose means are greater, in absolute value, than these SDs, are considered as having 'signal components'.

Fig. 6 Subject writing after insertion of micro wire electrodes with indigenous EMG prototype

Fig. 7 A close up of writing and signal recording with Indigenously developed EMG prototype

3 Results

12 patients (namely, A1, A2,…, A12) with writer's cramp (8 with concordant and 4 with discordant MMs) were assessed. The signals recorded (see Figs. 6, 7 and 8) and the number of signal units computed in RHWS and in LHWS muscles of patient A7 is shown in Fig. 7. Each patient was asked to write initially with their right hand and then with their left hand using a standard paragraph dictated to them, while the EMG was recorded from all the five channels. Each test consisted of four randomized trials, each trial lasted for 10 s

duration, with a rest period of 1–2 min between each trials. All five channels of EMG signals data were recorded digitized using a 12-bit A/D converter and processed on-line. The target muscles under EMG monitoring of active movement and movement of the needle was also observed visually. A close up of the signal recording can be viewed, depicted in Figs. 6 and 7.

Sterile nylon coated innocuous fine wire electrodes were introduced into five muscles for a detailed and muscle specific EMG recording. As most discordant muscle movements are those of wrist, 4 muscles causing flexion and

Fig. 8 **a** LH muscle signals of patient 1 D group **b** RH muscle signals of patient 1D group
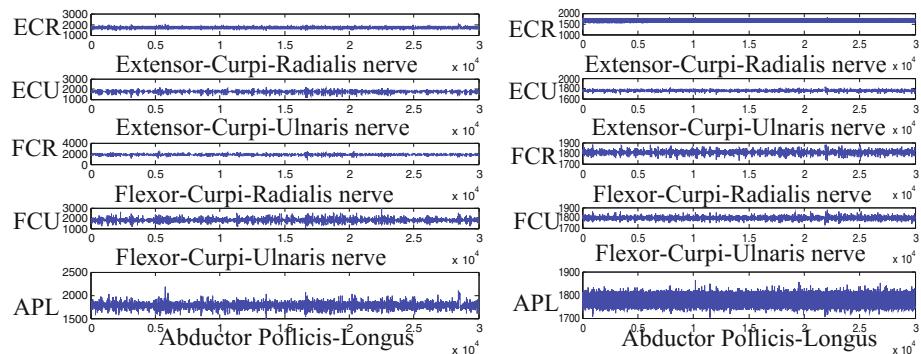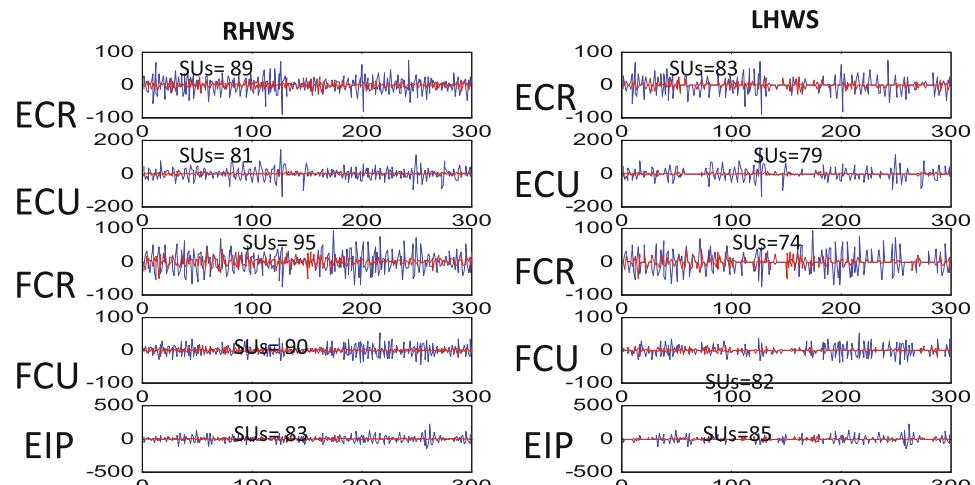
Fig. 9 A7 (Discordant group). RHWS: Right hand writing signal; LHWS: left hand writing signal

extension of wrist viz, ECR, ECU, FCR, FCU were analyzed in all patients and one more muscle (as decided by the Neurologist, for example, ADP, APL, etc. which showed the maximum discordance of mirror dystonia [13–16]) on the right hand was included. EMG signals were simultaneously recorded from all five muscles while the patients inscribed with their right hand (Right hand writing signal—RHWS) and then with their left hand (left hand writing signal—LHWS) (Fig. 8a, b).

For the patient A1, the signal units in RHWS: 101 in ECR, 81 in ECU, 84 in FCR, 85 in FCU, and 65 in 5th muscle. Signal units in the LHWS: 150 in ECR, 107 in ECU, 96 in FCR, 94 in FCU, and 151 in 5th muscle, similarly, for patients A2, A3,…, A12 can be seen. The same is depicted in the computed graphs (Fig. 9). Blue: RHWS, Red: LHWS, Left half signals are with noise, and Right half signals are with noise suppressed. Due to large space only one patient A1 data (signal) is shown here.

4 Conclusions

At present, the system is able to record five channels data. The duration of EMG noise distribution changes according to the duration of muscle activity. However, the noise distribution occurs most commonly in regions with underlying muscle, specifically flexor aspect of fore arm muscles. Thus, EMG noise most commonly occurs in channels including the frontal and temporal electrodes. This study showed significant quantifiable EMG differences in the signals seen while writing with the right and left hands between those writer's cramp patients with concordant mirror movements (C group see Fig. 9) versus those with discordant mirror movements (D group). In our computation, we found that the number of signal units in other words motor neurons in dominant intrinsic right hand is more than in the non dominant intrinsic left hand, and hence there is a quantifiable difference between the two groups (concordant and discordant).

Our future study involved longitudinal follow-ups and correlations with a normal control population in future to better comprehend Writer's cramp phenomena.

References

1. John, V. Basmajian., Carlo, J. De Luca: Muscles Alive: Their Functions Revealed by Electromyography. Williams and Wilkins (1985).
2. Ronald, S. Le Fever., Carlo, J. De Luca.: A Procedure for Decomposing the Myoelectric Signal Into Its Constituent Action Potentials—PART I: Technique, Theory, and Implementation. Journals of IEEE Trans. Biomed. Eng 29 (3), 149–157 (1982).
3. Ronald, S. Le Fever., Carlo, J. De Luca.: A Procedure for Decomposing the Myoelectric Signal Into Its Constituent Action Potentials—PART II: Execution and Test for Accuracy. Journals of IEEE Trans. Biomed. Eng 29 (3), 158–163 (1982).
4. Kevin, C. McGill., Leslie, J. Dorfman.: High—Resolution Alignment of Sampled Waveforms. IEEE Transactions on Biomedical Engineering 31(6), 462–468 (1984).
5. Kevin, C. McGill.: Optimal Resolution of Superimposed Action Potentials. IEEE Transactions on Biomedical Engineering 49 (47), 640–650 (2002).
6. L, J. Dorfman., K, C. McGill.: AAEE minimonograph #29: Automatic quantitative electromyography. Muscle and Nerve 11, 804–818 (1988).
7. Stashuk, D., De Luca, C. J.: Update on the decomposition and analysis of EMG signals. In: Desmedt, J.E. (Ed.): Computer-Aided Electromyography and Expert Systems. Holland, Elsevier 39–47 (1989).
8. D, Stashuk., H, De. Bruin.: Automatic decomposition of selective needle-detected myoelectric signals. IEEE Trans. Biomed. Eng 35, 1–10 (1988).
9. McGill, Kevin. C., Dorfman, L.J.: Automatic Decomposition Electromyography (ADEMG): Validation and normative data in the brachial biceps. Electroencephalography Clinical Neurophysiology 61, 453–461 (1985).
10. Lauren, H. Smith., Todd, A. Kuiken., Levi, J. Hargrove.: Evaluation of Linear Regression Simultaneous Myoelectric Control Using Intramuscular EMG. IEEE Trans. Biomed. Eng 63 (4), 737–746 (2016).
11. Jia-Jin, Jason. Chen., Richard, Shiavi.: Temporal feature Extraction and Clustering Analysis of Electromyographic Linear Envelopes in Gait Studies. Journals of IEEE Trans Biomed. Eng. 46(7), 797–809 (1999).
12. LiQun, Zhang., Richard, Shiavi.: Clustering Analysis and Pattern Discrimination of EMG Linear Envelopes. Journals of IEEE Trans. Biomed. Eng 38(8), 777–784(1991).
13. Grundmann, K.: Primary torsion dystonia. Arch Neurol 62, 682–685 (2005).
14. Jancovic J.: A text book movement disorders. 5th Edition 2007.
15. V, Rama. Raju.: A Study of Advanced Multi-Channel EMG in Writer's Cramp. MD/PhD Thesis sub-mitted to Nizam's Institute of Medical Sciences, Hyderabad, India, Aug (2009).
16. V. Rama Raju, A Study of Multi-Channel EMG in Writer's Cramp Signals. PhD Thesis submitted to Nizam's Institute of Medical Sciences, Hyderabad, India, Dec (2003).

Design of Linear Phase Filter by Using q-Bernstein Polynomial

Boonchana Purahong, Isoon Kanjanasurat, Vanvisa Chutchavong,
Kanok Janchitrapongvej, and Tuanjai Archevapanich

Abstract

The aim of this paper presents a design of IIR filter by using q-Bernstein polynomial. There are two parameters for adjusting a characteristic of frequency response. Stopband and slope of phase are adjusted by varying parameter ε. The advantage is a linear phase and maximally flat more than Butterworth and Chebyshev. The stability can guarantee with Mihailov's criterion.

Keywords

q-Bernstein polynomial • Linear phase • Mikhailov's stability

1 Introduction

In a type of filter, there are two forms that recursive and non-recursive. A linear phase is achieved by non-recursive filters. However, the feedback paths can be unstable, and the realization of recursive filters is less costly regarding hardware. Transformation is a part of the technique to design transfer functions. These changes maintain magnitude characteristics indeed, and the behavior is not predictable for the phase characteristics.

The advantage of Butterworth filter is maximally flat magnitude response in passband and simple to create a circuit. A Chebyshev filter has a slope of cutoff frequency better than Butterworth. But it has a ripple in the passband and a lot of parameter for adjusting magnitude response. Both of this filter has a non-linear phase.

The advantages of a filter are designed by using Bernstein polynomials are parameters that adjust magnitude and phase [1, 2]. Moreover, it flexible for the variable of phase. In this paper use the advantage of Bernstein filter to obtain a low-pass transfer function and present a technique to design linear phase filters using q-Bernstein Polynomials in the analog domain.

2 Mathematical Model

The q-Bernstein polynomial is a part of approximation theory that a uniform approximation by polynomials to continuous functions [3]. Let f(x) is a function defined in the interval [0, 1]. The q-Bernstein polynomial $B_n(f,q; x)$ of n degree and which approximates f(x) is

$$B(f; x, a) = \sum_{i=0}^{n} f\left(\frac{i}{n}\right) \binom{n}{i}_q x^i (1-x)_q^{n-i} \qquad (1)$$

Function in Bernstein that use to approximate for low-pass filter is

$$f\left(\frac{i}{n}\right) = \begin{cases} 1, & 0 \le i \le n-k \\ 0, & n-k+1 \le i \le n \end{cases} \qquad (2)$$

where k is the point of zero.

Let q > 0 For any n = 0, 1, 2… the q-integer $[n]_q$ is defined by

$$[n]_q \triangleq 1 + q + \ldots + q^{n-1} \qquad (3)$$

If n is zero, $[0]_q = 0$ and the q-factorial $[n]_q!$ is

$$[n]_q! \triangleq [1]_q[2]_q \ldots [n]_q \ldots, [0]_q! = 1 \qquad (4)$$

B. Purahong (✉) · I. Kanjanasurat · V. Chutchavong
Department of Computer Engineering, Faculty of Engineering,
King Mongkut's Institute of Technology Ladkrabang, Bangkok,
Thailand
e-mail: yuna001@gmail.com

I. Kanjanasurat
e-mail: pe_win99@hotmail.com

K. Janchitrapongvej
Faculty of Science and Technology, Southeast Bangkok College,
Bangkok, Thailand

T. Archevapanich
Faculty of Engineering and Architecture, Rajamangala University
of Technology Suvarnabhumi, Nonthaburi, Thailand

the q-binomial or the Gaussian coefficient for integers $0 \leq k \leq n$ is defined by

$$\begin{bmatrix} n \\ i \end{bmatrix}_q \triangleq \frac{[n]_q!}{[i]_q![n-i]_q!} \qquad (5)$$

and

$$(1-x)_q^{n-i} = \prod_{s=0}^{n-i-1}(1-q^s x) \qquad (6)$$

Substituting (2) in (1), and using an additional subscript k is

$$B(f;x) = \sum_{i=0}^{n-k} \binom{n}{i}_q (1-x)_q^{n-i} \qquad (7)$$

the interval of q-Bernstein is C(0, 1) for x is changed to C(0, α) for Ω by the transformation [4]

$$x = \frac{\Omega^2}{\Omega^2 + 1} \qquad (8)$$

Ω is low pass prototype filter axis. Transformation from Ω-axis to ω-axis is −1/ω and substitute to (8) is

$$x = \frac{1}{\omega^2 + 1} \qquad (9)$$

moreover, ω is s/j that s-domain

$$x = \frac{1}{1-s^2} \qquad (10)$$

Finally, q-Bernstein polynomial for approximate low pass filter is

$$B(f;s) = \sum_{i=0}^{n-k} \binom{n}{i}_q \left(\frac{1}{1-s^2}\right)^i \left(\frac{s^2}{s^2-1}\right)_q^{n-i} \qquad (11)$$

Classical approximation theory for analog filters requires first specifying the characteristic function. transfer and characteristic functions by q-Bernstein polynomial is

$$|N(s)|^2 = \frac{H_0^2}{1 + \varepsilon^2 \left(\sum_{i=0}^{n-k} \binom{n}{i}_q \left(\frac{1}{1-s^2}\right)^i \left(\frac{s^2}{s^2-1}\right)_q^{n-i}\right)^2} \qquad (12)$$

The transfer function magnitude squared lowpass filter have poles and zeros. For stability, the poles are selected in the left-hand-side of the s-plane and the left-hand-side zeros for minimum phase.

3 Results

Characteristic of low pass filter by using q-Bernstein can vary three parameters. First, H_0 is direct variation magnitude. If a value of H_0 is large, magnitude response starts in a large value. but phase is still stable. Magnitude and phase of vary H_0 are shown in Fig. 1 that fix $\varepsilon = 50$ and q = 1.

Magnitude and phase can change by adjusting ε. If ε near zero, it can make constant phase. Characteristic of vary ε are shown in Fig. 2 that fix $H_0 = 50$ and q = 1.

Last of the parameter is q. It changes a cut off frequency and effect to phase. Characteristic of vary q are shown in Fig. 3 that fix $H_0 = 0.02$ and $\varepsilon = 50$.

The transfer function of q-Bernstein filter order four is created by using parameter n = 2, e = 50, $h_0 = 0.02$ and

Fig. 1 A convergence of low pass filter by varying H_0
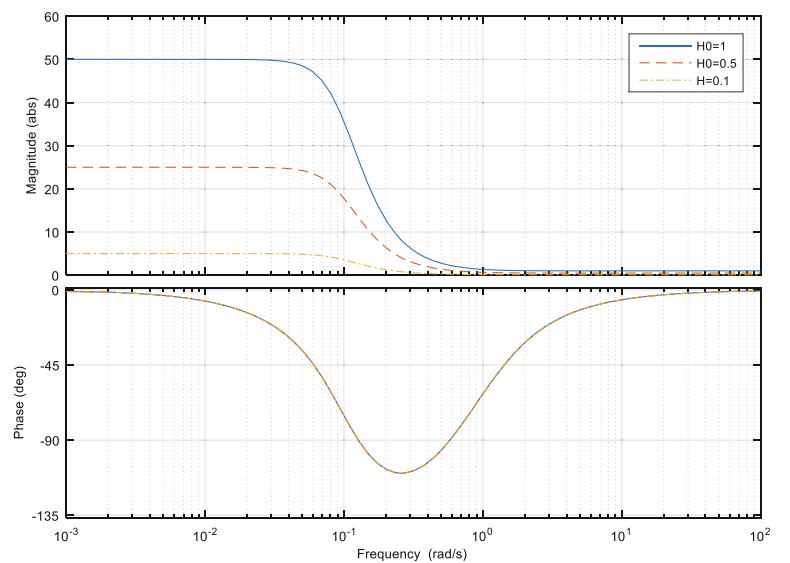
Fig. 2 Magnitude and phase by varying ε
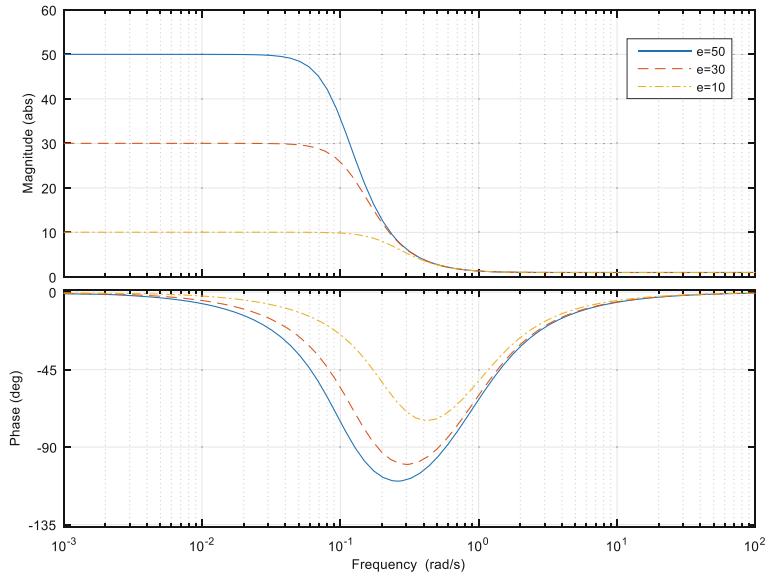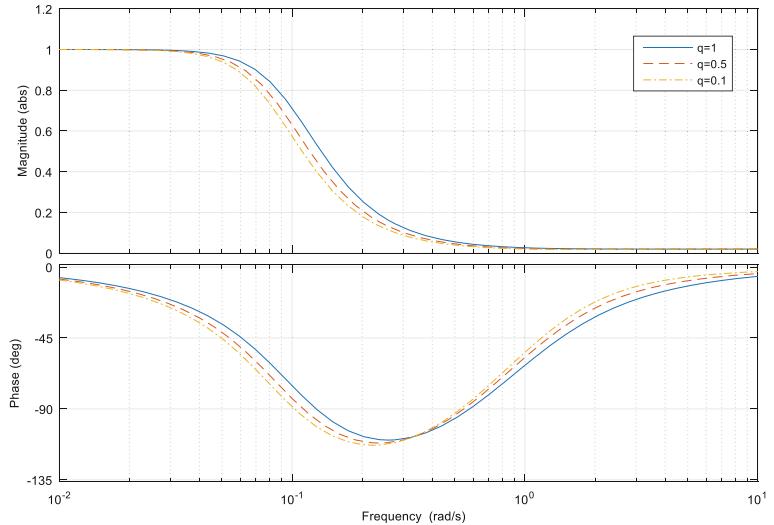
Fig. 3 Magnitude and phase of the q-Bernstein filter

q = 1. It selects pole and zeroes in the left-hand-side of s-plan. Finally, transfer function of this filter is shown in Eq. 13

$$N(s) = \frac{0.02s^4 \ + \ 0.08s^3 \ + \ 0.12s^2 + \ 0.08s \ + \ 0.02}{s^4 \ + \ 2.971s^3 \ + \ 2.413s^2 \ + \ 0.3132s \ + \ 0.02} \tag{13}$$

Comparison of frequency response between q-Bernstein in Eq. 13, Butterworth and Chebyshev in order 4 is shown in Fig. 4. q-Bernstein is similar Butterworth that maximally flat magnitude response in passband. Phase response of q-Bernstein is close to constant more than Butterworth and Chebyshev.

The Mikhailov's criterion that one of the criteria for the stability of linear systems of automatic control. Defines which nth order polynomials be defined as

$$D(j\omega) = u(\omega) + jv(\omega) \tag{14}$$

where

$$u(\omega) = a_0 - a_0\omega^2 + \cdots a_{2n}\omega^{2n}$$
$$v(\omega) = a_1\omega - a_3\omega^3 + \cdots a_{2n-1}\omega^{2n-1}$$

This method is used widely in the analog control system that the contour is encircled around the original in the anticlockwise direction. It has proven to be stable.

Fig. 4 a comparison of frequency response between q-Bernstein, Butterworth, and Chebyshev
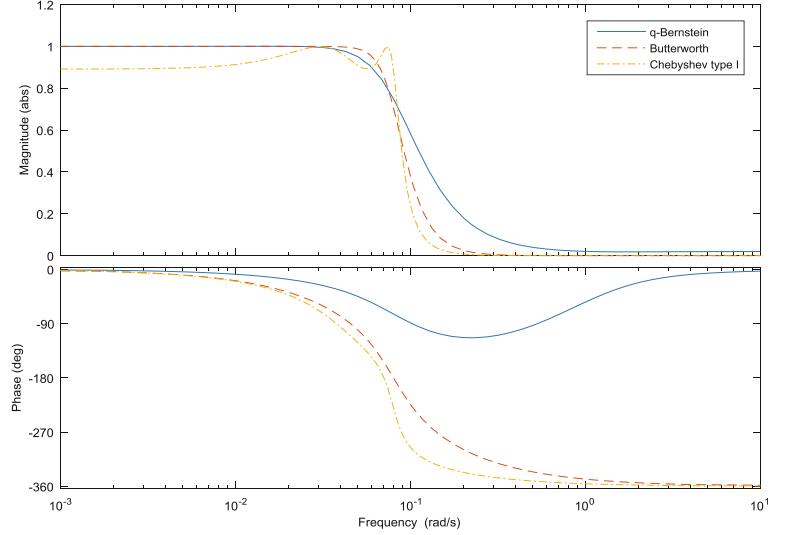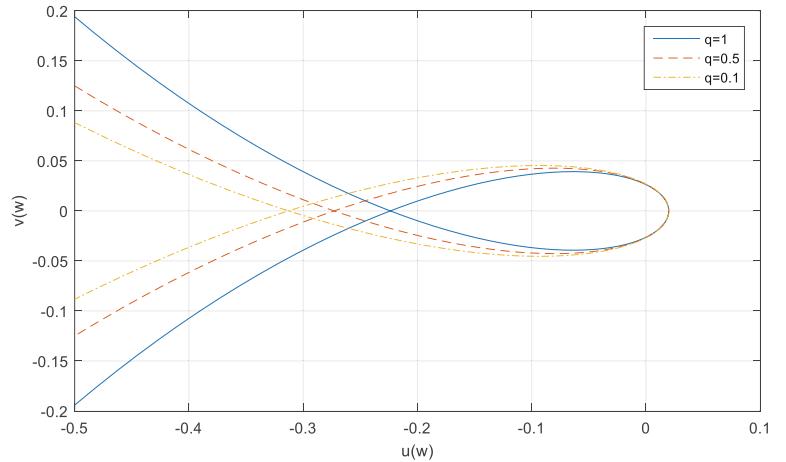
Fig. 5 Mikhailov's stability of q-Bernstein filter

Mikhailov's hodograph is plotted in Fig. 5. It shows a contour of q-Bernstein which vary parameter q. All of the q-Bernstein filter design has a stability that encircled the origin point of the Cartesian coordinate in the anticlockwise direction.

4 Conclusion

Design of low pass filter by using q-Bernstein is better than Bernstein because it has parameter q for adjusting. This filter has maximally flat magnitude response, and phase is constantly more than Butterworth, and Chebyshev. Finally, it has stability that proves by Mikhailov.

Conflict of Interest The authors declare that they have no conflict of interest.

References

1. D. Baez-Lopez.: The Bernstein filter-a new class of linear phase filter approximation. J CIRCUITS AND SYSTEMS 1991, pp. 704–707. IEEE.
2. D. Baez-Lopez.: Linear Phase IIR Digital Filters Using the Bernstein Polynomial. ICASSP-91, vol. 3, pp. 1661–1664 (1991).
3. Sofiya Ostrovska.: q-Bernstein polynomials and their iterates. Journal of Approximation Theory, Volume 123, Issue 2, 232–255 (2003),
4. Isoon Kanjanasurat.: Gain Equalizer by Four Parameters Logistic Bézier Bernstein Polynomial. ICEIC 2017, pp. 330–333 (2017).

Analysis of Kinematic Parameters Relationships in Normal and Dysgraphic Children

Diamante Morello, Milos Ajcevic, Iolanda Perrone, and Agostino Accardo

Abstract

Kinematic analysis of handwriting, using digital tablet together with appropriate tests and processing software, allows evaluation of subject graphomotor abilities. Several studies focused on the kinematic parameters extracted from the writing of both normal subjects and subjects with specific disorder, such as dysgraphia, recorded during simple tasks. However, relationships between these parameters have not yet been analyzed. The aim of this study was to examine and identify possible links between kinematic parameters like Amplitude (SA), Duration (SD) and Peak Velocity (PkVS) of Strokes extracted from handwriting and their changes between normal and dysgraphic children. Fifty normal and eighteen dysgraphic children, attending classes from 2nd to 5th grade of primary school, were involved in the study; three cursive tests were administered and analyzed. Results showed a linear relation between SA and PkVS parameters with a similar slope in both groups and reduced peak velocities in some dysgraphic children. A linear relationship was also present between SA and SD parameters in all tests for normal children while an unclear relation was found for dysgraphic children. The latter showed longer durations and slightly lower amplitudes than in normal subjects, in all tasks, as expected in case of poor fluency.

D. Morello (✉) · M. Ajcevic · A. Accardo
Department of Engineering and Architecture,
University of Trieste, Trieste, Italy
e-mail: dmorello@units.it

M. Ajcevic
e-mail: majcevic@units.it

A. Accardo
e-mail: accardo@units.it

I. Perrone
Department of Childhood Development,
ULSS7 Pieve di Soligo, Italy
e-mail: iolanda.perrone@ulss7.it

Keywords

Kinematic parameters • Handwriting • Dysgraphia

1 Introduction

Handwriting is the widest taught fine motor skill for school-age children and its development is crucial for performance in school, motor and cognitive development [1]. Digital tablets technology has brought an innovative approach to measure kinematic characteristics of handwriting movements allowing evaluation of the level of graphomotor abilities acquired by a subject. Many recent studies were carried out through writing acquisitions performed by means of these tablets that allow objective quantitative analyses of the writing quality as well as characterization of the handwriting process [2, 3]. The results of these studies indicate that some kinematic parameters could be used to discriminate poor from good hand motor performance [4].

In particular, several studies focused on the kinematic parameters extracted from the writing of both normal subjects and those with specific disorders, such as dysgraphia, recorded during simple tasks. This latter condition, defined as a disorder or a difficulty in the production of written language related to writing mechanics [5], is recognized as representing a distinct deficit. Mainly duration, length and velocity parameters were extracted to describe the hand movement and to provide information on the level of development achieved by a subject [6]. A high number of segments per letter and multiple direction reversals were used to provide information about subject's writing fluency and its ability to plan and execute the task in an efficient and accurate manner [7]. The number of velocity peaks, stroke velocity, pause time per stroke and the ratio between in air and on paper measures showed that dysgraphic children have increased pause time per stroke and number of directional velocity changes in respect of normal children [8]. Furthermore, handwriting quality and velocity varied with

the length of the writing task and these changes were different between children with and without dysgraphia [9]. In particular, horizontal stroke velocity, grip force and pressure have increased over time while vertical stroke velocity have decreased in children.

On the other side, few studies [10–12] focused on the relationships among writing kinematic parameters. An analytical expression of the relationship between curvature and velocity during hand-curved movement was derived in the freehand drawing of ellipse and spiral figures: in this case, the elliptical movement follows the 1/3 power law while the spiral movement follows the 2/3 power law [10]. A previous study [11] confirmed the isochrone principle (i.e. movement mean velocity increased with trajectory linear extension) and also found a 2/3 power law between tangential and curvature velocities, asserting that trajectory and kinematic of drawing movements are mutually constrained by functional relationships that decrease degrees of freedom of hand movement. Finally, a family of lognormal models, that provide analytical representations of strokes of a generated trajectory of the pen tip, were considered as the basic unit of handwriting [12]. This kind of mathematical model well describes the impulse response of the neuromuscular system. The log normality of the velocity patterns can be interpreted as reflecting the behavior of subject who correctly controls his movements.

The aim of this study was twofold: (a) to examine and identify possible relationships between kinematic parameters extracted from handwriting (e.g. amplitude, duration and peak velocity of strokes), and (b) to evaluate possible differences between normal and dysgraphic children, useful for an early identification of dysgraphia.

2 Materials and Methods

2.1 Subjects

In order to determine existing relation among kinematic parameters involved in writing, 68 (50 normal and 18 dysgraphic) children from 2nd to 5th grade of the Primary School with a medium cognitive level, right-handed and Italian mother tongue, were recruited. The Department of Childhood Development at the ULSS 7 of Pieve di Soligo (TV), Italy, followed the dysgraphic children. Normal children did not exhibit organic pathologies or handwriting problems while dysgraphic children presented graphomotor difficulties diagnosed by a child psychiatrist in collaboration with a logopedist, a psychologist and a neuropsychomotor therapist by using standard evaluation protocols. For each child, the informed consent from the parents was previously acquired.

2.2 Tasks

A series of three cursive tests (nominally LE, A and F tests), involving base motor skills, was performed. The LE test consisted in the writing, for a minute, of a sequence of *lelele* as fast as possible without pen lifting. This task did not involve linguistic competences. On the other hand, the A and F tests required the children to copy as accurately as possible (A test) and as fast as possible (F test) a sentence containing all the letters of Italian alphabet and some specific combinations (such as *br*, *pr*, *ll*, *ss* and *zz*), requiring adequate linguistic competences. The sentence was: *in pochi giorni il bruco diventò una bellissima farfalla che svolazzava sui prati in cerca di margherite e qualche quadrifoglio* (in a few days the caterpillar became a beautiful butterfly that fluttered on the grass looking for daisies and four-leaf clover).

2.3 Procedures and Parameters

The handwriting movements of children were acquired by using a commercial tablet (Wacom, Inc., Vancouver, WA, Model INTUOS 2.0). In order to reproduce a daily school context, a sheet of paper (adequate to the class of schooling) was placed on the tablet surface and a specific ink pen was used. The vertical and horizontal displacements of the pen were sampled at 100 Hz and acquired with a spatial resolution of 0.01 mm. From curvilinear velocity, obtained by combining horizontal and vertical instantaneous position derivatives, the strokes were identified as the tracts between two successive minima of this velocity profile. Mean stroke duration (SD, in ms), mean stroke amplitude (SA, in mm) and mean stroke peak velocity (PkVS, in mm/s) were calculated and the SA versus SD as well as the SA versus PkVS linear relationships were extracted and compared between normal and dysgraphic children. In particular, for all tasks the slope and intercept values of each linear relation were calculated and separately compared between the two groups by using t-Student statistical test; the differences were considered significant for p-value <0.05. All the analyses were carried out using a proprietary software written in MATLAB®.

3 Results

Figure 1 shows the relationships between Amplitude (SA), Duration (SD) and Peak Velocity (PkVS) of Strokes for normal and dysgraphic children in the three tests. A linear relation was found in the group of normal children both in the SA versus SD and in the SA versus PkVS plots for all the three tests. A similar trend with comparable slopes but

Fig. 1 Relationships between mean Amplitude (SA), Duration (SD) and Peak Velocity (PkVS) of strokes in normal (red circles) and dysgraphic (black crosses) children, in the three writing tests. Dotted lines represent linear fitting of data (slopes and intercepts in Tables 1 and 2) (Color figure online)
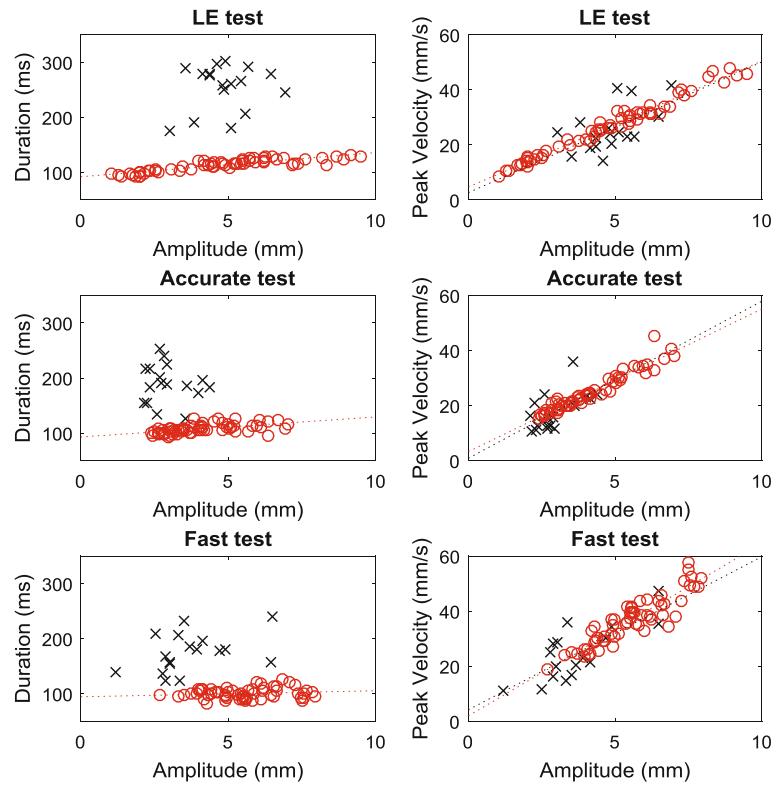
Table 1 Amplitude/Peak velocity linear relationship parameters

	Normal children		Dysgraphic children	
	Slope (s^{-1})	Intercept (mm/s)	Slope (s^{-1})	Intercept (mm/s)
LE test	4.57	4.73	4.75	2.65
A test	5.18	3.26	5.70	0.87
F test	6.26	1.97	5.56	4.19

Table 2 Amplitude/Duration linear relationship parameters

	Normal children		Dysgraphic children	
	Slope (ms/mm)	Intercept (ms)	Slope (ms/mm)	Intercept (ms)
LE test	4.39	92.2	7.81	216.3
A test	3.63	93.0	−5.71	206.6
F test	1.09	94.6	10.46	136.1

slightly different intercepts (Tables 1 and 2) was present in dysgraphic children only in the SA versus PkVS diagram. In fact, an unclear relation between SA and SD was found for dysgraphic children. In the SA/PkVS relation, dysgraphic and normal children presented in the LE test comparable SA and PkVS values with a greater variability for PkVS in children with dysgraphia. In fact, there were not significant differences in the slope and intercept values between the two groups of children (Table 3). In the other two tests,

Amplitude and Peak velocity values were generally lower in dysgraphic than in normal children with greater PkVS variability in the Fast test than the Accurate test, in both groups. Significant differences were found only between the intercept values (Table 3). In all cases, the PkVS increased with SA. In the SA/SD relation, dysgraphic children showed Duration values significantly longer and greater variability than normal children in all tests. In all tests, there were significant differences in the slope and intercept values

Table 3 p-Value of the differences between slopes and intercepts both in the amplitude/duration and the amplitude/peak velocity relationships in the normal and dysgraphic children

	Amplitude/Duration		Amplitude/Peak velocity	
	Slope	Intercept	Slope	Intercept
LE test	n.s.	<0.001	n.s.	n.s.
A test	0.037	<0.001	n.s.	0.044
F test	0.014`	<0.001	n.s.	0.037

except for the slope values of the LE test (Table 3). In normal children, Stroke Duration slightly increased with Amplitude.

4 Discussion

Kinematic parameters extracted from handwriting reflect the influence that the motor development and the cognitive maturation have on the writing skills providing information about the gained grade [1, 2, 4, 9, 12–14]. It is also know that graphomotor difficulties produce some alterations in these parameters [9, 13] but their mutual relation in normal and dysgraphic subjects haven't been explored yet. Our results concerning the relation between SA and PkVS parameters show a linear trend with a similar slope in both groups (confirmed by the statistical analysis) but shorter trajectories (lower SA), with corresponding reduced peak velocities, in dysgraphic children, in the tests requiring linguistic competences. This result could be due to a high fragmentation of the writing movement present in dysgraphic children [13].

A linear relationship was also found between SA and SD parameters in normal children, in the three tests, while unclear relations were observed in children with writing difficulties. The latter showed longer durations (in all tests) and slightly lower amplitudes (in the Accurate and Fast tests) than in normal subjects. This confirms the results of previous studies [8, 13] in which dysgraphic children had longer stroke duration during tasks than normal subjects, as expected in case of poor fluency, reflecting the maturation and automation lower grade of the motor ability in children with writing difficulties [14]. Furthermore, reduced amplitudes and increased durations produce smaller mean velocities despite comparable peak velocities resulting in a different stroke velocity profile. Finally, the slight differences found between test LE and the other two tests could be due to different attentive levels depending on the task (especially when linguistic competences are required [13]) that should be taken into account when choosing the test to be performed. It is worth noting that despite the considered children had different ages, with consequent probable different parameter values, the difference in the

amplitude/duration relationship were however significant for all the tests, except the slope of the LE test.

In conclusion, this study analyzed kinematic parameters extracted from handwriting movement identifying possible relationships between Amplitude (SA), Duration (SD) and Peak Velocity (PkVS) of Strokes. Clear differences were found between normal and dysgraphic children demonstrating in the latter some reduced motor performance. The differences in the relationships among some kinematic parameters found in this study could serve to create a prediction model useful for an early identification of children with dysgraphia.

Conflict of Interest Statement The authors declare that they have no conflict of interest.

References

1. Accardo, A.P., Genna, M., Borean, M.: Development, maturation and learning influence on handwriting kinematics. Human Movement Science 32(1), 136–146 (2013).
2. Rosenblum, S., Chevion, D., Weiss, P.L.: Using data visualization and signal processing to characterize the handwriting process. Pediatric Rehabilitation 9(4), 404–417 (2006).
3. Van Galen, G.P., Weber, J.F.: On-line size control in handwriting demonstrates the continuous nature of motor programs. Acta Psychologica 100(1), 195–216 (1998).
4. Mavrogiorgou, P., Mergl, R., Tigges, P., El Husseini, J., Schröter, A., Juckel, G., Zaudig, M., Hegerl, U.: Kinematic analysis of handwriting movements in patients with obsessive–compulsive disorder. Journal of Neurology, Neurosurgery and Psychiatry 70 (5), 605–612 (2001).
5. Hamstra-Bletz, L., Blote, A.W.: A longitudinal study on dysgraphic handwriting in primary school. Journal of Learning Disabilities 26(10), 689–99 (1993).
6. Mergl, R., Juckel, G., Rihl, J., Henkel, V., Karner, M., Tigges, P., Schröter, A., Hegerl, U.: Kinematical analysis of handwriting movements in depressed patients. Acta Psychiatrica Scandinivica 109(5), 383–391 (2004).
7. Rosenblum, S., Dvorkin, A.Y., Weiss, P.L.: Automatic segmentation as a tool for examining the handwriting process of children with dysgraphic and proficient handwriting. Human Movement Science 25(4–5), 608–621 (2006).
8. Chang, S.H., Yu, N.Y.: Handwriting movement analyses comparing first and second graders with normal or dysgraphic

characteristics. Research in Developmental Disabilities 34(9), 2433–2441 (2013).

9. Kushki, A., Scwellnus, H., Ilyas, F., Chau, T.: Changes in kinetics and kinematics of handwriting during a prolonged writing task in children with and without dysgraphia. Research in Developmental Disabilities 32(3), 1058–1064 (2011).

10. Huh, D., Sejnowski, T.J.: Spectrum of power laws for curved hand movements. Pnas 112(29), E3950–E3958 (2015).

11. Viviani, P., Schneider, R.: A developmental study of the relationship between geometry and kinematics in drawing movements. Journal of Experimental Psychology. Human Perception Performance 17(1), 198–218 (1991).

12. Plamondon, R., O'Reilly, C., Rémi, C., Duval, T.: The lognormal handwriter: learning, performing, and declining. Frontiers in Psychology 945(4), 1–14 (2013).

13. Accardo, A., Costa, F., Perrone, I.: The Influence of the Spatio-Temporal Terzi Treatment on the Kinematics of Cursive Writing of Dysgraphic Subjects. IEEE Transactions on Human-Machine Systems 47(2), 249–258 (2017).

14. Lin, Q., Luo, J., Wu, Z., Shen, F., Sun, Z.: Characterization of fine motor development: Dynamic analysis of children's drawing movements. Human Movement Science 40, 163–175 (2015).

Multiscale Analysis of Microvascular Blood Flow and Oxygenation

Marjola Thanaj, Andrew J. Chipperfield, and Geraldine F. Clough

Abstract

The purpose of this study is to investigate the feasibility of nonlinear methods for differentiating between haemodynamic steady states as a potential method of identifying microvascular dysfunction. As conventional nonlinear measures do not take into account the multiple time scales of the processes modulating microvascular function, here we evaluate the efficacy of multiscale analysis as a better discriminator of changes in microvascular health. We describe the basis and the implementation of the multiscale analysis of the microvascular blood flux (BF) and tissue oxygenation (OXY: oxyHb) signals recorded from the skin of 15 healthy male volunteers, age 29.2 ± 8.1y (mean $\pm$ SD), in two haemodynamic steady states at 33 °C and during warming at 43 °C to generate a local thermal hyperaemia (LTH). To investigate the influence of varying process time scales, multiscale analysis is employed on Sample entropy (MSE), to quantify signal regularity and Lempel and Ziv (MSLZ) and effort to compress (METC) complexity, to measure the randomness of the time series. Our findings show that there was a good discrimination in the multiscale indexes of both the BF ($p = 0.001$) and oxyHb (MSE, $p = 0.002$; METC and MSLZ, $p < 0.001$) signals between the two haemodynamic steady states, having the highest classification accuracy in oxyHb signals (MSE: 86.67%, MSLZ: 90.00% and METC: 93.33%). This study shows that "multiscale-based" analysis of blood flow and tissue oxygenation signals can identify different microvascular functional states and thus has potential for the clinical assessment and diagnosis of pathophysiological conditions.

1 Introduction

Blood flow in microvascular networks has been investigated in a range of physiological and pathophysiological states [1]. Recent studies have shown that in many disease states, such as metabolic disease and ageing, appears to be a reduction in the adaptive capabilities of the microvascular network and a consequent loss of physiological information content [2, 3].

Previously [4], we have investigated the time-dependent behaviour of microvascular blood flux and tissue oxygenation using time series analysis, power spectral density and complexity. We found differences in the spectral composition of the signals that were influenced by local skin warming such that differences in complexity were observable in the two haemodynamic steady states.

Nonlinear methods such as entropy and complexity techniques have been used widely to quantify the regularity and the randomness, respectively, of physiological signals and are well suited for the analysis of short length signals [5–8]. We and others have applied these approaches to BF signals derived from the skin in humans [4] and in animal models [7, 9], demonstrating clear differences in Lempel and Ziv (LZ) complexity between haemodynamic states. These studies demonstrate a diagnostic potential for complexity analysis of microvascular BF signals.

However, traditional algorithms for measuring entropy and complexity have the drawback that they can only study the behaviour at one scale. To address this, Costa et al. [2] introduced an improved multiscale entropy algorithm to

M. Thanaj (✉) · A. J. Chipperfield
Bioengineering Science Group, Faculty of Engineering and the Environment, University of Southampton, Highfield, Southampton, SO17 1BJ, UK
e-mail: M.Thanaj@soton.ac.uk

G. F. Clough
Human Development & Health, Faculty of Medicine, University of Southampton, Southampton, UK

estimate the entropy over multiple scales. Such multiscale analyses have been shown to be effective in quantifying the complexity of physiological signals in multiple spatial and temporal scales [2, 6, 10]. Similar studies [11], applied the multiscale entropy in the cardiac inter-beat interval to measure the regularity of the cardiac signal of young, elderly and subjects with heart failure in both waking and sleeping periods. They found good discrimination between these periods for all groups and reported that the multiscale entropy analysis was a valid method for quantifying the complexity of the cardiac signal across multiple scales.

In this study, we aim to investigate the feasibility of nonlinear methods for differentiating between signals derived from the microvasculature during two haemodynamic steady states. We explore the changes in entropy and complexity of the microcirculatory dynamics using multiscale analysis of sample entropy (SampEn), LZ and effort to compress (ETC) complexity methods in order to understand the effect of scale on these nonlinear metrics and their efficacy in classifying these haemodynamic steady states.

2 Methodology

2.1 Subjects

Microvascular blood flux (BF) and oxygenation (OXY: oxyHb) signals were recorded from the skin of 15 healthy male volunteers, age 29.2 ± 8.1y (mean $\pm$ SD). BF and OXY recordings were obtained at the skin of the forearm using a combined laser Doppler flowmetry (LDF) and white light reflectance (WLS) probe mounted in a heating block (Moor Instruments Ltd, Axminster UK) in two haemodynamic steady states, with the heating block clamped at 33 °C and during warming to 43 °C to generate a local thermal hyperaemia (LTH).

2.2 Study Procedure

All recordings were captured at a sampling rate of 40 Hz using the manufacturer's software. Figure 1 illustrates the BF, oxyHb and the temperature outputs and the selection of the 10 min artefact free segments marked as grey at 33 °C and at 43 °C, respectively. The truncated data could then be analysed and calculations made for the multiscale analysis. We elected to focus on the oxyHb output as the prime OXY signal for the nonlinear analysis as suggested by our previous studies [4].

2.3 Signal Analysis

Encoding
Nonlinear methods such as complexity measures are based on the complex information content of a finite time series to calculate the regularity of a binary time series representation. From previous studies [12, 13], it was reported that the binary conversion is sufficient to estimate the complexity in biomedical signals. As suggested by Yang et al. [14] a straightforward way to maintain the important characteristics of the dynamics contained in the original physiological signal is by using the increase and decrease encoding method whereby a zero is recorded if a value is less than the previous value in the time series or a one otherwise. Here this method will be referred to as delta encoding.

Nonlinear Analysis
The nonlinear methods employed here are estimated as follows:

Sample entropy: Sample entropy (SampEn) [15] was used to quantify signal regularity a time series. SampEn provides an applicable finite sequence formulation that discriminates the data sets by a measure of regularity, from totally regular to completely random. This method measures the logarithmic likelihood that runs of samples that are close for m continuous observations that remain close (within the same tolerance window r) on subsequent incremental comparisons.

$$SampEn(m, r, N) = \ln \frac{\Phi^m(r)}{\Phi^{m+1}(r)}$$

As suggested in the literature [15, 16], the parameter values to calculate SampEn can be chosen as $m = 2$ and $r = 0.15$ times the standard deviation of the binary time series.

Lempel and Ziv complexity: Lempel and Ziv (LZ) [17] complexity is a method for quantifying the randomness present in a sequence by estimating the number of production processes contained in a binary sequence, S. The production process called production history, $H(S)$, is denoted as:

$$H(S) = S(1, h_1)S(h_1 + 1, h_2) \ldots S(h_{m-1} + 1, h_m),$$

where m are the "words" of the history, h. The sequence is parsed from left to right and the complexity increases by one unit when a new sub-sequence of continuous symbols is encountered.
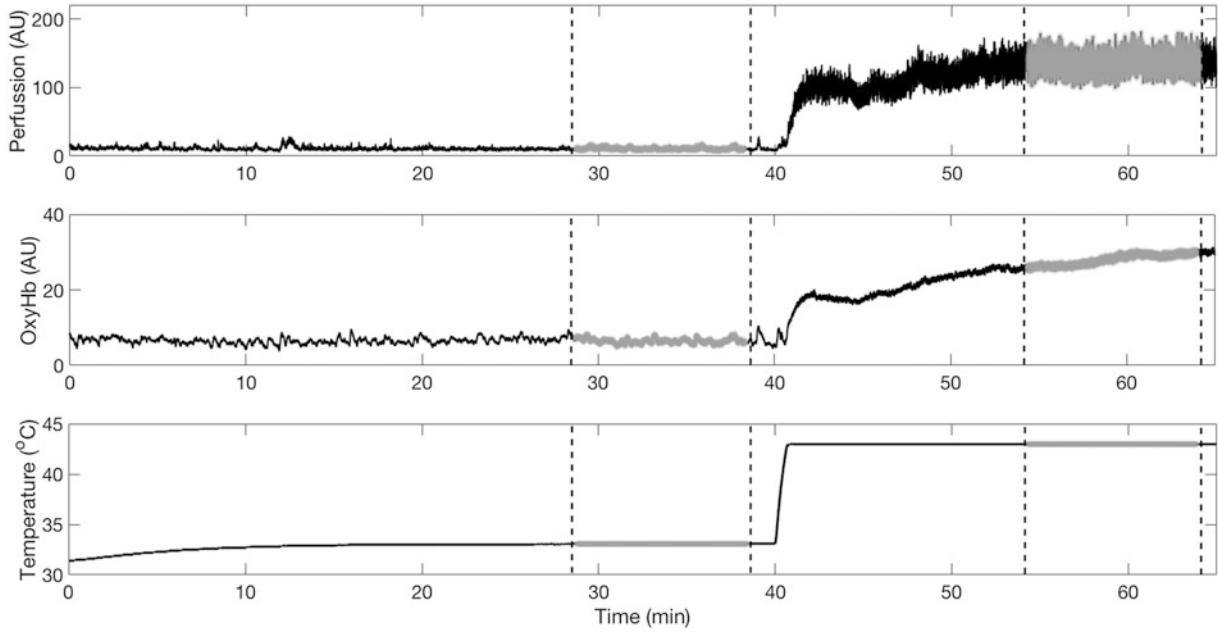
Fig. 1 Selection of the 10 min segments (grey area) for the data analysis at 33 and 43 °C. Blood flow in arbitrary perfusion units (PU), oxygenated haemoglobin (oxyHb) and temperature (°C) plots were obtained from one individual (Color figure online)

In order to define the complexity $c(S)$ of a sequence S, let denote $c_H(S)$ the least number of the components generated form the history $H(S)$ so,

$$c(S) = \min\{c_H(S)\}$$

To obtain a complexity measure independent of the length of the sequence, $c(S)$ should be normalized as:

$$C(S) = \frac{c(S)}{\frac{n}{log_2(n)}}$$

Effort to compress complexity: Effort to compress (ETC) complexity [18] is a similar complexity method based on the lossless compression algorithm known as Non-sequential Recrusive Pair Substitution (NSRPS) [19]. ETC complexity is defined by the pair of symbols with the maximum occurrence and replaces all its non-overlapping occurrences with a new symbol at each iteration.

$$N \rightarrow Number\ of\ iterations\ of\ NSPRS\ algorithm\ for\ entropy$$
$$\rightarrow zero$$

Therefore, N is the number of iterations, of NSPRS algorithm, required for the given sequence to be transformed to a constant sequence with zero entropy. Here the ETC complexity is normalized as: $\frac{N}{L-1}, 0 \leq N-1 \leq 1$, with $L =$ length of the sequence.

Multiscale Analysis

These nonlinear measures are used to analyse signals on a single scale, however, when applying these methods in physiological complex systems, it is essential to take into account the multiple time scales in that system. Costa et al. [2], proposed the Multiscale Entropy (MSE) technique for analysing biological signals using the coarse-graining method that resamples the original signal by reducing the scale factor, τ, of the time series and then determining the sample entropy for each scale. So, for a time series $\{x_1,\ldots,x_N\}$, the coarse-grained time series, y^τ, will be:

$$y_i^\tau = \frac{1}{\tau} \sum_{i=(i-1)\tau+1}^{i\tau} x_j, 1 \leq i \leq N/\tau. \qquad (1)$$

Here, the coarse graining method was applied in entropy and complexity methods and we call these procedure multiscale entropy (MSE), multiscale Lempel and Ziv complexity (MSLZ) and multiscale effort to compress complexity (METC).

Statistical Analysis

A Student t-test statistical test was performed to evaluate the differences between of the multiscale analysis of the two haemodynamic steady states for both BF and oxyHb signals. p-values less than 0.05 were taken to indicate statistical significance. Discriminant analysis with leave-one-out

cross-validation (LOO) was applied on multiscale methods of both BF and oxyHb signals, to find the classification accuracy in of all methods between the two haemodynamic steady states.

3 Results and Discussion

We set out to investigate whether the information content in the BF and oxyHb signals could be used to discriminate between two microvascular haemodynamic states in a cohort of healthy volunteers. The results showed a decrease in MSE during LTH in both BF (p = 0.001) and oxyHb signals (p < 0.001). MSLZ and METC also showed a significant

reduction in the complexity in BF signals (p = 0.001, for both) and oxyHb signals (p < 0.001, for both). The decline in randomness of the skin BF signal that we observe in healthy human skin during LTH is consistent with that reported by Tigno et al. [8] in the skin of primates during skin warming. Recent studies [1, 20] have suggested that the greater variability of the blood flux signal may indicate a more effective microvascular perfusion, whereas a lower variability in microvascular activity may correspond to a loss of the system's ability to adapt to pathophysiological conditions [21].

As shown in Fig. 2 the estimates for entropy and complexity of both BF and oxyHb signals showed a lower variability during LTH compared with the signals at 33 °C.
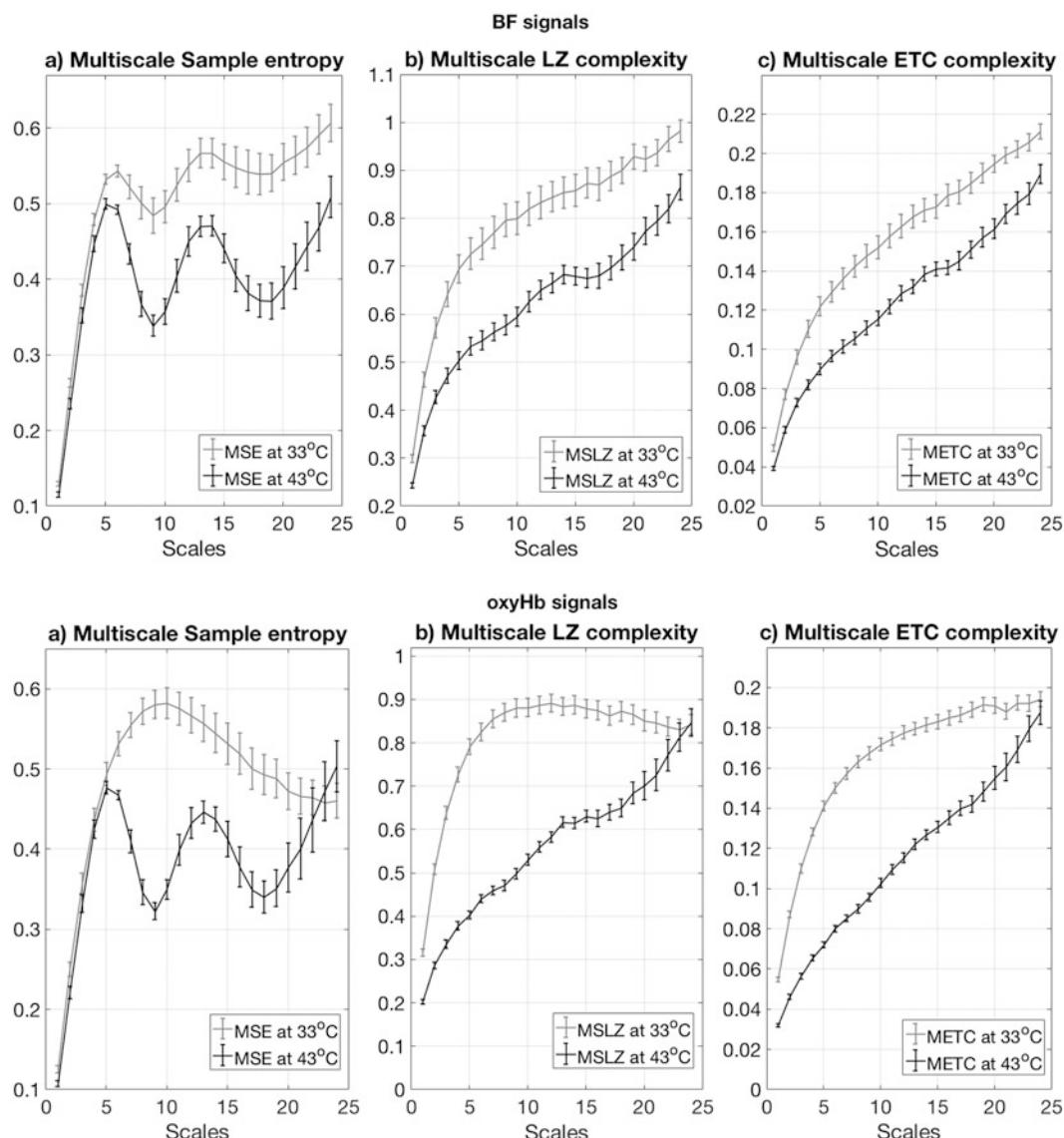
Fig. 2 The average multiscale analysis for BF (upper plots) and oxyHb (lower plots) signals at 33 °C (grey) and at 43 °C (black). **a** MSE, **b** MSLZ, **c** METC. Values are presented as means ± mean standard errors, (n = 15) (Color figure online)

Table 1 Statistical analysis and classification accuracy for all multiscale methods of both BF and oxyHb signals between the two haemodynamic steady states

Methods	BF		oxyHb	
	p-value	Classification accuracy (%)	p-value	Classification accuracy (%)
MSE	0.001	70.00	0.002	86.67
MSLZ	0.001	73.33	<0.001	90.00
METC	0.001	73.33	<0.001	93.33

We also observe that the separation between the haemodynamic states is greater in the oxyHb signal than in the BF signal. It is also worth noting that at the largest scales, the oxyHb signals during local heating become more complex than the ones at 33 °C when using the MSE method and approaches the signals at 33 °C when using both MSLZ and METC complexity measures. This increase of the complexity on larger scales may be a useful new index of increased adaptive capacity in larger time scales.

From Table 1 it is interesting to note that all three multiscale measures relating to the oxyHb signal indicate a good classification accuracy of the two haemodynamic steady states. The highest classification accuracy rates of 90.00% and 93.33% were reached with the MSLZ and METC complexity, respectively. By this test we showed that the characteristics of the multiscale analysis can be used in classification algorithms to separate two different data sets. High accuracy was achieved using the multiscale complexity analysis (MSLZ, METC), which indicates a classification effectiveness of the two haemodynamic steady states using the multiscale complexity measures and therefore, this may be valuable in clinical applications. Kalev et al. [22], using multiscale LZ complexity to examine the EEG signals for objective measures of depression, were able to demonstrate an 86% classification accuracy by accounting for the different frequencies of information content in the EEG. These authors also showed more statistically significant results using the multiscale LZ complexity than using the traditional LZ complexity.

We found that all the multiscale analysis methods we used were able to distinguish between the two haemodynamic steady states. However, we noticed that MSLZ and METC showed a more significant separation than MSE. These findings were consistent with those of Costa et al. [11], who found a good discrimination between wake and sleep periods. We note that the microvascular oxyHb signals showed better separation between the two haemodynamic steady states than the BF signals. This suggests that these measures may be valuable in clinical assessment of conditions of tissue under-perfusion [23].

Recent studies in an animal model have shown that the loss of adaptability throughout the microvascular network may be a major indicator of cardio-metabolic disease risk [21]. They further suggested that the spatial distribution and temporal behaviour of flow in a microvascular network may be more suitable measures with which to understand the impact of disease risk on the microcirculation. More experiments need to be conducted in pathological groups to examine changes in complexity arising from external perturbation for evaluating the microvascular dysfunction.

4   Conclusions and Future Work

In this work, we estimated the regularity and the complexity of microvascular blood flow signals in multiple scales, to inform how a change in system flexibility may allow a microvascular network to adapt to an imposed stressor. All multiscale methods showed a good discrimination between the two imposed haemodynamic steady states. They particularly showed a good discrimination between the oxyHb signals at low and high flows which make these methods a promising tool for further analysis of the microvascular function. For a better understanding of the nonlinear indexes of the microvascular function these methods need now to be extended to disease state.

References

1. Clough GF, Kuliga KZ and Chipperfield AJ. (2017) Flow motion dynamics of microvascular blood flow and oxygenation: Evidence of adaptive changes in obesity and type 2 diabetes mellitus/insulin resistance. *Microcirculation* 24.
2. Costa M, Goldberger AL and Peng CK. (2002) Multiscale entropy analysis of complex physiologic time series. *Physical Review Letters* 89.
3. Frisbee JC, Goodwill AG, Frisbee SJ, et al. (2016b) Microvascular perfusion heterogeneity contributes to peripheral vascular disease in metabolic syndrome. *J Physiol* 594: 2233–2243.
4. Kuliga KZ, Gush R, Clough GF, et al. (2017) Time-dependent Behavior of Microvascular Blood Flow and Oxygenation: a Predictor of Functional Outcomes. *IEEE Transactions on Biomedical Engineering* PP: 1–1.
5. Balasubramanian K and Nagaraj N. (2016) Aging and cardiovascular complexity: effect of the length of RR tachograms. *Peerj* 4.
6. Humeau A, Buard B, Mahe G, et al. (2010) Multiscale entropy of laser Doppler flowmetry signals in healthy human subjects. *Medical Physics* 37: 6142–6146.

7. Liao FY, Garrison DW and Jan YK. (2010) Relationship between nonlinear properties of sacral skin blood flow oscillations and vasodilatory function in people at risk for pressure ulcers. *Microvascular Research* 80: 44–53.

8. Tigno XT, Hansen BC, Nawang S, et al. (2011) Vasomotion becomes less random as diabetes progresses in monkeys. *Microcirculation* 18: 429–439.

9. Liao F, O'Brien WD, Jr. and Jan YK. (2013) Assessing complexity of skin blood flow oscillations in response to locally applied heating and pressure in rats: implications for pressure ulcer risk. *Physica A* 392.

10. Humeau A, Mahe G, Chapeau-Blondeau F, et al. (2011) Multiscale Analysis of Microvascular Blood Flow: A Multiscale Entropy Study of Laser Doppler Flowmetry Time Series. *IEEE Transactions on Biomedical Engineering* 58: 2970–2973.

11. Costa M, Goldberger AL and Peng CK. (2005) Multiscale entropy analysis of biological signals. *Physical Review E* 71.

12. Aboy M, Hornero R, Abasolo D, et al. (2006) Interpretation of the Lempel-Ziv complexity measure in the context of biomedical signal analysis. *IEEE Trans Biomed Eng* 53: 2282–2288.

13. Zhang XS, Zhu YS, Thakor NV, et al. (1999) Detecting ventricular tachycardia and fibrillation by complexity measure. *IEEE Transactions on Biomedical Engineering* 46: 548–555.

14. Yang AC, Hseu SS, Yien HW, et al. (2003) Linguistic analysis of the human heartbeat using frequency and rank order statistics. *Phys Rev Lett* 90: 108103.

15. Richman JS and Moorman JR. (2000) Physiological time-series analysis using approximate entropy and sample entropy. *American Journal of Physiology-Heart and Circulatory Physiology* 278: H2039–H2049.

16. Pincus SM. (2001) Assessing serial irregularity and its implications for health. In: Weinstein M, Hermalin AI and Stoto MA (eds) *Population Health and Aging: Strengthening the Dialogue between Epidemiology and Demography.* 245–267.

17. Lempel A and Ziv J. (1976) On the complexity of finite sequences. *IEEE Trans. Inf. Theory* IT-22: 75–81.

18. Nagaraj N, Balasubramanian K and Dey S. (2013) A new complexity measure for time series analysis and classification. *European Physical Journal-Special Topics* 222: 847–860.

19. Ebeling W and Jiménez-Montaño MA. (1980) On grammars, complexity, and information measures of biological macro-molecules. *Mathematical Biosciences* 52: 53–71.

20. Gryglewska B, Necki M, Zelawski M, et al. (2011) Fractal dimensions of skin microcirculation flow in subjects with familial predisposition or newly diagnosed hypertension. *Cardiology Journal* 18: 26–32.

21. Frisbee JC, Butcher JT, Frisbee SJ, et al. (2016a) Increased peripheral vascular disease risk progressively constrains perfusion adaptability in the skeletal muscle microcirculation. *Am J Physiol Heart Circ Physiol* 310: H488–504.

22. Kalev K, Bachmann M, Orgo L, et al. (2015) Lempel-Ziv and Multiscale Lempel-Ziv Complexity in Depression. 2015 37th Annual International Conference of the Ieee Engineering in Medicine and Biology Society. 4158–4161.

23. Papaioannou, V. E., Chouvarda, I. G., Maglaveras, N. K. and Pneumatikos, I. A. (2012) 'Temperature variability analysis using wavelets and multiscale entropy in patients with systemic inflammatory response syndrome, sepsis, and septic shock', *Critical Care,* 16(2), pp. 15.

Low- and High-Speed Arrivals Decomposition in 10–19 kHz Transmission Sounding of Human Lungs

Vladimir Korenbaum, Anton Shiryaev, Anatoly Kostiv, and Maria Safronova

Abstract

The possibility of decomposition of received signals into high-speed (150–1000 m/s) and low-speed components (50–150 m/s) previously revealed is verified in independent sample. Four types of the ratio between the amplitudes of high- and low-speed arrivals and their changes depending on air-filling of lungs (inspiration/exhalation) are found. Only one of these types, representing predominance of amplitudes of high-speed arrivals, both during inspiration and exhalation is found in one elderly patient with a long-term course of hormone-dependent asthma, but not in 3 other young healthy volunteers. For medium frequency 15 kHz of the range low-speed arrivals velocities result in wavelengths between 0.33 and 1 cm. Such small wavelengths may provide the spatial resolution in lung parenchyma about the first centimeters. Thus transmission sounding of lungs in the range of 10–19 kHz seems promising to provide high-resolution acoustic imaging or may be even transmission tomography of pulmonary parenchyma.

Keywords

Sound propagation • Lung parenchyma • Complex signals

1 Introduction

The unexpected phenomenon of 10–40 kHz sound transmission through human lungs with speed of about 1000 m/s was revealed recently [1]. While later our team in pilot experiment, using signal compression technique, found low- and high-speed sound propagation components in the frequency range of 10–19 kHz [2].

The objective is a more detailed study of the characteristics of sound transmission in human lungs in the frequency range of 10–19 kHz.

2 Materials and Methods

The 14-channel apparatus previously used [3] was provided with new accelerometer sensors having own resonance frequency near 35 kHz, which made possible a linear performance in the frequency range between 10–20 kHz. Signals from accelerometer sensors were registered with the 16-channel recorder Powerlab (ADInstruments), sampling frequency was 40 kHz. Chirp signals 10–19 kHz (6 min duration) were emitted into human thorax (4 positions) by small shaker installed on chest surface fed from professional external computer sound card through sonic power amplifier.

A convolution of emitted (at sound card analog output) and received signals (16-channel recorder channels) technique was used. The emitted chirp signal, reply of the sensor No. 7, and normalized convolution curve R_{xy} (amplitude and envelope) with detected peaks labeled with red marks as dependence on time delay are shown in Fig. 1 for example. Each peak of the envelope in accordance with hydroacoustic, radar considerations and our experience [4] is treated as a separate signal arrival (red mark) with its time delay. Sound velocity of each arrival is calculated as direct distance between shaker position and current sensor measured with pelvis-meter divided by time delay, and it is represented in Fig. 1 and other figures as black numbers above peaks.

Sound propagation in human lungs was studied for opposite positions of shaker and sensors (Fig. 2) at the chest surface in 4 volunteers, signed informed consents.

V. Korenbaum (✉) · A. Shiryaev · A. Kostiv · M. Safronova
Pacific Oceanological Institute, Russian Academy of Sciences,
Baltiiskaya Str. 43, 690041 Vladivostok, Russia
e-mail: v-kor@poi.dvo.ru
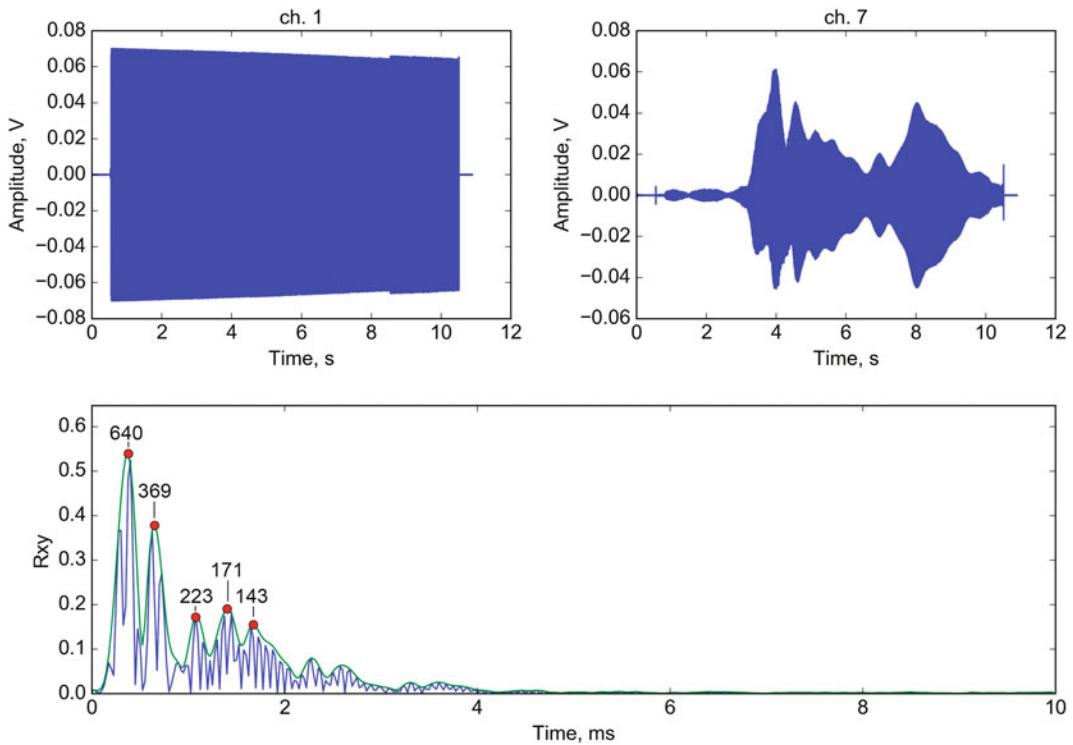
Fig. 1 Emitted chirp signal (ch. 1); reply of the sensor (ch. 7); and normalized convolution curve (blue) with its envelope (green) in dependence on time delay (volunteer Sh.) provided with envelope detected peaks (red marks) and sound velocities (black numbers above peaks) (Color figure online)
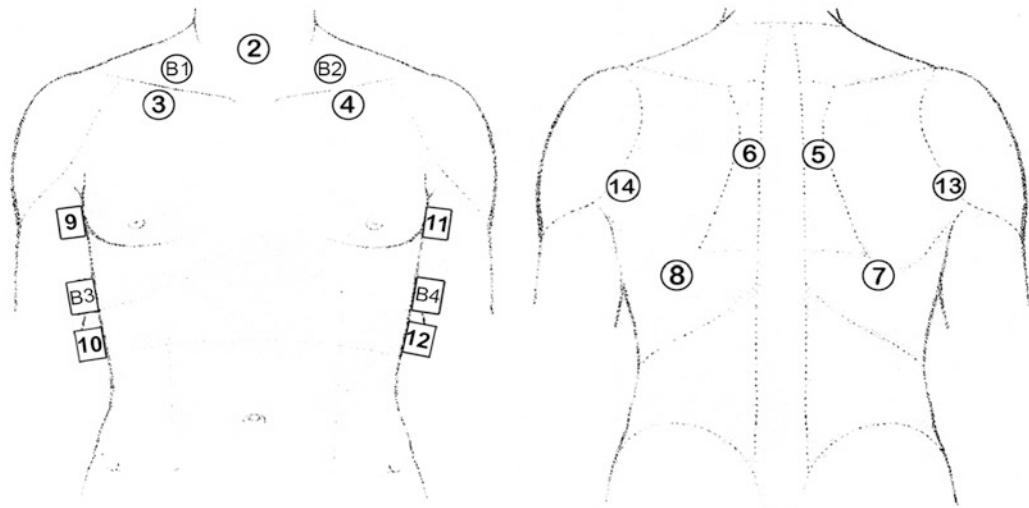
Fig. 2 The scheme accelerometers mounting (no. 2–14) and shaker positions (B1–B4) at torso

3 Results and Discussion

Sounding of thorax was performed in two respiratory maneuvers—breathe hold in maximum inspiration (HF2) and breathe hold in maximum exhalation (HF3).

Convolution curves (envelopes) of weighted correlation function T_{xy} with peaks-arrivals (sound velocities) are presented in diagrams Figs. 3, 4, 5 and 6 with log scale to include both inspiration (HF2) and exhalation (HF3) data.

A possibility of decomposition of received signals into high-speed and low-speed arrivals [2] is verified in this

Fig. 3 The log-scale envelopes of convolution curve (B1–11) of the type 1 (volunteer K1.) with detected peaks (red marks) in dependence on time delay (ms) and sound velocities (black numbers above peaks) in breathe-holds during inspiration (blue) and expiration (green) (Color figure online)
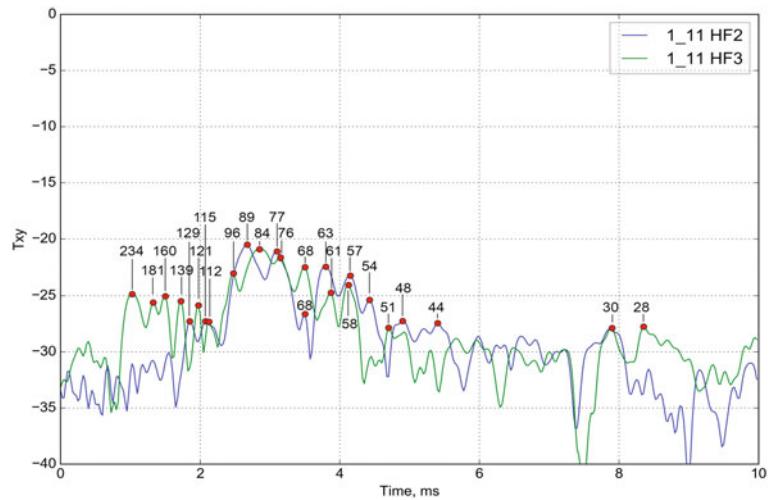
Fig. 4 The convolution curve (B3–11) of the type 2 (volunteer S.), other indication as in Fig. 3
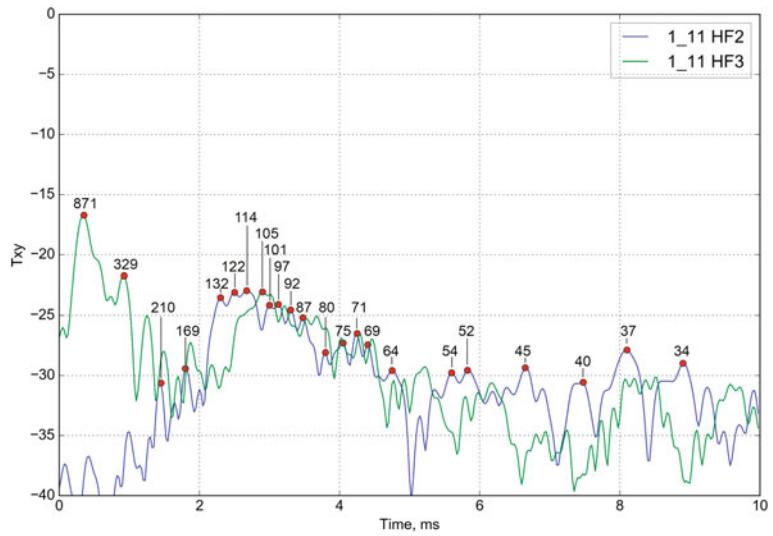
Fig. 5 The convolution curve (B4–10) of the type 3 (volunteer S.), other indication as in Fig. 3
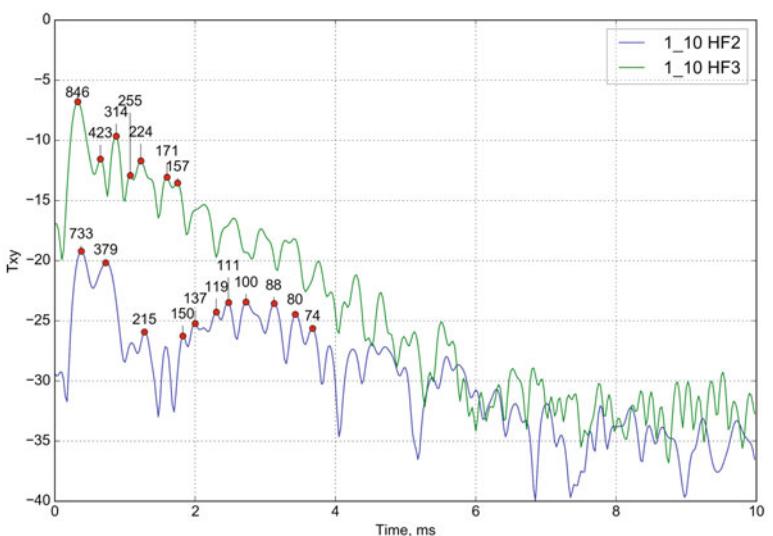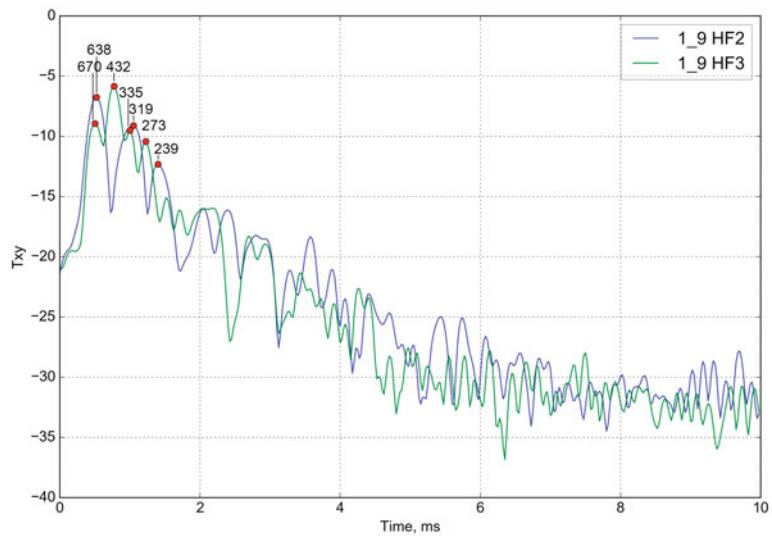
Fig. 6 The convolution curve (B2–9) of the type 4 (volunteer K2.), other indication as in Fig. 3

independent sample of subjects. An existence of low-speed arrivals with propagation velocities of 50–150 m/s is revealed, which velocities are inversely dependent on air-filling of lungs (inspiration/exhalation). Therefore these arrivals may be treated mainly as the result of sound wave propagation through the lung parenchyma. On the contrary, the amplitudes of high-speed arrivals found had velocities of 150–1000 m/s. Their amplitudes and/or velocities are enhanced with a decrease in air-filling of the lungs in breath hold during exhalation. Thus the high-speed arrivals may be connected to dominant sound propagation through high-density tissues of thorax.

Four characteristic types of convolution curves for opposite transmission traces were found. Type 1 (Fig. 3)— an appearance of high-speed arrivals in exhalation (HF3) re inspiration (HF2) without significant changing basic low-speed arrivals. Type 2 (Fig. 4)—an essential increase of high-speed arrivals amplitudes in exhalation (HF3) re inspiration (HF2). Type 3 (Fig. 5)—a dramatic increase of high-speed as well as low-speed arrivals amplitudes in exhalation (HF3) re inspiration (HF2). Type 4 (Fig. 6)—an absence of any amplitude or velocity dynamics in ratio of high-speed and low-speed arrivals between exhalation (HF3) and inspiration (HF2).

Only one of these types (the type 4—Fig. 6) is characterized by the predominance of amplitudes of high-speed arrivals, both during inspiration and exhalation. It may be acoustically interpreted as a local reduction in air-filling and ventilation of lung parenchyma. It is seen only in one elderly patient with a long-term course of hormone-dependent asthma, but not in 3 other young healthy individuals. Thus the method may be promising to reveal reduced air-filling and ventilation in pulmonary parenchyma.

Since found low-speed arrivals have sound velocity about 150–50 m/s for medium frequency 15 kHz of the range these velocities result in wavelengths between 1 and 0.33 cm. Such small wavelengths may provide the spatial resolution in lung parenchyma of about the first centimeters!

Thus transmission sounding of lungs in the range of 10–19 kHz seems very promising to provide high-resolution acoustic imaging or may be even tomography of pulmonary parenchyma.

What mechanism may be considered for the theoretical model of sound transmission in 10–19 kHz frequency range? For air bubbles in water the well-known Minnaert (1933) formula for resonant frequency may be simplified to

$$f = 3.26/r. \tag{1}$$

With alveoli diameter 0.2 – 0.3 mm, $f \approx 22$–33 kHz according to Eq. 1. Therefore in low-frequency 80–1000 Hz [4] as well as in high-frequency 10–19 kHz ranges the transmission is below fundamental alveoli resonance. Consequently in both frequency ranges a sound velocity should be governed by air compliance in alveoli and density of alveoli wall tissue.

Thus in both frequency ranges sound velocities through normal (air-filled) parenchyma must be close. This really is seen in our current experiments for low-speed arrivals with found velocities of 50–150 m/s in comparison with previous study made for frequency range 80–1000 Hz, where sound velocities of 20–50 m/s were seen [4].

However the question is why there is no sound transmission in lungs for the frequency range of 1–10 kHz [1] lying between 80–1000 Hz and 10–19 kHz bands, where sound propagation is evident?

4 Conclusions

The transmission sounding of lungs in the frequency range of 10–19 kHz seems promising to provide high-resolution acoustic imaging or may be even transmission tomography of pulmonary parenchyma. New studies using clinical models are welcome, for example, patients with focal pneumonia verified by CT.

Conflict of Interest The authors declare that they have no conflict of interest.

References

1. Rueter, D., Hauber, H., Droeman, D. et al.: Low-frequency ultrasound permeates the human thorax and lung: a novel approach to non-invasive monitoring. Ultraschall in Med. 31(1), 53–62 (2010).
2. Korenbaum, V., Shiryaev, A., Tagiltsev, A., Kamenev, S.: Features of 10–19 kHz sound propagation through human lungs. In 26-th Congress of the European Federation of Societies for Ultrasound in Medicine and Biology, pp. 66. Tel-Aviv, Israel (2014).
3. Korenbaum, V., Shiriaev, A.: Sound propagation through human lungs, under transmission sounding with acoustic signal of 80–1000 Hz frequency band. Proceedings of Meetings on Acoustics (POMA) 23, 020002 (2015).
4. Korenbaum, V., Nuzhdenko, A., Tagiltsev, A., Kostiv, A.: Investigation into transmission of complex sound signals in the human respiratory system. Acoustical physics 56(4), 568–575 (2010).

Analysis of Biological Response to Pleasure Elicited by Video

Masaji Yamashita, Takeshi Aikawa, Masataka Kitama, and Toru Yokoyama

Abstract

To study the objective evaluation of emotions, and pleasure in particular, biological responses to emotional videos were investigated. Fifteen adult males participated in the experiment. Five videos were used, which engendered "exhilaration," "happiness," "being comforted," "disgust," and "control." Impedance plethysmography, electrocardiogram, photo plethysmography, continuous blood pressure, and respiration were measured and analyzed. Self-rated scores for "pleasure–displeasure" adequately varied among emotional-video stimuli. Biological changes were observed in the "exhilaration" condition, such as heart rate (HR), pulse wave amplitude, and pulse pressure. However, no biological changes in common were found among pleasurable emotions. To determine biological responses common to pleasurable emotions, the pulse wave was assessed in detail. Consequently, arterial compliance tended to decrease for each pleasurable emotion, albeit non-significantly. The maximum of the differentiated pulse wave (dP) changed significantly for "exhilaration" and "happiness." Moreover, the combined parameter, which involved dP, HR, and mean blood pressure changed significantly for all pleasurable emotions.

Keywords

Pleasure • Bio-response • Video • Blood circulation

1 Introduction

Determining the autonomic responses associated with emotions has been an active research topic for almost a century [1]. However, there is no scientific consensus on whether there exists a relationship between emotions and autonomic nervous system activity [1]. We have studied biological responses to emotion-eliciting stimuli in test subjects to evaluate selected emotions objectively [2, 3]. However, our previous studies have only evaluated biological responses to "excitement" and "tension" as emotional stimuli. Russell's circumplex model of affect [4], characterized by two orthogonal axes of pleasure–displeasure and arousal–sleep, is widely accepted for the analysis of emotion: the pleasure–displeasure axis has been crucial for the analysis of emotion in many studies. In pleasurable emotions, there exist emotions of "exhilaration," "happiness," and "being comforted" along the arousal–sleep axis. As autonomic responses during a state of arousal differ from the responses during sleep, the responses during "exhilaration" would differ from those during "being comforted." Furthermore, autonomic responses and changes in blood flow may indicate contradictory reactions to similarly pleasurable emotions [1]. For example, viewing a pleasant picture evoked an increase in heart rate (HR) [5], whereas a happy scene in the film *Bambi* decreased HR in children [6]. Thus, it is necessary to develop new approaches to analyze responses to pleasurable emotions.

To study the objective evaluation of emotions, and pleasure in particular, we measured the biological responses of test subjects to video stimuli that elicited pleasurable and unpleasant emotions and characterized biological responses via a novel pulse-wave analysis.

2 Methods

2.1 Experiment

The ethics committee of Hokkaido University of Science approved this study. The experiments [7] were performed in a room that was electrically shielded, temperature-controlled (24.5–25.5 °C), and humidity-controlled (50–65%). Fifteen healthy adult males participated in the experiments after providing informed consent. The subjects were asked to

M. Yamashita (✉) · T. Aikawa · M. Kitama · T. Yokoyama
Hokkaido University of Science, 7-15-4-1 Maeda, Teine, Sapporo, Japan
e-mail: yamashita@hus.ac.jp

refrain from eating, drinking, or smoking for 3 h before the experiments.

Electrocardiography (ECG) data were recorded using a standard lead II on the chest, and the blood pressure-pulse wave was measured using tonometry at the left wrist. Respiratory wave activity was measured using a thermistor sensor placed in front of the subject's nostrils, and photo plethysmography was measured from the right index finger. Finally, cardiac stroke volume was measured by impedance plethysmography on the chest. All data were recorded with 16-bit 200-Hz sampling and subsequently analyzed using a computer program.

Videos projected onto a screen were used as stimuli. The experimental protocol was as follows: After a 15-min habituation period, the subject watched a familiar "campus" movie for 90 s in the pre-rest period, an emotional stimulus movie for 150 s in the stimulus period, and a similar "campus" movie for an additional 60 s in the post-rest period. Emotional stimulus movies were either "exhilaration," "happiness," "being comforted," "disgust," or "control" movies. A "sports highlight" movie was used for "exhilaration," a "delighted baby" movie was used for "happiness," a "puppy" movie was used for "being comforted," a "carcass" movie was used for "disgust," and a similar but different "campus" movie was used as a "control." Biological responses were measured during each session from the onset of the pre-rest period to the end of the post-rest period. The sections of the session were defined for analysis as follows: The pre-rest period was divided into two sections of 70 s (rest 0) and 20 s (rest 1). The stimulus period was divided into 7 sections of 20 s each (stim. 1 to stim. 7). The post-rest period was divided into 3 sections of 20 s each (rest 2 to rest 4). To adjust for individual variation, each data point was normalized to each rest 0 period. After each session, the subject rated his emotional state during the emotional stimulus video using a questionnaire. The questionnaire was composed of three 11-point scales (pleasure-displeasure, excitement-calmness, tension-relaxation) that were rated +5 to −5. Each session was repeated 5 times and emotional stimulus movies were presented in a randomized order.

2.2 Analysis

ECG data were used to calculate heart rate variability (HRV), the Mayer Wave component (MW; 0.04–0.15 Hz), and the respiratory sinus arrhythmia component (RSA; 0.15–0.4 Hz). Systolic blood pressure (SBP), diastolic blood pressure (DBP), mean blood pressure (MBP), and pulse pressure (PP) were obtained from the pulse wave. Total

peripheral resistance (TPR) was calculated from stroke volume (SV), HR, and MBP values. Pulse wave amplitude (PWA) was obtained from photo plethysmography. Finally, respiration frequency (RF) and amplitude (RA) were obtained from respiratory wave data [7]. Normalized data were averaged across a stimulus period for comparison among emotions.

To investigate the compliance of the aorta for each emotion, the pulse wave was differentiated to obtain the maximum rate of change of the pulse wave (dP). Using mean dP, HR and MBP, the combined value dP/HR/MBP was obtained.

Statistical analyses consisted of analyses of variance (ANOVAs) with post-hoc Bonferroni/LSD multiple comparisons.

3 Results

3.1 Self-rating

Self-rated scores in response to each emotional stimulus video were as follows: "pleasure–displeasure" mean scores for the "exhilaration," "happiness," "being comforted," "disgust," and "control" videos were 3.0, 2.2, 2.9, −4.1, and 1.1, respectively. A positive score indicates a "pleasure" rating and a negative score indicates a "displeasure" rating. "Pleasure–displeasure" scores in response to the "exhilaration" and "being comforted" videos were significantly greater (p < 0.001), and the "happiness" video was non-significantly greater (p = 0.17), than those in response to the "control" video. Scores in response to the "disgust" video were significantly lower (p < 0.001) than those in response to the "control" video [7]. Thus, self-rated scores for "pleasure–displeasure" adequately varied among emotional-video stimuli.

3.2 Biological Responses

Biological changes were observed in response to the "exhilaration" video, such as in HR, PP, and PWA [7]. Figure 1 compares HR response to each emotional stimulus video. HR significantly decreased relative to control in response to "exhilaration" (p < 0.05), but no changes in HR were observed in response to other emotional stimuli. PWA and PP also showed similar responses [7]. Further, RF increased relative to control in response to "happiness" (p < 0.05). No significant differences relative to control were noted for other parameters (SBP, DBP, MBP, SV, TPR, MW, RSA, or FA). Thus, no biological changes were common to pleasurable emotions.

Fig. 1 Comparison of normalized heart rate (HR) among emotions
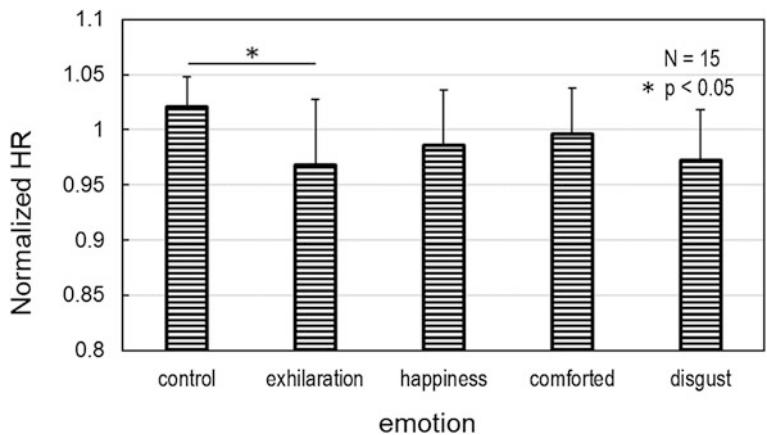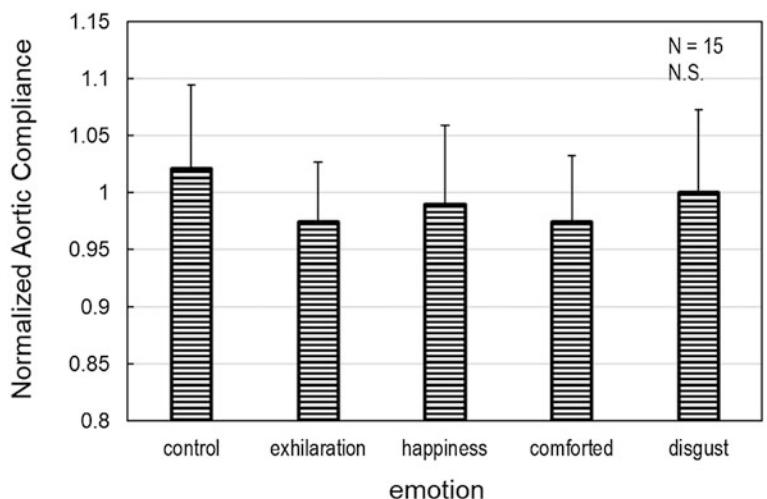
Fig. 2 Comparison of normalized aortic compliance among emotions

3.3 Features of Pulse Wave

To find any biological responses common to pleasurable emotions, detailed study of the pulse wave was executed. The parameter of SV/PP was considered to represent aortic compliance [8]; SV/PP values are shown in Fig. 2. Aortic compliance tended to decrease for each pleasurable emotion versus control, albeit non-significantly. The maximum of the differentiated pulse wave (dP) is shown in Fig. 3; dP changed significantly for "exhilaration" and "happiness" videos. Moreover, the combined parameter dP/HR/MBP changed significantly for every pleasurable emotion (Fig. 4).

4 Discussion

In general, the autonomic response pattern of happiness is characterized by increased cardiac activity due to vagal withdrawal, vasodilation, increased electro-dermal activity, and increased respiratory activity [1]. In the present study, we observed decreases in HR in response to "exhilaration"

emotional stimuli but no change to stimuli engineered to engender feelings of "happiness" and "being comforted." Further, we observed no change in RSA, which is indicative of parasympathetic nerve activity, in response to all pleasurable stimuli. This indicates the difficulty in describing the human response to pleasurable stimuli by only autonomic responses.

The use of aortic compliance provided a novel means by which to investigate commonalities among pleasurable emotions. As aortic compliance is relevant to dP, the changes in dP for "exhilaration" and "happiness" increased and the change for "being comforted" showed a tendency toward increasing. In contrast, MBP is related to peripheral resistance of blood vessels [8]. Therefore, the ratio dP/MBP indicated aortic and peripheral vessel's responses to pleasurable emotions. Moreover, HR drives blood circulation. Therefore, the combined parameter dP/HR/MBP was generated and found to change in individuals experiencing pleasurable emotions.

Many studies have explained the responses of pleasurable emotions such as amusement, contentment, happiness, and

Fig. 3 Comparison of
normalized value of the
maximum of the differentiated
pulse wave (dP) among emotions
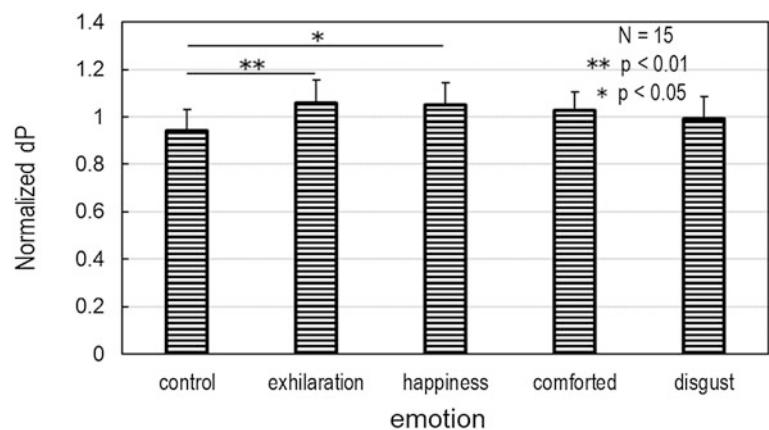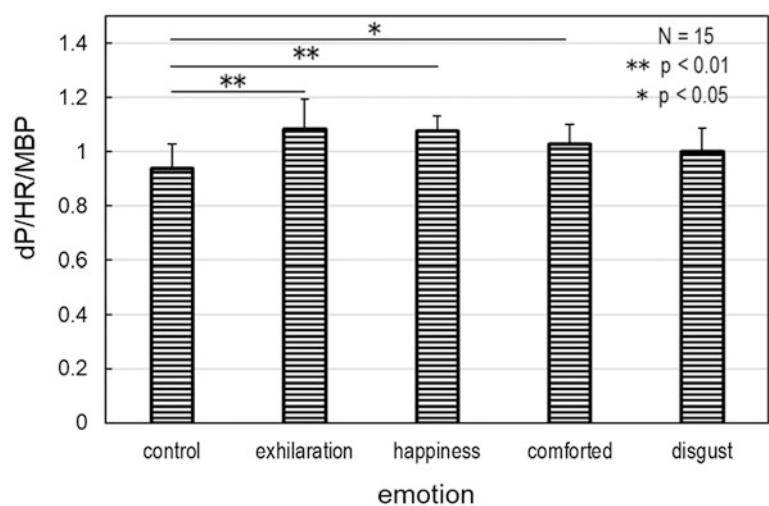
Fig. 4 Comparison of the value
of dP/HR/MBP among emotions

joy [1]. However, these responses were not unified, but were sometimes disjointed [1]. Therefore, biological responses are needed that represent the valence of pleasantness according to affective dimensional models [9]. The combined parameter discussed above would represent the valence of pleasantness. The primary limitation of this study is that the combined parameter was derived from the responses to video stimuli only. Therefore, further studies are required to confirm the results through experiments using stimuli of different modalities.

5   Conclusions

To investigate the biological responses common to pleasurable emotions, autonomic responses to video stimuli eliciting a variety of pleasurable emotions were measured. It was seen that HR, PWA, and PP changed during the experience of emotional exhilaration. However, no response was common to different aspects of emotional pleasure. The

novel use of pulse-wave analysis produced results that revealed responses common to pleasurable emotions.

Conflict of Interest   There are no conflicts of interest to declare.

References

1. Kreibig, S. D.: Autonomic nervous system activity in emotion: A review. Biological Psychology 84, 394–421 (2010).
2. Yamashita, M.: Experimental verification of psychophysiological index of excitement. International Journal of Affective Engineering 14(1), 65–71 (2015).
3. Yamashita, M., Aikawa, T., Mamorita, N., Arisawa, J., Kitama, M., Shimizu, H.: Study on the blood circulation responses caused by tension/unpleasant evoking stimulus. Proceedings of Life Engineering Symposium 2013, 305–307 (2013).
4. Russell, J. A.: A circumplex model of affect. Journal of Personality and Social Psychology 39, 1161–1178 (1980).
5. Jönsson, P., Sonnby-Borgström, M.: The effects of pictures of emotional faces on tonic and phasic autonomic cardiac control in women and men. Biological Psychology 62 (2), 157–173 (2003).
6. Sternbach, R.A.: Assessing differential autonomic patterns in emotion. Journal of Psychosomatic Research 6, 53–68 (1962).

7. Yamashita, M., Shimizu, H. O., Kitama, M.: Biological responses to emotional exhilaration elicited by video stimuli. KEER2016 188, 1–6 (2016).

8. Ozawa, T.: Clinical measurement of pulse pressure. Arterial Stiffness 8,1–7 (2005).

9. Jerritta S., Murugappan M., Nagarajan R., Wan K.: Physiological signals based human emotion recognition: A review, IEEE 7th International Colloquium on Signal Processing and its Applications, 410–415 (2011).

Pulse Rate Variability Analysis to Enhance Oximetry as at-Home Alternative for Sleep Apnea Diagnosing

Gonzalo C. Gutiérrez-Tobal, Daniel Álvarez, Fernando Vaquerizo-Villar, Verónica Barroso-García, Adrián Martín-Montero, Andrea Crespo, Félix del Campo, and Roberto Hornero

Abstract

This study focuses on the at-home Sleep apnea-hypopnea syndrome (SAHS) severity estimation. Three percent oxygen desaturation index (ODI_3) from nocturnal pulse-oximetry has been commonly evaluated as simplified alternative to polysomnography (PSG), the standard in-hospital diagnostic test. However, ODI_3 has shown limited ability to detect SAHS as it only sums up information from desaturation events. Other physiological signs of SAHS can be found in respiratory and cardiac signals, providing additional helpful data to establish SAHS and its severity. Pulse rate variability time series (PRV), also derived from nocturnal oximetry, is considered a surrogate for heart rate variability, which provides both cardiac and respiratory information. In this study, 200 oximetric recordings obtained at patients home were involved, divided into training (50%) and test (50%) groups. ODI_3 and PRV were obtained from them, the latter being characterized by the extraction of statistical features in time domain, as well as the spectral entropy from the commonly used very low (0–0.04 Hz.), low (0.04–0.15 Hz.), and high (0.15–0.4 Hz.) frequency bands. The ODI_3 and PRV features were joined in a multi-layer perceptron artificial neural network (MLP), trained to estimate the apnea-hypopnea index (AHI), which is the PSG-derived parameter used to diagnose SAHS. Our results showed that single ODI_3 rightly assigned 62.0% of the subjects from the test group into one out the four SAHS severity degrees, reaching 0.470 Cohens kappa, and 0.840 intra-class correlation coefficient (ICC) with the actual AHI (accuracies of 90.0, 88.0 and 82.0% in the increasing AHI cutoffs used to define SAHS severity). By contrast, our MLP model rightly assigned 75.0% of the subjects into their corresponding SAHS severity level, reaching 0.614 κ and 0.904 ICC (accuracies of 93.0, 88.0 and 90.0%). These results suggest that SAHS diagnosis could be accurately conducted at-patients home by combining ODI_3 and PRV from nocturnal oximetry

1 Introduction

The sleep apnea-hypopnea syndrome (SAHS) is a chronic and prevalent disease in which patients show recurrent episodes of respiratory pauses (apneas) and airflow reductions (hypopneas) while sleeping [1]. Apneic events boost a number of undesirable physiological processes that lead to a harmful impact both in health and quality of life of affected people [2].

The number of apneas and hypopneas per hour of sleep, i.e., the apnea-hypopnea index (AHI), is the parameter used to determine the presence and severity of SAHS [1, 3]. Clinical specialists estimate AHI by examining multiple physiological signals recorded during in-lab nocturnal polysomnography (PSG), which is the standard diagnostic test [3]. However, simplifying SAHS diagnosis has become a major issue for biomedical engineering due to limitations related to the PSG complexity, costs, and demand of time from physicians [3]. These drawbacks, together with the high prevalence of SAHS [3], imply a limited availability of specialized facilities, which derives in long waiting lists and delays the access to both diagnosis and treatment [3].

G. C. Gutiérrez-Tobal (✉) · D. Álvarez · F. Vaquerizo-Villar
V. Barroso-García · A. Martín-Montero · A. Crespo · F. del Campo · R. Hornero
Biomedical Engineering Group, Universidad de Valladolid, Valladolid, Spain
e-mail: gonzalo.gutierrez@gib.tel.uva.es; gguttob@gmail.com
URL: http://www.gib.tel.uva.es/

D. Álvarez · A. Crespo · F. del Campo
Sleep Unit, Hospital Universitario Rio Hortega, Valladolid, Spain

In past years, a wide range of simpler diagnostic alternatives have been evaluated. In contrast to 32 signals recorded during PSG, most of the alternatives focused on analyzing a single one [4, 5]. Nocturnal pulse-oximetry (NPO) is a simple test often used for this purpose [6, 7]. It only requires a sensor on a finger to record the blood oxygen saturation (SpO_2). This signal monitors the oxygen in the hemoglobin of the blood, which falls due to apneic events [1].

Promising results have been derived from the investigation of the SpO_2 signal, which include the use of automatic signal processing techniques and the assessment of clinically-used oxygen desaturation indexes (ODI) [6, 7]. However, recent studies have reported substantial redundancy between the 3% ODI (ODI_3), and the remaining information usually extracted from SpO_2 [8]. Moreover, SAHS is known to change the normal profile of the cardiac signals by the recurrence of bradycardia/tachycardia patterns [4]. Particularly, a recent work from our group reported that spectral entropy (SE) from VLF (0–0.04 Hz), LF (0.04–0.15 Hz), and HF (0.15–0.40 Hz) bands of the heart rate variability signal (HRV) provides more useful information than the corresponding power-based traditional features [9]. This kind of information is not available when using SpO_2 signal alone. Hence, we hypothesize that the usefulness of ODI_3 to simplify SAHS diagnosis test can be improved adding cardiac data of interest.

In this regard, NPO sensor is not only able to record SpO_2 but pulse rate too. Several studies have evaluated the use of cardiac information obtained from the pulse rate variability signal (PRV) as a surrogate of HRV [10, 11]. These works showed the usefulness of PRV in pediatric SAHS context. However, they did not evaluate adult subjects, they focused on the analysis of the classic spectral power-based HRV parameters [10], or only used time-domain PRV information to detect specific apneic related events [11]. Additionally, the signals used in these works were acquired in a laboratory, i.e., under supervised conditions.

In accordance with the above mentioned, we aim at evaluating the joint usefulness of ODI_3 from SpO_2 together with time and frequency domain features obtained from PRV. The extraction of SE from VLF, LF, and HF of PRV spectrum is proposed. Additionally, first to fourth order statistics ($Mt1$–$Mt4$) are also obtained with the purpose of characterizing the whole PRV time series. Moreover, in contrast to previous studies, both PSG and NPO are conducted at patients home. Hence, our proposal can be evaluated under those conditions which best reflect the usual sleep environment and behavior of patients. The eight features extracted from NPO (SpO_2 and PRV) are subsequently used as the only source of information to train a multi-layer perceptron (MLP) artificial neural network with ability to automatically estimate AHI. We chose MLP in view of its success in previous studies focused on automatic AHI estimation [12, 13]. The diagnostic performance of this estimated AHI is compared with ODI_3 to assess whether the use of PRV information can improve the ability of oximetry to detect SAHS and its severity.

2 Subjects and Signals

The study involved 200 adult subjects (67.5% males). All of them where referred to the sleep unit of the Hospital Universitario Rio Hortega in Valladolid (Spain) due to clinical suspicious of SAHS. The subjects gave their informed consent to participate in the study and the Ethics Committee of the Hospital approved the protocol. A physician examined at-home PSG (Embletta MPR ST+ , Embla Systems, USA) tests from all patients to compute an AHI for each of them. Apneas and hypopneas were scored following the rules of the American Academy of Sleep Medicine (AASM) [1]. According to the computed AHI, subjects were diagnosed in four SAHS-severity degrees: 12 no-SAHS (AHI < 5 e/h), 46 mild (5 $\leq$ AHI < 15 e/h), 46 moderate (15 $\leq$ AHI < 30 e/h), and 96 severe (AHI $\geq$ 30 e/h). The sample was randomly divided into a training (50%) and a test (50%) set, with the two of them having the same number of subjects from each SAHS-severity degree. Table 1 shows the demographic and clinical data of the subjects under study for the whole group and the training and test sets.

A NPO (WristOx$_2^{TM}$, Nonin, USA) was conducted at the same time that each PSG. SpO_2 and PRV were obtained at sampling rates of 1 Hz and 3 Hz, respectively. Artifacts were removed from both of them. In SpO_2, zero values and differences between consecutive samples $\geq 4\%$ were removed and substituted by interpolated data [14]. In PRV, values <0.33 s or >1.5 s, as well as differences in consecutive PRV values >0.66, were considered arrhythmia-related artifacts [4]. All of them were also removed and substituted by interpolated samples [4].

Table 1 Demographic and clinical data of the subjects under study

Data	All	Training	Test
Subjects (n)	200	100	100
Male (%)	67.5	64.0	71.0
Age (years)	55.4 ± 12.6	55.0 ± 11.9	55.8 ± 13.3
BMI (Kg/m^2)	29.5 ± 5.3	29.7 ± 5.3	29.3 ± 5.4
AHI (e/h)	34.3 ± 24.5	35.1 ± 25.3	33.5 ± 23.8

3   Methodology

3.1 SpO_2 and PRV Features

One feature was obtained from the SpO_2 signal (ODI_3) whereas 7 more were extracted from PRV: first- to fourth order statistical moments $Mt1$–$Mt4$ in time domain and the spectral entropy from the VLF (SE_{VLF}), LF (SE_{LF}), and HF (SE_{HF}) frequency bands. Next we briefly describe each of them:

- ODI_3 is a clinical parameter widely used to help in SAHS diagnosis. It computes the number of drops from the SpO_2 signal baseline $\geq 3\%$, divided by the number of hours of the recording [14].
- $Mt1$–$Mt4$ are the well-known mean ($Mt1$), standard deviation ($Mt2$), skewness ($Mt3$), and kurtosis ($Mt4$), which characterize the central tendency, dispersion, asymmetry, and peakedness of a time series, respectively. They have shown its utility to analyze oximetric signals in the past [12].
- SE measures the flatness of the spectrum of a biomedical signal [9]. Higher SE values (closer to 1) are reached when the spectral power is spreaded throughout frequencies. By contrast, SE values closer to 0 are reached in the presence of spectrums where power is condensed [9]. SE can be computed by applying Shannon's entropy to a normalized version of the power spectral density in a frequency range [9].

These eight features were used to characterize the recordings of each subject under study and train (and test) a MLP model with ability to automatically estimate AHI.

3.2   Multi-layer Perceptron Artificial Neural Network

MLP is a supervised learning algorithm typically arranged in three fully connected layers (input, hidden, and output) [13]. The layers are formed by neurons, each of them characterized by an activation function $g(\ )$ and their connections (or weights) to neurons from other layers ($w_{i,j}$, being i and j different layers). In this study, the input layer has eight neurons due to the number of the extracted features. Moreover, according to the AHI regression task, a single unit with a linear activation function was used in the output layer. Linear activation functions were also used for each neuron in the hidden layer (N_H). The number of hidden neurons finally arranged is a tuning parameter optimized using the training set [13]. In order to prevent overfitting, a regularization parameter (α) was introduced during the MLP training

process [13]. It was also optimized along with N_H. All weights $w_{i,j}$ were optimized using the sum of squares error function minimization criterion by means of the scaled conjugate gradient algorithm [13].

3.3   Statistical Analysis

Intra-class correlation coefficient (ICC) was used to measure the concordance between our estimation and the actual AHI. Cohen's kappa (κ) assessed the diagnostic ability of the estimated AHI in the four class classification task. Estimated AHI was also evaluated in the three AHI thresholds that define the severity groups to further assess its potentiality as screening tool. Sensitivity (Se), specificity (Sp), and accuracy (Acc) were used for this purpose. Regarding the optimization of the N_H and α parameters in the MLP model, a leave-one-out cross-validation (loo-cv) procedure was applied only in the training test. The whole training set, without the loo-cv process, was used to obtain the final MLP model.

4   Results

4.1   MLP Optimization and Training (Training Set)

Figure 1 shows the optimization of N_H and α during the loo-cv procedure. The pair $N_H = 45$ and $\alpha = 0.3$ reached the highest κ (0.597). These values were chosen as optimum, and used to train the model with the whole training set.

4.2   Diagnostic Ability of Our Proposal (Test Set)

Figure 2 displays a Bland-Altman plot facing the estimated AHI and the actual AHI. A small overestimation of our AHI can be observed (mean = 1.2) with the limits of the 95% confidence interval in the range (−19.2, 21.6). Table 2 displays the confusion matrices of both ODI_3 alone and the AHI estimated by our MLP model in the test set. ODI_3 rightly estimates the severity of 62.0% of the subjects, showing an $ICC = 0.840$ between it and the actual AHI, and a Cohen's $\kappa = 0.470$ in the four-class classification task. By contrast, our estimated AHI rightly classifies 75.0% of subjects into their actual severity degree, achieving $ICC = 0.904$ and $\kappa = 0.614$. Table 3 summarizes the diagnostic statistics for the three AHI thresholds that limit the SAHS-severity levels, i.e., AHI = 5, 15, and 30 e/h. The estimated AHI reaches the highest Acc for the three thresholds, outperforming ODI_3 in AHI = 5 and 30 e/h.

Fig. 1 N_H and α optimization process with loo-cv
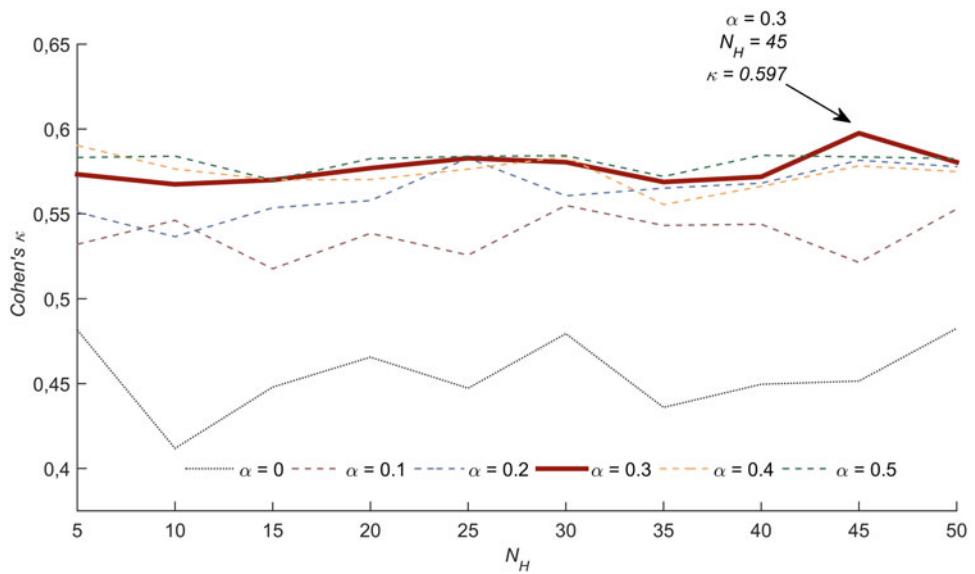
Fig. 2 Bland-Altman plot facing estimated and actual AHI
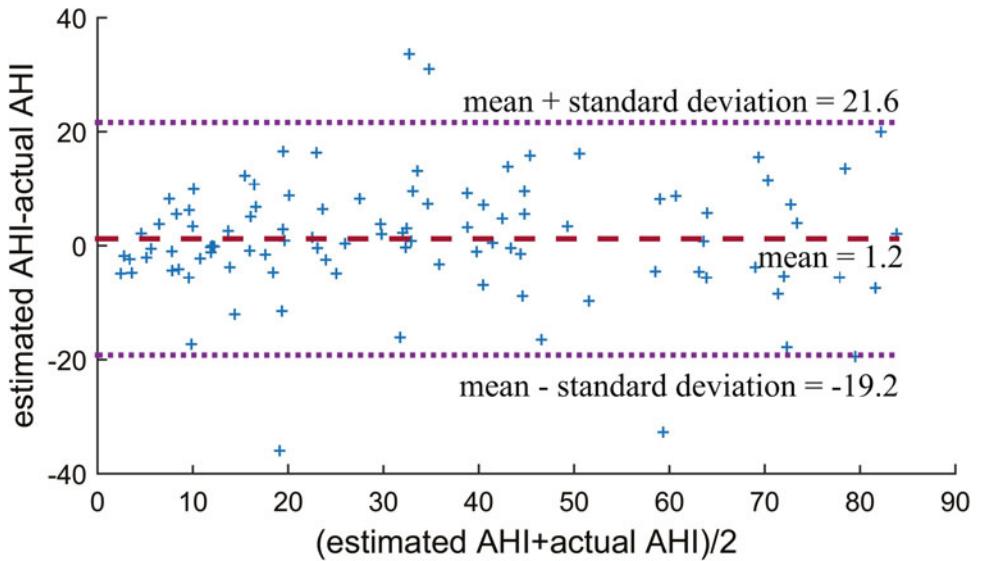
Table 2 Confusion matrices for ODI_3 and the AHI estimation derived from our MLP model (Test set). Rows correspond to the actual SAHS severity degree

	no-SAHS	Mild	Moderate	Severe
ODI_3				
no-SAHS	**6**	0	0	0
Mild	9	**13**	1	0
Moderate	0	10	**12**	1
Severe	1	0	16	**31**
Estimated AHI				
no-SAHS	**3**	3	0	0
Mild	2	**14**	6	1
Moderate	1	3	12	7
Severe	1	0	1	46

Table 3 Evaluation of AHI thresholds (5, 15, and 30 e/h) for both ODI_3 and our AHI estimation from MLP (Test set)

	5 e/h	15 e/h	30 e/h
ODI_3			
Se. (%)	89.4	84.5	64.6
Sp. (%)	100.0	96.6	98.1
Acc. (%)	90.0	**88.0**	82.0
Estimated AHI			
Se. (%)	95.7	92.9	95.8
Sp. (%)	50.0	75.9	84.6
Acc. (%)	**93.0**	**88.0**	**90.0**

5 Discussion and Conclusions

In this study, we obtained an MLP model with ability to estimate AHI from oximetric recordings acquired at patient's home. This model was trained with ODI_3 from SpO_2 as well as 7 features from PRV that reflect cardiac information not showed by the former. Our proposal reached very high agreement with actual AHI ($ICC = 0.904$) and diagnostic ability ($\kappa = 0.614$; 93.0%, 88.0%, 90.0% Acc for 5, 15, and 30 e/h, respectively), outperforming the single use of the widespread clinical parameter ODI_3 at each statistics.

Three studies have been found evaluating the diagnostic usefulness of at-home NPO. All of them only analyzed the SpO_2 signal. Olson et al. conducted a univariate analysis through delta index which showed moderate Se/Sp pairs in the three AHI thresholds (82.7%/54.2%, 88.5%/39.6%, 92.6%/34.1%, 5 e/h, 15 e/h, and 30 e/h, respectively) [15]. Chung et al. directly assessed the usefulness of at-home ODI_3, reaching 87.0, 84.0, 93.7% Acc for the same AHI thresholds [16]. Finally, Schlotthauer et al. estimated ODI_3 by means of the empirical mode decomposition, and its diagnostic assessment for AHI = 15 e/h reached 83.8% Se and 85.5% Sp [17]. Our proposal achieved an overall higher diagnostic ability than those reported in these works.

Notwithstanding these considerations, some limitations need to be pointed out. In accordance with the high prevalence of SAHS, and the pre-test symptoms referred by the patients involved in the study, the number of no-SAHS subjects is low comparing to the other SAHS-severity groups. A higher proportion of them would enhance the soundness of our results. This issue will be addressed in future studies. In addition, although the features extracted from the PRV signal have shown their usefulness, another future goal is the assessment of the information extracted by means of different analytical approaches.

Summarizing, our automatic estimation of the AHI has shown very high diagnostic ability using a MLP model only trained with at-home oximetric recordings. It outperformed the state-of-the-art studies found. Adding PRV features to ODI_3 enhanced the performance of the oximetric index alone. These results suggest that the information contained in the PRV signal complement ODI_3, leading to an accurate at-home diagnostic alternative.

Conflict of Interest The authors declare no conflict of interest.

References

1. Berry, R. B., et al.: Rules for scoring respiratory events in sleep: update of the 2007 AASM manual for the scoring of sleep and associated events. J. Clin. Sleep. Med., 8, 597, (2012).
2. Lopez-Jimenez, F. et al.: Obstructive sleep apnea: implications for cardiac and vascular disease. Chest, 133, 793–804 (2008).
3. Flemons, W. W., et al.: Home diagnosis of sleep apnea: a systematic review of the literature. Chest, 124, 1543–79 (2003).
4. Penzel, T., et al.: Comparison of detrended fluctuation analysis and spectral analysis for heart rate variability in sleep and sleep apnea. IEEE Trans. Biomed. Eng., 50, 1143–51 (2003).
5. Gutiérrez-Tobal, G. C., et al.: Utility of adaboost to detect sleep apnea-hypopnea syndrome from single-channel airflow. IEEE Trans. Biomed. Eng., 63, 636–46 (2016).
6. Bloch, K. E.: Getting the most out of nocturnal pulse oximetry. Chest, 124, 1628–30, (2003).
7. Sánchez-Morillo, D., et al.: Novel multiclass classification for home-based diagnosis of sleep apnea hypopnea syndrome. Expert Syst. Appl., 41, 1654–62 (2014).
8. Hornero, R., et al.: Nocturnal Oximetry based Evaluation of Habitually Snoring Children. Am. J. Respir. Crit. Care Med., 196, 1591–98 (2017).
9. Gutiérrez-Tobal, et al.: Assessment of time and frequency domain entropies to detect sleep apnoea in heart rate variability recordings from men and women. Entropy, 17, 123–41 (2015).
10. Garde, A., et al.: Development of a screening tool for sleep disordered breathing in children using the phone Oximeter. PloS ONE, 9, e112959 (2014).
11. Lázaro, J., et al.: Pulse rate variability analysis for discrimination of sleep-apnea-related decreases in the amplitude fluctuations of pulse photoplethysmographic signal in children. IEEE J. Biomed. Health. Inform., 18, 240–46, (2014).
12. Marcos, J. V., et al.: Automated prediction of the apnea-hypopnea index from nocturnal oximetry recordings. IEEE Trans. Biomed. Eng., 59, 141–49 (2012).
13. Gutiérrez-Tobal, G. C., et al.: Pattern recognition in airflow recordings to assist in the sleep apnoeahypopnoea syndrome diagnosis. Med. Biol. Eng. Comput., 51, 1367–80 (2013).
14. Magalang, U. J., et al.: Prediction of the apnea-hypopnea index from overnight pulse oximetry. Chest, 124, 1694–1701 (2003).
15. Olson, L. G., et al.: Prediction of sleep-disordered breathing by unattended overnight oximetry. J. Sleep. Res., 8, 51–55 (1999).
16. Chung, F., et al.: Oxygen desaturation index from nocturnal oximetry: a sensitive and specific tool to detect sleep-disordered breathing in surgical patients. Anesth. Analg., 114, 993–1000 (2012).
17. Schlotthauer, et al.: Screening of obstructive sleep apnea with empirical mode decomposition of pulse oximetry. Med. Eng. Phys., 36, 1074–80 (2014).

Are Extensor Digitorum Brevis and Gastrocnemius Working Together? Surface EMG Analysis in Healthy Children

Francesco Di Nardo, Annachiara Strazza, Michela Sara Palmieri, Alessandro Mengarelli, Stefano Cardarelli, Laura Burattini, Ornella Orsini, Federica Verdini, Antonio Bortone, and Sandro Fioretti

Abstract

A relationship between intrinsic and extrinsic foot muscles is acknowledged during walking. Literature on foot-muscle recruitment in children is not very extensive. Purpose of the study was the surface-EMG-based evaluation of possible concomitant recruitment of intrinsic and extrinsic foot muscles during healthy-children walking. Gastrocnemius lateralis (GL) was analyzed as representative for extrinsic foot muscles (ankle plantar flexor). Extensor digitorum brevis (EDB) is one of the main intrinsic foot muscles, controlling foot movement and stability. In this study, EDB was considered as representative of foot muscles. Surface-EMG signals during 4-min walking trial were acquired in eight healthy school-age children (mean $\pm$ SD: age 8.3 ± 1.7 years; height 136 ± 8 cm; mass 30.9 ± 6.2 kg) to fulfill the goal of the study. Then, Statistical gait analysis, a recent methodology performing a statistical characterization of gait, was applied to process EMG data. An exceptional number of strides were analyzed to consider the expected variability (mean $\pm$ SD = 265 ± 30 strides for each child, nearly 2500 in total). The research was undertaken in compliance with ethical principles of Helsinki Declaration and approved by institutional expert committee. Results showed that EDB activity is localized in two separate regions of gait cycle: mid-stance (from 8.2 ± 7.0 to $50.3 \pm 15.0\%$ of gait cycle) and swing phase, from 73.8 ± 13.8 to $95.1 \pm 4.7\%$. Main GL activity occurred in the same regions: mid-stance (from 5.7 ± 2.5 to $49.7 \pm 4.6\%$ of gait cycle) and swing phase, from 69.2 ± 18.7 to $95.4 \pm 5.4\%$. These findings showed that regions of activity of EDB and GL were practically overlapped, suggesting that EDB and GL worked synergistically for foot and ankle-joint control in children walking, in a large percentage of strides. Present study produced novel data on the variability of the reciprocal role of EDB and GL during children walking, providing a deeper insight in mechanisms regulating ankle-foot stability.

Keywords

Surface EMG • Ankle • Foot • Children
Statistical gait analysis

1 Introduction

The main functions of foot during human walking are: absorbing the shock of impacting the heel on the floor, in the attempt of isolating the rest of body; sustaining body weight during stance phase; and propelling the body [1]. A fundamental role in these functions are exercised by the recruitment of intrinsic and extrinsic foot muscles. Intrinsic foot muscles are located within the foot and define the plantar flexion and the dorsi-flexion of toes. Extrinsic foot muscles are located in the lower part of the leg and control foot movement, exercising different functions [2].

In adults, a relationship between intrinsic foot muscles and extrinsic foot muscles involved in ankle joint movement is acknowledged during walking [3]. In children, literature on foot-muscle recruitment is not very extensive, in particular focusing on the reciprocal role of intrinsic and extrinsic muscles. Purpose of the present study was the surface-EMG-based evaluation of possible concomitant recruitment of extrinsic (in particular ankle flexors) and intrinsic foot muscles during healthy-children walking. Gastrocnemius lateralis (GL) was analyzed as representative muscle for ankle plantar flexors. Extensor digitorum brevis (EDB) is one of the main intrinsic foot muscles; EDB is a relatively

F. Di Nardo (✉) · A. Strazza · A. Mengarelli · S. Cardarelli
L. Burattini · F. Verdini · S. Fioretti
Department of Information Engineering, Università Politecnica delle Marche, Via Brecce Bianche, 60131 Ancona, Italy
e-mail: f.dinardo@univpm.it

M. S. Palmieri · O. Orsini · A. Bortone
Centro ambulatoriale di Riabilitazione Santo Stefano, 62018 Porto Potenza Picena, Italy

flat muscle which occupies an exposed position on the dorsum of the foot. EDB controls the movements of the foot toes, assisting with extension of the second, third and fourth toes at the metatarsophalangeal joints [4]. In this study, EDB was considered as representative of foot muscles. A previous study of the present group of researchers reported data on EDB and GL in children [5], but a direct comparison has not been performed. Besides this, to our knowledge no other studies analyzed the concomitant activity of these two muscles in able-bodied children.

2 Materials and Methods

2.1 Subjects

Surface EMG signals from extensor digitorum brevis (EDB) and gastrocnemius lateralis (GL), together with foot-floor contact data, in eight able-bodied children have been taken from a previous study performed at Centro ambulatoriale di Riabilitazione Santo Stefano, Porto Potenza Picena (MC), Italy [5]. Characteristics of participants (mean ± SD and range) were reported in Table 1. Exclusion criteria: necessity of aided walking, neuromuscular diseases, disorders in balance and previous surgical intervention at ankle and/or foot. The present research has been undertaken following the ethical principles of the Helsinki Declaration and was approved by local ethical committee.

2.2 Signal Acquisition and Processing

Children were instrumented bilaterally with bipolar electrodes for surface EMG (sEMG) measurement over EDB and GL. Electrode location and orientation have been performed by a skilled licensed physical therapist, following the SENIAM recommendations [6]. Three foot-switches were also applied under the heel, the first and the fifth metatarsal heads of each foot. Participants were asked to walk barefoot back and forth over a 12-m straight path at their self-selected speed and cadence, for around 4 min. sEMG signals were acquired (sampling rate: 2 kHz; resolution: 12 bit), band-pass filtered (20–450 Hz) and treated by a double-threshold statistical detector, in order to identify myoelectric activation intervals. Briefly, this detector is

based on the observation of m successive samples once the signal exceeded the first threshold section; if at least r_0 (second threshold) out of successive m samples are still above section, activation is acknowledged. Detailed algorithm description is reported by Bonato et al. [7]. Foot-switch signals were converted into four different levels, corresponding to four different gait phases: the heel strike (H), foot-contact (F), push-off (P) and swing (S). Then, foot-switch signals were processed to identify each gait cycle [8]. Further details on signal acquisition and processing can be found in a previous study [5].

2.3 Statistical Gait Analysis

sEMG pattern analysis was performed through a recently developed methodology [9] characterizing human walking on the basis of spatial-temporal and sEMG parameters, considered hundreds of consecutive strides. This methodology relies on the cycle-dependency of muscle-activation during walking. Thus, sEMG parameters are averaged only over those cycles including the same number of activations, i.e. over each single activation modality. The activation modality defines the number of times a muscle activates during a single gait cycle: the n-activation modality consists of n active intervals for the considered muscle during a single gait cycle. To get mean activation intervals for each activation modality, muscle activations relative to every gait cycle were identified, computing onset/offset instants in temporal space. Then muscle activations were grouped according to the number of active intervals, i.e. relative to their activation modality and onset/offset time instants of each activation modality were averaged over the entire population. Averaged onset/offset percentage time instants were normalized, providing mean activation intervals in percentage of gait cycle.

3 Results and Discussion

Numerous strides have been studied for each child: a mean value (±standard deviation, SD) of 265.1 ± 30.4 strides. Data were presented as average value over right and left lower limbs. Detailed mean activation intervals for EBD and GL were reported in Tables 2 and 3, respectively. Data were

Table 1 Characteristics of participants

	Mean ± SD	Range
Age (months)	98.6 ± 12.6	81 ÷ 127
Height (cm)	136 ± 8	100 ÷ 140
Mass (Kg)	30.9 ± 6.2	18 ÷ 33

Table 2 Activation intervals of extensor digitorum brevis. Activation intervals of extensor digitorum brevis in its main modalities of activation, expressed as the timing, in the percentage of gait cycle, of signal onset and offset. Values are expressed as mean ± standard deviation (SD)

EDB	First activation		Second activation		Third activation	
	On	Off	On	Off	On	Off
1-activation mod	17.5 ± 14.7	79.1 ± 15.3				
2-activation mod	8.25 ± 7.0	50.3 ± 15.0	73.8 ± 13.8	91.5 ± 7.2		
3-activation mod	4.0 ± 3.6	36.6 ± 18.9	52.1 ± 13.6	66.4 ± 8.7	83.8 ± 8.3	95.1 ± 4.7

Table 3 Activation intervals of gastrocnemius lateralis. Activation intervals of gastrocnemius lateralis in its main modalities of activation, expressed as the timing, in the percentage of gait cycle, of signal onset and offset. Values are expressed as mean ± standard deviation (SD)

GL	First activation		Second activation		Third activation	
	On	Off	On	Off	On	Off
1-activation mod	9.7 ± 4.3	49.7 ± 4.6				
2-activation mod	5.7 ± 2.5	41.3 ± 7.5	69.2 ± 18.7	87.3 ± 7.5		
3-activation mod	2.0 ± 1.6	18.9 ± 10.4	31.8 ± 9.4	52.2 ± 13.7	85.1 ± 7.2	95.4 ± 5.4

reported for the three main activation modalities of each muscle.

Table 2 showed as muscular activity of EDB was gathered mainly during the stance phase. Figure 1 (upper grey-level-coded horizontal bar) indicated that the most frequent EDB recruitment occurred in the second half of stance phase between 30 and 55% of gait cycle.

This activity is acknowledged as the typical EDB recruitment during able-bodied walking [10]. It was interpreted as the participation of EDB in controlling mid-tarsal dorsiflexion in order to regulate shock absorbing mechanism; then, advancing the body, the action of EDB is suggested to be present to control mid-foot stability developing

Fig. 1 Muscle activation intervals over the population for EDB and GL. Values are expressed in percentage of gait cycle (0–100%). The three main activation modalities were considered all together in computing the horizontal bars. Horizontal bars are grey-level coded, according to the number of children where a certain condition is observed; black: condition observed for all subjects in every modality of activation, white: condition never met. The duration of gait phases, Heel contact (H), Flat foot contact (F), Push off (P), Swing (S), are indicated with vertical dashed lines

muscle tension for weight-bearing [4, 10]. This physiological interpretation has been extended also at children walking [5]. One more zone of activity has been detected during swing (Table 2 and Fig. 1); it occurs for a further control of the foot before touching the ground.

Table 3 showed as muscular activity of GL was gathered mainly during the stance phase. Figure 1 (lower grey-level-coded horizontal bar) indicated that the most frequent GL recruitment occurred in the second half of stance phase between 25 and 50% of gait cycle. This activity is acknowledged as the typical GL recruitment during able-bodied walking, both in adults and children [9–11]. It was interpreted as GL participation in slowing down the forward progression of tibia over the talus during the second rocker, therefore controlling ankle dorsiflexion [9–11]. Shorter and less frequent GL activity was detected also during swing (Fig. 1).

The activity of GL and EDB were virtually overlapped during stance (Fig. 1), suggesting that in child walking they worked cooperatively for controlling the foot and the ankle joint during foot-floor contact. A synergistic action of these two muscles has been detected also during swing around 85% of gait cycle (Fig. 1). It is likely for accurately positioning of the foot, in preparation of the following heel strike.

4 Conclusion

The findings of the present study showed that regions of activity of EDB and GL were virtually overlapped in children during walking, suggesting that EDB and GL worked cooperatively for foot and ankle-joint control, in a large percentage of strides. In this way, present study produced

novel data on variability of the reciprocal role of intrinsic and extrinsic foot muscles during child walking, providing a deeper insight in mechanisms regulating ankle-foot stability.

References

1. Dixon PC, Böhm H, Döderlein L (2012) Ankle and midfoot kinetics during normal gait: a multi-segment approach. J Biomech 45: 1011–1016.
2. Wright WG, Ivanenko YP, Gurfinkel VS (2012) Foot anatomy specialization for postural sensation and control. J Neurophysiol 107: 1513–21.
3. Zelik KE, La Scaleia V, Ivanenko YP, et al (2015) Coordination of intrinsic and extrinsic foot muscles during walking. Eur J Appl Physiol 115: 691–701.
4. Mckeon PO, Hertel J, Bramble D, et al (2014) The foot core system: a new paradigm for understanding intrinsic foot muscle function. Br J Sports Med. 1–9.
5. Di Nardo F, Strazza A, Palmieri MS, et al (2017) Detection of surface-EMG activity from extensor digitorum brevis muscle in healthy children walking. Physiol Meas 26.
6. Freriks B, Hermens HJ, Disselhorst-Klug C, et al (2000) The recommendations for sensors and sensor placement procedures for surface electromyography. J Electromyogr Kinesiol 10: 361–374.
7. Bonato P, D'Alessio T, Knaflitz M (1998) A statistical method for the measurement of muscle activation intervals from surface myoelectric signal during gait. IEEE Trans Biomed Eng 45: 287–299.
8. Agostini V, Balestra G, Knaflitz M (2014) Segmentation and classification of gait cycles. IEEE Trans Neural Syst Rehabil Eng 22: 946–952.
9. Agostini V, Nascimbeni A, Gaffuri A, et al (2010) Normative EMG activation patterns of school-age children during gait. Gait Posture 32: 285–289.
10. Perry J 1992 Gait Analysis: Normal and Pathological Function vol 12.
11. Di Nardo F, Fioretti S (2014) Emg-based analysis of treadmill and ground walking in distal leg muscles. IFMBE Proceedings 41: 611–614.

A Time-Frequency Approach for the Assessment of Dynamic Muscle Co-contractions

Annachiara Strazza, Federica Verdini, Alessandro Mengarelli,
Stefano Cardarelli, Laura Burattini, Sandro Fioretti,
and Francesco Di Nardo

Abstract

Co-contraction is defined as the activity of agonist and antagonist muscles around a joint, enhancing stability and balance. The quantitative assessment of muscle co-contractions would be meaningful for deepening the comprehension of this physiological mechanism. Thus, the purpose of this work is to quantify muscle co-contraction using energy localization in time-frequency domain of sEMG signal during straight walking. To this purpose, sEMG from tibialis anterior (TA) and gastrocnemius lateralis (GL) and basographic signals were acquired in five healthy subjects during walking. Basographic signals were analyzed to quantify foot-floor contact. sEMG signals were processed using Wavelet Transform (WT) to identify muscular co-contractions, according to the following steps. Daubechies (order 4 with 6 levels of decomposition) was chosen as mother wavelet. A denoising algorithm based on Daubechies mother wavelet was applied for removing noise from raw signals. Denoised signals were decomposed into WT coefficients with different frequency content, and then recombined to achieve the co-scalogram function, a localized statistical assessment of cross-energy density between signals. The localization of regions with maximum cross-energy density provided the assessment of co-contractions in time-frequency domain. This methodology applied to TA and GL signals was able to detect GL/TA co-contractions during mid-stance (30–34% of GC) phase, matching with literature. Moreover, WT approach was able to provide also the frequency band of information content for muscle co-contractions: 65–164 Hz. In conclusion, this study proposed WT cross-energy density as a reliable estimation of muscle co-contraction in time-frequency domain.

1 Introduction

Muscular co-contraction is defined as the simultaneous activity of agonist and antagonist muscles around a joint in the same plane [1]. This mechanism represents a known strategy for improving postural stability, joint stiffness and movement accuracy [2]. The quantitative assessment of muscle co-contractions is meaningful for deepening the comprehension of this physiological mechanism. In particular, co-activations of ankle muscle couple defined by tibialis anterior (TA) and gastrocnemius lateralis (GL) were documented in normal [3] and pathological [4] gait. The antagonist role of TA and GL is well-known during walking; TA is recruited in loading response and swing phase, while GL is active in stance period [5]. However, co-contractions between these two muscles during weight acceptance and stance phases were quantified by means of different EMG-based approaches [6–8]. Instead, poor information are available in literature to assess the frequency band where the muscles showed the reported co-contractions. Thus, it could be meaningful identifying the time-interval and the frequency band where the muscles showed their concomitant recruitment during gait. To pursue these goals, wavelet transform (WT) analysis of surface EMG (sEMG) signals seems to be an appropriate approach. WT is an advanced signal processing technique that maps a time waveform into frequency-time domain providing a good localization in both time and frequency domains [9, 10]. WT methodology is able to provide the co-scalogram function, a localized statistical assessment of the time-frequency cross-energy density, that represents the information content of the sEMG signal in both time and frequency domain. Thus, the purpose

A. Strazza (✉) · F. Verdini · A. Mengarelli · S. Cardarelli
L. Burattini · S. Fioretti · F. Di Nardo
Department of Information Engineering, Università Politecnica
delle Marche, Via Brecce Bianche, 60131 Ancona, Italy
e-mail: a.strazza@pm.univpm.it

of this work is to quantify ankle muscle co-contraction using cross-energy localization in time-frequency domain of sEMG signal during straight walking.

2 Materials and Methods

A. Subjects

Five healthy young adults (3 females and 2 males) were recruited for the study. Mean ($\pm$SD) characteristics are: age 22.7 ± 0.5 years; height 166 ± 8 cm; weight 53.6 ± 8.1 kg; body mass index (BMI) 18.9 ± 1.5 kg m^{-2}. Exclusion criteria included pathological or chronic joints pain, neurological pathology, orthopedic surgery within previous year, abnormal gait or BMI ≥ 25. Participants signed informed consent. The present research was undertaken in compliance with the ethical principles of Helsinki Declaration and approved by institutional expert committee.

B. Signal Acquisition

Participants were bilaterally instrumented with surface EMG (sEMG) probes and three foot-switches. sEMG signals were acquired through the Step 32 system (Medical Technology, Italy), with a sampling rate of 2 kHz and a resolution of 12 bit. Fixed geometry sEMG probes (Ag/Ag-Cl disk; electrode diameter 0.4 cm; inter-electrode distance 0.8 cm; gain 1000, input impedance > 1.5 GΩ, CMRR > 126 dB), placed on TA and GL, following the SENIAM recommendations for electrode location-orientation over muscles with respect to tendons, motor points and fiber direction [11], were used to acquire sEMG signals. Foot-switches were placed beneath the heel and the first and fifth metatarsal heads of the foot; each sensor had a surface of 1.21 cm^2 and an activation force equal to 3 N. After positioning the sensors, subjects were asked to walk barefoot over the floor for 5 min at their natural pace, back and forth over a 12-m long straight track.

C. Signal Processing

Footswitch signals were debounced, converted to four levels, Heel contact (H), Flat foot contact (F), Push-off (P), Swing (S), and processed to segment and classify the different gait cycle (GC). Then, foot-switch signals were processed to identify each gait cycle (GC) [12]. sEMG signals were amplified and band-pass filtered (20–450 Hz). sEMG signals were processed by means of Continuous Wavelet Transform (CWT). CWT is a time-frequency analysis method that quantifies temporal changes of the frequency content of non-stationary signals without losing resolution in time or frequency [13]. CWT of the input signal x(t) is defined as the inner product between the analyzed signal $x(t)$ and the basis function $\psi_{a,b}(t)$, as in the following expression (Eq. 1):

$$CWT_{x(a,b)} = \int x(t)\psi_{a,b}^*(t)dt \quad a \neq 0 \tag{1}$$

The basis function $\psi_{a,b}(t)$, the mother wavelet, is reported in Eq. 2:

$$\psi_{a,b}(t) = \frac{1}{\sqrt{a}}\psi\left(\frac{t-b}{a}\right) \tag{2}$$

where a represents the scale parameter, b represents the translation parameter (time shifting), and $\psi_{a,b}(t)$ is obtained by the mother wavelet function $\psi(t)$ at time b and scale a. WT approach provides multiresolution analysis: the global information of the signal is associated to low frequencies and the detailed information to high frequencies [14].

In this work, mother wavelet Daubechies of order 4 with 6 levels of decomposition (db4) has been chosen to implement the wavelet transform, for its suitability to detect signal changes and for the shape similarity between its shape and the shape of motor unit action potentials [15]. The sEMG signal was decomposed into its frequency content, performing a series of high- and low-pass filter operations followed by down-sampling, and then was reconstructed. Moreover, CWT has been applied for removing noise from sEMG [13]. The SNR values were computed according to the following definition (Eq. 3):

$$SNR = 20 \cdot log \frac{(\Delta EMG)}{(4 \cdot std(sEMG))} \tag{3}$$

where ΔEMG is a signal-measure representing maximum-minus minimum amplitudes of signal and $std(sEMG)$ is a noise-measure representing the sEMG standard deviation. Thus, SNRraw represents the SNR values of sEMG signals before the WT denoising, while SNRclean represents the SNR values of denoised signals after the WT denoising.

The assessment of muscular co-contractions in time-frequency domain has been identified starting from CWT co-scalogram function. Co-scalogram function is defined as (Eq. 4):

$$P_W x(a,b) = W_x(s,\tau) W_y^*(s,\tau) \tag{4}$$

providing a localized statistical assessment of cross-energy density between signals. The cross-energy density between signals identifies their local correlation. Co-scalogram of denoised sEMG signal was computed for each single stride and for every muscle during walking. The localization of regions with maximum cross-energy density has been identified as the interval in time-frequency where the co-scalogram is exceeding the 72% of the peak value of cross-energy density in both time and frequency domain. In time, periods shorter

than 30 ms were not considered as actual co-activations, because a muscular activity performs an active control on joints motion only when it lasts at least 30 ms [16].

3   Results and Discussion

Raw and denoised sEMG signals from tibialis anterior and gastrocnemius lateralis in subject 1 is presented in Fig. 1, panel a and b respectively. Comparable results were obtained in subjects 2–5.

SNR values of sEMG signals before the WT filtering (SNRraw) and SNR values of denoised signals after the WT filtering (SNRclean) of TA and GL muscles are reported in Table 1.

In a two-dimensional graph, co-scalogram and scalogram are expressed in function of time (% of GC) and scale, depend on frequency (Hz). The 2D color representation of the co-scalogram and scalogram for sEMG signals from TA, GL is reported in Fig. 2, panel a, b and c respectively.

For GL, the scalogram (Fig. 2b) showed that the maximum energy density in time occurred from 13 to 17% of GC

Fig. 1 Example of raw and denoised tibialis anterior (panel **a**) and gastrocnemius lateralis (panel **b**) sEMG signal during gait cycle

Table 1 SNR for tibialis anterior and gastrocnemius lateralis before (SNRraw) and after (SNRclean) WT denoising alghoritm

Subjects	Tibialis anterior		Gastrocnemius lateralis	
	SNRraw	SNRclean	SNRraw	SNRclean
#1	16.4	17.2	17.9	19.1
#2	16.8	17.6	16.7	18.3
#3	14.9	16.2	16.1	17.1
#4	17.7	19.1	18.6	19.2
#5	15.2	17.4	18.9	20.2
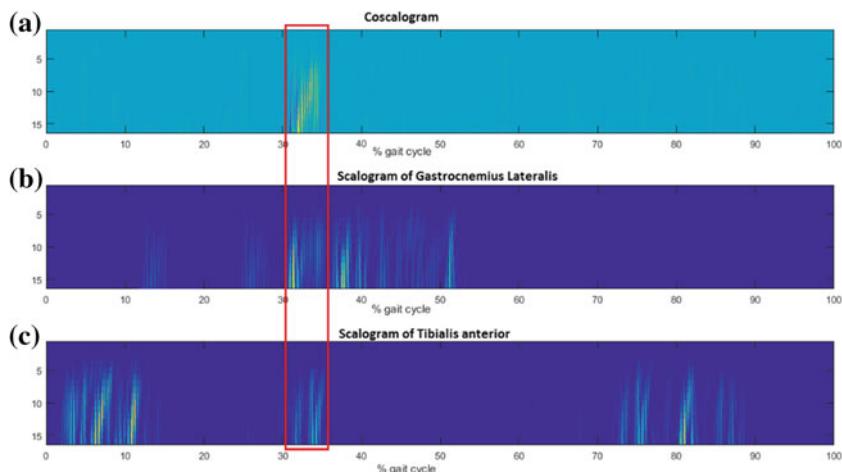
Fig. 2 2D color representation of cross-energy density for GL, TA in time-frequency domain (**a**) 2D color representation of scalogram for GL, TA (**b**, **c**). The color-level coded scale represents the logarithm of

the squared modulus of the wavelet coefficients; Yellow colors indicate higher cross-energy; blue colors indicate low cross-energy (Color figure online)

with a lower energy, and in mid-stance (P-phase), from 25 to 53% of GC. The maximum energy density in frequency was detected in frequency band between 65 and 167 Hz.

For TA, the maximum energy density in time occurred in early stance (H-phase), from 2 to 14% of GC and in swing phase from 73 to 88% of GC (Fig. 2c). During mid-stance phase, a lower energy density of TA is detected between 30 to 34% of GC. The energy density in frequency was detected in frequency band between 60 and 220 Hz. The co-scalogram, i.e. cross-energy density, was able to detect GL/TA co-contractions in time and frequency domain. During gait cycle, the localization of regions with maximum cross-energy density was assessed in mid-stance phase, between 30 and 35% of GC (Fig. 2a). This period is longer than 30 ms [16]; this region of maximum cross-energy density could be considered as an actual co-activation, matching with the literature [1, 3]. Moreover, co-scalogram function was able to provide also the maximum frequency band of information content for ankle muscle co-contractions: 65–164 Hz.

The localization in time of maximum cross-energy density, performed in the present study, could be interpreted as the time-interval where the sEMG signal reached its peak value of cross-energy, i.e. the region of GC where the ankle muscles showed their concomitant recruitment. The localization in frequency of maximum cross-energy density, was interpreted as the frequency-band where EMG signals of TA and GL showed the maximum frequency content of their superimposition.

4 Conclusion

The present study could be suitable for both supporting WT approach for sEMG denoising and providing a quantitative assessment of muscle concomitant recruitment during walking. In conclusion, this study proposed WT cross-energy density as a reliable estimation of muscle co-contraction in time-frequency domain.

References

1. Olney SJ (1983) Quantitative evaluation of cocontraction of knee and ankle muscles in normal walking. In: Biomechanics IX: International Congress of Biomechanics. pp 431–436.
2. Falconer K, Winter DA (1985) Quantitative assessment of co-contraction at the ankle joint in walking. Electromyogr Clin Neurophysiol 25:135–149.
3. Di Nardo F, Mengarelli A, Maranesi E, et al (2015) Assessment of the ankle muscle co-contraction during normal gait: A surface electromyography study. J Electromyogr Kinesiol 25:347–354.
4. Rosa MCN, Marques A, Demain S, et al (2014) Methodologies to assess muscle co-contraction during gait in people with neurological impairment - A systematic literature review. J. Electromyogr. Kinesiol. 24:179–191.
5. Perry J (1992) Gait Analysis: Normal and Pathological Function.
6. Strazza A, Mengarelli A, Fioretti S, et al (2017) Surface-EMG analysis for the quantification of thigh muscle dynamic co-contractions during normal gait. Gait Posture 51:228–233.
7. Hansen S, Hansen NL, Christensen LOD, et al (2002) Coupling of antagonistic ankle muscles during co-contraction in humans. Exp Brain Res 146:282–292.
8. Draganich LF, Jaeger RJ, Kralj R (1989) Coactivation of the hamstrings and quadriceps during extension of the knee. J Bone Joint Surg Am 71:1075–1081.
9. Strazza A, Verdini F, Burattini L, et al (2017) Time-frequency analysis of surface EMG signals for maximum energy localization during gait. Gait Posture 57:9–10.
10. Rioul O, Flandrin P (1992) Time-Scale Energy Distributions: A General Class Extending Wavelet Transforms. IEEE Trans Signal Process 40:1746–1757.
11. Hermens HJ, Freriks B, Disselhorst-Klug C, Rau G (2000) Development of recommendations for SEMG sensors and sensor placement procedures. J Electromyogr Kinesiol 10:361–374.
12. Agostini V, Balestra G, Knaflitz M (2014) Segmentation and classification of gait cycles. IEEE Trans Neural Syst Rehabil Eng 22:946–952.
13. Reaz MBI, Hussain MS, Mohd-Yasin F (2006) Techniques of EMG signal analysis: detection, processing, classification and applications (Correction). Biol Proced Online 8:163–163.
14. Mallat SG (1989) A Theory for Multiresolution Signal Decomposition: The Wavelet Representation. IEEE Trans Pattern Anal Mach Intell 11:674–693.
15. Farge M (1992) Wavelet Transforms and their Applications to Turbulence. Annu Rev Fluid Mech 24:395–458.
16. Bonato P, D'Alessio T, Knaflitz M (1998) A statistical method for the measurement of muscle activation intervals from surface myoelectric signal during gait. IEEE Transactions on Biomedical Engineering 45(3):287–99.

Scalp Level Connectivity for Representative Channels in Emotional Status

Jia Wen Li, Xu Tong Cui, Shovan Barma, Sio Hang Pun,
Pedro Antonio Mou, Hui Juan Huang, U. Kin Che, Mang I. Vai,
and Peng Un Mak

Abstract

Emotion can be regarded as a special brain status and it can be captured by Electroencephalography (EEG) via deploying number of channels all over the scalp. To find out the characteristics of emotional responses, the scalp level connectivity is one of the interests that considered. Nevertheless, to distinguish the significant EEG channels, which can imply the special regions at scalp level, has not yet been studied well. Therefore, in this work, we aim to identify the representative channels towards different emotional status by considering the connectivity derived from the values of coherence and correlation. In this purpose, DEAP, an online database has been investigated. Certainly, the emotional status can be evaluated on the valence-arousal (V-A) space and here, four groups contain HVHA, HVLA, LVHA, and LVLA have been studied. The results from 16 subjects show that the EEG channels AF3, F7, P7 and O1 have higher percentages in term of the connectivity and they could be considered as the representative channels in this case. Such findings could be useful to understand the scalp responses in emotional status.

J. W. Li (✉) · X. T. Cui · P. A. Mou · U. K. Che · M. I. Vai
P. U. Mak (✉)
Faculty of Science and Technology, Department of Electrical
and Computer Engineering, University of Macau, Macau SAR,
China
e-mail: gzcat29@gmail.com

P. U. Mak
e-mail: fstpum@umac.mo

J. W. Li · X. T. Cui · S. H. Pun · H. J. Huang · U. K. Che
M. I. Vai
State Key Laboratory of Analog and Mixed-Signal VLSI,
University of Macau, Macau SAR, China

S. Barma
Department of Electronics and Communication Engineering,
Indian Institute of Information Technology Guwahati, Guwahati,
India

1 Introduction

Emotion is an affective reaction to an event or stimulation, which can be observed by facial expression, voice, body movement, and so on. As usual, emotion is regulated by the brain and certainly, it can be recognized by electroencephalography (EEG), a non-invasive electrophysiological monitoring technique to record the electrical signals of the brain. Furthermore, because the EEG technique can detect the changes within millisecond timeframe and has the best time resolution than other approaches such as positron emission tomography (PET) and functional magnetic resonance imaging (fMRI), it has been widely used to analyze the emotional status of brain [1–5]. Based on EEG signals analysis, the emotion recognition can be realized so that to identify individual emotions in various areas like artificial intelligence and disease treatment can be accomplished. Such applications reflect the significances of emotional studies by using EEG signals in biomedical engineering field.

In literatures, EEG-based emotional studies mainly concentrate on the extractions of distinct features for distinguishing the emotions by using various algorithms, such as relative power values by fast Fourier transform (FFT) [6], prominent frequency wave by time-frequency analysis [7], and event-related potentials (ERPs) by signal-to-noise ratio maximizer (SIM) algorithm [8], etc. Nonetheless, the studies related to the scalp responses in the emotional status, especially the representative channels, have not yet been investigated well. Thereby, this work aims the representative channels based on the analysis of connectivity at scalp level. In

this purpose, two methods containing coherence in frequency domain and correlation in time domain have been employed. Then, with the values of coherence and correlation among all pairs of the channels, the representative channels can be selected. For experimental validation, DEAP, an online EEG emotional database has been considered [9]. Sixteen subjects from this database including female and male with different emotional status have been investigated. The representative channels are obtained from the statistical results of the values in term of the connectivity. The paper has been organized as follows. Section 2 introduces the usage of DEAP database in this work. Section 3 concentrates on how to find the representative channels by considering the connectivity based on coherence and correlation values. Section 4 discusses the statistical results from the subjects. Finally, conclusions have been drawn in Sect. 5.

2 DEAP Database

To study the responses in emotional status at scalp level through the EEG signals, it is required an EEG database that contains different emotional status and provides the technical parameters such as the number and locations of the scalp electrodes, sampling rate, time epoch, and so on. Then, DEAP database [9] is appropriate in this case. In DEAP, the EEG signals of 32 subjects have been denoted as each watched 40 different one-minute long music videos, i.e., there are 40 trails for one subject. After watching these videos, the subjects rated each video in terms of the levels of valence (V) and arousal (A). Based on the V-A scores, the emotions can be classified into four groups, high valence high arousal (HVHA), high valence low arousal (HVLA), low valence high arousal (LVHA), and low valence low arousal (LVLA). In this work, the chosen scores for classifications are: HVHA (V $\geq$ 5, A 5), HVLA (V $\geq$ 5, A < 5), LVHA (V < 5, A $\geq$ 5), and LVLA (V < 5, A < 5) respectively, where the thresholds of V and A scores are 5 [10]. Additionally, the EEG signals presented in the database have been recorded by 10–20 system consisting of 32 scalp channels (FP1, AF3, F3, F7, FC5, FC1, C3, T7, CP5, CP1, P3, P7, PO3, O1, OZ, PZ, FP2, AF4, FZ, F4, F8, FC6, FC2, CZ, C4, T8, CP6, CP2, P4, P8, PO4, and O2). The sampling rate is 128 Hz and the analog pass band of 0.01–100 Hz had been applied for preprocessing the EEG signals. For each group of emotion, 6 subjects have been studied. Due to the amount of trials is limited for some subjects, especially in HVLA and LVLA group, we made adjustments of the number and finally, 96 trials from 16 subjects have been selected. The details have been summarized into Table 1 in which the first column specifies the types of

emotion groups, and the rest displays the selection of corresponding subjects and the number of trails.

3 Connectivity for Representative Channels

Normally, the reaction of brain in term of the electrical activities can be expressed by the EEG signals recorded from the scalp. Based on the analysis of EEG signals, several connections between the channels can be considered and via the connectivity, the channels with prominent responses in the emotional status can be presented. Therefore, based on the values of connectivity, the representative channels can be selected for denoting the special regions that correlates with the emotional status. To map the connectivity from the EEG signals, several approaches have been applied to quantify the communication between the EEG channels, such as coherence method in frequency domain and correlation method in time domain. Because EEG represents a set of continuous voltage and time values, hence, it can be considered as a multivariate time series that belongs to the stochastic processes and this stochastic nature of EEG allows the use of correlation and coherence to indicate the scalp level connectivity [11]. In this light, to attain the representative channels from the connectivity, the methods of coherence and correlation have been applied in this work.

On one hand, the correlation metric is a conventional connectivity technique derived in time domain and it can be used to reveal the signal similarity including EEG [12]. The correlation is mathematically expressed as:

$$correlaion_{xy} = \frac{\sum_{i=1}^{n}(x_i - \bar{x})(y_i - \bar{y})}{\sqrt{\sum_{i=1}^{n}(x_i - \bar{x})^2 \sum_{i=1}^{n}(y_i - \bar{y})^2}} \quad (1)$$

where x and y are two sets of signals for the correlation calculation, and n is the amount of each set elements. Certainly, the higher correlation means the higher connection existing between the two signals. On other hand, the coherence is another typical metric that quantifying the phase synchrony between a pair of signals in the frequency domain [13] and it is a normalized coefficient which is mathematically expressed as:
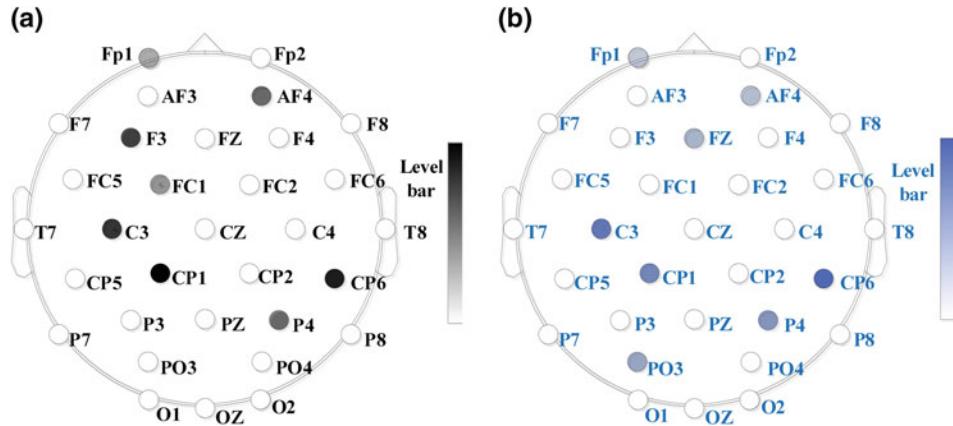
$$coh_{xy}(\omega) = \frac{|S_{xy}(\omega)|}{\sqrt{S_{xx}(\omega)S_{yy}(\omega)}} \quad (2)$$

In (2), the numerator and denominator represent the averaged cross-spectral densities and the averaged power estimations between signals x and y at frequency ω respectively. Again, the higher coherence indicates the higher

Table 1 Subjects and trials studied in this work

Group	Subject id in DEAP	No. of trials	Total trials
HVHA	2; 7; 21; 26; 27; 28	5 for each subject	30
HVLA	3; 5; 7; 11; 15; 28	3 for each subject	18
LVHA	2; 11; 13; 22; 24; 31	5 for each subject	30
LVLA	2; 4; 26; 27; 28; 29	3 for each subject	18

Fig. 1 Representative channels by the connectivity methods. **a** Coherence; **b** correlation

connection existing between the two signals. Additionally, from [14], for the EEG-based studies, the connection between a pair of signals can be regarded as strong when the value of correlation and coherence exceed 0.7 and 0.6 respectively. Thereby, in this work, the strong connections have been considered when the values exceed these thresholds (correlation $\geq$ 0.7; coherence $\geq$ 0.6). Based on the connectivity, the channels with larger summation of the connectivity values (correlation or coherence) among all pairs of the EEG channels have been regarded as the representatives. As a preliminary study, we consider the top 4 EEG channels which have larger summation of both coherence and correlation among all the channels as the representative channels for implying the special regions that have relationships with the emotional status. Therefore, by using the connectivity methods of coherence and correlation, the representative channels can be figured out.

4 Results and Discussion

Figure 1 is a sample result of the representative channels from trial 17 (HVHA) of Subject 2 and Fig. 1a is by coherence method, while Fig. 1b is by correlation method. In these two scalp maps, the channels enclosed with deeper color mean they have stronger responses in term of the connectivity, which decentralized in the central, frontal, and parietal lobes of both right and left hemispheres. Besides, the results of representative channels are similar (C3, CP1, CP6
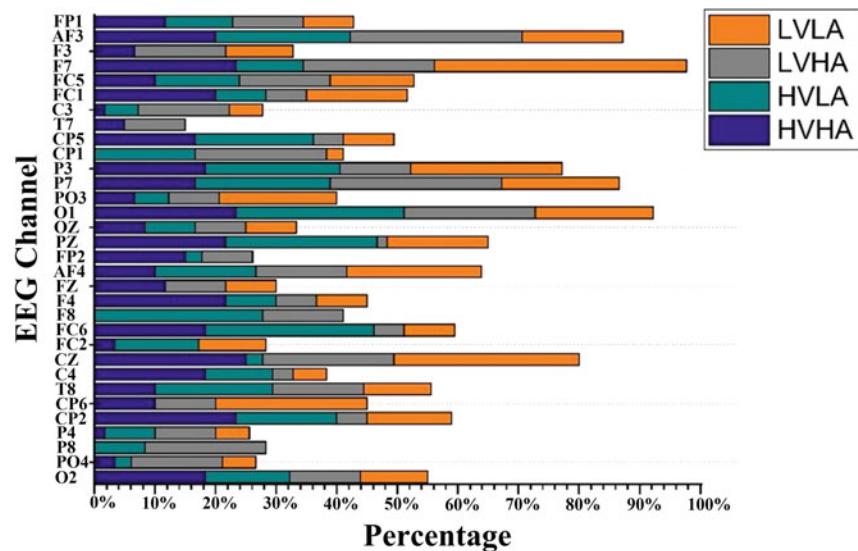
and P4) by the two applied methods. As seen, both of coherence and correlation are available to construct the scalp level connectivity via the EEG signals and to select the representative channels with prominent responses.

Figure 2 presents the statistical results of the representative channels from 16 subjects by using the mentioned methods. In Fig. 2, for LVLA, LVHA, HVLA, and HVHA groups, the representative channels with higher percentages are F7, CZ, CP6 and P3; AF3, F7, P7 and O1; F8, FC6, PZ and O1; F7, CZ, CP2 and O1, respectively. Additionally, to sum up the results of all 16 subjects in four kinds of emotions, the channels AF3, F7, P7 and O1 have relatively higher percentages. Thus, these EEG channels seem to have more connections in the emotional status. However, considering the individual results, the representative channels are not always very consistent and hence, it can be said that the emotional reaction seems subjective. Although there are common EEG channels can be found among different subjects, in our future study, the individual characteristics will be taken into as one of the significant considerations for the analysis of emotional status via EEG.

5 Conclusion

To investigate the scalp responses of the emotional status through the EEG signals, the data from DEAP database has been considered in this work. Then, the representative channels have been selected based on the two connectivity

Fig. 2 Statistical results of the representative channels in different groups of emotional status

methods including coherence and correlation. According to the mapping results of connectivity, both the coherence and correlation approaches are available to find the representative channels. Furthermore, from the statistical results of 16 subjects in four groups of emotions, the representative channels are found as: LVLA (F7, CZ, CP6 and P3); LVHA (AF3, F7, P7 and O1); HVLA (F8, FC6, PZ and O1); HVHA (F7, CZ, CP2 and O1). Moreover, the overall results with higher percentages of the connectivity are AF3, F7, P7 and O1. Therefore, these EEG channels can be regarded as significant with the emotional status. Although several channels can be found based on the statistical results, the individual characteristics can be observed so that it can be said that the emotional reactions are quite subjective. In short, the coherence and correlation methods can be used to obtain the scalp level connectivity and to select the channels presenting the special regions of scalp responses. Based on the connectivity, we can also study the relevant channels at scalp level in various neurological conditions, such as autism, sleep apnea, Alzheimer's disease, and so on.

References

1. Kumar N., Khaund K., Hazarika S.M.: Bispectral Analysis of EEG for Emotion Recognition. Procedia Computer Science 84, 31–35 (2016).
2. Soleymani M., Asghari-Esfeden S., Fu Y., *et al.*: Analysis of EEG Signals and Facial Expressions for Continuous Emotion Detection. IEEE Transactions on Affective Computing 7(1), 17–28 (2016).
3. Petrantonakis P.C., Hadjileontiadis L.J.: Emotion Recognition from EEG Using Higher Order Crossings. IEEE Transactions on Information Technology in Biomedicine 14(2), 186–197 (2010).
4. Zheng W.L., Lu B.L.: Investigating Critical Frequency Bands and Channels for EEG-Based Emotion Recognition with Deep Neural Networks. IEEE Transactions on Autonomous Mental Development 7(3), 162–175 (2015).
5. Lin Y.P., Wang C.H., Jung T.P., *et al.*: EEG-Based Emotion Recognition in Music Listening. IEEE Transactions on Biomedical Engineering 57(7), 1798–1806 (2010).
6. Ko K.E., Yang H.C., Sim K.B.: Emotion Recognition using EEG Signals with Relative Power Values and Bayesian Network. International Journal of Control, Automation, and Systems 7(5), 865–870 (2009).
7. Mehmood R.M., Lee H.J.: Exploration of Prominent Frequency Wave in EEG Signals from Brain Sensors Network. International Journal of Distributed Sensor Networks 2015(5), 1–9 (2015).
8. Jiang J., Zeng Y., Tong L., *et al.*: Single-trial ERP Detecting for Emotion Recognition. In: 17th IEEE/ACIS International Conference on Software Engineering, Artificial Intelligence, Networking and Parallel/Distributed Computing, pp. 105–108. IEEE, Shanghai, China (2016).
9. Koelstra S., Mühl C., Soleymani M., *et al.*: DEAP: A Database for Emotion Analysis Using Physiological Signals. IEEE Transactions on Affective Computing 3(1), 18–31 (2012).
10. Aguin A.R., Lo M.A.: Classification Model of Arousal and Valence Mental States by EEG Signals Analysis and Brodmann

Correlations. International Journal of Advanced Computer Science and Applications 6(6), 230–238 (2015).

11. Bastos A.M., Schoffelen J.M.: A Tutorial Review of Functional Connectivity Analysis Methods and Their Interpretational Pitfalls. Frontiers in Systems Neuroscience 9(1), 1–23 (2016).

12. Guevara M.A., Corsi-Cabrera M.: EEG coherence or EEG correlation? International Journal of Psychophysiology 23, 145–153 (1996).

13. Wang G., Sun Z., Tao R., et al.: Epileptic Seizure Detection Based on Partial Directed Coherence Analysis. IEEE Journal of Biomedical and Health Informatics 20(3), 873–879 (2016).

14. Lithari C., Klados M.A., Bamidis P.D.: Graph Analysis on Functional Connectivity Networks during an Emotional Paradigm. In: Bamidis P.D., Pallikarakis N. (eds) XII Mediterranean Conference on Medical and Biological Engineering and Computing 2010, IFMBE Proceedings, vol. 29, pp. 115–118. Springer, Heidelberg (2010).

Investigation of Changes in Causality Throughout Life—A Magnetoencephalogram Study Using Granger Causality and Transfer Entropy

Elizabeth Shumbayawonda, Alberto Fernández, Michael P. Hughes, and Daniel Abásolo

Abstract

The use of magnetoencephalogram (MEG) signals in cognitive neuroscience research to investigate the functioning of the brain has increased over recent years. In this sensor space study, Granger Causality (GC) and Transfer entropy (TE) were applied to resting state MEGs from 220 healthy volunteers (aged 7–84) to characterise the possible changes in causality due to age and gender. Additionally, graph theory principles were used to evaluate different network components such as integration (global efficiency), segregation (clustering coefficient and modularity), centrality (betweenness), and resilience (strength and assortativity). Results showed that males had higher GC than females until mid-adulthood (~60 years). However, this gender difference was not observed using TE. Moreover, complex network analysis results of low global efficiency, high clustering coefficient, and low node strength, suggest that at rest, the brain topology resembled a network made up of loosely connected modules that had segregated and disassortative nodes with low resistance to change. Statistical analyses of results from both techniques, using pairwise t-test and two-way ANOVA, showed that age had a significant effect ($p < 0.05$) in all brain regions for both genders with significant gender differences being observed over the anterior, posterior, left lateral and right lateral regions of the brain. The results from this study could be used to develop a fingerprint of healthy ageing, which can potentially be used to assist with the identification of alterations to background brain activity due to pathology.

1 Introduction

Graph theory principles of complex network analysis applied to functional brain networks have become a useful analysis technique in neuroscience [1, 2]. Network parameters such as centrality, modularity, strength, and efficiency have enabled better understanding of the structure of complex multidimensional brain networks [2]. Depending on the aspect of the brain under investigation, different techniques such as functional magnetic resonance imaging (fMRI), magnetoencephalography (MEG), and electroencephalography (EEG), can be employed to record brain activity [3, 4]. The information gathered from these recordings can then be potentially used to detect modifications to brain networks as a result of different pathologies, and might be useful in early diagnosis.

Measures such as Granger causality (GC) and transfer entropy (TE) have been used to study maturation [5], as well as to analyse the effects of pathology [6] on the brain. However, it is also important to evaluate how the brain networks change with healthy ageing and gender, as this can yield useful information about the background functioning of the brain. Therefore, in this study we analysed causality in MEG signals from healthy patients using GC and TE. The aim of this work was to investigate and identify the age and gender effects, network structural changes, as well as the nature of the causality (linear/non-linear) that might be present in background MEG recordings.

E. Shumbayawonda (✉) · M. P. Hughes · D. Abásolo
University of Surrey, Guildford, GU2 7XH, UK
e-mail: e.shumbayawonda@surrey.ac.uk

A. Fernández
Universidad Politécnica de Madrid, Madrid, Spain

2 Materials and Methods

2.1 Materials

More than 5 min of MEG signals were recorded using a 148 channel whole head magnetometer (MAGNES 2500WH, 4D Neuroimaging) in a shielded room at Centro de Magnetoencefalografía Dr. Pérez-Modrego (Madrid, Spain), with subjects sitting down and awake during the recording. A hardware bandpass filter (BPF) with bandwidth 0.1–200 Hz and sampling frequency 678.17 Hz was used, after which MEG signals were down sampled to 169.55 Hz following Nyquist criteria. Further preprocessing to isolate the frequencies of interest, lying between 1.5 and 40 Hz, was done using a 560 order finite impulse response BPF. 220 subjects with ages ranging between 7 and 84 [no significant age-gender differences with mean ages of: (mean $\pm$ standard deviation) males 42.92 ± 21.0 and females (45.0 ± 22.1)] had their MEGs recorded after which the acquired data were grouped according to age as summarised in Table 1.

2.2 Methods

This is a sensor space analysis where sensors were grouped and named according to the brain region they lay over, or are closest to, in a similar manner to that done by Shumbayawonda et al. [4].

2.3 Granger Causality

GC is a linear asymmetrical method which can be used to determine causality between two simultaneous signals. In this study, GC was used to estimate the causality between each pair of MEG signals. Thus the GC between signals $x(n)$ and $y(n)$ (predicting $x(n)$ from $y(n)$) recorded at sensors x and y is [7, 9]:

$$GC_{x \to y} = In\left(\frac{V_{x|\bar{x}}}{V_{x|\bar{x},\bar{y}}}\right) \quad (1)$$

where the notation $x|\bar{x}, \bar{y}$ refers to the prediction of signal x (n) by the past of signals $x(n)$ and $y(n)$, $V_{x|\bar{x}}$ and $V_{x|\bar{x},\bar{y}}$ are the

variances of the residuals u_{xy} and u_{yx} which are associated with the past values of both signals [7]:

$$x(n) = \sum_{k=1}^{X} a_{x|x,k} x(n-k) + \sum_{k=1}^{X} a_{x|y,k} y(n-k) + u_{xy}(n) \quad (2)$$

$$y(n) = \sum_{k=1}^{X} a_{y|x,k} x(n-k) + \sum_{k=1}^{X} a_{y|y,k} y(n-k) + u_{yx}(n) \quad (3)$$

$$V_{y|\bar{x},\bar{y}} = var\left(u_{yxp}\right) \quad (4)$$

$$V_{x|\bar{x},\bar{y}} = var\left(u_{xy}\right) \quad (5)$$

Additionally, X is the autoregressive model order, and $a_{x|x,k}$, $a_{x|y,k}$, $a_{y|x,k}$, and $a_{y|y,k}$ are model parameters. GC values lie between $0 \leq G_{p \to q} < \infty$, where the lower limit reflects that the past of $y(n)$ does not improve the prediction of $x(n)$, while the upper limit shows that $x(n)$ is causal to $y(n)$ [7].

2.4 Transfer Entropy

Transfer entropy (TE) is an information theoretic measure which approximates the causality between two time series $x(t)$ and $y(t)$ using Markov processes [10]. Though similar in concept to GC, TE is more sensitive and does not assume any kind of dependence between the two signals $x(t)$ and $y(t)$. Therefore, the TE between two MEG signals $x(t)$ and y (t) can be calculated as follows [7]:

$$T_{X \to Y} = \sum_{y_{n+1}|\mathbf{y_n^p},\mathbf{x_n^m}} p\left(y_{n+1}|\mathbf{y_n^{dy}}, \mathbf{x_n^{dx}}\right) \log\left(\frac{y_{n+u}|\mathbf{y_n^{dy}}, \mathbf{x_n^{dx}}}{p\left(y_{n+u}|\mathbf{y_n^{dy}}\right)}\right) \quad (6)$$

$$p\left(y_{n+1}|\mathbf{y_n^p}, \mathbf{x_n^m}\right) = p\left(y_{n+1}|\mathbf{y_n^p}\right) \quad (7)$$

$$\mathbf{x_n^{dx}} = \left(x(n), x(n-\tau), \ldots, x(n-(d_x-1)\tau)\right) \quad (8)$$

$$\mathbf{y_n^{dy}} = \left(y(n), y(n-\tau), \ldots, y(n-(d_y-1)\tau)\right) \quad (9)$$

where $T_{X \to Y}$ measures the amount of information flow (directed) from x to y, dx and dy are dimension delay vectors for time series $\mathbf{x_n}$ and $\mathbf{y_n}$, u is the prediction time, and, $\mathbf{x_n^m}$ and $\mathbf{y_n^p}$ are m and p orders of the Markov processes [7]. TE values

Table 1 Groups, age and number of male and female subjects used in this causality study

Group	1	2	3	4	5
Age	<19	19–40	41–60	61–70	>70
Male	11	44	20	11	12
Female	11	40	19	37	15

range between $0 \leq TE_{X \to Y} < \infty$ where the lower limit reflects no causality between the two signals x and y, and the upper limit shows that x is 'causing' y [7].
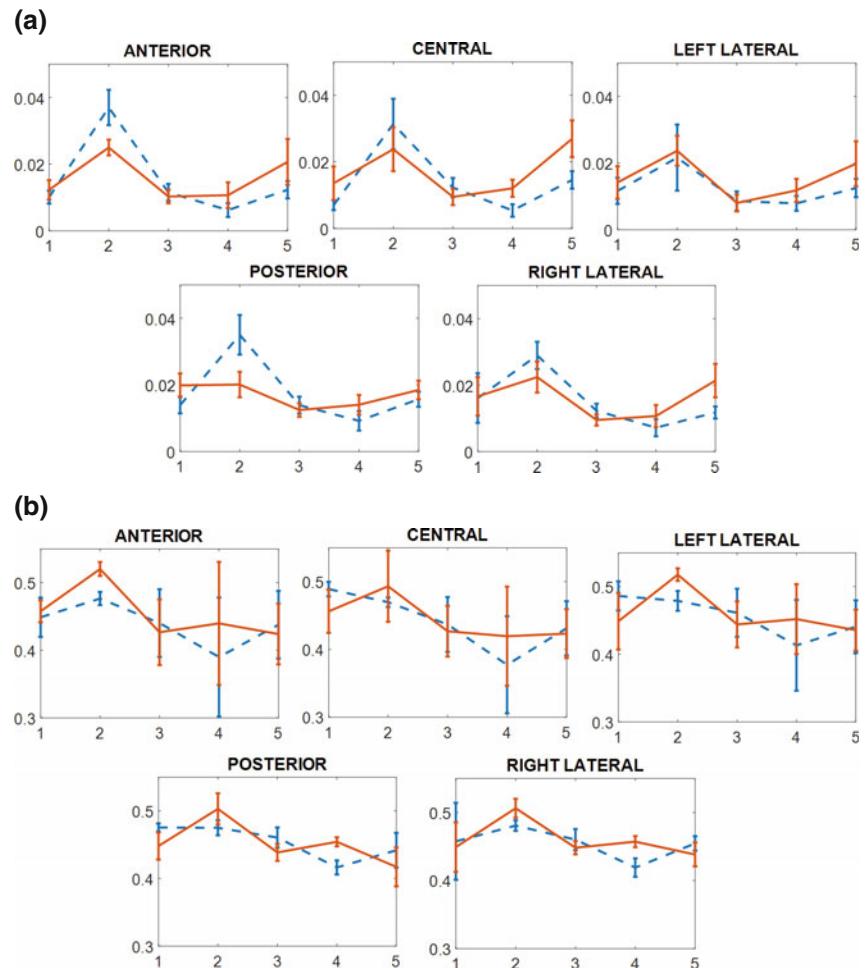
The HERMES toolbox [7] was used to obtain GC and TE values, which were stored in weighted adjacency matrices. Additionally, the Brain Connectivity Toolbox (BCT) [8] was used to calculate global efficiency, clustering coefficient, modularity, betweenness, strength and assortativity, so as to evaluate the integration, segregation, centrality, and resilience of the brain networks. Statistical analyses were performed using nonparametric two-tailed pairwise t-tests (Wilcoxon test) and nonparametric two-way ANOVA (Friedman 2-way ANOVA) to determine the effects of age and gender on each brain region respectively. All statistical analyses was done using IBM Statistical Package for the Social Sciences (SPSS) Statistical Data Editor 23, with all probabilities $p < 0.05$ considered significant.

3 Results

The evolution of average regional GC and TE values is shown in Fig. 1 for both males and females. Both GC and TE values were low, therefore suggesting there is little causal information present in the brain during resting state.

Results also showed that for groups 1–3 (ages up to 60 years old), males generally had higher GC values than females. When the significance of the changes due to age were evaluated in each brain region using GC and TE results, statistical analyses showed that age had a significant effect for ($p < 0.05$) both genders. Additionally, results using non-parametric two-way ANOVA showed significant gender GC differences over the anterior ($p = 0.001$), posterior ($p = 0.001$), left lateral ($p = 0.0021$), and right lateral ($p = 0.010$) regions. However, no significant TE gender differences were obtained ($p > 0.05$).

Fig. 1 Progression of average regional **a** GC values and **b** TE values with age for each brain region, age group (x-axis) and gender (male—blue dashed lines, females—orange solid lines) (Color figure online)

The investigation of network properties revealed that the resulting network resembled a regular globally integrated network, with disassortative network nodes, and low resistance to change. Nevertheless, the analysis using GC detected that the network nodes had low segregation (with clustering coefficient of between 0.05 and 0.3), while with TE it detected high segregation between network nodes with clustering coefficients between 0.1 and 0.6. In addition to this, results using GC showed that male global efficiencies (3.5%) were higher than female efficiencies (2.5%), while results using TE showed that both males and females has similar efficiencies ranging between 4–5%.

4 Discussion and Conclusion

Resting state can be described as a transition stage between sleep and task [11]. Thus, according to suggestions by Rubinov et al. [11], Deco et al. [12], and Stam et al. [13] it is possible that the causality detected using TE is supportive of the linear causality detected by GC. Consequently, this shows that in the absence of any inputs the brain network operates in a metastable and energy conservative manner with little information flow between different areas of the brain. The results from this pilot study seem to agree with these findings. Furthermore, it is possible that the different stages of brain maturation and ageing have an effect on the interactions between the different brain regions, which in turn have an effect on the causality in the brain. Consequently, this implies that the variations in causality with age observed in this study could be associated (directly/indirectly) with these changes [14, 15].

The results from this study have also highlighted some gender differences, with significant differences between males and females in the MEG signals from sensors over the anterior, posterior, left-lateral and right-lateral regions of the brain using GC.

A limitation to this study, which could have had an impact on the gender differences obtained, was the use of unbalanced numbers of subjects such as in group 4. Therefore, future work will involve the use of balanced gender groups. Moreover, future work will also involve additional studies to understand the potential relevance and implications of the gender differences found herein.

In conclusion, the results from this study have provided useful information that can be used to obtain a more detailed representation of the changes in brain activity associated with healthy ageing. GC and TE were used to analyse changes in causality due to age across the human lifespan in MEG signals and it was found that both age (for GC and TE) and gender (for GC) had significant effects.

References

1. Sporns, O., Chialvo, D., Kaiser, M., Hilgetag, C., 2004. Organization, development and function of complex brain network. TRENDS in Cognitive Sciences, 8(9), pp. 418–425.
2. Dehemer, M., 2010. Structural Analysis of Complex Networks. Illustrated ed. Vienna: Springer Science & Business Media.
3. Niedermeyer, E., Lopes da Silva, F. H., 2005. Electroencephalography: Basic Principles, Clinical Applications, and Related Fields. 5th ed. London: Lippincott Williams & Wilkins.
4. Shumbayawonda, E., Fernández, A., Hughes, M. P. & Abasolo, D., 2017. Permutation Entropy for the Characterisation of Brain Activity Recorded with Magnetoencephalograms in Healthy Ageing Entropy. Entropy, 19(141), pp. 1–17.
5. Lavanga, M., O. De Wel, A. Caicedo, K. Jansen, A. Dereymaeker, G. Naulaers and S. Van Huffel. Monitoring Effective Connectivity in the Preterm Brain: A Graph Approach to Study Maturation. Complexity, 2017(9078541), pp. 1–13.
6. Wang, L., Zhang, J., Zhang, Y., Yan, R., Liu, H., Qiu, M., 2016. Conditional Granger Causality Analysis of Effective Connectivity during Motor Imagery and Motor Execution in Stroke Patients. BioMed Research International, 2016(3870863), pp. 1–9.
7. Niso, G., Bruña, R., Pereda, E., Gutiérrez, R., Bajo, R., Maestú, F., del-Pozo, F., 2013. HERMES: towards an integrated toolbox to characterize functional and effective brain connectivity. Neuroinformatics, Volume 11, pp. 405–434.
8. Rubinov, M. & Sporns, O., 2010. Complex network measures of brain connectivity: Uses and interpretations. NeuroImage, Volume 52, pp. 1059–69.
9. Granger, C., 1969. Investigating causal relations by econometric models and cross-spectral methods. Eonometrica: Journal of Econometric Society. 37(3) 3, pp. 424–438.
10. Vicente, R., Wibral, M., Lindner, M. & Pipa, G., 2011. Transfer entropy-a model-free measure of effective connectivity for the neurosciences. Journal of Computational Neuroscience, 30(1), pp. 45–67.
11. Rubinov, M., Sporns, O., Thivierge, J., Breakspear, M., 2011. Neurobiologically realistic determinants of self-organized criticality in networks of spiking neurons. Public library of Science Computational Biology, 7(6), pp. 1–14.
12. Deco, G., Ponce-Alvarez, A., Mantini, D., Romani, G.L., Hagmann, P., Corbetta, M., 2013. Resting-state functional connectivity emerges from structurally and dynamically shaped slow linear fluctuations. The Journal of Neuroscience, 33(27), pp. 11239–11252.
13. Stam, C. J., van Straaten, E.C., Van Dellen, E., Tewarie, P., Gong, G., Hillebrand, A., Meier, J., Van Mieghem, P.: 2016. The relation between structural and functional connectivity patterns in complex brain networks. International Journal of Psychophysiology, Volume 103, pp. 149–160.
14. Peters, R., 2005. Ageing and the brain. Postgraduate Medical Journal, 82(964), pp. 84–88.
15. Ingalhalikar, M., Smith, A., Parker, D., Satterthwaite, T.D., Elliot, M.A., Rupare, H.H., Gur, R E., Gur, R.C., Verma, R., 2013. Sex differences in the structural connectome of the human brain. PNAS, 111(2), pp. 823–828.

EEG Functional Connectivity Detects Seasonal Changes

Laura Päeske, Maie Bachmann, Jaan Raik, and Hiie Hinrikus

Abstract

Seasonal alterations in human health, mood, and basal cortisol level have been reported in several studies. Despite the interest in these factors, seasonal changes in brain functional connectivity as a possible base of these phenomena have not been studied before. The aim of the current study is to analyse seasonal effects using two resting electroencephalogram (EEG) functional connectivity measures: magnitude-squared coherence (MSC) and imaginary coherence (iCOH). Recordings from 80 healthy Estonians were used: 25 recordings from spring, 8 from summer, 10 from autumn and 37 from winter months. Eyes-closed resting EEG was recorded from 30 channels using Neuroscan Synamps2 acquisition system and five frequency bands were analysed: delta, theta, alpha, beta and gamma. Multivariate permutation test revealed significant influence of seasons on beta MSC. Furthermore, statistical analysis between different seasons showed increased beta MSC in spring and winter months compared to summer and autumn months, increased beta iCOH in spring, autumn and winter months compared to summer months and increased gamma MSC in spring and summer months compared to autumn months. The increase in beta MSC and iCOH in spring and winter months compared to summer months may be the result of increased stress or deficiency in Vitamin D. Current study is the first to bring out seasonal changes in brain functional connectivity, but the shortcoming of the study is the limited number of recordings in summer and autumn months. Therefore, further studies are required for more reliable results.

Keywords

EEG • Coherence • Imaginary coherence
Functional connectivity • Seasons

L. Päeske (✉) · M. Bachmann · J. Raik · H. Hinrikus
Tallinn University of Technology, Ehitajate Tee 5, 12616 Tallinn, Estonia
e-mail: laura.paeske@ttu.ee

1 Introduction

Electroencephalograms (EEG) of different populations, for example patient and control groups, are often compared. In these cases, it is important to keep consistency throughout the study to ensure that the difference between populations is in fact caused by the condition of interest (disease, mental disorder etc.). Therefore, it is important to acknowledge, which factors influence EEG and should be taken into consideration. The influence of seasons is one of the factors that could possibly interfere with the studies, for example, when EEG of patients is recorded in one season while EEG of control group is recorded in another season. Therefore, current study investigates the influence of seasons on EEG.

Most apparent change in seasons is perhaps the duration of daily sunshine. Praschak-Rieder et al. [1] found that serotonin binding potential values were negatively correlated with average duration of daily sunshine. Brain serotonin level in turn influences energy, mood, feeding, mating and sleep. Sun also influences vitamin D level, which is highest in summer and lowest in winter [2, 3] and basal cortisol level, which depends on the time of the sunrise [4]. Another important factor that is influenced by seasons is seasonal affective disorder (SAD), which most commonly occurs in winter, but may also occur in spring.

Few studies have investigated seasonal changes in EEG. Peterson and Harmon-Jones [5] found that relative right frontal alpha activity was increased in autumn. However, Velo et al. [6] did not find any seasonal changes in frontal alpha asymmetry. They emphasized the importance of photoperiod instead.

An increasing number of studies are focusing on functional connectivity and connectome rather than discrete brain regions [7]. The aim of the current study is to analyse seasonal effects on two functional connectivity measures, magnitude-squared coherence (MSC) and the imaginary coherence (iCOH), in five different frequency bands.

2   Methods

2.1   Subjects

EEG recordings from 80 healthy subjects (38 female and 42 male) were used: 25 recordings from spring (March, April and May), 8 from summer (June, July and August), 10 from autumn (September, October and November) and 37 from winter months (December, January and February). Subjects' age varied from 19 to 75 years. The average age was 37.0 years with the standard deviation of 14.5 years.

All subjects completed Estonian self-report questionnaire (Emotional State Questionnaire—EST-Q) for major depressive disorder. Only subjects without inclination to depression were included in the current study.

The study was formally approved by the Tallinn Medical Research Ethics Committee and conducted in accordance with the Declaration of Helsinki. Subjects confirmed their participation with a signed written informed consent.

2.2   Estonian Seasons

EEG signals were recorded in Tallinn, Estonia (latitude 59 North and longitude 25 East). The average length of daylight and sunlight in Tallinn are longest in the summer months, followed by spring, autumn and winter (Table 1) (ClimaTemps.com). The average temperature is also highest in summer and lowest in winter, but average temperature in autumn months is higher compared to spring (yr. no).

2.3   Data Acquisition

EEG signals were recorded using Neuroscan Synamps2 acquisition system (Compumedics, NC, USA) from 30 channels. Channels were referenced to linked mastoids with additional two bipolar electro-oculograms (EOG) channels: horizontal and vertical. Electrodes were placed according to the extended international 10–20 system and electrode impedances for all electrodes were less than 10 kΩ. Signals were recorded for 6 min at a sampling rate of 1000 Hz.

2.4   Data Preprocessing

MATLAB (The Math-works, Inc.) was used for data processing. Signals were re-referenced to approximate point at infinity, constructed according to the reference electrode standardization technique (REST) [8]. Using Butterworth filter, the following sub-bands were obtained: delta (1–4 Hz), theta (4–8 Hz), alpha (8–12 Hz), beta (12–30 Hz) and gamma (30–45 Hz). Signals were downsampled to 200 Hz and divided into 20.48-s (4096 sample) segments. After visual inspection, first 10 artifact-free segments were kept for further processing.

2.5   Coherence and Imaginary Coherence

In the current study, two measures of functional connectivity were calculated: the magnitude-squared coherence (MSC) or coherence [9] and the imaginary coherence (iCOH) [10]. MSC is a commonly used functional connectivity measure, but iCOH is less sensitive to volume conduction. Test-retest reliability of both measures depends on artefacts, signal length and frequency band, but reliability of MSC is higher compared to iCOH [11]. Both measures are calculated from coherency, which describes linear relationship between two signals x(t) and y(t) at specific frequencies f. The cross-spectrum between x(t) and y(t) is:

$$S_{xy}(f) \equiv \langle X(f)Y^*(f) \rangle, \tag{1}$$

where $X(f)$ and $Y(f)$ are Fourier transforms of x(t) and y(t) respectively, * is complex conjugation and $\langle \rangle$ is expectation value. Coherency is defined as:

$$C_{xy}(f) \equiv \frac{S_{xy}(f)}{\left(S_{xx}(f)S_{yy}(f)\right)^{1/2}}. \tag{2}$$

MSC is calculated from coherency:

$$MSC_{xy}(f) \equiv \left| C_{xy}(f) \right|^2 \tag{3}$$

and iCOH is

$$iCOH_{xy}(f) \equiv Imag\left(C_{xy}(f)\right). \tag{4}$$

Table 1 Average daylight, sunlight and temperature by seasons in Estonia

Season	Average daylight (h/day)	Average sunlight (h/day)	Average temperature (°C)
Spring	14	7	3.6
Summer	17	9	15.4
Autumn	10	3	6.1
Winter	7	1	−4.7

2.6 Statistical Analysis

Ages and EST-Q depression scores were statistically compared between recordings from different seasons using Wilcoxon rank sum test. Wilcoxon rank sum test is a nonparametric statistical test for independent populations.

MSC and iCOH were calculated between all 30 channels for each EEG segment, frequency band and subject. Obtained 30×30 matrices were averaged over all channel connections. Statistical analysis were conducted in two parts: (1) statistically significant frequency bands were determined using multivariate permutation test and (2) differences between seasons were found using Wilcoxon rank sum test.

Multivariate permutation test is a statistical test where the distribution of the test statistic under the null hypothesis is obtained by randomly rearranging data labels. Each season is represented by a different label and analysis of variance (ANOVA) is used to calculate initial t-value for each frequency band. Season labels are randomly rearranged 10,000 times and at each permutation, the highest t-value of all frequency bands is added to the null distribution. By only considering highest t-values, multi-comparison problems are avoided. p-Value for each frequency band is the proportion of permutation t-values, which are higher than the initial t-value for this band. The confidence level of $p < 0.05$ was considered statistically significant.

Wilcoxon rank sum test was used to compare different seasons in statistically significant frequency bands.

3 Results

Wilcoxon rank sum test showed that recordings in spring were conducted on younger subjects than recordings in winter ($p < 0.05$), but no other age differences occurred between recordings from different seasons. EST-Q depression scores were significantly higher in summer ($p < 0.05$) and spring ($p < 0.005$) recordings compared to winter.

ANOVA showed that seasons influenced MSC in beta and gamma frequency bands (ANOVA $p < 0.05$) and iCOH in beta frequency band (ANOVA $p = 0.08$). However, when multivariate permutation test was applied (repeated tests of five frequency bands), only MSC in beta frequency band was statistically significant.

Wilcoxon rank sum test further showed that MSC in beta frequency band was significantly lower in summer and autumn compared to winter and spring (Fig. 1). In addition, MSC in gamma frequency band was significantly lower in autumn compared to spring and summer and iCOH was significantly lower in summer compared to all other seasons.

4 Discussion

The most surprising result was that EST-Q depression scores were higher in summer compared to winter. This result could be influenced by the limited number of recordings in summer, as only eight recordings were performed, compared to 37 recordings in winter. However, we believe this is unlikely a coincidence, as depression scores were also significantly higher in spring with 25 recordings compared to winter.

Beta MSC and iCOH were significantly decreased in summer recordings compared to winter and spring. Previous studies have linked decrease in beta fluctuations to relaxation [12], while increase in beta activity may be associated with anxiety [13]. Furthermore, we have found in our earlier study that beta functional connectivity increased in major depressive disorder [14]. Therefore, it can be presumed that subjects were more relaxed and less stressful in summer months. Although EST-Q depression scores were higher in summer months, it is plausible that stress levels were lower. In addition, the result may be influenced by average sunlight, which was highest in summer months. Sunlight increases vitamin D level and decreases serotonin and basal cortisol levels. Kull et al. [3] showed that Estonians are strongly influenced by sunlight: 73% of subjects had 25-(OH) vitamin D insufficiency in winter and 29% in summer.

In the current study, gamma MSC was significantly decreased in autumn compared to summer and spring. Previous studies have associated gamma with cognitive processes such as working memory and attention [15, 16].
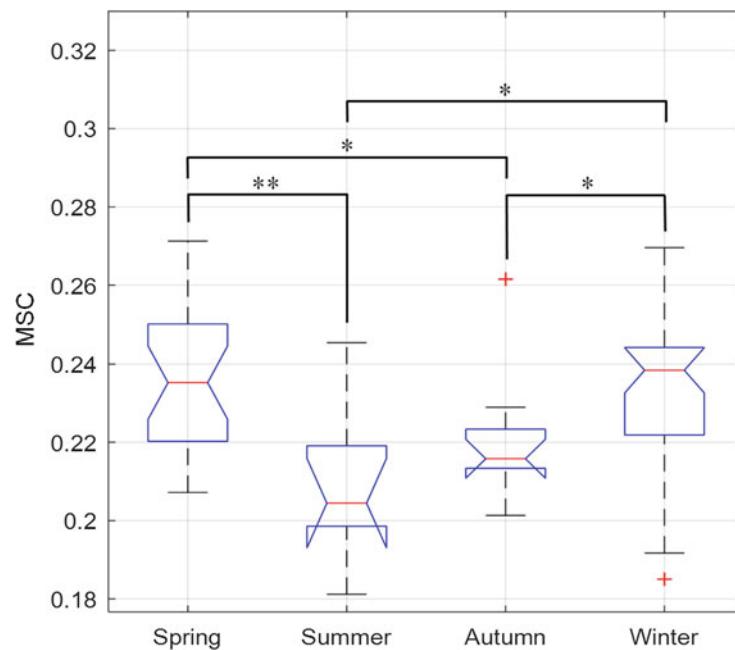
The results of the study indicate that seasons have a significant ($p < 0.05$) influence on MSC. Therefore, when comparing two populations, it is important to ensure that the recordings of different populations are not conducted in different seasons. The shortcomings of the study were the limited number of recordings in summer and autumn months and significant age difference of the subjects between spring and winter recordings. Therefore, further seasonal studies with more subjects are needed.

5 Conclusions

Current study is the first to analyse seasonal effects on EEG magnitude-squared coherence and imaginary coherence. We found that seasons significantly influence magnitude-squared coherence in beta frequency band.

Fig. 1 Beta MSC for different seasons. Central mark indicates the median, the bottom edge of the box indicates 25th percentile and the top edge indicates 75th percentile. The whiskers show most extreme data points and outliers are presented with "+". Statistical differences are marked as follows: * = p < 0.05 and ** = p < 0.01

References

1. Praschak-Rieder, N., Willeit, M., Wilson, A. A., Houle, S., Meyer, H.: Seasonal Variation in Human Brain Serotonin Transporter Binding. Arch Gen Psychiatry 65(9), 1072–1078 (2008).
2. Rosecrans, R., Dohnal, J. C.: Seasonal vitamin D changes and the impact on health risk assessment. Clinical Biochemistry 47(7–8), 670–672 (2014).
3. Kull, A. J., Kallikorm, R., Tamm, A., Lember, M.: Seasonal variance of 25-(OH) vitamin D in the general population of Estonia, a Northern European country. BMC Public Health, 9(22) (2009).
4. Hadlow, N. C., Brown, S., Wardrop, R., Henley, D.: The effects of season, daylight saving and time of sunrise on serum cortisol in a large population. Chronobiol Int., 31(2), 243–251 (2014).
5. Peterson, C. K., Harmon-Jones, E.: Circadian and seasonal variability of resting frontal EEG asymmetry. Biological Psychology, 80, 315–320 (2008).
6. Velo, J. R., Stewart, J. L., Hasler, B. P., Towers, D. N., Allen, J. J.: Should it matter when we record? Time of year and time of day as factors influencing frontal EEG asymmetry. Biological Psychology, 91, 283–291 (2012).

7. Deco, G., Kringelbach, M. L.: Great expectations: using whole-brain computational connectomics for understanding neuropsychiatric disorders. Neuron, 84, 892–905 (2014).
8. Yao, D.: A method to standardize a reference of scalp EEG recordings to a point at infinity. Physiol Meas, 22(4) 693–711 (2001).
9. Kay, S. M.: Modern Spectral Estimation. Englewood Cliffs, NJ: Prentice-Hall (1988).
10. Nolte, G., Bai, O., Wheaton, L., Mari, Z., Vorbach, S., Hallett, M.: Identifying true brain interaction from EEG data using the imaginary part of coherency. Clinical Neurophysiology, 115, 2292–2307 (2004).
11. Höller, Y., Uhl, A., Bathke, A., Thomschewski, A., Butz, K., Nardone, R., Fell, J.,Trinka, E.: Reliability of EEG Measures of Interaction: A Paradigm Shift Is Needed to Fight the Reproducibility Crisis. Frontiers in Human Neuroscience, 11(441) (2017).
12. Gregg, D. J., Herbert, B.: Topographic EEG Mapping of the. Biofeedback and Self-Regulation, 21(2), 121–129 (1996).
13. Aftanas, L. I., Pavlov, S. V.: Trait anxiety impact on posterior activation asymmetries at rest and during evoked negative emotions: EEG investigation. International Journal of Psychophysiology, 55(1), 85–94 (2005).
14. Orgo, L., Bachmann, M., Kalev, K., Järvelaid, M., Hinrikus, H.: Brain Functional Connectivity in Depression: Gender Differences in EEG. In: IEEE - EMBS Conference on Biomedical Engineering and Science, pp. 270–273 (2016).
15. Debener, S., Herrmann, C. S., C. Kranczioch, C., Gembris, D., Engel, A. K.: Top-down attentional processing enhances auditory evoked gamma band activity. Neuroreport, 14, 683–686 (2003).
16. Hermann, C. S., Senkowski, D., Röttger, S.: Phase-locking and amplitude modulations of EEG alpha: two measures reflect different cognitive processes in a working memory task. Exp Psychol, 51, 308–311 (2004).

Influence of Dysgraphia on Kinematic Characteristics of Handwriting in Italian Primary School Children

Giulia Silveri, Federica De Dea, Iolanda Perrone, and Agostino Accardo

Abstract

Handwriting is a complex skill that improves with schooling and it is accomplished after the child has achieved and integrated underlying perceptual-motor performance components. Even though nowadays children are expected to acquire a level of handwriting proficiency, even on the first day of school, at least 27% of the school population has difficulty with handwriting and needs to be screened for (with) an intervention program. In this paper, we examined the influence of dysgraphia on kinematic characteristics of normal and dysgraphic Italian children from 2nd to 5th grade of primary school. Three cursive tasks (sequence of *lelele* and Accurate and Fast copy of a sentence) were proposed and several kinematic parameters were evaluated. Since differences were present among grades both in normal and dysgraphic children, each parameter was compared between children coming from corresponding grades by means of the Wilcoxon rank sum test. The main results showed significant differences between the two groups within each grade for curvilinear velocity, total length and number of letters per second. Pen-lift durations were significantly different only in the Accurate and Fast tasks while number of strokes per second as well as stroke duration and length showed significant differences depending on the task and grade. These differences support the hypothesis of a lower fluency and automation as well as a different motor planning in dysgraphic subjects. Finally, many kinematic parameters could be useful for an early identification of dysgraphia in order to activate an immediate rehabilitative treatment.

1 Introduction

Handwriting is a sophisticated human activity that involves complicated cognitive, kinesthetic and perceptual-motor skills that improve with age and schooling [1, 2]. During the first years of school, children are expected to acquire a level of handwriting proficiency that enables them to make skillful use of handwriting. The proficiency of their handwriting is reflected by their ability to produce legible text with minimum effort [3]. However, it is widely accepted that at least 27% of the school population has difficulty with handwriting [4]. Children, who demonstrate no proficient handwriting skill, are defined as dysgraphic, a disturbance or difficulty in the production of written language concerning the mechanics of writing [5–7].

Previous studies indicated that children with motor skill difficulties present poor size control and spatially inconsistent behaviour [3, 8]. Handwriting difficulties are mainly related to readable writing and efficiency. The latter could be measured by the rate of letter production while readable writing considers the letter alignment and spacing of letter and words [9]. Some authors suggest that spatial inaccuracy in handwriting might be due to less-than-optimal strategies to manage neuro motor noise in the neuro muscular system [10, 11]. Increasing use of digitalization tablets allows quantitative analysis of writing quality [12]. Until now, the influence on the kinematics of writing due to rehabilitation treatment of dysgraphia has been examined only for the Chinese language; which uses very different symbols from

G. Silveri (✉) · F. De Dea · A. Accardo
Department of Engineering & Architecture, University of Trieste, Via Valerio, 10, 34127 Trieste, Italy
e-mail: giulia.silveri@phd.units.it

F. De Dea
e-mail: federica.dedea@phd.units.it

A. Accardo
e-mail: accardo@units.it

I. Perrone
Department of Childhood Development, USSL7 of Pieve Di Soligo, Treviso, Italy
e-mail: iolanda.perrone@ulss7.it

those of the Latin alphabet [13]. In literature some kinematic handwriting analysis of children have been mentioned [14, 15] but only few papers show the influence by new rehabilitation protocol on kinematics due to cursive writing [16].

This paper is a preliminary study in which we evaluate the effects of dysgraphia on handwriting abilities in order to identify parameters able to early recognise graphomotor difficulties in Italian school-aged children.

2 Material and Method

In this study, fifty normal children were recruited from 2nd to 5th grade of primary school (12 children both from 2nd and 3rd grade and 13 children both from 4th and 5th grade). Their handwriting were examined together with those of 18 children (4 from 2nd grade, 4 from 3rd grade, 5 from 4th grade, 5 from 5th grade) with dysgraphia followed by the Department of Childhood Development at the ULSS 7 of Pieve di Soligo (TV), Italy. Normal children did not exhibit organic pathologies or handwriting problems while dysgraphic children presented graphomotor difficulties diagnosed by a child psychiatrist in collaboration with a logopedist, a psychologist and a neuropsychomotor therapist by using standard evaluation protocols. All children were right-handed Italian mother tongue. For each child, informed consent was previously acquired from the parents.

The children performed a series of three cursive tasks: the first (LE test) required children to write a sequence of *lelele*, as quickly as possible for one minute. The other two tests, which required adequate linguistic competences, concerned copying, as Accurately as possible (A test) and as Fast as possible (F test), a phonetically balanced sentence. The sentence contained all the letters of the Italian alphabet and some specific problematic combinations of them (like *ll*, *ss* *zz*, *br* and *pr* patterns).

The writing was acquired by using a commercial digitalization tablet (Wacom, Inc., Vancouver, WA, Model Intuos 2.0) and a suitable program based on the Software Development Kit (SDK, LCS/Telegraphics). A sheet of lined paper of the adequate school grade was placed on the tablet surface and an ink pen was used to reproduce the usual school context.

The frequency used to sample the pen displacement across the tablet was 100 Hz and the spatial resolution was of 0.01 mm. The analysis was performed by using a proprietary program written in MATLAB® [17] that calculated at first the curvilinear velocity and identified the strokes as the tracts between two successive minima of this velocity profile. Several kinematic parameters were considered for each task: the path length (PL), the mean curvilinear velocity (CV), the number of strokes per letter (#S/letter) and per

second (#S/s), the number of letters per cm (#letter/cm) and per second (#letter/s), the stroke length (SL) and duration (SD), the pen lift duration (PLD) and the horizontal (SHVp), vertical (SVVp) and curvilinear (SCVp) peak velocities of stroke.

For all tasks, each parameter was averaged across students of the same class. In order to compare parameter values in the two groups, Wilcoxon rank sum test was used. Differences were considered significant for a p-value <0.05.

3 Results

Figures 1 and 2 show the parameter values extracted from handwriting in normal and dysgraphic children (p-values of their differences in Tables 1 and 2) in the three tests for each school grade examined.

The CV and PL (Fig. 1 and Table 1) values were significantly greater in normal rather than in dysgraphic children in all grades and tests. Their trend with grades was almost constant for CV in both groups and in PL for children with difficulties; only in normal children an increase after the 3rd grade was present. The values of pen lift duration decreased with grades presenting significantly lower values in normal than in the dysgraphic group only for A and F tests in almost all the grades (Table 1). The number of letters per second increased with schooling in all tests with significant higher values in normal than in dysgraphic children for all grades. Similarly, the number of letters per cm increased with schooling but the values were similar in the two groups without significant differences in the three tests. On the contrary, the number of strokes per letter decreased with grades (Fig. 1) presenting significant differences between normal and dysgraphic children only in 2nd and 3rd grades for both A and F tests (Table 1) in which normal children presented lower values than the other group.

The number of strokes per second, with schooling, was about constant in the three tests (Fig. 2), with values in normal children significantly greater than those in children with dysgraphia (Table 2). This was true for all grades. The SL trend with schooling was opposite in the two groups with comparable values significantly different only in 4th and 5th grades, where the normal group showed lower values than the other group. In addition, the SD parameter showed significant lower values in normal than in dysgraphic children in 4th and 5th grades for all tests with an about constant trend with schooling. The SHVp as well as the SVVp presented similar characteristics with significant greater values in normal than in dysgraphic children for A and F tests in all grades with an almost constant trend with schooling. On the contrary, the SCVp values were similar in the two groups in the three tests for all the grades.
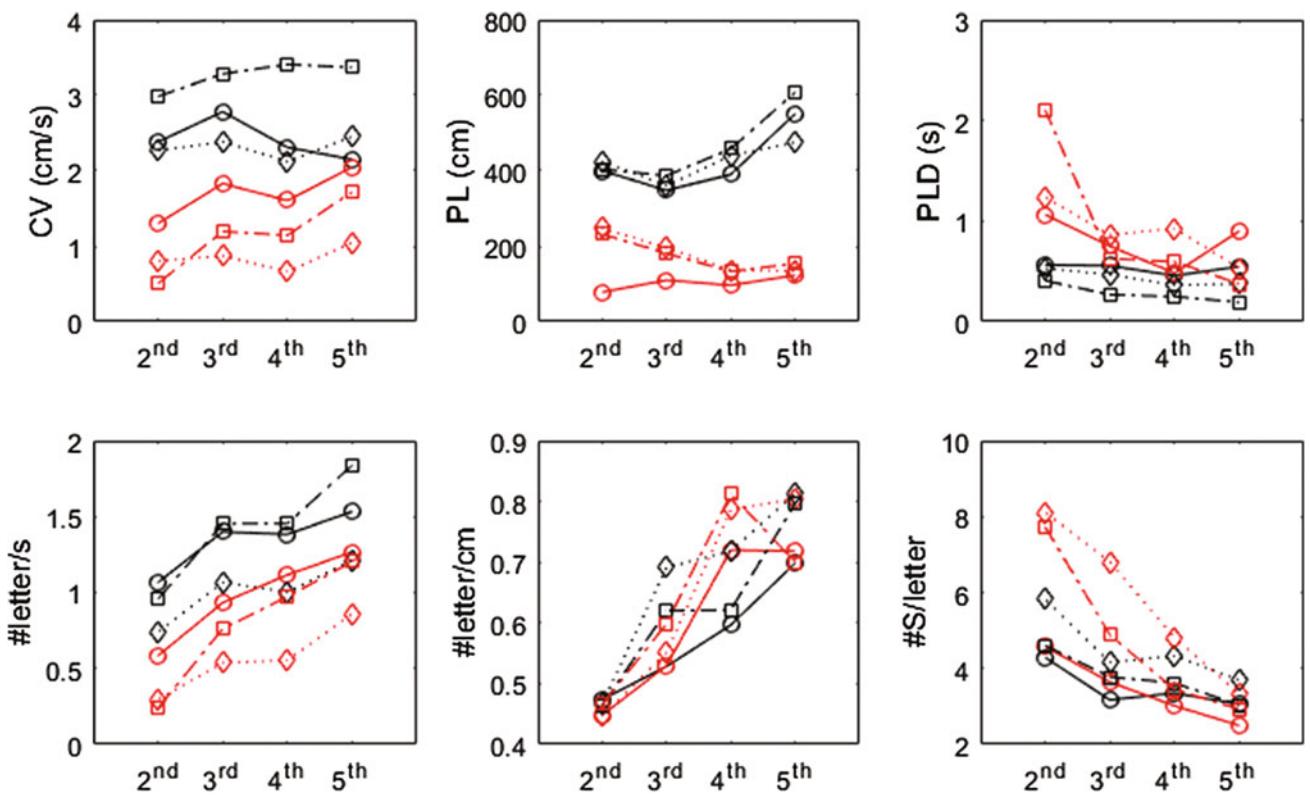
Fig. 1 Curvilinear velocity (CV), path length, pen lift duration (PLD), number of letters per second and per cm, number of strokes per letter parameters calculated in normal (black) and dysgraphic (red) children in the LE (circle), accurate (diamond) and fast (square) tests for the four school grades considered (Color figure online)

4 Discussion

Handwriting is a complex skill that is accomplished after a child has achieved and integrated underlying perceptual-motor performance components that can be quantified by means of kinematic analysis of writing [14–16]. This paper has compared several handwriting kinematic characteristics of normal Italian children, from 2nd to 5th grade of primary school, with those of children with dysgraphia by using three different tests in order to evaluate them as they change in the two groups. The results showed significant differences in the values of many parameters, especially in the two tests requiring linguistic competences. However, as in the LE test, some parameters changed significantly, confirming that dysgraphia is identifiable even when there is no linguistic involvement [18].

Particularly, greater #letter/s and CV as well as SHVp and SVVp in normal children support the hypothesis that dysgraphic children write significantly slower (less fluently) than normal ones [8, 16] whatever the test they have to do. Moreover, the CV, SHVp and SVVp values are almost independent of the class they attend while the #letter/s strongly depend on the class so that the school grade must be

taken into account if this parameter is used to evaluate dysgraphia. Since major differences are present in tests A and F, the grammatical and linguistic characteristics present in these tests seem to require greater attention and engagement levels by subject's, producing a slowing down of handwriting movement in dysgraphic children.

The significantly longest mean duration of the pen lift in dysgraphic children performing A and F tests underlines their lower ability to quickly plan motor action, thus producing a text in a less efficient way. This confirms that these tests are more appropriate to distinguish the two groups of children. Furthermore, lower #S/s and longer SD values in dysgraphic children suggest that these subjects need more time to construct a letter indicating less motor automation whatever the test used.

The shortest path length in dysgraphic children, even with the same number of letters to write (as in A and F tests), is mainly due to the writing of smaller letters than in normal children. Finally, the #letter/cm, #stroke/letter, stroke length and SCVp does not seem parameters able to distinguish between the two groups since they present values that are in large part not significantly different.

In conclusion, the analysis of handwriting kinematics, allowed by the use of digital tablets and suitable software,
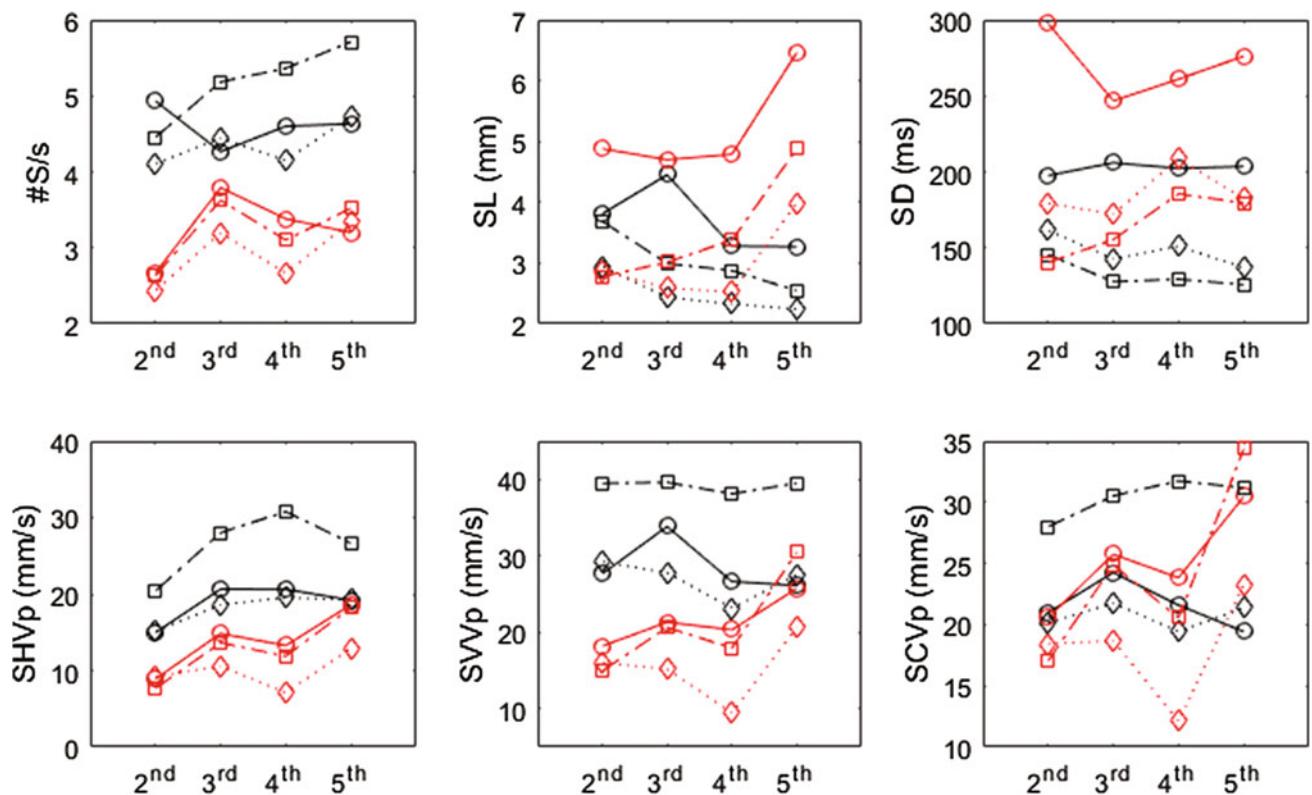
Fig. 2 Number of strokes per second, stroke length (SL) and duration (SD), horizontal (SHVp), vertical (SVVp) and curvilinear (SCVp) Peak velocities parameters calculated in normal (black) and dysgraphic (red) children in the LE (circle), accurate (diamond) and fast (square) tests for the four school grades considered (Color figure online)

Table 1 p-Values of the differences between normal and dysgraphic children of the parameters in Fig. 1, in the four grades for the three tests

Test	Grade	CV (cm/s)	PL (cm)	PLD (s)	#letter/s	#letter/cm	#S/letter
LE	2nd	0.0140	0.0250	n.s.	0.0071	n.s.	n.s.
	3rd	0.0034	0.0230	n.s.	0.0059	n.s.	n.s.
	4th	0.0004	0.0020	n.s.	0.0270	n.s.	n.s.
	5th	n.s.	0.0008	n.s.	n.s.	n.s.	n.s.
Accurate	2nd	0.0017	0.0034	0.0017	0.0008	n.s.	0.0230
	3rd	0.0008	0.0008	0.0034	0.0008	0.0230	0.0150
	4th	0.0001	0.0032	0.0170	0.0032	n.s.	n.s.
	5th	0.0036	0.0036	0.0390	0.050	n.s.	n.s.
Fast	2nd	0.0036	0.0250	0.0036	0.0036	n.s.	0.0140
	3rd	0.0008	0.0034	0.0008	0.0008	n.s.	0.0420
	4th	0.0005	0.0089	n.s.	0.0020	n.s.	n.s.
	5th	0.0036	0.0036	0.0036	0.0036	n.s.	n.s.

gave us the possibility to examine the dynamic construction of letters and to identify the significant writing differences produced by normal and dysgraphic children. These differences support the hypothesis of a lower fluency and automation as well as different motor planning in dysgraphic subjects and a relative dependence on the used test and the class attended. A series of kinematic parameters seem to be able to discriminate dysgraphia from normal handwriting and could be utilized for an early identification of dysgraphia in order to quickly activate a rehabilitative treatment. Further studies on a greater number of subjects are recommended to confirm the results of this research.

Table 2 p-Values of the differences between normal and dysgraphic children of the parameters in Fig. 2, in the four grades for the three tests

Test	Grade	#S/s	SL (mm)	SD (ms)	SHVp (mm/s)	SVVp (mm/s)	SCVp (mm/s)
LE	2nd	0.0036	0.0250	n.s.	n.s.	n.s.	n.s.
	3rd	n.s.	n.s.	n.s.	n.s.	0.0320	n.s.
	4th	0.0089	0.0043	0.0071	0.0009	0.0055	n.s.
	5th	0.0036	0.0071	0.0036	n.s.	n.s.	n.s.
Accurate	2nd	0.0320	n.s.	n.s.	n.s.	n.s.	n.s.
	3rd	0.0151	n.s.	0.0230	0.0034	0.0008	n.s.
	4th	0.0009	n.s.	0.0001	0.0001	0.0001	0.0092
	5th	0.0036	0.0140	0.0036	0.0036	0.0036	n.s.
Fast	2nd	0.0071	n.s.	n.s.	0.0036	0.0036	n.s.
	3rd	0.0017	n.s.	0.0320	0.0008	0.0008	0.0230
	4th	0.0110	0.0270	0.0043	0.0004	0.0015	n.s.
	5th	0.0036	0.0036	0.0036	0.0390	n.s.	n.s.

References

1. Reisman, J.E.: Development and reliability of the Research version of the Minnesota handwriting test. Physical & Occupational Therapy In Pediatrics 13(2), 41–55 (1993).
2. Jones, D., Christensen, C.: Relationship between automaticity in handwriting and students' ability to generate written text. Journal of Educational Psychology 91(1), 44–49 (1999).
3. Smits-Engelsman, B.C., Van Galen G.P.: Dysgraphia in Children: Lasting psychomotor deficiency or transient developmental delay. Journal of Experimental Child Psychology 67(2), 164–184 (1997).
4. van Hartingsveldt, M.J., de Groot, I.J.M.: Standardized tests of handwriting readiness: a systematic review of the literature. Developmental Medicine & Child Neurology 53(6), 506–515 (2011).
5. van Galen, G.P., de Jong, W.P.: Fitts' law as the outcome of a dynamic noise filtering model of motor control. Human Movement Science 14, 539–571 (1995).
6. Rosenblum, S., Livneh-Zirinski, M.: Handwriting process and product characteristics of children diagnosed with developmental coordination disorder. Human Movement Science 27(2), 200–214 (2008).
7. Graham, S., Harris, K.R.: Is handwriting causally related to learning to write? Treatment of handwriting problems in beginning writers. Journal of Educational Psychology 92 (4), 620–633 (2000).
8. Di Brina, C., Niels, R.: Dynamic time warping: A new method in the study of poor handwriting. Human Movement Science 27 (2), 242–255 (2008).
9. Feder, K.P., Majnemer, A.: Handwriting development, competency, and intervention. Developmental Medicine & Child Neurology 49 (4), 312–317 (2007).
10. Wing, L., Gould, J.: Severe impairments of social interaction and associated abnormalities in children: epidemiology and classification. Journal of Autism and Development Disorder 9 (1), 11–29 (1979).
11. Denton, P.L., Cope, S.: The effects of sensorimotor-based intervention versus therapeutic practice on improving handwriting performance in 6- to 11-year-old children. American Journal of Occupational Therapy 60(1), 16–27 (2006).
12. Rosenblum, S., Parush S., Weiss P.L.: Computerized temporal handwriting characteristics of proficient and non-proficient handwrites. American Journal of Occupational Therapy 57(2), 605–612 (2001).
13. Chang, S.H., Yu, N.Y.: Handwriting movement analyses comparing first and second graders with normal or dysgraphic characteristics. Research in Developmental Disabilities 34(9), 2433–2441 (2013).
14. Rueckriegel, S.M., Blankenburg, F.: Influence of age and movement complexity on kinematic hand movement parameters in childhood and adolescence. International Journal of Development Neuroscience 26(7), 655–663 (2008).
15. Accardo, A., Genna, M., Borean, M.: Development, maturation and learning influence on handwriting kinematics. Human Movement Science 32(1), 136–146 (2013).
16. Accardo, A., Costa, F., Perrone, I.: The Influence of the Spatio-Temporal Terzi Treatment on the Kinematics of Cursive Writing of Dysgraphic Subjects. IEEE Transactions on Human-Machine Systems 47(2), 249–258 (2017).
17. Accardo, A., Chiap, A., Borean, M., Bravar, L., Zoia, S., Carrozzi, M., Scabar, A.: A device for quantitative kinematic analysis of children's handwriting movements. In: IFMBE Proceedings, vol. 16, 445–448 (2007).
18. Tressoldi, P.E., Cornoldi C.: Batteria Per La Valutazione Della Scrittura E Della Competenza Ortografica Nella Scuola Dell'Obbligo. Giunti, Florence (2000).

Power Spectral Density Analysis in Spindles Epochs in Healthy Children

Federica De Dea, Caterina Zanus, Marco Carrozzi, Matteo Stecca, and Agostino Accardo

Abstract

Sleep spindles are important components of the N-REM stage-2 in the sleep electroencephalogram (EEG). They are oscillatory EEG activities of fusiform morphology in the range of 10–16 Hz [1], and a duration between 0.5 and 3 s. Spindles have been associated with cognitive skills and sleep-dependent memory consolidation. The aim of this study is to assess differences in the before ("pre"), during ("dur") and after ("post") spindle epochs by means of main power spectral bands delta (2–4 Hz), theta (4–8 Hz), alpha (8–12 Hz), beta (12–30 Hz), gamma (30–44 Hz), total (2–44 Hz) and sigma bands (12–16 Hz), calculated by the Welch periodogram, and by Fractal dimension (FD). The analysis was carried out on 7 healthy children (mean age = 8.90 ± 1.34 years) deprived of sleep on the day of the acquisition to enhance the deep sleep during the recording. For each EEG record (standard 10–20, 19 electrodes, sampling rate 512 Hz), two neurophysiologists labeled the start and the end points of the three sleep epochs. The results showed statistical differences between "dur" and both "pre" and "post" epochs in almost all channels (except O1 and O2) for all bands, except gamma. Furthermore, the values of FD were significantly different between "dur" and both "pre" and "post" epochs, for all channels. The FD values in "dur" epochs were smaller than in both "pre" and "post" ones, showing a lower EEG complexity during spindles, compared with the "pre" and "post" epochs. FD values in "post" epochs were found similar to those in "pre" periods. These differences could be useful to comprehend the spindles changes during sleep time. Moreover, these data could help on understanding the system generator of the spindles.

Keywords

Power spectral density • Sleep spindle • Children

1 Introduction

Sleep spindles are oscillatory EEG activities that characterize the Non-REM sleep. They display a fusiform morphology between 10–16 Hz and their duration varies from 0.5 to 3 s [1]. In the last decades, the interest in sleep spindle has been increased after Gibbs and Gibbs [2] discovered that children with disabilities exhibit high amplitude and long sleep spindles. Sleep spindles have also been associated with cognitive faculties and intelligence. Shibagaki and Kyono [3] found that children with IQ scores lower than normal had abnormal spindles with epileptiform morphology. On the other hand, children with higher IQ, better procedural knowledge and skills had a high number of spindles and more sigma power than those with normal IQ [4].

Moreover, sleep spindle have been correlated with certain pathological conditions (e.g., schizophrenia, mental retardation, abnormal maturation) and post stroke recovery processes. They are also considered to be significantly involved in sleep-dependent memory consolidation [5].

De Gennaro and Ferrara [6] highlighted that inter-individual characteristics of the spindles could be used as an "electrophysiological fingerprint".

F. De Dea (✉) · A. Accardo
Department of Engineering and Architecture, University of Trieste, Trieste, Italy
e-mail: federica.dedea@phd.units.it

A. Accardo
e-mail: accardo@units.it
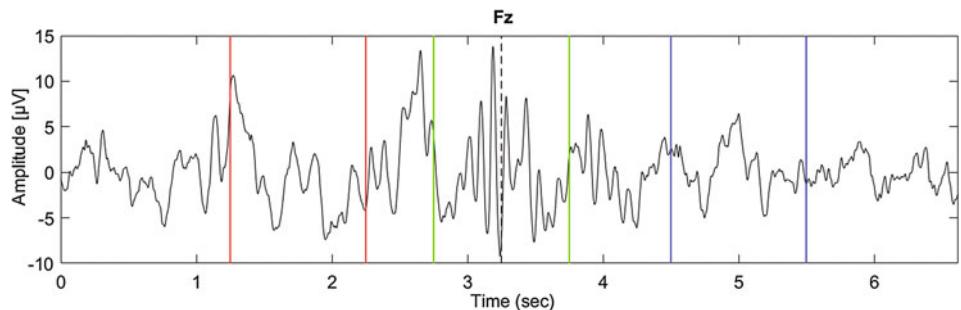
F. De Dea
Department of Life Science, University of Trieste, Trieste, Italy

C. Zanus · M. Carrozzi · M. Stecca
Child Neuropsychiatry, IRCCS Children's Hospital "Burlo Garofolo", Trieste, Italy
e-mail: caterina.zanus@burlo.trieste.it

M. Carrozzi
e-mail: marco.carrozzi@burlo.trieste.it

M. Stecca
e-mail: matteo.stecca.92@gmail.com

Sleep spindle were classified into slow, with a peak between 12 and 14 Hz and anterior distribution, and fast spindles, with a peak in the interval 14–16 Hz and centro-parietal distribution [7]. The dichotomy between slow and fast spindles starts from the age 2 and continues until the adulthood [8]. Children of 4–6 years of age presented only frontal low frequency peaks between 11 and 12.75 Hz, but from 6 to 13 years they presented also centro-parietal peaks at almost low frequency (12.5–13.5 Hz). Shinomiya et al. [8] in addition found that by the age of 13, the centro-parietal peaks at low frequencies disappeared and recurred in the new range of 13.5–14.5 Hz. Spindle density, amplitude and duration have been largely explored, but power density and temporal changes before and after spindle occurrence remain still elusive. To the best of our knowledge, only Ueda et al. [9] evaluated the spatiotemporal changes of slow wave activities before and after sleep spindle in a group of subjects between 20 and 26 years age.

The aim of this study is to analyze the temporal changes of EEG characteristics among before, during and after sleep spindle appearance in children. According to Shinomiya [8], we decided to analyze the entire frequency band (12–16 Hz), with no distinction between fast and slow spindle bands.

2 Materials and Methods

Seven healthy children (mean age of 8.9 ± 1.34 years) were recruited from the Children's Hospital "Burlo Garofolo" of Trieste, and the inform consent was obtained from their parents. The children were deprived of sleep on the day of acquisition in order to enhance the deep sleep during the recording. The inclusion criteria were the absence of neurological disorders and medical drug treatment.

The EEG was recorded using 19 electrodes, placed according to the 10–20 standard, with a sampling rate of 512 Hz. For each EEG, two neurophysiologists labeled the start ("Rstart") and the end ("Rstop") points of a single spindle. For each subject, 6–11 artifact free spindles were selected.

In order to achieve the homogeneity of the spindles durations among the children, the "Rstart" and "Rstop" are not used for epoching, but as a guideline to roughly estimate the locations of the spindles in the EEG data. Based on the power spectral density of Fz channel [3], for each spindle, the maximum power peak in the range of 12–16 Hz was calculated and always found between "Rstart" and "Rstop" labels. "Dur" epoch was obtained by cutting the EEG 0.5 s before and after the maximum power peak (1-s lasting epoch in total). The end of the pre-spindle epoch ("pre") and the start of the post-spindle epoch ("post") were set at the time at which the power value underwent the 95% of the maximum power peak, before and after spindle respectively. The durations of "pre" and "post" epochs were set to one second (Fig. 1).
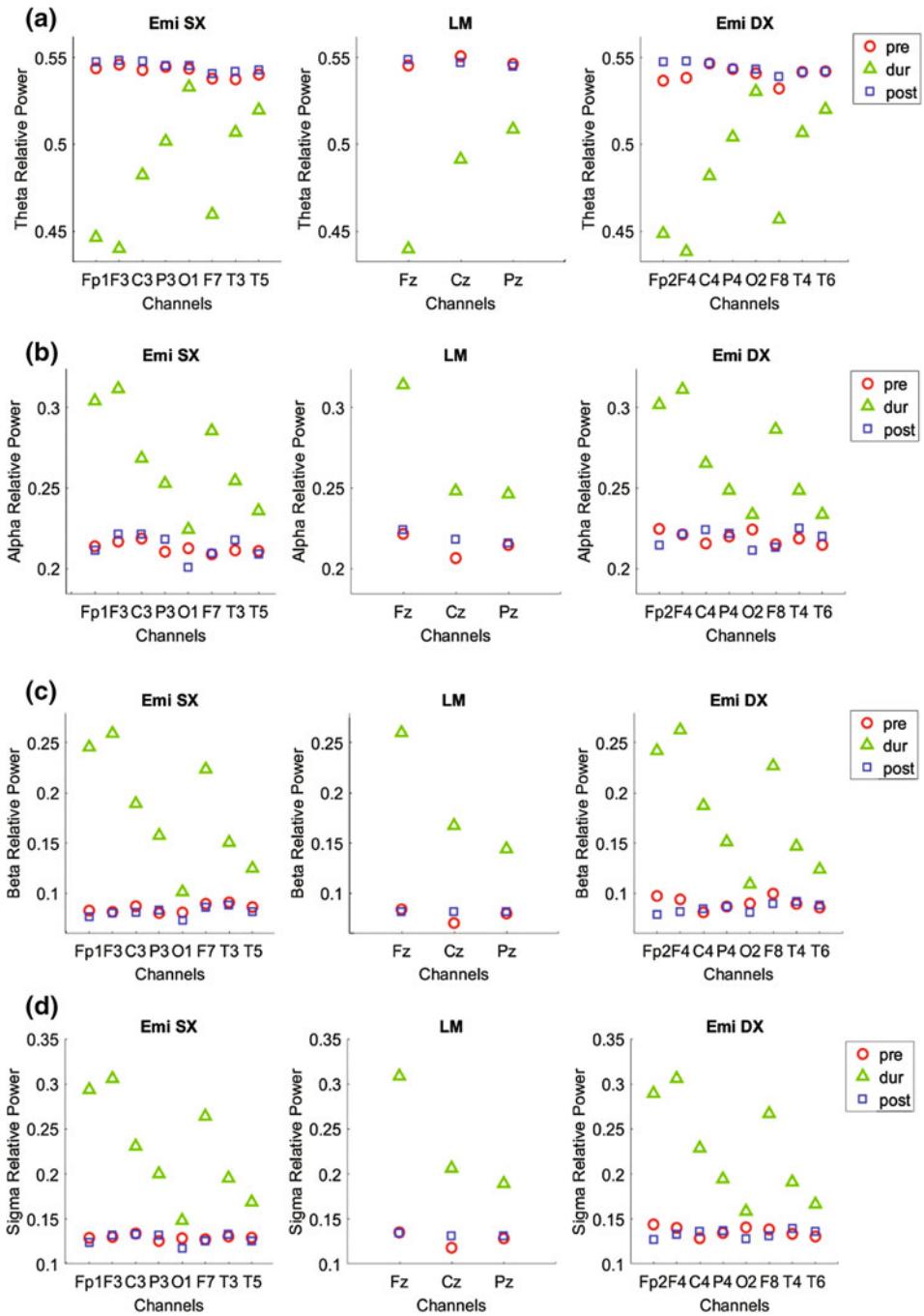
For each subject, the obtained segments were concatenate in order to achieve sequences of 6–11 s, depending on the number of spindles, for each type of epoch. Therefore, every sequence of each subject was band-pass filtered in the interval 2–44 Hz. Spectral power in the delta (2–4 Hz), theta (4–8 Hz), alpha (8–12 Hz), beta (12–30 Hz), gamma (30–44 Hz), total (2–44 Hz) and sigma bands (12–16 Hz) was calculated by using the power spectral density obtained by Welch periodogram with Hamming window, overlapped of 50%. Then the spectral powers of delta, theta, alpha, beta, gamma and sigma bands were divided by the total power to obtain the relative power spectral values. Moreover, for each sequence the Fractal Dimension (FD) was computed with the Higuchi algorithm [10, 11].

To evaluate the statistical differences among the three epochs ("pre-dur", "dur-post" and "pre-post"), Wilcoxon sign rank test for paired samples was used and Bonferroni correction for epochs correction was applied. Differences with a p-value lower than 0.05 were considered statistically significant.

3 Results

Figure 2a shows that spectral power in the theta band is lower in the "dur" epoch than in the "pre" one with significant differences in Fp2, F4, F8 and C4 of the right hemisphere and in all channels, except O1, of the left hemisphere, in addition all channels in the middle line result significant.

Fig. 2 Theta (a), Alpha (b), Beta (c) and Sigma (d) spectral power for each channel, in the "pre" (red circle), "dur" (green triangle) and "post" (blue square) epochs (Color figure online)

The difference between "dur" and "post" epochs, with "dur" value lower than "post", is significant for almost all channels except for T4, T6 and O2. Finally, the only significant difference between "pre" and "post" epochs is in the T3 channel. In delta band, "pre" values statistically differs from "dur" ones in all channels of the left hemisphere (except O1 and T5), in middle line (except Pz) and only in F4, C4 and F8 of the right hemisphere. Significant differences between "dur" and "post" are present in all channels except Cz, P4, T4 and T6.

"Pre" and "post" epochs show similar trend of relative spectral power for both alpha (Fig. 2b) and beta (Fig. 2c) bands over all channels. The differences between "dur" and "post" are significant in all channels for beta band (except T4 and T6) and almost all for alpha band except in the Cz, Pz, P4, T4 and T6 channels. On the other hand, the differences between "pre" and "dur" epochs are noteworthy in almost all channels, except P4, T4, T6, O1 and O2 for beta bands, meanwhile in alpha band significant differences are in almost all channels of left hemisphere and middle line
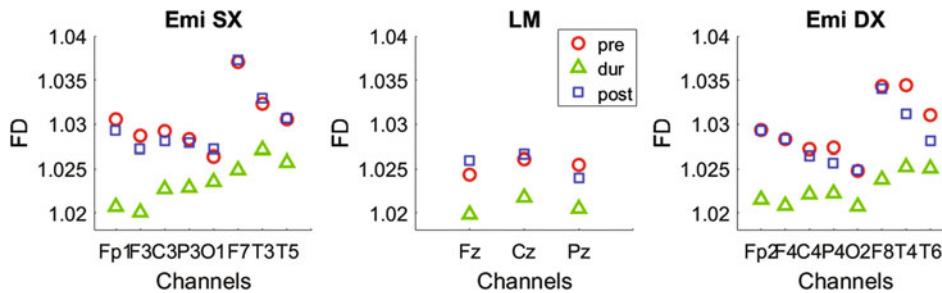
Fig. 3 FD values for each channel, in the "pre" (red circle), "dur" (green triangle) and "post" (blue square) epochs (Color figure online)

(except T5, O1 and Pz) and only in F4 and F8 of the right hemisphere.

For the sigma band (Fig. 2d), almost all channels highlight statistically different values between both "pre" and "dur" and "dur" and "post" with the exceptions of Fp2, P4, T4, T6, Pz and O1 in "pre-dur" comparison and of P4, T4, T6 and O2 in "dur-post" one.

Meanwhile, for total band the Fp1, C3, Fz, Cz, Fp2, F4, F8, and C4 channels have significant different values between "pre" and "dur", while only Fp1, F3, F7 and Fz significantly differ between "dur" and "post" epochs. In gamma band there is only one significant difference between "pre" and "dur" in P3 channel.

For alpha, beta and sigma bands, in "dur" epoch, relative power values are greater in the centro-frontal (Fp1, Fp2, F3, F4, F7, F8, C3, C4, Fz) channels than in temporolateral, parietal and occipital ones, while in delta and theta the trends are opposite. Moreover, for alpha, beta and sigma bands the "post" values are greater than "pre" ones in temporolateral and parietal channels, conversely in delta band only in frontal channels "post" values are greater than "pre". In theta and total bands "post" relative power values are greater than "pre" in all channels, except for Cz and Pz in theta band. Post values in delta band were higher than "pre" relative power values only in frontal channels.

The FD (Fig. 3) highlights lower values in "dur" epoch than in the other two epochs in which the values were very similar. Significant differences are found between "pre" and "dur" in almost all channels, except Fz, P4, T3, T4, T5, O1 and O2, and between "dur" and "post", except for C4, P4, T4 and T6 channels.

The values of FD are lower in prefrontal, central, parietal and occipital channels than fronto-temporal (F7, F8, T3, T4, T5 and T6) ones.

people instead of children [9]. Our results show that in alpha, beta and sigma bands, the spectral power values during "dur" epoch are greater than both "pre" and "post" epochs, highlighting that the power changes have an inverted V-shape. On the contrary, in delta and theta bands the "dur" epoch values are lower than both "pre" and "post", highlighting a V-shape. Moreover, in "dur" epoch, the relative power values of fronto-central channels are lower than temporolateral and occipital ones in all bands.

Furthermore, the values of FD in the three epochs are greater in fronto-temporal channels (F7, F8, T3, T4, T5 and T6) than in the others. Since FD is associated to complexity of a signal, its values indicate lower source generator complexity during the spindle compare with the "pre" and "post" epochs.

The role of sleep spindle in childhood is still not fully understood, but it is well known that spindle abnormality can be related to certain neurodevelopmental pathologies, strokes and mental disorders. In conclusion, this study tried to understand the behavior of the spindle generator. We discovered that sleep spindles are most likely involved in sleep maintenance, as indicated by the increasing of delta and theta power after the "dur" epoch and the decrease of power values in beta and alpha bands after spindle onset. All the increasing and decreasing power value changes among the epochs were higher in the frontal regions of all bands. Moreover, in "dur" epoch the complexity decrease, apparently indicating a relaxation of the brain, in particular in the fronto-central region.

Conflict of Interest The authors declare no conflict of interest.

4 Discussion

In literature, to the best of our knowledge, only one paper concerns the spectral power values changes in "pre", "dur" and "post" epochs of sleep spindles, but it analyzed adult

References

1. Jankel, W. R., & Niedermeyer, E. (1985). "Sleep spindles", *Journal of clinical neurophysiology: official publication of the American Electroencephalographic Society*, vol. *2,* no. 1, pp. 1–35.

2. E. L. Gibbs and F. A. Gibbs, "Extreme spindles: correlation of electroencephalographic sleep pattern with mental retardation," *Science (80-.).*, vol. 138, no. 3545, pp. 1106–1107, 1962.

3. M. Shibagaki and S. Kiyono, "Duration of spindle bursts during nocturnal sleep in mentally retarded children." Electroencephalogr. Clin. Neurophysiol. 55, 645–651, 1983.

4. R. S. Nader and C. T. Smith, "The relationship between stage 2 sleep spindles and intelligence," *Sleep*, vol. 24, no. 1, p. A160, 2001.

5. S. Diekelmann and J. Born, "The memory function of sleep," *Nature Reviews Neuroscience*, vol. 11, no. 2. pp. 114–126, 2010.

6. L. De Gennaro and M. Ferrara, "Sleep spindles: An overview," *Sleep Medicine Reviews*, vol. 7, no. 5. pp. 423–440, 2003.

7. S. M. Fogel and C. T. Smith, "The function of the sleep spindle: A physiological index of intelligence and a mechanism for sleep-dependent memory consolidation," *Neuroscience and Biobehavioral Reviews*, vol. 35, no. 5. pp. 1154–1165, 2011.

8. S. Shinomiya, K. Nagata, K. Takahashi, and T. Masumura, "Development of Sleep Spindles in Young Children and Adolescents," *Clin. EEG Neurosci.*, vol. 30, no. 2, pp. 39–43, 1999.

9. K. Ueda, H. Nittono, M. Hayashi, and T. Hori, "Spatiotemporal changes of slow wave activities before and after 14 Hz/12 Hz sleep spindles during stage 2 sleep," in *Psychiatry and Clinical Neurosciences*, 2001, vol. 55, no. 3, pp. 183–184.

10. T. Higuchi, "Approach to an irregular time series on the basis of the fractal theory," *Phys. D Nonlinear Phenom.*, vol. 31, no. 2, pp. 277–283, 1988.

11. A. Accardo, M. Affinito, M. Carrozzi, and F. Bouquet, "Use of the fractal dimension for the analysis of electroencephalographic time series.," *Biol. Cybern.*, vol. 77, pp. 339–350, 1997.

RF Ultrasound Based Longitudinal Motion Estimation of Carotid Artery Wall: Feasibility Study

Monika Zambacevičienė and Rytis Jurkonis

Abstract

Arteriosclerosis is a chronic, systemic, inflammatory disease of arteries. Arteriosclerosis reveals itself when complications when as constricted artery lumen and (or) its thrombosis, enlarged and thinner wall (aneurysm) build up. Nonetheless, it has been proved than significant changes of the mechanical properties of common carotid artery (CCA) wall are present much earlier than the anatomical changes appear. The aim of this work is to propose and evaluate an algorithm for analysis of longitudinal and radial movements of CCA wall from registered radiofrequency (RF) ultrasound (US) signals. The proposed method uses RF US signals, phase correlation and sub-sample algorithm to estimate radial and longitudinal movements of CCA wall which was monitored continuously for four cardiac cycles. A physical phantom and in vivo test were employed for testing the algorithm. The results with phantom show that a normalized root mean square error (NRMSE) of detected motion amplitude is from 0.21 to 0.41 μm and the coefficient of correlation is from 0.95 to 0.98 in case of any determined longitudinal motion function when the phase correlation, sub-pixel algorithm and additional filtering were used. The results from this validation study demonstrate the feasibility of CCA longitudinal and radial movement assessment in vivo using phase correlation and sub-sample algorithm. Radiofrequency ultrasound signals algorithm could be used to characterize radial and longitudinal displacements in early stage arteriosclerotic artery.

M. Zambacevičienė (✉) · R. Jurkonis
Biomedical Engineering Institute, Kaunas University
of Technology, Kaunas, Lithuania
e-mail: monika.zambaceviciene@ktu.edu

1 Introduction

Arteriosclerosis is chronic, systemic, inflammatory disease of the coronary, carotid and peripheral arteries, and the aorta [1]. Arteriosclerosis reveals only at the beginning of the complications: constricted artery lumen and (or) its thrombosis, enlarged and thinner artery wall (aneurysm) [2]. Nonetheless, it has been proved than significant changes of the mechanical properties of arterial wall (i.e. longitudinal and radial motion) are present much earlier than anatomical changes appear (i.e. *intima-media* thickness) [3]. Longitudinal movement is defined as the movement of arterial wall (intima-media complex) in the same direction as the blood flow in the artery during a cardiac cycle [4].

In addition, longitudinal motion has the same amplitude as radial movement and reaches about one millimetre [5]. Block Matching method is a widely used approach for tracking longitudinal motion of CCA through B-mode image sequences [4, 5, 7–9]. Current research investigated the association between reduced longitudinal motion of artery wall, arterial stiffness and cardiovascular disease [3]. Despite the preliminary evidence of a link between CCA longitudinal wall motion and cardiovascular health, the determinants of CCA longitudinal wall motion remain unknown [6].

The aim of this work is to propose and evaluate an algorithm for analysis of artery wall longitudinal and radial movements from registered RF US signals. The proposed method is based on phase correlation and sub-sample algorithm. A physical phantom and in vivo tests were employed for verification of the algorithm.

2 Materials and Methods

2.1 Data Acquisition

RF US signal sequences were acquired using a clinical scanner Ultrasonix SonixTouch (Analogic Ultrasound,

Canada), equipped with a 5–14 MHz linear array probe. RF US signals sequence frame rate was 52 fps, a sample size in longitudinal direction was 62.5 μm, and in radial direction was 19.25 μm. Our method was applied on phantom with determined longitudinal motion and on three healthy subjects (24, 45 and 80 years old).

2.2 Determined Longitudinal Motion Phantom

A phantom of fixed longitudinal displacements has been used to find out how precisely the proposed phase correlation and sub-sample algorithms are capable to measure determined longitudinal displacements. Figure 1 shows the structure of this phantom.

The eccentric ring was placed on disk which has been rotated by step motor. Ring center offset from disk center was 2 mm. The step motor is included in the device, which is used to verify performance of ultrasonic Doppler systems [10]. With disc of 42 mm diameter and preset linear speed of 10 m/s we obtained 1.22 s period of motion. Rotating eccentric caused motion of lever arm. Motion of lever arm transferred displacement to frame. The displacements of frame we assumed as sinus waveform reference longitudinal displacements. Frame displacement amplitude was verified with micrometer and we found 170, 200, 500, 700, 900, and 1100 μm double amplitudes. Both, ultrasound transducer and determined longitudinal motion phantom were firmed stationary in order to prevent random motions which may act as noise during registration of determined displacements.

2.3 RF Ultrasound Signals Processing Algorithm

Firstly, ultrasound RF signals had uploaded into a Matlab (Mathworks, Natick, MA). After that, B-mode ultrasound image had formed according to the classic B-mode image-formatting algorithm. The image was formed in

order to select the region of interest (ROI). Only RF signals in the ROI had been used for further analysis.

Phase correlation is a frequency domain technique based on the Fourier shift theorem. It states that a shift between two images will cause a phase shift in the Fourier domain. For example, two RF signal matrixes $a1(x, y)$ and $a2(x, y)$, with $a2$ shifted by an amount $[\Delta x, \Delta y]$ relative to $a1$. Their 2D discrete Fourier transforms are denoted as $A1(u, v)$ and $A2(u, v)$. The normalized cross-power spectrum is defined as:

$$R(u,v) = \frac{A_1(u,v)A_2^*(u,v)}{|A_1(u,v)A_2^*(u,v)|} = e^{-i(u\Delta x + v\Delta y)}, \quad (1)$$

where * is the complex conjugate. If we apply the inverse Fourier transform to $R(u, v)$, we get phase-correlation surface, which is so-called a 2D impulse (Dirac delta) function located at $[\Delta x, \Delta y]$:

$$r(x,y) = \mathcal{F}^{-1}(R(u,v)) = \delta(x - \Delta x, y - \Delta y) \quad (2)$$

Then the displacement between two RF signal matrixes $a1$ and $a2$:

$$(\Delta x, \Delta y) = \arg \max_{x,y} |r(x,y)| \quad (3)$$

However, the estimated displacement had integer accuracy, i.e. the coordinates of the maximum of the Dirac delta function had rounded version of the true peak location [11]. Due to this, phase correlation method was extended with sub-sample algorithm [12]. According to it, second degree surface was fitted to phase-correlation matrix maximum and neighborhood values to obtain sub-sample accuracy displacement. Finally, displacement between the two RF signal matrixes $a1$ and $a2$ are:

$$\begin{cases} x_{displacement} = x_{\text{sub}} + \Delta x \\ y_{displacement} = y_{\text{sub}} + \Delta y \end{cases} \quad (4)$$

Radial movement or pulsations of diameter of artery were estimated analyzing RF US signals in ROI2. Algorithm of
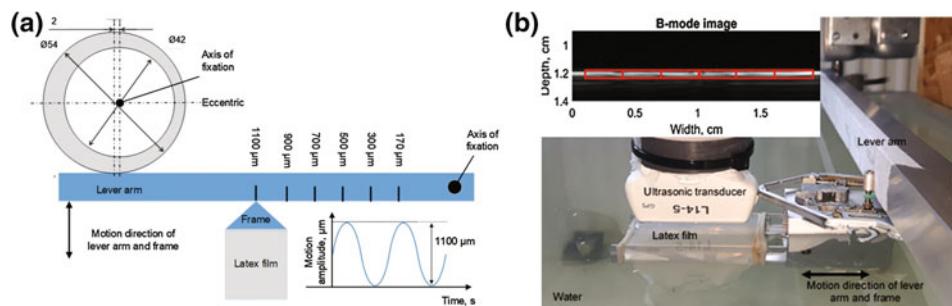
Fig. 1 Structural scheme (**a**) of phantom which ensures longitudinal displacements of determined amplitude. In experiments (**b**) we obtained US RF sequences of latex film. On B-mode image of film we selected 6 analysis regions (ROI1)

radial movement estimation is started with manual selection of ROI2 which covers anterior and posterior walls of CCA. From the center of ROI2, algorithm is searching for the maximums and their indices in RF US signals which amplitudes are above preset threshold. These maximums are assumed as boundary between CCA lumen and anterior or posterior walls. These indices found on both walls were used for calculation of radial movement. Estimate of radial movement is obtained as mean value of diameters estimated in ROI2. The displacements in phantom were obtained selecting ROI1 size of 3×0.4 mm. In case of CCA ROI1 size was 2×0.5 mm.

It has been observed that the longitudinal displacement signals were noisy and had outliers. Due to this, additional filtering was used. This filter had been designed using Matlab *smooth* function setting *rloess* method with 5% span.

The Pearson's correlation coefficient (R) and a normalized root-mean-square error (NRMSE) were used to evaluate the feasibility of RF US signals processing algorithm. NRMSE and R were calculated between sinus waveform (as a reference) of displacements in phantom and detected longitudinal displacement waveforms.

3 Results

Implemented algorithm was firstly applied on RF US signals acquired from motion phantom. Accuracy of estimates of phantom displacements is presented in Fig. 2. We selected 6 ROI1 in each of 7 RF signal sequences acquired from phantom. In detected waveforms of determined amplitude of longitudinal displacement three periods were used to evaluate the feasibility of the proposed algorithm. Mean values and standard deviations were calculated from n = 6 × 7 = 42 longitudinal displacement estimates.

Estimates shown that NRMSE was from 0.28 to 0.58 μm and R was from 0.88 to 0.96 at any preset longitudinal motion values. Raw motion waveforms were corrupted with spike outlier samples, therefore smoothing filter was employed. If additional filtering was employed, NRMSE was ranging from 0.21 to 0.41 μm, while R was from 0.95 to 0.98. Also, the standard deviation of the NRMSE was higher at all displacement values before filtering. This standard deviation indicated that the longitudinal motion curves are noisy or evaluated longitudinal displacement does not significantly correspond to the longitudinal displacement pattern. Before filtering standard deviation of the NRMSE was from 0.19 to 0.55 and standard deviation of R was from 0.04 to 0.14. After filtering standard deviation of the NRMSE was from 0.11 to 0.16 and standard deviation of R was from 0.01 to 0.03. It shown that filtering reduced noise and outliers in longitudinal motion estimates.

Implemented algorithm was also applied on RF US signals acquired from CCA in vivo. The estimated movements of the posterior wall of CCA are presented in Fig. 3. Waveforms of longitudinal movement of posterior wall and pulsations of diameter are matched on time axis.

We did an evaluation of longitudinal movements of CCA wall in volunteer subjects of different age. The purpose was to examine the capability of proposed algorithm to evaluate longitudinal motion in vivo. In CCA RF US sequence, we selected single ROI1, in which we detected motion waveforms. From waveforms of movement, we estimated amplitudes. Double amplitudes of artery wall movements are compared in Table 1. We calculated mean value and standard deviation of double (or peak-to-peak value) amplitudes estimated during four cardiac cycles (n = 4).

Comparing the 46-year-old subject with a 24-year-old one, a decrease in longitudinal and radial movement of the
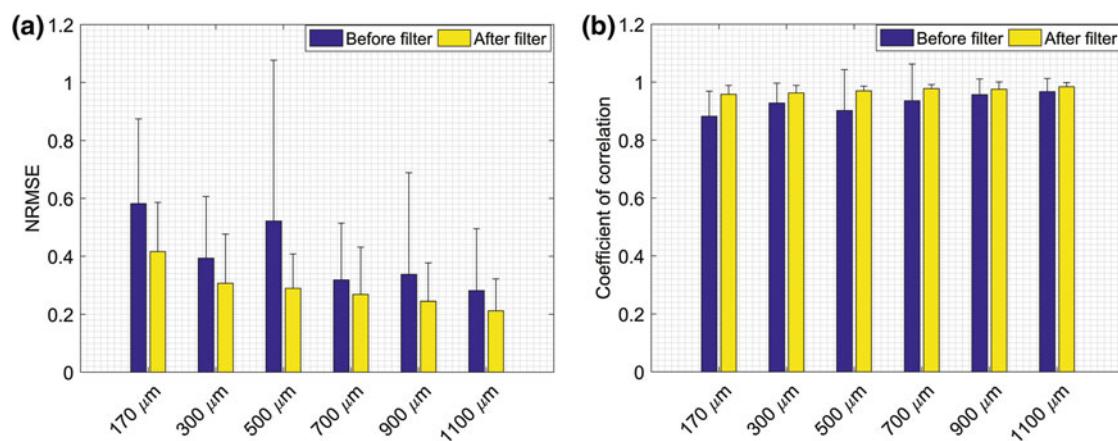
Fig. 2 Accuracy of estimates of phantom displacements: **a** NRMSE dependence for determined longitudinal displacement (n = 42) and **b** coefficient of correlation dependence for determined longitudinal displacement (n = 42) before and after filter
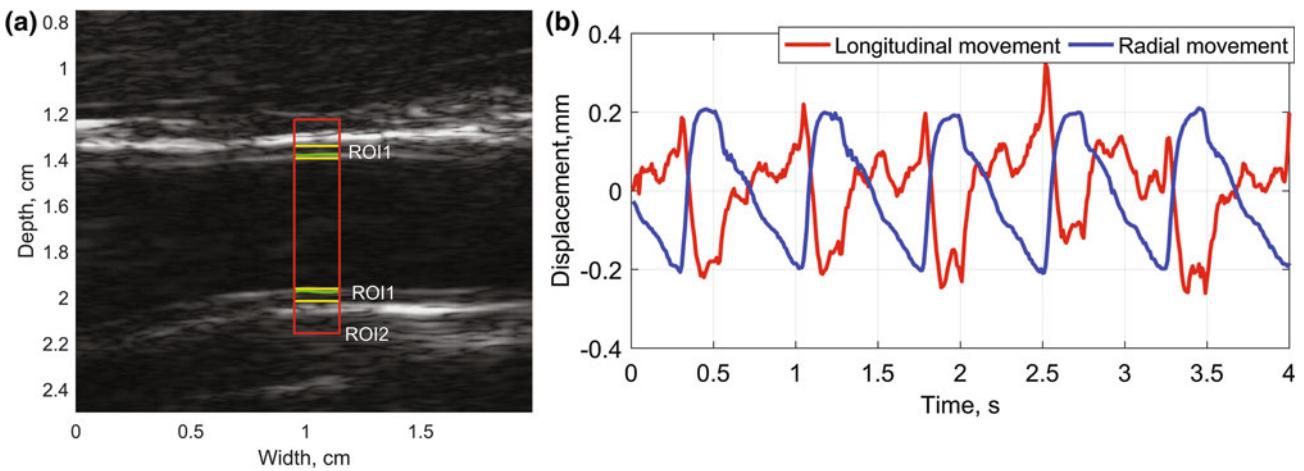
Fig. 3 Evaluation of CCA wall longitudinal motion: **a** B-mode US image and selected ROI1 (yellow), ROI2 (red) and boundary between lumen and CCA anterior and posterior walls (green lines); **b** detected waveforms of longitudinal movement of posterior wall and radial movement (Color figure online)

Table 1 Comparison of longitudinal and radial movements of CCA posterior wall

Age (year)	24	45	80
Radial movement (mm) (n = 4)	0.75 ± 0.02	0.39 ± 0.01	0.76 ± 0.12
Intima-media complex longitudinal movement (mm) (n = 4)	0.79 ± 0.08	0.34 ± 0.03	0.19 ± 0.03

carotid artery had observed and reached about 50%. However, in the 80-year-old subject, evaluated longitudinal movement was even more reduced. The longitudinal movement of the arterial wall had characterized bi-directional motion and link with radial movement. In this study result of longitudinal movement of CCA shown from three subjects. Therefore, further study in subjects groups is planned in the future.

4 Conclusions

In this paper, we present an algorithm for detection of longitudinal displacements from RF US signals. Proposed method is based on phase correlation and sub-sample algorithm. The results from in vitro validation study demonstrate the feasibility of proposed algorithm. A preliminary in vivo evaluation was conducted. It shown that proposed algorithm was capable to evaluate longitudinal movement in CCA. Also we observe the difference between young and the old subject. Future work will focus on increasing the amount of in vivo data of CCA and validating longitudinal movement of arterial wall as new biomarker of atherosclerosis.

Conflict of interest The authors declare that they have no conflict of interest.

References

1. NICOLAIDES, A., BEACH, K.W., KYRIACOU, E. and PATTI-CHIS, C.S. *Ultrasound and Carotid Bifurcation Atherosclerosis.* Springer Science & Business Media, 2011.
2. STALIORAITYTĖ, E.i.k. *Patologinė Anatomija.* 2-asis leid. ed. Kaunas: Naujasis lankas, 2001 ISBN 995503095X.
3. ZAHND, G., BOUSSEL, L., SÉRUSCLAT, A. and VRAY, D. *Intramural Shear Strain can Highlight the Presence of Atherosclerosis: A Clinical in Vivo Study.* IEEE, 2011.
4. ZAHND, G., et al. Evaluation of a Kalman-Based Block Matching Method to Assess the Bi-Dimensional Motion of the Carotid Artery Wall in B-Mode Ultrasound Sequences. *Medical Image Analysis*, 2013, vol. 17, no. 5. pp. 573–585.
5. CINTHIO, M., et al. Evaluation of an Ultrasonic Echo-Tracking Method for Measurements of Arterial Wall Movements in Two Dimensions. *IEEE Transactions on Ultrasonics, Ferroelectrics, and Frequency Control*, 2005, vol. 52, no. 8. pp. 1300–1311.
6. TAT, J., AU, J.S., KEIR, P.J. and MACDONALD, M.J. Reduced Common Carotid Artery Longitudinal Wall Motion and Intramural Shear Strain in Individuals with Elevated Cardiovascular Disease Risk using Speckle Tracking. *Clinical Physiology and Functional Imaging*, 2015.
7. GASTOUNIOTI, A., GOLEMATI, S., STOITSIS, J. and NIKITA, K. Adaptive Block Matching Methods for Carotid Artery Wall Motion Estimation from B-Mode Ultrasound: In Silico Evaluation & in Vivo Application. *Phys. Med. Biol*, 2013, vol. 58, no. 24. pp. 8647–8661.
8. GOLEMATI, S., et al. Carotid Artery Wall Motion Estimated from B-Mode Ultrasound using Region Tracking and Block Matching. *Ultrasound in Medicine & Biology*, 2003, vol. 29, no. 3. pp. 387–399.

9. AU, J.S., DITOR, D.S., MACDONALD, M.J. and STOHR, E. J. Carotid Artery Longitudinal Wall Motion is Associated with Local Blood Velocity and Left Ventricular Rotational, but Not Longitudinal, Mechanics. *Physiological Reports*, Jul, 2016, vol. 4, no. 14. pp. https://doi.org/10.14814/phy2.12872 ISSN 2051-817X.

10. *Doppler Ultrasound Quality Assurance Phantom with Moving String Target. Model no. 84–360. Mark 4. JJ&A Instruments, Duvall, WA.*

11. ALBA, A., AGUILAR-PONCE, R.M., VIGUERAS-GÓMEZ, J.F. and ARCE-SANTANA, E. *Phase Correlation Based Image Alignment with Subpixel Accuracy*. Springer, 2012.

12. SUN, C. Fast Optical Flow using 3D Shortest Path Techniques. *Image and Vision Computing*, 2002, vol. 20, no. 13. pp. 981–991.

Models of Physiological Parameters for Runners and Cyclists

Milan Stork, Jaroslav Novak, and Vaclav Zeman

Abstract

The study of physiological parameters dynamic is currently the main area of research in exercise physiology. The most common physiological data to collect include heart rate, oxygen saturation, core body and skin temperature, blood pressure, ECG, oxygen consumption and others. The data obtained are often related to various forms and intensities of physical activity, and in accordance with the principles of personalized medicine evaluated. Mathematical models are able to simulate some physiological parameters e.g. heart rate, oxygen consumption etc. during cycling exercise on bicycle ergometer or running exercise on treadmill. Workload intensity (in Watts) on bicycle ergometer and running velocity (in km/h) on the treadmill are taken as input for dynamic models. Determination of dynamic models of physiological parameters is fundamental for athletic training methodology, as well as evaluation of cardiorespiratory capacity and fitness. The present work demonstrates the application of dynamic systems models to the simulation of heart rate kinetics and oxygen consumption during workloads of time-varying intensity. Optimization of free model parameters could be used as important information about the health condition of the subject with special reference to the cardiorespiratory capacity and fitness age. The models could be used both for athletes as well as for untrained sedentary population.

1 Introduction

For study of physiological parameters kinetics during exercise usually the treadmill or bicycle ergometers are used. Heart rate (HR), oxygen uptake (VO_2), CO_2 expenditure (VCO_2), pulmonary ventilation (VE) and other parameters are continuously measured within test. The results are applied in training methodology and in many cases also for medical conclusions. Using physiological parameters obtained during any form of physical activity the dynamic models can be derived. Models are described by means set of nonlinear differential equations. Most relevant is dynamics of HR as a response to running velocity (on treadmill) or workload intensity (on cycle ergometer). It must be pointed out that besides of workload intensity there are other factors influencing HR, e.g.: ambient temperature and humidity, previous training and fatigue, over-training, altitude, medication, prodromal phase of infectious diseases, pre-start psychical state, mental activity, nutrition and others. $\dot{V}O_2$ is defined as the volume of oxygen used per time unit to cover energy demands of the body, either resting or during physical activity. $\dot{V}O_{2max}$ is the maximal capacity for oxygen consumption by the body during maximal physical exertion. Further increase in intensity doesn't yield a larger $\dot{V}O_2$. It is also known as aerobic power, maximal oxygen intake, maximal oxygen uptake, maximal oxygen consumption, aerobic capacity, and/or cardio-respiratory endurance capacity [1]. Anaerobic (lactate) threshold (LT) is defined as the point (borderline intensity of physical activity) at which the metabolic demands of physical exercise can no longer be met by available aerobic sources and at which an increase of

M. Stork (✉)
Department of Applied Electronics and Telecommunications/RICE, University of West Bohemia, Pilsen, Czech Republic
e-mail: stork@kae.zcu.cz

J. Novak · V. Zeman
Medical Faculty in Plzen, Department of Sports Medicine, Charles University in Prague, Prague, Czech Republic
e-mail: novakj@lfp.cuni.cz

V. Zeman
e-mail: vaclav.zeman@lfp.cuni.cz
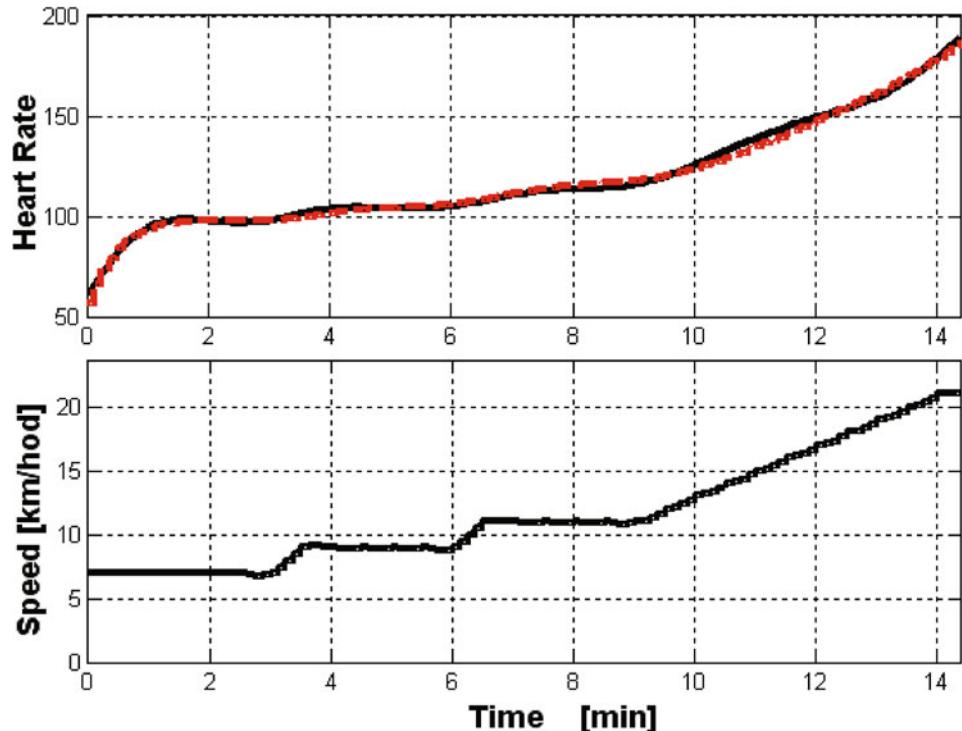
anaerobic metabolism occurs, reflected by an increase of blood lactate concentration. At the intensities lower then anaerobic threshold the rate of increase in $\dot{V}O_2$ uptake is approximately linear function of exercise intensity, whilst at the intensities higher then the LT the function is nonlinear. $\dot{V}O_2$ can be measured as a time series using equipment for expired air analysis (O_2–CO_2 analyzer). The measuring of that kind is possible in the exercise-test laboratory where the athlete performs either a running load on a treadmill at various speeds and/or cycling load on bicycle ergometer at various loads (in Watts) [2]. In this paper, pulmonary ventilation, breathing frequency, oxygen uptake and CO_2 expenditure are measured and registered every 30 s (sampling period T_s) throughout the whole test duration.

2 Materials and Methods

A two types of models can be used linear and nonlinear [3]. In this paper the linear state space approach was used. The state-space representation is a mathematical model of a physical system as a set of input, output and state variables related by first-order differential equations. The state of the system can be represented in vector forms with input $\boldsymbol{u}$, state $\boldsymbol{x}$ and output $\boldsymbol{y}$

$$\begin{aligned} \dot{\boldsymbol{x}} &= A\boldsymbol{x} + B\boldsymbol{u} \\ \boldsymbol{y} &= C\boldsymbol{x} + D\boldsymbol{u} \end{aligned} \tag{1}$$

where matrices A, B, C, D ($D = 0$ in this medical application) are

$$A = \begin{bmatrix} a_{11} & a_{12} & \cdots & a_{1n} \\ a_{21} & a_{22} & \cdots & a_{2n} \\ \vdots & \vdots & \ddots & \vdots \\ a_{n1} & a_{n2} & \cdots & a_{nn} \end{bmatrix}; \quad B = \begin{bmatrix} b_1 \\ b_2 \\ \vdots \\ b_n \end{bmatrix} \tag{2}$$
$$C = \begin{bmatrix} c_1 & c_2 & \cdots & c_n \end{bmatrix}; \quad D = 0$$
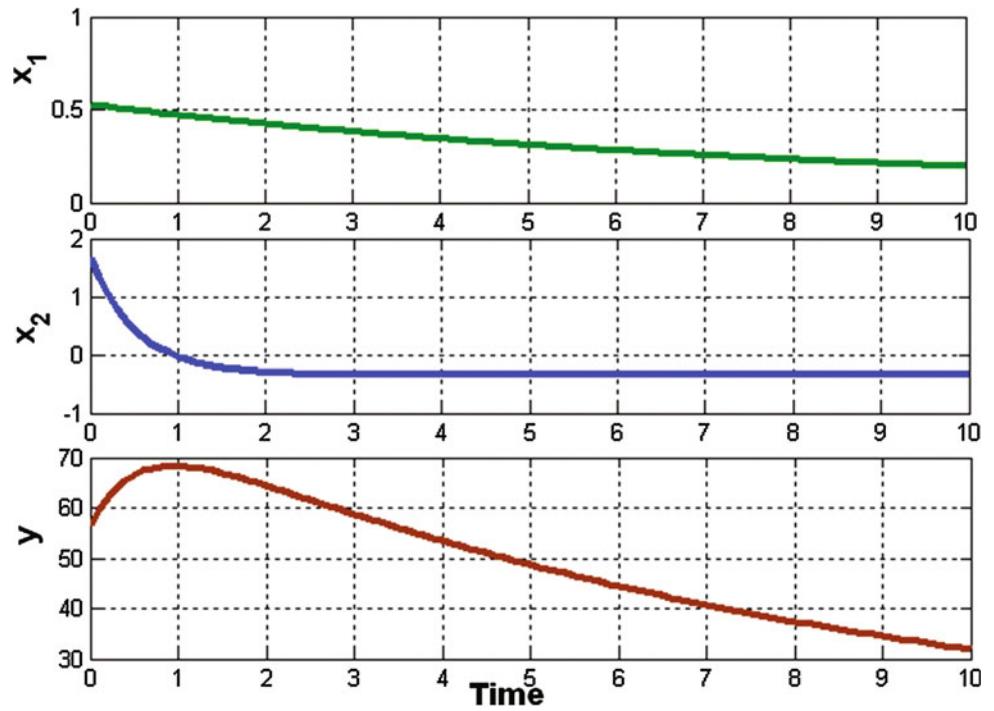
Before model estimation, the data were resampled at a higher rate using low-pass interpolation and after matrices A, B, C and initial conditions were estimated by means of optimization method. The model was converted to real block diagonal form. In real diagonal form, the complex eigenvalues are in 2-by-2 blocks on the diagonal. The example of state space for 4th order system (matrix A), with 2 real poles and 2 complex conjugate poles is given as Eq. (3).

$$A = \begin{bmatrix} a_{11} & 0 & 0 & 0 \\ 0 & a_{22} & 0 & 0 \\ 0 & 0 & a_{33} & a_{34} \\ 0 & 0 & -a_{34} & a_{44} \end{bmatrix} \tag{3}$$

3 Results

As first example, HR estimation versus speed for the male subject M1 is shown in Fig. 1 [4]. Estimation is based on state space approach.

Fig. 1 Measured HR (solid, black) and estimated HR (dash, red)—top, treadmill speed—bottom, subject M1 (Color figure online)

Fig. 2 Time evolution of Eq. (5), x_1—top, x_2—middle, y—bottom, subject M1

State space continuous time model is (for all state space models in this work, instead $T_S = 0.5$ min, $T_S = 0.5$ s is used, where T_S is sampling period)

$$\frac{dx_1}{dt} = -0.122x_1 + 0.0066u; \quad x_1(0) = 0.53$$
$$\frac{dx_2}{dt} = -1.846x_1 + 0.642u; \quad x_2(0) = 1.66 \quad (4)$$
$$y = 144 \cdot x_1 - 11.5 \cdot x_2$$

Time solution of $x_1(t)$ and $x_2(t)$ for unit step ($u = 1$) is

$$x_1(t) = 0.42 \cdot \exp(-0.122 \cdot t) + 0.054$$
$$x_2(t) = 2.0 \cdot \exp(-1.846 \cdot t) - 0.348 \quad (5)$$

From result of (5) can be seen that time solution consists from slow and fast part (top and middle), shown in Fig. 2.

It must be pointed out that not only *HR* can be estimated, but also other parameters can be modeled [5, 6]. In next example for the female person F1 oxygen uptake versus load is identified. Matrix *A* has form

$$A = \begin{bmatrix} -2.88 & 0 & 0 \\ 0 & -0.34 & 0.74 \\ 0 & -0.74 & -0.34 \end{bmatrix} \quad (6)$$

therefore estimated system has 1 real pole and 2 complex conjugate poles. Result of estimation of oxygen consumption is displayed in Fig. 3.

The presented estimation based on linear state space approach has a advantage that for estimated system is

possible derive e.g. step response, transfer function, Bode diagram etc. Example of the Bode diagram, magnitude and phase for subject F1 is shown in Fig. 4.

The last example concerns the male subject M2, for prolonged endurance running performance (approx. 2 h). For this example, for *HR* model the 5th order of state space model must be used. Matrix *A* has form

$$A = \begin{bmatrix} -5.33 & 0 & 0 & 0 & 0 \\ 0 & -1.5 & 3.87 & 0 & 0 \\ 0 & -3.87 & -1.5 & 0 & 0 \\ 0 & 0 & 0 & -0.003 & 0 \\ 0 & 0 & 0 & 0 & -1.24 \end{bmatrix} \quad (7)$$

The simulation result, *HR* as a time response on treadmill speed is shown in Fig. 5.

4 Conclusions

The aim of this paper was primarily to verify the usefulness of systems approach to modeling and analyzing the physiological response of the body to exercise. It was experimentally demonstrated that dynamic changes of selected physiological parameters obtained during different ergometric physical workloads can be simulated by set of first order differential equations with good agreement. Mathematical models can be e.g. used for appropriate load test run setting [7, 8]. Main advantage of take linear state space approach is that brings possibility of use e.g. Bode diagram,

Fig. 3 Measured oxygen consumption (solid, black) and estimated (dash, red)—top, versus bicycle ergometer power—bottom, subject F1 (Color figure online)
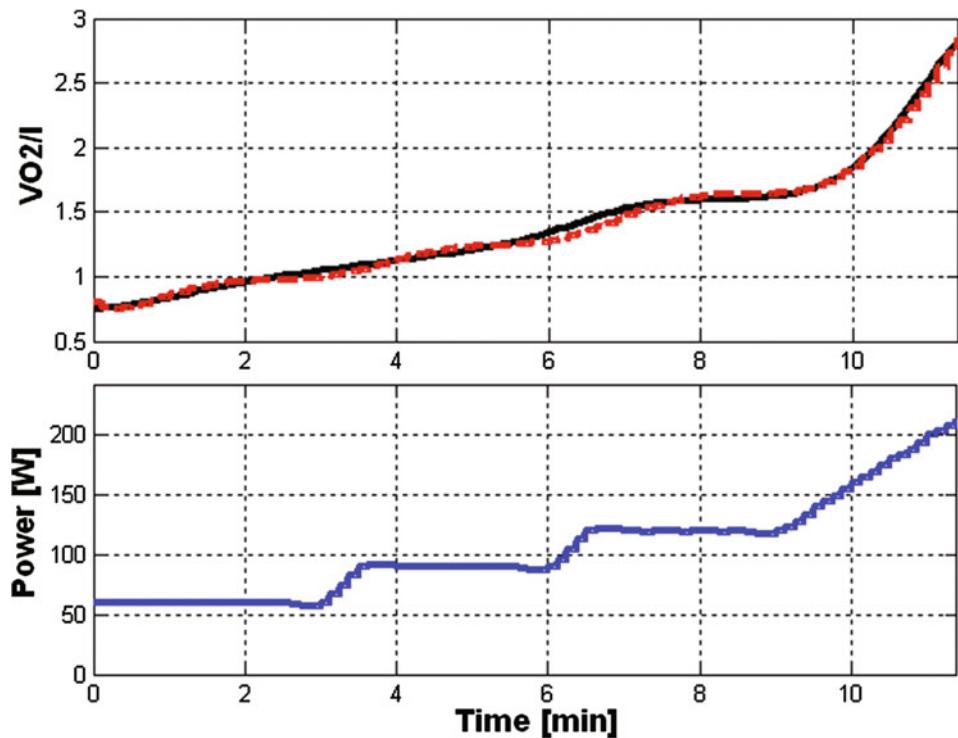
Fig. 4 Bode diagram, magnitude in dB (top) and phase in deg (bottom) of subject F1 estimated from data measured on exercise on bicycle ergometer
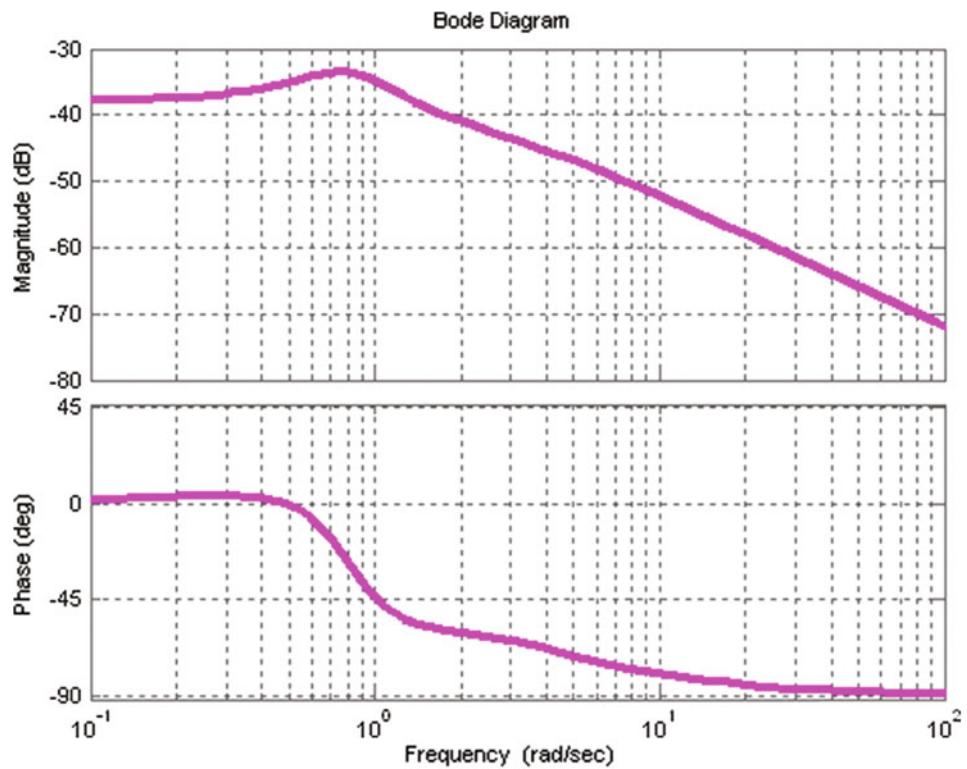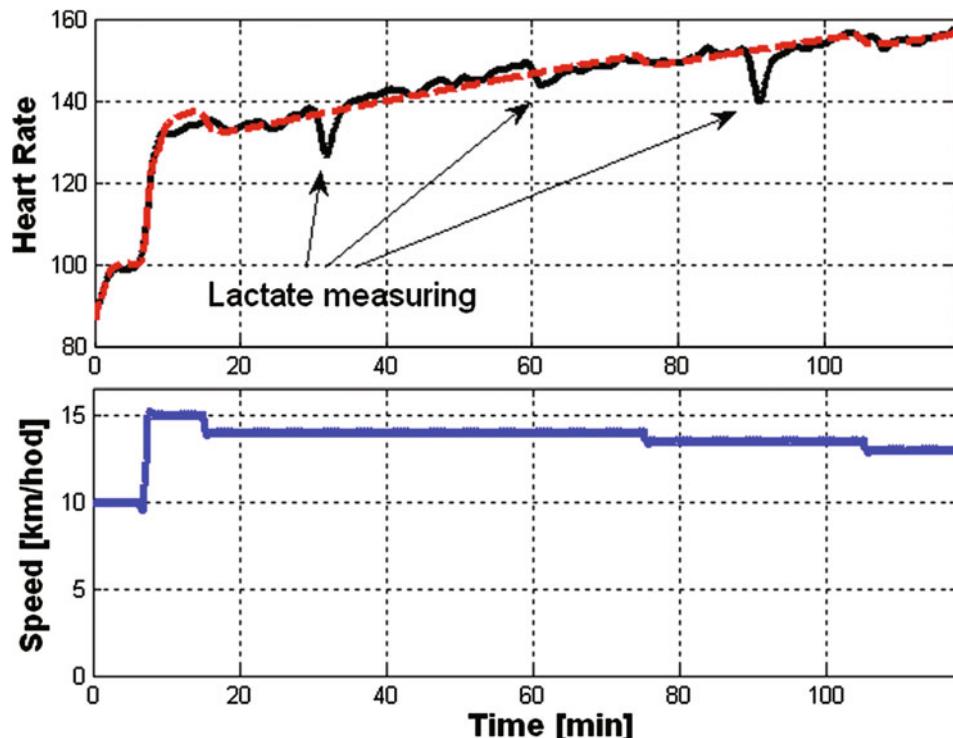
Fig. 5 Measured *HR* (solid, black) and estimated *HR* (dash, red)—top, treadmill speed—bottom, subject M2. During lactate measuring treadmill is stopped and therefore *HR* is decreasing (Color figure online)

step response, impulse response and therefore compare results of different subject.

It is evident that there are many open problems in the field of fitness determination (intensity, duration, procedure, choice of equipment, laboratory or field etc.). The application of more modern and sophisticated techniques of analysis and modeling could provide very interesting results.

Conflict of Interest None of the authors have actual or potential conflicts of interest to be disclosed.

References

1. Wasserman, K., Hansen, J.E., Sue, D.Y., Whipp, B. J. and Casaburi, R.: Principles of exercise testing and interpretation, including pathophysiology and clinical applications, Lippincott Williams and Wilkins (1999).

2. Guyton, A.C. and Hal,l J. E.: Textbook of Medical Physiology. Saunders and Company, 11th edition (2005).

3. Eskinat E., Johnson S., and Luyben W.: Use of Hammerstein models in identification of nonlinear systems. AIChE J., vol. 37, pp. 255–268, 1991.

4. Su, S., Wang, L., Celler, B., Savkin, A., and. Guo, Y.: Modelling and control for heart rate regulation during treadmill exercise. Proc. 28th Annu. Int. Conf. IEEE Engineering in Medicine and Biology Society (EMBS), New York, 4299–4302 (2006).

5. Su S., Wang L., Celler B., and Savkin A.: Estimation of oxygen consumption for moderate exercises by using a Hammerstein model. Proc. 28th Annual Int. Conf. IEEE Engineering in Medicine and Biology Society (EMBS), New York, 3427–3430 (2006).

6. Beck, K.C., Randolph, L.N., Bailey, K.R, Wood, C.M, Snyder, E. M. and Johnson, B.D.: Relationship between cardiac output and oxygen consumption during upright cycle exercise in healthy humans. J Appl Physiol 101: 1474–1480 (2006).

7. Nes, B. M., Janszky, I., Wisloff, U., Stoylen, A., and Karlsen, T.: Age-predicted maximal heart rate in healthy subjects: The HUNT Fitness Study. Scand. J. Med. Sci. Sports, 23(6): 697–704, (2013).

8. Mazzoleni, M. J., Battaglini, C. L., Martin, K. J. Coman, E. M., and Mann, B. P.: Modeling and predicting heart rate dynamics across a broad range of transient exercise intensities during cycling. Sport. Eng., (2016).

Cyclostationary Analysis of Respiratory Signals with Application of Rate Determination

Esra Saatci, Ertugrul Saatci, and Aydin Akan

Abstract

Respiratory signals are periodic-like signals where the noisy periodic pattern repeats itself. Therefore, based on a stationarity assumption, autocorrelation function contains noisy cycles in time-lag with the same rate as the respiration rate. In this work, cyclostationarity test is performed on the respiratory signals in order to determine cyclic characteristics of the time varying autocorrelation function. Our specific aim is to check whether the cycle period in time corresponds to the respiration rate. Lung simulator was used to generate the respiratory signals. Time varying autocorrelation variance was computed by using both the modified windowed, and the blocked signal methods. Our simulations resulted that the cycle period was the same as the respiration period. Moreover, we observed that cyclic frequencies corresponded to the respiratory rate and its harmonics.

Keywords

Respiratory rate determination • Cyclostationary analysis of respiratory signals • Time varying autocorrelation

1 Introduction

There are many methods to determine the respiratory rate from respiratory signals [1]. During regular breathing, measured airflow signal and mouth pressure are periodic-like signals, which contain additive white noise from the flow or pressure sensor and the environment. Thus, it may be seen as a basic peak-count problem to count the cycles. However, it is known that airflow signals are modulated during speech, cough or any other disturbances to airflow. In this case we require to employ solid methods to extract the cyclic properties. Moreover, determination of the respiratory mechanics requires the utilization of the respiratory signals and in this process measured signals are assumed to be statistically stationary signals. However respiratory signals have changing statistics due to variations in the biological systems by which signals sprang out [2, 3]. Hence, we propose to perform cyclostationary analysis [4] on the respiratory signals to test the cyclic behavior of the signals and more importantly to determine the cycle period. Here, our specific aim is to check whether the cycle period corresponds to the respiratory rate.

On this way, we have used both the variability method [5] and the windowing method [6]. In this work, we modified the windowing method, by which the variations in the time varying autocorrelation were shown to be a function of the window length. Cyclic frequencies were also found by using the cyclic autocorrelation.

2 Cyclostationary Signals

A signal $x(n)$, $n \in Z$ is called wide-sense cyclostationary with a cycle period p $(p > 0)$ if its mean $m_x(n) = m_x(n + lp)$ and autocorrelation $R_{xx}(n, k) = R_{xx}(n + lp, k), \forall l, k \in Z$ are periodic with the period p. If $p = 1$, the signal is regarded as a stationary signal. In this study we assume that N samples of the signal are available for the processing, $0 \le n \le N - 1$. Before the estimation, the signal must be represented by stationary intervals [5]. Blocking operator is used to map the signal $x[n]$ into m dimensional vector $\bar{x}_m$:

E. Saatci (✉) · E. Saatci
Department of Electrical and Electronics Engineering, Istanbul Kultur University, Istanbul, Turkey
e-mail: esra.saatci@iku.edu.tr

E. Saatci
e-mail: e.saatci@iku.edu.tr

A. Akan
Department of Biomedical Engineering, Izmir Katip Celebi University, Izmir, Turkey
e-mail: aydin.akan@ikc.edu.tr

$$x(n) \rightarrow \bar{x}_m, \quad \bar{x}_m = \begin{bmatrix} x(0) & x(m) & x(2m) & \cdots \\ x(1) & x(m+1) & x(2m+1) & \cdots \\ \vdots & \vdots & \vdots & \vdots \\ x(r) & x(m+r) & x(2m+r) & \cdots \\ \vdots & \vdots & \vdots & \vdots \\ x(m-1) & x(2m-1) & x(3m-1) & \cdots \end{bmatrix}$$

(1)

where each row is one of the stationary intervals that the signal contains if the blocking fold index is an integer multiples of the cycle period, $m = lp$.

2.1 Estimation of Time Varying Autocorrelation

Autocorrelation $R_{xx}(n, k)$ can be estimated by using both the blocked signal in (1) and windowed signal. Time average autocorrelation estimator of the windowed signal is defined as [6]:

$$\hat{R}_{xx}(n, k; h) = \frac{1}{W_h} \sum_{i=0}^{h-1} w_h(i) x(n+i) w_h(i+k) x(n+i+k)$$

(2)

where $0 \leq n \leq N - h - k$, k is the time lag for the time average autocorrelation, $0 \leq k \leq h - 1$, w_h is the length h window function and $W_h = (\|w_h\|_1)^2$. The prior information regarding to the stationary intervals of the signal is required for the window length to compute the autocorrelation at time instant n.

Another estimator for the autocorrelation can be defined by using the blocked signal in (1) as defined in [5]:

$$\hat{R}_{x_m^{r_1} x_m^{r_2}}(\hat{k}) = \frac{1}{\lfloor \frac{N}{m} \rfloor} \sum_{i=0}^{\lfloor \frac{N}{m} \rfloor - \hat{k} - 1} x(im + r_1) x(im + r_2 + \hat{k}m)$$

(3)

where $x_m^{r_1}$ and $x_m^{r_2}$ are r_1th and r_2th rows of the vector $\bar{x}_m$ respectively ($0 \leq r_1, r_2 \leq m - 1$), $\hat{k}$ is the time lag for the blocked signal autocorrelation, $0 \leq \hat{k} \leq \lfloor \frac{N}{m} \rfloor - 1$. In practice, it is stated that $\hat{k} = 0$ or 1 is effective for the cyclostationary signal analysis [5]. It is proved in [5] that, if $m = lp$, blocked signal autocorrelation estimator $\hat{R}_{x_m^{r_1} x_m^{r_2}}(\hat{k})$ approaches to the time average autocorrelation estimator of the windowed signal $\hat{R}_{xx}(n, k)$, in which window length is the same as the cycle period, $h = p$. That is expressed as $\hat{R}_{x_m^r x_m^{r+k}}(0) = \hat{R}_{xx}(r, k; h)$, where $0 \leq r \leq m - 1$.

We can observe variability in both $\hat{R}_{x_m^r x_m^{r+k}}(0)$ for different rows r of the blocked signal and $\hat{R}_{xx}(r, k)$ for different centered time instances r of the windowed signal. Furthermore, variability of $\hat{R}_{x_m^{r_1} x_m^{r_2}}(\hat{k})$ and $\hat{R}_{xx}(r, k)$ can be measured by the sample variance [5]:

$$\frac{1}{m} \sum_{r=0}^{m-1} \left(\hat{R}_{x_m^r x_m^{r+k}}(0) - \frac{1}{m} \sum_{r=0}^{m-1} \left(\hat{R}_{x_m^r x_m^{r+k}}(0) \right) \right)^2$$

(4)

Thus, stationary time intervals can be detected by observing the autocorrelation variance with respect of blocked index and window length for both estimators.

2.2 Cyclic Autocorrelation Function

Since $R_{xx}(n, k)$ is a periodic function in n, discrete Fourier series can be utilized to obtain spectral representation of the cyclic behavior of the cyclostationary signals. In this case cyclic autocorrelation can be estimated as in [7]:

$$\hat{C}_{xx}(\alpha_i, k) = \frac{1}{N} \sum_{n=0}^{N-1} R_{xx}(n, k) e^{-j\alpha_i n} = \frac{1}{N} \sum_{n=0}^{N-1} x(n) x(n+k) e^{-j\alpha_i n} \quad (5)$$

where α_i is the set of cyclic frequencies, $\alpha_i = i\frac{2\pi}{p}$ for $-\frac{p}{2} \leq i < \frac{p}{2}$, which has to be known before calculating the cyclic autocorrelation. In case of the known cycle period, $\hat{C}_{xx}(\alpha_i, k)$ are computed by following steps:

1. set cyclic frequencies $\alpha_i = i\frac{2\pi}{p}$ for $-\frac{p}{2} \leq i < \frac{p}{2}$,
2. compute the frequency shifted signal by $x(n)e^{-j\alpha_i n}$,
3. compute the correlation between $x(n)e^{-j\alpha_i n}$ and $x(n)$,
4. observe α_i's when $\hat{C}_{xx}(\alpha_i, k)$ is different from zero.

$\hat{C}_{xx}(\alpha_i, k)$ gets non zero values only at the distinct set of the cyclic frequencies [8]. If the signal is wide-sense stationary, $\hat{C}_{xx}(\alpha_i, k)$ will be non zero only at $\alpha_0 = 0$. Thus the presence of the cyclic frequency set can be used for the cyclostationarity test [9].

In case of the unknown cyclic frequency, $\hat{C}_{xx}(\alpha_i, k)$ are computed by following steps [10]:

1. compute the time varying autocorrelation $\hat{R}_{xx}(n, k; h)$,
2. compute the Fourier transform of $\hat{R}_{xx}(n, k; h)$,
3. observe α_i's when $\hat{C}_{xx}(\alpha_i, k)$ exceeds a given significance level.

3 Cyclo-stationarity Analysis of Respiratory Signals

Respiratory signals, which are airflow and mask pressure were produced by the artificial lung simulator (ASL 500, IngMar Medical, USA) and measured by pneumotachograph and pressure transducer system (Hans Rudolph Inc. Research pneumotachograph system). Sampling rate was 100 Hz. At least 10 breathing cycle ($N = 5000$) of airflow and mask pressure were recorded by data acquisition system (National Instrument DAQCard-6036E ADC-16bit). Airflow and mask pressure signals in time domain are shown in Fig. 1a and Fig. 1b respectively. We tested the applicability of the cyclostationarity analysis to the signals by computing both time varying autocorrelation (2), (3) and cyclic auto-correlation function (5).

3.1 Respiratory Rate Determination by Estimation of Time Varying Autocorrelation

First, time varying autocorrelation was estimated by using both (2) and (3) with different window length ($10 < h < 100$) and blocking fold index ($1 < m < N/2$), and then the autocorrelation variance was computed by (4). Hanning window was used with $h/2$ overlap. Autocorrelation at zero time lag ($k = 0$) was computed for different window lengths. In the blocked signal analysis autocorrelation at zero time lag ($\hat{k} = 0$) was also found effective to show the cycle period. Figure 1c and Fig. 1d show the autocorrelation variances versus window length and blocking fold index respectively, when the airflow signal was processed.

Cycle period p is visually picked up in both figures. It is known that artificial lung simulator gives the breaths at a rate of 12, that makes approximately 500 data points per tidal breath. In Fig. 1c maximum variance is observed at the window lengths around 500 data points. This result can be explained as that data samples are highly correlated by themselves within one breath cycle. Thus the number of data points in one breath cycle will be the best choice for the window length to search the correlation between or within respiratory signals. Hence, dividing the whole data into partitions equal to the breath cycle (not more and not less) leads to the significant correlation.

As it is explained in the Sect. 2.1, autocorrelation variance becomes maximum when the blocking fold index is the integer multiples of the cycle period. Thus we can easily conclude that respiratory signals are stationary only if one breath cycle is considered. This can be seen from Fig. 1d as

Fig. 1 Airflow (**a**) and mask pressure (**b**) signals in time domain, autocorrelation variance versus (**c**) window length computed by the windowed signals and (**d**) blocking index computed by the blocked signals
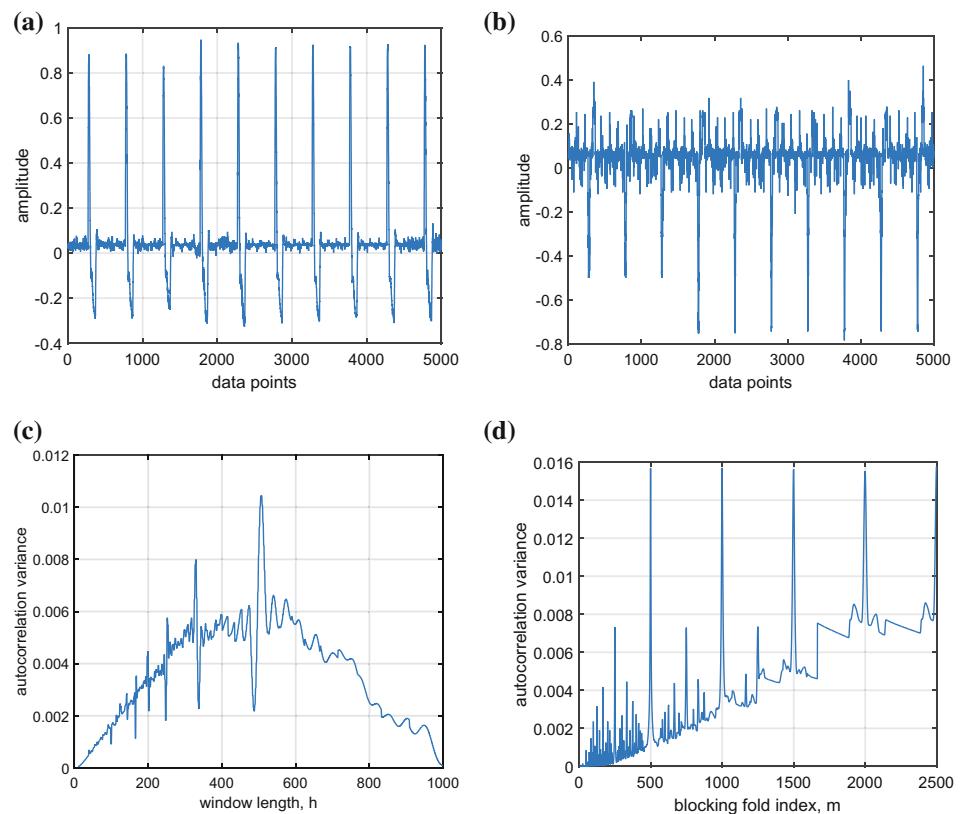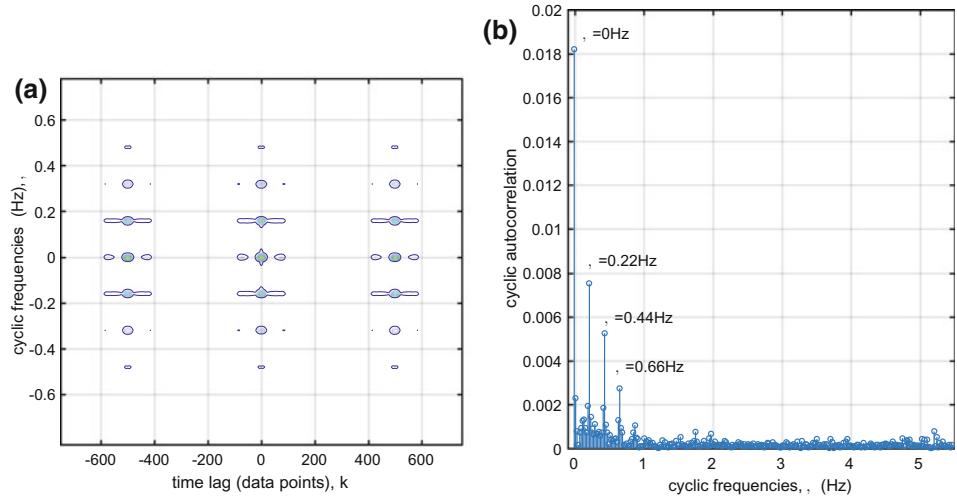
Fig. 2 $\hat{C}_{xx}(\alpha_i, k)$, **a** at cyclic frequencies versus time lag and **b** at the zero time lag $(k = 0)$ showing the respiratory rate and its harmonics

well. That result is also prominent when the signals are used in the respiratory mechanics determination problem in the form of power spectral density.

3.2 Cyclostationarity Test of the Respiratory Signals

In order to test whether respiratory signals are indeed cyclostationary signals, we follow the method explained in [7]. Accordingly, $\hat{C}_{xx}(\alpha_i, k)$ was evaluated at cyclic frequencies calculated by $\alpha_i = i \frac{2\pi}{p}$ for $-\frac{p}{2} \leq i < \frac{p}{2}$ and showed in Fig. 2. We used the cycle period $p = 500$ as explained in the Sect. 3.1. In both method, the same portion of the signal segment was used.

Figure 2a shows the contour plots of cyclic autocorrelation $\hat{C}_{xx}(\alpha_i, k)$ in which cyclic frequencies α_i was converted to frequency in Hz by using sampling frequency. First of all, it should be noted that since the cyclic frequencies exist at only very low frequencies, the non-zero components of $\hat{C}_{xx}(\alpha_i, k)$ was zoomed in the figure. Distinct cyclic frequencies at $\alpha_i = 0, \pm 0.22, \pm 0.44, \pm 0.66$ Hz confirm the cyclic behavior of the signals. In order to analyze the spectrum further, cyclic autocorrelation values versus cyclic frequencies were plotted when the time lag is zero $(k = 0)$ in Fig. 2b. Distinct peaks which correspond to the cyclic frequencies in Fig. 2a can be also observed from the Fig. 2b. Here cyclic frequency $\alpha = 0.22$ Hz represents the respiratory frequency which can be verified by the setting of the lung simulator. It is also seen that high frequency harmonics appeared as a cyclic frequencies in the cyclic autocorrelation.

4 Conclusion

In this paper, we propose a new approach for the cycle period estimation of respiratory signals by utilizing the time averaged windowing method. We applied both the proposed method and the blocking method to the respiratory signals which are cyclic signals in the time domain. Time varying autocorrelation variance was calculated and plotted for various values of the the window length and the blocking fold index. In the simulations, we observed that cycle period was the same as the respiratory period. In addition, cyclic frequencies correspond to the respiratory rate and its harmonics. In the future studies, cyclic spectrum and time-frequency representation [11] which characterize the cyclostationary signals will be utilized.

References

1. V. P. Seppa, J. V. Viik and J. Hyttinen, *Assessmet of pulmonary flow using impedance pneumography*, IEEE Trans. Biomed. Eng., vol. 57, no. 9, pp. 2277–2285, 2010.
2. B. Suki and K. R. Lutchen, *Pseudorandom signals to estimate apparent transfer and coherence functions of nonlinear systems: applications to respiratory mechanics*, IEEE Trans. Biomed. Eng., vol. 39, no. 11, pp. 1142–1152, 1999.
3. T. Li, H. Tang, T. Qui and Y. Park *Heart sound cancellation from lung sound record using cyclostationarity*, Med. Eng. and Physics, vol. 35, pp. 1831–1836, 2013.
4. W.A. Gardner and L. E. Franks, *Chracterization of cyclostationary random signal processes*, IEEE Trans. Infor. Theory, vol. 21, no. 1, pp. 4–14, 1975.
5. J. Wang, T. Chen and B. Huang, *Cyclo-period estimation for discrete-time cyclo-stationary signals*, IEEE Trans. Sig. Pro., vol. 54, no. 1, pp. 83–94, 2006.

6. A. Napolitano, *Cyclostationarity: limits and generalizations*, Signal Processing, vol. 120, pp. 323–347, 2016.

7. G. B. Giannakis, *Cyclostationary signal analysis*, Digital Signal Processing Handbook, Ed. V. K. Madisetti and D. B. Williams, Boca Raton: CRC Press LLC 1999.

8. J. Antoni, *Cyclic spectral analysis in practice*, Mech. Sys. Sig. Proc, vol. 21, pp. 597–630, 2007.

9. A. Napolitano, *Cyclostationarity: new trends and applications*, Signal Processing, vol. 120, pp. 385–408, 2016.

10. J. Antoni, *Cyclostationarity by examples*, Mech. Sys. Sig. Proc, vol. 23, pp. 987–1036, 2009.

11. L.F. Chaparro, E. Sejdic, A. Can, O.A. Alkishriwo, S. Senay and A. Akan *Asynchronous representation and processing of nonstationary signals*, IEEE Sig. Pro. Mag, vol. 42, 2013.

A New Approach for Brain Source Position Estimation Based on the Eigenvalues of the EEG Sensors Spatial Covariance Matrix

Lucas F. Cruz, Marcela G. Magalhães, Jonas A. Kunzler, André A. S. Coelho, and Rodrigo P. Lemos

Abstract

Direction of Arrival (DOA) estimation methods, like MUSIC, can be applied to EEG signals for brain source localization. However, they show a severe degradation at small signal-to-noise ratios on the EEG sensors and for large amounts of brain sources. Inspired on the SEAD method, this article introduces a new method that analyses the eigenvalues of a modified spatial covariance matrix of the EEG signals to produce a two-dimensional spectrum whose peaks more robustly estimate the source positions on a horizontal section of the brain. The key approach is to select the eigenvalues that are less affected by the noise and use them to produce the spectrum. To assess the accuracy and robustness of the proposed method, we compared its root-mean-square-error performance at different noise conditions to those of MUSIC and NSF. The proposed method showed the lowest estimation errors for different amounts of brain sources and grid densities.

Keywords

Biomedical engineering • DOA • Eigenvalues
Source estimation

L. F. Cruz (✉) · M. G. Magalhães · J. A. Kunzler
A. A. S. Coelho · R. P. Lemos
School of Electrical, Mechanics and Computer Engineering,
Universidade Federal de Goiás - UFG, Goiânia, Goiás, Brazil
e-mail: fiorini.cruz@gmail.com

M. G. Magalhães
e-mail: mar.cela.gm@hotmail.com

J. A. Kunzler
e-mail: k.jonasaugusto@gmail.com

A. A. S. Coelho
e-mail: andreproj1@gmail.com

R. P. Lemos
e-mail: V.lemos@ufg.br

1 Introduction

The human body produces several biopotentials related to its electrochemical activities, which are an important source of information. Electroencephalography (EEG) was born by the hands of Hans Berger and it is characterized by measurements of those biopotentials on the scalp [1]. For its non-invasive nature, EEG still is a fairly current tool to diagnose several brain disorders, including epilepsy syndromes.

Nearly 1–2% of world population are affected by epilepsy disorder, which is divided in two categories: partial and generalized epilepsy. Partial epilepsy is defined as a seizure that is originated only on a neuron group and shows high drug resistance. There is a surgical indication for those cases, however such indications and the surgical technique to be employed are both related to the location and number of epileptogenic foci (EFs) [2]. Therefore, estimation methods are useful to identify the sources positions which in turn allow classifying signals regarding their frequencies and determining the EFs after the use of beamforming algorithms.

Source position estimation can be accomplished with DOA (Direction of Arrival) techniques. The MUSIC (MUltiple SIgnal Classification) algorithm, a widespread method due to its easy implementation, can be used to brain source estimation [3]. Based on orthogonal subspaces, this algorithm makes a sweep in a search grid, where the orthogonality between a simulated signal subspace and an estimated noise subspace generates peaks in the source positions.

Another largely used DOA method is the NSF (Noise Subspace Fitting) [4], such that we decided to apply it for the first time to the brain source position estimation in this paper due to its versatility. The NSF explores the subspace fitting between an estimated noise subspace and a simulated signal subspace through the inverse of Frobenius norm. A sweep of the simulated signal creates peaks in the source positions, where the Frobenius norm attains its minimum. Under low

spatial resolution, the cited methods are highly affected by low SNRs (Signal-to-Noise Ratio) conditions.

Inspired on the DOA method known as SEAD [5, 6], this paper proposes a new kind of spectrum using a combination of the eigenvalues of the spatial covariance matrix, aiming a higher accuracy and a better noise robustness. This article begins with a brief description of the signal model, followed by an analysis of the eigenvalues' behavior and the proposition of a new estimation approach. To assess the performance of the cited methods we compared their estimation RMSEs (Root Mean Square Error) versus the SNR in different situations. Finally, conclusions and future work are presented.

2 Signal Model

Several models are used for the mathematical representation of neural activities, among them: spherical models, representation by geometric finite elements and boundary element methods [7–9]. We adopted the spherical model which consider the head as a homogeneous conductivity volume σ whose center is at the reference point of the coordinate system [10–12].

Consider M electromagnetic wavefronts impinging on an EEG sensor array with K electrodes. The electrodes are placed at positions $\mathbf{r}_{s,j}$, for $j = 1, \ldots, K$ on the scalp. Each wavefront is produced by a different source located at position $\mathbf{r}_{f,i}$ inside the brain, for $i = 1, \ldots, M$, with M assumed to be known. So, the $K \times 1$ vector of the sensor outputs in time instant n can be represented in the presence of noise by:

$$\mathbf{y}(n) = \mathbf{A}\mathbf{s}(n) + \mathbf{e}(n), \tag{1}$$

where $\mathbf{y}(n) \in \mathbb{R}^{K \times 1}$ is the noisy data vector (*snapshot*), $\mathbf{s}(n)$ is the $M \times 1$ source waveform vector, $\mathbf{e}(n)$ is the additive gaussian noise vector and $\mathbf{A} = [\mathbf{a}(\mathbf{r}_{f,1}), \quad \mathbf{a}(\mathbf{r}_{f,2}), \quad \ldots, \mathbf{a}(\mathbf{r}_{f,M})]$ is a $K \times M$ matrix representing the amplitude relations between sensors. Each column vector $\mathbf{a}(\mathbf{r}_{f,i}), i = 1, \ldots, M$, is given by:

$$\mathbf{a}(\mathbf{r}_{f,i}) = \left[\frac{cos(\theta_{1,i})}{4\pi\sigma|\mathbf{r}_{s,1} - \mathbf{r}_{f,i}|^2} \cdots \frac{cos(\theta_{K,i})}{4\pi\sigma|\mathbf{r}_{s,K} - \mathbf{r}_{f,i}|^2} \right]^T, \tag{2}$$

whose terms are related to the potentials

$$V(\mathbf{r}_{s,j}, \mathbf{r}_{f,i}, p_i) = \frac{p_i cos(\theta_{j,i})}{4\pi\sigma|\mathbf{r}_{s,j} - \mathbf{r}_{f,i}|^2} \tag{3}$$

produced by the i-th source on the j-th sensor. Each brain source is modelled as an infinitesimal dipole to represent brain activity within a limited area [7]. The term p_i stands for the dipole moment and is a part of vector $\mathbf{s}(n)$ in (1); $\theta_{j,i}$ is the angle between $(\mathbf{r}_{s,j} - \mathbf{r}_{f,i})$ and $\mathbf{a}_z$, the unitary vector in vertical direction. Since dipole lengths are close to 0, we assumed their orientation at $\mathbf{a}_z$ [7, 11].

The $K \times K$ spatial covariance matrix of the vector $\mathbf{y}(n)$ can then be written as $\mathbf{R} = E\{\mathbf{y}(n)\mathbf{y}^H(n)\}$ but, in practice $\mathbf{R}$ can be approximated by the sample covariance matrix:

$$\widehat{\mathbf{R}} = \frac{1}{N} \sum_{n=1}^{N} \{\mathbf{y}(n)\mathbf{y}^H(n)\}, \tag{4}$$

where N is the number of snapshots.

3 Proposed Method

Inspired on the Differential Spectrum of eigenvalues introduced in [5, 6], this paper investigates the behavior of the eigenvalues of an augmented spatial covariance matrix $\widetilde{\mathbf{R}}$ to propose a new method for brain source position estimation. To make $\widetilde{\mathbf{R}}$ dependent on a search position $\widehat{\mathbf{r}}_f = (x, y, z)$, we can write it as [5]:

$$\widetilde{\mathbf{R}}(\widehat{\mathbf{r}}_f) = \widehat{\mathbf{R}} + \boldsymbol{\Phi}(\widehat{\mathbf{r}}_f), \tag{5}$$

where $\widehat{\mathbf{R}}$ is the sample covariance matrix and $\boldsymbol{\Phi}(\widehat{\mathbf{r}}_f)$ is $K \times K$ and defined by:

$$\boldsymbol{\Phi}(\widehat{\mathbf{r}}_f) = E\{\mathbf{a}(\widehat{\mathbf{r}}_f)\mathbf{a}(\widehat{\mathbf{r}}_f)^H\}\Psi, \tag{6}$$

where Ψ assumes the value of the average signal power. For uncorrelated sources, the $(M+1)$ largest eigenvalues of $\widetilde{\mathbf{R}}(\widehat{\mathbf{r}}_f)$ and their corresponding eigenvectors span the signal subspace, while the remaining eigenvalues and eigenvectors span the noise subspace. If $\widehat{\mathbf{r}}_f$ is swept along a horizontal section of the brain and coincides with the position of a brain source, then the dimension of the signal subspace is reduced to M. As a consequence, more power is concentrated on the signal subspace and the noise eigenvalues $\tilde{\lambda}_{M+1}(\widehat{\mathbf{r}}_f), \cdots, \tilde{\lambda}_K(\widehat{\mathbf{r}}_f)$ attain their minima [6]. So, we exploit this behavior to introduce a new spectrum defined as:

$$S(\widehat{\mathbf{r}}_f) = \frac{1}{\prod_{i=M+1}^{K} \tilde{\lambda}_i(\widehat{\mathbf{r}}_f)} \tag{7}$$

whose peaks indicate the brain source positions, as shown in Fig. 1, where $S(\widehat{\mathbf{r}}_f)$ is evaluated only along the x-axis alone at a horizontal slice of the brain. According to [7], $|\widehat{\mathbf{r}}_f|$ must be less than 8 cm for a spherical model with a 9.2 cm radius due to the thickness of the skull and the scalp.
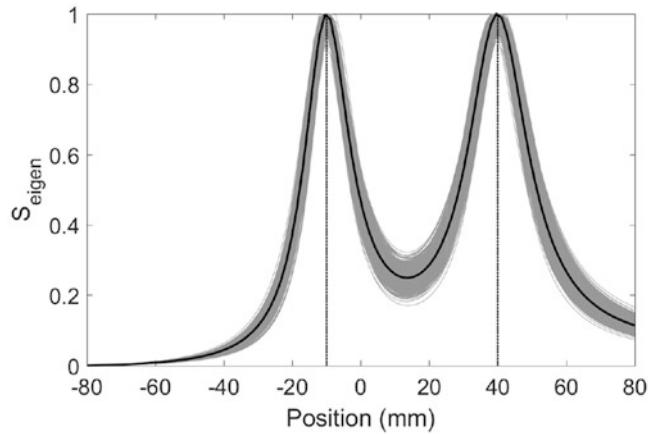
Fig. 1 Superimposition of the spectra $S(\widehat{\mathbf{r}}_f)$ normalized in the interval $[0, 1]$ of 1000 experiments at SNR = 20 dB for brain sources located at $(-10, 0, 0)$ and $(40, 0, 0)$ mm. Gray lines represent the spectra for each experiment, the black line shows the average spectrum and vertical lines indicate the sources positions

4 Results

In order to assess both the estimation performance and robustness of the proposed method against noise, we compared its root mean square estimation error (RMSE) to those of MUSIC and NFS algorithms. We simulated the measurement of EEG signals by $K = 21$ electrodes disposed according to the international measurement system 10/20 and took $N = 200$ samples from each electrode at the sampling frequency of 200 Hz. A thousand experiments were run at each SNR ranging from 10 to 25 dB for different amounts of brain sources placed on a horizontal section of the brain at $z = 0$.

Figure 2 shows the performance of the simultaneous estimation of three sources located at $(-3.4730, -19.6962, 0)$, $(-4.3412, 24.6202, 0)$ and $(57.9555, 15.5291, 0)$ mm.

For a single source, the RMSEs stood between 0.4 and 0.8 mm for the entire SNR range, although the proposed method performed slightly better than the others. For three brain sources, althogh the RMSE increased for all methods, the proposed approach provided a RMSE of approximately 1 mm at SNRs above 20 dB, therefore significantly lower than the RMSEs of MUSIC and NSF that were respectively 11 and 12 mm under the same conditions. We observed that our proposition consistently provided this performance improvement for a larger amount of brain sources when compared to the other methods.

Fig. 2 RMSE performance of MUSIC, NSF and the proposed method for one and three sources
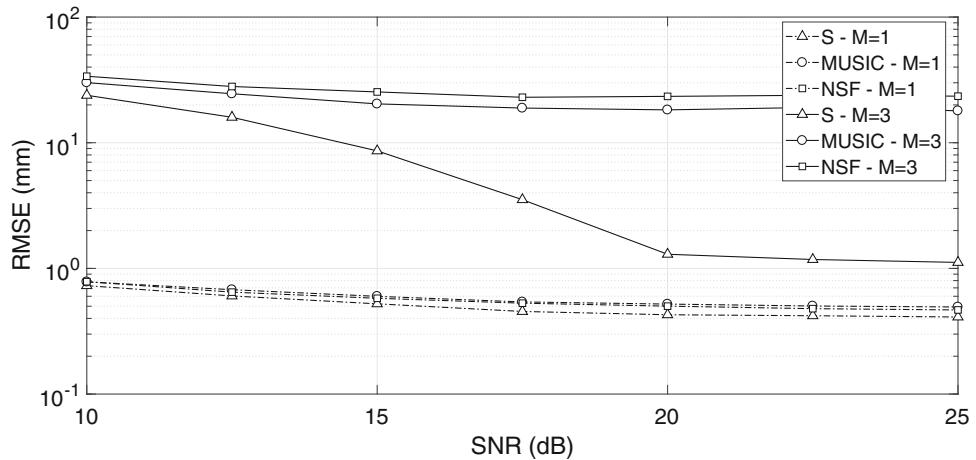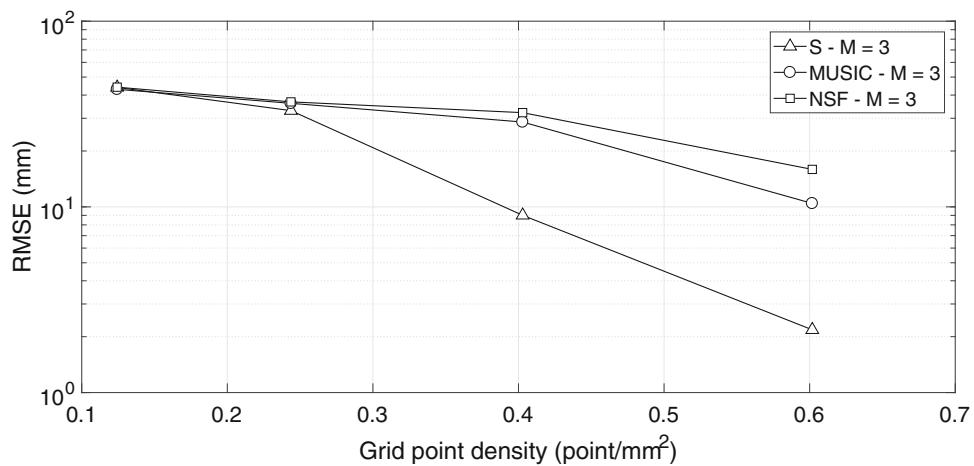
Fig. 3 RMSE versus grid point density for three sources and $SNR = 20$ dB

Another issue is the grid density, as shown in Fig. 3. From the 0.4 to 0.6 points/mm^2, which was the one used in Fig. 2, there was a significant decrease on the RMSE. Thus, the higher the grid density, the better the estimation accuracy.

5 Conclusions

We proposed a new noninvasive method for brain source position estimation using EEG. This algorithm is based on the eigenvalues of the noise subspace of the spatial covariance matrix of the EEG signals acquired on electrodes disposed according to the international measurement system 10/20. The new approach produces a spectrum whose peaks indicate the source positions. Our proposition showed RMS estimation errors significantly lower than those of MUSIC and NSF algorithms for one and three sources, especially in the last case for SNRs above 20 dB. Additionally, we observed that the higher the grid density of the search, the better the estimation accuracy of the proposed method.

Such improvements will further contribute to beamforming performance and source classification, in order to provide a more accurate diagnosis. As a future work, we will employ maximum likelihood procedures to refine the estimates and improve them at high SNR.

References

1. Vaid, S., Singh, P., Kaur, C.: EEG Signal Analysis for BCI Interface: A Review. In: 2015 Fifth International Conference on Advanced Computing Communication Technologies, pp. 143–147 (2015). https://doi.org/10.1109/acct.2015.72.
2. Schuele, S., Lders, H.: Intractable epilepsy: management and therapeutic alternatives. Lancet Neurol (2008).
3. Vergallo, P.; Lay-Ekuakille, A.: Brain source localization: A new method based on multiple signal classification algorithm and spatial sparsity of the field signal for electroencephalogram measurements. AIP Publishing (2013).
4. Krim, H., Viberg, M.: Two decades of array signal processing research: the parametric approach. IEEE Signal Processing Magazine, v. 13, n. 4, pp. 6794 (1996).
5. Ferreira, Y. R., Lemos, R. P.: A new DOA estimation algorithm based on differential spectrum. Proceedings of the Eighth International Symposium on Signal Processing and Its Applications, v. 1, pp. 283286 (2005).
6. Kunzler, J. et al.: Further investigation on frobenius spectrum for DOA estimation. In: 2015 IEEE 6th Latin American Symposium on Circuits Systems (LASCAS). [S.l.: s.n.], pp. 1–4 (2015).
7. Malmivuo, J., Plonsey R.: Bioelectromagnetism. Oxford University Press (1995).
8. Murzin V., Fuchs A., Kelso, J. A. S.: Anatomically constrained minimum variance beamforming applied to EEG. Springer-Verlag (2011).
9. Salu, Y. et al.: An improved method for localizing electric brain dipoles. IEEE Transactions on Biomedical Engineering, v. 37, n. 7, pp. 699–705 (1990).
10. Vergallo P. et al.: Processing EEG signals through beamforming techniques for seizure diagnosis. In: 2012 Sixth International Conference on Sensing Technology (ICST), pp. 497–501 (2012).
11. Vergallo P., Lay-Ekuakille A.: Brain source localization: A new method based on MUltiple SIgnal Classification algorithm and spatial sparsity of the field signal for electroencephalogram measurements. AIP Publishing (2013).
12. Vergallo P. et al.:Spatial filtering to detect brain sources from EEG measurements. In: 2014 IEEE International Symposium on Medical Measurements and Applications (MeMeA). pp 1–5 (2014).

Discrimination Between Day and Night ECG Recordings Based on the Morphology of *P* and *T* Waves

Dimitrios Zavantis, Ermioni Mastora, Prokopis Kontogiannis, and George Manis

Abstract

This paper investigates the possibility to discriminate day-night periods based exclusively on morphological characteristics extracted from *P* and *T* waves. Daytime values were determined between 13:00 and 15:00 and nighttime values between 1:00 and 3:00. Initially, *P* and *T* waves were selected manually and afterwards in an automatic way, employing a new algorithm. After delimiting the position of *P* and *T* waves, thirty four features, most of which employed for the first time for this purpose, were extracted using geometrical measures. All these features were examined for both waves. The results revealed a very clear discrimination for the majority of the features, leading to the conclusion that *P* and *T* wave morphology is very different during day and night, whilst the correlation coefficient indicated an association and not an arbitrary alteration. Despite the fact that the selected features were rich descriptors, machine learning techniques were also employed to confirm the discrimination capability.

Keywords

P wave • *T* wave • Classification • Day and night

1 Introduction

There is a growing body of literature which focuses on ECG and especially on *P* and *T* waves due to the clinically useful information that they provide. Many researchers studied these waves for certain time periods of day and night or for the whole 24 hour recording. Neyroud et al. [7] concluded that there are differences between day and night in the behavior of ventricular re-polarization. Braga et al. [3] and

Ramirez et al. [8] studied QT/RR differences between day and night for both genders. Many of them [2, 6] reported differences in RR intervals and Heart Rate Variability (HRV). Dilaveris et al. [4] presented the diurnal pattern of *P* wave duration, *P* area, and *PR* interval.

The objective of this paper is to show that the discrimination between day and night periods is possible even when we are based exclusively on the morphology of *P* or *T* waves. A large number of innovative features have been calculated accompanied with the more conventional ones which have been used widely before [1, 10]. The major advantage for some of the newly examined features is the independence between the metric and the detection accuracy of waves boundaries. Hence, these features have been proved good descriptors in capturing day-night differences in ECG waveform.

2 Materials and Methods

2.1 Wave Detection

In this study the MIT-BIH Normal Sinus Rhythm Database was used. The Normal Sinus Rhythm is the characteristic rhythm of the healthy human heart. The dataset includes 18 long-term (24-hour) ECG recordings with no significant arrhythmia. They include 5 men, aged 26–45, and 13 women, aged 20–50. Each data file contains two channels of ECG signal. The digitization was done using 12 bit analog-to-digital converter with sampling frequency 128 Hz and the data is available at uniform intervals of 7.8125 ms [5].

We used two approaches in order to identify and select the *P* and the *T* waves: a manual and an automatic detection. Getting coherent result from two complementary methods reinforces reliability and ensures independence from potential limitations of each method. Manual detection can ensure that typical waves have been selected in an accurate way. Totally, 2700 *P* and 2700 *T* waves were selected between

D. Zavantis · E. Mastora · P. Kontogiannis · G. Manis (✉)
Department of Computer Science & Engineering,
University of Ioannina, Ioannina, Greece
e-mail: manis@cs.uoi.gr

times 1:00 and 3:00 in the night and the same number of P and T waves between times 13:00 and 15:00 in the afternoon in order to study the discrimination in diametrically opposed day and night time intervals. An auxiliary visual inspection tool was implemented to assist the fast and accurate selection. Automatic detection can provide a very large number of waveforms. The large number of waves reinforces the statistical significance of the results. In the automatic method, the pAD detection algorithm was used [9]. With this method we selected approximately 100,000 P and 100,000 T waves from the examined periods.

2.2 Feature Extraction

All extracted features are selected to describe the morphology of the waveforms and can be grouped into five categories: distances, areas, secondary areas, slopes and ratios. Totally, 34 features were considered and examined.

For simplicity, the set *wave* was defined as:

$$wave = \{f(x_i) : x_i \in \mathscr{D}\}, i = 1, \ldots, n$$
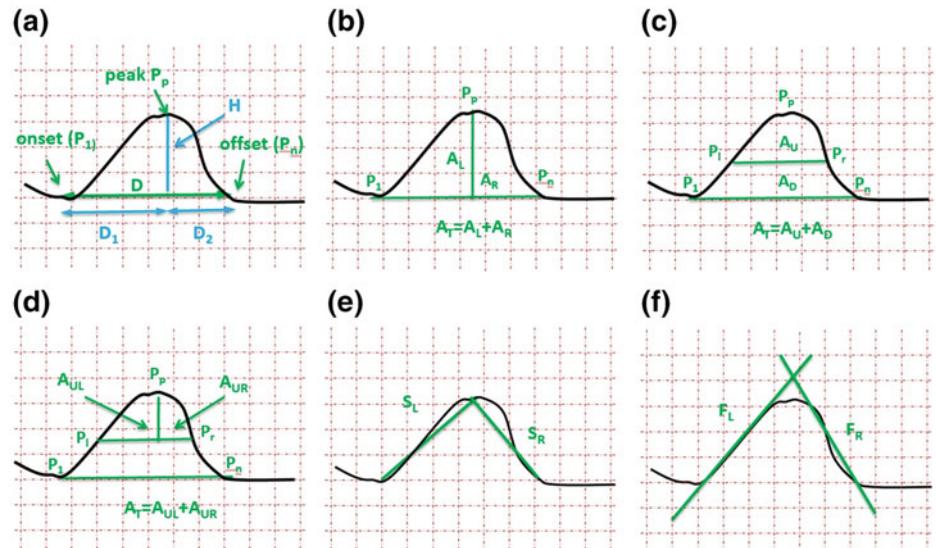
where $P_i = (x_i, f(x_i))$ corresponds to ith point and $\mathscr{D} = [onset\,point, offset\,point]$. Each feature category is described analytically below:

Distances:

Amplitude or Height (H): The Amplitude or Height is the distance between the line segment $P_1 P_n$, defined by the onset P_1 and the offset P_n, and the peak point P_p (Fig. 1a):

$$H = max(f(x_i)) - f(x_1).$$

Duration (D): *Duration* is the difference between the abscissa x_1 of the onset point P_1 and the abscissa x_n of the offset point P_n (Fig. 1a):

$$D = x_n - x_1.$$

Onset Duration (D_1): Onset Duration is the difference between the abscissa x_p of the peak point P_p and the abscissa x_1 of the onset point P_1 (Fig. 1a):

$$D_1 = x_p - x_1.$$

Offset Duration (D_2): Offset Duration is the difference between the abscissa x_n of the offset point P_n and the abscissa x_p of the peak point P_p (Fig. 1a):

$$D_2 = x_n - x_p.$$

Areas:

Total Area (A_T): Total Area is defined as the area under the curve starting from the onset point P_1 and ending to the offset point P_n (Fig. 1b):

$$A_T = \sum_{i=1}^{n-1} \int_{x_i}^{x_{i+1}} (\alpha(x - x_i) + f(x_i)) dx,$$

where the amount in the integral is the line between two consecutive points P_i and P_{i+1} and α the slope of this line:

$$\alpha = \frac{f(x_{i+1}) - f(x_i)}{x_{i+1} - x_i}.$$

Left Area (A_L): Left Area is defined as the area under the curve between the onset P_1 and the peak P_p (Fig. 1b):

Fig. 1 Features based on distances, areas and slopes

$$A_L = \sum_{i=1}^{p-1} \int_{x_i}^{x_{i+1}} (\alpha(x - x_i) + f(x_i)) dx.$$

Right Area (A_R): Right Area is defined as the area under the curve between the peak P_p and the offset P_n (Fig. 1b):

$$A_R = \sum_{i=p}^{n-1} \int_{x_i}^{x_{i+1}} (\alpha(x - x_i) + f(x_i)) dx.$$

Secondary areas:

Upper Area (A_U): Upper Area is defined as the area under the curve between the points P_l and P_r and the line segment $P_l P_r$ (Fig. 1c):

$$A_U = \sum_{i=l}^{r} \int_{x_i}^{x_{i+1}} (\alpha(x - x_i) + f(x_i)) dx - (f(x_r) - f(x_n))(x_r - x_l),$$

where x_l and x_r the abscissas of P_l and P_r, respectively.

Lower Area (A_D): Down or Lower Area is defined as the area under the curve between the onset P_1 and the point P_l, under the line segment $P_l P_r$ and under the curve between P_r and the offset point P_n (Fig. 1c):

$$A_D = A_1 + A_2 + A_3, \quad \text{where:}$$
$$A_1 = \sum_{i=1}^{l-1} \int_{x_i}^{x_{i+1}} (\alpha(x - x_i) + f(x_i)) dx, A_2 = (f(x_r) - f(x_n))(x_r - x_l),$$
$$A_3 = \sum_{i=r}^{n-1} \int_{x_i}^{x_{i+1}} (\alpha(x - x_i) + f(x_i)) dx.$$

Upper Left Area (A_{UL}): Upper Left Area is defined as the area under the curve between the point P_l and the peak point P_p and above the line segment $P_l P_r$ (Fig. 1d):

$$A_{UL} = \sum_{i=l}^{p-1} \int_{x_i}^{x_{i+1}} (\alpha(x - x_i) + f(x_i)) dx - (f(x_l) - f(x_n))(x_p - x_l).$$

Upper Right Area (A_{UR}): Upper Right Area is defined as the area under the curve between the peak point P_p and the point P_r and above the line segment $P_l P_r$ (Fig. 1d):

$$A_{UR} = \sum_{i=p}^{r-1} \int_{x_i}^{x_{i+1}} (\alpha(x - x_i) + f(x_i)) dx - (f(x_l) - f(x_n))(x_r - x_p).$$

Slopes:

Onset Slope (S_L): Onset or Left Slope is defined as the slope of the line segment connecting the onset point P_1 and the peak point P_p (Fig. 1e):

$$S_L = \frac{f(x_p) - f(x_1)}{x_p - x_1}.$$

Offset Slope (S_R): Offset or Right Slope is defined as the slope of the line segment connecting the peak point P_p and the offset point P_n (Fig. 1e):

$$S_R = \frac{f(x_n) - f(x_p)}{x_n - x_p}.$$

Fitting Onset Slope (F_L): Fitting Onset or Left Slope is defined as the slope of the straight line fitting the points $P_i, i = 1, \ldots, p$ (Fig. 1f). This line minimizes the sum of squared residuals of the linear regression model $min_{\alpha, \beta} Q(\alpha, \beta)$ for:

$$Q(\alpha, \beta) = \sum_{i=1}^{n} \hat{\varepsilon}_i^2 = \sum_{i=1}^{n} (f(x_i) - \beta - \alpha x_i)^2,$$

where β is the y-intercept and α is the slope F_L.

Fitting Offset Slope (F_R): Fitting Offset or Right Slope is defined as the slope of the straight line fitting the points $P_i, i = p, \ldots, n$ (Fig. 1f).

Ratios:

The rest of the features are computed by ratios of the above features (see Table 1). The ratios show the relationship between features, something that usually hides extra information.

2.3 Feature Selection

A paired t-test was applied to our data and proved that there is a statistically significant difference between day and night features ($p < 0.0001$), revealing that the extracted features are good descriptors and able to capture differences between the two examined time periods.

In general, the usage of a large number of features is computationally expensive and also may lead to suboptimal results. Therefore, the correlation coefficient (r) has been employed to decide the most important features, which will be used later for the classification process. We computed the correlation coefficient for all examined features between day and night periods and selected those with $r > 0.3$ for P waves and $r > 0.7$ for T waves. The coefficients for all features (extracted with the automated method) are presented in Table 1.

3 Results

In our experiments, four classification methods were used for the automatic discrimination of day and night periods: Naive-Bayes (*NB*), Decision Tree (*DT*), K-Nearest Neighbor

Table 1 Correlation coefficient for T and P waves

Feature	P wave	T wave	Feature	P wave	T wave	Feature	P wave	T wave
H	0.4140	0.7895	S_L	0.2762	0.7286	A_U/A_T	0.2474	0.3920
D	0.2449	0.2572	S_R	0.3803	0.7431	A_D/A_T	0.2508	0.4043
D_1	0.1576	0.2305	F_L	0.2652	0.6957	A_U/A_D	0.0036	0.2890
D_2	0.3509	0.2272	F_R	0.3783	0.7495	A_{UL}/A_L	0.2423	0.3144
A_T	0.4253	0.8408	D/H	0.3167	0.8285	A_{UR}/A_R	0.2328	0.3700
A_L	0.4249	0.8252	D_1/D_2	0.1102	0.1897	A_{UL}/A_{UR}	0.3567	0.0607
A_R	0.3946	0.8321	D_1/D	0.1189	0.1756	A_{UL}/A_U	0.3424	0.0721
A_U	0.2011	0.5384	D_2/D	0.1189	0.1756	A_{UR}/A_U	0.1313	0.0728
A_D	0.4064	0.8630	A_L/A_T	0.3777	0.2793	A_{UL}/A_T	0.1615	0.3426
A_{UL}	0.2048	0.5265	A_R/A_T	0.3762	0.2767	A_{UR}/A_T	0.3102	0.3453
A_{UR}	0.2437	0.5058	A_L/A_R	0.3944	0.3343	S_L/S_R	0.2023	0.2476
						F_L/F_R	0.1714	0.3510

Table 2 Mean success rate without feature selection

	P wave		T wave	
	C_M	C_A	C_M	C_A
NB	0.87	0.86	0.94	0.90
DT	0.87	0.82	0.94	0.91
KNN	0.88	0.91	0.95	0.93
SVM	0.82	0.90	0.95	0.90

Table 3 Mean success rate with feature selection

	P wave		T wave	
	C_M	C_A	C_M	C_A
NB	0.86	0.85	0.95	0.90
DT	0.87	0.88	0.95	0.92
KNN	0.88	0.90	0.95	0.93
SVM	0.89	0.91	0.96	0.93

(KNN), and Support Vector Machines (SVM). A 10-fold cross validation was applied twice, the first time using all the features and the second time using the selected ones. The results are shown in Tables 2 and 3.

Comparing the performance of the four classifiers, it can be noticed that in the case of P waves SVM presents a poorer classification performance for manual selection (C_M), while NB and DT seem to achieve a poorer classification in automatic detection (C_A). However, all mean success rates are very high. In T waves all classifiers, both in manual and automatic detection, present impressively high accuracy levels, higher than 90%. Table 3 outlines the performance of each classifier using only the selected features as input.

4 Conclusions

Morphological features of both P and T waves have been employed to prove the discrimination between day and night ECG recordings. The hypothesis of discrimination has been extensively studied in terms of statistics and classification. In order to ensure decoupling of conclusions from possible limitations of the detecting method, both manual and automatic detection was used. Finally, all experimental results reveal a clear discrimination with high mean success classification rates, close or above 90% for both P and T waves.

Conflicts of Interest The authors declare that they have no conflict of interest.

References

1. Arsenos, P., Manis, G.: The variability of the T-wave shape can discriminate young and elderly subjects. In: 10th IEEE International Conference on Information Technology and Applications in Biomedicine (ITAB), pp. 1–3 (2010)
2. Boudreau, P., Dumont, G., Kin, N., Walker, C.D., Boivin, D.B.: Correlation of heart rate variability and circadian markers in humans. In: Engineering in Medicine and Biology Society, EMBC, 2011 Annual International Conference of the IEEE, pp. 681–682 (2011)
3. Braga, F., Caiani, E., Locati, E., Cerutti, S.: Automated QT/RR analysis based on selective beat averaging applied to electrocardiographic holter 24 h. In: Computers in Cardiology, pp. 9–12 (2004)
4. Dilaveris, P.E., Färbom, P., Batchvarov, V., Ghuran, A., Malik, M.: Circadian behavior of P-wave duration, P-wave area, and PR

interval in healthy subjects. Annals of Noninvasive Electrocardiology **6**(2), 92–97 (2001)

5. Goldberger, A.L., Amaral, L.A., Glass, L., Hausdorff, J.M., Ivanov, P.C., Mark, R.G., Mietus, J.E., Moody, G.B., Peng, C. K., Stanley, H.E.: Physiobank, physiotoolkit, and physionet components of a new research resource for complex physiologic signals. Circulation **101**(23), e215–e220 (2000)

6. Massin, M.M., Maeyns, K., Withofs, N., Ravet, F., Gérard, P.: Circadian rhythm of heart rate and heart rate variability. Archives of Disease in Childhood **83**(2), 179–182 (2000)

7. Neyroud, N., Maison-Blanche, P., Denjoy, I., Chevret, S., Donger, C., Dausse, E., Fayn, J., Badilini, F., Menhabi, N., Schwartz, K., et al.: Diagnostic performance of QT interval variables from 24 h

electrocardiography in the long QT syndrome. European Heart Journal **19**(1), 158–165 (1998)

8. Ramrez, J., Cygankiewicz, I., Laguna, P., Malik, M., Pueyo, E.: Circadian pattern and sex differences of QT/RR and T-peak-to-end/RR curvatures and slopes in chronic heart failure patients. In: Computing in Cardiology Conference, pp. 173–176 (2014)

9. Zavantis, D., Mastora, E., Manis, G.: Robust automatic detection of P wave and T wave in electrocardiogram. In: Proc. of Computing in Cardiology (2017)

10. Zeraatkar, E., Kermani, S., Mehridehnavi, A., Aminzadeh, A., Zeraatkar, E., Sanei, H.: Arrhythmia detection based on morphological and time-frequency features of T-wave in electrocardiogram. Journal of Medical Signals and Sensors **1**(2), 99 (2011)

Automated Neurons Recognition and Sorting for Diamond Based Microelectrode Arrays Recording: A Feasibility Study

Ondřej Klempíř, Radim Krupička, Vladimíra Petráková, Jan Krůšek, Ivan Dittert, and Andrew Taylor

Abstract

Microelectrode arrays (MEA) are extensively used for recording and stimulating neural activity in vitro and in vivo. Depositing nanostructured boron doped diamond (BDD) onto the neuroelectrodes makes it possible to obtain dual mode low-noise neuroelectrical and neurochemical information simultaneously. The signal processing procedure requires finding and distinguishing individual neurons spikes in the recordings. Spike identification is usually done manually which is inaccurate and inappropriate for complex datasets. In this paper, we present a methodology and two algorithms for neurons recognition and evaluation based on unsupervised learning. Forty-five extracellular randomly selected signals from 26 unique measurements of embryonic hippocampal rat neurons (20 kHz, 6 min) were recorded on the commercial 60 TiN channels MEA. The signals were filtered in the 300–3000 Hz band and an amplitude detector (4x std of the background noise) was used for spike detection. WaveClus features were computed and its 3 PCA components were extracted for every spike. The optimal number of clusters were evaluated by an expert rater. K-means + gap criterion (alg. 1) and the Gaussian Mixture Model + Bayesian Information Criterion (alg. 2) were implemented and compared. The total IntraClass Correlation showed a significant inter-rater agreement for all 3 rater procedures (ICC = 0.69, $p < 0.001$), when post hoc weighted Cohen's Kappas for 2 raters were 0.85 (expert vs. alg. 1; $p < 0.001$) and 0.62 (expert vs. alg. 2; $p < 0.001$). This will contribute to the objective definition of dual mode BDD MEA performance criteria and for a comparison with the current system.

1 Introduction

Several approaches can be used to study individual neuronal cell activity. One of them is to record action potentials on the surface of the nerve cell membrane. Normally, needle electrodes would be used to monitor the electrical activity of a neuron, but it is less demanding and less invasive to apply an electrode array and measure the potentials between individual electrodes.

Microelectrode arrays (MEA) biosensors are extensively used for recording and stimulating neural activity in vitro and in vivo. They serve as a valuable tool for neurotoxicology screening of various neuroactive compounds and in pharmacological studies [1–4]. Depositing nanostructured boron doped diamond (BDD) onto the neuroelectrodes makes it possible to obtain dual mode low-noise neuroelectrical and neurochemical information simultaneously [5].

To be able to evaluate BDD MEA performance (sensitivity, specificity), we will define a methodology and two algorithms for neuron recognition based on unsupervised learning. To the best of our knowledge, this study excels in the originality of the studied data and the overall number of records that are being evaluated.

The MEA signal processing procedure requires finding and distinguishing individual neuron spikes in the recordings. The specific number of visible neurons around the microelectrode is from a practical point of view only putative, estimated based on action potential characteristics (accurate positioning and

O. Klempíř (✉) · R. Krupička · V. Petráková
Faculty of Biomedical Engineering, Czech Technical University,
Nám. Sítná 3105, 27201 Kladno, Czech Republic
e-mail: klempond@fbmi.cvut.cz

J. Krůšek · I. Dittert
Institute of Physiology CAS, Vídeňská 1083, 14220 Prague,
Czech Republic

A. Taylor
Institute of Physics CAS, Na Slovance 2, 18221 Prague,
Czech Republic
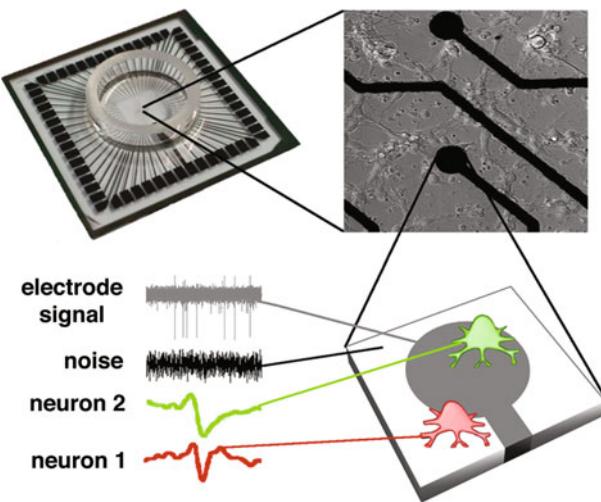
Fig. 1 MEA signals contain spikes generated by different neurons. Scheme reprinted from [7], with quoting

neural growth measuring is possible via optical methods). Valuable information can be obtained by clustering spikes according their features. Spike sorting follows a sequence of several steps which enables the extraction of action potentials (spikes) from raw data, ideally divided into groups (clusters) according to their neuron of origin (see Fig. 1) [6, 7]. For example, Rossant et al. reported a novel complex approach, especially suitable for large dense MEA, for detecting overlapping spikes in more than one electrode [8]. However, spike identification is usually done manually which is inaccurate and inappropriate for complex datasets.

2 Materials and Methods

2.1 Data Acquisition and Storing

Forty-five randomly selected extracellular signals from 26 unique measurements of an embryonic hippocampal rat neurons (daily recording, 6 min) were recorded on a commercial 60 titanium nitride (TiN) channels MEA (USB-ME64-System by Multi Channel Systems MCS GmbH). The electrodes are aligned in an 8×8 grid. Measured data was recorded using MC_Rack in a compressed.mcd format. One file contains 60 records from individual measuring electrodes. Raw signals in the MEA.mcd file format is loaded or converted (to csv or plain text) by developed batches of MATLAB scripts. All data files are stored on a shared e-infrastructure repository. One file takes about 700 MB of memory.

Typically, signal sources are within a radius of 30 μm around the electrode center. The peak amplitude values of spikes are in the range of tens to hundreds of microvolts. The

total duration of one spike is about 1.6 ms, which corresponds to the dominant frequency of 625 Hz. Data was recorded at a sampling frequency of 20 kHz.

However, since the signal is recorded extracellularly, directly from a cultivation medium, there is a significant amount of background noise, arising from three main sources: biological noise (mainly other cells in the electrode vicinity), electrode-electrolyte noise (liquid-metal interface) and device noise (especially the amplifier) [9].

2.2 Neurons Recognition and Sorting Procedures

Signals were band-pass filtered (Butterworth 2nd) in the 300–3000 Hz band (BPF). Since the detection tradeoff is related to the signal to noise ratio of the recording, an amplitude detector was used for spike detection. The value of the threshold (automatic or adaptive) is typically given by a multiplication of the standard deviation of the signal noise by a factor from 3–5 [10]. The number of samples corresponding to the minimum refractory period was considered as 36 (i.e. 1.8 ms). The threshold for extracellular detection was automatically set to (1) [11].

$$Thr = -4\sigma_n \quad \sigma_n = median\left\{\frac{|filtered\ signal|}{0.6745}\right\} \quad (1)$$

Each detected spike was modulated by a cubic spline curve and 64 equidistant shape-based features were computed with the WaveClus MATLAB toolbox [12]. The three largest Principle Component Analysis (PCA) components from total, previously computed, 64 shape-based features were extracted for every spike and mainly 2D PCA were used in successive steps. Unsupervised cluster analyses K-means + gap criterion (alg. 1) and the Gaussian Mixture Model (GMM) + Bayesian Information Criterion (BIC) (alg. 2) for an automatic estimation of the number of clusters in reduced 2D PCA spikes data were investigated (see Fig. 2) and statistically compared. All three principal components served solely for exploratory data analysis in a 3D space and detailed expertise rating.

In the case of the proposed alg. 1, we used the K-means algorithm with Euclidean distance from MATLAB, in combination with gap criterion (GC), which is not restricted to a certain type of metric distances. The GC is defined even for clustering solutions that contain only one cluster. The GC utilizes estimating the most dramatic decrease in error measurement during several proposed numbers of clusters with the largest gap value. The formula and implementation details can be found in [13].
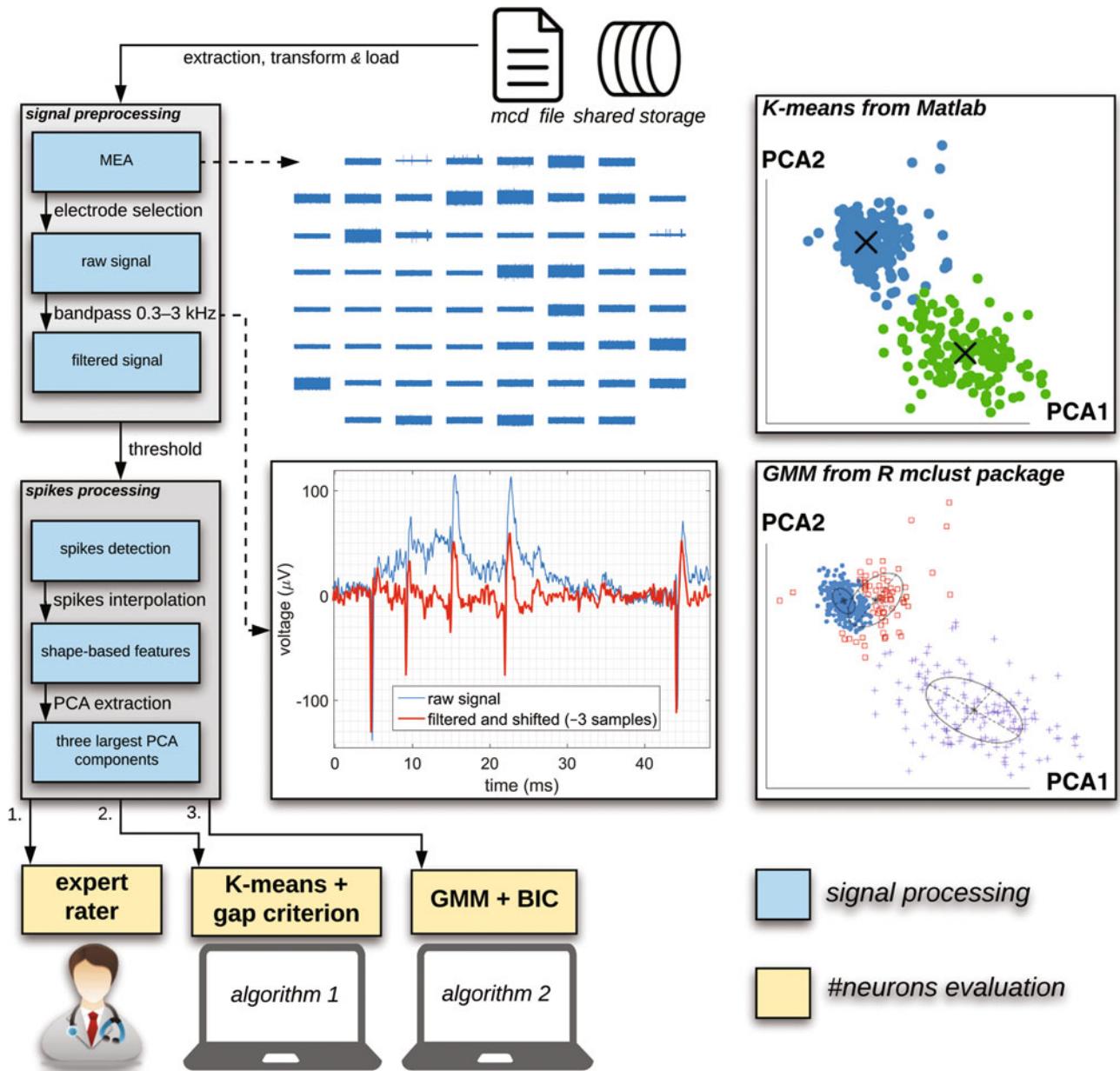
Fig. 2 The methodology of the designed spike sorting processing experiment. The pipeline schematically lists all the steps for working with the MEA signals. The bandpass filter is used to remove the slow shift, which can significantly influence spike detection. The graphs on the right side indicate that the GMM estimated different numbers of neurons compared to the K-means on the same example 2D PCA data

Neuron recognition with the proposed alg. 2 was performed in R Shiny's NeuroEDA web application for Bio-Data assesment [14]. The mclust R package provides models and methods to estimate the number of clusters in the multivariate dataset. The algorithm uses 10 models to calculate the default from 1 to 10 GMM components (clusters) and choose the minimal value of BIC to select the final number of clusters. BIC uses the optimal loglikelihood function value and penalizes for more complex models, i.e., models with additional parameters. The penalty of BIC is a function of the sample size (2).

$$BIC = -2(\log L) + numParam * \log(numObs) \quad (2)$$

2.3 Inter-rater Statistical Evaluation

As the real number of neurons in the vicinity of each microelectrode is not known during data analysis, we can only consider the similarity among the scores.

The optimal number of clusters (neurons) were then further evaluated by an expert rater. Inter-rater reliability

Tab. 1 Coefficients of inter-rater reliability and agreement

Single score intraclass correlation	Squared Cohen's Kappa (expert vs. alg. 1)	Squared Cohen's Kappa (expert vs. alg. 2)
Subjects = 45 Raters = 3 ICC = 0.69	Subjects = 45 Raters = 2 ICC Kappa = 0.85	Subjects = 45 Raters = 2 ICC Kappa = 0.62
F-Test H0: r0 = 0; H1: r0 > 0 F(44,49.1) = 9.02, p-val = 1.5e−12 **95%-CI:** 0.53 < ICC < 0.81	Absolute agreement = 32/45 z = 5.85 p-val = 5.07e−09	Absolute agreement = 27/45 z = 4.64 p-val = 3.55e−06

analysis of the detected neuron numbers was conducted. Additionally, F-test and confidence interval were computed. Statistical analyses were performed using R Statistical Software and irr library [15]. P-values of 0.05 or lower were considered statistically significant.

3 Results

The results are shown in Table 1. The total Intra Class Correlation showed a significant inter-rater agreement for all 3 rater procedures (ICC = 0.69, p < 0.001), when post hoc weighted Cohen's Kappas for 2 raters were ICC = 0.85 (expert vs. alg. 1; p < 0.001; relative agreement = 0.71) and ICC = 0.62 (expert vs. alg. 2; p < 0.001; relative agreement = 0.6). The largest 3 PCA components could explain the 80.2% (±13.6 (std)) variability of unreduced data.

A final fully automated procedure for MEA recordings based on alg. 1 has been proposed and developed using the three largest PCA components (Fig. 3) for offline processing in MATLAB R2015a (Mathworks, USA).

4 Discussion

Evaluation of the recorded data remains a major challenge due to the large amount of generated data and the presence of complex patterns in the behavior of neural cells. Neuroscientists have argued that a generally functioning spike sorting approach is not yet feasible, but the design of this study may be the next step towards this goal.

There were many general observations. Alg. 2 often estimated more neurons in 2D PCA space than both the expert rater and alg. 1, preferring Gaussian shapes. An expert could also (under)overestimate and should not be considered as an etalon. Generally, overall consistency is

important. Despite the small range of potential neuron counts estimated by individual approaches (alg. 1 vs. alg. 2 vs. expert), we used a quadratic weighting criterion to include penalties for consistency evaluation (Cohen's Kappa for 2 Raters with squared weights). Relative and absolute exact matches are also given. We did not consider any outliers. The analyses presented herein were based on all available data. The outliers detection may yield more accurate results in the future.

In a relevant publication, Novak et al. suggests a precise methodology for estimating the number of neurons in extracellular recording based on GMM with more parameters than in our study [16]. But in our case, we show a comparison of GMM + BIC with K-means + GC.

The device used for neurochemical detection is important for the research and treatment of neurological diseases. For example, preparing the first functional BDD electrodes with suitable mechanical and electrical properties and biocompatibility for deep brain stimulation/monitoring of Parkinson's (PD) and dystonia. Monitoring of neurochemical activity (neurotransmitters or metabolites) can bring new insights in describing dopaminergic neurons, e.g. in Substantia nigra in PD [17].

5 Conclusions

In this paper, we proposed two unsupervised spike sorting algorithms. Both algorithms can detect the optimal number of clusters (neurons) in neural recording. The results of our analysis confirm the possibility of using our sorting approach for BDD MEA evaluation. A substantial agreement of algorithms and expertise in detecting the number of neurons has been achieved. Beyond this work, the functionality of the procedure was successfully tested on pilot BDD MEA data and on real microelectrode signals from
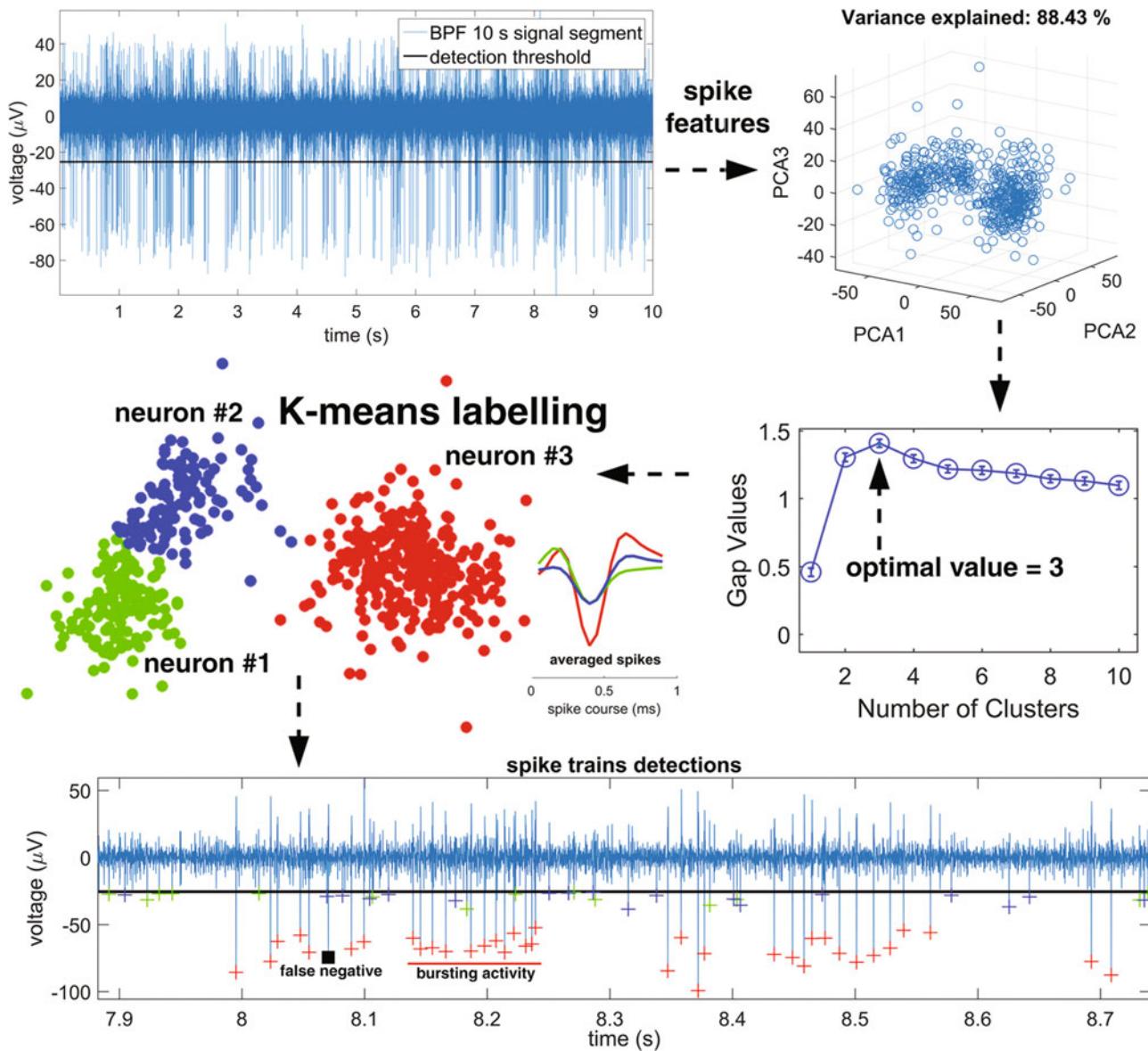
Fig. 3 An example of the fully automated procedure based on alg. 1 applied to a 10 s signal segment. Implementation was provided in Matlab. Objectivization of processing MEA data led to finding 3 neurons. As a result, bursting activity is evident. The black square refers to a false negative detection due to the refractory period

human basal ganglia. This will contribute to the objective definition of the dual mode BDD MEA performance index and for comparison with the current system.

Conflict of Interest The authors declare that they have no conflict of interest.

References

1. Johnstone, A.F., Gross, G.W., Weiss, D.G., Schroeder, O.H., Gramowski, A., Shafer, T.J.: Microelectrode arrays: a physiologically based neurotoxicity testing platform for the 21st century. Neurotoxicology 31(4), 331–350 (2010).
2. Vassallo, A., Chiappalone, M., Lopes, R.D.C., Scelfo, B., Novellino, A., Defran-chi, E., Johnstone, A.F.: A multi-laboratory evaluation of microelectrode array-based measurements of neural network activity for acute neurotoxicity testing. Neurotoxicology 60, 280–292 (2017).

3. Colombi, I., Mahajani, S., Frega, M., Gasparini, L., Chiappalone, M.: Effects of antiepileptic drugs on hippocampal neurons coupled to micro-electrode arrays. Front Neuroeng 6(10), 1–11 (2013).

4. Jones, I.L., Livi, P., Lewandowska, M.K., Fiscella, M., Roscic, B., Hierlemann, A.: The potential of microelectrode arrays and microelectronics for biomedical research and diagnostics. Anal Bioanal Chem 399(7), 2313–2329 (2011).

5. Alcaide, M., Taylor, A., Fjorback, M., Zachar, V., Pennisi, C.P.: Boron-doped nanocrystalline diamond electrodes for neural interfaces: in vivo biocompatibility evaluation. Front Neurosci 10(87), 1–9 (2016).

6. Lewicki, M.S.: A Review of Methods for Spike Sorting: The Detection and Classification of Neural Action Potentials. Comput Neural Syst 6, 53–78 (1998).

7. Bestel, R., Daus, A.W., Thielemann, Ch.: A novel automated spike sorting algorithm with adaptable feature extraction. Journal of Neuroscience Methods 211(1), 168–178 (2012).

8. Rossant, C., Kadir, S.N., Goodman, D.F.M, Schulman, J., Hunter, M.L.D., Saleem, A.B., Grosmark, A., Belluscio, M., Denfield, G. H., Ecker, A.S., Tolias, A.S., Solomon, S., Buzsaki, G., Carandini, M., Harris, K.D.: Spike sorting for large, dense electrode arrays. Nat Neurosci 19(4), 634–641 (2016).

9. Obien, M., Deligkaris, K., Bullmann, T., Bakkum, D., Frey, U.: Revealing neuronal function through microelectrode array recordings. Front Neurosci 8, 423 (2015).

10. Rey, H.G., Pedreira, C., Quiroga, R.Q.: Past, present and future of spike sorting techniques. Brain research bulletin 119, 106–117 (2015).

11. Spike sorting, http://www.scholarpedia.org/article/Spike_sorting, last accessed 2018/1/14.

12. WaveClus spike detection and sorting, https://github.com/csn-le/wave_clus, last accessed 2018/1/14.

13. Tibshirani, R., Walther, G., Hastie, T.: Estimating the number of clusters in a data set via the gap statistic. Journal of the Royal Statistical Society: Series B 63(2), 411–423 (2001).

14. Klempíř, O., Shala, L., Tesař, J., Krupička, R.: NeuroEDA – an interactive web tool for neuroinformatics data analysis and teaching biomedical statistics. MEFANET Journal 5(2), 62–68 (2017).

15. R package irr, https://cran.r-project.org/web/packages/irr/irr.pdf, last accessed 2018/1/14.

16. Novak, D., Wild, J., Sieger, T., Jech, R.: Identifying number of neurons in extracellular recording. In: Proceedings of the 4th International IEEE EMBS Conference on Neural Engineering, pp. 742–745. IEEE, Antalya, Turkey (2009).

17. Bennet, K.E., Tomshine, J.R., Min, H., Manciu, F.S., Marsh M.P., Paek, S.B., Settell, M.L., Nicolai, E.N., Blaha, C.D., Kouzani, A. Z., Chang, S., Lee, K.H.: A Diamond-Based Electrode for Detection of Neurochemicals in the Human Brain. Front Hum Neurosci, 1–12 (2016).

Ultra-Short Entropy for Mental Stress Detection

Rossana Castaldo, Luis Montesinos, and Leandro Pecchia

Abstract

Approximate Entropy (*ApEn*) and Sample Entropy (*SampEn*) are measures of signals' complexity and are widely used in Heart Rate Variability (HRV) analysis. In particular, recent studies proved that almost all the features measuring complexity of RR series statistically decreased during the stress and therefore, thus showing ability to detect stress. However, the choice of the similarity threshold r and minimum data length N required for their computation are still controversial. In fact, most entropy measures are considered not reliable for recordings shorter than 5 min and different threshold values r have shown to affect the analysis thus leading to incorrect conclusions. Therefore, the aim of this study was to understand the impact of changing parameters r and N for the computation of *ApEn* and *SampEn* and to select the optimal parameters to detect stress in healthy subjects. To accomplish it, 84 RR series, extracted from electrocardiography signals acquired during real-life stress, were analyzed. *ApEn* and *SampEn* were estimated for two different values of r computed using previously published methods and for N = {100, 200, 300, 400, 500} data points. The statistical significance for the differences in mean *ApEn* and *SampEn* values was assessed by non-parametric tests. The two methods used to compute r produced entropy values significantly different over different N values. In contrast, *ApEn* and *SampEn* showed consistency in differentiating rest and stress conditions for different input parameters. More specifically, ApEn$_{Chon}$ and *SampEn*$_{Chon}$ showed to have a better discrimination power between stressed subjects and resting subjects on ultra-short recordings ($N < 500$).

1 Introduction

Heart rate variability (HRV), the variation of the time interval between consecutive heartbeats (i.e. R-to-R intervals), is a consequence of the dynamical and complex regulation of the heart rate. Since the overall cardiac response to external stimuli and the related state of the autonomic nervous system can be investigated noninvasively by HRV, a large number of indices to characterize the latter have been developed [1]. In particular, entropy measures have shown great potential for physiological time-series analysis [2]. Hence, they have been widely used to quantify HRV [3], with the hypothesis that decreasing entropy values reveal perturbations of the underlying physiological mechanisms or disease. Moreover, recent studies have proved that almost all measures of complexity of RR series statistically decreased during stress, therefore were deemed able to detect it [3].

Generally speaking, Approximate Entropy (*ApEn*) and Sample Entropy (*SampEn*) measure the probability that vectors of length m built from a time-series of length N that are similar within a tolerance range given by $\pm r$ times the standard deviation of the time-series, remain similar for vector of length $m + 1$. Hence, for any fixed m, their computation requires the selection of parameters N (data length) and r (similarity threshold). The use of $m = 2$ has been previously suggested [2, 4]. As for N, values normally range between 100 and 5000, whereas for r values usually range between 0.1 and 0.25 [2, 4]. However, there are still open questions about the minimal data length (N) and the optimal

R. Castaldo (✉) · L. Montesinos · L. Pecchia
School of Engineering, University of Warwick, Coventry, CV4 7AL, UK
e-mail: r.castaldo@warwick.ac.uk

L. Montesinos
e-mail: l.montesinos-silva@warwick.ac.uk

L. Pecchia
e-mail: l.pecchia@warwick.ac.uk

L. Montesinos
Tecnologico de Monterrey, Campus Ciudad de Mexico, 14380 Mexico City, Mexico

threshold value r required to compute *ApEn* and *SampEn* measures. In fact, some studies have shown that *ApEn* values for recordings shorter than 3 min are considered unreliable [7, 8]. Additionally, some studies have shown that the selection of r, the similarity threshold, is critical in human HRV studies [5, 6]. In this regard, a study recommended that the threshold value r is the one that provides the maximum *ApEn* value [5], whereas another study recommended to compute r using a formula proposed by its authors [9].

Therefore, this study aimed to understand the impact of changing parameters N and r for the computation of *ApEn* and *SampEn* and to select the best parameters to detect stress in healthy subjects based on ultra-short recordings ($N < 500$).

2 Methods and Materials

2.1 Data Description

Eighty four stationary RR series extracted from electrocardiographic recordings acquired during real-life stress were analyzed. The dataset consisted of 42 students with an age range from 18 to 25 years old. The data were acquired using a commercial electrocardiograph (Easy ECG Pocket. ATES MEDICA Device s.r.l., Verona, Italy), which allows 3-lead clinical research ECG acquisitions, with a sampling frequency of 500 Hz and a resolution of 12 bits. The data were acquired on two different conditions: rest and stress. The stress session was recorded during a university verbal examination. The participants were examined under standard conditions during rest and stress phases: in the same quiet room, at a comfortable temperature, while sitting. From each record, subsequent RR time series of 5-min length were extracted. A detailed description of the protocol can be found in [3].

2.2 Algorithms for *ApEn* and *SampEn* Computation

A detailed description of the algorithms for the computation of *ApEn* and *SampEn* can be found elsewhere [3]. Briefly, given a RR time series of length N, such as RR_1, RR_2, …, RR_N, a sequence of vectors of length m: X_1, X_2, …, X_{N-m+1} is constructed as follows: $X_i = [RR_i, RR_{i+1}, …, RR_{i+m-1}]$. The distance $d[X_i, X_j]$ between vectors X_i and X_j is defined as the maximum absolute difference between their respective scalar components. For each vector X_i, the number of vectors X_j for which $d[X_i, X_j] < r$ is computed as

$$C_i^m(r) = \frac{number\ of\ \{d[X_i, X_j] \le r\}}{N - m + 1} \quad \forall j \quad (1)$$

Then, the index $\Phi^m(r)$ is computed by taking the natural logarithm of each $C_i^m(r)$ and averaging them over i.

$$\Phi^m(r) = \frac{1}{N - m + 1} \sum_{i=1}^{N-m+1} \ln C_i^m(r) \quad (2)$$

Finally, the approximate entropy is computed as:

$$ApEn(m, r, N) = \Phi^m(r) - \Phi^{m+1}(r) \quad (3)$$

In this study, we computed the *ApEn* for N = {100, 200, 300, 400, 500} samples, m = 2 and two different values of the threshold r:

- r = r_{Max}, that is, the value of r in the interval (0.01 * SDNN, 1.0 * SDNN) which maximizes the *ApEn*;
- r = r_{Chon} that is the value computed according to the formula proposed by Chon et al. [9]:

$$r_{Chon} = (-0.036 + 0.26\sqrt{SDDS/SDNN})/\sqrt[4]{N/1000} \quad (4)$$

where SDDS and SDNN are the short-term and long-term variability of the RR sequence, respectively. Formally, SDDS is the standard deviation of the difference sequence of the series RR, that is, $[RR_{i+1} - RR_i, RR_{i+2} - RR_{i+1}, …, RR_N - RR_{N-1}]$, and; SDNN is the standard deviation of the RR series.

To compute *SampEn*, $C_i^m(r)$ is computed as reported in Eq. 5, $\Phi^m(r)$ as reported in Eq. 2 and finally *SampEn* as in Eq. 6.

$$C_i^m(r) = \frac{number\ of\ \{d[X_i, X_j] \le r\}}{N - m + 1} \quad \forall j \neq i \quad (5)$$

$$SampEn(m, r, N) = \log \frac{\Phi^m(r)}{\Phi^{m+1}(r)} \quad (6)$$

Note that *ApEn* and *SampEn* differ in that the latter does not take into account vector self-matches. Additionally, the dependence on the parameter r is different: *SampEn* decreases when increases. On the other hand, it has been shown that *SampEn* and *ApEn* often provide comparable results for large values of N and r [10].

2.3 Statistical Analysis

Since a previous study showed that *ApEn* and *SampEn* did not follow normal distribution [11], the following descriptive statistics were computed: median (MD), standard deviation (SD), and the 25th and 75th percentiles. The statistical significance of the differences in median values estimated

using the two methods to compute r for N = {100, 200, 300, 400, 500} were assessed by a non-parametric statistical test (namely, the Wilcoxon signed rank test). Moreover, Spearman's correlation coefficients (rho) and their associated p-values (p_{rho}) were computed between the estimates of *ApEn* and *SampEn* varying N and r for rest and stress. The differences between *ApEn* and *SampEn* values for different N and r were also investigated to assess whether *Apen* and *SampEn* calculated for different N and r could discriminate between rest and stress conditions.

In-house Matlab scripts were used to compute *ApEn* and *SampEn* and perform the statistical analysis.

3 Results

Tables 1 and 2 show summary statistics for *ApEn* computed for N = {100, 200, 300, 400, 500} and r = {r_{Chon}, r_{Max}} during rest and stress, respectively. Moreover, Tables 1 and 2 also report the p-values calculated using Wilcoxon signed rank and the Spearman's correlation coefficient (rho). Statistically significant differences (p < 0.001) were observed between the $ApEn_{Max}$ and $ApEn_{Chon}$, as shown in Tables 1 and 2 for rest and stress respectively. These results were supported by rho values below 0.7, which demonstrate

a very low correlation. Moreover, Fig. 1 shows the median and standard deviation for $ApEn_{Max}$ and $ApEn_{Chon}$ during rest and stress, over different N values with m = 2.

The same analysis was run also for *SampEn*. Tables 3 and 4 show summary statistics for *SampEn* evaluated for N = {100, 200, 300, 400, 500} and r = {r_{Chon}, r_{Max}} during rest and stress, respectively. Moreover, Tables 3 and 4 also report the p-values calculated using Wilcoxon signed rank and the Spearman's correlation coefficient (rho). Statistically significant differences (p < 0.001) were observed between the $SampEn_{Max}$ and $SampEn_{Chon}$, as shown in Tables 1 and 2 for rest and stress respectively. However, rho showed to be above 0.7 highlighting a correlation between $SampEn_{Max}$ and $SampEn_{Chon}$ over different N values.

Figure 2 shows the median and standard deviation of $SampEn_{Max}$ and $SampEn_{Chon}$ during rest and stress over different N values with m = 2.

Table 5 presents the p-values for differences in $ApEn_{Chon}$, $ApEn_{Max}$, $SampEn_{Chon}$ and $SampEn_{Max}$ values between rest and stress conditions for different lengths N. $ApEn_{Chon}$ showed ability to discriminate between rest and stress for N = {200, 300, 400}. $ApEn_{Max}$ could not discriminate between rest and stress conditions for N < 500. $SampEn_{Chon}$ and $SampEn_{Max}$ showed discriminative power between rest and stress conditions for all data lengths analyzed in this study.

Table 1 *ApEn* during rest computed for N = {100, 200, 300, 400, 500} and r = {r_{Chon}, r_{Max}}

N	r_{Chon}				r_{Max}				r_{Chon} versus r_{Max}	
	MD	SD	25th	75th	MD	SD	25th	75th	*p*-value	rho
100	0.350	0.901	0.001	0.278	0.323	0.088	0.260	0.381	<0.001	0.232[*]
200	0.820	1.341	0.003	1.161	0.538	0.098	0.477	0.599	<0.001	0.070[*]
300	1.301	1.692	0.042	2.411	0.730	0.091	0.685	0.790	<0.001	−0.108[*]
400	1.821	1.953	0.212	2.642	0.897	0.101	0.831	0.931	<0.001	−0.283[*]
500	1.896	1.954	0.219	2.662	0.896	0.101	0.836	0.931	<0.001	−0.283[*]

[*]p_{rho} < 0.05

Table 2 *ApEn* during stress computed for N = {100, 200, 300, 400, 500} and r = {r_{Chon}, r_{Max}}

N	r_{Chon}				r_{Max}				r_{Chon} versus r_{Max}	
	MD	SD	25th	75th	MD	SD	25th	75th	*p*-value	rho
100	0.021	0.131	0.000	0.002	0.398	0.142	0.322	0.496	<0.001	−0.075[*]
200	0.305	0.912	0.012	0.06	0.609	0.124	0.510	0.691	<0.001	0.195[*]
300	0.523	1.070	0.044	0.376	0.772	0.123	0.671	0.854	<0.001	0.151[*]
400	0.716	1.532	0.021	0.766	0.853	0.125	0.759	0.920	<0.001	−0.019[*]
500	0.895	1.586	0.21	1.041	0.954	0.101	0.905	1.016	<0.001	0.027[*]

[*]p_{rho} < 0.05

Fig. 1 $ApEn_{Max}$ and $ApEn_{Chon}$ for N = {100, 200, 300, 400, 500} with m = 2. Error bars represent the standard deviation
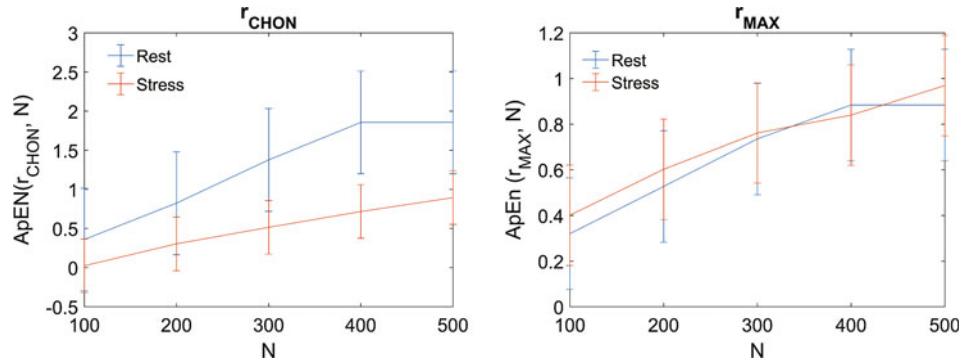
Table 3 *SampEn* during rest computed for N = {100, 200, 300, 400, 500} and r = {r_{Chon}, r_{Max}}

N	r_{Chon}				r_{Max}				r_{Chon} versus r_{Max}	
	MD	SD	25th	75th	MD	SD	25th	75th	*p*-value	rho
100	1.130	0.203	1.005	1.250	2.134	0.398	1.788	2.319	<0.001	0.716*
200	1.290	0.166	1.169	1.394	2.120	0.361	1.907	2.386	<0.001	0.861*
300	1.403	0.156	1.321	1.497	2.082	0.266	1.859	2.284	<0.001	0.621*
400	1.447	0.142	1.319	1.542	2.075	0.281	1.847	2.294	<0.001	0.704*
500	1.457	0.148	1.329	1.543	2.073	0.283	1.848	2.294	<0.001	0.704*
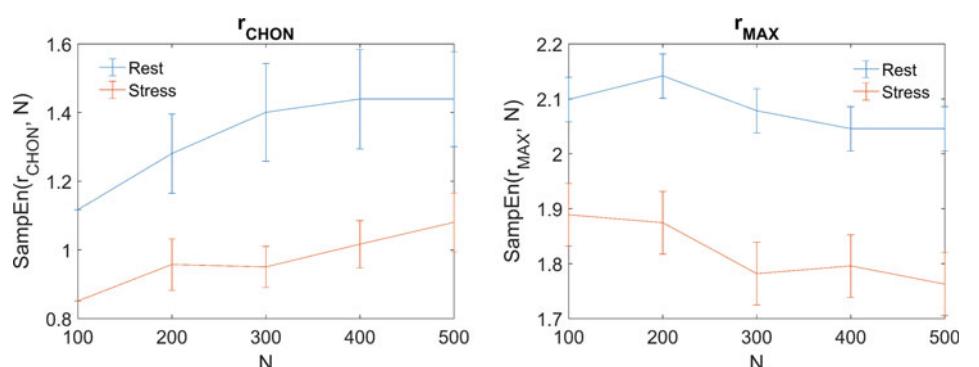
*p_{rho} < 0.05

Table 4 *SampEn* during stress computed for N = {100, 200, 300, 400, 500} and r = {r_{Chon}, r_{Max}}

N	r_{Chon}				r_{Max}				r_{Chon} versus r_{Max}	
	MD	SD	25th	75th	MD	SD	25th	75th	*p*-value	rho
100	0.845	0.292	0.668	1.059	1.876	0.503	1.557	2.174	<0.001	0.490*
200	0.962	0.327	0.683	1.171	1.898	0.425	1.595	2.247	<0.001	0.702*
300	0.946	0.301	0.746	1.148	1.777	0.469	1.477	2.131	<0.001	0.806*
400	1.028	0.308	0.833	1.236	1.785	0.466	1.490	2.073	<0.001	0.769*
500	1.068	0.343	0.852	1.347	1.692	0.503	1.385	2.180	<0.001	0.854*

*p_{rho} < 0.05

Fig. 2 *SampEn*$_{MAX}$ and *SampEn*$_{Chon}$ over different N values with m = 2. Error bars represent the standard deviation

4   Discussion and Conclusion

In this paper, we reported the methods and results of an analysis performed on 84 RR series to assess the appropriateness of using two different values of the parameter r,

namely r_{Chon} and r_{max}, for the computation of *ApEn* and *SampEn* on ultra-short HRV time series. $ApEn_{Chon}$ was significantly different from the $ApEn_{Max}$ over different N for both rest and stress conditions. These findings were consistent with those of previous studies on smaller time series (N = 120) [6, 11] and larger time series (N = 500) [12]. On

Table 5 Wilcoxon signed rank test between Rest and Stress for $ApEn_{Chon}$, $ApEn_{Max}$, $SampEn_{Chon}$ and $SampEn_{Max}$

N	$ApEn_{Chon}$	$ApEn_{Max}$	$SampEn_{Chon}$	$SampEn_{Max}$
	p-value	p-value	p-value	p-value
100	0.001	0.120	<0.001	0.031
200	<0.001	0.180	<0.001	0.004
300	<0.001	0.254	<0.001	0.002
400	<0.001	0.088	<0.001	0.006
500	0.002	<0.001	<0.001	0.004

the other hand, $SampEn_{Chon}$ was significantly different from but highly correlated to $SampEn_{Max}$ over different N for both rest and stress conditions. These results make evident that entropy values computed using different r parameter values should be carefully compared.

Additionally, the $ApEn_{Chon}$ and $SampEn_{Chon}$ appeared to be able to discriminate better than $ApEn_{Max}$ $SampEn_{Max}$ between rest and stress in ultra-short recordings (N < 500). Consequently, this may lead to the conclusion that the $ApEn_{Chon}$ and $SampEn_{Chon}$ have a good discrimination power in distinguishing stressed subjects from resting subjects.

References

1. Force, T., Heart rate variability guidelines: Standards of measurement, physiological interpretation, and clinical use. European Heart Journal, 1996. 17: p. 354–381.
2. Pincus, S., Approximate entropy as a measure of system complexity. Proc Natl Acad Sci USA, 1991. 88: p. 2297–2301.
3. Melillo, P., M. Bracale, and L. Pecchia, Nonlinear Heart Rate Variability features for real-life stress detection. Case study: students under stress due to university examination. BioMedical Engineering OnLine, 2011. 10(1): p. 1–13.
4. Pincus, S. and A. Goldberger, Physiological time-series analysis: what does regularity quantify? Am J Physiol, 1994. 266: p. H1643–H1656.
5. Lu, S., et al., Automatic selection of the threshold value r for approximate entropy. IEEE Transactions on Biomedical Engineering, 2008. 55(8): p. 1966–1972.
6. Castiglioni, P. and M. Di Rienzo. How the threshold "r" influences approximate entropy analysis of heart-rate variability. in Computers in Cardiology, 2008. 2008.
7. Salahuddin, L., et al., Ultra short term analysis of heart rate variability for monitoring mental stress in mobile settings. Conf Proc IEEE Eng Med Biol Soc, 2007. 2007: p. 4656–9.
8. Yentes, J.M., et al., The appropriate use of approximate entropy and sample entropy with short data sets. Annals of biomedical engineering, 2013. 41(2): p. 349–365.
9. Chon, K.H., C.G. Scully, and S. Lu, Approximate Entropy for all Signals Is the Recommended Threshold Value r Appropriate? Ieee Engineering in Medicine and Biology Magazine, 2009. 28(6): p. 18–23.
10. Rajendra Acharya, U., et al., Heart rate variability: a review. Med Biol Eng Comput, 2006. 44(12): p. 1031–51.
11. Liu, C.Y., et al., Comparison of different threshold values r for approximate entropy: application to investigate the heart rate variability between heart failure and healthy control groups. Physiological Measurement, 2011. 32(2): p. 167–180.
12. Melillo, P., et al. Approximate Entropy for Short-Term Heart Rate Variability Analysis: Is the Threshold Value Computed by Chon's Formula Appropriate? in The International Conference on Health Informatics. 2014. Springer.

Assessment of In-ear Photoplethysmography as a Surrogate for Electrocardiography in Heart Rate Variability Analysis

Timo Tigges, Thomas Büchler, Alexandru Pielmuş, Michael Klum, Aarne Feldheiser, Oliver Hunsicker, and Reinhold Orglmeister

Abstract

Heart rate variability (HRV) analysis is a valuable tool in the investigation of cardiovascular regulation by the autonomic nervous system. Generally, beat-to-beat interval time series, which are necessary for calculating quantitative HRV parameters, are extracted from electrocardiographic (ECG) recordings. However, in situations like home monitoring, acute medical care or the perioperative setting, the recording of ECG signals is inconvenient. Here, in-ear photoplethysmography (PPG) is a promising alternative technology for the acquisition of beat-to-beat intervals. In this work, the accuracy of HRV parameters derived from in-ear PPG recordings is compared to ECG-derived parameters in order to the accuracy of the in-ear PPG as a surrogate for ECG in HRV analysis. For this purpose, recordings of 28 volunteers were collected. Common HRV features from both the time and frequency domain have been calculated from the in-ear PPG signal and a reference ECG signal. For comparison, HRV parameters were also derived from the common fingertip PPG. It could be shown that the in-ear PPG is a viable alternative measurement modality for continuous HRV monitoring when ECG recording is not applicable. Nevertheless, care has to be taken in the selection of HRV parameters that are calculated from the in-ear PPG.

T. Tigges (✉) · T. Büchler · A. Pielmuş · M. Klum · R. Orglmeister
Chair for Electronics and Medical Signal Processing, Technische Universität Berlin, Berlin, Germany
e-mail: timo.tigges@tu-berlin.de
URL: http://www.emsp.tu-berlin.de

A. Feldheiser · O. Hunsicker
Department of Anaesthesiology and Intensive Care Medicine, Campus Virchow-Klinikum, Charité University Medicine Berlin, Berlin, Germany

1 Introduction

Heart rate variability (HRV) analysis is a valuable tool in the investigation of cardiovascular regulation by the autonomic nervous system. Generally, beat-to-beat interval time series, which are necessary for calculating quantitative HRV parameters, are extracted from electrocardiographic (ECG) recordings. However, in situations like home monitoring, acute medical care or the perioperative setting, the recording of ECG signals is inconvenient. Here, in-ear photoplethysmography (PPG) is a promising alternative technology for the acquisition of beat-to-beat intervals.

Recent research has already shown that HRV parameters can be derived from fingertip PPG signals with sufficient accuracy under various conditions [5]. In this work, the accuracy of HRV parameters derived from in-ear PPG recordings is compared to ECG-derived parameters in order to the accuracy of the in-ear PPG as a surrogate for ECG in HRV analysis. Furthermore, a comparison of HRV parameters from PPG recordings measured at the index finger to ECG-derived features is also conducted. The analysis is carried out based on data from healthy subjects at rest.
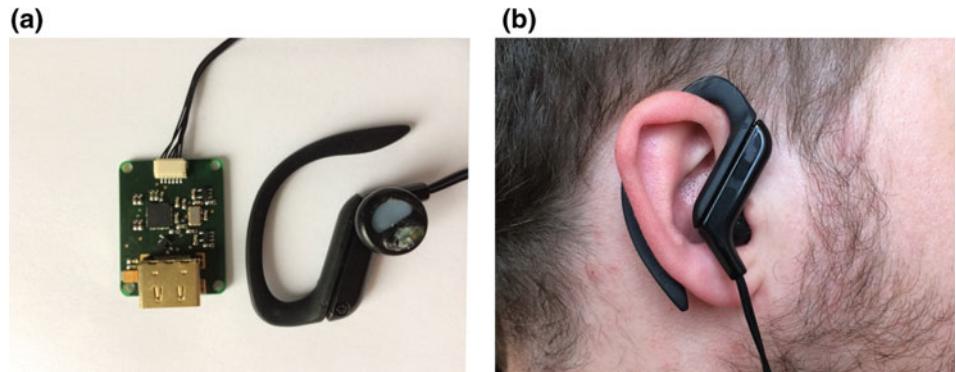
2 Materials and Methods

2.1 Collected Data

The dataset that this study is based on consists of recordings from 28 healthy participants (19 male, 9 female) having a mean age of 26.2 ± 4.3 years and a mean body mass index of 23.8 ± 3.5 kg/m^2. From each participant, we recorded an ECG signal (Einthoven lead II) as well as PPG signals from the right index finger and from within the ear canal of the right ear for a total duration of 4 min. During this period, the volunteers remained seated and at rest. This study was approved by the local ethics committee and written informed consent was obtained from all participants. One recording

Fig. 1 In-ear PPG Sensor. **a** In-ear PPG earpiece with optical sensor element (left) and analog front-end PCB (right). **b** In-ear PPG earpiece attached to the head

was excluded from the analysis due to insufficient signal quality of the in-ear PPG signal, supposedly caused by incorrect sensor placement.

All signals were collected with a multi-channel signal acquisition system that is based on the *rBSN* [3] wireless body sensor network platform. The novel in-ear PPG sensor front-end is described in more detail in the next section (Sect. 2.2). The sampling rate of the ECG signal was set to 500 Hz, whereas the PPG signals were digitized at a rate of 250 Hz. Prior to any further calculations, the PPG signals were upsampled to the sampling rate of the ECG signal. The ECG signal was filtered by an 4th-order infinite impulse response (IIR) comb filter with 2 Hz wide notches at multiples of 50 Hz in order to remove powerline interference from the signal. It was refrained from applying a lowpass filter to preserve the exact R-peak locations in the ECG signal. Both PPG signals were preprocessed by an 8th-order Butterworth bandpass filter having cut-off frequencies at 0.5 and 18 Hz for the purpose of baseline removal and suppression of high frequent noise while ideally preserving the PPG pulse waveforms. All signal processing and data analysis was performed using MATLAB R2017b®.

2.2 In-ear Photoplethysmography Sensor Front-End

The measurement of the in-ear PPG signals was conducted with a novel in-ear PPG sensor front-end [6]. The front-end exclusively consists of off-the-shelf components and is mainly composed of two parts, specifically a miniaturized optical sensor that can be introduced into the ear canal and an analog front-end that performs analog signal conditioning, analog-to-digital conversion and communication with a microcontroller via an SPI interface.

The optical sensor is based on the OSRAM SFH 7051, an integrated sensor element that combines three green LEDs (530 nm) with a matching photodiode. For easy application and robust positioning, we integrated the sensor element, which measures only 4.7 mm × 2.5 mm × 0.9 mm, into a modified headphone earpiece (see Fig. 1). The sensor is oriented radially so that the light is coupled directly into the tissue of the inside of the tragus.
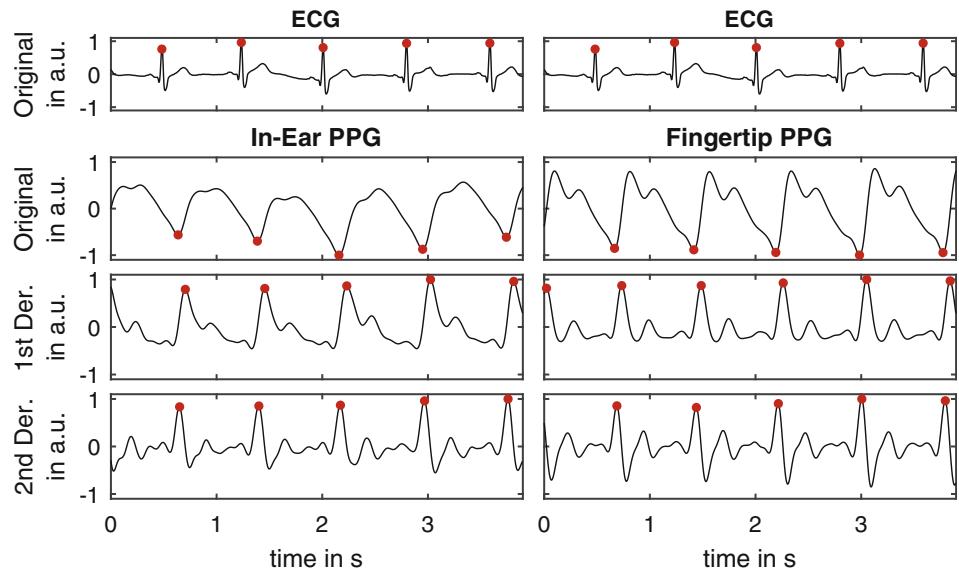
The optical sensor element is connected to the Texas Instruments AFE4490 integrated analog front-end. The AFE4490 incorporates a LED driver and a configurable receive channel that performs analog signal conditioning prior to a 22-Bit analog-to-digital conversion. After digitization, the sample values are transferred to a microcontroller that stores all data on a microSD flash memory card.

The fingertip PPG was recorded with the same setup except for the optical configuration. Here, the finger PPG was recorded in transmission mode by placing a red led (645 nm) and a matching photodiode on opposing sites into a standard PPG fingerclip case.

2.3 Tachogram Calculation

In order to calculate HRV parameters, it is necessary to extract beat-to-beat interval time series, so-called tachograms from the raw signals. This is achieved by calculating the time intervals between consecutive fiducial points in the assessed signals. In Fig. 2, fiducial_points_example, a short excerpt from one recording is presented that shows the examined fiducial points and their corresponding beat-to-beat intervals in the three signals. In the ECG signal, the time between the maximum points of two consecutive R-peaks was used to calculate the corresponding heart rate. It remains an open question which fiducial points from the

Fiducial points in the ECG (top row), the in-ear PPG (left column) and the fingertip PPG (right column) signals. Both columns show the same signal interval. All signals are shown in arbitrary units (a.u.)

PPG are most advisable for beat-to-beat heart rate derivation. Therefore, in this study, the following set of fiducial points of PPG pulses were analysed with respect to their impact on HRV parameters: the pulse onset (i.e. the local minimum), the local maximum of the pulse's first and second derivative.

Subsequent to the initial tachogram calculations, a careful elimination of intervals which are affected by artefacts was performed. For this purpose, a 25 s sliding window was incrementally shifted over the tachograms in steps of 5 s, where all intervals that differed by more than 20% from the mean inside the window were excluded. This measure was repeated until no more outliers were identified.

2.4   Calculation of HRV Parameters

The calculation of HRV parameters was performed in windows with a length of 180 s. In order to cover the complete 5 min recordings, this window was incrementally shifted over the recordings in steps of 3 s. For each time step, eight common HRV features [2] were individually calculated for the different fiducial points in the assessed signals.

From the time domain, the mean heart rate (Mean), the standard deviation of normal-to-normal (NN) intervals (SDNN), the standard deviation of differences between adjacent NN intervals (SDSD), and the ratio of beat interval pairs differing more than 50 ms (pNN50) were calculated.

The frequency domain features calculated were the normalized spectral energies in the very low frequency (VLF) band ranging from 0.003 to 0.04 Hz, the low frequency (LF) band ranging from 0.04 Hz, and the high frequency (HF) band ranging from 0.15 to 0.4 Hz. The Lomb-Scargle method was used for spectral estimation [1].

2.5   Methods of Evaluation

In this study, the accuracy of in-ear PPG as a surrogate for ECG in HRV analysis is evaluated. Therefore, the heartbeat intervals extracted from the in-ear PPG signal are compared to those derived from the ECG. Furthermore, for reasons of comparison, the heartbeat intervals from the common fingertip PPG are also assessed.
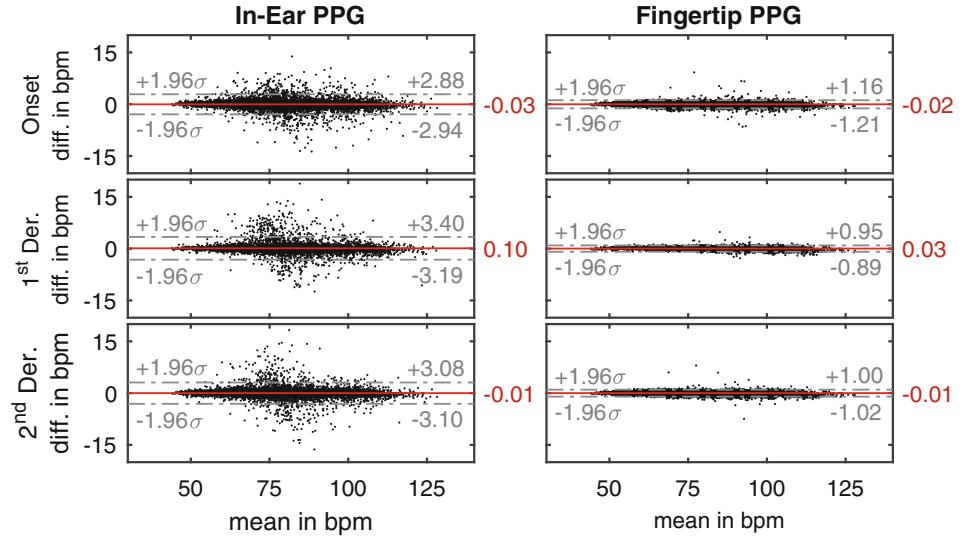
A Bland-Altman analysis was conducted to evaluate the beat-to-beat agreement between the PPG signals and the ECG signal. In order to analyze the accuracy of the derived HRV parameters, these were derived for all fiducial points from both PPG signals. The ECG-derived parameters were taken as reference. Then, the Spearman's rank correlation r_s was calculated as a measure of their monotonic relation. Furthermore, the normalized root-mean-square error $RMSE$ was calculated to evaluate their relative accuracy. Here, the mean parameter value from the ECG reference was taken as normalizing factor.

3   Results and Discussion

3.1   Bland-Altman Analysis of Beat-to-Beat Heart Rates

The results of the Bland-Altman analysis are presented in Fig. 3. Here, heartbeat intervals of all participants are converted to heart rates, given in beats per minutes (bpm), by taking their reciprocal values for the sake of a more convenient interpretation. For the in-ear PPG, the best agreement to the reference is found for the onset as fiducial point for time interval calculations. Here, the mean difference is

Fig. 3 Bland-Altman plots showing the agreement of beat-to-beat heart rates from the in-ear PPG (left column) and the fingertip PPG (right column) with the ECG reference for three ficuial points (onset, 1st derivative, 2nd derivative). All values are given in beats per minute (bpm)

−0.03 bpm and the 95% confidence interval is confined to −2.94 and 2.88 bpm. In comparison, the best beat-to-beat agreement of the fingertip PPG was found for the 1st derivative fiducial point, resulting in a mean difference of 0.03 bpm with limits of agreement at −0.89 and 0.95 bpm. In general, the accuracy of the beat-to-beat heart rates from the in-ear PPG is lower than for the fingertip PPG. This can be attributed to the sensor configuration in reflectance mode, which is more susceptible to movement artifacts, and the generally less pronounced systolic slope in the in-ear PPG pulse waveform resulting in a more diffuse fiducial point localization (cf. Fig. 2).

3.2 Evaluation of HRV Parameters

In Table 1, the mean and standard deviation of the Spearman rank correlation coefficient between the HRV parameters derived from the in-ear PPG and the ECG is presented. Again, results of the fingertip PPG are also given. There generally exists a strong monotonic relation between the

in-ear PPG and the ECG in most of the evaluated HRV parameters. An exception is presented by the time domain features SDSD and pNN50, which quantify high frequent oscillations in the tachograms. This is in agreement with our findings from the beat-to-beat evaluation in the previous section and is likely described by the more inaccurate beat localization in the in-ear PPG signal compared to the ECG R-peak. Furthermore, these findings match the results of a previously reported analysis of the index finger PPG as a source for HRV parameters [4]. Expectedly, the fingertip PPG shows a stronger monotonic relation to the PPG than the in-ear PPG.

From Table 2, one can see that the HRV features Mean, SDNN, and LF show a good agreement with the ECG reference for both PPG measurement sites. Those features quantify rather low-frequent oscillations and are therefore less affected by the lower pulse location accuracy in the PPG signals. In contrast, the features SDSD, HF and HF/LF show a much higher estimation error, which is a result of over-estimating heart rate fluctuations due to the depicted inaccuracies.

Table 1 Mean and standard deviation of Spearman's Rank Correlation r_s (given in %) between PPG-derived HRV features and features derived from ECG beat-to-beat heart rate time series

	In-ear PPG			Fingertip PPG		
	Onset	1st Der.	2nd Der.	Onset	1st Der.	2nd Der.
Mean	97.5 ± 8.8	97.2 ± 8.0	97.7 ± 8.1	99.3 ± 1.0	99.2 ± 1.0	99.3 ± 0.8
SDNN	87.6 ± 18.9	84.2 ± 24.7	87.4 ± 18.0	96.7 ± 5.5	95.4 ± 9.8	97.3 ± 4.8
SDSD	61.4 ± 47.8	70.7 ± 44.3	63.3 ± 50.6	94.0 ± 7.5	95.7 ± 4.4	95.8 ± 4.1
pNN50	61.2 ± 41.9	71.1 ± 39.4	50.9 ± 55.7	81.4 ± 29.6	75.0 ± 34.5	80.0 ± 32.0
HF	88.7 ± 13.8	87.0 ± 18.1	85.8 ± 19.7	96.2 ± 7.2	95.7 ± 7.2	96.1 ± 7.4
LF	92.2 ± 11.7	88.9 ± 15.5	90.8 ± 13.4	97.6 ± 3.7	97.4 ± 3.4	97.7 ± 3.0
HF	84.1 ± 21.7	87.4 ± 14.7	79.2 ± 39.7	93.1 ± 8.9	91.4 ± 13.1	92.6 ± 9.4
LF/HF	85.5 ± 17.4	81.5 ± 25.6	81.7 ± 21.9	94.5 ± 7.9	93.9 ± 7.6	94.5 ± 7.2

Table 2 Mean and standard deviation of normalized root-mean-square error *NRMSE* (given in %) between PPG-derived HRV features and features derived from ECG beat-to-beat heart rate time series

	In-ear PPG			Fingertip PPG		
	Onset	1st Der.	2nd Der.	Onset	1st Der.	2nd Der.
Mean	0.1 ± 0.2	0.1 ± 0.2	0.1 ± 0.2	0.1 ± 0.2	0.1 ± 0.2	0.1 ± 0.1
SDNN	6.6 ± 6.0	7.5 ± 9.9	6.9 ± 7.7	3.6 ± 2.5	3.3 ± 2.2	3.3 ± 2.2
SDSD	27.2 ± 29.8	29.2 ± 38.6	26.3 ± 26.7	8.7 ± 6.2	6.3 ± 4.5	7.0 ± 5.4
pNN50	121.5 ± 92.4	72.8 ± 124.9	68.0 ± 92.2	40.2 ± 53.5	27.2 ± 32.9	33.7 ± 42.7
LF	11.7 ± 9.2	10.3 ± 12.9	10.2 ± 9.5	3.8 ± 3.2	3.3 ± 3.0	3.5 ± 3.0
HF	26.8 ± 30.0	22.3 ± 23.0	24.5 ± 24.1	17.5 ± 15.7	15.3 ± 13.3	16.1 ± 14.3
LF/HF	27.0 ± 15.0	21.5 ± 17.6	23.7 ± 15.6	16.2 ± 10.6	14.4 ± 9.5	15.2 ± 10.0

For the three assessed PPG pulse fiducial points, both the Spearman rank correlation analysis and the *NRMSE* results do not show a conclusive pattern in both PPG modalities.

4 Conclusion

In this work, the in-ear PPG is investigated as a surrogate measurement site for the derivation of HRV parameters from healthy individuals under resting conditions. For this purpose, recordings of 28 volunteers were collected. Common HRV features from both the time and frequency domain have been calculated from the in-ear PPG signal and a reference ECG signal. For comparison, HRV parameters were also derived from the common fingertip PPG.

Our results show, that the HRV parameters Mean, SDNN and LF can be derived from the in-ear PPG with moderate accuracy. In contrast, HRV parameters that quantify high frequent fluctuations like SDSD, pNN50, HF and LF/HF show a more limited agreement with the ECG reference. Therefore, it could be shown, that the in-ear PPG is a viable alternative measurement modality for continuous HRV monitoring when ECG recording is not applicable. Care has to be taken in the selection of HRV parameters that are calculated from the in-ear PPG.

In further studies, we want to examine the accuracy of the in-ear PPG-derived HRV parameters during non-resting conditions like physical exercise.

Conflict of Interest The authors declare that they have no conflict of interest.

References

1. Lomb, N.R.: Least-squares frequency analysis of unequally spaced data. Astrophysics and Space Science **39**(2), 447–462. (1976)
2. Malik, M., Camm, A.J., Bigger, J.T., Breithardt, G., Cerutti, S., Cohen, R.J., Singer, D.H.: Heart rate variability. standards of measurement, physiological interpretation, and clinical use. European Heart Journal **17**(3), 354–381 (1996)
3. Pflugradt, M., Mann, S., Tigges, T., Görnig, M., Orglmeister, R.: Multi-modal signal acquisition using a synchronized wireless body sensor network in geriatric patients. Biomedical Engineering **60**(1), 57–68 (2015)
4. Pinheiro, N., Couceiro, R., Henriques, J., Mühlsteff, J., Quintal, I., Goncalves, L., Carvalho, P.: Can PPG be used for HRV analysis? In: 2016 38th Annual International Conference of the IEEE Engineering in Medicine and Biology Society (EMBC), pp. 2945–2949. Orlando, FL (2016)
5. Schäfer, A., Vagedes, J.: How accurate is pulse rate variability as an estimate of heart rate variability?: A review on studies comparing photoplethysmographic technology with an electrocardiogram. International Journal of Cardiology **166**(1), 15–29 (2013)
6. Tigges, T., Rockstroh, J., Pielmus, A., Klum, M., Feldheiser, A., Hunsicker, O., Orglmeister, R.: In-ear photoplethysmography for central pulse waveform analysis in non-invasive hemodynamic monitoring. In: Current Directions in Biomedical Engineering, vol. 3, pp. 587–590. (2017)

Statistical Guideline of Threshold Determination for Cardiac Spiral Wave Center Detection Using Phase Variance Analysis

Naoki Tomii, Masatoshi Yamazaki, Nitaro Shibata, Haruo Honjo, and Ichiro Sakuma

Abstract

Spiral wave (SW) plays a key role in generation and termination of fatal tachyarrhythmia. In our previous study, we proposed a novel objective tracking method of SW center trajectories by using phase variance (PV) analysis. This method evaluates local variance of phase values around each point to detect the position of SW center as the peak of PV map. PV analysis improved the detection accuracy of meandering SW centers and complex multiple SW centers significantly. However, the algorithm still includes some hyperparameters, the window size for the evaluation of phase variance and the binarization threshold for the peak detection. Thus, some guideline for proper determination of those parameters has been required. In this study, we hypothesized that the appropriate binarization threshold depends on the window size, and it can be determined as the level of PV value with specific p-value on Rayleigh's test. We compared the detection results with various window sizes (3, 6, 9, 12 pixels) and various thresholds (from 0.4 to 0.9). Optical mapping measurement data with single SW center and four SW centers were evaluated. As a result, proper numbers of SW centers were detected with the thresholds corresponding to the p-value of 0.05, even with the smallest window size (3 pixels). From these results, it was indicated that the suggested method based on Rayleigh's test is valuable for proper determination of PV analysis parameters.

N. Tomii (✉)
Faculty of Medicine, The University of Tokyo, Tokyo, Japan
e-mail: tomii@m.u-tokyo.ac.jp

M. Yamazaki · I. Sakuma
Faculty of Engineering, The University of Tokyo, Tokyo, Japan

N. Shibata
Shinjuku Mitsui Building Clinic, Tokyo, Japan

H. Honjo
Research Institute of Environmental Medicine, Nagoya University, Nagoya, Japan

1 Introduction

Spiral waves (SWs) play a significant role in fatal arrhythmia mechanisms such as tachycardia and fibrillation, and the dynamics of SWs in hearts is quite complex [1]. There have been many studies for clarifying such SW dynamics by using high spatiotemporal measurement system or computer simulations. In 1998, Gray et al. suggested that complex SW dynamics can be analyzed objectively by defining the SW center as a phase singularity (PS) point in a spatial phase map [2]. This concept have been accepted widely in many studies, and several quantitative methods for PS detection has also been suggested [3–5]. However, due to many positive and negative errors, it has been difficult to analyze the SW dynamics standing on the quantitative detection results.

In our previous study, we suggested a novel PS detection algorithm named phase variance (PV) analysis [6]. In this study, it was demonstrated that PV analysis enables stable and robust tracking of SW centers than the conventional PS detection method using closed-curve convolution of phase value gradients [3].

The remaining issue of PV analysis, on the other hand, is defining the several hyperparameters in the PV analysis properly. The following equation is the definition of the PV around a target point.

$$PV = 1 - \left\| \sum_{i=1}^{N} e^{i\theta_i} \right\| \tag{1}$$

θ_i is a phase value at each point inside a window which is set around a target point, and N is the number of the points. Then, a PV map can be derived by calculating the PV value at each point, and PSs can be detected as peak points in the PV map by binarizing the PV map with a certain threshold.

299

In this PS detection process, two major hyperparameters are remaining, the window size and the threshold for binarization.

We hypothesized that hyperparameters of PV analysis can be decided properly based on the Rayleigh test, a statistical testing method for a group of angle values [7]. The null hypothesis of Rayleigh test is that there is no bias in those angle values. Regarding to phase values in a window in a phase map, phase values are biased in most cases except for when the window is set around a PS point. Therefore, the null hypothesis will be rejected with a certain level of significance in most cases except the case where the window is set around a PS point. The probability of the null hypothesis being accepted in the Rayleigh test is defined by the following equation.

$$P \sim e^{-N(1-V)^2} \tag{2}$$
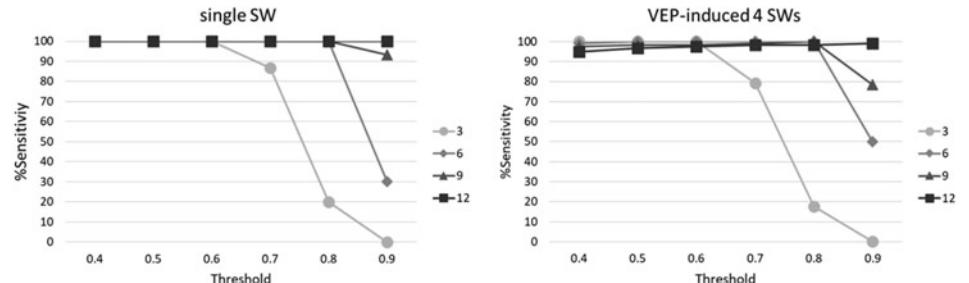
N is the number of samples, and V is the angle variance. The number of sample points N is the square of each window size. Based on this property of probability, we hypothesized that the proper threshold for each window size can be decided by deciding a certain significance level of null hypothesis rejection in the Rayleigh test, and therefore, the proper threshold for PS detection depends the window size of PV evaluation in (1). To test this hypothesis, we performed PS detection for 2D optical measurement results with various window size and thresholds and evaluated those detection results.

2 Methods

2.1 Evaluation Episodes

The experimental models and system used in this study have been described in our previous study [6]. Two isolated rabbit heart samples were used in this study. In each sample, a single SW and four VEP-induced SWs were induced by electric stimulations respectively. In each episode, sensitivity and specificity of PS detection were evaluated. The number of frames in each evaluation was 30 ($\approx$30 ms) in both episodes.

2.2 PS Detection

PS detection algorithm is described in detail in our previous paper [6]. At first, the action potential map was derived by reverse normalization of captured camera images. Subsequently, the phase map was derived from the action potential map using pseudo-EMD and the Hilbert transform [6]. Then PSs at each frame was detected by the PV analysis, with the window size in range from 3 to 12 pixels with an interval of 3 pixels, and the threshold in range from 0.4 to 0.9 with an interval of 0.1.

3 Results

In both episodes of single SW and VEP-induced SWs, no false positive (FP) detection was observed in any of 30 frames i.e. the specificity was 100%. Figure 1 shows the sensitivities with different window sizes for each evaluation episode. The left column in Fig. 1 shows the result of the single SW episode, and the right column shows the result of the VEP-induced four SWs episode, respectively. The X-axis of each graph denotes the threshold for PS detection.

In the result of single SW (Fig. 1 left), no false negative (FN) error was observed with any window size with a threshold smaller than 0.6. On the other hand, with thresholds larger than 0.6, sensitivity decreased with larger thresholds. Such tendency was noticeable particularly with smaller window size.

On the other hand, in the result of VEP-induced four SWs episode (Fig. 1 right), FN errors were observed even with small threshold. Figure 2 show examples of PS detection results of this episode. The top left panel shows a phase map at a certain time. The gray images in the most left column show the PV maps with different window sizes. The right side binary images show the PS detection results with different thresholds. Especially, Fig. 2 right shows the timing just before the PSs' collision, and PSs are close. In this case, FN errors were observed in the cases where the window size was too large to distinguish those PSs. The FN errors with small window sizes and large thresholds was also observed in the results of both Fig. 2.

Fig. 1 Sensitivity of PS detection with each window size and threshold. Left: single SW. Right: four VEP-induced SWs
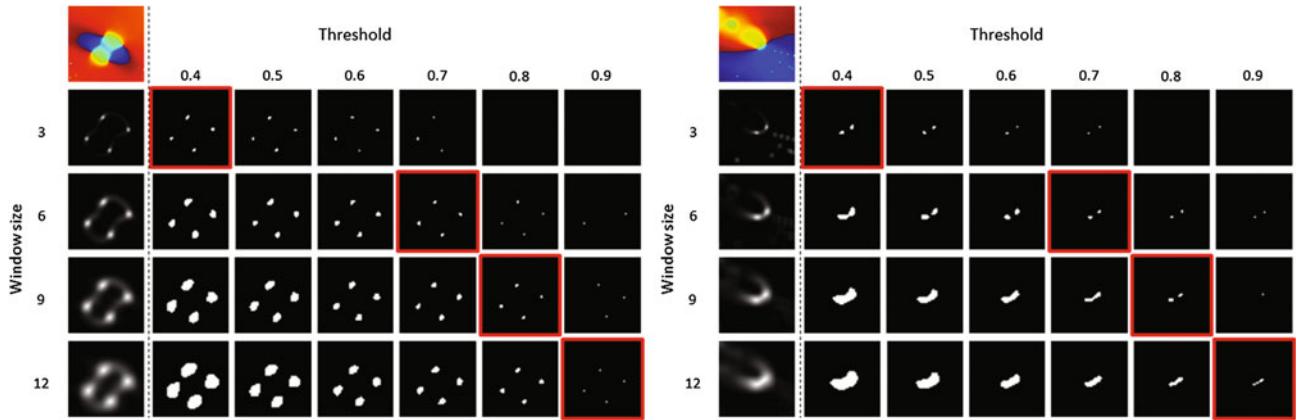
Fig. 2 Examples of PS detection results for the four VEP-induced SWs episode with different window size and different threshold. Left: Detection results of all four SWs. Right: The timing just before the PSs' collision. The region of interest of each image is focused on the region of the close PSs (Color figure online)

4   Discussion

To test our hypothesis about the proper hyperparameters of PV analysis and the Rayleigh test (Fig. 1), we performed PS detection for 2D optical measurement results with various window sizes and thresholds and evaluated those detection results.

4.1   Factors of Errors

In the results of PS detection with different parameters, two different factors of FN errors were observed. The first factor was that the threshold is larger than the peak value on the PV map. This kind of FN errors were noticeable particularly with smaller window size (Figs. 1 and 2). The second factor was that the window size for PV evaluation in (1) is too large in relation to the distance of close PSs. In fact, the PV map was quite ambiguous with too large window sizes (Fig. 2 right, the most left column, bottom) and it was impossible to distinguish close PSs in the PV map.

From these results, it seems that small window sizes and small thresholds are preferable compared to large window sizes and large thresholds to reduce FN errors. On the other hand, a predictable problem with small window sizes and small thresholds is the increase in FP errors. In the results in this paper, no FP error was observed. But some noise in measurement signal can increase the PV value at non-PS points, and robustness to such noise would be lost if the window size is too small. Therefore, to reduce total errors, window size should be enlarged properly while taking S/N ratio of the measurement signal into consideration.

4.2   Performance of the Threshold Decided by Rayleigh Test

Once the window size was decided considering S/N ratio, the next issue is defining the proper threshold. Figure 3 shows
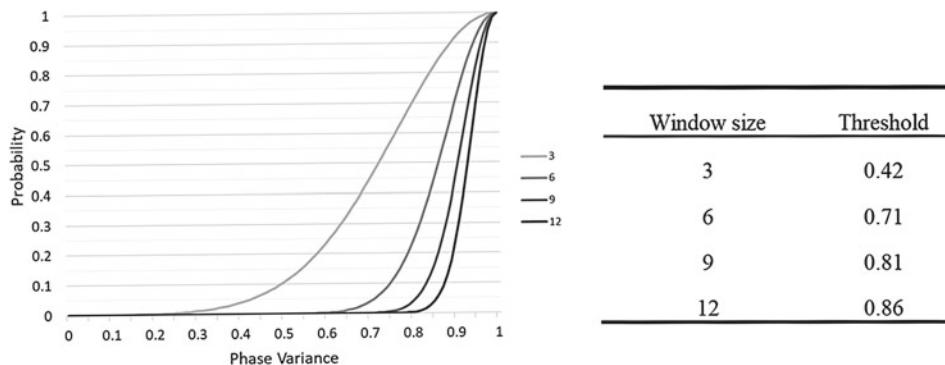
Fig. 3 The threshold determination based on Rayleigh test. Left panel: probabilities of phase variance based on Rayleigh test with each window size (3, 6, 9, 12 pixels) in a 2D phase map. Right table: calculated proper thresholds for each window size based on Rayleigh test (p = 0.05)

the probabilities for each window size in a 2D phase map. Table 1 shows the calculated threshold for each window size based on the probability of Rayleigh test (2), with p = 0.05. The result images of the nearest threshold for each window size is surrounded by thick red lines in Fig. 2. In these results, the PS detection results was almost the same, and the sensitivity and specificity was 100% in most cases (window size 3, 6, and 9). Just one exception was the case where the distance between close PSs were smaller than the window size (Fig. 2 right, window size 12, sensitivity was 99.2%). Therefore, the window size determines the minimum distance allowed for PSs to detect them identically. If there is no need to consider the measurement of noise, for example in the simulation results, the smallest window size 3 is the best to distinguish close PSs (Fig. 2 right, window size 3).

5 Conclusion

In the phase singularity detection based on the phase variance analysis, smaller window size is better to avoid false negative errors, and it should be enlarged properly while taking S/N ratio of the measurement signal into consideration. Once the window size is decided, the proper threshold can be calculated by the Rayleigh test.

References

1. Jalife, J.: Spatial and Temporal Organization in Ventricular Fibrillation. Trends Cardiovasc. Med. 9, 119–127 (1999)
2. Gray, R.A., Pertsov, A.M., Jalife, J.: Spatial and temporal organization during cardiac fibrillation. Nature. 392, 75–78 (1998). https://doi.org/10.1038/32164
3. Bray, M.-A., Wikswo, J.: Considerations in phase plane analysis for nonstationary reentrant cardiac behavior. Phys. Rev. E. 65, 51902 (2002). https://doi.org/10.1103/physreve.65.051902
4. Zou, R., Kneller, J., Leon, L.J., Nattel, S.: Development of a computer algorithm for the detection of phase singularities and initial application to analyze simulations of atrial fibrillation. Chaos. 12, 764–778 (2002). https://doi.org/10.1063/1.1497505
5. Geberth, D., Hütt, M.-T.: Combining spiral and target wave detection to analyze excitable media dynamics. Phys. A Stat. Mech. its Appl. 389, 249–258 (2010). https://doi.org/10.1016/j.physa.2009.09.034
6. Tomii, N., Yamazaki, M., Arafune, T., Honjo, H., Shibata, N., Sakuma, I.: Detection Algorithm of Phase Singularity Using Phase Variance Analysis for Epicardial Optical Mapping Data. IEEE Trans. Biomed. Eng. 63, 1795–1803 (2016). https://doi.org/10.1109/tbme.2015.2502726
7. Wilkie, D., Wilkie, D.: Rayleigh Test for Randomness of Circular Data. Appl. Stat. (1983)

A Brain Connectivity Metric Based on Phase Linearity Measurement

Fabio Baselice, Antonietta Sorriso, Rosaria Rucco, and Pierpaolo Sorrentino

Abstract

The analysis of brain connectivity is gaining interest in recent years due to the relevant information it carries about the functioning of the brain in health and in disease. In brief, it consists in measuring the statistical dependencies between signals generated by different brain regions. Several metrics have been proposed in literature, related to three families: amplitude based, phase based on jointly amplitude and phase based. Due to the large amount of noise that typically affects the estimation of the connectivity maps, averaging over several epochs of a population is normally carried out. We propose a novel phase based metric, namely the Phase Linearity Metric (PLM), that is resilient to noise and volume conduction, bearing promise to lower the number of epochs needed for a reliable measurement. The comparison with the widely adopted PLI connectivity metric confirms the effectiveness of the PLM.

Keywords

Brain connectivity • EEG • MEG

F. Baselice (✉) · A. Sorriso · P. Sorrentino
Department of Engineering, Parthenope University, Naples, Italy
e-mail: fabio.baselice@uniparthenope.it

A. Sorriso
e-mail: antonietta.sorriso@uniparthenope.it

P. Sorrentino
e-mail: pierpaolo.sorrentino@uniparthenope.it

R. Rucco
Department of Motor Sciences and Wellness, Parthenope University, Naples, Italy
e-mail: rosaria.rucco@uniparthenope.it

R. Rucco · P. Sorrentino
Hermitage-Capodimonte Hospital, Naples, Italy

1 Introduction

In this work we present a novel metric to estimate connectivity between brain areas. In brief, the aim is to evaluate the amount of information exchanged between two brain regions, and this is done by measuring the similarities between the recorded signals [1, 2]. The proposed metric, named the Phase Linearity Metric (PLM), is designed to exploit Electroencephalographic (EEG) or Magnetoencephalographic (MEG) signals. More in detail, the behavior of the phase differences of two signals is analyzed in order to find linear trends over time [3]. The measurement of the linear components is done by computing their energies in the Fourier domain. The PLM can be seen as an evolution of a widely adopted phase based metric, the Phase Lag Index (PLI) [4]. Our approach has been designed to be more resilient to noise as compared to other metrics, while remaining a purely phase based metric insensitive to volume conduction. To achieve these features, PLM takes into account small differences between the central frequency of the two considered signals. The performances of the PLM have been evaluated in a simulated scenario. In particular, a comparison between PLM and PLI on the coupling sensitivity and on the robustness to noise has been carried via a Monte Carlo simulation. Results show that PLM is capable of interesting performances and that it performs significantly better than the PLI when dealing with noise. This is an interesting feature of the PLM, since it allows a reduction of the number of epochs required to obtain a reliable measurement of phase based connectivity [5]. This might in turn allow the estimation of connectivity at the single subject level.

2 Methodology

The proposed metric, named the Phase Linearity Metric (PLM), is designed to exploit the phase of Electroencephalographic (EEG) or Magnetoencephalographic

(MEG) signals [6]. The behavior of the phase differences of two signals is analyzed in order to find linear trends over time. The measurement of the linear components is done by computing their energies in the Fourier domain. More in detail, starting from a couple of acquired signals $x(t)$ and $y(t)$, the so-called interferometric signal is computed:

$$z(t) = x(t) \cdot y'(t) \qquad (1)$$

Given $z(t)$, its power spectral density $S(f)$ is computed by implementing the Fast Fourier Transform (FFT) algorithm. The shape of $S(f)$ is related to the coupling level of $x(t)$ and $y(t)$. In particular, if the two signals are uncorrelated, $S(f)$ will spread over a wide range of frequencies, while in case of coupling it will be much more concentrated around $f = 0$. By computing the amount of energy in a narrow band $[-B, B]$ centered at $f = 0$, the amount of coupling between signals can be measured. Thus, PLM is defined as:

$$PLM = \frac{1}{E} \int_{-B}^{B} S(f) \mathrm{d}f \qquad (2)$$

where E is the energy of the interferometric signal $z(t)$.

The PLM can be seen as an evolution of a widely adopted phase based metric, the Phase Lag Index (PLI). The approach has been designed to be more resilient to noise as compared to other metrics, while remaining a purely phase based metric insensitive to volume conduction.

3 Results

The performances of the PLM have been evaluated and compared to PLI results in case of a simulated dataset. The realization of two Gaussian processes $g_1(t)$ and $g_2(t)$ have been generated in the *alpha* band ([7, 13] Hz). More in details, epochs of 6.5552 s sampled at 625 Hz have been generated, each one composed of 4097 samples. Subsequently, the signals have been mixed with different correlation values c according to [7]:

$$\begin{aligned} x(t) &= c \cdot g_1(t) + (1 - c) \cdot g_2(t) \\ y(t) &= (1 - c) \cdot g_1(t) + c \cdot g_2(t) \end{aligned} \qquad (3)$$

In Figs. 1 and 2, two couples of signals are reported in the uncorrelated ($c = 0$) and correlated ($c = 0.8$) cases, respectively. The power density spectra of the two related interferometric signals are reported in Fig. 3. It can be appreciated that, in case of $c = 0$, $S(f)$ extends over a wide range of frequencies (blue line of Fig. 3), while in the correlated case a peak at $f = 0$ is well delineated (red line of Fig. 3).
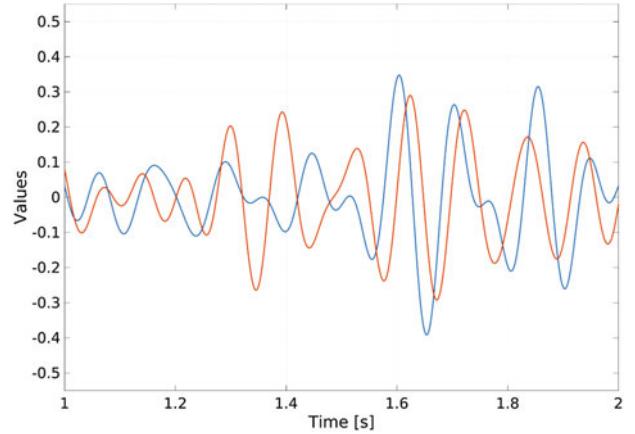
Fig. 1 1 s of the simulated signal couples in case of uncorrelated ($c = 0$) sources
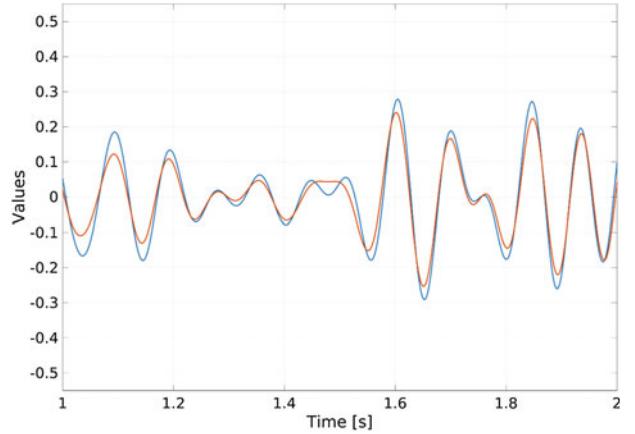
Fig. 2 1 s of the simulated signal couples in case of correlated ($c = 0.8$) sources
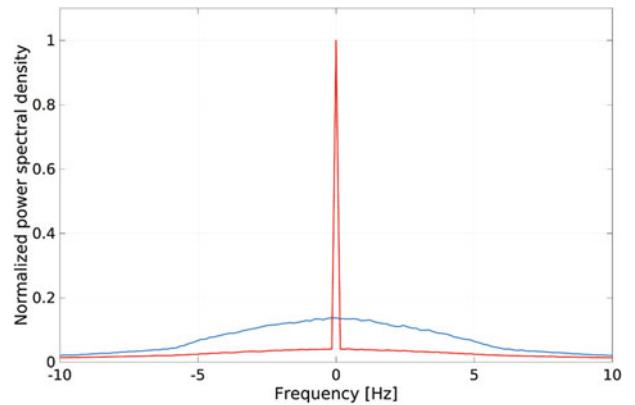
Fig. 3 Normalized power spectral densities in case of the uncorrelated (blue line) and correlated (red line) signals (Color figure online)

Both PLM and PLI have been computed in case of different coupling values, producing the results reported in

Fig. 4 PLM (blue line) and PLI (red line) measured values in case of different correlation between signals (Color figure online)

Fig. 5 Mean and standard deviation of PLM (blue lines) and PLI (red lines) values in case of different SNR levels. Results refer to a pair of signals with coupling coefficient $c = 0.3$ (Color figure online)

case of different Signal to Noise Ratio (SNR) levels (between 10 and 30 dB). Also in this analysis, PLI metric has been included in order to provide a reference. Results are reported in Fig. 5. It can be appreciated that the PLM performs significantly better than the PLI when dealing with noise. More in details, PLM values are characterized by a much smaller standard deviation for all considered noise levels.

4 Conclusions

A novel metric for measuring connectivity between brain areas has been proposed. The method, called Phase Linearity Measurement (PLM), analyzes the behavior of the phase difference between two signals in the frequency domain. The approach has been tested on a simulated dataset. Compared to PLI, which is a widely adopted connectivity metric based on the phase of the signals, PLM has shown to be more resilient with respect to noise, producing stable results.

Conflict of Interest Authors declare that there is no conflict of interests regarding the publication of this manuscript.

References

1. Stam, C.J., Modern network science of neurological disorders, Nature Reviews Neuroscience, 15, 683–695, (2014).
2. Greenblatt, A.R.E., Pflieger, M.E., Connectivity measures applied to human brain electrophysiological data, Journal of Neuroscience Methods, 207, 116, (2012).
3. Buzsaki, G., Rhythms of the Brain, (2006).
4. Stam, C.J., Nolte, G., Daffertshofer, A., Phase lag index: assessment of functional connectivity from multi channel EEG and MEG with diminished bias from common sources., Human Brain Mapping, 28, 117–893, (2007).
5. Rosenblum, M., Pikovsky, A., Kurths, J., Schafer, C., Tass, P.A., Phase synchronization: from theory to data analysis, Handbook of Biological Physics, 4, 279–321, (2003).
6. Lopes da Silva, F., EEG and MEG: Relevance to neuroscience, Neuron, 80, 1112–1128, (2013).
7. Ross, S.H., Stochastic Processes, Second Edition, John Wiley and Sons, (1996).

Fig. 4. The two indexes produce a monotonically increasing function, proving that both PLM and PLI are effective in measuring the coupling strength between two signals.

A study on the robustness with respect to noise of the PLM has also been carried out by analyzing the results in

Modeling of the Microvascular Pulse for Tracking the Vasoconstriction Response to Deep Inspiratory Gasp

Michele Sorelli, Antonia Perrella, and Leonardo Bocchi

Abstract

This work demonstrates the suitability of a microvascular pulse decomposition algorithm (PDA) for evaluating the vasoconstriction response to a deep inspiratory gasp (DIG). Synchronous ECG, respiratory, and laser Doppler flowmetry (LDF) signals of 13 healthy subjects (age: 26 ± 3 years) were analyzed, and a four-Gaussian PDA was applied to reconstruct the LDF heartbeat pulsations. To assess the tracking of the transient vasoconstriction, the goodness-of-fit achieved during the DIG was compared with the performance at baseline. Moreover, the heart rate (HR) derived from the model's systolic component was validated against the ECG, comparing the agreement with the one obtained from the wavelet transform analysis (WTA) of the LDF signal. The model's normalized root-mean-square error and average R^2 did not decrease during the DIG ($p = 0.249$, $p = 0.552$), and a nearly optimal pulse modeling accuracy was maintained ($p = 0.286$). Furthermore, the proposed PDA could better reproduce the reference HR than WTA, with a 46.8% reduction of the median root-mean-square error ($p < 0.001$), which did not worsen during the DIG ($p = 0.861$). Therefore, this method might find valuable application in the evaluation of neurovascular deterioration.

M. Sorelli (✉) · A. Perrella · L. Bocchi
Department of Information Engineering, University of Florence, Via di S. Marta 3, 50139 Florence, Italy
e-mail: michele.sorelli@unifi.it

L. Bocchi
e-mail: leonardo.bocchi@unifi.it

1 Introduction

The respiratory activity is known to produce blood flow oscillations which propagate through the circulatory system, showing a high degree of self-synchronization when evaluated at different body sites with non-invasive optical techniques, such as laser Doppler flowmetry (LDF) [1]. Breathing has also been associated with characteristic vasomotor responses induced by the sympathetic nervous system. In 1936, Bolton et al. [2] were the first to show how a deep inspiratory gasp (DIG) can evoke a transient vasoconstriction of the cutaneous circulation of the finger, which was inhibited after the impairment of sympathetic pathways. This vasomotor effect is indeed believed to be mediated by the vasoconstriction of arterio-venous shunts, which are densely innervated and abound particularly in the cutaneous circulation of toes and fingertips. The factor triggering the vasoconstrictive reflex has been identified with either the expansion of the thoracic cavity or the stretch of intra-thoracic veins; however, the exact physiological mechanism has not been unequivocally clarified yet [3]. In [4], Allen et al. have applied LDF and photo-plethysmography in order to evaluate the quantitative changes in cutaneous perfusion which followed a DIG manoeuvre, and to assess their repeatability. However, in a subsequent work, the same author has regretted the unavailability of reliable algorithms which allow for the automatic tracking and quantitative characterization of the peripheral pulse waveform [5]. Therefore, the aim of the present study was to demonstrate the suitability of a microvascular pulse decomposition algorithm (PDA) for the quantification of the transient physiological vasoconstriction induced by a DIG. This may help the clinical implementation of this test for the assessment of peripheral neuropathies.

2 Materials and Methods

13 healthy volunteers were recruited in this study (age: 26 ± 3 years). Microvascular perfusion was measured on the pulp of the right forefinger with a LDF Periflux 5000 system (Perimed, Sweden). Furthermore, a BioHarness 3.0 monitoring chest band (Zephyr Technologies, US) was used to record synchronous ECG and breathing activity signals, which were transmitted to a PC via Bluetooth protocol. All the acquired physiological signals were sampled at a rate of 250 Hz. The measurement sessions were conducted in an acclimatized room (T $\approx$ 23 °C), with the subjects sitting comfortably and leaning their ipsilateral forearm on a table, so as to minimise the probability of causing detrimental movement artefacts in the LDF signals. The contraction and expansion of the thoracic cavity, detected by the pressure transducer pad of this wearable device, were exploited so as to accurately define the actual DIG time window. Specifically, the start and end of the manoeuvre were respectively identified with the maximum and minimum extension of the chest strap. In order to improve the standardization of the measurement protocol, the interface of the data acquisition software provided the subjects with visual cues which triggered the DIG manoeuvre and, 5 s later, the subsequent exhalation. After recording the baseline perfusion for 60 s, the test was performed as a fast profound inhalation, followed by another post-DIG phase of 60 s, thus resulting in a total measurement time of 125 s. The present study was carried out according to the guidelines of the Declaration of Helsinki: the enrolled participants received a detailed explanation of the research protocol, and filled an informed consent before the measurement sessions.

Blood perfusion was analyzed with an improved version of a recent PDA [6], which allows for breaking each heartbeat-related pulsation of LDF signals into four Gaussian components. Thanks to the detection of a reference *incisura* on the dicrotic limb of the waveform, parameter identification can accurately reconstruct the transmitted systolic pulse, separately from the diastolic phase of the wave. More specifically, model identification was carried out with the Levenberg-Marquardt algorithm [7]; specific amplitude and time features of each detected waveform were exploited in order to tune the initialization and constraints of the optimization problem and, therefore, improve its stability. Afterwards, on each LDF signal, 3-σ limits were imposed on the (detrended) amplitude of the systolic term, a_{sys}, and the overall duration of the pulse, so as to decrease the rate of merged cardiac cycles and short spurious pulsations. Moreover, mis-modeled pulse waves were excluded by detecting lower outliers of the goodness-of-fit (GOF) R^2, in combination with abnormal σ values of the systolic Gaussian.

The a_{sys} amplitude of the selected systolic pulses was adopted for assessing the physiological vasoconstrictive response to the DIG manoeuvre; in order to perform a reliable evaluation of its trend, even in presence of varying baseline perfusion levels among different subjects, the above amplitude parameter was normalized with respect to the average, $\bar{a}_{sys}$, obtained during the 60 s preceding the DIG. The method's ability to track the DIG-induced transient vasoconstriction was evaluated by comparing the GOF achieved at baseline with the one obtained within the time window of the manoeuvre. To this end, the present evaluation was based on the average coefficient of determination R^2 associated with these respective phases and, furthermore, on the estimation of a normalized root-mean-square error (NRMSE), defined as:

$$\text{NRMSE} = 1 - \frac{\|S_{LDF}(t) - M_{4G}(t)\|}{\|S_{LDF}(t) - \overline{S}_{LDF}\|} \quad (1)$$

where $S_{LDF}(t)$ and $\overline{S}_{LDF}$ respectively indicate the LDF perfusion and its mean, while $M_{4G}(t)$ represents the adopted four-Gaussian model. Thus, given the expression above, a perfect fit of the signal pulsations would correspond to a theoretical unitary NRMSE, whereas a value of 0 would mean that the performance of the multi-Gaussian model is in fact equivalent to fitting the signal with a horizontal line corresponding to the mean $\overline{S}_{LDF}$. To further validate the proposed method, the reference ECG provided by the wearable chest band was exploited so as to verify whether the ratio of reconstructed pulse waves to the actual number of cardiac cycles worsened during the DIG phase. Moreover, in order to provide additional information on the modeling accuracy of the proposed method, the mean of the systolic Gaussian, μ_{sys}, was used for reconstructing the subjects' heart rate, HR_{PDA}, throughout the baseline, DIG, and post-DIG phases of the protocol; this estimate was then compared with the heart rate derived from the time interval in between the R peaks detected by the BioHarness' sensor (HR_{ECG}). It is relevant to emphasize that the post-modeling selection of the pulse waves was carefully taken into consideration at this stage, by neglecting those HR_{PDA} values estimated from μ_{sys} parameters of *unreliable* instances. For each subject, the root-mean-square error (RMSE) between the HR_{PDA} estimate and the reference HR_{ECG} was calculated separately for the baseline and DIG time windows. Next, the accuracy of the PDA was juxtaposed to the performance achieved with the wavelet transform (WT) analysis of the LDF signals [8]. The Morlet mother wavelet, with central frequency $f_0 = 1$, was used in this context. In detail, the instantaneous frequency characteristic of the cardiac modulation of blood perfusion

was estimated by reconstructing the ridge of the wavelet spectrogram inside the frequency range [0.6–2] Hz, and outside the time window of the so-called *cone of influence* [9].

3   Results and Conclusion

Because of the significant non-normality of all data distributions, which was preliminarily assessed with the Shapiro-Wilk test, the non-parametric Wilcoxon signed-rank test for dependent samples was applied to perform the statistical comparisons required in this study. The analysis of the GOF attained by the multi-Gaussian model during the manoeuvre yielded promising results, whose median and interquartile ranges (IQR) are hereby reported. Indeed, within the time window of the DIG, the PDA did not exhibit a significant worsening of the NRMSE (0.90, IQR: 0.81–0.94) relative to baseline (0.92, IQR: 0.87–0.94, p = 0.249), as shown in Fig. 1a. Furthermore, no statistically significant deviation was demonstrated between the distributions of the mean R^2 (Fig. 1b), obtained from the baseline (0.973, IQR: 0.958–0.978) and DIG phases of each subject (0.973, IQR: 0.953–0.980, p = 0.552). The multi-Gaussian PDA further demonstrated its accuracy showing a median pulse detection rate at baseline of 98.5% (IQR: 97.3–99.4%), which did not appear to be negatively affected by the manoeuvre (100%,

IQR: 100–100%, p = 0.286), as displayed in the box plot of Fig. 1c.

Consistent results were found regarding the validation of the HR_{PDA} estimates. As hypothesized in light of the GOF performance of the model, the ability to reproduce the reference HR_{ECG} was confirmed by the low RMSE levels found at baseline (1.8 bpm, IQR: 1.4–2.7 bpm), which did not appear to undergo a significant increase during the DIG (1.9 bpm, 1.4–3.2 bpm, p = 0.861), as shown in Fig. 2b. Moreover, the multi-Gaussian PDA outperformed the WT-based tracking of the heart rate (Fig. 2c), showing a significantly lower RMSE on the whole domain of the LDF signals (1.6 bpm, IQR: 1.4–2.6 bpm, vs. 3.2 bpm, IQR: 2.4–5.1 bpm, p < 0.001), with a 46.8% decrease of the median error score.

The baseline-normalized median trend of the subjects' HR_{PDA} can be appreciated in Fig. 3a; this plot highlights a substantial level of agreement to the quartiles of the reference HR_{ECG}, within all phases of the measurement protocol, including the DIG. In accordance with the results obtained by Allen et al. [5], the fast deep inhalation was found to induce an increase in the HR_{PDA}, that appears to peak in correspondence with the maximum expansion of the thorax, with a relative median rise of 13.3% (IQR: 7.1–18.9%) above the baseline mean. Furthermore, as expected the DIG manoeuvre determined a reduction of the a_{sys} amplitude of the LDF pulse waves, whose normalized median trend is displayed in Fig. 3b: it can be observed that the maximum
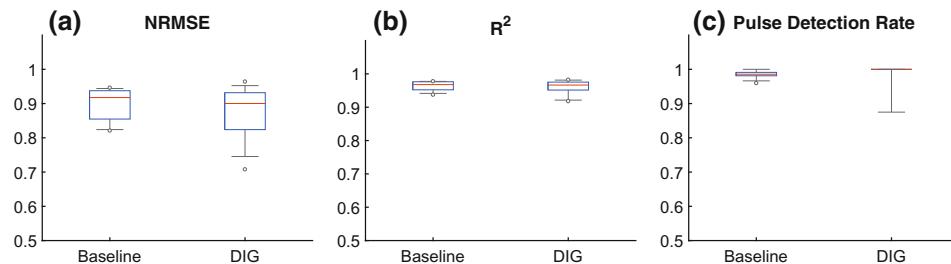

Fig. 1 GOF performance of the four-Gaussian modeling algorithm: baseline versus DIG
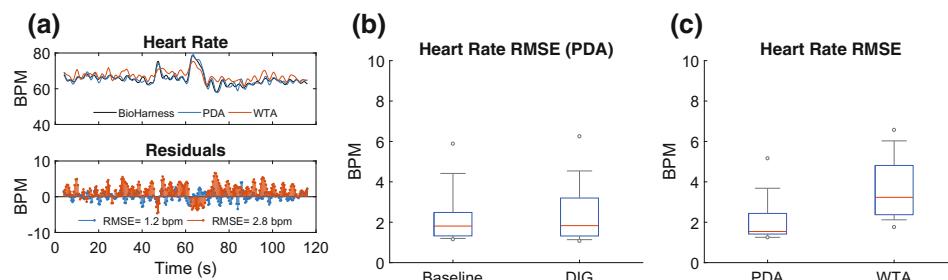
Fig. 2 Heart rate estimation and validation. **a** Example comparison of the PDA- and WT-based heart rate estimates to the reference ECG provided by the BioHarness 3.0 device; **b** PDA-based heart rate: baseline versus DIG; **c** heart rate tracking: PDA versus WT analysis
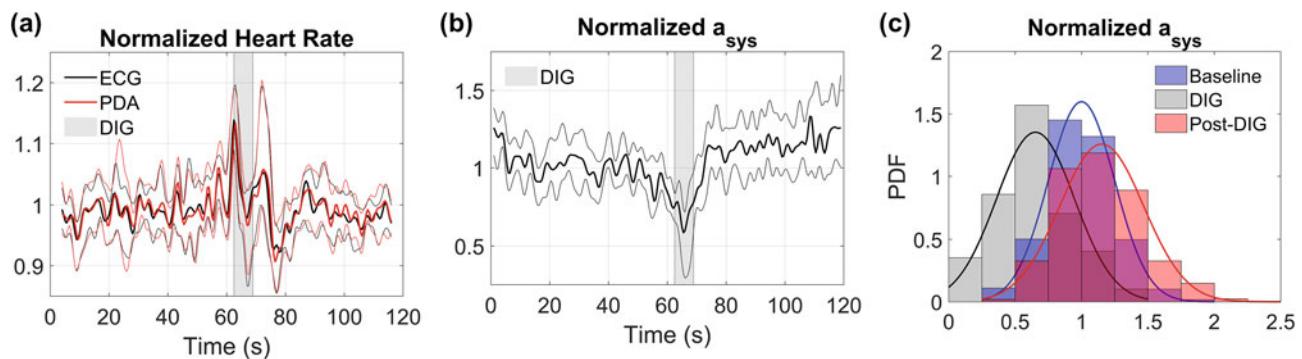
Fig. 3 **a** Normalized trend of the heart rate throughout the measurement protocol; **b** normalized trend of the systolic pulse amplitude, a_{sys}; **c** probability density functions of the a_{sys} parameter derived from the baseline, DIG and post-DIG phases of the protocol

vasoconstrictive effect appears to occur approximately 3.0 s after the end of the rapid inspiratory phase, where a 41.4% median amplitude decrease (IQR: 26.5–68.2%) is detected. Figure 3c shows the probability density functions of the latter parameter, estimated for the baseline, DIG and post-DIG time windows.

Collectively, the present results not only indicate that the developed PDA can reliably detect and model the microvascular pulse waveform, but also show that the achieved accuracy is not significantly affected by the attenuation determined by the vascular reflex, which follows a rapid deep inspiration. Therefore, the proposed methodology may be suitable for the characterization of neurogenic vasomotor responses, allowing to track transient changes in physiological features of the peripheral pulse, which have been related to vascular stiffness, e.g. the pulse arrival time, and the Reflection Index [10].

References

1. Stefanovska, A., Hožič, M.: Spatial synchronization in the human cardiovascular system. Progress of Theoretical Physics Supplement 139, pp. 270–282 (2000). https://doi.org/10.1103/physreve.60.857
2. Bolton, B., Carmichael, E. A., Sturup, G.: Vasoconstriction following deep inspiration. Journal of Physiology 86, pp. 83–94 (1936)
3. Mayrovitz, H. N., Groseclose, E. E.: Neurovascular responses to sequential deep inspirations assessed via laser-Doppler perfusion changes in dorsal finger skin. Clinical Physiology & Functional Imaging 22, pp. 49–54 (2002). https://doi.org/10.1046/j.1475-097x.2002.00404.x
4. Allen, J., Frame, J. R., Murray, A.: Microvascular blood flow and skin temperature changes in the fingers following a deep inspiratory gasp. Physiological Measurement 23, pp. 365–373 (2002). https://doi.org/10.1088/0967-3334/23/2/312
5. Allen, J., Di Maria, C., Mizeva, I., Podtaev, S.: Finger microvascular responses to deep inspiratory gasp assessed and quantified using wavelet analysis. Physiological Measurement 34, pp. 769–779 (2013). https://doi.org/10.1088/0967-3334/34/7/769
6. Sorelli, M., Perrella, A., Bocchi, L.: Cardiac pulse waves modeling and analysis in laser Doppler perfusion signals of the skin microcirculation. In: CMBEBIH 2017: Proceedings of the International Conference on Medical and Biological Engineering, pp. 20–25, Springer, Singapore (2017). https://doi.org/10.1007/978-981-10-4166-2_4
7. Moré, J. J.: The Levenberg-Marquardt algorithm: implementation and theory. In: Numerical analysis, pp. 105–116, Springer, Berlin (1978)
8. Stefanovska, A., Bračič, M., Kvernmo, H. B.: Wavelet analysis of oscillations in the peripheral blood circulation measured by laser Doppler technique. IEEE Transactions on Biomedical Engineering 46, pp. 1230–1239 (1999). https://doi.org/10.1109/10.790500
9. Iatsenko, D., McClintock, P. V. E., Stefanovska, A.: Linear and synchrosqueezed time-frequency representations revisited: overview, standards of use, resolution, reconstruction, concentration, and algorithms. Digital Signal Processing 42, pp. 1–26 (2015). https://doi.org/10.1016/j.dsp.2015.03.004
10. Millasseau, S. C., Kelly, R. P., Ritter, J. M., Chowienczyk, P. J.: The vascular impact of aging and vasoactive drugs: comparison of two digital volume pulse measurements. American Journal of Hypertension 16, pp. 467–472 (2003). https://doi.org/10.1016/s0895-7061(03)00569-7

Wavelet Phase Coherence Between the Microvascular Pulse Contour and the Respiratory Activity

Antonia Perrella, Michele Sorelli, Francesco Giardini,
Lorenzo Frassineti, Piergiorgio Francia, and Leonardo Bocchi

Abstract

A wavelet phase coherence (WPC) analysis was conducted in order to evaluate the time-phase relationships between the respiratory activity and the pulse of the peripheral perfusion. The investigation involved a group of 21 young healthy subjects, aged from 20 to 30 years. Cutaneous perfusion was measured by laser Doppler flowmetry, while breathing was simultaneously monitored with a wearable chest band. A multi-Gaussian modeling algorithm was used to decompose the pulse waveform thus enabling the separate characterization of the forward-travelling systolic pulse and the diastolic components arising from vascular impedance mismatch. The WPC between model-derived shape features and the breathing rhythm was assessed, to determine whether their characteristic oscillations were somehow synchronized. In 17 subjects a significant degree of phase coherence was detected in the respiratory frequency band for the area beneath the diastolic phase of the cardiac pulse. This result indicates that the microvascular reflection waves exhibit a marked periodicity linked to the breathing activity.

Keywords

Pulse decomposition • Laser Doppler flowmetry Wavelet phase coherence

A. Perrella · M. Sorelli (✉) · F. Giardini · L. Frassineti · L. Bocchi
Department of Information Engineering, University of Florence,
Via di S. Marta 3, 50139 Florence, Italy
e-mail: michele.sorelli@unifi.it

L. Bocchi
e-mail: leonardo.bocchi@unifi.it

P. Francia
Department of Clinical and Experimental Medicine, University
of Florence, Viale Pieraccini 6, 50139 Florence, Italy

1 Introduction

Oscillations in the microvascular blood flow originate from both central mechanisms and local physiological processes. Several studies, involving the wavelet transform (WT) analysis of laser Doppler flowmetry (LDF) signals, have associated these mechanisms with specific frequency ranges [1]. When two or more interactive physiological processes are being simultaneously monitored, it is interesting to assess whether their characteristic oscillations are mutually related. Based on the analysis of ECG and respiratory signals, cardio-respiratory interactions have been studied extensively at central level with two main methods, namely wavelet phase coherence analysis and Bayesian inference [2, 3]. The former has found widespread application in the assessment of time-phase relationships existing between physiological parameters oscillating at similar frequencies [4]. However, to the authors' knowledge, only few studies have been conducted to evaluate the quantitative effects of the respiratory function on the peripheral circulation. For instance, in this regard Chalacheva et al. [5] have investigated the role of spontaneous and induced sighs in the vasoconstrictive responses mediated by the sympathetic nervous system, and proposed a model of the cardiovascular system which incorporates a respiratory-peripheral vascular conductance coupling component. It is known that the microvascular pulse contour is affected by the biomechanical properties of the circulation and, thus, conveys information on the state of the vascular system [6]. Pulse decomposition algorithms (PDAs) represent a promising approach for evaluating such peripheral oscillations. PDAs decompose each pulse wave into a number of basic components which allow the separate reconstruction of forward-travelling systolic waves and reflected secondary pulsations arising from vascular impedance mismatch. Despite being established that the respiratory activity affects the amplitude of peripheral blood flow signals, until now no study has exploited a PDA in order to highlight a potential time-phase relationship between breathing and microvascular pulse. Therefore, in the present

study, a four-Gaussian PDA was implemented and applied in the context of a WPC analysis, with the aim to determine whether and which feature of the peripheral pulse profile are synchronized with the central respiratory rhythm.

2 Materials and Methods

A group of 21 non-smoking, healthy volunteers, aged from 20 to 30 years, was enrolled in the measurement sessions, involving the simultaneous acquisition of breathing and microvascular perfusion signals. Experimental data were collected in accordance with the guidelines of the Helsinki declaration. All the participants agreed to be included in the study and signed an informed consent form, after complete information on the purpose of the research and the procedures involved was provided. Peripheral perfusion signals were acquired from the tip of the right forefinger using a Periflux 5000 LDF system (Perimed, Sweden). The respiratory activity was recorded with a BioHarness 3.0 physiological monitoring telemetry device (Zephyr Technology, US), and synchronously transmitted to a PC via Bluetooth. The latter instrument consists of an electronic module and a chest strap, which houses a pressure sensor pad that detects the expansion of the rib cage due to the breathing action. Both signals were digitized at a sampling frequency of 250 Hz. Measurements lasted 5 min and were performed in resting conditions, during spontaneous breathing (Fig. 1), in a temperature-controlled room (T ≈ 23 °C). Moreover, a proper delay was included at the start of the experiments, to allow for the subjects to stabilize their body temperature.

Perfusion signals were analyzed with a novel PDA, which can accurately fit each cardiac pulse waveform with a four-Gaussian model. Thus, the available temporal window allowed to analyze 350–370 cardiac cycles for each subject. The method adopted in this study uses an approach similar to recent works regarding the modeling of photoplethysmographic pulses [7, 8], and is a direct improvement of a former two-Gaussian PDA, presented in [9]. More specifically, the algorithm is able to detect the perfusion wave directly transmitted to peripheral blood vessels after systole, and accurately discriminate it from secondary pulsations which arise during diastole. Next, the former phase is used to identify a systolic Gaussian model, while the latter is fitted with the remaining three components. After the identification of the model parameters, the shape of each reconstructed pulse is characterized through the following features (Fig. 2): the amplitude of the four Gaussian curves, α_1, α_2, α_3, α_4; the area beneath the systolic component, A_s; and, finally, the overall area under the model of the diastolic phase, A_d.

A general definition of phase coherence between two signals is provided by the following expression [10]:

$$C_\phi(w_k) = \frac{1}{N} \left| \sum_{n=1}^{N} e^{i(\phi_1(w_k,t_n) - \phi_2(w_k,t_n))} \right| \qquad (1)$$

where $\phi_1(w_k, t_n) - \phi_2(w_k, t_n)$ is the phase difference between oscillatory components with characteristic frequency w_k at time t_n. If these oscillations remain phase-locked (i.e. they are coherent) throughout the analyzed time window, then $C_\phi(w_k) = 1$; conversely, if $C_\phi(f_k) = 0$, there is no tendency to preserve a particular phase difference. In the present study, the WPC between the respiratory activity and the signals derived from the spline interpolation of the shape-features, estimated for each
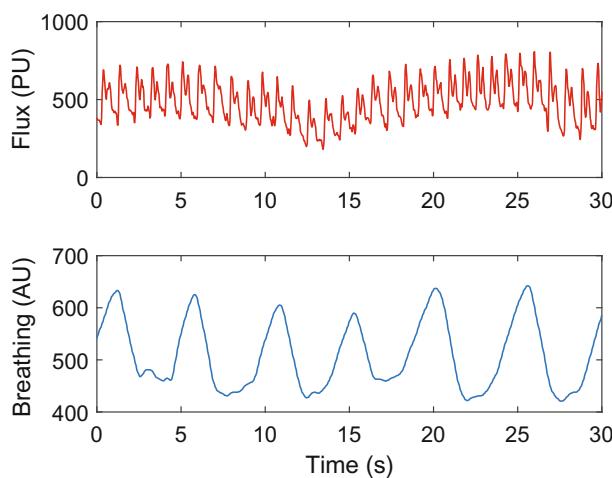

Fig. 1 30-s time window of a LDF signal of peripheral perfusion (top) and corresponding breathing trace (bottom)
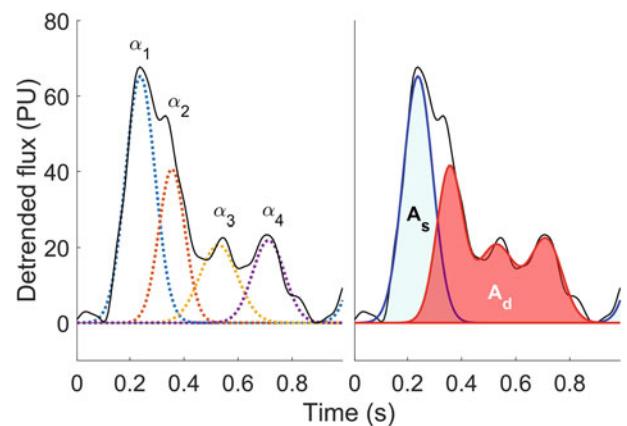

Fig. 2 Multi-Gaussian modeling of the LDF pulse and model-derived shape features

modeled LDF pulse (Fig. 2), was assessed. To this end, the method previously described in [11] was followed. In detail, the WT of breathing ($x_b(t)$) and feature ($x_{f,i}(t)$) signals was computed using the complex Morlet mother wavelet, with central frequency $f_0 = 1$ Hz, so as to achieve good resolution in both time and frequency domains. Before performing the WPC analysis, the time-averaged WT power spectra of the six shape-feature signals, $x_{f,i}(t)$, were assessed in order to verify whether they exhibited a significant power content within the frequency range of the respiratory activity, i.e. [0.145–0.6] Hz. Next, for each LDF signal, the estimated WT coefficients were used to derive the cosine and sine functions of the phase difference, $\Delta\phi$, between each $x_{f,i}(t)$ and $x_b(t)$ couple:

$$\cos(\Delta\phi_{k,n}) = \frac{\Re(w_{bk,n}) \cdot \Re(w_{fk,n}) + \Im(w_{bk,n}) \cdot \Im(w_{fk,n})}{\sqrt{\Re(w_{bk,n})^2 + \Im(w_{bk,n})^2}\sqrt{\Re(w_{fk,n})^2 + \Im(w_{fk,n})^2}},$$

$$(2)$$

$$\sin(\Delta\phi_{k,n}) = \frac{\Im(w_{bk,n}) \cdot \Re(w_{fk,n}) - \Re(w_{bk,n}) \cdot \Im(w_{fk,n})}{\sqrt{\Re(w_{bk,n})^2 + \Im(w_{bk,n})^2}\sqrt{\Re(w_{fk,n})^2 + \Im(w_{fk,n})^2}},$$

$$(3)$$

where $\Re(w_{\star k,n})$ and $\Im(w_{\star k,n})$ respectively represent the real and imaginary parts of the WT coefficients at the k-th frequency sample and the n-th time instant. A global WPC score was finally estimated as follows:

$$C_\phi(w_k) = \sqrt{\langle\cos(\Delta\phi_{k,n})\rangle^2 + \langle\sin(\Delta\phi_{k,n})\rangle^2} \qquad (4)$$

where $\langle\cdot\rangle$ is the average over the time domain of the signals, at each analyzed frequency w_k. The interpretation of $C_\phi(w_k) \geq 0$ values significantly depends on the number of oscillation periods available in the acquired signals. Indeed, it is important to recall that WPC rarely approaches 0 and tends to increase when moving toward the lowest observable frequencies, even when the dynamics underlying the couple of assessed time series is actually unrelated. Additionally, some physiological signals are characterized by spurious high WPC values, which are in fact associated with autocorrelation phenomena. Nevertheless, the undesired influence of low-frequency biases and autocorrelation can be overcome by comparing the resulting $C_\phi(w_k)$ against the phase coherence obtained between each original signal and a corresponding surrogate, produced through phase randomization, thus destroying the original temporal properties, while preserving the spectral amplitude information [12]. Namely, this allows to selectively disrupt the properties associated with the null hypothesis to be tested, i.e. that the instantaneous phase of each assessed

($x_b(t)$, $x_{f,i}(t)$) couple is not reciprocally related. Surrogate signals were generated with the amplitude-adjusted Fourier transform (AAFT) method [13]. In detail, a set of N = 100 surrogates was created for each $x_b(t)$ and $x_{f,i}(t)$ signal, where N was set in order to ensure statistical repeatability. Therefore, N = 100 $C_{\phi,b,surr}(w_k)$ and $C_{\phi,f,surr}(w_k)$ surrogate curves were respectively obtained for each breathing signal and parameter of interest. These sets were then used to identify the following significance threshold:

$$T_{C_{\phi,surr}}(w_k) = \overline{C}_{\phi,surr}(w_k) + 2 \cdot \sigma_{C_{\phi,surr}}(w_k) \qquad (5)$$

where $\overline{C}_{\phi,surr}(w_k)$ represents the mean WPC over the 100 surrogates, while $\sigma_{C_{\phi,surr}}(w_k)$ is their standard deviation. Each couple ($x_b(t)$, $x_{f,i}(t)$) was considered to be significantly phase-coherent at frequency w_k, if $C_\phi(w_k) > T_{C_{\phi,surr}}(w_k)$ held for both the breathing and shape-feature signals.

3 Results and Conclusion

A relevant respiratory peak was indeed identified in the wavelet power spectrum of most subjects (Fig. 3a), thus confirming the hypothesis of a considerable breathing-related modulation of the features obtained with the multi-Gaussian PDA. Furthermore, a significant WPC with respect to the breathing rhythm was detected in 17 out of the 21 healthy subjects (i.e. 81.0%) regarding the diastolic area of the LDF pulse, A_d (Fig. 3b), which was associated with an overall WPC median value of 0.78 (interquartile range: 0.63, 0.83). On the other hand, the A_s and α_1 features did not exhibit a significant coherence except in a relatively small number of cases (Table 1), whereas no apparent WPC was instead detected for the α_2, α_3 and α_4 Gaussian amplitudes.

In summary, the synchronism between the oscillations of quantitative shape features of the LDF pulse and the rhythm of the respiratory function has been investigated in this study. The presented results indicate that A_d shows a strong degree of phase coherence with the breathing function, which confirms the hypothesis of a significant coupling between the latter and the diastolic contour of the perfusion pulse and, in turn, with the reflection waves arising in the circulatory tree.

Therefore, this method may represent a novel valuable approach for assessing the physiological couplings between the oscillations which characterize the cardiovascular system, and their potential deterioration with ageing and/or pathological conditions. Indeed, a decrease of the respiratory modulation of the cardiac activity has been revealed in the elderly by several authors [2, 3], who have suggested a progressive loss of stability of the normal respiratory-sinus
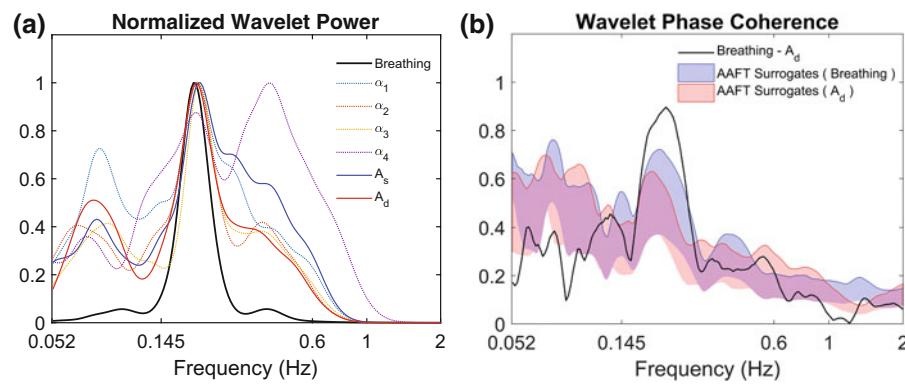
Fig. 3 a Time-averaged normalized WT power spectra of the model-derived shape features, showing a peak in correspondence of the respiratory rhythm. **b** Sample WPC between breathing and A_d. The upper thick colored lines depict the significance thresholds, $T_{C_{\phi,surr}}(w_k)$, while the lower boundary of the shaded areas corresponds to the mean surrogate WPC (Color figure online)

Table 1 Wavelet phase coherence analysis: results

Feature	Coherence	Median	IQR
A_d	17/21 subjects	0.78	(0.63, 0.83)
A_s	6/21 subjects	0.62	(0.64, 0.66)
α_1	8/21 subjects	0.65	(0.67, 0.69)

arrhythmia. Future work will deal with the acquisition and analysis of a wider set of signals and, furthermore, with the physiological interpretation of the proposed morphological features and their relationship with the respiratory dynamics.

References

1. Stefanovska, A., Bračič, M., Kvernmo, H. B.: Wavelet analysis of oscillations in the peripheral blood circulation measured by laser Doppler technique. IEEE Transactions on Biomedical Engineering 46, pp. 1230–1239 (1999). https://doi.org/10.1109/10.790500

2. Iatsenko, D., Bernjak, A., Stankovski, T., Shiogai, Y., Owen-Lynch, P. J., Clarkson, P. B. M., McClintock, P. V. E., Stefanovska, A.: Evolution of cardiorespiratory interactions with age, Philosophical Transactions A 371, (2013). https://doi.org/10.1098/rsta.2011.0622

3. Stankovski, T., McClintock, P. V. E., Stefanovska, A.: Cardiorespiratory coupling functions, synchronization and ageing. In: Cardiovascular Oscillations (ESGCO), 8th Conference of the European Study Group on Cardiovascular Oscillations, pp. 181–182, IEEE (2014). https://doi.org/10.1109/esgco.2014.6847579

4. Bandrivskyy, A., Bernjak, A., McClintock, P. V. E., Stefanovska, A.: Wavelet phase coherence analysis: application to skin temperature and blood flow, Cardiovascular Engineering 4, pp. 89–93 (2004). https://doi.org/10.1023/b:care.0000025126.63253.43

5. Chalacheva, P., Khoo, M. C.: Modeling of deep breath vasoconstriction reflex, In: EMBC, 37th Annual International Conference of the IEEE, pp. 7792–7795, IEEE (2015). https://doi.org/10.1109/embc.2015.7320199

6. Alastruey, J., Passerini, T., Formaggia, L., Peiró, J.: Physical determining factors of the arterial pulse waveform: theoretical analysis and calculation using the 1-D formulation. Journal of Engineering Mathematics 77, pp. 19–37 (2012). https://doi.org/10.1007/s10665-012-9555-z

7. Baruch, M. C., Warburton, D. E. R., Bredin, S. S. D., Cote, A., Gerdt, D. W., Adkins, C. M.: Pulse Decomposition Analysis of the digital arterial pulse during hemorrhage simulation. Nonlinear Biomedical Physics 5 (2011). https://doi.org/10.1186/1753-4631-5-1

8. Couceiro, R., Carvalho, P., Paiva, R. P., Henriques, J., Quintal, I., Antunes, M., Muehlsteff, J., Eickholt, C., Brinkmeyer, C., Kelm, M., Meyer, C.: Assessment of cardiovascular function from multi-Gaussian fitting of a finger photoplethysmogram. Physiological Measurement 36, pp. 1801–1825 (2015). https://doi.org/10.1088/0967-3334/36/9/1801

9. Sorelli, M., Perrella, A., Bocchi, L.: Cardiac pulse waves modeling and analysis in laser Doppler perfusion signals of the skin microcirculation. In: CMBEBIH, Proceedings of the International Conference on Medical and Biological Engineering, pp. 20–25, Springer (2017). https://doi.org/10.1007/978-981-10-4166-2_4

10. Sheppard, L. W., Vuksanović, V., McClintock, P. V. E., Stefanovska, A.: Oscillatory dynamics of vasoconstriction and vasodilation identified by time-localized phase coherence, Physics in Medicine and Biology 56, pp. 3583–3601 (2011). https://doi.org/10.1088/0031-9155/56/12/009

11. Tankanag, A. V., Grinevich, A. A., Kirilina, T. V., Krasnikov, G. V., Piskunova, G. M., Chemeris, N. K.: Wavelet phase coherence analysis of the skin blood flow oscillations in human, Microvascular Research 95, pp. 53–59 (2004). https://doi.org/10.1016/j.mvr.2014.07.003

12. Sheppard, L. W., Stefanovska, A., McClintock, P. V. E.: Testing for time-localized coherence in bivariate data, Physical Review E 85, (2012). https://doi.org/10.1103/physreve.85.046205

13. Schreiber, T., Schmitz, A.: Surrogate time series, Physica D: Nonlinear Phenomena 142, pp. 346–382 (2000). https://doi.org/10.1016/s0167-2789(00)00043-9

Selection of Entropy-Measure Parameters for Force Plate-Based Human Balance Evaluation

Luis Montesinos, Rossana Castaldo, and Leandro Pecchia

Abstract

Human balance is commonly evaluated through the center of pressure (COP) displacement measured with a force plate, producing 2D time-series that represent COP trajectories in the anteroposterior and mediolateral directions. Entropy measures have been previously used to quantify the regularity of those time-series in different groups and/or experimental conditions. However, these measures are computed using multiple input parameters, the selection of which has been scarcely investigated within this context. This study aimed to investigate the behavior of COP time-series entropy measures using different parameters values, in order to inform their selection. Specifically, we investigated Approximate Entropy (ApEn) and Sample Entropy (SampEn), which are very sensitive to their input parameters: m (embedding dimension), r (tolerance) and N (length of data). A dataset containing COP time-series for 159 subjects with no physical disabilities was used. As a case study, subjects were grouped in young adults (age < 60, n = 85), and older adults (age $\geq$ 60) with (n = 18) and without (n = 56) history of falls. ApEn and SampEn were computed for $m = \{2, 3\}$ and $r = \{0.1, 0.15, 0.2, 0.25, 0.3, 0.35, 0.4, 0.45, 0.5\}$ with a fixed data length (N = 1200 points). ApEn and SampEn values were compared between groups using one-way ANOVA. Our results suggest that ApEn and SampEn are able to discriminate with ease between young and older adults for a wide range of m and r values. However, the selection becomes critical for the discrimination between non-fallers and fallers. An $m = 2$ and $r = \{0.4, 0.45\}$ are suggested in this case.

Keywords

Entropy • Balance • Posturography

1 Introduction

Human balance is the result of a complex process which relies on the adequate integration of several physiological systems (i.e. visual, vestibular, somatosensory and musculoskeletal) [1]. Age-related disabilities and certain illnesses may affect one or more of those systems, potentially producing impaired balance and increasing the risk of falling [2]. Therefore, the characterization of human balance is of paramount importance for researchers and clinicians alike.

The most common measurement technique of body balance is static posturography (a.k.a. stabilography), i.e. the measure of the center of pressure (COP) displacement during quiet standing. The COP is the point location of the vertical ground reaction force vector. It is typically acquired with a force plate which outputs 2D time-series representing its trajectory in the anterior-posterior (AP) and medial-lateral (ML) directions. Subsequently, various measures are computed to characterize COP excursions and to investigate differences between groups and/or testing conditions. Linear and frequency measures have been extensively used for this purpose (e.g. total length, range in the AP/ML direction, mean and median frequencies of the time-series) [3–5].

More recently, nonlinear measures such as Approximate Entropy (ApEn) and Sample Entropy (SampEn) have been used to quantify the regularity or predictability within COP time-series in different groups or testing conditions [6–13]. Broadly speaking, ApEn and SampEn measure the likelihood that subseries of length m (from a time-series of length N) that are similar within a tolerance range given by

L. Montesinos (✉) · R. Castaldo · L. Pecchia
University of Warwick, CV4 7AL Coventry, UK
e-mail: l.montesinos-silva@warwick.ac.uk

R. Castaldo
e-mail: r.castaldo@warwick.ac.uk

L. Pecchia
e-mail: l.pecchia@warwick.ac.uk

L. Montesinos
Tecnologico de Monterrey, Campus Ciudad de Mexico, 14380
Mexico City, Mexico

$\pm r$ times the standard deviation of the time-series, remain similar for subseries of length $m + 1$. A regular/predictable time-series (e.g. a signal containing patterns) produce relatively small entropy values, whereas a less predictable process (e.g. random noise) produce higher entropy values [14, 15]. The appropriate selection of parameters m (embedding dimension), r (similarity criterion) and N (data length) is critical; yet it has been scarcely investigated in COP time-series analysis.

This study aimed (1) to determine the adequate choice of input parameters m and r on the computation of ApEn and SampEn on the analysis of COP time-series; and (2) to determine the ability of ApEn and SampEn to discriminate between groups of young adults, and older adults with and without history of falls.

2 Methods

2.1 Data Set Description

A public data set of human balance evaluations was used in this study [16]. This dataset contains posturography data for 163 subjects, recorded while the subjects were standing still for 60 s in four different conditions: with eyes open on a firm surface, with eyes open on a foam mat, with eyes closed on a firm surface, and with eyes closed on a foam mat. Three trials per condition were recorded, producing 1930 trials in total (26 trials from 5 subjects were excluded). During these trials, 3D force (Fx, Fy, Fz) and moment (Mx, My, Mz) data were recorded at a sampling frequency of 100 Hz using a force plate. Subsequently, these data were smoothed using a 4th order zero lag Butterworth low-pass filter with a cut-off frequency of 10 Hz and were used to compute the center of pressure in the anterior-posterior and medial-lateral directions (COPx and COPy, respectively). Additionally, the dataset contains subjects' basic demographic, anthropometric, and health status data (e.g. age, height, weight, morbidities and disabilities), as well as other qualitative evaluations related to balance, fear of falling, physical activity and cognitive function. A detailed description of the protocol and resulting data set can be found in [16].

2.2 Data Processing

Firstly, COP time-series were downsampled with a factor of 5 to achieve an effective frequency of 20 Hz, which resulted in time-series with a length of $N = 1200$ data points (20 Hz $\times$ 60 s). This operation was performed in order to introduce a time lag of 5 for the computation of ApEn and SampEn (i.e. including every 5th point of the original time-series in their computation). This procedure has been applied in previous studies in order to reduce redundancy while preserving essential information [6, 7, 11, 13].

Subsequently, Approximate Entropy (ApEn) and Sample Entropy (SampEn) were computed for each COP time-series using all possible combinations of $m = \{2, 3\}$ and $r = \{0.1, 0.15, 0.2, 0.25, 0.3, 0.35, 0.4, 0.45, 0.5\}$. A detailed description of the algorithms used to compute ApEn and SampEn can be found in [14, 15].

2.3 Data Analysis

Firstly, subjects were classified in three groups based on their age and history of falls in the past 12 months (falls 12 m): young adults (Y: age < 60), older adults non-fallers (NF: age $\geq$ 60 and falls 12 m = 0) and older adults fallers (F: age $\geq$ 60 and falls 12 m $\geq$ 1). Subjects with physical disabilities were excluded from all groups, thus were not considered in the analysis. Subsequently, a one-way analysis of variance (ANOVA) was performed on basic demographic and anthropometric variables (i.e. age, height, weight and body mass index) to discard potential confounders, particularly in the investigation of differences in entropy values between the NF and F groups.

Finally, mean and standard deviation for each group were estimated for the ApEn and SampEn measures previously computed. The statistical significance of the differences in mean ApEn and SampEn values between groups was investigated by means of a one-way ANOVA. A p-value < 0.05 was taken as evidence of statistically significant differences between groups. Due to space constraints, only the results for anterior-posterior COP component are shown in this paper.

The scripts for data processing and analysis were written in MATLAB R2016b.

3 Results
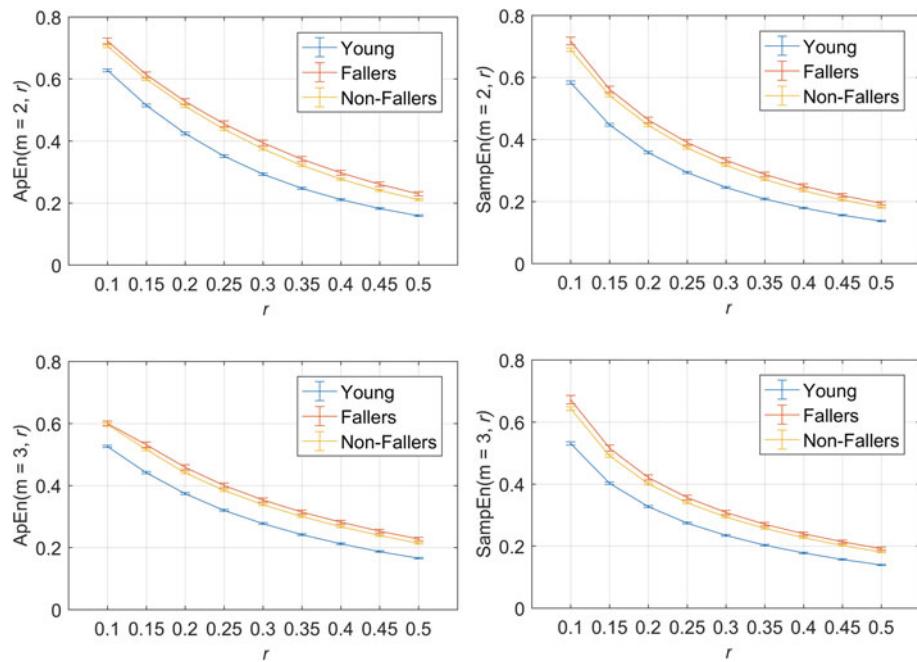
Four subjects were discarded from the study due to physical disabilities (namely, poliomyelitis and cerebral palsy), leaving 159 subjects (115 females, 44 males) for the analysis: 85 subjects were classified as young adults (Y), 56 as older adults non-fallers (NF) and 18 as older adults fallers (F). Table 1 shows mean (standard deviation) by group for basic demographic and anthropometric variables: age, height, weight and body mass index (BMI). Moreover, it shows the p-values obtained from a one-way ANOVA test. Importantly, no significant differences were found between groups NF and F, suggesting homogeneity between them with regards to age and basic anthropometric variables (thus discarding them as potential confounders).

Figure 1 shows the mean and standard error of the mean by group for ApEn and SampEn values computed for

Table 1 Subjects' basic demographic and anthropometric variables: mean (standard deviation) by group and p-values for a one-way ANOVA test

Variable	Young (Y)	Non-fallers (NF)	Fallers (F)	Y versus NF	Y versus F	NF versus F
Age, years	27.72 (7.78)	71.54 (6.35)	71.20 (7.12)	**<0.001**	**<0.001**	0.984
Height (cm)	166.81 (8.75)	157.77 (8.73)	155.19 (6.16)	**<0.001**	**<0.001**	0.502
Weight (kg)	61.62 (7.73)	63.96 (8.43)	60.01 (8.10)	0.207	0.718	0.163
BMI (kg/m^2)	22.20 (2.82)	25.71 (2.97)	24.88 (2.84)	**<0.001**	**<0.001**	0.540

Fig. 1 Approximate Entropy (left) and Sample Entropy (right) for $m = \{2, 3\}$ and $r = \{0.1, 0.15, 0.2, 0.25, 0.3, 0.35, 0.4, 0.45, 0.5\}$. Error bars represent the standard error of the mean

$m = \{2, 3\}$ and $r = \{0.1, 0.15, 0.2, 0.25, 0.3, 0.35, 0.4, 0.45, 0.5\}$. Lower mean entropies are observed for Y group compared to the NF/F groups for all combinations of m and r. The one-way ANOVA test revealed that those differences were statistically significant with a p-value < 0.001 in all cases (thus not shown in this paper). Moreover, lower mean entropies can be observed for the NF group compared to the F group for all combinations of m and r. However, statistical testing revealed significant differences only for:

- ApEn($m = 2$, $r = \{0.35, 0.4, 0.45\}$) and ApEn($m = 3$, $r = 0.5$)
- SampEn($m = 2$, $r = \{0.4, 0.45, 0.5\}$) and SampEn ($m = 3$, $r = \{0.15, 0.2\}$).

Tables 2 and 3 show mean (standard deviation) by group for ApEn and SampEn, respectively, as well as p-values from the test of differences between NF and F.

4 Discussion and Conclusions

The use of ApEn and SampEn to characterize the regularity of COP trajectories is an emerging practice in human balance research. While previous studies have achieved promising results regarding the use of those entropy measures to discriminate between groups and/or testing conditions, the adequate selection of input parameter values has been scarcely investigated. This study aimed (1) to determine correct input parameters for the computation of ApEn and SampEn for the analysis of COP time-series; and (2) to investigate the ability of ApEn and SampEn to discriminate between groups of young adults, and older adults with and without history of falls.

Overall, the results confirm that the selection of input parameters for the computation of entropy measures for COP time-series is a very critical for the discrimination between experimental groups. Certainly, our results suggest that

Table 2 Approximate entropy: mean and standard deviation (SD) by group and p-value for a one-way ANOVA test

r	Young (Y)		Non-fallers (NF)		Fallers (F)		NF versus F
	Mean	SD	Mean	SD	Mean	SD	p
m = 2							
0.1	0.628	0.129	0.705	0.108	0.723	0.138	0.178
0.15	0.515	0.134	0.599	0.104	0.613	0.131	0.298
0.2	0.424	0.136	0.512	0.110	0.527	0.133	0.280
0.25	0.351	0.131	0.438	0.113	0.455	0.133	0.176
0.3	0.293	0.121	0.374	0.110	0.394	0.129	0.093
0.35	0.247	0.109	0.321	0.104	0.341	0.122	**0.049**
0.4	0.211	0.098	0.277	0.096	0.297	0.113	**0.024**
0.45	0.182	0.087	0.241	0.087	0.260	0.104	**0.014**
0.5	0.159	0.077	0.211	0.079	0.229	0.094	0.009
m = 3							
0.1	0.526	0.109	0.597	0.094	0.600	0.114	0.939
0.15	0.441	0.113	0.516	0.103	0.531	0.128	0.170
0.2	0.374	0.106	0.441	0.093	0.459	0.117	0.080
0.25	0.320	0.099	0.384	0.085	0.400	0.107	0.073
0.3	0.277	0.094	0.338	0.081	0.353	0.099	0.088
0.35	0.242	0.089	0.300	0.078	0.314	0.094	0.084
0.4	0.212	0.084	0.267	0.075	0.282	0.089	0.064
0.45	0.187	0.078	0.239	0.072	0.253	0.084	0.057
0.5	0.166	0.073	0.214	0.068	0.228	0.079	**0.043**

Table 3 Sample entropy: mean and standard deviation (SD) by group and p-value for a one-way ANOVA test

r	Young (Y)		Non-fallers (NF)		Fallers (F)		NF versus F
	Mean	SD	Mean	SD	Mean	SD	p
m = 2							
0.1	0.583	0.158	0.689	0.140	0.718	0.179	0.051
0.15	0.447	0.136	0.542	0.116	0.562	0.146	0.125
0.2	0.358	0.124	0.445	0.109	0.463	0.133	0.149
0.25	0.294	0.113	0.373	0.102	0.390	0.123	0.116
0.3	0.245	0.101	0.316	0.095	0.333	0.114	0.082
0.35	0.208	0.090	0.271	0.087	0.288	0.104	0.058
0.4	0.179	0.080	0.235	0.079	0.250	0.095	**0.040**
0.45	0.156	0.071	0.205	0.071	0.220	0.085	**0.030**
0.5	0.137	0.063	0.181	0.064	0.194	0.077	**0.025**
m = 3							
0.1	0.531	0.163	0.643	0.156	0.672	0.199	0.064
0.15	0.403	0.125	0.491	0.120	0.515	0.152	**0.037**
0.2	0.327	0.106	0.401	0.098	0.421	0.124	**0.041**
0.25	0.274	0.094	0.339	0.085	0.356	0.107	0.051
0.3	0.234	0.085	0.294	0.077	0.308	0.096	0.069
0.35	0.203	0.078	0.257	0.071	0.270	0.087	0.073
0.4	0.178	0.071	0.227	0.066	0.240	0.080	0.066
0.45	0.157	0.066	0.202	0.062	0.214	0.074	0.061
0.5	0.139	0.060	0.181	0.058	0.192	0.069	0.053

ApEn and SampEn are able to discriminate with ease between two highly heterogeneous groups, e.g. young adults and older adults, for a wide range of m and r values. However, the choice of parameter values becomes crucial for the discrimination between groups that are closer to each other; e.g. older-adult non-fallers and older-adult fallers. Our current findings suggest that using combinations of $m = 2$ and $r = \{0.4, 0.45\}$ allows both ApEn and SampEn to discriminate between the latter.

Future studies should determine whether these entropy measures have a higher discriminative power under specific balance testing conditions (e.g. eyes open versus eyes closed) and whether it remains for shorter data lengths (e.g. $N = 600$).

Conflict of Interest Statement The authors declare that they have no conflict of interest.

References

1. Winter DA (1995) Human balance and posture control during standing and walking. Gait Posture 3:193–214
2. Kannus P, Sievänen H, Palvanen M, Järvinen T, Parkkari J (2005) Prevention of falls and consequent injuries in elderly people. The Lancet 366:1885–1893
3. Duarte M, Freitas SM (2010) Revision of posturography based on force plate for balance evaluation. Braz J Phys Ther 14:183–192
4. Visser JE, Carpenter MG, van der Kooij H, Bloem BR (2008) The clinical utility of posturography. Clin Neurophysiol 119:2424–2436. https://doi.org/10.1016/j.clinph.2008.07.220
5. Paillard T, Noé F (2015) Techniques and Methods for Testing the Postural Function in Healthy and Pathological Subjects. BioMed Res Int 2015:1–15. https://doi.org/10.1155/2015/891390
6. Sabatini AM (2000) Analysis of postural sway using entropy measures of signal complexity. Med Biol Eng Comput 38:617–624
7. Cavanaugh JT, Mercer VS, Stergiou N (2007) Approximate entropy detects the effect of a secondary cognitive task on postural control in healthy young adults: a methodological report. J NeuroEngineering Rehabil 4:42. https://doi.org/10.1186/1743-0003-4-42
8. Donker SF, Roerdink M, Greven AJ, Beek PJ (2007) Regularity of center-of-pressure trajectories depends on the amount of attention invested in postural control. Exp Brain Res 181:1–11. https://doi.org/10.1007/s00221-007-0905-4
9. Santarcangelo EL, Scattina E, Carli G, Balocchi R, Macerata A, Manzoni D (2009) Modulation of the postural effects of cognitive load by hypnotizability. Exp Brain Res 194:323–328. https://doi.org/10.1007/s00221-009-1740-6
10. Stins JF, Michielsen ME, Roerdink M, Beek PJ (2009) Sway regularity reflects attentional involvement in postural control: Effects of expertise, vision and cognition. Gait Posture 30:106–109. https://doi.org/10.1016/j.gaitpost.2009.04.001
11. Borg FG, Lax\a aback G (2010) Entropy of balance-some recent results. J Neuroengineering Rehabil 7:38
12. Hansen C, Wei Q, Shieh J-S, Fourcade P, Isableu B, Majed L (2017) Sample Entropy, Univariate, and Multivariate Multi-Scale Entropy in Comparison with Classical Postural Sway Parameters in Young Healthy Adults. Front Hum Neurosci 11. https://doi.org/10.3389/fnhum.2017.00206
13. Vassimon-Barroso V de, Catai AM, Buto MSDS, Porta A, Takahashi ACDM (2017) Linear and nonlinear analysis of postural control in frailty syndrome. Braz J Phys Ther 21:184–191. https://doi.org/10.1016/j.bjpt.2017.03.015
14. Pincus SM, Gladstone IM, Ehrenkranz RA (1991) A regularity statistic for medical data analysis. J Clin Monit Comput 7:335–345
15. Richman JS, Moorman JR (2000) Physiological time-series analysis using approximate entropy and sample entropy. Am J Physiol-Heart Circ Physiol 278:H2039–H2049
16. Santos DA, Duarte M (2016) A public data set of human balance evaluations. PeerJ 4:e2648. https://doi.org/10.7717/peerj.2648

Assessment of Similarity Between Finger and Wrist Photoplethysmography According to the Light Wavelength

Sangjin Han and Hangsik Shin

Abstract

The purpose of this paper is to investigate optimal measurement site of wrist PPG by comparing wrist PPG with conventional finger PPG in terms of pulse quality index (PQI). PPGs are obtained from left index finger and five specific sites around the wrist during 40 s with multiple wavelengths; green (530 nm) and infrared (960 nm). To evaluate the PQI, we calculated PQI using existing PQI metrics such as perfusion index (PI), zero crossing rate (ZCR) in every pulse of PPG. As a result, in PQI_{PI}, significant differences $(P < 0.05)$ were found between finger PPG and wrist PPG in all measuring position. On the other hand, in PQI_{zcr}, no significant differences were founded in all measuring site on wrist in case of infrared PPG.

Keywords

Photoplethysmography • Pulse quality index
Wearable photoplethysmography • Wrist band
Wrist photoplethysmography

1 Introduction

1.1 Wearable Phytoplehysmography

Developing information and communication technology, digital healthcare, a new healthcare paradigm mainly based on the ubiquitous bio-signal measurement technology without spatiotemporal restriction, is wide-spreaded. Moreover, various wearable systems and devices have been developed for acquiring bio-signals in daily life, especially, these technology is often specified as 'wearable healthcare'.

S. Han · H. Shin (✉)
Department of Biomedical Engineering, Chonnam National University, 50, Daehak-ro Yeosu, Gwangju, Jeollanam-do 59626, Republic of Korea
e-mail: hangsik.shin@jnu.ac.kr

The wrist band is one of the popular form-factor in wearable healthcare due to its high usability and convenience [1]. In most cases, heart beat based on optical sensing or activity based on initial sensing have been commonly measured on wearable platform because photoplethysmography (PPG) for heart beat measurement and accelerometry for activity measurement have simple hardware structure, and they are easy to implement. Though the need of measuring bio-signal on wrist has increased, there are less validation results of PPG measurement on wrist. In other words, we use wrist-type heartbeat monitoring devices in our daily lives, but optimal measurement schemes about measuring site, sensor placement or optical characteristics are still covered in veil. Therefore, it is necessary to find that optimal signal measurement condition by systemic approaches. The purpose of this paper is to investigate optimal measurement site of wrist PPG by comparing wrist PPG with conventional finger PPG in terms of pulse quality index (PQI). PQI is a kind of quality index for signal reliability assessment based on pulse morphology. Thus, we expected that the PQI could be an index for detecting optimal signal measurement site in wrist PPG. Therefore, we calculated PQI in finger and multi-site wrist PPG and investigated the difference between the PQI of finger PPG and the PQI of wrist PPG as an assessment criteria of the similarity finger PPG and wrist PPG.

1.2 Measurement Technique of Photoplethysmography

PPG is a non-invasive measurement technique that measures changes in the volume of blood vessels under the skin tissue. PPG are easily used in wearable devices because they have the advantages of non-stimulation, continuous monitoring and relatively simple system configuration [2]. Generally, PPG is measured at the terminal of the body, such as the finger tip, toe or earlobe. PPG is known to be used for obtaining subject's cardiovascular system information such as heart rate, oxygen saturation (SpO_2) and breathing.

Usually, PPG is measured using red light or infrared light, but because of the anatomical structure and optical tissue characteristics of the wrist are different from finger, which is widely used site in measuring conventional PPG, green light is used in most of commercialized devices when measuring PPG at the wrist [3]. Therefore, if we want to use wrist PPG as a surrogate of finger PPG, it is necessary to understand the difference in wrist PPG measurement such as absorption coefficient, anatomical structure or influence of measuring site. In this study, we will compare signal quality of PPG according to the measuring site and wavelength to investigate optimal position with specific wavelength in wrist PPG measurement.

2 Methodology

2.1 Multiwavelength Optical Sensor

In experiment, we use a house-made sensor module with green (530 nm) and infrared (960 nm) LEDs for measuring PPG. Four LEDs of each wavelength were placed on circle with 4.8 mm radius to maintain the uniform distance between all LEDs and photodetector (PD). Totally, 8 LEDs were used for multiwavelength PPG sensor module.

2.2 Measurement Sites of Wrist PPG

PPG is measured from subject's left index finger and from five specific measuring sites on wrist in sitting position. Here, five measuring site of wrist is defined as center of ventral (CV), radial artery (R), ventral ulnar artery (VU), center of dorsal (CD) and dorsal radial vein (DR). The site of CV and CD were selected by considering general wearable condition of wrist band, and other measuring sites are selected according to the location of blood vessels. At every measuring site, signal was recorded for 40 s with 500 Hz sampling frequency.

2.3 Pulse Quality Index

To emphasize a important feature of the cardiac activity from the acquired signal, we used band pass filter with 2–5 Hz passband. Filtered signal was divided into individual beats after beat detection. Then PQI was calculated in every beat. As a PQI metric, perfusion index-based PQI (PQI_{PI}) and zero crossing rate-based PQI (PQI_{zcr}) were used. The PQI_{PI} was calculated by using detected peaks. And the PQI_{zcr} was calculated after removing DC component of PPG waveform by highpass filtering.

Perfusion index-based PQI (PQI_{PI})

Perfusion index (PI), which indicates the ratio of the pulsatile and non-pulsatile component of the tissue under the skin, is a frequently used index in evaluating the signal quality of PPG waveform. Therefore, in several literature [4, 5], PI is regarded as one of the PQI evaluation technique, thus PI sometimes represented as PQI_{PI}. PQI_{PI} is defined as the ratio of the AC to DC component of the PPG waveform, and it can be calculate using following equation, Eq. (1) [6]:

$$PQI_{PI} = (y_{max} - y_{min})/y_{\min} \tag{1}$$

where y_{max} and y_{min} are maximum systolic peak and baseline of the single beats after filtering.

Zero crossing rate based PQI (PQI_{zcr})

PQI_{zcr} is the rate of sign-changes in the processed signal, that is, the rate at which the signal changes from positive to negative or back [7], which is defined in Eq. (2).

$$PQI_{zcr} = 1/N \sum_{n=1}^{N} \Gamma\{y < 0\} \tag{2}$$

where y is the filtered PPG signal of length N, and the indicator function, $\Gamma\{A\}$, is 1 if its argument A is true and 0 otherwise (Fig. 1).

3 Result

To quantify the similarities between the finger PPG and the wrist PPG, PQI difference between finger and wrist PPG is calculated. Table 1 shows mean and standard deviation of PQIs at each measuring site. In Table 1, we can find that the PQI_{PI} and PQI_{zcr} are different according to the wavelength and the measuring site. In statistical validation, we performed Kolmogorov-smirnov test for checking a distribution within group and confirmed that all groups haven't a normal
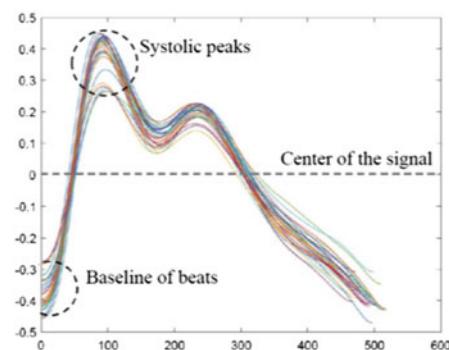
Fig. 1 Accumulated beats from PPG measured on finger tip
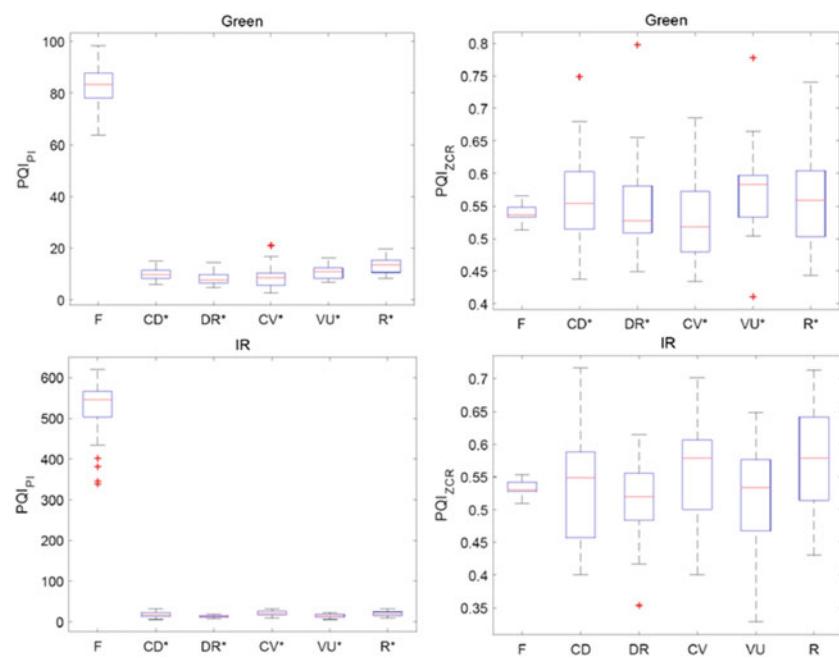
Table 1 Stastistical values of PQIs of the different wavelengths and measuring sites (N: number of beats, *P < 0.05)

Light source	Green (530 nm)		Infrared (960 nm)	
PQI metric	PQI_{PI}	PQI_{zcr}	PQI_{PI}	PQI_{zcr}
Finger (N = 30)	82.56 ± 7.31	0.54 ± 0.01	521 ± 73.09	0.53 ± 0.01
CD (N = 27)	9.84 ± 2.4	0.54 ± 0.07*	18.39 ± 6.78*	0.53 ± 0.08
DR (N = 25)	7.69 ± 2.28*	0.53 ± 0.7*	12.84 ± 2.82*	0.49 ± 0.06
CV (N = 28)	7.76 ± 3.82*	0.51 ± 0.06*	20.12 ± 5.51*	0.54 ± 0.08
VU (N = 27)	10.59 ± 2.5*	0.54 ± 0.07*	14.37 ± 4.37*	0.48 ± 0.08
R (N = 24)	13.03 ± 3.15*	0.55 ± 0.07*	18.55 ± 5.73*	0.57 ± 0.08

distribution. Then, we used paired *wilcoxon*-test to validate whether there is significant difference or not in between measuring sites. As a result, wrist PQI_{PI} was significantly different (P < 0.05) compared with finger PQI_{PI} in all measuring sites regardless of the wavelength. The difference was minimized on R and on CV compared with finger in green light-based PQI_{PI} and IR-based PQI_{PI}, respectively. In terms of PQI_{zcr}, minimum difference between wrist PPG and finger PPG was found on DR with green light, however, significant difference was not found in IR-based PQI_{zcr} regardless of measuring site. In the comparison of PQIs by wavelength, IR-based PQI_{PI} is significantly (P < 0.05) higher than green light-based PQI_{PI} in all measurement sites. This result implies that PPG peaks can be detected easier by using IR light than using green light (Fig. 2).

4 Discussion and Conclusion

In this study, we measured finger PPG and wrist PPG using multi-wavelength optical sensor, and calculated signal quality of PPG in terms of PQI_{PI} and PQI_{zcr} to investigate the similarity of between PPGs measured at finger and at five specific site around wrist. Result of this study conducted by PQI assessment suggests that, in wrist PPG measurement, radial artery or center of ventral site shows better signal quality and that infrared is more suitable than green light. This study has following limitations; first, wrist PPGs were not recorded simultaneously, and it could cause the error in comparing PQI value because the non-stationary characteristic of physiological signal. Moreover, in this study, we

Fig. 2 Boxplot of PQIs according to the measuring site and wavelength (*P < 0.05)

only use two PQI metrics for evaluation. Therefore, in further study, we will compare the simultaneously measured PPGs, and use additional PQI metrics to evaluate quality of signals for more reliable result.

References

1. Z. Zhang, P. Zhouyue and L. Benyuan, "TROIKA: A general framework for heart rate monitoring using wrist-type photoplethysmographic signals during intensive physical exercise," IEEE Transactions on Biomedical Engineering, vol. 62, no. 2, pp. 522–531, 2015

2. J. Allen, "Photoplethysmography and its application in clinical physiological measurement," Physiological measurement vol. 28, no. 3: R1, 2007

3. V. Vizbara, "Comparison of green, blue and infrared light in wrist and forehead photoplethysmography," Biomedical Engineering, vol. 17, no. 1, 2013

4. G. Hartmut Gehring, M. Holger, and S. Peter, "The effects of motion artifact and low perfusion on the performance of a new generation of pulse oximeters in volunteers undergoing hypoxemia," Respiratory Care, vol. 47, no. 1, pp. 48–60, 2002

5. M. Cannesson, B. Delannoy, A. Morand, P. Rosamel, Y. Attof, O. Bastein and J.-J. Lehot, "Does the pleth variability index indicate the respiratory-induced variation in the plethysmogram and arterial pressure waveforms?," Anesthesia & Analgesia, vol. 106, no. 4, pp. 1189–1194, 2008

6. M. Elgendi, "Optimal Signal Quality Index for Photoplethysmogram Signals," Bioengineering, vol. 3, no. 4, pp. 21, 2016

7. C.H. Chen, "Signal Processing Handbook," CRC Press: New York, NY, USA, 1988

EEG Coherence Analysis in Subjects After Rehabilitation from Stroke with Motor Imagery

L. C. P. da Silva, C. C. S. C. Paz, A. M. F. L. Miranda de Sá,
and C. J. Tierra-Criollo

Abstract

Stroke is caused by a lack of blood supply in a particular region of the brain that may be a consequence of clot formation or rupture of the blood vessel. It presents high incidence, generating permanent neurological sequelae, which leads to motor impairment and functional limitations. It is necessary to identify techniques of motor rehabilitation that favour the cortical reorganization and the functional recovery of affected individuals. Motor imagery (MI) is a technique used in motor rehabilitation of individuals with motor deficit, defined as mental simulation of movements without movement actually occurring. MI activates the same cortical regions as the execution of the movement, especially the motor area and the somatosensory cortex. The objective of this study was to investigate changes in cortical activity related to MI rehabilitation (during 1 month—three session/week) in hemiparetic individuals after stroke. EEG signals from eight post-stroke individuals were registered one week before MI rehabilitation (BMI) and 1 month after rehabilitation (*Follow-up*), during motor task execution (MOV) and motor task imagination (IMG). Magnitude squared of coherence (MSC) was evaluated, using 50 epochs of the EEG signal considered without artefact. The delta band presented the highest MSC values in both conditions (MOV and IMG), mainly in frontal and central regions. Only two volunteers presented MSC values in the *Follow-up* period higher than in the period before mental rehabilitation, mainly on electrodes F3 (p = 0.04), C3 (p = 0.036) and F4 (p = 0.02).

1 Introduction

Stroke affects about 15 million people annually, with one-third of individuals showing some sort of permanent neurological sequelae. This disease presents high incidence and prevalence, generating sequels that lead to motor impairment and functional limitations. Due to the clinical relevance of this condition, it is necessary to identify motor rehabilitation techniques that improve cortical reorganization and functional recovery of these individuals [1, 2]. Motor imagery (MI) is one of these techniques for rehabilitation after stroke [3].

The definition of MI is a mental simulation of movements without actual movement [3]. MI promotes activation of motor and somatosensory cortex areas, which are the same cortical regions activated during movement [4]. Studies considered 1st person MI (MI kinesthetic) an important therapeutic tool in motor recovery of post-stroke individuals, mainly due to hemiparesis, which affects active movement, making it difficult for motor rehabilitation [2, 5].

Electroencephalography (EEG) signals are used in the evaluation of sensory and cognitive processes. One of the main methods of electrophysiological analysis is the identification of process-related or event-related cortical activation by EEG signal analysis. Magnitude-Squared Coherence is a technique used in the analysis of somatosensory responses in individuals without neurological dysfunctions [6]. The MSC evaluates the linear dependence between the harmonic components of the stimulus (or motor task) and the brain response. In post-stroke individuals, cortical patterns have been poorly evaluated, requiring further studies to

L. C. P. da Silva · A. M. F. L.Miranda de Sá (✉)
C. J. Tierra-Criollo
LAPIS/PEB – COPPE/UFRJ, Rio de Janeiro, Brazil
e-mail: amflms@peb.ufrj.br

L. C. P. da Silva
e-mail: coutinhol@peb.ufrj.br

C. J. Tierra-Criollo
e-mail: carjulio@peb.ufrj.br

C. C. S. C.Paz
Department of Physical Therapy, UNB, Brasília, Brazil
e-mail: clarissacardoso@unb.br

understand how and to what degree the MI influences the brain electrical activity of these individuals [5].

The objective of this study was to investigate changes in cortical activity based on MSC of EEG signals related to MI rehabilitation in hemiparetic individuals after stroke.

2 Methodology

2.1 Volunteers

The EEG signals of post-stroke individuals were recorded following the protocol approved by the Ethics Committee of the Federal University of Minas Gerais (ETIC 467/08). Signal analysis was realized at the Laboratory of Signal Processing and Medical Imaging (LAPIS) at the Federal University of Rio de Janeiro.

The sample consisted of nine volunteers (5 women) with mean age of 42.2 ± 12.2 years (between 23 and 54 years) and injury time ranging from 7 to 24 months (mean of 13 ± 6.5 months), with 5 right-handed individuals. Inclusion criteria: age between 20 and 60 years; diagnosis of unilateral stroke for more than 6 months; participation in a physiotherapy program for strengthening and stretching the muscles of the paretic upper limb since the acute phase of the stroke; commitment of its dominant side; without cognitive deficit (score > 18 in Mini Mental Health Examination—MESM); capability to perform active flexion of at least $10°$ from the neutral wrist, metacarpophalangeal and interphalangeal position of the thumb [2]. Participants did not use any medication that would interfere with the EEG signal. Exclusion criteria: Difficulty in performing motor imagery, identified by score ≤ 4 in the questions of the revised motor imagination questionnaire (MIQ-RS) (Gregg et al. 2007).

Motor rehabilitation consisted of conventional physiotherapeutic intervention (CPI) associated with MI. A physical therapy practitioner performed CPI in post stroke subjects for 4 weeks (30 min per session, 3 times per week). The CPI emphasized stretching of the flexor muscles and strengthening of the flexor and extensor muscles of the shoulder, elbow and wrist, in addition to the scapular muscles. The IM tasks were in first-person perspective (where the individual imagines to perform the movements) and selected according to the individual's goal, being specific to each one. For example, individual #1 focused on picking glass and can (1st week), manipulating objects (2nd week), using cutlery (3rd week) and combing hair (4th week), while individual #9 focused on opening and closing jars to direct, to use cutlery and to button clothes and shoes in the first, second, third and fourth weeks, respectively. The intensity of the tasks was progressive, starting with simpler tasks and evolving to more complex tasks, focusing on the reach and grasp of certain objects [2]. Further details of the rehabilitation process can be found at [2].

Data acquisition. The experiment started with volunteers positioned in a comfortable armchair, with supported upper limbs. EEG signals acquired in two periods: a week before MR (BMR) and 1 month after MR (*Follow-up*). At each recording session, there were collected: (1) 15 min of spontaneous EEG; (2) 15 min of grasping movement in dominant hand (MOV) and (3) 15 min of grasping MI in dominant hand (IMG). EEG signal was recorded at 17 electrodes placed according to the international 10–20 system. A biological signal amplifier (BrainNET BNT-36) was used, presenting bandpass filter between 0.1 and 100 Hz, notch filter at 60 and 600 Hz sampling frequency.

The EEG signal was recorded using a protocol similar to that in Santos Filho et al. (2009). The red LED was triggered 4 s before the motor task, remaining until the beginning of the task. The yellow LED was activated 3 s after the red LED was, remaining on for 1 s until the motor task start. The LEDs had different functions in the protocol: the red LED was used to focus the attention of the participant in the procedure and the yellow LED indicated preparation for task. After the 4-s interval, both LEDs were turned off indicating the order of accomplishment of the task. Individuals performed the task after the shutdown of both LEDs.
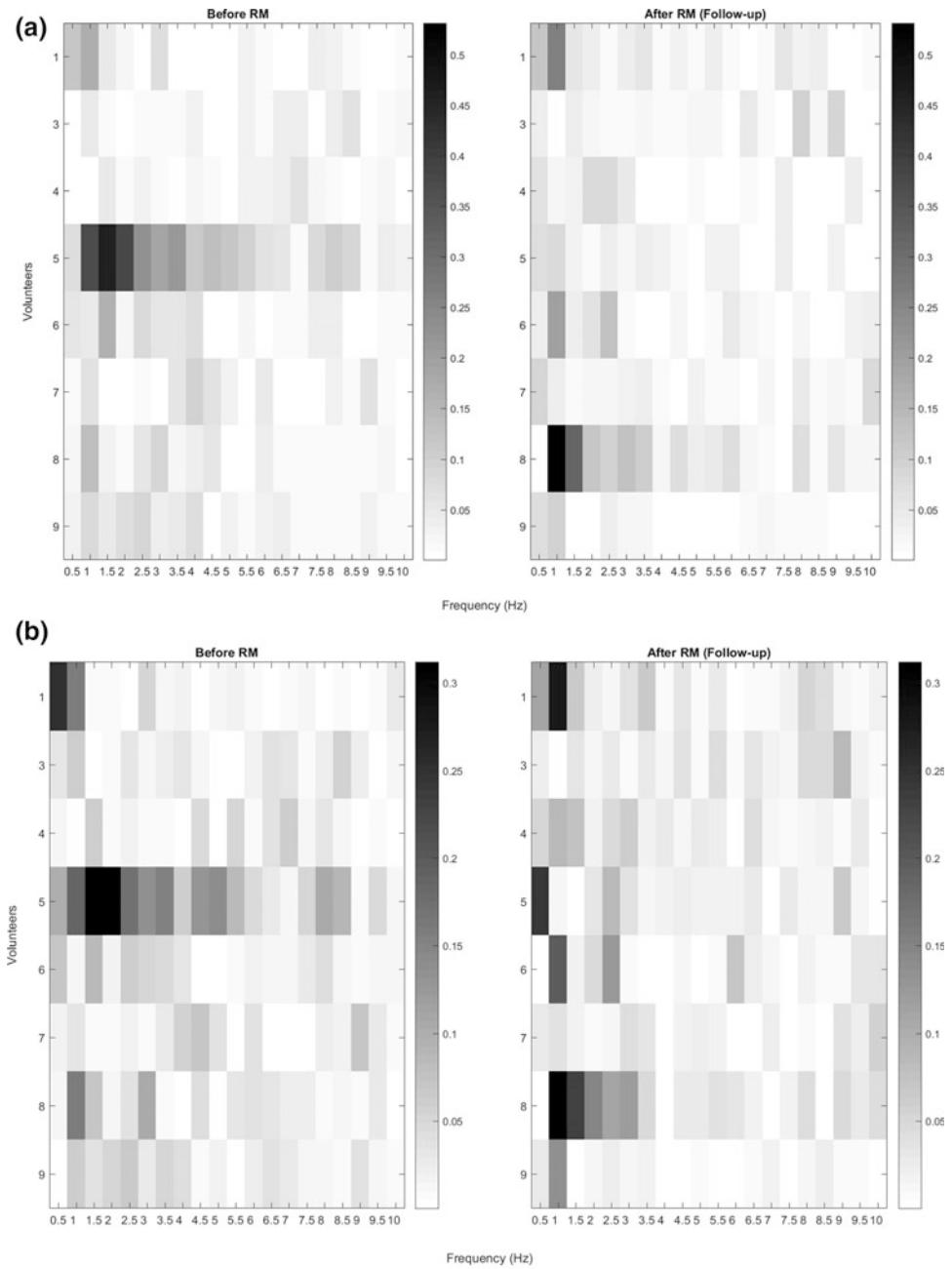
EEG signals were filtered with a 2nd-order *Butterworth* bandpass (0.1–40 Hz) and segmented into 14-s epochs (−4 to 10 s), synchronized with the motor task execution (t = 0 s). The interval (−1 and 3 s) was selected, where the response related to the motor task would be expected [6]. Epochs considered to have artefacts (visually identified) were rejected. Finally, Magnitude-Squared Coherence (MSC) was estimated for each volunteer in both conditions MOV and IMG. EEG signal from one of the individuals was excluded because it was highly contaminated by artefacts. For statistical analysis, the Wilcoxon test was used to compare the BMR and *Follow-up* periods for each volunteer, both in the MOV and IMG conditions, considered as statistically significant values of p < 0.05.

Magnitude-Squared Coherence (MSC). Technique proposed to test for the presence of evoked responses in EEG signal [6, 7]. Coherence between two signals $x(n)$ and $y(n)$ is defined as the cross-correlation spectrum between these signals and quantifies the linear dependence between their harmonic components. Assuming $x(n)$ to be the EEG signal registered from the scalp and $y(n)$ identical in all epochs of these signal (i.e. an intermittent stimulation or given task), MSC can be estimated as:

$$MSC(f) = \frac{\left| \sum_{i=1}^{M} X_i(f) \right|^2}{M \sum_{i=1}^{M} |X_i(f)|^2} \tag{1}$$

where $X_i(f)$ is the Discrete Fourier Transform (DFT) of the i-th epoch of $x(n)$ and M, the number of epochs in the signal.

For the case of lack of coherence between the signals $x(n)$ and $y(n)$ (null hypothesis), MSC follows a beta distribution with the following parameters [8]:

$$MSC(f) \sim \beta(1, M - 1) \quad (2)$$
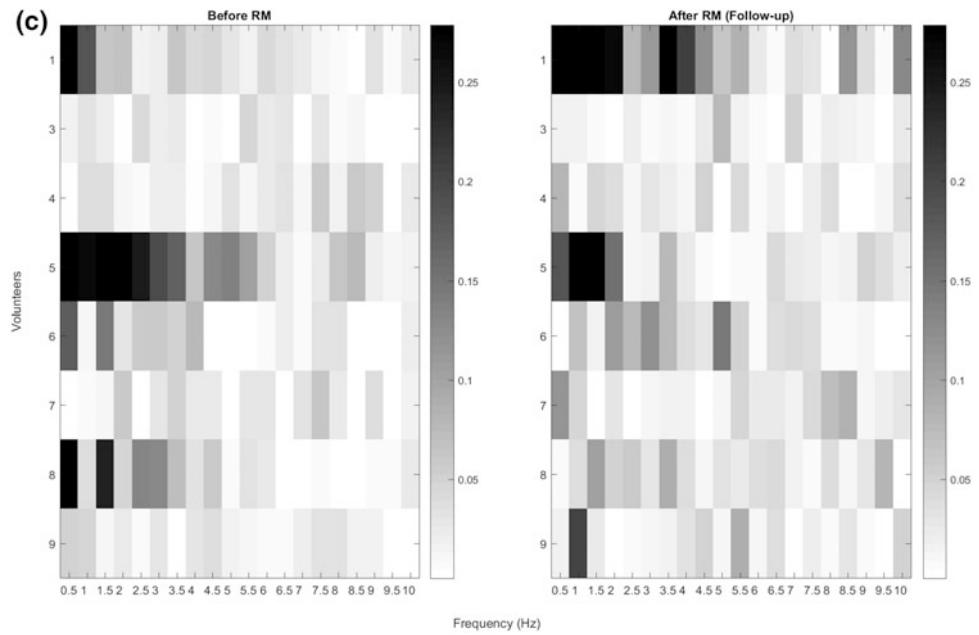
where $\beta_{(1,M-1)}$ is the standard beta distribution with parameters 1 and $M - 1$. The critical value of MSC for a significance level α, considering the null hypothesis test for the absence of stimulus, is calculated by [8]:

$$MSC_{crit} = 1 - \alpha^{\frac{1}{M-1}} \quad (3)$$

In the absence of response to the event, MSC tends asymptotically to 0 when M tends to infinity. At frequency f, the presence of synchronized response to the event is expected for $MSC(f) > MSC_{crit}$.

3 Results

The number of epochs without artefacts was 50 ($M = 50$), leading to MSC_{crit} equal to 0.0593 (Eq. 3). The delta band (<4 Hz) presented higher MSC values, especially in frontal and central cortical regions in both conditions, MOV and

Fig. 1 (continued)

Table 1 Summary of volunteers that presented differences between periods *Follow-up* and BMR

Volunteer	Condition	Comparison	Channel	*p*-value
#1	MOV	*Follow-up* > BMR	F4	0.02
	IMG	*Follow-up* > BMR	C3	0.036
#8	IMG	*Follow-up* > BMR	F3	0.04
#5	MOV	BMR > *Follow-up*	C3	0.015
	MOV	BMR > *Follow-up*	F3	0.025
	IMG	BMR > *Follow-up*	F3	0.01

IMG (Fig. 1). In this band, the *Follow-up* and BMR periods were compared, for each volunteer, in each conditions MOV and IMG.

Three volunteers (#1, #5 and #8) presented statistically significant differences (p < 0.05) in MSC values between periods *Follow-up* and BMR (Table 1). In volunteers #1 and #8, F3 (Fig. 1a) and C3 (Fig. 1b) electrodes in condition IMG and F4 electrode in condition MOV (Fig. 1c) had higher MSC values in period *Follow-up*. On the other hand, volunteer #5 exhibited opposite behaviour (i.e., BMR > *Follow-up*) in C3 and F3 electrodes in condition MOV and F3 electrode in condition IMG.

4   Discussion

Acute influence of motor rehabilitation with MI on cortical activity has been the focus of recent studies [9, 10]. In volunteers without neurological dysfunctions, Paz et al. [10] found increased values of MSC in the delta band (≤ 4 Hz) after MI training [10]. The delta band is related to the

accomplishment of mental tasks, mainly to the difficulty of the task and to the inhibition of stimuli unrelated to the performance of the task [11]. The increase in neural efficiency and the favoring of motor learning are related to higher values of coherence in the delta band [10].

Our work showed that, during the execution of the motor task in individuals after stroke, the delta band had the highest MSC values. The initial hypothesis, in relation to the conditions studied (BMR and *Follow-up*), was that the effect of training with MI would be similar to that occurring in normal volunteers (MSC in *Follow-up* > MSC in BMR) [10].

Post-stroke volunteers showed motor improvement after MI training, assessed by the Minnesota Manual Dexterity Test (MMDT) and gait speed [2]. However, despite motor improvement, the MSC of 5 volunteers did not present statistically significant differences between BMR and *Follow-up* conditions. Only Two volunteers presented MSC values in the *Follow-up* period higher than in BMR (p < 0.05) at F3, C3 and F4 electrodes. The other volunteer presented opposite results, exhibiting higher values in the BMR period (p < 0.05), at C3 and F3 electrodes.

In the volunteers who presented difference, the results suggest that the motor task in *Follow-up* was more synchronized to the stimulus than in BMR because it presented higher MSC values. However, in most individuals, there was no difference between the periods studied. It is speculated that the brain region and extension of the lesion may influence this aspect. Damage to the sensorimotor cortex due to a cortical stroke can result in a reduction in the size of the sensorimotor cortex and thus to the processing capacity of the cortex, as assessed by neurophysiological markers [12].

Future studies will be needed to improve results. Evaluation of individuals (e.g., laterality and stroke extension), in addition to EEG signal analysis by other processing techniques (e.g., Event-related EEG synchronization and desynchronization and Entropy) will be important for understanding the physiological mechanisms involved.

Conflicts of Interest The authors declare that they have no conflict of interest. And the Federal University of Minas Gerais (UFMG) Ethics Committee approved the project.

References

1. WHO Stroke, Cerebrovascular accident, http://www.who.int/topics/cerebrovascular_accident/en/, last accessed 2016/11/15.
2. Paz, CCSC., Teixeira-Salmela, LF., Tierra- Criollo, CJ. The addition of functional task-oriented mental practice to conventional physical therapy improves motor skills in daily functions after stroke. Braz J Phys Ther. 17(6):564–571 (2013).
3. Jeannerod, M. The representing brain: Neural correlates of motor intention and imagery. Behavioral and Brain Sciences, 17 (2):187–245 (1994).
4. Jackson PL et al. Potential role of mental Practice using motor imagery in neurologic rehabilitation. Archives of Physical Medicine Rehabilitation. 82:1133–41 (2001).
5. Sharma, N., Pomeroy, V.M., Baron, J.C. Motor Imagery A Backdoor to the Motor System After Stroke? Stroke 37:1941–1952 (2006).
6. Santos Filho et al. Magnitude Squared of Coherence to Detect Imaginary Movement. EURASIP Journal on Advances in Signal Processing. 2009(1): 1–10 (2009).
7. Gregg et al. The MIQ-RS: A Suitable Option for Examining Movement Imagery Ability. eCAM Advance Access (2007).
8. Miranda de Sá, AM., Felix, LB., Infantosi AF. A matrix-based algorithm for estimating multiple coherence of a periodic signal and its application to the multichannel EEG during sensory stimulation. IEEE Trans Biomed Eng. 51(7):1140–6 (2004).
9. Page et al. Cortical plasticity following motor skill learning during mental practice in stroke. Neurorehabil Neural Repair. 23(4):382–8 (2009).
10. Paz CCSC et al. A influência aguda da prática mental sobre as oscilações corticais delta – um estudo piloto. Rev. Bras. Eng. Biom., 28(4): 375–386 (2012).
11. Harmony T et al. Do specific EEG frequencies indicate different processes during mental calculation? Neuroscience Letters. 266:25–8 (1999).
12. Campfens at al. Poor motor function is associated with reduced sensory processing after stroke. Experimental Brain Research. 233 (4):1339–1349 (2015).

Optimal Window for the Estimation of Very Low Frequency Content in Heart Rate Variability Analysis

B. Becerra-Luna, R. Martínez-Memije, R. Cartas-Rosado,
O. Infante-Vázquez, J. C. Sánchez-García, and G. Sánchez-Pérez

Abstract

The spectral analysis of heart rate variability (HRV) is an accepted method for assessing the autonomic control of the cardiovascular system. The electrocardiographic recordings used to extract the time interval between consecutive R waves (RR intervals or tachogram) should last 5 min or 24 h, according to the guidelines published in 1996 by the European Heart Journal (TASK FORCE). The three frequency bands recognized are the VLF (0.003–0.04 Hz), the LF (0.04–0.15 Hz) and the HF (0.15–0.4 Hz), which are associated with cardiovascular modulatory mechanisms. Given that the estimation of VLF in 5 min recordings is unreliable and that in some circumstances (orthostatism, controlled breathing, etc.) it is not possible to obtain 24 h recordings, it becomes necessary to consider other window sizes in order to estimate it with greater certainty. To show how the size of the window affects the estimation of the power spectral density, synthetic signals were evaluated using the Welch periodogram, comparing the power and spectral resolution obtained with conventional 5 min windows versus results obtained with windows that ranged from 300 to 3000 s in steps of 300 s, plus an additional one of 4000 s. Noise-free signals were generated, contaminated with White Gaussian Noise and mounted on a linear trend, to approximate the conditions of a real tachogram. The results suggest that the optimal size of the analysis window is 50 min, decreasing the power estimation error of the VLF band from 24.91 to 8.06%, increasing the spectral resolution and increasing the confidence in the evaluation of the three frequency bands defined for the HRV, especially for the VLF. These results suggest an alternative analysis for recordings with duration less than 24 h but that require evaluating the VLF, as in the HRV recordings of patients during their haemodialysis session.

Keywords

Heart rate variability • Very low frequency
ECG

1 Introduction

Heart rate is the most commonly noninvasive parameter used in the analysis and evaluation of cardiac activity [1]. The variations in this parameter, obtained by measuring the time interval between consecutive heart beats (tachogram), give rise to the concept of Heart Rate Variability (HRV), whose analysis is widely used to characterize, indirectly, the functions of the autonomous nervous system [2].

The HRV can be evaluated in several ways, being the time-domain and frequency-domain methods, the classical analyses performed. The spectral analysis of HRV is a widely accepted approach to quantitatively assess the functions of the autonomous nervous system [3]. One way to do this assessment is through the analysis of the Power Spectral Density (PSD) to estimate how the power of the tachogram (i.e., variance) distributes along its frequency content.

The methods used for calculating the PSD can generally be classified as parametric and non-parametric [4], each one having its advantages and disadvantages. Non-parametric methods estimate the PSD directly from the signal itself, and although it is directly proportional to the power of the frequency components of the process, they depend strongly on the length of the analyzed signal, which in turn influences the spectral resolution obtained. In 1996, the European

B. Becerra-Luna (✉) · R. Martínez-Memije · O. Infante-Vázquez
Electromechanical Instrumentation Department, Instituto Nacional de Cardiología "Ignacio Chávez", Mexico City, Mexico
e-mail: bbecerral0500@alumno.ipn.mx;
pacorro28144@hotmail.com

B. Becerra-Luna · J. C. Sánchez-García · G. Sánchez-Pérez
Posgraduate Studies and Research Department-ESIME
Culhuacan, Instituto Politécnico Nacional, Mexico City, Mexico

R. Cartas-Rosado
Electromechanical Instrumentation Department, CONACYT, Mexico City, Mexico

Society of Cardiology and the North American Society of Pacing and Electrophysiology published jointly a document with guidelines aimed to standardize terms, classifications and methods for the measurement of the HRV. The directives issued in this document, establish two lengths of time for the analysis of the HRV; the first one is defined by a 5 min window and is known as short-term recording; and the second one, contained within a 24 h window is known as long-term recording [1].

The spectral analysis performed in short-time recordings allows the identification of three frequency intervals identified as very low frequency (VLF), low frequency (LF) and high frequency (HF) bands, with spectral components within frequency ranges of 0.003 Hz–0.04 Hz, 0.04 Hz–0.15 Hz and 0.15 Hz–0.4 Hz, respectively. In long-term recordings, it is also distinguishable an ultra-low frequency (ULF) band with spectral components below 0.003 Hz, in addition to the three bands previously described. While the power distribution and the central frequency of the LF and HF bands obtained from the spectral analysis of the HRV vary according to the modulation of the sympathetic and parasympathetic systems, the VLF content of the HRV is not associated to a single physiological phenomenon, but several studies show that this is associated with the modulation of the sympathetic system, temperature and renin-angiotensin system [5].

According to the guidelines for the assessment of the HRV, a minimum of 5 min length ECG is required for the extraction of the VLF content; however, sometimes there are certain problems that impede the acquisition of 5 min or 24 h ECG recordings, such as controlled breathing, postural changes, etc. Also, the preprocessing of tachograms negatively affects the spectral estimation of the VLF components, given that it removes baseline and trends that might contribute to the VLF spectrum. Another difficulty that appears when short time recordings are processed is related to the minimum lower frequency that can be estimated with certainty. Taking into account that tachograms are multi-frequency signals, and assuming stationarity within an analysis window of 300 s (5 min, as recommended by the task force [1]), the spectral estimation of the whole VLF band would not be reliable because the minimum frequency obtained with certainty would be of 0.0033 Hz, which is above the lower limit of the VLF band. These drawbacks show that it is necessary to adjust the length of the analysis window.

The reliable assessment of the VLF, as part of the HRV analysis, is important in several areas of medicine, because it is believed that it could be linked to events such as long-term changes in blood pressure. The aforementioned limitations related to the spectral estimation of VLF band in short time recordings, along with the lack of stationarity in long time recordings; suggest the necessity to adapt the time length of the analysis window used for spectral estimation of the HRV, which is the objective of this work.

2 Materials and Methods

The method used in this work for the evaluation of the PSD is non-parametric, based on Fast Fourier Transform (FFT). To evaluate the influence of the time length of the analysis window on the estimation of the power spectral density, two synthetic signals formed by the sum of 3 sine waves with frequencies of 0.003 Hz, 0.1 Hz and 0.2 Hz, and amplitudes of 0.2, 0.15 and 0.1 units, respectively, plus a DC component, were generated. One of the signals was kept noiseless, while the other was contaminated with White Gaussian Noise (WGN). The generated signal-to-noise ratio (SNR) was of −4 dB. Firstly, the power spectral density of each signal was obtained with an analysis window equal to the length of the testing signals to use it as reference value for comparison purposes. Secondly, the PSD was obtained by varying the length of the analysis window from 300 s up to 3000 s in steps of 300 s in order to evaluate the error generated with respect to the reference values. An additional window of 4000 s length was included in the analysis to check for the tendency in the spectral estimation when the window increases. The power spectral density was obtained using the Welch periodogram and Hamming window with 50% of overlap. This periodogram employs the Fast Fourier Transform (FFT) for its calculation. The chosen method offers the advantage of being simple in its algorithm with high processing speed [6]. All processing was done using Matlab R2016b (MathWorks®).

2.1 Description of the Synthetic Model

The model corresponding to the synthetic signals is shown in Eq. (1), where the noise amplitude can be set to zero to create the noiseless signal. The sampling period was 0.25 s and the total time was 10,800 s. A short segment of the synthetic signals used to test this approach are plotted in Fig. 1.

$$y(t) = 0.2\sin(2\pi f_1 t) + 0.15\sin(2\pi f_2 t) + 0.1\sin(2\pi f_3 t) + DC + WGN$$
(1)

The frequencies of the three oscillatory components were chosen in correspondence to the bandwidths of interest, associated with the phenomenon of heart rate variability (HRV). White Gaussian Noise was chosen to include the whole frequency band of interest (limitation is sampling frequency) and have control over the DC level added to the
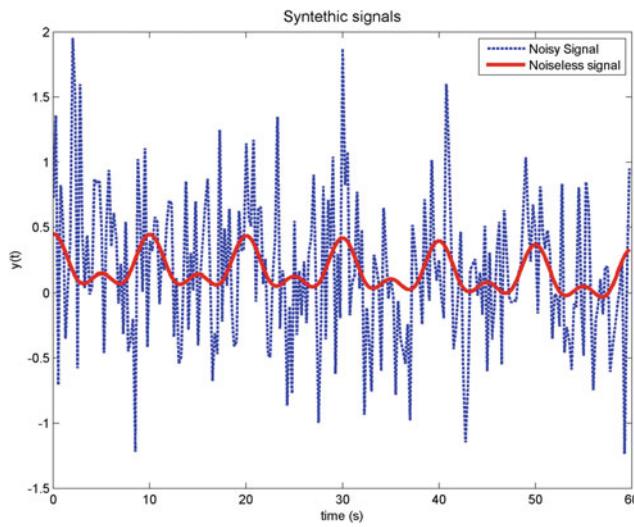
Fig. 1 The figure shows a 60 s segment of the signals used in the experiment. The plot in blue the noisy signal contaminated with WGN, the red plot is the noiseless signal

synthetic signals. For both signals (noisy and noiseless), the mean power of each band of interest was calculated according to the methodology and analysis windows described above.

3 Results

The results obtained were compared against the powers obtained in 0.003, 0.1 and 0.2 Hz using the whole signal. The percentage error was calculated according to Eq. 2.

$$\%Error = \frac{|Reference\ power - Variable\ power|}{Reference\ power} \times 100 \quad (2)$$

The errors obtained from comparing the power estimated using analysis windows of variable length against the power estimated using the entire signal are contained in Table 1 for the three bands of interest. Each test is indicated in the column Number of Window, while the corresponding time length is indicated in the column Window length. Results obtained for the noiseless synthetic signal (P Signal) show that using an analysis window of 5 min length, yields a small difference in the estimation of the PSD for the LF and HF bands, but not for the VLF band, where the difference is very high; however, the error in this band begins to decrease as the length of the analysis window increases. In contrast, the power estimated in the LF and HF bands is very close to the reference values, regardless the length of the analysis window.

For the noisy signal (N Signal), the percentage error obtained for each analysis window also shows a decreasing trend, as the results obtained for the noiseless signal, but with small bumps due to the random nature of the noise. The plot in Fig. 2a shows how the error percentage varies according to the window length for the noiseless synthetic signal. For the case of the noisy signal, the corresponding variations in error percentages are plotted in Fig. 2b.

4 Discussion

To perform an analysis of HRV using a 5 min length window leads to an incorrect spectral estimation of the VLF, in accordance with the Task Force [1]. Due to the fact that in many cases it is not possible to record long-time ECGs, and given that the analysis for the VLF band is not reliable for short-time recordings, it was proposed in this work to increase the length of the recording, as well as the analysis

Table 1 Percentage error for VLF, LF and HF bands obtained with a noiseless signal (P Signal) and signal contaminated with WGN (N signal). Windows varied from 300 to 3000 s, plus an additional one of 4000 s

Number of window	Window length (s)	% Error (VLF)		% Error (LF)		% Error (HF)	
		P signal	N signal	P signal	N signal	P signal	N signal
1	300	24.912	23.230	0.003	1.250	0.001	2.023
2	600	24.611	21.203	0.006	1.704	0.002	0.720
3	900	24.445	20.111	0.008	2.262	0.003	0.260
4	1200	24.117	18.534	0.008	3.311	0.003	0.634
5	1500	23.449	19.192	0.007	2.534	0.002	0.921
6	1800	22.279	18.190	0.005	2.700	0.001	0.204
7	2100	20.376	16.813	0.003	2.962	0.001	0.440
8	2400	17.509	14.080	0.002	2.333	0.001	0.680
9	2700	13.451	10.251	0.001	2.301	0.001	0.433
10	3000	8.061	7.735	0.001	3.332	0.001	0.620
11	4000	8.062	8.220	0.001	2.670	0.001	0.541

Fig. 2 Results obtained with a
noiseless signal and with
contaminated signal with WGN,
show how the tendency of error
decreases when the length of the
window increases

window, to 50 min. The results obtained show that it is
possible to improve the power estimation in the very low
frequency (VLF) band either for noiseless synthetic signals
and synthetic signals contaminated with WGN. The increase
in power estimation for the VLF band is due to the spectral
resolution enhancement obtained with the proposed window
length. This provides greater accuracy at locating the com-
ponents contained in the VLF band, while preserving the
powers in LF and HF bands.

5   Conclusion

The estimation of the spectral content depends strongly on
the length of the recording under analysis, and hence, on the
length of the analysis window used. In studies of HRV,
where it is important to extract the information contained in
the VLF band, in addition to the content in the LF and HF
bands, the analysis should be done in recordings of at least
50 min, according to our results. This makes feasible its use
in cases where it is not possible to have 24 h recordings, e.g.,
in ECGs recorded from patients undergoing haemodialysis
sessions [7], which last approximately from 3 to 4 h.

References

1. TaskForce of the Esc and the NASPE (1996) Heart rate variability:
   standards of measurement, physiological interpretation and clinical
   use. Eur Heart J 17:354–381
2. Sassi R, Cerutti S, Lombardi F et al (2015) Advances in heart rate
   variability signal analysis: joint position statement by the
   e-Cardiology ESC Working Group and the European Heart Rhythm
   Association co-endorsed by the Asia Pacific Heart Rhythm Society.
   Europace 17(9): 1341–1353
3. Draghici AE, Taylor JA (2016) The physiological basis and
   measurement of heart rate variability in humans. J Physiol Anthro-
   pol 35(22): 1–8
4. Stoica P, Moses R (2004) Spectral analysis of signals. Prentice Hall,
   New Jersey
5. Cavalcanti S, Severi S, Chiari L et al (1997) Autonomic nervous
   function during haemodialysis assessed by spectral analysis of
   heart-rate variability. Clin Sci 92:351–359
6. Welch PD (1967) The use of fast Fourier transform for the
   estimation of power spectra: a method based on time averaging over
   short, modified periodograms. IEEE Trans Audio Electroacoustic
   AU-15: 70–73
7. Martinez-Memije R, Meza-Campos S, Morales-Alvarez PR et al
   (2015) Heart Rate Variability during Hemodialysis in Two
   Ultrafiltration Profiles. In: Braidot A., Hadad A. (eds) VI Latin
   American Congress on Biomedical Engineering CLAIB 2014,
   Paraná, Argentina 29, 30 & 31 October 2014. IFMBE Proceedings,
   vol 49. Springer, Cham

Optimization of Algorithms for Real-Time ECG Beats Classification

Rolando González Tejeda and Maité Cañizares Falcón

Abstract

Beats classification is an essential step in the ECG signal analysis for cardiac arrhythmias detection. There are multiple alternatives to solve this problem, but these are considerably reduced when real-time restrictions are added to the analysis. The goal of this work is to expose an optimal solution based mainly on the use of voltage values of the signal in the time domain and compare it with other based on Daubechies' Wavelets analysis. Several measures are used in both feature spaces to determine the similarity of every beat to a patient's specific patterns and, after that, a method similar to clustering's algorithms is used to assign a class to each. To evaluate the performance of the proposed algorithms, ECG signal records extracted from the MIT-BIH database are used. With the method used in the analysis, we obtained *93.25%* of sensitivity and *91.43%* on premature ventricular contractions predictivity, which allow us to conclude that it is very feasible for their application in real time systems, due to their low computational cost.

Keywords

ECG • Beat classification • Real time • Cluster

1 Introduction

Cardiovascular diseases are among the main causes of mortality in the world. It has been shown that 90–95% of patients with acute myocardial infarction have an associated cardiac arrhythmia [1]. Some of the most common arrhythmias, which may warn of the possible occurrence of acute myocardial infarction, are those associated with the presence of premature ventricular contractions. Therefore, the early detection of this type of beat has great importance.

From the observation of the patient's electrocardiographic (ECG) signal, it can be determined if arrhythmias are present or not. That's why, the use of computational tools that automate this signal monitoring, is essential for this purpose and have great boom in recent times. If, in addition, the processing is done in real time, quick assistance and decision-making to protect the patient's life is guaranteed.

Before classifying the beats, the execution of two phases in the ECG analysis is required. The first phase is the pre-processing of the signal. This consists mainly of the application of filters in order to eliminate noise from it. The second phase is the QRS complex detection, where the information necessary to compare the beat is found.

Starting from the information obtained from these phases, several methods are used for the classification of beats. Some use supervised learning techniques [2]; that base their operation on the extraction of the distinctive features of a particular type of beat from the training with records of ECG signal. Other methods consist of unsupervised learning such as Kmeans or Hierarchical clustering [3, 4], which group beats with similar patterns. Algorithms based on Hidden Markov Model [5] have also been used because the order and existence of P, Q, R, S and T waves can be determinant in beat's classification. Similarly, principal component analysis (PCA) [4] has been used to reduce the dimensions of the ECG signal feature vector, in order to find the most relevant. Recently, the use of wavelets to represent signals has become very frequent because of its good results in similar problems, and because it has implicit noise reduction.

Due to the high computational cost, many of these algorithms, like the case of PCA, are discarded. Others, such as Kmeans or Hierarchical clusters, cannot be applied in the way they were originally conceived, since they require the entire dataset for the clustering and the aim of this work is to perform the classification in real time.

R. G. Tejeda (✉) · M. C. Falcón
ICID-Digital Medical Technologies, 1704, 202 St., Havana, Cuba
e-mail: rolo.gonzaleztejeda@gmail.com

2 Materials and Methods

2.1 Pre-processing and QRS Complex Detection

Pre-processing consists mainly in the reduction of the noise present in the ECG signal. The interference of the power line with a frequency of 60 Hz is eliminated using a second order Notch filter. The noise coming from the movement and bad contact of the electrodes for different causes is eliminated using a third order Butterworth filter.

In this work, the article Pan and Tompkins [6] was used for the QRS complex detection. After filtering, the signal is differentiated to provide the QRS complex slope information. We use a five-point derivative (1). Later the signal is squared point by point. This make all data points positive and does nonlinear amplification of the output of derivative emphasizing the higher frequencies. Finally, the last N values obtained corresponding to 150 ms are taken to calculate the moving-window integration (2). The QRS complex is detected when the integration waveform exceeds a threshold.

$$\hat{x}(nT) = (1/8T)[-x(nT - 2T) - 2x(nT - T) \\ + 2x(nT + T) + x(nT + 2T)] \quad (1)$$

$$y(nT) = 1/N \sum_{i=1}^{N} \hat{x}(nT - iT)^2 \quad (2)$$

where T is the sampling period and N is the number of samples in the width of integration window.

2.2 Discrete Wavelet Transform

Wavelets are considered a time-frequency representation of a function. From the projection of the signal in translations and expansions of functions called mother wavelets and scaling wavelets, a decomposition of the signal in several coefficients is obtained. These give a measure of the energy value of a frequency band in a time interval. For practical applications, the Discrete Wavelet Transform (DWT) is used, which consists in using a discrete set of wavelets depending on the values of scale and translation.

2.3 Features Extraction

Detection of referents peaks within the QRS complex. The features will be extrac-ted from the knowledge of R peak position or another peak (Q or S wave) within the QRS complex that will take as a reference if R peak is not present. One case that involves a complication is when there is an R' wave. In this case, R′ becomes a candidate to be recognized by the algorithm implemented as R. Figure 1 shows several cases that complicate the easy detection of the R wave. Therefore, for each QRS complex, several peaks (at most 3) are calculated, which are candidates for reference. To calculate them, the following is done:

- The detail coefficients of the Haar wavelets are calculated at scale level 3 [7], let's call it DWTHaar3. In Fig. 2 it is clearly seen how the positive maximums in the DWTHaar3 correspond to the descending portion in the ECG signal and the negative minimums to the ascending one.
- Within QRS time interval, the pair of local extrema (Max and Min) whit greatest sum of absolute values is searched in DWTHaar3. Between both extrema there will be a peak P1 in the ECG signal that must correspond to the zero crossing of the DWTHaar3. If the 1st extremum is a maximum then P1 is a local maximum, otherwise it is a local minimum.
- If adjacent to Max there is another local minimum Min′ with an approximate value to Min then between Max and Min′ there is another candidate peak P2 to be reference. In case there is a local maximum Max′ adjacent to Min, same analysis is done to know if there is a 3rd peak P3 between Min and Max′

Features. In this work we compare the results obtained from two feature spaces. The 1st are the values of the ECG

**Fig. 1** Cases where reference point detection is complex
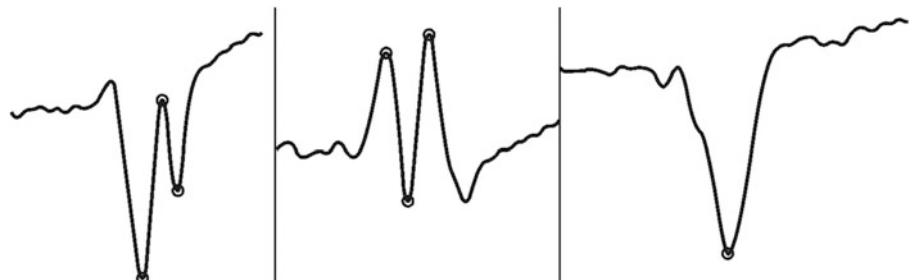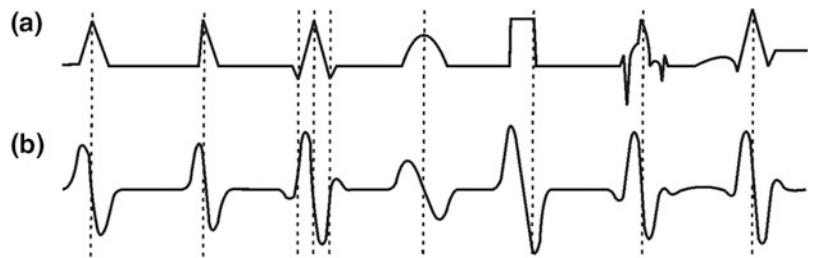
Fig. 2 **a** Different waveforms.
b DWTHaar3 function response

signal in the interval [Pn − N, Pn + N], where Pn is the reference point of the QRS complex. The 2nd are the coefficients of the second order Daubechies wavelets associated with the time interval [Pn − N, Pn + N]. The frequency bands corresponding to different decomposition levels of these wavelets with sampling frequency of 256 Hz are [8]: D1 (37.5–75 Hz); D2 (18.75–37.5 Hz); D3 (9.375–18.75 Hz); D4 (4.6875–9.375 Hz); A4 (0–4.6875 Hz). Coefficients of the levels A4, D4 and D3 are chosen because they contain the main frequency bands of QRS waves.

2.4 Clustering

To measure the distance from a beat to the centroid of a cluster, the following measures are used [4]:

- Cityblock

$$1/N \sum_{i=1}^{N} |C_i - X_i| \qquad (3)$$

- Correlation

$$\frac{\sum_{i=1}^{N} (X_i - \bar{X}) * (C_i - \bar{C})}{\sqrt{\sum_{i=1}^{N} (X_i - \bar{X})^2} * \sqrt{\sum_{i=1}^{N} (C_i - \bar{C})^2}} \qquad (4)$$

where C and X are feature vectors of a cluster and a beat respectively; $\bar{C}$ and $\bar{X}$ are their means.

The clustering stage consists of grouping the beats with similar features. When a beat is detected, it is compared to all clusters, which contain the different beat patterns of a patient. If there is no pattern similar to the beat in question, or if it is the 1st beat to be analyzed, then a new cluster is added with that beat as the only element. For this cluster, the reference point (Prc) is set as follows:

- If there is only one candidate to reference point, it is chosen.
- If there are 2, the one between the pair of local maxima in DWTHaar3 with greatest sum of absolute values is

selected. This is because the absolute value of the DWTHaar3 reaches its maximum when the slope has a greater inclination.
- If there are 3, the center peak is chosen.

To determine the similarity of a beat with a cluster one of the measures mentioned above is used. If its value exceeds a predefined threshold, then it is determined that the beat belongs to the cluster. The reference point of the analyzed beat is selected according to the features of cluster reference point. If it is a local minimum, the reference point in the beat will be a local minimum too, else it will be the local maximum. If there are two local minima or two local maxima like Prc, then the one with highest absolute value is chosen.

The clusters that have a high similarity with the current beat join in a single cluster. To calculate the centroid of this, the features vectors of all its beats are averaged.

2.5 Classification

In this work three classifications are defined for the beats: N, PVC and Q. N are the normal beats, PVC are the premature ventricular contractions, and Q are those that cannot be classified. Every cluster has associated one of this classes. Cluster containing the highest number of beats is classified as N and the rest are classified as PVC. If there are more than one cluster with the highest number of beats (e.g. when there is bigeminy, where the PVC occurs with the same frequency as normal beat), class N is given to the cluster that represents the beats with the lowest QRS width. When two or more clusters are joined, and one of them is of class N, then the resultant cluster also takes class N. A beat takes the class of the cluster to which it belongs. If it does not belong to any then it is classified as Q.

3 Results

The Massachusetts Institute of Technology (MIT) has available databases of ECG signals for public use. 32 records of this database were chosen. These were acquired through two channels, with a sampling frequency of 360 Hz. Each

Table 1 Results obtained with different algorithms

Measure	Daub. %Sen	Daub. %Pred	Volt. %Sen	Volt. %Pred
Cityblock	92.90	88.84	91.34	89.62
Correlation	93.25	91.43	88.66	93.52

record contains annotations made by specialized doctors, where they specify the classification of the beats.

To evaluate the results of the classification with this database, measures of sensitivity (5) and positive predictivity (6) were used, defined as:

$$Sen = \frac{TP}{TP + FN} * 100 \qquad (5)$$

$$Pred = \frac{TP}{TP + FP} * 100 \qquad (6)$$

TP   True Positive. A beat is correctly classified.
FN   False Negative. A beat is classified by the algorithm as negative, however, it is positive.
FP   False Positive. A beat is classified by the algorithm as positive, however, it is negative.

Tables 1 show the results obtained with the different spaces of features and measures used. As observed, the best results were obtained using Daubechies wavelets with the correlation measure.

4 Conclusions

In this paper we present a solution to the problem of classifying ECG beats in real time. The methods that gave the best results were those using the Daubechies wavelets with the correlation measure with 93.25% sensitivity and 91.43% positive predictivity. The algorithm described has a low computational cost. The application of the filters and the calculation of the DWTHaar3 require a constant number of steps for each voltage value of the ECG signal. The maximum and minimum of the DWTHaar3 is stored in memory, which also makes constant the number of operations for

peaks' selection. Calculate the cityblock and correlation measures is linear with respect to the 60 points time window centered in the reference point. Wavelets' calculation is also linear. The classification, deciding which cluster is more correlated with the annalyzed beat, has a constant cost. The implementation of this algorithm is being used in a patient's monitor based on the ARM9 architecture without problems.

Conflict of Interest The authors declare that they have no conflict of interest.

References

1. Chuang-Chien, C.; Tong-Hong, L. and Ben-Yi, L.: "Using correlation coefficient in ECG waveform for arrhythmia detection", Biomedical Engineering Applications, Basis & Communications, 17, 147–152 (2005).
2. Gaurav, K. J.; Ranbir, P: "ECG Classification with the Help of Neural Network", International Journal of Electrical and Electronics Research, 2, 42–46, (2014).
3. Peluffo-Ordoñez, D. H.: "Estudio comparativo de métodos de agrupamiento no supervisado de latidos de señales ECG", Master's Thesis, National University of Colombia, Manizales, (2009).
4. Micó, P.: "Nuevos desarrollos y aplicaciones basados en métodos estocásticos para el agrupamiento no supervisado de latidos en señales electrocardiográficas", Doctoral Thesis, Polytechnic University of Valencia, Valencia, (2005).
5. Andreao, R.; Dorizzi, B. and Boudy, J.: ECG signal analysis through hidden Markov models. IEEE Transactions on Biomedical Engineering, 53(8):1541–1549, (2006).
6. Pan, J. and Tompkins, W. J.: "A real-time QRS detection algorithm", IEEE Transactions on Biomedical Engineering, 32(3), 230–235, (1985).
7. Bensegueni, S. and Bennia, A.: "R- Peak detection using wavelet transforms technique", U.P.B, (77), 135–148, (2015).
8. Cvetkovic, D.; Übeyli, E. D. and Cosic, I.: "Wavelet transform feature extraction from human PPG, ECG, and EEG signal responses to ELF PEMF exposures: A pilot study", Digital Signal Processing, 18, 861–874, (2008).

Wave Kurtosis: A Novel, Specific Parameter for TUG-Turn Quantification

Slavka Viteckova⑩, Radim Krupicka, Patrik Kutilek, Vaclav Cejka,
Zoltan Szabo, Martina Hoskovcova, and Evzen Ruzicka

Abstract

The Timed Up and Go test (TUG) is widely used in both research and clinical settings. The most common parameter for quantification of functional decline is the duration of a performed TUG. Analysis of the turn part of the TUG could provide valuable information about functional decline. Notwithstanding, there are only a few studies that deals with the TUG turn processing. This study proposes a novelty parameter—wave kurtosis (WK) that provides quantitative metrics for describing and comparing turn patterns. The WK is designed to evaluate the shape of the signal waveform. The WK quantifies the peak of the signal, its position and tails. The TUG-turn angular rate was analysed. Intra-class correlations (ICC) of WK and the strength of a linear association between WK and established turn parameters (turn duration, peak angular rate, and mean angular rate) were calculated. The reliability of WK about the vertical axis was moderate (ICC > 0.50), while reliabilities of the frontal axis and sagittal axis varied according to the subject group. The WK about the vertical axis was moderately correlated with turn duration, mean value and peak value. Utilization of waveform parameters opens a new area of TUG turn analysis and may allow for a more sensitive determination of movement disorders or fall risk assessment. Therefore, future studies utilizing turn movement may benefit from the use of the wave kurtosis.

S. Viteckova (✉) · R. Krupicka · P. Kutilek · V. Cejka · Z. Szabo
Faculty of Biomedical Engineering, Czech Technical University in
Prague, Kladno, Czech Republic
e-mail: slavka.viteckova@fbmi.cvut.cz

M. Hoskovcova · E. Ruzicka
Department of Neurology and Centre of Clinical Neuroscience,
First Faculty of Medicine and General University Hospital in
Prague, Charles University in Prague, Prague, Czech Republic

1 Introduction

The Timed Up and Go test (TUG) provides information on functional decline and changes exhibited amongst populations with different conditions. Originally, only the time it took to perform a TUG test by a participant was assessed [1]. Beyond TUG timing, instrumented TUG allows for conducting a detailed quantitative assessment of the movement. A substantial amount of work focuses on the analysis of the gait component of a TUG. Although the turn is a challenging task and could provide valuable information for the determination of safe ambulation and functional independence [2], there is much less research which includes turn assessment. Of the parameters employed are parameters for assessing the turn duration [3–6], step-based parameters [3, 4, 6] and statistical properties of the angular rate [4, 5, 7]. While these are valuable parameters of turn assessment, they are not capable of capturing the complex properties of the turn signal, such as changes to the signal over turn time. This limitation emphasizes the need for a more complex parameter of turn quantification.

The current study presents the newly developed turn parameter—wave kurtosis (WK). The objectives were to define the WK parameter and to investigate its association with established discrete turn parameters.

2 Wave Kurtosis

An a priori analysis of the angular rate signal was conducted using qualitative observation. The results of the analysis suggest that angular rate signals when a turn is performed are stochastic non-stationary signals. The angular rate about the vertical axis is single bell shaped (Fig. 1 (left)). The angular rate about the frontal (Fig. 1 (middle)) and sagittal axis is multi-peaked (Fig. 1 (right)). The number, position and magnitude of peaks vary among subjects. Based on the observation of the signal shape, we developed a novel

parameter that we refer to as wave kurtosis (WK). This parameter is inspired by statistical central higher order moments, namely sample kurtosis (4th order moment):

$$K = \frac{\frac{1}{n}\sum_{i=1}^{n}(x_i - \mu)^2}{\left[\frac{1}{n-1}\sum_{i=1}^{n}(x_i - \mu)^2\right]^2},\tag{1}$$

$$\mu = \frac{1}{n}\sum_{i=1}^{n}x_i.\tag{2}$$

The kurtosis summarises the shape of the distribution function so that it quantifies the relative peakedness or flatness of the variable distribution. Similar to its statistical counterpart that measures the shape of distribution, wave kurtosis is a measure of the shape of the signal.

The core idea of this novel parameter calculation is that the calculation considers the signal as a distribution function. Based on knowledge of the distribution function, it is possible to infer virtual source data, i.e. a virtual random variable. Then it is possible to apply the statistical kurtosis calculation to the virtual random variable to get its statistical kurtosis, i.e. wave kurtosis of the original signal. The results describe the shape of the distribution function of the virtual random variable, which is actually the measured signal.
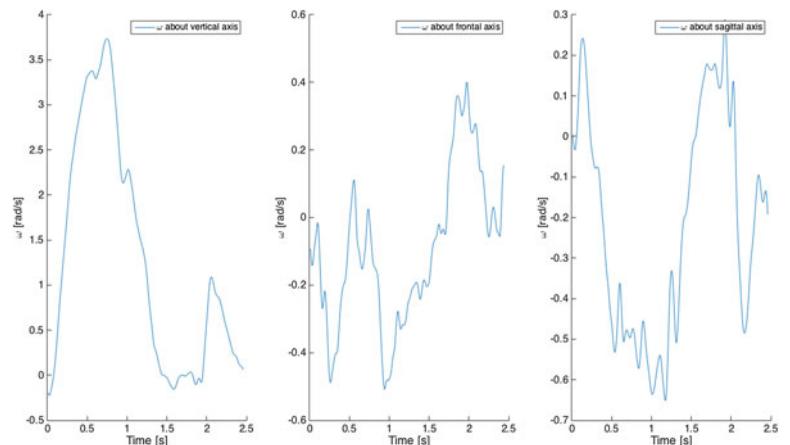
The measure of wave kurtosis utilizes statistical kurtosis to the assessment of the turn signal shape in the following manner. As the value of each signal element, ω_i, corresponds to the same number (i.e. ω_i) of i-th sample (element) in the virtual random variable, the total number of elements in the virtual random variable is calculated as a sum of the signal values:

$$m = \sum_{i=1}^{n}\omega_i,\tag{3}$$

where is the analyzed angular velocity and n is the signal length.

Then the mean of the virtual random variable is calculated:

$$\mu = \frac{\sum_{i=1}^{n}\omega_i t_i}{m},\tag{4}$$

where t is a unit-spaced vector with elements [1, 2, …, n] representing time.

Finally, the wave kurtosis value, WK, is computed:

$$WK = \frac{\frac{1}{n}\sum_{i=1}^{n}(t_i - \mu)^2\omega_i}{\left[\frac{1}{n-1}\sum_{i=1}^{n}(t_i - \mu)^2\omega_i\right]^2}.\tag{5}$$

The WK value is always positive, i.e. greater than zero.

2.1 Characteristics of Wave Kurtosis

To demonstrate responses of WK to different inputs we utilized artificially generated signals with respect to turn signals waveform characteristics, e.g. number of peaks. Figure 2 demonstrates various examples of signals characteristics via artificially generated time series data. In Fig. 2 (left), the two waves demonstrate the shift of the peak towards the beginning of turn. In this case, the offset is −30% of the signal length. Whilst the WK value for the centered peak is 220, the WK value for the shifted waveform is 191 indicating an early onset of the TUG-turn. The multipeak signal about the frontal and sagittal axis is represented by the sinusoidal wave in the artificial time series (Fig. 2 (right)). The two waves have periods 0.07 and 0.3, the corresponding WK are 176 and 180.

3 Methods

3.1 Participants

We included 38 Parkinson's disease (PD) patients (29 males, 9 females), mean age 66.3 years (SD 8.9). The control group included 20 older adult volunteers (12 males, 8 females), mean age 64.5 (±8.0) years without history or signs of balance

Fig. 1 Angular movement of the turn
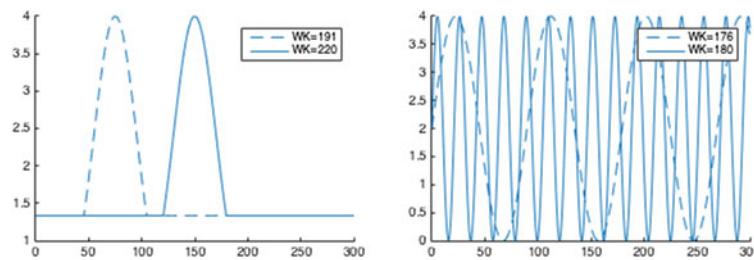
Fig. 2 Different characteristics of the turn signal. Left: different peak locations; Right: sin waves with different period

problems or any neuropsychiatric disorders. A written consent was obtained prior to participation in the study, and all procedures were approved by the Ethics Committee of the General University Hospital in Prague, Czech Republic, and therefore performed in accordance with the ethical standards established in the 1964 Declaration of Helsinki.

3.2 Data Acquisition

All subjects performed an instrumented extended Timed Up and Go Test [8] two times to obtain the gait and turn kinematics. All subject wore three gyro-accelerometers (MTx units, Xsens Technologies B.V.). The units were symmetrically attached on the lateral shank of each lower leg, 4 cm above the ankle joint, and the chest, 2 cm below the sternal notch. Following a standing calibration trial, subjects were observed while they rose from their chair during an ETUG, walked 7 m, turned, walked back, and sat down again.

3.3 Data Processing

Kinematic data was collected at 120 Hz. The kinematic data was low-pass filtered at 60 Hz with a zero-phase second-order Butterworth filter [5]. An automated analysis algorithm identified the sit-to-stand, gait, turning and the turn-to-sit components of the TUG [4]. From the automatic analysis, we employed a trunk angular rate signal and calculated the wave kurtosis parameter about all three axes. Additionally, established TUG-turn parameters; namely turn duration, peak angular rate, and mean angular rate, were also computed.

Positive angular velocity means the rotation direction of the axis of rotation was clockwise, while negative means a counter-clockwise rotation. It is possible to use two options to achieve only positive values. The first is to use absolute values of the signal. In this way we get angular velocity without direction information. The second option is to shift the signal above zero by its minimal value. In this way we preserve direction information, i.e. the threshold

$$T = \text{abs}(\min(\text{signal})) \qquad (6)$$

differentiates between directions. We performed further analysis for both cases, i.e. absolute values of the signal (WK_{abs}) and shifted signal (WK_{shift}).

3.4 Statistical Analysis

To evaluate the reliability of the proposed parameters, Intra-Class Correlation (ICC) among two measurements was used. Since the same subjects and the same device was used, an ICC (1, 1) was performed. Absolute agreement, ρ, and a 95% confidence interval was reported. Reliability greater than 0.90 is considered as excellent, reliability greater than 0.75 is considered as good, greater than 0.50 is moderate, and lower than 0.50 is poor.

To assess the relationship between wave kurtosis and other turn parameters, Pearson correlation coefficients were calculated. A value of $p < 0.05$ was considered significant.

Shapiro-Wilk test was used to verify the normality of WK parameters. The assumption of normal data distribution has been rejected (significance level $p = 0.05$). Therefore, non-parametric Wilcoxon rank sum test was used to compare PD patient data to control group data. The significance level was set to $p < 0.05$.

All analysis algorithms, as well as statistical evaluation of outcomes were run using MATLAB environment (MatLab R2015b, Mathworks, Inc., Natick, MA, USA).

4 Results

Both WK_{abs} and WK_{shift} of PD patients about all vertical axes showed moderate reliability (Table 1). The WK reliability of the control group was lower (Table 1). The WK_{shift} and WK_{abs} about the vertical axis showed moderate reliability ($\rho = 0.57$ and 0.64, respectively). Other WK of the control group were poor ($\rho < 0.50$).

The WK values about the vertical axis were moderately correlated for mean and peak parameters. The WK about the

Table 1 Correlation of turn parameters. Axis: v—vertical axis, f—frontal axis, s—sagittal axis. CG—control group, PD—Parkinson disease patients

	Axis	ICC (ρ)		Correlation (ρ)					
		CG	PD	CG			PD		
				Mean	Peak	Duration	Mean	Peak	Duration
WK$_{shift}$	v	0.57	0.60	0.62	0.64	−0.59	0.54	0.47	−0.54
	f	0.23	0.61	−0.09	−0.24	−0.03	0.22	−0.06	−0.28
	s	0.18	0.61	0.48	−0.22	−0.36	0.43	−0.14	−0.16
WK$_{abs}$	v	0.64	0.74	0.47	0.56	−0.50	0.63	0.60	−0.55
	f	0.43	0.74	−0.10	0.02	0.08	0.41	−0.05	−0.28
	s	0.32	0.65	0.21	−0.34	−0.19	0.44	0.08	−0.25

vertical axis was negatively correlated for duration. Other correlations vary from weak negative to weak positive.

The turn assessment via WK parameters revealed a significant difference between the control group and PD in the WK$_{abs}$ and WK$_{shift}$ of the angular rate about the vertical-axis ($p = 0.03$ and 0.04, respectively). The WK parameter about the horizontal and sagittal axes did not exhibit a statistically significant difference in any of the evaluated cases. For detailed statistical evaluation see Table 2.

5 Discussion

The first purpose of this study was to propose a parameter to turn angular rate quantification that considers the shape of the signal. We proposed the wave kurtosis parameter and demonstrated its outputs to different waveforms.

The results of the first aim of this study suggests that the novelty quantifier of the turn is reliable enough for turn assessment. Herewith, it seems to be capable of capturing the personal nature of the turn. Specifically, the WK of the angular rate about all axes showed moderate reliability.

We analysed the performance of the WK parameter on two cases of source signals. First, the signal was shifted up so that the minimal signal value equaled 0, WK$_{shift}$. Second, the absolute value of the signal was employed, WK$_{abs}$. The performance of WK$_{abs}$ and WK$_{shift}$, i.e. ICC and correlation with other parameters, were similar. Therefore, we can recommend the computation of WK parameters based on the absolute value of the turn signal as well as its shifted counterpart.

Interestingly, the ICC for both WK (WK$_{shift}$, WK$_{abs}$) about the frontal and the sagittal axis for the control group was significantly lower than for PD patients. However, the aim of the study was not to deeply investigate or interpret the results of the WK parameter relating to different subject group. Therefore, future studies should provide elucidation of WK parameters relating to different diseases.

The angular rate about the vertical axis is the characteristic component of the turn signal. It is usually a single peak signal formed predominantly by the angular velocity of the subject rotation about 180°. Lower values indicate higher values of the analysed signal, while higher values indicate lower values of the signal.

The angular rate about the frontal axis is mainly generated by backward/forward bends of the body, i.e. extension/flexion. According to a previous demonstration, lower values may indicate an earlier onset of forward leaning, i.e. earlier peak position, and higher turn rate. On the contrary, higher values represent a lower non-peak angular rate.

The angular rate about the sagittal axis is contributed by lateral bends of the body, i.e. abduction/adduction. The multistep turn strategy generates multi-peak signals by reciprocal inclinations, while the single step strategy usually results in a single peak signal. Thus, lower values are attributed to multi-step turn strategy, and higher values to a single step strategy. In the case of single step strategy, the value is influenced by non-peak angular rates - the lower the rate, the higher value.

The second aim of this study was to investigate the association between the newly proposed parameter and other turn parameters, namely turn duration, signal mean and peak values. Regardless the signal, i.e. absolute or shifted, the correlations of WK parameters were moderate. Based on the association between the variables in question, we can gather that WK introduces new point of view on TUG-turn quantification.

The approach for computing signal wave kurtosis presented here is intended for trunk turn angular rate waveform only, and would not be appropriate for assessment of discrete data derived from a turn. Based on the achieved results, parameter computations should be applied to the angular rate signal about all axes. Applications to other turn signals may not result in meaningful outcomes.

The results obtained by this novel parameter showed a discriminative ability between evaluated subjects groups.

Table 2 Discriminative ability of WK parameters between subject groups (*p*-value). Axis: v—vertical axis, f—frontal axis, s—sagittal axis. CG —control group, PD—Parkinson disease patients. *Statistically significant difference

		CG (*p*-value)		
		v	f	s
PD	WK$_{shift}$	**0.04***	0.08	0.28
	WK$_{abs}$	**0.03***	0.07	0.28

The difference in the turn maneuver of PD patients is in agreement with other works [4, 5]. The detailed analysis and interpretation of wave kurtosis parameter with regard to PD patients should be the subject of further investigation.

6 Conclusion

This paper introduced and analysed a newly proposed parameter for TUG-turn angular rate quantification. The presented parameter, referred to as wave kurtosis, is based on turn signal shape assessment. We can designate that this parameter is suitable for the evaluation of turns both in research and practice. Quantitative waveform analysis of complex turn signals may allow for more sensitive fall risk assessment or determination of movement disorders. Therefore, future studies of TUG-turn movement may benefit from the use of the wave kurtosis.

Compliance with Ethical Standards The authors declare that they have no conflict of interest.

References

1. H. A Bischoff, H. Staehelin, A. Monsch, M. Iversen, A. Weyh, M. von Dechend, R. Akos, M. Conzelmann, W. Dick, R. Theiler, Identifying a cut-off point for normal mobility: A comparison of the timed 'up and go' test in community-dwelling and institutionalised elderly women, Age Ageing. 32 (2003) 315–320.
2. J.E. Harris, J.J. Eng, D.S. Marigold, C.D. Tokuno, C.L. Louis, Relationship of Balance and Mobility to Fall Incidence in People With Chronic Stroke, Phys. Ther. 85 (2005) 150–158. https://doi.org/10.1093/ptj/85.2.150.
3. W. Dite, V. Temple, Development of a Clinical Measure of Turning for Older Adults, Am J Phys Med Rehabil. 81 (2002) 857–66; quiz 867.
4. A. Salarian, F.B. Horak, C. Zampieri, P. Carlson-Kuhta, J.G. Nutt, K. Aminian, ITUG, a sensitive and reliable measure of mobility, IEEE Trans. Neural Syst. Rehabil. Eng. 18 (2010) 303–310. https://doi.org/10.1109/tnsre.2010.2047606.
5. B.R. Greene, A. O'Donovan, R. Romero-Ortuno, L. Cogan, C.N. Scanaill, R.A. Kenny, Quantitative Falls Risk Assessment Using the Timed Up and Go Test, IEEE Trans. Biomed. Eng. 57 (2010) 2918–2926. https://doi.org/10.1109/tbme.2010.2083659.
6. C.D.C. de M. Faria, B. de Carvalho-Pinto, S. Nadeau, L.F. Teixeira-Salmela, 180° turn while walking: characterization and comparisons between subjects with and without stroke, J. Phys. Ther. Sci. 28 (2016) 2694–2699. https://doi.org/10.1589/jpts.28.2694.
7. J. Silva, I. Sousa, Instrumented timed up and go: Fall risk assessment based on inertial wearable sensors, in: 2016 IEEE Int. Symp. Med. Meas. Appl., 2016: pp. 1–6. https://doi.org/10.1109/memea.2016.7533778.
8. J. Wall, C. Bell, S. Campbell, J. Davis, The Timed Get-up-and-Go test revisited: Measurement of the component tasks, J Rehabil Res Dev. 37 (2000) 109–113.

Investigation of the Feasibility of Postoperative Pain Assessment Using Frequency Analysis of Photoplethysmogram Variability

Yoon La Yang, Hyeon Seok Seok, and Hangsik Shin

Abstract

Quantifying of pain is necessary for optimal dose of opioid. In pain quantification, there have been many attempts to analyze the photoplethysmography (PPG) waveform as a promising maker of autonomic function. In this paper, we investigate the feasibility of PPG amplitude variability (PPGV) as a novel marker of pain quantification. We derived 8 parameters related to the PPG amplitude and amplitude variability: $ACA_{baseline}$, ACA_{dia}, $PPGAV_{sys}$, $PPGAV_{dia}$, $PPGAV_{sys}/ACA_{baseline}$, $PPGAV_{sys}/ACA_{dia}$, $PPGAV_{dia}/ACA_{baseline}$ and $PPGAV_{dia}/ACA_{dia}$, and calculated frequency domain variables, TP, VLF, LF, HF, nLF, nHF and LF/HF, that have been used for heart rate variability analysis. Every parameter was derived in clinical dataset obtained before and after surgery, and a significant difference was statistically verified using paired t-test. Consequently, a significant difference ($p < 0.05$) was found in every derived variable except for most variables in $ACA_{baseline}$, ACA_{dia}, $PPGAV_{sys}$, $PPGV_{dia}$, in nHF of $PPGAV_{sys}/ACA_{baseline}$, in nHF, LF/HF of $PPGAV_{sys}/ACA_{dia}$, in nLF, nHF of $PPGAV_{dia}/ACA_{dia}$, and in nLF, nHF of $PPGAV_{dia}/ACA_{baseline}$. This result suggests that the possibility of frequency domain analysis of PPGV as a novel indicator of surgical pain quantification.

Keywords

Frequency analysis • Pain quantification
Photoplethysmography • Photoplethysmography variability

1 Introduction

Assessment of surgical pain has been attempted with difficulties because it is not easy to describe degree of pain objectively. There have been many attempts to quantify pain such as skin conductance-based method [1, 2], analgesia nociception index (ANI, Mdoloris Medical System, Lille, France) [3, 4] and surgical plethysmographic index (SPI, GE Healthcare, Chicago, USA) [5]. Skin conduction was reported to correlate significantly with a numeric rating scale (NRS) in postoperative pain [6] and ANI seems more sensitive than heart rate and systolic blood pressure to moderate nociceptive stimuli in propofol-anaesthetized patients [7]. Especially, SPI which based on continuous cardiovascular variables like heartbeat intervals (HBI) and photoplethysmography amplitude (PPGA) was evaluated as a promising index of postoperative pain assessment [8]. The result of SPI could be interpreted as changes of heart rate and blood volume with sympathetic activation [9, 10]. In this study, we consider the possibility of assessing surgical pain by analyzing PPG amplitude variability (PPGV) as another pain indicator. For this, we assumed that the PPGV has relevance with blood pressure variability (BPV), which is a method to measure systolic blood pressure and detect changes in the short or long term and estimates the physiological state via the mean of the measured blood pressure or a standard deviation [11], because blood volume could be proportionally changed with blood pressure excluding the consideration of vascular property. In analyzing PPGV, we adapted frequency domain analysis metric of heart rate variability (HRV).

Y. L. Yang · H. Shin (✉)
Interdisciplinary Program in Biomedical Engineering, Chonnam National University, Gwangju, Republic of Korea
e-mail: hangsik.shin@jnu.ac.kr

H. S. Seok · H. Shin
Department of Biomedical Engineering, Chonnam National University, Yeosu, Republic of Korea

2 Methods

2.1 Dataset

Sixty surgical patients (29 males, 31 females, 52.1 ± 11.4 years old) were enrolled to the experiment, and 58 pair of dataset was used except 2 pair of dataset which has recording error. According to the protocol, PPG data was recorded before and after surgery, and dataset recorded before and after surgery were regarded as a painless and pain dataset, respectively. Every record has 6-min length of 300 Hz sampling frequency. To calculate the area of PPG waveform, every upper and lower peak location of the PPG waveform was detected and validated by proficient researchers.

2.2 Parameter Extraction

Derived parameters were defined as the amplitude from baseline to systolic peak ($ACA_{baseline}$), the amplitude from diastolic peak to systolic peak (ACA_{dia}), the amplitude difference of adjacent systolic peaks ($PPGAV_{sys}$), the amplitude difference of adjacent diastolic peaks ($PPGAV_{dia}$), the ratio of $PPGAV_{sys}$ to $ACA_{baseline}$ ($PPGAV_{sys}/ACA_{baseline}$), the ratio of $PPGAV_{sys}$ to HPH ($PPGAV_{sys}/HPH$), the ratio of
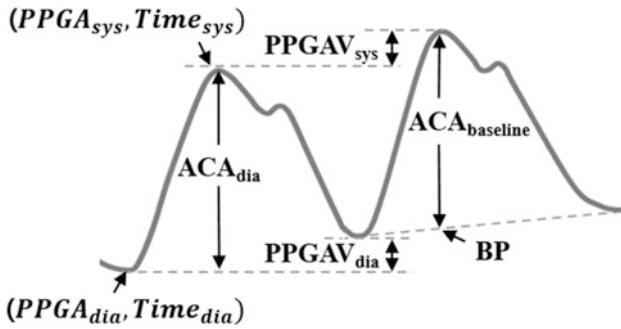
Fig. 1 PPG waveform and derived parameters

$PPGAV_{dia}$ to ACA ($PPGAV_{dia}/ACA$), and the ratio of $PPGAV_{dia}$ to HPH ($PPGAV_{dia}/HPH$). Figure 1 shows the graphical representation of parameters, and Eqs. (1)–(5) represents mathematical equation of ACA_{dia}, BP, $ACA_{baseline}$, $PPGAV_{sys}$, $PPGAV_{dia}$, respectively (see Table 1).

$$ACA_{dia} = PPGA_{sys}(k) - PPGA_{dia}(k) \tag{1}$$

$$BP(k) = \frac{PPGA_{dia}(k+1) - PPGA_{dia}(k)}{Time_{dia}(k+1) - Time_{dia}(k)} \\ \left\{ Time_{sys}(k) - Time_{dia}(k) \right\} + PPGA_{dia}(k) \tag{2}$$

$$ACA_{baseline} = PPGA_{sys}(k) - BP(k) \tag{3}$$

$$PPGAV_{sys} = PPGA_{sys}(k+1) - PPGA_{sys}(k) \tag{4}$$

$$PPGAV_{dia} = PPGA_{dia}(k+1) - PPGA_{dia}(k) \tag{5}$$

2.3 Validation

Every parameter was derived in pain and painless dataset, and it was verified whether there is significant different using paired t-test.

3 Result and Discussion

Table 2 shows that the mean, standard deviation, coefficient of variation and significance of difference of the result according to the nociceptive pain. As a result, statistical difference was not found in TP, VLF, LF, HF, nLF of $ACA_{baseline}$, TP, LF, HF, nLF of ACA_{dia}, TP, VLF, KF, HL, nHF of $PPGAV_{sys}$, TP, VLF, LF, HF, nLF, nHF of $PPGV_{dia}$, nHF of $PPGAV_{sys}/ACA_{baseline}$, nHF, LF/HF of $PPGAV_{sys}/ACA_{dia}$ and nLF, nHF of $PPGAV_{dia}/ACA_{dia}$, nLF, nHF of $PPGAV_{dia}/ACA_{baseline}$. LF component of BPV reflects sympathetic vasomotor activity which is known as Mayer wave [12–17]. Otherwise, high frequency component of BPV reflects mechanical function of hemodynamics

Table 1 Extracted parameters

No.	Parameter name	Unit	Parameter definition
1	$ACA_{baseline}$	a. u.	AC amplitude from baseline to systolic peak
2	ACA_{dia}	a. u.	AC amplitude from diastolic peak to systolic peak
3	$PPGAV_{sys}$	a. u.	Systolic PPGA variation
4	$PPGAV_{dia}$	a. u.	Diastolic PPGA variation
5	$PPGAV_{sys}/ACA_{baseline}$	n. u.	Ratio of $PPGAV_{sys}$ to $ACA_{baseline}$
6	$PPGAV_{sys}/ACA_{dia}$	n. u.	Ratio of $PPGAV_{sys}$ to ACA_{dia}
7	$PPGAV_{dia}/ACA_{baseline}$	n. u.	Ratio of $PPGAV_{dia}$ to $ACA_{baseline}$
8	$PPGAV_{dia}/ACA_{dia}$	n. u.	Ratio of $PPGAV_{dia}$ to ACA_{dia}

Table 2 Statistical changes of derived parameters

No.	Parameters		Mean (standard deviation)		Coefficient of variation		p-value
			Before	After	Before	After	
1	ACA$_{baseline}$	TP	8.75 (12.53)	8.50 (11.43)	143.16	134.50	0.348
2		VLF	1.43 (1.59)	1.20 (1.42)	110.68	118.55	0.052
3		LF	0.72 (0.60)	0.60 (0.57)	83.72	95.34	0.108
4		HF	0.44 (0.37)	0.51 (0.50)	84.42	98.49	0.990
5		nLF	13.55 (5.04)	11.92 (5.58)	37.23	46.81	0.059
6		nHF	8.42 (3.63)	9.96 (4.39)	43.11	44.08	<0.05
7		LF/HF	1.73 (0.58)	1.29 (0.58)	33.30	44.60	<0.001
8	ACA$_{dia}$	TP	9.35 (16.07)	9.16 (12.57)	171.97	137.27	0.321
9		VLF	1.48 (1.95)	1.23 (1.51)	131.85	122.09	0.039
10		LF	0.73 (0.61)	0.61 (0.58)	83.58	95.41	0.115
11		HF	0.48 (0.41)	0.55 (0.58)	85.22	100.72	1.000
12		nLF	12.94 (5.05)	11.43 (5.49)	39.01	48.09	0.078
13		nHF	8.56 (3.76)	10.11 (4.51)	43.98	44.62	<0.05
14		LF/HF	1.63 (0.55)	1.22 (0.5)	33.54	44.85	<0.001
15	PPGAV$_{sys}$	TP	8.47 (36.17)	5.58 (7.28)	426.92	130.55	0.526
16		VLF	1.10 (5.37)	0.61 (0.88)	488.30	145.36	0.171
17		LF	0.22 (0.27)	0.40 (0.66)	124.88	163.13	0.059
18		HF	0.28 (0.23)	0.42 (0.50)	81.81	119.38	0.423
19		nLF	8.65 (4.72)	10.51 (5.32)	54.52	50.60	<0.05
20		nHF	13.13 (7.01)	12.65 (5.58)	53.39	44.09	0.642
21		LF/HF	0.78 (0.58)	0.85 (0.29)	74.41	33.83	<0.01
22	PPGAV$_{dia}$	TP	4.62 (13.77)	3.09 (3.33)	298.19	107.88	0.515
23		VLF	0.55 (2.00)	0.25 (0.26)	362.65	104.57	0.251
24		LF	0.18 (0.18)	0.29 (0.33)	103.11	115.52	0.160
25		HF	0.23 (0.21)	0.35 (0.40)	88.84	114.23	0.459
26		nLF	9.49 (5.09)	10.74 (4.91)	53.60	45.66	0.091
27		nHF	14.01 (6.69)	13.58 (4.88)	47.79	35.97	0.646
28		LF/HF	0.77 (0.56)	0.79 (0.23)	72.73	29.31	<0.05
29	PPGAV$_{sys}$/ACA$_{baseline}$	TP	5.56 (32.57)	3.76 (5.36)	585.51	142.62	<0.001
30		VLF	0.78 (4.82)	0.41 (0.65)	620.06	158.08	<0.001
31		LF	0.08 (0.21)	0.30 (0.63)	258.91	210.15	<0.001
32		HF	0.08 (0.05)	0.31 (0.45)	68.66	145.99	<0.001
33		nLF	8.29 (4.68)	10.07 (5.04)	56.44	50.01	<0.05
34		nHF	12.84 (7.06)	12.30 (5.39)	54.97	43.79	0.592
35		LF/HF	0.75 (0.57)	0.87 (0.34)	75.26	39.55	<0.01
36	PPGAV$_{sys}$/ACA$_{dia}$	TP	2.35 (11.53)	1.82 (1.82)	490.70	99.84	<0.001
37		VLF	0.31 (1.71)	0.16 (0.15)	542.32	95.16	<0.001
38		LF	0.06 (0.08)	0.17 (0.20)	138.54	118.12	<0.001
39		HF	0.07 (0.04)	0.20 (0.20)	62.41	100.84	<0.001
40		nLF	9.38 (4.88)	10.45 (4.53)	52.04	43.38	0.133
41		nHF	14.04 (6.60)	13.35 (4.83)	47.03	36.17	0.447
42		LF/HF	0.76 (0.57)	0.79 (0.24)	74.90	30.44	<0.01

(continued)

Table 2 (continued)

No.	Parameters		Mean (standard deviation)		Coefficient of variation		*p*-value
			Before	After	Before	After	
43	PPGAV$_{dia}$/ACA$_{baseline}$	TP	5.05 (28.66)	4.03 (5.99)	567.37	148.51	<0.001
44		VLF	0.70 (4.24)	0.44 (0.75)	604.91	169.14	<0.001
45		LF	0.08 (0.18)	0.34 (0.78)	237.98	229.36	<0.001
46		HF	0.08 (0.05)	0.34 (0.53)	64.32	158.31	<0.001
47		nLF	8.22 (4.65)	10.08 (5.10)	56.58	50.54	<0.05
48		nHF	12.83 (7.11)	12.34 (5.42)	55.44	43.90	0.635
49		LF/HF	0.75 (0.57)	0.87 (0.36)	75.83	42.05	0.050
50	PPGAV$_{dia}$/ACA$_{dia}$	TP	2.20 (10.21)	2.06 (2.31)	464.54	112.24	<0.001
51		VLF	0.29 (1.51)	0.17 (0.18)	519.13	106.60	<0.001
52		LF	0.05 (0.07)	0.19 (0.26)	126.73	131.65	<0.001
53		HF	0.07 (0.04)	0.24 (0.28)	64.80	120.16	<0.001
54		nLF	9.20 (4.81)	10.36 (4.48)	52.25	43.27	0.113
55		nHF	13.91 (6.66)	13.44 (4.82)	47.88	35.87	0.606
56		LF/HF	0.75 (0.56)	0.78 (0.25)	74.27	31.57	<0.01

according to the pressure change inside thoracic cage [15]. In the result of this study, LF value of ACA$_{baseline}$ and ACA$_{dia}$ was decreased but there is no statistical significance, moreover, PPGAV$_{sys}$ and PPGAV$_{dia}$ also shows increases with no significance. However, in every normalized parameter, LF value is increased with statistical significance ($p < 0.05$). This result could be interpreted that normalization reduced the ambiguity of PPG amplitude which is measured as an arbitrary unit. In terms of parameters, amplitude variability parameter, PPGAV$_{sys}$, PPGAV$_{dia}$ shows clear classification result compared with simple amplitude-based variables, ACA$_{baseline}$ and ACA$_{dia}$. This result suggests that the frequency domain variables of PPGV has a possibility in pain quantification and that the significant changes were reflected better in normalized variables.

4 Conclusion

In this study, we investigated PPGV in surgical pain quantification. We derived frequency domain variable of PPGV before and after surgery and found that there is a significant difference ($p < 0.05$) in PPGV variables according to the pain stimuli. Especially, result indicated that a clear difference was found in normalized PPGV variables. Consequently, the result of this study suggests that the possibility of frequency domain analysis of PPGV as a novel indicator of surgical pain quantification.

References

1. Dube A. A., Duquette M., Roy M., Lepore F., Duncan G., Rainville P.: Brain activity associated with the electrodermal reactivity to acute heat pain. Neuroimage 45, 169–180 (2009)
2. Burton A. R., Birznieks I., Bolton P. S., Henderson L. A., Macefield V. G.: Effects of deep and superficial experimentally induced acute pain on muscle sympathetic nerve activity in human subjects. The Journal of Physiology 587(1), 183–193 (2009)
3. Luginbiihl M., Ypparila-Wolters H., Riifenacht M., Petersen-Felix S., Korhonen I.: Heart rate variability does not discriminate between different levels of haemodynamic responsiveness during surgical anaesthesia. British Journal of Anaesthesia 98(6), 728–736 (2007)
4. Seitsonen E. R. J., Korhonen I. K. J., Van Gils M. J., Huiku M., Lötjönen J. M. P., Korttila K. T., Yli-Hankala A. M.: EEG spectral entropy, heart rate, photoplethysmography and motor responses to skin incision during sevoflurane anaesthesia. Acta Anaesthesiologica Scandinavica 49(3), 284–292 (2005)
5. Huiku M., Uutela K., Van Gils M., Korhonen I., Kymäläinen M., Meriläinen P., Yli-Hankala A.: Assessment of surgical stress during general anaesthesia. British journal of anaesthesia 98(4), 447–455 (2007)
6. Ledowski T., Bromilow J., Wu J., Paech M. J., Storm H., Schug S. A.: The assessment of postoperative pain by monitoring skin conductance: results of a prospective study. Anaesthesia 62(10), 989–993 (2007)

7. Jeanne M., Clement C., De Jonckheere J., Logier R., Tavernier B.: Variations of the analgesia nociception index during general anaesthesia for laparoscopic abdominal surgery. Journal of clinical monitoring and computing 26(4), 289–294 (2012)

8. Ahonen J., Jokela R., Uutela K., Huiku, M.: Surgical stress index reflects surgical stress in gynaecological laparoscopic day-case surgery. British journal of anaesthesia 98(4), 456–461 (2007)

9. Awad A. A., Ghobashy M. A. M., Ouda W., Stout R. G., Silverman D. G., Shelley K. H.: Different responses of ear and finger pulse oximeter wave form to cold pressor test. Anesthesia & Analgesia 92(6), 1483–1486 (2001)

10. Korhonen I., YLI-HANKALA A.: Photoplethysmography and nociception. Acta Anaesthesiologica Scandinavica 53(8), 975–985. (2009)

11. Mancia G.: Short-and Long-term blood pressure variability. Hypertension 60(2), 512–517. (2012)

12. Pagani M., Lombardi F., Guzzetti S., Rimoldi O., Furlan R. A. F. F. A. E. L. L. O., Pizzinelli P., Piccaluga E.: Power spectral analysis of heart rate and arterial pressure variabilities as a marker of sympathovagal interaction in man and conscious dog. Circulation research, 59(2), 178–193. (1986)

13. Van De Borne P., Montano N., Pagani M., Oren R., Somers V. K.: Absence of low-frequency variability of sympathetic nerve activity in severe heart failure. Circulation, 95(6), 1449–1454. (1997)

14. Pagani M., Montano N., Porta A., Malliani A., Abboud F. M., Birkett C., Somers V. K.: Relationship between spectral components of cardiovascular variabilities and direct measures of muscle sympathetic nerve activity in humans. Circulation, 95(6), 1441–1448. (1997)

15. Radaelli A., Bernardi L., Valle F., Leuzzi S., Salvucci F., Pedrotti L., Sleight P.: Cardiovascular autonomic modulation in essential hypertension. Effect of tilting. Hypertension, 24(5), 556–563. (1994)

16. Montano N., Cogliati C., Porta A., Pagani M., Malliani A., Narkiewicz K., Somers V. K.: Central vagotonic effects of atropine modulate spectral oscillations of sympathetic nerve activity. Circulation, 98(14), 1394–1399. (1998)

17. Malliani A., Pagani M., Lombardi F., Cerutti S.: Cardiovascular neural regulation explored in the frequency domain. Circulation, 84(2), 482–492. (1991)

A Decision-Making Fusion Method for Accurately Locating QRS Complexes from the Multiple QRS Detectors

Feifei Liu, Chengyu Liu, Xinge Jiang, Lina Zhao, Jianqing Li, Chuanjie Song, and Shoushui Wei

Abstract

QRS detection for electrocardiogram (ECG) signal plays a fundamental role in monitoring cardiovascular diseases. Lots of QRS detection algorithms exist and most of them are verified with high sensitivity and positive predictivity on the standard ECG databases. Recent progress in mobile ECG rises the challenge of accurate QRS detection for real-time dynamic ECG recordings since the variety of noises. In this study, a decision-making fusion method for accurately locating QRS complexes from the multiple QRS detectors were proposed. First, the ECG signals were detected by these nine detectors. Then, the voting fusion rule had been established that a heartbeat was determined when more than five detectors showed their detections in a time moving window respectively. And the mean value of the middle three detections' positions in the window was served as a corrected heartbeat. Moreover, the comprehensive post processing technology was used to eliminate the false detection and to search the missed beats. The new proposed method was tested on high and poor signal quality ECG databases. For comparison, the best detection accuracy for the single algorithm was only 75.50% while the new proposed fusion method with 200 ms time moving window reported a detection accuracy of 80.43% for the poor-quality ECG signals. The proposed fusion method can significantly improve locating QRS complexes accuracy for the ECG signals with poor signal quality. Thus, it has a potential usefulness in the real-time dynamic ECG monitoring situations.

1 Introduction

Accurate heart rate detection for ECG signal plays a fundamental role in monitoring cardiovascular diseases (CVD), which has been the most common cause of death globally. The QRS complex is the most striking waveform within the Electrocardiogram (ECG) signal; it serves as the basis for the automated determination of the heart rate, as well as the benchmark point for classifying the cardiac cycle and identifying any abnormality. Lots of QRS detection algorithms exist and most of them are verified with high sensitivity and positive predictivity (>99%) on the open-access ECG database, such as MIT-BIH arrhythmia database [1].

Recently, the rapid development in wearable and telehealth technologies promotes the real-time, remote and continuous ECG individual monitoring. Real-time ECG remote monitoring is an effective means for the early warning of CADs. However, the quality of signals monitored by mobile devices also bring the new challenge. The subject of the PhysioNet/CinC Challenge 2011 was to develop an efficient algorithm to detect the quality of ECGs collected using mobile phones. Liu et al. [2] reported that the classical QRS detection method proposed by Pan and Tompkins [3] only had a relatively low detection accuracy on the low-quality ECG signals. Khamis et al. [4] developed new QRS detection method based on the artifact masking technology, which reported the good detection performance. The methods about locating QRS complexes on the low-quality signal was not insufficient. In this study, a

F. Liu · C. Liu (✉) · L. Zhao · J. Li
School of Instrument Science and Engineering, Southeast University, Nanjing 210096, China
e-mail: chengyu@seu.edu.cn

F. Liu · C. Song
Shandong Zhong Yang Software Limited Company, Jinan, Shandong, China

X. Jiang · L. Zhao · S. Wei
School of Control Science and Engineering, Shandong University, Jinan, China

X. Jiang
Shandong College of Electronic Technology, Jinan 250200, China

decision-making fusion method for locating QRS complexes based on up to nine QRS detectors were proposed.

2 Methods

2.1 The Decision-Making Fusion Method

In this study, we proposed a new decision-making fusion method for accurately locating QRS complexes based on up to these nine QRS detectors, including RS-slope algorithm [5], Sixth-power algorithm [6], Finite State Machine algorithm (FSM) [7], U3 transform algorithm (U3) [8], Difference operation algorithm (DOM) [9], Pan and Tompkins algorithm (Pan) [3], 'jqrs' algorithm [10], UNSW algorithm (UNSW) [4], Optimized knowledge based algorithm (OKB) [1]. Figure 1 shows the flow diagram of the proposed decision-making fusion method.

First, the ECG signals were detected by nine detectors. Then, the voting fusion rule had been established that a heartbeat was determined when more than five detectors showed their detections in a time moving window respectively. Considering it is almost impossible that all detectors showed their detections at the same time, time moving window was introduced. The voting decision-making fusion rule was shown by Eqs. (1)–(3) defined as follows:

$$R\left(i, \mathrm{w}_j\right) = \begin{cases} 1 & if\ R_i \in w_j \\ 0 & if\ R_i \notin w_j \end{cases} \quad (1)$$

$$V\left(\mathrm{w}_j\right) = \sum_{i=1}^{9} R\left(i, \mathrm{w}_j\right) \quad j = 1, 2, 3, \ldots, n \quad (2)$$

$$S(\mathrm{j}) = \begin{cases} 1 & if\ V\left(\mathrm{w}_j\right) \geq 5 \\ 0 & if\ V\left(\mathrm{w}_j\right) < 5 \end{cases} \quad (3)$$

where, R_i was the QRS complexes location detected by the nine QRS detectors, $i = 1, 2, 3, \ldots, 9$; w_j was the time moving window for the voting and was set as 50 ms,
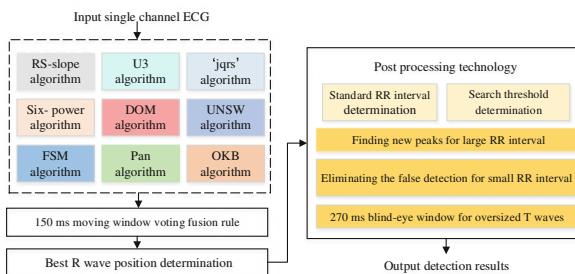
100 ms, 150 ms, 200 ms and 250 ms respectively in this study; $V\left(\mathrm{w}_j\right)$ represented the voting result of these nine detectors in the w_j window. if $V\left(\mathrm{w}_j\right) \geq 5$, $S(\mathrm{j})$ was equaled to one, and this time moving window w_j was regarded as a potential heartbeat. Then the first R wave detected point outside the current window on the right side was regarded as the next time window left side. Otherwise, $S(\mathrm{j})$ was equaled to zero, and this time moving window w_j was rejected, and the first (and left-most) R wave detected point inside the current window was given up, and the second point regarded as the next time window left side. And the mean value of the middle three detections' positions in each selected time window was served as a corrected QRS complexes position. The position of maximum absolute value was located as R wave points the in a window of 100-ms.

Then, the post-processing technology was applied to eliminate the possibility of a false detection and search the missed beats. First, the standard RR interval was determined as the median value of 70% central range of RR-interval series. And the search threshold was determined as 0.6 times the mean value of 50% central range of R waves value. If the current RR interval was larger than the 1.66 times the standard RR interval, the search threshold was used to find new peaks as the new heart beats. If the current RR interval was smaller than the 0.6 times the standard RR interval, the search threshold was used to eliminate the false detection. Moreover 270 ms blind-eye window was employed to avoid the oversized T waves to be taken as detections.

2.2 Database

For the comparison, two databases were selected from the PhysioNet/CinC Challenge 2014 [11]. One was the training set with good signal quality, consisted of single II-lead 100 recordings (named 100–199), sampled at 250 Hz, with 12-bit resolution. This database was used as the high-quality ECG database in this study. Another one was an augmented training set with very low quality also consisted of 100 recordings, sampled at 360 Hz. This database was used as low-quality database in this study. Each recording had a 10 min in duration. All ECG recordings had the manually annotated QRS complex locations and these locations were used as the references for evaluating the four automatic QRS detection algorithms.

2.3 Evaluation Methods

The evaluation metrics of sensitive (Se), positive predictivity (+P) and F1 measure were calculated as follows:

Fig. 1 The flow diagram of the new proposed decision-making fusion method

$$Se = \frac{TP}{TP + FN} \times 100\% \tag{4}$$

$$+P = \frac{TP}{TP + FP} \times 100\% \tag{5}$$

$$F1 = \frac{2 \times TP}{(2 \times TP + FP + FN)} \times 100\% \tag{6}$$

where TP is the number of QRS complexes truly detected, FP is the number of false positive (extra falsely detected QRS complexes) and FN is the number of false negative (missed detected QRS complexes).

3 Results and Discussion

Tables 1 and 2 show the performances of nine single QRS detectors and the proposed fusion method on the high and poor signal quality ECG databases, respectively. All these ten methods had good detection results for the high signal quality ECG database (all >99%, shown in Table 2). However, the detection results decrease significantly for the poor signal quality ECG signals. The best detection accuracy for the nine single algorithms was only 75.50% from the OKB method, while the new proposed fusion method with 200 ms time moving window reported a detection accuracy of 80.43%.

For these two databases, compared with these nine QRS detection methods, the new fusion method all reported the best performance. For the high signal quality database, although the fusion method showed the best the detection results, the nine single QRS detectors all had high detection accuracy (all >99%). In this way, considering the computational efficiency, it was no need to use fusion method to pursue a little improvement on the detection accuracy.

However, for the poor signal quality database, the new fusion method with 200 ms time moving window reported higher detection accuracy (80.43%) compared with the nine single QRS detectors (all <75.5%). Figure 2 shows an example from the recording 1019 in the poor signal quality ECG database. The red crosses represent the reference annotations, and the magenta asterisks represent the detected points of nine single QRS detectors, and the green asterisks represent the detected points of the new fusion method. Different QRS detectors had different robust performance for different noise. This figure illustrates that voting fusion rule could extract the best R wave points from nine QRS detectors detection results, which can improve noise immunity. And the comprehensive post processing technology could eliminate the false detection and search the missed beats, which improves the detection accuracy further. The influence of the time moving window width was not obvious for the high signal quality ECG database. For the poor signal quality ECG database, 200 ms time window showed the best performance.

4 Conclusion
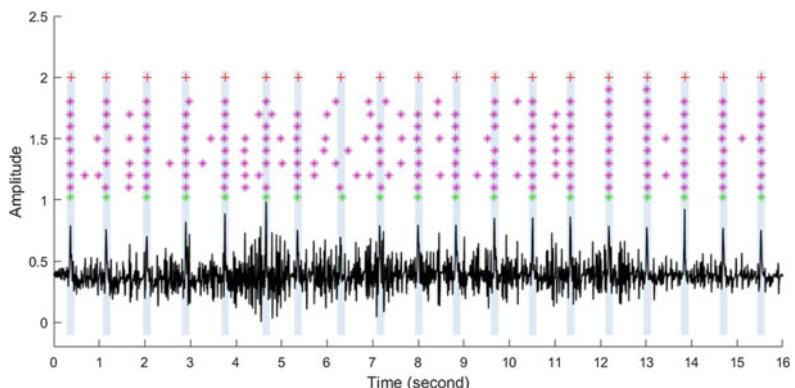
In this study, a new decision-making fusion method for QRS complexes location based on up to nine QRS detectors were proposed. High and poor ECG signal quality databases were used to analyze the performance of this new method. For these two databases, compared with these nine QRS

Table 1 Performances of the ten methods on high signal quality database

Methods	Time moving window (ms)	Poor signal quality ECG database						
		Total beat	TP	FN	FP	Se (%)	+P (%)	F1 (%)
RS-Slope	/	72,415	72,106	309	80	99.57	99.89	99.73
Sixth-power	/	72,415	72,095	320	220	99.56	99.70	99.63
FSM	/	72,415	72,249	166	216	99.77	99.70	99.74
U3	/	72,415	72,211	204	388	99.72	99.47	99.59
DOM	/	72,415	72,055	360	225	99.50	99.69	99.60
Pan	/	72,415	72,185	230	239	99.68	99.67	99.68
'jqrs'	/	72,415	72,263	152	125	99.79	99.83	99.81
UNSW	/	72,415	72,304	111	639	99.85	99.12	99.48
OKB	/	72,415	72,194	221	56	99.69	99.92	99.81
Fusion algorithm	50	72,415	72,315	100	63	99.86	99.91	**99.89**
	100	72,415	72,325	90	76	99.88	99.90	**99.89**
	150	72,415	72,333	82	86	99.89	99.88	99.88
	200	72,415	72,331	84	95	99.88	99.87	99.88
	250	72,415	72,323	92	107	99.87	99.85	99.86

Table 2 Performances of the ten methods on poor signal quality database

Methods	Time moving window (ms)	Poor signal quality ECG database						
		Total beat	TP	FN	FP	Se (%)	+P (%)	F1 (%)
RS-Slope	/	78,618	38,904	39,714	13,047	49.48	74.89	59.59
Sixth-power	/	78,618	52,985	25,633	24,717	67.40	68.19	67.79
FSM	/	78,618	54,974	23,644	25,347	69.93	68.44	69.18
U3	/	78,618	57,484	21,134	23,280	73.12	71.18	72.13
DOM	/	78,618	56,558	22,060	18,722	71.94	75.13	73.50
Pan	/	78,618	57,801	20,817	20,479	73.52	73.84	73.68
'jqrs'	/	78,618	58,476	20,142	20,516	74.38	74.03	74.20
UNSW	/	78,618	60,395	18,223	22,746	76.82	72.64	74.67
OKB	/	78,618	57,354	21,264	15,969	72.95	78.22	75.50
Fusion algorithm	50	78,618	60,875	17,743	13,782	77.43	81.54	79.43
	100	78,618	62,496	16,122	14,487	79.49	81.18	80.33
	150	78,618	62,936	15,682	14,973	80.05	80.78	**80.42**
	200	78,618	63,227	15,391	15,375	80.42	80.44	**80.43**
	250	78,618	62,591	16,027	16,481	79.61	79.16	79.38

Fig. 2 Example from the recording 1019 in the poor-quality ECG database

detection methods, the new fusion method all reported the best performance. Especially for the poor-quality ECG signals, this fusion method with 200 ms time moving window reported higher detection results (F1 = 80.43%), while the best detection accuracy for the single algorithm was only 75.50%.

The proposed fusion method can significantly improve the QRS detection accuracy for the ECG signals with poor signal quality. Thus, it has a potential usefulness in the real-time dynamic ECG monitoring situations.

References

1. Elgendi, M.: Fast QRS Detection with an Optimized Knowledge-Based Method: Evaluation on 11 Standard ECG Databases. Plos One 8, e735571–735518 (2013).
2. Liu, F., Wei, S., Li. Y., Jiang, X., Zhang, Z., Zhang, L., Liu, C.: The accuracy on the common Pan-Tompkins based QRS detection methods through low-quality ECG database. Journal of medical Imaging and Health Informatics 7(5), 1039–1043 (2017).
3. Pan, J., Tompkins, W.: A real-time QRS detection algorithm. Biomedical Engineering, IEEE Transactions on bio-medical engineering 32(3), 230–236 (1985).
4. Khamis, H., Weiss, R., Xie, Y., Chen, C., Lovell, N., Redmond, S.: QRS Detection Algorithm for Telehealth Electrocardiogram

Recordings. IEEE Transactions on Biomedical Engineering 63(7), 1377–1388 (2016).

5. Podziemski, P., Gieraltowski, J. Fetal heart rate discovery: algorithm for detection of fetal heart rate from noisy, noninvasive fetal ECG recordings. In: Computing in Cardiology Conference 2013, vol. 40, pp. 333–336. IEEE, Zaragoza (2013).

6. Dohare, A., Kumar, V., Kumar, R., An efficient new method for the detection of QRS in electrocardiogram. Computers & Electrical Engineering 40(5), 1717–1730 (2013).

7. Gutierrez-Rivas, R. Garcia, J., Marnane, W., Hernandez, A.: Novel Real-Time Low-Complexity QRS Complex Detector Based on Adaptive Thresholding. IEEE Sensors Journal 15(10), 6036–6043 (2015).

8. Paoletti, M., Marchesi, C.: Discovering dangerous patterns in long-term ambulatory ECG recordings using a fast QRS detection algorithm and explorative data analysis. Computer Methods & Programs in Biomedicine 82(1), 20–30 (2006).

9. Yeh, Y., Wang, W., QRS complexes detection for ECG signal: The Difference Operation Method. Computer Methods and Programs in Biomedicine 91(3), 245–254 (2008).

10. Behar, J., Oster, J., Clifford, G.: Non-invasive FECG extraction from a set of abdominal sensors. In: Computing in Cardiology Conference 2013. pp. 297–300. IEEE, Zaragoza (2013).

11. Silva I., Moody B., Behar J., Johnson A., Oster J., Clifford G.D., Moody G.B., Robust detection of heart beats in multimodal data, Physiological Measurement 36, 1629–1644 (2015).

Effect of Myocardial Infarction Size on the Simulated ECG Morphology Based on a 3D Torso-Heart Model

Zhipeng Cai, Jianqing Li, Kan Luo, Zhigang Wang, Xiangyu Zhang, Jian Zhang, and Chengyu Liu

Abstract

Objective: Myocardial infarction (MI) is a big threat to human health. Underlying linkage between changes in standard electrocardiography (ECG) waveforms and different MI conditions is important. A three-dimensional (3D) bidomain torso-heart model was proposed for stimulating the MI effect. In this study, we aimed to quantify the effect of MI size on the simulated ECG morphology from this model. Methods: Using a simplified 3D torso-heart model, the electrical activation of heart and its conduction were simulated. The adopted 3D torso-heart model consists of torso, lung, and the whole heart components, including atria, ventricles, and blood chambers. Simulation of MI was performed by changing the control parameters of the infarcted region. All infarcts were located in the anterior wall of the left ventricle. The effect of MI size (three sizes: 168.1, 914.8 and 2,210 mm^3) on the QRS complex from the stimulated standard 12-lead ECGs was explored. Results: The results demonstrated the progressions of heart depolarization and repolarization and revealed the difference of electrical conduction between the normal and MI hearts. Compared with Q-wave amplitude ratios (QARs) and S-wave amplitude ratios (SARs), the R-wave amplitude ratios (RARs) showed their superiority in the distinguish of lesion size, as they are in sequential order with the lesion size. However, the cooperation of QARs and SARs can also help determine the size of infarcted myocardium, especially in the chest ECG leads. Significance: This study provided a quantitative analysis for the effect of MI size on the simulated standard 12-lead ECG morphology. The simulated results confirmed the changes in ECG QRS complex due to the MI changes are consistent with the clinical futures. Thus, it provides an alternative tool for understanding the inherent conduction mechanism of ECG signal.

Z. Cai (✉) · J. Li (✉) · X. Zhang · C. Liu (✉)
Southeast-Lenovo Wearable Heart-Sleep-Emotion Intelligent
Monitoring Lab, School of Instrument Science and Engineering,
Southeast University, Nanjing, China
e-mail: 230169212@seu.edu.cn

J. Li
e-mail: ljq@seu.edu.cn

C. Liu
e-mail: chengyu@seu.edu.cn

J. Li
School of Basic Medical Sciences, Nanjing Medical University,
Nanjing, China

K. Luo
School of Information Science and Engineering, Fujian University
of Technology, Fuzhou, China

Z. Wang
Institute for Medical Science and Technology, University of
Dundee, Dundee, DD2 1FD, Scotland

J. Zhang
Sir Run Run Hospital, Nanjing Medical University, Nanjing,
China

1 Introduction

Non-communicable diseases (NCDs) have become the leading cause of death globally, killing 38 million people each year [1]. Cardiovascular diseases (CVDs) account for the most deaths annually, leading to 17.5 million of deaths every year [2]. Among the fatal heart diseases, myocardial infarction (MI) is one that may cause acute death without any prior signs or symptoms before onset. However, at least 80% of premature deaths from CVDs can be avoided by early detected, diagnosed and treated.

The standard 12-lead electrocardiograms (ECGs) have been proved to have the capability to locate the site of infarcted myocardium [3]. While there is still not an effective method to determine the size of lesion. Fortunately,

computer models provide a promising method for us to understand the relationship between cardiac electrical activity and different anomalies in the heart.

An intact canine heart model was adopted to investigate restitution property of cardiac tissue using the modified two-variable FitzHugh-Nagumo (FHN) model [4]. But this model only simulated the cardiac electrical activity of the heart, it did not investigate the performance of cardiac electrical activity mapping on the body surface and the influence of heart disease on the body surface potentials (BSPs). The changes in the waveforms of standard 12-leads ECGs and body surface potential mapping (BSPM) were studied using a detailed heart model embodied in a torso [5]. However, they only roughly simulated anterior and anterior transmural ischemia and infarction and anterior subendo-cardial, the detailed effect of sites and sizes of ischemic myocardium on ECG morphology need further research.

Most of the models mentioned above can simulate the electrical activities and the standard 12-leads ECGs, some even can simulate the pathological ECGs in different MI conditions. However, the linkage between the ECG wave-forms and MI sizes needs further research to assess left ventricular function. In the current study, a model based method was proposed to evaluate the effect of MI sizes on ECGs and a practical, clinically useful tool for improved electrocardiographic diagnosis was provided based on this model.

2 Methodology

In this paper, the model we adopted is a simplified three-dimensional (3D) bidomain torso-heart model, con-sisting of torso, lungs and entire heart (Fig. 1a), which can simulate 12-lead ECGs under normal and pathological heart states. The details of the model have been published in [6]. Briefly, the torso, lungs and blood chambers were defined as passive volume conductor regions and the governing equa-tion for the extracellular voltage was given by the Laplace formulation of Maxwell's equations. The heart region was divided into seven subdomains according the anatomical structure of heart, including sinoatrial node, atria, atrioven-tricular node, His bundle, bundle branches, Purkinje fibers and ventricular myocardium. Although the torso morphol-ogy can have an impact on BSPMs, these effects are beyond the scope of this article. The mathematical model of the heart tissue is bidomain model and the bidomain equations were based on modified FHN equations. We can simulate different heart states by adjusting different parameters in these seven subdomains of the simple ideal model.

As showed in Fig. 1b, the research in this study was focused on the single anterior MI, therefore the study of single MI was conducted in the center of anterior left ventricular wall. According to anatomical studies, the size of single myocardial infarction in the left ventricle was sim-plified into three types: small, moderate and large. In the model, a approximative frustum region was used to represent the infarcted myocardium (Fig. 1b). The small infarcts were 2–3 cm in diameter, and only located in the endocardium, while the moderate infarcts were 4–6 cm in diameter, cov-ering the endocardium and midmyocardium, the large infarcts were transmural, spanning the endocardium, mid-myocardium and epicardium [5]. Therefore, the final sizes of the infracted myocardium are set as 168.1 mm^3, 914.8 mm^3 and 2,210 mm^3 respectively in our study.

The numerical solutions of the transmembrane potentials and ECGs were calculated using finite element method (FEM). The total simulation process was carried out in a multi-physical simulation software (COMSOL, Switzer-land), as it can realize the simulation of real physical phe-nomena by solving partial differential equations (PDEs) based on the FEM. The simulation of one second cardiac activity took about 5 h at the resolution of 1 ms (Intel Core i7-7700 CPU, @3.6 GHz, 8 G RAM). The average finite element mesh of different conditions was 45,690 tetrahedral elements with 105,712 degrees of freedom.
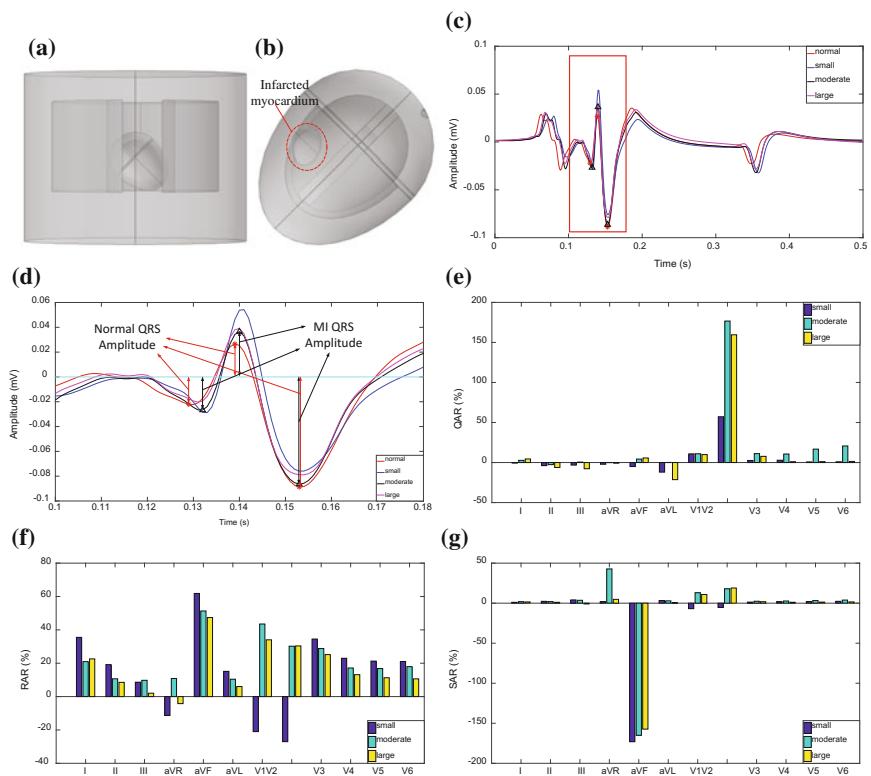
After obtaining different simulation results, several characteristic coefficients were calculated to quantify the effect of infarct sizes on ECG morphology. The commonly used method to evaluate the degree of cardiac ischemia is to detect the ST segment changes in ECG signals, but the changes in the QRS complex were more sensitive to the sizes of infarcted myocardium, therefore we mainly com-pared the amplitudes of Q wave, R wave and S wave [5]. Another evaluation measure is the accuracy of morpholog-ical classification of QRS complex in ECG signals, which was based on our previous rule-based method [7].

3 Experiments and Results

3.1 Simulated Lead aVF ECGs of the MI Models

To verify the validation of the model, we compared the simulated lead aVF ECG morphology between normal heart and MI heart. Figure 1c–d illustrated the lead aVF ECGs of three sizes of anterior MIs. It can be seen that the changes of ECG morphology were similar as the MI lesion expands. It is reported that QRS complex can reflect more details of the changes of MI size [8], then we mainly investigated the changes in QRS complex. The amplitudes of R wave and S wave from MI heart are different with normal ECG. Mean-while, it can also be seen that the change trends of QRS complex under three sizes are consistent. However, the variation range were inconsistent. Therefore, there needs quantitative investigation of relationship between the ECG

Fig. 1 The simplified 3D torso-heart model and the simulated results of the model. **a** The geometry of the original torso-heart model; **b** the back view of the anterior MI heart; **c** comparison of lead aVF signals between normal heart and MI heart under three sizes; **d** the details of the QRS complexes of the simulated lead aVF ECGs, marked as red box in (**c**); **e** the Q-wave amplitude ratio of three sizes MIs; **f** the R-wave amplitude ratio of three sizes MIs; **g** the S-wave amplitude ratio of three sizes MIs

3.2 QRS Quantitative Parameters for Determination of MI Sizes

To simplify the quantitative criteria, we only calculated three parameters of QRS complex: Q-wave amplitude ratio (QAR), R-wave amplitude ratio (RAR) and S-wave amplitude ratio (SAR). These parameters are the quotient of the absolute amplitudes of normal QRS divided by the difference amplitudes between pathological QRS and the normal ones, as shown in Eq. (1). The sign of the parameters indicates the elevation or depression of the ECG segment. In addition, since the theoretical waveforms produced by the model are stable and constant, therefore, only one beat data is compared in this study.

$$QRS_{parameters} = (Amplitudes_{normal} - Amplitudes_{MI})/Amplitudes_{normal} \tag{1}$$

The Q-wave amplitude changes of standard 12-lead ECGs in three sizes are illustrated in Fig. 1e. The variation of the QAR is irregular in limb leads. However, the QARs of three sizes in leads V2–V6 present a roof shape with all the signs are positive, meaning that the Q waves of anterior MI elevate in most chest leads. In addition, the value of small size is greater than that in large size in these leads. Obviously, the elevation of Q wave in lead V2 are all greater than 50% in three sizes, while in other leads are less than 50%. Figure 1f illustrates the R-wave amplitude changes of pathological ECGs relative to the normal ECGs. Although the variation of the RARs in most leads are significant, they are sequenced in order with a descending trend in leads II, aVF and V3–V6. These amplitude changes are not represented as expected, especially in lead I, aVL and aVR. However, we consider these drawbacks are caused by using of the simplified model. However, the results can still indicate that the RARs in these leads are sensitive to the MI sizes at anterior sites. Figure 1g shows the comparison of SARs among different sizes of infarcts. The SARs showed a similar trend as QARs in leads II and V3–V6. It is noteworthy that the SARs are all negative in lead aVF, with their absolute values larger than 150%. Meanwhile, they present an upward tendency with the expansion of infarcted myocardium. The change trends of QARs and SARs in most chest leads do not match the expectation. Although it may be

consistent with the clinical results in some conditions, it still reflects the drawbacks of this model. However, it can still simulate the electrical activity during cardiac cycle and reveal the inherent conduction mechanism of ECG signal.

4 Discussion

In the current study, a model based method was proposed to evaluate the effect of MI sizes on ECGs and a practical, clinically useful tool for improved electrocardiographic diagnosis was provided based on this model.

The RARs present a descending trend in leads II, aVF and V3–V6, indicating the RAR can be used as a diagnostic tool for quantifying MI sizes [8]. From the view of cardiac electric axis theory, leads II and aVF are the axes closest to the lesion on transverse plane. In addition, the chest leads V3–V6 are the axes pointing to the lesion on coronal plane. The QARs and SARs both present a roof shape trend in most chest leads, with their signs are all positive. However, they cannot distinguish lesion size solely, while their cooperation can serve as a good diagnostic method for detection of MI sizes. For small size, the value of QAR is positive and the value of SAR is negative in lead V2, together with all the values of QAR and SAR are positive in leads V3–V6. While the QARs are all greater than 10% and SARs are all greater than 3% in leads V3–V6 when the size is moderate. As to determine large size lesion, the QARs and SARs are all positive in leads V2–V6, and the values in V2 are several times than those in other leads. The results indicate the superiority of chest leads in the distinction of lesion size.

Limitations should be motioned. It still needs more works to optimize the model for more accurate BSPMs, such as considering the myocardial anisotropy, or constructing the geometry of the model by CT/MRI data. Moreover, the more precise changes on the ECG morphology need to be studied on more refined MI sizes. We also need to conduct more experiments on the MI patients to confirm the clinical usefulness of the method, and compare these characteristic coefficients between real normal ECGs and real MI ECGs.

5 Conclusion

In this study, a theoretical method for determining the anterior myocardial infarction sizes was proposed, based on the simulated ECGs obtained from a torso-heart model. The results showed the superiority of RARs in the distinguish of MI size. The theoretical comparison results of other parameters suggested the significance of multi-parameter fusion in the detection of lesion sites. The cooperation of QARs and SARs are also efficient in the detection of anterior MIs.

Conflicts of Interest The authors declare no conflict of interest.

References

1. Allen, L., Cobiac, L., Townsend, N.: Quantifying the global distribution of premature mortality from non-communicable diseases. J PUBLIC HEALTH-UK, 1–6 (2017).
2. World Health Organization: Hearts: technical package for cardiovascular disease management in primary health care. Geneva: WHO, 1–73 (2016).
3. Clemmensen, P., Ohman, E.M., Sevilla, D.C., Peck, S., Wagner, N. B., Quigley, P.S., Grande, P., Lee, K.L., Wagner, G.S.: Changes in standard electrocardiographic ST-segment elevation predictive of successful reperfusion in acute myocardial infarction. The American journal of cardiology, 66(20), 1407–1411 (1990).
4. Aliev, R.R., Panfilov, A.V.: A simple two-variable model of cardiac excitation. Chaos, Solitons & Fractals, 7(3), 293–301 (1996).
5. Miller, W.T., Geselowitz, D.B.: Simulation studies of the electrocardiogram. II. Ischemia and infarction. CIRC RES, 43(2), 315–323 (1978).
6. Sovilj, S., Magjarević, R., Lovell, N.H., Dokos, S.: A simplified 3D model of whole heart electrical activity and 12-lead ECG generation. COMPUT MATH METHOD M (2013) https://doi.org/10.1155/2013/134208.
7. Xu, M., Wei, S., Qin, X., Zhang, Y., Liu, C.: Rule-based method for morphological classification of ST segment in ECG signals. J MED BIOL ENG, 35(6), 816–823 (2015).
8. Wagner, G.S., Freye, C.J., Palmeri, S.T., Roark, S.F., Stack, N.C., Ideker, R.E., Harrell, F.E., Selvester, R.H.: Evaluation of a QRS scoring system for estimating myocardial infarct size. I. Specificity and observer agreement. CIRCULATION, 65(2), 342–347 (1982).

Effect of Ectopic Beats on Heart Rate Variability Indices in Heart Failure Patients

Chengyu Liu, Lina Zhao, Zhipeng Cai, Feifei Liu, Yaowei Li,
Shoushui Wei, Jianqing Li, and Alan Murray

Abstract

Heart rate variability (HRV) provides a valuable tool for early detection of cardiovascular abnormalities. Ectopic beats have been proven to have an influence on HRV results, but the effect of different amount of ectopic beats on analysis of congestive heart failure (CHF) patient rhythms has not been quantified. In this study, we tested the commonly used HRV indices for significant differences between 5-min RR segments with and without ectopic beats. Eight long-term CHF RR interval recordings from http://www.physionet.org were studied. Each recording was divided into non-overlapping segments of 5-min RR segments without or with different numbers of ectopic beats. Two time-domain HRV indices of SDNN and RMSSD and two frequency-domain indices of normalized low frequency (LFn) and high frequency (HFn) powers were employed. Results showed that ectopic segments had significantly larger values for SDNN (39 ± 18 vs. ectopic free segments 28 ± 16 ms, $P < 0.05$), RMSSD (47 ± 29 vs. 24 ± 23 ms, $P < 0.05$) and HFn (0.66 ± 0.13 vs. 0.52 ± 0.14, $P < 0.01$), and significantly lower values for LFn (0.34 ± 0.13 vs. ectopic free segments 0.48 ± 0.14, $P < 0.01$). Compared with the indices of RMSSD and frequency-domain indices, SDNN was least affected by a relatively small amount of ectopic beats (one to six beats). Compared with the time-domain indices, the frequency-domain indices responded more quickly to the appearance of ectopic beats.

1 Introduction

Heart rate variability (HRV) studies the slight fluctuations in RR interval time series and has become an important tool for the assessment of cardiovascular autonomic regulation during various physiological and clinical conditions. However, ectopic beats consists in RR interval time series may cause bias in the reliable measurement of HRV [1, 2]. Researchers reported that some HRV time-domain parameters are more sensitive to the ectopic beats than others [1]. Researchers also stated that the presence of only one ectopic beat can introduce an increase in the high frequency (HF) power in HRV of around 10% [3]. The reason is that ectopic beats can induce the sudden changes in RR intervals and increase the high-frequency fluctuation in the tachogram of HRV, distorting the true measure of an HRV metric [4].

Although many detecting and editing (correcting) methods for ectopic beats have been proposed [2, 5–7], there is no agreed conclusion on which method is more efficient to handle the ectopic beats to obtain accurate HRV estimation [2, 4, 7]. Meanwhile, the effect of different amount of ectopic beats on the common time-domain and frequency-domain HRV indices for special cardiovascular disease has not been widely documented. This paper, therefore, aims to quantify the differences between ectopic-free and ectopic RR interval time series for congestive heart failure (CHF) patients and to quantify the effect of different amount of ectopic beats on the

C. Liu (✉) · L. Zhao · Z. Cai · F. Liu · Y. Li · J. Li
Southeast-Lenovo Wearable Heart-Sleep-Emotion Intelligent
Monitoring Lab, School of Instrument Science and Engineering,
Southeast University, Nanjing, 210096, China
e-mail: chengyu@seu.edu.cn

L. Zhao · S. Wei
School of Control Science and Engineering, Shandong University,
Jinan, 250061, China

J. Li
School of Basic Medical Sciences, Nanjing Medical University,
Nanjing, 211166, China

A. Murray
School of Engineering, Newcastle University, NE1 7RU
Newcastle upon Tyne, UK

commonly used time-domain and frequency-domain HRV indices.

2 Methods
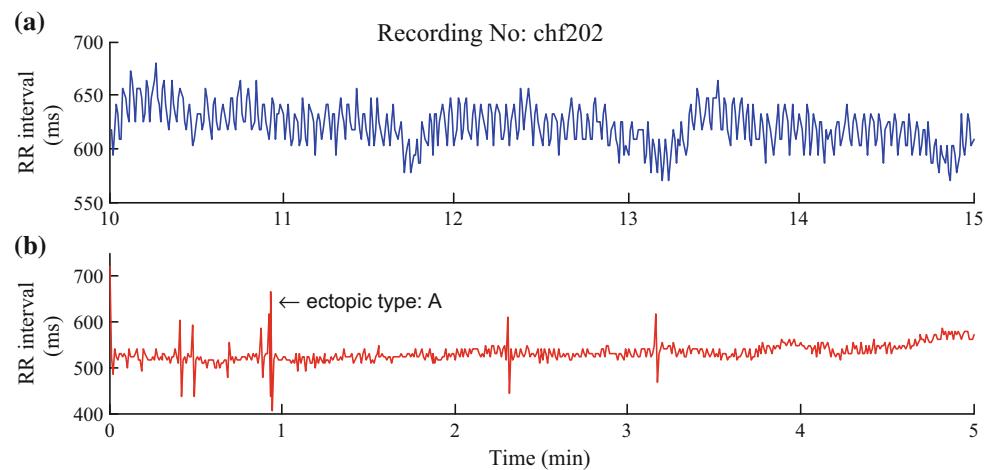
2.1 Database

All data used were from the PhysioNet CHF RR Interval Databases [8], a free-access, online archive of physiological signals. This database included 29 long-term RR interval records of subjects aged 34–79, with CHF. The original ECGs were digitized at 128 Hz, and the beat annotations were obtained by automated analysis with manual review and correction. A 5-min time window was used to segment the long-term RR interval records. In each 5-min RR segment, RR intervals greater than 2 s were first removed to exclude the influence from artifacts [9]. Then 5-min RR segments were classified as an ectopic segment if at least one ectopic beat was included or ectopic-free segment if no ectopic beat existed. Ectopic beats were from supraventricular or ventricular beats, depending on the localization of ectopic focus. Figure 1 shows the examples of an ectopic-free and ectopic 5-min RR segments. To exclude the record effect, only eight records with approximately equal amounts of ectopic-free and ectopic RR segments were selected for the following analysis (see Table 1).

2.2 HRV Indices

For a 5-min RR segment $x(i)$, $(i = 1, 2, \ldots, N)$, four common HRV indices were calculated in this study.

(1) Time-domain indices:
The standard deviation of 5-min RR segment (SDNN) and the square root of the mean of the sum of the squares of differences between adjacent intervals of 5-min RR segment (RMSSD) were used and were defined as:

$$\text{SDNN} = \sqrt{\frac{1}{N-1} \sum_{i=1}^{N} (x(i) - \bar{x})^2} \qquad (1)$$

$$\text{RMSSD} = \sqrt{\frac{1}{N-1} \sum_{i=1}^{N-1} (x(i+1) - x(i))^2} \qquad (2)$$

where $\bar{x} = \frac{1}{N} \sum_{i=1}^{N} x(i)$ is the mean value of RR intervals.

(2) Frequency-domain indices:
Frequency-domain analysis provides a quantitative evaluation of sympathetic and parasympathetic activation. The low frequency (LF) component (between 0.04 and 0.15 Hz) reflects both sympathetic and parasympathetic nervous systems while the HF component (between 0.15 and 0.40 Hz) mainly reflects vagal activity [4, 10]. Burg modern spectrum estimation was used to acquire frequency parameters. The spectral powers of LF and HF were normalized using $\text{LFn} = \frac{\text{LF}}{\text{LF}+\text{HF}}$ and $\text{HFn} = \frac{\text{HF}}{\text{LF}+\text{HF}}$.

2.3 Statistical Analysis

Group t-student test was used to determine whether the results obtained from the ectopic-free and ectopic RR segments had significant differences. Comparisons were also performed between the ectopic-free group and the groups

Fig. 1 Examples of 5-min RR segments: **a** ectopic-free RR segment and **b** RR segment with 'a' (atrial) type ectopic beat

Table 1 Recordings selected from the PhysioNet CHF RR interval databases

Record	# Beats			# 5-min RR segments		
	Normal	Ectopic	Total	Ectopic-free	Ectopic	Total
chf202	109,003	273	109,276	97	150	247
chf203	98,473	496	98,969	75	187	262
chf209	108,758	507	109,265	70	156	226
chf215	141,898	5,851	147,749	110	166	276
chf220	136,929	820	137,749	138	143	281
chf224	134,367	356	134,723	137	150	287
chf225	91,161	242	91,403	97	121	218
chf228	117,459	1,467	118,926	71	204	275

with different amount of ectopic beats. All statistical analyses were performed using the SPSS software (Ver. 20, IBM, USA). A statistical significance was accepted at $P < 0.05$.

3 Results

Table 2 gives the overall means and SDs of HRV indices (i.e., SDNN, RMSSD, LFn, and HFn) from both ectopic-free and ectopic 5-min RR segments. As shown in Table 2, there were significant differences in all four indices between the two groups (all $P < 0.05$). For time-domain indices, SDNN in ectopic group was significantly larger by 11 ms (39 ± 18 vs. 28 ± 16 ms, $P < 0.05$) and RMSSD was significantly larger by 23 ms (47 ± 29 vs. 24 ± 23 ms, $P < 0.05$). For frequency-domain indices, LFn in ectopic group was significantly lower by 0.14 (0.34 ± 0.13 vs. 0.48 ± 0.14, $P < 0.01$) while HFn was significantly larger by 0.14 (0.66 ± 0.13 vs. 0.52 ± 0.14, $P < 0.01$).

Then we divided the ectopic RR segments into sub-groups with different amount of ectopic beats. Figure 2 shows the distribution of RR segments classified by the number of ectopic beats. There are total 795 ectopic-free RR segments (also as shown in Table 2). For ectopic ones, there are 464, 243, 138, 81, 50 and 33 segments when ectopic beast are from one to six respectively, and there are 217 ectopic segments with ectopic beats more than six. Figure 3 shows the corresponding mean and SDs values of the four HRV indices for each RR segment group, to allow the

ectopic beat number-related HRV changes to be observed and compared.

For time-domain indices, SDNN increased with increasing ectopic beat number. When compared with the ectopic-free group, statistically significant increases were observed at the group with one ectopic beat ($P < 0.01$), the group with two ectopic beats ($P < 0.01$) and the group with more than six ectopic beats ($P < 0.01$). However, the groups with three to six ectopic beats did not show the statistical significance. The reason maybe come from the small amount of RR segments. RMSSD also increased with the increase of ectopic beat number for each group. When compared with the ectopic-free group, statistically significant increases were observed for all seven ectopic groups (all $P < 0.01$).

For frequency-domain indices, LFn gradually decreased with the increase of ectopic beat number for each group. When compared with the ectopic-free group, statistically significant decreases were observed for all seven ectopic groups (all $P < 0.01$). HFn showed a reverse trend to LFn since mathematically, the sum of LFn and HFn was a constant.

For comparison of the results from time-domain and frequency-domain HRV indices, the latter responded more quickly to the appearance of ectopic beats. With the increase of ectopic beats from one to six, LFn (HFn) quickly decreased (increased) at these situations with relatively small amount of ectopic beats. When the number of ectopic beats was large and increased up to more than six, the decrease trend in LFn (increase trend in HFn) was not obvious.

Table 2 HRV results for ectopic-free and ectopic 5-min RR segments

Index	Ectopic-free	Ectopic	P-value
# segment	795	1277	
SDNN (ms)	28 ± 16	39 ± 18	<0.05
RMSSD (ms)	24 ± 23	47 ± 29	<0.05
LFn	0.48 ± 0.14	0.34 ± 0.13	<0.01
HFn	0.52 ± 0.14	0.66 ± 0.13	<0.01

Fig. 2 Distribution of the ectopic-free and ectopic 5-min RR segments classified by the number of ectopic beats
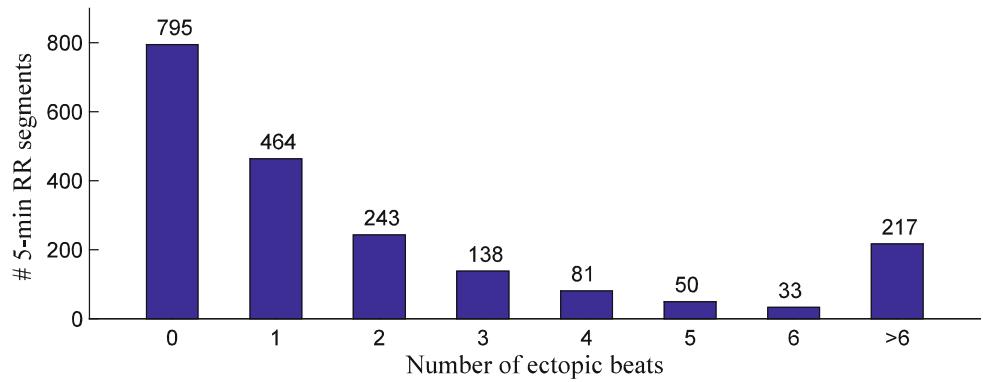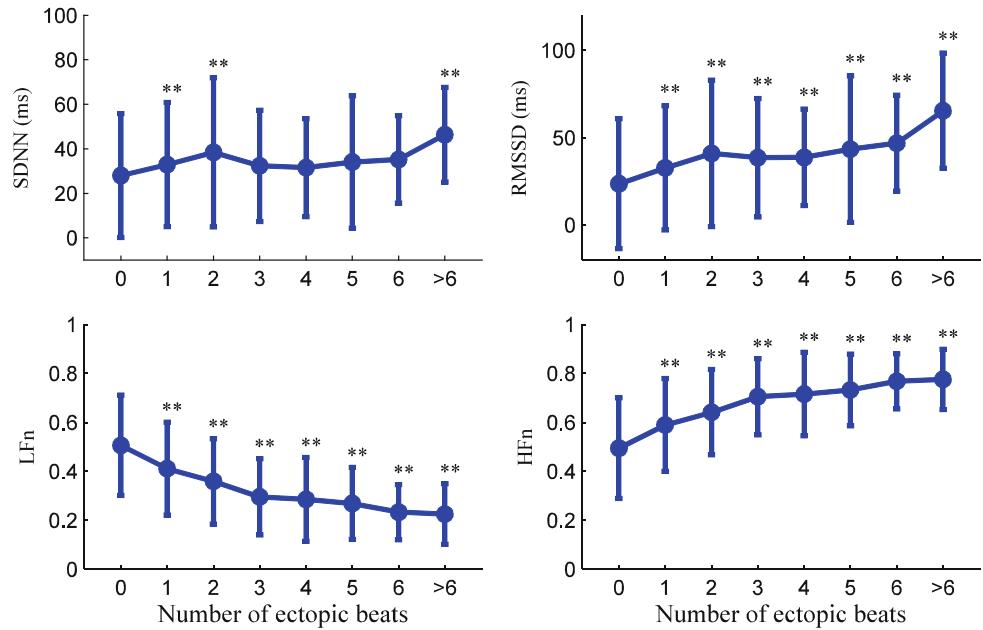

Fig. 3 Group mean and standard standards (SDs) of four HRV indices at each RR segment group with different numbers of ectopic beats. Compared with ectopic-free group, statistically significant differences at the $P < 0.01$ level are marked as '**'

However, time-domain indices showed distinct changes when applied on the RR segments with more than six ectopic beats.

4 Discussion

In this study, we quantified the effect of different amount of ectopic beats on the common time-domain and frequency-domain HRV indices for CHF patients. The results showed that the ectopic RR segments had larger SDNN, RMSSD, and HFn but lower LFn values than the ectopic-free RR segments. Compared with the indices of RMSSD and frequency-domain indices, SDNN was least affected by a relatively small amount of ectopic beats (one to six beats). Compared with the time-domain indices, the frequency-domain indices responded more quickly to the appearance of ectopic beats. The results confirmed that

ectopic beats in RR segments have a significant influence on the HRV results for CHF patients.

Ectopic beats are routinely removed/edited from the RR tachogram prior to HRV analysis. Our results agreed with the previously reported works. Salo et al. found that SDNN was least affected by the editing of RR intervals, and compared with the indices of SDNN and RMSSD, frequency-domain indices were more sensitive to the editing of RR intervals and reported larger errors after the ectopic beat editing [1]. This finding was consistent with our current study, where we showed that RMSSD and frequency-domain indices were more sensitive to the appearance of a small amount of ectopic beast (one to six beats). The reason is that the ectopic beats are usually step-like shapes and can result in sudden changes in RR interval time series. This effect is significant on the transient change of HRV reflected by RMSSD and the spectral components of HRV reflected by the frequency-domain LFn and HFn indices [4].

References

1. M. A. Salo, H. V. Huikuri, and T. Seppänen, "Ectopic beats in heart rate variability analysis: effects of editing on time and frequency domain measures," *Ann Noninvasive Electrocardiol,* vol. 6, no. 1, pp. 5–17, 2001.
2. D. Nabil and F. B. Reguig, "Ectopic beats detection and correction methods: A review," *Biomedical Signal Processing and Control,* vol. 18, no. 4, pp. 228–244, 2015.
3. G. G. Berntson and J. R. Stowell, "ECG artifacts and heart period variability: don't miss a beat," *Psychophysiology,* vol. 35, no. 1, pp. 127–132, 1998.
4. G. D. Clifford and L. Tarassenko, "Quantifying errors in spectral estimates of HRV due to beat replacement and resampling," *IEEE Trans Biomed Eng,* vol. 52, no. 4, pp. 630–638, 2005.
5. T. H. Tarkiainen, T. A. Kuusela, K. U. Tahvanainen, J. E. Hartikainen, P. Tiittanen, K. L. Timonen, and E. J. Vanninen, "Comparison of methods for editing of ectopic beats in measurements of short-term non-linear heart rate dynamics," *Clin Physiol Funct Imaging,* vol. 27, no. 2, pp. 126–133, 2007.
6. C. Y. Liu, L. P. Li, L. N. Zhao, D. C. Zheng, P. Li, and C. C. Liu, "A combination method of improved impulse rejection filter and template matching for identification of anomalous intervals in RR sequences," *Journal of Medical and Biological Engineering,* vol. 32, no. 8, pp. 245–250, 2012.
7. M. A. Peltola, "Role of editing of R-R intervals in the analysis of heart rate variability," *Front Physiol,* vol. 3, p. 148, 2012.
8. A. L. Goldberger, L. A. Amaral, L. Glass, J. M. Hausdorff, P. C. Ivanov, R. G. Mark, J. E. Mietus, G. B. Moody, C. K. Peng, and H. E. Stanley, "PhysioBank, PhysioToolkit, and PhysioNet: components of a new research resource for complex physiologic signals," *Circulation,* vol. 101, no. 23, pp. 215–220, 2000.
9. L. N. Zhao, S. S. Wei, C. Q. Zhang, Y. T. Zhang, X. E. Jiang, F. Liu, and C. Y. Liu, "Determination of sample entropy and fuzzy measure entropy parameters for distinguishing congestive heart failure from normal sinus rhythm subjects," *Entropy,* vol. 17, no. 9, pp. 6270–6288, 2015.
10. K. Zhu, D. Chemla, G. Roisman, W. Mao, S. Bazizi, A. Lefevre, and P. Escourrou, "Overnight heart rate variability in patients with obstructive sleep apnoea: a time and frequency domain study," *Clin Exp Pharmacol Physiol,* vol. 39, no. 11, pp. 901–908, 2012.

Heart Rate Monitoring for the Detection of Changes in Mental Demands During Computer Work

Ramtin Zargari Marandi, Pascal Madeleine, Nicolas Vuillerme, and Afshin Samani

Abstract

The detection of variations in mental demands is a key factor for optimizing the balance between occupational health and work performance. With the advances in heart rate acquisition technologies, heart rate monitoring is now easy and affordable. In this study, we recorded the heart rate of 18 healthy young participants while they performed three consecutive 5-min cyclic computer tasks with low, medium and high mental demands in two days with at least one week apart. The cycles began with memorizing a pattern of connected points following by the disappearance of the pattern, and then replicating it using computer mouse clicks on an incomplete version of the pattern. The mental demand of the tasks was manipulated by changing the complexity of the displayed patterns. The participants rated their perceived mental load after each task. The mean, range, and standard deviation of heart rate, MHR, RHR, and SDHR respectively, along with the performance (in terms of accuracy and speed of pattern replication) for each cycle was calculated and averaged for each task. The RHR and SDHR increased with increasing mental demands ($p < 0.001$), whereas the MHR did not significantly change in response to the different task demands. The responses remained consistent across days for RHR, MHR, but not SDHR. As expected, the performance decreased and the perceived mental load increased as the task demands increased. These results suggest that the variations in heart rate would provide useful information regarding the quantification of mental load.

1 Introduction

The advent of information technology has led to significant changes in work conditions. Many occupations emerged with different mental demands. It is important to monitor the mental load variation of workers to prevent overload and its detrimental effects, e.g., accidents. Various approaches and modalities have been introduced in the literature to detect changes in mental/cognitive load [1, 2]. However, there are serious limits to some modalities (e.g., electroencephalography) since they still are uncomfortable and can limit the user's motion or dexterity in most of the occupations. In recent years, wearable sensors have been developed to monitor biosignals such as heart rate [3]. These devices are getting more popular in recent years [4]. The unobtrusiveness of these devices is a key feature to use them in mental load monitoring.

The study of the relationship between characteristics of heart rate and mental load levels dates back to more than half a century ago [5]. Heart rate and its variability are known to be associated with mental load variations [6]. Many features have been introduced to characterize cardiac activity; however, a subset of them might be useful in practice due to the limited data access provided in commercial wearable sensors (e.g., fitness trackers). This may constrain the features to basic statistical features, such as the mean and the range of heart rate.

The aim of this study was to investigate whether there is an association between heart rate characteristics and mental load variations in a standardized model of computer work. We have employed a fitness tracker to record heart rate while people performed a computer task with different levels of mental

R. Zargari Marandi (✉) · P. Madeleine · N. Vuillerme
A. Samani (✉)
Sport Sciences, Department of Health Science and Technology, Aalborg University, Aalborg East, Denmark
e-mail: rzm@hst.aau.dk

A. Samani
e-mail: afsamani@aau.dk

R. Zargari Marandi · N. Vuillerme
Université Grenoble-Alpes, AGEIS, Grenoble, France

N. Vuillerme
Institut Universitaire de France, Paris, France

demands. We statistically analyzed the association between the heart rate features and the levels of the mental demands.

2 Materials and Methods

2.1 Participants

Eighteen healthy young participants (six females and 12 males, aged 23 ± 3 years) voluntarily participated in this study. They were right-handed, had normal or corrected to normal vision, and reported no background of mental or psychological disorders. The participants were asked to obstinate alcohol for 24 h, and caffeine, smoking and drugs for 12 h prior to experimental days. The study was approved by The North Denmark Region Committee on Health Research Ethics, project number N-20160023, and conducted in accordance with the Declaration of Helsinki.

2.2 Experimental Procedure

A task (WAME 1.0, [1]) was developed in a graphical user interface (MATLAB R2015b) based on standard models of computer work [7]. The participants were sitting behind a desk to perform the task on a computer screen using a computer mouse. The task has been described in our previous work [1]. Briefly, the task was displayed to the participants on a 19 in. LCD monitor (1280 × 1024 pixels). The participants underwent five episodes (5-min) of the task, with 1-min pauses in between. The first two episodes were conducted for the acclimatization with the task. The three remaining episodes were performed under a sequence of three levels of mental demands (low, medium, and high). The order of the episodes was counterbalanced across participants to avoid carry-over effect. Each episode of the task included cyclic operations. Each cycle began with memorization of a pattern of connected points in different shapes. It was followed by fixating on a single point while the pattern was not displayed. Afterwards, the points without connecting lines appeared and the participant had a limited time to click on the points in a specific order to replicate the recently memorized pattern. An extra point (distracting point) was also shown during the replication period which must not have been clicked. A new cycle with a new pattern appeared after the offset of each cycle with no pause in between. The patterns were generated randomly subject to some constraints. No loop or crossings were allowed for the lines connecting the points. The length of the lines and the angles made in the connection of two lines were limited to ensure central location of the connected pattern in the center of computer screen. The experiments were performed in two days with at least seven days in between, and in the same time of the day (10–12 a.m. or 1–3 p.m.) to lower the possible effects of variation in circadian rhythms. Each of the first two sections of a cycle took 2.06, 2.34, and 2.62 s, respectively for low, medium, and high levels. Likewise, the third section of a cycle took 4.11, 5.06, and 6.02 s, respectively for low, medium, and high levels.

2.3 Measurements

The heart rate was recorded during each task episode using A300 fitness tracker (Polar Electro Oy, Finland). This device provides instantaneous heart rate in one second intervals. The asserted accuracy of the heart rate measurement is about $\pm 1\%$ or 1 bpm in stable conditions which may also apply in our experimental setting with sedentary computer work. The validity and usability of this device have been approved in an independent study [8]. From the heart rate data, we extracted the mean, range, and standard deviation of heart rate (respectively indicated by MHR, RHR, and SDHR) during each cycle and averaged them across cycles for each of the three task episodes.

We also measured the performance of doing the task based on the clicking accuracy and speed. As described previously [1], the accuracy was computed based on how complete the patterns were replicated considering all clicks. The speed referred to how fast the pattern replication was drawn by the participants. The performance measure was monotonically related to how well the participants performed the task.

In addition, we acquired the subjective ratings of perceived mental load using national aeronautics and space administration task load index (NASA-TLX) questionnaire [9] after each task episode.

2.4 Statistics

Repeated-measures analysis of variance used to examine the effects of change in the levels of mental demands (low, medium and high) and experiment days (day 1, and day 2) on cardiac features (MHR and RHR), performance, and NASA-TLX scores. If the assumption of sphericity was not met, a Greenhouse-Geisser correction was applied. Bonferroni adjustment was used for pairwise comparison across the mental load levels.

3 Results

Table 1 illustrates the overall results regarding the effects of different levels of mental demands. The RHR significantly increased with the levels of mental demands,

Table 1 Overview of the experimental results (Mean ± standard deviation). Statistically significant changed metrics affected by the levels of mental demands are bolded (*$p < 0.05$)

	Day 1			Day 2		
	Low	Medium	High	Low	Medium	High
MHR (bpm)	72 ± 11	72 ± 10	73 ± 10	75 ± 11	74 ± 11	75 ± 12
RHR (bpm)	2 ± 0	2 ± 0	3 ± 1	2 ± 1	3 ± 1	3 ± 1
SDHR (bpm)	0.71 ± 0.24	0.77 ± 0.27	0.93 ± 0.43	0.82 ± 0.35	0.91 ± 0.38	0.98 ± 0.48
Performance	0.49 ± 0.07	0.42 ± 0.08	0.38 ± 0.09	0.52 ± 0.06	0.46 ± 0.07	0.43 ± 0.07
Perceived mental load	14 ± 5	18 ± 7	19 ± 7	14 ± 6	17 ± 7	17 ± 8

$F(1.4, 24.6) = 28.5, p < 0.001, \eta_p^2 = 0.6$. No significant difference between days was observed in RHR. No interaction between the days and levels was found. The pairwise comparisons exhibited increase in RHR from low to medium, $p = 0.002$, low to high, $p < 0.001$, and medium to high levels, $p = 0.002$. The SDHR also increased significantly with the levels of mental demands, $F(1.5, 49.2) = 14.2, p < 0.001, \eta_p^2 = 0.3$. Significant differences between days were found in SDHR, $F(1, 33) = 4.4, p = 0.043, \eta_p^2 = 0.1$. Pairwise comparisons revealed that the SDHR significantly increased from low to medium, $p = 0.042$, low to high, $p < 0.001$, and medium to high, $p = 0.003$, levels in the first day, and from low to high level, $p = 0.030$, in the second day in SDHR. No interaction between days and levels was found in SDHR. The MHR did not change significantly in response to the different levels of mental demands. Neither a significant difference between days was found.

The performance decreased significantly as the mental demands increased, $F(2, 34) = 24.9, p < 0.001, \eta_p^2 = 0.6$. It was also significantly increased with the day of the experiment, $F(1, 17) = 4.9, p = 0.040, \eta_p^2 = 0.2$. No interaction between the days and levels were observed. Pairwise comparison revealed that the decrease in the performance was significant from the low to medium, $p = 0.005$, medium to high, $p = 0.015$, and low to high levels, $p < 0.001$, in the first day. In the second day, the decrease in the performance was also significant from low to medium, $p = 0.018$, and low to high levels, $p < 0.001$.

The perceived mental load increased significantly with the levels, $F(2, 36) = 7.6, p = 0.002, \eta_p^2 = 0.3$. No significant difference in the perceived mental load was observed across days. No interactions between the days and levels were found. Pairwise comparisons revealed that the perceived mental load was significantly higher in the high level compared with the low level, $p = 0.021$, higher in the medium level than in the low level, $p = 0.022$.

4 Conclusion

The results showed that the RHR was sensitive to three different levels of mental load. The performance and perceived mental load changed in concordance with the changing demands of the task. This, in sum, lends support to the possibility of using the range of heart rate as an index to detect overload in computer work. Furthermore, the consistency of responses across days also warrants its applicability. Although SDHR was also sensitive to the mental load levels, its inconsistent response across days disproves its appropriateness.

Although commercially available heart rate sensors may not provide access to data (e.g., RR intervals) required to compute some parameters of heart rate variability (HRV) such as standard deviation of RR intervals a.k.a. SDNN, statistical features of variation in instantaneous heart rate such as RHR would partially capture this information. The association between the levels of mental demands and RHR was in agreement with previous findings showing that the variability of heart rate correlates with mental load levels [10, 11]. Heart rate and HRV in relation to mental load variation were reported in computer tasks [12]. The study was performed using an imaging technique [13] to measure HRV and heart rate with no contact which despite its privacy concerns is a promising approach to mental load monitoring. As such, the mean heart rate corresponded to very light work [14]. It also worth noting that the mean of heart rate by itself may not show the change in mental load, but its variability contained the relevant information to capture the changes. This is also in line with previous studies showing that the associated metrics to HRV usually perform superior to the mean of heart rate [12, 15].

There are some issues regarding the limitations to use RHR. Since HRV is linked to autonomic nervous system [16], RHR should be examined on its specificity to discriminate mental load variation from various emotional

states and other interrelated psychophysiological states [17]. Another issue is to choose an appropriate time window to compute RHR and MHR in long-term monitoring. One suggestion in computer work would be to take consideration of task specifications (e.g., repetitiveness) into account for choosing the time window.

The consistency of RHR responses across days warrants its applicability in monitoring mental load. Future work will consider incorporating this cardiac feature together with relevant features from other unobtrusive modalities such as eye-tracking [1] to develop a robust model of mental workload.

References

1. Marandi R.Z., Samani A., Madeleine P.: The level of mental load during a functional task is reflected in oculometrics. In: Eskola H., Väisänen O., Viik J., Hyttinen J. (eds) EMBEC & NBC 2017. IFMBE Proceedings, vol 65. pp. 57–60 Springer, Singapore (2017).
2. Dhamala M., Pagnoni G., Wiesenfeld K., Berns G.S.: Measurements of brain activity complexity for varying mental loads. Physical Review E, 65(4), 1–7 (2002).
3. Mukhopadhyay SC. Wearable sensors for human activity monitoring: A review. IEEE Sens J 15(3), 1321–1330 (2015).
4. Phan D., Siong L.Y., Pathirana P.N., Seneviratne A.: Smartwatch: Performance evaluation for long-term heart rate monitoring. In: 2015 Int. Symp. Bioelectron. Bioinforma. pp. 144–147, IEEE, Beijing (2015).
5. Blitz P.S., Hoogstraten J., Mulder G.: Mental load, heart rate and heart rate variability. Psychol Forsch 33(4), 277–288 (1970).
6. Taelman J., Vandeput S., Vlemincx E.: Instantaneous changes in heart rate regulation due to mental load in simulated office work. Eur J Appl Physiol 111(7), 1497–1505 (2011).
7. Samani A., Holtermann A., Søgaard K., Madeleine P.: Active pauses induce more variable electromyographic pattern of the trapezius muscle activity during computer work. J Electromyogr Kinesiol, 19(6), e430–e437 (2009).
8. Vooijs M., Alpay L.L., Snoeck-Stroband J.B.: Validity and usability of low-cost accelerometers for internet-based self-monitoring of physical activity in patients with chronic obstructive pulmonary disease. J Med Internet Res 3(4):e14 (2014).
9. Hart S.G., Staveland L.E.: Development of NASA-TLX (Task Load Index): Results of Empirical and Theoretical Research. Adv Psychol 52:139–183 (1988).
10. Cinaz B., La Marca. R., Arnrich B., Tröster G.: Monitoring of mental workload levels. In: Proc. of the IADIS Int. Conf. e-Health pp. 189–193 (2010).
11. Vandeput S., Taelman J., Spaepen A., Van Huffel S.: Heart rate variability as a tool to distinguish periods of physical and mental stress in a laboratory environment. In: Proc. 6th Int. Work. biosignal Interpret. (BSI), New Haven, CT. pp. 187–190 (2009).
12. McDuff D.J., Hernandez J., Gontarek S., Picard R.W.: COGCAM: Contact-free Measurement of Cognitive Stress During Computer Tasks with a Digital Camera. Proc 2016 CHI Conf Hum Factors Comput Syst pp. 4000–4004 (2016).
13. McDuff D., Gontarek S., Picard R.W.: Improvements in remote cardiopulmonary measurement using a five band digital camera. IEEE Trans Biomed Eng 61(10), 2593–2601 (2014).
14. Åstrand PO.: Textbook of Work Physiology: Physiological Bases of Exercise. 4th edn. Human Kinetics, US (2003).
15. Schneider F., Martin J., Hapfelmeier A.: The validity of linear and non-linear heart rate metrics as workload indicators of emergency physicians. PLoS One 12(11), p. e0188635 (2017).
16. Luque-Casado A., Perales J.C., Cárdenas D., Sanabria D.: Heart rate variability and cognitive processing: The autonomic response to task demands. Biol Psychol 113:83–90 (2015).
17. Nickel P., Nachreiner F.: Sensitivity and Diagnosticity of the 0.1-Hz Component of Heart Rate Variability as an Indicator of Mental Workload. Hum Factors J Hum Factors Ergon Soc 45(4), 575–590 (2003).

Indirect Cardiac Output and Stroke Volume Assessment During Spiroergometric Examination

Jaroslav Novak, Milan Stork, and Vaclav Zeman

Abstract

Cardiac output can be accurately estimated from VO_2 (oxygen consumption) during exercise in normal subjects and in patients with heart failure by measuring the *LAT* (lactate acidosis threshold) or VO_{2peak} (peak oxygen consumption) during bicycle ergometer test. Hence, during step-vice increased workload on bicycle ergometer with continuous measurement of oxygen consumption changes in cardiac output and stroke volume (*SV*) can be calculated. Our measurement documented usefulness of this method in subjects of different performance level, both men and women. Non-invasive evaluation of cardiac output and stroke volume during spiroergometric stress test enables to extent the information about the health status of the subject and about the functional reserve of his circulatory apparatus. The examples presented in this study prove the applicability of this method in evaluation of fitness level in healthy male and female subjects of different age. The data of cardiac output and stroke volume will be added into the software program of final protocol of complex sports medical examination. This method can enrich the scale of parameters testifying the functional capacity of the subjects.

J. Novak (✉) · V. Zeman
Department of Sports Medicine Medical Faculty in Plzen, Charles University in Prague, Prague, Czech Republic
e-mail: novakj@lfp.cuni.cz

V. Zeman
e-mail: vaclav.zeman@lfp.cuni.cz

M. Stork
Department of Applied Electronics and Telecommunications/RICE, University of West Bohemia, Pilsen, Czech Republic
e-mail: stork@kae.zcu.cz

1 Introduction

Cardiac output (*CO*) is a measure of the amount of blood pumped by either ventricle. In steady state, the outputs of both ventricles are the same. In a healthy adult male, *CO* is approximately 5 L/min [1]. *CO* can vary, however, according to the body's physiological needs; for example, a well-trained athlete, while exercising, can increase *CO* to up to 30 L/min to increase the rate of transport of oxygen, nutrients, and wastes [2]. Abnormally low levels of *CO* can also be an indication of pathology.

The primary function of the heart is to import energy to blood to generate and sustain an arterial blood pressure sufficient to adequately perfuse organs. The heart achieves this by contracting its muscular walls around a closed chamber to generate sufficient pressure to propel blood from the left ventricle, through the aortic valve, and into the aorta. Each time the left ventricle contract, a volume of blood is ejected into the aorta. This *SV*, multiplied by the number of beats per minute (*HR*), equals the *CO*:

$$CO = SV * HR [\text{ml/min, ml/min/beat, beats/min}] \quad (1)$$

CO indicates how well the heart is performing this function. *CO* is regulated principally by the demand for oxygen by the cells of the body. If the cells are working hard, with a high metabolic oxygen demand then the *CO* is raised to increase the supply of oxygen to the cells, while at rest when the cellular demand is low, the *CO* return to baseline. *CO* is regulated not only by the heart as it pumps, but also by the function of the vessels of the body as they actively relax and contract thereby increasing and decreasing the resistance to flow.

When *CO* increases in a healthy but untrained individual, most of the increase can be attributed to an increase in *HR*. Increased sympathetic nervous system activity, and decreased parasympathetic nervous system activity can also increase *CO*. *HR* can vary by a factor of approximately 3,

between 60 and 180 beats per minute, while SV can vary between 70 and 120 ml, a ratio factor of only 1.7 ml.

The ability to accurately measure CO is important in clinical medicine as it provides for improved diagnosis of abnormalities, and can be used to guide appropriate management. CO measurement, if it were accurate and non-invasive, would be adopted as part of every clinical examination from general observations to the intensive care ward, and would be as common as simple blood pressure measurements are now. Such practice, if it were adopted, may revolutionize the treatment of many cardiovascular diseases including hypertension and heart failure. This is the reason why CO measurement is now an important research and clinical focus in cardiovascular medicine.

Current invasive procedures for monitoring CO increase the potential for complications, including the higher risk of infection and sepsis. Other methods of measuring CO exist, but require additional measurements, tests, and/or equipment:

Impedance cardiography is a non-invasive method of measuring CO. Impedance changes are due to changes in intrathoracic fluid volume and respiration, so changes in blood volume per cardiac cycle can be measured and used to estimate SV and CO [3].

The **Doppler ultrasound method** uses reflected sound waves to calculate flow velocity and volume to obtain CO and is a non-invasive.

The **Pulse Pressure** (PP) methods measure the pressure in an artery over time to derive a waveform and use this information to calculate cardiac performance. The problem is that any measure from the artery includes the changes in pressure associated with changes in arterial function (compliance, impedance, etc.).

The **Fick method** derives CO through calculating oxygen consumed over a given period of time by measuring oxygen consumption per minute with a spirometer, oxygen concentration of venous blood from the pulmonary artery, and oxygen concentration of arterial blood from a peripheral artery [4]. CO can be calculated from these measurements: VO_2 consumption per minute using a spirometer (with the subject re-breathing air) and a CO_2 absorber

- the oxygen content of blood taken from the pulmonary artery (representing mixed venous blood)
- the oxygen content of blood from a cannula in a peripheral artery (representing arterial blood)

From these values, it is known (2):

$$VO_2 = (CO * C_A) - (CO * C_V) \qquad (2)$$

where C_A is oxygen content of arterial blood and C_V is oxygen content of venous blood and CO is:

$$CO = VO_2/(C_A - C_V) \qquad (3)$$

While considered to be the most accurate method for CO measurement, Fick method is invasive, requires time for the sample analysis, and accurate oxygen consumption samples are difficult to acquire. There have also been modifications to the Fick method where respiratory oxygen content is measured as part of a closed system and the consumed oxygen calculated using an assumed oxygen consumption index which is then used to calculate CO. Other modifications use inert gas as tracers and measure the change in inspired and expired gas concentrations to calculate CO.

Athletic training, mainly endurance training, evokes significant adaptive changes both in cardiac output and in many other body functions. Maximal oxygen uptake (VO_{2max}) as the highest rate of oxygen consumption during maximal or exhaustive exercise, is considered as the best objective laboratory measure of endurance capacity. It markedly depends on the oxygen transport capacity (cardiac output, red blood cell count, plasma volume) and oxidative capacity of muscles. While measuring of heart rate is practicable method how to evaluate response and adaptability to physical load, assessment of cardiac output was not so easy.

In this paper, CO was estimated noninvasively from oxygen uptake during exercise on cycle or treadmill ergometer.

2 Materials and Methods

Because both HR and VO_2 can be easily measured during standard incremental cardio-pulmonary exercise testing [5], both CO and SV could be accurately quantified if the simultaneous arteriovenous O_2 content difference ($C_A - C_V$) could be estimated [6, 7]. For noninvasive CO estimation, exercise tests were performed on an electronically braked cycle ergometer (or treadmill) controlled by computer. Subjects were familiarized with the apparatus and performed a continuous incremental symptom-limited maximal test for determination of VO_{2max} and lactic acidosis threshold (LAT). The samples of expired gas were connected to gas analyzer (O_2 and CO_2 analyzer). All electrical signals from sensors and from gas analyzer were processed in personal computer. From the measured values workload (W) for cycle ergometer or (km/h) for treadmill, HR (beats/min) and VO_2 (l/min) the CO was estimated [8]. Also SV was calculated. The CO was estimated according formula (4):

$$CO = \frac{100 * VO_2}{\left[5.721 + 0.1047 \frac{100 * VO_2}{VO_{2MAX}}\right]} \qquad (1/\text{min}) \qquad (4)$$

Six subjects (3 men and 3 women) of our data-base with very different athletic background were used to demonstrate

Table 1 Spiroergometric values of 6 subject. Sub = Subject M-male F-female, He = Height (cm), We = Weight (kg), VO2m = VO_{2max} (l), VO_{2mk} = VO_{2max}/kg (ml/min/kg)

Sub	Age	He	We	VO_{2m}	VO_{2mk}
M1	28	177	70.3	5.75	81
M2	49	170	66.7	4.2	63
M3	65	166.5	65.2	3.15	39.7
F1	31	168.5	63.2	4.33	68.5
F2	11	156.5	42.8	1.6	37.5
F3	40	165.5	72	2.69	37.4
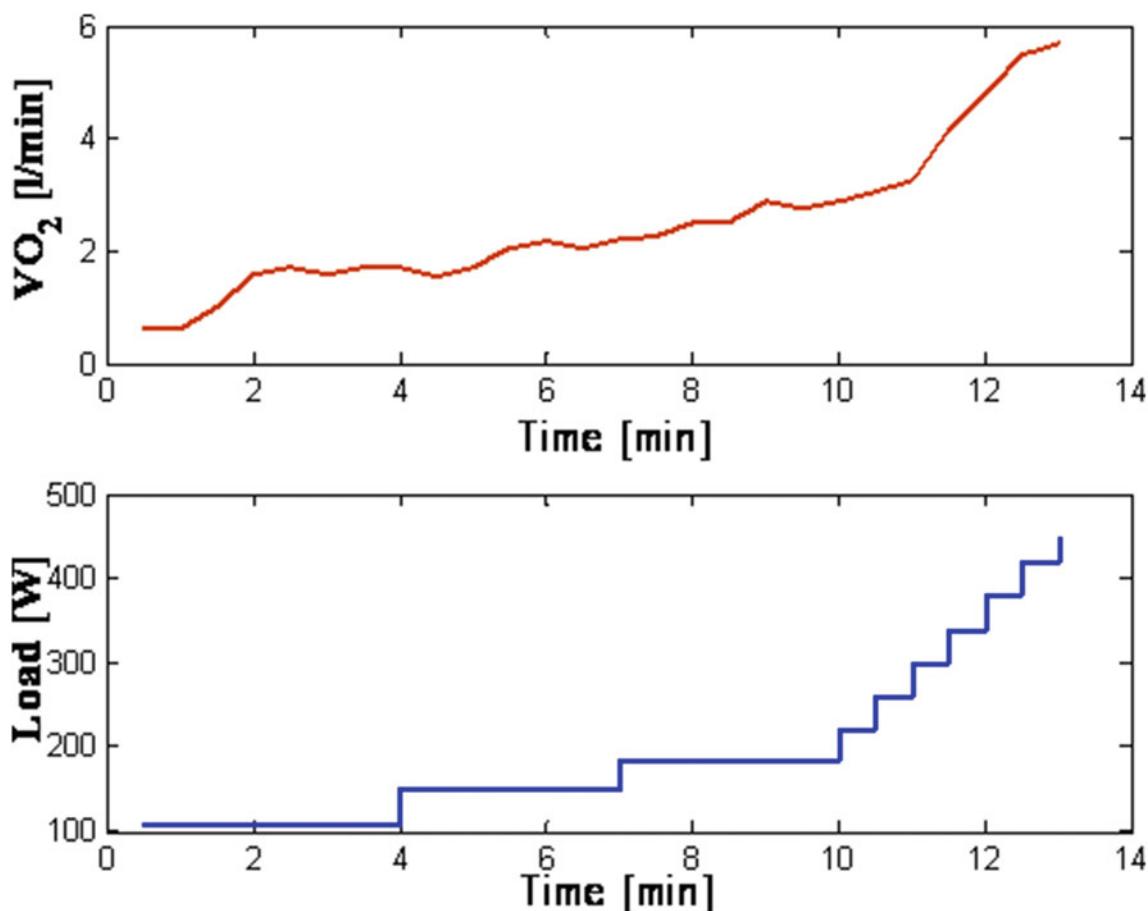
Fig. 1 Workloads (in W) and VO_2 (l/min) during stress-test in M1 on cycle ergometer

the dynamics of *CO* and *SV* during standard spiroergometric stress test (Table 1). M1—top-class cross-country skier, M2—leisure "hobby" athlete, M3—pre-surgery patient, F1—top-class triathlete, F2—young swimmer, F3—leisure "hobby" athlete. The test used 3 three-minute sub-maximal worming-up workloads followed by step-vise increased workload up to the exhaustion

3 Results

Figure 1 illustrates the changes in oxygen consumption (*VO₂*) during step-vise increased workload in standard stress-test in top-class cross-country skier. *VO₂* values were used to calculate estimated *CO* and *SV* values. Results of
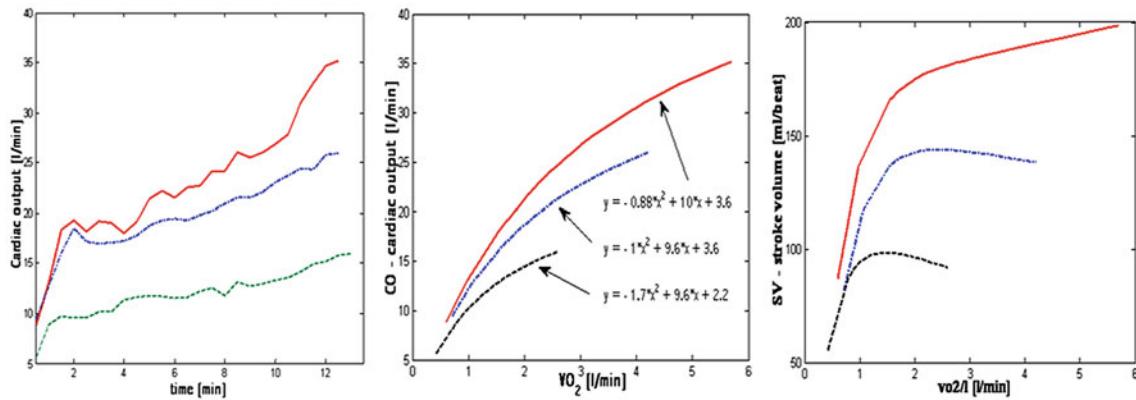
Fig. 2 CO and SV changes during the stress-test in men. Left: CO related to time during stress-test. Middle—CO related to VO_2 during stress-test. Right: SV related to VO_2 during stress-test (red—top class cross-country skier, blue—former top class cross-country skier, now "masters" age group; black—leisure "hobby" athlete) (Color figure online)
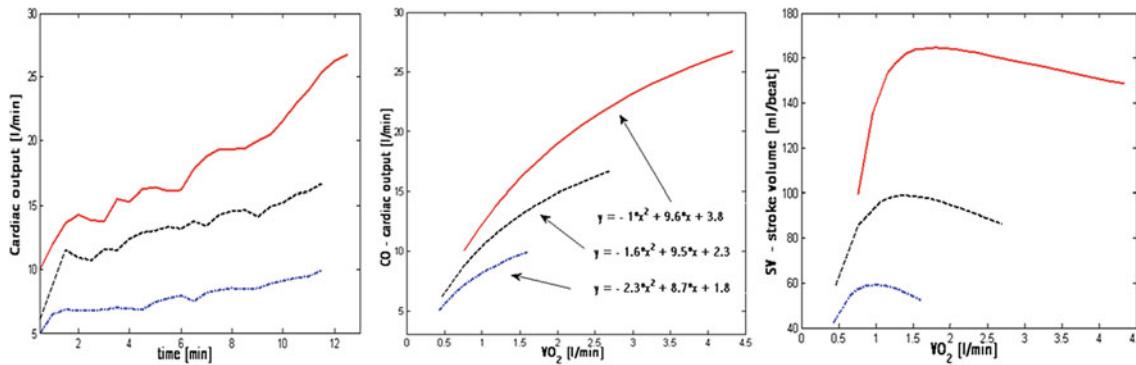
Fig. 3 CO and SV changes during the stress-test in women. Left: CO related to time during stress-test. Middle—CO related to VO_2 during stress-test. Right: SV related to VO_2 during stress-test (red—top class cross-country skier, blue—leisure "hobby" athlete, black– pre-surgery patient) (Color figure online)

those calculations are presented in Fig. 2 for men and in Fig. 3 for women. VO_2 isopleths according to Stringer et al. [7] experience were used to illustrate the difference in highly trained endurance athlete and less trained or even untrained subjects. The data clearly documented the difference in the heart's pumping efficiency during increasing peripheral tissue needs. Higher cardiac output as a function of higher stroke volume plays important role in increased transporting capacity of blood for oxygen and enables well trained subject to achieve significantly higher physical performance.

4 Discussion

A totally noninvasive determination of CO and SV during exercise would be very useful in healthy subjects as well as in patients with various degrees of cardiac insufficiency [6, 7]. Having estimated CO and corresponding HR, SV can

be calculated. This can provide a simple and low-cost assessment of cardiac function in response to exercise.

Although it is generally assumed that CO increases linearly with VO_2, the pattern of variation in VO_2 and CO as maximal O_2 consumption is approached has not been extensively investigated and may vary among individuals. According to Frank-Starling mechanism the amount of blood that the heart pumps works up to a limit of 3 times the resting normal cardiac output. When the peripheral tissues demand excessive amounts of blood flow, the nervous signals increase cardiac output [9]. Our examples document that the time course of these changes is very similar in the subjects of very different cardio-respiratory fitness level (see Figs. 2 and 3). However, these findings still need to be proved in the groups of subjects of different lifestyle, different athletic background, men and women, and even patients. Our pilot study indicates that top level endurance athletes can reach outstanding values of CO and SV at about

40 l/min and 200 ml/beat respectively [10]. Hence, this method seems to offer another useful data to evaluate cardio-respiratory capacity and adaptation to physical activity and/or inactivity.

Conflicts of Interest None of the authors have actual or potential conflicts of interest to be disclosed.

References

1. Costanzo, L. S.: Physiology. Saunders and Company, 3rd edition (2006).
2. Guyton A.C., and Hall J.E.: Textbook of Medical Physiology. Saunders and Company, 11th edition (2005).
3. White S.W., Quail A.W, De Leeuw P.W, Traugott F.M., Brown W.J., Porges W.L., and Cottee, D.B.: Impedance cardiography for cardiac output measurement: an evaluation of accuracy and limitations. European Heart Journal, 11:79 (1990).
4. Fick, A.: The output of the heart. Phys. Med. Gesellschaft 16, (1870).
5. Wasserman, K., Hansen, J.E., Sue, D.Y., Whipp, B. J. and Casaburi, R.: Principles of exercise testing and interpretation, including pathophysiology and clinical applications, Lippincott Williams and Wilkins (1999).
6. Sullivan M.J., Knight J.D., Higginbotham M.B. and Cobb F.R.: Relation between central and peripheral hemodynamics during exercise in patients with chronic heart failure. Circulation 80: 769–781 (1989).
7. Stringer W.W., Hansen J.E. and Wasserman K.: Cardiac output estimated noninvasively from oxygen uptake during exercise. J. Appl. Physiol. 82(3): 908–912 (1997).
8. Beck K.C., Randolph L.N., Bailey K.R, Wood C.M, Snyder E.M. and Johnson B.D.: Relationship between cardiac output and oxygen consumption during upright cycle exercise in healthy humans. J Appl Physiol 101: 1474–1480 (2006).
9. Guyton A.C., Hall J.E., Lohmeier T.E., Jackson T.E.: Modern concepts of circulatory function. In: Hayase S., Murao S.: Cardiology. Exc. Med, Amsterdam-Oxford-Princeton (1979).
10. Ekblom B., Hermansen L.: Cardiac output in athletes. J. Appl. Physiol. 25, 619–625 (1968).

An Impulsive Noise Rejection Filter for Wearable ECG Signal Processing

Xiangyu Zhang, Jianqing Li, Zhipeng Cai, Shengyi Ma, Jian Zhang, and Chengyu Liu

Abstract

Objective: QRS detection is essential for ECG signal processing. For real-time dynamic ECG, QRS detection is usually performed on a fixed time window, lengths from several to dozens of seconds. However, the unexpected impulsive noise (usually short-term but large amplitude) within the ECG episode is a disaster for QRS detectors. Thus we aimed to propose a new filter to handle this impulsive noise to improve the QRS detection accuracy in wearable ECG measurement. Methods: ECG signals were acquired by the Lenovo Smart-vest, which is a 12-lead wearable ECG collection device, with a sample rate of 500 Hz. The consecutive ECG signals were manually visual-scanned to pick out the episodes including impulsive noises. A fixed time window of 10 s was used for segmenting the ECG episodes. Then, each 10-s ECG episode was processed by Butterworth band-pass filter (0.5–35 Hz). The common Pan & Tompkins (P&T) QRS detector was performed on the filtered signals. A flexible threshold of 60 ms was used to confirm the true positive detection for QRS complex. One hundred episodes with the detection accuracy less than 60% were selected as the test data for the new proposed impulsive noise rejection (INR) filter. The new INR filter was designed with the combination of first order difference, fast Fourier transformation (FFT) and adaptive filtering. Results: Before the INR filtering, the average QRS detection accuracy of the 100 challenging ECG episodes was only 50.62%. As contrast, with the help of the INR filter, P&T detector can achieve a high detection accuracy of 76.32%. Significance: Impulsive noise is a challenging noise existing in the wearable ECG signals. The new designed INR filter can efficiently reject the impulsive noise, and make benefit for the accurate QRS detection in the dynamic environment.

1 Introduction

The World Health Organization (WHO) states that the widespread cardiovascular disease (CVD) accounts for 29% of global deaths every year [1]. It is reported that 1 out of 3 deaths was dead for CVD in the United States [2]. Besides, the prevalence of CVD in China is on the rise, there are about 3 million deaths caused by CVD yearly [3].

Electrocardiogram (ECG) is widely used in past decades as it is a non-invasive measuring method to obtain the cardiac arrhythmias [4]. However, these CVDs-related deaths can be avoided if the diseases have been early detected, diagnosed and treated [5]. Recently wearable ECG has attracted lots of attention in health-care applications [6]. Wearable ECG acquisition system provides a convenient method for people to record their real time ECG signals in their daily life and offers an alternative way to guarantee their lives by early warning a variety of CVDs. To achieve the precisely classification of each heartbeat, the key technique was ECG signal processing and analyzing.

X. Zhang (✉) · J. Li · Z. Cai · C. Liu
School of Instrument Science and Engineering, Southeast University, Nanjing, China
e-mail: 230179249@seu.edu.cn

J. Li
e-mail: ljq@seu.edu.cn

C. Liu
e-mail: chengyu@seu.edu.cn

J. Li
School of Basic Medical Sciences, Nanjing Medical University, Nanjing, China

S. Ma
School of Biological Sciences & Medical Engineering, Southeast University, Nanjing, China

J. Zhang
Sir Run Run Hospital, Nanjing Medical University, Nanjing, China

Accurate QRS detection is an important progress for ECG signal processing, especially in dynamic environment. The ECG signals collected by wearable ECG devices integrated with dry electrodes usually contains lots of noises, particularly, the impulsive noise caused by the displacement or shedding of the electrode. Impulsive noises can destroy the ECG information significantly [7], and seriously affect the accuracy of the QRS detection due to the variations in noise amplitudes [8]. In addition, the instantaneous huge change of impulsive noise in amplitude is much larger than that in QRS complex, while the first order difference can perfectly locate the impulsive noise [9].

After locating the position of the impulsive noise, the data processing algorithms was developed to extract ECG signals from the impulsive noise annihilated data. The simple approach to remove the impulse noise is reducing the amplitude of the surrounding signal. The mean filter and the median filter method was also used, as it can effectively remove the noise caused by the sharp change of the amplitude of a certain point. However, the impulsive interference caused by the detachment of the electrode usually lasts for a period of time. Therefore, the traditional sliding filtering method cannot effectively remove the impulsive noise occurred in Wearable ECG signals. Li Su and Guoliang Zhao proposed an improved thresholding de-noising method based on Donoho's method to suppress impulsive noise to some extent [10]. Besides, Alina proposed a State Space Recursive Least Square (SSRLS) algorithm based enhanced adaptive impulsive noise cancellation technique. Alina's method shows a good performance on reducing the impulsive noise occurring just on one point. Although these algorithms can help remove impulsive noise, there still need to develop a fast method to extract ECG signal from noise-contaminated signal detected by wearable devices. Therefore, a new pulse interference detection and processing algorithm based on first order difference and Fast Fourier Transformation (FFT) was proposed.

2 Method

2.1 Data

The data source was ECG signals recorded by the Lenovo Smart-vest, which is a 12-lead wearable ECG monitoring device (Sampling @ 500 Hz). The consecutive ECG signals were manually visual-scanned to pick out the episodes including impulsive noises. A fixed time window of 10 s was used for segmenting the ECG episodes. These ECG signals. A fixed time window of 10 s was used for segmenting the ECG episodes. We finally find 100 challenge recording which is collected from 10 people with a totally 1433 beats. Each episode was processed individually.

2.2 Proposed Method

The new INR filter was designed with the combination of first order difference, fast Fourier transformation (FFT) and adaptive filtering. The first order difference was used to detect the position of impulsive noise.

Firstly, the baseline drift was removed by Butterworth band-pass filter, the band-pass cutoff frequency was 0.5–35 Hz. Then, the baseline drift removed data was defined as s(x), and the first order difference was used to locate the position of impulsive noise.

$$S'(x) = \text{diff}(s(x)) \tag{1}$$

$S'(x)$ is data after the first order difference. It is known that every 10 s ECG data contains 10–20 beats, then the mean value of the largest 20 peaks was set as the threshold.

$$T(x) = \text{sort}(\text{findpeaks}(S'(x))) \tag{2}$$

$$\text{Thr} = \text{mean}(T(\text{end} - 19 : \text{end})) \tag{3}$$

Secondly, the point larger than 1.5 times of the threshold was defined as the position where impulse occurs. Thereafter, the impulse was recognized as the range between the intersection points of the ECG signal and detected baseline around the impulse. Then, the values of the detected impulse episode were set to the value of its initial point, due to the limited range of the Operational Amplifier in the ECG collection device. Then cycle detection and processing steps, until there is no large pulse.

Finally, a FFT based band-pass filter, with a frequency range of 5–25 Hz, was designed by combining FFT and Hamming window. This progress will enhance the R-wave by reducing the influence of other frequencies. This is the reason that this filter was only used in the detection of the R-wave rather than the reconstruction of the ECG. After that, the Pan's method was used to locate the position of R peaks.

The flow chart for the progress can be seen from Fig. 1.
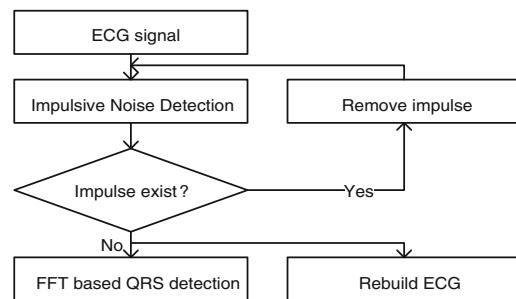
Fig. 1 Flow chart of ECG processing for the new proposed method

Step 1: In this step, we use the first order difference based impulse detector to find the impulsive noise from the data after preprocessing.

Step 2: In this step, the impulsive noise was removed.

Step 3: Repeat step 1 and step 2, until there is no impulsive noise.

Step 4: In this step, the impulse removed signal was filtered by the FFT filter. Then we use the Pan's method to detect the QRS.

3 Result

The Fig. 2 shows one example from the 100 ECG episodes. For the ECG signal, we firstly use the Butterworth filter to remove the based-line drift and the high frequency noises and the result was showed in Fig. 2a, then Pan's method was used to detect the QRS position. The result in Fig. 2b presents a bad accuracy because of the impulse amplitude influence. But it can easily find the QRS wave after the impulse was removed. The detected impulsive noise is showed in Fig. 2c. The Fig. 2d shows the final result of QRS detection with data processed by the proposed INR filter. Before processing, the QRS-detection method only can

locate the impulse. After processing, most R-wave was detected, indicating the QRS detection result has been improved significantly.

After the QRS detection, the true positive (TP), false positive (FP) and false negative (FN) was used to evaluate the QRS detections result. And the evaluation metrics of positive predictivity (P+), sensitivity (Se), and 1 score were calculated as:

$$P_+ = \frac{TP}{TP+FP} * 100\% \tag{4}$$

$$S_e = \frac{TP}{TP+FN} * 100\% \tag{5}$$

$$F_1 = \frac{TP*2}{TP*2+FN+FP} * 100\% \tag{6}$$

Table 1 shows the performance of the result of QRS detector on the selected data. The QRS detector (P&T method) reported Se value of 41.38%. P+ value of 65.16% and F1 value of 50.62% with the data after pre-processing. And a performance of Se value of 79.83%, P+ value of 73.10% and F1 value of 76.32% with the data processed by the INR filter. The result shows the superiority of the proposed method in the improvement of QRS detection.
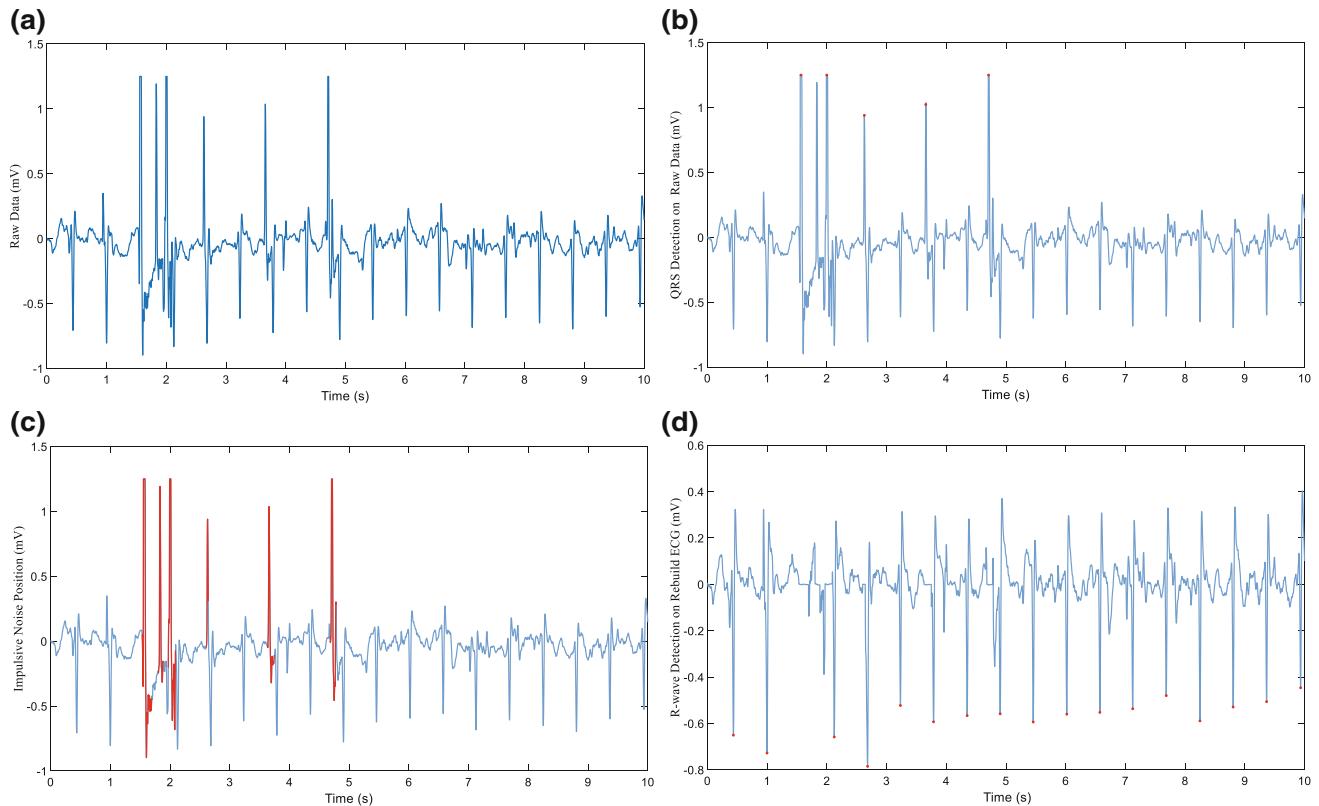
Fig. 2 The result of one example from the challenge ECG data. **a** The ECG signal after preprocessing; **b** ECG signal after preprocessing & the result of QRS detection; **c** the impulsive noise position on the ECG signal after preprocessing; **d** ECG signal after impulsive noise remove & the result of R-wave detection

Table 1 Performance of the QRS detection method on the selected data

Data	Total beat	TP	FN	FP	SE (%)	P+ (%)	F1 (%)
Before INR filter	1433	593	840	317	41.38	65.16	50.62
After INR filter	1433	1144	289	421	79.83	73.10	76.32

4 Conclusion

In this study, we proposed a INR filter aiming to remove the impulsive noise from wearable ECG signals and improve the QRS detection accuracy. The results show that the proposed filter has a good performance in impulse elimination, and provides a promising method to enhance QRS detection accuracy.

References

1. World Health Organization: Hearts: technical package for cardiovascular disease management in primary health care. Geneva: WHO, 1–73 (2016).

2. Mozaffarian, D., Benjamin, E. J., Go, A. S. et al.: Heart disease and stroke statistics—2016 update: a report from the American Heart Association. Circulation 133(4), e38–e360 (2016).

3. Weiwei, C., Runlin, G., Lisheng, L. et al.: China cardiovascular diseases report 2015: a summary. Journal of geriatric cardiology: JGC (2017).

4. Liu, S., Cai, G., Huang, Y., Chen, Y.: A wearable ECG apparatus for ubiquitous health care. In: 2016 IEEE International Conference on Systems, Man, and Cybernetics (SMC), pp. 004471–004476, IEEE, Budapest (2016).

5. Hernandez, A. I., Mora, F., Villegas, M., Passariello, G., Carrault, G.: Real-time ECG transmission via Internet for nonclinical applications. IEEE Transactions on information technology in biomedicine 5(3), 253–257 (2001).

6. Nagai, S., Anzai, D., Wang, J.: Motion artefact removals for wearable ECG using stationary wavelet transform. Healthcare technology letters 4(4), 138 (2017).

7. Mirza, A., Kabir, S M., Ayub, S., Arslan, M., Sheikh, S. A.: Enhanced impulsive noise cancellation based on SSRLS. In: 2015 International Conference on Computer, Communications, and Control Technology (I4CT), pp. 31–35 Kuching (2015).

8. Bhateja, V., Urooj, S., Verma, R., Mehrotra, R.: A novel approach for suppression of powerline interference and impulse noise in ECG signals. In: 2013 International Conference on Multimedia, Signal Processing and Communication Technologies (IMPACT), pp. 103–107, IEEE, Aligarh (2013).

9. Rasheed, S., Hussain, A.: Impulse Noise Detection and Removal Using First Order and Second Order Difference with Multistage Directional Statistics. In: 12th International Conference on Frontiers of Information Technology (FIT), pp. 325–329, IEEE, Islamabad, (2014).

10. Li S., Guoliang, Z.: De-noising of ECG signal using translation-Invariant wavelet de-noising method with improved thresholding. In: 27th Annual International Conference of the Engineering in Medicine and Biology Society, pp. 5946–5949, IEEE, Shanghai (2006).

Automatic Detection of P Wave in ECG During Ventricular Extrasystoles

Lucie Maršánová, Andrea Němcová, Radovan Smíšek,
Tomáš Goldmann, Martin Vítek, and Lukáš Smital

Abstract

This work introduces a new method for P wave detection in ECG signals during ventricular extrasystoles. The authors of previous works which deal with detection of P waves tested their algorithms mainly on physiological records (sinus rhythm) and they reached good results for these records. Testing of P wave detection algorithms using pathological records is usually not provided and if it is, the results are notably worse than in the case of physiological records. The automatic and reliable detection of atrial activity in pathological situations is still an unsolved problem. In this work, phasor transform in combination with classification algorithm is used for P wave detection. Phasor transform converts each ECG sample into a phasor which enhances changes in the ECG signal. The classification is based on extraction of morphological features which are derived from each QRS complex. The results of classification are used for demarcation of areas in which P waves are searched using phasor transform. The proposed algorithm was tested on signals no. 106, 119, 214 and 223 from MIT-BIH arrhythmia database, in which the ventricular extrasystoles are present. For validation whether the algorithm is functional also for signals with physiological rhythm, it was tested on the signals no. 100, 101, 103, 117, and 122.

The accuracy of the P wave detection in signals with ventricular extrasystoles is Se = 98.94% and PP = 98.30% and in signals without pathology is Se = 98.47% and PP = 99.99%.

1 Introduction

Cardiovascular disorders are still the most common cause of death worldwide [1]. Due to the ease of use, non-invasiveness and cheapness, electrocardiogram (ECG) is nowadays still the most available and widely used method for the cardiovascular system examination. Automatic computer analysis of ECG (especially detection of QRS complex, P wave and T wave) is a fundamental task in cardiac monitoring and mainly in long-term ECG monitoring [1, 2].

Commonly used algorithms for P wave detection usually fail on the ECG signals with ventricular extrasystoles (VE) even though for signals without pathology these algorithms show good results [3–6]. The main problem of the majority P wave detection algorithms is that they search for the P wave before QRS complex and always assume presence of P wave. However, in the case of VE, the P wave is not present before QRS complex. It is due to the fact, that the heart beat originates in ventricles and atria are not contracted.

2 Methods

For the P wave detection, the phasor transform (PT) [4] is used together with classification of VE. For differentiation between VE and normal (other) beats, morphological features

L. Maršánová (✉) · A. Němcová · R. Smíšek
M. Vítek · L. Smital
Faculty of Electrical Engineering and Communication,
Department of Biomedical Engineering, Brno University
of Technology, Technická 12, 616 00 Brno, Czech Republic
e-mail: marsanova@feec.vutbr.cz

R. Smíšek
Institute of Scientific Instruments, The Czech Academy of
Sciences, Královopolská 147, 612 64 Brno, Czech Republic

T. Goldmann
Faculty of Information Technology, Department of Intelligent
Systems, Brno University of Technology, Božetěchova 2, 612 66
Brno, Czech Republic
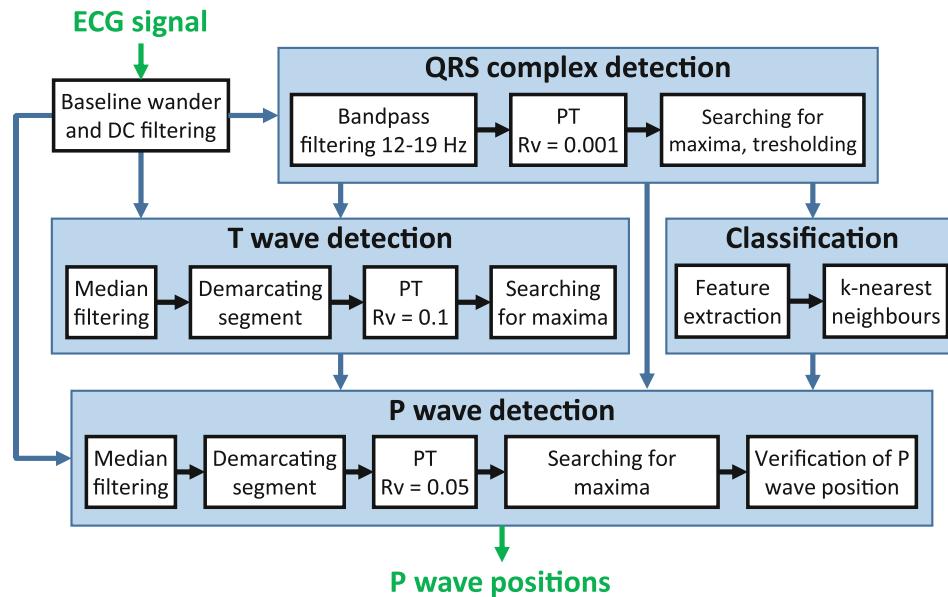
Fig. 1 The overall process of P wave detection

and k-nearest neighbours (k-NN) classification method were used. The proposed algorithm consists of four parts—QRS complex and T wave detection, classification, and P wave detection. The overall process is shown in Fig. 1. Each block is described in the next subchapters in detail.

2.1 Phasor Transform

Phasor transform [4] is new method which was used in previous work [4] for P wave detection with great results. PT transforms each sample of the ECG signal into a complex number, while the signal information is preserved. PT enhances ECG waves changes and makes their detection and delineation easier. The degree of ECG waves enhancement is determined by the value of $R_V \in <0, 1>$. The constant R_V value is considered as a real part of the complex signal. Imaginary part of the complex signal is the original value of the ECG sample. Calculation of the complex signal is shown in Eq. (1)

$$y(n) = R_V + jx(n),\qquad(1)$$

where $y(n)$ is the complex signal and $x(n)$ is the original signal.

The phase (phasor) $\varphi(n)$ is computed as

$$\varphi(n) = tan^{-1}\left(\frac{x(n)}{R_V}\right).\qquad(2)$$

In phasor signal $\varphi(n)$, the QRS complexes have higher amplitudes than the other ECG components, even if the original ECG signal has smaller amplitudes of QRS

complexes than T waves. The P waves and T waves are highlighted in the phasor signal as well, although less than QRS complexes.

2.2 Classification and Feature Extraction

The main innovation of our approach is using classification algorithm, which is able to detect ventricular extrasystoles. From each detected QRS complex, several morphological features were computed. Specifically: area under the curve (AUC) of the original ECG signal demarcated from $R(i) - 0.05$ s to $R(i) + 0.05$ s, actual length of RR interval ($RR(i)$), differences of area under the curve of the actual and previous QRS complex, length of previous RR interval ($RR(i-1)$), differences of $RR(i)$ and $RR(i-1)$, amplitude of QRS complex, and differences of amplitudes of the actual and previous QRS complex. Some of these features were already used in our previous work [2]. These features represent the QRS complex in classification into VE and other QRS complexes classes.

For differentiation between VE and normal (other) beats we used k-nearest neighbours (k-NN) classification method. The number of neighbours was selected as k = 1. The results of classification are used for decision whether the P wave will be searched or not.

2.3 QRS Complex Detection

Before QRS complex detection itself, the ECG signal is firstly filtered by the high-pass filter with cut-off frequency

of 0.67 Hz to eliminate baseline wander and DC component and by band-pass filter with cut-off frequencies of 12 and 19 Hz for suppressing P and T waves. For QRS complex detection, phasor transform of ECG signal is performed; R_V is set to 0.001. In phasor signal $\varphi(n)$, we search for maxima in a sliding window, which length is set to 300 ms. Then it is checked, whether the maxima are higher than the adaptive threshold, which values are calculated as a double of standard deviation of phasor signal calculated in a sliding window of 2 s length. The positions of maxima higher than the threshold are positions of QRS complexes. Finally, the positions of QRS complexes are precised—they are gone through again and the intervals between two subsequent QRS complexes (RR intervals) are checked. If the current RR interval is 1.75× (or more) longer than previous one, backward searching is performed. The maximum is searched in the same segment, but in different signal—the original signal $x(n)$ and with different threshold—set as 0.3× previously detected R wave size. Newly found maximum marks the position of missed QRS complex. If the current interval is lower than 1.75× the previous RR interval, we assume that no QRS complex is missing.

2.4 T Wave Detection

Firstly, the ECG signal is smoothed using the nonlinear median filter with 40 ms window length. T wave detection algorithm uses previously detected QRS complex positions to demarcate the area, where the T wave will be searched. The area is demarcated from $R(i) + 0.16 \times RR(i + 1)$ to $R(i) + 0.57 \times RR(i + 1)$, where R($i$) is the actual QRS complex. The signal in this area is then transformed using PT with $R_V = 0.1$ and the maximum is searched. Found maximum is a position of the T wave.

2.5 P Wave Detection

Firstly, the ECG signal is smoothed using nonlinear median filter with 40 ms window length. For P wave detection, the QRS complex as a reference is used as well. According to the result of classification (described in Sects. 2.2 and 2.3), the P wave is or is not searched. If the actual QRS complex is classified as VE, the P wave is probably not present and due to this fact it is not searched. If the $RR(i)$ interval is shorter than 0.4 s, the P wave is not searched either (because it is probably hidden in the T wave of the previous heartbeat).

If the QRS complex is classified as normal (other), the P wave is searched for in the limited area. The area before

actual QRS complex is demarcated with respect to the length of $RR(i)$ from $R(i) - 0.7 \times RR(i)$ to $R(i) - 0.07 \times RR(i)$. PT with $R_V = 0.05$ is applied only on this segment.

In demarcated P wave segment in phasor signal, the maximum is found and this is considered as a potential P wave. Thereafter it is verified, whether the position of currently detected P wave is located after the position of T wave in the previous heartbeat. If this criterion is not met, it means that instead of the P wave, the T wave of the previous heartbeat was detected. The P wave is probably not present in actual heartbeat or it is hidden in previous heartbeat T wave. In this case, the position of such P wave is deleted.

Finally, the last condition is applied. The voltage of the P wave must be higher than the value computed as 0.1× voltage of the actual R wave. To precise the position of the P wave peak, the maximum is searched in the original signal 20 ms before and after the maximum detected in the phasor signal.

2.6 Testing Database of ECG Signals

For complex testing of our algorithm we needed both physiological and pathological ECG records. Therefore, we tested the algorithm on signals from the most commonly used [1] standard database of electrocardiograms - The MIT-BIH Arrhythmia Database [7]. This database contains 48 half-hour two-channel ECG records. The sampling frequency is 360 Hz. From this database we selected 9 signals for testing purposes. Signals no. 106, 119, 214, 223 contain a large number of pathologies including VE and signals no. 100, 101, 103, 117, 122 which do not contain pathologies (or only a few), so these are considered as physiological signals. Exactly the same records were used in [8]. To evaluate the accuracy of our algorithm, we need the P wave annotations, which are unfortunately not publicly available. Therefore, we manually annotated all 12 selected signals and we also published these annotations on Physionet [7].

3 Results

3.1 Detection of P Waves in ECG During VE

Proposed P wave detection algorithm was tested on the signals no. 106, 119, 214 and 223 from the MIT-BIH Arrhythmia Database. These signals contain altogether 1,542 VE (isolated, bigeminy, trigeminy and tachycardia) and 7,227 P waves. The authors of [8] used the same signals for testing their P wave detection algorithm. Nevertheless, they used only a part of each signal and they did not specified

Table 1 Performance of the P wave detection algorithms on signals with ventricular extrasystoles (Se—sensitivity, PP—positive predictivity, Nr—not reported)

Rec. No.	Ecgpuwave [3]		PP rhythm [8]		PT [5]		WT [6]		Proposed method	
	Se (%)	PP (%)	Se (%)	PP (%)	Se (%)	PP (%)	Se (%)	PP (%)	Se (%)	PP (%)
106	Nr	Nr	Nr	Nr	99.87	74.25	90.98	91.83	99.73	99.34
119	Nr	Nr	Nr	Nr	99.51	78.06	99.38	99.69	98.83	99.44
214	Nr	Nr	Nr	Nr	99.55	88.14	98.55	99.50	98.75	99.35
223	Nr	Nr	Nr	Nr	99.95	80.75	94.62	93.72	98.43	95.08
Mean	90.82	68.65	98.85	84.45	99.72	80.30	95.88	96.18	98.94	98.30

which one (the only available information is that testing was done on 610 P waves). Therefore, it is not possible to test these two (our and [8]) P wave detection algorithms on the same data. For comparison, very popular algorithm for detection of ECG significant points (ecgpuwave [3]), our previously published algorithm based on PT [5], and publicly available algorithm for delineation of ECG based on wavelet transform (WT) [6] were tested on the same data as our new algorithm. The results—sensitivity (Se) and positive predictivity (PP) of all tested algorithms are shown in Table 1.

3.2 Detection of P Waves in ECG During Physiological Rhythm

For validation that the proposed algorithm is functional also in the case of signals with physiological rhythm, it was tested on the signals no. 100, 101, 103, 117 and 122 from the MIT-BIH Arrhythmia Database (these signals contain altogether around 10,216 P waves). For comparison, we also tested our previously published algorithm [5] and also publicly available algorithm for delineation of ECG [6] on the same signals as we used for testing of our newly

proposed algorithm. We also show the results of algorithms ecgpuwave [3] and PP rhythm [8]—in case of physiological signals, the algorithms were probably tested on the whole signals (not only on some parts as in the case of pathological records). The results are summarized in Table 2.

4 Conclusion

The results of P wave detection in ECG during ventricular extrasystoles using proposed algorithm (Se = 98.94%, PP = 98.30%) are significantly better than the results presented in other works [3, 8] (Se = 90.82%, PP = 68.65% and Se = 98.85%, PP = 84.45%, respectively) or achieved by using other available algorithms [5, 6] (Se = 99.72%, PP = 80.30% and Se = 95.88%, PP = 96.18%, respectively). In the case of physiological signals, our results (Se = 98.47%, PP = 99.99%) are comparable with results proposed in [3, 8] (Se = 99.68%, PP = 99.84% and Se = 99.57%, PP = 99.83%, respectively) and notably better than the results of algorithms [5, 6] (Se = 79.79%, PP = 75.02% and Se = 77.84%, PP = 75.03%, respectively). These results confirmed, that the proposed algorithm can be used well for detection of P waves in signals with ventricular extrasystoles

Table 2 Performance of the P wave detection algorithms on physiological signals (Se—sensitivity, PP—positive predictivity, Nr—not reported)

Rec. No.	Ecgpuwave [3]		PP rhythm [8]		PT [5]		WT [6]		Proposed method	
	Se (%)	PP (%)	Se (%)	PP (%)	Se (%)	PP (%)	Se (%)	PP (%)	Se (%)	PP (%)
100	Nr	Nr	Nr	Nr	100.00	99.30	99.34	99.91	99.96	100.00
101	Nr	Nr	Nr	Nr	99.84	99.79	98.02	99.95	98.93	100.00
103	Nr	Nr	Nr	Nr	46.76	41.84	39.95	40.53	98.80	100.00
117	Nr	Nr	Nr	Nr	100.00	99.93	99.48	100.0	96.48	99.93
122	Nr	Nr	Nr	Nr	52.35	34.25	52.41	34.77	98.18	100.00
Mean	99.68	99.84	99.57	99.83	79.79	75.02	77.84	75.03	98.47	99.99

as well as in signals with physiological rhythm. The proposed algorithm produces only a few false positive P wave detections.

References

1. Smíšek, R., Maršánová, L., Němcová, A., Vítek, M.; Kozumplík, J.; Nováková, M. CSE database: extended annotations and new recommendations for ECG software testing. Medical and Biological Engineering and Computing, 54(12), (2016).
2. Maršánová, L., Ronzhina, M., Smíšek, R., Vítek, M., Němcová, A., Smital, L., Nováková, M. ECG features and methods for automatic classification of ventricular premature and ischemic heartbeats: A comprehensive experimental study. Scientific Reports (7), 1–11 (2017).
3. Martínez, J. P., R. Almeida, S. Olmos, et al. A Wavelet-Based ECG Delineator: Evaluation on Standard Databases. IEEE Transactions on Biomedical Engineering 51(4), 570–581 (2004).
4. Martínez, A., R. Alcaraz A J. J. Rieta. Application of the phasor transform for automatic delineation of single-lead ECG fiducial points. Physiological Measurement 31(11), 1467–1485 (2010).
5. Maršánová, L. Detection of P, QRS and T Components of ECG Using Phasor Transform. In: IEEE Student Branch Conference, 55–58 (2016).
6. Vítek, M., Hrubeš, J.; Kozumplík, J. A Wavelet-Based ECG Delineation in Multilead ECG Signals: Evaluation on the CSE Database. In: World Congress on Medical Physics and Biomedical Engineering 177–180 (2009).
7. M Goldberger, A.L., Lan, A., Glass L., Hausdorff J.M., Ivanov P. Ch., Mark R.G., Mietus J.E., Moody G.B., Peng C.K., Stanley H.E. PhysioBank, PhysioToolkit, and PhysioNet: Components of a New Research Resource for Complex Physiologic Signals. Circulation 101(23), 215–220 (2000).
8. Portet, F. P wave detector with PP rhythm tracking: evaluation in different arrhythmia contexts. Physiological Measurement 29(1), 141–155 (2008).

An Ensemble Empirical Mode Decomposition Based Method for Fetal Phonocardiogram Enhancement

Dragos Daniel Taralunga and G. Mihaela Neagu (Ungureanu)

Abstract

Nowadays, fetal monitoring standard relies mainly on the analysis of fetal heart rate. However, signals like fetal electrocadiogram (fECG) and fetal phonocardiogram (fPCG) can offer complementary diagnostic information derived from the waveform analysis. The limitations of using, in particular, fPCG are: the signal to noise ratio (SNR) is very low because the recorded signal is a mixture of acoustic components originating not only from the fetus heart but also from the mother (maternal heart sounds (MHS), maternal organ sounds (MOS)) and other sources (power line interference, reverbaration noise, sensor and background noise). Moreover, it is dependent on gestational age, fetal and maternal positions, the data acquisition location. From the noise components the MHS presents a high correlation in the frequency domain with the fetal heart sounds (FHS). Thus, separation of MHS from acoustic recordings is not straightforward. In addition the MHS is a narrowband non-stationary signal. Thus, in this paper is proposed a method for fPCG enhancement from the recorded acoustic mixture based on the Esemeble Empirical Mode Decomposition (EEMD). This approach allows to analyze heart sounds into Intrinsic Mode Functions (IMFs) and it is adaptive and data driven. The performance of the proposed method is evaluated on a database with simulated fPCG signals.

Keywords

Fetal monitoring • Phonocardiography • Esemble empirical mode decomposition

D. D. Taralunga (✉) · G. Mihaela Neagu (Ungureanu)
Faculty of Electronics, Telecommunications and Information Technology, Faculty of Medical Engineering, Polithenica University Bucharest, Bucharest, Romania
e-mail: dragos.taralunga@upb.ro; taralungad@yahoo.com

1 Introduction

The fetal heart rate (fHR) is the primary diagnostic parameter used in today's standard of fetal monitoring. It is estimated usually using the cardiotocograph [1] which consists of placing two sensors on the maternal abdomen: one is a Doppler sensor used for auscultation (estimating the fHR) and the second one is used to record the uterine. contractions. However, some complementary fetal monitoring methods exist which can bring more diagnostic information about the fetus's health status: pulse oxymetry, magneto-cardiography, fetal electrocardiography (fECG) and fetal phonocardiography (fPCG). The latter is a simple and low cost method which has the following advantages: it can be used for long term monitoring, it is non-invasive and it offers, beside the instantaneous fHR, also the fPCG signal morphology that can be used to extract additional information about the well being of the fetus during pregnancy.

The fPCG consists of the sounds produced during a fetal cardiac cycle, fetal heart sounds (fHS). The sounds are recorded passively, no energy is transmitted in the maternal body, by placing an acoustic sensor on the mother's abdomen. The recorded sounds can have multiple origins: (i) *fetal components* generated during a cardiac cycle by: opening/closing of the valve leaflets, vibrations of the heart muscle, blood flow. In adults usually four sounds are audible, while in the fetus only the first (S1) and second (S2) heart sounds are detectable [2, 3]. In Fig. 1 the fHS are depicted. The S1 is the result of asynchronous closure, during the isovolumic contraction, of the atrioventricular valves, i.e. the mitral and tricupsid valves. The time between the closure of the mitral valve, which closes first, and the closure of the tricupsid valve represents the split time. Usually S1 has low frequency components which varies with the gestational age [4]. After the S1, ventricular ejection takes place, where the volume of blood is ejected out from the ventricles and first the aortic and then the pulmonary valves are closing. The asynchronous closure of these two
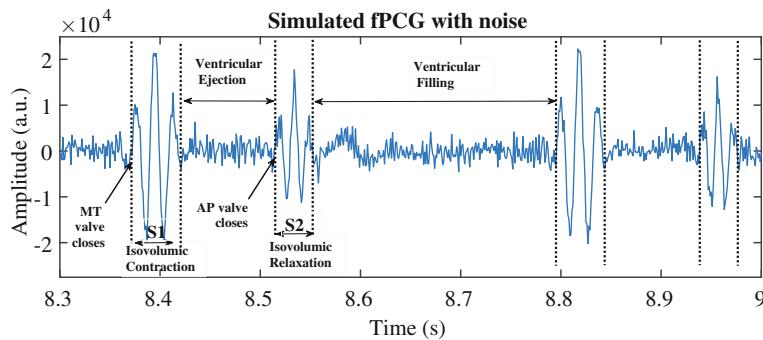
Fig. 1 The sounds generated by the fetal heart and other acustic components

valves produces the S2. It has also low frequencies and in comparison with S1 it has a smaller duration, lower amplitude and higher frequency [5]. It seems that the spectrum of the fHS is between 20–110 Hz [4]. However, there are many studies in literature reporting frequency range for fHS which are not in agreement with each other [4]. Diagnostic information is available in the time and frequency features of the fHS like: distance between two consecutive S1 (the fHR can be estimated from this time feature), duration of S1 and S2, duration of the split time, intra-beat distance (S1–S2), frequency range of S1 and S2, center frequency, relative intensities ($S1\S2$). Other fetal sounds can be produced by fetal movement, fetal hiccup and respiration [6]; (ii) *maternal components*: maternal heart sounds—mHS, and maternal organ sounds—mOS: digestive sounds, uterine contractions, respiration. The mHS is a non stationary, periodic signal with the frequency range 10–40 Hz and the central frequency between 15 and 20 Hz [4]; (iii) *other components*: movement artefacts, power line interference, reverberation noise, sensor noise [4].

From a signal processing perspective, the mHS and the other component must be reduced or removed, to ensure that the enhanced time and frequency features of the fPCG signal are of diagnostic quality. Thus, highly accurate fHR information can be derived from the fPCG. A number of methods for fPCG enhancement are proposed in literature, and methods based on linear decomposition show good results in estimating fHR (Short Time Fourier Transform—STFT [7], Wigner Ville Distribution—WVD [8], Wavelet Transform—WT [9], blind source separation [10]). However, the fHS and mHS are non stationary signals, thus, in the present study Esemble Empirical Mode Decomposition (EEMF) is used to decompose the signal recorded by the acoustic sensor in basic oscillations, in order to separate the fPCG from mHS and other noise components. The instantaneous frequency is calculated from each oscillation using the Hilbert Transform, and the ones having the frequency range of the fHS are used to reconstruct the signal. Next, a simple method is used to enhance fast rising oscillation in order to detect the position

of the S1. Based on the time between the S1 sounds, the fHR is estimated.

2   Materials and Methods

2.1   Simulated FPCG

The proposed method for fHR estimation is evaluated on simulated data generated as described in [11] and available on PhysioBank [12]. Thus, the fPCG can be defined as a mixture of the fHS $s(t)$ and noise components $n(t)$:

$$x(t) = s(t) + n(t) \qquad (1)$$

First, the fHR signal is simulated using an artificial R-R tachogram with real fetal characteristics: the low frequency (LF) components of the fHR are set to 0.03–0.2 Hz and the high frequency components (HF) to 0.2–1 Hz, the LF/HF ratio is set to 5, the standard deviation (SD) of the HF band to 0.03, the mean fHR is set to 140 bpm and to 80 bpm or 200 bpm for bradycardia and tachycardia, respectively. Next, the fHS are modelled using two pseudo-periodic Gaussian-modulated sinusoidal pulses, with central frequencies between 36.89 and 53.55 Hz for S1 and 55.18–65.64 Hz for S2. The intra-beat distance (SSID), S1–S2, is set to $SSID = 210 - 0.5 * fHR$. The maternal components are simulated similarly having the central frequency 16.93 Hz for mS1, SD 4.64, and 30.44 Hz for mS2, SD 14.61 Hz. The intra-beat distance (mSSID), mS1–mS2 is determined with the following expression: $mSSID = 0.2 * (60,000/mHR) + 160$ ms. The mOS are simulated using a 5th order Butterworth low-pass filter with 25 Hz cut-off frequency. Other noise components are simulated as following: generic noise–white Gaussian noise with zero mean; acoustic sensor noise, movement artefacts, maternal coughing—random spikes of limited duration, 0.5–1.5 s. According to (1) the noise components are linearly added to the fHS. The simulated databases in [12] contain fPCG with different signal to noise ratio (SNR).

2.2 The Proposed Method

Pre-processing and denoising: The EEMD is used to cancel out the noise components present in the acoustic recording, in order to enhance the fHS and to obtain an accurate estimate of the fHR. EEMD is an improved version of the Empirical Mode Decomposition (EMD). The latter is an adaptive method to decompose non-linear and non-stationary signals [13]. Thus, based only on the local characteristics of the signal, it extracts the intrinsic mode functions (IMF) by a sifting process. The IMF has to satisfy the following conditions: (i) the number of zero crossings and the number of extrema must be equal or differ at most by one, and (ii) the mean value of the envelopes defined by the local maxima and minima, respectively, has to be zero at any point.

The sifting process has the following steps:

(1) determine the local maxima and minima;
(2) using spline interpolation, construct the upper and lower envelopes;
(3) compute the mean envelope, $m_1(t)$;
(4) subtract the mean envelope from the initial signal, $x(t)$:
$h_1(t) = x(t) - m_1(t)$;
  (a) check if $h_1(t)$ satisfies the IMF conditions. If yes, then $h_1(t)$ is considered the first IMF, $c_1(t) = h_1(t)$, and jump to step (5);
  (b) if $h_1(t)$ doesn't satisfy the IMF conditions, then repeat steps (1), (2), (3) and (4). Thus, $h_{1,1}(t)$ is obtained: $h_{1,1}(t) = h_1(t) - m_{1,1}(t)$. After k cycles, $h_{1,k}(t) = h_{1,k-1}(t) - m_{1,k}(t)$, the IMF is obtained, $c_1(t) = h_{1,k}(t)$;
5. after the IMF is identified its separated from the rest of the data and the residue $r_1(t)$ is obtained: $r_1(t) = x(t) - c_1(t)$;
6. the process starts from the beginning, considering $r_1(t)$ as starting signal. The steps are repeat p times, where p is the number of the IMFs obtained and the last residue, $r_p(t)$. The sifting process stops when the stopping criterion is satisfied: $SD = \sum_{t=0}^{T} \frac{|h_{1,k-1}(t) - h_{1,k}(t)|^2}{h_{1,k-1}(t)^2}$, where SD is the standard deviation of two consecutive sifting results. Thus, when SD is between 0.2–0.3, the stopping criterion is satisfied [13].

However, the most significant disadvantage of the EMD is the mode mixing, which implies that a signal of the same scale appears in different IMFs or a single IMF consists of signals with disparate scales. Mode mixing is often a consequence of signal intermittency, which makes the physical meaning of individual IMF unclear [13]. To overcame this drawback, Wu et al. proposes a new noise assisted analysis method, EEMD, which eliminates the mode mixing phenomenon.

The steps of the EEMD method are the following: (1) white noise is added to the data set; (2) the data with white noise is decomposed into IMF using EMD; (3) steps (1) and (2) are repeated, each time with different white noise series; (4) obtain the means of the IMFs obtained after decomposition, as the final result.

The white noise series cancel each other in the final mean of the corresponding IMFs [13].

S1 detection: Once the signal is decomposed with EEMD, the components which contain the most information about fHS are selected and used for reconstruction of the signal. In order, to identify the components to be selected, the instantaneous frequency is computed and the components which have the most information in the frequency range of the fHS are considered for reconstruction. The instantaneous frequency is computed using the Hilbert Transform (HT):

$$y(t) = \frac{P}{\pi} \int_{-\infty}^{+\infty} \frac{x(\tau)}{t - \tau} d\tau \qquad (2)$$

$$z(t) = x(t) + y(t) = a(t)e^{i\phi(t)} \qquad (3)$$

$$a(t) = \sqrt{x^{(}t) + y^2(t)}\phi(t) = arctan\frac{y(t)}{x(t)} \qquad (4)$$

where P is the Cauchy principal value, $z(t)$ is the analytical signal formed from the initial signal $x(t)$ and its HT, $y(t)$, $a(t)$ is the instantaneous amplitude and the $\phi(t)$ is the instantaneous phase. The time derivative of the $\phi(t)$ represents the instantaneous frequency: $\omega(t) = \frac{\partial \phi(t)}{\partial t}$.

Next, the reconstructed signal is squared and then a moving average window of 20 samples is applied in order to enhance the S1 from the fHS. The resulted signal, $d(t)$ consists of clearly delimited spikes which correspond to the maxima of S1. A threshold is used to identify possible S1 candidates: $T = \frac{0.7}{M} \sqrt{\sum_{i=1}^{M} d(i)^2}$ where M is the total number of samples. The estimation of the fHR is determined as follows: $fHR = \frac{60}{T_{S_1,S_1}}$, where T_{S_1,S_1} is the time between two consecutive detected S1. In order to reduce the number of erroneous detections of S1, characteristics of the fHR are used: if the time between two consecutive S1 candidates is smaller than 0.2 s, the one with the lowest amplitude is rejected and if the time between two consecutive S1 candidates is higher than 0.6 s, it is interpreted that a S1 was not detected. In this case, the mean of the difference between the

last eight consecutive S1 is used in order to introduce the missed S1 in the time series.

3 Results and Conclusions

Figure 2a depicts the simulated fPCG with noise. After the signal is decomposed with EEMD method and the IMFs are selected, the reconstructed fPCG is obtained, without noise, Fig. 2b. Figure 3a illustrates the signal obtained after squaring and superimposed the signal after the moving average is applied. It can be observed that the S1 are enhanced. S1 detection is depicted in Fig. 3b.

Figure 4 depicts the estimated fHR. The black arrow indicates the outliers which can appear when a S1 is omitted. It is recovered with the second rule from the fHR estimation block and its location is considered to be the location of the current S1 plus the mean S1 interval for the last eight detected S1.

The proposed method shows high robustness, being able to detect all S1 even in very noisy conditions. However, the critical step is the selection of the IMFs which are used to reconstruct the signal, in order to separate and enhance the fHS from the other unwanted acoustic components. Thus, more criteria should be identified and introduce in the IMFs selection procedure, in order to make the method fully automated. Another perspective is to evaluate the performance of the method on real fPCG signals. Nevertheless, the proposed EEMD based method shows reliable and robust results in estimating fHR.
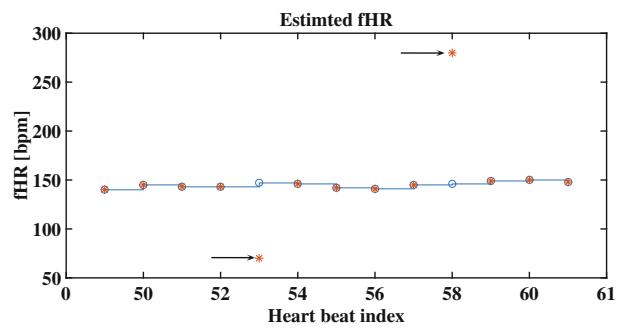
Fig. 4 Estimated fHR
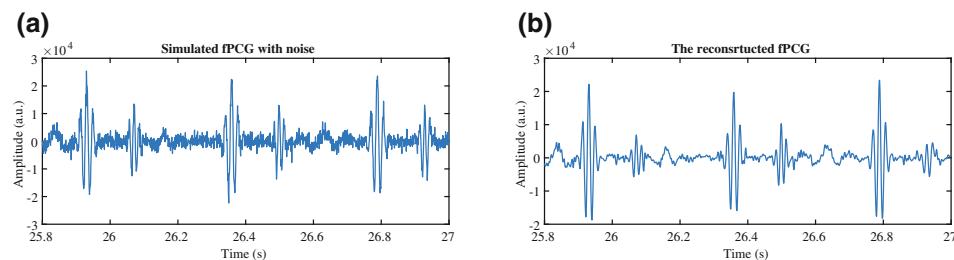
Fig. 2 a The simulated fPCG with added noise; **b** the Denoised fPCG signal
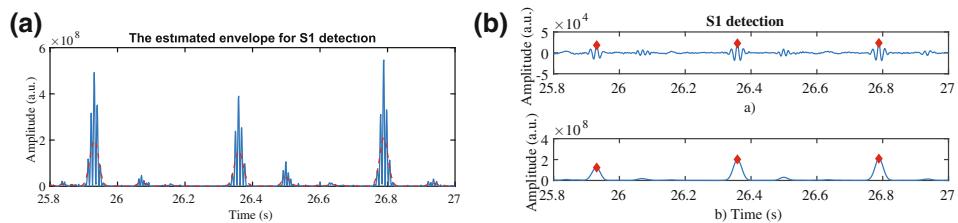
Fig. 3 a S1 enhancement; **b** S1 detection

References

1. Miller, D.A., Miller, L.A.: Electronic fetal heart rate monitoring: applying principles of patient safety. American Journal of Obstetrics & Gynecology **206**(4), 278–283 (2018). https://doi.org/10.1016/j.ajog.2011.08.016. http://dx.doi.org/10.1016/j.ajog.2011.08.016

2. Nagel, J.H.: Progresses in fetal monitoring by improved data acquisition. IEEE engineering in medicine and biology magazine: the quarterly magazine of the Engineering in Medicine & Biology Society **3**, 9–13 (1984). https://doi.org/10.1109/memb.1984.5006080

3. Mittra, A.K., Choudhary, N.K., Zadgaonkar, A.S.: Development of an artificial womb for acoustical simulation of mother's abdomen. International Journal of Biomedical Engineering and Technology **1**(3), 315–328 (2008). https://doi.org/10.1504/ijbet.2008.016964. https://www.inderscienceonline.com/doi/abs/10.1504/IJBET.2008.016964

4. Chetlur Adithya, P., Sankar, R., Moreno, W.A., Hart, S.: Trends in fetal monitoring through phonocardiography: Challenges and future directions. Biomedical Signal Processing and Control **33**, 289–305 (2017). https://doi.org/10.1016/j.bspc.2016.11.007

5. Jabloun, M., Ravier, P., Buttelli, O., Lédée, R., Harba, R., Nguyen, L.D.: A generating model of realistic synthetic heart sounds for performance assessment of phonocardiogram processing algorithms. Biomedical Signal Processing and Control **8**(5), 455–465 (2013). https://doi.org/10.1016/j.bspc.2013.01.002

6. Kovács, F., Horváth, C., Török, M., Hosszú, G.: Fetal breathing transmission in phonoeardiographic monitoring telemedicine systems. In: Annual International Conference of the IEEE Engineering in Medicine and Biology - Proceedings, pp. 5226–5229 (2006). https://doi.org/10.1109/iembs.2006.260360

7. Mittra, A.K., Choudhari, N.K.: Time-frequency analysis of foetal heart sound signal for the prediction of prenatal anomalies. Journal of Medical Engineering and Technology **33**(4), 296–302 (2009). https://doi.org/10.1080/03091900802454384

8. Balogh, Á.T., Kovács, F.: Application of phonocardiography on preterm infants with patent ductus arteriosus. Biomedical Signal Processing and Control **6**(4), 337–345 (2011). https://doi.org/10.1016/j.bspc.2011.05.009

9. Chourasia, V.S., Tiwari, A.K., Gangopadhyay, R.: A novel approach for phonocardiographic signals processing to make possible fetal heart rate evaluations. Digital Signal Processing: A Review Journal **30**, 165–183 (2014). https://doi.org/10.1016/j.dsp.2014.03.009

10. Soysa, W.N., Godaliyadda, R.I., Wijayakulasooriya, J.V., Ekanayake, M.P., Kandauda, I.C.: Extraction and analysis of fetal heart signals with abnormalities an Eigen-analysis based approach. In: 2013 IEEE 8th International Conference on Industrial and Information Systems, ICIIS 2013 - Conference Proceedings, pp. 294–299 (2013). https://doi.org/10.1109/iciinfs.2013.6731998

11. Cesarelli, M., Ruffo, M., Romano, M., Bifulco, P.: Simulation of foetal phonocardiographic recordings for testing of FHR extraction algorithms. Computer Methods and Programs in Biomedicine **107**(3), 513–523 (2012). https://doi.org/10.1016/j.cmpb.2011.11.008

12. Goldberger, A.L., Amaral, L.A.N., Glass, L., Hausdorff, J.M., Ivanov, P.C., Mark, R.G., Mietus, J.E., Moody, G.B., Peng, C.K., Stanley, H.E.: PhysioBank, PhysioToolkit, and PhysioNet: Components of a New Research Resource for Complex Physiologic Signals. Circulation **101**(23), e215–e220 (2000). https://doi.org/10.1161/01.cir.101.23.e215. URL http://circ.ahajournals.org/cgi/doi/10.1161/01.CIR.101.23.e215

13. Wu, Z., Huang, N.E.: E nsemble Empirical Mode Decomposition: A Noise-Assited Data Analysis Method. Advances in Adaptive Data Analysis **01**(01), 1–41 (2009). https://doi.org/10.1142/s1793536909000047

The Automatic Detection of Epileptic Seizures Based on EEG Signals Processing: Investigation of Different Features and Classification Algorithms

Alexandra-Maria Tăuţan, Ioana Mândruţă, Ovidiu-Alexandru Băjenaru,
Rodica Strungaru, Dragoş Ţarălungă, Bogdan Hurezeanu,
and G. Mihaela Neagu (Ungureanu)

Abstract

Automatic detection of epileptic seizures has been extensively studied and documented in literature. However, the topic continues to be of interest as reliable algorithms for general use are still being investigated. The challenge comes from the complex nature of the EEG signal and of the epileptic seizure, as both show patient specific characteristics. This makes highly performing algorithms developed on specific datasets difficult to translate to a more general use case. To provide more insights into the characteristics of seizure and non-seizure EEG segments, this paper proposes and investigates several features. Feature combinations are selected and fed per patient to both an Support-Vector Machine and Random Forest classifier. The performance of the trained models varied per patient, feature combination and training algorithm, with the highest accuracy reaching 94%.

1 Introduction

Epilepsy is a neurological condition characterized by the recurrent presence of epileptic seizures. An epileptic seizure is a transient occurrence of signs and/or symptoms due to abnormal excessive or synchronous neuronal activity in the brain [1]. The presence and frequency of these seizures significantly decrease the quality of life of the sufferer and can even become life-threatening.

The physicians propose a treatment method by using either scalp or invasive electroencephalographic (EEG) recordings. The characterization of an individual's epilepsy through EEG signals requires several hours or even days of recordings. These need to be carefully analyzed by the EEG technologist before a diagnostic is placed or the next step in treatment is determined. However, the process of manual analysis is cumbersome and time consuming. Automatic seizure detection software would make the process faster.

Automatic seizure detection has been thoroughly investigated since the 1970s [2] and a large variety of methods have been proposed in literature [3]. Nonetheless, the topic still proves challenging due to the interindividual variability of EEG signals and also to the variability of the seizure signals. Epileptic EEG seizure signals show an extreme variation in appearance and can include changes in amplitude, changes in frequency and sometimes unnoticeable changes during small seizures [3]. Thus, prediction models developed for some datasets are difficult to translate to other datasets while maintaining accuracy.

The aim of this study is to investigate several time and frequency domain features across multiple patients and analyze their suitability for the automatic detection of seizures across the entire database. Section 2 presents the database used and the general processing of EEG recordings for this study. Section 3 provides a description of the proposed features, while Sects. 4 and 5 present the method of classification and the outcome. Finally, Sect. 6 summarizes the conclusions.

A.-M. Tăuţan (✉) · R. Strungaru · D. Ţarălungă · B. Hurezeanu ·
G. Mihaela Neagu (Ungureanu)
Faculty of Electronics, Telecommunications and Information
Technology/Faculty of Medical Engineering, Polithenica
University of Bucharest, Bucharest, Romania
e-mail: alexandra.tautan@gmail.com

G. Mihaela Neagu (Ungureanu)
e-mail: g.mihaela.ungureanu@upb.ro

I. Mândruţă · O.-A. Băjenaru
University of Medicine and Pharmacy "Carol Davila" Bucharest,
Dionisie Lupu no. 37, Bucharest, Romania

2 Methodology

2.1 Database

The database used in this study was the CHB-MIT Scalp EEG Database which is freely available on PhysioNet [4]. It comprises scalp EEG recordings of 24 pediatric subjects with intractable seizures, monitored after the withdrawal of anti-seizure medication. A total of 23 EEG channels were recorded for most of the subjects. All signals were acquired at a sampling rate of 256 Hz with 16-bit resolution [5].

2.2 Processing

All processing was performed in Matlab. No pre-processing was applied and all patient data was included. Annotations of the epileptic seizures were made available with the data and no further alterations were made.

Seizure and non-seizure EEG segments were selected: 20 s from the seizure onset annotation and 20 s prior to the annotated onset, respectively. Both time and frequency domain features were extracted from both segment types, as described in Sect. 3.1. For better classification results, these features should provide a clear difference between normal and seizure EEG. After a statistical selection, the features are fed into two classifiers whose performances are then compared, see Sects. 4 and 5.

3 Feature Extraction

3.1 Description

A total of 12 features were extracted from both the seizure and non-seizure EEG segments. A brief description of these features is available in Table 1. The time domain features were computed on the entire 20 s available. The frequency domain features were extracted from the power spectral density (PSD) estimated using Welch's method on a 5 s window and 90% overlap.

The amplitude of an EEG signal during an epileptic seizure might increase, decrease or stay within the same range [6]. Thus, the amplitude by itself cannot be used as an indicator of seizure onset but might bring a significant contribution to the detection of seizure and non-seizure segments when combined with the other features. Higher order statistics, in particular, skewness and kurtosis, are also assumed to indicate the frequency of extreme signal deviations [7]. Entropy is regarded as a statistical measure of the sample values spread and can be a good indicator of an epileptic EEG signal [8].

The spectral content of a seizure segment may overlap the content of a non-seizure one, however the dominant spectral components might be different. The dominant frequency and the PSD are investigated through maxPSD and maxF. Additionally, we also defined varPSD to examine the variation around the spectrum peak. The intensity of the other

Table 1 Brief description of features extracted from seizure and non-seizure segments

Feature	Description
Time domain	
Amplitude	maximum amplitude of the EEG signal
Skewness	measuring the asymmetry of the sample distribution
Kurtosis	measuring the 'peakedness' of the sample distribution
Entropy	Shannon's Entropy [8]
Frequency domain	
maxPSD	maximum PSD
maxF	corresponding frequency of the maximum PSD
meanGamma	mean PSD in the Gamma Band (20–100 Hz)
meanBeta	mean PSD in the Beta Band (13–30 Hz)
meanAlpha	mean PSD in the Alpha Band (8–12 Hz)
meanTheta	mean PSD in the Theta Band (4–7 Hz)
meanDelta	mean PSD in the Delta Band (0–4 Hz)
varPSD	variation of PSD around maxF

frequency components is taken into account through the mean PSD of the specific EEG bands.

3.2 Selection

Ideally, a set of features that can discriminate all types of seizure and non-seizure segments should be chosen for classification purposes. Figure 1 provides a graphical illustration of some of the features identified for the two patients. For patient 24, a clear discrimination exists between seizure and non-seizure characteristics (see Fig. 1a–d).While for patient 15, there is no clear visual discrimination between the two states (see Fig. 1e–h).

Paired t-tests were performed for all features to determine which bring more value to the differentiation between the two classes. The maxPSD value proved itself to be a good differentiator for most of the recordings, while the proposed varPSD the least favorable for providing discrimination. Based on the rejection of the null hypothesis (H = 1, $p < 0.01$) for the majority of patients and corresponding recordings, six features were selected: Amplitude, Kurtosis, maxPSD, maxF, meanTheta and meanAlpha.

4 Classifier Training and Validation

For each individual patient, the available EEG segments were split into a training set (80%) and a test set (20%). Three feature vectors are supposed to indicate the seizure and non-seizure states, whose components are:

- all 12 features identified in Table 1 (see Sect. 3.1)
- only selected features (see Sect. 3.2)
- only maxPSD and maxF.

Two algorithms are used for classification: support-vector machine (SVM) and random forest (RF).

SVMs are adequate for datasets that contain two classes, in our case those would be seizure and non-seizure segments. Numerous examples can be found in literature on the usage of SVMs for automatic epileptic seizure detection with excellent results [5, 9]. When using frequency features as input, the accuracy of the SVM classification reached 93%. A value which was improved with the use of blind source separation techniques (ICA—independent component analysis, PCA—principle component analysis) and reached 98–99% accuracy [9]. The SVM algorithm applied in this study

Fig. 1 Examples of feature clusters for patients with ID 24 and 15. Blue dots are extracted from the seizure EEG segments, while red dots for the non-seizure EEG segments (Color figure online)

uses the sequential minimum optimization method with a linear kernel function for finding the separation plane.

The RF algorithm is an ensemble learning method based on growing a multitude of decision trees. Several decision tree based algorithms used in scalp EEG automatic seizure detection (mostly employed on frequency features) were reported in literature [9]. Their accuracies are above 90%. The RF algorithm trained in this study used 100 classification trees with a leaf size of 1.

The six trained models are then applied to the test dataset for validation. The performance is evaluated using accuracy, sensitivity (true positive rate) and specificity (true negative rate).

5 Results and Analysis

Figure 2 presents the accuracy of the 6 models for each patient. There is a high variability in accuracy among patients and models and no clear trend can be observed. The highest value accuracy is 94% and is obtained using the RF algorithm. This result is similar to other reported accuracies, as briefly outlined in Sect. 4

In most cases, RF performs better for all feature vectors when compared to the SVM accuracy. Using the selected feature vector yielded similar results when compared to the use of all proposed features. Hence similar accuracies were obtained when using a half the number of features. Interestingly, using only the frequency components as input to the random forest proved to be efficient in some of the cases which otherwise presented significantly lower performance, i.e. patients 13 and 14.

The best results were obtained on patient 24: an accuracy of over 90% for all 6 models. In contrast, patient 15 shows an accuracy of around 50% for all models. Some of the features obtained from the seizure and non-seizure segments of these two patients are plotted in Fig. 1 with respect to the PSD. The separation between the two classes for patient 24

Fig. 3 Example of EEG segments for S24
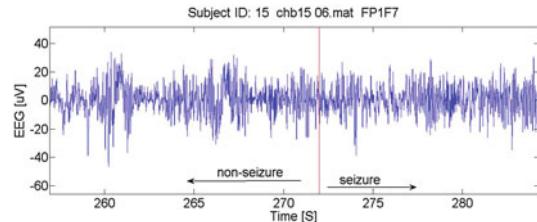
Fig. 4 Example of EEG segments for S15

are visually very clear. For patient 15, the boundary between the two is difficult to spot, making the classification problem more challenging.

Figures 3 and 4 provide representative samples of seizure and non-seizure EEG recordings. For S24, the epileptic moments can be noticed visually as being very different from normal activity. However, for S15 the signal quality seems to be pourer and no significant difference can be visually spotted before and after the seizure annotation. Taking into account the amount of noise present in the recording, it can be considered that the resulting features would also be impacted.

Mean values for accuracy, sensitivity and specificity were computed for all patients, see Fig. 5. Overall, the average differences between the 6 models for all three performance


Fig. 2 Accuracy of seizure and non-seizure segment identification of the four trained models
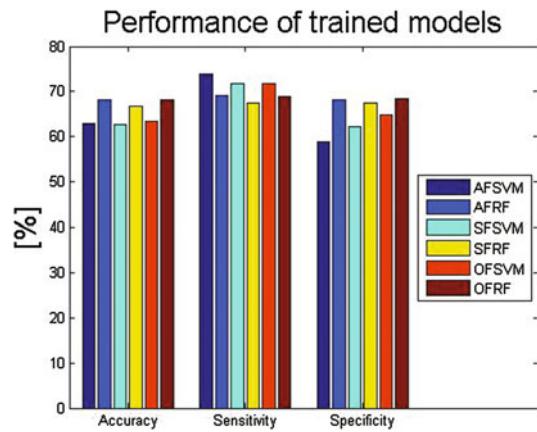
Fig. 5 Mean values for performance of the SVM and RF classifiers having as input all features and the selected features. The following abbreviations are used: AF—All Features; SF—Selected Features; OF—Only Frequency

measures were relatively small. The RF algorithm presented higher accuracy than SVM. A higher sensitivity was presented by SVM, while a higher specificity by RF.

6 Conclusions

The proposed combination of time and frequency domain features can be used for the classification of seizure and non-seizure EEG segments. Our analysis showed that frequency features (maxPSD, maxF) had a higher impact on the differentiation of the two states. From the time domain, kurtosis and maxAmp were the most significant among a higher number of patients from the dataset. Results suggest an individualized feature selection would prove more beneficial in terms of class differentiation. We believe that developing a general framework for seizure detection independent of individual patients would be difficult due to the high interindividual variability of seizure EEG signals.

The random forest algorithm outperformed the support-vector machine classifier. Accuracy and specificity were a few percentage points higher for RF than for SVM. For the SVM classification, a clear boundary between the features describing the two classes is recommended. This was not the case for several subjects, where the boundary was fuzzy. A decision on classification of test data based on the separation plane constructed from such training data is prone to errors. Hence, a forest of decision trees would be more suitable for boundary test points, slightly improving the final result.

The outcome of the classification depends highly on the input signal quality. The selected dataset contains only scalp EEG recordings. Scalp EEGs are noisy and prone to external interference. The quality of the EEG segments could be improved through a better pre-processing of the signals. Filters or other methods of removing unwanted interference could also remove important components of seizure signals.

Seizure signals overlap and mix with background activity, making the differentiation between seizure and non-seizure segments more unreliable. Invasive recording methods might provide features that should be used, as interference from other sources would be reduced. These features could then be transposed on scalp EEG studies. Using blind source separation techniques (ICA, PCA) or wavelet transforms in feature extraction prior to classifier training can enhance the classification accuracy.

Conflict of Interest Statement The authors declare that they have no conflict of interest.

References

1. Robert S. Fisher, Walter Van Emde Boas, Warren Blume, Christian Elger, Pierre Genton, Phillip Lee, and Jerome Engel. Epileptic seizures and epilepsy: Definitions proposed by the International League Against Epilepsy (ILAE) and the International Bureau for Epilepsy (IBE). *Epilepsia*, 46(4):470–472, 2005.
2. A. T. Tzallas, M. G. Tsipouras, and D. I. Fotiadis. Automatic seizure detection based on time-frequency analysis and artificial neural networks. *Computational Intelligence and Neuroscience*, 2007, 2007.
3. Jagriti Saini and Maitreyee Dutta. An extensive review on development of EEG-based computer-aided diagnosis systems for epilepsy detection. *Network: Computation in Neural Systems*, 28 (1):1–27, 2017.
4. Ary L Goldberger, Luis A N Amaral, Leon Glass, Jeffrey M Hausdorff, Plamen Ch Ivanov, Roger G Mark, Joseph E Mietus, George B Moody, Chung-kang Peng, and H Eugene Stanley. PhysioBanl, PhysioToolkit, and PhysioNet, Components of a New Research Resource for Complex Physiologic Signals. *Circulation*, 101(23):E215–20, 2000.
5. Ali Shoeb and John Guttag. Application of Machine Learning To Epileptic Seizure Detection. *Proceedings of the 27th International Conference on Machine Learning (ICML-10)*, pages 975–982, 2010.
6. J. Gotman. Automatic recognition of epileptic seizures in the EEG. *Electroencephalography and Clinical Neurophysiology*, 54(5):530–540, 1982.
7. Bedeeuzzaman Mohamed, Omar Farooq, and Yusuf Uzzaman Khan. Automatic Seizure Detection Using Higher Order Moments. *2010 International Conference on Recent Trends in Information, Telecommunication and Computing*, pages 159–163, 2010.
8. N. Kannathal, Min Lim Choo, U. Rajendra Acharya, and P. K. Sadasivan. Entropies for detection of epilepsy in EEG. *Computer Methods and Programs in Biomedicine*, 80(3):187–194, 2005.
9. U. Rajendra Acharya, S. Vinitha Sree, G. Swapna, Roshan Joy Martis, and Jasjit S. Suri. Automated EEG analysis of epilepsy: A review. *Knowledge-Based Systems*, 45:147–165, 2013.

Atrial Fibrillation Detection from Wrist Photoplethysmography Data Using Artificial Neural Networks

Zeinab Rezaei Yousefi, Jakub Parak, Adrian Tarniceriu, Jarkko Harju, Arvi Yli-Hankala, Ilkka Korhonen, and Antti Vehkaoja

Abstract

Atrial fibrillation (AF) can be detected by analysis of the rhythm of heartbeats. The development of photoplethysmography (PPG) technology has enabled comfortable and unobtrusive physiological monitoring of heart rate with a wrist-worn device. Therefore, it is important to examine the possibility of using PPG signal to detect AF episodes in real-world situations. The aim of this paper is to evaluate an AF detection method based on artificial neural networks (ANN) from PPG-derived beat-to-beat interval data used for primary screening or monitoring purposes. The proposed classifier is able to distinguish between AF and sinus rhythms (SR). In total 30 patients (15 with AF, 15 with SR, mean age 71.5 years) with multiple comorbidities were monitored during routine postoperative treatment. The monitoring included standard ECG and a wrist-worn PPG monitor with green and infrared light sources. The input features of the ANN are based on the information obtained from inter-beat interval (IBI) sequences of 30 consecutive PPG pulses. One of the main concerns about the PPG signals is their susceptibility to be corrupted by noise and artifacts mostly caused by subject movement. Therefore, in the proposed method the IBI reliability is automatically evaluated beforehand. The amount of uncertainty due to unreliable beats was 15.42%. The achieved sensitivity and specificity of AF detection for 30 beats sequences were $99.20 \pm 1.3\%$ and $99.54 \pm 0.64\%$, respectively. Based on these results, the ANN algorithm demonstrated excellent performance at recognizing AF from SR using wrist PPG data.

1 Introduction

Atrial fibrillation (AF) is the most common cardiac arrhythmia in which electrical activity in the atria is rapid and disorganized. AF causes increased risk of heart failure and stroke. Therefore, early screening and diagnosis can reduce the AF impact. In healthy heart the electrical excitation for each beat starts at the sinus node and subsequently spreads over the atrium and ventricles and heart beats at a regular rhythm with approximately 60–80 beats per minute (normal sinus rhythm, SR). In contrast, during atrial fibrillation the heart electrical signal does not begin in sinus node, but other parts of atrium muscle tissue are providing abnormal electrical signals to stimulate the atrium, which causes a chaotic heart rhythm and quasi constantly circulating excitation. Therefore, the time intervals between two heartbeats become irregular [1].

Even if the AF mechanism is caused by electric disturbances in the heart, this pathology can also affect the photoplethysmography (PPG) signal, since it produces an irregular flow in the blood vessels [1]. The advantage of the PPG signal is that it can be obtained unobtrusively and the recording time is not limited e.g. by skin irritation as with ECG. Moreover, the sensing device is easy-to-set up and economically efficient.

Recently, there has been a growing research interest in wearable sensing technologies that have enabled real-time and long-term health monitoring. Recent studies have shown that PPG is a promising technique and can be helpful for

Z. Rezaei Yousefi (✉) · J. Parak · I. Korhonen · A. Vehkaoja
Faculty of Biomedical Sciences and Engineering,
BioMediTech Institute, Tampere University of Technology,
and PulseOn Ltd., Espoo, Finland
e-mail: rezaeiyo@student.tut.fi; zeinab.rezaeiyousefi@pulseon.fi

A. Tarniceriu
PulseOn SA, Neuchatel, Switzerland

J. Harju · A. Yli-Hankala
Department of Anesthesia, Tampere University Hospital,
Tampere, Finland

continuous cardiac and respiratory event monitoring, early screening and diagnostic of various cardiac diseases [2, 3]. It should be noted that the reliability of information obtained from the PPG devices is highly important when using their data in clinical decision making. A fast and accurate quality estimation of the signal is needed to recognize corrupted data from valid data before any diagnosis and prediction.

Automatic detection of atrial fibrillation from ECG signals has been the base of research during many years and a large number of methods have been developed mostly employing time-frequency analysis techniques [4] and statistical tools [5–8]. However, AF detection from PPG signals has not been extensively studied. There are a few proposed algorithms designed to be used with smart-phone camera sensors that can capture PPG data from the finger tip of the patients [9–11]. Smart-phone sensor however, is an intermittent-type measurement solution and cannot be applied continuously in ambulatory applications. Methods for classifying arrhythmias from PPG signals obtained from wearable devices in longer time periods are less developed [12, 13].

In the present study we built an ANN trained by features acquired from inter-beat-interval series for AF detection. The aim of our research is to develop a method for automatic classification of each beat into two target classes: AF and SR. Since the PPG signal is often disturbed by movement artifacts, it is inevitable to discard a portion of the acquired data in long-term monitoring due to the low reliability of the estimation.

2 Methodology

The block diagram of the proposed algorithm is presented in Fig. 1. The explanation of each block is given in the following sections.

2.1 Data Acquisition

The wrist PPG signal together with a tri-axis accelerometer data was recorded using the PulseOn Optical Heart Rate monitor (PulseOn Technologies Ltd, Espoo, Finland, www.pulseon.fi). The PulseOn device (shown in Fig. 2) is a wrist worn device that uses reflection mode PPG with utilizing two light wavelengths (green and infrared) to record the PPG signal. The reference ECG signal was recorded with GE Carescape B850 patient monitor. The data recordings were performed in the post-anesthesia care unit of Tampere University Hospital. In total 30 subjects having either SR or AF rhythm during the measurement participated to the study. All types of AF (paroxysmal, persistent and permanent) were present in the study population. It was visually verified that the cardiac rhythm of the patients assigned to the two groups was either SR or AF during the whole time of the recording. However, one of the AF patients was later excluded from the final analysis because it was noticed that the cardiac rhythm of that patient was switching between SR and AF several times during the recording. The patient population consisted of adult patients who had undergone an elective surgery and whose cardiac rhythm was not controlled by any drug: 15 subjects (7 females, 67.5 ± 10.7 years old) with normal SR and 14 subjects (8 females, 74.8 ± 8.3 years old) with continuous AF. The average recording length was 1.5 h. The subjects were lying down in bed during the data collection, but their hands were free to move. Example waveforms for SR and AF subjects are depicted in Figs. 3 and 4, respectively.

An ethical approval was obtained from the local ethical committee of Pirkanmaa Hospital District (ETL R17024), and the study was registered at clinicaltrials.gov (NCT03081793) before study initiation. The procedures followed in this study were in accordance with the ethical standards of the responsible committee on human experimentation (institutional and
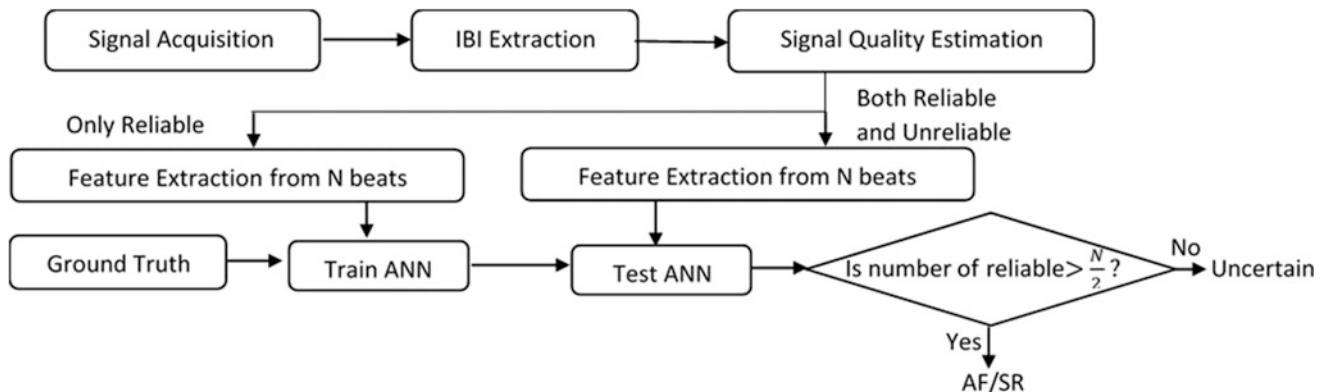
Fig. 1 Block diagram of AF detection algorithm

Fig. 2 PulseOn optical heart rate tracker

national) and with the Helsinki Declaration of 1975, as revised in 2000 and 2008.

2.2 IBI Extraction and Signal Quality Estimation

A proprietary signal processing algorithm was applied to segment the PPG signal beat by beat and to identify the individual PPG pulses. RR intervals used as reference were obtained from the simultaneously recorded ECG signal using Kubios HRV software (www.kubios.com) [14]. Beat-to-beat detection accuracy of Kubios output was visually verified by an expert.

The raw PPG signals can be heavily corrupted by motion and other sources of interferences. Therefore, a signal quality estimation algorithm is applied in our method to classify the pulses into correct and artifact beats. This binary classification is designed based on the morphology of the PPG signal and the amount of motion of the subject during each inter-beat time interval. Accuracy of estimated HR and inter-beat intervals (IBI) from PPG signals obtained from the PulseOn device have already been evaluated in [15, 16].

2.3 Feature Extraction and Artificial Neural Network

Atrial fibrillation in the ECG can be diagnosed by analysis of the morphological properties of the electrocardiogram—usually the absence of the p-wave. However, there are no morphological properties in the PPG signal to enable us to detect abnormal atrial activity to distinguish between AF and SR. Therefore, other diagnostic metrics such as high disparity of the length of IBI's can be helpful for automatic detection of AF. The method applied in this study is based on the analysis of the rhythm of the pulses and more precisely based on the analysis of the inter beat intervals. As it can be seen in Fig. 3, the SR IBIs in the area with low motion are almost constant. However, AF arrhythmia variations will lead to IBI with large amplitude variations (Fig. 4).

In order to extract the features used in ANN based classification, we divided the IBI time series into sliding windows of N = 30 consecutive IBIs. The length of the analyzed window has to be taken into consideration. Although, a longer window is more effective for AF detection, short segments are preferable due to less computational demands and faster detection of AF especially in case of short-lasting AF episodes. For each segment we calculated

Fig. 3 Example of measured waveforms (ECG, ACC, PPG) and corresponding IBI and RRI for an SR patient
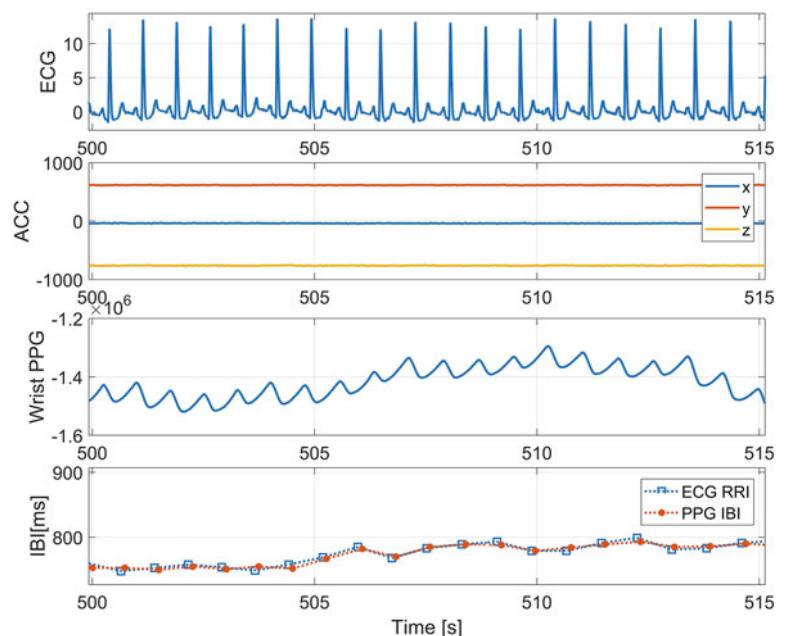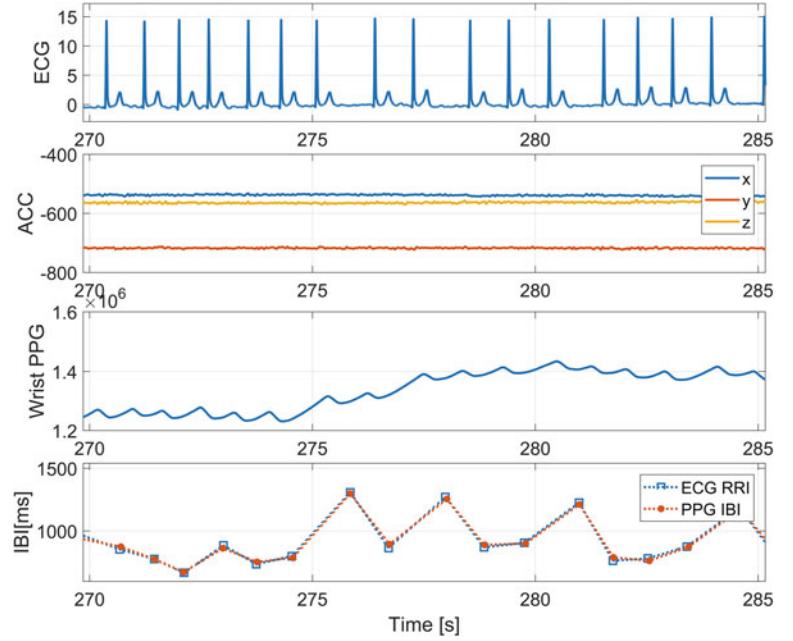
Fig. 4 Example of measured
waveforms (ECG, ACC, PPG)
and corresponding IBI and RRI
for an AF patient

the following features: the transition matrix containing the probabilities of successive IBI lengths (short, medium, or long) introduced in [17], the fraction of successive IBIs that differ by more than 50 ms (pNN50), the standard deviation (SD) of IBIs and the root mean square of successive difference (RMSSD) of IBIs as the input features for the ANN.

Given the above features, we built a multilayer perceptron as a classifier to discriminate between AF and SR. An ANN architecture including 12 input units (9 inputs for the transition matrix and 3 for the other features), 10 hidden layers and one output neuron is proposed in this work. Only reliable or correct beats obtained from the signal quality estimation algorithm were used in training the network. However, to test the network we imported IBIs of all beats (both correct and artifact beats) and based on the output of signal quality estimation we decided to reject those decision which are affected by artifacts so that within each window if more than the half of beats were artifact (unreliable), the output decision will be assigned as uncertain.

2.4 Evaluation and Performance Metrics

In order to assess the generalization performance of our AF detection algorithm, we applied k-fold cross-validation, that each time one of the 29 subsets were used as the test set and the remaining 28 subsets were put together to form a training set. By pooling the predicted probabilities of outcome from all test sets across all 29 folds, the final sensitivity $(Se = \frac{TP}{TP+FN})$, specificity $(Sp = \frac{TN}{TN+FP})$ and area under curve (AUC) were calculated and used to evaluate the model. Here positive and negative are associated to AF and SR frames, respectively. The AUC represents the overall accuracy of a test and can be applied in comparative studies. Since this study utilizes simultaneously recorded ECG signal, we can take advantage of that to compare the results of RRI-analysis based features for AF detection against IBI-based features. The ECG signals are less affected by artifacts and noise normally present in ambulatory conditions.

3 Results and Discussion

In this algorithm, we tried to consider the minimum number of beats required to trigger an AF detection. The used window length is 30 beats. Table 1 summarizes the performance metrics of the RRI-based classifier and of the IBI-based classifier for both cases of "All IBI" (considering all beats, be it reliable or not) and "Proposed method" (considering the beat reliability). According to the signal quality estimator applied in this study 26.7% of the detected heartbeats were

Table 1 AF/SR classification results for all data sets

	RRI-based	All IBI	Proposed method
Se	97.63 ± 8.67	97.87 ± 4.84	93.64 ± 21.6
Sp	99.65 ± 0.73	95.83 ± 6.31	99.16 ± 1.8
AUC	0.994	0.976	0.996

Table 2 Results after excluding problematic dataset

|	RRI-based	All IBI	Proposed method
Se	99.8 ± 0.51	98.04 ± 1.94	99.2 ± 1.3
Sp	99.8 ± 0.52	95.58 ± 6.54	99.54 ± 0.64
AUC	0.999	0.984	0.997
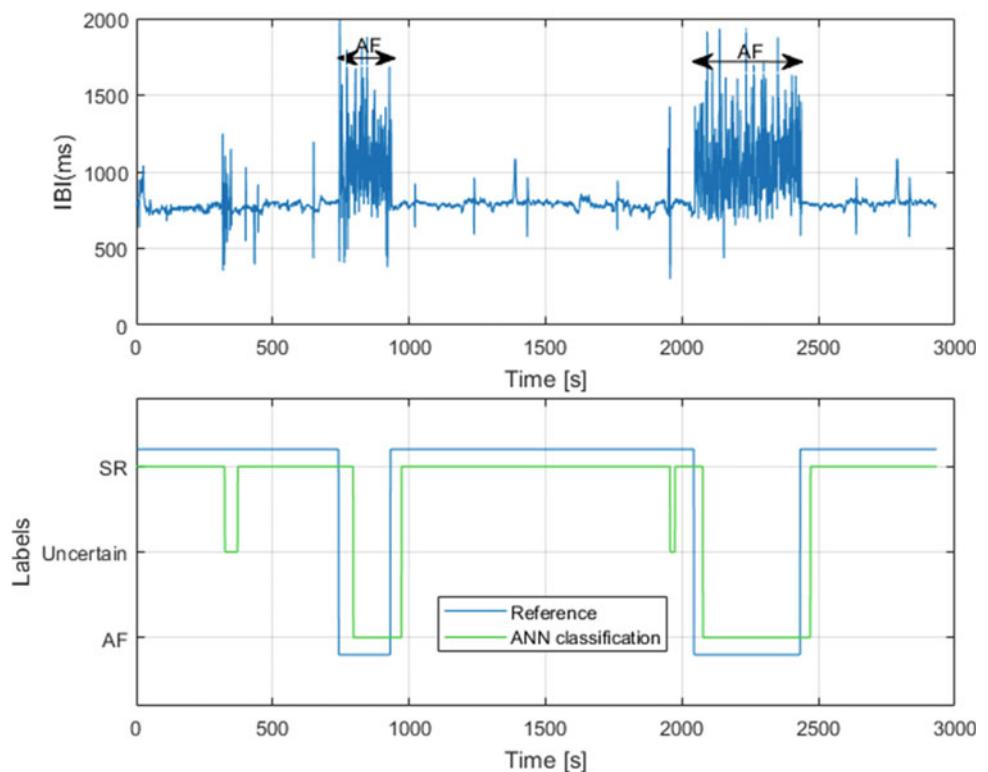
classified as unreliable or artifact beats. However, based on the proposed IBI-based algorithm approach, 84.58% of the data was classified as AF/SR and only 15.42% of the data was labeled as uncertain due to the low quality or too many unreliable beats. The reason for higher value of Sensitivity (the ability to detect true AF events) of the "All IBI" approach compare to the "Proposed method" is that the artifact beats (26.7% of the data) produce irregularity in IBI sequences and the algorithm recognizes these irregularities as AF events. In addition to that, further investigation revealed that the reason of low mean and very high standard deviation values of Sensitivity for the proposed method is related to one dataset acquired from a patient which were classified as AF since there were not any visible p-wave in the ECG signal. However, compared to the other AF patients there was more regularity in the IBI sequence of this patient that made it similar to the SR cases. The results after excluding this patient from the experiment are shown in Table 2.

These results demonstrate that the wrist PPG technology is accurate enough to detect AF and has the ability to become an alternative for the ECG-based AF detection that is cumbersome and more expensive. The presented results are for patients with either continuous SR or continuous AF during the whole time of the recording. However, the method cab be equally applied for patients with paroxysmal AF episodes. The only restriction is that the AF episodes need to last for at least 30 beats. We have tested this on artificially concatenated data from both sets that is shown in Fig. 5. We have inserted two AF episodes in an SR data set at times 700–900 s and 2000–2500 s. It can be seen that the proposed algorithm is able to detect correctly AF episodes.

4 Conclusion

In this paper, an ANN-based algorithm for the detection of atrial fibrillation on a beat-by-beat basis from PPG signals was proposed and evaluated. The algorithm provides very

Fig. 5 ANN classification results for an artificially mixed data set (artificial paroxysmal AF data)

satisfying detection accuracy/reliability in terms of sensitivity and specificity. It has been confirmed that PPG-based monitoring technique is very promising in AF detection and has the potential to induce a dramatic change in medical screening and monitoring by wearable sensing technology. As the subject of our future work for AF detection, we plan to apply Recurrent Neural Networks (RNN) particularly those using Long Short-Term Memory (LSTM) which are popular models for learning from sequence data.

Conflict of Interest Rezaei Yousefi Z, Parak J, Tarniceriu A and Vehkaoja A are employees of PulseOn Ltd.

References

1. Waktare, J.E.P.: Atrial Fibrillation. Circulation, Volume 106, Issue 1. July 2 (2002).
2. Conroy, T., Guzman, J. H., Hall, B., Tsouri, G., Couderc, J. P.: Detection of atrial fibrillation using an earlobe photoplethysmographic sensor. Physiological measurement 38, no.10, 1906 (2017).
3. Gil, E., Vergara, J. M., Laguna, P.: Detection of decreases in the amplitude fluctuation of pulse photoplethysmography signal as indication of obstructive sleep apnea syndrome in children. Biomedical Signal Processing and Control 3, no. 3, pp. 267–277 (2008).
4. Couceiro, R., Carvalho, P., Henriques, J., Antunes, M., Harris, M., Habetha, J.: Detection of atrial fibrillation using model-based ECG analysis. In: 19th International Conference on Pattern Recognition. pp. 1–5. IEEE Press (2008).
5. Moody, G. B., Mark, R. G.: A new method for detecting atrial brillation using R-R intervals. Computers in Cardiology, pp. 227â€"230, (1983).
6. Petrucci, E., Balian, V., Filippini, G., Mainardi, L. T.: Atrial fibrillation detection algorithms for very long term ECG monitoring. In: Computers in Cardiology, pp. 623–626. IEEE, (2005).
7. Ghodrati, A., Marinello, S.: Statistical analysis of RR interval irregularities for detection of atrial fibrillation. In: Computers in Cardiology, pp. 1057–1060. IEEE, (2008).
8. Smiley, A., Simon, D.: Evolutionary optimization of atrial fibrillation diagnostic algorithms. International Journal of Swarm Intelligence 2, no. 2–4: pp. 117-133. (2016).
9. Lee, J., Reyes, B. A., McManus, D. D., Maitas, O., Chon, K. H.: Atrial fibrillation detection using an iPhone 4S. IEEE Transactions on Biomedical Engineering 60, no. 1. pp. 203–206. (2013).
10. Chong, J. W., Esa, N., McManus, D. D., Chon, K. H.: Arrhythmia discrimination using a smart phone. IEEE journal of biomedical and health informatics, 19(3), pp. 815–824. (2015).
11. Krivoshei, L., Weber, S., Burkard, T., Maseli, A., Brasier, N., Kühne, M., Conen, D., Huebner, T., Seeck, A., and Eckstein, J.: Smart detection of atrial fibrillation. Europace 19, no. 5. pp. 753–757. (2016).
12. Nemati, S., Ghassemi, M. M., Ambai, V., Isakadze, N., Levantsevych, O., Shah, A., Clifford, G. D.: Monitoring and detecting atrial fibrillation using wearable technology. In Engineering in Medicine and Biology Society (EMBC), 38th Annual International Conference of the IEEE, pp. 3394–3397. IEEE, (2016).
13. Bonomi, A.G., Schipper, F., Eerikainen, L.M., Margarito, J., Aarts, R.M., Babaeizadeh, S., de Morree, H.M. and Dekker, L.: Atrial fibrillation detection using photo-plethysmography and acceleration data at the wrist. In: Computing in Cardiology Conference (CinC). pp. 277–280. IEEE, (2016).
14. Tarvainen, M. P., Niskanen, J. P., Lipponen, J. A., Ranta-Aho, P. O., Karjalainen, P. A.. Kubios HRV heart rate variability analysis software. Computer methods and programs in biomedicine, 113(1), pp. 210–220. (2014).
15. Parak, J., Tarniceriu, A., Renevey, P., Bertschi, M., Delgado-Gonzalo, R., Korhonen, I.: Evaluation of the beat-to-beat detection accuracy of PulseOn wearable optical heart rate monitor. In Engineering in Medicine and Biology Society (EMBC), 37th Annual International Conference of the IEEE, pp. 8099–8102. IEEE, (2015).
16. Pietila, J., Mehrang, S., Tolonen, J., Helander, E., Jimison, H., Pavel, M., Korhonen, I: Evaluation of the accuracy and reliability for photoplethysmography based heart rate and beat-to-beat detection during daily activities. In EMBEC & NBC. pp. 145–148. Springer, (2017).
17. Artis, S. G., Mark, R. G., Moody, G. B.: Detection of atrial fibrillation using artificial neural networks. In Computers in Cardiology, Proceedings, pp. 173–176. IEEE, (1991).

EEG Spectral Asymmetry Is Dependent on Education Level of Men

Toomas Põld, Maie Bachmann, Laura Päeske, Kaia Kalev, Jaanus Lass, and Hiie Hinrikus

Abstract

An objective indicator based on the asymmetry of electroencephalographic (EEG) signal spectrum has been shown promising for screening of population to discover occupational stress. However, the factors other than stress affect the EEG spectrum. The aim of the current study is to investigate the role of education level on EEG signals' band relative powers. For this purpose, 18-channel resting eyes-closed EEG was recorded from 30 men having Bachelor or higher education (tertiary education) and 16 men declaring to have lower, upper or post-secondary education (secondary education). For those signals, relative theta, alpha, beta and gamma powers were calculated. The results indicated increase in relative gamma power for the subgroup of men having tertiary education compared to the subgroup of men having secondary education. No significant alterations were revealed in other relative band powers. Higher relative gamma power of men having higher level of education could be related to the higher cognitive load in their everyday life, as widespread gamma activation has been previously demonstrated during cognitive tasks. The results of the current study suggest that the level of education is one of the factors to be taken into account in EEG based evaluation of occupational stress or mental disorders.

1 Introduction

The problems of stress and mental disorders have become important in labour force nowadays and, consequently, need more attention also in occupational health. One in five people at the workplace experience a mental health condition. This statistic is predicted to worsen if early intervention and awareness is continuously avoided [1]. Exposure to stressful working conditions can have direct influence on safety and health [2]. Currently the diagnosis of stress, depression and other mental disorders are based on the evaluation of the intensity of subjective symptoms by general practitioner, occupational physician or psychiatrist using questionnaires and interview—no objective criteria exist in clinical practice. As a result, it is highly important to have an inexpensive objective measure to screen employees for early detection of stress.

The brain behaviour and its mental state are related to its bioelectric activity determined by neuronal oscillations. The oscillations are a prominent feature of neuronal processes and the synchronization of the oscillations is a likely mechanism for cerebral integration for neural communication [3, 4]. Therefore, the spectrum of the resting electroencephalographic (EEG) signal is determined by the state of the brain. Consequently, EEG methods can be highly promising in early detection of mental disorders including occupational stress. For example, a method, spectral asymmetry index, has been shown to differentiate depression from controls [5]. Spectral asymmetry index was also elevated for the group of leaders compared to non-leaders [6]. However, EEG, and therefore different objective parameters calculated from EEG, indicate changes also in variation of normal conditions or under consumption of different substances, like coffee [7], which need to be taken into account while studying stress or different brain disorders. What is more, Veldhuizen et al. [8] found significant gender differences for the temporal theta power for healthy subjects, while Orgo et al. [9] demonstrated significant differences in

T. Põld (✉) · M. Bachmann · L. Päeske · K. Kalev · J. Lass
H. Hinrikus
Tallinn University of Technology, Ehitajate tee 5, 12616 Tallinn, Estonia
e-mail: toomas.pold@qvalitas.ee

T. Põld
Qvalitas Medical Centre, Pärnu mnt 102C, 11312 Tallinn, Estonia

synchronization likelihood between EEG male and female major depressive disorder. In addition, Marciani et al. [10] concluded that young subjects indicate more pronounced fast activity compared to elderly subjects, while some studies have indicated changes in EEG depending on the cognitive load [10]. Cognitive load can be indirectly related to the subjects' education level.

As it is shown, several factors other than mental disorders or stress are capable of changing the EEG relative band powers.

Current study aims to identify whether EEG relative band powers differ for men having tertiary or secondary education. The results would give valuable information about the dependence of EEG on the level of education that is important in EEG-based estimation of occupational stress and explains whether and how the education level could be revealed in spectral asymmetry of the EEG signal.

2 Methods

2.1 Subjects

The experiments were carried out in Qvalitas Medical Center on a group of healthy volunteers. The group consisted of 46 subjects: 30 subjects having tertiary education with the mean age of 42.1 and standard deviation of 9.4 years and 16 subjects having secondary education with the mean age of 37.6 and standard deviation 7.5. The age difference between two education levels of interest were statistically compared ($p > 0.05$) to exclude the influence of age on the results.

At least 1.5 h before the experiment the subjects did not consume any caffeinated drinks and up to 8 h before no alcoholic beverages.

2.2 Experiment Procedure and EEG Recording Equipment

The experimental study was performed according to the recording protocol identical for all subjects: eyes closed resting EEG recorded for 7 mins. During the EEG recordings, subjects were lying in a relaxed position with eyes closed and ears blocked. The room was dimly lit but no other special conditions were provided.

The Cadwell Easy II EEG (Kennewick, WA, USA) measurement equipment was used for the EEG recordings. The 18-channel EEG was recorded according to the international 10–20-electrode position classification system (common reference Cz). Raw signals in frequency band 0.3–70 Hz were stored at sampling frequency 400 Hz. The notch filter was applied at 50 Hz.

2.3 EEG Analysis

The visually checked artefacts-free EEG segments with the duration of 10 s were selected from the EEG signal. First 30 of the segments (5 mins) were used in further analysis. Spectral asymmetry and also the relative theta, alpha, beta and gamma band powers were calculated for each of those segments, to clarify, which part of the EEG spectrum is responsible for alterations in EEG spectral asymmetry.

The spectral asymmetry was calculated as relative difference between powers of EEG bands at frequencies higher and lower than the central alpha band. In spectral asymmetry, the alpha band was excluded from the calculations.

To calculate the EEG segments' relative band powers, the power spectral density was estimated by means of Welch's averaged periodogram method for each subject's EEG channels. The signal was divided into overlapping epochs (50%), with the length of 2048 samples and extracted through a Hanning window. Afterwards, the average of relative powers were computed for theta (3.5–7.5 Hz), alpha (7.5–12.5 Hz), beta (12.5–30 Hz) and gamma (30–46 Hz) bands. Next the relative band powers and also the spectral asymmetry were averaged over all channels and the difference in those parameters between groups with secondary and tertiary education was evaluated using the Mann-Whitney statistical test. The confidence level of 0.05 was selected for evaluation. In case any of the parameters gave significant difference between the two groups, those parameters were re-evaluated for group differences in nine more specific brain regions, each comprising of two nearby channels: Fp1&Fp2, F7&F3, F8&F4, T3&C3, T4&C4, Fz&Pz, T5&P3, T6&P4, O1&O2.

All the EEG data processing was performed using MATLAB (The Math-works, Inc.).

3 Results

The groups with different education levels were not statistically significantly different considering the age ($p > 0.05$). We found statistically significant difference between the group of men having tertiary education compared to the group of men having secondary education in spectral asymmetry values averaged over all channels ($p < 0.05$). Therefore, also the difference between the groups in nine more specific brain regions was studied (Fig. 1). As can be seen all the posterior regions and also left anterior regions indicate statistically significant increase in spectral asymmetry in case of tertiary education.

While calculating the relative band powers of theta, alpha beta and gamma band averaged over all channels for group of males with tertiary and secondary education, only the relative gamma band power indicated statistically significant
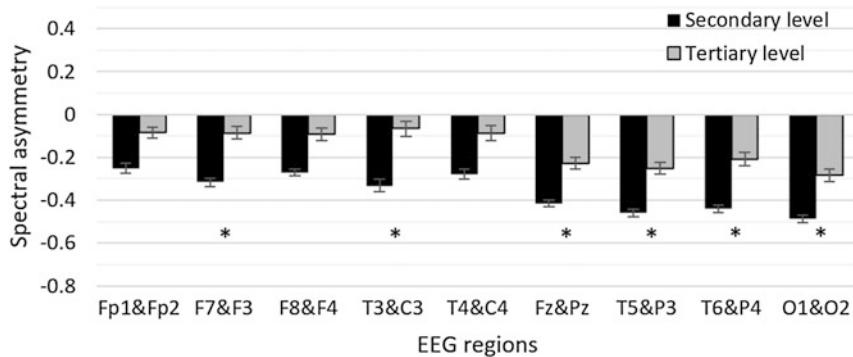
Fig. 1 Mean and standard error of the spectral asymmetry values for the group of men having secondary education and group of men having tertiary education in 9 brain regions. Asterisk represent statistically significant difference (p < 0.05)
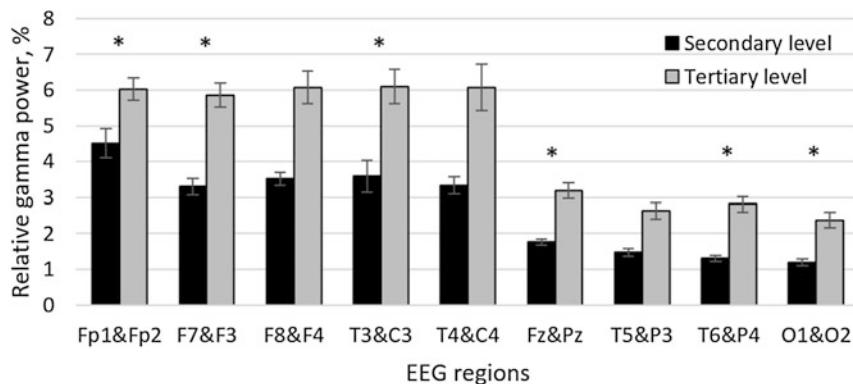

Fig. 2 Mean and standard error of the relative gamma power for the group of men having secondary education and group of men having tertiary education in 9 brain regions. Asterisk represent statistically significant difference (p < 0.05)

difference (p < 0.05) between the groups. Therefore, only the behaviour of relative gamma band power was studied in more specific brain regions. Figure 2 presents the average relative gamma band powers for the group of men having secondary education and group of men having tertiary education in nine brain regions. The results indicate increased relative gamma power for the group of men having tertiary education compared to group of men having secondary education in all regions. The increase was statistically significant in all regions, except F8&F4 (p = 0.08) and T5&P3 (p = 0.07) indicating increase close to statistical significance, and T4&C4 indicating non-significant increase. In other words, it can be generalized that all brain regions, except left fronto-central region, indicate increased relative gamma band power for men with tertiary education compared to men with secondary education.

4 Discussion

The results indicated significant increase in spectral asymmetry for men with tertiary education compared to men with secondary education. While clarifying which EEG frequency band is responsible for those differences, it was revealed that only relative gamma power is able to differentiate those groups. As relative gamma power in combination with spectral asymmetry gave good results while classifying depressive disorder [11], the education level of subjects needs to be considered in future studies to better classify mental disorders. Higher relative gamma power of men having higher level of education could be related to the higher cognitive load in their everyday life, as widespread gamma activation has been previously demonstrated during cognitive load [12].

Considering the current results, one has to keep in mind that the study included only men. Additional study is needed to understand how variations in education level reveal in women's EEG, as there have been found significant sex differences in theta power [8]. In addition, the research of mental health charity Mind reveals that men are twice as likely to suffer work-related mental health problems compared to women [1].

The results of the current study suggest that the level of education is one of the factors to be taken into account in EEG based evaluation of occupational stress or mental disorders.

5 Conclusions

The results of the performed study indicate that men with tertiary education have increased relative gamma band power compared to men with secondary education, influencing also the EEG spectral asymmetry. The level of education is one of the factors to be taken into account in EEG based evaluation of stress or mental disorders.

Compliance with Ethical Requirements The experiments were conducted with the understanding and the written informed consent of each human subject. Complete anonymity of recorded EEG signals and the results of analysis was guaranteed.The study was in accordance with the ethical standards and formally approved by the Tallinn Medical Research Ethics Committee. The procedures followed were in accordance with the Helsinki Declaration of 1975, as revised in 2000 and 2008.

Conflict of Interests The authors declare that they have no conflict of interest.

References

1. Mamo, E. Men more likely to suffer work-related mental health issues https://www.openaccessgovernment.org/men-work-related-mental-health-issues/36371/ (2017) last accessed 2018/02/02.
2. Levy, B. S., Wegman, D. H., Baron, S. L., Sokas, R. K. et al.: Occupational and environmental health. 6th edition. Oxford University Press, New York, 14, 296–312 (2011).
3. Buzsáki, G., Draguhn, A.: Neuronal oscillations in cortical networks. Science 304, 1926–1929 (2004).
4. Schnitzler, A., Gross, J.: Normal and pathological oscillatory communication in the brain. Nature Rev Neurosci 6, 285–296 (2005).
5. Hinrikus, H., Suhhova, A., Bachmann, M. et al.: Electroencephalographic spectral asymmetry index for detection of depression. Med Biol Eng Comp 47, 1291–1299 (2009).
6. Põld T., Bachman M., Orgo L., Kalev K., Lass J., Hinrikus H.: EEG Spectral Asymmetry Index Detects Differences Between Leaders and Non-leaders. In: Eskola H., Väisänen O., Viik J., Hyttinen J. (eds) EMBEC & NBC 2017. EMBEC 2017, NBC 2017. IFMBE Proceedings, vol 65, pp. 17–20, Springer, Singapore (2018).
7. Saifudinova M., Bachmann M., Lass J., Hinrikus H.: Effect of Coffee on EEG Spectral Assymmetry. In: Jaffray D. (eds) World Congress on Medical Physics and Biomedical Engineering, June 7–12, 2015, Toronto, Canada. IFMBE Proceedings, vol 51, pp. 1030–1033 Springer, Cham (2015).
8. Veldhuizen, R. J., Jonkman, E. J., Poortvliet, D. C.: Sex differences in age regression parameters of healthy adults–normative data and practical Implications. Electroencephalogr Clin Neurophysiol. 86(6), 377–84 (1993).
9. Orgo, L., Bachmann, M., Kalev, K., Hinrikus, H., Järvelaid, M.: Brain functional connectivity in depression: Gender differences in EEG. 2016 IEEE EMBS Conference on Biomedical Engineering and Sciences (IECBES), pp. 270–273. Kuala Lumpur (2016).
10. Marciani, M. G., Maschio, M., Spanedda, F., Caltagirone, C., Gigli, GL., Bernardi, G.: Quantitative EEG evaluation in normal elderly subjects during mental processes: age-related changes. Int J Neurosci. 76(1–2), 131–40 (1994).
11. Bachmanna, M., Päeske, L., Kalev, K., Aarmaa, K., Lehtmets, L., Ööpik, P., Lass, J., Hinrikus, H.: Methods for classifying depression in single channel EEG using linear and nonlinear signal analysis. Computer Methods and Programs in Biomedicine, 155, pp. 11–17 (2018).
12. Werkle-Bergner, M., Shing, Y.L., Müller, V., Li, S.C., Lindenberger, U.: EEG gamma-band synchronization in visual coding from childhood to old age: evidence from evoked power and inter-trial phase locking. Clinical Neurophysiology 120(7), 1291–1302 (2009).

Artificial Neural Network Applied like Qualifier of Symptoms in Patients with Parkinson's Disease by Evaluating the Movement of Upper-Limbs Activities

J. P. Bermeo, M. Huerta, M. Bravo, and A. Bermeo

Abstract

The Movement Disorder Society (MDS-UPDRS) defines characteristics to qualify various symptoms of PD, the present works propose to apply an Artificial Neural Network ANN to qualify symptoms based upon movement of upper-limbs activities. In this way, a system based on Arduino and Android mobile app were developed, where accelerometers are used to acquire and store the acceleration data from upper-limbs while PD patients were doing three activities: rest sitting, eating and brushing teeth, meanwhile their symptoms were classified by doctor between 0 (normal) to 4 (most severe impairment). After that, store data were processed and estimation on Power Spectral Density (PSD) was done, then this information and doctor's diagnosis were used into the ANN training to evaluate the symptoms in PD patients. For the ANN training was used back-propagation model and many ANN configurations, until get the best fit between inputs (processed data) and output (doctor's diagnosis). The results showed that trained ANN can be used like qualifier with a high degree of accuracy over the 90%, for the tests performed. Moreover, even though MSD-UPDRS allows to get an accurate diagnosis, there is not objective, so ANN could be fixed to be completely objective, being a great advantage with manual evaluation.

J. P. Bermeo (✉) · M. Huerta · M. Bravo · A. Bermeo
Universidad Politécnica Salesiana, Cuenca, 010105, Ecuador
e-mail: jbermeo@ups.edu.ec

1 Introduction

The "Paralisis Agitans" syndrome named the first time by James Parkinson in 1817, is a neurodegenerative disease caused by reduction of dopaminergic cells in the substantia nigra, however the most famous name is Parkinson Disease named by Jean-Martin Charcot [1]. Between 1 and 2% of population over 70 years are affecting by PD [2]; the tremor at rest, muscle stiffness, bradykinesia (slowness in voluntary and involuntary movements, but mainly difficulty to start and finish them), loss of postural reflexes and segmental cephalic tremor are the most common movement disorders.

In 1980, the Unified Parkinson's Disease Rating Scale UPDRS was developed, but the Movement Disorder Society (MDS) asked a revision about scale, resulting in the MDS-UPDRS scale [3], where start in 0 (normal) to 4 (most severe impairment).

The measurement process of MDS-UPDRS is large and complex, furthermore is subjective and potentially error prone, so there are a lot of methods and devices to evaluate the PD's motor symptoms. In [4] 3D visualization techniques are applied to monitoring and assessment of Parkinson's disease. The severity of symptoms had been assessed by Wii console [5], Kinetic sensor [6, 7], but the main problem is the weight in the first case because is a constraint for the free movement, and in the second case, the problem is a limited distance and the necessity of adequate light. A system based on Arduino and Android mobile App was developed in [8] to evaluate motor assessments. Neither all these approaches apply their measurements to evaluate the movement disorders of PD's patients in a MDS-UPDRS scale.

This paper takes advantages of Artificial Neural Networks ANN to classify a wide range of inputs, for this work, the inputs are processed signals measured by triaxial accelerometers from the system developed in [9], and ANN was trained with doctor's diagnosis such as output. The results showed a high accurate between ANN's output and diagnosis. The measures were taken form upper limbs in

four activities of daily life such as lying rest, eating, rest sitting, and brushing teeth.

2 Methodology

For this work, begin with the training of ANN, after that the ANN is used to make diagnosis with measurement took and processed from acquisition system. The first step, to train ANN, is take measurement from system developed in [9], then data are processed to become in inputs to ANN, and doctor's diagnosis are the reference outputs. With inputs and reference outputs, ANN trains until get ANN's outputs are like reference outputs. ANN changes while training, so the last configuration is known as a "trained network", Fig. 1 show the process to train ANN.

The trained ANN could be applied to evaluate Parkinson's patients in a MDS-UPDRS scale. Figure 2 sketched what was described above.

In the next sections, every block is detailed.

2.1 Acquisition System

The acquisition system [9] has a digital accelerometer and gyroscope MPU-6050, Arduino Pro Mini, microSD module, HC-05 Bluetooth module and a Li-ion battery. The information is stored in CSV format in Android mobile device, information was sent by Bluetooth module from Arduino

Pro Mini to Android mobile device. Figure 3 outlined block diagram of acquisition system.

The information measured from triaxial accelerometers, has a sampling frequency of 14 Hz, for each test 450 samples were used to data processing, information is registered by sensor in Arduino device and data is sent to personal computer by Bluetooth in CSV format. Figure 4 shows acceleration of each axes and the module received from acquisition systems for one Parkinson disease's patient X

2.2 Data Processing

The ANNs are sensitive to variations of amplitude and time displacement [10], so the data should be processed before introduced to ANN. To generate invariance to time displacements, the module of the Fast Fourier Transform FFT [11] and Welch's power spectral density estimate [12] are used.

The FFT is applied to acceleration, and Welch's power spectral density is applied to displacement. The acceleration's integral is equal to velocity, and velocity's integral is the displacement [13]. For each integral, interpolation is applied to evaluate the middle point, its mean that N original points will become $2*N-1$ points for first integral and $2*(2*N-1)-1$ points for second integral, so for N = 450 acceleration's points there are 1797 displacement's points. Figure 5 shows calculated displacement for each axes and module.

The accelerometers measure the gravity, furthermore a constant velocity could be affect the estimation of
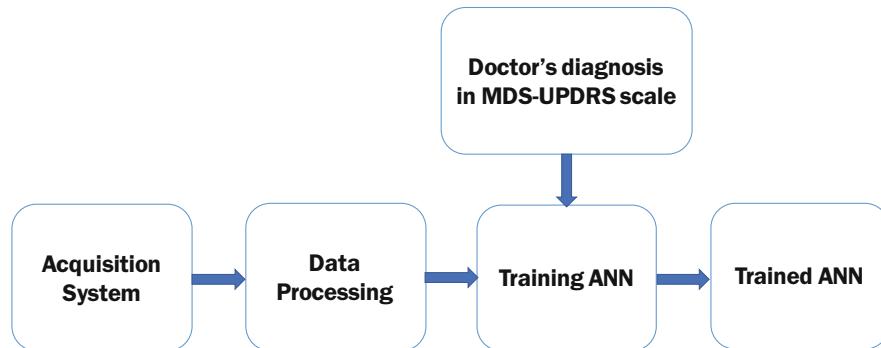
Fig. 1 Flow chart of the artificial neural network (ANN) training process
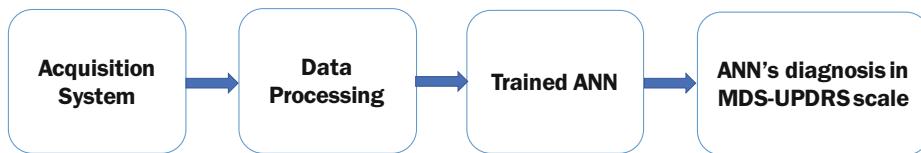
Fig. 2 Trained ANN applied like evaluator
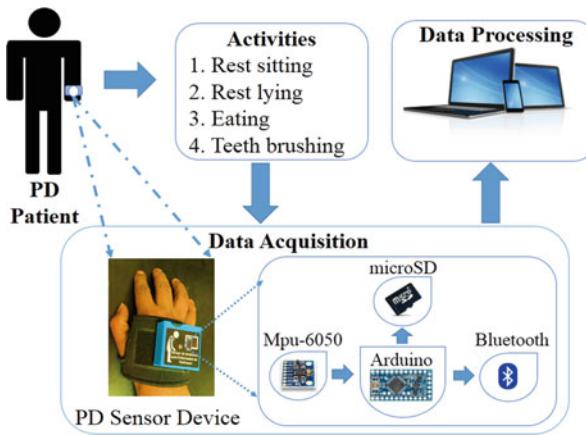
Fig. 3 Block diagram of acquisition system [9]
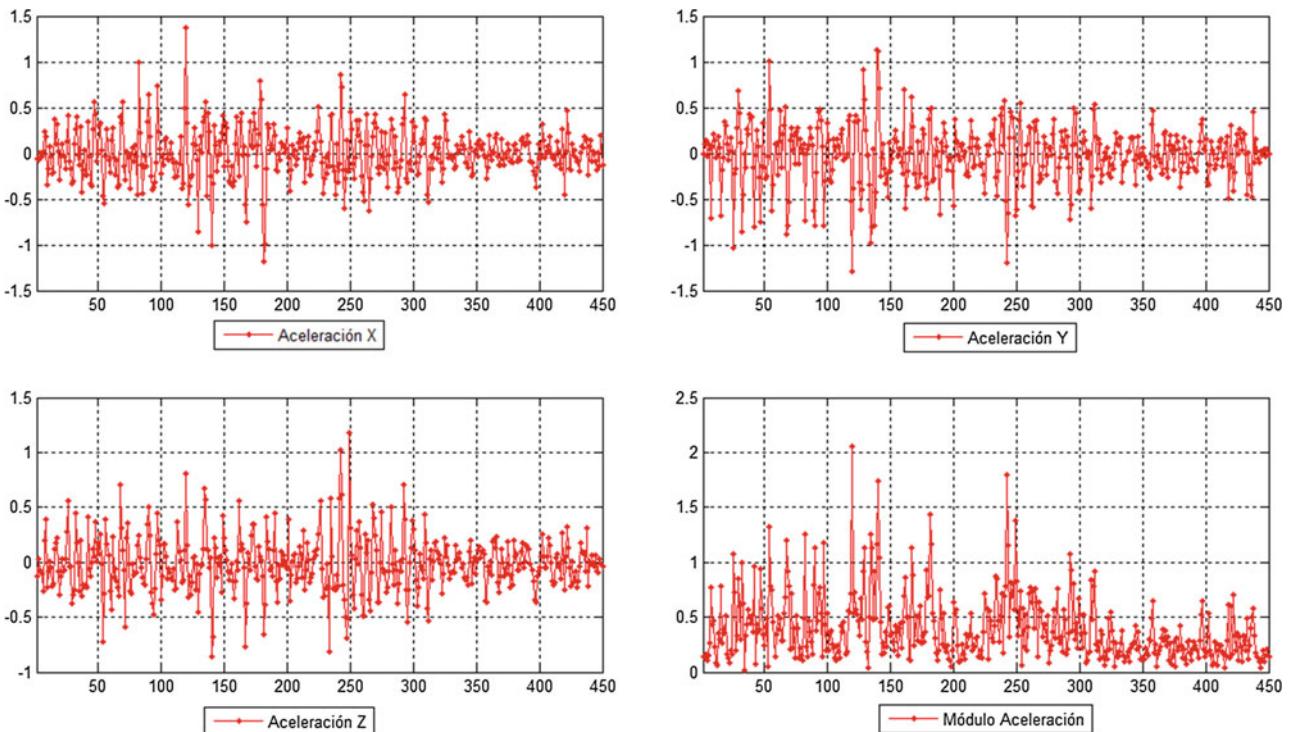
Fig. 4 Acceleration measured from triaxial accelerometers

displacement, so before each integral, a digital high pass filter was applied to eliminate frequencies below 0.5 Hz, Matlab's functions [14] were used to get this aim. Figure 6 shows the Fast Fourier Transform of acceleration and Welch's power spectral density estimated from displacement.

2.3 Artificial Neural Network ANN

The ANN's has several applications like pattern recognition [15], sales forecasting [16], evaluation of health index of power transformers [17], and others. In this paper ANN was used like evaluator for patients with PD.

After data processing, information can be entered to ANN to start the training. Some configurations were tried, at the end, the ANN with the best results, had three layers, 357 inputs, thirty neurons in hidden layer and one output; logsig function to hidden layer and lineal function to last layer. The ANN is sketched in the next Fig. 7.

With the trained ANN, in the Fig. 8 a comparative between net's output and doctor's diagnosis is showed. There is a high equivalence between both diagnoses, its
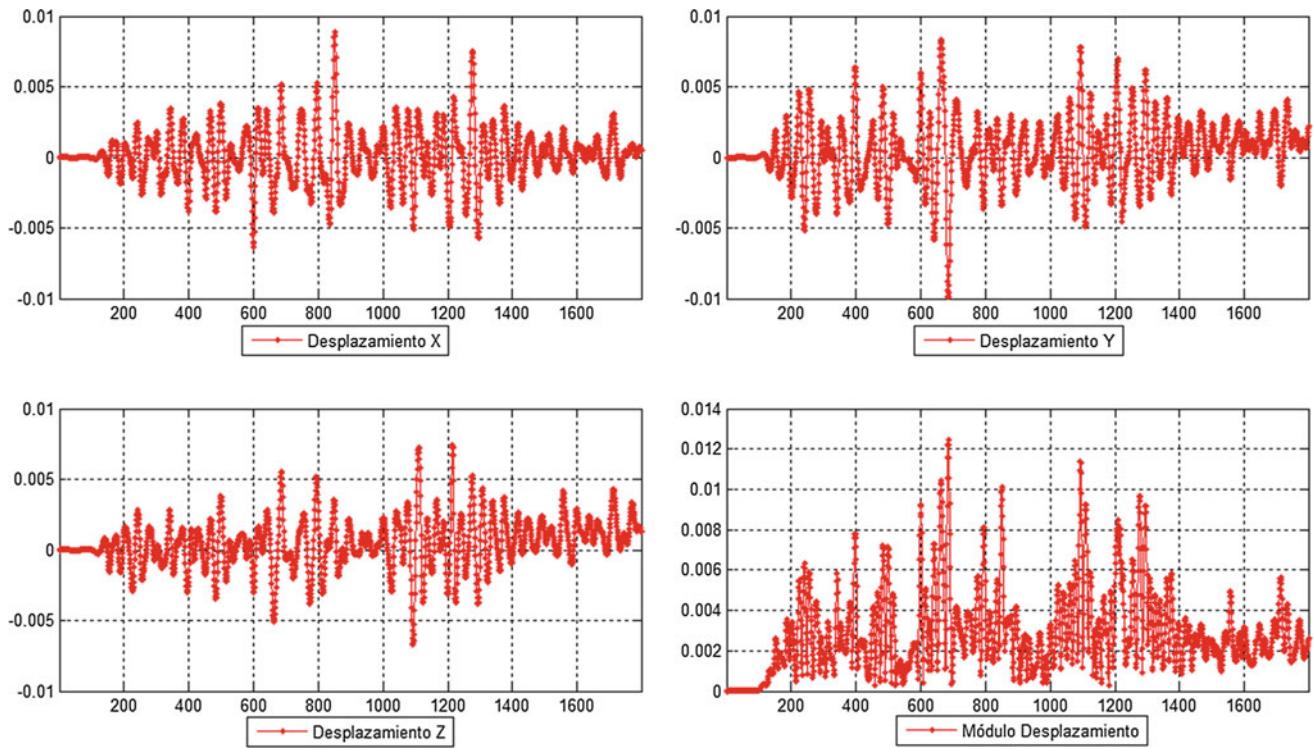
Fig. 5 Displacement calculated from twice integrated acceleration
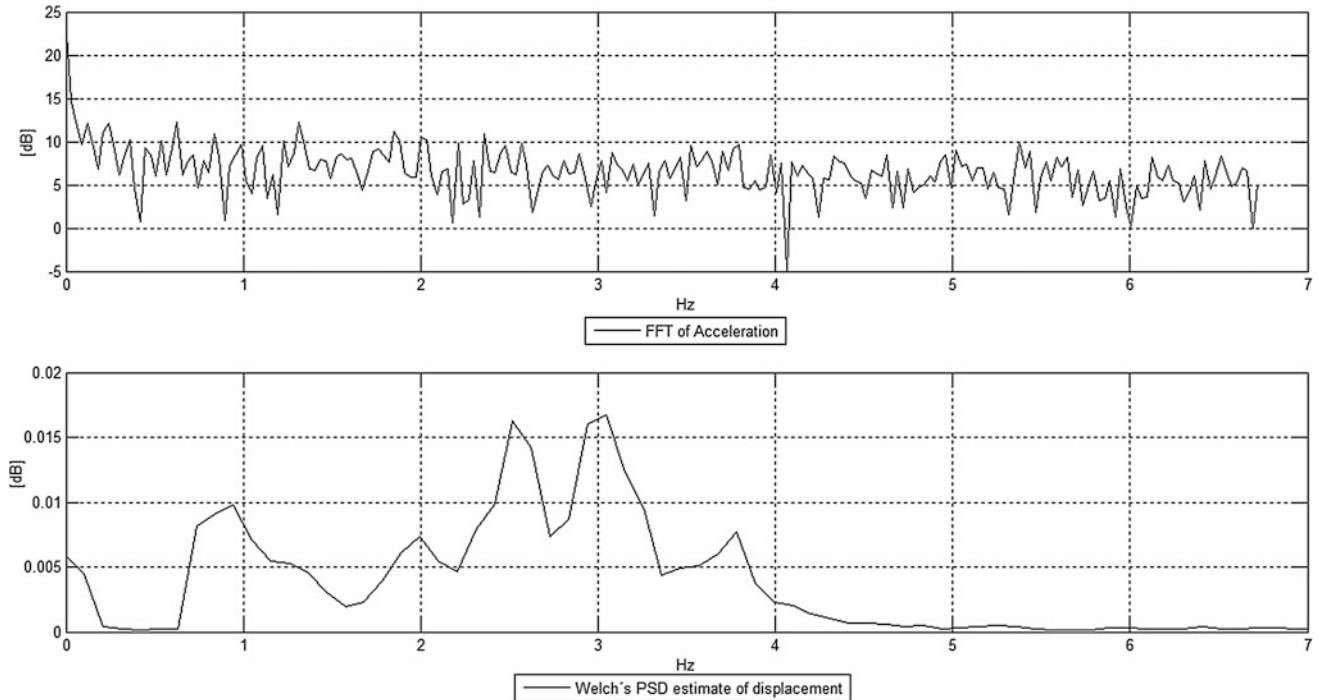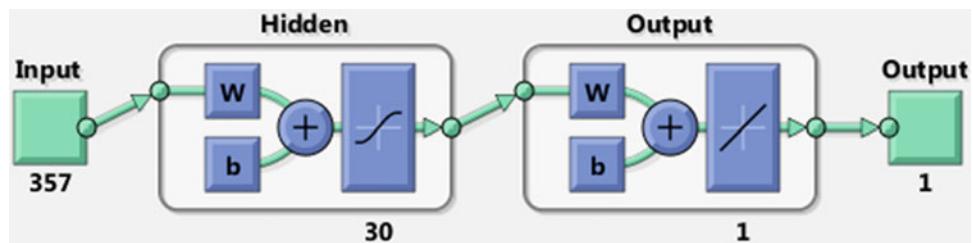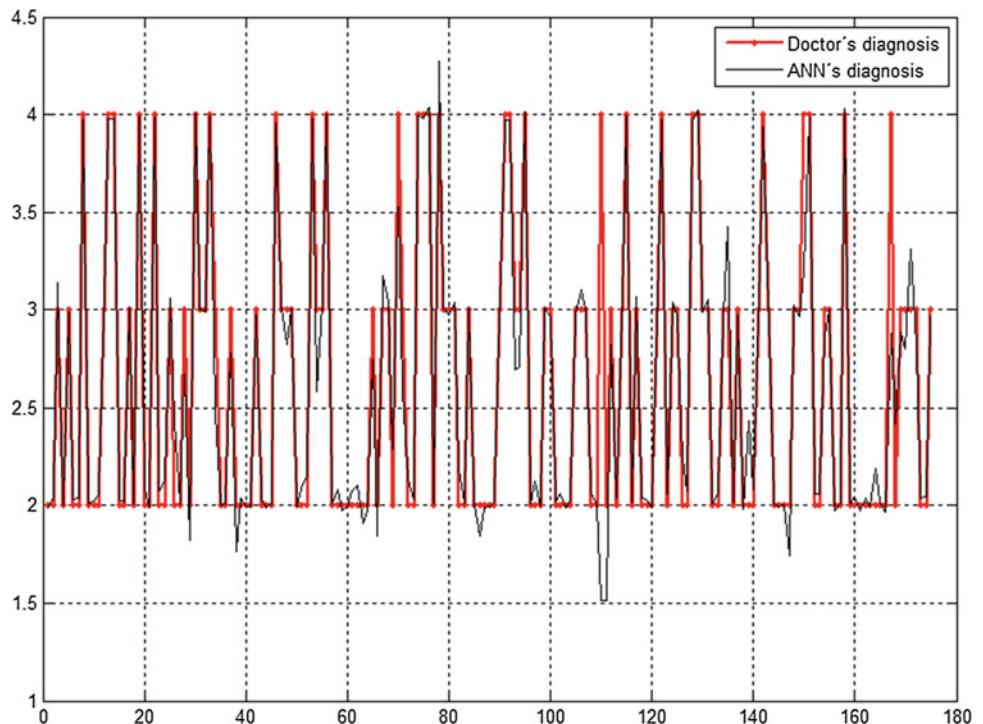
Fig. 6 FFT and Welch's PSD estimate

Fig. 7 ANN's scheme

Fig. 8 Comparative between ANN and Doctor's diagnosis

mean, the ANN have a good performance to make an estimation in a MDS-UPDRS scale, with over 90% of success.

3   Conclusions

This method evaluates the patients in shorter time than traditional method, so it should have less inconveniences to doctor and patients, furthermore this tool is objective without the subjective influence of evaluator.

At least thirty minutes are needed to evaluate PD's patients in a MDS-UPDRS scale [3], with the equipment and software claimed in this work, the evaluation time is rough ten minutes, and this is a big advantage in the process. Furthermore, the high level of certainty (>90%), shows that ANN could be used to diagnosis.

The inputs for ANN must be processed to eliminate invariance like to displacement in time or others, so the FFT and Welch's PSD estimate are good tools to get this aim.

References

1. N. Titova, C. Padmakumar, S. J. G. Lewis y K. R. Chaudhuri, Parkinson's: a syndrome rather than a disease?, *Journal of Neural Transmission,* pp. 907–914, 2016.
2. A. Villa-Velarde, M. Rodriguez, K. Cruz y A. Cervantes, State of research on Parkinson's disease in Mexico of 1988 to 2010, *Neurociencia,* vol. 18, no 10, pp. 27–38, 2013.
3. C. Goetz, B. Tilley, S. Shaftman, G. Stebbins, S. Fahn, P. Martinez-Martin, W. Poewe, C. Sampaio, M. Stern, R. Dodel, B. Dubois, R. Holloway, J. Jankovic, J. Kulisevsky, A. Lang, A. Lees, S. Leurgans, P. LeWitt, D. Nyenhuis, C. Olanow, O. Rascol,

A. Schrag, J. Teresi, J. van Hilten y N. LaPelle, Movement Disorder Society-sponsored revision of the Unified Parkinson's Disease Rating Scale (MDS-UPDRS): Scale presentation and clinimetric testing results., *Movement Disorders,* vol. 23, no 15, pp. 2129–2170, 2008.

4. J. Synnott, L. Chen, C. Nugent y G. Moore, Assessment and visualization of Parkinson's disease tremor, de *Proceedings of the 10th IEEE International Conference on Information Technology and Applications in Biomedicine*, Corfu, Greece, 2010.

5. L. Chiuchisan, O. Geman, L. Chiuchisan, A. Coriolan Iuresi Y. A. Graur, NeuroParkinScreen—A health care system for Neurological Disorders Screening and Rehabilitation, de *International Conference and Exposition on Electrical and Power Engineering (EPE 2014)*, Iasi, Romani, 2014.

6. S. Sooklal, P. Mohan y S. Teelucksingh, Using the Kinect for detecting tremors: Challenges and opportunities, de *International Conference on Biomedical and Health Informatics (BHI)*, Valencia, Spain, 2014.

7. B. Dror, E. Yanai, A. Frid, N. Peleg, N. Goldenthal, I. Schlesinger, H. Hel-Or y S. Raz, Automatic assessment of Parkinson's Disease from natural hands movements using 3D depth sensor, de *IEEE 28-th Convention of Electrical and Electronics Engineers*, Eilat, Israel, 2014.

8. A. Bermeo, M. Bravo, M. Huerta y A. Soto, A System to Monitor Tremor in Patients with Parkinson's Disease, de *The 38th Annual International Conference of the IEEE Engineering in Medicine and Biology Society*, Orlando, Florida, 2016.

9. M. Bravo, A. Bermeo, R. Contreras, M. Huerta, A. Soto, J. Bermeo, G. Sagbay y C. Llumiguano, An upper-limbs activities analysis of PD patients in OFF and ON state of medication, de *Ecuador Technical Chapters Meeting (ETCM), IEEE*, Guayaquil, 2016.

10. M. T. Hagan, H. B. Demuth, M. H. Beale y O. De Jesús, Neural Network Design, Oklahoma: M. Hagan, 2014.

11. A. V. Oppenheim y R. W. Schafer, Discrete-Time Signal Processing, Harlow: Pearson, 2014.

12. F. Attivissimo, M. Savino y A. Trotta, A study on nonlinear averagings to perform the characterization of power spectral density estimation algorithms, *IEEE Transactions on Instrumentation and Measurement,* vol. 49, no 5, pp. 1036–1042, 200.

13. B. S. Thomson, The Calculus integral, 2da Ed. ed., Burnaby: ClassicalRealAnalysis, 2009.

14. J. M. Giron-Sierra, Digital Signal Processing with Matlab Examples, vol. 1, Madrid: Springer, 2017.

15. B. Ripley, Pattern Recognition and Neural Networks, Cambridge: Cambridge University Press, 2007.

16. J. Bermeo, H. Castillo y S. Serrano, Neural Networks and Genetic Algorithms Applied for Implementing the Management Model "triple A" in a Supply Chain. Case: Collection Centers of Raw Milk in the Azuay Province, de *MATEC Web of Conferences*, Toulouse, 2016.

17. R. Medina, J. Lata, D. Chacón, D. Morales, A. Medina y J. Bermeo, Health Index assesssment for power transformers with thermal upgraded paper up to 230 kV using fuzzy interference systems, de *51st International Universities Power Engineering Conference (UPEC)*, Coimbra, 2016.

Nonlinear Dimensionality Reduction and Feature Analysis for Artifact Component Identification in hdEEG Datasets

Vlastimil Koudelka, Jan Štrobl, Marek Piorecký, Martin Brunovský, and Vladimír Krajča

Abstract

The time-domain independent component analysis (ICA) is commonly used technique for neural and noise signal separation in electroencephalographic (EEG) data. Nevertheless, the estimated independent sources have to be further classified by an expert using predefined or learned features. Automatic algorithms on market suffer from unsatisfactory sensitivity and specificity mostly due to large inter-subject variability of the human EEG. Generalization of each learning machine depends on whether some discriminative features exist in inter and intra individual component space. We employ nonlinear dimension reduction technique called t-Distributed Stochastic Neighbor Embedding (t-SNE) to fit the data and visualize them in estimated feature space. Our approach is unsupervised and completely data driven. We focus on regularities in a real-world hdEEG component set that could be learned by robust feature classifier, e.g. a deep network. Furthermore, we also investigate relations between found data structure and commonly used criteria known from the literature.

V. Koudelka · M. Brunovský
National Institute of Mental Health, Topolova 748, 250 67 Klecany, Czech Republic
e-mail: Vlastimil.Koudelka@nudz.cz
URL: http://www.nudz.cz/en/research-programmes/rp6-brain-electrophysiology/profile/

J. Štrobl (✉) · M. Piorecký · V. Krajča
Faculty of Biomedical Engineering, CTU in Prague, Sitna Sq. 2105, 272 01 Kladno, Czech Republic
e-mail: jan.strobl@fbmi.cvut.cz

1 Introduction

Recently, Chaumon et al. published a practical guide to the selection of independent components (ICs), summarized automated selection tools, and proposed a comprehensive set of features for ICs recognition [1]. The mentioned study [1] was motivated by the fact that no automated method could accurately isolate artifacts without supervision.

More specificaly, in FASTER [2] and ADJUST [3] a priori selected features were exploited. The SASICA tool [1] then summarized and extended the fixed feature set. The MARA algorithm also applied a specific set of features and focused on supervised expert based learning [4]. Slightly different supervised method was used in CORRMAP [5], where the ICA inverse weights (topo-maps) were clustered based on supervised spatial cross correlation algorithm. Supervised based methods in [6] reflect specific conditions of the training set. This may increase bias and network generalization has to be carefully validated [4].

In contrast with the above mentioned tools, our approach is unsupervised, completely data driven, and no expert input is needed. More importantly, the proposed method doesn't operate on a pre-defined set of known features, the algorithm rather extracts intrinsic features form the data. This concept of learning from raw data is known from deep learning technology. Our goal is to approach the IC selection problem in sense of the deep learning.

Application of deep learning techniques in EEG physiological feature learning can be found in paper [7]. To the best of our knowledge, no method exploiting deep learning for IC identifications was published yet.

Here, we focus on the feature extraction and visualization, since it is an essential step to interpret the discriminating features. The t-SNE method [8] is used to fit and visualize data structure, see Sect. 2.3. Generally, methods and materials are described in Sect. 2. In this paper, we focus on IC spatial weights, time scores are not taken into account, see Sect. 2.2. The IC dataset is also analyzed in

sense of criteria selected in [1], see Sect. 2.5. The DBSCAN algorithm is used to label clusters observed in t-SNE map, see Sect. 2.4. Finally, we discuss relations between found IC clusters and commonly used metrics, see Sect. 3.

2 Materials and Methods

The testing dataset is composed of 5 min long, eyes open, resting state, EEG recordings from 40 subjects. The dataset consisted of two groups: schizophrenic patients and healthy controls. Both groups contained twenty subjects. Data acquisition was approved by the local ethical committee of National Institute of Mental Health, Czech Republic.

Data were recorded in a Faraday cage by EGI256-channel EEG system equipped by Net Amps 400 series amplifier, $F_s = 1000$ Hz, DC coupling with 256 HydroCel Geodesic Sensor Net, and Net Station 5 acquisition software.

The method was implemented in frame of FieldTrip MATLAB software toolbox [9].

2.1 Data Preprocessing

Each 256-channel recording was down-sampled to $F_s = 250$ Hz. Time courses exhibiting high values of variance were selected by Tuckey method and interpolated by weighted average of all neighbors. Signal was band pass filtered by two-way zero-phase FIR filter with critical frequencies $F_{low} = 0.5$ Hz and $F_{high} = 50$ Hz, see [3]. The raw data were inspected and artifacts what would significantly affect ICA decomposition were rejected.

2.2 ICA and Normalization

Data dimension was reduced by Principal Component Analysis (PCA) prior to ICA decomposition to prevent over-fitting of the source reconstruction algorithm. We obtained 35 components maintaining 99% of variance of the original data. Time-domain Extended Infomax ICA algorithm was used to separate signal sources [10]. Inverse weights $W_c(n)$ of all $n = 1, 2, \ldots, N$ channels were arranged into a row vector and all $c = 1, 2, \ldots, C$ components were shaped into a subject matrix. All $(N = 256) \times (C = 35)$ subject matrices were concatenated in one 1400×256 data matrix W. Each W row (each topomap) was normalized with respect to its Root Means Squared (RMS) value to emphasize the field spatial distribution rather then its total power. Dimension of W was finally reduced by PCA to 1400×45, which is a standard procedure before numerical t-SNE embedding.

2.3 t-SNE Component Embedding

Similarity between each pair of IC topomaps W_i and W_j is represented by conditional probability $P_{i|j}$ under some assumptions [8]:

$$P_{i|j} = \frac{exp\left(-\|W_i - W_j\|^2\right)/\sigma_i^2}{\sum_{k \neq i} exp\left(-\|W_i - W_k\|^2\right)/\sigma_i^2}, \quad (1)$$

where σ_i denotes variance of the i-th component Gaussian distribution of neighbors.

The same metric described in Eq. 1 is applied to a low dimensional (two-dimensional in our case), alternative distribution of topomaps. The mapping is provided by fitting an alternative low-dimensional IC distribution to the minimum of Kullback-Leibler divergence between high and low-dimensional map probabilities.

2.4 DBSCAN Labeling

Density based algorithms take advantage of different density distributions of classified objects in space to separate individual datasets, see [11]. Objects are in our case the topographical maps of IC signals. DBSCAN classifies objects based on density, so a range of objects with a similar density distribution is classified in the same class. In order to avoid classifing object regions from each other in very distant space, the DBSCAN defines a cluster as a high dot density region that is separated by a low density location. All objects with the low-density region are labelled as so-called noise cluster. The input parameters of the algorithm are the radius (Eps) and the number of objects in it (k).

2.5 Applied Criteria

In order to investigate relations between found data structure and common component features, RMS energy of each component was evaluated. Additionally, three criteria from [1] were addressed: Autocorrelation, Focal topography, and Focal trial activity.

The Autocorrelation A_c is supposed to reach high values in physiological ICs in contrast with some artifact components. The A_c can be calculated as follows [1]:

The Focal topography F_c is sensitive to ICs exhibiting spatially focused energy in one or a few channels. The maximal Z-score of energy across channels is purposed to evaluate the spatial focus [1]:

$$F_c = \max_n \left(\underset{N}{Z}(W_c(n)) \right), \tag{2}$$

here, $\underset{N}{Z}$ is a set of Z-scores in all channels, max_n is maximum in a channel n and $W_c(n)$ is and inverse weight at channel n and component c.

Focal trial activity FT_c measures facility in time within IC time series. High signal amplitudes, which are not regularly distributed in time indicate an artifact. The FT_c can be easily evaluated, see Eq. 3:

$$FT_c = \max_k \left(\underset{K}{Z} \left(\max_t(x(c,k,t)) - \min_t(x(c,k,t)) \right) \right), \tag{3}$$

where max_t is a maximum in a time sample t, min_t is a minimum in a time sample t, k denotes the k-th segment of the signal, $\underset{K}{Z}$ is a set of Z-scores in all segments, and $x(c,k,t)$ are time-domain data in the c-th component, the k-th segment and time sample t [1].

3 Results and Discussion

All 1400 topomaps projected into 2-dimensional space by the tSNE method can be observed in Fig. 1. Data are clearly formed into clusters. Each cluster contains ICs originating from various subjects. Thus, we concludes that the tSNE fits inter subject regularities in data, see Fig. 1a. The DBSCAN identified twelve clusters containing different number of members depicted in Fig. 1b. Labeled clusters without noise points filtered by the DBSCAN can be observed in Fig. 1c. The noise cluster containing 343 ICs was further evaluated as the thirteenth regular IC cluster.

In Fig. 2, mean (Fig. 2a), median (Fig. 2b), and variance (Fig. 2c) topomaps can be observed. Median and mean topomaps are qualitatively similar which indicates cluster homogeneity. However, Fig. 2c uncover badly mapped pulse-like ICs topomaps. In accordance with [1], we can estimate, that cluster CL1, CL3, CL6 and CL11 represents EOG artefact, clusters CL2, CL4, CL5, CL7 and CL10 represent brain activity. CL9 represents cardiac activity, which can be justified by observing corresponding IC time series (not presented). CL12 represents bad electrode ICs. A cluster CL8 represent mismatch of the topomaps located in the center of tSNE map, see Fig. 1c. Obviously, the noise point channel CL13 contains a mixture of noise components. In the following part of the paper we will use the interpretation mentioned above which is based on the practical guide in [1].

Figure 3 summarizes all addressed criteria (features) in standard boxplot form. Depicted boxplots approximate PDFs of analyzed features from [1]. On the other hand, Fig. 2
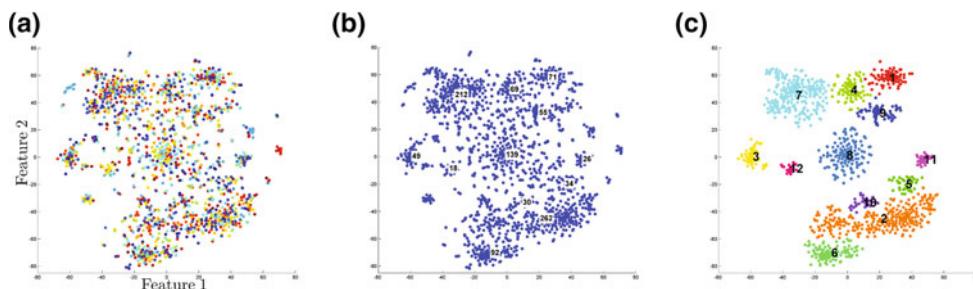

Fig. 1 Each point in the t-SNE map denotes an IC originating from a particular subject: **a** each subject is coded by unique color; **b** distribution of all ICs, a number of cluster members appears in averaged position within each cluster; **c** labeled IC clusters excluding noise points
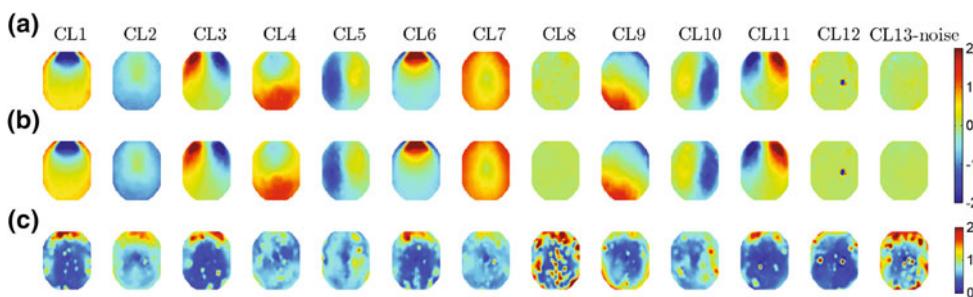

Fig. 2 Topomaps of clusters labeled by DBSCAN method (CL1–CL12 and noise CL13) depicted: **a** in average; **b** median; **c** variance across cluster members
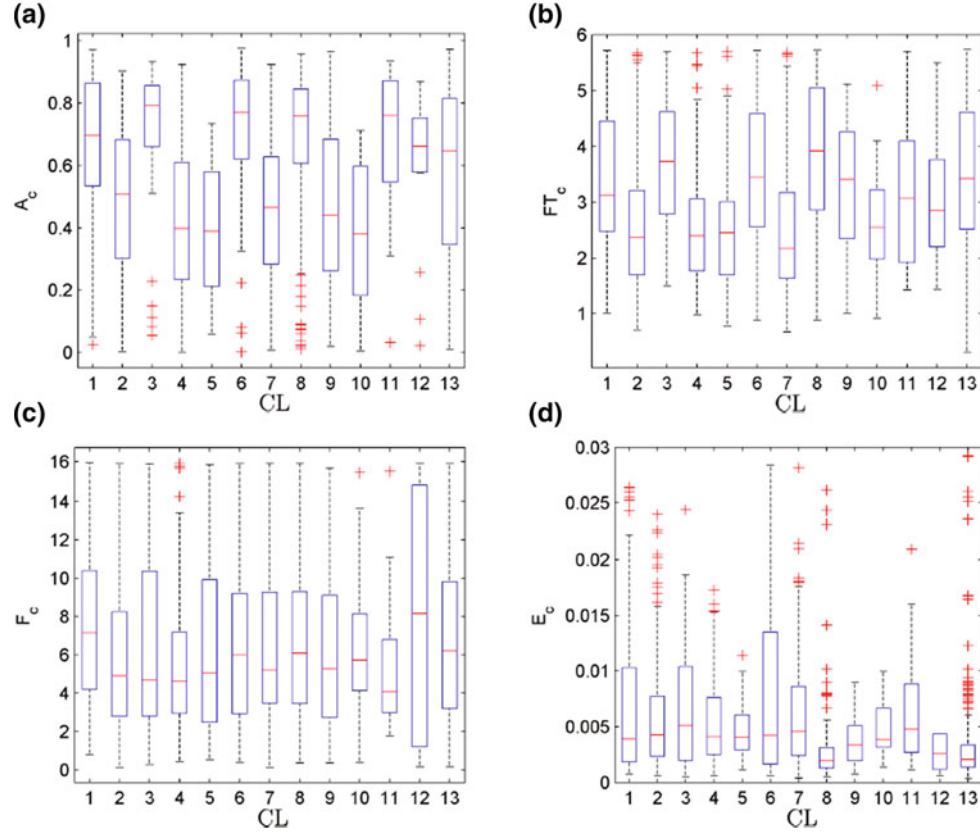
Fig. 3 Comparison of boxplots of independent cluster groups in terms of: **a** Autocorrelation; **b** Focal trial activity; **c** Focal topography; **d** Energy criterion

summarizes spatial features identified by our novel approach. Thus, comparison and analysis of Figs. 2 and 3 is the main connection between the purposed method and common approaches. Surprisingly, even if the purposed approach is based on spatial features, the found data structure also corresponds to time based criteria A_c and FT_c, see Fig. 3a, b.

More specifically, the A_c cluster distributions (see Sect. 2.5) depicted in Fig. 3a separate physiological and artificial like topomaps except cardiac cluster. However, detailed observation shows, that A_c values are in contrast with our expectations (IC maps exhibiting rather low level of A_c tend to be artifacts). Study [1] briefly mentioned, that this phenomenon is due to slow time fluctuations. We suggest, that this could be an effect of time domain blurring due to zero-phase FIR filters.

Regarding to the FT_c, the spatial structure in Fig. 2 corresponds well to the FT_c distributions in Fig. 3b. Clusters CL2, CL4, CL5, CL7, and CL10 exhibit the lowest median and low inter-quartile variance.

Surprisingly, space based F_c criterion depicted in Fig. 3c does not show very good separation of observed clusters. Slightly higher F_c can be observed in CL1 and CL6 (eye blinks), CL8 (mismatch), CL12 (bad electrode), and noise CL13 (mixed) clusters. Figure 2c also shows high pulse like variance distribution which indicate bad separation of bad electrode ICs in the tSNE map.

In Fig. 3d, the E_c Energy criterion (see Sect. 2.5) can be observed. In general, the lower IC topomap energy the less variance is explained by a particular IC. The least energy exhibit CL8 (mismatch of topomaps) and CL13, which is in accordance with [1], where the low energy ICs are suggested for rejection.

4 Conclusion

An unsupervised data driven approach was applied to independent component identification. Generally, the extracted data structure from 1400 IC topomaps showed

good correspondence with commonly applied criteria. The purposed method (at current development stage) can be used to check a dataset quality or it can extend existing user informing tools, e.g. SASICA. Thanks to promising results, this contribution is the very first step towards identification method based on IC feature extraction from the raw data (without a priory fixed criteria), capable to learn across datasets and providing a sufficient low level layer for IC classifiers. The next step would be integrating also spectral information of ICs and analysis of its effect on IC separation.

Statements by Authors The authors declare that there is no conflict of interest regarding the publication of this article.

The study protocol and patient informed consent have been approved by National Institute of Mental Health ethical committee.

The procedures followed were in compliance with the ethical standards of the responsible committee on human experimentation (institutional and national) and with the World Medical Association Declaration of Helsinki on Ethical Principles for Medical Research Involving Human Subjects.

References

1. M. Chaumon, D.V. Bishop, N.A. Busch, Journal of neuroscience methods **250**, 47 (2015).
2. H. Nolan, R. Whelan, R.B. Reilly, Journal of Neuroscience Methods **192**(1), 152 (2010). https://doi.org/10.1016/j.jneumeth.2010.07.015.
3. A. Mognon, J. Jovicich, L. Bruzzone, M. Buiatti, Psychophysiology **48**(2), 229 (2011). https://doi.org/10.1111/j.1469–8986.2010.01061.x.
4. I. Winkler, S. Brandl, F. Horn, E. Waldburger, C. Allefeld, M. Tangermann, Journal of Neural Engineering **11**(3) (2014). https://doi.org/10.1088/1741-2560/11/3/035013.
5. F. Campos Viola, J. Thorne, B. Edmonds, T. Schneider, T. Eichele, S. Debener, Clinical Neurophysiology **120**(5), 868 (2009). https://doi.org/10.1016/j.clinph.2009.01.015.
6. T. Radüntz, J. Scouten, O. Hochmuth, B. Meffert, Journal of Neural Engineering **14**(4), 046004 (2017). https://doi.org/10.1088/1741-2552/aa69d1.
7. R.T. Schirrmeister, L. Gemein, K. Eggensperger, F. Hutter, T. Ball, arxiv:1708.08012 (2017).
8. L.V.D. Maaten, G. Hinton, Journal of Machine Learning Research **9**, 2579 (2008). https://doi.org/10.1007/s10479-011-0841-3.
9. R. Oostenveld, P. Fries, E. Maris, J.M. Schoffelen, Computational intelligence and neuroscience **2011**, 1 (2011).
10. T.W. Lee, M. Girolami, T.J. Sejnowski, Neural computation **11**(2), 417 (1999).
11. M. Ester, H.P. Kriegel, J. Sander, X. Xu, et al., in *Kdd*, vol. 96 (1996), pp. 226–231.

Comparison of Spline Methods for 3D Brain Mapping

Václava Piorecká, Vladimír Krajča, and Tomáš Páleníček

Abstract

Brain mapping is a topographical method that is frequently used in human scalp electroencephalogram (EEG) for two-dimensional (2D) or three-dimensional (3D) visualisation of electrical potentials distributed across the surface of the brain. In human research, accepted standards for EEG recording and mapping exist, however to date, no such standards have yet been developed for use with laboratory rats. We have selected methods typically used for 3D brain mapping in humans and applied them to a brain model of the Wistar rat. Spherical and 3D splines were implemented as methods of the interpolation. The validation of 3D maps was created by using simulated signals of human and rat brain activity. The Root Mean Square error (RMS error) was calculated for the evaluation of interpolation methods. In conclusion, our results showed that the 3D spline interpolation yielded a better electrical potential map in both the human brain model and the rat brain model.

Keywords

Animal brain mapping • 3D spline • Spherical spline

1 Introduction

Current research in psychopharmacology has to always use EEG as one of the key methods for the evaluation of potential novel therapeutic compound's central effects an safety [1]. Therefore it is obvious that translational approaches using the same methods of evaluation of animal and human EEG signal should be applied.

EEG brain mapping is one of the most simple standardized approaches how to characterize spatial patterns in EEG activity. There are lots of methods which can be used for mapping in humans, however spline mapping yields one of the best results in terms of accuracy and spatial localization on the surface of the human head/brain [2]. In our work we have depicted two methods, spherical and 3D spline mapping for application and comparison of their accuracy on a model of the rat's brain. Our main goal was to adapt and compare the methods of spline mapping of the signal from multiple electrodes recorded from the rat's brain in order to create a translational approach for comparison of animal and human EEG findings from pharmaco-EEG studies.

2 Methods

2.1 Brain Models

The 3D rat brain model of the Wistar's rat was downloaded from Brain Atlas Reconstructor (BAR). This work establishes the first magnetic resonance histology (MRH) atlas of the rat brain, with an emphasis on quantitation [3, 4].

For testing purposes we have selected positions of electrodes that are currently used in rat EEG studies in our laboratory and that cover frontal, parietal and temporal areas of the cortex [5].

The human head model was taken from Wave-Finder software (a set of EEG analysis methods written in C++) for imaging purpose of the human brain. The standard 10/20 system of electrode's positions were used [6].

2.2 3D Brain Mapping

Initially it is necessary to project each point of the brain model and of the electrodes positions on a sphere in both of

V. Piorecká (✉) · V. Krajča
Faculty of Biomedical Engineering, Czech Technical University in Prague, Nám. Sítná 3105, 272 01 Kladno, Czech Republic
e-mail: vaclava.piorecka@fbmi.cvut.cz

V. Piorecká · T. Páleníček
National Institute of Mental Health, Topolova 748, 250 67 Klecany, Czech Republic

these methods. The ideal center and the ideal radius of this sphere were computed as minimalization of the function 1. In Eq. 1 the variables $[x_0, y_0, z_0]$ describe the center point of the brain model and r represent the radius of the sphere [7].

$$(x - x_0)^2 + (y - y_0)^2 + (z - z_0)^2 = r^2 \qquad (1)$$

Spherical splines

The spherical spline method consists of two steps. The first part is coefficients computation. Concretely coefficients of brain model (Gx) and coefficients of electrodes (C) are computed. These coefficients describe relation between brain model points positions and electrodes positions. Algorithm of spherical spline computation used Legrende polynomial to describe the distance between points [7].

$$g_m(x) = (2^n n!)^{-1} \frac{d^n}{dx^n} \left[(x^2 - 1)^n \right] \qquad (2)$$

Computation of the electrode's coefficients describe Eqs. 3–5, where $\delta(r_i, r_j)$ is Euclidean distance between two electrodes and g_m represents Legrende polynoms [7].

$$D(j) = 1 - \delta(r_i, r_j) \qquad (3)$$

$$G_x(i, j) = g_m(D(j)) \qquad (4)$$

$$C = inv(G_x) \qquad (5)$$

Computation of the coefficients the brain models describe Eqs. 6–7, where $\delta(R_i, R_j)$ is Euclidean distance between two electrodes points of the brain model and g_m represents Legrende polynoms [7].

$$D(j) = 1 - \delta(R_i, R_j) \qquad (6)$$

$$Gx(i, j) = g_m(D(j)) \qquad (7)$$

The second part of spherical spline mapping represents potential distribution of the signal over the whole brain model. If V is the vector of potential values under each electrode, than U represents the vector of potential distribution [7].

$$C' = C \times V \qquad (8)$$

$$U(i) = \sum_{j=1}^{M} C'(j, 1) \cdot Gx(i, j) \qquad (9)$$

3D splines

The interpolated potential U_m at each point of the brain model $[x, y, z]$ is described by Eqs. 10–12, where P is represented by p_i coefficients and Q is represented by q_i coefficients. Matrixes F_m and H_m describe relations between brain model's points positions and electrode's positions [2, 8].

$$U_m(x, y, z) = \sum_{i=1}^{N} p_i \cdot H_m + \sum_{d=0}^{m-1} \sum_{k=0}^{d} \sum_{g=0}^{k} q_{dkg} \cdot F_m, \qquad (10)$$

$$F_m = \sum_{d=0}^{m-1} \sum_{k=0}^{d} \sum_{g=0}^{k} q_{dkg} \cdot x^{d-k} \cdot y^{k-g} \cdot z^g, \qquad (11)$$

$$H_m = \left((x - x_e)^2 + (y - y_e)^2 + (z - z_e)^2 \right)^{\frac{(2m-3)}{2}} \qquad (12)$$

Vectors P, Q are obtained by solving following system:

$$\begin{bmatrix} H & F \\ F^t & 0 \end{bmatrix} \begin{bmatrix} P \\ Q \end{bmatrix} = \begin{bmatrix} V \\ 0 \end{bmatrix}, \qquad (13)$$

where V is the vector of intensity under each of the electrodes. Matrix H represents distances between electrode's positions and matrix F describe realtion between the Cartesian coordinates of electrode's positions [2, 8].

2.3 Evaluation of the Interpolation Methods

We used root mean square error (RMSE) as a evaluation method of spline mapping algorithms. Once the models were created, we have used a simulated activity that was delivered in the model under each of the electrode individually and subsequently the mapping was performed. The final RMSE was calculated as a mean of all simulated activity. RMSE is described by Eq. 14, where $U^{analytical}$ is original value under electrodes and $U^{interpolated}$ is mean of th interpolated value under four nearest points to each of electrodes.

$$RMSE = \sqrt{\frac{\sum_{n=1}^{Nchannels} \left(U_{n,ori}^{analytical} - U_{n,ori}^{interpolated} \right)^2}{\sum_{n=1}^{Nchannels} \left(U_{n,ori}^{analytical} \right)^2}} \qquad (14)$$

3 Results
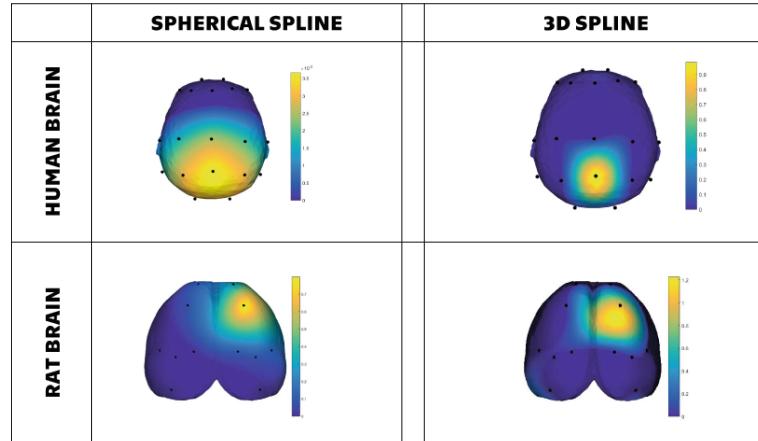
Results of RMSE on human brain model implicated that 3D spline method is in this case better method of spline interpolation. For rat's brain model is 3D spline method of interpolation better too. Concrete values of RMSE are described in Table 1.

3D spline method gives a better potential map with respect to testing signal as we can see on Fig. 1. This method localized signal with better accuracy close to the electrode. In case of spherical spline method, there was larger area around electrode with unit voltage. Spherical spline method

Table 1 RMS error of spline interpolation methods on rat and human brain

	Root mean square error (RMS), (–)	
	Human brain	Rat brain
3D spline	0.0669	0.0694
Spherical spline	0.5702	0.5934

Fig. 1 This figure depicts simulated activity on human and rat brain phantom. In order to compare the spherical spline and 3D spline behavior, we set one particular electrode to unit voltage while the other electrodes were set to zero voltage

detected non-zero voltage signal under electrodes with zero voltage signal.

4 Conclusion

Our results showed that the 3D spline interpolation yielded a better electrical potential map in both the human brain model and the rat brain model.

Conflict of Interest Declaration The authors declare that there is no conflict of interest regarding the publication of this article.

References

1. Drinkenburg, W. H., Ahnaou, A., Ruigt, G. S.: Pharmaco-EEG Studies in Animals: A History-Based Introduction to Contemporary Translational Applications. Neuropsychobiology. 2015;72(3–4):139–50. https://doi.org/10.1159/000443175

2. Nouira, I., Ben Abdallah, A., Bedoui, M. H.: EEG potential mapping by 3D interpolation methods. In: 2014 International Conference on Multimedia Computing and Systems (ICMCS), pp. 469–474. IEEE, 2014. https://doi.org/10.1109/icmcs.2014.6911297. ISBN 978-1-4799-3824-7.

3. Calabrese, E., Badea, A., Watson, C., Johnson, G. A.: A quantitative magnetic resonance histology atlas of postnatal rat brain development with regional estimates of growth and variability. NeuroImage, 2013, vol. 71, p. 196–206. https://doi.org/10.1016/j.neuroimage.2013.01.017

4. Majka, P., Kowalski, J. M., Chlodzinska, N., Wójcik, D. K.: 3D Brain Atlas Reconstructor Service Online Repository of Three-Dimensional Models of Brain Structures. Neuroinformatics, 2013, vol. 11, p. 507–518. https://doi.org/10.1007/s12021-013-9199-9

5. Tylš, F., Páleníček, T., Kadeřábek, L., Lipski, M., Kubešová, A., Horáček, J.: Sex differences and serotonergic mechanisms in the behavioural effects of psilocin. Behavioural Pharmacology. 2016, 27(4), 309–320. ISSN 0955-8810. https://doi.org/10.1097/fbp.0000000000000198.

6. Krajča, V., Petránek, S., PietilÃ¤, T., Frey, H.: Wave-Finder: a new system for an automatic processing of long-term EEG recordings. In: Rother, M., Zwiener, U. (eds.), Quantitative EEG Analysis-Clinical Utility and New Methods, Universitts verlag Jena, 1993, pp. 103–106.

7. Perrin, F., Pernier, J., Bertrand, O., Echallier, J. F.: Spherical splines for scalp potential and current density mapping. Electroencephalography and Clinical Neurophysiology, 1989, vol. 72, pp. 184–187. https://doi.org/10.1016/0013-4694(89)90180-6

8. Law, S. K., Nunez, P. L., Wijesinghe, R. S.: High-resolution EEG using spline generated surface Laplacians on spherical and ellipsoidal surfaces. In Proceedings of the IEEE IEEE transactions on bio-medical engineering. United States, 1993, vol. 40, p. 145–153. https://doi.org/10.1109/10.212068

Simulation, Modification and Dimension Reduction of EEG Feature Space

Marek Piorecký, Eva Černá, Václava Piorecká, Vladimír Krajča, and Vlastimil Koudelka

Abstract

An automate classification of EEG time segments is frequently used technique across many neuro-scientific fields. Generally, segment classification results in labeled EEG time segments (e.g. physiological brain activity, epileptic activity, muscle artifacts or electrode artifacts). However, currently used methods are usually tested on artificial surrogate data and more general validation approach is needed. Here, a generalized statistical model of commonly used discriminating features obtained from real EEG data is presented for the first time. Multivariate probability density functions (PDFs) of classes are fitted on more than twenty thousand of testing segments from human EEG. An unique testing set is designed using a recent non-linear dimension reduction technique. Parametric and non-parametric PDF estimators are applied and compared in sense of feature space model.

Keywords

EEG • Dimension reduction • Feature space

1 Introduction

Electroencephalography (EEG) is most commonly used method of examining of the electric brain activity. Records are examined in the time and frequency domain [1]. Signal preprocessing and automatic segmentation and classification help expert to recognize the pathological segments in EEG records [2].

Adaptive segmentation creates segments containing one kind of characteristic waveform and so it helps to make the classification easier [3, 4].

Features are counted for each segment of the EEG record. EEG segments are classified into the same classes based on similarity of their features.

There are many features, some of them are typically used to determine concretely waveform [1, 5].

Automatic methods were used for the classification of segments as well as learning methods, which required user's intervention [1]. Generally, learning methods require usage of etalons, which describe the typical content of the class.

Dimension reduction helps to speed up the data processing and brings a new perspective on them.

Principal component analysis (PCA) is one of most commonly used linear method, which can be applied on EEG. t-Distributed Stochastic Neighbor Embedding (tSNE) is a nonlinear method, which constructs a probability distribution over pairs of high-dimensional objects in such way that high probability is assigned to similar objects, while low probability is connected with dissimilar points [6].

2 Methods

2.1 Data

The data comes from the measurement of patients from Bulovka Hospital in Prague. The data was recorded by using the Brain-Quick (Micromed). It was obtained on the basis of the project proposal, which was approved by the ethics committee of Bulovka Hospital on June 28 2011. These are clinical examinations lasted from 15 to 40 min. Test data were measured on patients who had been diagnosed with suspected epilepsy disease. Patients were 6 men and 4 women aged between 26 and 60 years.

M. Piorecký (✉) · E. Černá · V. Piorecká · V. Krajča
Faculty of Biomedical Engineering, CTU in Prague,
Nám. Sítná 3105, 272 01 Kladno, Czech Republic
e-mail: marek.piorecky@fbmi.cvut.cz

V. Koudelka
National Institute of Mental Health, Topolová 748,
250 65 Klecany, Czech Republic

2.2 Segmentation

Our software in C++ and Matlab R2015a were used to process the data. The sampling frequency in the record was 128 Hz. The filter was set on a bandpass (0.4 and 70 Hz). Computational operations were applied in the average montage. We used an adaptive estimation of mean value described by Grießbach [7]. Multichannel adaptive segmentation [4] was used after the filtration. The Varri's adaptive segmentation method is based on two joint windows sliding along the signal and detecting local maxima in the total difference if the measurement calculated from the amplitude and the frequency difference (Eqs. in [3, 4]). The adaptive segmentation is simultaneously processed for all the channels.

Adaptive segmentation parameters were: the window length—128 samples, the window length for local maxima identification—30 samples, the moving step of the two connected windows—1 sample, minimum segment length—70 samples. The fluctuation eliminating threshold varied from patient to patient.

2.3 Features

23 features based on time and frequency domain were used in practice. The features were: (1) signal variability, (2) maximal positive and (3) negative value (amplitude) in segment, delta (4, 5) band as square root of power spectral density (PSD) in band 0.5–2.0 Hz as delta 1 and 2.0–3.5 Hz as delta 2. The same partition was in (6, 7) theta (4.0–6.0 Hz, 6.0–7.5 Hz) and (8, 9) alpha (8.0–10.5 Hz, 10.5–12.5 Hz) band. Sigma (10) was in 18.0–29.0 Hz and beta (11) in 13.5–29.0 Hz. To estimate the spectrum was used Welch method [8] of averaged modified periodograms instead of single periodogram (by FFT) to get a better estimation of the spectra. Next features were maximum of the first (12) and second derivation (13), medium frequency (14), medium of the first (15) and second derivation (16),

Hjorths parameter [5]: mobility (17), complexity (18) and activity (19), length of the curve (20), nonlinear energy (21), number of the passes by zero (22) and the maximum peak frequency in the spectrum (23) [1, 9].

2.4 Training Set Development

We obtained 23D space after feature computation. The goal is to separate four classes distributed within the feature space: physiological activity (PHYSIO), epileptic activity (EPI), EMG artifacts (EMG) and wrong electrode contact artifacts (WRONGEL), see Fig. 1.

At first, a homogenous cluster was selected by using DBSCAN and k-means algorithm. Further processing can be summarized in following 4 points [2, 10]:

1. When DBSCAN ranked point (segment described by 23 features) as a center in the specific cluster and the k-means included this segment near the center of the same cluster, the segment was selected as a representative of that cluster (class).
2. Classes across patients and across measurements were merged and created one big class of specific segments of EEG signal.
3. The expert discarded segments whose character did not match the specific class.
4. Final classified dataset consisted of 335 segments of EMG, 1239 EMG and noise, 2200 epileptic activity, 17390 physiological activity, 19763 physiological activity with noise, 495 wrong electrode contact segments. The dataset with noise was created for realistic simulation feature space of EEG.

Pleas note that each feature was normalized by its minimum and maximum values within each class. We had to use normalization was necessary to use because of the different ranges of the original features.
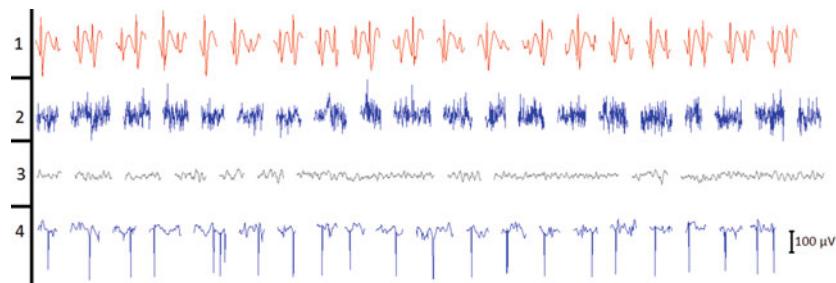

Fig. 1 A sample of segments of each created class, from the top: epilepsy activity, EMG artifacts, physiological activity and wrong electrode contact

2.5 Training Set Validation

At first, a linear PCA method based on singular-value decomposition was applied to visually inspect testing dataset in two dimensional space, see Fig. 2.

Since PCA method was sufficient for our purpose, we further investigated tSNE dimension reduction technique in order to depict the data structure. tSNE is a non-linear projection technique developed by van Maaten and Hinton [6]. 2D space was created by using parameters of tSNE: perplexity = 30 and initial dimension = 23.

2.6 Feature Space Modeling

In order to show all feature distributions, we calculated and depicted BOX plots. This is a standard approach to data analysis in EEG studies [11, 12]. Based on tSNE map, data points lying out of the interquartile span were rejected from the training set. The cleaned dataset was than used in fitting the PDF function. Both normal distribution and kernel density estimator were fitted to the training set. Finally, obtained probability distributions (kernel and normal) were used to simulate general feature space.

3 Results and Discussion

The investigated EEG segments were randomly selected from various datasets, subjects, and events (e.g. EPI, PHYSIO, EMG, etc.). This way an appropriate generalization of the model could be obtained.

Physiological activity has the most outliers, see Fig. 4. More segments with a wider range of the features (e.g. freq. wave spectrum) are assigned to the physiological activity. Medium frequency and second derivation features separate well physiological activity and EMG artifacts. Hjorth parameter activity effectively isolates Epilepsy from all others classes, see Fig. 4.

Nonlinear methods create 2D feature space separated from clusters created separable classes. From this point of view, DBSCAN seems to be a better option (opposite k-means) as it is able to distinguish interlacing clusters. Physiological segments match normal distribution, see Fig. 3. Kernel distribution has 2 local maximum in EMG class, Epilepsy class and wrong electrode class, see Fig. 3. There are two possibilities to use the simulation. Interquartile span enables its users to create clear etalons for learning classifiers. The use of the entire span offers the creation of an infinite number of segments that can be used as a simulated
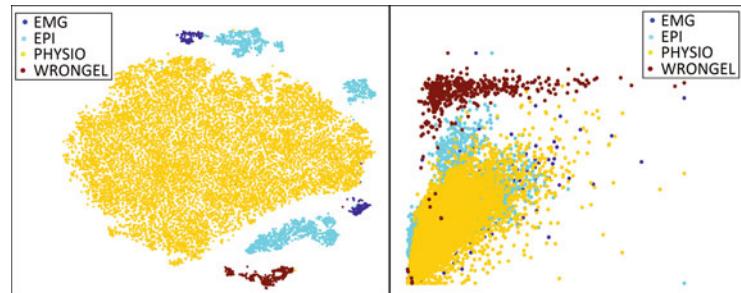

Fig. 2 EEG feature space reduced by the nonlinear and linear method. Left: Feature space after tSNE dimension reduction, 700 iteration steps. Right: Reduced space after PCA. Axes are modified features by dimension reduction
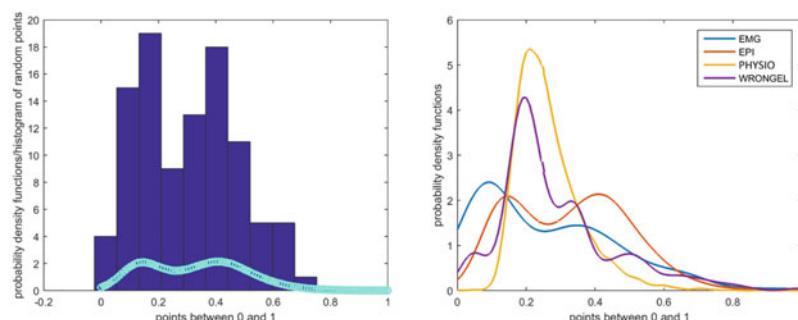

Fig. 3 Left: fitted kernel distribution on segments of epilepsy activity of feature 20 (white circles) and histogram shows the distribution of randomly generated dataset from the fitted function (dark bars); Right:

Fitted kernel distribution on EMG artifacts, epilepsy and physiological activity and wrong electrode contacts segments
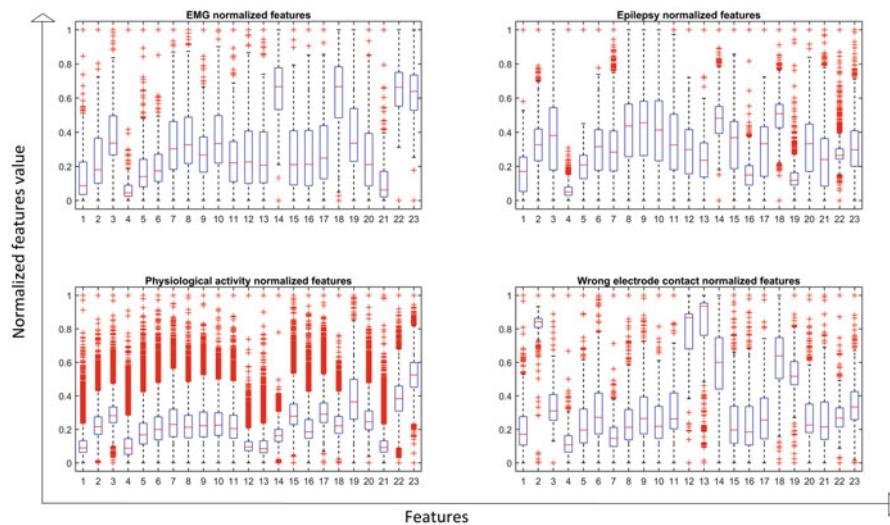
Fig. 4 Boxplot shows the distribution of features. The bottom and top of the box are the first and third quartiles, and the band inside the box is the second quartile—the median. The ends of the whiskers are the minimum and maximum of all of the data. Red markers represent outliers (Color figure online)

realistic feature space to test algorithms. The user can simulate any number of segments of the selected activity. In the case of simulation of the "whole record" (all classes at once), the recommended ratio of classes is 1:12:246:6—EMG:EPI:PHYSIO:WRONGEL.

We assume that EEG records contain also noise from the recording device. In order to compare data across the device, it was appropriate to deduce general technical noise. General noise was subtracted from each feature. In our case segment white noise (power 75%) was of the same length as EEG segment.

4 Conclusion

A methodology for simulation feature space has been developed. The database of physiological, epileptic and artifact segments was created together with this work. Segments database offers the possibility to examine other features. We assume that nonlinear methods are better for examining EEG space dimension reduction as they maintain segments class separability. The simulation of feature space is needed to test the effectiveness of the selected features and to verify the classification methods. The Kernel distribution could be used for simulation EMG and Epileptic activity feature space because we do not want to suppress the second local maximum that occurs in this activity.

Conflict of Interest Declaration The authors declare that there is no conflict of interest regarding the publication of this article.

Protection of Human Subjects and Animals in Research The procedures followed were in compliance with the ethical standards of the responsible committee on human experimentation (institutional and national) and with the World Medical Association Declaration of Helsinki on Ethical Principles for Medical Research Involving Human Subjects.

Statement of Informed Consent The study protocol and patient informed consent have been approved by the Bulovka Hospital.

References

1. Krajca, V., Petranek, S., Patakova, I., Värri, A.: Automatic identification of significant graphoelements in multichannel EEG recordings by adaptive segmentation and fuzzy clustering. In: International Journal of Bio-Medical Computing, 1991, vol. 28(1–2), pp. 7189. https://doi.org/10.1016/0020-7101(91)90028-d.
2. Prabhakar, S., K., Rajaguru, H.: Pca and k-means clustering for classification of epilepsy risk levels from eeg signals - A comparitive study between them. In: 2015 International Conference on Intelligent Informatics and Biomedical Sciences (ICIIBMS), 2015, pp. 83–86. IEEE. https://doi.org/10.1109/iciibms.2015.7439467.
3. Paul, K., Krajca, V., Roth, Z., Melichar, J., Petranek, S.: Comparison of quantitative EEG characteristics of quiet and active sleep in newborns. In: Sleep Medicine, 2003, vol. 4(6), pp. 543–552. https://doi.org/10.1016/j.sleep.2003.08.008.

4. Värri, A.: Algorithms and systems for the analysis of long-term physiological signals. In: Tampereen teknillinen korkeakoulu. Julkaisuja. Tampere University of Technology, 1992.

5. Sana Tmar-Ben Hamida, Beena Ahmed, and Thomas Penzel. A novel insomnia identiffcation method based on hjorth parameters. In: 2015 IEEE International Symposium on Signal Processing and Information Technology (ISSPIT), Abu Dhabi, 2015, pp. 548–552. IEEE, ISBN 9781509004812. https://doi.org/10.1109/isspit.2015.7394397.

6. Van der Maaten, L., Hinton, G.: Visualizing Data using t-SNE. In: Journal of Machine Learning, 2008, vol. 9, pp. 2579–2605.

7. Grießbach, G., Witte, H.: Complex adaptive procedures for EEG monitoring. In: Witte, H., Zwiener, U., Schack, B., Doering, A. (eds.) Quantitative and Topological EEG and MEG Analysis, In: Druckhaus Mayer Verlag Gmbh Jena - Erlangen, 1997, pp. 295–297.

8. Welch, P.: The use of fast fourier transform for the estimation of power spectra: A method based on time averaging over short, modiffed periodograms. In: IEEE Transactions on Audio and Electroacoustics, 1967, vol. 15(2), pp. 70–73. https://doi.org/10.1109/tau.1967.1161901.

9. Krajca, V., Petranek, S., Pietilä, T., Frey, H.: WaveFinder: A new system for an automatic processing of long-term EEG recordings. Quantitative EEG analysisclinical utility and new methods, 1993, pp. 103–106.

10. Ware, S., V., Bharathi HN.: Study of density based algorithms. In: International Journal of Computer Applications, 2013, vol. 69(26). https://doi.org/10.5120/12132-8235.

11. De Haan, W., Al Pijnenburg, Y., Lm Strijers, R., Van Der Made, Y., Van Der Flier, W. M., Scheltens, P., Stam, C. J.: Functional neural network analysis in frontotemporal dementia and Alzheimer's disease using EEG and graph theory. In: BMC Neuroscience. 2009, vol. 10(1), 101. https://doi.org/10.1186/1471-2202-10-101. ISSN 1471-2202.

12. Easwaramoorthy, D., Uthayakumar. R.: Analysis of EEG signals using Advanced Generalized Fractal Dimensions. In: 2010 Second International conference on Computing, Communication and Networking Technologies. IEEE, 2010, pp. 1–6. https://doi.org/10.1109/icccnt.2010.5591775. ISBN 978-1-4244-6591-0.

Can Textile Electrode for ECG Apply to EMG Measurement?

Daisuke Goto and Naruhiro Shiozawa

Abstract

Electromyograms (EMG) are used as not only evaluation of muscle strength and muscle fatigue in medical but also those in sports science and biomechanics fields. It needs the expert knowledge to set electrodes on a certain muscle position every day to monitor EMG for long terms. We assumed that this problem would be solved by textile electrodes. In our previous study, we revealed that the stretchable conductive elastomers enabled to measure precise electrocardiogram (ECG) waveform compared with conventional Ag/AgCl electrodes (Okuno et al, Proceedings of international conference on healthcare, pp 42–43, 2014 [1]). However, EMG measurement has not been evaluated so far. Because EMG has a wider frequency band than the ECG, we need to be clear the electrode's characteristics for EMG measurement use. The purpose of this research is to clarify whether the developed electrode can adapt to the EMG measurement. Healthy eleven adults were participated in our experiment as subjects (Age: 21.4 ± 0.8: mean $\pm$ S.D.). EMG was recoded from the tibial anterior muscle. EMG signal were collected by self-making myoelectric amplifier. The frequency band of the EMG amplifier was 30–500 Hz and sampled at 1 kHz. EMG was measured isometric contraction motion of the load 0, 1.25, 2.5, 3.75 and 5 kg. As the results, the correlation coefficients between the load and the RMS of the developed electrode and the Ag/AgCl electrode were r = 0.918 and r = 0.912, respectively. This result showed that the development electrode can be used for muscle strength evaluation.

1 Introduction

In recent years, reductions in the number of steps and the amount of activity arise with increase of the transportation network [2]. In the world, physical activity tends to decrease rapidly. The worldwide epidemic of physical inactivity is related to morbidity and early mortality rate of adult disease such as coronary heart disease, type 2 diabetes mellitus, breast cancer and colon cancer [2, 3]. Physical inactivity is one of the factors of increasing medical expenses. In order to solve these problems, interest in attempt based more accurate evidence has been heightened. On the other hand, technologies that measure the activity amount in daily life have been improved by novel wearable sensors. These sensors/devices enable to monitor changes in daily activity. Monitoring the amount of activity on a daily basis permits people to grasp the state of lifestyle habits and is expected to be utilized in daily life and medical scene [4, 5].

Devices such as pedometers and acceleration sensors are used in the measurement of the amount of physical activity. However, movement with only the upper limbs makes it difficult to evaluate the physical activity level [6]. Electromyograms (EMG) are used as not only evaluation of muscle strength and muscle fatigue in medical but also those in sports science and biomechanics fields. The spread of EMG in daily life is expected to be useful for various subjects. However, the use of Ag/AgCl electrodes in long-term measurement causes some problem that electric characteristics change due to drying and that the decrease in adhesive strength makes electrodes fall off due to perspiration. Also, it needs the expert knowledge to set electrodes on a certain muscle position every day. Therefore, development of

D. Goto · N. Shiozawa (✉)
Ritsumeikan University, 1-1-1 Noji-higashi, Kusatsu, Shiga, Japan
e-mail: shiozawa@fc.ritsumei.ac.jp

D. Goto
e-mail: daisuke.goto519@gmail.com

special biological electrodes for long-term measurement instead of the Ag/AgCl electrodes is demanded.

We assumed that this problem would be solved by textile electrodes. In our previous study, we developed novel textile electrode with the stretchable conductive film (COCOMI, Toyobo Co., Ltd.) attached to a textile and revealed that the electrodes enabled to measure precise electrocardiogram (ECG) waveform compared with conventional Ag/AgCl electrodes [1]. Since the electrode is embedded on the shirt and set electrodes on the optimum position, expert knowledge is not required. Moreover, the electrode without electrolyte gel is suitable for long-term measurement. As described above, the electrode has proved for ECG, but EMG measurement has not been evaluated so far.

The purpose of this research is to clarify whether the developed electrode can adapt to the EMG measurement in comparison the Ag/AgCl electrodes.

2 Method

2.1 Textile Electrode

Figure 1 shows the overall view of textile EMG electrode and structure of the electrodes. The electrodes were made from stretchable conductive elastomers. As shown in Fig. 1, textile electrodes and polyurethane sheet were embedded on the back side of sleeve (M6566, McDavid). Moreover, polyurethane sheets were used to cover the electrodes except to position sensing myogenic potential. The electrodes were connected to the EMG amplifier with lead wires from the surface of the sleeve. EMG was recoded from the tibial anterior muscle. A common ground reference was placed on fibular head.

2.2 Data Collection

Healthy eleven adults were participated in our experiment as subjects (Age: 21.4 ± 0.8). This study was conducted with the approval of the Ethics Committee of Faculty, Ritsumeikan University. All subjects who participated gave their informed consent. For each electrode, the following two procedures were performed in order.

(1) Impedance

Each subject was seated in sedentary state on the bed. The impedance between human body and electrodes (around 0.1–10 kHz) was measured with an impedance analyzer (3522–50, Hioki). At each frequency, impedance values which were averaged four recorded impedance values were measured. The impedance measurement was performed within 15 min of setting the electrodes.

(2) EMG measurement

Each subjects remained seated on the bed to avoid the right tibialis anterior contraction. Each dorsiflexor isometric contractions at 90° in 5 s were maintained after sedentary in 10 s. EMG was measured isometric contraction motion of the load 0, 1.25, 2.5, 3.75 and 5 kg. The load was set weight which was hung by pulley. The root mean square (RMS) was computed using 2 s of the myoelectric potential from each isometric contraction. The relation between the RMS values from each isometric contraction and the weight loads was shown as a correlation coefficient.

In this research, EMG signal were collected by self-making myoelectric amplifier. This self-making myoelectric amplifier consisted of an instrumentation amplifier


*Electric wire to connect between electrode and the lead wire
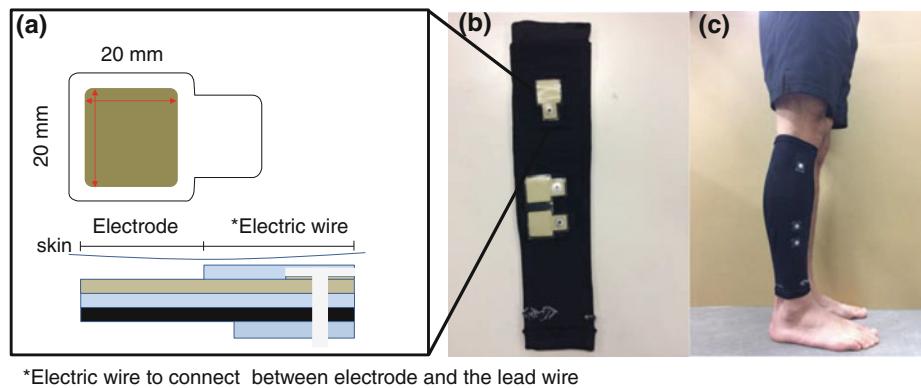
Fig. 1 **a** Textile electrode. **b** The entire textile electrodes. **c** Wearing textile electrodes

(AD620, ANALOG DEVICES, Massachusetts), a high pass filter, a noninverting amplifier circuit using high input impedance operational amplifier (TL071, Texas Instruments, Texas) and a low pass filter. The instrumentation amplifier was set a gain about 10 and the noninverting amplifier circuit was set a gain of about 100. Total gain for the EMG amplifier circuit was 60 dB. The frequency band of the EMG amplifier was 30–500 Hz to remove motion artifacts and sampled at 1 kHz. Myoelectric potential measured from a COCOMI and Ag/AgCl electrodes via the myoelectric amplifier were converted into digital signal by an AD conversion device (AI-1608AY-USB, CONTEC, Osaka, Japan) with 16 bits resolution. The input impedance of the instrumentation amplifier was 10 GΩ.

The above experiment carried out with the textile electrodes and Ag/AgCl electrodes. Before Ag/AgCl electrodes were set, skin of subjects was cleaned with alcohol wipe. The textile electrodes and Ag/AgCl electrodes were adjusted to the same electrode position.

3 Result

3.1 The Impedance Value Between Human Body and Electrodes

There were individual differences in impedance values at each frequency. Figure 2 shows the average impedance values at each frequency for the textile electrode and Ag/AgCl electrode. The impedance values between human body and electrodes of the Ag/AgCl electrode were lower from 31.6 Hz to 1 kHz ($p < 0.05$) compared with our developed electrode. The impedance values between human body and electrodes greatly decreased at above 1 kHz for both electrodes.

3.2 EMG Measurement

It was confirmed that both the RMS of the textile electrodes and Ag/AgCl electrodes enlarged with increasing loads. The correlation coefficients between the load and the RMS of the developed electrode and the Ag/AgCl electrode were $r = 0.918$ and $r = 0.912$, respectively. There were strong correlations between the load of the add weight and the myoelectric potential for the textile electrodes and Ag/AgCl electrodes.

4 Discussion

The impedance between human body and electrodes is depends on temperature, skin condition and fixing time of electrodes. It is desirable that the impedance between human body and electrodes is minimized as much as possible to reduce errors in biometric measurement. As the results of our experiment, it was found that the impedance values differ interindividually at below 1 kHz. Some previous studies reported that the impedance of the dry electrodes was higher than that of the Ag/AgCl electrodes [7, 8]. Also, it is possibility considered that differences in impedance values between COCOMI electrodes and Ag/AgCl electrodes occurred due to difference of the electrodes size and the effect of cleaning skin with alcohol wipe.

In previous study, some simplified models as impedance of skin were proposed [8, 9]. The simplified models contain resistances and capacitors. In this study, the result of impedance measurement showed greatly reduction the impedance value at above 1 kHz. From this result, a factor of capacitor in the impedance between human body and electrodes may cause the greatly reduction the impedance value. Further studies are needed in order to validate the result.
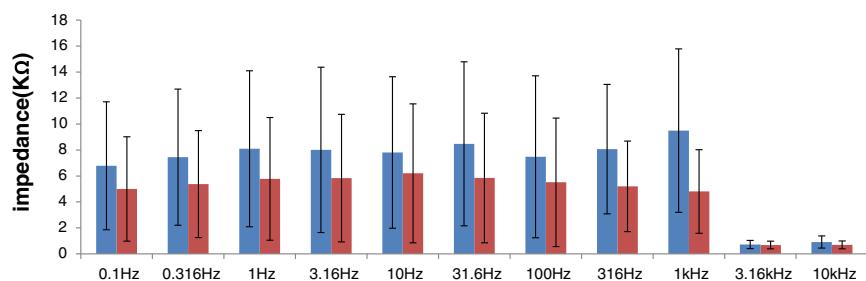

Fig. 2 The average impedance values at each frequency for the textile electrode (blue bars) and Ag/AgCl electrode (red bars) (Color figure online)

The result of EMG measurement showed there were strong correlations between the loads added weight and the myoelectric potential for both electrodes. These results indicated the possibility of using the textile electrodes in EMG measurement for isometric contraction movements. It is important to note that in this experiment EMG data was sampled as 1 kHz and the impedance values at above 500 Hz were not influenced.

References

1. Okuno, A., Lee, J., Shiozawa, N., Makikawa, M. (2014) Comparison of Signal-to-Noise Ratio of Electrocardiogram Measured by Different Size of Electrode during Running, Proc. International Conference on Healthcare 2014: pp. 42–43.
2. Chang and Yu-Kai (2017) Combined effects of physical activity and obesity on cognitive function: independent, overlapping, moderator, and mediator models. Sports Medicine 47.3: 449–468.
3. Lewis and Beth A. (2017) Future directions in physical activity intervention research: expanding our focus to sedentary behaviors, technology, and dissemination. Journal of behavioral medicine 40.1: 112–126.
4. Paradiso, R., Loriga, G., Taccini, N., Gemignani, A., and Ghelarducci, B. (2005) WEALTHY-a wearable healthcare system: new frontier on e-textile. Journal of Telecommunications and Information Technology: 105–113.
5. Shafti, A., Manero, R. R., Borg, A. M., Althoefer, K., and Howard, M. J. (2016, May) Designing embroidered electrodes for wearable surface electromyography. In Robotics and Automation (ICRA), 2016 IEEE International Conference on: pp. 172–177.
6. Gant, Katie, Jorge Bohorquez, and Christine K. Thomas. (2017) Long-term recording of electromyographic activity from multiple muscles to monitor physical activity of participants with or without a neurological disorder: Biomedical Engineering/Biomedizinische Technik.
7. Hewson, D. J., Duchêne, J., and Hogrel, J. Y. (2001) Changes in impedance at the electrode-skin interface of surface EMG electrodes during long-term EMG recordings. In Engineering in Medicine and Biology Society, 2001. Proceedings of the 23rd Annual International Conference of the IEEE: Vol. 4, pp. 3345–3348.
8. Hewson, D. J., Hogrel, J. Y., Langeron, Y., & Duchêne, J. (2003). Evolution in impedance at the electrode-skin interface of two types of surface EMG electrodes during long-term recordings. Journal of Electromyography and Kinesiology, 13(3), 273–279.
9. Lin, C. T., Liao, L. D., Liu, Y. H., Wang, I. J., Lin, B. S., and Chang, J. Y. (2011) Novel dry polymer foam electrodes for long-term EEG measurement. IEEE Transactions on Biomedical Engineering, 58(5):1200–1207.
10. Assambo, C., Baba, A., Dozio, R., and Burke, M. J. (2007, February) Determination of the parameters of the skin-electrode impedance model for ECG measurement. In Proceedings of the 6th WSEAS international conference on electronics, hardware, wireless and optical communications, Corfu Island, Greece: pp. 90–95.
11. Laferriere, P., Lemaire, E. D., and Chan, A. D. (2011) Surface electromyographic signals using dry electrodes. IEEE Transactions on Instrumentation and Measurement, 60(10): 3259–3268.
12. Finni, T., Hu, M., Kettunen, P., Vilavuo, T., and Cheng, S. (2007) Measurement of EMG activity with textile electrodes embedded into clothing. Physiological measurement, 28(11): 1405.

Automatic Detection of Strict Left Bundle Branch Block

Radovan Smisek, Pavel Jurak, Ivo Viscor, Josef Halamek,
Filip Plesinger, Magdalena Matejkova, Pavel Leinveber,
and Jana Kolarova

Abstract

Strict (true) left bundle branch block (tLBBB) ECG morphology is a new diagnostic marker in cardiology that was proposed to predict cardiac resynchronization therapy (CRT) responders. In this paper we present an algorithm for the automatic detection of tLBBB. This algorithm includes mid-QRS notching and slurring detection, QRS duration measurement and tLBBB morphology detection. All required morphologies are detected in the time domain using thresholding of simple features of signal. In order to test our algorithms, three experts labelled 78 ECG records (12 leads, fs = 5 kHz, 15 min); 51 records were labeled as tLBBB. The proposed algorithms were tested showing overall sensitivity and specificity 98 and 86%, respectively, in cases where all three experts reached full consensus (82% of the dataset). Our method showed lower sensitivity and higher specificity 96% and 88%, respectively, for the dataset including cases where experts mutually disagreed, consensus has been reached through expert discussion in these records.

Keywords

Strict left bundle branch block • QRS notching
QRS slurring • QRS morphology • ECG

R. Smisek (✉) · P. Jurak · I. Viscor · J. Halamek · F. Plesinger
Institute of Scientific Instruments of the CAS, v.v.i, Kralovopolska
147, 61264 Brno, Czech Republic
e-mail: smisek@isibrno.cz; smisek@vutbr.cz

R. Smisek · J. Kolarova
Brno University of Technology, Antoninska 548, 60190 Brno,
Czech Republic

M. Matejkova · P. Leinveber
International Clinical Research Center, St. Anne's University
Hospital, Brno, Czech Republic
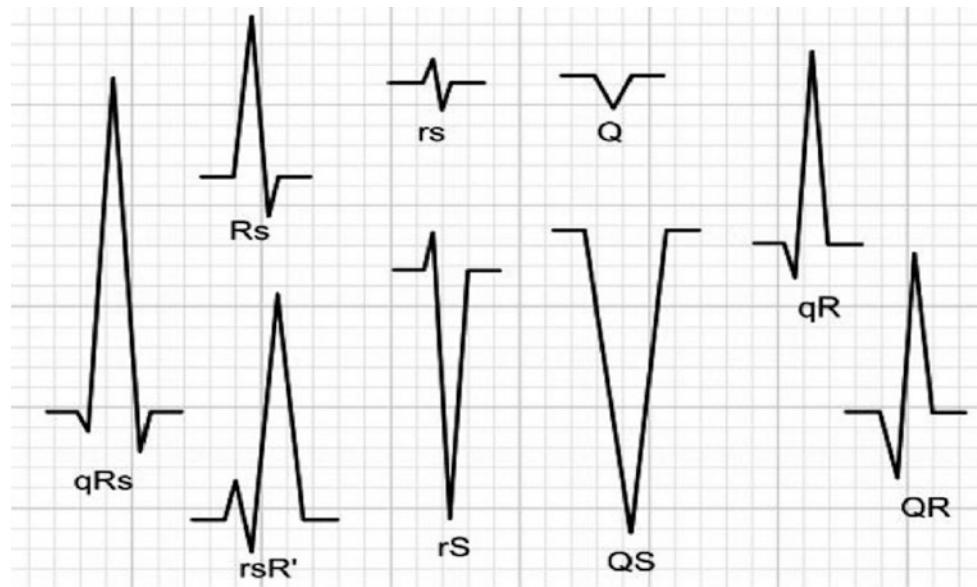
1 Introduction

Several studies have shown that individuals with LBBB have a great benefit from CRT, on the other hand, individuals with right bundle branch block (RBBB), hypertrophy and non-specific cardiac diseases have less or no benefit [1, 2]. However, the success rate of therapy is only two-thirds of patients with LBBB [1, 2]. For this reason, it was necessary to update the criteria for determining LBBB. The new criteria were defined in [1]. This criteria include the presence of tLBBB morphology in V1 and V2—it means the shape (see Fig. 1) QS (QRS is completely negative) or rS (the dominant wave of the QRS is negative and the positive wave is only before this dominant wave) the presence of mid-QRS notching or slurring in at least two of leads V1, V2, V5, V6, I and aVL and finally a QRS duration (QRSd) of more than 130 ms for women and more than 140 ms for men. Mid-QRS notching and slurring must begin after 40 ms after the onset of QRS and before 50% of QRS. The end of mid-QRS notching and slurring must be before 2/3 of QRS.

Mid-QRS notching and slurring are not precisely defined. One of the definitions states that the QRS notching is a sudden change in the direction of curve in the QRS complex, the notch has at least 2 turning points located on the same side of the isoelectric line. QRS slurring is defined as the QRS complex in which its ascending or descending part contains a sharp change of slope. It is not defined in which sampling frequency these morphologies should be evaluated and it is also not defined how deep and wide the notch can already be considered as QRS notching. Similarly, it is not defined what change in gradient is large enough to determine the QRS slurring. Because of these uncertainties, automatic mid-QRS notching and slurring detection is very difficult [3, 4].

This paper describes an algorithm for automatic detection of tLBBB. A reliable tool for pathology detection is highly needed because a large number of records are often needed to be analyzed and manual processing is very

Fig. 1 Examples of the nomenclature for QRS complexes [7]

time-consuming. Automatic detection also eliminates the subjectivity of decision making and the potential inexperience of the evaluator.

2 Data

The ECG data was collected over 10–15 min in the resting supine position with a standard 12-lead ECG setup and sampling frequency 5 kHz. Measurements were performed at the International Clinical Research Center at St. Anne's University Hospital, Brno, Czech Republic. A total of 78 records were available, included 60 men and 18 women of the age 67.27 ± 9.87. Three experts determined in each record whether mid-QRS notching or slurring is present. In case of disagreement, the consensus was determined on the basis of expert discussion. Two experts further manually measured QRSd and one expert evaluated the morphology in V1 and V2. Altogether, 51 records were evaluated as t-LBBB. The tLBBB morphology was determined in 71 records, mid-QRS notching or slurring in at least 2 leads was determined in 55 records, and the broad QRSd according to the criteria set in [1] was labeled in 70 records. Diagnosis of non-tLBBB records was not determined.

3 Methods

The proposed algorithm verifies all parts of the tLBBB criteria step by step. The parts of the algorithm will be described in the subchapters below.

3.1 QRS Duration Measurement

The ECG signal was resampled at a sampling rate of 1250 Hz before detection because the applied measurement algorithm was not optimized for the higher sampling frequency. The freely available program called ecgpuwave [5] was used for QRSd measuring. This program detected the onset and offset of each QRS complex in the entire record in all leads. The median distance between the QRS onset and offset and the corresponding dominant peak of QRS was calculated after this detection. The positions of these dominant peaks were detected using the program described in [6]. QRSd was determined by adding two calculated distances.

3.2 QRS Morphology Determination

In this part is described the detection of tLBBB morphology (the shape of QRS is rS of QR, see Chap. 1 and Fig. 1) One representative QRS complex was created in each analyzed lead (V1 and V2). In the first step, the signal was resampled to 250 Hz. Subsequently, bandpass filtering was performed with 0.1 and 45 Hz cut-off frequencies. Eventually, all detected QRS complexes (section from start to end of each QRS) were separated from the signal. The resulting representative QRS was given by the median of all QRS.

The morphology of the QRS was determined from the representative complex. First, it was determined whether the dominant wave of the QRS complex was positive or negative. If the dominant wave was negative, it was determined whether there was a positive wave after the dominant wave.
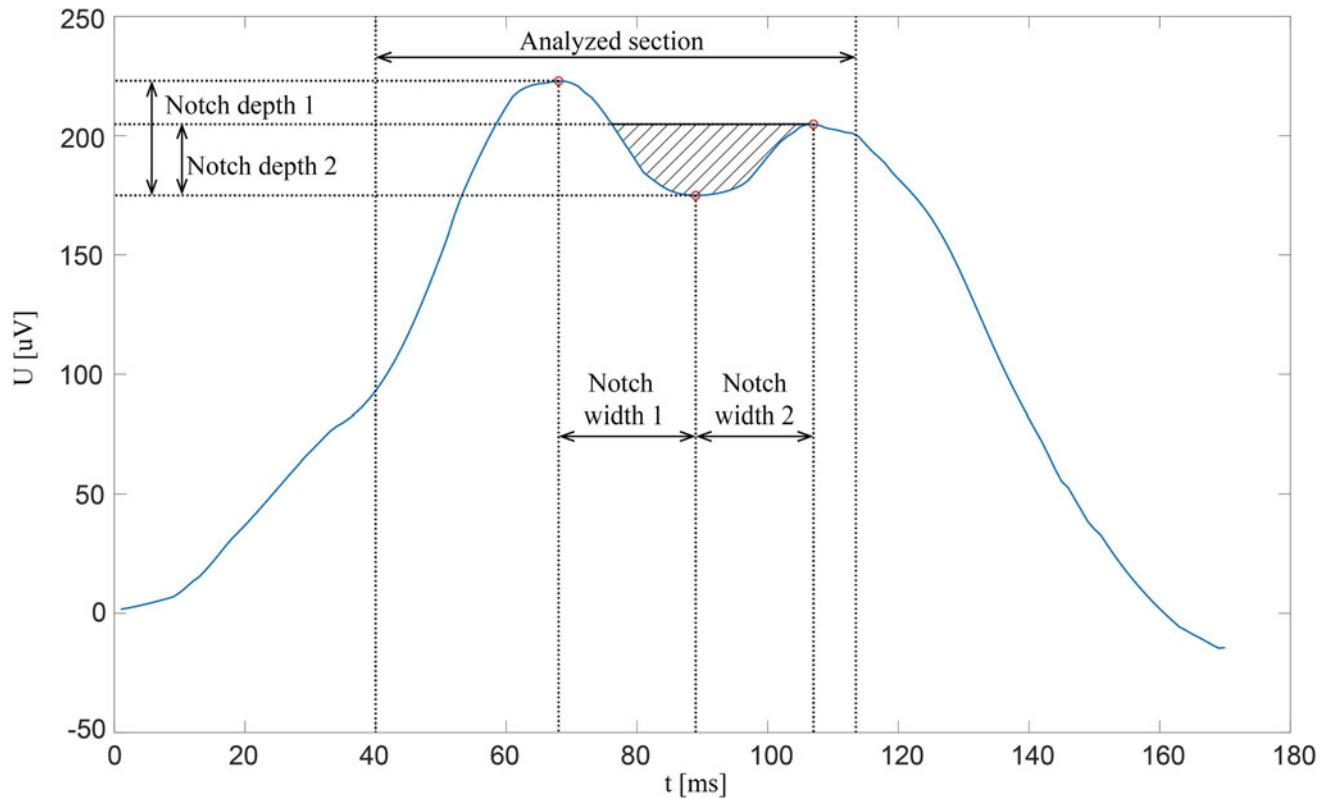
Fig. 2 Mid-QRS notching and features suitable for QRS notching detection (notch depth 1 and 2, notch width 1 and 2 and the area inside the notch—hatched area)

This positive wave was detected when one of the samples between dominant wave S and QRS offset was higher than the first sample of QRS. Another condition was that the curve has to decrease sufficiently after a point with a higher value than the first QRS element, but before the end of the QRS complex. The QRS morphology according to the tLBBB criteria was determined if the dominant wave was negative and no positive wave was detected after wave S.

3.3 QRS Notching and Slurring Detection

The representative QRS was created (in the same way as in QRS morphology determination) in each lead in which QRS notching and slurring was analyzed (V1, V2, V5, V6, I and aVL). The analyzed section of signal was shortened only to a part where mid-QRS notching and slurring can occur—the section between 40 ms after the QRS onset and 2/3 of QRSd was selected. This section of signal enters QRS notching and slurring detection algorithms.

QRS notching detection. The first step in detecting QRS notching was to detect all local extremes. Consequently, a combination of local extremes, which can form QRS notching, was sought. QRS notching was detected if at least 3 consecutive local extremes was on the one side of the isoelectric line. The second condition was that the first local extreme had to be the maximum if the samples were above the isoelectric line or the first local extreme had to be the minimum if the samples were below isoelectric line.

If the 3 consecutive local extremes meeting these conditions were found the geometric parameters describing QRS notching (the time difference between all three local extremes, the area inside the notch and the depth of notch—it was calculated as the difference in voltage at the edges of the notch and the extreme between them) were calculated. The features used are on the Fig. 2. Thresholding of these values was determined whether there was mid-QRS notching in the signal.

QRS slurring detection. Several features of QRS slope change were calculated between every two consecutive local extremes. The first feature was the ratio of the maximum and minimum of the first difference of the signal. Another feature was the ratio of the maximum and minimum of sum of the first difference samples in a floating window of 12 ms. The

last feature was the maximum difference between the sum in the adjacent windows of 12 ms. The same features were also counted for the 20 ms window.

3.4 Final Classification of TLBBB

The last step was to decide on the presence of tLBBB. The tLBBB was classified if a wide QRS was detected and the tLBBB morphology was in leads V1 and V2 and in at least two leads (of the analyzed leads I, aVL, V1, V2, V5 and V6) was mid-QRS notching or slurring.

4 Results and Discussion

4.1 QRS Duration Measurement

The median and quartiles (75% and 25%) of the absolute difference between the reference and the automatically measured QRSd was calculated to determine accuracy of QRSd measurement. The reference values were measured manually by two experts. The results are shown in Table 1. We can see that the smallest difference is between manually two experts measured values. However, the deviation of the automatically measured QRSd is comparable with the difference between the manually measured values.

4.2 QRS Morphology Determination

Sensitivity (Se), specificity (Sp) and accuracy (Acc) were used to evaluate the success of the determination tLBBB morphology. The Se, Sp and Acc were 98.59%, 100% and 98.72%, respectively. The 70 records were correctly evaluated as tLBBB morphology, the 7 records were correctly evaluated as non-tLBBB morphology and only 1 record was misclassified by the software (SW). This record has tLBBB morphology, but the SW evaluated it as non-tLBBB.

Table 1 Deviation of QRSd measurement (Ref1 and Ref2 are QRSd values measured manually by experts; SW is the QRSd value measured by the software)

Compared values	Median (ms)	Quartile 75% (ms)	Quartile 25% (ms)
Ref1—Ref2	5.4	12.4	3
Ref1—SW	6.5	14	3
Ref2—SW	8	15	4

Table 2 Success of QRS notching and slurring detection (Ref1, Ref2 and Ref3 are detection determined by experts; SW is created software)

Detection method	Se (%)	Sp (%)	Acc (%)
Ref1	89.10	91.30	89.74
Ref2	100.00	78.26	93.59
Ref3	80.00	100.00	85.90
SW	90.16	100.00	92.31

4.3 QRS Notching and Slurring Detection

QRS notching and slurring detection is less accurate than previous QRS morphology determination. This is due to the above-mentioned inaccurate definition of QRS notching and slurring. Table 2 compares the Se, Sp and Acc of detection by three experts and SW, the reference value is the consensus reached by the discussion among experts. The SW Se and Sp is comparable to manual annotation.

The 55 records were correctly evaluated as QRS notching/slurring, the 17 records were correctly evaluated as non-QRS notching/slurring and 6 records were incorrectly evaluated as non-QRS notching/slurring. The SW did not label QRS notching or slurring when this pathology was not found in the signal.

4.4 Final Classification of tLBBB

The Se, Sp and Acc of the final tLBBB classification by SW is 96.23%, 88.00% and 93.59%, respectively. We further divided the records into a group where all three experts chose the same diagnosis without the need to discuss each other (64 records, 82%) and to the group where the same diagnosis was not chosen (14 records, 18%). In the group where all the same diagnosis was chosen, the SW Se, Sp and Acc is 95.56%, 94.74% and 95.31%, respectively. In the second group, SW Se, Sp and Acc is 100%, 66.67% and 85.71%, respectively. Table 3 is the confusion matrix of tLBBB classification by SW (all records).

Table 3 Confusion matrix of tLBBB classification

		Manual annotations	
		tLBBB	Non-tLBBB
SW	tLBBB	51	3
	Non-tLBBB	2	18

Table 4 Se and Sp of mid-QRS notching and slurring and tLBBB classification in this paper and in paper [2]

	Se notch/slur (%)	Sp notch/slur (%)	Se tLBBB (%)	Sp tLBBB (%)
Paper [2]	95 ± 5	85 ± 21	95 ± 5	86 ± 22
This paper	90.16	100.00	96.23	88.00

4.5 Comparison with Earlier Results

Study [2] also dealt with the tLBBB classification. Comparison with this study is provided in Table 4. The sensitivity of the classification is better in the study [2], otherwise all the rates of success are better in this article.

5 Conclusion

This paper describes the fully automatic algorithm for classification of tLBBB based on the criteria set in [1]. QRSd was measured, QRS morphology was determined in leads V1 and V2, and mid-QRS notching and slurring was detected. The resulting diagnosis was determined in the end. The achieved results are comparable to the manual classification by the experts as well as compared to the results of paper [2]. The limitation of this paper is the low number of classified records on which the algorithm was tested.

References

1. Strauss, D., Selvester, R., Wagner, G.: Defining Left Bundle Branch Block in the Era of Cardiac Resynchronization Therapy. Am J Cardiol 107(6), 927–934 (2011).
2. Xia, X., Ruwald, A., Ruwald, M., Ugoeke, N., Szepietowska, B., Kutyifa, V., Aktas, M., Thomsen, P., Zareba, W., MOSS, A., Couderc, J.: Automatic Diagnosis of Strict Left Bundle Branch Block from Standard 12-lead Electrocardiogram. In: Computing in Cardiology, pp. 665–668, Vancouver (2016).
3. Macfarlane, P., Clark, E.: ECG measurements in end QRS notching and slurring. Journal of Electrocardiology 45(5), 385–389 (2013).
4. Clark, E., Katibi, I., Macfarlane, P.: Automatic detection of end QRS notching or slurring. Journal of Electrocardiology 47(2), 151–154 (2014).
5. Jane, R., Blasi, A., Garcia, J., Laguna, P.: Evaluation of an automatic threshold based detector of waveform limits in Holter ECG with the QT database. In: Computing in Cardiology, pp. 295–298, Lund (1997).
6. Plesinger, F., Jurco, J., Jurak, P., Halamek, J.: Robust multichannel QRS detection. In: Computing in Cardiology, pp. 557–560, Cambridge (2014).
7. Xia, X., Ruwald, A-C., Ruwald, MH.,, et al.: Validation of an automatic diagnosis of strict left bundle branch block criteria using 12-lead electrocardiograms. Ann Noninvasive Electrocardiol 22(2), pp. 1–8 (2017).

Classification of Children with SLI Through Their Speech Utterances

Pavel Grill

Abstract

Many young children have speech disorders. The research focused on one such disorder, known as specific language impairment (SLI) or developmental dysphasia in Czech (DD). A major problem in treating this disorder is the fact that specific language impairment is detected in children at a relatively late age. For successful speech therapy, early diagnosis is critical. This paper provides the issue of identifying SLI in children on the basis of their speech and presents two different approaches to this issue using. The First access is a new method for detecting specific language impairment based on the number of pronunciation errors in utterances. The success rate of detection of children with SLI is higher than 93%. An advantage of this method is its simplicity in the form of a simple test. This test is used in a mobile application SLIt Tool which is designed for iPad. The second method is based on the acoustic features of the speech signal. The feature set used to analyze speech data contains 1582 acoustic features and the success rate is almost 97%. An advantages of these different methods is that they could be used together to develop of the robustness automatic detection system.

Keywords

Specific language impairments • Disorder speech
Artificial neural networks

1 Introduction

The ability to communicate via spoken language is one of the most important human attributes. Inabilities to communicate using speech can isolate individuals from society. Isolation resulting from speech impairments is significant for children with specific language impairments. Specific Language Impairment (SLI), or Developmental Dysphasia (DD), [1–4] is chosen as a diagnosis when a child has delayed or disordered language development for no apparent reason. It has been described as a language disorder that delays the mastery of language skills in children who have no hearing loss or other developmental delays. These children fail to acquire their native language properly/completely, despite having normal nonverbal intelligence, no hearing problems, and no known neurological dysfunctions or behavioral, emotional or social problems [5]. It is estimated that SLI affects approximately 5–7% of the kindergarten population [6]. Various heritability studies, e.g., genetic etiology studies, family evaluations and stud-ies of twins, have demonstrated that SLI includes a significant genetic component [7]. Another study showed that SLI affects boys much more frequently than girls [8]. The manifestation of impairments occurs mainly in reduced vocabulary development at early ages and typically difficulty in manipulating linguistic rules of inflection and derivation, resulting in incorrect syntactic structures, in their native tongue. Usually, their own production of language is worse than their language comprehension. Various difficulties can be present in children with SLI in non-linguistic cognitive skills, e.g., executive functions, mental rotation, or motor ability [9]. Other difficulties occur particularly in other cognitive domains, such as working memory [10, 11], and these difficulties can be associated with reading impairments [12, 13]. Numerous studies have addressed the question of the problem underlying and causing the observed language difficulties. In these studies, theories of language acquisition and language representation and processing have been applied [4, 14].

Research addresses the issue of identifying specific language impairments in children on the basis of their speech. The aim is to develop methods and procedures that could be utilized to unambiguously classify these children. The procedures described in this paper are intended to be used as a basic building blocks of the software tools for evaluating treatment progress and assisting physicians in clinical praxis

P. Grill (✉)
R&D Laboratory, Military Technical Institute, Prague, Czech Republic
e-mail: pavel.grill@vtusp.cz

and a partial result will be in creation a simple tool for identifying this disorder that can be used anywhere by anyone.

2 Methods

2.1 Ethics Statement

This study was conducted in the Department of Circuit Theory of the Faculty of Electrical Engineering of the CTU in Prague. The Ethics Committee of Motol University Hospital in Prague, Czech Republic approved the research. All of the parents provided written informed consent on behalf of their children prior to participation in the study.

2.2 Participants

The database of children with SLI and typically children [15] was created in the research group of the LANNA. The specific section of the database for our research contains two different types of speakers: children without disorder (controls) and children with SLI (cases). The children's speech was recorded in a schoolroom or a speech and language therapist's consulting room in the presence of surrounding background noise during the period 2003–2013. This state simulates the natural environment of children and is important for capturing the normal children's behavior.

The participants included in the research had to be examined by a clinical psychologist. The examinations were performed in the Department of Pediatric Neurology of the 2nd Faculty of Medicine of Charles University in Prague. The parents were present during the examinations, which required one day. The children did not take any medications. The following tests were administered during the examination: Gessel Developmental Diagnosis [16] and the Stanford-Binet Intelligence Test (Fourth Edition) [17], Additional tests were standardized for the Czech language (sound differentiation test, world differentiation test, auditory analysis and synthesis test), including special tests of perceptual skills, graphomotor skills and visuomotor coordination, spontaneous talk evaluations and figure drawing and tracing [1, 2, 5, 18]. The inclusion criteria were the following: performance intelligence quotient (PIQ) $\geq$ 70; disturbed phonemic discrimination; and disturbed language at various levels—phonologic, syntactic, lexical, semantic and pragmatic [6]. Neurological examinations showed no abnormalities. Motor milestones were within normal ranges. None of the children had hearing impairments. No child was diagnosed with a pervasive developmental disorder or other dominating behavioral problem. None of the children had a history of language or other cognitive regression [6].

Controls consisted of 15 boys and 29 girls (a total of 44 children) 70–131 months of age (mean age = 106 $\pm$ 15.4 and median = 110). Cases consisted of 35 boys and 19 girls (a total of 54 children) 70–131 months of age (mean age = 96 $\pm$ 16.3 and median = 94).

2.3 Hardware and Software

The database was recorded on the digital dictaphone (SONY MZ-N710 with parameters: fs = 44.1 kHz, 16-bit resolution in stereo mode and wav standardized format) and an iBook laptop computer by Apple Inc., with professional solution software by Avid Technology (fs = 44.1 kHz, 16-bit resolution in mono mode and wav standardized format). The speech was recorded in the natural environment of a schoolroom and in a clinic. For the preprocessiing data were used the followings software: Cool Edit Pro 2 [19], Labelling [20] for the phonetic transcription and Matlab [21]. The input data consisted of the speech signal in.wav format. The phonetic transcription was output as an lbl file (text format). The process of labelling was entirely manual. For statistical computing, it used a Statistics Toolbox in MATLAB and R software [21].

2.4 Speaking Tasks

The suitable utterences for the recordings were created by the clinical psychologists and speech therapists. They compiled the speech test relying on the acknowledged tests. With this speech test, the participants repeated spoken utterances, which were necessary to ensure the same conditions for all of the participants. It is from reason because the younger children could not yet read. The structures of the utterances included a range of words and phrases, for a total of 68 different utterances. All of the utterances used were described in [15, 22, 23].

The test was performed as follows: The speech therapist read a chosen text, and the participant repeated it. Only they were present during the recording.

2.5 Statistics

It is necessary to verify the validity of the obtained results [24–28]. For correctness of our results we used following tests; *Shapiro-Wilk (S-W) normality test*, *Student's t-test*, *F-test*. For obtained data, which did not conform to the normal distribution of data, we used a non-parametric test for data. We chose *Wilcoxon's rank-sum test*. A p-value set to the maximum level of $p < 0.001$ for the *t-test* and the *F-test* and $p < 0.05$ was considered statistically significant for the

S-W test and *Wilcoxon's rank-sum test*. The results obtained at these levels have significant interpretive value.

3 Results

3.1 First Approach: Error Analysis

This method based on the description of errors in individual words [15, 22, 23]. I attempted to analyze the words pronounced by cases and compare them with those pronounced by controls. During the study, it was found that utterances from cases include many more errors than those of controls. Basis for this approach is an identification number of pronunciation errors in the utterances using the parameter indicated as penalty score (see simplified equation):

$$PS = wp + up + mp \tag{1}$$

where *PS* is the penalty score, *wp* is the number of wrong phonemes, *up* is the number of unspoken phonemes, *mp* is the number of missing phonemes. The input data for error analysis are the recorded ut_1 (text reading by speech therapist) and ut_2 (repeating text by children), and the output from error analysis is a *PS* of the analyzed ut_2, which is calculated in CM (confusion) matrix. A detailed description of the error analysis is in [22] and simplified process diagram is provided in Fig. 1.

The obtained score for the Wilcoxon's rank-sum test, S-W test did not confirm the normality, is *p-val* = 1.01e−15, *zval* = −8.3166, and *ranksum* = 963; hypothesis of equal medians was rejected. Controls and cases are distinguishable at the default 5% significance level. The results of the analysis of utterance errors are displayed in Fig. 2.
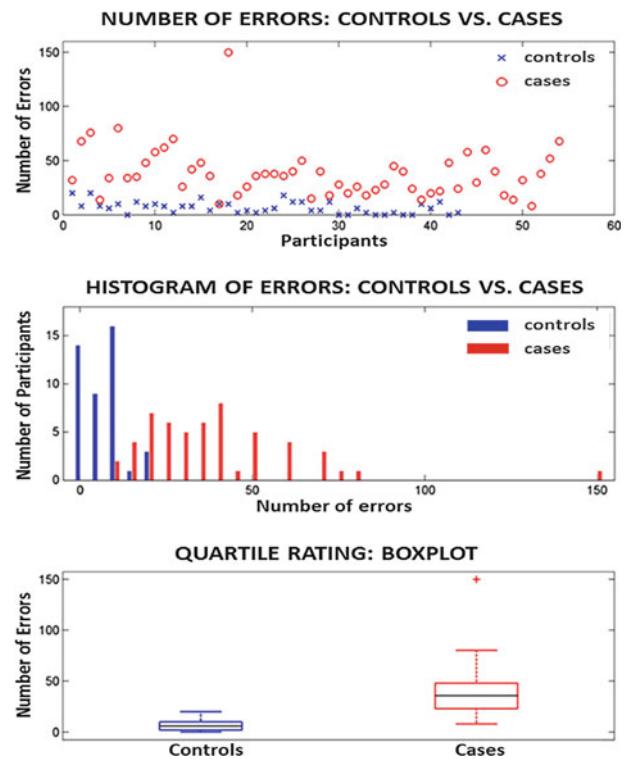
Fig. 2 Evaluation of the error analysis. Data from controls are shown in blue (or at a lower position), and data from cases are shown in red (or at a higher position) or in grayscale (Color figure online)

The cases had a total number of errors in their utterances that was much greater than the number of errors for the controls. Table 1 shows the difference in the average number of errors between controls and cases. The final percentage success rate for the evaluation of the error analysis was **93.81%**.
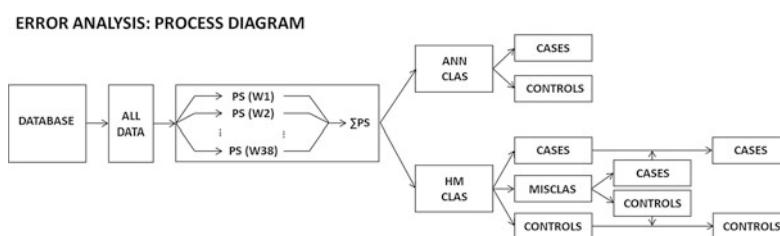

Fig. 1 Process diagram illustrating the principle of error analysis

Table 1 Error analysis: comparison both groups: average number of errors for controls and for cases

Error analysis: controls versus cases: participants				
Age	Average error		Difference	Difference
Category	Cases (2)	Controls (1)	2 versus 1	(%)
All	38.89	4.93	33.96	688.84

3.2 Second Approach: Feature Analysis

This method based on the auditory signal features specific to the acoustic features of speech [15, 22, 23]. Children with SLI show impaired perception and production of spoken language and can also present with motor, auditory, and phonological difficulties. The main challenge was to maximize the variability between classes, i.e., cases versus controls by using to compare the words spoken by participants from cases with those spoken by participants from controls. I focused on acoustic speech parameters, which were extracted from individual words without using the Labeling program.

The examined issue can be divided into four parts whose respective key components can be described as follows:

1. Input data: Data used for experiments—speech data from controls and cases.
2. Feature extraction: The tool for audio feature extraction —the OpenSMILE toolkit [29] was used to extract acoustic parametres. The obtained feature set for description of the speech signal contains a total of 1582 acoustic features, i.e., 21 statistical functionals used for 34 low-level descriptors (LLDs) and their deltas, which were calculated every 25-ms from the speech signal. The names and numbers of the 34 low-level descriptors as they appear in the output file are as follows: *pcm_loudness (1), mfcc (15), logmelfreqband (8), lspfreq (8), f0finenv (1),* and *voicingfinalunclipped (1).* The names of the 21 functionals are as follows: *maxpos, minpos, amean, linregc1, linregc2, linregerra, linregerrq, stddev, skewness, kurtosis, quartile1, quartile2, quartile3, iqr1-2, iqr2-3, iqr1-3, percentile1.0, percentile99.0, pctlrange0-1, upleveltime75,* and *upleveltime90.*
3. Feature selection: Methods and procedures used to reduce of the number of features—the procedure of selection of parameters for the feature selection into three classes: a value of 1 indicates correct classification, and a value of 2 indicates incorrect classification or so-called *"misclassification".* The data were evaluated using Spearman's rank correlation coefficient. All of the data were compared using this correlation. For each feature,

the sum of the correlation coefficients was calculated, and the 30 features with the highest values were selected. The selected features were those that contained the best information about the internal dependencies of the data. The whole process is provided in Fig. 3.

4. Classification: Describes the decision-making procedures used for the final classification—the resulting classification for each participant was evaluated from the winning class based on the number of classifications, i.e., 1 for a correct classification and 2 for a misclassification, and a class is assigned based on the number of classifications. The winning class was based on a larger number of classifications. Features could be selected in two ways: For each word, it was chosen the feature set with either the same number of features or a variable number of features, feature selection—FS: constant and FS: variable). First, it was necessary to determine the rate of successful classification. First class features distinguished healthy children from children with SLI with a success rate higher than 90%; second class features had a success rate between 80 and 90%, and so on. For each word, it was selected the properties with the highest accuracy rate. The participants were classified using a total of 268 features (preferred final feature set) obtained from 38 words. If a constant number of features was used, each participant was classified using a total of 760 features.

A detailed description of the feature analysis is provided in Fig. 4, which shows the process diagram for the classification of the error analysis.

The obtained score for the Wilcoxon's rank-sum test, S-W test did not confirm the normality, for controls is (correct vs. wrong classification) $p\text{-}val = 1.7510e{-}15$, $zval = 7.9578$, and $ranksum = 2911$ and for cases is (correct vs. wrong classification) $p\text{-}val = 3.3145e{-}19$, $zval = -8.9577$, and $ranksum = 1485$ and therefore, the null hypothesis of equal medians was rejected. Controls and cases are distinguishable at the default 5% significance level. The results of the feature analyses for all of the participants are displayed in Fig. 5. The classification as a controls are displayed on the left, and the classification as a cases displayed on the right. Results of the participants from controls

FEATURE ANALYSIS: SELECTING ACOUSTIC FEATURES
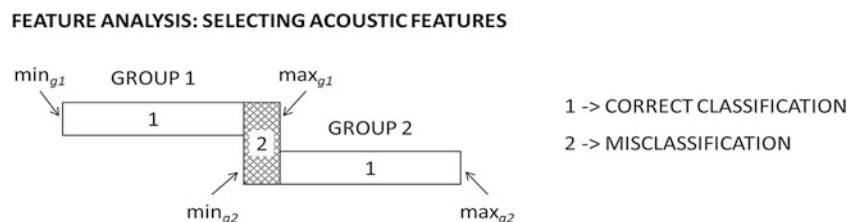
Fig. 3 Procedure for selecting appropriate acoustic features. The value of 1 indicates correct classification, and the value of 2 indicates incorrect classification. Parameters "maxg1" and "ming2" indicate maximum and minimum threshold limits for incorrect classification
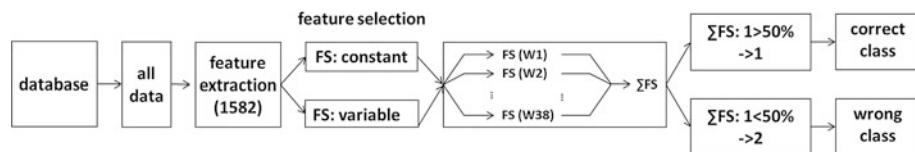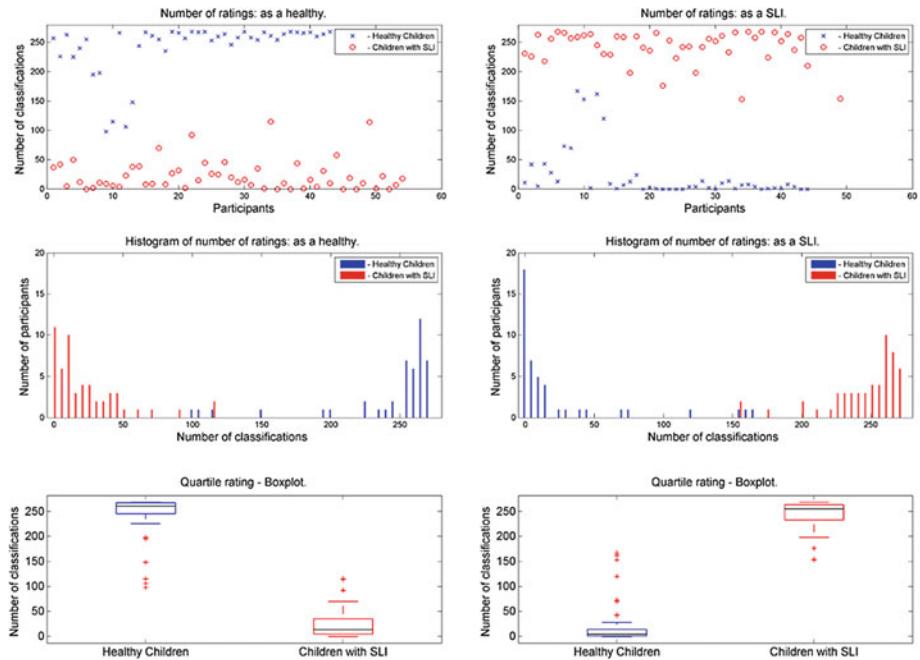
Fig. 4 Overview of the classification children with SLI through acoustic features

Fig. 5 Evaluation of the feature analysis. Data from controls are shown in blue colour, and data from cases are shown in red colour. Samples with a higher number of classifications are in a higher position (Color figure online)

are displayed in blue, and results of the participants from cases are displayed in red. The total numbers of classifications are displayed in the upper graphs. A higher value indicates more obvious inclusion of the participant in his group. The results show that the participants from the controls had a higher number of classifications as "healthy" (values in blue on the left chart), and the participants from the cases had a higher number of classification as "SLI" (values in red on the right chart).

Table 2 presents the final results used to distinguish the two groups and their percent success rate. It was achieved a 96.94% success rate for both groups. Only 3 participants out of 98 were misclassified. These participants were from the controls group, i.e., the typically children. This result proved that it is possible to find acoustic features that can distinguish typically children from children with SLI with high accuracy. The final percentage success rate for the evaluation of the feature analysis was **96.94%**.

Table 2 The success of classification. The percentage rates of correct classification of the method used to distinguish the two groups

Controls versus cases: final percent success rate				
Classification of participants				Success rate
Group	Total number	Correct	Wrong	(%)
Controls (2)	54	54	0	100.00
Cases (1)	44	41	3	93.18
$\sum$(1 + 2)	**98**	**95**	**3**	**96.94**

4 Conclusion and Discussion

The methods described in this paper was developed to analyze disordered children speech. It was focused on children with specific language impairments and believe that the utilization of these methods in clinical practice will bring more insight into progression and treatment of the disease and help to think out efficiently treatment of the disease. This research was a part of the research project that is focused on treatment of SLI.

4.1 Error Analysis

Error analysis is based on the number of errors in the utterances. The advantage of this access is that its function does not require complex computational methods and can be performed by anyone. This approach provides complete information about the most common errors and substitutions between speech sounds in the utterances of the children with SLI. The results of the error analysis show that the number of errors in utterances is an important cue that can be used as a border line to determine typically children and children with SLI. This approach enabled the creation of a simple test to detect children with SLI, specifically mobile application SLIt Tool [15, 22, 23]. The initial goal of creating a test originated when we solved the problems with the creation of a children's speech database.

4.2 Feature Analysis

This method, called feature analysis, for identifying children with SLI based on the auditory signal features specific to the acoustic features of speech. These features can be easily obtained and can be calculated without complicated modifications of the speech signal. Modern techniques permit the calculation of as many different acoustic features of audio recording as possible. This approach reduces the need for difficult decisions about which features and methods are relevant to the task but adds the need for optimization and classification methods. These experiments show that feature analysis can distinguish typically children and children with SLI on high level of resolution.

4.3 Conclusion

These results prove that it is possible for children with specific language impairments to be clearly identified and distinguished from healthy children, based on their speech and speech skills. It was combined traditional and alternative approaches to this issue and obtained a resistance tools that

is not dependent on the quality of the captured recordings. It found several different classification methods for children with SLI. All of these methods can be used separately for the classification of these children. Each method yields a high level of success in classifying children with SLI, but each has its particular limiting factors and shortcomings. Using these methods together, it is able to eliminate these shortcomings and obtain a powerful tool for diagnosing children with SLI.

References

1. Bishop D VM (2014). Uncommon Understanding (Classic Edition): Development and Disorders of Language Comprehension in Children. England Psychological Press. ISBN 9780203381472.
2. Leonard L B (2014). Children with specific language impairment., MA: MIT Press. ISBN 9780262027069.
3. Hulme C, Snowling M J (2009). Developmental Disorders of Language Learning and Cognition. Wiley. ISBN 9780631206118.
4. Specific Language Impairment. Available: http://www.nidcd.nih.gov/health/voice/pages/specific-language-impairment.aspx Accessed 02 February 2017.
5. Vranova M, Tuckova J, Kyncl M, Grill P, Komarek V, et al. (2011). MRI abnormalities of speech and computerised processing of speech of children with Developmental Dysphasia. (in Czech). In AKL Congress, Tabor, Czech Republic.
6. Tučková J, Komarek V (2008). Effectiveness of Speech Analysis by Self-Organizing Maps in Children with Developmental Language Disorders. In: Neuroendocrinology Letters. Ed.: Peter G. Fedor-Freybergh. Society of Integrated Sciences, vol. 29, No. 6, Nov/Dec 2008, ISSN 0172-780X.
7. Schuller B, Steidl S, Batliner A, Burkhardt F, Devillers L, Müller Ch, Narayanan S (2013). Paralinguistics in speech and language-State-of-the-art and the challenge, Computer Speech and Language, v. 27 n. 1, p. 4–39, January, 2013, ISSN 0885-2308.
8. Tomblin J B, Records N L, Buckwalter P, Zhang X, Smith E, O'Brien M (1997). Prevalence of Specific Language Impairment in Kindergarten Children. Journal of Speech, Language, and Hearing Research, December 1997, Vol. 40, 1245–1260. https://doi.org/10.1044/jslhr.4006.1245.
9. Bishop D V M, Adams C V, Norbury C F (2006). Distinct genetic influences on grammar and phonological short-term memory deficits: Evidence from 6-year-old twins. Genes, Brain and Behavior. 2006. PMID: 16507007. https://doi.org/10.1111/j.1601-183x.2005.00148.x.
10. Kohnert K, Windsor J, Ebert K D (2009). Primary or/Specific/Language Impairment and children learning a second language. Brain and Language. https://doi.org/10.1016/j.bandl.2008.01.009.
11. Archibald L M, Gathercole S E (2006). Short-term and working memory in Specific Language Impairment. In Alloway, T. P. & Gathercole, S. E. (Eds), Working memory in neurodevelopmental

conditions, pp. 139–160. Psychology Press. https://doi.org/10.1080/13682820500442602.

12. Montgomery JW, Magimairaj B M, Finney M C (2010). Working memory and specific language impairment: An update on the relation and perspectives on assessment and treatment. American Journal of Speech-Language Pathology 19, Vol. 19, 78–94. https://doi.org/10.1044/1058-0360.

13. Bishop D V M, Snowling M J (2004). Developmental dyslexia and specific language impairment: Same or different? Psychological Bulletin, 130(6), 858–886. https://doi.org/10.1037/0033-2909.130.6.858.

14. van Weerdenburg M, Verhoeven L, Bosman A, van Balkom H (2011). Predicting word decoding and word spelling development in children with Specific Language Impairment. Journal of Communication Disorders 44. https://doi.org/10.1016/j.jcomdis.2010.12.002.

15. Grill P, Tučková J (2016). Speech Databases of Typical Children and Children with SLI. PLoS ONE 11(3): e0150365. https://doi.org/10.1371/journal.pone.0150365.

16. Knobloch H, Stevens F, Malone A F (1980). Manual for developmental diagnosis. The administration and interpretation of the revised Gesell and Amatruda developmental and neurologic examination. Hagerstown: Harper and Row, 1980.

17. Thorndike R L, Hagen E P, Sattler J M (1995). Stanford-Binet Intelligence Test (Terman-Merrill): Fourth revision. Itasca, IL: Riverside Publishing.

18. Swierkoszova J (1990). Specific Learning Disabilities. (in Slovak). Bratislava: SPN. ISBN 80-08-00447-9.

19. Cool Edit Pro 2 Adobe Systems Inc. Available: http://www.adobe.com/special/products/audition/syntrillium.html. Accessed 11 February 2016.

20. Tuckova J, Bartu M, Zetocha P (2009). Applications of artificial neural networks for signal processing. (in Czech) Prague: Czech Technical University in Prague. ISBN 978-80-01-04400-1.

21. MATLAB MathWorks Inc. Available: http://www.mathworks.com/products/matlab/. Accessed 11 February 2016.

22. Grill P (2015). Specific language impairments and possibilities of classification and detection from children's speech. Prague: Czech Technical University in Prague. In https://dspace.cvut.cz/bitstream/handle/10467/62582/Disertace_Grill_2015.pdf?sequence=1.

23. Grill, P., Tuckova, J. (2017). Classification and detection of specific language impairments in children from their speech skills. Edited by Carolyn S. Ryan, Learning Disabilities - An International Perspective, ISBN 978-953-51-5386-3, Publisher: InTech. doi:http://dx.doi.org/10.5772/intechopen.69464.

24. Meloun M, Militký J (2004). Statistická analýza experimentálních dat (book in the Czech). Praha: ACADEMIA, 953 p. ISBN 80-200-1254-0.

25. Jaros F, Rosa Z (1980). CSN 01 0225 - Aplikovana statistika. Testy shody empirickeho rozdeleni s teoretickym (book in the Czech). Cesky normalizacni institut, Praha.

26. Shapiro S S, Wilk M B (1965). An analysis of variance test for normality (complete samples). Biometrika, 52(3/4), 591{611. https://doi.org/10.1093/biomet/52.3-4.591.

27. Panik M J (2005). Advanced statistics from an elementary point of view. Boston: Elsevier/Academic Press., xvii, 802 p. ISBN 01-208-8494-1.

28. Gibbons J D, Chakraborti S (2011). Nonparametric Statistical Inference, 5th Ed., Boca Raton, FL: Chapman & Hall/CRC Press, Taylor & Francis Group, 2011. ISBN 0-8247-4052-1.

29. Eyben, F., Wöllmer, M., Schuller, B. (2010)"openSMILE - The Munich Versatile and Fast Open-Source Audio Feature Extractor", In Proc. ACM Multimedia (MM), ACM, Florence, Italy, ACM, ISBN 978-1-60558-933-6, pp. 1459-1462, October 2010. https://doi.org/10.1145/1873951.1874246.

30. The R Project for Statistical Computing. Available: http://www.r-project.org/index.html. Accessed 11 February 2016.

31. Tučková, J. (2009). Selected applications of the artificial neural networks at the signal processing. (book in the Czech). Prague: Czech Technical University in Prague, ISBN 978-80-01-04229-8.

32. Kohonen T (2001). Self-Organizing Maps. Berlin Heidelberg, 3rd Edition, Springer Series in Information Sciences, Springer-Verlag, ISBN 3-540-67921-9.

Research on Respiratory Signal Based on Angular Velocity

Guo Dan, Junhao Zhao, Huanyu Yang, Xiaohong Weng, and Zhemin Zhu

Abstract

Precise monitoring of human respiration is crucial to the diagnosis of a wide range of respiratory and cardiovascular disorders and (thus) is of great interest to both clinicians and researchers. Existing measurements may include electrocardiography (ECG), nasal cannula and respiratory plethysmography. However, low comfort levels and signal shifts which are often observed in these techniques pose limitations for long-term, accurate monitoring of human respiration. In this paper, we develop a convenient respiratory signal acquisition method based on angular velocity derived from suprasternal notch. Research has found that waveforms collected from the suprasternal notch display higher robustness, as well as less gender variability. We use the median filter method and intersection detection technique to extract the respiratory waveform, respiratory frequency and respiratory phase parameters. And validated the respiratory signals derived from suprasternal angular velocity in both males and females. The extracted parameters are validated against a carbon dioxide concentration acquisition device, which serves as our golden reference platform. The results demonstrate the potential of suprasternal-derived angular velocity as a simple, low-cost and unobtrusive method for monitoring human respiration.

1 Introduction

With the significant advances in technology and an enormous increase in public health awareness, an increasing amount of innovative technologies have been applied to traditional physiological parameter monitoring. Breathing (or respiration) is the biological process of gas exchange between an organism (human body) and the surrounding environment; therefore, orderly execution is vital to the normal metabolism of every human being. The measurement of human respiration is crucial to the diagnosis and monitoring of a wide range of respiratory, pulmonary and cardiovascular disorders, such as chronic obstructive pulmonary disease (COPD). Moreover, with the help of big data analysis, long-term monitoring could help to reveal potential respiratory diseases, ensure early-stage treatment and reduce the risks that accompany the late stages of these diseases.

A number of methods have been proposed for respiratory monitoring. For example, Cao et al. developed an impedance respiratory monitoring system, which shares a pair of electrodes with the electrocardiography (ECG) monitor. However, using electrodes to collect respiratory signals is uncomfortable for the participants, thus making the user experience poor. Gao et al. used a carbon dioxide detector to obtain respiratory waveforms by placing a nasal cannula under the nose of each participant. This method has limitations since the cannula significantly hampers both the convenience and comfort levels. A respiratory plethysmography was used by Leino et al. however, due to its poor dynamic stability, this method can display obvious signal shifts during long-term monitoring. Hung et al. demonstrated a method based on tri-axial accelerometers to evaluate

G. Dan (✉) · J. Zhao · H. Yang
School of Biomedical Engineering, Health Science Center, Shenzhen University, Guangdong 518060, People's Republic of China
e-mail: danguo@szu.edu.cn

G. Dan · Z. Zhu
Shenzhen Institute of Neuroscience, Guangdong 518057, People's Republic of China

X. Weng
Service Center for Societies, China Association for Science and Technology, Beijing 100000, People's Republic of China

respiratory waveforms. By placing the accelerometers in the thoracic region of the participant, Hung demonstrated the feasibility of capturing and distinguishing different respiratory waveforms under conditions of normal breathing, apnea and deep breathing. Despite Hung's results, it has been argued that the optimal location of the accelerometer would not be on the suprasternal notch. Research has found that waveforms collected from the suprasternal notch display higher robustness, as well as less gender variability. Therefore, with both convenience and comfort being taken into consideration, this study used angular velocity for respiration measurement. We validated the respiratory signals derived from suprasternal acceleration in both males and females.

2 Method

2.1 Respiration Detection Mechanisms

Respiration is the biological process of gas exchange between organisms (e.g., humans) and the surrounding environment. Expansion and contraction of the thoracic cavity cause the lung to inflate (breathing in) and deflate (breathing out). The sternum, or breastbone, is located in the center of the chest and is raised and pushed out by the attached respiratory muscles during inhalation. The suprasternal notch is located at the superior border of the sternum. The inertial sensor is positioned such that its upper side touches the skin of trachea and its lower side touches the skin of the suprasternal notch. During respiration, the sensor area undergoes a slight upper motion and an obvious lower motion. The chosen location is insensitive to gender and can be used to accurately detect respiratory signals.

Angular velocity has the advantages of high accuracy, low levels of noise, and better amplitudes than for acceleration. Therefore, this study used angular velocity to measure respiration. The inertial sensor attached to the suprasternal notch rotates with each breathing movement, resulting in a change in the angular velocity and thus the output of angular velocity signals. As shown in Fig. 1, the ZOY surface of the sensor is close to the skin; the sensor rotates around the Y axis during respiration. During inhalation, the X axis rotates upwards following the Y axis, forming an angle of theta1 with the original X axis at rest. The direction of angular velocity during inhalation is Y positive. During exhalation, the X axis rotates downwards following the Y axis, forming an angle of theta2 with the original X axis at rest. The direction of angular velocity during exhalation is now Y negative. Since the direction of angular velocity differs between normal inhalation and exhalation, it can be used to distinguish the inhalation phase from the exhalation phase. When the breathing motion is at a resting portion of the breathing cycle, the detected angular velocity represents the baseline of respiratory signals. With continuous breathing, the respiratory signals fluctuate around the baseline.
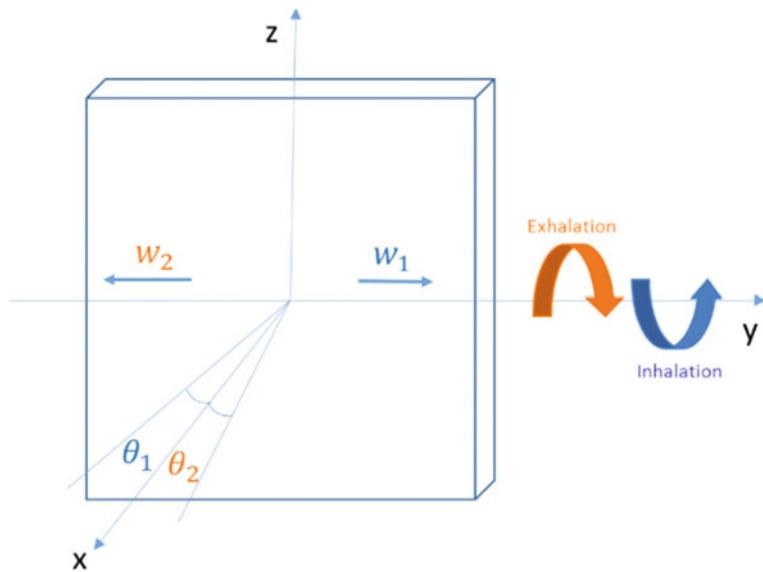

Fig. 1 Inertial sensor motion diagram

2.2 Platform Setup

Two platforms were set up in this study: an inertial sensor platform and a carbon dioxide concentration platform. The CO_2 concentration platform is used as the gold standard reference platform to test the accuracy of the inertial sensor platform and is set up such that the data acquisition of both platforms can be synchronized. The CO_2 concentration platform uses a RESPLIVE/TiniStream CO_2 measurement module from Witleaf Co. Ltd. This system uses a bypass for signal acquisition and a serial port for data transfer to the connected PC and has a sampling frequency of 25 Hz. The inertial sensor platform uses an INVENSENSOR MPU6050 sensor to detect respiratory signals and has a sampling frequency of 50 Hz. MPU6050 is small, energy efficient and low cost. Moreover, the system can read the data directly and does not require data fusion, which makes the data processing substantially faster. Figure 2 shows the inertial sensor and the CO_2 concentration platforms used in our experiments. For data acquisition, the inertial sensor was mounted in the suprasternal notch of the patients using double-sided polyurethane foam tape and further secured using 2 strips of over-the-top paper tape. A nasal cannula was placed in the direct air pathway of the respiratory airflow below the nasal cavity. The collected data were transmitted to the PC and were synchronized by PC software. The synchronized data were then used for subsequent processing.

2.3 Waveform Meaning and Introduction

The meaning of the respiratory angular velocity differs depending on the location chosen for the sensor. The inertial sensor attached to suprasternal notch rotates around a Y axis, which is parallel to the superior-inferior axis of the human anatomical position. During inhalation, the chest cavity expands until the inhalation ends, and the corresponding angular velocity gradually increases and then decreases. During exhalation, the angular velocity again gradually increases and then decreases but toward an opposite direction. The turning points for inhalation and exhalation correspond to the points where the breathing waveform intersects the baseline when no respiration is detected or allowed. As a summary, the waveform of the respiratory angular velocity is shown in Fig. 3. The X axis represents time. The Y axis represents the angular velocity. The area above the baseline represents the inhalation phase, and the
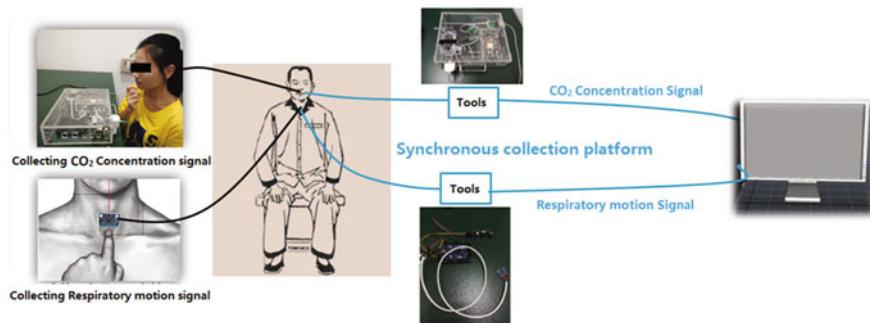

**Fig. 2** Synchronous acquisition system for respiratory data
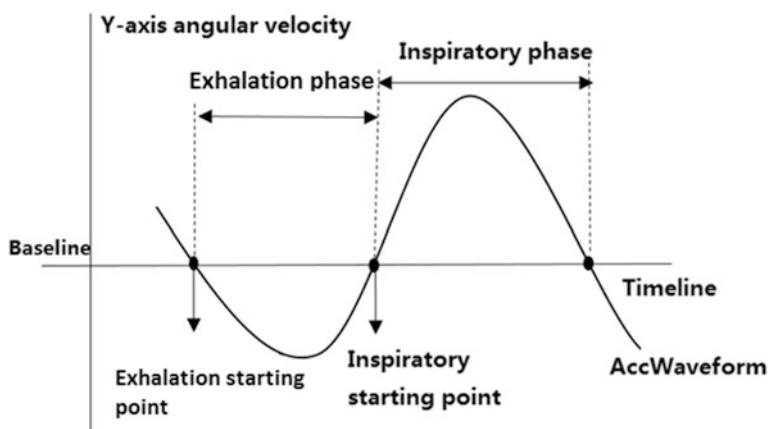

Fig. 3 Respiratory angular velocity signal
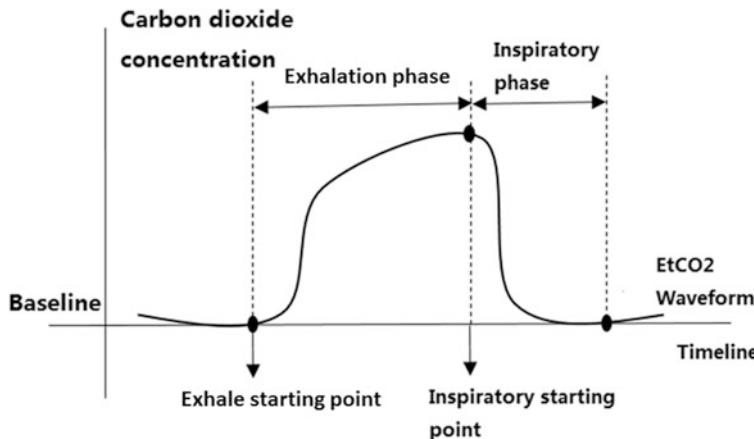
Fig. 4 Respiratory carbon dioxide concentration signal

area below represents the exhalation phase. As indicated in the figure, the waveform fluctuates around the baseline with each breathing movement.

The waveform of the respiratory carbon dioxide concentration at the end of the breath is shown in Fig. 4. The waveform consists of four phases: the first phase is the inspiratory baseline, the second phase is the expiratory ascending branch, the third phase is the alveolar plateau, and the forth phase is the inspiratory descending branch. During exhalation, the mixed gas of the alveolus and dead space, that is, the gas of the alveolus and the respiratory tract above the alveolus, are first breathed out at the same time; afterward, during the plateau, only alveolar gas is exhaled. During inhalation, the carbon dioxide concentration curve decreased to the baseline rapidly and steeply, and fresh gas entered the respiratory tract. The starting point of the ascending branch is the beginning of exhalation, and the starting point of the inspiratory descending branch is the starting point of the inhalation. The frequency and phase of the reference breathing waveform can be determined from the expiratory and inspiratory starting point information for comparison and verification.

2.4 Data Acquisition

To verify the accuracy of respiratory angular rate signals, the respiratory signals of 10 healthy subjects were collected simultaneously; these subjects included 5 males and 5 females, with ages between 21.75 and 28.25 years, heights between 162.38 and 173.62 cm and weights between 49.88 and 80.12 kg. All subjects understood and agreed to the experiment contents before the experiment. The experiment

used a single channel angular velocity signal acquisition module to collect the respiratory signal placed on the suprasternal notch of the subjects as the sample signal. The use of wired devices ensured the stability of signal transmission.

The speed of respiration varies in different people. Studies have shown that the respiratory phases of different frequencies have differences in the accuracy. This paper selected three different frequencies of respiratory signals for the experiments: a normal frequency, a high frequency and a low frequency. In the experiment, we controlled the breathing frequency by asking the subjects to breathe at the pace set by a metronome. The normal frequency was 0.25 Hz, the low frequency was 0.15 Hz, and the high frequency was 0.4 Hz.

In the experiment, the subjects were asked to breathe 10 times and then hold their breath for 10 s, with 3 repetitions of this process. To reduce the interference resulting from changing between breathing at different frequencies, each participant was provided a 2 min break before switching the frequency, which can ensure the reliability of data.

3 Algorithms

The acquired data needed to be pretreated and the parameters extracted before being used for evaluation. The noise and phase differences were eliminated by preprocessing, which can help identify the inspiratory and expiratory points of the target signal and the reference signal; the relevant parameters were then obtained from these points for further evaluation. Figure 5 shows the block diagram for processing respiratory signals.
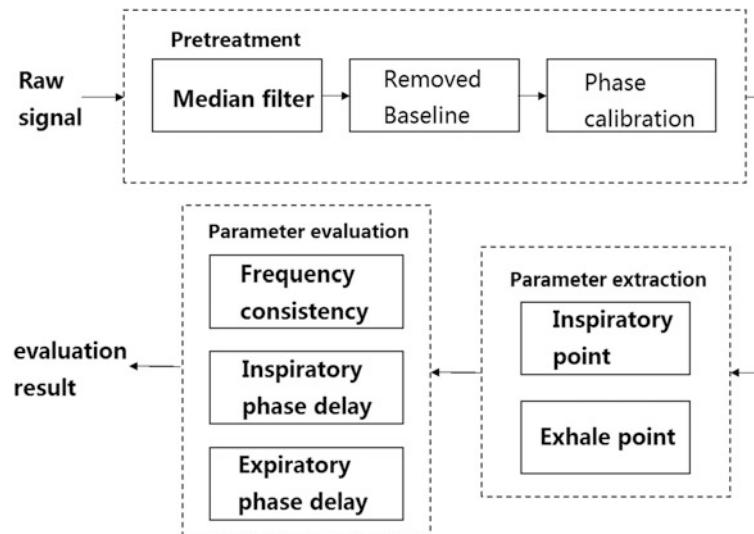
Fig. 5 Block diagram for processing respiratory signals

3.1 Preprocessing

The pretreatment first resamples the two signals to obtain a frequency of 25 Hz. The special position of the sensor causes noise in the signal, including the spike noise caused by heartbeat, in addition to the random noise of the system. The median filter replaces the data in the fixed window by its median to filter the noise, which can filter the pulse noise and spike noise points very well. This method is simple and conductive to hardware implementation. After testing, the median filter window size was chosen to be 20.

After filtering, we performed the process of baseline identification to differentiate between inspiratory and expiratory phases. The median of a fixed length signal in the condition of holding breathing was selected as the baseline value. The intersection of the respiratory angular velocity signal obtained by subtracting the baseline value from the denoised signal and the coordinate axis was considered the starting point of inspiration and expiration.

The reference breathing signal has an overall delay relative to the respiratory angular velocity signal. Because the instrument for measuring the carbon dioxide concentration is a bypass type, it is necessary to collect the breath gas into a small chamber for analysis and processing. The system has an overall delay, so phase shifting must be removed. For this purpose, we selected the respiratory waveform of the signal that remained to be processed after the first time of labored breathing to obtain the average delay for the calibration of the whole respiratory delay. The phase calibration was based on the starting point of the expiratory phase. According to the data test results, the mean value of the system delay was 41 data points, and the variance was 4 data points, between 1.48 and 1.8 s.

3.2 Calculation of Respiratory Parameters

The intersection of the respiratory angular velocity waveform and the transverse axis was identified by the method of intersection point detection to obtain the initial information regarding the starting point of inspiration and expiration. According to the meaning of the waveform, the intersection of the waveform ascending branch and the horizontal axis is the starting point of the inspiration, and the intersection of the waveform descending branch and the horizontal axis is the starting point of the expiration. The inspiration is identified by finding the data point where the previous data point is less than or equal to zero and the subsequent data point is greater than zero The expiration is identified by finding the data point where the previous data point is greater than or equal to zero and the subsequent data point is less than or equal to zero. For the reference breathing waveform, the inspiration and expiration starting points of the waveform are determined by manual identification. According to the waveform meaning, the starting point of the expiratory ascending branch is the beginning of expiration, and the starting point of the inspiratory descending branch is the beginning of inspiration. Figure 6 shows the flow chart for identifying phase points, among which T_IN and T_EX are used to store the inspiratory and expiratory start times, respectively.

In the design, the respiratory verification parameters are the respiratory rate, inspiratory phase delay and expiratory phase delay. The formula is as follows [12]:

$$RR = \frac{1}{\left\{ \sum_{I=1}^{N-1} \frac{\left| T_{IN_{i+1}} - T_{IN_i} \right|}{(n-1)} \right\}} \tag{1}$$
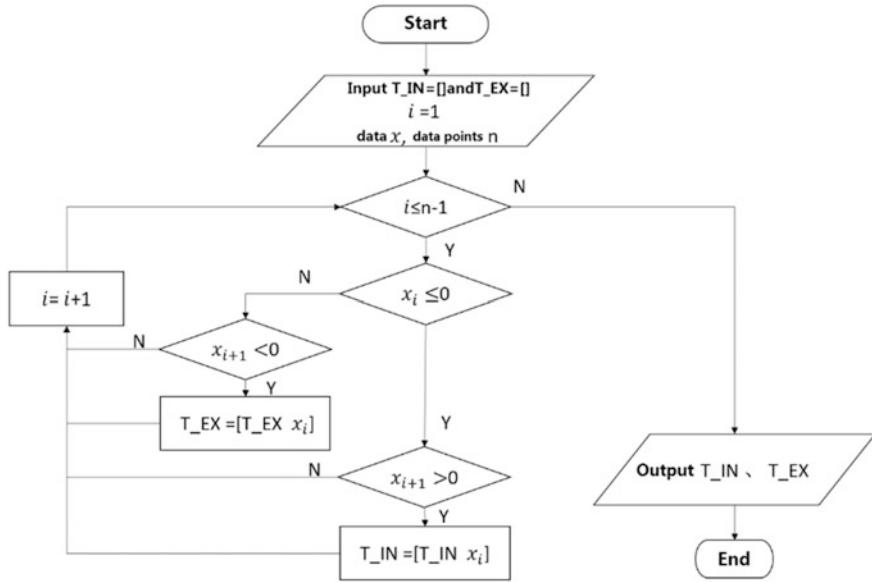
Fig. 6 Flow chart for identifying phase points

$$\Delta T_{in} = \sum_{i=1}^{n-1} \frac{\left(T_{Acc_{IN_{i+1}}} - T_{EtCO2_{IN_i}}\right)}{(n-1)} \quad (2)$$

$$\Delta T_{ex} = \sum_{i=1}^{n-1} \frac{\left(T_{Acc_{Ex_{i+1}}} - T_{EtCO2_{Ex_i}}\right)}{(n-1)} \quad (3)$$

In the formula, RR is the respiratory frequency. ΔT_{in} is the inspiratory phase delay. ΔT_{ex} is the expiratory phase delay. T_IN is the inspiratory time. Acc_{RR} is the mean value of the respiratory angular velocity frequency. $EtCO2_{RR}$ is the respiratory frequency mean of the respiratory carbon dioxide concentration waveform. T_Acc_IN is the inspiratory starting point of the angular velocity. T_EtCO2_IN is the inspiratory starting point of the respiratory carbon dioxide concentration waveform. T_Acc_EX is the expiratory starting point of the angular velocity. $T\_EtCO2\_EX_i$ is the expiratory starting point of respiratory carbon dioxide concentration waveform.

4 Results and Discussion

The consistency between the respiratory angular velocity and the respiratory frequency obtained from reference signal can be shown by the Bland-Altman diagram. From the diagram, we can see whether the respiratory frequency obtained from the respiratory angular velocity is able to replace the respiratory frequency obtained from the reference signal. Figure 7 is the Bland-Altman diagram of two types of

signals, corresponding to the consistency evaluation charts of normal frequency breathing, high frequency breathing and low frequency breathing. In the chart, the abscissa represents the mean value of the respiratory frequency measured by two methods, and the vertical axis represents the difference between the two methods of measuring the respiratory frequency. As shown in the diagram, the respiratory angular velocity and the reference respiration frequency are within the confidence interval at three different types of breathing rates. Regarding dispersion, the high frequency respiration of the two signals is more dispersed. The mixed processing result of the three frequencies indicates that there is a high frequency data point outside of the confidence interval. In general, for normal frequency breathing, high frequency breathing and low frequency breathing, the respiratory rate obtained by the breathing angular velocity can meet the requirements, and the respiratory rate can be determined using the respiratory angular velocity acquisition device.

The delay in the respiratory angle velocity signal relative to the reference signal at the starting point of inspiration and expiration is used to evaluate the respiratory phase, and the data can be analyzed by a boxplot of the delay value. The boxplot provides key information about the location and dispersion of the data. As shown in Fig. 8, this project compares the statistical information about the inspiratory and expiratory phase delays of three different respiratory frequencies and mixed respiratory frequencies. The chart shows that delays exit in both the inspiratory and expiratory starting points. For three types of frequencies, the delay in the inspiratory phase starting point is generally less than that
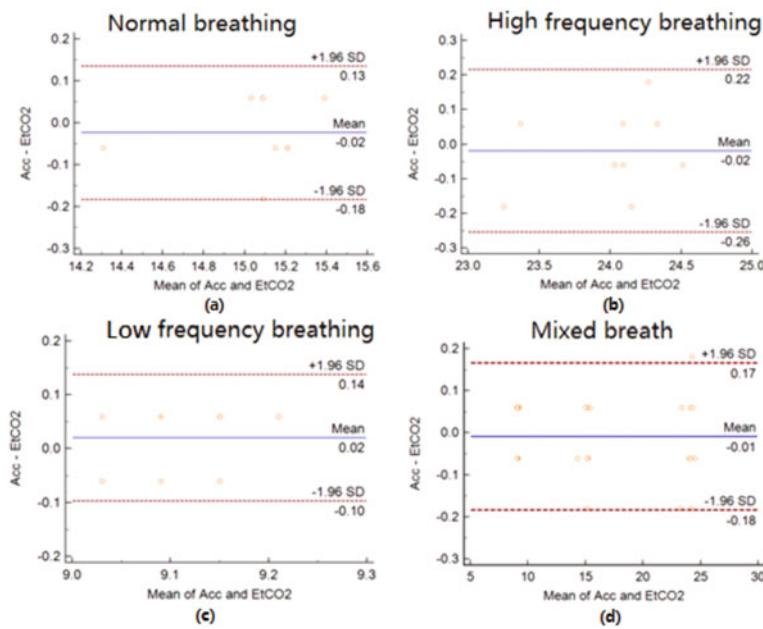
**Fig. 7** Assessment chart for the respiratory rate
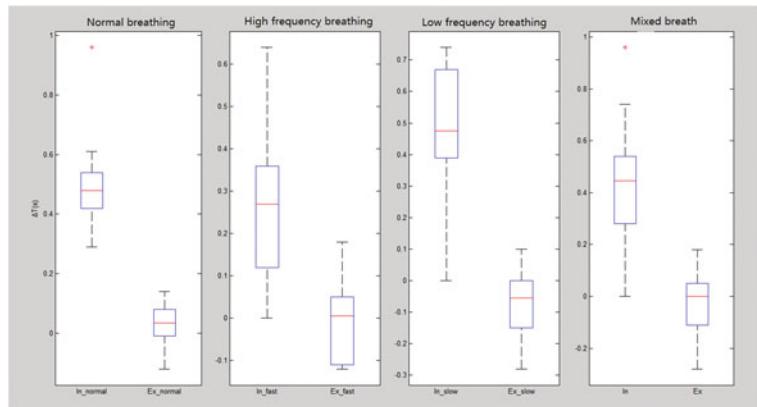
Fig. 8 Assessment chart for the respiratory phase

of the starting point of the expiratory phase. This finding occurs because the expiratory starting point is the reference point for calibrating the signal, and the delay time will be entirely focused on the inspiratory starting point. As indicated by the middle position of the boxplot, the median value of the expiratory delay is almost zero, and the median value of the inspiratory delay is generally less than 0.5 s. Regarding dispersion, the range for the inspiratory and expiratory starting point delay values of the high frequency signals and low frequency signals is larger than that for the normal frequency, indicating that the respiratory angular velocity signal acquisition device can obtain more stable information from normal respiratory signals. In general, the delay in the respiratory phase is within an acceptable range.

5 Conclusion

The present results have demonstrated that suprasternal acceleration can provide an accurate measurement of human respiration. The obtained angular velocity can be used to extract the respiratory waveform, calculate the respiratory rate, and retrieve accurate respiratory phase information. Compared with traditional monitoring methods, the use of the angular velocity from an inertial sensor has been demonstrated to be a convenient, low cost and reliable way to measure human respiration without the constraints of location. Therefore, our proposed method is suitable for long-term respiratory monitoring.

Conflict of Interest None

Ethics Statement In this study, all the participants included in the acquisition of respiratory signals provided written informed consent according to specific procedures approved by the IRB of Shenzhen University and Health Science Center Research Ethics Committee. Therefore, all the participants have given written informed consent in accordance with the Declaration of Helsinki.

References

1. XIE Yingying. Research and Design of Respiratory Training System Based on Biofeedback. Beijing Jiaotong University, 2010.
2. CAO Xiwu, DENG Qinkai, LUO Lihui. Development of Impedance Respiratory Monitoring System. Chinese Journal of Medical Physics 2000, 17(4):213–214.
3. GAO Lijun, ZHONG Shike, YUAN Jun. CO_2 concentration test system. Journal of Nanchang University, 1994, 18(2):181–185.
4. Leino K NS, Valta P. Validation of a new respiratory inductive plethysmograph. Acta Anaesthesiologica Scandinavica, 2001, 45 (1):104–111.
5. Hung PD BS, Guillemaud R. Estimation of respiratory waveform using an accelerometer. 5th IEEE International Symposium on Biomedical Imaging. Paris, FRANCE: 1493–1496.
6. David Barbosa Rendón JLRO, Luis F. Crespo Foix, Daniel Sánchez Morillo, Miguel A. Fernández Mapping the Human Body for Vibrations using an Accelerometer. Proceedings of the 29th Annual International. Lyon, France: 1671–1674.
7. ZHAO Wei, LI Man, LI Junjie. Discussion on Respiratory Mode in the Primary Practice of Ba Duanjin Fighting. Wushu Science, 2014, (01):90–91.
8. HUANG Zengming.Design of human respiratory movement model. Journal of Wenzhou Teachers College. Natural Science Edition, 1996, (06): 87–88.
9. Bates A LM, Mann J. Respiratory rate and flow waveform estimation from tri-axial accelerometer data. 2010 International Conference on Body Sensor Networks. Singapore, Singapore: 144–150.
10. HOU Haijia, TAN Wei, DAI Bing et al. Comparison of clinical application value of dynamic monitoring of carbon dioxide at different end expiratory rates. Shanxi Medical Journal, 2014, (18): 2123–2126.
11. Kotani K HI, Yamamoto Y. Analysis of Respiratory Sinus Arrhythmia with Respect to Respiratory Phase. Methods Of Information In Medicine, 2000, 39(2):153–156.
12. Phan DH BS, Guillemaud R, Castelli E, Thi NYP. Estimation of respiratory waveform and heart rate using an accelerometer. 30th Annual International Conference of the Ieee Engineering in Medicine and Biology Society. Vancouver, CANADA: 4916–4919.

Comparison of Brain Computer Interface for Selecting Menus that Utilize EEG and NIRS

Akihiko Hanafusa, Keiyo Arai, and Yukari Okawa

Abstract

The authors attempted to develop an environment control system for severely handicapped bed-ridden patients. In this study, we used electroencephalograms (EEG) and near infrared stereoscopy (NIRS) to test and compare a system called "brain computer interface" for the purpose of selecting menus. The feature of the EEG-based system is that wavelet analysis is used to detect the event-related potential P300, and then, to determine the selected menu. Additionally, an appropriate stimulus-to-stimulus interval time of the menu was derived to be approximately 0.50–0.75 s. Regarding the NIRS-based system, real-time feedback was effective in increasing oxygenated hemoglobin (Oxy-Hb) signal, which resulted in a higher success ratio. The average success ratio of EEG-based system was higher than that of NIRS-based system. In general, using the proposed system, the time required to select a menu is shortened, and the feeling of restraint is reduced.

1 Introduction

Brain computer interface (BCI) [1, 2] is a system that is expected to assist severely-disabled person who cannot move their muscles because of muscular dystrophy and amyotrophic lateral sclerosis (ALS). The authors attempted to develop an environment control system that requires the use a computer or control household appliances such as motorized bed, air conditioner and room light. To achieve this purpose, a menu selection interface by means of near infrared spectroscopy (NIRS) [3] or electroencephalogram (EEG) [4] is developed. In the EEG system, a powerful P300 [5], which is a typical event-related potential (ERP) [6, 7], is used. P300 has a positive potential which occurs approximately 300–500 ms after stimulation. In the NIRS system, increased oxygenated hemoglobin (Oxy-Hb) when concentrated to a specified menu is used.

There have been attempts to use NIRS and EEG simultaneously for the BCI [8]. However, the system becomes larger, more complex, and expensive. Our goal is to propose a better and simpler method. In this paper, an overview and features of the system are described and the success ratio of the two methods are compared.

2 Configuration and Signal Processing

2.1 EEG-Based System

Figure 1 shows the configuration of the EEG-based system. The system consists of a wireless bio-amplifier (mobile+, g.tec medical engineering GmbH) and a PC. We developed a series of software that inputs and processes the EEG signals and offers a graphical user interface using MATLAB (MathWorks, Inc.). The active electrodes were set at Cz and Pz according to the international ten–twenty electrode system, and the voltage variation was measured using the right earlobe (A2) as a reference electrode. The Bluetooth wireless bio-amplifier was used to measure the EEG and electro-oculogram (EOG). The EOG was measured to detect an eye blink. The sampling frequency of the bio-amplifier was set to 256 Hz, and the band pass cutting frequency was set to 0.5–100 Hz. Additionally, infrared remote-controlled devices can be connected to the PC by an infrared remote-controlled interface.

The developed software can display characters and the menu (Fig. 1) on the desktop, measure the EEG signal, and

A. Hanafusa (✉) · K. Arai · Y. Okawa
Department of Bio-Science and Engineering, Shibaura Institute of Technology, 307 Fukasaku, Minuma-Ku, Saitama, 337-8570, Japan
e-mail: hanafusa@shibaura-it.ac.jp
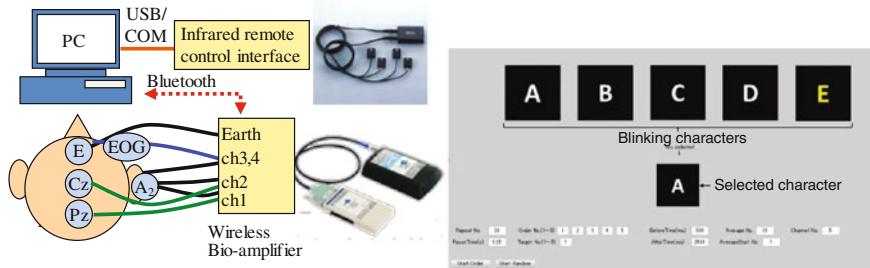
Fig. 1 Configuration of EEG-based BCI system and display of menu interface


(a) Without MRA   (b) With MRA
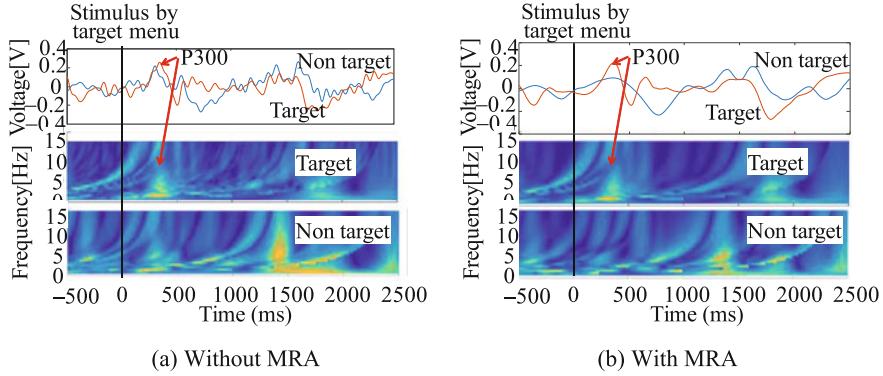
Fig. 2 Configuration of EEG-based BCI system and display of menu interface

output synchronized signals when the color of a displayed illuminated character changes. The characters "A", "B", "C", "D", and "E" change to yellow, and the blinking time interval can be changed. Subjects were asked to count the number of illuminated characters.

The input EEG signal is filtered by a 13-Hz low-pass filter and averaged 15 times. Thereafter, a multi-resolution analysis (MRA) is performed using Daubechies4 as a mother wavelet, and a residual component is selected. Finally, wavelet analysis [9] with a complex-type Morlet mother wavelet is conducted to automatically detect the existence of P300. Figure 2 shows two cases without MRA (Fig. 2a) and with MRA (Fig. 2b). The middle and bottom graphs denote the results of the wavelet analysis of the target and non-target, respectively. The signal becomes smoother with MRA and the difference between the target and non-target becomes clearer with the case in the figure. Further, where the sum of amplitude signal of wavelet signal around P300 area is maximum is selected as a target menu.

2.2 NIRS-Based System

Figure 3 shows the configuration of the NIRS-based system. The system consists of an NIRS measurement system (ETG-4000, Hitachi Ltd.) and a PC. The menu displayed on

the PC is similar to that displayed in the EEG-based system; however, the blinking time is set to more than 10 s. Additionally, the PC and NIRS measurement system is connected by LAN and a feedback bar graph can be shown in the PC window nearly in real time.

ETG-4000 can measure oxyhemoglobin (Oxy-Hb), de-oxyhemoglobin (Deoxy-Hb), and total hemoglobin. Among these signals we used oxyhemoglobin measured from two channels placed on the frontal lobe. The subjects were told to concentrate when menu "C" was displayed, and to try to increase the feedback signal when displayed. An example of the measured signal is shown in Fig. 4. The red line denotes the raw signal, and a pulse wave can be observed. The green line denotes the signal after a spline
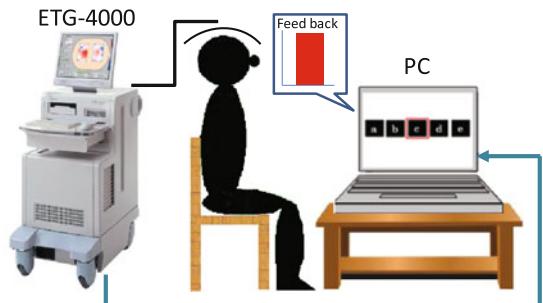

**Fig. 3** Configuration of NIRS-based BCI system
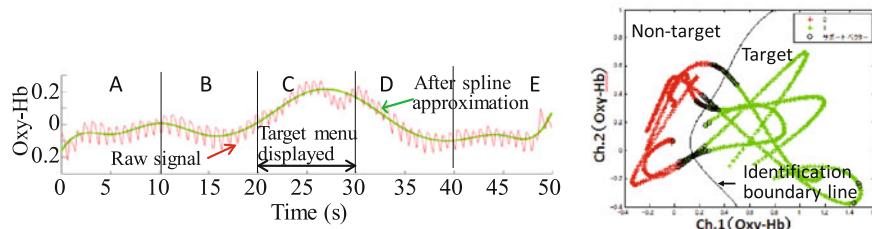
Fig. 4 Measured and processed signal from the NIRS system and scatter plot of two channels used for discrimination by SVM (Color figure online)

approximation and the signal is smoothed. The methods for determining the selections are as follows:

- Max: Where the maximum value of Oxy-Hb is obtained.
- ΔOxy: Where the difference of Oxy-Hb between start and peak is maximum.
- ΔOxy_15 s: Same as above, however processed time region is increased from 10 to 15 s.
- SVM: Discrimination using machine learning method by support vector machine (SVM). An example of scatter plot by two channels and identification boundary line calculated by SVM are shown in Fig. 4.
- SVM_15 s: Same as above, however processed time region is increased from 10 to 15 s.

3   Experimental Results

3.1   EEG Based System

Experiments using the EEG-based system were performed by changing the menu blinking interval time, called stimulus to stimulus interval (SSI). SSIs were changed to 0.25, 0.50, 0.75, and 1.00 s. Eleven healthy subjects tried four cases of SSI ten times. The success ratios with and without MRA were also compared, and the results are shown in Fig. 5.

When SSIs are 0.50 and 0.75 s, the average success ratio was higher than that of when the SSI s are 0.25 and 1.0 s. Additionally, the standard deviation of 1.00 s was larger than the standard deviation of the other cases. The result of the statistical test using Holm method exhibited significant differences between SSI 0.75–0.25 s and 0.50–0.25 s ($P < 0.05$). However, there was no significant difference between the case with MRA and the case without MRA by the two-way analysis of variance (significance level of 5%).
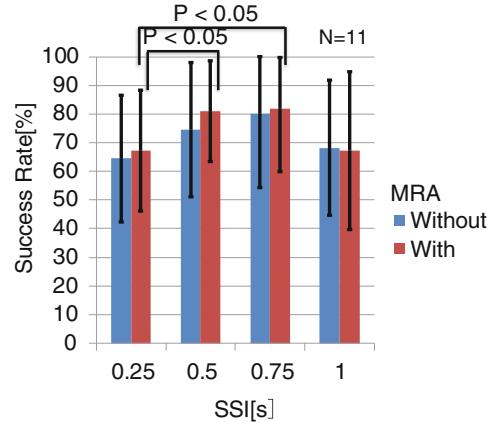
Fig. 5 Success ratio using EEG signal with and without MRA when SSIs were changed to 0.25, 0.50, 0.75, and 1.00 s

3.2   NIRS-Based System

Experiments using NIRS-based system with and without feedback were performed. Out of ten healthy subjects, seven tried the case without feedback and ten tried the case with feedback for six days and fifteen trials for each day. The success ratios were compared by changing the discriminant method. Regarding the SVM case, the first five trials were used as the training data of SVM, and the remaining ten trials were used for discrimination. The results are shown in Fig. 6.

There was significant difference between the case with feedback and the case without feedback by the two-way analysis of variance (significance level of 5%). Additionally, there were trends showing that the average success ratio increased when the processing time region was extended from 10 to 15 s, as in the cases between ΔOxy to ΔOxy_15 s and SVM to SVM_15 s. However, statistical tests showed that there was no significant difference by the discriminant methods.
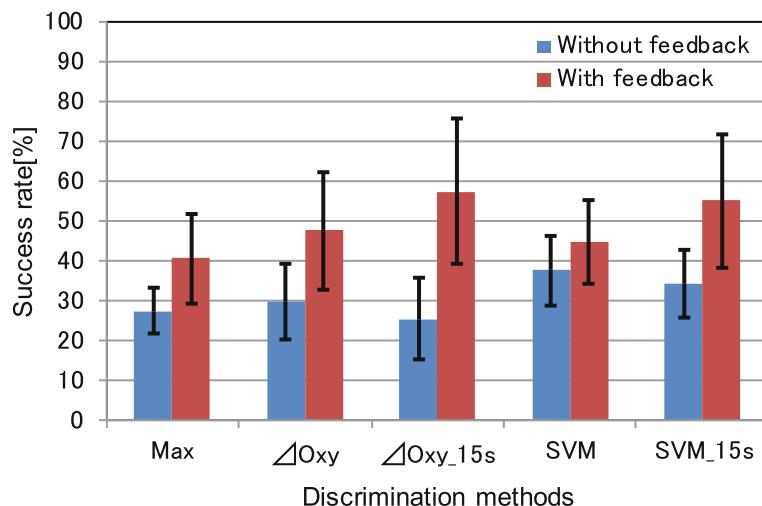
Fig. 6 Success ratio using NIRS signal with and without feedback when the discrimination methods are changed

4 Discussion

From the results of the EEG-based system (Fig. 5), the appropriate SSI time was approximately 0.50–0.75 s. Additionally, an SSI of 0.25 s was very short, and an SSI of 1.00 s was very long. Table 1 lists the time required for one task for each SSI condition. As the EEG signal needs to be averaged 15 times, the blinking time of a character is also repeated fifteen times. When the SSI is 1.00 s, the time for one task is too long and the subjects find it difficult to concentrate on the menu. However, when the SSI is 0.25 s, the P300 signal becomes unclear as it occurs after 0.30 s, which is after the next menu is blinked.

From the results of the NIRS-based system, the success ratio with feedback was higher than that without feedback. By looking at the feedback signal, subjects understand the current level of Oxy-Hb signal and may feel easier to concentrate on the menu to increase it. As the current SSI of the system is 10 s, the time required for selecting one character from 5 characters is 50 s.

In general, in comparison with the NIRS-based system, the success ratio of the EEG-based system is higher, and the time required for one set of experiments is shorter when the illuminating time is less than 0.50 s. Additionally, when

comparing the current system, EEG system is wireless; however, head set of NIRS system is connected to the main enclosure via the optical fiber cable. Thus, the subject may feel stronger restraint feeling when using NIRS-based system.

5 Conclusion

BCI systems based on EEG and NIRS were developed. The feature of the EEG-based system is that wavelet analysis is used to determine the selected menu. An appropriate SSI time of the menu was approximately 0.50–0.75 s. Regarding the NIRS-based system, real time feedback was effective in increasing the success ratio. The average success ratio of the EEG-based system was higher than that of NIRS-based system. In general, using the proposed system, the time required to select a menu was shortened and the feeling of restraint feeling was reduced.

To increase the success ratio and reduce the necessary time, further improvement of menu display and signal processing method is necessary. Additionally, experiments on patients are necessary to ensure the effectiveness of the method.

Table 1 Necessary time for one task for each SSI condition

SSI condition (s)	Necessary time (s)
0.25	18.75
0.50	37.50
0.75	56.25
1.00	75.00

References

1. M. A. Lebedev and M. A. Nicolel, Brain machine interfaces: past, present and future. Trends in Neurosciences, 29(9), pp. 536–546 (2006).

2. L. F. Nicolas-Alonso, J. Gomez-Gil, Brain computer interfaces, a review. Sensors 12(2), pp. 1211–1279 (2012).
3. L. C. Schudlo, S. Weyand, T. Chau: A review of past and future near-infrared spectroscopy brain computer interface research at the PRISM lab. Proc. of 36th Annual International Conference of the IEEE, pp. 1996–1999 (2014).
4. J. Minguillon, M. Angel, L. Gordo, F. Pelayo: Trends in EEG-BCI for daily-life: Requirements for artifact removal, Biomedical Signal Processing and Control 31, pp. 407–418 (2017).
5. A. Furdea, S. Halder, et al: An auditory oddball (p 300) spelling system for brain-computer interfaces. Psychophysiology, 46: pp. 617–625 (2009).
6. S. Sutton, et al: Evoked-Potential Correlates of Stimulus Uncertainty. Science, 150(3700), pp. 1187–1188 (1965).
7. N. Kanou, K. Sakuma, K. Nakashima, Communication of ALS Patients by Detecting Event-Related Potential. IEE J Trans. EIS, 127(3), pp. 305–311 (2007).
8. Y. Tomita, F. B. Vialatte, G. Dreyfus, et al: Bimodal BCI Using Simultaneously NIRS and EEG, IEEE Transactions on Biomedical Engineering 61(4), pp. 1274–1284 (2014).
9. I. Daubechies: Ten Lectures on Wavelet (CBMS-NSF Regional Conference Series in Applied Mathematics). Springer, 98(2007).

Preprocessing of the BSPM Signals with Untraditionally Strong Baseline Wandering

Michal Huptych, Matěj Hrachovina, and Lenka Lhotská

Abstract

The BSPM is a special setup of the ECG measurement with many of electrodes (20–256) on the body surface. Results of the measurement are strongly dependent on many conditions like body shape, contact of electrodes and skin, patient position and movements. Of course, these conditions are crucial also for standard ECG measurement, but obviously, problems with the conditions are more probable during the BSPM signals acquisition. In this paper, we would like to present a problem with the Body Surface Potential Mapping (BSPM) ECG preprocessing caused by unexpected signal interruption due to the significant baseline wandering and derivate problems which are generated by solving of this baseline wandering filtration. This problem is major for next signal processing (mainly ECG delineation) because the baseline wandering problem is closely connected with the determination of ECG signals' isoline. We use a system of 120 electrodes on body front and back. The experimental measurements are arranged in the clinical environment with maximal treatment to electrodes position and contact of electrodes and skin at the beginning of the measurement. Unfortunately, obtained signals contain often extreme baseline wandering bedsides of standard artefacts. This baseline wandering seems to be created most likely by patient movements and a change of the electrodes contact. Moreover, we have observed that the standard artefact filtration and the extreme baseline wandering filtration are against each other.

M. Huptych (✉) · L. Lhotská
Czech Institute of Informatics, Robotics and Cybernetics, Czech Technical University in Prague, Prague, Czech Republic
e-mail: Michal.Huptych@cvut.cz

M. Hrachovina
Department of Cybernetics, FEE CTU, Prague, Czech Republic

L. Lhotská
Faculty of Biomedical Engineering, Czech Technical University in Prague, Prague, Czech Republic

1 Introduction

Cardiac resynchronization therapy (CRT) is a relevant treatment of the heart failure. Its influence on decreasing morbidity and mortality was demonstrated in many studies, e.g. [1–3]. Indicators for the CRT intervention are symptomatic chronic heart failure with symptoms lasting despite optimized pharmacological treatment and simultaneously systolic dysfunction of the left ventricle with an ejection fraction ≤35% [4]. One of the open issues is an evaluation of the CRT intervention result with non-invasive measurement and diagnosis techniques. In our project, we aimed at studying of the electrical dyssynchrony by Body Surface Potential Mapping (BSPM) processing in order to quantify the ICT therapy progress. The first step of BSPM is specific measurement (multichannel ECG), which provides, unlike conventional 12-leads electrocardiography, the non-invasive acquisition of cardiac activity from 24–300 electrodes. The example of our electrodes settings (system Biosemi [5]) is depicted in Fig. 1. The multichannel ECG increases spatial sampling of the measurement on the body surface and thus provides more detailed information on the electrical activity of the heart. Therefore, this approach can lead in many cases to better diagnostic value regarding spatial and temporal information of the electrical activity of the heart [1, 4].

Besides providing the whole information on the cardiac electric field available at the body surface, the multichannel ECG is more sensitive in detecting local electrical events, such as local conduction disturbances or regional heterogeneities of ventricular recovery. On the other side, the multichannel ECG has also disadvantages, especially more demanding measurement given mainly by request to place many electrodes. The final product of multichannel ECG
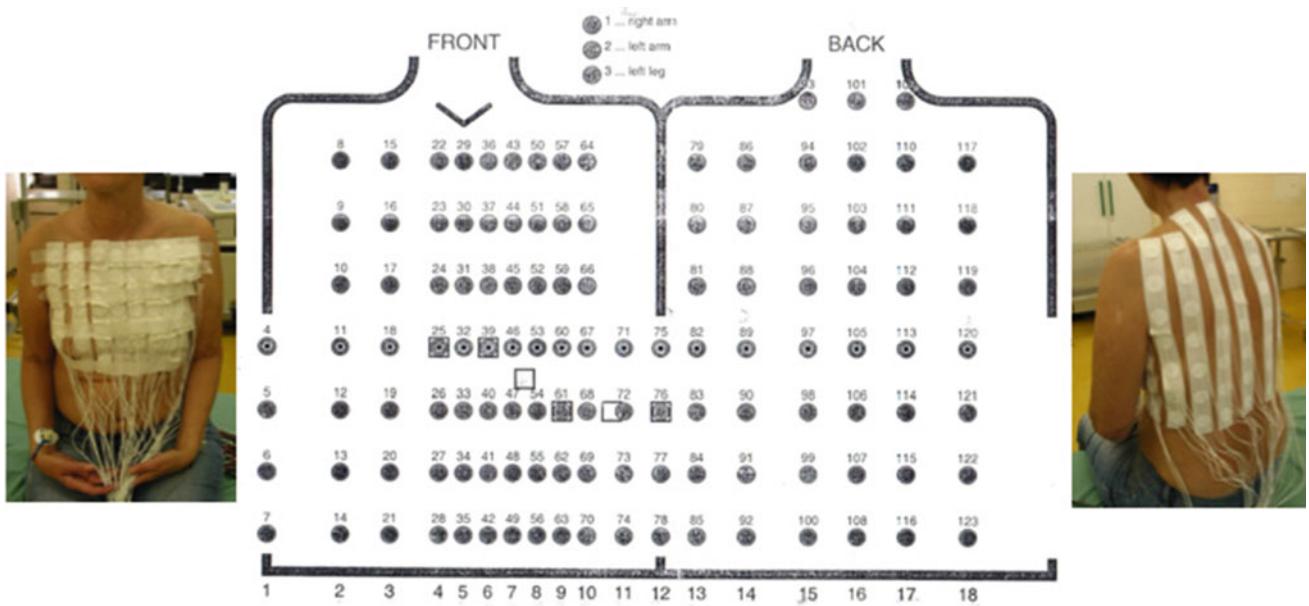
Fig. 1 The electrodes' grid of 120 leads Biosemi system (in the middle) and example of electrodes placed on the chest (on left) and the back (on right) in practice

measurement is a collection of Body Surface Potential Maps (BSPM). These maps are a visualization of the time-spatial electrical activity of heart on body surface and there are several modes how is possible this activity visualize and analyze. The most frequently used body surface maps are isopotential map, depicting a distribution of the potential in each moment of the measurement, and isointegral map, providing a distribution of the sum of potentials over a specified time interval.

In a joint project with the Department of Cardiology of the University Hospital Motol Prague, we focus on the BSPM data processing and analysis. Electrical dyssynchrony is analyzed and quantified from BSPM and for selected patients also from endocardial electrical mapping of the left ventricle using electro-anatomical mapping system CARTO. There are several studies describing this topic, e.g. [6, 7]. However, the preprocessing and filtration techniques are either not described or they are not reproducible for our data. Thus, in the paper we describe an important step in multi-channel ECG preprocessing, namely signal filtration, which proved to be crucial for the next steps in signal analysis.

BSPM is traditionally used for mapping of electrical activity propagation along chest and back. Moreover, there is an idea to use the BSPM for finding early activation sites of the cardiac muscle. This approach would be less burdensome and more comfortable for a patient because BSPM is the non-invasive method while diagnosis by the catheter is the invasive method. In both of BSPM applications, the quality of signals is crucial for next processing, e.g. labeling the ECG and extracting feature timing. Therefore, the aim of

filtration is to cancel as much noise as possible without altering the ECG components (mainly Q, R, S and T waves).

2 Materials and Methods

2.1 Signal Acquisition

BSPM Signals are recorded from unipolar leads referenced against Wilson's central terminal (WCT), which is formed by the mean of the bipolar limb signals.

$$V_{WCT} = \frac{(RA + LA + LL)}{3}$$

The raw signals are saved referenced to a virtual floating reference though, so the WCT signal needs to be subtracted from each lead. The recorded signals contain the direct current (DC) offset induced during amplification. The easiest and most commonly used method of eliminating DC offset during post-processing is subtracting the mean of the signal itself.

2.2 Signal Noise Background

Although the measurements are arranged with maximal treatment to electrodes position and contact of electrodes and skin, there are three important sources of noise in the signal: mains hum, motion artefacts, and bad electrodes' contact. The most impacted problem for us is the bad electrodes'

contact. Usually, the electrode-skin impedance is slightly changed during the ECG measurement. However, these changes are slow and have a minimal effect on the useful signal. In the case of bad contact of electrode and skin, the impedance changes strongly, the amplitude of the measured signal changes accordingly, but with weak correspondence to the ECG signal [8]. This is the common problem at multichannel measurements generally that an electrode does not stick to the skin well enough and lose contact. Unfortunately, in our case, we do not have any indication of the electrode-skin impedance change and it is impossible to monitor the electrodes constantly. Moreover, it is very complicated and unreliable to record impedance of the electrode during the measurement. Therefore, there is no way of reconstructing the signal from the lead where electrode impedance is unstable.

2.3 Filtration Methods

The baseline wander caused by breathing or (slow) movement is a low frequency induced noise under 1 Hz (AHA guidelines state 0.67 Hz threshold). This noise is possible to remove by high pass filters. There has to be a compromise between filter strength, signal distortion, and filtering duration. The higher order of the filter, the better filtration result, but the filtration is longer (here it is necessary to realize we have 2048 Hz sample rate). Moreover, the type of the filter is also very important. The Infinite Impulse Response (IIR) filters need lower order to achieve good attenuation, but their phase is not linear, which can corrupt the ECG signal morphology. This fact is crucial for ECG filtration. Therefore, Finite Impulse Response (FIR) filters are preferred, although they need higher order and thus take longer time to filter. However, even filters with linear phase can have a problem with signal distortion as shown in [9]. A further problem is that it shows that even when using cutoff frequency of 0.67 Hz, according to guidelines, the higher frequency components of the QRS complex are phase shifted and consequently mixed with the signal of the S wave, thus causing the wrongly high amplitude of the S wave. The problem of hum noise removing is problem of removing of a narrow band signal. For this process, a FIR filter cannot be effectively used and we use an IIR filter. If we suppose that all other noise is represented by random (relatively stationary) signals with the even probability distribution and it is sufficient to use a single beat of the resulting processed signal, we can use averaging of the signal to improve the final quality. The first step in this processing is annotating the individual beats. We have used R peak detection because its detection is the most robust in the whole signal. The second step is verifying that the beats, that were selected for the averaging, are similar. Our chosen

criteria were defined for R-R intervals, where the R-R intervals must be within ±5% of the median R-R interval within the whole recording and the inter-beat R-R variability must not be over 3% of the median.

3 Results

In Fig. 2, there are depicted original signal (the green line) and three variants of the filtration. The baseline wandering in Fig. 2 is not the strongest one which we have observed in records, but it is a good example because it contains many types of others signal disturbing. Further, here it is necessary to mention that the rapid spike in the green signal is not R peak but the stimulation impulse from implanted artificial cardiac pacemaker. In order to remove the motion artefacts and baseline drift, we use a sequence of a low-pass and a high-pass filters. We use two separate filters of lower order instead of the band-pass filter with the significantly higher order.

The first variant of the filtration (the red line in Fig. 2) is performed by two Butterworth filters of the first order, the low pass filter with cutoff frequency 45 Hz and the high pass filter with cutoff frequency 0.67 Hz. This filtration appears to be very useful but only up to the moment where we want to detect individual components of the ECG, as it distorts the Q, S and T waves, which are of upmost importance in the analysis of the CRT therapy.

For the second filtration (the black signal in Fig. 2), there are used sequence of three filters. The first one is moving average low pass with cutoff frequency of 80 Hz. The second filter is same like in the first variant IIR notch filter with cut-off frequency 50 Hz and 3 dB bandwidth of 6 Hz. The last filtration is again moving average but now the high pass filter with cutoff frequency of 0.6 Hz.

The third variant of the filtration (the blue signal in Fig. 2) use the low pass FIR filter with cutoff frequency 100 Hz and length of filter a half of sample rate. The high pass filtration is performed by the FIR filter with cutoff in 0.67 Hz, moving average filter with length 1.2 times sample frequency. The hum noise was removed by IIR notch filter with cut-off frequency 50 Hz and 3 dB bandwidth of 6 Hz. As we can see in Fig. 2, this filter sequence is very soft on attenuating high frequencies, thus it barely removes the pacing spike. It is a compromise between computational efficiency and phase distortion of the onset of Q and S wave.

Final effect of the filtration methods on the potential maps is difficult to evaluate. Theoretically, what we can test is the difference between the labeled signal features. However, the problem is complicated by the fact that the ECG waveforms are pathological and we cannot use simple automatic waveform delineation methods, but they need to be labeled by experts. Moreover, we do not have still enough patient
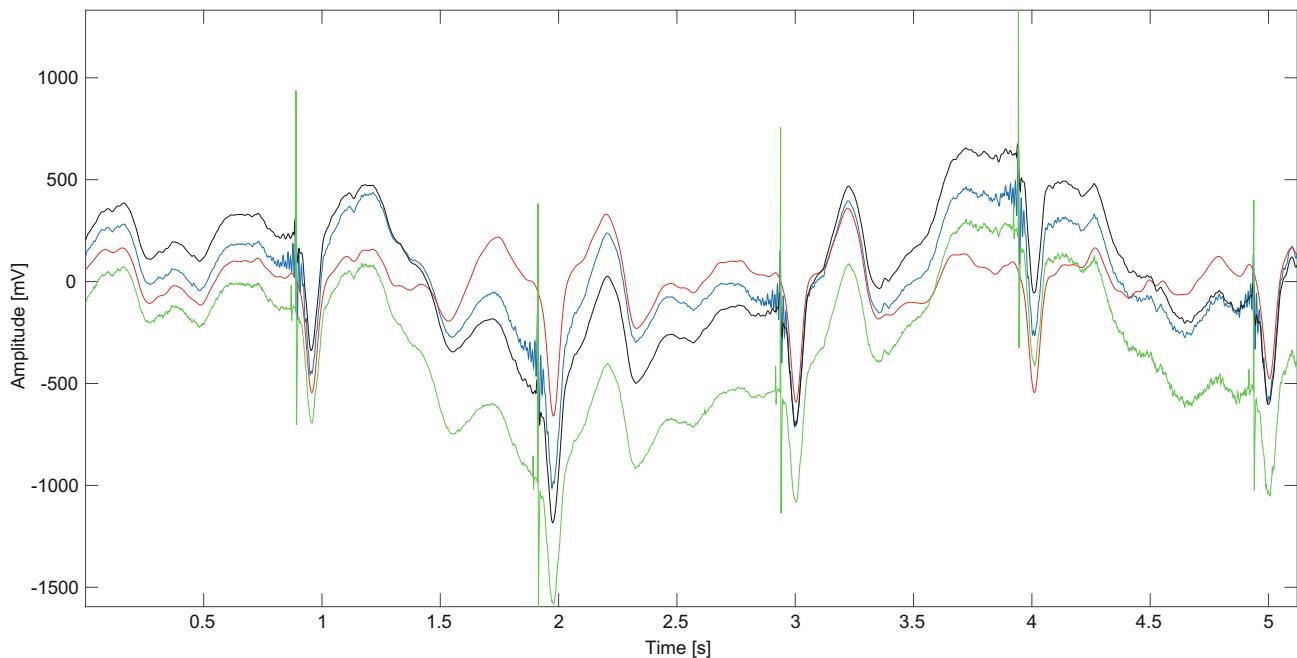
Fig. 2 Example of one channel from multichannel ECG measurement, the green line is the original signal, the red one is the first filtration variant (2nd paragraph of the chapter Result), the black is the second variant (3rd paragraph of the chapter Result) and the blue is the third variant of filtration (4th paragraph of the chapter Result) (Color figure online)

data to compare. However, current results prove that the designed experimental protocol and pre-processing methods are correct and we can acquire unique data.

4 Conclusion

The multichannel measurement is a complex task where must be considered aspects like electric noise, noise-induced from breathing and motion, patient proportions influencing electrode placement, and proper electrode-skin contact. As expected, the next step of data preprocessing is similarly challenging since the artefacts and noise vary in particular channels. Thus, there is not possible to apply only one method of filtration and expect perfect results in all channels. Especially, if there is one more pronounced noise type combined with others. We tried to present three sequences of the filtration, which each has several advantages and disadvantages not only from the perspective of filtration result but also from the perspective of the next processing. Momently, our conclusion is the compromise between better baseline wandering filtration and preserving of proper morphological ECG shapes. Even though the methods were not evaluated quantitatively, they have been justified as sufficient for accurate delineation of ECG signals by the clinicians and physiologist experts that were assessing them.

Conflict of Interest The authors declare that they have no conflict of interest.

Statement of Informed Consent The study protocol and patient informed consent have been approved by the University Hospital Motol ethical committee.

Protection of Human Subjects and Animals in Research The procedures followed were in compliance with the ethical standards of the responsible committee on human experimentation (institutional and national) and with the World Medical Association Declaration of Helsinki on Ethical Principles for Medical Research Involving Human Subjects.

References

1. Abraham WT, Fisher WG, Smith Al, et al. Cardiac resynchronization in chronic heart failure. N Engl J Med 2002; 346(24):1845–53.
2. Cleland JG, Daubert JC, Erdmann E, et al. The effect of cardiac resynchronization on morbidity and mortality in heart failure. N Engl J Med 2005;352(15):1539–49.
3. Bristow MR, Saxon LA, Boehmer J, et al. and the Comparison of Medical Therapy, Pacing And Defibrillation in Heart Failure Investigators. Cardiac resynchronization therapy with or without an implantable defibrillator in advanced chronic heart failure. N Engl J Med 2004; 350:2140–2150.

4. Brignole M, Auricchio A, Baron-Esquivias G, et al. 2013 ESC Guidelines on cardiac pacing and cardiac resynchronization therapy: the Task Force on cardiac pacing and resynchronization therapy of the European Society of Cardiology (ESC). Developed in collaboration with the European Heart Rhythm Association (EHRA). Eur Heart J 2013; 34:2281–2329.

5. Biosemi. https://www.biosemi.com/, Available 02/04/2018.

6. Giffard-Roisin, S., T. Jackson, L. Fovargue, et al. 'Noninvasive Personalization of a Cardiac Electrophysiology Model from Body Surface Potential Mapping', IEEE Transactions on Biomedical Engineering, vol. 64/no. 9, (2017), pp. 2206–2218.

7. Wang, Yong, and Yoram Rudy. 'Application of the Method of Fundamental Solutions to Potential-Based Inverse Electrocardiography', Annals of Biomedical Engineering, vol. 34/no. 8, (2006), pp. 1272–1288.

8. Taji, Bahareh, Shervin Shirmohammadi, Voicu Groza, and Izmail Batkin. 2014. Impact of skin-electrode interface on electrocardiogram measurements using conductive textile electrodes. IEEE Transactions on Instrumentation and Measurement 63 (6): 1412–22.

9. Buendía-Fuentes, F., M. A. Arnau-Vives, A. Arnau-Vives, et al. 'High-Bandpass Filters in Electrocardiography: Source of Error in the Interpretation of the ST Segment', ISRN Cardiology, vol. 2012 (2012), 10 pages.

Empirical Mode Decomposition in Analysis of Hemodynamic Response to Static Handgrip

Norbert Olenderek, Gerard Cybulski, Krzysztof Krzemiński, Wiktor Niewiadomski, Anna Gąsiorowska, and Anna Strasz

Abstract

The empirical mode decomposition (EMD) of biological signals is used to detect reaction to physiological stimuli and to identify global trends in slowly changing variables. We applied EMD to analyze hemodynamic reaction to handgrip in 9 healthy males (aged 21.3 ± 0.3 years) and 10 male patients following coronary artery bypass grafting (aged 55 ± 6 years). Subjects squeezed a dynamometer with 30% of individually determined maximal force for 3 min. The aim of the study was to check whether the application of EMD to the signals could bring any objective quantitative or qualitative measures allowing one to distinguish physiological states of healthy subjects and patients. Hemodynamic data were collected using a battery-powered, ambulatory impedance cardiography device (ReoMonitor) incorporating a single ECG channel. Heart rate (HR), R-R interval (RR), stroke volume (SV), cardiac output (CO), left ventricular ejection time (ET), pre-ejection period (PEP), maximum amplitude of the dz/dt signal (Amp), and basic chest impedance (Z0) were calculated automatically using the software earlier developed for ReoMonitor. The dedicated computer program allows to calculate and display the dynamics of basic and derivative parameters, describing the impact of systolic time intervals on RR intervals, or the relationship between them (e.g. PEP/ET). The EMD procedure was applied to identify the components of each basic hemodynamic parameter and all their derivatives. We observed the most pronounced effect of handgrip in second and third intrinsic mode functions (IMF), which particularly manifested in parameters describing the ratio of systolic time intervals to the length of RR.

Keywords

Empirical mode decomposition • Hemodynamic response to Handgrip • Impedance cardiography

1 Introduction

1.1 Motivation

Static exercise causes increase in heart rate (HR) and cardiac output (CO) and raises systolic (SBP) and diastolic (DBP) blood pressures, whereas effect on stroke volume (SV) is unclear. These responses are related mainly to the neural effects on the heart, including changes in the activities of both the parasympathetic and sympathetic systems induced by central command modulated by signals from mechanoreceptors and metaboreceptors [1, 2]. The hemodynamic response to this specific exercise was analyzed in several papers showing the dynamics of the response [2–6]. They used impedance cardiography (ICG) for noninvasive beat-to-beat acquisition of hemodynamic parameters.

1.2 Aim of the Study

The empirical mode decomposition (EMD) of biological signals is used to detect reaction to physiological stimuli and to identify global trends in slowly changing variables [7]. In this study, we used some data from previously published researches [2, 6] with the aim of checking whether the application of EMD to the signals could bring any objective quantitative or qualitative measures allowing one to distinguish physiological states of healthy subjects and patients.

N. Olenderek · G. Cybulski (✉)
Faculty of Mechatronics, Institute of Metrology and Biomedical Engineering, Warsaw University of Technology, Św. Andrzeja Boboli 8, Warsaw, Poland
e-mail: G.Cybulski@mchtr.pw.edu.pl; cybulski@mchtr.pw.edu.pl

K. Krzemiński · W. Niewiadomski · A. Gąsiorowska · A. Strasz
Department of Applied Physiology, Mossakowski Medical Research Centre, Polish Academy of Sciences, Warsaw, Poland

2   Materials and Methods

2.1   Impedance Cardiography (ICG)

Hemodynamic data were collected using a battery-powered, ambulatory impedance cardiography device with a single built-in ECG channel (ReoMonitor) [8–11]. Heart rate (HR), length of R-R interval (RR), stroke volume (SV), cardiac output (CO), left ventricular ejection time (ET), pre-ejection period (PEP), maximum amplitude of the dz/dt signal (Amp), andbasic chest impedance (Z0) were calculated automatically using the dedicated software developed earlier for the ReoMonitor system. Hemodynamic data from ReoMonitor system had previously been verified using pulsed Doppler echocardiography [12].

2.2   Dedicated Computer Program

We developed a new program (running in the MATLAB environment) whose features include importing hemodynamic parameters for subsequent time periods and plotting their changes over time. It also allows calculation and display of the dynamics of basic and derivative parameters, describing the impact of systolic time intervals on the lengths of RR intervals or related parameters, or the relationships between them (e.g. ET/RR, PEP/RR, PEP/ET, (ET + PEP)/RR). The program also applied the EMD procedure to identify the components of each basic hemodynamic parameter and all their derivatives.

2.3   Subjects and Protocol

The analyses were performed using data from two groups of people – 9 healthy males aged 21.3 ± 0.3 years and 10 male patients following coronary artery bypass grafting (aged 55 ± 6 years). Subjects in both groups were instructed to squeeze a dynamometer with a force of 30% of their maximal force and keep up the effort for 3 min or until exhaustion, whichever happened first. The detailed characteristic of the patients was described in earlier papers [2, 6].

2.4   Data Analysis

The EMD procedure was applied to identify the components of each basic hemodynamic parameter and all their derivatives.

   The EMD method—decomposition into empirical modes named intrinsic mode functions (IMF)—allows the presentation of non-stationary and non-linear signals as the sum of simpler components in the time domain. It separates components that overlap in time and frequency. The method allows time-domain determination of the signal energy distribution for the frequencies occurring in them—from the largest to the smallest. The lower-frequency components are successively separated from the highest-frequency component.

   An IMF is defined as a function that satisfies the following requirements [7]:

1. In the whole data set, the number of extrema and the number of zero-crossings must not differ by more than one.
2. At any point, the mean value of the envelope defined by the local maxima and the envelope defined by the local minima is zero.

   "It represents a generally simple oscillatory mode as a counterpart to the simple harmonic function. By definition, an IMF is any function with the same number of extrema and zero crossings, whose envelopes are symmetric with respect to zero" [7].

3   Results

3.1   Empirical Mode Decomposition

An example of a decomposed stroke volume (SV) signal obtained from a young, healthy man during handgrip is presented in Fig. 1. The original signal is visualized in the top left subplot. In subsequent subplots, the consecutive intrinsic mode functions are presented. Time is shown in seconds. The handgrip exercise started at 180 s and finished at 360 s. An example of a decomposed handgrip SV signal inform a patient following coronary artery bypass grafting is presented in Fig. 2. Table 1 and Table 2 present summarized hemodynamic parameters in healthy subjects and patients, respectively.

4   Discussion and Conclusions

4.1   Main Findings

We did not find in the literature papers describing the application of EMD to ICG signals collected during a static handgrip exercise. The EMD procedure was used to identify the components of each basic hemodynamic parameter. We observed the most pronounced effect of handgrip in the second and third intrinsic mode functions (IMF) in some hemodynamic parameters (e.g. SV, CO, ET). We found differences between the groups in time course of HR, CO
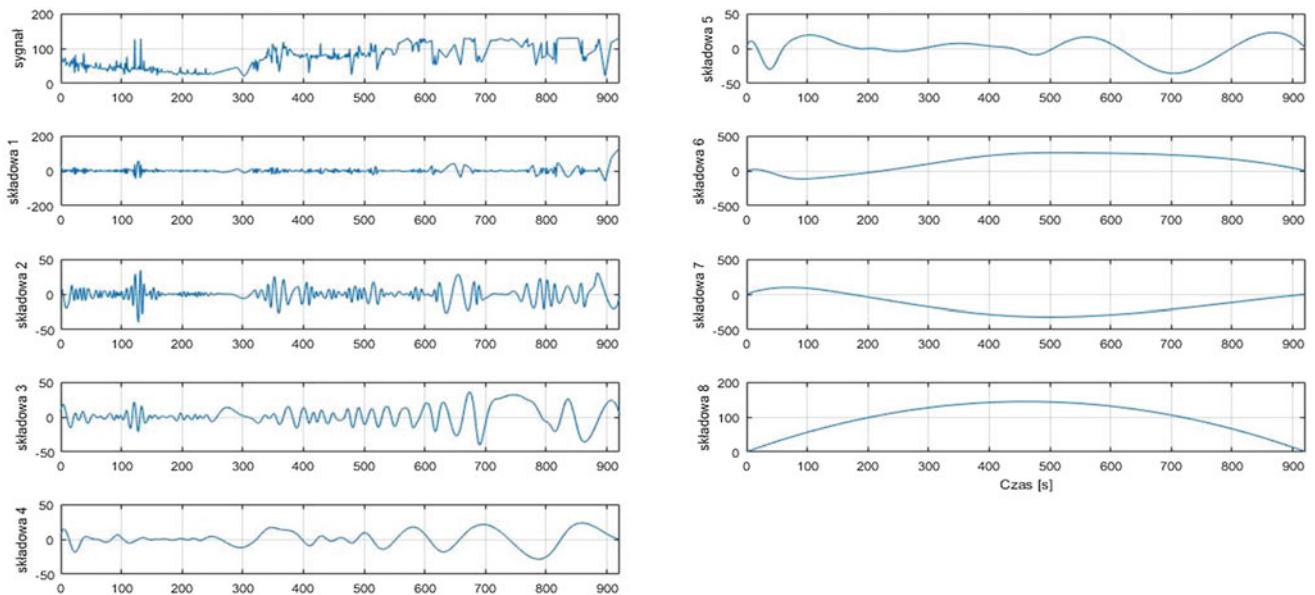
Fig. 1 An example of a decomposed stroke volume (SV) signal obtained during the handgrip exercise, performed by a young, healthy man. In the top left subplot, the original signal is presented. In subsequent subplots, the consecutive intrinsic mode functions are presented. Time is presented in seconds. The handgrip exercise started at 180 s and finished at 360 s
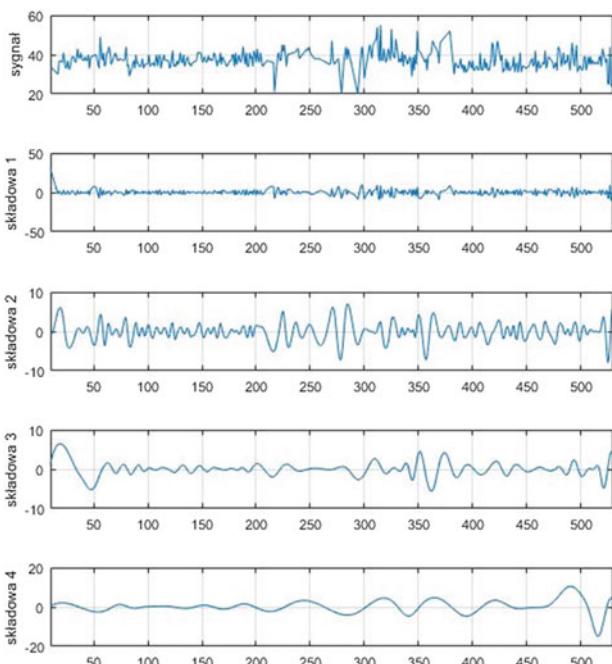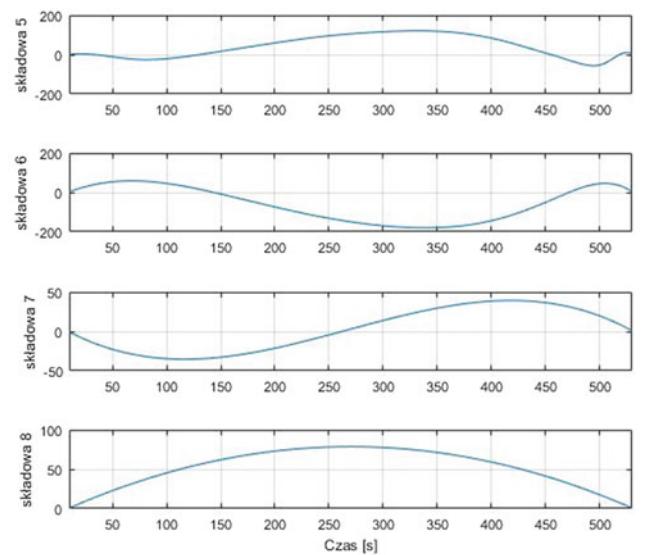

Fig. 2 An example of a decomposed stroke volume (SV) signal obtained during handgrip, performed by a patient following coronary artery bypass grafting. In subsequent subplots, the consecutive intrinsic mode functions are presented. Time is presented in seconds. The handgrip exercise started at 180 s and finished at 360 s

Table 1 Summarized hemodynamic parameters in healthy subjects expressed as mean ± SD. Symbol (*) denotes statistical significance of (p < 0.05) of the difference Δ (180–0 s) within the group, symbol (#) denotes statistical significance of (p < 0.05) between the patients and healthy subjects

Parameter	Rest (0 s)	E (90 s)	E (180 s)	Rec. (60 s)	Δ (180–0 s)
HR (1/min)	77.0 ± 16.6	87.4 ± 7.4[#]	89.5 ± 13.4	91.9 ± 14.8[#]	12.6 ± 12.2[*]
SV (ml)	62.4 ± 15.6	62.5 ± 16.2	70.0 ± 12.9	65.5 ± 9.1	7.6 ± 15.6
CO (l/min)	4.79 ± 1.58	5.76 ± 1,78	5.96 ± 0.79	5.81 ± 0.79[#]	1.17 ± 1.14[*,#]
ET (ms)	286 ± 24[#]	271 ± 26[#]	285 ± 17[#]	284 ± 13[#]	−2 ± 21
PEP (ms)	79 ± 22	71 ± 18	69 ± 11	78 ± 15	−10 ± 14
PEP/ET	0.28 ± 0.08	0.26 ± 0.08	0.26 ± 0.06	0.28 ± 0.06	−0.03 ± 0.05

Table 2 Summarized hemodynamic parameters in patients. Description as for Table 1

Parameter	Rest (0 s)	E (90 s)	E (180 s)	Rec. (60 s)	Δ (180–0 s)
HR (1/min)	66.2 ± 11.0	71.5 ± 11.3	76.8 ± 17.0	60.6 ± 8.7	10.6 ± 11.7*
SV (ml)	41.8 ± 23.0	42.7 ± 29.2	42.6 ± 23.9	39.6 ± 21.8	0.8 ± 7.4
CO (l/min)	2.99 ± 2.01	3.21 ± 2.24	3.54 ± 2.05	3.05 ± 1.99[#]	0.55 ± 0.88[#]
ET (ms)	334 ± 24[#]	340 ± 25[#]	329 ± 49[#]	331 ± 43[#]	−5 ± 32
PEP (ms)	95 ± 17	94 ± 23	90 ± 19	86 ± 12	−5 ± 14
PEP/ET	0.28 ± 0.05	0.28 ± 0.07	0.28 ± 0.08	0.27 ± 0.05	0.00 ± 0.06

and ET, exemplified in Tables 1 and 2. However, in our opinion EMD did not reveal any significant difference between healthy subjects and patients in patterns of hemodynamic parameter signals.

4.2 Importance of Applied Analysis and Study Limitations

There is growing interest in the use of non-invasive holter-type tests (e.g., portable ICG) under the conditions of daily activity, which is associated with increased occurrence of artifacts. Software that analyzes changes in hemodynamic parameters under the influence of various stimuli may support basic cardiovascular studies. The amplitude of the intrinsic mode function of non-stationary and non-linear biological signals is sensitive to disruptions, which helps to determine the times when these occurred. Also, we hope that signals decomposed by EMD (IMF 2 and IMF 3) might be used in automatic detection of characteristic points in signals recorded during handgrip exercises (the onset of exercise, the end of exercise, and occasionally higher intensity of exercise). However, it must be emphasized that this study was performed on a very limited data set.

References

1. Shepherd, JT., Blomqvist, GB., Lind, AR., Mithell JH., Saltin, B. Static (isometric) exercise. Supp. I. Circ Res 48(I), 179–188 (1981).
2. Krzemiński K., Cybulski G., Ziemba A., Nazar K. Cardiovascular and hormonal responses to static handgrip in young and older healthy men. European Journal of Applied Physiology 112 (4), 1315–1325 (2012).
3. Grucza, R., J F Kahn, JF., Cybulski, G., Niewiadomski, W., Stupnicka, E., Nazar, K. Cardiovascular and Sympatho-Adrenal Responses to Static Handgrip Performed With One and Two Hands" Appl Physiol Occup Physiol 59 (3), 184–188 (1989).
4. Grucza, R., Smorawski, J., Cybulski, G., Niewiadomski, W., Kahn, JF., Kapitaniak, B., Monod, H. Cardiovascular response to static handgrip in trained and untrained men. Eur J Appl Physiol 62, 337–341 (1991).
5. Krzemiński, K., Cybulski, G., Nazar K.. Relationships between plasma adrenomedullin concentration and systolic time intervals during static handgrip in patients with heart failure. Clinical Physiology and Functional Imaging. 29(2), 114–22 (2009).
6. Bilinska M., Kosydar-Piechna M., Gasiorowska A., Mikulski T., Piotrowski W., Nazar K., Piotrowicz R. Influence of dynamic training on hemodynamic, neurohormonal responses to static exercise and on inflammatory markers in patients after coronary artery bypass grafting. Circ J. 74(12), 2598–604 (2010).
7. Huang, N. E., Shen, Z., Long, S. R., Wu, M. C., Shih, H. H., Zheng, Q., Yen, N. C., Tung, C. C., Liu, H. H. (1998). The Empirical Mode Decomposition and the Hilbert Spectrum for

Nonlinear and Nonstationary Time Series Analysis. Proceedings of the Royal Society of London A. 454, 903–995 (1971).

8. Cybulski, G., Książkiewicz, A., Łukasik, W., Niewiadomski, W., Pałko T. Ambulatory monitoring device for central hemodynamics and ECG signals recording on PCMCIA flash memory cards, Computers in Cardiology 1995, IEEE, Vienna, Austria, September 10–13, Computers in Cardiology 1995, IEEE. 1995, pp. 505–7 (1995).

9. Cybulski G. Computer method for automatic determination of stroke volume using impedance cardiography signals, Acta Physiologica Polonica, 39 (5–6), 494–503 (1988).

10. Cybulski G., Ambulatory Impedance Cardiography, Lecture Notes in Electrical Engineering, 76, https://doi.org/10.1007/978-3-642-11987-3_2, Springer-Verlag, Berlin Heidelberg (2011).

11. Cybulski, G., Ziółkowska, E., Kodrzycka, A., Niewiadomski, W., Sikora, K., Książkiewicz, A., Łukasik, W., Pałko T. Application of Impedance Cardiography Ambulatory Monitoring System for Analysis of Central Hemodynamics in Healthy Man and Arrhythmia Patients. Computers in Cardiology 1997, IEEE., 509–12 (1997).

12. Cybulski G., Michalak E., Koźluk E., Piątkowska A., Niewiadomski W., Stroke volume and systolic time intervals: beat-to-beat comparison between echocardiography and ambulatory impedance cardiography in supine and tilted positions, Medical and Biological Engineering and Computing, 42, 707–711 (2004).

A Rapid Assessment Method on Fistula Stenosis Staging for Hemodialysis Patients

Yu-Yao Wang, Chung-Dann Kan, Wei-Ling Chen, and Kuo-Sheng Cheng

Abstract

The AV access is usually evaluated by feeling thrill and pulsation through palpation, listening for the bruit by using a stethoscope, Doppler ultrasound imaging, or angiography, etc. However, these techniques require specific equipment and operator. Phonoangiography is a noninvasive tool for identifying vascular diameter change. In this study, a mock model has been set up to simplify the simulation of blood flow condition. Phonographic signal is recorded by electronic stethoscope and further signal processed. The relationship of phonographic signals and stenotic lesions is studied. Early detection of hemodialysis access problems such as stenosis and thrombosis is very important issue. The purpose of this study is to develop a phonographic system to evaluate arteriovenous shunt (AVS) stenosis of hemodialysis patients. The degree of stenosis (DOS) is used as an index to classify the AV access condition, and is determined by the narrowing percentage of normal vessels. In this mock model, the DOS is set to be varied from 0, 50, 70, 80, 85, 90, 92.5 to 95%. The empirical mode decomposition (EMD) method is applied to analyze the relationship between DOS and spectrogram. Verification is based on Doppler ultrasound which is the golden standard in clinical application. From the experimental results, the proposed method is demonstrated to be feasible for charactering the staging of DOS conditions. There is a great correlation between the phonoangiography and the severity of DOS in AV access. This noninvasive method may be useful and potential for early detection in home-care use.

1 Introduction

1.1 Background

According to the United States Renal Data System (USRDS) report in 2015, both number of end-stage renal disease, also called end-stage kidney disease (ESRD) incidence and prevalence are the most in the world [1]. Although the number of kidney disease patients is not the most in Taiwan, but the health insurance cost is the highest in 2015 [2]. It implies that kidney disease treatment is definitely an important issue in Taiwan.

1.2 Arteriovenous Shunt (AVS)

Hemodialysis patients need a particular blood vessel which can draw enough blood flow to do dialysis. Currently, there are two types of AVS in arms, i.e., Arteriovenous Fistula (AVF) and Arteriovenous Graft, respectively. AVF is connected by patients' own brachial artery and cephalic vein. In contrast, AVG refers to the connection of brachial artery and cephalic vein with an artificial blood vessel in between.

1.3 Arteriovenous Shunt Problem

Hemodialysis patients must visit the hospital two or three times per week for hemodialysis treatment. During each

Y.-Y. Wang (✉) · K.-S. Cheng
Department of Biomedical Engineering, National Cheng Kung University, Tainan, Taiwan
e-mail: wert7774@mail.com

K.-S. Cheng
e-mail: kscheng@mail.ncku.edu.tw

C.-D. Kan
National Cheng Kung University Hospital, Tainan, Taiwan

W.-L. Chen
Department of Engineering and Maintenance, Kaohsiung Veterans General Hospital, Kaohsiung City, Taiwan

time, the brachial artery and cephalic vein will be inserted with the needle for dialysis. As the time passed, some symptoms such as thrombosis, aneurysmal deformability, and intimal hyperplasia caused by needle will occur in AVS. AVS is the basis for sustaining the patients' life, so early diagnosis is necessary. These problems would result in a poor blood flow that could reduce the performance and decrease the efficiency of the dialysis process [3].

1.4 Standard Evaluation in Clinical

Ultrasound Doppler and angiography is the evaluation method with high accuracy. For monitoring AVSs, Doppler ultrasound imaging is often used [4]. The blood flow rate, velocity, and vascular diameter are determined and correlated with the level of stenotic severity. But there are some disadvantages. These techniques require specific equipment, place, and operator. Compared to the former, Angiography is an invasive diagnosis, but not suitable for everyone. The purpose of this study is to develop a noninvasive assessment which will be useful and potential for early detection in home-care use.

1.5 Literature Review

Some research groups have shown that the phonoangiography technique could identify as many as 20% of vascular diameter changes as well as its frequency characteristics due to hemodialysis access problems [5] (Table 1).

They confirmed that the bandwidth of interest in stenotic studies ranges within 0–1000 Hz and the increase of spectral energy intensity is related to the increase of blood flow and velocity. However, when approaching high frequencies, the energy tends to decrease [5].

The Empirical Mode Decomposition (EMD) is a method to decompose non-linear, non-stationary time series signal into a sum of different modes, so-called Intrinsic Mode Functions. Each IMF has its own characteristic frequencies. The mean energy and mean instantaneous frequency per IMF was proved to be good features for classification [6].

2 Materials and Methods

2.1 Experimental Design

In this study, the experimental design is depicted in Fig. 1.

2.2 Mock Model

The degree of stenosis (DOS) as defined in Eq. (1) is used as an index to classify the AV access condition, and is determined by the narrowing percentage of normal vessels. In this mock model (as shown in Fig. 2), a cardiopulmonary circulation is simulated and the stenosis is set from 0, 50, 70, 80, 85, 90, 92.5 to 95% [7]. The flow sound is recorded using 3M^{TM} Littman Electronic Stethoscope Model 3200. AVS flow is set at 900 ml. In this study, the stenosis status is divided into three stages: healthy (0–50%), suspicion (50–85%), and severe (85% up).
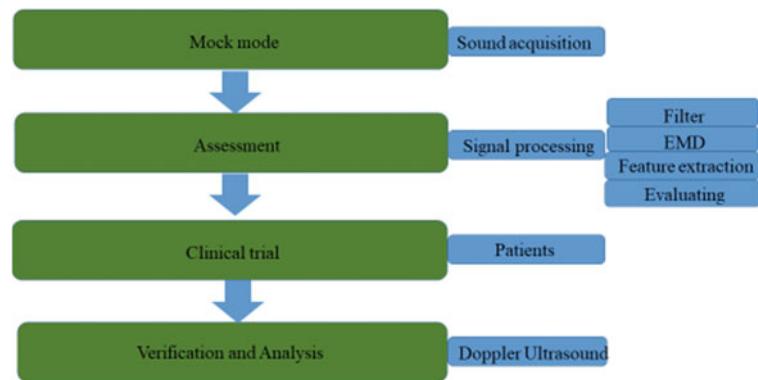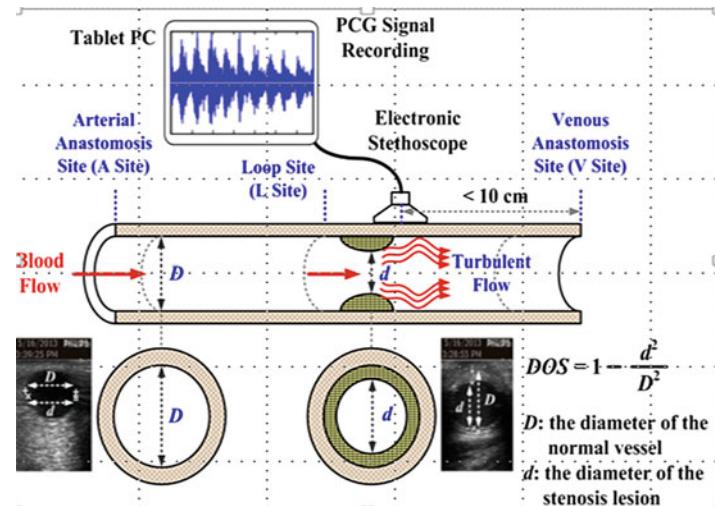
$$DOS = 1 - \frac{d^2}{D^2} \qquad (1)$$

2.3 Data

In mock model, we recorded sound before and after stenosis sites, respectively. In Fig. 2 A site indicates the measurement before stenosis, and V site the measurement after stenosis. In clinical trial, there are fifty patients from National Cheng Kung University Hospital recruited in the study with IRB approval.

Table 1 Comparison of different algorithm

|	Fourier	Wavelet	Hilbert
Basis	Apriori	Apriori	Adaptive
Frequency	Convolution: global	Convolution: regional	Differentiation: local
Presentation	Energy-frequency	Energy-time-frequency	Energy-time-frequency
Nonlinear	No	No	Yes
Non-stationary	No	Yes	Yes
Feature extraction	No	Discrete: No Continuous: Yes	Yes

Fig. 1 Flowchart of experiment

Fig. 2 The configuration of mock model and the degree of stenosis simulation

2.4 Signal Processing

As mentioned previously, the bandwidth of interest in stenosis ranges within 0–1000 Hz. So, a band-pass filter is set to be 0–1 kHz and the sampling rate of signal is 4 kHz. Then, the sound signal is decomposed into Intrinsic Mode Functions (IMF) using Empirical Mode Decomposition (EMD). After the decomposition, the original signal s(t) can be expressed as,

$$s(t) = \sum_{j=1}^{n} c_j(t) + r_n(t) \tag{2}$$

n denotes the number of components after sifting process. In Eq. (2), c1(t), …, c_n(t) are the IMFs and r_n(t) is the residue which can be regarded as a constant. Then, the Hilbert Transform is applied to each IMFs and the signal may be represented as energy-time-frequency form z(t).

$$z(t) = c_j(t) + v_j(t) \tag{3}$$

v_j(t) is the Hilbert Transform of c_j(t).

$$s(t) = \sum_{j=1}^{n} A_j(t) \cos \theta_j(t) + r_n(t) \tag{4}$$

$$A_j(t) = \sqrt{c_j(t)^2 + v_j(t)^2} \tag{5}$$
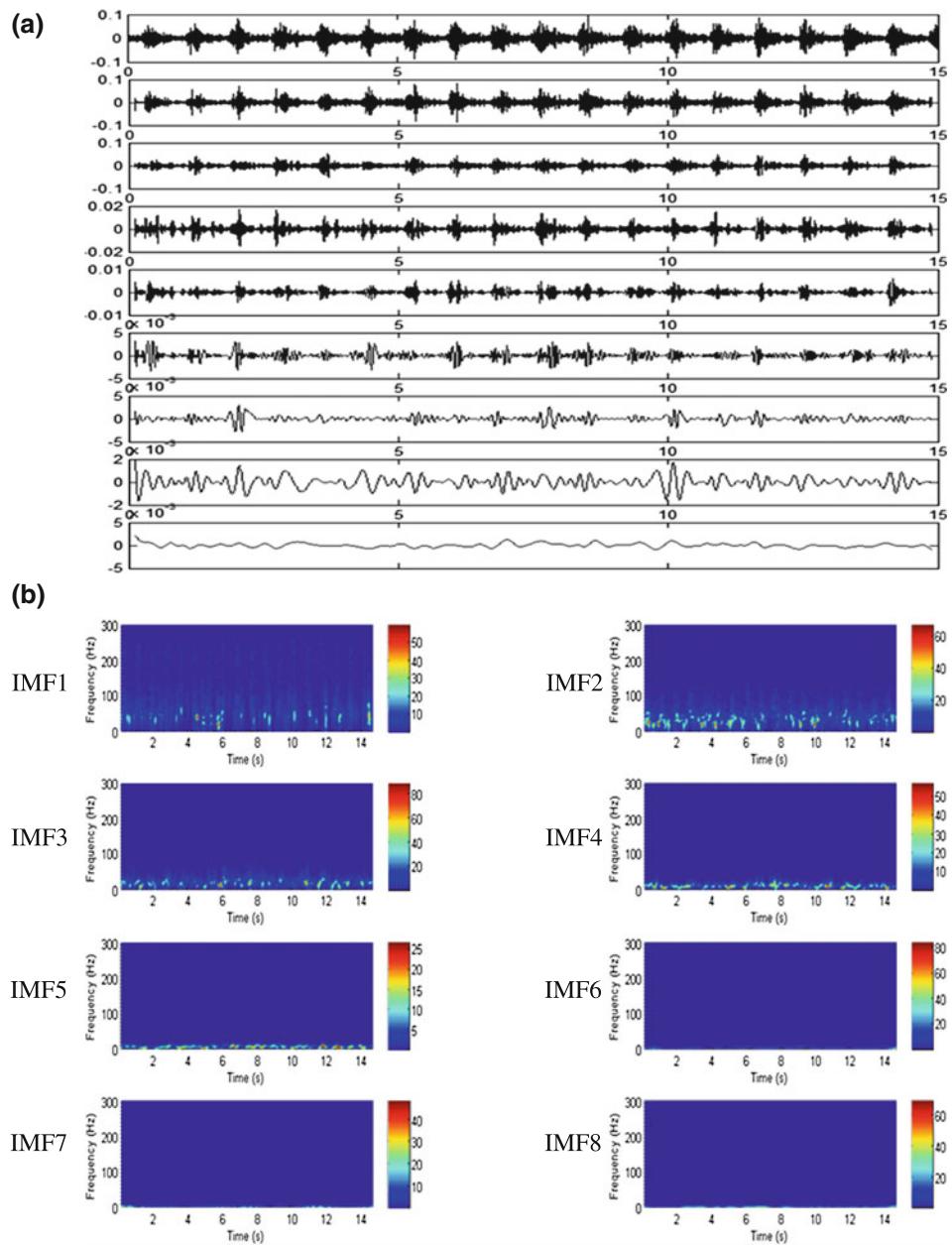
$$\theta_j(t) = \arctan \left(\frac{v_j(t)}{c_j(t)} \right) \tag{6}$$

According to literature review, it is expected that some high frequency components caused by stenosis AVS will show up. Thus, we focus on analyzing IMFs features in Fig. 3b such as specific frequency, mean energy, phase etc.

3 Results and Discussion

Both mock model signals and clinical trial signals are shown to have a great correlation between the phonoangiography and the severity of DOS in AV access. Certain high frequency energy in the first IMF is seen to increase due to stenosis problem. However, as the severity of DOS

Fig. 3 **a** The first one is original signal, the others are IMF1–IMF8. **b** Hilbert Energy spectrum of IMFs which can provide us visual aid in certain frequency. The first two IMFs usually have obvious change when we compare with different degree of stenosis

increases, the energy will gradually decreases. The first four IMFs' phase also have obvious changes. All of these features could be used as the index of stenosis staging.

4   Conclusion

In this study, the Hilbert Spectrum shows that the high frequency content change of the sounds produced by stenosis. It is demonstrated to be feasible that the features such as frequency, phase, energy extracted from IMFs may be useful in staging the severity of DOS. This noninvasive method may be useful and potential for early detection in home-care use.

References

1. United States Renal Data System, "USRDS Annual Data Report Volume 2: ESRD in the United States", p 133–134, 2015.
2. https://www.nhri.gov.tw/Resource/webdata/, last accessed 2018/2/3.
3. Mickley, V., *Stenosis And Thrombosis In Haemodialys is Fistulae and Grafts: The Surgeon's Point of View*, Nephrology Dialysis Transplantation, 19(2), pp. 309–311, 2004.
4. Tonelli, M., James, M., Wiebe, N., Jindal, K., Hemmelgarn, B., & Alberta Kidney Disease Network, "*Ultrasound Monitoring to Detect Access Stenosis in Hemodialysis Patients: A Systematic*

Review", American Journal of Kidney Diseases, 51(4), pp. 630–640, 2008.

5. Anas Mohd Noor, "Non-Imaging Acoustical Properties in Monitoring Arteriovenous Hemodialysis Access. A Review", J. Eng. Technol. Sci., Vol. 47, No. 6, 2015.

6. Pablo V´asquez, Marco Mungu´ıa M, Elisabeth Mattsson, Bengt Mandersson, "Application of the Empirical Mode Decomposition in the study of murmurs from Arteriovenous Fistula Stenosis", 32nd Annual International Conference of the IEEE EMBS Buenos Aires, Argentina, August 31–September 4, 2010.

7. Yi-Chu Li, Fan-Ming Yu, Chung-Dann Kan, "Evaluation of Arteriovenous Shunt Stenosis induced Phonographic Signal on Hemodynamics in Hemodialysis Patients", Master's Thesis of Department of Aeronautics and Astronautics, National Cheng Kung University, June. 2015.

Accuracy Comparison of ML-Based Detection Algorithms Using Two Different Acceleration Derived Feature Vectors

Sara Zulj, Goran Seketa, Igor Lackovic, and Ratko Magjarevic

Abstract

Falls among the elderly are an important health issue which can lead to serious consequences. Unintentional falls in the elderly are the most common cause of nonfatal injuries. Different algorithms have been proposed for fall detection using vision based, ambient or inertial sensors. In this experiment, we used data collected from 16 subjects performing 15 tasks: 12 activities of daily living and 3 simulated falls. Subjects were equipped with a waist-mounted IMU to collect tri-axial accelerometer data during the activities. We derived features from accelerometer data on time-windowed identified activities and divided them into 2 different feature vectors (FV) that are used for fall detection algorithm. The selection was made based on the computational complexity of the features. We used different machine learning (ML) techniques to distinguish fall events from non-fall events (i.e. activities of daily living). In this paper, we compared and analyzed the accuracy of fall detection for different ML-based algorithms using the two accelerations-derived feature vectors for potential real-time implementation. The accuracy of the selected models ranged from 80.1 to 90.0% for FV1 and from 87.2 to 98.6% for FV2. The support vector machines algorithm achieved the best performance with accuracy 98.6%, sensitivity 98.7% and specificity 98.6% for FV2.

Keywords

Fall detection • Machine learning • Classification

1 Introduction

With an ageing population, the number of persons over 60 years old was estimated to be 688 million in 2006, and is projected to grow to almost two billion by 2050. Falls among the elderly are an important health issue and a leading cause of injury-related hospitalizations. Falls can lead to serious consequences and are accounted for 40% of all injury deaths. Unintentional falls in the elderly are the most common cause of nonfatal injuries. Prevention is a challenge to population ageing [1]. Another important issue to address, is the time the elderly remains lying on the floor after falling—long lie. Long lie is associated with the fear of falling, muscle damage, pneumonia, pressure sores, dehydration and hypothermia [2]. The robust fall detection system is a key to lessen the number of long lie in elderly.

The aim in the field of fall detection is to develop a robust fall detector which can classify the falls as falls and the non-falls as non-falls even under real life conditions. A review of challenges and trends in the fields is given in [3]. Another related issue is the performance under real-life conditions, usability, and user acceptance. Due to the rarity of occurrence of falls, there may be insufficient or no training data available for the real-life conditions [4]. Many authors opt for a laboratory setting with voluntary simulated falls performed by young volunteers, rarely testing the system in older adults and real-life setting [5].

Different fall detection solutions have been proposed using vision based, ambient or wearable devices—mostly inertial sensors [6]. The scoping review of the state of knowledge on technologies used in fall detection is given in [7]. Moreover, algorithms for fall detection using wearable devices can roughly be divided in two groups: threshold-based algorithms and machine learning algorithms, some combining the two approaches [8]. Accurate fall detection systems in the existing literature generally use multiple sensors, but the increase in the number of sensor

S. Zulj (✉) · G. Seketa · I. Lackovic · R. Magjarevic
Faculty of Electrical Engineering and Computing,
Department of Electronic Systems and Information Processing,
University of Zagreb, Zagreb, Croatia
e-mail: sara.zulj@fer.hr

nodes has a negative impact on the adoption of the system by the user [9].

In our previous study, a threshold-based fall detector using accelerometer was designed and evaluated using the data of subjects simulating falls and performing activities of daily living (ADL) in a laboratory setting [10]. In this paper, we present the machine learning (ML) approach by extracting acceleration-derived features for the two feature vectors for potential real-time implementation of fall detection.

2 Materials and Methods

2.1 Participants

The data used in this study were previously collected for a study on threshold methods for fall detection [10], where 16 volunteering subjects have performed activities of daily living (ADL) and simulated falls. Subjects were ranging in age from 15 to 44 years (mean 23.1, SD 6.7), height from 159 to 192 cm (mean 176.4, SD 8.9) and body mass 55–93 kg (mean 75.2, SD 12.8).

2.2 Experimental Protocol

In each trial, subjects performed 13 tasks in the laboratory: 10 activities of daily living (ADLs) and 3 falls. The ADLs were: walking, fast walking, running, fast running, jumping, high jumping, sitting down, standing up, lying down and getting up from a lying position. Subjects simulated three types of falls: forward fall, sideways fall and backward fall. During all fall trials, the floor was covered with a 2 cm thick mat. Subjects were instructed to fall relaxed and avoid any compensatory strategies during the trials. Two additional ADLs, walking up the stairs and walking down the stairs were recorded separately, outside the laboratory. The number of trials for each subject is shown in Table 1. The total number of activities recorded during the trials was 866, 186 falls and 680 ADL events.

2.3 Data Acquisition

During each trial, we recorded data of a wide range accelerometer in the range ±8 g using Shimmer3 IMU (ShimmerSensing, Dublin, Ireland). The IMU was mounted on the right side of the subject's waist using a Velcro belt, with its x-axis pointing forward, y-axis pointing up and z-axis pointing away from the body. Data acquired at 204.8 Hz were live streamed to a PC using the Bluetooth connection for the total duration of the trial (i.e. 13 activities in the laboratory setting or 2 activities for stairs).

3 Data Analysis

3.1 Feature Vector Selection

In each trial, the center for each event (fall or ADL event) was identified and marked in the data record, and a 2.5-s window centered around the event was applied. All further computations were made over the 2.5 s window data. The width of the window was selected to include all significant samples of nonrepetitive activities (e.g. fall, standing up, sitting down, jumping, etc.).

For this study, we computed two different accelerometer-derived feature vectors by selecting different features based on the computational expensiveness of the measure. First feature vector (FV1) was computed for each activity as a maximum value of the following measures: sum vector magnitude (SVMAG), differential SVM (DSVM), gravity weighted SVM (GSVM), gravity weighted DSVM (GDSVM) and Euler angle between the vertical device axis and the direction of the gravitational field (theta), using the following Eq. [8]:

$$SVMAG(n) = \sqrt{a_x(n)^2 + a_y(n)^2 + a_z(n)^2}, \quad (1)$$

$$DSVM(n) = \left[\begin{array}{c} (a_x(n) - a_x(n-1))^2 + (a_y(n) - a_y(n-1))^2 \\ + (a_z(n) - a_z(n-1))^2 \end{array} \right]^{1/2}, \quad (2)$$

$$theta(n) = \text{atan2}\left(\frac{\sqrt{a_x(n)^2 + a_z(n)^2}}{a_y(n)} \right), \quad (3)$$

$$GSVM(n) = \frac{theta(n)}{90} \times SVMAG(n), \quad (4)$$

$$GDSVM(n) = \frac{theta(n)}{90} \times DSVM(n). \quad (5)$$

where $a_x(n)$, $a_y(n)$, $a_z(n)$ represent x, y and z acceleration of the n-th sample, respectively.

Second feature vector (FV2) was computed to comprise 6 features: mean and variance of x, y and z acceleration components over 2.5 s window for each trial [11]. Each feature vector contains one observation for every activity per trial, issuing 866 observations.

Table 1 Participant trials per activity

Activity	Participant ID																Total per activity
	1	2	3	4	5	6	7	8	9	10	11	12	13	14	15	16	
Backwards fall	5	5	5	5	5	3	4	2	2	6	6	2	2	2	4	4	**62**
Forward fall	5	5	5	5	5	3	4	2	2	6	6	2	2	2	4	4	**62**
Sideways fall	5	5	5	5	5	3	4	2	2	6	6	2	2	2	4	4	**62**
Fast running	5	5	5	5	5	3	4	2	2	6	6	2	2	2	4	4	**62**
Fast walking	5	5	5	5	5	3	4	2	2	6	6	2	2	2	4	4	**62**
High jumping	5	5	5	5	5	3	4	2	2	6	6	2	2	2	4	4	**62**
Jumping	5	5	5	5	5	3	4	2	2	6	6	2	2	2	4	4	**62**
Lying down	5	5	5	5	5	3	4	2	2	6	6	2	2	2	4	4	**62**
Standing up from lying	5	5	5	5	5	3	4	2	2	6	6	2	2	2	4	4	**62**
Sitting down	5	5	5	5	5	3	4	2	2	6	6	2	2	2	4	4	**62**
Standing up from sitting	5	5	5	5	5	3	4	2	2	6	6	2	2	2	4	4	**62**
Running	5	5	5	5	5	3	4	2	2	6	6	2	2	2	4	4	**62**
Walking	5	5	5	5	5	3	4	2	2	6	6	2	2	2	4	4	**62**
Walking downstairs	7	6	–	–	–	–	–	–	–	–	–	6	5	6	–	–	**30**
Walking upstairs	7	6	–	–	–	–	–	–	–	–	–	6	5	6	–	–	**30**
Total per participant	**79**	**77**	**65**	**65**	**65**	**39**	**52**	**26**	**26**	**78**	**78**	**38**	**36**	**38**	**52**	**52**	**866**

3.2 Classification Methods and Comparison

In their paper, Albert et al. [12] evaluated accuracy of five supervised classifiers of fall detection on accelerometer data gathered using a mobile phone and wearable accelerometer. They found support vector machines and sparse multinomial logistic regression (SMLR) were found to be the best performing methods in this study, both identifying simulated falls with 98% accuracy.

Similarly, we selected five common machine learning algorithms for human activity recognition to solve this binary classification task: decision tree (DT), logistic regression (LR), naïve Bayes (NB), k-nearest neighbor (kNN) and support vector machines (SVM). Both feature vectors were split into training and evaluation sets by choosing data from participants 6–16 (11 participants, 404 ADL trials, and 102 fall trials) for training, and the remaining for evaluation (5 participants, 276 ADL trials, and 75 fall trials). To select the parameters for each algorithm, we performed tenfold cross-validation with the training set and selected parameters which provided best cross-validation accuracy. All five final models were trained on the entire training set.

For comparison of all five algorithms using two different feature vectors, we calculated accuracy, sensitivity and specificity, as follows:

$$accuracy =$$
$$\frac{True\ positive + True\ negative}{True\ positive + False\ positive + True\ negative + False\ negative}$$
(6)

$$sensitivity = \frac{True\ positive}{True\ positive + False\ negative}$$
(7)

$$specificity = \frac{True\ negative}{True\ negative + False\ positive}$$
(8)

Furthermore, we examined occurrences of misclassified samples, i.e. false positive and false negative predictions depending with respect to the activity. The data analysis and algorithms were implemented in MATLAB (R2016b, The MathWorks Inc.).

4 Results

The accuracy of all ten ML-algorithms are shown in Fig. 1. All accuracy ranged from 80.1 to 90.0% for FV1 and from 87.2 to 98.6% for FV2. Overall, algorithms performed better when using FV2. The SVM algorithm achieved the best accuracy for both feature vectors, followed by kNN algorithm for FV2 (98.6%, the same accuracy as SVM) and DT for FV1 (87.7%).

Sensitivity and specificity for all algorithms are shown in Fig. 2. The SVM algorithm provided the best combination of sensitivity and specificity (FV2–98.7 and 98.6%, FV1–85.3 and 91.3%), followed by kNN algorithm for FV2 (96.0% sensitivity and 99.3% specificity) and DT for FV1 (77.3% sensitivity and 90.6% specificity). All algorithms using FV2 showed high specificity. LR showed poorest sensitivity for both FV1 and FV2 (49.3% and 41.3% for FV1 and FV2 respectively). Relaxation of threshold on confidence criterion did not improve results.
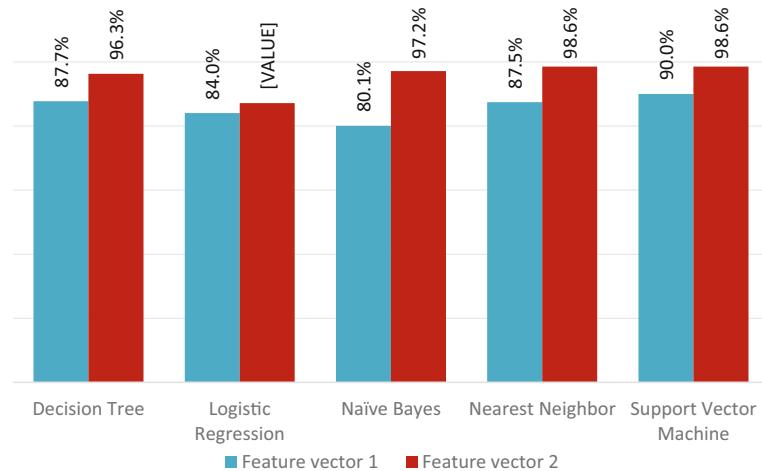
Fig. 1 Accuracy comparison chart between five machine learning algorithms using two different feature vectors
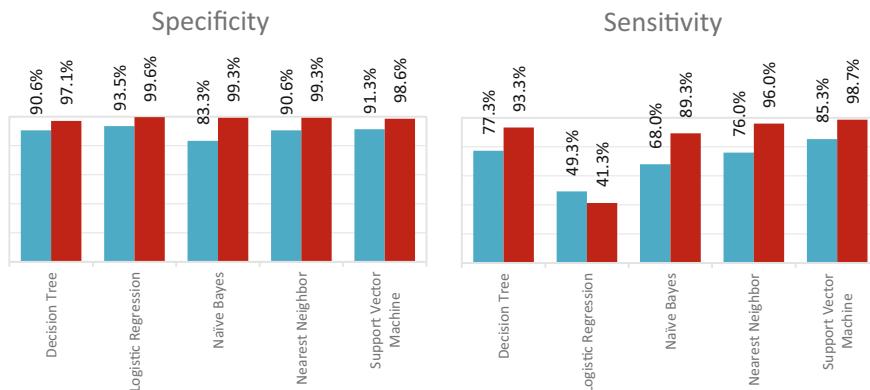
Fig. 2 Sensitivity and specificity comparison chart between five machine learning algorithms using two different feature vectors

Table 2 Number of false positives and false negative results for each feature vector and machine learning algorithms per activity

		Feature vector 1					Feature vector 2				
		DT	LR	NB	kNN	SVM	DT	LR	NB	kNN	SVM
False negative											
Backwards fall	(25)	7	18	11	10	5	4	20	7	3	1
Forward fall	(25)	8	18	13	8	6	1	20	1	0	0
Sideways fall	(25)	2	2	0	0	0	0	4	0	0	0
False positives											
Fast running	(25)	11	11	22	13	13	0	1	0	0	0
Fast walking	(25)	0	0	0	1	0	0	0	0	0	0
High jumping	(25)	4	1	8	2	3	1	0	0	0	0
Jumping	(25)	2	1	3	2	2	0	0	0	0	0
Lying down	(25)	2	1	1	1	1	1	0	2	0	4
Standing up from lying	(25)	0	0	0	0	0	0	0	0	0	0
Sitting down	(25)	0	0	0	0	0	2	0	0	0	0
Standing up from sitting	(25)	0	0	0	0	0	0	0	0	0	0
Running	(25)	7	4	12	7	5	3	0	0	1	0
Walking	(25)	0	0	0	0	0	1	0	0	0	0
Walking downstairs	(13)	0	0	0	0	0	0	0	0	1	0
Walking upstairs	(13)	0	0	0	0	0	0	0	0	0	0

Misclassified activities are shown in Table 2. Missed falls occurred in all three types of falls, with overall least missed sideways falls. False positive results using FV1 occurred mostly in activities fast running and running, followed by high jumping and jumping, whereas in FV2 most false positives occurred during lying down activity. Activity of standing up from both lying and sitting, as well as walking upstairs, was never misclassified regardless of the feature vector.

5 Conclusions and Future Work

This paper presents results of accuracy comparison of ML-based fall detection algorithms using two different acceleration derived feature vectors. We used the accelerometer data of activities of daily living and simulated falls recorded from a laboratory setting study. We selected two different sets of accelerometer-derived features for two feature vectors and trained them separately using five machine learning techniques. Feature vector 2 showed better overall accuracy, using each ML model. From the five models selected, SVM showed the best performance with accuracy 98.6%, sensitivity 98.7% and specificity 98.6%. For the feature vector 1, extra features could be used to improve the accuracies of machine learning algorithms for fall detection.

The authors are aware of the limits of the trials performed due to having mostly young participants involved in the study. The falls were simulated in safe laboratory settings, and it is possible that those voluntary falls may differ from real-life falls.

The aim of this study was to find the best ML-model for potential real-time implementation depending on the different features. In our future work, we plan to evaluate models using new features, and combine threshold and machine learning algorithms for fall detection.

Conflict of Interest The authors declare no conflict of interest.

References

1. WHO, "Who global report on falls prevention in older age," 2007.
2. S. R. Lord, C. Sherrington, H. B. Menz, and J. C. Close, *Falls in older people: risk factors and strategies for prevention*. Cambridge University Press, 2007.
3. R. Igual, C. Medrano, and I. Plaza, "Challenges, issues and trends in fall detection systems," *BioMedical Engineering OnLine*, vol. 12, p. 66, Jul 2013.
4. S. S. Khan and J. R. Hoey David, "Review of fall detection techniques: A data availability perspective," *Medical Engineering and Physics*, vol. 39, pp. 12–22, 2016.
5. S. Chaudhuri, H. Thompson, and G. Demiris, "Fall detection devices and their use with older adults: A systematic review," Oct–Dec 2014.
6. M. Mubashir, L. Shao, and L. Seed, "A survey on fall detection: Principles and approaches," *Neurocomputing*, vol. 100, pp. 144–152, 2013. Special issue: Behaviours in video.
7. N. Lapierre, N. Neubauer, A. Miguel-Cruz, A. Rios Rincon, L. Liu, and J. Rousseau, "The state of knowledge on technologies and their use for fall detection: A scoping review," 2018.
8. D. Lim, C. Park, N. H. Kim, S.-H. Kim, and Y. S. Yu, "Fall-Detection Algorithm Using 3-Axis Acceleration: Combination with Simple Threshold and Hidden Markov Model," *Journal of Applied Mathematics*, vol. 2014, pp. 1–8, sep 2014.
9. A. T. Ozdemir, "An analysis on sensor locations of the human body for wearable fall detection devices: Principles and practice," *Sensors*, vol. 16, no. 8, 2016.
10. G. Seketa, J. Vugrin, and I. Lackovic, "Optimal threshold selection for acceleration-based fall detection," in *Precision Medicine Powered by pHealth and Connected Health* (N. Maglaveras, I. Chouvarda, and P. de Carvalho, eds.), (Singapore), pp. 151–155, Springer Singapore, 2018.
11. O. Aziz, M. Musngi, E. J. Park, G. Mori, and S. N. Robinovitch, "A comparison of accuracy of fall detection algorithms (threshold-based vs. machine learning) using waist-mounted tri-axial accelerometer signals from a comprehensive set of falls and non-fall trials," *Medical & Biological Engineering & Computing*, vol. 55, pp. 45–55, Jan 2017.
12. M. V. Albert, K. Kording, M. Herrmann, and A. Jayaraman, "Fall classification by machine learning using mobile phones," *PLOS ONE*, vol. 7, pp. 1–6, 05 2012.

The Value of New Atomic Sensors in Medical Diagnostic Procedures

Kazimierz Peczalski and Tadeusz Palko

Abstract

The new generation of atomic magnetic sensors with sensitivity of 10 pT/rtHz provides new tool for assessment of biological magnetic signals such as MCG, MEG or other neurological signals. The atomic sensors with such high sensitivity always require attenuation of the spurious magnetic signals with shielding of the sensor and the subject. Additionally the best sensitivity of sensors is achieved in the total magnetic earth field close to zero. Authors have designed, based on a Vacuumschmelze room, the laboratory for the atomic sensors measurements with the compensation coils system zeroing out the magnetic field of the earth within whole area inside the shielded volume. The preliminary measurements have proven that diagnostic signal of MCG can be monitored by two parallel sensors. The results confirmed the ability of the multisensors examination of the distribution of the magnetic field magnitude on the surfaces of chest, scalp or other fragments of human body. In most practical situations the vector of the magnetic field is perpendicular to the surface of tissue generating it and the field maximum is exactly over the area of interest e.g. where the neurons are placed. Therefore the maps measured by the atomic sensor arrays can be more precise than isopotential maps where the magnetic field gradient parallel to the surface is detected. We could also expect that the measured magnetic field will have high amplitude because of the smaller dimensions of sensors and low attenuation of the magnetic field by bones.

K. Peczalski (✉) · T. Palko
Warsaw University of Technology, 02525 Warsaw, Poland
e-mail: k.peczalski@mchtr.pw.edu.pl

1 Introduction

The new generation of atomic magnetic sensors with sensitivity of 10 pT/rtHz provides new tool for assessment of biological magnetic signals such as Magnetocardiography (MCG), Megnetoencephalography (MEG) or other neurological signals. The atomic sensors with such high sensitivity always require attenuation of the spurious magnetic signals with shielding of the sensor and the subject. Additionally the best sensitivity of sensors is achieved in the total magnetic earth field close to zero. Such conditions are provided by the three dimensional system of compensation coils situated within a magnetically shielded room.

2 The Magnetic Shielded Room Dedicated for Atomic Sensors

Authors have designed the laboratory for the atomic sensors measurements, based on a Vacuumschmelze room, with the compensation coils system zeroing out the magnetic field of the earth within whole area inside the shielded volume [1]. The inner dimensions of the room are height = 2.85 m, width = 3.35 m, length = 4.33 m.

The Magnetic Shielded Room (MSR) designated for the Spin Exchange Relaxation Free (SERF) magnetometers studies has to fulfill two basic conditions: provides the sufficiently low level of magnetic noises and external magnetic DC (direct current) field of the earth close to zero. The design of the MSR, providing the satisfactory attenuation factor in the required spectrum of frequency, is based on application of multiple layers of materials in order to filter the magnetic noises for particular frequencies. The most common used materials are the nickel alloy called Mumetal and aluminum. The MSR consists usually of aluminum layer between two Mumetal layers.

The listed below layers were applied in the MSR located in the Department of Mechatronics fascilities:

Table 1 The damping factors of MSR measured at different frequencies

Frequency (Hz)	Dumping factor
>0	500
>0.01	38
>0.1	55
>1	400
>10	4000
>100	10,000
>1000	10,000

- 2 mm Mumetal
- 8 mm aluminum
- 3 mm Mumetal

The damping factors of magnetic fields measured at different frequencies for the MSR located in the Mechatronics Department of Warsaw University of Technology are presented in Table 1.

The MSR provides the magnitude of the DC magnetic field of the earth inside the room in the range of 20 nT. The additional active compensation was applied in order to provide an external magnetic DC field inside of MSR close to zero. The two systems of the Helmholz coils, global for whole MSR capacity and local for the object under test and sensors were tested. Each of them consists of three sets of coils dedicated for the x, y, z axes. The compensation system is intend to produce magnetic induction vector with the same value and opposite direction to the earth induction vector thus providing of sum of vectors inside of the MSR close to zero. The finite element simulation of the compensation of induction vector of the earth by the 3 dimensional system of modified Helmholz coils is presented in the Fig. 1. The results of simulation was confirmed by measurements.

3 The Magnetic Sensors Development

The atomic magnetometers are designed for measurements of the induction of small magnetic fields. The main components of the sensor is a glass cell consisting of vapors of alkali metals such as cesium, rubidium or potassium. The atoms of alkali metals are characterized by one valence electron [2]. The two perpendicular laser beams: pumping and measuring passing through the vapor stored in the sensors cell. The block diagram of system is presented in the Fig. 2.

The magnitude of the magnetic induction depends on the changes of the Larmor precession angle of atoms. The vapor inside measuring cell is excited by so called pumping laser in order to align the polarization of the spins of vapor atoms (the length of laser wave is set up on the optic resonance frequency). The process of pumping is indented to increase the energy of circulating atoms of vapor in order to preserve its coherence of spins. The small changes of the magnetic field cause the proportional changes of angle of Larmor precession. The angle of polarization of the measuring laser beam passing by the cell with volume of approximately one cubic centimeter is changed according to the changes of angle of Larmor precession. The values of polarization angle of measuring laser beam are related to the values of induction of magnetic field. The sensitivity of atomic magnetometers is limited by the density of alkali metals in the cell and the time of spins coherence.

The system with the described above sensor is presented in the Fig. 3.
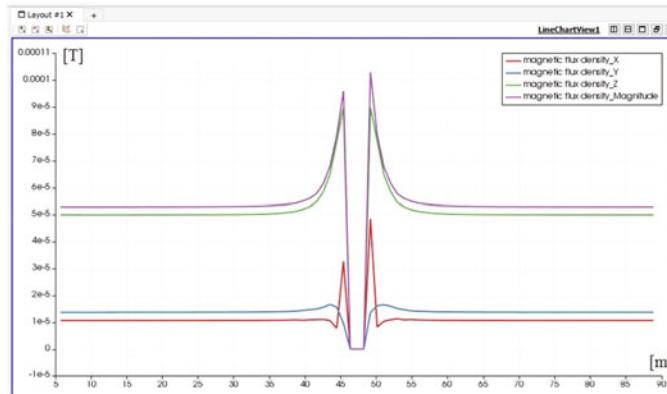
Fig. 1 The simulation of compensation of induction vector of the earth inside MSR
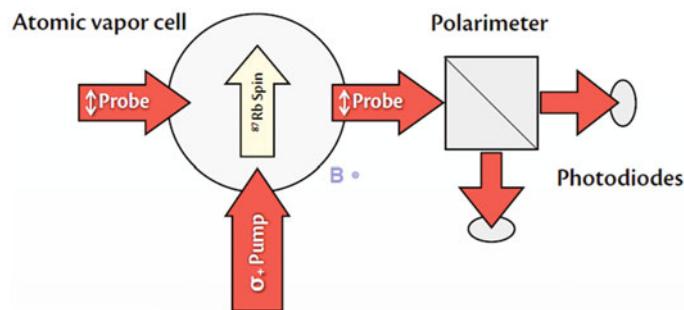
Fig. 2 The block diagram of SERF sensor
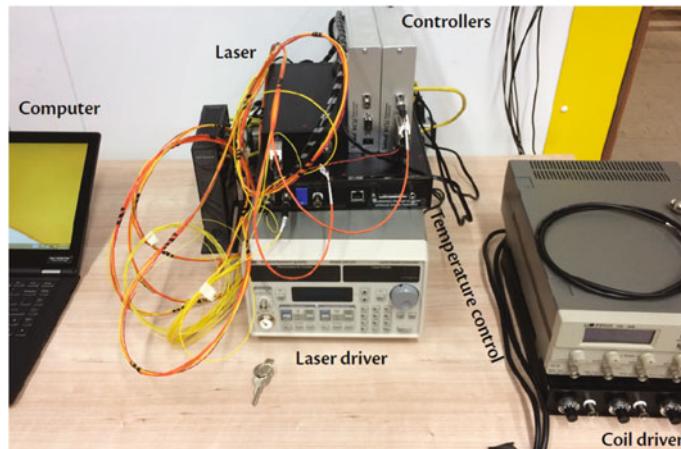
Fig. 3 The former system for SERF sensor
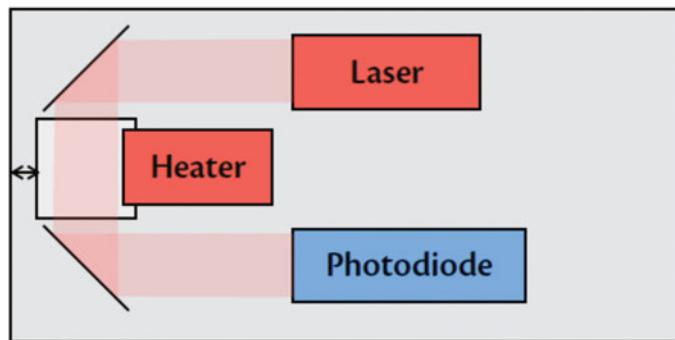
Fig. 4 The block diagram of the new SERF sensor

In this system the transmission of the high energy by the optical fiber caused excessive heating due to the optical impedance mismatch and losses in the area of the attachment to the connectors. In some cases optic fibers just exploded. The optical fibers were intended to replace current supply wires that always generate spurious magnetic fields. Because of the difficulties in transmitting high power over the optical fibers the second generation of miniaturized systems with

new sensors were introduced. In the new sensors the resistive heating elements replaced the former laser systems. The block diagram of the new sensor is presented in the Fig. 4 and the new miniaturized system with the magnetic sensor is presented in the Fig. 5.

Both systems were connected directly to PC which allows for the sensor calibration and data acquisition with a custom developed software.

Fig. 5 The new SERF system

4 The Prevails of Diagnostic of Magnetic Versus Electric Signals

The newly developed non cryogenic sensor is more effective and practical than the presently used cryogenic sensors for the measurements of magnetic microsignals generated by human organs such as the heart or brain. But the new method is still more complicated and expensive than other existing sensor of the electrical signals in heart, brain and other organs. So, what are the advantages of system equipped in magnetic atomic sensors that justify its application in medical diagnostic procedures? The first advantage is related to all medical magnetometers. The vector of the magnetic field is perpendicular to the surface of tissue generating it e.g. neuron and the field maximum is exactly over the area of interest e.g. where the neuron is placed. Therefore the maps measured by the atomic sensor arrays can have a better spatial resolution than the izopotential maps of the electric field gradient parallel to the surface. The second advantage is related to the small physical dimension of magnetic sensors especially versus of so far commonly used cryogenic superconducting quantum interference device (SQUID) [3]. For example the new sensor dimensions are height = 10 width = 20 length = 140 mm and the very small one liter,

round dewar of SQUID dimension are diameter 127 length = 279 mm. Therefore the atomic sensor could be located directly on the surface of the body and the distance between measuring cell and edge of transducer is smaller than in the SQUID case. The smaller distance between the source of signal and measuring cell of the magnetic transducer provides higher amplitude of recorded signal. Similarly the planar location of the magnetic signal will be determined with better accuracy because of smaller dimension of the sensing volume. The monitoring of the magnetic signal of the brain will take advantage of low attenuation of the magnetic field by the scalp tissues and bones and ability to bring the sensing volume very close to the head. The atomic magnetic sensor compared to SQUID's avoids the big and expensive cooling systems necessary for superconducting conditions.

5 Conclusion

The novel magnetic sensors seems to be a promising diagnostic tool for the brain and heart magnetic signal and should provide the opportunity for new diagnostic applications such as monitoring of disturbances of the fetal cardiac rhythm [4] and functionality of the brain and other regions of nervous system.

References

1. Peczalski K., Palko T. New methods of examination of biomagnetic fields of human organs. Elektronika, vol. 12, 65–66 (2016).
2. Kominis I.K. et. al.: A subfemtotesla multichannel atomic magnetometer. Nature, vol. 422, pp. 596–599 (2003).
3. Hansen P.C., Kringerlbach M.L., Salmedin R. (eds). MEG; an intruduction to methods. Oxford Press University (2010).
4. Sinstra J. et. al. Multicentre study of cardiac fetal time intervals using magnetocardiography. BJOG: an International Journal of Obstetrics & Gynaecology, vol. 102, 1235–1243 (2002).

Assessment of Micro T-Wave Alternans Using T-Wave Morphology-Based Methods

Thaís Winkert, Paulo Roberto Benchimol-Barbosa, and Jurandir Nadal

Abstract

Microvolt T-wave alternans (MTWA) is a risk marker for life threatening arrhythmias, defined as beat-by-beat alternation of the T-wave amplitudes. Sensitive to noise, MTWA classical method (CM) requires accurate determination of T-wave peaks. This study assessed alternative methods prescinding this limitation. Fifty ECG recordings from PhysioNet T-Wave Alternans Database were assessed (channels 1 and 2). A sequence of 128 sinus beats was extracted from each signal. The FFT of the 128 T-wave peak value series was employed to perform CM, taken as reference. Further, T-waves were isolated and consecutively concatenated, composing an artificial continuous (AC) signal. Over AC two methods were investigated: (i) Hilbert Transform approach (HT)—assessed by the FFT of the AC envelope, calculated by HT; (ii) Short-time spectral approach (STS)—assessed in the average of 96 FFT obtained from moving windows with 32 consecutive T-waves, displaced one by one. MTWA was calculated as 'alternans ratio', (alternans peak divided by the SD of 10 vicinal harmonics). CM versus HT and CM versus STS were compared by correlation coefficient, Bland-Altman charts and ROC. Correlation coefficient were, respectively, channel 1: 0.787 and 0.797 and channel 2: 0.835 and 0.836 ($p < 0.001$ for all). Bland-Altman plots showed non-significant (NS) differences for both channels. The area under ROC curves of CM, HT and STS were, respectively, 0.75, 0.80 and 0.71 (channel 1) and 0.77, 0.80 and 0.70 (channel 2) ($p = NS$ for all). As a conclusion, quantification of MTWA based on T-wave morphology analysis is feasible, accurate and reproducible, and have potential clinical application.

1 Introduction

T-wave expresses ventricle repolarization and represents transmural action potential phase 3 gradient across ventricle wall [1]. In this way, Microvolt T-Wave Alternans (MTWA) is linked to increased vulnerability to life-threatening ventricular tachyarrhythmias [2]. Defined as a tenuous fluctuation beat-by-beat on T-waves amplitude, MTWA can be associated with impaired intra-sarcoplasmic calcium influx and efflux dynamics [3, 4]. It has demonstrated that MTWA is an independent risk factor of inducible malignant ventricular arrhythmia during electrophysiological testing and considered a valuable arrhythmia risk stratification tool [5].

Introduced in the early 90s, the classical method of MTWA requires the application of a Fourier Transform over time series of T-wave peak amplitudes [6]. Therefore, it depends on accurate determination of T-waves fiducial points, requiring appropriate assessment of T-wave amplitudes.

As a consequence of respiratory-derived amplitude modulation, power line and muscular interferences, the morphology of T-waves undergoes continuous variation. In clinical settings, the accurate measurement of T-wave amplitudes may be challenging due to its morphological aspects allied to external interferences.

MTWA assessment methods that do not require accurate peak determination may be an applicable alternative to overcome the peak measurement limitation. This study assessed methods prescinding T-wave peak detection, for MTWA assessment.

T. Winkert (✉) · P. R. Benchimol-Barbosa · J. Nadal
Biomedical Engineering Program, COPPE, Universidade Federal do Rio de Janeiro, Rio de Janeiro, RJ, Brazil
e-mail: thaiswinkert@peb.ufrj.br

P. R. Benchimol-Barbosa
Hospital Universitário Pedro Ernesto, Universidade do Estado do Rio de Janeiro, Rio de Janeiro, RJ, Brazil

2 Materials and Methods

2.1 The Physionet Signals

The data analyzed by this study were multichannel ECG records downloaded from T-Wave Alternans Database, available at Physionet website [6]. The records were sampled at 500 Hz with 16-bit resolution over a ±32 mV range and came from several collaborative institutions, some with the standard 12-lead ECG and some only with 2 leads available. In its hole, the database contains 100 signals, 32 synthesized and 68 real signals, from patients with myocardial infarctions, transient ischemia, ventricular tachyarrhythmias, and other risk factors for sudden cardiac death, as well as healthy controls. Only the first and the second channels were available in all data and were analyzed in this study.

2.2 Preprocessing

The preprocessing step aimed at reducing interference, correcting baseline drifting and discontinuities, and providing improvement for the appropriate identification of MTWA. All ECG signals were preprocessed by a three-stage process: **(1) Low-Pass Filter**—To reduce external interferences, all signals were low-pass filtered: Butterworth, second order, cutoff frequency on 30 Hz; **(2) Baseline drifting correction** —In each ECG all R-waves were detected using absolute first order derivative method. Three points were identified from each detected R-wave: 220, 200 and 80 ms before it peak and were defined as references to the baseline of this heartbeat. A cubic spline was fitted to those points over the whole signal. Drifting correction was the result of the subtraction of cubic spline by the ECG; and **(3) Respiratory**

fluctuation correction—Using the peak of consecutive R-waves, it was set another cubic spline. The ECG was, then, divided by inter R-wave-derived spline to correct for the modulatory effect of thoracic movement due to respiratory fluctuation.

These procedures provided a corrected output ECG in which MTWA analysis was carried out. Additionally, on corrected ECG, ectopic beats were identified by visual inspection based on prematurity and QRS complex waveform comparisons.

2.3 MTWA Assessments Methods

After the preprocessing approach, a sequence of 128 consecutive sinus beats were extracted from each signal, ensuring the absence of ectopic rhythms in-between. Signals that did not present at least 128 consecutive T-wave were discharged from analysis. Three methods were applied to the remaining sequences.

Classical Method (CM)—Taken as reference, the first approach consisted in measuring the T-wave amplitudes of every sinus beat in the sequence previously taken. The detection of the T-wave peak was carried out calculating the maximum value form a 300 ms width window, started at 100 ms after R-wave peak, and stored in a vector. For CM, T-wave peak vector was then Fourier transformed and the peak on the PSD spectra at 0.5 cycles per beat measured [7] (Fig. 1).

Hilbert Transform Approach (HT)—An artificial continuous (AC) signal embracing consecutive isolated T-waves morphologies were created by concatenating 128 consecutives T-waves, extracted as in CM. The signal was clipped below its mean value to reduce its amplitude, and improve
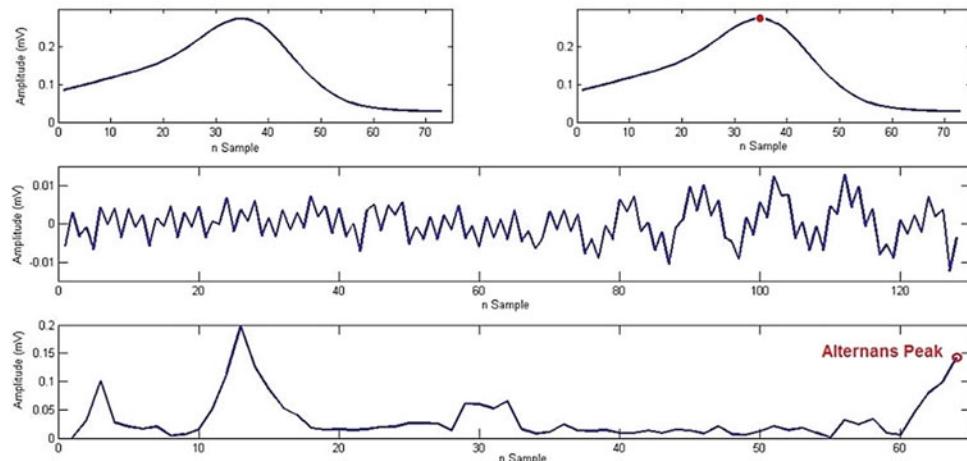
Fig. 1 MTWA identification using CM for TWA17, channel 1. Upper panel in the left shows the 300 ms window containing one T-wave and the right one the same T-wave and it peak. The middle panel shows T-wave peak vector (alternans vector) and lower panel shows FFT of alternans vector. The red dot indicates the alternans peaks (Color figure online)

Fig. 2 MTWA identification using HT approach for TWA29, channel 1. Upper panel show the part of the ECG signal with 128 consecutive T-waves. The middle AC signal (blue) and it envelope (red). Lower panel shows FFT AC envelope. The red dot indicates the alternans peaks (Color figure online)
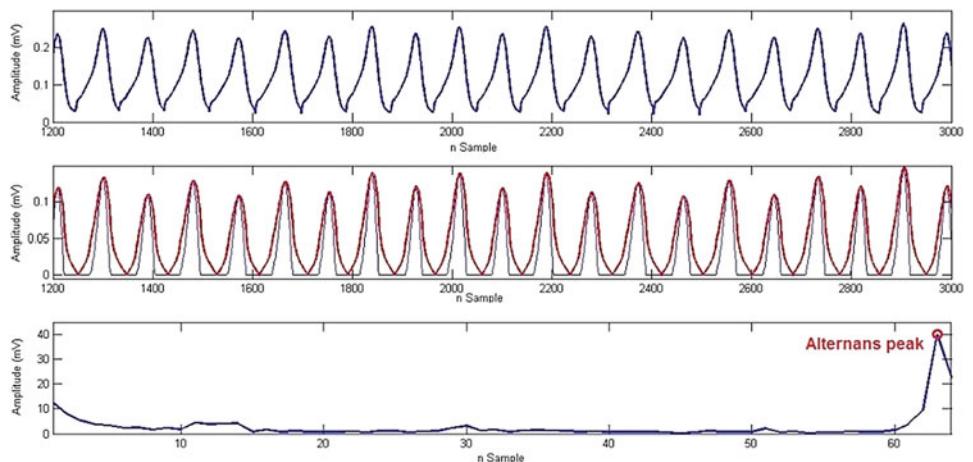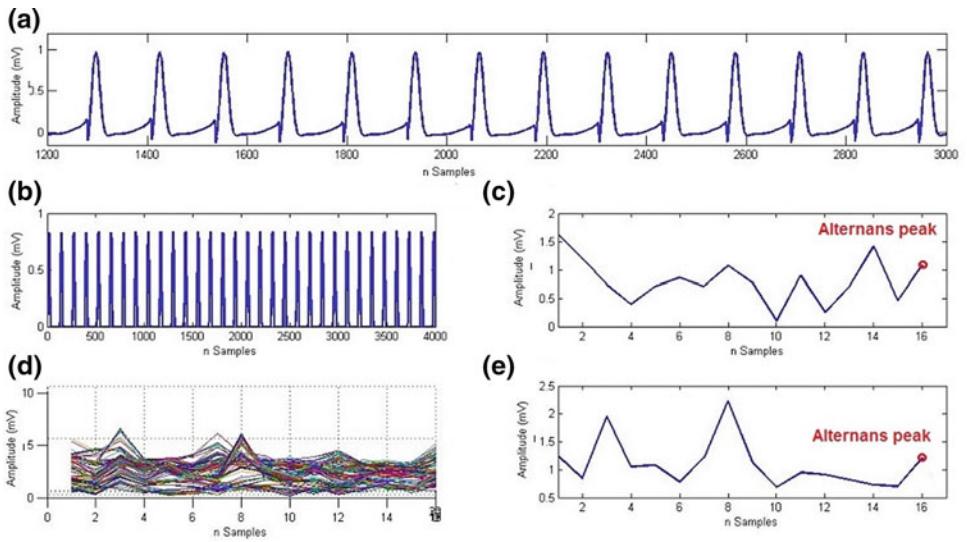
Fig. 3 MTWA identification using STS approach for TWA82, channel 1. **a** Upper panel show the part of the ECG signal with 128 consecutive T-waves. **b** The middle left brings AC signal windowed in 32 T-waves and right, **c** show its FFT amplitude. **d** Lower panel in the left shows 96 FFTs and, on the right **e** the average all 96 consecutive amplitude spectra. The red dot indicates alternans peaks (Color figure online)

analysis. The envelope of this signal was assessed by the Hilbert Transform (the absolute value the of sum of the actual signal and its Hilbert Transformed version multiplied by the imaginary unit). It was hypothesized MTWA may be captured by the envelope of the T-waves sequences [8]. The envelope function was Fourier transformed to isolate a T-wave peak amplitude alternation. The peak at the frequency corresponding to half of the whole T-wave series frequency was isolated and quantified, defining alternans peak [8] (Fig. 2).

Short-time spectral approach (STS)—For this approach, it was used the same artificial signal as in HT. Instead of calculating the envelope of the signal, here we used a 'moving-average' approach to asses MTWA. The artificial signal was divided into 96 windows containing a 32 consecutive T-waves. Consecutive windows were one-by-one T-wave displaced. All 96 windows were Fast
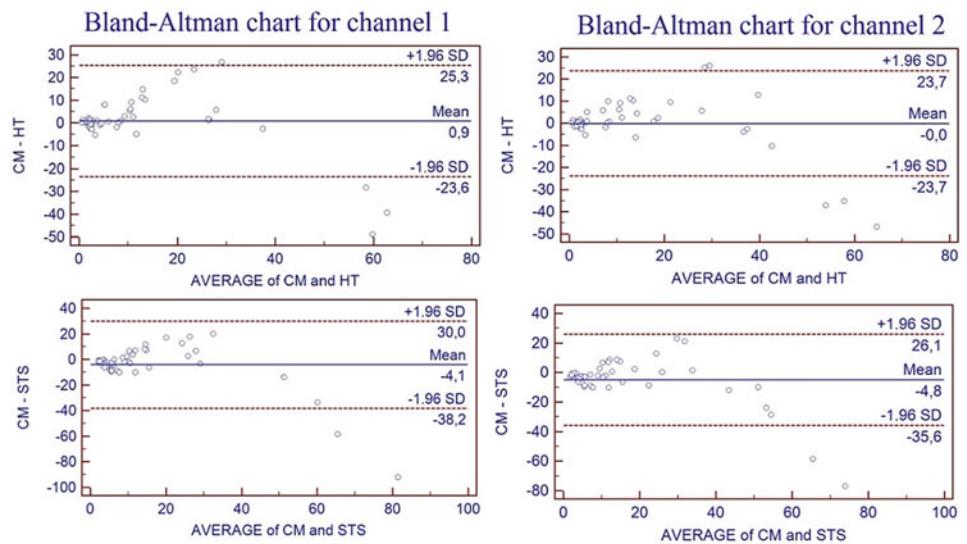
Fourier Transform and averaged. To assessed MTWA, in this approach, the peak at the frequency corresponding to half of the whole T-wave series frequency (in this case 32) was isolated and quantified, defining alternans peak (Fig. 3).

For all methods alternans was calculated as 'alternans ratio', defined as the alternans peak divided by the standard deviation of ten consecutive harmonics immediately neighbor to the peak. 'Alternans ratio' above three units are considered abnormal [6].

2.4 Statistical Analysis

The classical method was used as reference and compared to Hilbert Transform approach and to short-time spectral approach by correlation coefficient, Bland-Altman charts and the area under ROC. To offer a quantitative assessment of

Fig. 4 Bland Altman charts. The left panel shows channel 1 results, respectively, CM versus HT and CM versus STS. The right panel shows channel 2 results, also CM versus HT and CM versus STS

Bland-Altman chart significance, the percentage of points outside the 95% confidence interval was compared against zero percentage using a Chi-squared method. The alternans peaks were also compared by linear correlation using the Pearson correlation coefficient. Alpha error level was always set at 0.05.

3 Results

Signals preprocessing and the three methods were developed using MATLAB® code. Statistical analyses were implemented by MedCalc® platform. All data were successfully submitted for preprocessing analysis. The 32 simulated signals were considered able to MTWA analysis. Some real signals did not fit the MTWA requirements profile: 13 were too short (did not convey 128 consecutive normal beats, at least), 11 signals were excluded due to excessive baseline noise by visual inspection (Excessive noise group median 0.092 mV, [lower quartile 0.049 mV; upper quartile 0.264 mV]). Additional nine signals were excluded, since no sequence of 128 consecutive sinus beats could be extracted due to ectopic beats and 17 did not present T-wave. Thus, 18 real and 32 synthesized signals were used for MTWA evaluation (8 control cases and 42 pathological cases).

In CM, alternans frequency was found at 0.5 cycles per beat, in HT approach and in STS approach alternans frequency was found exactly at half of the corresponding whole T-wave series frequency (harmonics 64 and 16 respectively). The numeric comparison of alternans ratio was performed by correlation coefficient. By comparing classical method with Hilbert Transform approach correlation coefficient were 0.787 for channel 1 and 0.835 for channel 2 ($p < 0.001$), and for short-time spectral analysis, the obtained correlation

coefficients were, respectively, 0.798 for channel 1, and 0.836 for channel 2 (also $p < 0.001$).

Bland-Altman chart for alternans ratio comparison between CM versus HT presented only four cases outside the 95% confidence interval for channel 1 and 5 cases for channel 2 (respectively, $\chi^2 = 0.13$; $p = 0.72$, $\chi^2 = 0.40$; $p = 0.52$). By comparing CM versus STS using Bland-Altman chart it presented two cases outside the 95% confidence interval for channel 1 and 2 ($\chi^2 = 0.04$; $p = 0.83$ for both channels. Figure 4). Non-significant differences for CM versus HT and CM versus STS comparison were found after Bland-Altman chart analyses, in both channels.

Comparison of ROC curves also resulted non-significant differences between CM versus HT and CM versus STS. The area under ROC curves of CM, HT and STS were, respectively, 0.75, 0.80 and 0.71 for channel 1 ($p < 0.05$ for all), and 0.77, 0.80 and 0.70 for channel 2 ($p < 0.05$ for all).

4 Discussion

This study assessed two alternative methods for micro T-wave alternans based on T-wave morphology instead of precise T-wave peak detection. Both methods were applied to an AC signal, composed by 128 sequences of windowed T-waves clipped at its mean value. HT approach applied Hilbert Transform to calculate the envelope of AC signal, which prescinded T-wave peaks detection for MTWA identification. In STS approach, a 'moving-average' over 32 consecutive FFT amplitude spectra was applied to AC signal, also prescinding T-wave peak detection. Methods were applied to standard database, provided for Physionet, containing 42 pathologic ECGs with tracings of T-wave alternans and 8 control cases. Compared to CM, both methods

showed high numeric correlation and reproducibility, turning them to be promising tools for MTWA clinical application.

The proposed methods overcome the accurate T-wave peak detections, showing high numeric correlation. ROC curves results showed that HT present higher sensitivity above the three methods.

This evaluation was based in manly synthesized data, because real data do not fit the MTWA requirements. STS method indicate MTWA may be assessed using less than 128 consecutive sinus beats, thus overcome this limitation. Also, it allows patients with many extra systoles ECGs to perform an MTWA analysis. Further analysis are need to confirm this statement.

The analysis was automatic performed based on the available database. For other analysis the methods require some improvements regarding preprocessing, identification of R-wave, differences sample frequencies.

The requirement of T-wave morphology clipping may influence the amplitude of the Hilbert transform envelope, which is a potential limitation of HT approach. Alternans detection also may be compromised in both HT and STS approaches by flat T-waves, making MTWA indeterminate. Further clinical analyses are needed to validate the utility of both methods for arrhythmia risk stratification, extra systoles detection.

Assessment of micro T-wave alternans based on T-wave morphology approaches is feasible, accurate and reproducible.

References

1. Smith, JM, et al. Electrical alternans and cardiac electrical instability. Circulation, 77:110–121 (1988).
2. Shimizu W, Antzelevitch C. Cellular and ionic basis for T-wave alternans under long-QT conditions. Circulation, 99:1499–507 (1999).
3. Akar FG, et al. Transmural Electrophysiological Heterogeneities Underlying Arrhythmogenesis in Heart Failure. Circ Res, 93:638–645 (2003).
4. Walker ML, et al. Hysteresis Effect Implicates Calcium Cycling as a Mechanism of Repolarization Alternans. Circulation, 108:2704–2709 (2003).
5. Rosenbaum, DS et al. Electrical alternans and vulnerability to ventricular arrhythmias. The New England Journal of Medicine, 330:235–241 (1994).
6. Detecting and Quantifying T-Wave Alternans. Physionet. http://www.physionet.org/challenge/2008, last assessed 2017/10/15.
7. Benchimol-Barbosa PR, et al. Alternância elétrica da onda T: Bases eletrofisiológicas e aplicações clínicas baseadas em evidências. [In Portuguese] Revista da SOCER J, 17:227–242 (2004).
8. Winkert,T. et al. Comparison of two methods for assessment of Microvolt T-Wave Alternans: discrete versus continuous T-wave analysis, Computing in Cardiology 2016, 43:45–48.

Electrode Optimization for Bioimpedance Based Central Aortic Blood Pressure Estimation

Margus Metshein, Hip Kõiv, Paul Annus, and Mart Min

Abstract

Evidence suggests that assessment of the central aortic pressure (CAP) of blood is vital for accurate detection of cardiovascular events and for making treatment decisions. Direct CAP measurement is possible and is used in clinical environment, however it is both costly and carries increased risk, therefore it is not suitable for preliminary screening and monitoring. Indirect noninvasive assessment of CAP has been around for several years. Applanation tonometry which is largely based on the research by O'Rourke et al. is method of choice and sometimes even described as gold standard for the noninvasive assessment of the central pressures, the pulse wave velocity and the heart rate variability. Pressure sensor is typically placed on the radial artery, and central aortic pressure is estimated by generalized mathematical transformation of the recorded waveform. While widely used the method has serious drawback—strong dependence on operator skills. The electrical bioimpedance (EBI) has emerged as viable alternative in search for the measurement methods with better repeatability. Its applicability has been confirmed in several studies involving simultaneous invasive CAP measurement, and comparative measurements with AtCor Medical SphygmoCor device. Further refinement of the method is considered in proposed paper. Electrical attachment of the bioimpedance measurement unit to the body is investigated and discussed.

Keywords

Bioimpedance • Electrodes • Pressure • Current distribution

1 Introduction

Measurement system must be connected to the tissue under investigation with electrodes. Yet it turns out to be the most vulnerable part of the system. Around 85% of the problems in EBI measurement can be associated with the electrodes [1]. First of all sensitivity distribution depends on the number and placement of the electrodes [2, 3]. There are also simultaneous parasitic couplings distorting the current distribution inside the object [4]. Current investigation tackles the problem of coupling uncertainties in case of the bioimpedance based CAP estimation [5]. Different flexible electrode materials are compared, and impact of the contact pressure is investigated in case of tetrapolar electrode configuration. The tetrapolar impedance measurement should minimize the impact of the electrode impedances to the EBI measurement, even if it cannot be fully eliminated [6]. Minimal or optimal pressure on the electrodes is desirable in order to avoid deformation of the artery under them, and to ensure true noninvasiveness of the measurement. Both the invariable part of the EBI of the local volume (Z_0) and the information carrying time varying part of the impedance ($\Delta Z(t)$) caused by the blood pulsation will be investigated:

$$Z = Z_0 + \Delta Z(t) \qquad (1)$$

Frequency dependence of the measured bioimpedance should also be investigated, as well as the impact of the electrode materials on different parameters. The HF2IS impedance spectroscope [7] together with the HF2TA transimpedance amplifier was used as measurement instrument of choice in all of the experiments.

M. Metshein · H. Kõiv · P. Annus (✉) · M. Min
Thomas Johann Seebeck Department of Electronics, School of Information Technologies, Tallinn University of Technology, Ehitajate tee 5, 19086 Tallinn, Estonia
e-mail: paul.annus@ttu.ee

2 Effect of the Increasing Distance Between the Electrodes on the Measured Impedance of the Wrist

It is proposed in the literature that blood is mainly resistive in kHz region of frequencies. The measured change in the impedance, because of the varying amounts of the blood, can be however complex, due to the actual current distribution. There is also tissue that lies between the electrode and the blood vessel and an unknown sensitivity distribution. Experiments were performed to evaluate the effect of the increasing distance between the electrodes, by using the electrocardiogram (ECG) electrodes. Standard ECG monitoring electrodes with foam tape (type 2228—3 M) were cut narrower (width of 9 mm) and attached in line on radial artery with the gap of 1 mm between the electrodes (center distance: 10 mm) (Fig. 1a).

The following four setups were used to measure the magnitude and the phase in the tetrapolar electrode configuration with the excitation signal amplitude of 500 mV and at the frequency of 128 kHz:

- Distance between the electrodes was increased in 10 mm steps by lifting the pair of exciting and measuring electrodes by one step (1).

- Distance between the electrodes was increased in 10 mm steps by lifting the pair of exciting and measuring electrodes by one step and removing the unused electrodes from in between the measuring electrodes (2).
- Distance between the electrodes was increased in 10 mm steps by lifting one measuring electrode by one step while the exciting electrodes were permanently set to outermost positions (3).
- Placing the electrodes in setup (1) on top of the ulnar bone region (4).

Graphical representation of the measured magnitude and phase can be seen on Fig. 2. Concerning the phase in the case of setups (1)–(2), the result is maintaining its horizontal trend, which was expected if the underlying tissues do not change much. The setup (3) shows the effect of the increasing phase shift for the increasing distance, which needs explanation. In the case of setup (4), the phase shift is bigger, indicating different tissues under the electrodes, which is true due to different location.

The magnitude in all of the setups is increasing quite linearly—approximately by 13 Ω per 10 mm in the case of setup (1) and by shorter steps in the case of setup (4)—about 8.5 Ω per 10 mm. One can realize that the presence of unused electrodes on the volume of the wrist in between the

Fig. 1 Electrodes and setup for EBI measurement on the wrist in tetrapolar configuration: **a** in the case of the increasing distance between the electrodes and **b** for comparison between different conductive electrode fabrics under the pressure
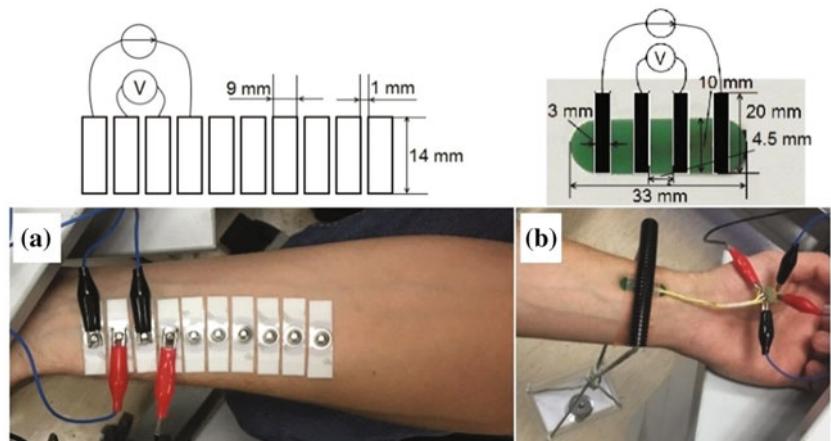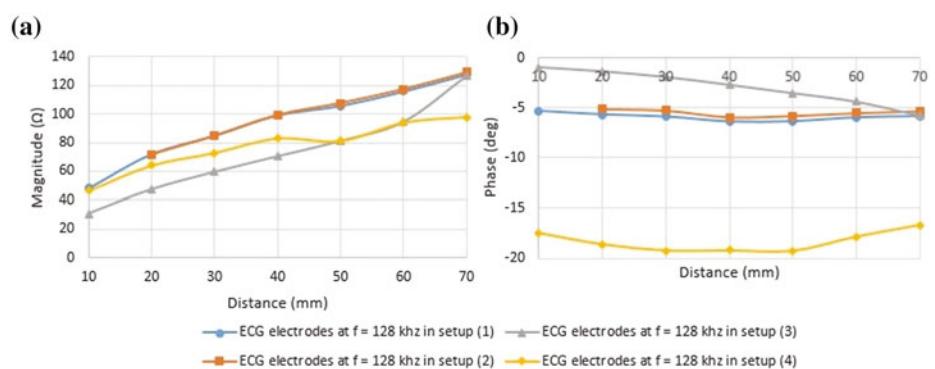
Fig. 2 Influence of the increasing distance between the measuring electrodes in the cases of different setups on: **a** the magnitude and **b** the phase of the EBI on the wrist

measuring electrodes does not influence the result. In the case of setup (3), the effect of excitation by distant electrodes is present, appearing in approximately 22 Ω lower magnitudes than in case of the setups (1)–(2).

Quite often it is assumed that [8, 9] electric current prefers to flow through blood in vessels because of the low resistivity, typically 1.5 Ωm. In reality also the presence of the skin, muscles, radial bone, radial artery and two radial veins should be considered. Calculation of the impedance of just the blood vessels in the local volume per 10 mm gives 830 Ω instead of the measured value of 13.3 Ω. Inner diameters of the radial artery and veins where taken to be 2.7 mm, and volumes of the blood were summed. This leads to speculations about the actual distribution of the current in the local volume of the wrist. Sizable impact of the muscles is expected because of their longitudinal resistivity of 2.4 Ωm. If the area of the hypothetical cylindrical volume of the muscle is taken to be ten times larger than the summed area of the radial artery and the two veins, then the calculated impedance is 140 Ω per 10 mm, still an order of magnitude larger than the measured value. Presence of other layers of lower resistivity like tendons and vessel walls should be taken into account as well, and complex current distribution picture will emerge. Further research is due here.

3 Influence of the Usage of Different Electrode Materials for Monitoring Pulse Wave by Measuring the Impedance of Wrist

From one side it seems plausible that the change in the electrode pressure will have some impact also on the EBI value. Question however is how big that impact is, and does it significantly depend on the electrode material. On the other side it seems beneficial to acquire also some information regarding the applied pressure during the measurement, which could enable to control it in more deterministic manner. Therefore specific pressure sensitive fabric was included in the list of potential candidates for the EBI electrodes. The goal therefore was investigation of the influence of the different electrode materials on the value of the measured Z_0 and on the magnitude of the $\Delta Z(t)$ under different pressures. Three different materials were chosen for evaluation as electrodes.

1. Nickel/cuprum (Ni/Cu) polyethylene terephthalate polyurethane conductive foam of part number Sui-78-20 (Seiren Co., Ltd.) with surface resistivity of 0.07 Ω/m^2.
2. Ni/Cu polyester taffeta conductive fabric of part number 3035-535 (Laird Technologies) with surface resistivity of 0.07 Ω/m^2.
3. EeonTex pressure sensing fabric of part number COM-14111 (SparkFun Electronics) with surface resistivity of 2 kΩ/m^2 at non-pressured state.

All of the electrodes were cut into equivalently sized pieces and attached onto a rigid printed circuit board (PCB) (Fig. 1b) for the experiments. The crocodile clips were attached to the ends of the fabric, and external pressure was applied on other side of the PCB. Single comfortably sitting volunteer was participating in the experiment. The hand was lying on the armrest at the height of about the lower rib. The weights used to apply the controlled pressure onto the radial artery where in the range of 0…700 g, with the step of 100 g. EBI of the wrist was measured by using tetrapolar electrode configuration with the excitation signal amplitude of 500 mV and at the frequency of 128 kHz. The graphical representation of the resulting EBI values can be seen in Fig. 3.

Out of three candidates the pressure sensitive textile has the worst highly nonlinear result. 2nd material however performs rather well showing slight nearly linear increase in magnitude. Graphical representation of the dependence of the magnitude of $\Delta Z(t)$ for all three fabrics can be seen in Fig. 4. The rising trend of $\Delta Z(t)$ is visible for all chosen materials when the external pressure on the radial artery is increasing.
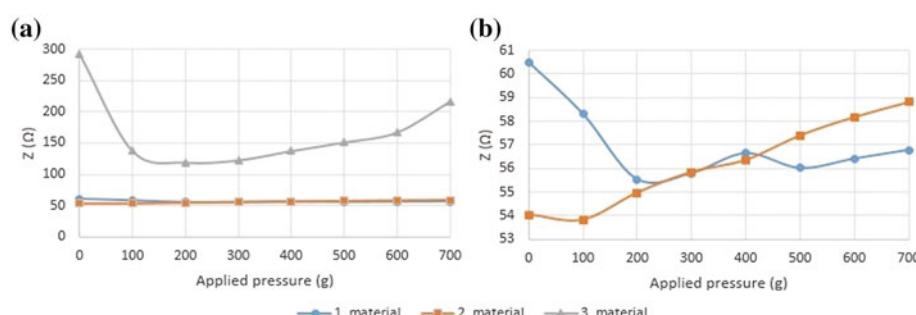
Fig. 3 Influence of the increasing external pressure on the magnitude of the EBI on the wrist for three different electrode materials: **a** all three materials, **b** zoomed in picture of the two best options

Fig. 4 Influence of the increasing external pressure on the value of ΔZ(t) for three different materials: **a** all three materials, **b** zoomed in picture of the two best options
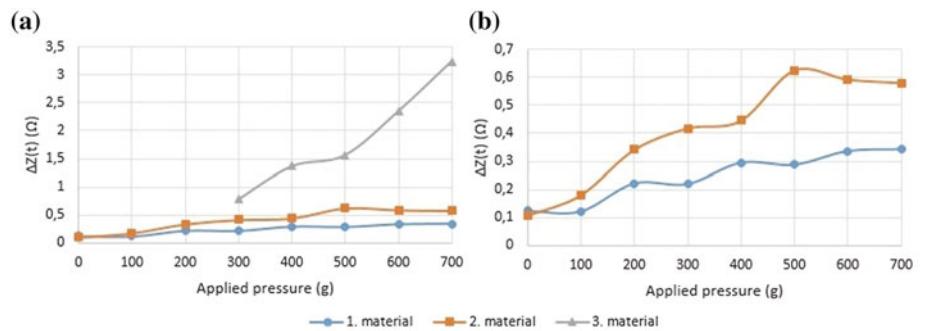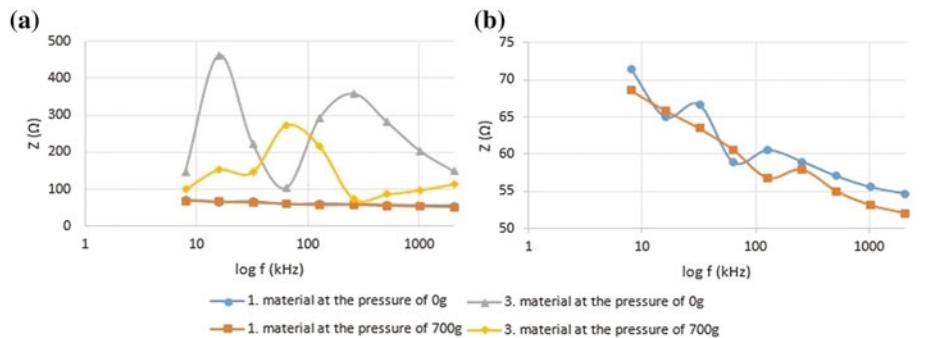

Fig. 5 Influence of the frequency of the excitation signal on the magnitude of: **a** all results, **b** zoomed in picture of the two best options

Last but not least the frequency dependence of the acquired EBI was investigated. The graphical representation of the magnitude of the EBI for 1st and 3rd electrode material can be seen in Fig. 5. As the 1st and 2nd material tend to behave quite similarly, only the first one is presented in the following figure. Also, only the results at two pressures are shown: 0 and 700 g. Clearly 3rd material exhibits strange nonlinear properties under different pressure and frequency combinations.

4   Conclusions

In some works it is assumed that the current density is greater in the path of least impedance i.e. in the blood in the artery under the electrodes, than in the surrounding tissue. In other works it is regarded as a largely unsolved basic problem: "To what extent does an externally applied electric current follow blood vessels?" [1]. Cause for the time variance of the impedance is also still debatable [1]. Is it blood volume change or orientation of the erythrocytes, or something else? Measurement results seem to suggest that the current is distributed more widely and in more complex manner than expected, as the roughly calculated impedance of the blood vessels in the local volume is about 830 Ω per 10 mm, instead of the measured value of 13.3 Ω.

Attempt to get multimodal readings form the same textile electrodes, both the EBI and the pressure, has failed with tested material, which is behaving very poorly for the EBI assessment. Nevertheless the idea is appealing, and further investigation will follow with different pressure sensitive materials. It is probably safe to conclude that there is optimal pressure point (roughly 300 g of applied weight), where the artery is not deformed too much, and the EBI readings are good. Placement and configuration of the electrodes plays an essential role as well, and should be investigated further.

The results should be considered preliminary, experiments were conducted only on a single person, and conclusions debatable, but hopefully provoking some thoughts. The authors declare that they have no conflict of interest.

References

1. Grimnes, S.: Bioimpedance and bioelectricity basics. Elsevier, Boston, MA (2014).
2. Grimnes, S., Martinsen, Ø.G.: Sources of error in tetrapolar impedance measurements on biomaterials and other ionic conductors. J. Phys. Appl. Phys. 40, pp. 9–14 (2007).

3. Patterson, R.P.: Impedance cardiography: What is the source of the signal? J. Phys. Conf. Ser. 224, 012118 (2010).
4. Aliau-Bonet, C., Pallas-Areny, R.: On the Effect of Body Capacitance to Ground in Tetrapolar Bioimpedance Measurements. IEEE Trans. Biomed. Eng. 59, pp. 3405–3411 (2012).
5. Min, M., Annus, P., Koiv, H., Krivosei, A., Uuetoa, T., Lamp, J.: Bioimpedance sensing - a viable alternative for tonometry in non-invasive assessment of central aortic pressure. In: Proc. 12th IEEE Int. Symp on Med. Meas. and Appl. (MeMeA), pp. 373–378 (2017).
6. Cömert, A., Hyttinen, J.: Impedance spectroscopy of changes in skin-electrode impedance induced by motion. Biomed. Eng. OnLine. 13, 149 (2014).
7. HF2 User Manual ziControl, https://www.zhinst.com/, (2017).
8. Bang, S., Lee, C., Park, J., Cho, M.-C., Yoo, Y.-G., Cho, S.H.: A pulse transit time measurement method based on electrocardiography and bioimpedance. In: Proc. of Biomed. Circuits Syst. Conf. (BioCAS), pp. 153–156. IEEE, Beijing, China (2009).
9. Lee, W., Cho, S.H.: Integrated all electrical pulse wave velocity and respiration sensors using bio-impedance. IEEE J. Solid-State Circuits 50(3), 776–785 (2015).

Photoplethysmographic Measurements on Clinical Patients (>65 y) and Healthy Cohorts Between Ages of 18–75 y

Matti Huotari, Juha Röning, Kari Määttä, and Pekka Romsi

Abstract

The biomedical information on different indexes like arterial elasticity index (AEI), arterial age (AA) is used in many cases. However, they applicability for diseases earlier prediction like arteriosclerosis (AS) is seldom applied. Many illnesses are becoming common, especially cardiovascular disorders (CVD) among elderly people, and in females. It is predicted that the negative impacts of AS on young people can be greater than on the elderly people in the long run because of sedentary lifestyle. Degenerative changes in the arteries have many causes in addition to the lifestyle. Arterial elasticity (AE) would provide a direct indicator for cardiovascular healthiness and predict AS. AE can be challenging in the cases of elderly, but also in the case of the young persons whose endothelial functions have been earlier very good. The vessel properties would be important to know for characterization of both arterial diseases and the development of reliable devices. Photoplethysmography (PPG), and especially its response pulse wave decomposition, envelope analysis, and its second order derivative (SDPPG) open the new health information for clinics. PPG signals are correlated with the alterations in blood pressure, blood flow, arterial elasticity, and health indexes. Exposure of human to physical exercise has been shown to improve endothelial function in patients with risk factors and heart failure. Exercise has been shown to be protective to cardiovascular disease. In addition according to this study, the exact mathematical solution for the pulse wave analysis has be replaced by numerical analysis method. In addition, a probability density function and a coherence function suits well to the inherent resting PPG process, and giving some intrinsic properties of the arterial pulsation phenomena.

1 Introduction

Photoplethysmographic (PPG) waveform represents peripheral blood flow. Electrocardiogram (ECG) produces information from the heart, but it does not provide any simple information on the arterial tree. PPG wave reflects both peripheral and central hemodynamic properties. PPG device uses infrared and red light emitting diodes which transmit light through the tissue to noninvasively measure hemodynamic parameters such as pulse wave form, and is thus a useful measure of vascular dysfunction and heart rate variability (HRV). HRV in subjects at rest, we can have the fingertip PPG, which is as accurate as ECG based HRV. On the other hand, the blood systolic and diastolic pressures exhibit short and long term pressure variabilities. However, PPG signals are sensitive to motion artefacts even in presence of small motion, both physical and psychological. Physiological and cardiovascular changes can be phasic related to the stimulus exposure but also tonic without close relation to exposures. The tonic response is related to the baseline.

M. Huotari (✉) · J. Röning
Faculty of Information Technology and Electrical Engineering (ITEE), BISG, Oulu University, Pentti Kaiteran Katu 1, FI-90014 Oulu, Finland
e-mail: matti.huotari7@gmail.com

J. Röning
e-mail: juha.roning@oulu.fi

K. Määttä
Faculty of Information Technology and Electrical Engineering (ITEE), CAS, Oulu University, Pentti Kaiteran Katu 1, FI-90014 Oulu, Finland
e-mail: kari.maatta@oulu.fi

P. Romsi
Vascular Surgery, Oulu University Hospital, 90029 Oulu, Finland
e-mail: pekka.romsi@ppshp.fi

Many mathematical relations exist between blood pressure, blood flow, and arterial elasticity. However, in clinics blood pressures are measured on the periphery. If two PPG signals correspond to each other perfectly at a given frequency, the magnitude of coherence is 1, as in the case of finger IR and RED PPG. If they are totally unrelated coherence will be 0, as in the case of any PPG and phonocardiography (PCG). In PPG technology, the main difficulty is its quantitative analysis, namely calibration, and comparison of PPG wave measurement obtained from different patients and skin areas. Coherence is to explain cause and effect relations and their linearity. Coherence function is calculated as follows. The two parallel signals have their FFT transforms for coherence function. Coherence measures the degree of linear dependency of the two PPG signals for equal frequency components. In our measurements the light intensities and wavelengths (red 640 nm and infrared 920 nm) are fixed. In practice, the arterial pulse waveform is based on the propagating pulse wave from the left ventricle. It travels through the arterial circulatory system and arrives the multiple peripheral, parallel capillary arteries. Capillaries can be identified visually by the naked eye, so we do use no clearing material such as propylene glycol for the PPG measurements. The propagation velocity depends on heart generated pulse and arterial wall elasticity, which is not well understood. The composed pulse waveform can be decomposed with different mathematical analysis domains, such as time or frequency-based. A single PPG wave is the summation of forward and backward waves. It is likely sure that the PPG pulse waveform is composed at least five components. The more elastic the arterial wall is, the slower the PPG pulse wave velocity is. Elasticity of the arterial wall changes as a function of aging, and blood pressure, as in the case of hypertension. This change can be measured by an inexpensive and operator independent PPG device. It has been worked with analysis of the arterial pulse wave and the second derivative of the PPG signal. The raw PPG signal reflects peripheral circulation, which is related both to arterial vasoconstriction and vasodilatation controlled by the autonomic nervous system in the long term and modulated by the heart cycle beat intervals in the short term. However, the challenges with clinical subjects are the variability of the PPG signals from finger, toe, and nose, or even in the ear. Our need to analyse the signal on a case by case basis so long we don't have the proper electronic automation. For automated diagnosis also based on photoplethysmography would be important. The intensity of the PPG signal is a function of the blood volume in the tissue, and it fluctuates due to the cardiovascular cycle. The pulsation carries many kinds of information about the function of the cardiovascular system, which is not yet known [1].

New bioengineering measurements and devices are needed to overcome the burden of healthcare system. Notwithstanding its simplicity, PPG measurements and analysis have many challenges. Essential factors affect PPG pulse amplitude either increasing or decreasing. Especially decreased amplitude (smaller pulses) are caused by vasoconstriction pharmacologically, physiologically (by cold, surgical-induced stress, increased tissue congestion (venous), hand or toe position lower than the heart (when measured at the finger or toe), or in Valsalva, low stroke volume (when critically reduced). Increased PPG amplitude (larger pulses) are caused by vasodilation pharmacologically, physiologically (by warming, sedation, sepsis), anesthetically (by regional blocks, decreased tissue congestion (venous)), and hand or toe position held above the heart (when measured at the finger or toe). We calculate numerically the second derivative of the finger, toe, and nose PPG pulse waveform. The closed form solution for the arterial pulse waveform can be obtained from the fluid dynamic equations, but due to the variability of parameters of the equations means that a closed form exact solution is impossible to derive or it would not have any closed form solution. The non-linear form of the equations prevents from deriving a closed form, analytic solution which could be used in studying the short-term control produced by the autonomous nervous system. Without accurate functional modelling of the PPG dynamics, we use its envelopes (upper and lower), in the application of normalization which provides very satisfactory results. Our envelope curve is the source data enveloped so that it is tangent to every peak in the raw or filtered PPG data. Origin software obtains the upper, lower, or both envelopes of the PPG data by applying a local maximum method combined with a cubic spline interpolation. Also arterial elasticity could be more exactly determined for the arterial stiffness indicator. For example, inter beat interval (IBI) plots are interesting measured from the subject finger versus toe. In this case it is calculated based on the second derivatives of PPG waveforms from the finger and toe. The nose and ear PPG signal could give more information on the head and neck arteries. The PPG signal is caused by the heart beat causing the percussion wave, followed by the tidal wave generated in the aorta. The other reflected waves are coming from the periphery as follows, dicrotic wave, repercussion wave, and retidal wave. However, the origins of the waveforms of the PPG signal are not fully understood, it is generally accepted that PPG can provide valuable clinical knowledge on the cardiovascular

system under study. Tthe fluctuating flow of blood is measured as an alternating signal superimposed on a steady signal that makes a PPG waveform [1].

2 Subjects and Methodology

The clinical patient measurements were conducted in Oulu University Hospital (Oulu, Finland) as a clinical device test (test II), where we studied 17 patients of who 10 subjects exhibited normal arterials and 7 patients with peripheral arterial disease according to the ankle brachial index (ABI). The data were acquired by means of USB-NI 6012 (16 bit) measurement card connected to the SignalExpress software (NI) having a sampling frequency of 1 kHz. The studies was approved by the ethical review boards of the Oulu University and University Hospital and the Finnish National Supervisory Authority of Health and Welfare (VALVIRA). Informed consents were obtained from the test subjects, who abstained from alcohol, caffeine, and strenuous exercise in the 24 h up to the day of the tests. The age causes changes in the PPG pulse shape and also on the second derivative of the PPG (SDPPG) wave forms on which the calculated ratio B/A (the first minimum, the first maximum, respectively, Fig. 2). Also an asynchronous PPG pulse appears as a time delay between the left forefinger PPG and left second toe PPG. The delays are the longer, the more elastic the person's arteries are. We see that automation is needed on the PPG analysis.

Theoretically in PPG measurements, the transmission (T) of light through a series of N attenuators (e.g. haemoglobin molecule) can be written as the product or summation of the transmission through each of the individual attenuator, since each one attenuates the light that is incident upon it:

$$T_{overall} = I_{out}/I_{in} = T_1 T_2 T_3 \ldots T_N \qquad (1a)$$

or in otherwise

$$\log[T_{overall}] = \log[I_{out}/I_{in}] = \log[T_1] + \log[T_2] + \log[T_3] \ldots + \log[T_N] \quad (1b)$$

where T_i are any attenuator, I_{in} and I_{out} are the incident and transmitted light intensities, respectively. Unity transmission indicates that all of the incident light I_{in} passes through the attenuators without loss and $I_{out} = I_{in}$ while transmission $I_{out} = 0$ is complete extinction, and $T_{overall} = 0$ by Eq. 1a and 1b.

When an absorbance term is inject in the similar case, we get for N attenuators being some biological components

$$A_{total} = E_1 C_1 L_1 E_2 C_2 L_2 \ldots E_N C_N L_N \qquad (2)$$

Transmittance (T), reflectance (R), and absorbance (A) added together as giving 1, accordingly
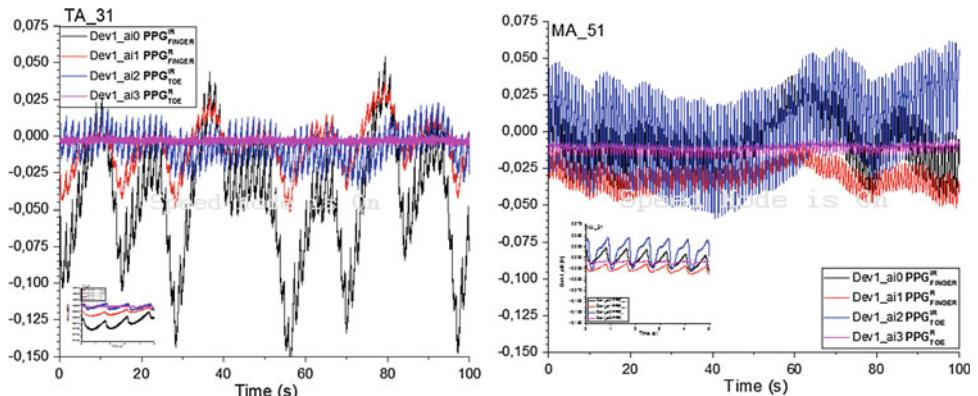
$$1 = T + R + A = 1 \qquad (3)$$

PPG signal is originating by the very small change in blood volume caused by each heartbeat. As the volume of blood in tissue changes, the absorption of light by red cells also changes because of their orientation. In decomposition analysis of the pulse waves produces five components: percussion wave, tidal wave, dicrotic wave, repercussion wave, and retidal wave. SDPPG waveform envelopes produce the distinction of five sequential waves called the initial positive wave, the early negative wave, the late upsloping wave, the late down sloping wave, and the diastolic positive wave.

3 Results and Discussion

As an example, Fig. 1 shows PPGs for red (620 nm) and infrared (920 nm) measured from the index finger, and second toe of a 31, and 51 years male, respectively. The data sets behaves differently compared with each other.

It is worth noting that the discussed system for arterial elasticity diagnosing is based on analysis of set of arterial finger, toe, and nose PPG pulses that are uncovered from the PPG envelopes. Figure 2 shows PPGs and PCG ratio as a function of time for from the left index finger for infrared (black) and red (red), and from the left second toe for

Fig. 1 PPGs measured from left index finger, left second toe by infrared led (black lines), by red led (red), from left second toe by infrared led (blue), by red led (violet) from a 31 and 51 years male healthy cohort. Inset for a 5 s PPG records (Color figure online)
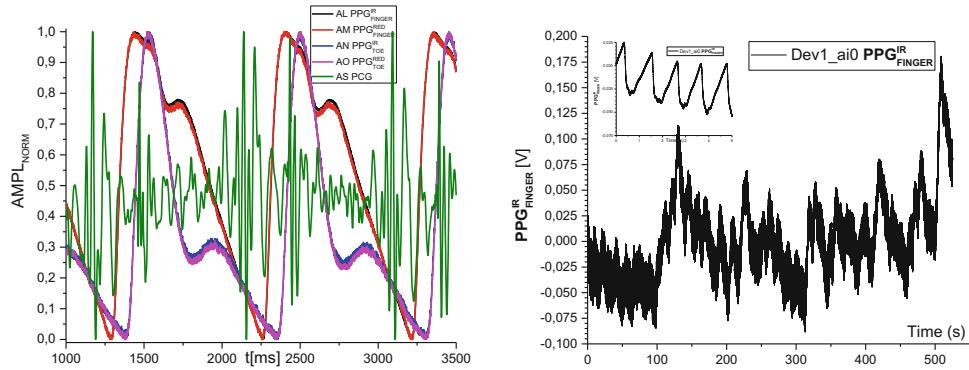
Fig. 2 On the lift side, PPG measured from left index finger by infrared led (black line), by red led (red), from left second toe by infrared led (blue), by red led (violet) (normalized 0,...,1), and by PCG (green) from a 22 years male healthy cohort. On the right side, raw PPG recording of finger infrared PPG for over 500 s from a 33 years male healthy cohort (Color figure online)
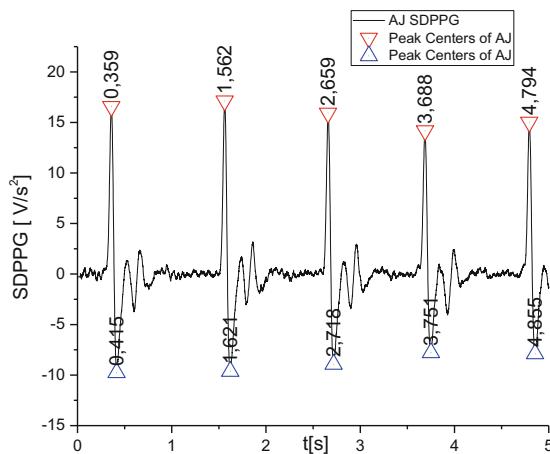

Fig. 3 SDPPG for 5 s from the left index finger by infrared led from a 32 years male healthy cohort, where A is marked by triangle pointing down (red) and B by triangle pointing up (blue) from Fig. 1 right side PPG (Color figure online)

infrared (blue) and red (magneta) from a 32 years male healthy cohort. We can see that the functions are dynamic changing much after about the first minute. The coherence is a statistic function that examines the relation between two signals, in this case two biomedical signals to estimate the power transfer between input and output of a linear system. If the signals are ergodic, and the system is linear. Here it is used to estimate the causality between the fingers and toe PPG. Values of coherence will always satisfy $0 \leq$ coherence ≤ 1 as a function of frequency (see also Fig. 4). Figure 4 shows the coherence as a function of frequency for each PPG pairs.

It is worth noting that arterial elasticity diagnosing is based on analysis of set of arterial finger, toe, and nose PPG pulses that are uncovered from the PPG envelopes. However, SDPPG can be used for evaluation of vascular aging. In Fig. 3 the SDPPG for 5 s is shown from the left index finger by infrared led from a 32 years male healthy cohort,
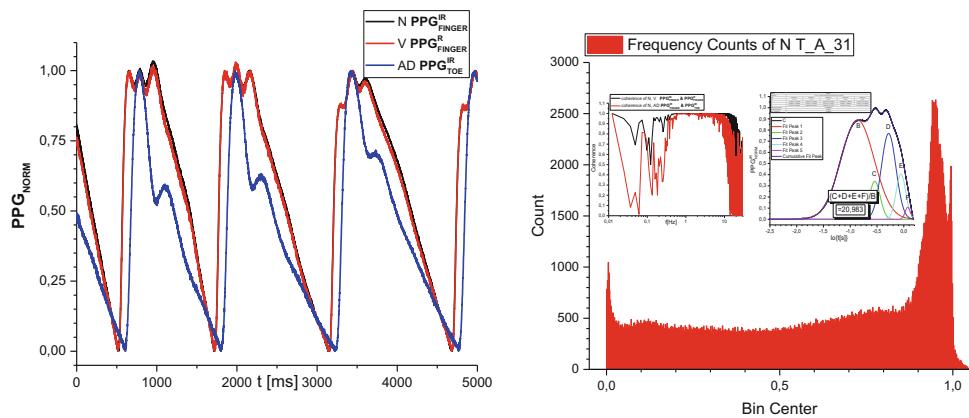
Fig. 4 The PPG signals (left) from the finger infrared led (black), red led (red), and toe infrared led (blue). On the right coherence functions of PPGs measured between the left index finger by infrared and red, and finger with the infrared led between the left second toe by infrared led. On the bandwidth the coherence is about 1 for finger-finger (black)

and finger-toe (red), and about 1 on the measurement band for the finger and toe, respectively. On the right side the decomposed single pulse waveform (0.999 correlation coefficient between the measured and model). Probability function is shown on the bottom of the Figure (Color figure online)
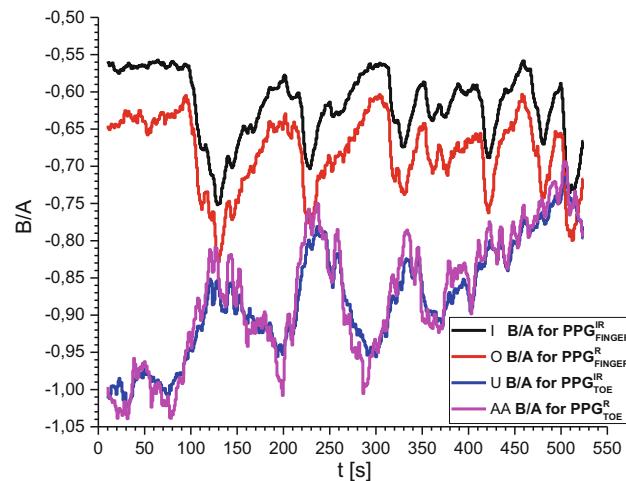
Fig. 5 SDPPG based B/A ratio from the left index finger for infrared (black) and red (red), and from the left second toe for infrared (blue) and red (magneta) from a 32 years male healthy cohort from Fig. 1 the whole right PPG (black) (Color figure online)
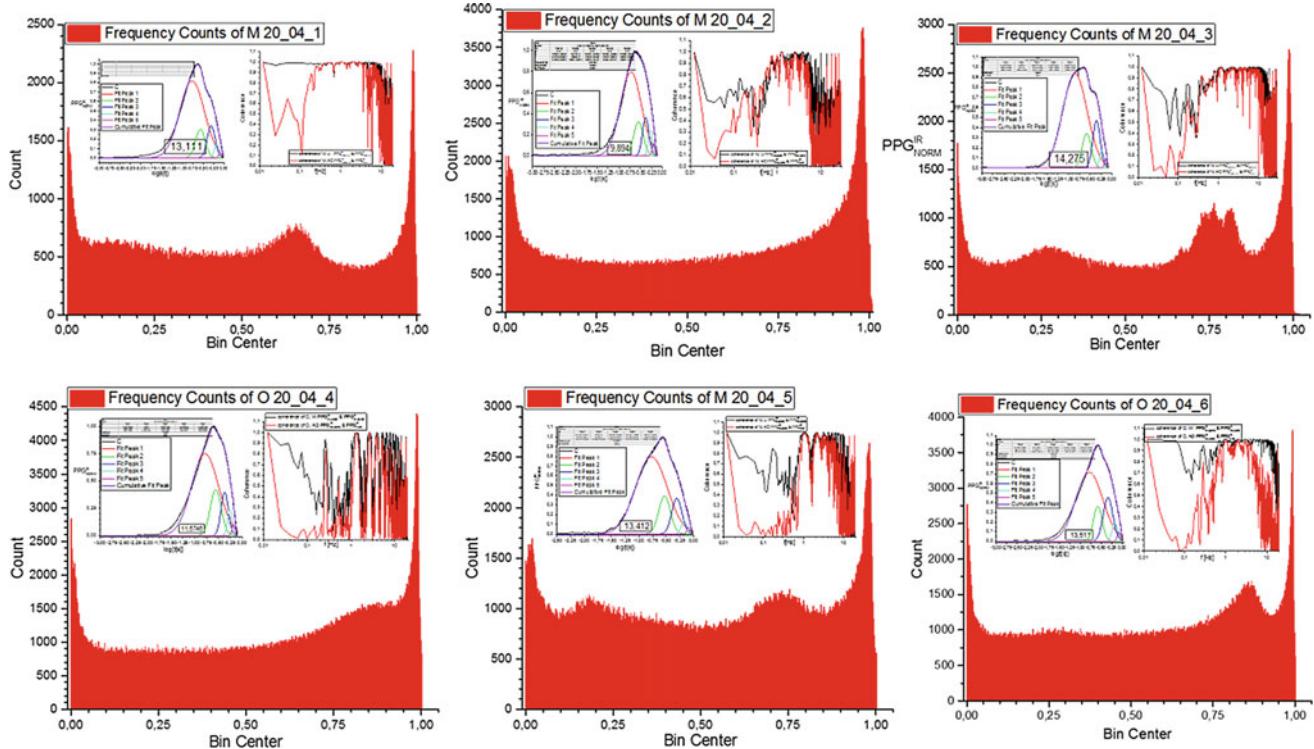
Fig. 6 The six patient data based decomposed functions, coherence and probability functions as examples

where A is marked by triangle pointing down (red) and B by triangle pointing up (blue) from Fig. 1 right side PPG. Figure 4 shows SDPPG based ration B/A for red as a function of corresponding ratio for infrared measured from the index finger for (a) a 34 years male, for (b) a 65 years male patient, for (c) a 65 years female healthy cohort, and

(d) a 22 years male healthy cohort. b/a ratio might reflect the large arterial elastic properties, or even AS. In Fig. 5 the case (b) is an AS patient and (c) is a healthy cohort. The arterial elasticity indexes are nowadays based on a single value. Figure shows, however, the elasticity is a variable parameter based on b/a ratio as a function of time. Figure 6 shows the
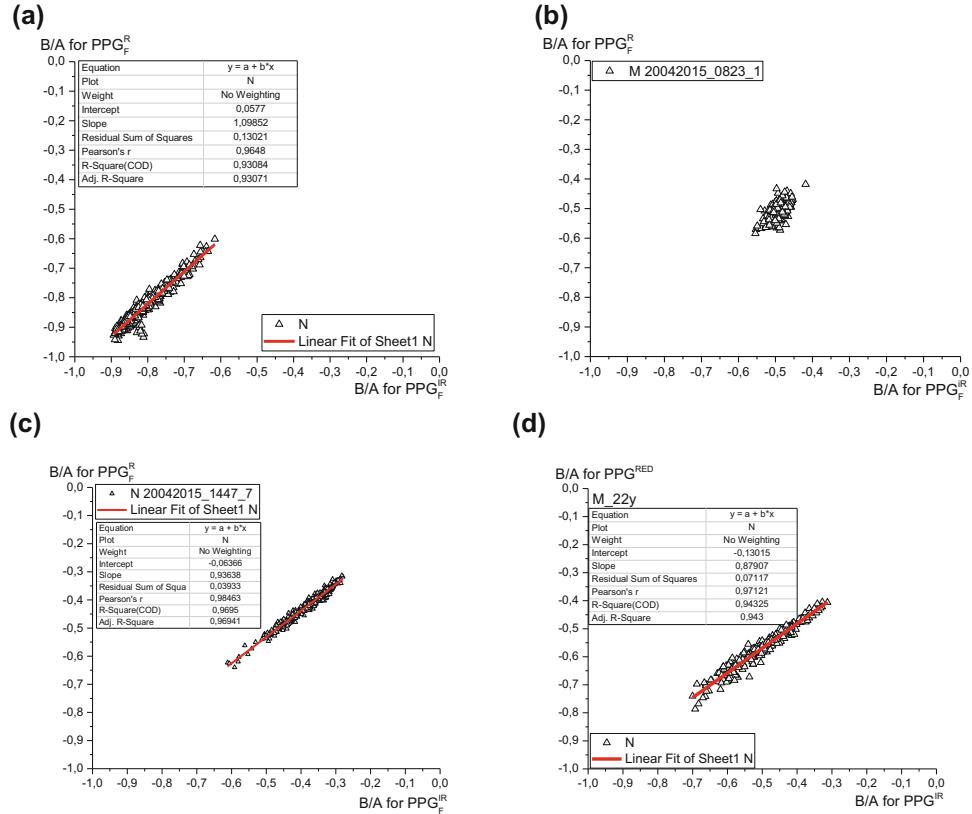
Fig. 7 SDPPG based ration B/A for red as a function of corresponding ratio for infrared measured from the index finger for **a** a 34 years male, for **b** a 65 years male patient, for **c** a 65 years female healthy cohort, and **d** a 22 years male healthy cohort
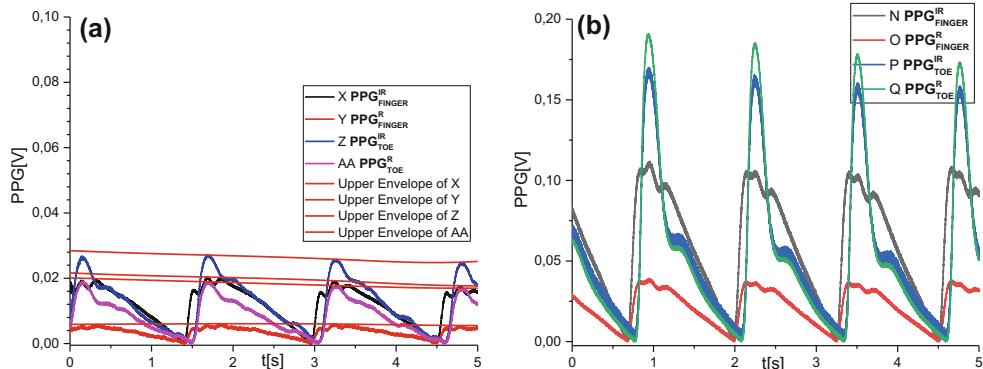
Fig. 8 PPGs measured from left index finger, left second toe by infrared led (black lines), by red led (red), from left second toe by infrared led (blue), by red led (violet) from a 33 years subject before

physical exercise (**a**) and after physical exercise (**b**), respectively, for a 5 s record shown (Color figure online)

six patient data based decomposed functions, coherence and probability functions as examples. They all have the different analysed functions, coherence, and also probability density functions (Fig. 7).

Figure 8 shows the male persons' data based on the physical exercise effect. The physical exercise exposure could be good input for testing purposes. Further test would be needed to make clear the different causes of response
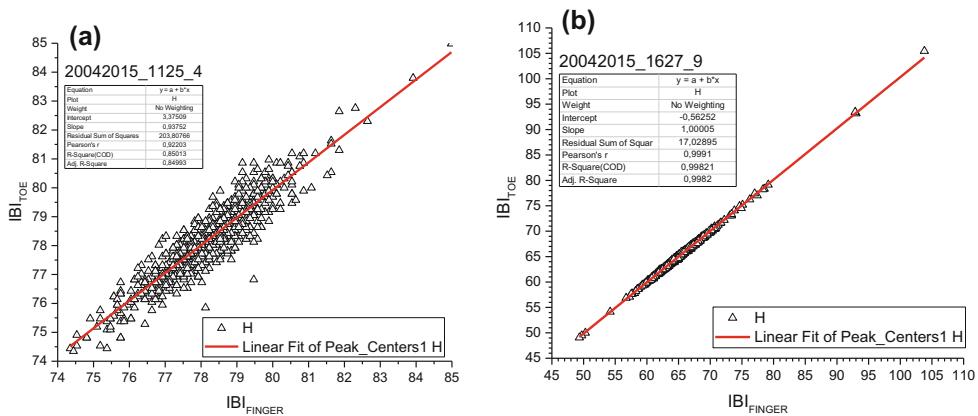
Fig. 9 IBI-plots of SDPPG based IBI for two patients (>65 y) measured from left index finger, left second toe by infrared led. The correlation coefficient for **a** 0,850, and **b** 0,998, respectively
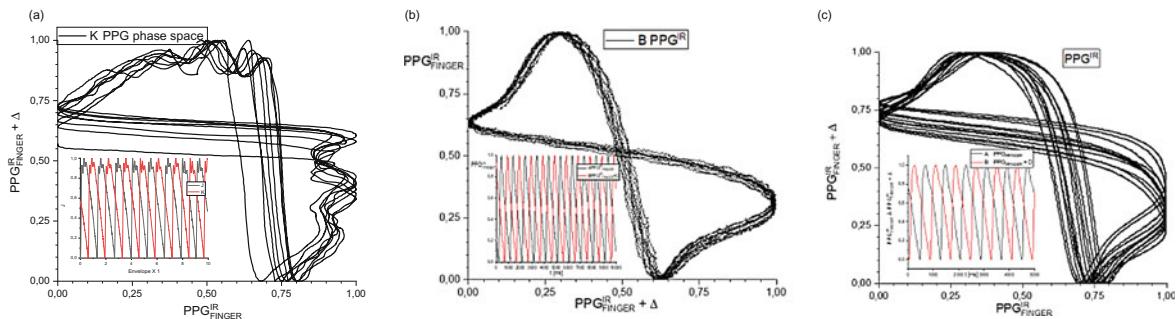
Fig. 10 Phase-space-plots of PPG from the index finger of a young male (36 y) (A), two patients (>65 y) (B), and (C). The pattern of the phase-space plots are different for the elderly. Inside the graph there is the corresponding PPG for 5–10 s in time (black the normalized PPG and red the phase delayed PPG, respectively) (Color figure online)

patterns before and after exercise. Figure 9 shows the correlation between the finger and toe IBI functions for two persons. In the case 8(a) the correlation coefficient is 0.850 and 8(b) it is 0.998. AA and AEI of the human arteries can be easily determined by PPG signal waveform. Patterns of the PPG waveforms are originating from the very small change in blood vessel walls caused by human ageing, Fig. 10.

References

1. Meglinski, I. (ed.), (2018) Biophotonics for Medical Applications, Woodhead Publishing Series in Biomaterials: Number 82.
2. Peltokangas, M, Vehkaoja, A, Huotari, M, Verho, J, Mattila, VM, Röning, et al. (2017). Combining finger and toe photoplethysmograms for the detection of atherosclerosis, Physiological Measurement, 38, (2).

Round Cosine Transform Based Feature Extraction of Motor Imagery EEG Signals

R. B. Braga, C. D. Lopes, and T. Becker

Abstract

Brain Computer Interfaces (BCIs) are systems with great potential for the rehabilitation of people with severe motor injuries. By analyzing a subject's brain waves, it is possible to detect patterns and translate his "thinking" into device commands, like prosthesis or a robotic arm. This research presents an EEG processing method, which is capable of detecting patterns of the subject's motor imagery, splitting the patters in left or right hand imagery. The proposed method considers the Round Cosine Transform (RCT), a low computational complexity transform, and an artificial neural network (ANN) module which identifies the patterns. The method has been tested in a real-time (RT) continuous EEG processing experiment simulation, controlling a mouse arrow horizontally on a screen based on the subject's imagery motor activity. The performance of the proposed method is evaluated in terms of the mutual information (MI), classification time and misclassification rate (%). The achieved results were 0.49 bits, 5.25 s and 15.6%, respectively.

R. B. Braga
Universidade Católica de Pelotas, Gonçalves Chaves, 373, Pelotas, Brazil
e-mail: rodrigobraga.fuzz@gmail.com

C. D. Lopes
Universidade Federal de Ciências da Saúde de Porto Alegre, Sarmento Leite, 245, Porto Alegre, Brazil
e-mail: carladiniz@ufcspa.edu.br

T. Becker (✉)
Universidade Federal do Rio Grande do Sul, Sarmento Leite, 425, Porto Alegre, Brazil
e-mail: tiago.becker@ufrgs.br

1 Introduction

There are several diseases that can lead to severe motor disabilities, including conditions where the fully conscious brain cannot use any of its natural paths to communicate with the external [1]. For these disorders, it would be very useful to have a communication system independent of the nerves and muscles of the body, interacting direct with the brain, translating the patient intents and thoughts directly into external actions. Then, brain computer interface (BCI) is an alternative to help severely disabled people to communicate with computers or control electronic devices through their thoughts [2].

Wolpaw et al. [3] define a BCI as "a communication system in which messages or commands that an individual sends to the external world do not pass through the brain's normal output pathways of peripheral nerves and muscles."

The signals of a BCI system are submitted to one or more feature extraction procedures, such as amplitude measurements and spectral or spatial filtering [3]. Those features normally encode messages or user commands. The BCI uses the time domain characteristics (like amplitudes of evoked potentials or firing rates of neurons) in the frequency domain, μ band (8–13 Hz) amplitude, β band (13–30 Hz) amplitude or both [3].

Important parts of the BCI systems are the algorithms of feature extraction and pattern classification. They are responsible for the correct patient intent translation, i.e., the correct interpretation of brainwaves. The significant features of a particular EEG signal characterize the behavior of the EEG signal [4, 5] and can be extracted from the samples and compressed into a few parameters. Using a smaller number of parameters to represent the EEG signal is crucial for recognition, classification and diagnosis purposes in a real-time (RT) system application.

The hypothesis was that using the Round Cosine Transform (RCT) method it is possible to classify the EEG signals of IEEE BCI Competition II, dataset III (a motor imagery

experiment) [6], with a better performance, when compared with the research [7], which also proposes an online continuous EEG processing experiment simulation.

The methodology proposed in this article is based on a fast Discrete Cosine Transform (DCT) approximation for the RCT [8]. The EEG features extracted by RCT are fed into a Multilayer perceptron (MLP) network, trained with the Backpropagation algorithm. The results obtained with this technique are compared with the results obtained by [7], which proposed a method that considers the Multivariate Gaussian Probability Density Function (MVGPDF) of Cepstral Coefficients (CC) to generate the probabilistic features over CC. Further, the extracted features are classified by linear classifiers: Naïve Bayes (NB) and discriminant analysis (DA).

2 Experimental Dataset

The experimental data used is from the BCI Competition II [6]. The dataset III is a motor imagery experiment. This dataset was recorded from a healthy subject (female, 25 years) during a feedback session. The subject sat in a relaxing chair with armrests. The task was to control a feedback bar in one dimension by imagination of left-hand or right-hand movements. The order of left and right cues was random. The experiment included 7 runs with 40 trials. Each one of these trials has a 9 s length. Three bipolar EEG channels were measured over C3, Cz and C4. The EEG was sampled with 128 Hz and was band pass filtered between 0.5 and 30 Hz [6].

3 Materials and Methods

3.1 Round Cosine Transform

The RCT is a fast approximation algorithm for the DCT [8], a well-known transform for its use in data compression [9]. The RCT approximates the DCT by rounding the elements of its transformation matrix to the nearest integer value. Due to the sinusoidal nature of the matrix elements, after the rounding process the transformation matrix will be composed only of zeros and ones, then the calculation of the product of the input vector (signal) by the matrix can be done using only sums. In the RCT no complete multiplier algorithms are needed [8], as a multiplication by multiples of 2 can be calculated by simple shifting operations in binary arithmetic.

These characteristics make the RCT a zero multiplicative complexity transform [8], which performs faster than the classic DCT algorithm [9]. Despite of being an approximation, Bayer and Cintra [8] reported that the RCT has a

comparable performance to the DCT, sometimes even better (in an image compression case study).

It is possible to use the brainwaves μ captured in the motor cortex to check the mental state of a person within the context of imagined movements [2]. The RCT [8] was applied in the frequency analysis of the μ as a method of preprocessing EEG signals, with a low computational cost.

3.2 Artificial Neural Networks

Artificial Neural Networks (ANNs) can be defined as a distributed parallel structure, composed by simple processing units, called artificial neurons. Multilayer perceptron (MLP) networks can be trained, in a supervised manner (i.e. showing the desired output for each input presented to the system), by an algorithm called Backpropagation [4, 10]. The idea of the Backpropagation consists in modifying the weights between neurons at the network, to minimize the output error (see details in [10]).

In this study, for validation purposes, a dataset is used to train the ANN (training data). After the training, the ANN is applied to a different dataset (test data) in order to validate the generalization of the system. A 10-fold cross validation analysis was implemented. The 280 trials were randomly separated into a training (140 trials) and a test (140 trials) set. The training set was used to train the ANNs, and the classifiers performance were measured over the 140 test trials.
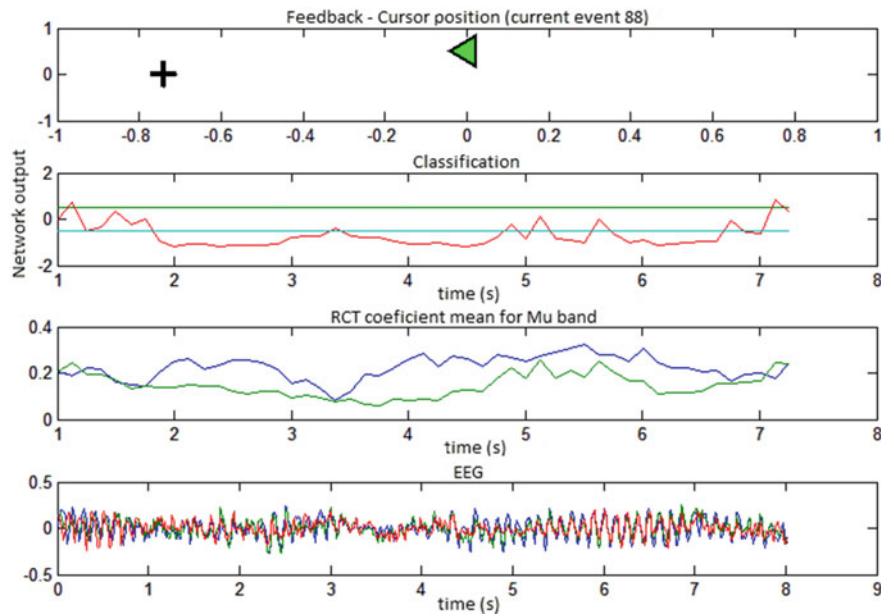
In the feature extraction method, a sliding window of 1 s of data (128 samples) issued for all the test trials to continuously generate the features. So, the analysis starts with 1 s delay. The selected features are then fed into the classifiers. The ANNs in this work have 10 neurons (best performance achieved with this number of neurons) in the hidden layer and 1 in the output layer (classifying the signal between left or right hand). The activation function of the hidden layer is the tangent sigmoid and the output neuron is linear.

The proposed methodology of a RT simulation for EEG signals classification is described below.

4 Proposed Methodology

The output of the ANN is used as the control signal to move the mouse pointer on the screen. The system simulates the capture of the EEG signal continuously by means of an electroencephalograph connected to a user. The test EEG signals came from the database [6]. An event of 9 s is chosen randomly from the 140 test signals. A window of size N slides along the signal, simulating the acquisition of new samples over time. As soon as the 9 s of the event is over, a new test event is randomly selected. Even though

Fig. 1 Interface of the developed system implemented in the RT simulation (example from event/trail 88) (Color figure online)

there is a discontinuity of waveforms between events, a signal is presented continuously to the classification system. The implemented system extracts the EEG characteristics with the RCT every time a new data is available, and uses the MLP previously trained for the classification. After initialization, the system waits for the buffer to be filled before processing starts. The feedback loop provides a device to be controlled (the mouse pointer) and visualization tools.

For each of the 280 trials of the dataset, the 128-point RCT was calculated, which means that a 1 s sliding window was used along the 9 s of each trial. For each time window, the RCT coefficients equivalent to the μ band over C3 and C4 were selected. The mean value for each channel was used to form the feature vector that feed the ANNs inputs. The algorithm developed with RCT and MLPs allows the classification system to run in RT, processing the EEG continuously, without requiring the structure of isolated events. The first step in feedback is to draw the curves on the screen. An experiment test of classification is described below in order to elucidate the process. All the algorithms were implemented in MATLAB®.

5 Results

The first graph in the Fig. 1 illustrates the control process. The cursor accompanies the direction of the mouse movement on the screen. The green arrow shows the side to which the volunteer should move the cursor in that event. The second graph shows the output of the ANN. The upper and the lower threshold were defined (straight blue and green). The third graph shows the value of the selected characteristics, i.e., the
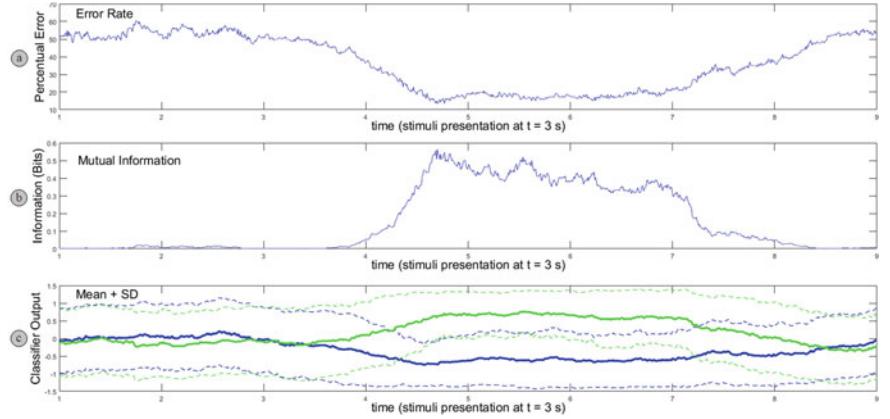
average of the RCT coefficients of the μ band for the channel C3 (blue) the channel C4 (green). The last graph in Fig. 1 shows the curves of the EEG measured. The signals of channels C3, Cz and C4 are drawn in blue, green and red respectively. These curves are updated in RT simulation as the signal is captured and processed.

The MLPs were trained to generate an output ranging from −1 to 1 based on the amplitude of the input characteristics. The value −1 indicate left hand movement, and the value 1 indicate right hand movement. The use of a continuous output signal allows the determination of the confidence with which the network performs the classification. The continuous output signal S of the network is discretized to control the mouse pointer by comparing it with a threshold value T. This value is adjustable but has a starting amplitude of 0.5 by default. The pointer is effectively controlled in RT as soon as the signal is sorted. The output of the ANN could be used in any application that requires one degree of freedom, or in a binary decision.

In order to evaluate the performance of the proposed method, the classification accuracy and the mutual information (MI) measured in bits are taken as the parameters of evaluation. These criteria were also chosen to allow the comparison with the results obtained previously [7] in an on line simulation of classification process.

The continuous output of the classifier has been used to compute the MI and the error rate for the test set. The system can identify the EEG signal from BCI Competition II (dataset III), as shown in Fig. 2. The MI is a measurement that has close relationship with the error rate, but takes into account the magnitude of the output (and not only the output class) of the classifier. It can be said that the MI is a measure

Fig. 2 Results of the test set classification. **a** Error rate. **b** MI. **c** Mean and SD of the output signal of the classifier for each class. Blue—Class 1. Green—Class 2 (Color figure online)

of the amount of information that a random variable contains about another [11]. Using the trained MLPs to classify the test dataset, one event at a time and in a continuous way, the curves of Fig. 2 were generated. As it was necessary to fill a buffer of 128 samples to perform the first calculation of the RCT and generate the characteristic vector, for the first 128 samples (first second) there is no classification (Fig. 2a).

The classifier output begins to differentiate for each class around time t = 3.5 s (Fig. 2a). This was expected, since the stimulus was given at t = 3 s, and the time required for the volunteer to produce conscious change in brain activity is around half a second [12]. Up to t = 3.5 s, the error rate was around 50%, as expected [12]. Since the volunteer did not perform imaging for either hand before the stimulus, no useful information could be extracted from his brain activity. When the subject begins to imagine the movement of a given direction, the classifier can detect its intention and the error rate decreases rapidly.

The same is true for MI (Fig. 2b). Before the stimulus, the volunteer did not perform any action for which the network was trained to recognize. Then, the information transmitted is nearly null, with the curve remaining at 0 bits. When the classifier recognizes the act of the volunteer performing the imagery, the information is transmitted, and the value of the MI increases.

The Fig. 2c shows the mean and standard deviation (SD) of the output classifier, being Class 1 the left hand and Class 2 the right hand movement. It is possible to see that the curves tend to return to their initial state before the end of the event (t = 9 s). It is known that the volunteer, expecting that

the recording of the event is about to end, unconsciously reduces the effort in performing the imagery.

In the present study, in a 10-fold cross validation analysis, in test data, a mean accuracy of 84.4% was obtained, with a signal-to-noise-ratio (SNR) of 0.99 and a classification time of 5.25 s. The maximum MI achieved was 0.49 for the classification of the EEG signal between the left and right hand classes (see Fig. 2).

6 Discussion and Conclusions

The main criterion of the BCI competition II, dataset III was the maximum MI. The winning group used the Morlet wavelet as a type of extraction and analysis of multivariate distribution for classification [13]. The results were a maximum MI of 0.61, a mean accuracy about 89%, a SNR of 1.34, and a classification time of 7.59 s for the classification of the EEG signals. The results of this group outstands in relation to others, because the algorithm used by the researchers was designed to work specifically in single event system, with a short recording of EEG signal. The classifier of this group has a cumulative result, which can be observed by the advanced time instant for which the maximum MI occurs [12]. That is, the algorithm developed by this group would not behave satisfactorily in a RT application.

A correlate recent study [14] proposes a RT process of EEG emotion (pleasant, happy, frightened and angry) recognition. The study evaluated the EEG emotion classification computing the Fractal Dimension, 2nd–6th statistics

and higher order crossings features from theta, alpha and beta band waves. The support vector machine was used to classify those features. The average accuracy achieved was 46.56–81.41%. The results of time classification and SNR were not described. In the study [7], which also considers a RT simulation process of EEG classification, on the dataset III of the BCI Competition II, using the MVGPDF of CC to generate the features over the EEG signals, the accuracy obtained was about 80.5%, and the maximum MI was about 0.33 in test data. The results of time classification and SNR were not provided.

Comparing the results obtained in [7, 13, 14] and this work, it can be observed that the RCT is a promising feature EEG extraction for RT applications. It was possible to classify the EEG signal continuously between the left and right classes, generating a minimum error rate of 15.6%, a SNR of 0.99, a classification time of 5.25 s, and a value of 0.49 for maximum MI bits.

Conflicts of Interest   The authors declare that they have no conflict of interest.

References

1. Liu, M., Chen, H., Chen, R., Wang, Z.: Low-power IC design for a wireless BCI system. In: IEEE International Symposium on Circuits and Systems (ISCAS), pp. 1560–1563, IEEE, Seattle (2008).

2. Thomas, K. P., Guan, C., Tong, L. C., Prasad, V. A.: Discriminative Filterbank Selection and EEG Information Fusion for Brain Computer Interface. In: IEEE International Symposium on Circuits and Systems (ISCAS), pp. 24–27, IEEE, Taiwan (2009).

3. Wolpaw, J. R., Birbaumer, N., McFarland, D.J., Pfurtscheller, G., Vaughan, T.M.: Brain–computer interfaces for communication and control. Clinical Neurophysiology 113(6), 767–791, 2002.

4. Lopes, C. D., Becker, T., Kozakevicius, A. J., Rasia-Filho, A. A., Macq, B., Susin, A. A.: A P300 potential evaluation wavelet method comparing individuals with high and low risk for alcoholism. Neural Computing and Applications 28(12), 3737–3748 (2016).

5. Dingyin, H., Wei, L., Xi, C.: Feature extraction of motor imagery EEG signals based on wavelet packet decomposition. IEEE International Conference on Complex Medical Engineering (ICME), pp. 694–697, Harbin, China (2011).

6. BCI Competition II Homepage, http://www.bbci.de/competition/ii/results, last accessed 2017/02/05.

7. Bhattacharyya, S., Mukul, M. K.: Cepstral Coefficients Based Feature for Real-time Movement Imagery Classification. International Journal of Engineering and Technology 8(1), 117–123 (2016).

8. Bayer, F. M., Cintra, R. J.: Image Compression Via a Fast DCT Approximation. IEEE Latin America Transactions 8(6), 708–713 (2010).

9. Feig, E., Winograd, S.: Fast algorithms for the discrete cosine transform. IEEE Transactions on Signal Processing 40(9), 2174–93 (1992).

10. Haykin, S.: Neural Networks: A comprehensive foundation. 2nd edn. Prentice Hall, PTR Upper Saddle River, NJ, USA (1998).

11. Guo, D., Shamai, S., Verdú, S.: Mutual Information and MMSE in Gaussian Channels. In Proceedings of IEEE International Symposium on Information Theory, pp. 349–349, IEEE, Chicago (2004).

12. Blankertz, B., Müller, K. R., Curio, G., Vaughan, T.M., Schalk, G., Wolpaw, J.R., Schlögl, A., Neuper, C., Pfurtscheller, G., Hinterberger, T., Schröder, M., Birbaumer, N.: The BCI Competition 2003: Progress and Perspectives in Detection and Discrimination of EEG Single Trials. IEEE Transactions On Biomedical Engineering 51(6), 1044–51 (2004).

13. Schlogl, A.: Outcome of the BCI-competition 2003 on the Graz dataset, http://www.bbci.de/competition/ii/results/TR_BCI2003_III.pdf, last accessed 2017/02/05.

14. Lan, Z., Sourina, O., Wang, L., Liu, Y.: Real-time EEG-based emotion monitoring using stable features. The Visual Computer 32 (3), 347–358 (2016).

Combined Phase and Magnitude Metric for Validation of Lower Limb Multibody Dynamics Muscle Action with sEMG

Carlos Rodrigues, Miguel Correia, João Abrantes, Jurandir Nadal, and Marco Benedetti

Abstract

This study presents and applies combined phase and magnitude metrics for validation of multibody dynamics (MBD) estimated muscle actions with simultaneous registered sEMG of lower limb muscles. Subject-specific tests were performed for acquisition of ground reaction forces and kinematic data from joint reflective markers during NG, SKG and SR. Inverse kinematics and dynamics was performed using AnyBody musculoskeletal personalized modeling and simulation. MBD estimated muscle activity (MA) of soleus medialis (SM) and tibialis anterior (TA) were compared on phase, magnitude and combined metric with simultaneous acquisition of sEMG for the same muscles. Results from quantitative metrics presented better agreement between MDB MA and sEMG on phase (P) than on magnitude (M) with combined (C) metric following the same pattern as the magnitude. Soleus medialis presented for specific subject lower P and M error on NG and SKG than at SR with similar P errors for tibialis anterior and higher error on M for TA at NG and SKG than SR. Separately and combined quantitative metrics of phase and magnitude presents as a suitable tool for comparing measured sEMG and MBD estimated muscle activities, contributing to overcome qualitative and subjective comparisons, need for intensive observer supervision, low reproducibility and time consuming.

1 Introduction

People walk for lower velocities and run for higher velocities. Under injury or pathology people frequently adopt modified gait (MG), namely stiff knee gait (SKG) and slow running (SR) as alternative to normal gait (NG). Despite redundancy of human muscular system, subjects tend to adopt stereotyped lower limb muscle recruitment during gait and running, with an open issue on lower limb muscle action (MA) on modified gait and running, namely SKG and SR in relation to NG [1].

Developments on multibody dynamics (MBD) have contributed for MA estimation during NG and MG from distribution of joint forces along with personalized musculoskeletal models using inverse methods and external data from kinematics and dynamics. MBD estimated MA require some validation based on direct measurements of muscle activity. Due to noninvasive nature sEMG is being used for muscle activity detection that can be compared with MBD MA estimation. Nonetheless, MBD MA estimation and sEMG present different natures with possible magnitude (M) and phase (P) differences requiring appropriate metrics for comparison [2]. The purpose of this study is to present and apply selected M and P metrics [3] for comparing MBD MA and corresponding lower limbs sEMG for assessment of MA during SKG and SR in relation to NG for a specific subject.

C. Rodrigues (✉) · M. Correia
Faculty of Engineering, FEUP, University of Porto, Porto, Portugal
e-mail: c.rodrigues@fe.up.pt

C. Rodrigues · M. Correia
INESC TEC, Institute for Systems and Computer Engineering, Technology and Science, Porto, Portugal

J. Abrantes
MovLab, Interactions and Interfaces Laboratory, Lisbon, Portugal

J. Nadal
UFRJ, Federal University of Rio de Janeiro, Rio de Janeiro, Brazil

M. Benedetti
UFPE, Federal University of Pernambuco, Recife, Brazil

2 Materials and Methods

2.1 Experimental Tests

The experiment was performed in accordance with the ethical guidelines of the North Denmark Region Committee on Health Research Ethics (N-20130014) and the participant provided full written informed consent prior to the experiment. The study subject, one adult healthy male was weighted 70 kg mass and height measured 1.86 m. Adhesive reflective markers were attached to subject palpable skin surface of the right and left anterior and posterior superior iliac spines, thigh superior, knee medial and lateral, shank superior, ankle medial and lateral and toes. Simultaneous recordings of ground reaction forces, skin markers attached to the lower extremity and EMG were obtained with two AMTI force plates sampling at 2000 Hz, eight camera Qualisys system at 100 Hz and Noraxon wireless system at 2000 Hz. sEMG was recorded during NG, SKG and SR for soleus medialis (SM) and tibialis anterior (TA) of the subject right leg and normalized to dynamic maximum voluntary contraction (MVC) with counter movement jump for SM and right leg swing for TA.

2.2 Musculoskeletal Modeling

Musculoskeletal analysis was performed using AnyGait v. 0.92 set up for the experimental setup, starting with generation of stick-figure model based on a static trial, over-determinate kinematic analysis over the dynamic trial and joint angles, morphing Twente Lower Extremity Model (TLEM) to match the size and joint morphology of the stick-figure model for inverse dynamic analysis based on joint angles and kinetic boundary conditions. TLEM model comprises eight rigid segments with twenty-one degrees of freedom (dof) including HAT (Head, Arms and Trunk), pelvis, right and left thigh, right and left calf, 3 dof for trunk orientation, 6 dof for 3D position and pelvic orientation, 3 dof for each of the right and left hip modelized as ball-and-socket joint, 1 dof for each joint of the knee, ankle and subtalar modeled as hinges. The mechanical effect of the 76 muscles of both legs were implemented through 264 muscular elements described by the 3D locations of their origins and insertion points in the corresponding segments, taken as independent actuators with specific muscle mass, pennation angle, physiological cross-sectional area (PCSA) and optimal length of tendon and muscle fibers. Attention was focused on MBD estimated muscle activities from the musculoskeletal model outputs and processed sEMG for

comparing different dynamic trials. AnyGait was set up to produce output using polynomial muscle recruitment criterion of power 3 and recorded sEMG was band-pass filtered at 10 and 400 Hz, rectified and low-pass filtered at 6 Hz to obtain linear envelope.

2.3 Data Analysis

Selected validation method splits metrics on amplitude (magnitude) and phase (time of arrival) of the measured (m) and computed (c) signal, providing independent error measures and combining it into a single metric based on integral wave form. For this purpose, considering $m(t)$ the measured signal and $c(t)$ the corresponding computed signal, the time integrals are calculated using (1) with $t_1 < t < t_2$ the time span of interest, in this case one complete stride for NG, SKG and SR.

$$v_{mm} = 1/(t_2 - t_1) \int_{t_1}^{t_2} m^2(t)dt$$
$$v_{cc} = 1/(t_2 - t_1) \int_{t_1}^{t_2} c^2(t)dt \qquad (1)$$
$$v_{mc} = 1/(t_2 - t_1) \int_{t_1}^{t_2} m(t)c(t)dt$$

Based on these measures the error magnitude is calculated using (2) that is phase invariant since it is based on the ratio of the area under the squared signals, with −1 ensuring zero metric when the two areas are equal.

$$M = \sqrt{v_{cc}/v_{mm}} - 1 \qquad (2)$$

The phase error is calculated using (3) that is invariant to magnitude differences, zero if $c(t) = m(t)$ and varies with τ if $c(t) = m(t - \tau)$.

$$P = 1/\pi \cos^{-1}(v_{mc}/\sqrt{v_{mm}v_{cc}}) \qquad (3)$$

Finally magnitude M and phase P error are combined using (4) into a single comprehensive error factor C as defined by [3].

$$C = \sqrt{M^2 + P} \qquad (4)$$

A complete stride corresponding to the time interval that mediates the beginning of two successive contacts of the right foot with the ground was selected for the analysis at NG, SKG and SR. The phases of the locomotion cycle were time limited based on ground reaction forces records, at NG and SKG from the instant start of the contact with the ground at the initial double limb stance (IDS), the start of the single

limb support (SLS), the start of terminal double limb support (TDS) and the start and end of the swing phase (SW), and at SR with beginning and end of the stance (ST), early float (EF), middle swing (MS) and late float (LF).

3 Results

Figure 1 presents synchronized %MVC of MBD estimated muscle action and linear envelope of registered sEMG of soleus medialis (SM) and tibialis anterior (TA) at various phases during a complete stride on NG, SKG and SR.

Processed sEMG and MBD muscle estimated activity presented for analyzed specific subject better agreement with lower error on phase (P) and lower agreement with higher error on magnitude (M), with combined (C) metric following the same pattern as the magnitude (M), Fig. 2 and Table 1.

Fig. 2 Absolute magnitude (M), phase (P) and combined (C) metric comparing of soleus medialis (SM) and tibialis anterior (TA) %MVC of MBD and sEMG at NG, SKG and SR

On phase NG and SKG presented for analyzed specific subject better agreement than SR for SM, Fig. 3. On

Fig. 1 Soleus medialis (SM) and tibialis anterior (TA) %MVC of MBD estimated muscle action and linear envelope of registered sEMG at NG, SKG and SR

Table 1 Quantitative of magnitude, phase and combined metrics between processed sEMG and normalized MVC of MBD muscle estimated activity

	% Magnitude (%)	% Phase (%)	% Combined (%)
NG–SM	−45.03	+30.95	+54.64
NG–TA	−63.37	+28.75	+69.59
SKG–SM	−44.01	+20.86	+48.70
SKG–TA	−64.39	+29.91	+71.00
SR–SM	+65.42	+39.90	+76.63
SR–TA	−47.16	+28.68	+55.20

Fig. 3 Absolute phase (P) and magnitude (M) metric of soleus medialis (SM) and tibialis anterior (TA) %MVC of MBD and sEMG at NG, SKG and SR
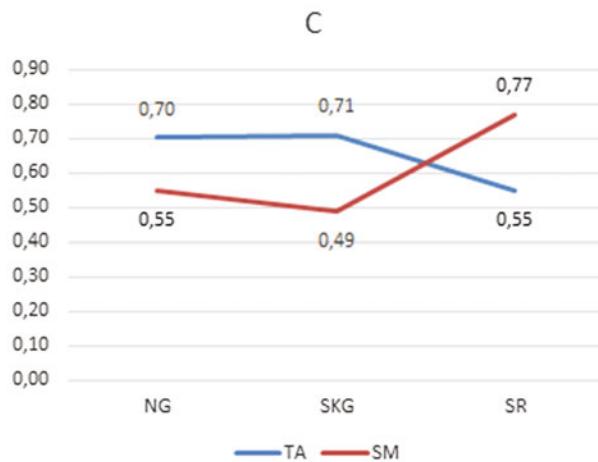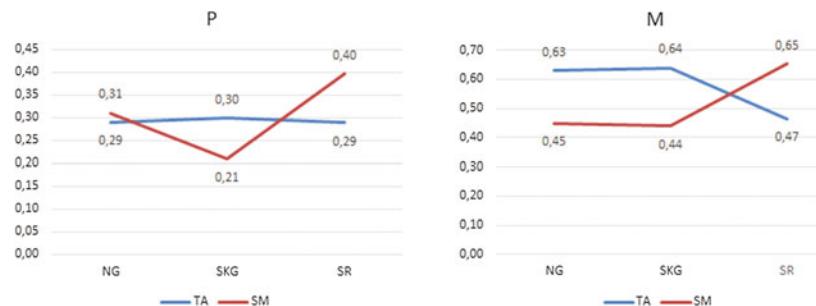
Fig. 4 Absolute combined (C) of phase (P) and magnitude (M) metric of soleus medialis (SM) and tibialis anterior (TA) %MVC of MBD and sEMG at NG, SKG and SR

magnitude SM presented better agreement than TA for NG and SKG with the opposite at SR, Fig. 3. Better combined agreement on SM for NG and SKG than at SR points to higher ability of the model to predict SM muscle actions in agreement with sEMG registered patterns at NG and SKG than at SR, with better ability for prediction of TA muscle actions on SR than NG and SKG, Fig. 4.

4 Discussion and Conclusion

Presented analysis showed that validation of the lower limb musculoskeletal model can be performed by comparing muscle activities predicted by MBD with the measured sEMG activity. Previous evaluations were mainly qualitative and based on the comparison between the instants of muscular activation and deactivation predicted by the model with the experimental results. Alternatively, with present study, the muscle activity estimated by MBD was compared to the sEMG recorded activity at tibialis anterior and soleus medialis muscles, using its entire time series, namely normal gait at self-selected speed, slow running and stiff knee gait. MBD estimated muscle activities compared well with processed sEMG for each considered gait mode, namely on antagonist nature of muscles tibialis anterior and soleus medialis, featured by their activities and time instants of activation and inactivation assessed by MBD predicted muscle activities and processed sEMG Despite estimated muscle actions with MBD and measured sEMG express different physical quantities, these were obtained under the same conditions of joint angles, angular velocities and accelerations, thus minimizing the error on acquisition and comparing under the same dynamic conditions. MBD estimated muscle activities presents as a powerful alternative when sEMG is not viable and sEMG as a tool

for MBD validation as well for modeling and simulation improvement. Separately and combined quantitative metrics of phase and magnitude presents as a suitable tool for comparing measured sEMG and MBD estimated muscle activities, contributing to overcome qualitative and subjective comparisons, need for observer intensive supervision, low reproducibility and time consuming.

Conflict of Interest The authors declare that they have no conflict of interest.

References

1. Perry, J., Burnfield, J. M.: Gait Analysis: Normal and Pathological Function. 2nd edn. SLACK Incorporated, Thorofare, NJ (2010).
2. Lund, M. E., de Zee, M., Andersen, M. S., Rasmussen, J: On validation of multibody musculoskeletal models. Journal of Engineering in Medicine 226(2), 82–94 (2012).
3. Schwer, L. E.: Validation metrics for response histories: perspectives and case studies. Engineering with computers 23(4), 295–309 (2007).

Detection of Sleep Stages in Temporal Profiles in Neonatal EEG—k-NN versus k-Means Approach: A Feasibility Study

Vladimir Krajca, Hana Schaabova, Vaclava Piorecka, Marek Piorecky, Jan Strobl, Lenka Lhotska, Vaclav Gerla, and Karel Paul

Abstract

The aim of this feasibility study is to experimentally verify the detection of changes of sleep stages in neonates with our proposed semi-automated approach using k-NN classification in comparison with a fully automated approach using simple k-means cluster analysis for classification (instead of k-NN). Our semi-automatic approach uses the k-NN classifier trained on etalons (prototypes) created by semi-automated etalons extraction (k-means for etalons suggestion and expert-in-the-loop for verification). Both methods are compared to labelling of sleep stages made by an experienced physician Dr. K. Paul. An EEG recording of full-term neonate is chosen from group of EEG recordings: full-term and preterm neonates recorded from eight electrodes positioned in standard conditions. The EEG recording is digitally preprocessed by mean-removal filter (no other filters are applied) and segmented adaptively. For each segment, 24 features are extracted and send to two classification processes: k-means and k-NN. Classified segments are plotted in temporal profiles (class membership in time) that are analysed for sleep stages using our method of creating a single detection curve from all channels and a threshold is applied on this detection curve to detect sleep stages.

V. Krajca · H. Schaabova (✉) · V. Piorecka · M. Piorecky
J. Strobl · L. Lhotska · K. Paul
Faculty of Biomedical Engineering, Department of Biomedical Technology, Czech Technical University in Prague, Kladno, Czech Republic
e-mail: hana.schaabova@fbmi.cvut.cz

V. Krajca
e-mail: krajcvla@fbmi.cvut.cz

V. Piorecka
e-mail: vaclava.piorecka@fbmi.cvut.cz

M. Piorecky
e-mail: marek.piorecky@fbmi.cvut.cz

J. Strobl
e-mail: jan.strobl@fbmi.cvut.cz

L. Lhotska
e-mail: lenka.lhotska@cvut.cz

K. Paul
e-mail: karelpaul@seznam.cz

L. Lhotska · V. Gerla
Czech Institute of Informatics, Robotics, and Cybernetics, Czech Technical University in Prague, Prague, Czech Republic
e-mail: vaclav.gerla@cvut.cz

1 Introduction

The aim of this study is to verify the feasibility of comparison of the result of our temporal detection curve applied on our semi-automated method (classification by k-NN and etalons extraction by k-means) from our previous paper [1] to the result of temporal detection curve applied on automated method of k-means cluster analysis as a golden standard method. Both methods are compared to a scoring of an experienced physician. The detection of sleep stages is also investigated in these papers [2–9].

2 Data

We process a full-term neonatal EEG recording from group of preterm and full-term neonate EEG (approximately 20 recordings in total). These EEG recordings are approximately 20–120 min long and they were measured in the Institute for the Care of Mother and Child in Prague. The data were recorded polygraphically from eight electrodes positioned in the standard "10-20" system (Fp1, Fp2, C3, C4, O1, O2, T3, T4). The electrodes were in unipolar montage with reference electrodes located on earlobes

(average from electrodes A1 and A2). Note that in full-term neonate recording we can see the difference between the quiet and active sleep stages visually compared to the pre-term neonate.

The data were scored by an experienced physician Dr. K. Paul into two sleep stages: quiet sleep (QS) and active sleep (AS), and two transitions: transfer to quiet sleep (TQ) and awake (AW).

3   Methods

3.1   Preprocessing and Adaptive Segmentation

The EEG recordings were collected using Brainquick (Micromed) system. This system has its own bandpass filter from 0.4 to 50.0 Hz. The multichannel EEG signal is digitally preprocessed by the mean removal filter and no other digital filter is applied. Another preprocessing step is the segmentation of EEG recording into EEG segments. For the purpose of this study, the adaptive segmentation is performed to create a mimetic approach that imitates the work of an expert. Using this method we obtain partly stationary segments of same characteristics from a generally non-stationary EEG. The methodology of A. Värri et al. [10] is used for adaptive detection of the segment borders with parameters stated in [1].

3.2   Feature Extraction

For each segment, we compute 24 features. The selection of the features is based on the results from clinical practice and on our previous experience [2, 4, 5]. Besides the traditional features based on the characteristics of the curve amplitude and bandpass frequency, we use the Hjorth's parameters [11], non-linear energy of segment [12], zero crossing [13] and others (see paper [1]). Each feature is normalized by maximum value of given feature in whole EEG signal.

3.3   Semi-automatic Etalon Selection

The semi-automatic etalon (prototype) selection (extraction) consists of cluster analysis (k-means algorithm) and an expert-in-the-loop which is described in our previous publication [1]. We already tried this approach on the epileptic adult EEG recordings [14]. Although there are 4 known classes in the neonate sleep EEG (QS, AS, TQ, AW), we use 12 classes of etalons from experience. In this study, we select $k = 15$ segments that are the nearest to the centre of the mean (in k-means) as the suggested etalons and the physician revises them.

3.4   Classification

For classification of EEG segments both supervised and unsupervised methods are used, so we can compare their feasibility for the sleep stage changes detection. The k-NN is used as a supervised method of classification (here with $k = 5$), it learns on a training set of etalons extracted with semi-automatic selection mentioned above.

The k-means cluster analysis is used as an unsupervised method of classification and it does not need any training set. The advantage should be that the cluster analysis is fully automated, so no expert-in-the-loop is needed, which can be also a disadvantage due to a missing context that the expert can bring to the classification process.
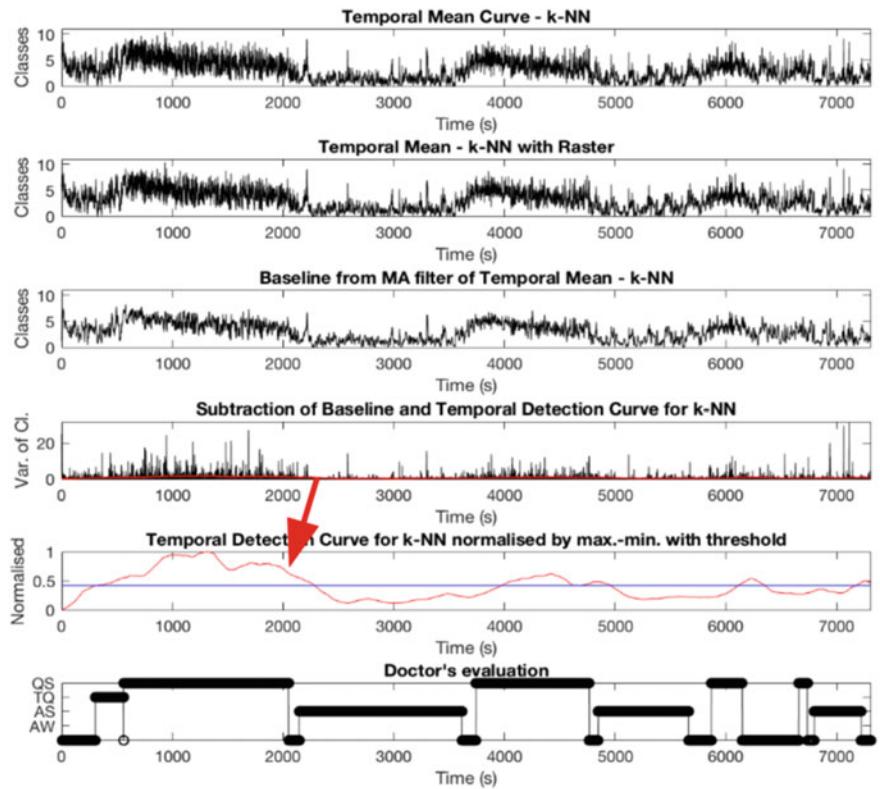
3.5   Detection of Sleep Stages Based on Temporal Profiles

The temporal (time) profile is the function of the class membership in course of time for one EEG channel [3]. The temporal profile is calculated and visualized for each EEG channel, so we get schematic plots of the EEG signal for each channel (8 channels in our case) that reflect the dynamics of EEG structure. The analysis of all temporal profiles can reveal hidden micro-structures and trends in the EEG recording. The derivative over several channels of temporal profiles can reflect topography of the EEG and possible asymmetry [15]. In this study, we analyse temporal profiles for detection of neonatal sleep changes as proposed in [3].

Note that for our detection purpose, the classes in each temporal profile for each channel are sorted from the highest to the lowest according to the feature: magnitude of amplitude variability. Also note that the classes containing only artefacts should be removed before the temporal detection process.

The detection of changes in the neonatal sleep stages (QS, AS) in temporal profiles consists of averaging the temporal profiles through all channels and getting one temporal mean curve (first subplot of Fig. 1). A raster of width WLBin is applied on the temporal mean curve (see second subplot of Fig. 1) to lower the amount of data (WLBin must be less than the minimal segment length). A baseline is extracted by using a MA filter with window length WLMean (see 3. subplot of Fig. 1). The baseline is subtracted from the rastered temporal mean curve and the result is squared to enhance the effect (see 4. subplot of Fig. 1). The resulting curve is smoothed twice with another MA filter of length WLSmooth which gives us the temporal detection curve. However, this curve has so low amplitude that it is not visible in the plot of the subtraction (subplot 4.), so the detection curve is normalised by its maximum and plotted in

Fig. 1 The process of creating the detection curve shown on results of k-NN classification method. The fourth subplot shows subtraction of rastered temporal mean and baseline from previous two subplots, which gives a red detection curve after MA filtering. The detection curve is then normalised (see the fifth subplot). A threshold is applied and the whole method is compared to the physician's evaluation (Color figure online)

subplot number 5 of Fig. 1 with a detection threshold (mean of the detection curve). See paper [1] for detailed description of the process.

The optimal parameters for the temporal analysis are chosen heuristically from experience. For a full-term neonate patient with EEG recording sampled with sampling frequency of 128 Hz, we used WLBin = 100, WLMean = 5, WLSmooth = 240.

4 Results

Comparison of k-means classification and k-NN classification is shown in Fig. 2. For each classification approach a normalised temporal detection curve is calculated from temporal profiles of 8 channels. Each detection curve has its own threshold experimentally calculated as a mean of its curve. The physician's labelling is shown in the lower part of the Fig. 2 and it represents 4 sleep stages (labels AS—active sleep, QS—quiet sleep, TQ—transition to sleep, AW—awake) in course of time. These labels should be aligned with the upper detection curve. But we can see that the detection curve is shifted due to the repeated MA filtering.

Note that the expert labelled only the parts of the signal that clearly qualify as sleep stages: AS, QS, TQ, AW. We can see that the crossing of the detection curves corresponds with the evaluation of the expert for most of the quiet sleep

stages. We can claim that if the detection curve is higher than the threshold then there is most probably a quiet sleep stage. The detection of quiet sleep stage seems to be possible from both classification approaches.

5 Conclusion

The feasibility study for comparison of fully automated k-means classification method (as a golden standard) and our semi-automated k-NN classification methods with expert-in-the-loop and cluster analysis for etalons extraction is investigated for improvement of detection of neonatal sleep changes. The temporal detection curves from both classification approaches are calculated. We can detect quiet sleep stage from both methods by detecting when the detection curve is higher than the threshold. The k-NN and k-means classifications detection curves give similar results in terms of crossing the detection threshold. This can be a result of the fact that the k-NN classification method is using etalons extracted as centres of k-means clusters, and usually this etalons are edited by the expert, but in this case no extensive editing was needed for this patient. This can be different for other patients as the physician will edit the training set of etalons. However, the advantage of the k-NN approach is the possibility that the expert can edit the etalons in the way he/she needs for the evaluation of the patient,
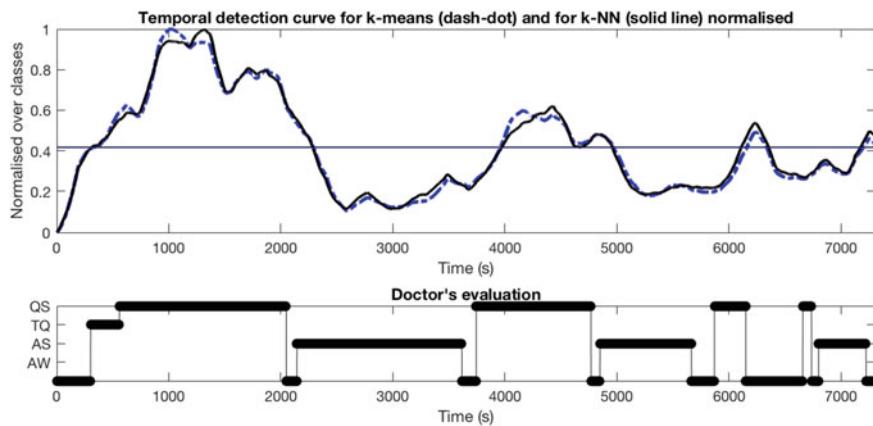
Fig. 2 Upper subplot shows two normalised temporal detection curves for sleep stages of a full-term neonate EEG recording calculated from temporal profiles of 8 channels. The blue dash-dot curve is the normalised temporal detection curve based on k-means classification. The black solid line curve is the normalised temporal detection curve based on k-NN classification. Each detection curve has its own threshold. The bottom subplot represents the evaluation of the expert (physician) into 4 sleep stages in course of time aligned with the upper detection curves (Color figure online)

where additional knowledge of the patient's treatment is entered by the expert. Further investigation is needed on full-term and pre-term neonates and also we aim at comparing our approach to other detecting methods suitable for neonatal sleep such as wavelet transform.

Conflict of Interest Declaration The authors declare that there is no conflict of interest regarding the publication of this article.

Statement of Informed Consent The study protocol and patient informed consent have been approved by the Institute for the Care of Mother and Child ethical committee.

Protection of Human Subjects and Animals in Research The procedures followed were in compliance with the ethical standards of the responsible committee on human experimentation (institutional and national) and with the World Medical Association Declaration of Helsinki on Ethical Principles for Medical Research Involving Human Subjects.

References

1. Krajca, V., Piorecka, V., Schaabova, H., Strobl, J., Piorecky, M., Lhotska, L., Paul, K.: Detecton of sleep stages in neonatal EEG records. In: Eskola, H., Väisänen, O., Viik, J., Hynen, J. (eds) *EMBEC & NBC 2017. IFMBE Proceedings*, vol 65. Springer, Singapore (2017).

2. Paul, K., Krajca, V., Roth, Z., Melichar, J., Petranek, S.: Comparison of quantitative EEG characteristics of quiet and active sleep in newborns. *Sleep Medicine*, 4: 543–552 (2005).

3. Krajca, V., Petranek, S., Paul, K., Matousek, M., Mohylova, J., Lhotska, L.: Automatic detection of sleep stages in neonatal EEG using the structural time profiles. In *27th Annual International Conference of the IEEE Engineering in Medicine and Biology Society*, 1–7 of *Proceedings of EMBC*, 6014-6016 (2005).

4. Gerla, V., Paul, K., Lhotska, L., Krajca, V.: Multivariate Analysis of Full-Term Neonatal Polysomnographic Data. *IEEE Transactions on Information Technology in Biomedicine*, 13: 104–110 (2009).

5. Djordjevic, V., Reljin, N., Gerla, V., Lhotska, L., Krajca, V.: Feature Extraction and Classification of EEG Sleep Recordings in Newborns. In *9th International Conference on Information Technology and Applications in Biomedicine*, 393+ (2009).

6. Piryatinska, A., Terdik, G., Woyczynski, W.A., Loparo, K.A., Scher, M.S., Zlotnik, A.: Automated detection of neonate EEG sleep stages. *Computer Methods and Programs in Biomedicine*, 95: 31–46 (2009).

7. Scher, M.S., Jones, B.L., Steppe, D.A., Cork, D.L., Seltman, H.J., Banks, D.L.: Functional brain maturation in neonates as measured by EEG - sleep analyses. *Clinical Neurophysiology*, 114: 875–882 (2003).

8. Krajca, V., Mohylova, J., Paul, K., Petranek, S.: Automatic detection of sleep stages in preterm neonates by exploring the time structure of the EEG. In *3rd European Medical and Biological Conference*, 1–5 (2005).

9. Krajca, V., Petranek, S., Mohylova, J., Paul, K., Gerla, V., Lhotska, L.: Modeling the Microstructure of Neonatal EEG Sleep Stages by Temporal Profiles. In *13th International Conference on Biomedical Engineering*, 133 Berlin, Heidelberg: Springer Berlin Heidelberg (2009).

10. Krajca, V., Petranek, S., Patakova, I., Värri, A.: Automatic identification of significant graphoelements in multichannel EEG recordings by adaptive segmentation and fuzzy clustering. *International Journal of Bio-Medical Computing*, 28: 71–89 (1991).

11. Hjorth, B.: EEG analysis based on time domain properties. *Electroencephalography and Clinical Neurophysiology*, 29: 306–310 (1970).

12. D'Alessandro, M., Esteller, R., Vachtsevanos, G., Hinson, A., Echauz, J., Litt, B.: Epileptic seizure prediction using hybrid feature selection over multiple intracranial EEG electrode contacts *IEEE Transactions on Biomedical Engineering*, 50: 603–615 (2003).

13. van Putten, M.J.A.M., Kind, T., Visser, F., Lagerburg, V.: Detecting temporal lobe seizures from scalp EEG recordings. *Clinical Neurophysiology*, 116: 2480–2489 (2005).

14. Schaabova, H., Krajca, V., Sedlmajerova, V., Bukhtaieva, O., Lhotska, L., Mohylova, J., Petranek, S.: Application of Artificial Neural Networks for Analyses of EEG Record with Semi-Automated Etalons Extraction: A Pilot Study. In *Engineering Applications of Neural Networks. Cham: Springer International Pub.*, 629: 94–107 (2016).

15. Paul, K., Krajca, V., Roth, Z., Melichar, J., Petranek, S.: Quantitative topographic differentiation of the neonatal EEG. *Clinical Neurophysiology*, 117: 2050–2058 (2006).

Muscle Synergies for Motor Control Evaluation

Fernando J. Muñoz Z., Natalia M. López C., Flavio Roberti, and Max E. Valentinuzzi

Abstract

Muscle synergies have been proposed to be a modular organization for muscle coordination that map high-level task goals, or motor intentions, into motor actions. Muscle synergies and other types of modular organization have been used to explain muscle coordination during a variety of motor behaviors in many different species. In some instances, new synergies may emerge when a new motor task is presented and the recruitment of the synergies may be altered. Here, we used a database to investigate muscle activity of the right hand during seven distinct limb motions in order to extract muscle synergies: hand open, hand close, supination, pronation, wrist flexion, wrist extension, and rest. Database content EMG signals collected from seven sites on the forearm and one site on the bicep, with an electrode placed on the wrist to provide a common ground reference. Classification scheme is based on the synergies between a functional group of muscles. The muscular synergy is evaluated using different techniques like the normalized power spectral densities (PSD), the cross-correlation matrix of muscular force (estimated through the root mean square (RMS) value of EMG amplitude) and the intermuscular coherence between different sets of muscles. We investigate the relationship between muscle synergy recruitment and functional motor outputs and hypothesized that a common pool of muscle synergies producing consistent task-level biomechanical functions is used to generate different motor behaviors.

1 Introduction

The upper limb is a fundamental part of the human body for the performance of our daily activities. This region extends from the deltoid region up to and including the hand, arm, axilla and shoulder. It enables us to grip, write, lift and throw among many other movements. The main purpose of the upper limb is to position the hand around the body during the execution of a task, a coordinate muscular interaction that involves a large magnitude of motor units interacting within muscle fibers.

Many studies have been conducted to establish the interaction between the central nervous system (CNS) and motor units during a movement [1]. A central issue in motor control is how the CNS generates the muscle activity patterns necessary to achieve a task. Some researchers postulate that the CNS creates a hierarchical architecture divided into specific building blocks that combine to create different movements [2–4]. Muscle synergies (MS) have been proposed as these blocks to the construction of motor tasks. In the spatial domain, MS captures a specific relationship in the strength of activation of a group of muscles. In the temporal domain, a MS may capture time-invariant or time-varying relationship among muscles [5]. Many studies analyze EMG data through correlational and computational methods in order to see if muscle synergies exist and if these synergies are relevant to the task [6–8].

F. J. Muñoz Z. (✉) · N. M. López C.
Universidad Nacional de San Juan—GATEME/CONICET,
San Juan, Argentina
e-mail: fmunoz@gateme.unsj.edu.ar

N. M. López C.
e-mail: nlopez@gateme.unsj.edu.ar

F. Roberti
Universidad Nacional de San Juan—INAUT/CONICET,
San Juan, Argentina

M. E. Valentinuzzi
Instituto Superior de Investigaciones Biológicas/CONICET,
San Juan, Argentina

2 Materials and Methods

2.1 EMG Database

The used database contains Surface EMG of the right arm (seven sites on the forearm and one site on the bicep) with an electrode placed on the wrist as a common ground reference (Fig. 1) [9]. Seven motor tasks were recorded: hand open (HO), hand close (HC), supination (SP), pronation (PN), wrist flexion (WF), wrist extension (WE), and rest (R). The order of these limb motions was randomized. The elbow was sustained at 90-degree flexion during the trials. Table 1 shows the muscle(s) associated with each channel (Ch.) position, and the motion limbs related these muscles.

2.2 Data Processing

Surface EMG signals were acquired and amplified with a gain of 1000 and bandwidth of 1 Hz to 1 kHz. EMGs were sampled at 3 kHz using an analog-to-digital converter board
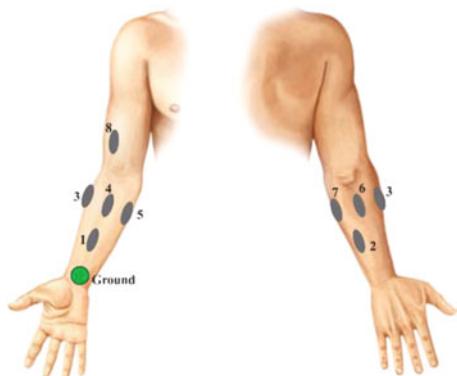
Fig. 1 Electrodes placement according to [9]

Table 1 Muscle and motion associated with each channel (Ch.)

Ch.	Muscles	Motion
1	Flexor carpi radialis	WF
2	Extensor carpi ulnaris	WE
3	Brachioradialis	WF
4	Between brachioradialis and flexor carpi radialis	WF
5	Flexor carpi ulnaris	WF
6	Extensor digitorum	WE, HO
7	Between extensor carpi ulnaris and flexor carpi ulnaris	WF, WE
8	Biceps	SP

[9]. Signals were processed using the MatLab® software, using a sampling frequency of 1 kHz. The DC offset was removed, and EMG signal was rectified and classified in the seven motions under study. A 5th order Butterworth IIR low pass filter (cut off frequency of 10 Hz) and a 5th order Butterworth IIR band pass filter (20–450 Hz) were applied. Finally, a windowing process was applied to the data, with a window length of 200 ms and 50% overlap that allows to assume stationarity of the signal within the chosen window [10] and produces a smoother response.

A set of features was extracted to evaluate the signals: root mean square (RMS), Mean Absolute Value (MAV), Integrated Absolute Value (IAV), Waveform length (WL), Cross-Correlation (CC), Coherence and Wiener–Granger Causality (GC).

Coherence analysis was used to evaluate the relation of two sets of EMG data in the frequency domain. The coherence spectra is defined as the magnitude squared of the cross spectrum, normalized by the product of the auto spectra of the two individual data sets [11]. Equation (1) shows the formula for Coherence between two data series, x and y. G_{xy} is the cross-spectral density between x and y. G_{xx} and G_{yy} are the autospectral density of x and y respectively. Coherence analysis provides a correlational value between 0 (no correlation) and 1 (perfect correlation).

$$C_{xy} = \left| G_{xy} \right|^2 \Big/ G_{xx} \cdot G_{yy} \tag{1}$$

Granger causality allows to identifying "causal" connectivity. Let X(t) and Y(t) be the time series from two data channels. Suppose that the temporal dynamics of X(t) and Y(t) are suitably represented by the following bivariate autoregressive process:

$$X(t) = \sum_{j=1}^{p} A_{11}(j)X(t-j) + \sum_{j=1}^{p} A_{12}(j)Y(t-j) + E_1(t) \tag{2}$$

$$Y(t) = \sum_{j=1}^{p} A_{21}(j)X(t-j) + \sum_{j=1}^{p} A_{22}(j)Y(t-j) + E_2(t) \tag{3}$$

Here A_{11}, A_{12}, A_{21}, A_{22} are the reduced regression coefficients, E_1, E_2 the reduced regression residuals end p the time lags. A variable X "G-cause" a variable Y if the past of X contains information that helps predict the future of Y over and above information already in the past of Y. The method provides a statistical description of observed responses. Computation of G-causality requires specification of the regression model order. Two suitable criteria are the Akaike information criterion (Akaike 1974) and the Bayesian information criterion (Schwartz 1978) [12].

3   Results

Each trial contains the information of the 8 electrodes. Figure 2 shows the acquired signal, offset reduction and rectification for channel 1, as a first stage of processing.

Movements were identified, extracted and regrouped into 7 groups corresponding to each movement (Fig. 3a). Fourier Transform was applied to each channel (Fig. 3b). Each group contain 8 signals, one per channel. The low pass filter and band pass filter are shown in Fig. 3c and 3d respectively.

The mean values of the extracted features were analyzed in order obtain the most significative channels to each motion limb, as shown in Table 2. The coherence analysis
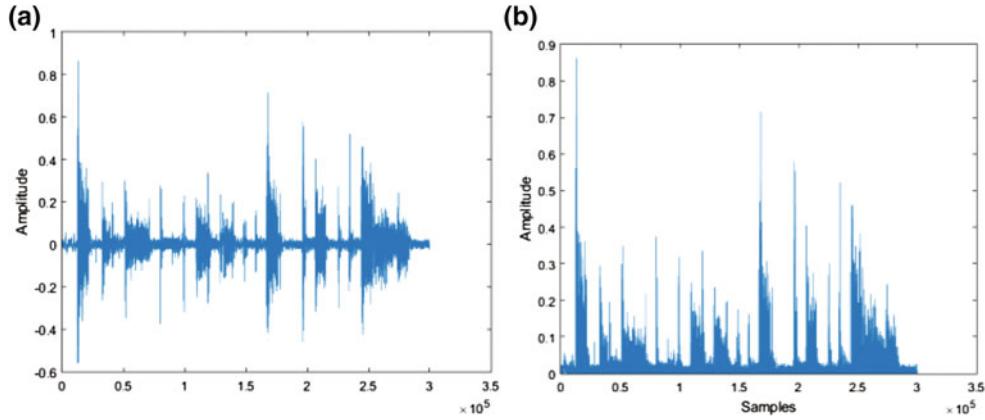
Fig. 2 **a** Acquired signal during a test (corresponding to channel 1). The subject performed all 7 movements. Signal has offset reduction. **b** Signal rectification
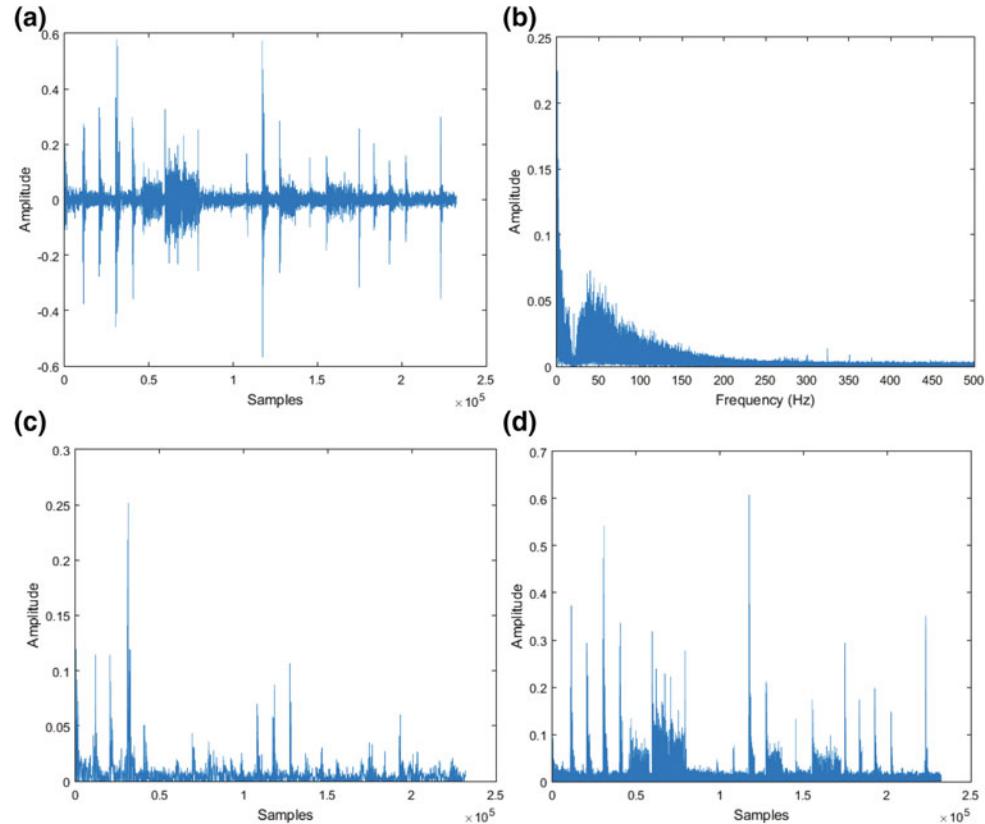
Fig. 3 **a** First channel data extraction corresponding to HO motion. **b** Fourier transform of the signal in **a**. **c** Low pass filter applied to data. **d** Band pass filter applied to data

Table 2 Channels whose mean values are the highest for each feature extracted

Motion limb	RMS	MAV	IAV	WL
Hand open	5, 6	5, 6	5, 6	5, 6
Hand close	3, 7	3, 7, 6	3, 6, 7	3, 7, 1
Wrist flexion	1, 5, 4	4, 1, 5	4, 1, 5	1, 5, 4
Wrist extension	3, 6	3, 6	3, 6	3, 6
Supination	8, 5	6, 8	8, 6	8, 6
Pronation	6, 7	6, 7	6, 7	6, 7
Rest	8, 4, 6	4, 8, 6	4, 6, 8	3, 6, 1

was carried out by comparing each band bass filter channel with the others for each motion limb. A total of 64 graphs were obtained for each movement analyzed, 8 per channel. Figure 4 shows coherence using channel 1 as reference for the WF task.

Figure 4 shows that channels 1, 4 and 5 have the best coherence levels for lowest frequencies, which correspond to common coherence frequency ranges of motor activity.

Horizontal red line represents a 95% confidence bound. We compute a G-Causality network in order to complement this information, stablishing a threshold of 0.85 [12]. Figure 5 shows the most important G-Causality during WF. We also notice a causal connection between channels 1, 4 and 5. It important to notice that some channels are placed at the ends of the muscles (1, 2), while others are in between the two muscles. That fact produces lower signals and coherence levels. Channels placed on the fleshy part of the muscles, are found to be most effective control input (3, 5, 6 and 8).

4 Conclusions

It is important to have a better understanding of neural control mechanisms and patterns involved in the execution of a movement, as well as the performance made by the central nervous system. In this study, synergic relationships between muscles were observed from EMG signals during tasks. It was shown that certain co-activation groups exist when analyzed through coherence analysis. Results indicate
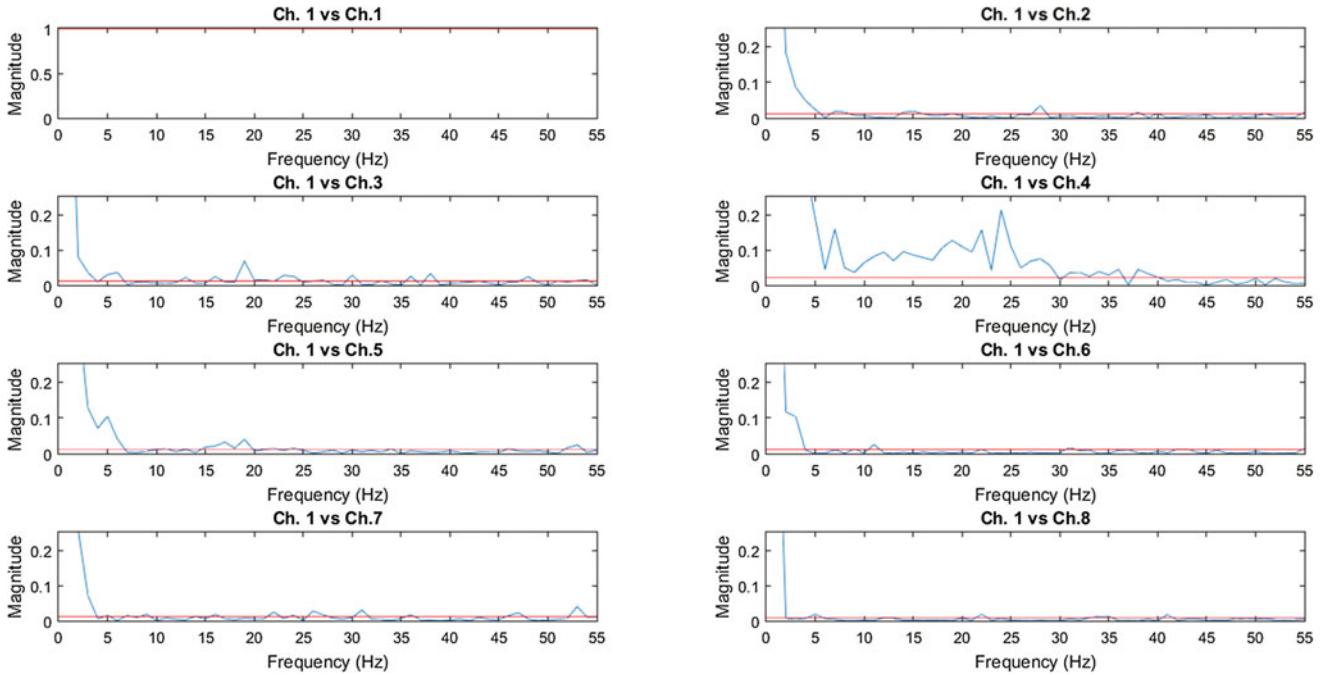
Fig. 4 Coherence corresponding to WF task. Channel 1 versus All

No peak found. Window: 1, Frequency: 1 - 30 Bins, Threshold: 0.95
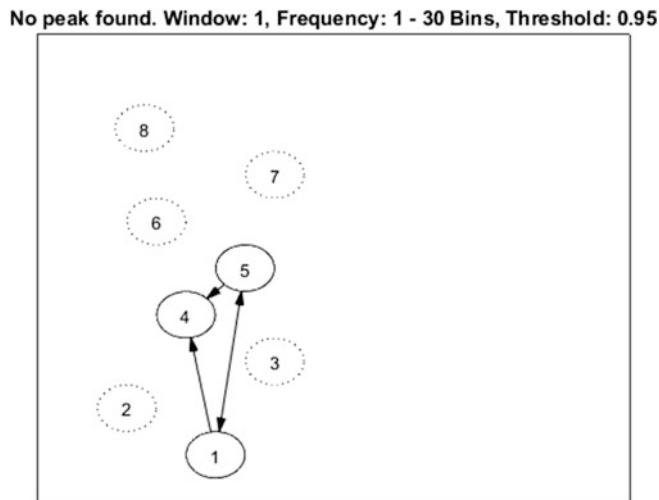
Fig. 5 G-Causality network for WF task

a low frequency range of the co-activation in which motor unit recruitment may take place for the central nervous system in motor output. It is hoped that this study provided much useful information in the way muscles are activated.

References

1. d'Avella, A., Saltiel, P., Bizzi, E.: Combinations of muscle synergies in the construction of a natural motor behavior. Nature Neuroscience. http://dx.doi.org/10.1038/nn1010.
2. Arbib, M.: Perceptual structures and distributed motor control: Brooks, V.B. (Ed.), Handbook of Physiology, Section 2: The Nervous System, Vol. II, Motor Control, Part I. American Physiology Society, pp. 1449–1480. (1981).
3. Bizzi E, Cheung VCK, d'Avella A, Saltiel P, Tresch M (2008). Combining modules for movement. Brain Res Reviews 57:125–133.
4. Cheung VCK, d'Avella A, Tresch MC, Bizzi E (2005.) Central and sensory contributions to the activation and organization of muscle synergies during natural motor behaviors. J Neurosci 25:6419–6434.
5. D'avella, A.- Lacquaniti, F.: Control of reaching movements by muscle synergy combinations. Frontiers in Computational Neuroscience. Vol. 7. pp. 42. (2013) https://www.frontiersin.org/article/10.3389/fncom.2013.00042.
6. Tresch M.C., Jarc A.: The case for and against muscle synergies. Curr Opin Neurobiol 19:1–7 (2009).
7. Boonstra, Breakspear. "Neural Mechanisms of Intermuscular Coherence: Implications for the Rectification of Surface Electromyography" J Neurophysiol 107:796–807, 2012.
8. Danna-Dos Santos, Poston, Jesunathadas. "Influence of Fatigue on Hand Muscle Coordination and EMG-EMG Coherence During Three-Digit Grasping" J Neurophysiol 104: 3576–3587, 2010.
9. Chan A., Green G.: Myoelectric control development toolbox. 30th Conference of the Canadian Medical & Biological Engineering Society, Toronto, Canada, M0100, 2007.
10. Englehart, K., Hudgins, B.: A robust, real-time control scheme for multifunction myoelectric control. IEEE Transactions on Biomedical Engineering, vol. 50, no. 7, pp. 848–854, 2003.
11. Boonstra T., Breakspear M.: Neural Mechanisms of Intermuscular Coherence: Implications for the Rectification of Surface Electromyography. J Neurophysiol. 2012 Feb; 107(3):796–807. https://doi.org/10.1152/jn.00066.2011. Epub 2011 Nov 9.
12. Jie Cui a, Lei Xua, Steven L. Bressler b, Mingzhou Ding c, Hualou Liang a.: BSMART: A Matlab/C toolbox for analysis of multichannel neural time series. Neural Networks 21 (2008) 1094–1104.
13. Barnett, L., Seth, A.K.: The MVGC Multivariate Granger Causality Toolbox: A New Approach to Granger-causal Inference, J. Neurosci. Methods 223, 2014.
14. Cram, J., Durie, M.: The History of Muscle Dysfunction and sEMG. Journal of Applied Psychophysiology and Biofeedback. Retrieved Oct. 15, 2012.

Methodology for Quantification of Frontal Muscle Electromyography Contamination in the Electroencephalogram

Gustavo Moreira da Silva, Fabio Henrique Monteiro Oliveira,
Luciano Brink Peres, Carlos Magno Medeiros Queiroz,
Luiza Maire David Luiz, Samila Carolina Costa,
Marcus Fraga Vieira, and Adriano O. Andrade

Abstract

The electroencephalogram (EEG) is the record of cerebral electrophysiological activity along the scalp in which it has been widely used in several applications, for example, the quantification of the cognitive capacity focusing on the diagnosis or even Brain Machine Interfaces (BCI). However, neural data are frequently contaminated by artifacts that may originate from recording devices or by non-brain physiological activities, such as the blink and the contraction of the scalp muscles. This last represents a considerable challenge in the removal of EEG artifacts due to high amplitude and broad frequency range, which makes it difficult to remove by conventional filtering. Thus, some applications such as BCI systems may occasionally be associated with frequent contractions of head muscles corrupting the EEG control signal. This requires the application of a number of filtering techniques. However, the standard gold techniques still contain limitations, such as not completely eliminating noise in all EEG channels. For this reason, besides to the study of the techniques is helpful to understand the electromyography (EMG) contamination along the scalp. The present work aims to quantitatively estimate EMG noise in 16 bipolar channels of EEG distributed along the scalp according to the 10–20 system. This estimation was based on experimental protocol considering the simultaneous acquisition of EEG and EMG of the frontal muscle sampled at 5 kHz. The protocol consisted of 15 beeps, while listening to these beeps the volunteer made a contraction of the frontal muscle. The mean power of the EEG contaminated by EMG of frontal muscle contraction was compare between the periods of muscle contraction and non-contraction. The results show a mean increase of approximately 74.9% in the power of EEG signals during the muscular contraction. Thus, we conclude that frontal muscular contamination is present on the all EEG rhythms and all over the scalp.

1 Introduction

The brain-computer interfaces (BCIs) translate the electrical signals of the brain activity detectable on the scalp into outputs that allow users to communicate without participation of the motor muscles [1]. However, electroencephalogram (EEG) data are typically contaminated with artifacts (e.g., by muscle activity). These artifacts can have order of magnitude greater than that of EEG amplitude, which may be strongly attenuated by meninges, skull bone and scalp [2].

Unrecognized EMG noise can mimic the actual EEG, thus mislead, and otherwise prevent an investigation aimed at improving these BCI systems. Thus, the EMG noise is a special problem and require the ability to recognize and eliminate EMG contamination so that the brain-detected information be workable. Consequently, the EMG artifact is, therefore, a limiting factor, mainly in applications that rely on measures and detection of EEG characteristics in real time, besides making it impossible to read the trace in cases of clinical EEG [3].

Recently, the characterization and filtering of the EMG-contaminated EEG has received attention because of those possible misinterpretations that may result from the

G. M. da Silva (✉) · F. H. M. Oliveira · L. B. Peres
C. M. M. Queiroz · L. M. D. Luiz · S. C. Costa · A. O. Andrade
Centre for Innovation and Technology Assessment in Health,
Federal University of Uberlândia, Uberlândia, Brazil
e-mail: gustavo.moreira@ufu.br

F. H. M. Oliveira
Federal Institute of Science and Technology, Campus Brasília,
Brasília, Brazil

M. F. Vieira
Bioengineering and Biomechanics Laboratory, Federal University
of Goiás, Goiânia, Brazil

presence of undesirable artifacts in the EEG signal. The removal methods most found in the literature are (1) independent components analysis (ICA), (2) canonical components analysis (CCA), (3) wavelet methods and (4) empirical mode decomposition (EMD). Of these methods, ICA uses an independence property to decompose a given signal into its original sources. One of the main limitations of this method is the hypothesis that as independent sources are not Gaussian. A canonical correlation analysis is a type of method for signal decomposition and second order statistics (i.e. correlation) in component estimation. One of the main limitations of the method with regard to the absence of linear correlations between studied variables. On the other hand, the tests that used a hybrid wavelet-EMD technique provide superior performance to ICA in all frequency bands [4–6].

Those methods of removal require a certain information about the noise, therefore, is necessary to understand and study how the contamination occurs, which depends on the arrangement of the electrodes in the different frequency bands of the EEG. This work aims to estimate the EMG contamination on the EEG signal by measuring the mean power of the signal over a sequence of muscular contractions used for the control of a cursor of a Human Computer Interface (HMI) [7].

2 Methods

2.1 Characterization of the Study

This study obeys Resolution 466/2012 of the National Health Council and the signal acquisitions were carried out at the Centre for Innovation and Technology Assessment in Health of the Federal University of Uberlândia (UFU) authorized by the Human Research Ethics Committee (CEP-UFU), CAAE Number: 43670815.4.0000.5152.

EEG datasets collected in this study are from ten healthy subjects, who were asked to sit in a comfortable chair. The protocol consisted of two equal trials, one performed with opened eyes and the other with closed eyes. Firstly, the subject heard 15 beeps with durations of 0.5 s, 1 s or 3 s, respectively and randomly. While listening to these beeps the volunteer made a contraction of the frontal muscle (raise the eyebrows). Those contractions were designated as short, medium and long according to Table 1.

Table 1 Frontal muscular contractions based on the HMI control [10]

Contraction	Duration (s)	Cursor command
Short	0.5	Rotate mouse
Medium	1	Move mouse
Long	3	Click

2.2 Data Acquisition

Figure 1 illustrates the whole procedure for data collection. This process starts at an acoustic stimuli that was created, as described in Table 1, those beeps have intervals of 2 s between them. The volunteer, instructed to raise the eyebrows as much as he can while listening to the beep, has his EEG and EMG signals recorded simultaneously. Thus, is generated the corrupted EEG signal used to characterize the contamination pattern of each electrode.

For the characterization of the EMG noise detected by the EEG electrodes, EEG and EMG signals were collected simultaneously. Figure 2a shows the positioning of EEG sensors with the EEG cap that adopted the 10–20 standard and bipolar reference totaling 16 differential channels as shown in Fig. 2b. The signal were amplified by RHD200 Intan, USA [8], shown in the Fig. 2a. After that, the signal was sampled at 5 kHz and passband filter with a cutoff frequency of 0.1 Hz and 1 kHz.

2.3 Data Analysis

The following sequence of signal processing steps was applied to the analysis of the signals:

a. Filtering of the rhythms—The signals were decomposed into distinct bandwidths (delta, theta, alpha, beta, gamma with higher brainwaves) according to definition of the EEG in the literature [9]. It was used a digital Butterworth filter with cutoff frequencies (0.1–4, 4–7, 7–13, 13–30, 30–1000 Hz).

b. Signal windowing—The EMG signal envelope was estimated for the detection of the beginning and the end of the muscular contraction. These landmarks were used for windowing EEG signals in periods of active and non-active muscular contraction.

c. Estimate of mean power of the signal within the window—Eq. 1 defines the mean power (P) of the signal, in which V is input discrete time series and N is the number of samples of the signal.

$$P = \sum_{n=1}^{N} \frac{V[n]^2}{N} \tag{1}$$

d. Normalization of mean power—For the comparative visualization of the power of the signal in the periods of active and non-active muscular contraction the mean power was normalized by Eq. 2. P_k is the power of the k-th signal window; P_{min} is the overall minimum power and P_{max} the overall maximum power.

Fig. 1 Procedure for EEG and EMG recording
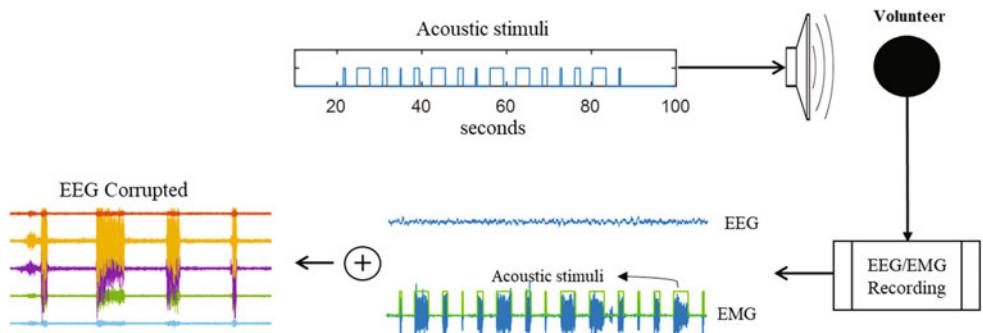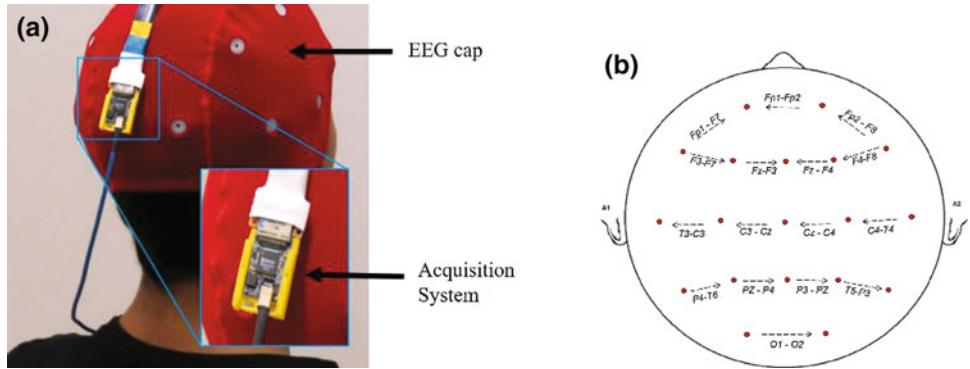
Fig. 2 a Positioning of EEG sensors and the acquisition system of EEG and EMG. **b** Bipolar reference for the EEG

$$P_{norm} = \frac{P_k - P_{min}}{P_{max}} \qquad (2)$$

e. Generate topographic maps of the power distribution over the head—The overall power distribution considered all subjects was estimated for each condition (with and without muscular contraction).

f. Estimate of the overall power—The overall power was estimated for each bipolar derivative.

3 Results

Figure 3 shows the overall mean of the power for all subjects in the 5 rhythms and for the raw EEG. Figure 3a shows the normalized mean power of the periods without muscular contraction and Fig. 3b the periods with muscular contraction.

Figure 4 presents the overall mean power of each derivative at the periods with and without muscular contraction.

The mean power of the derivatives at the times series without muscular contraction was 784.5 uV and with muscular contraction was 3.135 mV which represents an increase of approximately 74.9% in the power of EEG signals during the muscular contraction.

4 Discussion and Conclusion

This study described the EEG contamination by facial EMG activity. For this, the mean power of the signal estimated from a sequence of muscular contractions, typically used for the control of a cursor on computer screen [10], was employed. The purpose of this research comes from an actual demand of our research group, which is the evaluation of the learning process during the control of an HMI.

In order to do this, a periodic beep sound with three different periods was employed as a stimulus for the beginning of the muscular contraction, which resulted from the volunteer raising the eyebrows. The time series used to control the acoustic stimulus was compared to the envelope of the facial EMG signal, which presented a delay of around 100 ms, indicating an agreement between the beginning and end of the muscular contraction with the acoustic stimulus.

The energy distribution shown in Fig. 3 highlights a large contamination in frontal regions of the head, around 70% of power increase. The results are consistent with previous descriptions of the EMG contamination in the EEG caused
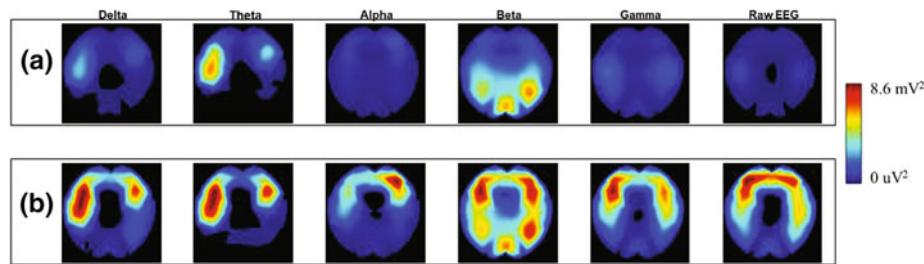
Fig. 3 a Power of EEG without muscular contraction in different rhythms. **b** Power of EEG with muscular contraction in different rhythms
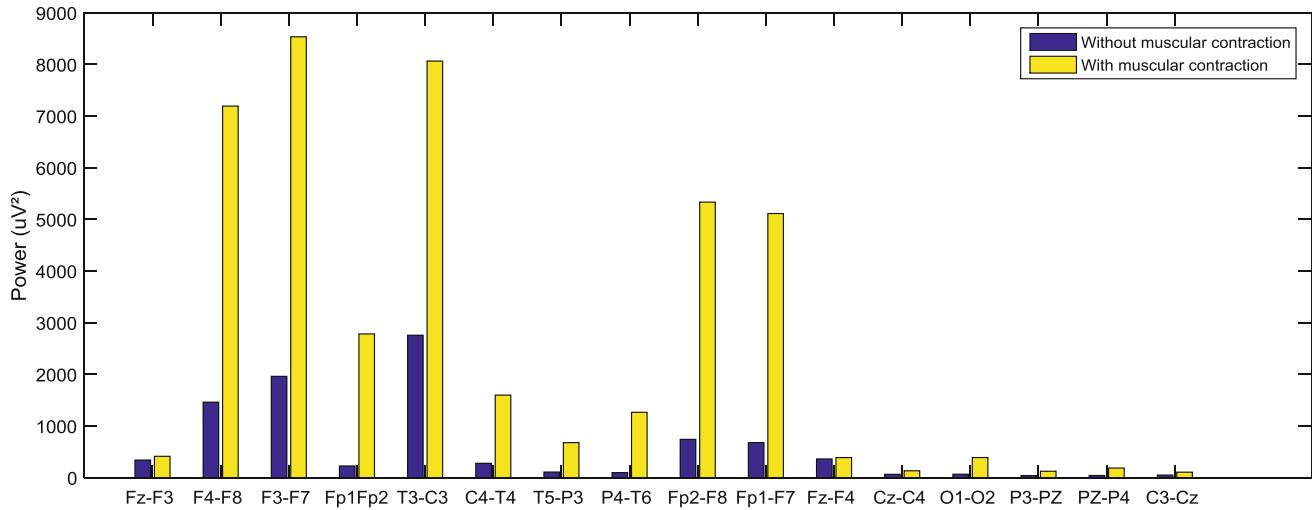
Fig. 4 Power of EEG signals for each bipolar derivation

by the frontalis muscle, in which has been demonstrated that the muscle artifacts contaminate the EEG activity at frequencies lower than 15 Hz [11]. By using this information, it may be possible to design specific filters for EMG artifact removal from the EEG, customizing them for specific frequency bands and each region of the scalp.

The next stage of this work is the characterization of the interference caused by other facial muscles (temporal, orbicularis oculi, zygomatic and orbicularis oris), and the development and assessment of filtering techniques that can be applied both offline and online.

Conflicts of Interest The authors declare no conflict of interest.

References

1. Wolpaw, J. R., Birbaumer, N., McFarland, D. J., Pfurtscheller, G., Vaughan, T. M.: Brain-computer interfaces for communication and control. Clinical Neurophysiology 113, 767–791 (2002).
2. Sanei, S., Chambers, J.A.: EEG Signal Processing. 1st edn. Chichester, Wiley (2007).
3. Gharieb, R.R., Thakor, N.V., Neurological EEG Monitors: A Review. Encyclopedia of Medical Devices and Instrumentation (2006).
4. Daly, I., Scherer, R., Billinger, M., Müller-Putz, G.: FORCe: Fully Online and Automated Artifact Removal for Brain-Computer Interfacing. IEEE Transactions on Neural Systems and Rehabilitation Engineering 23(5), 725–736 (2015).
5. Chen, X., Liu, A., Chiang, J., Wang, Z. J., McKeown, M. J., Ward, R. K.: Removing Muscle Artifacts From EEG Data: Multichannel or Single-Channel Techniques?. IEEE Sensors Journal 16(7), 1986–1997 (2016).
6. Bono, V., Das, S., Jamal, W., Maharatna, M.: Hybrid wavelet and EMD/ICA approach for artifact suppression in pervasive EEG. Journal of Neuroscience Methods 267 89–107 (2016).

7. Queiroz, C. M. Q., Luiz, L. M. D., Miranda, M., Lima, G. F. M., Andrade, A. O.: Proposta de uma Interface Gráfica para Aprendizagem. In: Annals of 8th Biomedical Engineering Symposium, pp. 310–315. Uberlândia (2015).

8. RHD2000-Series Amplifier Evaluation System. http://www.intantech.com/RHD2132_16channel_amp_board.html.

9. Niedermeyer, E., Lopes da Silva, F. H., Niedermeyer, E. Electroencephalography: basic principles, clinical applications, and related fields. Williams & Williams, Baltimore (1993).

10. Queiroz, C. M. M., Nasuto, S. J., Andrade, A. O.: Development and Evaluation of Human-Computer Interface Based on Facial Motor Unit Activity. In: 7th International Joint Conference on Biomedical Engineering Systems and Technologies, pp. 47–53. Angers (2014).

11. Goncharova, I.I., McFarland, D.J., Vaughan, T.M., Wolpaw, J.R.: EMG contamination of EEG: Spectral and topographical characteristics. Clinical Neurophysiology 114, 1580–1593 (2003).

Effects of Nitroglycerin to Ballistocardiography by EMFi

Jarmo Alametsä and Jari Viik

Abstract

The purpose of this work was to study the effect of nitroglycerin (glyceryl trinitrate) to ballistocardiographic signal (BCG) recorded in sitting position by using Electromechanical Film (EMFi) sensors. ECG, BCG, ankle pulse signal and carotid pulse (CP) signal from the neck near the carotid artery were recorded from a single person and duration of the signal components according to R wave of the ECG and amplitudes of the signals were studied. In the first study the effect of 1 nitroglycerin pill was studied and in the second study the effect of exercise and the intake of 2 nitroglycerin pills were examined. The time domain properties of BCG, CP and ankle pulse signals stayed somewhat stable due to nitroglycerin intake. Noticeable increase was seen in some systolic signal amplitudes. Diastolic signal amplitudes mainly decreased. Signal traces became smoother and the fluctuation of the ballistic signals decreased. Nitroglycerin intake had a major but temporary effect on the heart-vasculature system due to increased aortic elasticity.

Keywords

Ballistocardiography • Pulse wave • Nitro

1 Introduction

Ballistocardiography (BCG) is a non-invasive method for cardiac and respiratory evaluation and it reflects closely the strength of myocardial contraction revealing the condition of the heart [1]. The BCG waveforms have been divided into three groups, labelled with letters; Pre-ejection (FGH),
ejection (IJK) and diastolic part of the heart cycle (LMN) [1]. The peak of the H coincides with the end of the tension phase and the onset of the rapid expulsion of the blood from the heart into aorta [2]. The foot ward pointing I wave reflects the rapid acceleration of blood in the ascending aorta and pulmonary arteries around the aortic arch and into the carotid arteries. The J wave describes acceleration of blood in the descending and abdominal aorta and deceleration of blood in the ascending aorta. I-J amplitude reflects the force of contraction of the left ventricle and I-J velocity reflects contractility [1].

The carotid pulse (CP) indicates the variations in arterial blood pressure and volume with each heart beat. The CP rises abruptly with the ejection of blood from left ventricle to ascending aorta reaching a peak called percussion wave (P). The following secondary wave is called as a tidal wave (T), caused by a reflected pulse returning from the upper body. Dicrotic notch (D) is caused by a closure of aortic valve and this can be followed by dicrotic wave (DW), which is due to reflected pulse from the lower body [3].

In this paper a Mobile Physiological Signal Measurement Station [4] has been used to record seat BCG, carotid pulse and ankle pulse signals [5] with EMFi sensors. The main goal of this study is to test what changes happen in BCG, carotid and ankle pulse signals due to intake of nitroglycerin.

2 Methods

The EMFi acts as a sensitive movement sensor suitable for BCG recordings [6]. Signals from EMFi sensors were recorded with the recording device [4] into a notebook computer with a data acquisition card (Daqcard 6036E). In the recording device an active Butterworth 8 degree low pass filter was used, where the cut-off frequency was 256 Hz. In chair recordings the EMFi sensor (42 cm × 36 cm) was beneath the measured person. One EMFi sensor strip (15 cm × 2 cm) was attached on the right side of the neck

J. Alametsä
Tampere University of Applied Sciences, Tampere, Finland
e-mail: jarmo.alametsa@health.tamk.fi

J. Viik (✉)
Tampere University of Technology, Tampere, Finland
e-mail: jari.viik@tut.fi

near carotid artery and another to the ankle to get dorsalis pedis pulse.

3 Measurements

The recordings were made from the BCG, carotid and ankle pulse signal of single person in a sitting position. All the measurements lasted about 3, 2 min and the used sampling frequency was 500 Hz. Just before the measurements the blood pressure (BP) and the pulse were measured with Omron M5-I BP monitor device. Two different measurements were done; in recording 1 few recordings were made before (having normal resting pulse rate) and the rest after 1 nitroglycerin pill intake (Nitroglycerin Nycomed 0.5 mg under the tongue). In recording 2 physical exercise was done before recordings. Having done so, the pulse was higher but also the BP level was lower than having a resting pulse level. In recording 2 2 nitroglycerin pills were taken in order to test how heart-vasculature system reacted to BP fall.

The R wave of ECG was used as a reference in detecting the slopes of the signals. Temporal duration of signals (T_{HI}, T_{IJ} and T_{JK}) and their amplitudes H-I (A_{HI}), I-J (A_{IJ}), J-K (A_{JK}), K-L (A_{KL}), L-M (A_{LM}), and M-N (A_{MN}), from the BCG signal and E-P (A_{EP}), P-T (A_{PT}), P-D (A_{PD}), E-D (A_{ED}), from the carotid artery signal were extracted (Fig. 1). The signal points D (T_{RD}) and DW (T_{RDW}) from carotid artery signal were also extracted [2].

Signals were first band pass filtered (0.5–30 Hz FIR, 700 taps, time delay corrected), down sampled into 100 Hz and the analysis was done with 0.5 s window length. The index of the R point was detected first by differentiating (2 points), squaring and integrating (5 points) and by taking the maximum from the ECG signal. The I slope from the BCG was detected by local minimum method and then the J slope was detected by local maximum using the index of the I point as a starting point. Other slopes were detected at the same way. Amplitude spectrum was calculated from raw signal, cumulated (by adding current spectrum value to amplitude scaled value) and normalized.
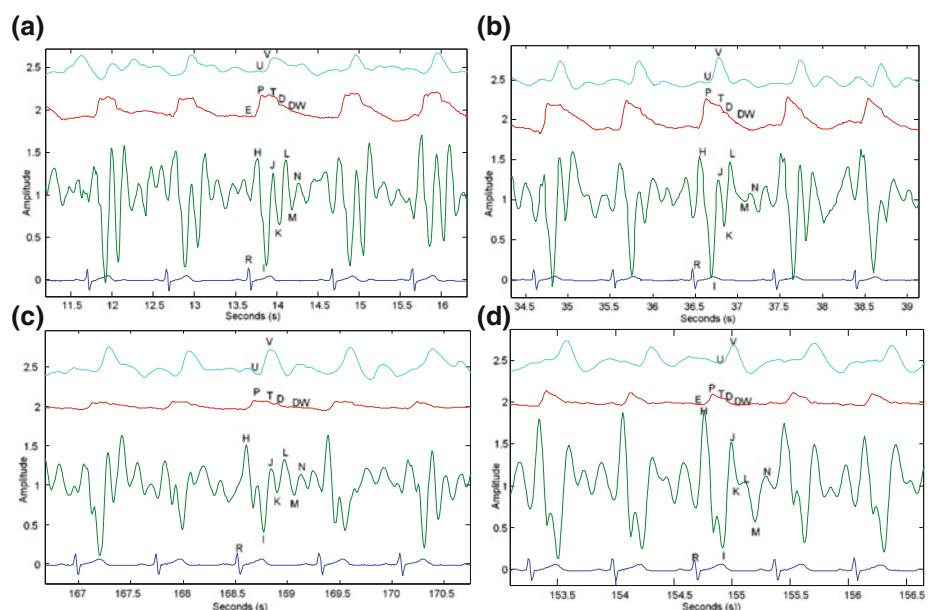
4 Results

After the intake of nitroglycerin it starts to effect very rapidly (but the effect is temporary; only from 5 to 10 min). Minor changes were seen in temporal BCG values (Fig. 2) being larger in diastolic values T_{RL}, T_{RM} and T_{RN} in recording 1. Systolic T_{HI} and T_{IJ} increased, but T_{JK} decreased. Systolic amplitude values A_{HI} and A_{IJ} in recording 1 increased (Fig. 3), but A_{JK}, A_{KL} and A_{LM} decreased (and started to rise again for a while). A_{MN} decreased steadily. CP and ankle pulse signals increased (A_{EP}, A_{PD}) as well as ankle pulse signal A_{UV}. A_{PT} increased and decreased at the end. In amplitude spectrum the nitroglycerin intake shifted frequency spikes and increased spike amplitudes (spikes in 1–4 Hz area shifted to higher and in 4–6 Hz to lower frequencies). The increase in pulse is seen in CP amplitude spectrum.

Recording 2 was done about 1 h after physical exercise and the resting pulse was higher than normally. Possibly for that reason, systolic T_{RH}, T_{RI} and T_{RJ} stayed almost constant (Fig. 1) while T_{RK}, T_{RL} and T_{RM} had a slight increase and a minor decrease in time after that. T_{RDW} in carotid pulse signal deceased. This is explained the cone alike shape of the carotid pulse signal (Fig. 1) expressing increased aortic

Fig. 1 **a** Recording 1 before. RR 148/96 p.57. **b** Recording 1 after nitro. RR 128/82 p.82. **c** Recording 2 before. RR 125/82 p.81. **d** Recording 2 after nitro. RR 101/67 p.90

(a)

Before 159/97p.62 4,67	Before 148/96p.57 4,46	After 155/97p.66 4,47	After 138/88p.66 4,37	After 128/82p.63 4,40	After 139/86p.63 4,47

(b)

Before 124/74p.80	Before 127/80p.78	Before 125/82p.81	After 119/81p.79	After 101/67p.90	After 106/72p.85	After 108/73p.87	After 113/78p.83

111/75p.82

4,72	4,53	4,33	4,37	4,24	4,24	4,26	4,28	4,32
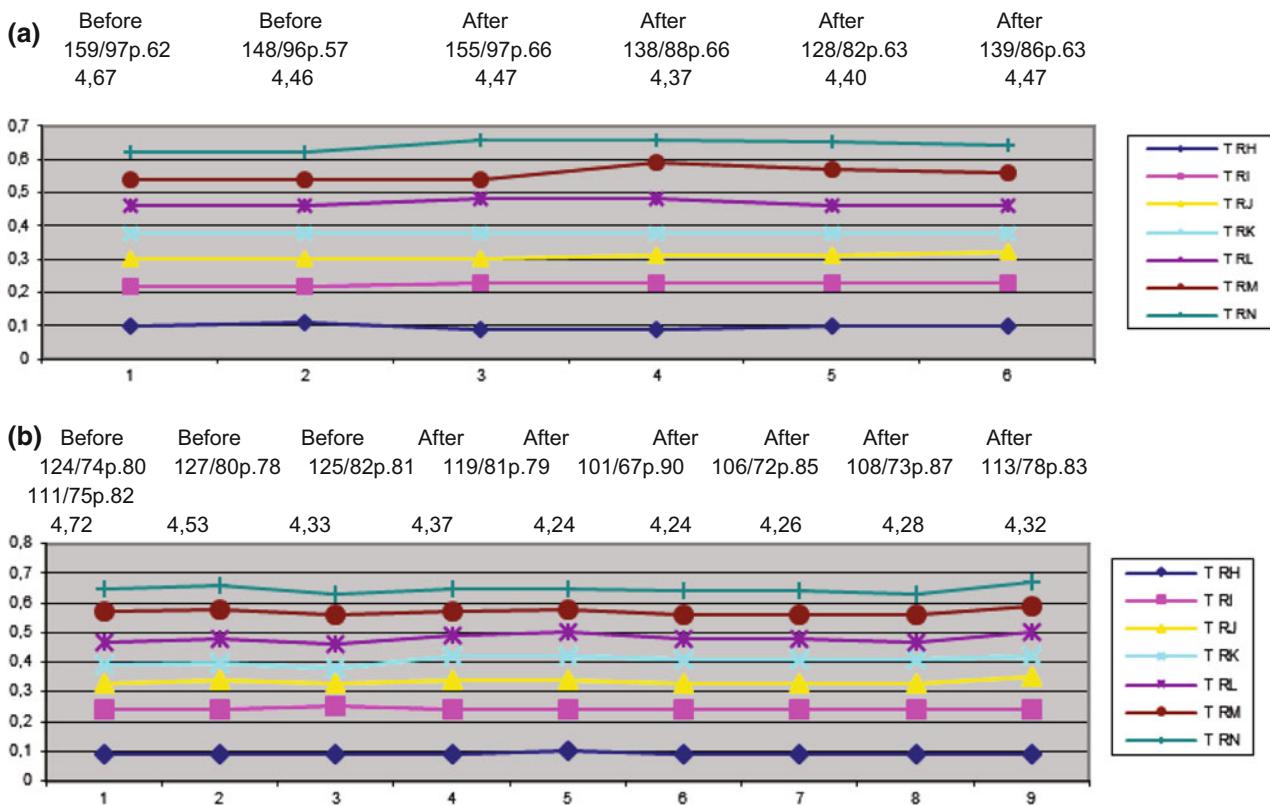
Fig. 2 Seat BCG time domain values from recording 1 (**a**) and recording 2 (**b**). From T_{RH} to T_{RK} denote systolic and T_{RL} to T_{RN} diastolic values. T_{RH} reflects the tension phase of the ventricles. T_{RK} is the duration of the entire mechanical systole. Normal ECG R-R interval is about 0.8 s. Pulse wave velocity (PWV) value after BP value

elasticity. Systolic T_{HI} decreased (at first, but recovered then in the last two recordings), T_{IJ} and T_{JK} increased. Systolic amplitude values A_{HI} and A_{IJ} increased strongly (Fig. 3), but A_{JK} increase was modest. A_{KL} decreased and A_{LM} was almost stable during recordings. A_{MN} increased slightly. The amplitudes of the CP signal decreased in recording 2 when compared to recording 1. A_{ED} was almost flat line whereas A_{EP} and A_{PT} increased being very stable after that. A_{PD} had a slight increase in amplitude and it became steady after that. In amplitude spectrum from the seat BCG the nitroglycerin intake seemed to shift frequency spikes a bit in 1–6 Hz area to higher and in 6–9 Hz to lower frequencies. In carotid amplitude spectrum changes due to nitroglycerin intake was seen.

The temporal properties of the BCG, ankle and carotid artery signals remained quite stable in both recordings (1 and 2). In T_{HI}, T_{IJ} and T_{JK} values differences were between recordings 1 and 2 as a react to nitroglycerin intake. In recording 2 quite a high pulse rate with 2 nitroglycerin pills caused dilatation of arteries and increased workload of the heart.

5 Discussion

Nitroglycerin has been used for more than a century as an agent in treating ischemic heart disease and congestive heart failure. It decays in metabolism to nitric oxide (NO) making arteries and veins to dilate thus reducing the workload of the heart. Dilated coronary arteries have more delivery capacity helping also in strain situations. It has been suggested also, that the usage of nitroglycerin may protect myocardium. The long-term usage of nitroglycerin develops a nitrate tolerance which limits its usage [7]. Usually, BCG amplitudes decreases while arterial pressure increases seen as elevated BP values [1]. Nitroglycerin increases BCG amplitudes. It might be used as a short-term usage in hypertension. It can also be used as a pre-medication before heavy physical work. The usage of nitroglycerin may help to maintain aortic elasticity and by doing so, may also decrease turbulent flow of blood in the veins. Aortic arch is naturally twisted and curvature and helical shape in aortic arch stabilizes the void unsteadiness making blood flow stable. Highly unstable flow
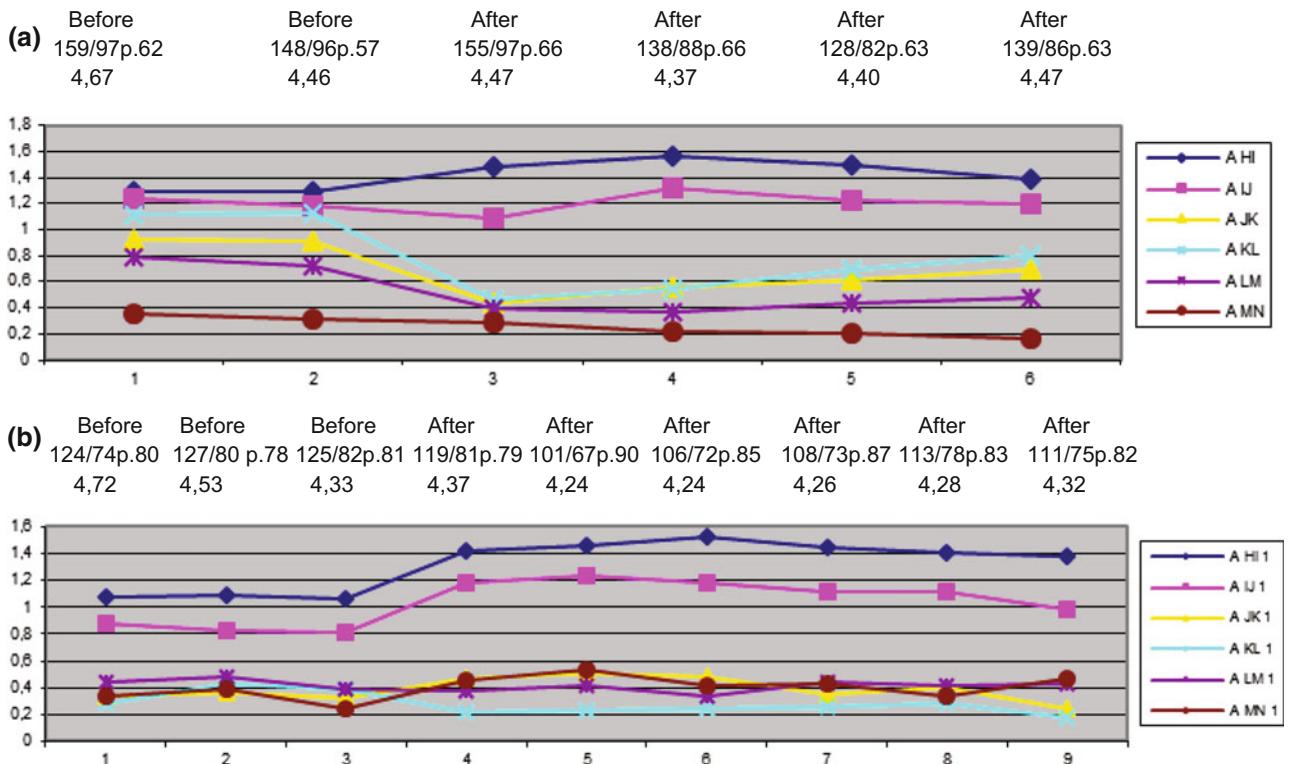
Fig. 3 Seat BCG amplitude values from recording 1 (**a**) and recording 2 (**b**). A_{JK} decreased **a** after nitroglycerin intake (after typical BP) thus reflecting the drop in BP. In **b** the BP was already very low; A_{JK} increases slightly, then decreases. In both A_{KL} dropped. As the device is not calibrated, the absolute force is not known and the values are in arbitrary units

can aggravate vessel wall and provoke an inflammatory response [8].

Our goal was to examine, what changes in BCG, aortic and ankle pulse signals occurs due to intake of nitroglycerin in the case of normal low resting pulse and after exercise with a higher pulse. Nitroglycerin usage induced temporal and amplitude changes being partly different with two different recording setups. Visually, the signal traces after nitroglycerin intake became smoother and the fluctuation of the signals decreased. This is due to increased aortic elasticity. In earlier studies BCG which have been abnormal in form, have improved in form or even restored to normal due to usage of nitroglycerin [9]. With healthy young people BCG amplitudes increased but its form stayed normal, heart rate increased and BP decreased moderately. With some healthy young people I wave was diminished due to nitroglycerin intake [9].

In the past mild exercise and BCG has been used to distinguish patients having abnormalities in cardiovascular function. The results were so diverse with normal people also that only marked abnormality was able to detect in that way. Changes not to be identified at rest but after physical exercise would be a sign of cardiac abnormality. Thus showing that a diseased heart could not to increase its cardiac output after exercise, or in attempt to do so, the heart would contract in an abnormal manner resulting a distortion in BCG [10]. The notching of H-I component in recording 2 (Fig. 1c, d) needs further study. However, in recording 1 without exercise no notching is seen (Fig. 1a, b). Notching may be due to effect of exercise. The notching of H-I component has been described as normal after exercise [11]. The usage of nitroglycerin increased ballistic amplitudes (Fig. 1b, d). However, the physical exercise induced no any kind of signs of coronary disease and not any kind of dizziness during exercise. Previous studies have also confirmed the benefits of vigorous physical training providing a remarkable improvement in BCG waveforms [12]. Physical training has also benefits in maintaining normal BP.

6 Conclusion

The usage of nitroglycerin increased systolic amplitudes but the temporal BCG components stayed pretty stable. Nitroglycerin may improve arterial elasticity and thus relieve the workload of the heart. Due to the small amount of measured

persons, this phenomenon with nitroglycerin needs further study.

References

1. Weissler A.M. The Ballistocardiographic waveforms, in Noninvasive Cardiology Monographs, (Grune & Stratton Inc. NY). 1974, pp. 55–125

2. Eeina Ye V. The Significance of the Time Interrelationships in Ballistocardiographic Analysis, October 25, 1960, ADA377004, Joint publications research service Arlington.

3. Rangayyan R.M. A Case -study Approach to Solve Problems in Biomedical Signal Analysis. The IEEE Press, Piscataway, NJ, 2000.

4. Alametsä, J. The Possibilities of EMFi Sensors in Heart Related Activity Monitoring with a new Mobile Physiological Signal Measurement Station, Proc. of the proactive comp. workshop PROW 2004, 25–26 November 2004, Helsinki, Finland.

5. Alametsä, J. Measurement of Carotid Pulse and Ankle pulse Signal with EMFi Sensor, ISEM 2005, 12th International Symposium on Interdisciplinary Electromagnetic, Mechanic & Biomedical Problems, 12–14.9.2005, Bad Gastein, Salzburg.

6. Kirjavainen K. Electromechanical film and procedure for manufacturing same, 1987. http://www.emfit.com

7. Hu R, Li XH, etc. Nitroglycerin-induced myocardial protection and tolerance: role for CGRP. Trends in Pharmacological Sciences, August 2014, Vol. 35, No. 8.

8. Mosley M. The Wonderful World of Blood with Michael Mosley. BBC 2015. www.bbc.co.uk/programmes/b05nyyhf.

9. Starr I, etc. The Effect of Nitroglycerine on the Ballistocardiogram of Persons with and without Clinical Evidence of Coronary Heart Disease. Circulation, Volume XII, October, 1955.

10. Makinson DH. Changes in the Ballistocardiogram after Exercise in Normal and Abnormal Subjects. Circulation, Volume II, August, 1950.

11. Wiard RM, etc. Estimation of Central Aortic Forces in the Ballistocardiogram under Rest and Exercise Conditions. 31st Annual International Conference of the IEEE EMBS Minneapolis, Minnesota, USA, September 2–6, 2009.

12. Alametsä, J. Spectral Properties of BCG Signal in Sitting and Supine Positions in Normal Blood Pressure and Hypertension. EMBEC05, Prague, Czech Republic.

The Evaluation of the Tremor: Signal Database of Healthy Control Subjects

Jan Havlík, Patrik Horák, Kamila Řasová, Jitka Řezníčková, and Josef Zeman

Abstract

A tremor an involuntary rhythmic oscillatory movement of a part of the body—belongs to one of the most disabling features of multiple sclerosis (MS). In clinical practice, the tremor is currently classified according to clinical scales. Unfortunately, this approach is fully subjective in principle, and the objective classification is still missing. As is shown in the literature, the tremor can be investigated by accelerometers and gyroscopes based on the frequency analysis and other advanced methods of signal processing. A condition of the successful development of these methods is an existence of a signal database of healthy subjects. This paper concerns with the collecting of the signal database of healthy control subjects. The signals were acquired on the group of healthy subjects aged from 18 to 50 years (20 subjects). For each patient, one-minute records of postural tremor (for both right and left hand, with and without closed eyes; 4 records together) have been acquired, and also several clinical tests have been passed (a measurement of a strength by a handgrip, a pinch key, and a trippod test, a nine-hole peg test, a coin rotation task test, and a tip pinch test). All records have been supplemented by anamnestic data.

Keywords

Tremor • Signal database • Healthy subjects
Signal analysis

J. Havlík (✉)
Faculty of Electrical Engineering, Czech Technical University in Prague, Technická 2, 16627 Prague 6, Czech Republic
e-mail: xhavlikj@fel.cvut.cz
URL: http://bmeg.fel.cvut.cz

P. Horák · K. Řasová · J. Řezníčková
Department of Rehabilitation, Third Faculty of Medicine, Charles University in Prague, Prague, Czech Republic

J. Zeman
Faculty of Engineering, Czech University of Life Sciences Prague, Prague, Czech Republic

1 Introduction

A tremor—an involuntary rhythmic oscillatory movement of a part of the body—belongs to one of the most disabling features of multiple sclerosis (MS). The different types of the tremor are currently classified according to clinical scales. Unfortunately, this approach is fully subjective in principle. The objective classification is still missing in clinical practice [1].

In MS, the tremor is frequently embedded in a complex movement disorder, which often includes dysmetria and other ataxic features [2]. From clinical observation, animal studies and some experimental evidence in humans it is apparent that the cerebellum and the thalamic nuclei connected to the cerebellum play an important role in a production of the tremor.

As it is shown in the literature, the tremor can be investigated by accelerometers and gyroscopes. This approach has been satisfactory proved many of researchers aim at the study of the tremor in patients with Parkinsons disease, for example [3–5], some of the studies also deal with other types of the tremors [6, 7]. A frequently used approach to the tremor analysis using accelerometers and gyroscopes is an acquiring data during pre-defined movements or exercising. Some studies which acquire data during long-term activity or daily activities are also described in the literature [6].

As it was written above, the tremor is an involuntary rhythmic oscillatory movement which accompanies several neurological diseases such as MS. The most important characteristics of the tremor from a technical point of view are a frequency range and an amplitude of the signal. Approximate frequencies of the human tremor in the upper limbs are 2–10 Hz for patients with MS, possibly up to 18 Hz for the other types of the tremor [8, 9]. The similar values are shown also in [10] for the physiological tremor or in [7] for the Parkinsonian tremor and the physiological tremor. The highest frequency of the tremor mentioned in

[11] is 25 Hz. The tremor signal is typically harmonic signal with amplitude lower than 2 g in most cases [7, 11].

The goal of the current project is to investigate the tremor by accelerometers and gyroscopes based on the frequency analysis and other advanced methods of signal processing and to use these objective parameters for the classification and evaluation of the tremor. A condition of the successful development of these methods is an existence of a signal database of healthy subjects. This paper concerns with the collecting of the signal database of healthy control subjects.

In our work, we did not measure finger [12] or hand [11] tremor. Our aim was to receive complex information about motor control of the subject. We did put the accelerometer on the end of the body to measure the longest circuit generating corticomuscular coherence [13–15].

2 Methods

2.1 Group of Probands

The group of healthy control subjects consists of 20 probands (6 males and 14 females) aged from 18 to 50 years, the averaged age was 27.6 ± 8.6 years (mean ± standard deviation). All the probands have been informed about the study and signed the informed consent. Each proband has filled an anamnestic questionnaire. The signal database is supplemented with anonymous data about the probands such as age, sex, height, weight, smoking, taking alcohol, visual analog scale etc.

2.2 Measuring Device

The measuring device used for the study uses the 3-axis accelerometer and 3-axis gyroscope chip (MotionTracking sensor MPU-6050) which can measure acceleration up to 16 g and rotation up to 2000 degrees per second. The sensor is fixed to the patient using a ring on a finger. Data from the chip are acquired by an own measuring device with microcontroller Atmel Mega 328 and stored on an SD card. For the signal analysis, the magnitude of acceleration—the root of sum of each component squares—was computed from separate axes.

2.3 Clinical Tests

Each proband has been examined by an independent examiner and passed 6 standard clinical tests—a measurement of a strength by a handgrip [16], a pinch key [17], and

a trippod test [18], a nine-hole peg test [19], a coin rotation task test [20], and a tip pinch test [21]. All the tests have been examined both for the left and right hand.

2.4 Tremor Bandwidth

A postural tremor has been measured for each patient. The tremor is measured with a sensor placed on the arm during stretching the whole arm forward. The measurement was realized as one-minute experiments, separately passed for left and right hand and with opened and closed eyes. The sampling frequency was 100 Hz. Thus, four signals with 6000 samples were recorded for each patient— records of postural tremor for right/left hand with opened/closed eyes.

For each record, the signal of acceleration was filtered by high-pass 2nd order Butterworth filter with cut-off frequency of 0.5 Hz (a filter of isoline), the power spectral density (PSD) was estimated and finally, the PSD was smoothed by low-pass 2nd order Butterworth filter with cut-off frequency of 0.5 Hz. The spectral characteristic was consequently parameterized by parameters f_{MAX} and f_{HIGH}. The f_{MAX} was determined as a frequency for which the smoothed PSD is maximal and f_{HIGH} was determined as a PSD bandwidth (it means that PSD for f_{HIGH} is about 3 dB smaller than for f_{MAX}).

2.5 Clinical Approvement

The study is approved by the institutional biomedical research ethics board of the Charles University in Prague, reg. nr. EK-VP/23/0/2014.

3 Results

3.1 Basic Statistics of the Clinical Trials

The clinical trials were evaluated separately for males and females, and right and left hands. For each record, the mean and the standard deviation (SD) of each trial were calculated. These basic statistical indicators are shown in Table 1.

3.2 Tremor Bandwidth
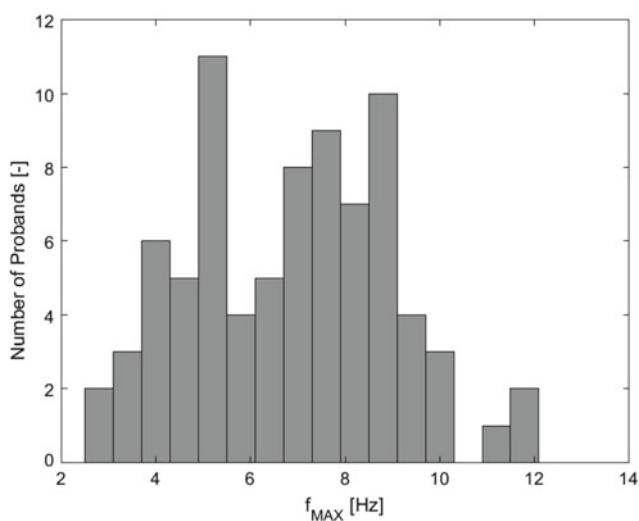
The postural tremor was evaluated for all 20 probands, the results are shown in Table 2, separately for left and right hand, and measurements with opened and closed eyes. For

Table 1 Clinical tests results (M/F male/female, L/R left/right)

	M-L	M-R	F-L	F-R
	Mean (SD)	Mean (SD)	Mean (SD)	Mean (SD)
Handgrip (kg)	40.7 (5.5)	42.5 (3.4)	26.7 (5.0)	27.7 (4.8)
Nine hole peg test (s)	18.0 (1.7)	18.0 (1.9)	18.4 (2.6)	17.9 (2.1)
Coin rotation test (s)	13.1 (1.3)	12.6 (2.1)	14.5 (2.5)	14.0 (2.4)
Pinch Key (kg)	7.6 (1.2)	8.2 (1.1)	6.3 (0.9)	6.7 (0.8)
Trippod (kg)	6.2 (1.2)	6.6 (1.2)	5.4 (0.7)	5.3 (0.7)
Tip-Tip (kg)	4.1 (0.6)	4.5 (0.5)	3.4 (0.4)	3.5 (0.5)
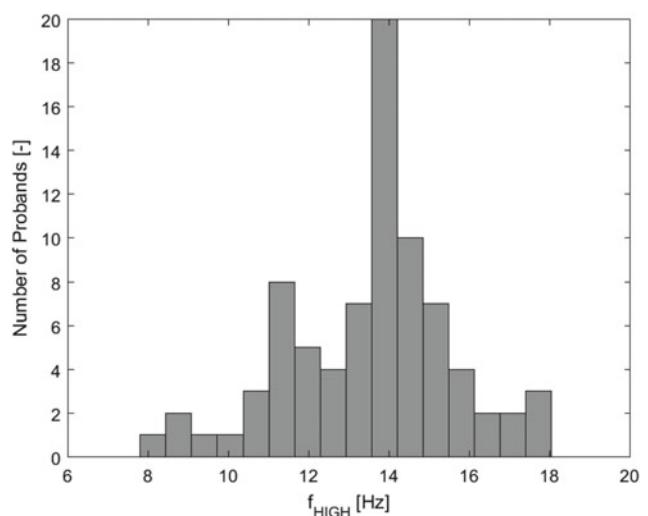
Table 2 Bandwidth of tremor and the frequency with maximal energy

	f_{MAX} (Hz)	f_{HIGH} (Hz)
	Mean (SD)	Mean (SD)
Left hand—opened eyes	7.1 (2.3)	13.5 (2.2)
Left hand—closed eyes	6.0 (1.6)	12.8 (1.9)
Right hand—opened eyes	7.2 (2.3)	13.9 (1.9)
Right hand—closed eyes	7.1 (2.2)	13.8 (2.3)
All together	6.8 (2.1)	13.5 (2.1)

Fig. 2 Histogram of tremor bandwidth

Fig. 1 Histogram of frequency with maximal energy

both parameters f_{MAX} and f_{HIGH}, the mean and the standard deviation are indicated. The last line of the table collects all the records together and shows averaged data from all 80 records.

The distribution of observed parameters are shown in histograms on Figs. 1 (for parameter f_{MAX}) and 2 (for parameter f_{HIGH}).

4 Discussion

The study deals with the objectification of tremor diagnosis problem. Currently, the tremor is classified according to clinical scales. The development of new methods for evaluating of the tremor based on the objective criteria requires the comparison of healthy subjects with diseased patients. The paper presents the collecting of signal database of healthy control probands and the processing of the recorded signals. The database of the healthy controls which was collected during the study is an essential condition of the future research.

The spectral characteristic of the tremor is parameterized by the parameters f_{MAX}) and f_{HIGH} which quantitatively describe the spectrum of the tremor. Based on the literature review, the authors speculate, that the bandwidth (parameter f_{HIGH}) should be significantly wider for healthy subjects than for the diseased patients. The reason is that the spectrum of

tremor has a dominant peak which is standing out from the rest of the spectrum. In contrast to this, the spectrum of healthy patients is more smoothed, which means that the bandwidth of the spectrum defined in methods is wider for them.

The future steps should be concerned with a collecting of signal database and clinical parameters of MS patients and to design and implementation of methods for evaluation of the tremor based on objective criteria [22].

5 Conclusion

The paper presents the signal database of the healthy control subjects, which is an essential condition of the design and implementation of methods for the evaluation and classification of the tremor. The accelerometry signals were collected from 20 probands aged 18–50 years. The signal database is supplemented with anonymous data about the probands and with the results of standard clinical trials.

References

1. Koch, M., Mostert, J., Heersema, D., Keyser, J.D.: Tremor in multiple sclerosis. Journal of neurology 254(2), 133–145 (2007)
2. Alusi, S.H., Glickman, S., Aziz, T.Z., Bain, P.G.: Tremor in multiple sclerosis. Journal of neurology, neurosurgery, and psychiatry 66(2), 131–134 (1999)
3. Boika, A.: Postural tremor in parkinson's disease (pd): Types of accelerometer traces. Parkinsonism & Related Disorders 13, S69 (2007)
4. Hossen, A., Muthuraman, M., Al-Hakim, Z., Raethjen, J., Deuschl, G., Heute, U.: Discrimination of parkinsonian tremor from essential tremor using statistical signal characterization of the spectrum of accelerometer signal. Bio-medical materials and engineering 23(6), 513–531 (2013)
5. LeMoyne, R., Mastroianni, T., Grundfest, W.: Wireless accelerometer configuration for monitoring parkinsons disease hand tremor. Advances in Parkinson's Disease 2(2), 62–67 (2013)
6. Heldman, D.A., Jankovic, J., Vaillancourt, D.E., Prodoehl, J., Elble, R.J., Giuffrida, J.P.: Essential tremor quantification during activities of daily living. Parkinsonism & Related Disorders 17(7), 537–542 (2011)
7. Pascoal-Faria, P., Patrcio, M., Leal, A., Caramelo, F., Freire, A., Janurio, C., Castelo-Branco, M.: Understanding tremor in rapid upper limb movements using 3d accelerometers data. Neuroscience & Medicine 5(5), 205–213 (2014)
8. Bain, P.G.: Parkinsonism & related disorders. tremor. Parkinsonism & Related Disorders 13, 369 (2007)
9. O'Suilleabhain, P.E., Matsumoto, J.Y.: Time-frequency analysis of tremors. Brain: a journal of neurology 121(Pt 11), 2127–2134 (1998)
10. Graham, B.B.: Using an Accelerometer Sensor to Measure Human Hand Motion. Ph.D. thesis (2000)
11. Stiles, R.N., Randall, J.E.: Mechanical factors in human tremor frequency. Journal of applied physiology 23(3), 324–330 (1967)
12. RANDALL, J.E., STILES, R.N.: Power spectral analysis of finger acceleration tremor. Journal of applied physiology 19, 357 (1964)
13. Watanabe, R.N., Kohn, A.F.: Fast oscillatory commands from the motor cortex can be decoded by the spinal cord for force control. The Journal of neuroscience: the official journal of the Society for Neuroscience 35(40), 13687 (2015)
14. Williams, E.R., Baker, S.N.: Circuits generating corticomuscular coherence investigated using a biophysically based computational model. i. descending systems. Journal of Neurophysiology 101(1), 31–41 (2009)
15. Williams, E.R., Soteropoulos, D.S., Baker, S.N., Kopell, N.J.: Spinal interneuron circuits reduce approximately 10-hz movement discontinuities by phase cancellation. Proceedings of the National Academy of Sciences of the United States of America 107(24), 11098–11103 (2010)
16. Massy-Westropp, N.M., Gill, T.K., Taylor, A.W., Bohannon, R.W., Hill, C.L.: Hand grip strength: age and gender stratified normative data in a population-based study. BMC research notes 4(1), 127 (2011)
17. Smaby, N., Johanson, M.E., Baker, B., Kenney, D.E., Murray, W.M., Hentz, V.R.: Identification of key pinch forces required to complete functional tasks. Journal of rehabilitation research and development 41(2), 215 (2004)
18. Videler, A.J., Beelen, A., van Schaik, I.N., Verhamme, C., van den Berg, L.H., de Visser, M., Nollet, F.: Tripod pinch strength and thumb opposition are the major determinants of manual dexterity in charcot-marie-tooth disease type 1a. Journal of neurology, neurosurgery, and psychiatry 81(8), 828–833 (2010)
19. Feys, P., Lamers, I., Francis, G., Benedict, R., Phillips, G., LaRocca, N., Hudson, L.D., Rudick, R.: The nine-hole peg test as a manual dexterity performance measure for multiple sclerosis (2017)
20. Heldner, M.R., Vanbellingen, T., Bohlhalter, S., Mattle, H.P., Mri, R.M., Kamm, C.P.: Coin rotation task: a valid test for manual dexterity in multiple sclerosis. Physical therapy 94(11), 1644–1651 (2014)
21. Dullinger, J., Pellegrino, A., Copney, J., Beltran, A., Kocian, E.: Pinch strength (2018), https://oth603competencysg.weebly.com/pinch-strength.html
22. Roberts, H.C., Denison, H.J., Martin, H.J., Patel, H.P., Syddall, H., Cooper, C., Sayer, A.A.: A review of the measurement of grip strength in clinical and epidemiological studies: towards a standardised approach. Age and Ageing 40(4), 423–429 (2011)

Design and Manufacture a Haptic System to Rehabilitate the Muscles of the Hand

Mina Zareei, Ali Zamani, Ali Tavakoli Golpaygani, and Mohammad J. Sadeghi

Abstract

The paper's objective is to fabricate a novel haptic system for hand muscular rehabilitation applications after hemiplegia that happens after stroke. This prototype is categorised as end-effectors. By using this equipment, patient can perform both active range of motion and passive range of motion. Each rehabilitation device equipped haptic technology for evaluation of force exerted by patient's limb using multi-axial force sensors. Unlike previous proposed devices and state of the art devices, our proposed device evaluates force exerted only receiving feedback of haptic device the current draw of DC motor. In fact, no force sensor has been used in our proposed haptic device.

Keywords

Haptic system • Rehabilitation of hand fingers
Stroke • Feedback of current • Fuzzy algorithm

1 Introduction

During the past decade, the applications of haptic technology in rehabilitation has been the subject of many investigations and studies. Various devices has been fabricated in this application. The Rutgers Master II-nd [1] glove is one of them which was fabricated by a team of researchers at Rutgers University in 2000. Their device was designed for dexterous interactions with virtual environment and uses five pneumatic actuators configured between the palm and the thumb and has five degrees of freedom (DoF). HIRO II designed by Kawasaki and Mouri [2] in 2007 is a haptic interface system for giving sense of force and tactile to each finger. The device is categorised as end-effector type which consists 18 DoF. Mechanism control self-motion mechanism has been employed in the system. There are many disadvantages to the system consisting high weight, high backlash, high friction, large work-space, high price, low-precision force sensation and so on [3]. HIRO III developed by Endo et al. [3] in 2011. The device was designed to reduce and improve HIRO II's disadvantages. The most noticeable disadvantages of all aforesaid devices are large work-space, limited access only to clinical centres, priceless, unportable and using expensive multi-axial force sensors. In this paper, An Smart way has got employed to receive its haptic feedback from the current of DC motor as a substitute for receiving feedback from force that is typical through the proposed haptic interface devices. Moreover, the prototype is able to measure the value of force exerted to haptic system. We used Fuzzy controller algorithm to implement protocols of hand rehabilitation being used in clinical centres.

This paper consists of five main sections: in the Sect. 2, the mechanical part of the system will be described. In the Sect. 3, the electronic part and fuzzy algorithm employed in the system will be introduced. Results and evaluations of the haptic system are in the Sect. 4. And finally, discussion and conclusion will be provided in the Sect. 5.

2 Mechanical Part

The proposed haptic system consists of an ergonomic hand-arm-rest (for user's forearm), finger holder and a housing are showed in Fig. 1. The finger holder or so-called Guide is location of attaching user's fingertips that its design is inspired Sale et al. [4]. The housing supports electrical

M. Zareei (✉) · A. Zamani
Department of Medical Physics and Engineering, Shiraz University of Medical Sciences, Shiraz, Iran
e-mail: zareimina67@gmail.com

A. T. Golpaygani
Iranian National Standardization Organization, Karaj, Iran

M. J. Sadeghi
Amirkabir University of Technology, Tehran, Iran

Fig. 1 Front view of the proposed haptic system. The user's forearm and fingertip are located to the hand-arm-rest and the guide respectively and then flexion/extension exercises are produced

printed circuit board, actuator, ballscrew [5] and encoder. The DC motor is coupled with the ballscrew to create both flexion/extension exercises and adequate torque.

3 Electronic and Controller Parts

This platform comprises two healing procedures, an assisted phase and a resisted phase. These two ones are proportional to hand therapy protocols which are prescribed by physiotherapists.

In resisted phase, the patient is requested to withstand motion of the Guide. Commensurate with the force exerted, electric current will increase. The Central Processing Unit (CPU) will process the electric current in real time. Whenever electric current increases, the CPU will command mechanical part to increase resistance of pathway by driving more electric current to terminals of the DC motor because the haptic platforms electric current have to be kept steady-state. By this method, the patient's impaired finger will meet various challenges to be encouraged and try recovering strengthen and stretch that are lost in order to stroke. In assisted phase, the patient is requested to give assistance to motion of the Guide. In this case, commensurate with the force exerted, the electric current will decrease.

The CPU senses that in real time, and will command the mechanical part to decrease current of DC motor since patient's impaired finger can perform its rehabilitation period actively-passively. This means whenever the impaired finger attempts to do flexion/extension functions by itself, the haptic platform's actuator will work with less electric power than the initial electric power because the haptic platforms electric current have to be kept steady-state. It should be mentioned that even if patient's impaired finger strengthen isn't sufficient to assist motion of the Guide, the gripping and grasping will be executed by the mechanical part entirely passive as if a physiotherapist in clinical centre helps patient with extension/flexion exercises if she/he isn't able to do them by herself/himself.

By this method, both this platform is able to realize active and passive rehabilitation that is the primary purpose of each haptic devices for hand rehabilitation and the patient is able to play an effective role in her/his rehabilitation period.

3.1 The Closed-Loop Feedback Control System of the Platform

To achieve steady-state electric current, we employed Fuzzy Logic Controller to handle this multi-input and multi-output system in the desired manner.

In control part as shown in Fig. 2, a current error or cost function e_a needs to be calculated which is the difference between the initial current I_s so-called setpoint current and the momentary current signal feedback I_a (Eq. 1).

$$e_a = I_s - I_a \tag{1}$$

The main object of the fuzzy controller is to minimize the cost function. One of strategies for minimizing the cost function is controlling Pulse Width Modulation (PWM) [6]. The AVR micro-controller can create the PWM signal using its clock source or its Timer counter register (TCNT). The PWM employs TCNT to count up and then wraps back to a low state(zero) continuously by comparing to the value of Output Compare Register (OCR) [7]. Notably, if value of
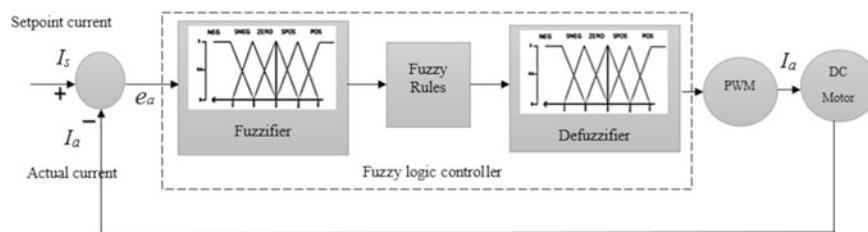
Fig. 2 The block diagram of the DC motor current controller model
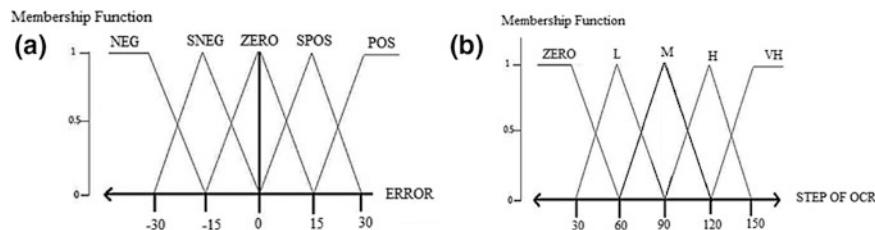
Fig. 3 **a** Membership function curve of fuzzy sets defining the electric current. **b** Membership function curve of defuzzy sets defining numerical values of OCR to control current output

OCR increases, inversely proportional to the value of OCR increased, value of the PWM and consequently value of current will decrease and vice verse. The closed-loop feedback controller is employed to control Output Compare Register. In general, Fuzzy logic controller comprises several design steps: defining inputs and outputs, defining fuzzy membership, set functions and rules, and tuning the DC motor.

The fuzzy logic controller has one input and two outputs defined as control variables. In fuzzifier block, current error crisp variables are converted into linguistic variables. All membership functions are considered the triangular waveform that are overlapped with each other and plotted into linguistic labels (Fig. 3a). By using triangular function, membership degree can be computed. The 5 sets classified the fuzzy sets includes Negative (NEG), Small negative (SNEG), Zero, Small positive (SPOS), and positive (POS).

In defuzzifier block, linguistic variables are translated into numerical values the Timer and the current. As shown in Fig. 3b membership functions for defuzzy sets are considered triangular functions. The 5 sets classified the defuzzy sets includes Zero, Low (L), Medium (M), High (H), and Very High (VH). All numerical values tabulated in Fig. 3a, b have been conducted by performing various performance tests using Oscilloscope. The fuzzifier inputs can be mapped into the required output via the rules, as indicated in Table 1. Notably, in order to have better and fast controller, fuzzy logic algorithm was implemented in the micro-controller.

Table 1 Fuzzy rules which were implemented according to IF … THEN in the micro-controller

Rule no.	If the error is	Then PWM output is
1	NEG	VH
2	SNEG	H
3	ZERO	M
4	SPOS	L
5	POS	Z

4 Evaluation of the Proposed Haptic System

To know whether the control unit can work well or not, we measured the period of each cycle in each test since electric current must be steady-state. Being stable current in each cycle means that speed of motor in each cycle must be stable. That is reason why we computed the amount of period in each cycle by exerting different forces. Meanwhile, each cycle consists of a flexion motion and an extension motion and for being under the same circumstance we measured four cycles with the same setpoint current in each test. Each test was repeated five times and generally thirty measurements was made under the same circumstance.
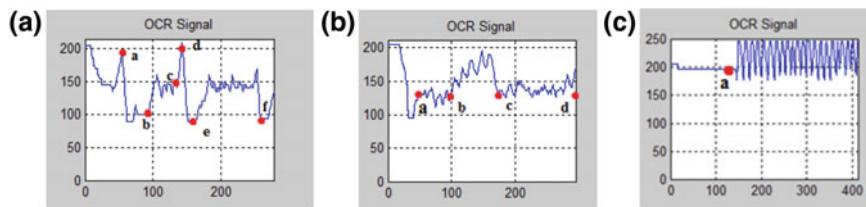
The Average of the period error was computed in terms of ms (Table 2). If value of error is zero, it means that speed of the system is stable in each cycle, this shows that the control unit is working efficiently. As indicated at Table 2, value of error is less than 0.003 ms and it's approximately zero.

To evaluate the subject's finger function, an exploratory study was examined on three subjects with different finger strengths and the results was conducted graphically (Fig. 4).

As seen in Fig. 4a after adjusting the setpoint current at point a, the first subject was asked to do flexion/extension exercises while resisting the motion direction of the Guide. Commensurate with force exerted to the Guide, drawn current of motor must be increased then value of OCR will decreased. As illustrated in Fig. 4a, the greatest resistance has taken place at intervals ab and de (values are much less than value of setpoint); on the other hand, the most amount of his finger strength has be exerted during these intervals. Over intervals bc and ef, his rehabilitation process was done passively-actively in fact the mechanical part helped the subject complete his motion cycle. The second subject was asked to assist the motion of the guide. In the assistance phase, after choosing setpoint current (point a), as seen in Fig. 4b the subject was trying to assist the motion of guide. During intervals ad and cd, the subject's impaired finger was attempting to do its flexion/extension exercises by itself since there is not any substantial difference between value of

Table 2 Period error computed. In this test values of force exerted are between 0–1/5 N. Each test were repeated five times

Number of test						
Actual value of force exerted (N)	1	2	3	4	5	Average error of period (ms)
0.25	0.003	0.001	0.005	0.002	0.002	0.0025
0.5	0.002	0.004	0	0.003	0.003	0.0028
0.75	0.005	0.003	0.001	0.004	0.004	0.0032
1	0.002	0.001	0.003	0.005	0.005	0.0028
1.25	0.003	0.003	0.002	0.001	0.002	0.0022
1.50	0.002	0.003	0.003	0.002	0.002	0.0024
Total average error						0.00265

Fig. 4 Performance of the OCR signal for 3 different subjects. Horizontal axis is time (ms) and the vertical axis is OCR value. **a** The first subject resisting. **b** The second subject assisting. **c** The third subject assisting. In whole curves, point a depicts the setpoint current

setpoint current and value of momentary current. It shows that its strength was not enough to perform them therefore the mechanical part helped her complete her motion cycle. During interval ab the finger applied more force to the guide therefore commensurate with force exerted, the current had to decrease. Because the subject's finger was able to complete her rehabilitation process by herself more actively and less passively. The third subject was asked to both assist and resist motion of the guide regardless of which in extension or flexion direction. As illustrated in Fig. 4c, the subject's finger strength in direction of motion is more than the subject's finger strength in upright motion.

5 Conclusion

This paper proposes a novel haptic system to rehabilitate hand in which controlled by fuzzy logic controller. Instead of using multi-axial force sensors, an intellectual method has been developed to receive its haptic feedback from the drawn current of DC motor. In addition, One of the most significant innovations in this system is that we employed fuzzy algorithm which was very close to treatment protocols in rehabilitating of hand. Although, quite a few systems for hand rehabilitation have already proposed, majority of them have been designed for clinical centres therefore these platforms are being commercialised. The proposed haptic system can provide these exercises for the patient forced to do the practices on their own at home with lower costs (leading to

reduce the therapeutic time period), higher accuracy. It assists repetitive grasping and releasing movements while allowing the subject to feel real object in his hands during therapy and in a parallel way, forces and torques are gained. Thus, this arrangement confers a more precise criterion to the physician to forecast the time duration elapses for the healing. The preliminary tests performed on several healthy subjects that results of 3 subjects have shown here.

References

1. Bouzit M, Burdea G, Popescu G, Boian R. The Rutgers Master II-new design force-feedback glove. IEEE/ASME Transactions on mechatronics (2002) https://doi.org/10.1109/tmech.2002.1011262
2. Kawasaki H, Mouri T. Design and control of five-fingered haptic interface opposite to human hand. IEEE Transactions on robotics (2007) https://doi.org/10.1109/tro.2007.906258
3. Endo T, Kawasaki H, Mouri T, Ishigure Y, Shimomura H, Matsumura M, et al. Five-fingered haptic interface robot: HIRO III. IEEE Transactions on Haptics (2011) https://doi.org/10.1109/toh.2010.62
4. Sale P, Lombardi V, Franceschini M. Hand robotics rehabilitation: feasibility and preliminary results of a robotic treatment in patients with hemiparesis. Stroke research and treatment (2012) https://doi.org/10.1155/2012/820931
5. http://www.kssballscrew.com/us/pdf/catalog/TechnicalDataSheet
6. Duran MJ, Barrero F. Recent advances in the design, modeling, and control of multiphase machines Part II. IEEE Transactions on Industrial Electronics (2016) https://doi.org/10.1109/tie.2015.2448211
7. https://www.microchip.com

Are Micro Back Markers on Thin Film of Scaffold Effective to Evaluate Contractive Movement of Myotube?

Yusuke Takahashi, Shigehiro Hashimoto, and Haruka Hino

Abstract

The scaffold of the transparent film with micro markers has been designed to evaluate the contractive movement of myotube under the electric pulse stimulations in vitro. The scaffold of a thin film (6 μm of thickness) of polydimethylsiloxane was made with ten million micro markers: 4 μm of diameter, 2 μm of height, and 30 μm of interval. Ten million markers were made on the backside of the scaffold by the photolithography technique. C2C12 (mouse myoblast cell line) was seeded on the film at the counter surface to the markers at the density of 5000 cells/cm^2. The cells were cultured for 12 days in the medium containing 10% fetal bovine serum and 1% penicillin/streptomycin at 310 K with 5% of CO_2 content. The electric pulses (1 s of pulse cycle, 1 ms of pulse width) were applied between platinum electrodes dipped in the medium. The myoblasts were able to be cultured on the film to be differentiated into myotubes. The thin film with micro markers was successfully made of polydimethylsiloxane, and had enough transparency for observation of myotubes by the microscope. The myotube was contracted synchronously with the stimulation of electric pulses. The contractile movement was able to be analyzed by the repetitive displacement of the length between backside micro markers of the film. The micro backside markers on thin film of scaffold are effective to evaluate contractive movement of the myotube.

Keywords

Micromachining • Myotube • Contractive movement

1 Introduction

The myotube can be made from myoblasts by the cell culture technique in vitro. The myotube contracts synchronously with the electric pulses, which is applied to the medium in vitro [1]. The macro movement of muscle tissue was measured by the conventional technique of mechatronics in previous studies. The movement can also be detected by the laser technique [2]. For the application to regenerative medicine, the functional quality of micro contraction of myotube should be evaluated in vitro.

The photolithography technique, on the other hand, enables machining of micro patterns on the scaffold [3, 4]. In the present study, the contractive movement of myotube cultured on the newly designed transparent thin film with micro markers under the electric pulse stimulations has been evaluated in vitro.

2 Methods

2.1 Thin Film with Micro Markers

The scaffold of the transparent film with micro markers has been designed. The scaffold of a thin film (6 μm of thickness) of polydimethylsiloxane was made with micro markers: 4 μm of diameter, and 2 μm of height, each. Ten thousand markers were arranged in a grid (30 μm of interval) on the backside of the scaffold by the photolithography technique.

A photomask is made for the micro pattern. Titanium (0.0002 mm thickness) was deposited on the surface of the glass plate in the electron beam vapor deposition apparatus. After oxygen ashing, HMDS (hexamethyldisilazane) was coated on the disk. The positive photoresist material of OFPR-800LB was coated on the disk, and was baked in the oven. The pattern for micro markers was drawn on the photoresist with a laser drawing system, and was baked on

Y. Takahashi · S. Hashimoto (✉) · H. Hino
Kogakuin University, Shinjuku, Tokyo 1638677, Japan
e-mail: shashimoto@cc.kogakuin.ac.jp

the heated plate. The photoresist was developed with tetra-methyl-ammonium hydroxide, rinsed by the pure water. The surface of titanium with photoresist material was etched with the plasma gas using reactive ion etching system. OFPR-800LB was removed by acetone, after confirmation of pattern of etching. The dimension of the micro-pattern of the mask was confirmed with a laser microscope.

The mold for the thin film of the scaffold with micro markers array was made on the surface of the glass plate. The surface of the glass was hydrophilized by the oxygen plasma ashing in the reactive ion etching system. To improve affinity between glass and photoresist material, HMDS was coated on the disk with a spin coater. The positive photoresist material of OFPR-800LB was coated on the disk with the spin coater, and was baked in the oven. The photomask was mounted on the surface of OFPR-800LB, and the photoresist was exposed to the UV light through the mask in the mask aligner. The photoresist was baked in the oven, and developed with NMD-3. The pattern was rinsed by the pure water, and dried by the spin-dryer. The morphology of the surface of the mold was confirmed with a stylus profiler, and the height of the step of the surface of the mold was used to estimate the thickness of the film.

PDMS (polydimethylsiloxane) was mixed with the curing agent. The volume ratio of PDMS to curing agent is ten to one. After degassing, PDMS was poured on the mold, which was placed on the spin coater, to make the thin film of scaffold with the micro pattern. PDMS ring, which was hydrophilized by the oxygen plasma ashing in the reactive ion etching system, was placed on the thin film of PDMS. The film supported with the ring was baked in the oven at 368 K for 30 min. After residual PDMS film outside of PDMS ring was cut off, PDMS film with PDMS ring was carefully peeled off from the mold using acetone. After rinsed by the pure water, PDMS film was sandwiched by another PDMS ring, and dried in the oven at 333 K for 1 h.

The morphology of the markers array on the rear surface of the film was observed by a scanning electron microscope. After exposure to the oxygen gas in a reactive ion etching system, the scaffold of PDMS film was preserved in the ultrapure water to keep the hydrophilic property of the surface before the cell culture.

2.2 Cell Culture

C2C12 (mouse myoblast cell line originated with cross-striated muscle of C3H mouse) was seeded on the film at the counter surface to the markers at the density of 5000 cells/cm^2. The cells were cultured for 12 days in D-MEM (Dulbecco's Modified Eagle's Medium) containing 10% fetal bovine serum and 1% penicillin/streptomycin at 310 K with 5% of CO_2 content.

2.3 Observation of Contractive Movement of Myotube

The electric pulses (1 s of pulse cycle, 1 ms of pulse width) were applied between platinum electrodes dipped in the culture medium. The contractive movement was observed by an inverted phase contrast microscope. The local repetitive displacements of the distance between backside micro markers (Fig. 1) of the film were traced at the image of the microscopic movie image. Strain (ε) is calculated by the following equation.

$$\varepsilon = \Delta x/x \tag{1}$$

In Eq. 1, Δx is amplitude of repetitive displacement of the distance (x) between neighboring markers. The amplitude (Δx) is evaluated as the distance between maximum and minimum values of x during repetitive contraction in the present study. At the image, the angle (0 rad $< \theta <$ 1.57 rad) between the longitudinal axis of the myotube and x was also measured.
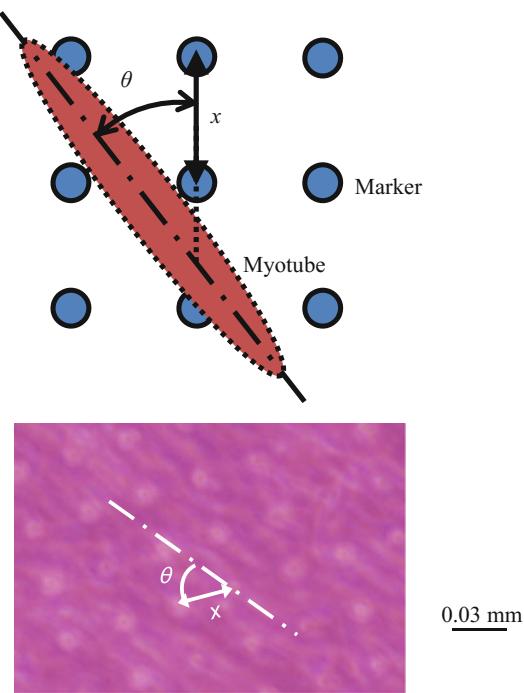
Fig. 1 The distance (x) between neighboring markers, and the angle (θ) between the longitudinal axis of the myotube and x (upper). They are traced at the microscopic movie image (lower)
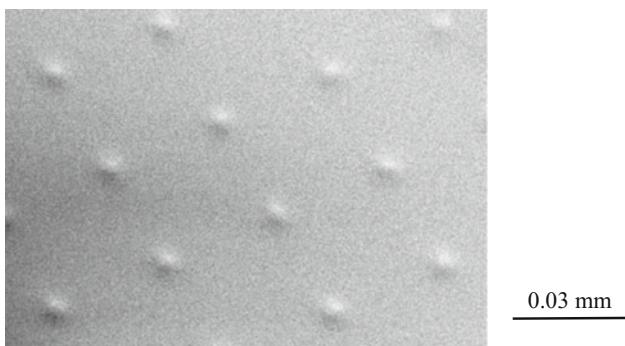
Fig. 2 A scanning electron microscopic image of the back side of the film of the scaffold. Micro markers were successfully able to be made with the interval of 0.03 mm

3 Results

The myoblasts were able to be cultured on the film to be differentiated into myotubes. The thin film with micro markers was successfully made of polydimethylsiloxane (Fig. 2), and had enough transparency for observation of myotubes by the inverted phase contrast microscope (Fig. 3).

The myotube was contracted synchronously with the stimulation of electric pulses. Figure 4 shows the local repetitive strain between the neighboring markers related to the angle of the contracting myotube. The higher strain sometimes occurs around 0 rad and around 1.5 rad. When myotube contracts, the scaffold film contracts at 0 rad. The counter movement synchronously occurs at 1.57 rad. The maximum value of ε was 0.33 at 1.3 rad.

4 Discussion

When the scaffold has high elasticity, the movement of the myotube is limited, and is hard to be detected [5]. The thin film of scaffold, which is designed in the present study, has
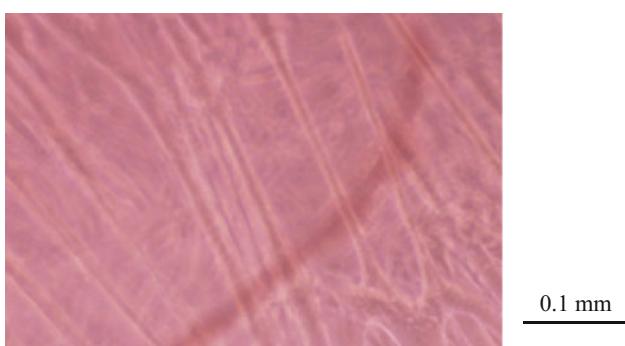
Fig. 3 Myoblasts were successfully cultured, and differentiated into myotubes on the film of polydimethylsiloxane
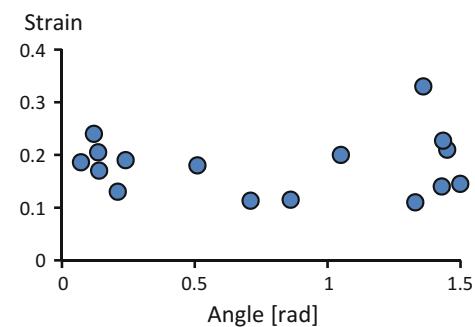
Fig. 4 Relationship between local strain (ε) and angle (θ)

enough compliance to follow the contraction of a myotube [6, 7]. It has also enough transparency to observe the movement of a myotube cultured on the film by an inverted phase contrast microscope. The arrangement of the backside micro markers, of which interval was short enough, was able to trace the local repetitive movement of the myotube cultured on the film. A cell might sensitive to the hardness of the surface of the scaffold, which is called mechanotacsis [8]. The local mechanical property of the film might be modified by each backside marker in the present study, but cells does not show local densely distribution according to the location of the backside marker. In the present study, the backside markers may not affect the distribution of cells on the film by mechanotacsis of cells. The contraction force of the myotube can be estimated using the related parameters of the film of the scaffold: strain, cross sectional area, and elasticity [6, 9]. The evaluation might contribute the quantitative process to make engineered tissue for regenerative medicine.

5 Conclusion

A scaffold of a thin film with micro markers can be realized by the photolithography technique. The micro back markers on thin film of scaffold are effective to evaluate contractive movement of the myotube.

Conflict of Interest This paper has no conflict of interests.

References

1. Yamasaki, K., Hayashi, H., Nishiyama, K., Kobayashi, H., Uto, S., Kondo, H., Hashimoto, S., Fujisato, T.: Control of myotube contraction using electrical pulse stimulation for bio-actuator. Journal of Artificial Organs 12(2), 131–137 (2009).

2. Hashimoto, S., et al.: Measurement of periodical contraction of cultured muscle tube with laser. Journal of Systemics, Cybernetics and Informatics 7(3), 51–55 (2009).

3. Hino, H., Hashimoto, S., Tamura, T., Takahashi, Y., Sugimoto, T., Yasuda, T.: Electric measurement of cultured myoblast oriented on scaffold with micro-pattern. In: Proceedings of the 21th World Multi-Conference on Systemics Cybernetics and Informatics, Vol. 2, pp. 209–214. International Institute of Informatics and Systemics, Orlando (2017).

4. Takahashi, Y., Sugimoto, K., Hino, H., Katano, T., Hashimoto, S.: Design of scaffold with array of micro projections to trace intra- and inter-cellular behavior. In: Proceedings of the 20th World Multi-Conference on Systemics Cybernetics and Informatics, Vol. 2, pp. 159–164. International Institute of Informatics and Systemics, Orlando (2016).

5. Takahashi, Y., Hashimoto, S., Hino, H., Takeda, T.: Electric stimulation for acceleration of cultivation of myoblast on micro titanium coil spring. In: Proceedings of the 20th World Multi-Conference on Systemics Cybernetics and Informatics, Vol. 2, pp. 153–158. International Institute of Informatics and Systemics, Orlando (2016).

6. Liu, M., Sun, J., Sun, Y., Bock, C., Chen, Q.: Thickness-dependent mechanical properties of polydimethylsiloxane membranes. Journal of Micromechanics and Microengineering 19(3), 1–4 (2009).

7. Alford, P.W., Feinberg, A.W., Sheehy, S.P., Parker, K.K.: Biohybird thin films for measuring contractility in engineered cardiovascular muscle. Biomaterials 31(13), 3613–3621 (2010).

8. Takahashi, Y., Sugimoto, K., Hino, H., Hashimoto, S.: Effect of mechanical property of scaffold surface with micro hybrid striped pattern on cell migration. In: Proceedings of the 21st World Multi-Conference on Systemics, Cybernetics and Informatics, Vol. 2, pp. 227–232. International Institute of Informatics and Systemics, Orlando (2017).

9. Nagayama, K., Adachi, A., Matsumoto, T.: Heterogeneous response of traction force at focal adhesions of vascular smooth muscle cells subjected to macroscopic stretch on a micropillar substrate. Journal of Biomechanics 44(15), 2699–2705 (2011).

Study on Walking Training System for Using High-Performance Shoes with Human Compatibility

Yasuhiro Hayakawa

Abstract

The number of elderly in the Japanese population has been increasing, and is expected to reach about 40% by 2060. This means that those aged 65 and over in Japan will be roughly every one in 2.5 persons (Cabinet office, Government of Japan, Director General for Policies on Cohesive Society, "H.26 Aged Society White Paper", 2014, [1]). With this are increases in the need for elder-to-elder nursing and shortage in and an increased burden on care takers. These developments have resulted in efforts to promote independence among the elderly—something that has brought walking to the attention of those promoting good health and independence among the elderly. The increasing number of accidental falls among the elderly while walking (Ministry of Health, Labour and Welfare, "Comprehensive Survey of Living Conditions" IV conditions of care, [2]). Among the main factors in falls are a deteriorating center of gravity of balance due to declining physical performance and weakening in the muscular strength of the lower limbs. In this study, we focused on shoes to be worn daily in walking aimed at both assisting walking and preventing falls. Further, we proposed training in walking that is continues and daily that detects and corrects the center of balance during walking. To add detection of staggering, we used a sponge-core soft-rubber actuator consisting of open-cell foam sponge coated in silicon rubber. This actuator changes stiffness with inner pressure. Equipping insoles, with it means that it can be used for both detecting the pressure distribution of the foot sole while prompting correct walking by changing the stiffness of the insole. We also developed a means of walking status presentation that confirms walking status on a display in real time.

1 Introduction

The number of elderly in the Japanese population has been increasing, and is expected to reach about 40% by 2060. This means that those aged 65 and over in Japan will be roughly every one in 2.5 persons [1]. With this are increases in the need for elder-to-elder nursing and shortage in and an increased burden on care takers. These developments have resulted in efforts to promote independence among the elderly—something that has brought walking to the attention of those promoting good health and independence among the elderly. The increasing number of accidental falls among the elderly while walking [2]. Among the main factors in falls are a deteriorating center of gravity of balance due to declining physical performance and weakening in the muscular strength of the lower limbs.

In this study, we focus on shoes to be worn daily in walking aimed at both assisting walking and preventing falls. We propose training in walking that is continues and daily that detects and corrects the center of balance during walking. To add detection of staggering, we use a sponge-core soft-rubber actuator (SCSRA) consisting of open-cell foam sponge coated in silicon rubber. This actuator changes stiffness with inner pressure. Equipping insoles, with it means that it can be uses for both detecting the pressure distribution of the foot sole while prompting correct walking by changing the stiffness of the insole. We also develop a means of walking status presentation that confirms walking status on a display in real time.

Y. Hayakawa (✉)
National Institute of Technology, Nara College, 22 Yata-cho, Yamatokoriyama, Nara, Japan
e-mail: hayakawa@ctrl.nara-k.ac.jp

2   High-Performance Shoes

2.1   Sponge-Core Soft Rubber Actuator (SCSRA)

We introduced the SCSRA for the insole. Figure 1 shows the structure of SCSRA. Sponge is coated and sealed in silicon rubber and a tube is attached for add or remove air. Thus, it can change the stiffness along with the inner pressure. Inner pressure is also changed by external pressure. So, the SCSRA is used both to detect pressure and assist in walking. Additionally, the actuator is more suitable for use on the human skin than others composed plastics or metals, because it's made up of these soft materials. Endurance test results confirmed that SCSRA endures up to 84.2 kPa when it kept hermetically-sealed, so that it has enough pressure resistance for use as an insole [3].

2.1.1   Insole

Using SCSRA as insole material, we developed High- Performance Shoes that both measure the pressure distribution of the foot sole enable the center of gravity to be corrected in walking. Figure 2 shows the weight transfer during the stance phase of the walking cycle. This determines the arrangement of the insole. According to this figure, it is pertinent that the measurement of the heel, little toe, thenar and big toe [4].

Based on these, we arranged the corresponding SCSRA as shown in Fig. 3
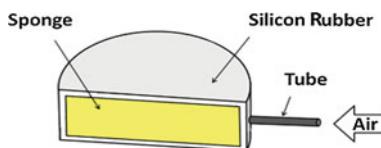
Fig. 1 SCSRA structure
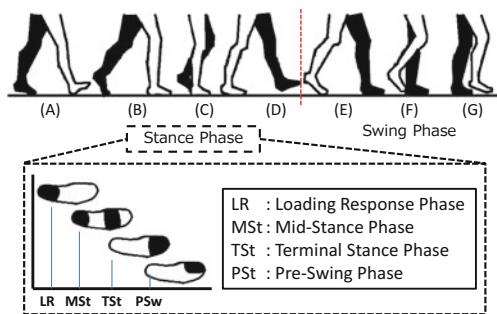
Fig. 2 Weight transfer during the stance phase of the walking cycle [4]
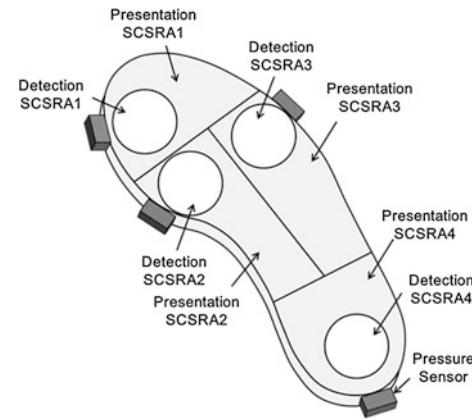
Fig. 3 SCSRA arrangement

2.2   High Performance Shoes

Our High-Performance Shoes, shown in Fig. 4, consist of an insole which is described in section B, an electrical circuit that measures pressure distribution, processes data and assists walking correction [5, 6]. These are separated into the shoes, which weigh 720 g, and a sin pad, which weighs 180 g. SCSRAs have small pressure sensors for measuring inner pressure of each SCSRA.

SCSRAs have small three-port two-position air solenoid valves for controlling of inner pressure. The electrical control circuit has an AVR microcomputer and a XBee, which is a wireless communication module, along with micro air pump for changing inner pressure mounted on the shin pad. Figure 5 shows the electrical circuit. The details of using components are listed in Table 1.

2.3   Walk-Assistance and Experimental Results

The objective of our walk-assistance system is to enable users to realize self-sustained walking training that stimulates the sole to walk correctly by changing insole stiffness
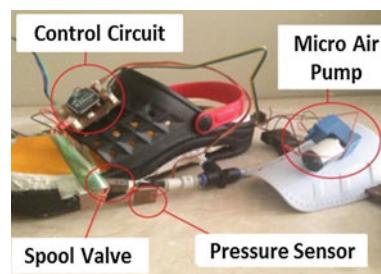
Fig. 4 High-performance shoes used in walking training
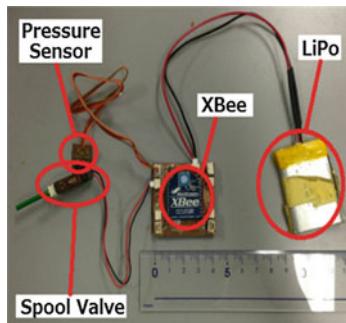
Fig. 5 Electrical circuit for system control

automatically when a constant pressure value is exceeded. Figure 6 shows the proposed configuration of walking assist system and experimental results of pressure distribution of each insole. In system operation, the pressure value from the SCSRA is sent to the electrical circuit. If it exceeds 10 kPa, the solenoid valve on the SCSRA corresponding to the SCSRA is turned on. Then, the impounded air from the

micro pump is introduced into the SCSRA through a tube, making it stiff. When pressure is less than the threshold, the valve is turned off and inner air is exposed to the atmosphere to make it soft.

3 Conclusions
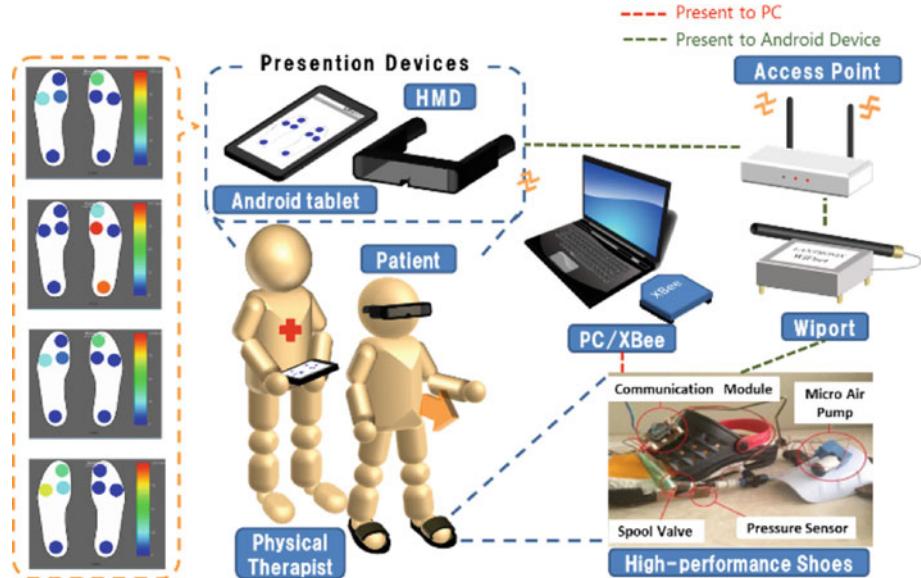
We have discussed the background, development and results for the High-Performance Shoes we developed in this study. These shoes detect and help correct the pressure distribution on the sole of the foot, helping to correct walking balance and to minimize falls in elderly through walking training.

Although our shoes had a certain effectiveness in support in walking by younger person's. However, these shoes have some problems to conduct walking experiments by elderly people such as weight of shoes, ease to wear and so on. Therefore, we have been improving in order to reduce size and weight and become easy to wear. After these improvements, we plan to conduct walking experiments involving

Table 1 Components manufacturers and models

Components	Manufacturer	Model
Pressure sensor	Fujikura	FGN-607P G SR
Solenoid valve	SMC	S070C-RDC-32
AVR microcomputer	ATMEL	ATMEGA64-16AU
XBee	Digi International	XBee S2
Micro air pump	Parker Hannifin	E164-11-060

Fig. 6 Walking training system using high-performance

pseudo elderly persons. Furthermore, we also plan to conduct walking experiments and sensory evaluation involving the elderly at welfare and rehabilitation facilities.

References

1. Cabinet office, Government of Japan, Director General for Policies on Cohesive Society, "H.26 Aged Society White Paper" Chapter 1, section 1–2 (2014)

2. Ministry of Health, Labour and Welfare, "Comprehensive Survey of Living Conditions" IV conditions of care

3. Yasuhiro HAYAKAWA, Kensuke MORISHITA, Mina AICHI and Ryuuji TIIUDA, "Development of a Pneumatic Silicon Outer Fence Mold Actuator", The Japan Society of Mechanical Engineers, C, Vol. 70, No. 690, pp. 433–439, 2004

4. Perry Jacqueline, "GAIT ANALYSIS Normal and Pathological Function second Edition" pp 2–47(2007)

5. Yasuhiro HAYAKAWA, Shogo KAWANAKA, Kazuma KANEZAKI, Shigeki DOI, "Development of Walking Training System using High-Performance Shoes", Robotics and Mechatronics Conference 2014, 1A1-A01(2014)

6. Yasuhiro HAYAKAWA, Shogo KAWANAKA, Kazuma KANEZAKI, Shigeki DOI, "Study on Presentation System for Walking Training using High-Performance Shoes", Robotics and Mechatronics Conference 2015, 1P2-L10 (2015)

Ergonomic Assessment of an Active Orthosis for the Rehabilitation of Flexion and Extension of Wrist

Adriano O. Andrade, Julien Bourget, Samila Costa, Adriano Pereira, Michael I. Okereke, and Marcus Fraga Vieira

Abstract

Muscular stiffness and limb rigidity are two main consequences of Parkinson's disease. These motor symptoms may be present in distinct parts of the body, influencing functional tasks executed by hands. To aid people suffering from these motor symptoms, we developed an active wrist orthosis whose purpose is to enable increase the flexion and extension range of motion of the wrist joint. We identified five relevant ergonomic variables that should be considered when using the orthosis in the clinical practice: (i) device stability, (ii) forearm position; (iii) muscular strength; (iv) amplitude of motion; and (v) mass of the device. These variables were identified based on the observation of movements while users executed the flexion and extension of the wrist with and without the device. In this research, we present a description of the developed orthosis and an evaluation of the ergonomic variables (i), (ii) and (iii). An enhanced support structure has been used with the orthosis and shown to lead to a stability improvement. Electromyographic analysis showed that the use of the orthosis does not introduce undue muscular load on the user at distinct angular positions of the forearm.

1 Introduction

Parkinson's disease (PD) is a neurodegenerative disease that leads to progressive loss of dopaminergic neurons from the substantia nigra [2]. Dopamine deficiency produces a severe extrapyramidal system effect, resulting in decreased muscular strength [5]. These pathophysiological changes generate typical neurological symptoms found in patients with PD such as bradykinesia, rest and postural tremor, postural instability, and muscular stiffness [3].

A research area that can contribute to patients with PD is the provision of physiotherapeutic aid based on robotic devices for safe and intensive rehabilitation of individuals with light to severe motor deficits. Such use of robotic devices has been shown to partially restore the function of the upper limb of individuals affected by PD [4, 7]. The work of Sangha et al. [6] is an example of the rehabilitation of flexion and extension movements of the wrist. However, as in most of the studies in this area, the authors do not present ergonomic assessment of the developed device. The ergonomics of any orthosis is vital for eventual adoption in PD-related physiotherapy. In this study, we present the description of an active wrist orthosis and the evaluation of ergonomic variables that may affect its practical use.

A. O. Andrade (✉) · J. Bourget · S. Costa · A. Pereira
Centre for Innovation and Technology Assessment in Health, Federal University of Uberlândia, Uberlândia, Brazil
e-mail: adriano@ufu.br

J. Bourget
e-mail: julien.bourget@etu.univ-lyon1.fr

S. Costa
e-mail: samilac.costa@gmail.com

A. Pereira
e-mail: a.alves.pereira@uol.com.br

J. Bourget
Biomedical Engineering, University Claude Bernard Lyon 1, Polytech Lyon, Lyon, France

M. I. Okereke
Department of Engineering Science, University of Greenwich, London, UK
e-mail: M.I.Okereke@greenwich.ac.uk

M. F. Vieira
Bioengineering and Biomechanics Laboratory, Federal University of Goiás, Goiânia, Brazil
e-mail: marcus.fraga.vieira@gmail.com
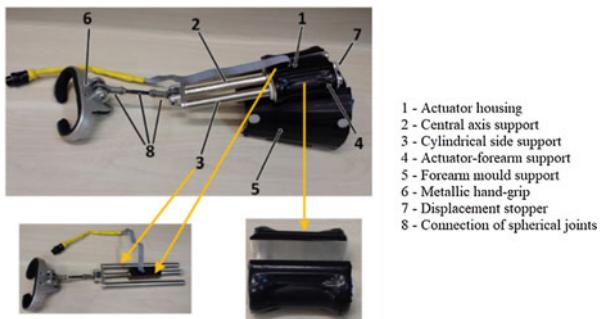
Fig. 1 Identification of the parts of the orthosis

2 General Description of the Orthosis

The active wrist orthosis (Fig. 1), was developed in the Centre for Innovation and Technology Assessment in Health (NIATS) of the Federal University of Uberlândia. The current design has been patented (INPI-BR10 2014 023282 6). Ethical approval for the development and assessment of the orthosis was granted by the National Committee for Ethics in Research (CAAE: 07075413.6.0000.5152).

The orthosis was manufactured mainly from aluminum and its overall weight is 909 g. The actuator is a linear DC-Servomotor (LM 2070-080-11, Faulhaber, Germany). Programmed motion of the orthosis is achieved via an external motion controller (MCLM-3006-S-RS, Faulhaber, Germany), which is not shown in Fig. 1. As the focus of this research is the ergonomic assessment of the orthosis in a passive scenario (i.e., without considering linear forces exerted by the actuator), all the evaluations were performed without the influence of the actuator, which means that it was turned off.

3 Methodology for Ergonomic Assessment

Based on preliminary tests with the orthosis, five ergonomic variables were identified: (i) device stability, (ii) forearm position; (iii) muscular strength; (iv) amplitude of motion; and (v) mass of the device. In this paper it is presented only results concerning the analysis of the variables (i), (ii) and (iii). It is expected that results related to variables (iv) and (v) are presented in complementary future work.

3.1 Orthosis Stability

For effective transfer of the actuator force to the hand, the orthosis must be securely fixed on the forearm. A special under-forearm support was manufactured (designed and 3D-printed) to securely fix the orthosis.

To evaluate the gain in stability (i.e., the steadiness of the orthosis on the forearm) provided by the support, a volunteer carried out the flexion and extension of the wrist with and without the support. A three-axial accelerometer (LSM303D, Microelectronics, Switzerland) was positioned with the x-axis perpendicular to the sliding axis of the orthosis (Fig. 1) on the forearm mould support (Fig. 1). The measure of stability was based on the estimate of displacement resulting from double integration of the measured acceleration on the x-axis, as no significant oscillations were observed in the other directions. Collected signals were sampled at 50 Hz with the arm laid on a flat surface at $0°$. Linear and nonlinear detrending methods were applied as described in [1] to the raw signals, for eliminating the influence of gravity and other low frequency components over the signal.

3.2 Muscular Strength

People suffering from PD experience reduced muscular strength. Hence, the relative muscular force for common daily tasks required by able-bodied persons is much lower than those of individuals with PD. Therefore, muscular strength (MS) was identified as a relevant ergonomic variable.

The Maximum Voluntary Muscular Contraction (MVC) of a healthy male was collected and analysed. The MVC was acquired during the resistive active movement of flexion and extension of the wrist over 12 s. This task was repeated three times with a 2 min rest interval to allow for adequate relaxation of the muscle fibre in-between tests.

To acquire EMG signals, a customized system based on the Intan Tech's RHD2000 Evaluation System was employed. EMG was collected simultaneously from the flexor and extensor muscles of the subject's dominant forearm, with and without the orthosis. Disposable sensors (Meditrace, 35 mm) were used for EMG detection.

EMG signals were filtered by a zero-phase high passband Butterworth digital filter (6th order, 30 Hz cut-off frequency). The envelope of the signal was estimated by means of the root mean square value (RMS) and the mean of its main peaks (based on a pre-defined threshold) was employed as the main feature extracted from EMG signals. Signal analysis was performed by using customized programs developed in MatLab (Mathworks, USA).

Figure 2 shows the test setup. Eight flexion-extension repetitions were carried out with the forearm-rest support in these angles: $0°$, $18°$, $45°$ and $90°$ relative to the horizontal line. This angular-variation study corresponds to the ergonomic variable of forearm positioning while wearing the orthosis. The EMG signal was expressed as a percentage of MVC.

The importance of this ergonomic variable is that the desired design of the orthosis should require an MS that is quite low, often 10% in comparison with the user not wearing the orthosis. This investigation identified: (a) the percentage of the subject's MVC required to do a flexion or an extension for a given inclination angle of the forearm; and (b) the percentage of additional MVC introduced by using the orthosis.

4 Results

4.1 Orthosis Stability

Figure 3 depicts a typical result obtained from a subject executing successive flexions and extensions, with and without the orthosis support.

The mean and standard error for the conditions with and without support were respectively 11.0 ± 3.9 mm and -7.0 ± 17.7 mm. The absolute amplitude was of 7.7 mm for the condition with support against 33.4 mm for the condition without the support. The relative difference between the absolute amplitudes was of 76.86%, meaning that there was an improvement in the orthosis stability.

4.2 Muscular Strength

Figure 4 shows the %MVC for the different arm positions, with and without the orthosis. Figure 5 shows the Ergonomic Index (EI) associated with the flexion and extension
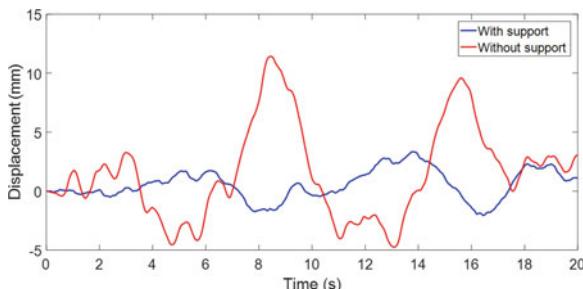
Fig. 3 Comparison of the displacement of the orthosis with and without the ergonomic support
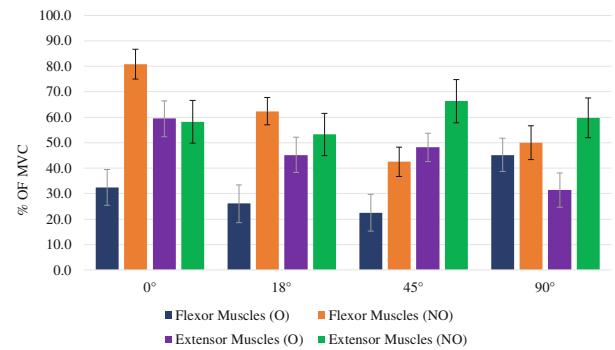
Fig. 4 Comparison of percentage MVC for flexor and extensor muscles. *Note* O and NO refers to Orthosis and No Orthosis. The overall mean and standard deviation are presented
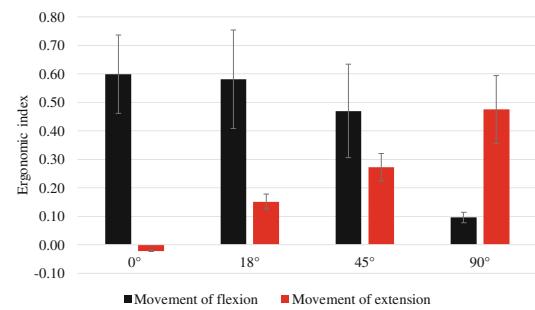
Fig. 5 Ergonomic Index from the flexion and extension movements at distinct angles. The overall mean and standard deviation are presented

movements for the different angles, where the EI is defined according to Eq. 1,

$$Ergonomic\, Index(EI) = 1 - \frac{\%MVC_{with\,orthosis}}{\%MVC_{without\,orthosis}} \quad (1)$$

where $\%MVC_{with\,orthosis}$ and $\%MVC_{without\,orthosis}$ is the percentage MVC with and without the orthosis respectively.

5 Discussion and Conclusion

In this study, it was presented an orthosis developed for rehabilitation of flexion and extension wrist activity following muscular stiffness resulting from PD. This communication has focused on the ergonomic assessment of the orthosis. An enhanced support structure has been designed and used with the orthosis and objectively shown to lead to a 76.86% stability improvement.

In Fig. 5 it is possible to verify an increase in the value of the EI for the extension movement as a function of the increase in the angle. This was expected because at 90° the weight of the orthosis contributed to the movement. The same reasoning is true for the movement of flexion, in which there was a reduction of the EI as function as the decrease of

the angle. This means that the EI, as it was defined, is not only capturing information about ergonomics but also on the way the muscles work. The results of this research have opened opportunities for further large-scale studies involving the use of the orthosis with healthy individuals and patients with PD.

Conflicts of Interest The authors declare no conflict of interest.

References

1. Andrade AO, Ferreira LCV, Rabelo AG, Vieira MF, Campos AR, Goncalves BF, Pereira AA, Gonçalves BF, Pereira AA (2017) Pelvic movement variability of healthy and unilateral hip joint involvement individuals. Biomed Signal Process Control 32:10–19. https://doi.org/10.1016/j.bspc.2016.10.008

2. Christofoletti G, Cândido ER, Olmedo L, Miziara SRB, Beinotti F (2012) Efeito de uma intervenção cognitivo-motora sobre os sintomas depressivos de pacientes com doença de Parkinson. J Bras Psiquiatr 61:78–83. https://doi.org/10.1590/s0047-20852012000200004

3. Dickson JM, Grünewald RA (2004) Somatic symptom progression in idiopathic Parkinson's disease. Parkinsonism Relat Disord 10:487–492. https://doi.org/10.1016/j.parkreldis.2004.05.005

4. Fasoli SE, Krebs HI, Stein J, Frontera WR, Hogan N (2003) Effects of robotic therapy on motor impairment and recovery in chronic stroke. Arch Phys Med Rehabil 84:477–482. https://doi.org/10.1053/apmr.2003.50110

5. Rossi B, Siciliano G, Carboncini MC, Manca ML, Massetani R, Viacava P, Al. E (1996) Muscle modifications in Parkinson's disease: Myoelectric manifestations. Electroencephalogr Clin Neurophysiol - Electromyogr Mot Control 101:211–218

6. Sangha S, Elnady AM, Member S, Menon C (2016) A Compact Robotic Orthosis for Wrist Assistance. 1080–1085

7. Stefano M, Patrizia P, Mario A, Ferlini G, Rizzello R, Rosati G (2014) Robotic Upper Limb Rehabilitation after Acute Stroke by NeReBot: Evaluation of Treatment Costs. Biomed Res Int 2014:1–5. https://doi.org/10.1155/2014/265634

Muscle Stiffness Estimation Using Center of Pressure Fluctuations Induced by Electrical Stimulation

Takanori Uchiyama and Ayana Sugiyama

Abstract

We proposed a novel technique to estimate muscle stiffness using center of pressure (COP) fluctuations induced by electrical stimulation. Six participants stood on a force plate and the COP displacement was measured with and without electrical stimulation applied to the gastrocnemius muscle. The displacement measured in the stimulated condition involved both intrinsic and electrically induced fluctuations. To obtain the intrinsic fluctuation, the measured displacement was smoothed using a Kalman filter constructed by approximating the displacement measured in the non-stimulated condition with an autoregressive model. The intrinsic fluctuation was subtracted from the measured displacement to obtain the electrically induced fluctuation. The fourth-order transfer function from the electrical stimulation to induced fluctuation was identified using a singular value decomposition method. The transfer function had natural frequencies of approximately 2 and 0.3 Hz. The former was close to the natural frequency of the gastrocnemius muscle, and the latter was close to the resonance frequency around the ankle joint. The proposed method can provide muscle and ankle joint stiffness in a standing posture.

Keywords

Center of pressure • Stiffness • System identification

1 Introduction

Human standing posture is often modeled as an unstable inverted pendulum stabilized by muscles around the ankle joint. Several standing posture control mechanisms have

T. Uchiyama (✉) · A. Sugiyama
Keio University, Yokohama, Kanagawa, Japan
e-mail: uchiyama@appi.keio.ac.jp
URL: http://www.bi.appi.keio.ac.jp

been proposed [1–3]. Winter et al. [2] proposed a mechanism based on muscle stiffness that was high enough to maintain standing posture by continuous muscle activation. Asai et al. [3] proposed a mechanism based on intermittent muscle activation. The muscle stiffness was not large enough to maintain the standing posture, however constant muscle stiffness was assumed. Muscle stiffness depends on the muscle activation level, therefore we suppose that the muscle stiffness varies to maintain the standing posture. The stiffness around the ankle joint while standing has been investigated by applying sudden movement to a plate on which a participant stands [4, 5]. However, the method could not estimate the muscle stiffness itself. We propose a novel method to estimate both the ankle and muscle stiffness in the standing posture by measuring the center of pressure (COP) fluctuations induced by electrical stimulation.

2 Methods

2.1 Measurements

Six male volunteers aged from 22 to 24 years participated in the experiments, and none of them had a history of neuromuscular disorders. This study was approved by our local ethics committee (No. 29-36, Faculty of Science and Technology, Keio University). All participants gave informed consent in accordance with the Declaration of Helsinki.

Each participant was instructed to stand on a force plate (SS-FP40A0-SY; Sports Sensing Co., LTD, Fukuoka, Japan) in Romberg's posture. The participant was instructed to look at a target at their eye height. The distance between the target and the participant was 2 m. Electrical stimulation was applied to the gastrocnemius muscles using an electrical stimulator (SEN-3301; Nihon Kohden, Tokyo, Japan) and isolator (S-104J; Nihon Kohden) through disposable Ag-AgCl surface electrodes (Vitrode F-150S; Nihon Kohden). The stimulation was a 700 μs wide monopolar rectangular pulse with an amplitude of 25–30 mA. The

stimulation was applied to the gastrocnemius muscles every 10 s. The COP was measured with the force plate and sampled with a 16-bit analog-to-digital converter (cRIO-9215, National Instruments, Austin, TX, USA) at 2,000 Hz, then stored on a computer. The measurement time was 120 s. The measurement was repeated five times. Measurements without electrical stimulation were also carried out.

2.2 Analysis

The displacement of the COP, d_s, involves both electrically induced and intrinsic fluctuations. We used a Kalman filter to eliminate the intrinsic fluctuation from d_s. The outline of the proposed method is shown in Fig. 1.

First, the COP measured without electrical stimulation was modeled with an autoregressive (AR) model. The AR coefficients were calculated using the least square method, and the order of the model was determined using Akaike's Information Criterion (AIC). The AR model was described as a state equation and an output equation. The AR model was used to construct a Kalman filter that was used as a fixed-interval smoother on the measured d_s. The smoothed d_s corresponds to the intrinsic fluctuation. Therefore, the smoothed d_s was subtracted from the measured d_s to extract the electrically induced fluctuation d_e. The d_e from the five measurements were then synchronously averaged and referenced to the input electrical stimulation for system identification.

The electrical stimulation was an input to the system and d_e was an output of the system. The d_e could be regarded as an impulse response. Therefore, the system was identified to obtain the transfer function from the electrical stimulation to d_e using a singular value decomposition method. The transfer function was factorized to the products of the second-order mass-spring-damper model. A mass-spring-damper model has one natural frequency whose square is proportional to k/m where m is the mass and k is the spring constant (i.e., stiffness) of the model. Therefore, the natural frequency of the transfer function was used as an index of the stiffness.

3 Results

3.1 Extraction of Electrically Induced Fluctuation

A typical example of the displacement of the COP is shown in Fig. 2, where the origin is the average COP position. The y-axis corresponds to the front-back direction and a positive value indicates that the COP moves forward from the origin. The COP displacement in the front-back direction represented in Fig. 3 showed a slow increase and decrease with a relatively high frequency oscillation.

The signal shown in Fig. 3 was approximated with a sixth to tenth order AR model, depending on the participants. The measured d_s (gray line) and smoothed d_s (black line) are shown in Fig. 4a. The smoothed d_s was subtracted from d_s to
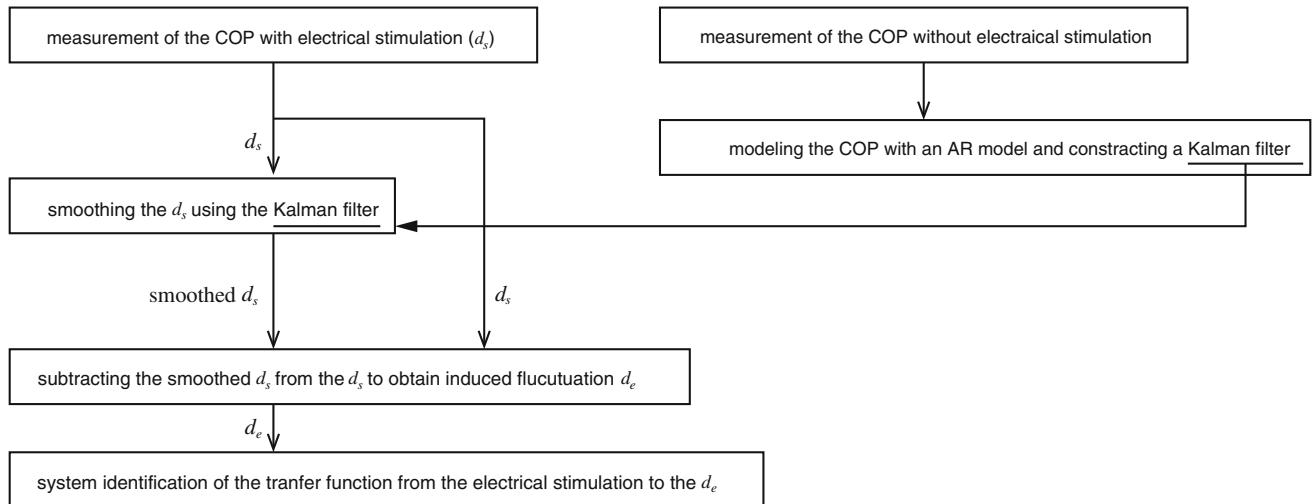
Fig. 1 Outline of the proposed method for eliminating the intrinsic COP fluctuation
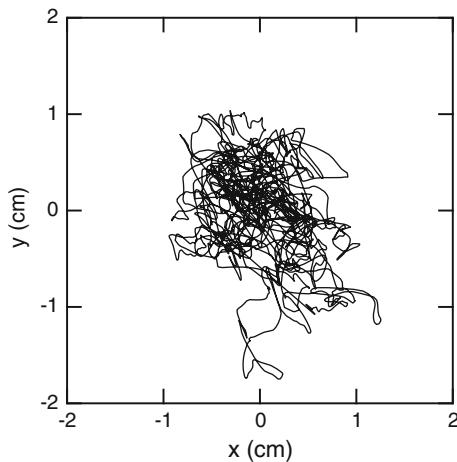
Fig. 2 Typical example of the COP displacement. The *y*-axis indicates the front-back direction
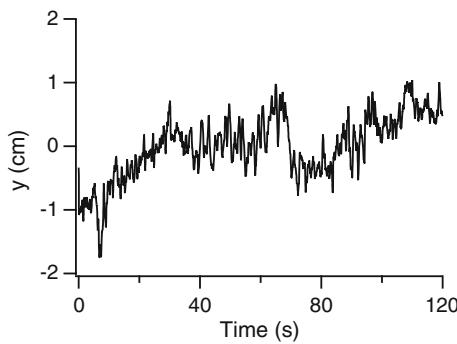
Fig. 3 Time course of the COP displacement in the front-back direction shown in Fig. 2


Fig. 4 Extraction of the electrically induced COP fluctuation. **a** Measured COP fluctuation with electrical stimulation and the smoothed signal. The gray line denotes the measured fluctuation, and the black line denotes the fluctuation smoothed with the Kalman filter. **b** Extracted electrically induced fluctuation, d_e
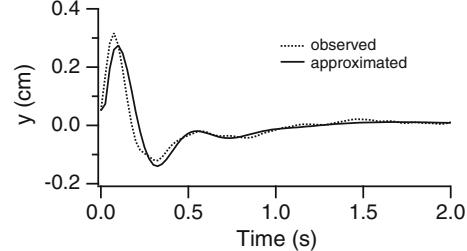

Fig. 5 Synchronously averaged induced fluctuation and its approximation. The dotted and solid lines denote the observed and approximated fluctuation, respectively

extract d_e, which is shown in Fig. 4b. The electrically induced fluctuation was extracted, although some high frequency noise remained. The extracted signal was synchronously averaged with reference to the electrical stimulation to eliminate the noise.

3.2 System Identification and Natural Frequency

The synchronously averaged signal is shown in Fig. 5. The COP moved forward around 0.3 cm in 0.1 s and then moved backward to −0.1 cm at 0.3 s. The fluctuation showed weak second positive and negative peaks and then went back to 0 cm around 1 s. The signal was well-approximated with a fourth-order model, as shown in Fig. 5. The fourth-order model has two natural frequencies, shown in Table 1. The average high natural frequency f_1 was around 2 Hz and the average low natural frequency f_2 was around 0.3 Hz. The high natural frequency was close to the resonance frequency of the gastrocnemius muscle [6]. The

low natural frequency was close to the frequency (0.7 Hz) at which the gain characteristics of the standing posture system were highest [4].

4 Discussion

The proposed method was able to extract the electrically induced fluctuation, as shown in Fig. 4b. The amplitude variation over time may have been caused by the muscle activation level and muscle length. When the muscle activation level is high, the muscle becomes stiff. Many of muscle fibers have already been activated and the number of muscle fibers activated with the electrical stimulation decreases. This results in the decreased amplitude of the

Table 1 Natural frequencies of the identified transfer function

Participant	f_1 (Hz)	f_2 (Hz)
A	1.85	0.298
B	1.82	0.296
C	1.71	0.307
D	1.91	0.589
E	1.56	0.414
F	1.79	0.386

induced fluctuation. When the muscle activation level is low, the muscle becomes soft and many inactivated muscle fibers remain. As a result, the amplitude of the induced fluctuation increased. This study used stimulation every 10 s and a synchronous averaging technique on the induced fluctuation. Therefore the estimated natural frequency corresponded to the average muscle mechanical characteristics. Further study is necessary to apply the electrical stimulation at an appropriate time interval based on the muscle activation level and the COP displacement.

The stiffness of the gastrocnemius muscle can be roughly estimated from the high natural frequency of a mass-spring-damper model of the gastrocnemius muscle. The stiffness was around 30 N/m. The stiffness around the ankle joint can also be roughly estimated when we assume that the low natural frequency is that of the inverted pendulum whose rotational center is the ankle joint. The stiffness was around 800 Nm/rad, which is similar to the value reported by Casadio et al. [5]. The proposed method provided muscle and ankle stiffness in a standing posture.

5 Conclusion

A novel muscle and ankle joint stiffness estimation method was proposed. In this method, the COP was measured with and without electrical stimulation. The electrically induced COP fluctuation was extracted, and the transfer function from the stimulation to the induced fluctuation was identified. The transfer function provided two natural frequencies that were proportional to square roots of the muscle stiffness and ankle joint stiffness.

References

1. Collins, J.J., De Luca, C.J.: Open-loop and close-loop control of posture. Exp. Brain Res. 95, 308–318 (1993).
2. Winter D.A., Patla A.E., Prince, F., Ishac, M., Gielo-Perczak K.: Stiffness control of balance in quiet standing. J. Neuro. Physiol. 83, 1211–1221 (1998).
3. Asai, Y., Tasaka, Y., Nomura, K., Nomura, T., Casadio, M., Morasso, P.: Model of postural control in quiet standing: Robust compensation of delay-induced instability using intermittent activation of feedback control. PLoS ONE 4, e6169 (2009).
4. Ishida, A., Imai, S., Fukuoka, Y.: Analysis of the posture control system under fixed and sway-referenced support condition. IEEE Trans. Biomed. Eng. 44, 331–336 (1997).
5. Casadio M., Morasso P.G., Sanguineti, V.: Direct measurement of ankle stiffness during quiet standing: implications for control modeling and clinical application. Gait & Posture 21, 410–424 (2005).
6. Takesita, D., Shibayama, A., Muraoka, T,. Muramatsu, T., Nagano., Fukunaga, T., Fukashiro, S.: Resonance in the human medial gastrocnemius muscle during cycle ankle bending exercise. J. Appl. Physiol. 101, 111–118 (2006).

Gait Ratios and Variability Indices to Quantify the Effect of Using Smartphones in Dual-Task Walking

Carlotta Caramia, Ivan Bernabucci, Carmen D'Anna,
Cristiano De Marchis, and Maurizio Schmid

Abstract

Smartphone use is one of the most common activities performed while walking: recent studies showed how this behaviour affected spatio-temporal, smoothness, symmetry and regularity gait parameters. In this study, we investigated a subset of additional gait parameters, potentially indicative of gait instability, to check whether concurrent smartphone activities cause deviations from stable walking. Ten young healthy adults were asked to walk outdoor normally and while performing five smartphone-based dual-task activities, with different levels of cognitive effort. Three groups of gait parameters, extracted by a single waist-mounted tri-axial inertial sensor, were analyzed: Gait Ratios group included Stride-to-Stance Time Ratio (SSTR)—equal to the golden ratio $\varphi \approx 1.618$ in normal walking—and Walk Ratio (WR)—the ratio between Step Length (SL) and cadence, roughly constant within healthy subjects—Variability Measures group included Coefficients of Variation (CV) of SL and step time; Acceleration Ratios group composed of Root Mean Squared acceleration Ratios (RMSR)—the ratio between rms along a single direction and the total rms acceleration. When a dual-task is present, SSTR did not show significant variations from Baseline. A continuous typing activity with low cognitive engagement caused a significant decrease of WR with respect to all the other tasks. RMSR in the mediolateral direction and the CV SL showed visible yet not significant proportion with the amount of experienced cognitive effort. The resulting alterations were in general inconclusive as to their possible link with a reduced ability to adapt the locomotion structure to the context changes, even if for some parameters the observed proportion with cognitive effort and visual domain may need to be deepened on a bigger sample size, possibly including more challenging dual-task demands.

1 Introduction

Different kinds of quantitative gait descriptors have been shown to provide deep insight onto the locomotor control strategies both in healthy users and in individuals with motor-related pathologies. The traditional analysis of spatio-temporal gait parameters, such as speed, cadence, and step length, is able to provide detailed indications regarding the walking performance. Other categories of indicators have been introduced among the gait analysis metrics, such as symmetry, harmonicity, smoothness and variability measures, and they have been shown to be accurate predictors of altered gait patterns, able to integrate the information provided by traditional spatial and temporal gait parameters [1, 2]. Within this multiplicity of measures related to walking behaviour, gait analysis literature has sought to derive synthetic descriptors of gait performance starting from combinations of the aforementioned metrics. Among these, some studies have analysed the so-called Walk Ratio (WR); Sekiya et al. [3] first introduced this parameter, defined as the ratio between Step Length (SL) and step cadence, showing its low variability within and among subjects across a wide range of walking speeds in healthy individuals [4]. Other studies have used this ratio to quantify gait performance in pathologies, highlighting how WR is reduced, reflecting higher energy expenditure, reduced stability and altered attentional demands [5]. Other synthetic gait descriptors have been introduced by Iosa et al. [6], defined by the ratios between specific gait phase timings (e.g. the

C. Caramia (✉) · I. Bernabucci · C. D'Anna · C. De Marchis ·
M. Schmid
Department of Engineering, Roma Tre University, 00146 Rome,
Italy
e-mail: carlotta.caramia@uniroma3.it

ratio between stride time and stance time: Stride-to-Stance Time Ratio, SSTR) are roughly constant across subjects and speeds in healthy subjects, and equal the golden ratio φ. More recent studies have analyzed the behaviour of such gait ratios in different populations, showing that variation with respect to φ are correlated to alterations in walking stability and energy expenditure as well [7, 8]. In an effort to bring gait analysis out of the lab, using data gathered from wearable inertial sensors, other parameters extracted from the acceleration signals have been shown to be related to walking stability, such as the root mean square acceleration components along the different directions. Sekine et al. [9] have reported common proportions among the root mean square acceleration values along three orthogonal sensing axes. By using a normalized version of the rms along each of the three axes and the total rms magnitude (Root Mean Square Ratio, RMSR), it was found that these common proportions were significantly altered along the mediolateral direction in neurological patients, thus reflecting gait abnormalities and disease severity [9, 10]. In this scenario, it emerges that the previously mentioned metrics can be used as general descriptors of human gait stability, risk of fall and energy consumption in different populations, in a unified framework of locomotion optimization strategies. Among the challenging walking situations, dual-task walking has been extensively studied in literature, and there is a large consensus that the alternative allocation of attentional resources during dual-task execution reduces walking stability and gait performance in general [11]. Among the most executed dual-task activities, nowadays walking while using a smartphone is one of the most common amongst young individuals, and it encompasses a series of risks and gait alterations [12, 13]. A recent study of ours has shown that a number of spatio-temporal, harmonicity and smoothness parameters are significantly altered during dual-task walking with a smartphone, with these alterations directly related to the amount of cognitive load [14]. Since these alterations are potentially indicative of reduced stability, we seek to describe these alterations using a set of indicators derived from a single waist mounted inertial sensor, by using the previously mentioned synthetic descriptors of gait behaviour. In particular, the aim of the present study is to check if SSTR, WR, RMSR and variability measures may be potential indicators of gait alterations during dual-task walking with a smartphone under different levels of cognitive engagement. All these parameters are measured in a real life outdoor setting by using a single waist mounted three-axial inertial sensor.

2 Materials and Methods

2.1 Participants and Procedure

Ten healthy young adults (4 women, age range 21–23) with no motor disorders provided written consent to participate to the experiment. They were chosen based on their dexterity in the use of smartphone (they used smartphone at least 2 h per day during the last 3 years). The experiment, performed in an external environment along a 200 m-long pedestrian straight path, consisted in a walking trial with several dual-task demands performed using their own smartphone—the most common activities were chosen, according to literature [15]—and each activity lasted 40 s. Participants were just informed on the path to follow and to walk holding the smartphone in the hand: during the test, the experimenter sent the instruction through an instant messaging app. The dual-task demands—exactly the same for all participants—are the following, sorted by increasing cognitive effort [16]:

- talking on the smartphone about daily activities—Talk;
- answering the experimenter to general knowledge questions through an instant messaging app—LCLtext;
- surfing on a page of a social network—Surf;
- playing a math game on the smartphone—Math;
- reversing a word sent from the experimenter and sending it back through an instant messaging app—HCLtext.

Moreover, a normal walking bout of 40 s was interspersed between each task; among these, the first one was used as the reference sequence task—Baseline—with whom comparing the dual-task activities.

2.2 Instrumentation and Data Recording

Gait data were acquired using an inertial sensor (Shimmer3, Shimmer sensing, Dublin, Ireland) located on the back of the lower trunk of each participant [17]. The linear accelerations along the three axes (anteroposterior, AP; vertical, VT; mediolateral, ML) were acquired at a sampling frequency of 102.4 samples/s, in the range ±2 g. During the experiments,

manual annotations were taken to differentiate the individual activities, and they were subsequently used to segment the different tasks within the recording.

2.3 Data Processing

To avoid the analysis of transitions between consecutive activities, the first and last 10 s of each task sequence were excluded and, thus, only the central 20 s were considered for the analysis. Measures relating to gait behaviour were extracted, gathering them in the following groups:

- Gait Ratios (GR), which included the SSTR and the WR parameters. SSTR, the ratio between stride time and stance time that is equal to φ—an irrational number of the value of about 1.6180—in a healthy walking pattern [6], represents the intrinsic harmonic and symmetric properties of gait. The estimation of this parameter required the extraction of all the initial contacts (IC) and final contacts (FC) of the foot during the trials: in this respect, the method proposed in [18] was used: it involved the smoothing of the vertical lumbar acceleration by integrating and then differentiating through Gaussian continuous wavelet transforms. Thus, minima from this signal corresponded to the IC events, while a further differentiation of this signal provided the FC events, identified as the maxima. We obtained a value of φ for each stride of each subject's trial. WR, the ratio between SL (m) and cadence (steps per min) [3], represents the relationship between the amplitude and frequency of the rhythmic legs movements when walking. It was estimated for each step of each subject's trial. SL was obtained following the method proposed by Zijlstra and Hof [19]—the inverted pendulum model—with the modification introduced by Gonzales et al. [20].
- Variability Measures (VR), which included Coefficients of Variation (CV) of SL and step time—the ratio of

standard deviation of the parameter over its mean value along the task (CV = 100 * SD/mean).

- Acceleration Ratios (AR), which included the RMSR along the three axes. The RMSR values are given by the ratio of the rms of acceleration signals in each direction and the rms vector magnitude, and they referred gait abnormality measures.

2.4 Statistical Analysis

Descriptive statistics was calculated for each parameter under each task condition. Normality of data distribution was tested through the Lilliefors test, and a repeated measures univariate ANOVA was performed to evaluate the overall effect of all the tasks on each parameter that passed the normality test described above. Post hoc analysis was then done to verify possible statistical differences between single pairs of tasks. The level of significance was set at 0.05.

3 Results

The effects of smartphone-based dual-task walking on gait parameters are reported separately for each group. All parameters passed the Lilliefors test for normality.

3.1 Gait Ratios

For this group (Fig. 1), SSTR did not result significantly affected by the task condition: in the Baseline condition, φ resulted equal to 1.582, and did not show a statistically difference from other dual-task conditions (see Fig. 1, left panel). Also, WR was influenced by the performed tasks (F = 4.34, p = 6E−4): WR during LCLtext was significantly
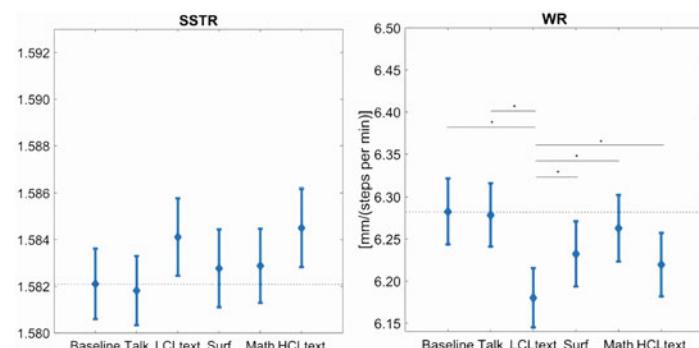
Fig. 1 SSTR (left panel) and WR (right panel) across different task conditions. Significant differences are represented between task pairs. Group mean values are drawn with error bars corresponding to standard errors
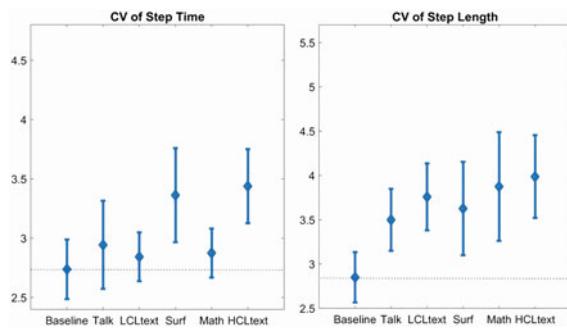
Fig. 2 Step time and step length variability across conditions, as measured by the coefficient of variation

lower as compared both to Baseline and to all the other dual-task activities (Fig. 1, right panel).

3.2 Variability Measures

In this group (Fig. 2, left panel), step time CV resulted independent from the amount of cognitive effort. For the CV SL, a lower mean value at Baseline than at all the other tasks resulted, even if the statistical analysis showed a value just above the significance threshold (F = 2.4, p = 0.052). A clear, though modest, CV SL increase appeared as a function of increasing cognitive engagement (Fig. 2, right panel).

3.3 Acceleration Ratios

Regarding the Acceleration Ratios (Table 1), no significant differences were found for RMSR along any of the axes. For the ML direction, an increasing trend with the amount of cognitive effort was visible, but this was not supported by the statistical analysis.

4 Discussion and Conclusion

Stride-to-Stance Time Ratio did not depart significantly from normal walking when an additional concurrent cognitive task is present. Thus, the ratio between stride and stance

time, which was demonstrated to be equal to φ in healthy subjects (as well as the ratio between stance and swing phases and the ratio between swing and double support phases), remained almost constant even if the amount of cognitive effort was increased. This result might be a consequence of optimization and stability of human walking; in order to successfully accomplish the task, subjects alter most traditional spatio-temporal gait parameters (step length, step time, stride frequency and gait speed), as reported in [14], but they preserve at the same time the temporal ratio among gait sub-phases. As shown in [14], the stride frequency decreases with the increase of the cognitive effort: what happened with all dual-task conditions was that the stride time increased with a correspondent increase of the stance time, leading to roughly stable values of SSTR. A deviation from φ would correspond to an incomplete adaptation of the locomotion structure to the context changes, contributing to an unstable walking, thus leading to sub-optimal energy expenditure. This aspect has been investigated in previous studies, hypothesizing that preservation of gait ratio constitutes a gait stabilization mechanism able to minimize energy expenditure [7, 8]. Regarding the measured values of SSTR, we obtained an average value across different conditions in the baseline condition of 1.582, thus slightly different from the analytical formulation of φ: this may be associated with the used instrumentation, as, to our knowledge, no other studies have up to now estimated gait ratios through acceleration data extracted from one inertial sensor located in the lumbar zone.

Regarding the walk ratio, contrary to what one could expect, this parameter resulted mainly affected only during the LCLtext activity and not during other activities with higher cognitive load. This might be explained considering the position and the attitude required when LCL texting: in this task, the subjects kept their smartphone head-on, constantly focussing on the screen and typing continuously. HCLtext, conversely, required a more interspersed typing, due to the time needed to elaborate on the proper answer. While reporting data on patients with multiple sclerosis, Kalron [21] found a significant positive relationship with the cognitive domains of visuo-spatial, verbal function and information processing; thus, we could associate this higher

Table 1 RMSR values across conditions (group means ± standard errors)

Activity	AP (μ ± s.e)	VT (μ ± s.e)	ML (μ ± s.e)
Baseline	0.527 ± 0.024	0.694 ± 0.015	0.476 ± 0.026
Talk	0.522 ± 0.022	0.687 ± 0.018	0.490 ± 0.030
LCLtext	0.529 ± 0.023	0.689 ± 0.015	0.483 ± 0.025
Surf	0.530 ± 0.021	0.677 ± 0.012	0.498 ± 0.028
Math	0.523 ± 0.020	0.682 ± 0.016	0.497 ± 0.032
HCLtext	0.527 ± 0.018	0.672 ± 0.018	0.508 ± 0.029

variation of walk ratio when continuously typing such as in LCLtext to the higher requests in the visuo-spatial domain. Also, other dual-task activities varied, but with no significant differences from Baseline. Interestingly, the trend found in SSTR is similar to the one shown by walk ratio; event if not significant, the main alterations in SSTR have been found in LCLtext and HCLtext, which may indeed constitute the more challenging tasks for gait stability. The walk ratio represents the coordinated pattern of spatial and temporal characteristics in a rhythmic movement, where the energy cost is optimized, and its value is approximately constant across a wide range of speeds [22]. Its decrease is thought of as a non-specific adaptive mechanism facilitating the neuro-mechanical control of walking, affecting the quality of gait control, at the expenses of an increase in the metabolic cost [5]. Kalron [21] found lower values of walk ratio in fallers compared to non-fallers, associating that to the attempt of adopting a cautious gait for the fear of falling and calling for a study to analyse whether changes in walk ratio occur during different cognitive-walking dual tests. With the present study we were able to show that some changes occurred, but these may be more probably associated with the emergence of a more cautious approach only when continuous typing is present and visuo-spatial affordances are at risk. Regarding the measures of acceleration ratios, it was shown that the mediolateral direction is primarily associated with walking balance [9]. The variations of gait ratio measures when an additional concurrent task is present during walking, could make us believe that a change in the RMSR along the mediolateral direction is the result of a less stable condition. Indeed, our data showed a possible increase of this latter quantity compared to the baseline condition when dual-tasks are present, even though these deviations were not statistically different. In the same way, we did not find significant differences among tasks in the coefficients of variation of step time and step length, even if in the latter one we observed a trend increase towards the significance threshold limits. It would be interesting to determine if the absence of significance is solely related to the rather small sample size, or if it is the result of a cognitive effort that may be not sufficiently challenging for the chosen population sample: increasing the population sample size, and studying the elderly—who may be less familiar with smartphone use, and thus experience an increased cognitive effort in the same conditions—may shed light on this specific aspect.

Conflict of Interest The authors declare that they have no conflict of interest.

References

1. Urbanek, J.K., Zipunnikov, V., Harris, T., et al.: Validation of gait characteristics extracted from raw accelerometry during walking against measures of physical function, mobility, fatigability, and fitness. The Journals of Gerontology, https://doi.org/10.1093/gerona/glx174 (2016).
2. Hausdorff, H.M.: Gait variability: methods, modeling and meaning. Journal of neuroengineering and rehabilitation 2(1), 19 (2005).
3. Sekiya, N., Nagasaki, H., Ito, H., et al.: The invariant relationship between step length and step rate during free walking. Journal of Human Movement Studies 30(6), 241–257 (1996).
4. Sekiya, N., Nagasaki, H.: Reproducibility of the walking patterns of normal young adults: test-retest reliability of the walk ratio (step-length/step-rate). Gait & posture 7(3), 225–227 (1998).
5. Rota, V., Perucca, L., Simone, A., et al.: Walk ratio (step length/cadence) as a summary index of neuromotor control of gait: application to multiple sclerosis. International Journal of Rehabilitation Research 34(3), 265–269 (2011).
6. Iosa, M., Fusco, A., Marchetti, F., et al.: The Golden Ratio of Gait Harmony: Repetitive Proportions of Repetitive Gait Phases. BioMed Research International 2013 (2013).
7. Iosa, M., Bini, F., Marinozzi, F., et al.: Stability and Harmony of Gait in Patients with Subacute Stroke. Journal of medical and biological engineering 36(5), 635–643 (2016).
8. Serrao, M., Chini, G., Iosa, M., et al.: Harmony as a convergence attractor that minimizes the energy expenditure and variability in physiological gait and the loss of harmony in cerebellar ataxia. Clinical Biomechanics 48, 15–23 (2017).
9. Sekine, M., Tamura, T., Yoshida, Y., et al.: A gait abnormality measure based on root mean square of trunk acceleration. Journal of neuroengineering and rehabilitation 10(1), 118 (2013).
10. Matsushima, A., Yoshida, K., Genno, H., et al.: Clinical assessment of standing and gait in ataxic patients using a triaxial accelerometer. Cerebellum & ataxias 2(1), 9 (2015).
11. Patel, P., Lamar, M., Bhatt, T.: Effect of type of cognitive task and walking speed on cognitive-motor interference during dual-task walking. Neuroscience 260, 140–148 (2014).
12. Lamberg, E.M., Muratori, L.M.: Cell phones change the way we walk. Gait & posture 35(4), 688–690 (2012).
13. Schabrun, S.M., van de Hoorn, W., Moorcraft, A., et al.: Texting and Walking: Strategies for Postural Control and Implications for Safety. PLoS One https://doi.org/10.1371/journal.pone.0084312 (2014).
14. Caramia, C., Bernabucci, I., D'Anna, C., et al.: Gait parameters are differently affected by concurrent smartphone-based activities with scaled levels of cognitive effort. PLoS One https://doi.org/10.1371/journal.pone.0185825 (2017).
15. Berolo, S., Steenstra, I., Amick, B.C. III, et al.: A comparison of two methods to assess the usage of mobile hand-held communication devices. Journal of Occupational and Environmental Hygiene 12(3), 276–285 (2015).
16. Haga, S., Sano, A., Sekine, Y., et al.: Effect of using a smart phone on pedestrians' attention and walking. Procedia Manufacturing 3, 2574–2580 (2015).
17. Caramia, C., Bernabucci, I., Conforto, S., et al.: Spatio-temporal gait parameters as estimated from wearable sensors placed at different waist level. In: Biomedical Engineering and Sciences

(IECBES), 2016 IEEE EMBS Conference on, pp. 727–730, Malaysia (2016).

18. McCamley, J., Donati, M., Grimpampi, E., et al.: An enhanced estimate of initial contact and final contact instants of time using lower trunk inertial sensor data. Gait & posture 36, 316–318 (2012).

19. Zijlstra, W., Hof, A.L.: Assessment of spatio-temporal gait parameters from trunk accelerations during human walking. Gait & posture 18(2), 1–10 (2003).

20. Gonzales, R.C., Alvarez, D., Lopez, A.M.: Modified Pendulum Model for mean Step Length Estimation. In: 29th Annual International Conference of the IEEE, EMBS 2007, pp. 1371–1374, Lyon, France (2007).

21. Kalron, A: Construct validity of the walk ratio as a measure control of gait control in people with multiple sclerosis without mobility aids. Gait & posture 47, 103–107 (2016).

22. Nagasaki, H., Itoh, K., Hashizume, K., et al.: Walking patterns and finger rhythm of older adults. Perceptual and motor skills 82(2), 435–447 (1996).

Split-Belt Treadmill to Study Reactive Responses to Unexpected Gait Perturbation

Slavka Viteckova, Patrik Kutilek, Veronika Kotolova, Radim Krupicka,
Zoltan Szabo, Jan Kauler, and Jan Hybl

Abstract

The aim is to presents a solution and realization of the design of new split-belt treadmill for controlled, unexpected perturbation during walking to study recovery responses and dynamic stability of the human gait. The construction of the split-belt treadmill consists of several subsystems. The most important subsystems are: actuator, control and sensory subsystem. Actuator subsystem is based on two asynchronous motors, two inverters and two gears (for each belt separately). Control subsystem is made up of Modbus communications between the control computer and two inverters with respect to the parameters of the asynchronous motors. The sensory subsystem is based on the incremental angular speed sensor used to record the behavior of the treadmill belts. The control itself is created through the MatLab software and special custom-made user interface that allows to define a wide range of perturbation schemes. It was then verified whether the belts had the desired speed. Verification of the system has shown that at the recommended speeds of running the belts (at 2.4 km/h), the system is stable, shows no variations in proband load, and real changes in belt velocities are achieved with minimum deviations from the desired values. The main benefit of the described

work is the creation of a functional control of the prototype of the treadmill for controlled, mechanical gait perturbations. The split-belt treadmill is designed to study reactive responses during walking that can be further used to fall-risk assessment, clinical or rehabilitation intervention.

1 Introduction

Split-belt treadmills are used to study dynamic stability of the human gait. There are only few commercial systems, which have introduced in recent years and can be used in clinical practice [1–3]. These systems are for example M-gait (Motekforce Link BV, Amsterdam, Netherlands) and Split-Belt (Woodway Inc., Waukesha, USA). These dual belt systems provide variable speed control of each leg independently. Split-belt treadmills can be used to gait rehabilitation [4, 5].

However, these systems have two basic disadvantages. The first disadvantage is the limited possibility or impossibility of adjusting the sequences allowing for a complex change in belt speeds under each limb. This is related to the impossibility of measuring complex gait perturbation [6, 7]. The second disadvantage is that the treadmills provide only approximate information on the speed of the belts for further motion analysis, which is determined by the behavior of the actuators of the belts, but it is not a real speed that would be measured by the sensor system. In this way, inaccuracies can occur in the detected belt velocity values, for example in the case of severe deformation or slippage of the belts. The aim of this article is to describe new split-belt treadmill. We developed split-belt treadmill that allows for complex changes in speeds of belt movements and direct measurement of belt speeds. These

S. Viteckova · P. Kutilek · V. Kotolova (✉)
R. Krupicka · Z. Szabo · J. Kauler · J. Hybl
Faculty of Biomedical Engineering, Czech Technical
University in Prague, Sitna sq., 3105 Kladno, Czech Republic
e-mail: kotolver@fbmi.cvut.cz

S. Viteckova
e-mail: slavka.viteckova@fbmi.cvut.cz

P. Kutilek
e-mail: kutilek@fbmi.cvut.cz

R. Krupicka
e-mail: krupicka@fbmi.cvut.cz

Z. Szabo
e-mail: szabo@fbmi.cvut.cz

J. Hybl
e-mail: jan.hybl@fbmi.cvut.cz

options are completely new, allow to induce controlled gait perturbations and will allow us to study complex reactive responses to these perturbations.

2 Structure Design and Methods

Based on the above mentioned drawbacks, subsystem and method of control and direct measurement of the speeds of belt movements are designed. Method provides left and right belt speed control separately, allowing realization of complex split belt walking protocol and direct measurement of belt speeds.

2.1 Conceptual Design of the System's Structure

The new treadmill consists, as usual belts, of the following basic subsystems: actuator subsystem, control subsystem, rollers, belts and passive structure. From a common treadmill, new split-belt treadmill differs in the duplication of actuator subsystem, control subsystem, rollers and belts. The difference from all current treadmills is that it has a new sensory subsystem, i.e. measuring subsystem, and modified and control subsystem with new possibilities and functions.

2.2 Actuator and Control Subsystem

The prototype of the treadmill consists of two separate belts powered by by two asynchronous motors Transtecno 803-4 type (Transtecno srl, Anzola Emilia, Italy) and two gearboxes Tramec XC B14 (Tramec LLC, Iola, USA). The motors are used to drive rollers with two belts. The belts have a total length of 3.3 m and are wide 0.25 m. The inclination of both belts can be adjusted up to 30° with the actuator subsystem still on the ground, see Fig. 1. The maximum speed of the belts is 2.4 km/h.

The Matlab (MathWorks Inc., Natick, USA) was used to create a graphical user interface to control the actuators and

data processing. User can define a sequence of changes in the belt movements by setting the relative time when the change in belt movement begins, final speeds, the duration of the speed changes (defines the acceleration or deceleration of the belt) and selects this setting for the right, left, or both belts. The created sequences can be saved and subsequently reused. When specifying a sequence, its predicted progression is displayed graphically, showing the changes in speeds and acceleration ramps. Data from the sequence of changes is transferred to the protocol for converters. Then, the user opens the COM port for serial communication and starts sending the data to the motors that control the individual belts, i.e. active rollers move with the belts and are powered by the motors.

2.3 Measurement Subsystem

In real time, information about the current belt speed is provided via the inverter and sensory subsystem back to the computer. The entire course of the current motion of the belts is plotted in real-time into the diagram. The sensory subsystem is based on the two incremental angular speed sensors used to record the real behavior of the treadmill belts. The sensors are applied on passive rollers which are on the opposite side of the treadmill than the active rollers, see Fig. 2.

2.4 Methods of Data Processing

Custom made software for treadmill control (Matlab-based) allows us to study the treadmill data. Data from sensory subsystem and control subsystem are graphically presented. The output from control software shows real-time velocity graphs of right belt (green line) and left belt (red line) with required changes and predicted values, see Fig. 3. Perturbation schemes (representing individual sequence lines) can be compared with real behavior of both belts, i.e. we can compare the relative time from sequence start, speed, time to change speed (representing acceleration) of left and right
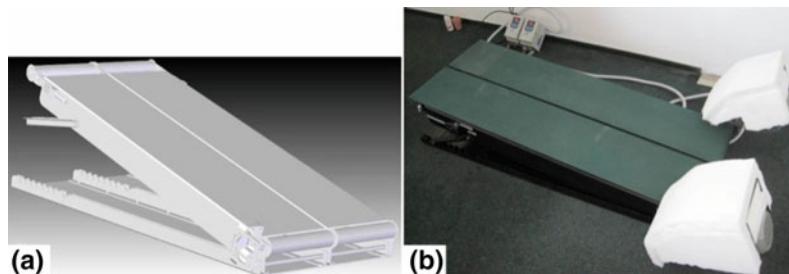
Fig. 1 3-D model of the split-belt treadmill (**a**) and split-belt treadmill with two asynchronous motors after realization (**b**)

Fig. 2 Detail of the sensory subsystem based on the incremental angular speed sensors used to record the behavior of the belts

belt. For the purposes of processing and comparing the values of the speeds required and executed, the values are stored in the Matlab workspace under the variables which contain the specified values for the left belt velocity and right belt velocity. The plot of the expected course of the changes in the speeds of individual belts is different in color. The actual speed of the belts should correlate with the assumed course, however slight variations are allowed, especially when changing speeds on so-called ramps.

2.5　Test Procedure

Experimental verification of the new split-belt treadmill was performed by comparing predefined speeds real speeds to determine system response and quality of control. It was checked whether the belts had the desired speed. The planned sequence of the perturbation scheme was predefined and displayed in the graph, see Fig. 3, and when the split-belt treadmill run the graph is continuously updated with the current/real values of speeds.

Verification was performed on a total of three sequences of perturbation schemes with a weight load (i.e. weight of the person) of 80 kg. The data comparison was focused on the time delay in the control of the speed change, the difference between the required and realized speeds after

Fig. 3 Graphical output from control software; real-time velocity graphs of right belt (green line) and left belt (red line) with required change and predicted values (Color figure online)

change realization, and the difference in the times (desired and achieved) of the duration of speed change. These differences were investigated at each change in the perturbation scheme.

3　Results

The results of verification for individual belts are summarized in Table 1. Due to the technical equipment of the split-belt treadmill, the start and end phases of the acceleration are not linear but have a sigmoidal course, see Fig. 4. When changing speeds with positive acceleration values, the ramp approaches the linear curve more than with speed change with negative acceleration values.

4　Discussion

The differences in required and real time and speed can be negligible in relation to the purpose of using the split-belt treadmill to be used to induce perturbations while walking.

An important part of the verification was confirmation of an optimal speed for treadmill running at 2.4 km/h. At higher speeds, the system became unstable—it did not maintain the required speeds and the belt slipped. For these reasons, the maximum speed of the belts should not exceed 2.4 km/h. From the validation results, we can assume that the split-belt treadmill requirements have been met and split-belt treadmill is a stable system. However, the maximum speed of 2.4 km/h is sufficient to simulate comfortable walks on the belts. The weakest part of the whole split-belt treadmill can be its maximum speed of the belt run of 2.4 km/h, which is given by the performance characteristics of the motors used for the split-belt treadmill.

However, the aim of the paper was to present the prototype and methodology of measurement and system structure, stability shortcomings can be eliminated in the future by choosing better but more expensive motors.

5　Conclusion

In this work was described new split-belt treadmill with new subsystems and methods of control, which ensure completely independent control of belts speeds. The control itself is through the Matlab user interface that allows us to define a wide range of perturbation schemes with the possibility of storing them and provides a summary report of the perturbation sequence being performed. The main benefit of the work is the creation of a functional control of the prototype of the split-belt treadmill that can be used in research or rehabilitation practice.
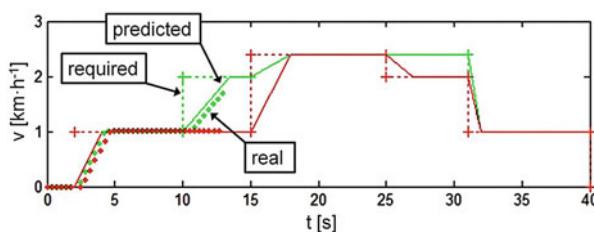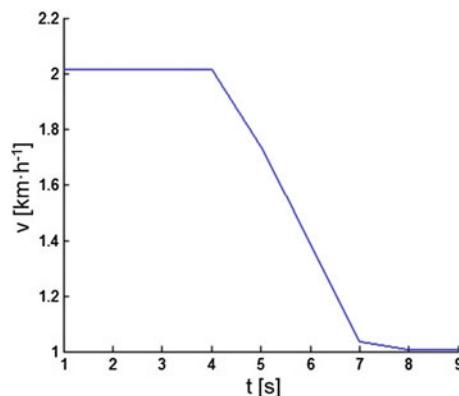
Table 1 Results of the experimental verification of the split-belt treadmill

Parameter	Left belt	Right belt
Average time delay in the control of the speed change (s)	0.43	0.48
Average difference between the desired and realized speeds (km/h)	4.8×10^{-4}	4.8×10^{-4}
Average difference in the times of the duration of speed change (s)	0.25	0.18

Fig. 4 Ramp acceleration graph when changing speed with negative acceleration value

Conflict of Interest The authors declare that they have no conflict of interest.

References

1. Fujiki, S., Aoi, S., Funato, T., Tomita, N., Senda, K., Tsuchiya, K.: Adaptation mechanism of interlimb coordination in human split-belt treadmill walking through learning of foot contact timing: a robotics study. Journal of The Royal Society Interface 12(110), 20150542 (2015).
2. Long, A.W., Finley, J.M., Bastian, A.J.: A marching-walking hybrid induces step length adaptation and transfers to natural walking. Journal of neurophysiology 113 (10), 3905–3914 (2015).
3. Gervasio, S., Farina, D., Sinkjær, T., Mrachacz-Kersting, N.: Crossed reflex reversal during human locomotion. J Neurophysiol 109, 2335–2344 (2013).
4. Fasano, A., Schlenstedt, C., Herzog, J., Plotnik, M., Rose, F.E.M., Volkmann, J., Deuschl, G.: Split-belt locomotion in Parkinson's disease links asymmetry, dyscoordination and sequence effect. Gait Posture. 48, 6–12 (2016).
5. Gervasio, S., Voigt, M., Kersting, U.G., Farina, D., Sinkjær, T., Mrachacz-Kersting, N.: Sensory feedback in interlimb coordination: contralateral afferent contribution to the short-latency crossed response during human walking. PLoS ONE 12(1), e0168557 (2017).
6. McCrum, C., Gerards, M.H.G, Karamanidis, K., Zijlstra, W., Meijer, K.: A systematic review of gait perturbation paradigms for improving reactive stepping responses and falls risk among healthy older adults. Eur Rev Aging Phys Act 14(3), eCollection (2017).
7. Malone, L.A., Bastian, A.J.: Thinking about walking: effects of conscious correction versus distraction on locomotor adaptation. J Neurophysiol 103, 1954–1962 (2010).

Measurement of Mechanical Properties of Enamel Based on Resonant Ultrasound Spectroscopy

Haijun Niu, Fan Fan, Rui Wang, Qiang Zhang, and Pengling Ren

Abstract

Mechanical properties is critical for developing dental materials and designing dental prosthesis. The aim of this study is to investigate the mechanical properties of human enamel material based on resonant ultrasound spectroscopy method (RUS). First, some pure enamel specimens were prepared carefully from five fresh human teeth. Under the assumption of transverse isotropic biomaterial, for all enamel specimens, the theoretical resonant frequencies were calculated using Rayleigh-Ritz method, the experimental resonant frequencies were extracted from resonant ultrasound spectroscopy, and then the optimal elastic constants was estimated based on based on the experimental and theoretical resonant frequencies using Levenberg-Marquardt method. In addition, the mechanical parameters, including Young's moduli, Shear moduli, and Poisson's ratios, were also calculated based on the optimal elastic constants. The result showed that RUS method exhibited more consistency of mechanical parameters than previous studies. This method may provide more precise measurement of mechanical properties of Enamel materials.

Keywords

Enamel • Elastic constants • Resonant ultrasound spectroscopy • Transverse isotropic

H. Niu (✉) · F. Fan · R. Wang · Q. Zhang · P. Ren
Key Laboratory of Ministry of Education for Biomechanics and Mechanobiology, School of Biological Science and Medical Engineering, Beihang University, Beijing, China
e-mail: hjniu@buaa.edu.cn

H. Niu
Beijing Advanced Innovation Center for Biomedical Engineering, Beihang University, Beijing, China

1 Introduction

Enamel is the hardest bone tissue of the human tooth, covering the crown surface and protecting the inner tissue [1]. Understanding the mechanical properties and the mechanisms in relation to the compositional and hierarchical microstructure of enamel is important for developing dental materials and designing dental prosthesis.

However, previous measurement results of enamel mechanical properties always vary widely due to the limitations of measurement methods. Ye et al. measured the elastic modulus of human molar enamel in the range of 20.8–26.8 GPa by using the stretching method [2]. Stanford et al's results shows elastic modulus is ranged from 62.74 to 95.84 GPa and Craig et al's result is from 8.27 to 37.23 GPa using compressed method [3, 4]. Cuy et al. measured the elastic modulus of human enamel surface to be greater than 115 GPa using the nano-indentation method [5]. Gilmore et al. measured the elastic modulus of bovine enamel in the range of 32.4–131.0 GPa using ultrasonic interferometry [6].

Resonant ultrasound spectroscopy (RUS) has been used as an accurate and efficient method to characterize material mechanical properties and has been considered as the most accurate method for measuring the elastic constants of high Q solid materials [7]. Recently, Bernard et al. applied RUS to bone materials, which broke the limit of the RUS method for measuring low Q materials [8]. Kinney et al. measured the mechanical properties of human dentin in both the dry and humid states using RUS [9]. Fan et al. used this method to estimate elastic constants, as well as Young's moduli, Shear moduli and Poisson's ratios of human dentin specimens [10].

This study evaluated the elastic constants of small-sized human enamel specimen base on RUS method. The mechanical parameters, Young's moduli, Shear moduli, and Poisson's ratios were also calculated and compared with the results of previous research.

2 Experiment and Methods

2.1 Experimental System

Figure 1a is the schematic of RUS experimental system. The system include a network analyzer (Bode 100, Austria), broadband amplifier (HQA-15 M-10T, Germany), two shear wave ultrasound transducers (V154RM, Panametrics, US) and a sample table.

2.2 Specimen Preparation

Five fresh enamel specimens were prepared from wisdom teeth provide by five younger (age 25–27 years). First, a low-speed diamond saw (SYJ-150, Shenyang Kejing. China) with 0.01-mm positioning accuracy was used to cut the enamel roughly. After being polished with 500-mesh, 800-mesh, and 2000-mesh abrasive papers, the standard rectangular parallelepiped specimens was complete (Fig. 1b). The specimens were stored in saline to maintain a hydrated state.

2.3 Methods

The step of RUS method include (1) to calculate theoretical resonant frequencies using the Rayleigh-Ritz method base on a priori elastic constants, (2) to measured and extracted the experimental resonant frequencies from the RUS, (3) to obtain the optimal elastic constants using the Levenberg-Marquardt (LM) method. And then, Young's moduli, Shear moduli, and Poisson's ratios, were calculated based on the optimal elastic constants.

Theoretical resonant frequency. Human enamel is assumed to be a transversely isotropic material, with 5

independent constants, as shown in (1). The initial values of the elastic coefficients is set based on previous study [11]. $C_{11} = 82.96$ GPa, $C_{12} = 36.04$ GPa, $C_{13} = 34.66$ GPa, $C_{33} = 92.89$ GPa, and $C_{44} = 22.90$ GPa.

$$C_{ij} = \begin{pmatrix} C_{11} & C_{12} & C_{13} & 0 & 0 & 0 \\ C_{12} & C_{11} & C_{13} & 0 & 0 & 0 \\ C_{13} & C_{13} & C_{33} & 0 & 0 & 0 \\ 0 & 0 & 0 & C_{44} & 0 & 0 \\ 0 & 0 & 0 & 0 & C_{44} & 0 \\ 0 & 0 & 0 & 0 & 0 & \frac{1}{2}(C_{11} - C_{12}) \end{pmatrix}$$

$$(1)$$

The theoretical resonant frequencies can be obtained by finding the stationary points of the Lagrangian L by

$$L = \frac{1}{2} \int \left(\sum_i \rho (2\pi f)^2 u_i^2 - \sum_{i,j,k,l} c_{ijkl} \frac{\partial u_i}{\partial x_j} \frac{\partial u_k}{\partial x_l} \right) dV, \quad (2)$$

where ρ is the specimen density, V is the specimen volume, C_{ijkl} is each initial elastic constant, f is the resonant frequency, and u_i is the displacement field. The equation was solved by the Rayleigh-Ritz method [18].

Experimental resonant frequency. To obtain the resonant frequency of the specimen, the frequency-sweeping ranges were set to include at least the range of the first 30 orders of resonant frequency. Six independent experiments were performed on each enamel specimen with the same parameters, and six groups of experimental resonant frequencies were obtained by seeking local maximum points [8].

Elastic constants and mechanical parameters calculation. To obtain the final elastic constants based on the experimental and theoretical resonant frequencies of the enamel specimen, a cost function $F(C)$ was defined as
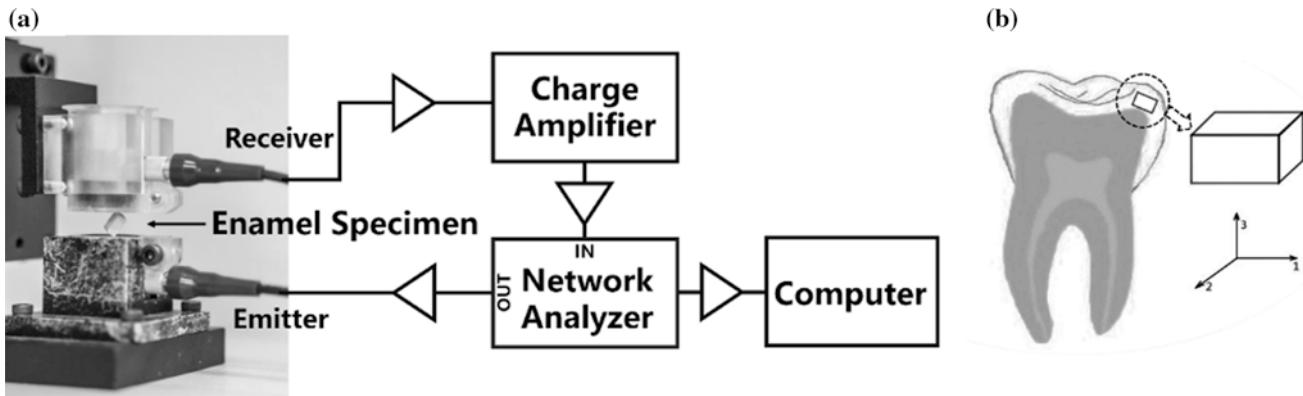
Fig. 1 **a** Platform of the RUS experiment system. **b** The enamel specimen

$$F(C) = \sum_{i=1}^{N} w_i \left(f_i^{exp} - f_i^{cal}(C) \right)^2 \qquad (3)$$

where f_i^{cal} is the i-th theoretical resonant frequency, f_i^{exp} is the i-th experimental resonant frequency, N is the number of theoretical resonant frequencies, C is the elastic constant of enamel and, w_i is the weight, given by (4),

$$w_i = \begin{cases} 0 & f_i^{cal} \text{ does not match } f_i^{exp} \\ 1/(f_i^{exp})^2 & f_i^{cal} \text{ matches } f_i^{exp} \end{cases} \qquad (4)$$

Under the convergent condition, the optimal elastic constants C were the ones that minimized $F(C)$, using the Levenberg-Marquardt (LM) method [7].

According to the generalized Hooke's law, the 6×6 stiffness matrix was constructed and numerically inverted to obtain the compliance matrix C_{ij}^{-1}, from which the engineering moduli were calculated

$$C_{ij}^{-1} = \begin{pmatrix} 1/E_{11} & -v_{12}/E_{11} & -v_{13}/E_{11} & 0 & 0 & 0 \\ -v_{12}/E_{11} & 1/E_{11} & -v_{13}/E_{11} & 0 & 0 & 0 \\ -v_{13}/E_{11} & -v_{13}/E_{11} & 1/E_{33} & 0 & 0 & 0 \\ 0 & 0 & 0 & 1/G_{13} & 0 & 0 \\ 0 & 0 & 0 & 0 & 1/G_{13} & 0 \\ 0 & 0 & 0 & 0 & 0 & 1/G_{12} \end{pmatrix}, \qquad (5)$$

where E_{ii} is Young's modulus (GPa), G_{ij} is Shear modulus (GPa), and v_{ij} is Poisson's ratio.

3 Results

The elastic constants and mechanical parameters of the enamel specimen are shown in Table 1. The five independent elastic constants C_{11}, C_{12}, C_{13}, C_{33} and C_{44} are 87.557 ± 12.165 GPa, 32.186 ± 10.428 GPa, 26.951 ± 6.545 GPa, 83.306 ± 10.714 GPa, and 41.394 ± 16.618 GPa, respectively. Young's moduli E_{11} and E_{33}, Shear moduli G_{13} and G_{12}, and Possion's ratios v_{12} and v_{13} were 70.937 ± 9.485 GPa, 70.802 ± 6.826 GPa, 41.394 ± 16.618 GPa, 27.686 ± 5.143 GPa, 0.293 ± 0.114 and 0.227 ± 0.059, respectively.

4 Discussion

As above mentioned, previous researchers used a variety of measurement techniques to obtain mechanical properties of dental materials [1–6]. However, due to the small size of human enamel specimens and the limitations of the measurement techniques have led to large differences in the measurement results.

Elastic constants and engineering moduli are the primary mechanical parameters that characterize the elastic properties of enamel. Due to the difference in microstructures and symmetries of different materials, the number of independent elastic constants for each material also varies. For simplification, it is generally assumed that enamel is isotropic, which may not be adequate for the real situation. To describe the enamel materials more accurately, Wen et al. assumed that enamel specimens are transversely isotropic and have five independent elastic constants [11]. Under the assumption of transverse isotropic biomaterial, this study estimated five constants of enamel specimens using RUS. Despite an extensive literature review, there were few studies found where measurement of the actual elastic constants of pure enamel material occurred under transversely isotropic conditions, except Wen evaluate elastic constants of enamel use FEA [11]. Compared with the elastic constants of dentin similarly calculated by the RUS method [2–6], the elastic constants of enamel obtained in our study were significantly larger, which might be attributed to the higher calcification of enamel and denser structure of enamel materials

Young's moduli of human enamel obtained in previous studies were significantly different due to measurement methods difference. For example, the compression method used by Stanford et al. yielded values between 8.27 and 37.23 GPa [3]. The Young's modulus obtained in this study were in the range of 60.069–80.462 GPa, which was consistent with the results of Craig et al. [4], but with less measurement deviation. In addition, Poisson's ratios v_{12} (0.33) and v_{13} (0.25) and Shear modulus G_{12} (24.8 GPa) computed by Wen et al. [11] with FEA were consistent with the measurement results of this study. For Poisson's ratio v_{12} and the Shear modulus G_{13}, the differences among the specimens were large. The main reason might from sample difference, including individual donor difference and material location difference.

Table 1 The elastic constants and mechanical parameters of enamel specimens (GPa)

No.	1	2	3	4	5	Mean	SD
C_{11}	92.038	96.716	84.804	96.626	67.603	87.557	12.165
C_{12}	26.302	43.465	41.792	30.534	18.838	32.186	10.428
C_{13}	32.68	23.41	29.555	31.892	17.216	26.951	6.545
C_{33}	94.128	72.316	93.776	83.569	72.743	83.306	10.714
C_{44}	29.648	51.855	27.333	32.606	65.526	41.394	16.618
E_{11}	77.921	74.69	61.516	80.462	60.097	70.937	9.485
E_{33}	76.079	64.497	79.976	67.571	65.885	70.802	6.826
v_{12}	0.185	0.402	0.43	0.217	0.232	0.293	0.114
v_{13}	0.283	0.193	0.18	0.299	0.182	0.227	0.059
G_{13}	29.648	51.855	27.333	32.606	65.526	41.394	16.618
G_{12}	32.868	26.626	21.506	33.046	24.382	27.686	5.143

The results of this study on the elastic constants and mechanical parameters of enamel may provide valuable information for understanding the mechanical properties of dental materials and developing dental repair material. However, to achieve more accurate mechanical parameters of human enamel materials, more regular and pure enamel specimens should be prepared in the future work.

References

1. He LH and Swain MV. Understanding the mechanical behaviour of human enamel from its structural and compositional characteristics. J Mech Behav Bio Mater, 1(1):18–29. (2008).
2. Wang B, Su Y, and Ye D. Measurement of Poisson's ratio of human enamel. West China Journal of Stomatology, 4:295–297. (1994).
3. Stanford JW, Paffenbarger GC, Kumpula JW and Sweeney WT. Determination of some compressive properties of human enamel and dentin. J Am Dent Assoc, 57(4): 487–495. (1958).
4. Craig RG, Peyton FA and Johnson DW. Compressive properties of enamel, dental cements, and gold. J Dent Res, 40(5): 936–945 (1961).
5. Cuy JL, Mann AB, Livi KJ, Teaford MF and Weihs TP. Nanoindentation mapping of the mechanical properties of human molar tooth enamel. Arch Oral Biol, 47(4): 281–291 (2002).
6. Gilmore RS, Pollack RP and Katz JL. Elastic properties of bovine dentine and enamel. Arch Oral Biol, 15(8):787–796 (1970).
7. Migliori A and Sarrao JL. Resonant ultrasound spectroscopy: Applications to physics, materials measurements, and nondestructive evaluation. New York: Wiley, (1997).
8. Bernard S, Grimal Q and Laugier P. Resonant ultrasound spectroscopy for viscoelastic characterization of anisotropic attenuative solid materials. J Acoust Soc Am, 135(5):2601–2613 (2014).
9. Kinney JH, Gladden JR, Marshall GW, Marshall SJ, So JH and Maynard JD. Resonant ultrasound spectroscopy measurements of the elastic constants of human dentin. J Biomech, 37(4):437–441 (2004).
10. Fan F, Wang R, Feng D, Zhang Q and Niu H. The Elasticity Coefficients Measurement of Human Dentin Based on RUS. Biomed Res Int, (2017) http://doi.org/10.1155/2017/7852971.
11. Wen M, Zheng J and Zhou Z. Finite element analysis on effect of organic phase on mechanical properties of human tooth enamel. Lubrication Engineering, 39(7):21–25 (2014). (in Chinese).

Evaluating the Effect of Changes in Bone Geometry on the Trans-femoral Socket-Residual Limb Interface Using Finite Element Analysis

Alex van Heesewijk, Andy Crocombe, Serge Cirovic, Mathew Taylor, and Wei Xu

Abstract

A prosthetic socket used by a lower limb amputee should accommodate the patient's geometry and biomechanical needs. The creation of a geometrically accurate subject-specific finite element model can be used to provide a better understanding of the load transfer between socket and limb. There has been a limited number of finite element studies of trans-femoral sockets with all current models only including the femur and ignoring the pelvis. This study looked to evaluate the effect that including the pelvic bone as well as the femur in a finite element model has on the contact interface between the prosthetic socket and residual limb. This was done by creating a finite element model from a computerised tomography scan of a trans-femoral amputee. This model included three-dimensional geometry, nonlinear material properties and frictional contact between the residual limb and prosthetic socket. It was found that without the pelvic bone the contact pressures peaked at the distal end region of the residual limb (peak of 95 kPa). However by including the pelvic bone the contact pressures were instead concentrated at the ischial loading region (peak of 364 kPa). The shear stresses experienced on the socket-residual limb interface were also simulated. The results obtained in this study can be used to provide more of an understanding of the loading on the residual limb for the design and creation of future trans-femoral sockets.

A. van Heesewijk (✉) · A. Crocombe · S. Cirovic · M. Taylor W. Xu
University of Surrey, Guildford, Surrey, GU2 7XH, UK
e-mail: a.vanheesewijk@surrey.ac.uk

1 Introduction

The amputation of a lower limb is a severely traumatic experience. The prosthetic solution to this aims to restore the self-esteem of the patient as well as to restore the best ambulation achievable for the patient. The prosthetic socket introduces an interface between the residual limb and prosthesis, which transfers the loading during ambulation between limb and prosthesis. The correct socket design for the individual is crucial in achieving comfort and optimal use of the prosthetic limb.

This residual limb—prosthetic socket interface alters the natural demand placed upon the residual limb, requiring the loads produced during gait to be borne by the soft tissue rather than the bone. To minimise detrimental interactions between the prosthetic socket and residual limb, the new situation that causes severe skin and vascular problems [1], needs to be understood. The stress-strain state of this interaction has been investigated in previous studies by the use of finite element analysis (FEA) [2–8]. The development of finite element models commonly use MRI [3, 4] or CT scans [5–8] to obtain the relevant bone and soft tissue geometry. FEA has been widely used to examine the aspects of lower limb prosthetics ranging from the donning procedure [6] and effects of dynamic loading [3] to multiple surgical and morphological factors [4]. However, the validity of these finite element models is reliant on the use of the correct geometry.

A number of previous FEA studies of the trans-femoral residual limb have modeled only the femur as the bony geometry without including the pelvis [2, 5–8]. However, the pelvic region has been shown to play a substantial part in bearing the load of the patient in both common types of trans-femoral prosthetic sockets; ischial containment socket where the proximal socket design is to encase the ischial tuberosity of the pelvis and the quadrilateral socket where the proximal socket brim sits just beneath the ischial tuberosity [9, 10].

A better understanding of the role the pelvic bone has on the load transfer between residual limb and socket is necessary to increase overall knowledge and to inform future socket design. The objective of this study is to simulate the loading between a residual limb and prosthetic socket, both with and without the inclusion of the pelvic bone to understand the effect it has on the contact interface.

2 Methods and Materials

2.1 Geometry Acquisition

The geometry of a residual limb and internal bone were collected from a trans-femoral amputee who was 39 years of age, 173 cm in height with an approximate body-weight of 74 kg. The geometries of the residual limb and bone were collected by a GE Lightspeed Plus CT scanner with a 512×512 pixel matrix, 0.703 mm pixel size, 1.25 mm slice increment and 0.0° gantry tilt.

During the CT scan the patient was lying supine without the addition of a liner or socket. The bone and residual limb surfaces were identified and segmented using Mimics version 19.0 (Materialise, Leuven, Belgium). For the first model the bone surface was taken only as the femur (non-pelvic model), whilst in the second model the bone surface was taken as the femur and pelvic bone combined (pelvic model).

These surfaces were loaded into 3-Matic version 11.0 (Materialise, Leuven, Belgium) to convert the surfaces into solid parts. During this process the muscle, fat and skin of the soft tissue were modelled as a single entity. The internal geometry of the socket was assumed to be the same as the external surface of the residual limb, which is the approach used in previous similar studies [4, 5]. The resulting solid three-dimensional models comprised of bone, soft tissue and socket (see Fig. 1) and were meshed with 4-node tetrahedral elements. The total number of elements ranged from approximately 534,000 to 565,000 depending on model configuration.

2.2 Mechanical Properties

The bone and socket materials were considered as linear elastic, homogeneous and isotropic. In previous studies, linear elasticity was also implemented for the soft tissues with a Young's modulus of 100–400 kPa and Poisson's ratio of 0.45–0.49 [1–3, 8]. However, as the loading of a residual limb exhibited large deformation Portnoy et al. [4] introduced the use of a hyper-elastic model for the soft tissue to account for this. For the soft tissue hyper-elastic and linear, homogeneous and isotopic properties were defined using the 3rd order Mooney-Rivlin strain energy function (see Table 1). The material constants were taken from literature [3–6].

2.3 Loads and Boundary Conditions

The interface between the bone and soft tissue was modeled as a tied constraint which prevents movement between the two parts. The soft tissue and socket interface was modeled as a surface to surface contact interaction using ABAQUS CAE 2017®, which prevented the slave surface (soft tissue) from penetrating the master surface (socket) during the analysis. For this interaction a friction coefficient of 0.45 was used as this was within a range of previously reported values [11].

The analysis was conducted as a two phase process. The first phase simulated the pre-stresses due to the donning procedure. This was done by applying a 50 N load to the distal end of the socket with the proximal region of the bone being constrained in movement; the proximal bone region was the femoral head for the non-pelvic model and the proximal pelvis for the pelvic model, respectively. The resulting stresses were kept in the second phase. In the second phase a walking load of 110% of the patient's bodyweight (800 N) was applied to the distal end of the socket with the proximal region of the bone remaining fixed.

Fig. 1 FE mesh of prosthetic socket, soft tissue, pelvic model bone and non-pelvic model bone

Socket   Soft tissue   Pelvic model   Non pelvic model
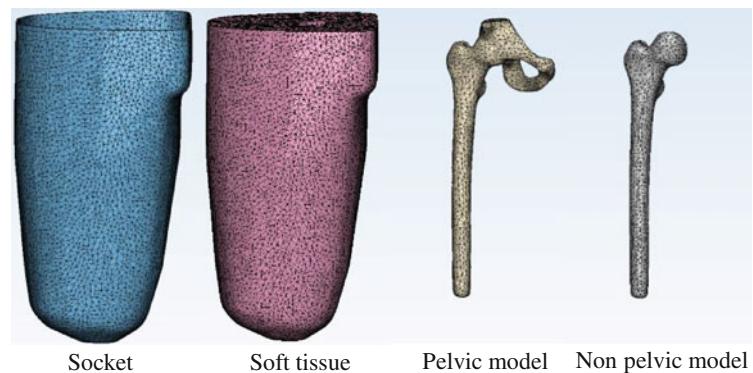
Table 1 Mechanical properties for the bone, socket and soft tissue

	Young's modulus (MPa)	Poisson's ratio
Bone	15,000	0.3
Socket	1500	0.3
Soft tissue	$C_{10} = 0.00425$, $C_{11} = 0$, $D_{01} = 2.36$	

Table 2 Peak values of stresses at the soft tissue-socket interface

Model	Donning contact pressure (kPa)	Loading contact pressure (kPa)	Loading circumferential shear stress (kPa)	Loading longitudinal shear stress (kPa)
Non-pelvic	3.48	94.91	+20.09/−20.89	+32.79/−25.76
Pelvic	5.48	364.40	+14.93/−78.06	+37.79/−38.85

3 Results

The stress distribution from the soft tissue—socket interaction was characterized in terms of contact pressure, circumferential shear stress and longitudinal shear stress (see Table 2). The pre-stress from the donning application produced a contact pressure peak of 3.48 and 5.48 kPa for the non-pelvic and pelvic models, respectively (see Fig. 2).

Figures 3, 4 and Table 2 show the contact pressure and shear stress distribution and peaks generated from the second loading phase. The contact pressure peaked at 94.91 kPa for the non-pelvic model and was located at the distal end of the residual limb, whilst the pelvic model peaked at 364.40 kPa and was produced at the ischial loading region. The circumferential and longitudinal shear stress for the non-pelvic model peaked at −20.89 and 32.79 kPa respectively (see Fig. 3), with both peaks occurring at the distal end of the soft tissue. The circumferential and longitudinal shear stress for the pelvic model peaked at −78.06 and −38.85 kPa respectively (see Fig. 4), with both peaks occurring at the ischial loading region.

4 Discussion

In previous studies it was often assumed that the socket geometry shares the same shape as the residual limb [4, 5], this was also the case for this study. The difference in geometry between the socket and residual limb socket leads itself to pre-stress conditions from the donning process. However as that was absent in this study, a 50 N load was used to replicate this in simulation as previously implemented by Zhang et al. [5]. The resulting maximum contact pressure from this was 3.48–5.48 kPa, which is close to the maximum pressure reported by Lacroix and Patino [6] (1.54–5.61 kPa) who implemented an explicit finite element method to accurately simulate the donning process.

The resultant peak contact pressure of 95 kPa for the non-pelvic model is in good agreement with the findings of Zhang and Mak [2] who reported a peak contact pressure peak of 63 kPa at the distal end of a distal loaded trans-femoral socket.

The pelvic model in this study resulted in a peak contact pressure of 364 kPa at the ischial support region and 36 kPa
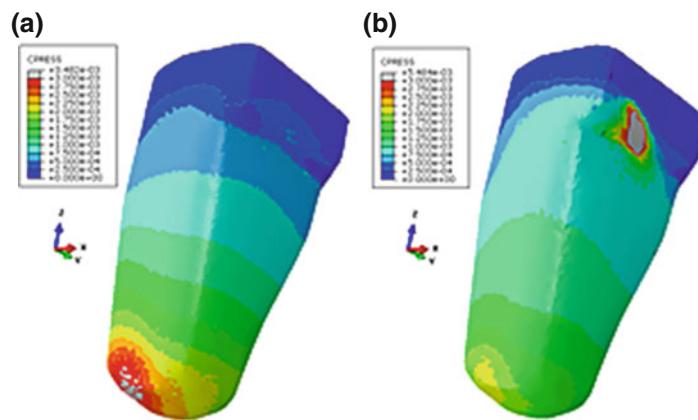
Fig. 2 Contact pressure at the soft tissue—socket interface due to donning. **a** Non pelvic model. **b** Pelvic model
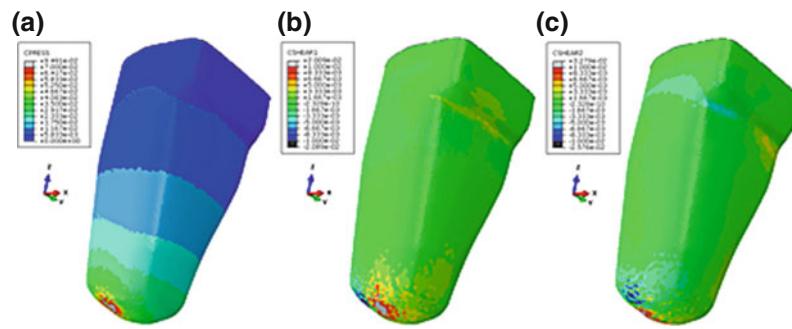
Fig. 3 **a** The contact pressure, **b** circumferential shear stress and **c** longitudinal shear stress for the non-pelvic model
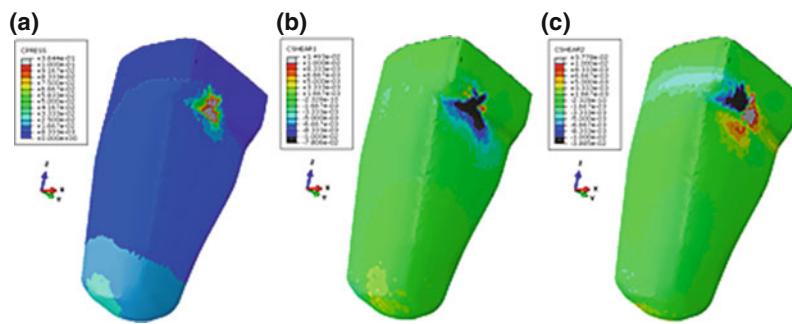
Fig. 4 **a** The contact pressure, **b** circumferential shear stress and **c** longitudinal shear stress for the pelvic model

at the distal end. Similarly, Zhang et al. [5] reported peak contact pressures of 119.30 and 80.57 kPa at the ischial support region and distal end, respectively. The study by Zhang et al. [5] did not include the pelvic bone and consequently their peak contact pressures at the ischial support region were considerably lower than obtained in this study. Their resultant stresses may be attributed to the socket brim geometry and the movement constraint placed on the proximal soft tissue.

The results of an experimental study by Kahle and Highsmith [10] which measured the interface between prosthetic socket and residual limb during walking using Tekscan F-Socket System, produced a peak contact pressure of 254.67 kPa in the ischial support region. The contact pressure and location reported by Kahle and Highsmith [10] are in agreement with those produced by the pelvic model in this study.

This study demonstrates the importance of implementing true bone geometry in the production of lower limb finite element models when examining the residual limb—prosthetic socket interface.

References

1. Zhang, M., Mak, A.F.T., Roberts, V.C.: Finite element modelling of a residual lower-limb in a prosthetic socket: a survey of the development in the first decade. Med. Eng. Phys. 20, 360–373 (1998).
2. Zhang, M., Mak, A.F.T.: A finite element analysis of the load transfer between an above-knee residual limb and its prosthetic socket – Roles of interface friction and distal-end boundary conditions. IEEE Trans. Rehabil. Eng. 4(4), 337–346 (1996).
3. Jia, X., Zhang, M., Lee, W.: Load transfer mechanics between trans-tibial prosthetic socket and residual limb – dynamic effects. J. Biomech. 37, 1371–1377 (2004).
4. Portnoy, S., Siev-Ner, I., Yizhar, Z., Kristal, A., Shabshin, N., Gefen, A.: Surgical and morphological factors that affect internal mechanical loads in soft tissues of the transtibial residuum. Ann. Biomed. Eng. 37(12), 2583–2605 (2009).
5. Zhang, L., Zhu, M., Shen, L., Zheng, F.: Finite element analysis of the contact interface between trans-femoral stump and prosthetic socket. In: 35th Annual International Conference of the IEEE EMBS, pp. 3–7. Osaka, Japan (2013).

6. Lacroix, D., Patino, J.F.R.: Finite element analysis of donning procedure of a prosthetic transfemoral socket. Ann. Biomed. Eng. 39(12), 2972–2983 (2011).

7. Restrepo, V., Villarraga, J., Palacio, J.P.: Stress reduction in the residual limb of a transfemoral amputee varying the coefficient of friction. J. Pros. Orthot. 26(4), 205–211 (2014).

8. Velez Zea, J.A., Goez, L.M.B., Ossa, J.A.V.: Relation between the length of the residual limb length and stress distribution over stump for transfemoral amputees. Revista EIA (Spanish) 12(23), 107–115 (2015).

9. Schuch, C.M., Pritham, C.H.: Current transfemoral sockets. Clin Orthop Relat Res 361, 48–54 (1999).

10. Kahle, J., Highsmith, M.J.: Transfemoral sockets with vacuum-assisted suspension comparison of hip kinematics, socket position, contact pressure, and preference: Ischial containment versus brimless. J Rehabil Res Dev 50(9), 1241–1252 (2013).

11. Ramirez, J., Pavon, J., Toro, A.: Experimental assessment of friction coefficient between polypropylene and human skin using instrumented sclerometer. J. Eng. Tribol. 229(3), 259–265 (2015).

Monitor Aided Radio Control Mobile Robot (MARCMR)

Kamran Hameed, Muddasir Hussain, and Ijlal Shahrukh

Abstract

The term robot comes from the Czech word robota, which when translated means "forced labor". Generally, all the robots in the world are designed for monotonous tasks. The robots handle the jobs that are difficult, dangerous or boring for a human to perform. In the medical world robots have now taken over many tasks; from a basic robotic helping hand to complex mimetic robotic arm based surgery and these chores have shown promising results. Our robotic arm is based on an innovative idea which provides help to the less mobile or paralyzed patients. Our robotic arm: Monitor Aided Radio-controlled Mobile Robot (MARCMR) is based on a robotic arm mounted over a moveable shaft, which can move from one place to another place by radio control. It uses simple gripping and dropping process to move the object which will assist paralyzed patients. MARCMR may also be helpful to work as laboratory equipment handing tool. MARCMR is controlled by using RF remote. The robot is also attached with a camera which enhances the real time view of the user. The MARCMR can be fixed by the side of a patient so that they can be able to perform their daily routine tasks and secondly they can be installed at various locations within an area where humans do not prefer to go or it might be hazardous. Keeping in mind the durability and flexibility, the MARCMR is built by using Aluminum, Plastic (PVC) and Iron. It has a wrist, elbow and shoulder joints to provide maximum closeness with a human arm. The joints are controlled with DC motors. The MARCMR revealed encouraging outcome as the patients will be able to perform their tasks with ease and they may also be allocated to the places where humans don't wish to go.

1 Introduction

1.1 Monitor Aided Radio Control Mobile Robot (MARCMR)

The Monitor Aided Radio Control Mobile Robot (MARCMR). It is based on the robotic arm fixed on the moveable cart, which can move from one place to another place by means of radio control cart. Which can assist the paralyze patients and can use as laboratory equipment handling tool [1] by using radio-control remote can control the robot function and movement real time video of the surrounding can also be recorded, the RF camera is attached to the wrist of the robot [2]. Rapid rate of accident cause paralysis to the people either short period of time or long period of time [3, 4]. The main idea to assembled designed project is to assist the paralyze patients to control robot using its control panel, so the patients can easily execute their work with the help of designed robot, proposed design can also be used to handle the lab equipments in many hazardous areas [5] or factories where the human being cannot work normally due to hazardous environment like (chemical industries, Atomic industries and some areas where extreme temperature required). Other areas where MARCMR can be used are: handling stuff from one place to another, handling laboratory

K. Hameed (✉) · I. Shahrukh
Department of Biomedical Engineering, Imam Abdulrahman Bin Faisal University, Dammam, Kingdom of Saudi Arabia
e-mail: khKhawaja@iau.edu.sa; kamranhameed@live.com

M. Hussain
Department of Biomedical Engineering, Sir Syed University of Engineering & Technology, Karachi, Pakistan

equipments, controlled by simple switch based RF controlling pad. Video and audio monitoring via RF camera [1].

2 Design Methodology

2.1 MARCMR's Mechanical Structure Components Selection and Its Designing

The proposed design (MARCMR) is based on the hardware assembly selections of the material is important to give the strength to the assembly. The hardware of the MARCMR is based on Aluminum (plastic PVC) and Iron (screw rods). The Aluminum is used in a designed project to give the rigidity to the assembly having less weight as compare to the other metals. It is used in wrist, elbow, shoulder, shaft and some movable cart of MARCMR. Plastic (PVC) has also used in MARCMR because it molds easily to give a desire shape to the structure. In MARCMR the plastic is used in Robotic hand and its covering. Iron screw rod is also used in MARCMR due to its high rigidity used in the MARCMR for the movement of Elbow and shaft. The basic unit of Robotic hand is shown in Fig. 1. The movement of the finger is controlled by gear and pulley support. The wrist which is connected to the gear motor which can rotate the hand up to 0–180° (Supination) as shown in Fig. 2 The Shoulder of the MARCMR shown in Fig. 3, is fixed with the steel rod, the rod is fixed with the gear which is supported by two motors. The vertical shaft as shown in Fig. 4, give the minimum height and maximum height to the hand to pick the object

Fig. 2 The wrist of MARCMR

Fig. 3 The shoulder of MARCMR

Fig. 1 Basic unit of MARCMR hand

Fig. 4 Shaft of the MARCMR hand

from the ground and from the height. The vertical shaft as shown in Fig. 5, is fixed at the moveable cart. The cart can move in the (Forward, Backward, Left, and Right) direction

Fig. 5 Moveable cart of MARCMR hand
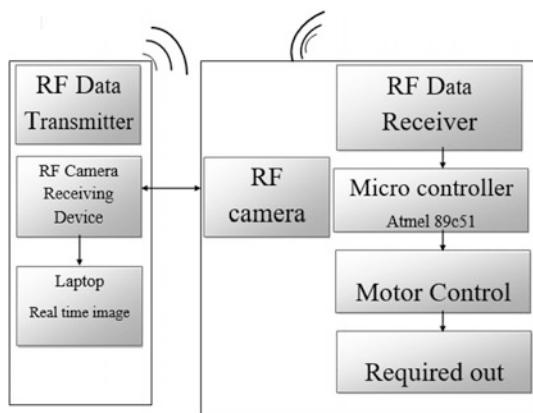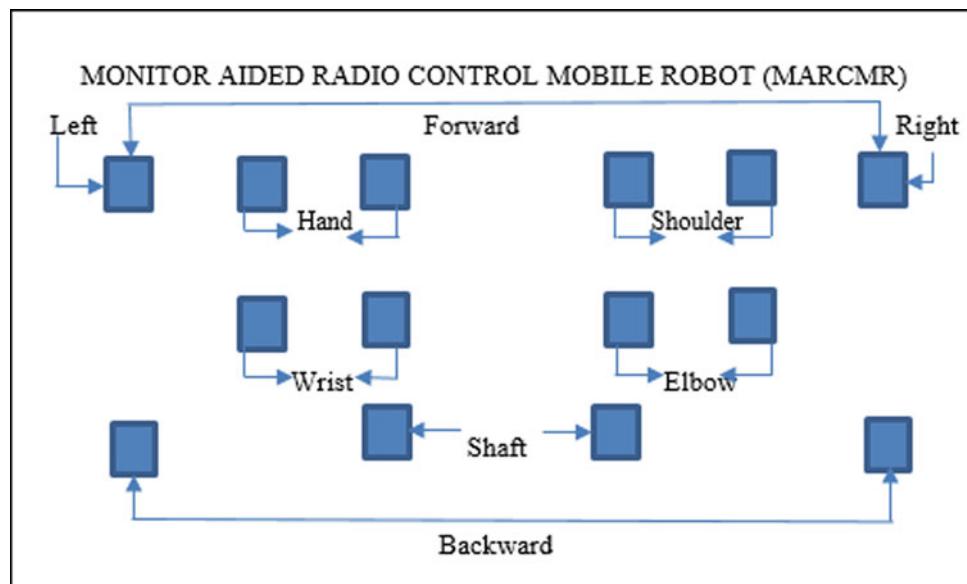
Fig. 6 MARCMR's system layout

[1, 2]. The high torque gear motor is fixed with the wheel to drag the load up to 8 kg. Four wheels are fixed with the base corners for support the movement and two wheels fixed with motor to give the movement.

2.2 MARCMR's Electronics Design Circuits and It's Description

A microcontroller has been used in this project to control the movements of the robotic hand over the input of desired function from the user. Each movement of the mechanical manipulator is done by using motors that are selected by considering various parameters. For the movement of the fingers (flexion and Extension) a small size DC motor FF050H is used, the assembly of the gear system make possible to flex and extends the finger while changing the polarity of the motor. Each motor is used to perform the specified function as produced by the human body. The overall design layout is shown in Fig. 6.

Microcontroller:
The data is received by the RF receiver, then microcontroller takes this data as input and generates output which is connected to different relays that are connected with H-bridge circuit to the movement of MARCMR.
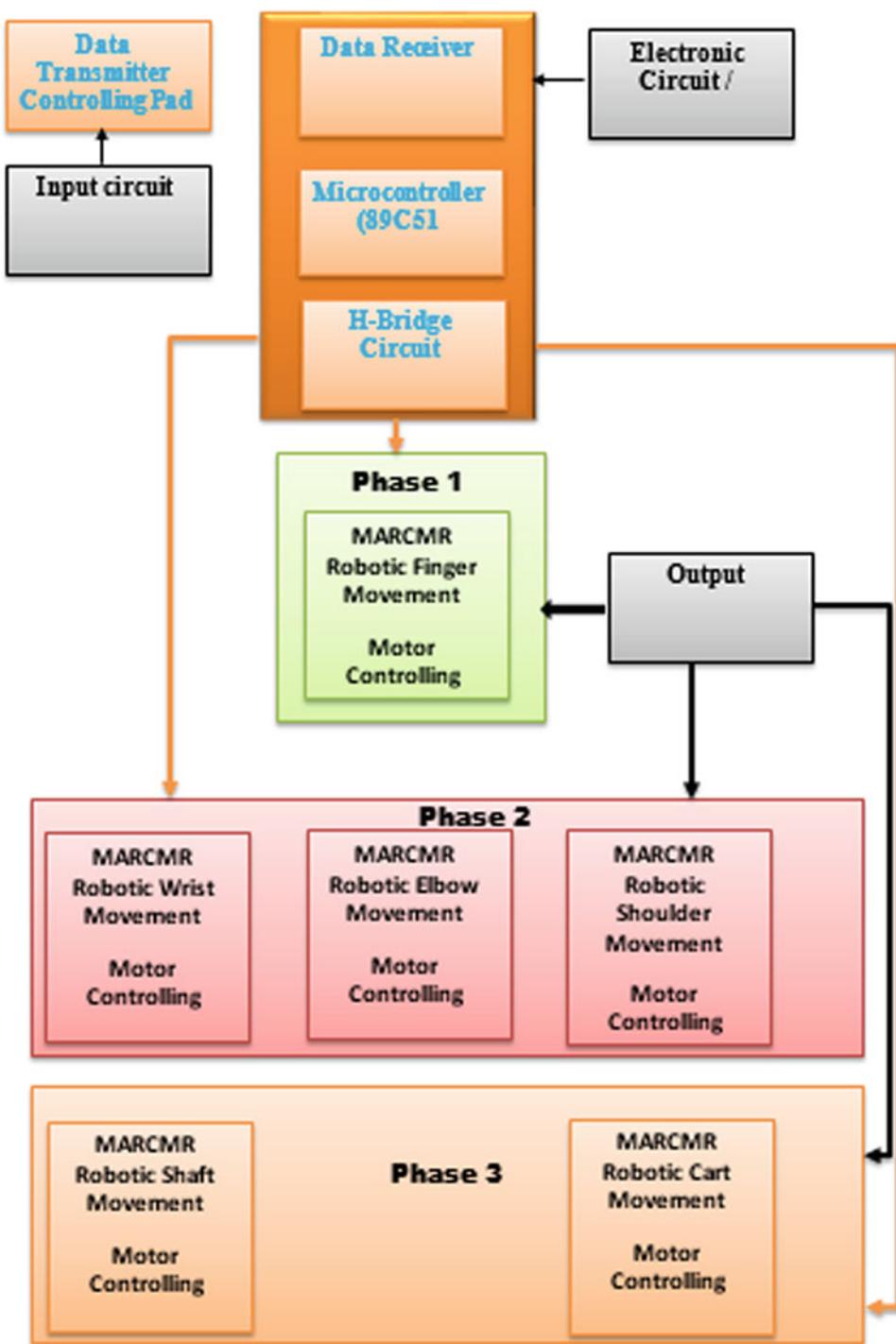
H Bridge Circuit:
The H bridge circuit is used in the project to control the polarity of the DC motor by the microcontroller. Each set of h bridge is responsible to control specified motor. The input to the H-bridge is given by the Micro Controller output pins.

RF Module:
There are four RF modules of different frequencies used in the project. Each module is able to transmit and receive four signals. The module operates at 5 V. The output of the module is DC 0 and 5 V. It's made easy to interlink with the Microcontroller input. The module is able to send and receive more than 1 signals at a time. The input of Micro Controller is connected to the output of the RF module. Four

Fig. 7 Controlling pad of MARCMR

Fig. 8 MARCMR's controlling
phase's layout

different frequencies (27, 35, 40, and 49 MHz) are used to control the movement wirelessly.

DC Power Supply:
In this project Dc batteries of 12, 6 and 7.4 V are used to power the Dc motors and wireless modules. The DC

batteries are rechargeable and they can run the system effectively for 4 h.
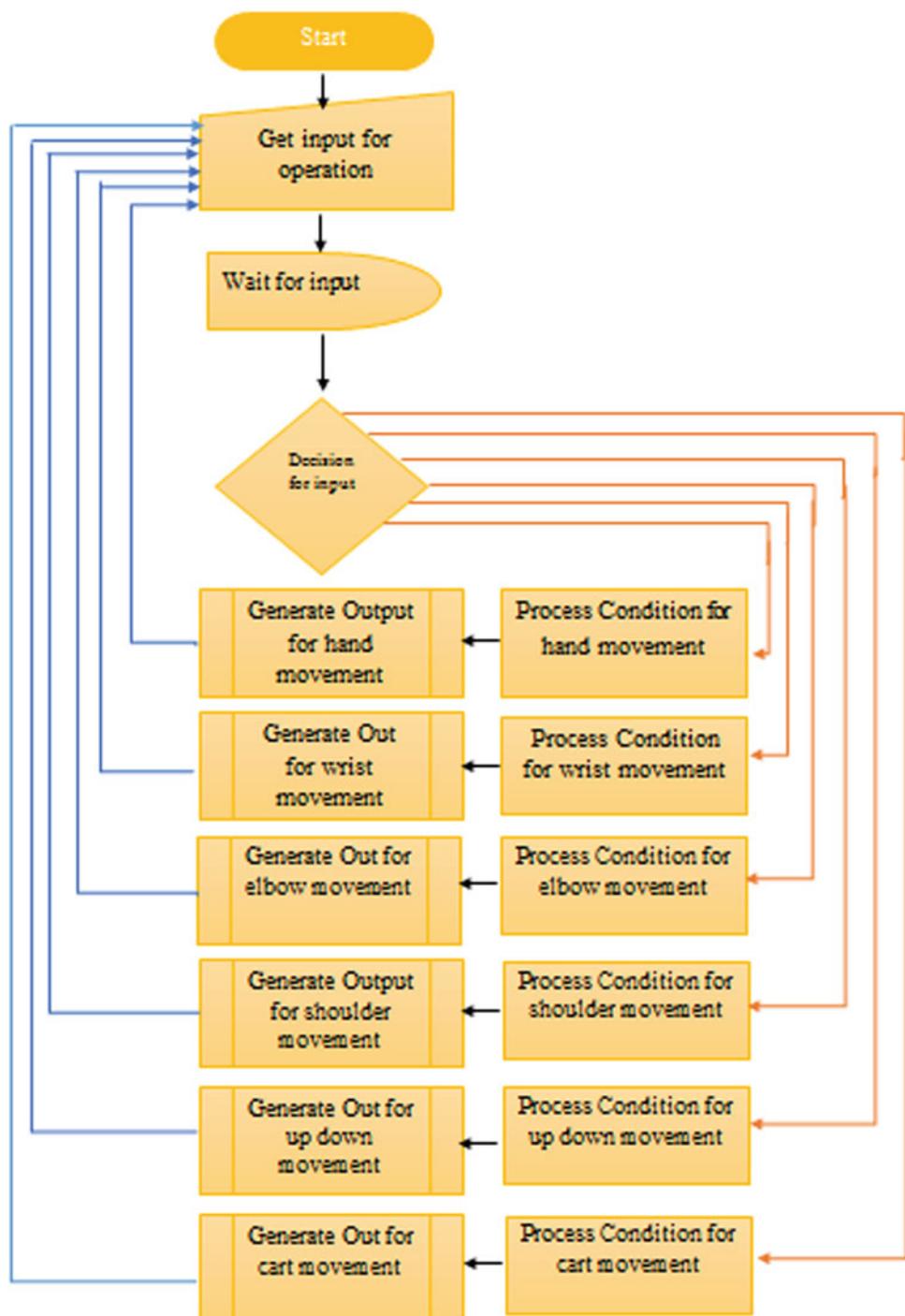
Wireless Camera:
The wireless camera is fixed at the arm of the MARCMR. The camera is used to receive the real time image within the

range of 200 feet which can be transmitted to the server by using RF module. Transmitter this feature enables the users to communicate with the system and perform guided movement the system lay out is shown in Fig. 6, and system phase diagram is shown in Fig. 8 the programing flow chart is shown in Fig. 9.

MARCMR Controlling Pad:

The controlling pad as shown in Fig. 7 is based on the switch board connected to the RF transmitter. The data is transmitted by the transmitter with the help of controlling pad and receive by the receiver for the movement. The 7 V battery is attached to the controlling pad to give the supply.

Fig. 9 MARCMR programming flow chart

3 Conclusion

The main idea to assemble this project was assist the para-
lyze patients so the patients can do their own work by using
the controller (control panel) [2] and as well as it is quit save
for the patients. Another main feature of proposed design is
that it can handle lab equipment so in many hazardous areas
[5] or in factories where the human being cannot work
normally like (chemical industries, Atomic industries and
some areas where extreme temperature required). The
Monitor Aided Radio Control Mobile Robot (MARCMR) is
the achievement to resolving the problems encounter by the
paralyze patients, object gripping and dropping and handle
object from one place to another facilitate them to do their
work [6, 2] that they are able to do their work and spend
normal life.

Conflict of Interest The authors declare that they have no conflict of
interest.

References

1. I. Firmansyah, B. Hermanto and L.T. Handoko (2007) Group for
   Theoretical and Computational Physic, Research Center for Physics
   Control and Monitoring System for Modular Wireless Robot,
   Indonesian Institute of Sciences, Indonesia.
2. Jegede Olawale, Awodele Oludele, Ajayi Ayodele, and Ndong
   (2007) Babcock University Development of a Microcontroller
   Based Robotic Arm, Ilisan–Remo.
3. International association of oil & gas producer land transport
   accident statistic 209–215 Black friars Road London SE1 8NL
   United Kingdom.
4. Department for transport Scottish executive assembly for wales road
   casualties' great Britain 2006 Published September 2007.
5. Hoa G. Nguyen* and John P. BottSpace and Naval Warfare
   Systems Center San Diego (2007) Robotics for law enforcement.
6. Yuru Zhang, Jiting Li, Jian Feng Li. (2007) Robotic Dexterous
   Hand: Modeling, Planning, and Simulation. Mechanical Press,
   Beijing.

Development of a New Method to Monitor Shoulder Girdle Motion for Ballerina with Shoulder Impingement Syndrome Based on DAid Smart Shirt Application

Guna Semjonova, Janis Vetra, Alexander Oks, and Alexei Katashev

Abstract

Shoulder impingement is the most common cause of shoulder pain. The ability to control the orientation and movement of the scapula is essential for optimal arm function and pain reduction in young adults with shoulder impingement signs. Smart garments find wide range of healthcare applications, including rehabilitation. One of the main parts of smart garment is the sensing system which can include one or several sensing elements for posture and joint motion control. The aim of present research was to verify the possibility of using DAid Smart shirt to capture and monitor shoulder gridle motion during motor control exercises and during training sessions out of laboratory environment for ballerina with shoulder impingement syndrome. Another aim was to develop method of this Smart shirt using in addition to conventional physiotherapy to reduce right side shoulder girdle elevation. As a monitoring tool, specially designed DAid Smart Shirt had been used. Specifically, embodied textile strain sensors gave possibility to capture spatiotemporally motion, but acquisition system provided visual feedback on the screen of remote electronic device. Conclusions: Designed DAid Smart shirt can be objective and convenient tool for shoulder motion monitoring for both: patient and physiotherapist. Thus, it can be used as

effective assisting device to conventional physiotherapy for shoulder girdle motion control.

Keywords

Smart garments • Shoulder girdle motion control
Shoulder girdle motion monitoring

1 Introduction

Shoulder injuries of professional ballet dancers occurred in 2.5% of cases in women [1]. Movement faults and changes in muscle function of the scapula are associated with shoulder symptoms [2, 3]. Shoulder impingement has been shown to be the most common cause of shoulder pain, constituting 74% of cases. Shoulder impingement is a compression of subacromial tissues because of narrowing of the subacromial space [2]. The etiology of subacromial can include anatomical and mechanical factors, rotator cuff pathology, shoulder joint instability, restrictive processes of the shoulder joint, imbalance of the muscles, and postural considerations [3]. Impingement syndrome can cause functional disability and reduce quality of life and may contribute to the development of rotator cuff disease [2]. Several biomechanical and physiological factors have been highlighted in shoulder impingement patients, including altered scapular movements and muscle activity [2, 4]. Physiotherapy is often the first line of management for shoulder impingement and physiotherapy methods such as motor control exercise intervention can improve function and pain in young adults with shoulder impingement signs [4].

It is known that smart garment is effective in simple motor learning tasks for shoulder patients in a clinical setting [5], but there is a lack amount of literature that wearable technologies are appropriate for posture monitoring and posture correction in advanced motor tasks such as shoulder motor control exercises and ballet training sessions. The aim of present research was to capture and monitor shoulder

G. Semjonova (✉)
Faculty of Rehabilitation, Rigas Stradins University,
Riga, Latvia
e-mail: guna.semjonova@gmail.com

J. Vetra
Faculty of Medicine, Institute of Anatomy and Anthropology,
Rigas Stradins University, Riga, Latvia

A. Oks
Institute of Design Technologies,
Riga Technical University, Riga, Latvia

A. Katashev
Institute of Biomedical Engineering and Nanotechnologies,
Riga Technical University, Riga, Latvia

gridle motion with DAid Smart shirt during training sessions and motor control exercises out of laboratory environment for ballerina with shoulder impingement syndrome and type I or Inferior scapular dysfunction (Kibler classification).

2 Materials and Methods

2.1 Case Study Participant

Participant was 24 years old professional ballet dancer (woman) with 14 years dancing experience, BMI (Body Mass Index) was 19.3. Diagnosed by right shoulder impingement signs, with type I or Inferior scapular dysfunction (Kibler cl.). DASH (The Disabilities of the Arm, Shoulder and Hand Measure) outcome score: 18.5. Clinical tests: Empty can, Neer's, Speed test were positive. Diagnostic ultrasound imaging results showed that no tears were found. Her main complain and problem was: she couldn't hold her right shoulder down in one straight line with left one because of pain and lack of stability of shoulder girdle. Also, she couldn't feel the right place or stable position for right side shoulder girdle, because of changed body awareness.

2.2 Instrumentation

DAid Smart shirt was used to capture and monitor shoulder gridle motion during physiotherapy intervention and training sessions. This smart garment was developed in collaboration of Riga Technical University and Riga Stradins University for posture monitoring and corrections in advanced motor tasks. DAid Smart shirt represents tight shirt with four embedded highly sensitive knitted strain sensors. Sensor reactions are transferred via sewn electro conductive lines to data acquisition electronic device and then via Bluetooth to computer or smartphone. Specific sensors placement provides independence of sensors reactions to patient's shoulder elevation-depression and protraction-retraction movements (Fig. 1). Quintix Biomechanics v26 (UK) optical motion capture system was used for reference, as well.

2.3 Intervention

The motor control retraining package was targeted at correcting movement impairments of the scapula by re-educating muscle recruitment [4, 6]. There were 2 components to the package: (1) motor control exercises to correct alignment and coordination, which involve (a) learning optimal scapular orientation at rest and then controlling optimal orientation during active arm movements in

scapular, frontal, sagittal plane [4], and (b) muscle specific exercises for *m.trapezius* lower part and *m.serratus anterior* [7].

During the motor control exercises, scapular position was optimized in relation to the thorax, initially by being altered manually by the therapist on a subject specific basis. This involved the therapist using observation and palpation to alter orientation/alignment of the scapula and clavicle using the following guidelines: acromion should be higher than the superior medial border of scapula; the spine of the scapula should be 15–25° rotated in the coronal plane; medial border and inferior angle of scapula should be tight against the rib cage; and the clavicle should have a slight posterior rotation in the frontal plane [4]. The participant was then taught to actively reproduce this orientation using visual (in a laptop screen line from DAid Smart Shirt should be as still as possible, approximately value should be <0.02 mV), auditory (from therapist there usually are instruction: *keep your shoulder down*).

Once the scapula was placed into an optimal position, the participant was asked to control the orientation of the shoulder girdle while lifting arm to 90° humeral elevation in the frontal, sagittal, and scapular planes. Movements were performed at a slow, controlled pace and repeated for 2 min.
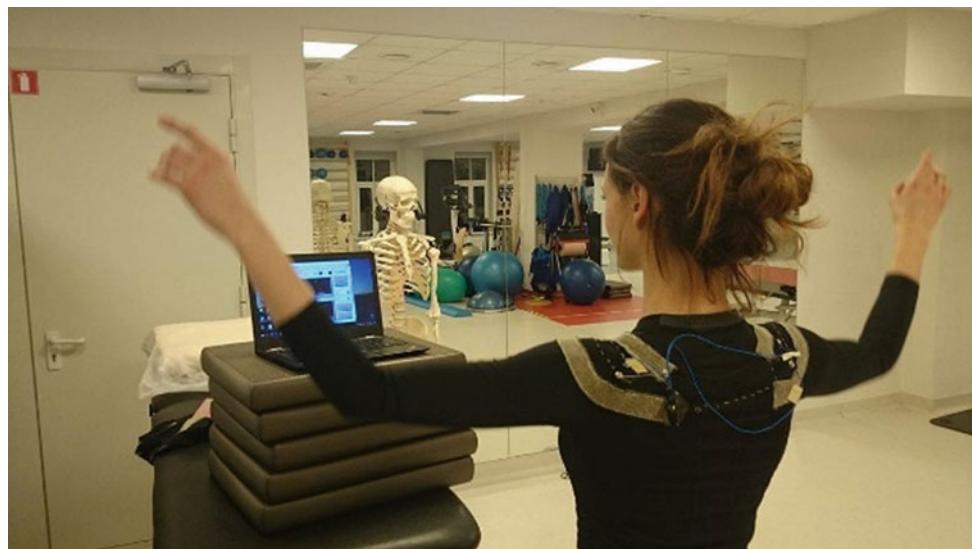
Once the participant had regained sufficient control of scapular orientation during arm movements, muscle specific motor control exercises were introduced (after 4 weeks).

These exercises required the participant to initiate and maintain optimal scapular orientation whilst recruiting *m. serratus anterior* and lower trapezius [7]. Retraining was performed 4 weeks, with 10 follow-up appointments with the physiotherapist during that time, once a week there was one monitored training session for ballet *Scheherezade and her tales* (Music by Nikolai Rimsky-Korsakov and Zoltan Kodaly), Sun variation theme out of laboratory environment, in real time and place, where she had training sessions.

2.4 Data Analysis Methods

Data from DAid Smart shirt were analyzed by using descriptive statistics and correlation methods and then compared with results obtained using Quintix Biomechanics v26 (UK) video analysis software. It was defined that Smart Shirt data values less than 0.02 mV corresponds to stable shoulder gridle during both left and right-side arm movements in motor control tasks, therapeutic exercises, ballet training sessions. Thus, sensor signal value 0.02 mV was assumed as threshold for scapular stability duration in ballet training sessions, motor control exercises and therapeutic exercises comparative studies. Amount of values less than 0.02 mV reflect scapular stability time during tasks and pointed out in percent (%).

Fig. 1 DAid smart shirt in clinical settings

3 Results

DASH Outcome Measure score after physiotherapy sessions was 4.2 points. DAid Smart shirt data and right shoulder girdle angular movement range and correlation coefficient of the DAid Smart shirt data and shoulder girdle angular movement was 0.96 (see Fig. 2), it means, that these both methods were coherent in time.

Right side scapular stability duration in motor control exercises increase for sagittal plane motion task from 59% in first session to 100%—last session, frontal plane motion task from 28 to 100%, scapular plane motion task from 49 to 99% (see Fig. 3).

Fig. 2 Smart shirt and movement video analysis data correlation
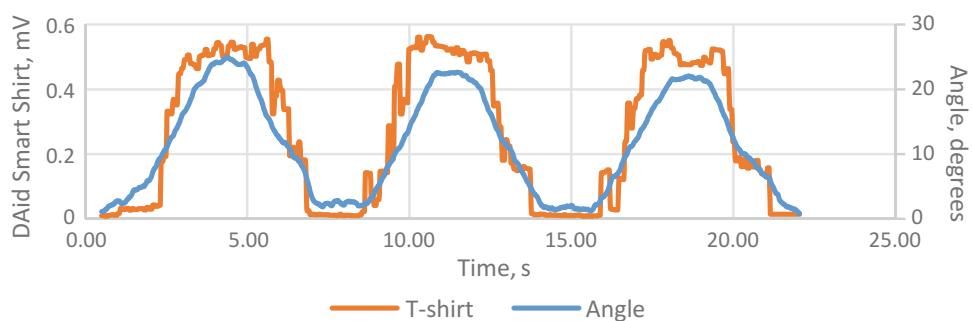
Fig. 3 Right side scapular stability duration before and after motor control exercises
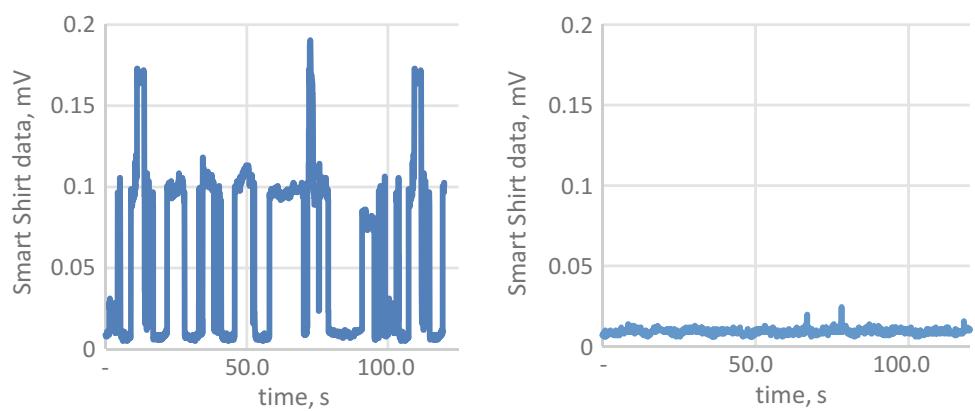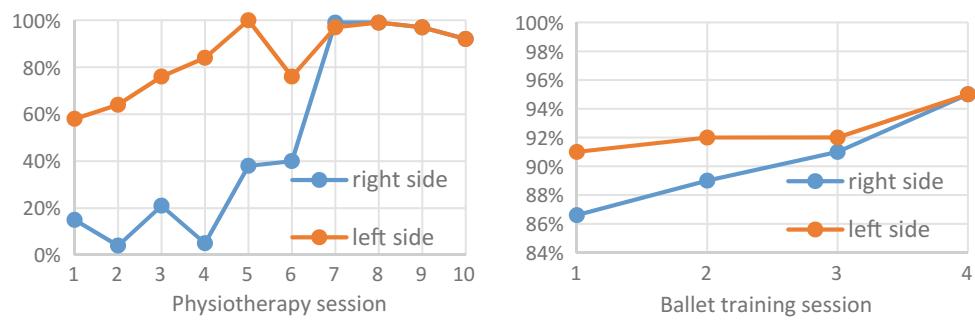
Fig. 4 Right side scapular stability during therapeutic exercise and during ballet training sessions

For therapeutic exercise right side shoulder girdle stability increase from 15 to 92% and scapular stability duration also increased in ballet training sessions (see Fig. 4).

4 Conclusions

Designed DAid Smart shirt can be objective and convenient device for shoulder motion monitoring. For both: patient and physiotherapist it can be used as effective assisting device in addition to conventional physiotherapy for shoulder girdle motion capture and monitoring during advanced motor tasks such as shoulder motor control exercises and ballet training sessions. During training tasks for shoulder joint patient can correct scapular position to look on the computer screen. For physiotherapist this is effective assisting device, because permanent presence of physiotherapist is not needful, as a result therapy process is more optimized, but still effective.

Conflicts of Interest The authors declare no conflict of interest.

Ethical Statements Participant gave her written, informed consent for inclusion before they participated in the study. The study was conducted in accordance with the Declaration of Helsinki, and the study protocol was approved by the Ethics Committee of Riga Stradins University (4/05.10.2017).

References

1. Arendt, Y. D., Kerschbaumer, F., Verletzungen und berlastungserscheinungen im professionellen Ballett, Zeitschrift für Orthopädie und Unfallchirurgie, Z Orthop Ihre Grenzgeb 141(3), 349–356 (2003)
2. Watts, A.R., Williams, B., Kim, S.W., Bramwell, D.C., Krishnan, J., Shoulder impingement syndrome: a systematic review of clinical trial participant selection criteria, Shoulder & Elbow 0(0) 1–11, (2016)
3. Sataloff, T.R., Brandfonbrenes, G.A., Lederman J.R., PERFORMING ARTS MEDICINE, 3rd Edition. Science and Medicine. Inc. USA. (2010)
4. Worsley, P., Warner, M., Mottram, S., Gadola, S., Veeger, H., Hermens, H., Morrisey,D., Little, P., Cooper, C., Carr, A.,Stokes, M. Motor control retraining exercises for shoulder impingement: effects on function, muscle activation and biomechanics in young adults, Journal of Shoulder and Elbow Surgery 22(4): e11–e19 (2013)
5. Wang, Q., De Baets, L., Timmermans, A., Chen., W., Giacolini, L., Matheve, T., Markopoulus, P. Motor Control Training for Shoulder with Smart Garments. Sensors (2017)
6. Comerford, MJ.; Mottram, SL. Kinetic control: the management of uncontrolled movement. Elsevier; Chatswood, N.S.W: (2012)
7. Ekstrom, R., Donatelli, R.,Soderberg, G., Surface Electromyographic Analysis of Exercises for the Trapezius and Serratus Anterior Muscles, Journal of Orthopaedic & Sports Physical Therapy, 33:247–258 (2003)

Detection of Excessive Pronation and Supination for Walking and Running Gait with Smart Socks

Peteris Eizentals, Alexei Katashev, Alexander Okss, Zane Pavare, and Darta Balcuna

Abstract

Excessive pronation and supination are gait conditions that could lead to such injuries as ankle sprains, shin splints, Achilles tendinitis and others. Early detection of excessive pronation and supination in running and walking gait are important for injury prevention not only for professional athletes but also for the general population. Unfortunately, the typical equipment necessary for detection of these conditions is relatively expensive and therefore is not widely used by non-professionals. Moreover, most of the typical equipment is either designed for operation under laboratory conditions only or is too bulky and consequently affects the performance of the wearer during the performed activity. This study proposes a method for pronation and supination detection by using smart textile socks with integrated pressure sensors and a specific sensor measurement processing algorithm. Each sock has five sensors, one on the heel, two in the middle and two in the front sole area. These sensors are knit from a conductive thread and have a resistivity inversely proportional to the pressure, which allows monitoring of the feet pressure at different parts during a physical activity. A special pressure vector is calculated from the sensor values to characterize the step. The value of this pressure vector give information about the step and allows detection of excessive supination and pronation in the gait. The preliminary tests demonstrated a significant difference between the pressure vector of a normal gait and gait performed with pronation and supination, thus allowing detection of these gait conditions.

1 Introduction

Foot pronation and supination are normal rolling movements occurring during the gait at the subtalar joint of the foot. Excessive pronation and supination, however, can lead to serious injuries such as shin splints, anterior compartment syndrome, patellofemoral pain syndrome, plantar fasciitis, tarsal tunnel syndrome, Achilles tendonitis, heel spurs and others. Typical approaches for detection of excessive pronation or supination are gait video analysis, pressure plates and special pressure insoles [1].

The smart textile sensor is a relatively recent approach to monitoring the foot plantar pressure. The main benefit of these sensors is the relatively low cost and ability to be directly embedded into socks, thus they can be used with any kind of shoes, both indoors and outdoors. Although a reasonably accurate plantar pressure measurement can be acquired with smart textile socks, it is generally unclear, how to use the acquired information for diagnostic and prophylactic purposes. As a result, such socks are typically used for step counting for runners, and only few researchers put attention to feet plantar pressure in general [2, 3] or for more specific applications, such as for patients with diabetic neuropathy [4].

P. Eizentals (✉) · A. Katashev
Institute of Biomedical Engineering and Nanotechnologies,
Riga Technical University, Riga, Latvia
e-mail: peteris.eizentals@gmail.com

A. Katashev
e-mail: aleksejs.katasevs@rtu.lv

A. Okss
Institute of Design and Technology, Riga Technical University,
Riga, Latvia
e-mail: aleksandrs.okss@rtu.lv

Z. Pavare · D. Balcuna
Medical Education Technology Centre, Riga Stradins University,
Riga, Latvia
e-mail: zane.pavare@rsu.lv

D. Balcuna
e-mail: darta.balcuna@rsu.lv

The main purpose of this paper is to introduce a novel method, specially designed for low sensor count smart textile socks for plantar pressure analysis and abnormal plantar pressure detection for excessive pronation and supination diagnostics. The proposed method converts the sensor values into a geometric vector, which in turn is used to describe a step. It has been shown in this paper that such constructed step vectors differ depending on the level of pronation or supination of the step.

This paper is organized as follows. First, a brief description of the used hardware is given. Then, the developed pressure vector algorithm is explained in details. Afterwards, a set of experiments is described and the results are provided. Finally, the results of the experiments are discussed and conclusions are drawn.

2 Materials and Methods

2.1 Smart Socks

This paper proposes a novel method for excessive pronation and supination detection using smart socks with textile pressure sensors and a special data processing algorithm. The smart socks used in this research is a custom built sock that contains 5 pressure sensors, two are under the front of the foot, two in the middle and one is on the heel (Fig. 1) [5].

The electronics of the smart socks consist of microcontroller that collects the sensor data, and a Bluetooth module for sending the collected data to a laptop for processing. Keeping electronics very simple allow creating the data

acquisition module compact and lightweight, which in turn minimizes its effect on the task performed by the wearer. For this experiment, the data receiving from the computer side was performed by a custom-designed LabView script while data analysis was performed with MatLab.

2.2 Pressure Vector

A special sensor measurement processing and visualization method is proposed in this paper. The proposed data processing algorithm conceptually is similar to the center of the mass information, provided by most of the typical foot plantar pressure calculation software. Although the used smart socks have sensor configuration as shown in Figs. 1 and 2, the method itself is applicable to any sensor configuration. First, each sensor measurement is first inverted and then normalized to values between 0 and 1 with a sliding window local normalization according to Eqs. 1–3,
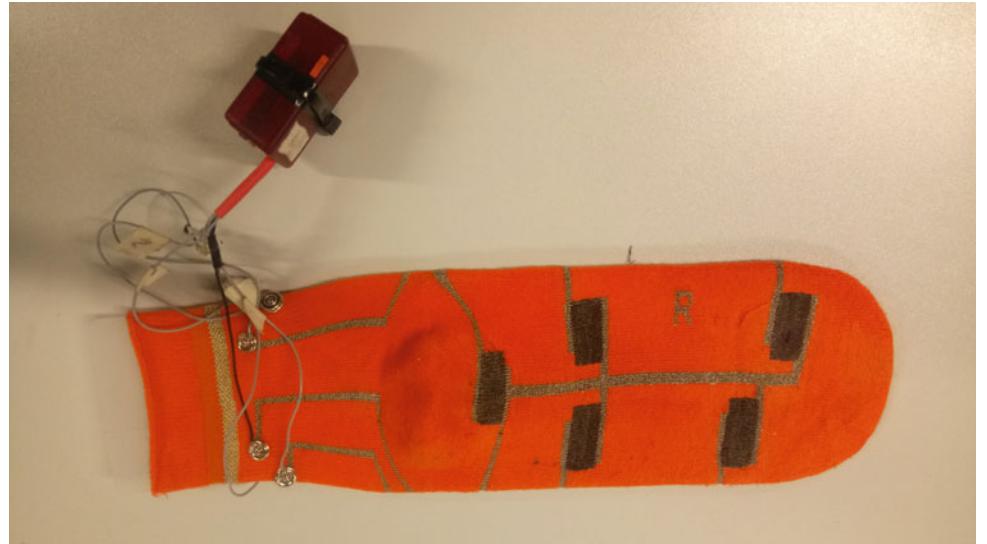
$$u_i' = \frac{u_i - \min_{a \le i \le b} u_i}{\max_{a \le i \le b} u_i - \min_{a \le i \le b} u_i} \tag{1}$$

$$a = i - 0.5w \tag{2}$$

$$b = i + 0.5w \tag{3}$$

where u_i is the corresponding measurement and w is the normalization window size. This allows ignoring the sensitivity difference between sensors. Next, all sensor measurements are summed to obtain the summary value of all used sensors, which is utilized for determining the

Fig. 1 Smart textile sock with 5 pressure sensors and data acquisition hardware

starting and ending points of separate steps. Finally, the endpoint coordinates of the pressure vector are calculated for each measured point of the step according to Eqs. 4 and 5,

$$V_x = \sum_{i=1}^{n=5} k_i u_i' \cos \varphi_i \tag{4}$$

$$V_y = \sum_{i=1}^{n=5} k_i u_i' \sin \varphi_i \tag{5}$$

where $k = [\, 1 \quad 1 \quad \cos\alpha \quad \cos\alpha \quad 1 \,]$ is a coefficient assigned to each sensor and $\varphi = [\, \pi - \alpha \quad \alpha \quad \pi \quad 0 \quad 3\pi/2 \,]$ is the assigned angle of the sensor ($\alpha = 75°$).

In short, the pressure vector is constructed by assigning a unit vector pointing from an arbitrary origin of coordinate space to each sensor. The moduli of these sensor vectors are equal to the value of each respective sensor measurement. All obtained vectors then are summed up to obtain a single vector, which points to the place of maximum pressure. The trajectory of the end-point of this vector during a single step is used to describe this step.

2.3 Performed Experiments

To verify the ability of the proposed method to distinguish between normal steps and steps with excessive pronation and supination, a set of experiments was performed. Three individuals walked for approx. 10 m (10–15 steps) long distance while simulating one of the three gait conditions, normal gait, gait with excessive pronation and gait with excessive supination. Additionally, to discover the optimal way of detection, the experiment was performed under three conditions, barefooted, wearing normal shoes, and wearing sports shoes. In total 37 normal, 22 over-pronated and 22 over-supinated walks were performed. Data of all performed algorithms was collected and processed according to the above-described algorithm.

3 Results and Discussion

To verify the applicability of the designed method for detection of excessive pronation and supination conditions using smart textile socks, foot plantar pressure measurements were performed for three individuals for three gait types under three conditions. The used gait types were a normal walk, walk with over-pronation and gait with over-supination. The used conditions were without shoes,

with normal street shoes, and with sports shoes. Measurements were processed according to the above-described algorithm.

Due to the space limitation, only some of the results are provided here. The results provided in Fig. 3 are of one person and are organized as follows, row 1 is normal gait, row 2 is gait with pronation, and row 3 is gait with supination, column 1 is a bare walk, column 2 is walk in normal shoes and column 3 is walk-in sports shoes. The lines in the presented graphs are the pressure vector end-point movement during each step.

Although the lines might seem chaotic at first, a pattern can be recognized if they are compared to the sensor configuration image in Fig. 2. Each of the lines starts from the bottom (sens. 5) as the heel is the first to touch the ground, then they trace the rest of the sensor activation time and power. For example, in Fig. 3a it can be clearly seen that the sensors activate in such order: heel (5) → outside of arch (4) → inside of arch (3) → outside of the sole (2) → inside of the sole/big toe (1). For comparison, the lines for Fig. 3 b and c doesn't show such a distinct pattern, which can be explained by additional pressure to the sock from shoes. Row 2 of the Fig. 3 shows a clear pronation, as the accent on the sensor 3 is dominant during the initial phase of the step and the pressure vector moves considerably to the left. Over-supination (row 3) seems pretty obvious when
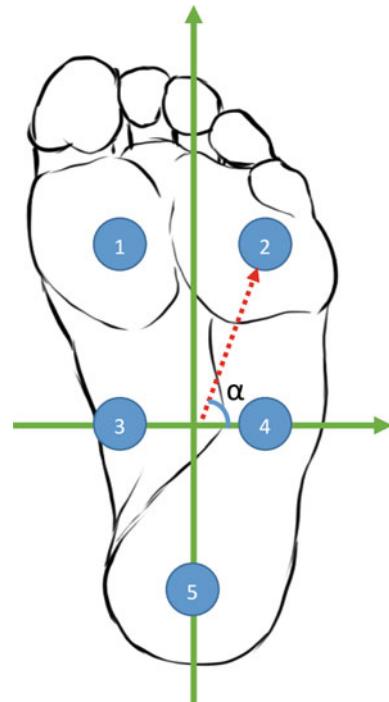
Fig. 2 Sensor locations and arbitrary coordinate frame of the pressure vector
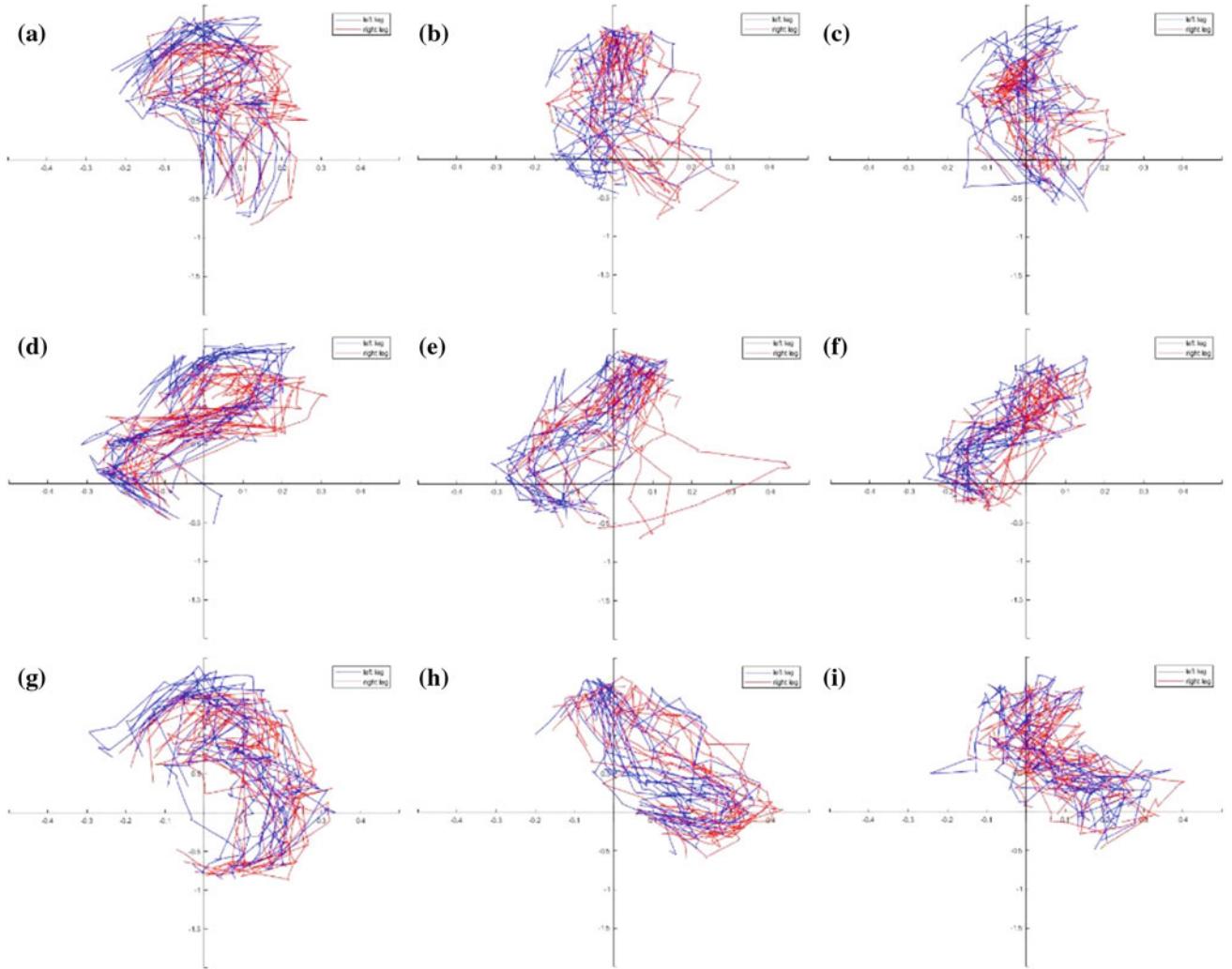
Fig. 3 Example of experimental result, **a–c** normal walk, **d–f** pronation, **g–i** supination, **a**, **d**, **g** no shoes, **b**, **e**, **h** normal shoes, **c**, **f**, **i** sport shoes

compared to the normal walk, as the force vector moves considerably to the right. Without normal walk as reference, however, it would be more difficult to decide if the supination is excessive or not. This is due to the fact that the normal gait is always to some degree with supination, provided by the arch of the foot. Some steps in most figures are with significantly different pressure vector shape. Such vectors are explained as missteps that participants reported making occasionally.

4 Conclusions

This paper described a novel method for excessive pronation and supination detection using smart textile socks. In the described method a pressure vector was constructed from the sensor pressure data to describe each step. It was proved experimentally that these pressure vectors can be used to

detect excessive pronation or supination of a step. It was concluded based on the experimental results that the used shoe type doesn't affect the measurement considerably as long as the shoe doesn't apply excessive pressure on the sock and well-fitting socks are used.

For future work, the data acquisition hardware will be improved, as it was concluded that the current sampling rate is too low for a good quality result. Additionally, it is necessary to collect measurements of a wider population sample, especially real patients, to develop guidelines for connecting the pressure vector image with physical conditions.

Conflicts of Interest The authors declare that there is no conflict of interest.

References

1. J. Berengueres, M. Fritschi, R. McClanahan, "A smart pressure-sensitive insole that reminds you to walk correctly: An orthotic-less treatment for over pronation", Engineering in Medicine and Biology Society (EMBC), 2014 36th Annual International Conference of the IEEE

2. O. Tirosh, R. Begg, E. Passmore, N. Knopp-Steinberg (2013), "Wearable Textile Sensor Sock For Gait Analysis", Seventh International Conference on Sensing Technology

3. Xiaoyou Lin and Boon-Chong Seet, "Battery-Free Smart Sock for Abnormal Relative Plantar Pressure Monitoring", IEEE Transactions on Biomedical Circuits and Systems, vol. 11, No. 2, April 2017

4. A. Perrier, N. Vuillerme, V. Luboz, M. Bucki, F. Cannard, B. Diot, D. Colin, D. Rin, J.-P. Bourg, Y. Payan, "Smart Diabetic Socks: Embedded device for diabetic foot prevention", IRBM 35 (2014) 72–76

5. A. Oks, A. Katashev, E. Bernans, V. Abolins, "Smart Socks System as an Equipment to Analyze Temporal Parameters of Human Gait and Running", Proceedings of the 11th International Scientific and Practical Conference. Vol. 3, 238–241

Development of a Customized Wrist Orthosis for Flexion and Extension Treatment Using Reverse Engineering and 3D Printing

Leonardo A. García-García●, Marisela Rodríguez-Salvador●, and Marcos David Moya-Bencomo

Abstract

Hand disability implies impairment and limitation in daily activities, affecting patient's life quality. Broken bones, congenital conditions or cerebrovascular diseases frequently demand the use of structural support in the form of orthoses. Orthoses are categorized according to their mechanical functions in: static, static progressive or dynamic. While static orthoses are usually made of a single piece and do not allow movement, static progressive and dynamic orthoses are made of a main body with assembled with mechanical elements such as rods, pins, straps, springs, etc., thus allowing a limited amount of movement. Hand orthoses demand a high degree of personalization to suit patients' anatomy and pathology. A new application of the reverse engineering is proposed. Here is described a new multidisciplinary method for the development of static progressive and dynamic orthoses for the hand for the rehabilitation of hand disabilities. The method involves the image acquisition of the patient's anatomy and the mechanical design of the orthosis by Computer Aided Design (CAD) software. This method offers a high degree of personalization and the development of low volume hand orthoses with a reduction of weight at low cost by using 3D printing. The case presented on this paper is the design of an original dynamic orthosis for flexion and extension treatment of the wrist. The main body of the orthosis was designed using the data from Computer Tomography (CT) scan images and a CAD software to fit the hand anatomy. Mechanical elements were chosen to provide a variation from 0° up to 90° of extension, and up to 90° of flexion with mechanical resistance to assist in the improvement of the wrist flexor muscles strength.

1 Introduction

Disabilities constrain daily activities, thus affecting life quality. Hand disability as a result of congenital conditions, injuries, or cerebrovascular diseases has a huge impact on patients' daily activity [1]. Orthoses are frequently used as a complement for physiotherapy as they provide structural support, helping to avoid spasticity. Several types of orthoses exist but, no practical guidelines have been defined so far [2–4]. The aims of splinting are protective sensation and prevention of contracture and deformity [5, 6]. The principal advantage of orthoses is the duration of their effectiveness, because they can be placed and left for several hours without the presence of a physiotherapist or nurse [4].

Orthoses are categorized according to their mechanical functioning in: static, dynamic, or static progressive [6–8]. Static splints constraint the movement as the structure is rigid, static progressive constraint the movement with rigid elements but can adjust the position as the tissue heals, and dynamic orthoses allows movements trough assemblies of mechanical elements such as springs, wires, or elastic bands [3, 9, 10]. The goal of both, dynamic and static progressive splints is to apply small amount of force over a prolonged period to influence the healing of tissue, where the cells respond to the tension applied, thus the necessity of a well-designed dynamic splinting, based on both, patient's anatomy and the outcome sought [11]. Dynamic Orthoses (DO) and Static Progressive orthosis (SPO) are

L. A. García-García (✉) · M. Rodríguez-Salvador · M. D. Moya-Bencomo
Tecnologico de Monterrey, Escuela de Ingeniería y Ciencias, Monterrey, Nuevo Leon, Mexico
e-mail: leonardogarcia@itesm.mx;
Leonardo.azael.garci@gmail.com

M. Rodríguez-Salvador
e-mail: marisrod@itesm.mx

M. D. Moya-Bencomo
e-mail: marcosmoya@itesm.mx

recommended in interventions for patient not which require more than the use of static orthoses [5]; their use has been well accepted and the improvement during and after training was demonstrated [6].

To accomplish these task, custom-made orthoses needs to be handmade by a skilled person. This is achieved using plaster of Paris or by forming sheets of thermoplastics to form the base of the orthosis according to the patients' anatomy. Thermoplastics are cut, heated, molded and adjusted, a complex stage requiring simultaneously of design and fabrication, a process prone to inaccuracies in the fit and functioning, causing discomfort and poor aesthetics, reducing the tendency to wear the orthosis as prescribed [4, 11]. If the design is poor, the functions can cause shear stress, misalignment, or excessive pressure. In the design of dynamic orthoses is poor or if the force is applied in the wrong direction, the tissue can be further damaged [11].

The use of reverse engineering has been proposed as the most suitable method for the fabrication of custom DO and SPO hand orthoses. This method is widely used to obtain digital models from existing physical parts and has been applied in industries such as software engineering, animation, and mechanical engineering, where the use of CAD/CAM/CAE systems are advantageous for this purpose [12]. This methodology can be applied for the making of dynamic orthoses, where a high degree of personalization is sought. The use of 3D printing, also known as Additive Manufacturing (AM) was developed to fabricate three dimensional objects from 3D models, designed in a computer aided design (CAD) software or by image acquisition methods, such as Computer Tomography (CT) scans, Magnetic Resonance Imaging (MRI), or 3D scanners. 3D printing provides a new method of fabrication for complex shapes and designs in a single process with a reduction of material waste, it is therefore advantageous over conventional manufacturing processes.

This research paper proposes a new methodology based on reverse engineering and 3D printing for a new application, the development of personalized dynamic or static progressive orthoses for the hand. The methodology involves the data acquisition, data processing, design and fabrication of the orthosis. A particular case is here presented, which discusses the development of a dynamic orthoses for flexion and extension of the wrist treatment to increase the Passive range of motion (PROM).

2   Materials and Methods

The methodology was based on common procedures described in the literature for the development of hand orthoses [11, 13], which involves at first the diagnostic and best selection of treatment, where the type of orthoses is chosen according to the number of joints involved and type of force required, followed by the drawing of the contour of the on a piece of paper. The contour is then transferred to the material, usually Low Temperature Thermoplastics (LTT), to be later cut and heated in hot water until it is flexible enough to shape it and be fitted to the patient, and adjust as required. Finally, selection or fabrication of the outriggers is done, and the mechanical active elements are chosen and the assembly is carried out. This process can be improved using emerging technologies, such as 3D scan and 3D printing.

The use of 3D printing for the development of static orthoses for the hand has been explore by authors such as Paterson [4, 13, 14], Palousek [15], Baronio [16], and Kim [17]. The methods involve the data acquisition using imaging techniques such as MRI or photogrammetry, followed by the data processing, where the 3D model of the hand is made for a further design of the orthosis. This model subsequently exported to a digital file to be 3D printed. There results offer advantages such as low cost and personalization, but the process can take up to 24 h from data acquisition to the final product, being the 3D printing the process that takes more time to be completed [13, 15, 17]. The time also is related to the volume to print, and this time can be improved adding fenestrations [13, 17]. However, if the patient needs a replacement for the orthosis, the 3D model can be used to print a new one.

The methodology here proposed includes the CAD design of the whole assembly using a 3D modeling package, as described in Fig. 1, which describes the flow chart followed for the development of a dynamic orthoses for the hand to aid in the improvement of the ROM at the flexion/extension of the wrist.

The first step is the definition of the type of orthoses. For this case, a 60 years old male patient of 65 kg weight and 1.60 m height was selected. The patient required rehabilitation to increase the wrist ROM, and the use of a dynamic orthoses was identified as an effective treatment. The identification of the elements were the base splint, two outriggers, two torsion springs, and the fasteners for the assembly. The image acquisition was carried out using MRI images. A total of 150 slices with a 0.97 mm thickness were obtained. A segmentation software was afterwards used to generate the 3D model, ScanIP® [18]. The model was exported as a point cloud file and processed in Solidworks® to generate a solid model of the hand. The design proposed used torsion springs for to applied a constant load.

The springs were selected from a commercial catalogue, as the fabrication of custom-made springs increases the cost. To select the springs the torque was calculated with the following considerations: as the joint lacks of force, only the weight of the hand was considered, which accounts for an average of 0.57% of the total body mass [19, 20]. The load was applied at 18 cm from the axis of rotation of the wrist,
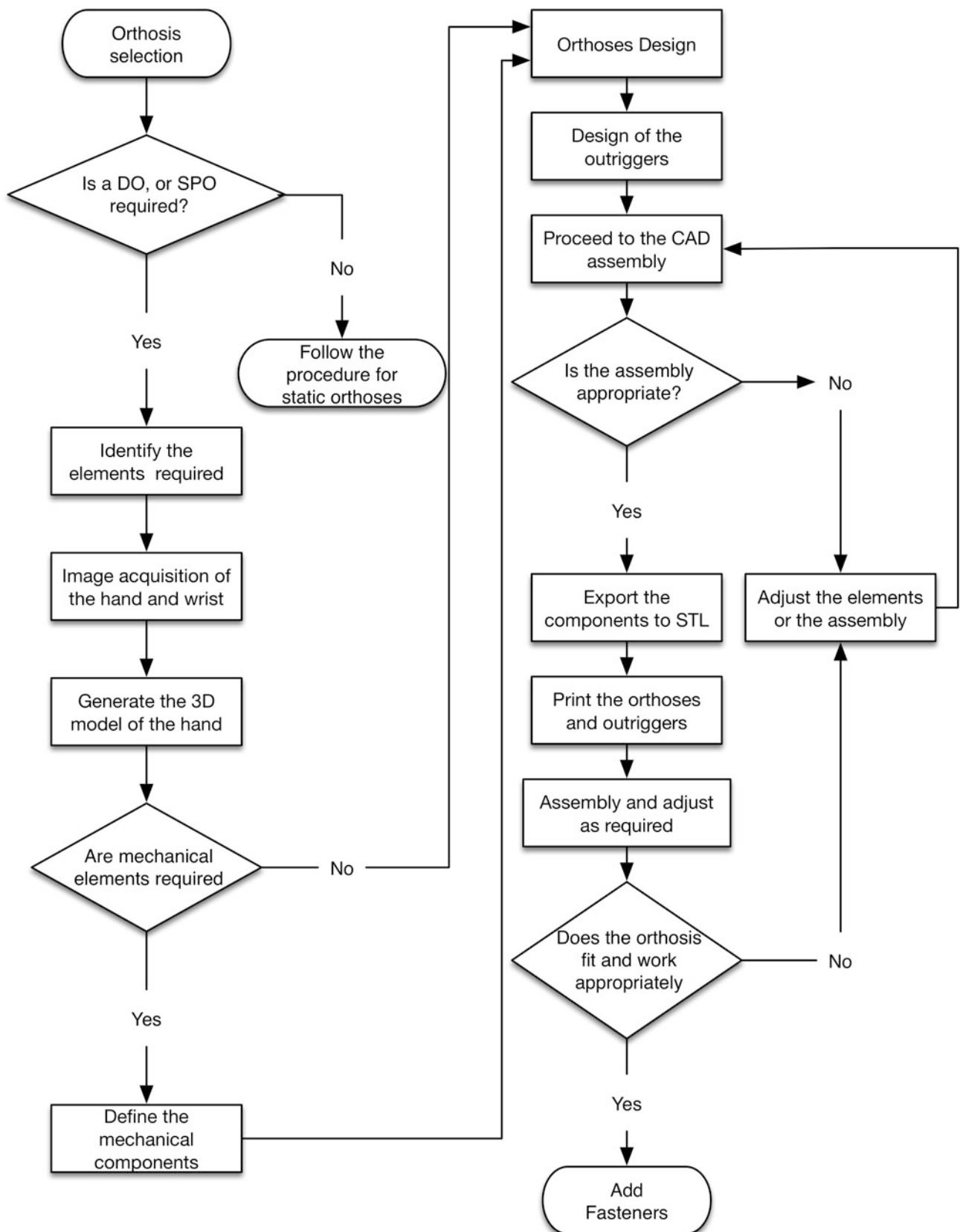
Fig. 1 Methodology developed for the fabrication of DO and SPO using additive manufacturing

located at the center of the capitate. For this case, the load was 3.65 N, and the torque of 0.65 N m. As a result, a pair of 180° torsion spring with wire diameter of 0.64 mm, outer dimeter of 5.72 mm and an arm length of 19 mm were chosen [21]. Each of the was placed at the outer and inner center of rotation of the outrigger axis.

The base splint base was first designed from the hand model and modifications were made to allow the full PROM. Lateral housings for the springs were added, for the assembly of the orthosis, outriggers, and springs. The outriggers designed based on the anatomy, force, and movement of the hand, considering the ROM. The elements were exported to as STL to be printed using PLA plastic, finally Velcro fasteners were added. The orthosis does not include grasp elements, as it was recommended to be able to adapt conventional handles as the patient condition progresses.

3 Results and Discussions

The CAD process followed and the final design are shown in Fig. 2. It is important to highlight that the handgrips for the palmar flexion to grasp the orthosis was not designed, as it was recommended to be able to adapt any shape required as the grip forces progresses, going from a bulky one up to a normal handgrip.

The application of the new methodology used for the development of DO and SPO the findings suggest that it is feasible the use of reverse engineering. Customization according to patient and treatment was also demonstrated, nevertheless, clinical trials are required. The use of MRI images for the construction of the 3D model for the fabrication of the DO for wrist flexion/extension was proven to be feasible. However, the processing of the images to generate the CAD model was longer than the expected, about 5 h. In this case, a new anatomy acquisition method needs to be considered to reduce the time of the data processing.

This methodology was well implemented and used by a person with high skills in the use of CAD software and design, however this has not been proven by therapist, and it is assumed that they do not possess experience on this topic. As a result, a multidisciplinary team is required for the implementation of the methodology developed, moreover, the overall time of the manufacturing needs to be reduced to be implemented by therapists. Furthermore, a clinical trial needs to be carried out to test the efficiency and the life span of the orthoses.
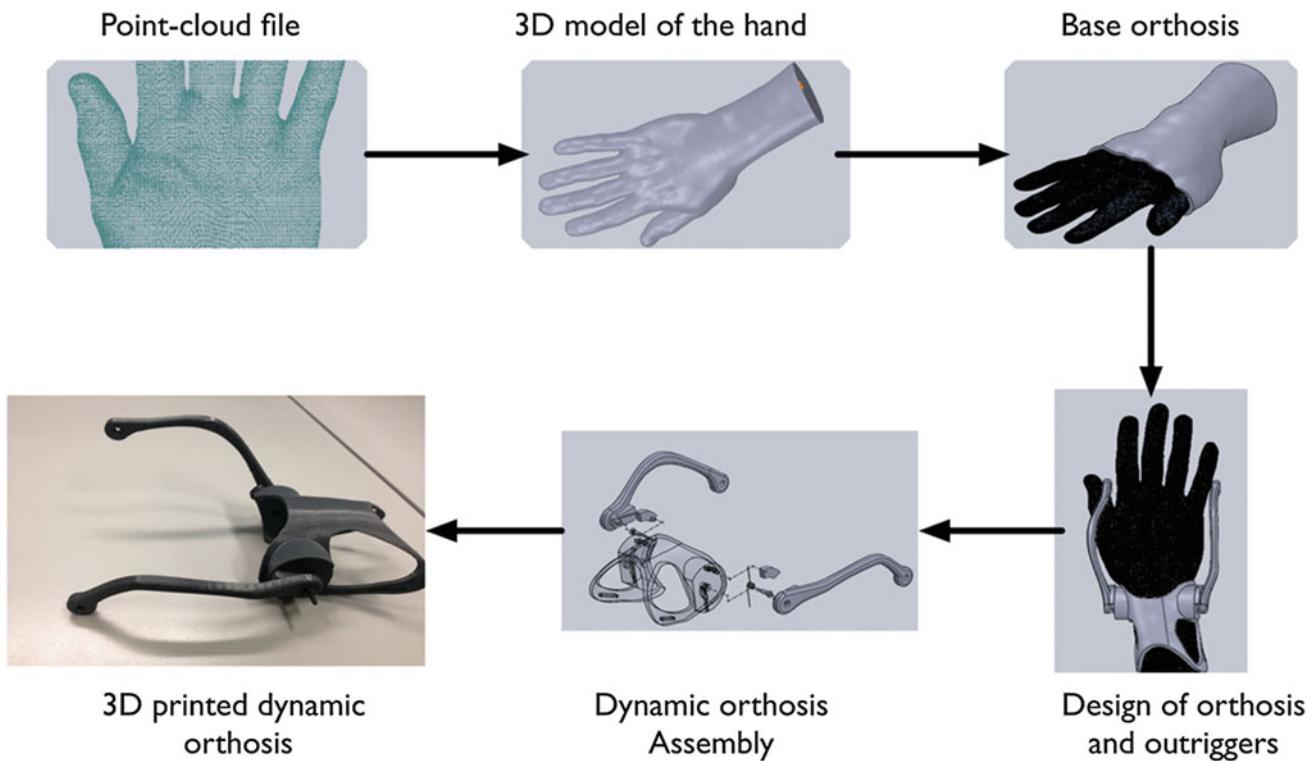
Fig. 2 CAD Process followed for the development of the dynamic orthosis for the wrist flexion/extension treatment

4 Conclusions

The use of DO and SPO have had a high level of acceptancy for rehabilitation, specially for acute-stroke patients. Although they are an effective treatment, the authors did not find strong evidence of their use. The reverse engineering method used offers a high degree of personalization of orthoses compared with standardized methods. The production of the orthosis using 3D printing is of advantage over methods where the hot material is place over patient's skin. Moreover, complex designs and patterns can be implemented to reduce weight and to allow skin to breath, improving their use and reducing the rejection, thus enabling patients to regain independence in daily life activities.

Competing Interests The authors declare that they have no conflict of interest.

References

1. Organization World Health. World report on disability. Available from: http://www.who.int/disabilities/world_report/2011/report.pdf, last Accessed 15th May 2017.
2. Colditz JC. Plaster of Paris: the forgotten hand splinting material. J Hand Ther. 2002; 15(2): 144–57. Available from: http://www.sciencedirect.com/science/article/pii/S0894113002500296.
3. Fess EE. A history of splinting: to understand the present, view the past. J Hand Ther. 2002; 15(2): 97–132.
4. Paterson AM, Bibb RJ, Campbell RI. Evaluation of a digitised splinting approach with multiple-material functionality using additive manufacturing technologies. In: Bourell D, editor. Twenty-Third Annual International Solid Freeform Fabrication Symposium. 2012. p. 656–72.
5. Andringa, A.,van de Port, I., Meijer, J.W.: Long-Term Use of a Static Hand-Wrist Orthosis in Chronic Stroke Patients: A Pilot Study. Stroke Research and Treatment. 1–5 (2013).
6. Franck, J. A., Timmermans, A. A. A., Seelen, A. M. Effects of a dynamic hand orthosis for functional use of the impaired upper limb in sub-acute stroke patients: A multiple single case experimental design study. Technology and Disability 25, 177–187 (2013).
7. Chinchalkar SJ, Pearce J, Athwal GS. Static progressive versus three-point elbow extension splinting: a mathematical analysis. J Hand Ther. 2009; 22(1): 37–43.
8. Taylor E, Hanna J, Belcher HJCR. Splinting of the hand and wrist. Curr Orthop. 2003; 17(6): 465–74.
9. Colditz J. Principles of splinting and splint prescription. Surgery of the hand and upper extremity. 1996. pp. 2389–410.
10. Fess E, Gettle K, Philips C, Janson JR. Hand and upper extremity splinting: Principles and methods. St L Missouri: Mosby; 2004. pp. 725.
11. Coppard BM, Lohman H. Introduction to orthotics: a clinical reasoning and problem-solving approach. St L. Mossouri: Mosby; 2015.
12. Kumar A., Jain, P. K., Pathak, P. Reverse engineering in product manufacturing: an overview: DAAAM International Scientific Book, DAAAM International Publishing, Vienna (2013).
13. Paterson AM, Bibb R, Campbell RI, Bingham G. Comparing additive manufacturing technologies for customised wrist splints. Rapid Prototyp J. 21(3), 2015.
14. Paterson AMJ, Bibb RJ, Campbell RI. A review of existing anatomical data capture methods to support the mass customisation of wrist splints. Virtual Phys Prototyp. 2010; 5(4).
15. Palousek D, Rosicky J, Koutny D, Stoklásek P, Navrat T. Pilot study of the wrist orthosis design process. Rapid Prototyp J. 20(1), 2014.
16. Baronio G, Harran S, Signoroni A. A critical analysis of a hand orthosis reverse engineering and 3D printing process. Appl Bionics Biomech. 2016.
17. Kim H, Jeong S. Case study: hybrid model for the customized wrist orthosis using 3D printing. J Mech Sci Technol, 29(12), 2015.
18. Simpleware 2010 Reference guide. scanip, scanfe, scancad, version 3.2 Technical report Ltd. Simpleware, Exeter, UK.
19. Clauser, C., McConville, J. T., Young, J. W.: Weight Volume, and center of mass of segments of the human body. National technical information service (1969).
20. Dempster, W. T., Gaughran, G.: Properties of body segments based on size and weight. American Journal of Anatomy 120:33–54 (1955).
21. Lee Spring: Resortes de catalogo hechos a la medida. Lee Spring (2015).

Development of a Gait System in Hypogravity Simulation for Physiological Studies on Earth and in Space

Ana Karla Oliveira Leite, Thais Russomano, Marlise dos Santos Araújo, and Júlio César Marques de Lima

Abstract

Running and walking stimulate and maintain the functioning of the musculoskeletal and cardiopulmonary systems, which are responsible for body posture, movement, strength and coordination on Earth and during space missions. This study aimed to develop a low-cost Gait System in Hypogravity Simulation (GSHS) for the study of human physiology. The developed construction consists of 5 subsystems: structural, suspension, simulation, force and communication. The GSHS is formed of a body suspension structure with a treadmill, connected to a force platform, welded upright at one end, with the volunteer suspended by a vest and elastic cables, and positioned in parallel to the ground. The maximum permitted weight for the system is 100 kg, taking into consideration the load capacity of the materials and components. A 72 kg object was pressed against the treadmill to test the force platform, and a motor with two rods and articulated mechanical feet was fastened close to the treadmill, allowing the surface to be touched during the human gait simulation. The results demonstrated the GSHS was able to suspend the object, maintaining it pressed against the treadmill without load variations. The communication subsystem stored and transferred the force platform CPU data to the computer. The force platform presented a 2.84% error in measurement of the object weight (72 ± 2.84 kg). The gait simulation test demonstrated the force platform was able to perform the real-time collection of touch time for each foot and the gait ground reaction forces. The GSHS was able to maintain communication between the force platform and data receiving system.

1 Introduction

The reduction in action of gravitational force encountered in space missions negatively affects the cardiovascular, muscular and bone systems. Muscle deconditioning may limit the ability of a crew to work due to atrophy and muscle weakness [1]. In microgravity and hypogravity, alterations also occur in the structure and function of bone cells, including changes in the cytoskeleton, cell morphology, and cell growth and differentiation, leading to osteopenia, which can progress to osteoporosis [2].

Walking and running produce a high impact that stimulates the activity of the muscles and bones responsible for maintaining posture [3], and reducing possible damage caused by exposure to hypogravity [1]. Therefore, research related to the walking pattern using reduced gravity simulator systems has grown considerably, as these are necessary to help diminish or avoid bone, muscle and cardiovascular deconditioning, before, during and after a space mission [1, 2].

Along with the evolution of space exploration, research on human physiology and biomechanics in reduced gravity also received close attention. Research on locomotion in hypogravity has been conducted since the 1960s [4–7]. The development of some gait simulators were used as a source of research and study [8–11], two of them stand out by simulating gait in the supine position as well as the Gait System in Hypogravity Simulation (GSHS), they are NASA's enhanced Zero-Gravity Locomotion Simulator (eZLS) [8] and the vertical treadmill exercises of Jordan and collaborators [11].

The development of a GSHS enables study of the influence of such reduced gravity environments while astronauts are in Earth orbit. The present study aimed to develop a

A. K. O. Leite (✉) · M. dos Santos Araújo · J. C. M. de Lima
Microgravity Centre, Pontifical Catholic University of Rio Grande do Sul, Porto Alegre, Brazil
e-mail: ana.karla@acad.pucrs.br

T. Russomano
Faculty of Life Sciences & Medicine, CHAPS, School of Basic and Medical Biosciences, KCL, London, UK

system for the simulation of walking in hypogravity, allowing evaluation of human physiology and biomechanical aspects.

2 Methods

The first phase of the project considered the definition of the functional and structural components. The prototype (see Fig. 1) consisted of the following subsystems: **structural**, based on frames and metallic supports; **suspension**, which involved the addition of a support for securing the treadmill in the vertical position, and adaptation of the straps and cables, as well as the harness used for suspension; **force**, composed of the ergometric treadmill and force platform with four load cells, the instrumentation circuit for these cells, 24-bit A/D converter, memory and a microcontroller to control the system; **communication**, responsible for the wireless transmission of the data collected from the force platform, with interaction between the microcontroller and a pair of ZigBee-type radios; **visualization and data storage**, with the use of a desktop computer and applications for data analysis; and finally, **simulation**, comprised of a set of elastic ropes. This elastic ropes allow the adjustment of different tensions, the software on the personal computer shows the data of the force platform (load), and with this, the researcher will adjust the tension of elastic ropes to simulate the application of different loads on the lower limbs of the volunteer.

2.1 Electronic Subsystems

An ergometric treadmill (Polimet, model EP-1600) was fixed in the pyramidal structure. Four load cells with a capacity of 50 kg were used to measure the ground reaction force. A printed circuit board used 4 integrated HX711 circuits for amplification and to perform the A/D conversion of the load cell signals, sending them to an MSP430F2619 microcontroller, which processed the data and sent it to the desktop computer (visualisation system) through a wireless communication port using a ZigBee radio.

The data collected by the MSP430F2274 from the force platform was transmitted in a "txt" format, which allows for manipulation of the data by different visualization and data analysis software. The data collected by the platform could also be viewed locally on an LCD display, to give flexibility to the tests and the system as a whole.

2.2 Force Platform Instrumentation

Four load cells with a capacity of 200 kg (total) were attached to each foot of the treadmill, connected to a printed circuit board containing four HX711 modules (one for each load cell), one MSP430F2619 microcontroller and one ZigBee module Xbee S2C.
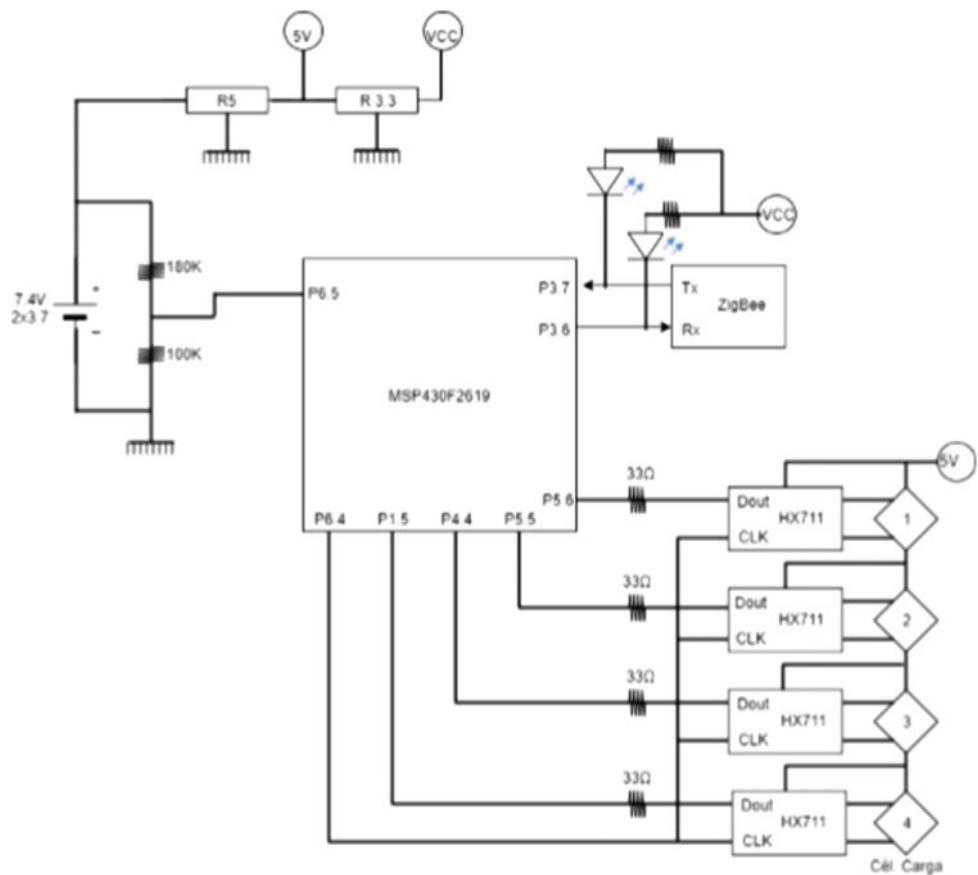
The low-cost load cells used employed only two strain gauges, and therefore, two resistors were added to complete the Wheatstone bridge circuit. The load cell signals were amplified by a factor of 128 times, corresponding to a signal of ± 20 mV when a 5 V power supply is used. The signal passed through a 24-bit A/D converter, responsible for digitizing the amplified signal and sending it via a serial port to the MSP430F2619 microcontroller. This process is carried out for each load cell.

The digitized signal arrives at the MSP430F2619 through inputs P1.5, P4.4, P5.5 and P5.6, one input for each HX711. The clock of each HX711 was placed on the same pin P5.4 to be synchronized. The MSP430 scans the digitized and amplified signal from the HX711 module integrating the four signals. To data transfer were used the USART communication ports (P3.7, P3.6) in the MSP430 and Rx, Tx in ZigBee Module (see Fig. 2). This system was powered by a 5 V voltage source.

Fig. 1 Prototype of gait system in hypogravity simulation

Fig. 2 Force platform electric instrumentation

2.3 Communication Instrumentation Subsystem

The communication subsystem consisted of a ZigBee radio module connected to an adapter that emulates a UART serial communication port in the computer. This radio connected to a further ZigBee radio module present on the force platform, allowing wireless data transmission. The data was transferred from the MSP430F2274 via the UART port, at a rate of 115,200 bps, in txt format.

An alphanumeric LCD display was connected to the microcontroller via a 4-bit parallel communication port for simplicity and hardware savings—(number of pins required for the microcontroller). It was possible to visualise on the display the load readings made by the force platform, which facilitated the tests to be conducted, such as the application of different loads on the volunteer, accomplished through the adjustment in tension of the elastic ropes.

2.4 Tests

Several experiments were performed to test the GSHS as a whole. The force platform was tested together with the communication and simulation subsystem, with a sampling rate of 80 samples per second. The aim was to evaluate the data acquisition subsystem, which is functionally interconnected with the communication and data storage subsystems. The GSHS structure was tested along with the body suspension system, and to this end, a cardiac massage simulation mannequin weighing approximately 15 kg was used. The mannequin was dressed in the KED harness and attached to the structure. A spirit level was placed on top of the chest area to help with proper alignment through the adjustment of the ropes and elastic bands used in the suspension system.

A boxing bag weighing approximately 72 kg was suspended and attached to the treadmill in order to validate the force measurement subsystem. This load was pressed against the platform and a reading of 100 samples was performed. This test was called "continuous pressure" as it applied a constant value load on the load cell strain gauges.

In order to test the force platform in a more realistic manner, a mechanical system was developed to simulate a person's walking pattern, using a motor and articulated feet mechanism, which converted rotational to linear movement. The foot mechanism used springs and shock absorbers and a

Continuous Pressure Test
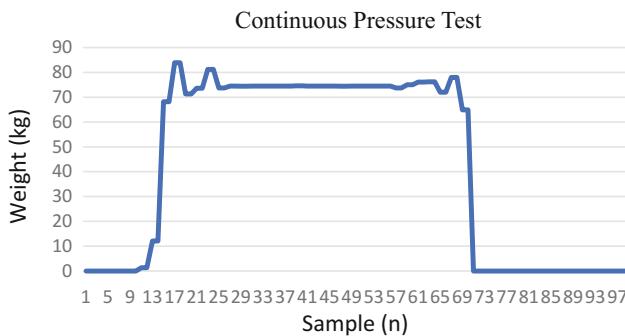
Fig. 3 Continuos pressure test at gait system in hypogravity simulation

platform composed of joints. This articulated mechanical foot simulated the walking pattern of a person in all the phases during walking.

The calibration process of the walking system was carried out using a commercially available weighing scale. This scale was placed on top of the treadmill, on which a load of known value was applied. The value displayed on the scale was used to calibrate the force platform, after which the unladen weight of the force platform was set. This procedure, however, is still in the process of improvement.

3 Results

The commercial scale measured a weight of 72 kg for the boxing bag, and the GSHS system presented a value of 74.4 kg, with a discrepancy of 2.84% between the two (see Fig. 3). A total of 100 samples of readings were performed to measure the applied load. During this procedure, variations in the load were observed, relating to the process of

placement and removal of weight from the platform, as well as the acquisition of signals without the presence of stimulus, simulating the periods preceding and following the contact of the mass (known weight) with the surface of the force platform.
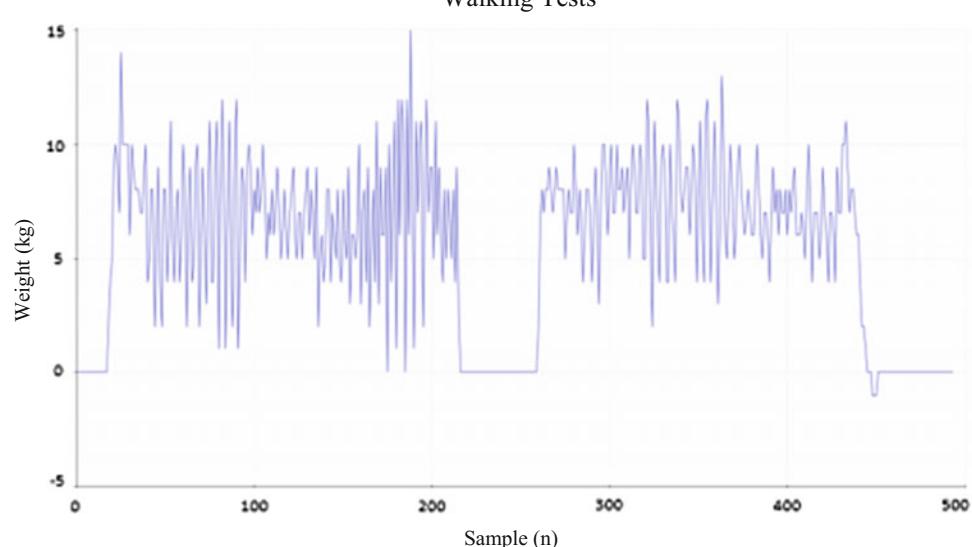
The error presented is partially due to the difficulty in performing the measurement of the load in a vertical position. The commercial scale is designed for use in the horizontal position. The GSHS is a low-cost project and, therefore, simple load cells in a half-bridge configuration were used and without calibration certification. Even with these limitations, the error reported for the equipment was less than 3%.

When using the GSHS and for the force platform to register the load, it is necessary for the mass placed to simulate the weight of the volunteer to be pressed against the surface of the treadmill, since the mass is placed perpendicular to the platform. This is possible with the use of elastic cords to adjust the tension applied, with the force platform indicating on the LCD display the apparent weight of the mass in relation to the vertical position of the force platform, and no longer the force weight. Therefore, it is possible to simulate a microgravity environment due to the postural inversion of the load used. The walking tests performed using the GSHS were conducted with a sampling rate of up to 80 samples per second, 500 samples were collected in almost 1 min (see Fig. 4).

4 Discussion

A study performed a series of tests to analyse the kinetics and kinematics of the walking pattern of 44 male volunteers, using two force platforms at a frequency of 60 Hz and six

Fig. 4 Walking test results using weight x sample in almost 1 min

Walking Tests

cameras. In addition to the expected results, the author recorded a pace of 128.7 ± 7.7 steps/min [12]. Another ones [13–15] noted 124.8 ± 5.4 steps/min, 111.6 ± 8.3 steps/min, and 119.0 ± 10 steps/min, respectively. Therefore, considering the four studies, the mean number of steps per second was of 2.01, indicating that a system that collects two samples per second is adequate. This suggests that the sample rate used to acquire data from slow or rapid walking using the GSHS platform is suitable.

5 Conclusion

The percentage error in measurement of the object weight was found to be greater than that of commercial scales, however, it is still at a threshold below 3%. The force platform was able to capture the signals, and amplified, converted, processed and transmitted them via a wireless communication port, in txt format, to a desktop computer for viewing and analysis of the data. In addition, the signals measured by the platform could be viewed on an LCD display, determining which load is being applied, and thus, simulating a microgravity environment It was possible to see through the analysis of loads that the structural and body suspension subsystems are able to safely support volunteers up to 100 kg.

The previously cited studies [12–15] support the conclusion that development of a collection system with a sampling frequency of up to 80 samples per second is sufficient and suitable for analysis of the intended data. The tests performed by these authors were conducted using adult volunteer gait analysis data, with the mean number of steps being 2 steps/second, in other words, two samples per second. By setting a rate of up to 80 samples/second, the GSHS is able to collect exercise data of a higher intensity, such as in the case of fast walking or even running.

In this first version of the prototype, the biomechanical data are summarized in the treadmill ground contact time. This data can be investigated through the graphs plotted with the force platform data. Implement GSHS with cameras for kinematic gait analysis, as well as sensors capable of showing ground reaction forces, contact time, load distribution between members, among other, are part of future projects.

References

1. Clément, G. Fundamentals of Space Medicine. France: Springer (2011).
2. Grimm, D; Grosse, J; Wehland, M; Mann, V; Reseland, J.E; Sundaresan, A; Corysom, T.J. The impact of microgravity on bone in humans. Bone 87, 44–56 (2016).
3. Cadore, E.L; Bretano, M.A; Kruel; Martins, L.F. Efeitos da Atividade Física na Densidade Mineral Óssea e na Remodelação do Tecido Ósseo. Revista Brasileira de Medicina do Esporte 11(9), 373–379 (2005).
4. Harris, R.L; Spady, Jr. A.A. Effects of pressure suits and backpack loads on man's self-locomotion in earth and simulated lunar gravity (1968).
5. Hewes, D.E; Spady, Jr. A.A. Evaluation of a gravity-simulation technique for studies of man's self-locomotion in lunar environment. Techn Note d-2176. NASA contractor report. NASA CR. United States. National Aeronautics and Space Administration, 1–34 (1964).
6. Spady, Jr. A.A; Krasnow, W. D. Exploratory study of man's self-locomotion capabilities with a space suit in lunar gravity. NASA TN D-2641. Technical note. United States. National Aeronautics and Space Administration, 1 (1966).
7. Harris, R. L; Hewes D. E; Spady, Jr. A.A. Comparative measurements of man's walking and running gaits in earth and simulated lunar gravity (1966).
8. Perusek, G.P; Lewandowski, B; Gilkey, K; Nall, M. Exercise countermeasures and a new ground-based partial-g analog for exploration.45th AAIA Aerospace Sciences Meeting and Exhibit, Nevada, 2007.
9. MIRVIS, Adam D. A Dynamics-Based Fidelity Assessment of Partial Gravity Gait Simulation Using Underwater Body Segment Ballasting. 2011. Master Dissertation. University of Maryland, 2011.
10. Disiuta, L. Desenvolvimento de uma câmara de pressão positiva para estudos em fisiologia aeroespacial. Porto Alegre: PUCRS, 2014. Master Dissertation, Faculty of Electrical Engineering, Pontifical Catholic University of Rio Grande do Sul, 2014.
11. Jordan, A.R; Barnes, A; Claxton, D; PurVIS, A; Fysh, M. Kinematics and neuromuscular recruitment during vertical treadmill exercise. Journal of Exercise Rehabilitation, 13(3), 307–314 (2017).
12. Chung, T.M. Avaliação cinética e cinemática da marcha em homens adultos do sexo masculino. Acta Fisiátrica 7(2), 61–67 (2000).
13. Cairns, M.A; Burdett, R.G; Pisciotta, J.C; Simon, S.R. A biomechanical analysis of racewalking gait. Medicine and Science in Sports and Exercise 18(4), 446–453 (1986).
14. Kabada, M.P; Ramakrishnan, H.K; Wooten, M.E. Measurement of lower extremity kinematics during level walking. J Orthop Rese 8 (3), 383–392 (1990).
15. Kerrigan, D.C; Todd, M.K; Della Croce, U; Lipsitz, L.A; Collins, J.J. Biomechanical gait alterations independent of speed in the healthy elderly: evidence for specific limiting impairments. Arch Phys Med Rehabil, 79, 317–322 (1998).

The Options in Robotic Control of Rehabilitating Patient's Lower Limbs

Karel Vosahlik and Jan Hosek

Abstract

The use of robotics is currently expanding in all spheres including healthcare. There are many fields of healthcare, where robotics is being or can be used. A design of new rehabilitation devices and aids has to come out from the knowledge of anatomy and physiology of specific body-part movements combined with proper analysis of body movements in particular rehabilitation methods. This article analyses physiological movements in selected rehabilitation methods focused on lower limbs rehabilitation. It also proposes options for realization proprioceptive neuromuscular facilitation by using robotic devices.

Keywords

Therapeutical rehabilitation • Robotization Construction

1 Introduction

Human population is exposed to many diseases and injuries. When we focus on neurological or orthopedic diseases, we should mention for example: brain vascular stroke, cerebral palsy in children, multiple sclerosis, paraplegia, central and peripheral paralysis, ataxia, scoliosis, muscular disorders, joint disorders, postoperative conditions.

The therapy is physically demanding for both patients and physiotherapists. Some therapeutic rehabilitation methods require active participation of patients, who follow instructions provided by physiotherapists. Other methods and techniques are carried out by physiotherapists and patients participate in active or passive way. However, there

are diseases and injuries in which a loco-motor system is severely damaged and a therapy of these patients requires an assistance of two or three physiotherapists. The most common case is the walk training, when patient's lower limbs are led by two physiotherapists and one physiotherapist supports the patient.

Hospital and rehabilitation devices can be divided into five groups. The first group includes urgent care beds. These beds are used in hospital wards like central admissions or operating rooms. The second group includes standard hospital beds for follow-up treatment which are placed in inpatient wards of medical facilities.

Patients in inpatient wards are treated after surgical interventions and some kinds of rehabilitation, that does not require special equipment and large space, are done here.

The third group is represented by special rehabilitation beds. These beds are designed in order to gradually put a strain on loco-motor system using increasing vertical walk training. When we focus on a subject of therapeutic rehabilitation, ErigoPro bed by Hocoma [1] company should be taken into consideration. This bed has an adjustable height with a possibility to be straighten up until 90° angle. ErigoPro bed is equipped with robotic system by which a movement of lower limbs is controlled. Patient's leg is attached to a footrest by ankle-straps. A lower limb is attached to propellent units in thigh area by turnback cuffs. A movement of lower limb is initiated by a propellent unit in thigh area which causes flexion and extension of a hip joint. Knee and hock movements are passive.

The second product is the BTS Anymov bed by BTS Bioengineering [2]. This is a full-sized height adjustable bed with several segments. A cephalic and a thoracic segment is adjustable up to 75°. A lower limb segment is adjustable from 0° to 35°. The bed is equipped with robotic braces that control movements of lower limbs. A simulated walk with robotic braces can be also done in vertical position. Both ErigoPro and BTS Anymov can be equipped with an electro-stimulation module.

K. Vosahlik (✉) · J. Hosek
Faculty of Mechanical Engineering, Department of Instruction and Control Engineering, Czech Technical University in Prague, Technicka 4, 166 07, Prague 6, Czech Republic
e-mail: karel.vosahlik@fs.cvut.cz

The next group of devices are rehabilitation robots used in gradual loading of loco-motor system and walk training. Lokomat by Hocoma [3] can be mentioned as an example of these robots. A patient is suspended on a harness, which can control a load and walking is trained on moving surface [4].

The last group of devices are exoskelets. These are used with patients with weakened loco-motor system. Exoskelet helps with walking and moving in space [5, 6].

Our work is focused on rehabilitation beds designed to simulate walking. A method of proprioceptive neuromuscular facilitation is used during this therapy. Unfortunately these beds [1, 2] perform inaccurate movement of lower limbs due to a lack of hip joint rotation, caused by planar solution of the motions of these mechanisms. The goal of this paper is to propose a mechanism design solution meeting all requirements of proprioceptive neuromuscular facilitation method concerning rotations in lower limbs.

2   Medical Rehabilitation of Patients

Doctors of various specializations are confronted with patients, who suffer from functional disorders of loco-motor system. The main specializations that encounter these disorders are neurology, orthopedics, neurosurgery a physiotherapy. There are many rehabilitation methods like Vojta's method, sensomotorical stimulation method and proprioceptive neuromuscular facilitation method.

The Vojta's method is a diagnostical and therapeutical system [7]. This method is based on application of manual pressure in specific initial postures and the pressure is applied to chosen body parts. Once pressed, these, so-called trigger zones, initiate automatic locomotion movements named as spontaneous crawling and turning. These spontaneous movements can be activated from three postures: both reclining positions (facing upwards and downwards) and in kneeling position.

The senzomotorical stimulation method was originally used for an unstable knee and ankle therapy. Later this method was used in functional disorders therapy. This technique includes a set of balance exercises in different postures. The most important exercises are those that are performed vertically. Facilitation of foot movements is considered to be crucial and it works with two-stage learning model [8].

The proprioceptive neuromuscular facilitation method (PNF) comes out of a basic neurophysiological mechanism. The PNF method is based on movement patterns, that are diagonal with a rotation. There are two diagonal lines for each part of the body. Each diagonal line is made by two patterns of flexion and extension component. Movements within the direction of these lines include three components

in various combinations: flexion or extension, abduction or adduction, outer or inner rotation [9, 10].

The use of robotics in Vojta's method is not suitable, because this method is carried out under variable conditions. It would be complicated to get a patient into requested position and the following pressure procedure is inappropriate to be done by robotics. Nonetheless, robotics is suitable for the PNF method of lower limb stimulation, when certain movements can be replaced by robotic control. The PNF method is characterized by complex movements, because there are many joints moved within one diagonal line. Beds and rehabilitation devices with the ability of using the PNF method are currently available, however their robotic movements are not precise enough. The goal of this thesis is to provide a robotic system design with elimination of imperfections in the PNF method.

3   Solution

A construction solution of robotic system, that is stated in here, is determined for special rehabilitation beds. The first part of the robotic system is located in the area of hip joint. This joint provides abduction and adduction, flexion and extension, inner and outer rotation. The mechanism responsible for abduction and adduction (see Fig. 1). This mechanism consists of a bed frame (position 1), revolving arm (position 2) and linear actuator (position 3).

A mechanism performing a flexion and extension of hip joint consists of a console (position 1) attached to revolving arm performing abduction and adduction of lower limb, a holder (position 2) and linear actuator (position 3), that provides flexion or extension of hip joint by changing the length (see Fig. 2). Linear actuator for flexion-extension and abduction-adduction movements is used in ErigoPro bed [1] a BTS Anymov bed [2].

The last possible movement of hip joint is inner and outer rotation. This movement is often ignored, even though this rotation is an essential movement in PNF method. "This technique involves executing diagonal, spiral-patterned movements against resistance several times through a full
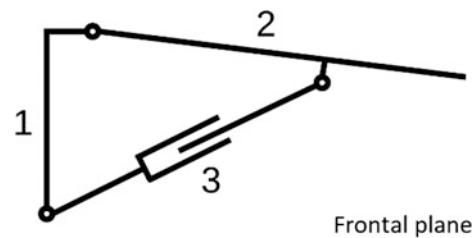

Fig. 1 A mechanism of abduction and adduction of right lower limb hip joint
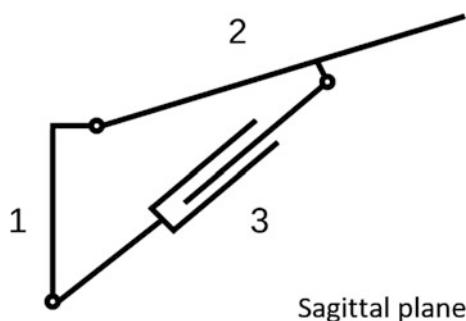
Fig. 2 A mechanism of flexion and extension of right lower limb hip joint

range of motion. A vital element in PNF is the diagonal spiral pattern, which serves as a basis of movement for the various techniques. These diagonal patterns with a rotary component involve movements in three dimensions with sequential, and at times, simultaneous movement at several joints" [9]. Designing the rotation mechanism of lower limb appears to be complicated concerning allocation of this mechanism in the thigh area (see Fig. 3). The mechanism includes a holder (see Fig. 3—position 1, see Fig. 2—position 2) with a stepping motor or servo-mechanism. A shaft ends with a cogwheel, that is in a mesh with cogs on arc line. The arc line is attached to a set with a thigh pad. This connection of the holder and a set of thigh pad is made with pulleys securing the right position of the arc line and its rolling movement.

The second joint, in which a movement is processed, is a knee. This movement is processed by a robotic system. The basic movement of this joint is flexion and extension. This robotic system (see Fig. 4) for a knee joint is made of thigh set (position 1), shank set (position 2) a linear actuator (position 3).

A hock joint movement and leg movements are quite complex. There are three pairs of movements—flexion and extension, pronation and supination, eversion and inversion. A flexion and extension mechanism is formed by a shank set, foot set and linear actuator. Eversion, inversion, pronation and supination movements are processed by two stepping motors or servo-mechanisms and two cogged arc lines. Propellent units and wires are placed on the outer and lower side of robotic braces. The safety of patients is provided both
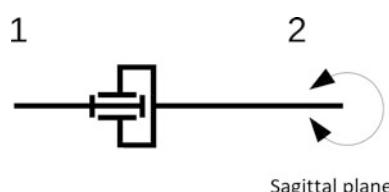
Fig. 3 A mechanism of outer and inner rotation of right lower limb hip joint
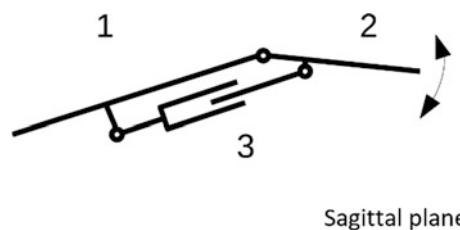
Fig. 4 A flexion and extension mechanism of a knee
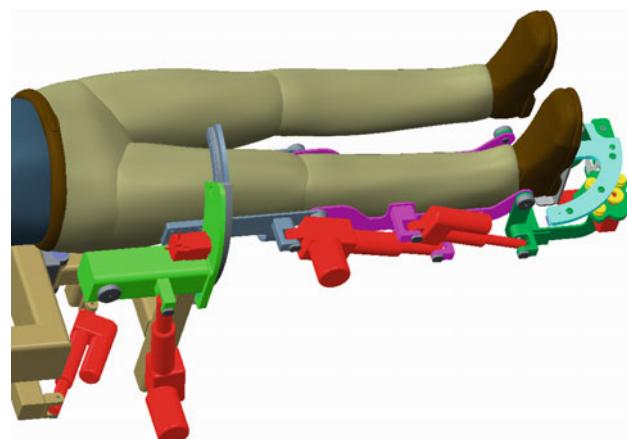
Fig. 5 A mechanism of right lower limb

mechanically and electronically. The mechanism of right lower limb (see Fig. 5).

4 Discussion

All of the mentioned mechanisms can be modified. There is for instance a possibility to switch a location of arc line and stepping motors. All the linear actuators providing hip, knee and hock flexion and extension can be replaced by stepping motors, or servo-mechanisms with a gearbox. A load of linear actuators comes from their attach position, a weigh of robotic system and a weigh of a patient.

Individual rehabilitation methods vary in selected movement and using of joint motion range. From this reason it is necessary to know movements from anatomical point of view and a range of each joint [9–11]. Every patient has different range of joints, so it is crucial to examine actual individual range by a doctor or physiotherapist in advance.

5 Conclusion

There are many kinds of beds and robotic devices mentioned in this thesis. They are used in healthcare and primarily in rehabilitation. As it was discovered, many cotemporary

special rehabilitation beds and robots do not allow a lower limb rotation, which is necessary in PNF method. We have proposed a solution that actively affects movements in lower limb movements including a rotation of hip joint. This suggested mechanism provides an ability of spatial movement in order to achieve diagonal movements of lower limbs based on the PNF method.

Compliance with Ethical Requirements Both authors comply the Springer's ethical policies and there are no conflicts of interest of this paper.

References

1. Hocoma Erigo, https://www.hocoma.com/solutions/erigo, last accessed 2018/1/26.
2. BTS Anymov, http://www.btsbioengineering.com/bts-anymov, last accessed 2018/1/26.
3. Hocoma Lokomat, https://www.hocoma.com/solutions/lokomat, last accessed 2018/1/26.
4. P.-Y. Cheng, P.-Y. Lai, Comparison of Exoskeleton Robots and End-Effector Robots on Training Methods and Gait Biomechanics, In: Intelligent Robotics and Applications, Springer Berlin Heidelberg, 2013, pp. 258–266.
5. Ferris, D-P.: The exoskeletons are here. Journal of Neuroengineering and Rehabilitation 6(17), 1–3 (2009).
6. Diaz, I.: Lower-Limb Robotic Rehabilitation: Literature Review and Challenges. Journal of Robotics 2011 (2011), 1–11 (2011).
7. Gajewska, E.: An attempt to explain the Vojta therapy mechanism of action using the surface polyelectromyography in healthy subjects: A pilot study. Journal of Bodywork and Movement Therapies, (2017).
8. Senzomotorika, http://medicina.ronnie.cz/c-3839-senzomotorika-ii-uvod-zaklady.html, last accessed 2018/1/26.
9. Surburg, P.R.: Proprioceptive Neuromuscular Facilitation Techniques in Sports Medicine: A Reassessment. Journal of Athletic Training 32(1), 34–39 (1997).
10. Choi, Y-K.: The Effects of Taping Prior to PNF Treatment on Lower Extremity Proprioception of Hemiplegic Patients. Journal of Physical Therapy Science 25(9), 1119–1122 (2013).
11. Hamilton, W. J..: Textbook of Human Anatomy. 2nd edn. The Mamillan press LTD, London (1976).

Knee and Ankle Powered Above-Knee Prosthesis Design and Development

Miljan Rupar, Adisa Vučina, and Remzo Dedić

Abstract

Amputation has vast influence on life of amputees. Despite technology advancements, above-knee leg amputees still have quite a problem ascending stairs. At Faculty of Mechanical Engineering and Computing, University of Mostar, we are developing above-knee prosthesis that would be able to perform stair ascent in natural manner. The goal is to mimic main leg muscles by using actuators. First tests of the prosthesis showed that it is not enough to power prosthesis using only knee actuator and that in order to achieve more natural stair ascent ankle actuator should be integrated into a prosthesis design. This paper presents our current design of the above-knee prosthesis and its functions. The prosthesis is powered in the knee and in the ankle by hydraulic actuators. With the ankle actuator integrated into the design, prosthesis showed much better results, closer to the natural stair ascent. Current prototype of the prosthesis was designed by using combination of custom-made and off-the-shelf components which proved to be good for initial tests and experimental purposes. However, novel components need to be developed in order to optimize the prosthesis and make its design less rough, more ergonomic and user friendly.

1   Introduction

Leg amputation has enormous influence on all areas of life of amputees. Besides psychological trauma and dealing with a limb loss, amputation defines every aspect of person's

M. Rupar (✉) · A. Vučina · R. Dedić
Faculty of Mechanical Engineering and Computing, University of
Mostar, Mostar, Bosnia and Herzegovina
e-mail: miljan_deus@yahoo.com

relation toward environment and vice versa. After successful psychological and physical rehabilitation, amputees also have to adapt to their ambulation limitations. Stairs usually present the most insurmountable obstacle to above knee amputees. Stair ascent is a high power demanding task, and vast majority of prostheses used by amputees are passive and unable to provide enough force to perform this activity.

At Faculty of Mechanical Engineering and Computing, University of Mostar, Bosnia and Herzegovina, we are developing above-knee prosthesis that would enable performing stair ascent in natural manner. The goal is to mimic main leg muscles by using externally powered actuators. Powered actuators would provide force needed for performing high power demanding task of ascending stairs. This paper presents our current and planned future design of the above-knee prosthesis and its functions.

2   Prosthesis Design

In order to be able to perform stair ascent in natural manner, prosthesis needs power. So firstly all forces and moments while performing this activity had to be calculated [1]. Calculations showed that worst load case occurs while leg is in loading response phase. At that point of stair ascent moment in the knee joint is largest, so the idea was to externally power knee joint and provide required forces, which, considering the design of the prosthesis at that point, showed to be 4–6 times of user weight [1, 2]. However, first tests of the prosthesis showed that it is not enough only to power prosthesis using only knee actuator, due to stability and kinematic issues, and that in order to achieve more natural stair ascent ankle actuator should be integrated into a prosthesis design [2]. So in our latest tests, the prosthesis was powered in the knee and in the ankle by hydraulic actuators. The prosthesis prototype showed much better results, closer to the natural stair ascent, with the ankle actuator integrated into design [3]. We have also devised a

novel prosthetic foot with passive forefoot flexion which additionally improves gait and makes it closer to natural stair ascent (see Fig. 1).

2.1 Current Design of the Prosthesis

Our latest prototype of the prosthesis consists of knee mechanism and carbon fiber prosthesis body, specialized pylon and novel prosthetic foot, hydraulic knee and ankle actuators, appropriate powering system and user customized stump socket. For proof of concept design we decided to modify existing commercially available passive prosthesis, so knee mechanism and carbon fiber prosthesis body are actually upper part of Endolite SFEUK prosthesis. This prosthesis was chosen due to its modifying ability to integrate knee actuator and also its financial availability.

Pylon serves the function of lower leg and it is designed in a way to enable connection of the foot to the upper part of the prosthesis and ankle joint movement, and is specially adapted so ankle actuator can be integrated into prosthesis design (see Fig. 2, left). Special attention was given to its design in regard to load bearing ability because it has to withstand large loads. Since it must be light so it does not burden the prosthesis design with its weight we chose to make it of aluminum alloy Al 2024, which is characterized by a favorable ratio of strength and specific weight [4]. We designed hydraulic actuators for knee and ankle, which were customized to be able to properly fit into a prosthesis design and provide adequate force (see Fig. 2, right).

Fig. 1 Prosthesis features: **a** powered knee, **b** powered ankle, **c** passive forefoot flexion [3]
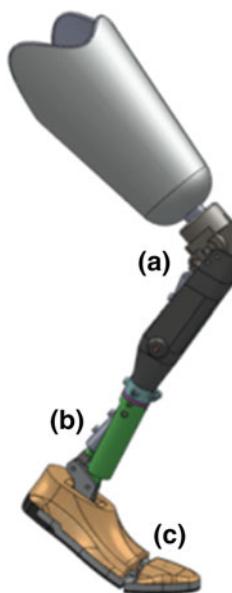
Fig. 2 3D model of prosthetic pylon (left) and integration of hydraulic actuator (right) [3]

2.2 Novel Prosthetic Foot Development

Development of our novel prosthetic foot began with the assumption that flexion of the entire foot (dorsal and plantar flexion) would improve overall gait. This flexion is enabled by hydraulic actuator, and adequate prosthetic foot had to be designed to support this feature. While in the phase of initial development, we came to an idea to implement forefoot flexion feature which would additionally improve gait. We assumed that having real joint flexion, instead of using elastic features of composite material or rubber will be a bigger step toward natural human gait with prosthesis. Human foot is a complex structure which consists of large number of bones, joints, muscles, tendons and ligaments. Reasons of its complexity are various movements that human foot can perform in all three dimensions. With current features of our novel prosthetic foot only flexion in sagittal plane is enabled, since sagittal plane movements are dominating while walking and performing other activities. Design of the foot is envisioned to be made from three basic units: cover, supporting structure, and elastic pad (see Fig. 3). The function of cover is to anatomically and aesthetically shape the foot in order to simulate outside appearance of human foot. This cover should be made of light and soft material and enable more pleasant feeling to its user.

Elastic pad has dampening function while walking or climbing stairs, which makes gait more natural. On posterior part pad is thicker and is in the shape of heel, which is important during heel strike. Elastic pad should be made of rubber or some other flexible material with good shock absorbing abilities. Supporting structure is conceived of two separate parts connected with joint so dorsal forefoot flexion is enabled. Optimal material for support structure would be carbon fibers. For testing purposes we used light aluminum alloy. Two supporting parts are connected with torsion

Fig. 3 Novel prosthetic foot 3D model and consisting three basic units: cover, supporting structure, and elastic pad [3]

spring which dampens forefoot movements and enables returning of forefoot in initial position. Special attention was given to the part of the foot that is connected to the pylon of the prosthesis and actuator, since this assembly simulates movements of human ankle.

2.3 Power and Control System of the Prosthesis

In order to simulate muscle strength of human leg, external hydraulic power system was used. The hydraulic power system consists of two hydraulic actuators powering knee and ankle joint, hydraulic power pack unit and hydraulic installation. We used unidirectional hydraulic system to power the prosthesis during stance phase and during swing phase prosthesis was free to swing. Testing proved that stair ascent, with both knee and ankle joints powered, along with forefoot flexion feature, was closer to natural. However, kinematics in swing phase was quite unnatural because prosthesis was free to move, so we started considering reversible hydraulic system, which would enable control of the prosthesis in both swing and stance phase. In order to make prosthesis intuitive and "smart", we are also considering the implementation of sensors and electronic control, so prosthesis is able to recognize intended motion of its user

and to automatically adapt according to different types of movements and speeds. Our current trails with prosthesis were performed without sensors, using either manual or Wi-Fi control. At this moment control implementation is in its initial stage and various control methods are being considered. We are testing the ability of inertial motion unit sensors, which consist of a gyroscope and an accelerometer.

3 Assembly of Hydraulic Prosthesis Physical Prototype

In order to assemble physical prototype of the prosthesis some components had to be designed from scratch and some were off-the-shelf components. Designed components first had to be checked for stress analysis before manufacturing. This is especially important for pylon and prosthetic foot structure which are critical in regard to load endurance. We used finite element method in SolidWorks to check for stress and displacement analysis. This analysis had much influence on final design of pylon and prosthetic foot (see Fig. 4).

After passing the stress analysis with satisfactory safety factor, we first made prototypes using 3D printing in order to check for any collisions or inconsistencies in the mechanisms (see Fig. 5), and after everything was satisfactory,
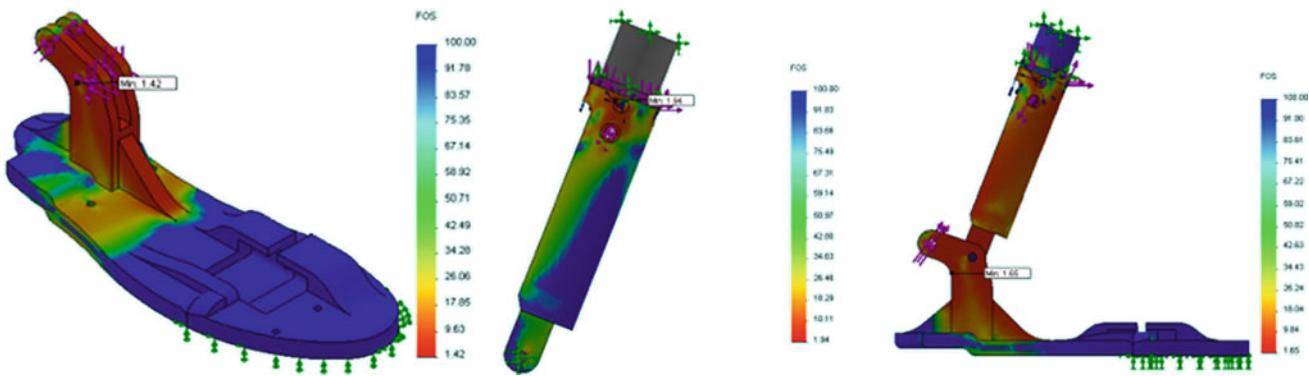
Fig. 4 Stress analysis of the prosthetic foot and pylon structure [3]

Fig. 5 Physical model of the prosthetic foot made by 3D prototyping method [3]

Fig. 6 Designing and manufacturing physical prototypes of hydraulic actuator [3]
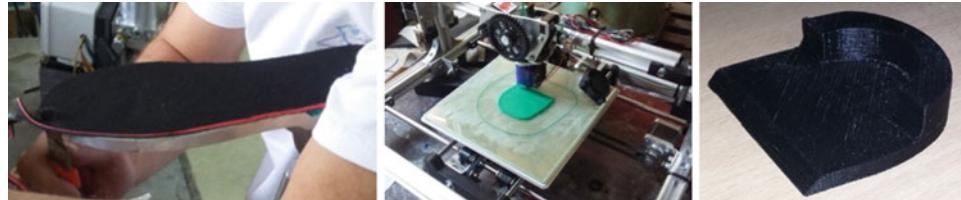
Fig. 7 Elastic pad and heel design and manufacturing [3]

pylon and foot were produced on CNC machine (see Fig. 8, left).

Hydraulic actuators were produced in workshop and were also 3D prototyped before producing in order to assure that mechanisms works without collisions (see Fig. 6). After calculating hydraulic features needed to power the prosthesis we obtained off-the-shelf hydraulic power pack unit which integrates all needed components of the hydraulic system into one whole. Due to its size and mass, especially with DC battery included, we added it externally to prosthesis design, which was suitable enough for testing purposes. For testing purposes we used DC lead battery, which was good in regard to time endurance, but quite heavy and unpractical for integration inside of the prosthesis design. For elastic pad of

Fig. 8 Prosthetic foot and pylon (left) and the prosthesis with hydraulic system (right) [3]

the foot we chose the material which is being used for making anatomic shoe pads, and thicker heel part was made out of rubber based on 3D prototyped model (see Fig. 7).

Prosthetic foot, pylon and hydraulic actuators for the knee and ankle were assembled and connected by hydraulic installation with hydraulic system which made physical prototype of the prosthesis completed. In order for the prosthesis to be used in the testing phase on amputee, we made prosthetic stump socked in prosthetic workshop and adapted it to user of the prosthesis (see Fig. 8, right).

4 Future Work on Prosthesis Design

With knee and ankle actuators and novel prosthetic foot integrated into design, prosthesis showed much better results, closer to the natural stair ascent. Current prototype of the prosthesis was designed by using combination of custom-made and of off-the-shelf components which proved to be good for initial tests and experimental purposes. However, unique, novel components need to be developed in order to optimize the prosthesis and make its design less rough, more ergonomic and user friendly.

Our future plans in regard to prosthesis design include work on: smaller hydraulic system that could be integrated into the prosthesis design, separated control of knee and ankle actuators, development of novel knee mechanism and prosthesis body, further development of prosthetic foot and consideration of using carbon fiber based materials, making prosthesis adjustable for wider range of users, considering the usage of electric actuators, further improvement of sensory control, enabling movements of the prosthesis in transverse and frontal plane etc.

Conflict of Interest Statement Authors declare that they have no conflict of interest.

References

1. Huđec, M., (2001) *Prilog analizi hidrauličkih komponenti za natkoljenične proteze*. Magistarski rad. Mašinski fakultet, Univerzitet Džemal Bijedić, Mostar.
2. Vučina, A., (2002) *Prilog istraživanju kinematike sila u natkoljeničnoj protezi pri gibanju na stepenicama*. Doktorska disertacija. Fakultet strojarstva i računarstva, Sveučilište u Mostaru.
3. Rupar, M., (2017) *Contribution to research of above knee prosthesis with active hydraulically powered knee and ankle joints and prosthetic foot with passive forefoot joint flexion*. Doctoral Thesis. Faculty of Mechanical Engineering and Computing, University of Mostar.
4. Rupar, M. & Dedić, R., (2014) *Analiza naprezanja protetskog stopala i pilona*. in *Zbornik radova Fakulteta strojarstva i računarstva Sveučilišta u Mostaru, 2012*, Fakultet strojarstva i računarstva, Sveučilište u Mostaru: Mostar. p. 131–138.

Adaptive Impedance Control of a Robotic Orthosis Actuated by Pneumatic Artificial Muscle

Quy-Thinh Dao and Shin-ichiroh Yamamoto

Abstract

In recent years, rehabilitation robots which help the neurological impaired patient regain the function of the lower limb via training sessions have been developed with great attention. Since these types of robot interact closely with humans, safety is always the top priority considered in the design. Besides, the compliance of the robot must also be controlled to give the subject the best comforts. To fulfill the above mentioned requirements, a two degrees of freedom (2-DOF) robotic orthosis power by pneumatic artificial muscles (PAMs) based on the human musculoskeletal system is developed in this study. The system is able to track any desired trajectories by using a computed torque control strategy. The impedance controller is also integrated into the system to adapt the robot compliance according to the external force. The feasibility and effectiveness of the developed system are verified by experiments.

1 Introduction

Pneumatic artificial muscles (PAM) have been used for many years as the actuators of the robots, including the industrial and service robots. In comparison to the motorized actuator, PAMs have many advantages such as natural compliance, lightweight, high ratio of weight to power. Especially PAM behaves quite similar to the human muscle since PAM is widely used in service robots which interacts with the human such as rehabilitation systems. Various prototype systems have been developed in research centers [1–5]. Most of these system actuated by two mono-articular muscles for hip and knee joints.

Similar to the human musculoskeletal system, the positive contribution of the bi-articular muscle to the robot motion already reported by Kumamoto et al. [6]. The existence of the additional muscles also provides the robot the redundancy in both its kinematic and dynamic. In our previous studies [7–9], a high compliant gait training system actuated by PAMs based on the treadmill and body-weight support (BWS) named AIRGAIT has been developed. In comparison with the existing systems [1–5], our robotic orthosis using the actuators base on the human musculoskeletal system with an additional bi-articular muscle connecting between hip and knee joints. Several strategies have been used for trajectory tracking control of the developed system such as co-contraction model, modified feedforward-feedback. However, the system only shows good performance without the participation of the subject at low walking speed [7, 8]. Although the tracking performance has been improved at higher walking speed in [9], the model of the robot has not considered since all controllers are designed independently.

In this research, our developed lower-limb rehabilitation system is continued to be improved. First, the dynamical model of the system is built in which the contribution of the bi-articular muscle is considered. Based on the mathematical model, a modified computed torque controller is proposed to enhance the tracking performance. Finally, the robot impedance controller is developed to adapt the robot compliance accordingly the external force effects on it. The effectiveness of the developed system is verified by experiments.

Q.-T. Dao (✉)
Graduate School of Engineering and Science, Shibaura Institute of Technology, Tokyo, Japan
e-mail: nb16505@shibaura-it.ac.jp

S. Yamamoto
Department of Bioscience Engineering, Shibaura Institute of Technology, Tokyo, Japan
e-mail: yamashin@se.shibaura-it.ac.jp

2 Model of 2DOF Robot Manipulators with Antagonistic Bi-articular Muscles

Figure 1a shows the typical configuration of a typical 2-DOF robotic. The dynamic of this system can be described by Euler-Lagrange formulation as following

$$D(\theta)\ddot{\theta} + C(\theta, \dot{\theta})\dot{\theta} + G(\theta) = T \qquad (1)$$

where $\theta = [\theta_1, \theta_2]^T$ is the matrix of the robot joint angle. $T = [T_1, T_2]^T$ is a matrix of input torques applied to the system; $D(\theta)$ is the system mass matrix, $C(\theta, \dot{\theta})$ is the Coriolis matrix and $G(\theta)$ is the gravity vector.

$D(\theta)$ is the nonsingular matrix and can be determined as

$$D(\theta) = \begin{bmatrix} D_{11} & D_{12} \\ D_{21} & D_{22} \end{bmatrix} \qquad (2)$$

where

$$D_{11} = m_1 l_{c1}^2 + m_2(l_1^2 + l_{c2}^2 + 2l_1 l_{c2}cos\theta_2) + I_1 + I_2 \qquad (3a)$$

$$D_{12} = D_{21} = m_2(l_{c2}^2 + l_1 l_{c2}cos\theta_2) \qquad (3b)$$

$$D_{22} = m_2 l_{c2}^2 + I_2 \qquad (3c)$$

l_i denotes the length of link i; l_{ci} denotes the distance from the previous joint to the center of mass (COM) of link i; m_i and $I_i = m_i l_{ci}^2$ denote the mass and inertia moment of link i, respectively.

The matrix $C(\theta, \dot{\theta})$ is given as

$$C(\theta, \dot{\theta}) = \begin{bmatrix} C_{11} & C_{12} \\ C_{21} & C_{22} \end{bmatrix} \qquad (4)$$

where $C_{11} = h\dot{\theta}_2$, $C_{12} = h\dot{\theta}_1 + h\dot{\theta}_2$, $C_{21} = -h\dot{\theta}_1$, $C_{22} = 0$ with $h = -m_2 l_1 l_{c2}sin\theta_2$.

The vector $G(\theta) = [G1, G2]^T$ where

$$G_1 = (m_1 l_{c1} + m_2 l_1)gcos\theta_1 + m_2 l_{c2}gcos(\theta_1 + \theta_2) \qquad (5a)$$

$$G_2 = m_2 l_{c2}gcos(\theta_1 + \theta_2) \qquad (5b)$$

and g is the acceleration of gravity.

As shown in Fig. 1b, in the AIRGAIT orthosis configuration, hip and knee joint are actuated by two mono-articular muscles, whereas the bi-articular, which connect between hip and knee joints and act to both joints simultaneously. Hence, the relation between the muscle torques $\tau = [\tau_1 \quad \tau_2 \quad \tau_3]^T$ provided by the corresponding pair of PAMs and the joints torques can be described by

$$T = W\tau \qquad (6)$$

in which W is the Jacobian matrix from the muscle space to the joint space. It is as follows

$$W = \begin{bmatrix} 1 & 0 & 1 \\ 0 & 1 & 1 \end{bmatrix} \qquad (7)$$

Since W is not a square matrix, τ can be derived from (6) and (7) by using the Moore-Penrose pseudo-inverse matrix W^+ of W as

$$\tau = W^+ T \qquad (8)$$

From Eqs. (1) and (8), the dynamic model of the AIR-GAIT robotic orthosis can be demonstrated by

$$\tau = \bar{D}(\theta)\ddot{\theta} + \bar{C}(\theta)\dot{\theta} + \bar{G}(\theta) \qquad (9)$$

Fig. 1 **a** Typical 2DOF robotic. **b** Robotic orthosis with two mono-articular and one bi-articular muscles

where $\bar{D}(\theta) = W^+ D(\theta)$, $\bar{C}(\theta) = W^+ C(\theta)$, and $\bar{G}(\theta) = W^+ G(\theta)$, respectively.

3 Robot Orthosis Control System

3.1 Trajectory Tracking Control

In this research, a computed torque control strategy is employed for the trajectory tracking purposed of the AIRGAIT robot orthosis.

$$T = D(\theta)(\ddot{\theta}^* + K_d\dot{e} + K_c e) + C(\theta,\dot{\theta})\dot{\theta} + G(\theta) \qquad (10)$$

where θ^* is the reference trajectory to track, $e = \theta^* - \theta$, and K_c, K_d are constant gain matrices. The error dynamics can be written as $D(\theta)(\ddot{e} + K_d\dot{e} + K_c e) = 0$, since $D(\theta)$ is always positive definite, we have
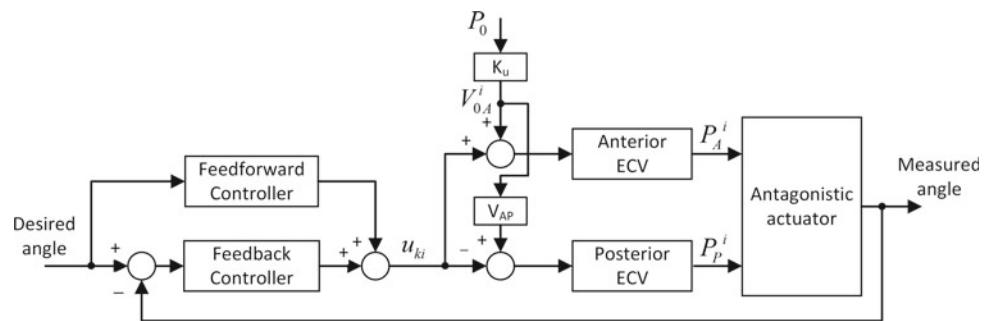
$$\ddot{e} + K_d\dot{e} + K_c e = 0 \qquad (11)$$

The control law (10) can be rewritten as

$$T = \underbrace{D(\theta)(\ddot{\theta}^*) + C(\theta,\dot{\theta})\dot{\theta} + G(\theta)}_{T_{ff}} + \underbrace{D(\theta)(K_d\dot{e} + K_c e)}_{T_{fb}}$$

$$(12)$$

By adjusting the controller parameters K_p and K_d, the required tracking performance can be achieved. In practice, the design matrices K_p and K_d may be chosen diagonal which results in a decoupled multi-variable linear system. Besides, it can be seen from (12) that, the controller is consist of two components including a feedforward and a feedback term. Therefore, the control system actually is consist of three decoupling channels of two mono- and one bi-articular muscles of which block diagram as in Fig. 2. The parameters of the controllers after being well tuned are provided in Table 1.

The reference trajectories of the hip ($\theta^*_{1,t}$) and knee ($\theta^*_{2,t}$) mono-articular actuator are modified from the gait data profile in text book [10] with the maximum of hip and knee flexion/extension are $+20°/-20°$ and $+45°/0°$, respectively. The reference value of the bi-articular actuator is the sum of the knee and hip reference values $\theta^*_{3,t} = \theta^*_{1,t} + \theta^*_{2,t}$.

3.2 Robot Impedance Control

Robot stiffness or compliance control is one of the most important requirements of the robot. The stiffness property of an antagonistic actuator is dominated by the nominal pressure supply to its two PAMs. In this study, the relationship between stiffness and the nominal pressure in the work by Choi et al. [4] is employed. The compliance γ_j of antagonistic actuator powered by n couple of PAMs is derived by

$$\gamma_j = \frac{\theta_j}{n\left[2R^2 K_{0j}\theta_j + K_{1j}(R^2\pi P_{A0} - P_{AP}y_A R) + \Delta P_j K_1 R^2\right]}$$

$$(13)$$

in which K_{0j} and K_{1j} are the parameters of spring element of the PAM (Table 2), and y_A is the length of anterior PAM in the case of joint angle θ_i. In (13), θ_i and ΔP_j are regulated by trajectory tracking controller, P_{AP} is unchanged for setting the initial position of the actuator. The nominal pressure P_{A0} becomes the manipulated signal of the actuator compliance.

The impedance control architecture of the AIRGAIT orthosis is shown in Fig. 3. The robot impedance can be controlled base on the external force effect to the robot orthosis F_{ex}. The concept of impedance control of robotic orthosis is to set the robot impedance high (low compliance) if the external force has the opposite direction (prevent the movement) with the rotation movement. In the other case, the robot impedance is decrease if the external force support

Fig. 2 The block diagram of decoupled channels

Table 1 The parameters of the trajectory tracking controller

Controller channel	K_c	K_d
Knee mono-articular	0.05	0.8e−3
Hip mono-articular	0.05	0.5e−3
Bi-articular	0.04	1.0e−3

Table 2 The spring parameters of each PAM

Actuators	K_0 [N]	K_1 [$\frac{N}{100\,kPa}$]
Hip PAMs	0.691	1.096
Knee PAMs	0.572	0.835
Bi PAMs	0.453	1.217

the movement of the robot. Based on the directions of the external force the control signal of the impedance controller is expressed by

$$\Delta P_{0i,t} = K_{ui}F_{ex}sign(F_{ex}) \tag{14}$$

in which K_{ui} is the proportional coefficient of the control pressure and external force. With assumption that, the initial compliance of the robot orthosis is set at the minimum value, since the impedance controller increase the joint compliance only. For the safety requirement, the control signal of the robot impedance controller is constraint by the following condition

$$0 < \Delta P_{0i,t} < P_{0i} \tag{15}$$

4 Experiment Evaluation

4.1 Experiment Setup

The proposed control strategy is examined on the AIRGAIT orthosis. In order to create the periodic external force, two

bicycle tubes are attached to the orthosis at the shank and thigh part. Two bar-shaped load cells are used to measure this force. The real image of the experiment setup is given in Fig. 4. The first step of the experiment, the robot is set to trajectory tracking mode. After the system reach the steady state, the impedance control is activated to control the robot joint compliance in the second step. Data of the desired, measured trajectories and compliance of each joint during experiments are collected for assessing.

The sampling frequency for the overall system is set at 100 Hz. The data from the load cells, pressure sensors, as well as the data of the angle sensors are processed by 6 Hz low pass filter.

4.2 Experiment Result

To evaluate the performance of the system during trajectory tracking mode, the mean of all measured trajectories are computed first. Then, the maximum tracking error (MTE) and the root mean square tracking error (RMSTE) between the average and the desired trajectory are evaluated. The trajectory tracking performance of the robotic orthosis in tracking and impedance control modes are depicted in Fig. 5. As can be observed in Table 3, the MTE and RMSTE are below 3.29° and 1.85° ± 1.01 for both hip and knee joints in trajectory tracking mode. In impedance control mode, the tracking performance is slightly degraded, i.e., $MTE = 6.11°$ and $RMSTE = 2.69°$. The joint compliances of the robotic orthosis in tracking control and impedance control mode in are shown in Fig. 6. It can be observed that in trajectory tracking mode, the compliance is set at low level, the maximum values are 2.75 rad/N m for hip joint and 4.55 rad/N m for the knee joint. When the impedance control mode is activated, the robot compliance increase according to the external force F_{ex} to 4.69 rad/N m and 7.07 rad/N m for hip and knee joints, respectively. The impedance controller can adapt its joints compliances to the external force while the tracking controller is still stable.
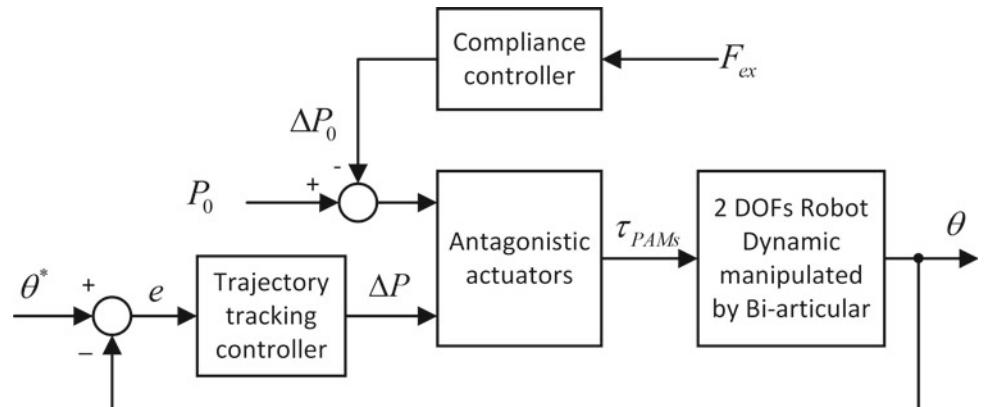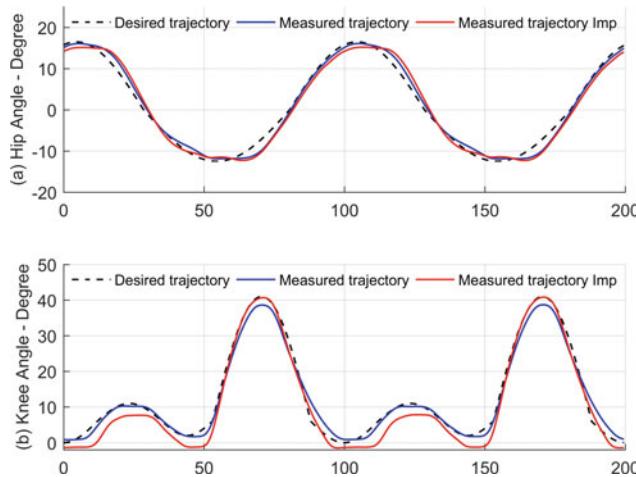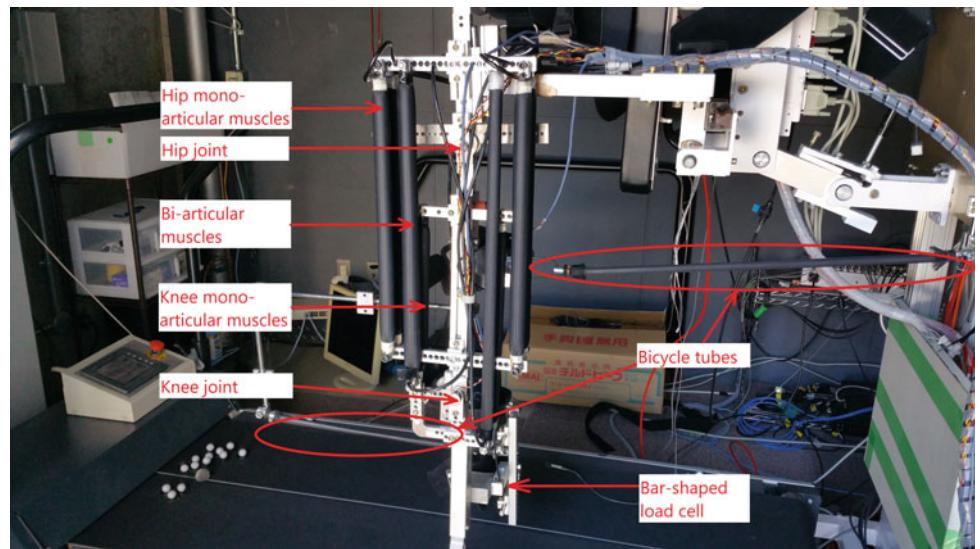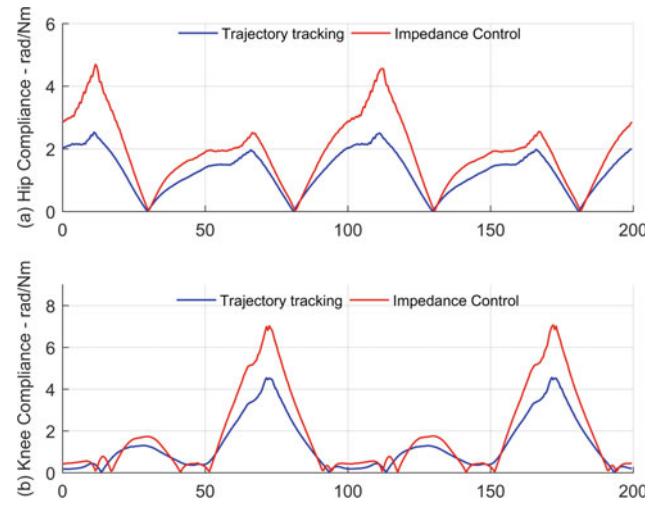
Fig. 3 Impedance control architecture of the AIRGAIT robotic orthosis

Fig. 4 The experiment system

**Fig. 5** Trajectory tracking performance of robotic orthosis in trajectory tracking and impedance control mode

Fig. 6 Joint compliance of the robot orthosis in trajectory tracking and impedance control mode

Table 3 Experimental evaluations

Parameter	Trajectory tracking control mode		Impedance control mode	
	Hip joint	Knee joint	Hip joint	Knee joint
MTE	2.75°	3.29°	3.17°	6.11°
RMSTE	1.25°	1.85°	1.76°	2.69°
Maximum compliance (rad/N m)	2.75	4.55	4.69	7.07

5 Conclusion

In this paper, the control system for the AIRGAIT robotic orthosis is continued to improve. First, the dynamic model which considering the contribution of the bi-articular muscle is built. Base on the mathematic model, the computed torque control strategy is employed for the trajectory tracking purpose. Then, an impedance controller is integrated to the system allows the robot adapt its joint compliances accordingly the external force. The effectiveness of the proposed system is verified by experiment. In future

works, the participation of the human subject will be considered to further improvement of the system. The human effort is possible estimated by the load cells, and the impedance controller can adapt the robot compliance accordingly to enhance the patient's voluntary in the gait training process.

Conflicts of Interest The authors declare that they have no conflict of interest.

References

1. K. E. Gordon, G. S. Sawicki, and D. P. Ferris, "Mechanical performance of artificial pneumatic muscles to power an ankle-foot orthosis," *J. Biomech.*, vol. 39, pp. 1832–1841, Jul. 2006.

2. P. Beyletal., "Safe and compliant guidance by a powered knee exoskeleton for robot-assisted rehabilitation of gait," *Adv. Robot.*, vol. 25, pp. 513–535, May 2011.

3. G. S. Sawicki and D. P. Ferris, "A pneumatically powered knee-ankle-foot orthosis with myoelectric activation and inhibition," *J. NeuroEng. Rehabil.*, vol. 6, 2009.

4. T. Y. Choi and J. J. Lee, "Control of Manipulator Using Pneumatic Muscles for Enhanced Safety," in *IEEE Transactions on Industrial Electronics*, vol. 57, no. 8, pp. 2815–2825, Aug. 2010. https://doi.org/10.1109/tie.2009.2036632.

5. S. Hussain, S. Q. Xie, P. K. Jamwal, and J. Parsons, "An intrinsically compliant robotic orthosis for treadmill training," *Med. Eng. Phys.*, vol. 34, pp. 1448–1453, Dec. 2012.

6. Kumamoto, M., T. Oshima, and T. Yamamoto, "Control properties induced by the existence of antagonistic pairs of bi-articular muscles Mechanical engineering model analyses," in *Human Movement Science*, 1994. 13(5): p. 611–634.

7. Y. Shibata, S. Imai, T. Nobutomo, T. Miyoshi and S. I. Yamamoto, "Development of body weight support gait training system using antagonistic bi-articular muscle model," *2010 Annual International Conference of the IEEE Engineering in Medicine and Biology*, Buenos Aires, 2010, pp. 4468–4471. https://doi.org/10.1109/iembs.2010.5625972.

8. M. A. Mat Dzahir, T. Nobutomo and S. I. Yamamoto, "Development of body weight support gait training system using pneumatic mckibben actuators -Control of Lower Extremity Orthosis-," *2013 35th Annual International Conference of the IEEE Engineering in Medicine and Biology Society (EMBC)*, Osaka, 2013, pp. 6417–6420.

9. Q. T. Dao and S. i. Yamamoto, "Tracking control of a robotic orthosis for gait rehabilitation: A feedforward-feedback control approach," *2017 10th Biomedical Engineering International Conference (BMEiCON)*, Hokkaido, Japan, 2017, pp. 1–5.

10. David A. Winter, "Biomechanics and motor control of human movement", Third edition. *University of Waterloo press*, Waterloo, Ontario, Canada.

Quantifying Movement of the Head and Shoulders During Quiet Standing Using MatLab Software and Promising Parameters

Petr Volf, Jan Hybl, Patrik Kutilek, Jan Hejda, Jiri Hozman, Vaclav Krivanek, Radek Doskocil, and Rudolf Cerny

Abstract

In this paper, we describe a method for quantifying movement of the head and shoulders during quiet standing. The method proposed allows for the determination of postural stability of the head and shoulders, especially during the Romberg's test, by recording the relative angular movements. The proposed software is used to calculate new parameters of the head and shoulder movements. These parameters are: the area of the confidence ellipse of the inclination of the head versus the inclination of the shoulders and the area of the confidence ellipse of the head rotation versus the shoulder rotation, the size of the main and minor axis of the confidence ellipse of the inclination of the head versus the inclination of the shoulders and the size of the main and minor axes of the confidence ellipse of the head rotation versus the shoulder rotation. The proposed method was implemented using MatLab software. To test this method, we compared the movements of the fourteen healthy subjects/volunteers and nine patients with an inner ear viral infection. Based on the data results, we identified that the parameters can be used to evaluate postural stability in neurology.

P. Volf (✉) · J. Hybl · P. Kutilek · J. Hejda · J. Hozman
Faculty of Biomedical Engineering, Czech Technical University in Prague, Sitna sq. 3105, Kladno, Czech Republic
e-mail: petr.volf@fbmi.cvut.cz

J. Hybl
e-mail: jan.hybl@fbmi.cvut.cz

P. Kutilek
e-mail: kutilek@fbmi.cvut.cz

J. Hejda
e-mail: jan.hejda@fbmi.cvut.cz

J. Hozman
e-mail: hozman@fbmi.cvut.cz

V. Krivanek · R. Doskocil
Faculty of Military Technology, University of Defence, Kounicova 65, Brno, Czech Republic
e-mail: vaclav.krivanek@unob.cz

R. Doskocil
e-mail: radek.doskocil@unob.cz

R. Cerny
2nd Faculty of Medicine, Department of Neurology, Charles University in Prague and Motol University Hospital, V Uvalu 84, Prague, Czech Republic
e-mail: rudolf.cerny@lfmotol.cuni.cz

1 Introduction

There are a large number of diseases that affect the skeletal, muscular and nervous systems of human body. Many of them can result in abnormal posture of both neck and shoulders, [1, 2]. This is one of the reasons why there is currently an ongoing development of new methods to quantify the relative angular movements of upper body parts [3, 4]. However, methods for quantification of kinematics data of the relative head and shoulders movements have not yet been tested or developed in a sufficient manner [3, 5].

The Romberg's test has become a standard test in the evaluation of postural instability during quiet standing, [6]. Today, the main tools for measuring postural instability during quiet standing include stabilometric platforms, [7]. It is possible to apply a similar technique for assessing the movement of the head and shoulders. All stabilometric platforms are based on measuring the coordinates of center of pressure (CoP). Thus, the methods for quantitative evaluation of coordinates can be adapted to assess the angles of angular movement of the head and shoulders. The main aim of this work is to present quantitative assessment methods, that allow for the evaluation of postural stability in quiet stance using angles of angular movement of the head and shoulders.

2   Methods

2.1   Participants

The main purpose of our preliminary study was to test new evaluation methods. The data was collected from fourteen healthy subjects (HS) (age of 24.6 (SD 1.6) years) and nine patients (Pts) (age of 52.3 (SD 13.0) years) with a viral infection of the inner ear, characterized by dizziness and nausea [5, 8].

2.2   Measurement Equipment and Test Procedure

The Motion capture (MoCap) system based on cameras and gyroscopes is described in detail in [9]. The system can be separated into 3 parts—two cameras attached to a camera stand, gyroscope in combination with a set of infrared LEDs that are both attached to a helmet, and another set of infrared LEDs attached to two shoulder clips [5]. The design of the system is shown in Fig. 1. The head and shoulder orientation was measured in standing position during the Romberg's test. The test subjects were asked to keep their eyes closed (EC) [5], and stand still for 60 s on both legs on a platform. The subject's feet were positioned next to one another at an angle of 30° and their arms were supposed to remain passively hanging. Each subject was measured two times with a 2-min interval between each measurement, [5]. The study protocol was approved by Ethical Committee and the University Hospital Motol.

2.3   Methods of Data Processing

During the measurements, the control software captures two images by two cameras and collects data from the gyro-accelerometer attached on the helmet, [5]. Marker coordinates are then extracted from the images [5], so that the angle of the shoulders and head rotation and inclination can be determined from these, see [9].

As the two coordinates characterize CoP, it is possible to use the methods of evaluation from these two data sets. Generally, a parameter frequently used is an area of a geometric shape, which describes the distribution of the measured CoP position. One of the methods for describing the point distribution is the application of confidence 95% ellipse. The observed parameters are the area of the ellipse and the size of the main and minor axis of the ellipse, [3, 4]. The 95% confidence ellipse characteristics are given by formulas described in detail in [10] and [11]. All calculations

were performed using custom-written programs created in MatLab software (MatLab R2010b, Mathworks, Inc., Natick, MA, USA) to determine the confidence ellipse characteristics. The output from the software is not only the calculated characteristics of the 95% confidence ellipse of the angular variables of head movement vs. movement of shoulders, but also the graphical presentation of the ellipse, see Fig. 2.

2.4   Statistical Analysis

After calculating the area of the ellipse and the size of the main and minor axis of the ellipse of each Pts and HS standing, the statistical analysis was performed using MatLab software. The Jarque-Bera test was used to test the normal distribution of the calculated ellipse characteristics. The median (Mdn), minimum (Min), maximum (Max), the first quartile (Q1) and the third quartile (Q3) of area and the size of the main and minor axis are then used to compare the results for Pts and HS. Also, the Wilcoxon rank sum test was used to assess the significance of the differences between the data. The significance level was set at $p < 0.05$.

3   Results

The Jarque-Bera test showed not normal distribution of data in most data sets. Then, the statistical data was used to illustrate the differences between the Pts and HS. The following Table 1. shows the results of our statistical evaluation. Only the comparison of size of minor axis of ellipse of head inclination vs. shoulders inclination plot of Pts with size of minor axis of ellipse of head inclination vs. shoulders inclination plot of HS ($p = 0.05$) found statistically significant differences. Other comparisons of parameter values between Pts and HS did not identify statistically significant differences.

4   Discussion

Using the parameters of confidence ellipse based on angles of rotation movements of the head and shoulders we were able to evaluate the relative movements of upper body parts. We quantitatively described the distribution of the measured data by a 2-D confidence ellipse. Testing of the functionality of the method occurred in the laboratory environment of Motol University Hospital, Charles University. The results showed statistically significant differences in only one case —comparison of size of minor axis of ellipse of head inclination versus shoulders inclination plot of Pts with the

Fig. 1 MoCap camera system (**a**); camera with vertical axis orientation (1), camera with horizontal axis orientation (2), special helmet with markers and gyro-accelerometer (3), and a platform (4) that is part of the lower part (**b**) of the structure of MoCap system
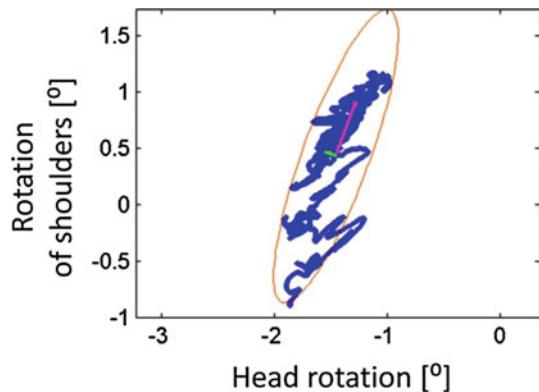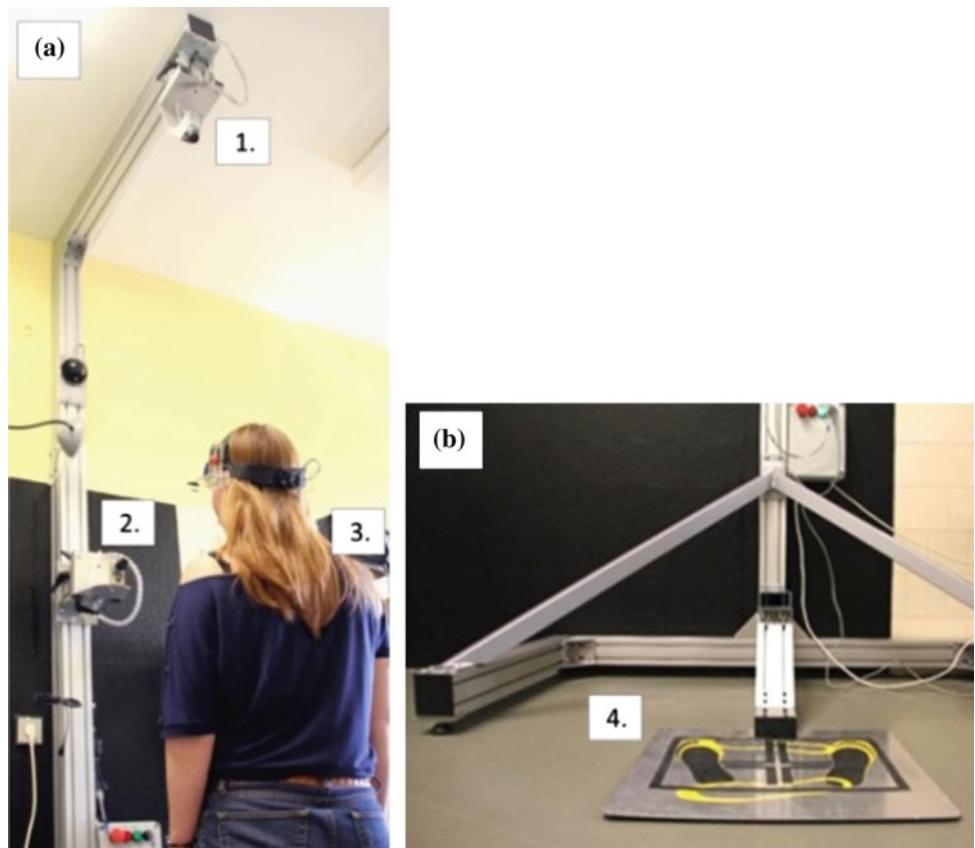

Fig. 2 Example of the output from a program, graph of the head rotation versus rotation of the shoulders and application of the method of data evaluation by confidence 95% ellipse

size of minor axis of ellipse of head inclination vs. shoulders inclination plot. However, in almost all cases, medians of parameter values are larger in patients. This result corresponds to the expectation of worse postural stability of patients, [5].

According to the method described above, the ellipse parameters may yield insight into the postural stability and postural balance problems in Pts with neurological disorders. This information is important for medical examination and

rehabilitation medicine. Thus, the method based on ellipse parameters could be used as an additional method for determining and evaluating postural instability of upper body parts. Nevertheless, there are potential limitations to our study. The most important limitation is that the sample of test subjects was small. Although statistically significant results were observed, it would be helpful to see these findings proven in a larger study. However, to test the basic features of the method proposed for the study of the Pts with viral infection of the inner ear, characterized by dizziness and nausea, a smaller sample of Pts and HS is sufficient.

5 Conclusion

We concluded that the study of postural instability in patients with neurological disorders based on confidence ellipse of the set of points obtained by plotting parameters of head movement versus parameters of shoulders movement could be suitable for identification of postural balance problems. The new method based on confidence ellipse has never been used prior to this study of relative movements of head and shoulder of patients diagnosed with neurological disorders. This can lead to using proposed methods in medical practice. The proposed techniques should be seen as

Table 1 Descriptive statistics of the parameters of confidence ellipse of the head movement versus shoulders movement of the subjects with eyes closed

Parameter	Statistical indicator	Pts	HS
Confidence ellipse area of rotation of head versus rotation of shoulders plot	Min (deg^2)	0.54	0.54
	Max (deg^2)	5.57	7.00
	Mdn (deg^2)	2.03	1.57
	Q1 (deg^2)	1.49	1.06
	Q3 (deg^2)	3.35	2.50
Confidence ellipse area of inclination of head versus inclination of shoulders plot	Min (deg^2)	0.54	0.26
	Max (deg^2)	4.62	3.41
	Mdn (deg^2)	1.23	0.97
	Q1 (deg^2)	0.73	0.65
	Q3 (deg^2)	1.66	1.37
Size of main axis of confidence ellipse of head rotation versus shoulders rotation plot	Min (deg)	0.82	0.65
	Max (deg)	3.57	4.74
	Mdn (deg)	1.55	1.48
	Q1 (deg)	1.25	0.98
	Q3 (deg)	2.08	2.25
Size of main axis of confidence ellipse of head inclination versus shoulders inclination plot	Min (deg)	0.58	0.38
	Max (deg)	3.65	2.32
	Mdn (deg)	0.99	1.12
	Q1 (deg)	0.75	0.75
	Q3 (deg)	1.26	1.41
Size of minor axis of confidence ellipse of head rotation versus shoulders rotation plot	Min (deg)	0.21	0.25
	Max (deg)	1.21	0.98
	Mdn (deg)	0.43	0.32
	Q1 (deg)	0.25	0.29
	Q3 (deg)	0.61	0.44
Size of minor axis of confidence ellipse of head inclination versus shoulders inclination plot	Min (deg)	0.25	0.18
	Max (deg)	0.83	0.51
	Mdn (deg)	0.39	0.28
	Q1 (deg)	0.29	0.25
	Q3 (deg)	0.43	0.36

a contribution to the study of postural stability of Pts with a neurological disorder. The next phase of our research is clear, it is to apply this new method to a larger group of Pts with different problems with postural stability.

References

1. Cerny, R., Strohm, K., Hozman, J., Stoklasa, J., Sturm, D.: Head in space – noninvasive measurement of head posture. In: Proceedings of The International Otorhinolaryngological Congress, pp. 39–42, Medimond S.r.l., Bologna (2006).
2. Martin, A. R., Reddy, R., Fehlings, M. G.: Dropped head syndrome: diagnosis and management, Evidence-Based Spine-Care Journal 2(2), 41–47 (2011).
3. Kutilek, P., Hejda, J., Socha, V., Vlckova, K., Cerny, R.: Evaluation of the relative position of the head and shoulders in neurological practice. In: Proceedings of the 19th International Conference on Applied Electronics, pp. 169–172, University of West Bohemia, Pilsen (2014).
4. Kutilek, P, Hozman, J., Cerny, R., Hejda, J.: Methods of measurement and evaluation of eye, head and shoulders position in neurological practice, Advanced Topics in Neurological Disorders, pp. 25–44, InTech Europe,, Rijeka (2012).
5. Kutilek, P., Volf, P., Hejda, J., Hozman, J., Viteckova, S., Krivanek, V., Doskocil, R., Cerny, R.: A technique for quantifying the relative angular movement of the head and shoulders, IFMBE Proceedings series 56, 310–313 (2017).
6. Khasnis, A., Gokula, R.M.: Romberg's test. Journal of Postgraduate Medicine 49(2), 169–72 (2003).
7. Oliveira, L.F., Simpson, D.M., Nadal, J.: Calculation of area of stabilometric signals using principal component analysis. Physiological Measurement 17(4), 305–12 (1996).
8. Strauss, M., Davis, G.L., Viral disease of the labyrinth: I. Review of the literature and discussion of the role of cytomegalovirus in congenital deafness, Ann. Otol. Rhinol. Laryngol. 82(4), 577–83 (1973).
9. Hejda, J., Kutilek, P., Hozman, J., Cerny, R., System for precise measurement of head and shoulders position, IFMBE Proceedings 41, 1555–1558 (2014).
10. Jørgensen, M.B., Skotte, J.H., Holtermann, A., Sjøgaard, G., Petersen, N.C., Søgaard, K.: Neck pain and postural balance among workers with high postural demands – a crosssectional study, BMC Musculoskelet. Disord. 12, 176 (2011).
11. Prieto, T. E., Myklebust, J. B., Hoffmann, R. G., Lovett, E. G., Myklebust, B. M.: Measures of postural steadiness: differences between healthy young and elderly adults, IEEE Trans. Biomed. Eng. 43, 956–966 (1996).

Validation of the Novel Body Weight Support System Using Pneumatic Artificial Muscle: A Case Study

Riichi Takiguchi, Van-Thuc Tran, and Shin-Ichiroh Yamamoto

Abstract

Locomotion gait training system plays a significant role in therapy for the patients who are in recovering from hemiplegia, paraplegia, spinal cord injury or after stroke. Modern gait training systems commonly use a Body Weight Support (BWS) system which is to enable the spinal cord injury or stroke patients bearing their weight during the walking practice. The conventional rope-pulley mechanism in conventional BWS systems could cause the "pendulum effect" during gait training and make subject be uncomfortable. Furthermore, using only one rope-pulley mechanism the conventional BWS system could not flexibly modulate the supported force, for example, the hemiplegic patient. This research is aimed to develop a novel BWS system which will be used to support the spinal cord injury patient during gait training. The novel BWS system will be applied Pneumatic Artificial Muscles (PAM) for generating the support force. The mechanical structure of the new BWS system is totally different from the conventional body weight support system. Therefore, the new BWS system will have several advantages, such as simplicity, low cost and flexibly adjusting the unloading force. The purpose is to develop a very simple BWS system for gait training, however, its capabilities generating active unloading forces. An experiment with a perturbation was conducted using the new BWS system and a representative conventional BWS system (Counter Weight system) to verify the performance of the new BWS system and to investigate the gait variance of the subject under both two BWS system. The results showed that the new BWS system presented a better performance in comparison with the Counter Weight system.

1 Introduction

Locomotion is a very essential functionality of human being. The patients with incomplete spinal cord injury or stroke is often restricted in daily activities and community ambulation due to the weakness of the muscles activations. Previously, the effort to recover the mobility function of hemiplegia patient took much labor cost and often required two or three therapists [1, 2]. Fortunately, locomotion gait training system has been developed for over two recent decades that enable the patients be able to walk on their legs. The main task of the locomotion gait training system is to improve the mobility capacity of the patient in recovering state after therapeutic. Currently, the modern gait training system often combine the treadmill Body weight Support system and a Robotic leg Orthosis such as DGO [3], or a well-known rehabilitation system Lokomat by Hocoma [4].

In walking rehabilitation system, the body weight support system is one of the main part and plays an important role in recovering progress of patient. The Body Weight Support system assists patient by reduce the load on the patient leg and plays as a safety part of the gait training system. At the early state of gait training course, the amount of unload is totally high up to 80% of patient weight due to the leg weakness and the patient might not carry the whole weight. According the recovery of the patient, the therapist may gradually increase the load on patients leg by reducing the unloading force from Body Weight Support system. One may see that the strategy of modulation the unloading force also contributes to the mobility recovery progress of the patient. Franz et al. [5] suggested that unloading force which was a variation of gait pattern may have more efficient.

R. Takiguchi (✉) · V.-T. Tran · S.-I. Yamamoto
Shibaura Institute of Technology, Tokyo, Japan
e-mail: mf17045@shibaura-it.ac.jp

However, in order to implement the strategy for gait training base Body Weight support system, at least two conditions must be fulfilled. First, we need a Body Weight Support system that could flexibly generate the unloading force. Second, we need investigate the walking balancing with stable and unstable environment under Body Weight Support system. The first condition could be achieved by the current development of the active Body Weight Support system for gait training. Meanwhile, the second condition is still a gap of current researches in gait rehabilitation.

Balance responses of human has been considered to study in recent decades. Previously, Bachmann et al. investigated the effects of unexpected and sudden changes in unloading force [6]. The electromyography (EMG) results indicated that the muscle activities changed following the perturbation. However, the gait parameters change during walking did not included. Hof et al. introduced the "extrapolated center of mass" (XCOM) which has an intimate relationship to the dynamic balancing during walking [7]. Current studies investigated the metabolic cost and locomotion control of spinal cord injury patient during under the unstable environment [8, 9]. However, in these study, the effect of body weight support system did not concern since the perturbation applied in lateral. In contrast, walking under Body Weight support system, the gait parameter of human could change due to the effect of the unloading force, especially the effect of lateral part of unloading force [10]. The gait parameter modification would be due to the adaptation human mobility mechanism of the external force on subject body.

In the previous study, we introduced a total new active body weight support system that applied the Pneumatic Muscle Actuators [11]. The mechanical structure, that contained several PAMs connecting directly to subject trunk, totally differed from the conventional systems in which the rope-pulley mechanism were applied. In this paper we interested in investigating the subject gait parameters during walking under the Body Weight support systems with the vertical perturbations partially. We hypothesis that, under the perturbation, the human walking balance with the active body weight support system would be more stable than the counter weight system.

2 Method

2.1 Experiment Setup
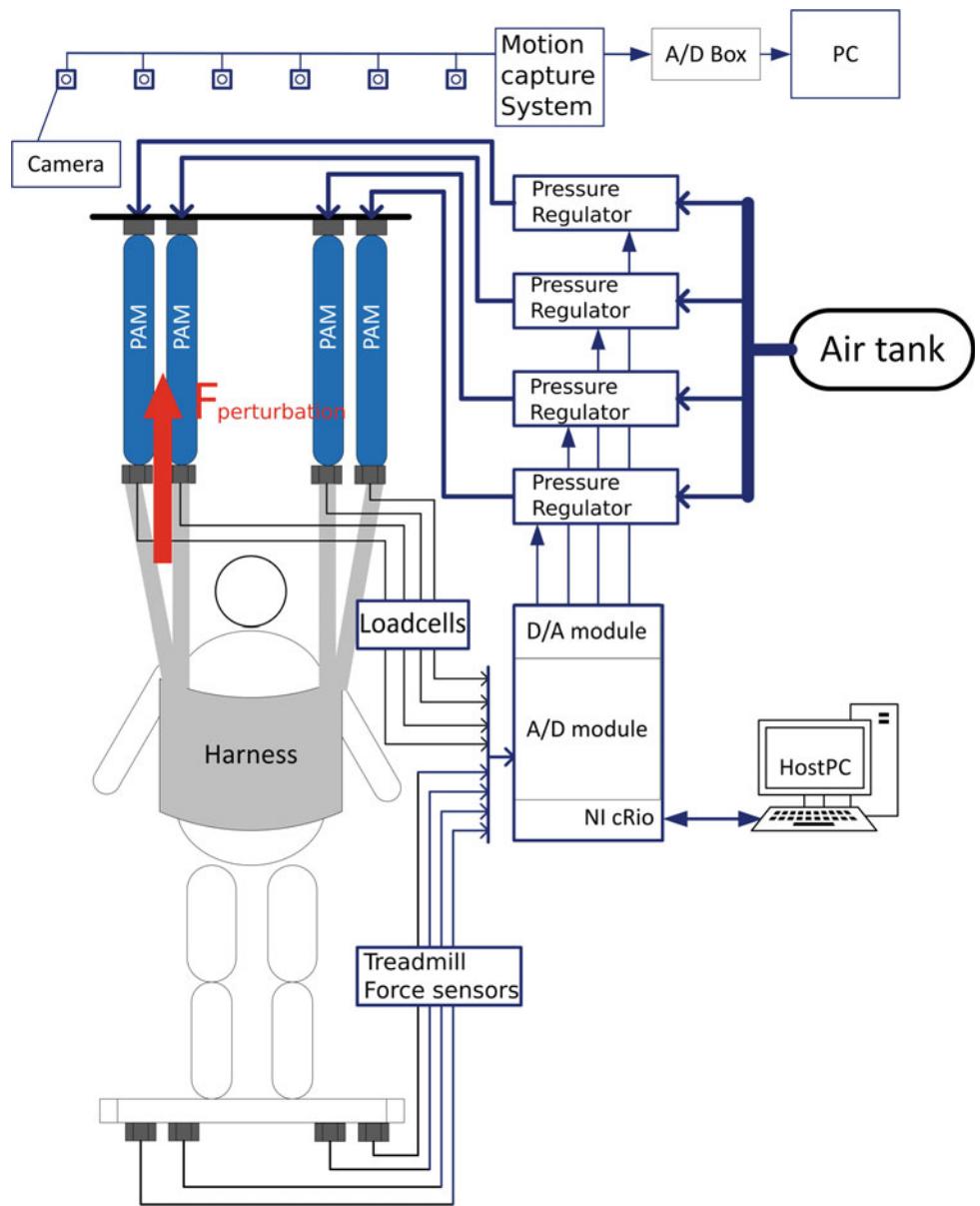
Six healthy subjects (age 23 ± 0.58 years, weight 61 ± 3.57 (Kg) and height 170.3 ± 6.18 (cm)) volunteered to conduct this experiment. The experiment was conducted base on the new active Body Weight Support system (see [11]) and Counter Weight system. In The new BWS system, the

Pneumatic Artificial Muscles (PAMs) with 1" (in.) diameter were used to generate the unloading force to support the subject carrying the body weight. The mechanism in the new active Body Weight Support system, such that the actuators connect directly to the subject's trunk, totally differs from the conventional Body Weight support system (such as Counter Weight system) since the main actuator often connecting to the subject body by a rope-pulley structure. Each PAM has a load-cell (LUR-A-2KNSA1 by Kyowa) integrated to feedback the force signal to the controller. In this paper, the unloading force, which is generated by the PAMs by regulating the compressed air using the pressure regulator (ITV 2050 by SMC), is considered to be constant for each level. The controller was designed and implemented base on NI LabVIEW and NI cRio 9176 (by National Instrument).

2.2 Protocol and Data Acquisition

In this study, five trials were conducted for each subject. First, the subject walked freely without wearing any Body Weight Support systems at speed 3.2 km/h of Treadmill; and this condition is also called the normal walking. Secondly, subject walking on the treadmill under BWS system at unloading force equals 30% of subject's weight. The foot-switch sensor was attached to the subject's sole at the ball-of-the-foot position to detect whenever the toe-on appeared during walking. The perturbation with the amplitude about 80% of unloading force was randomly added just from the rising edge of the foot-switch signal. The duration of each perturbation is always 250 ms. For each trial, the perturbations were randomly given 15 times after four to eight steps. Figure 1 shows the scheme of the perturbation generated under the new active BWS system. In the third trial, the subject walked under the Counter Weight system with treadmill speed similar to the first and the second trial. The same procedure of perturbation generated was also conducted for the third trial. Figure 2 shows the configuration of the perturbation in the case using the Counter Weight system. Notice that, in this study, we considered only the case that perturbation generated in the lateral direction only to investigate the variance of the gait parameters due to the unloading system. The Motion Capture System (by Motion Analysis Corp.) was used to capture the coordination from a set of sixteen markers positioned on the subject's legs (foot, ankle joint, knee joint and hip joint) and trunk by using ten high speed cameras at 200 Hz sampling frequency. The analog signal of the four force sensors embed under treadmill and foot-switch sensor were synchronized recorded by using Motion Capture System at 1 kHz sampling frequency. The data collection was used to calculate the step width, step length, "Extrapolated Center of Mass" (XCOM) and

Fig. 1 The scheme presents main components of the new body weight system. The red arrow represents the perturbation force added to the total unloading force (Color figure online)


3 Result and Discussion
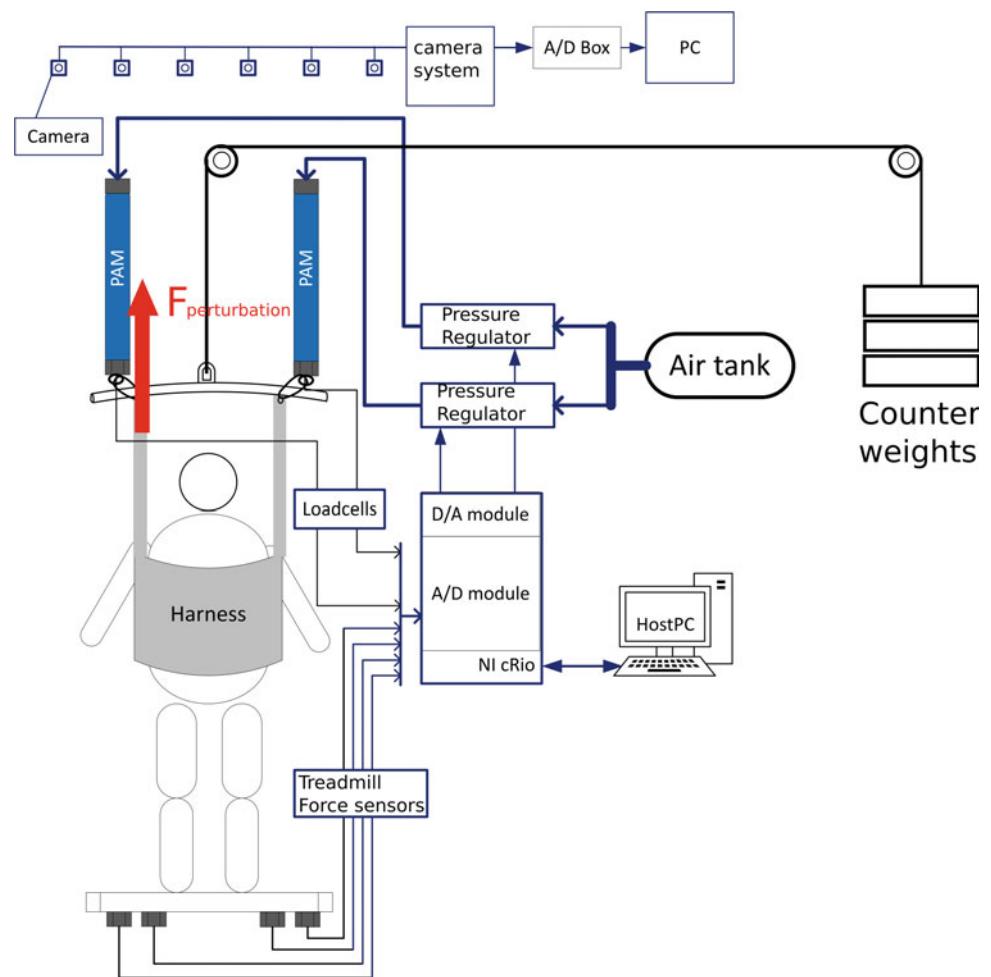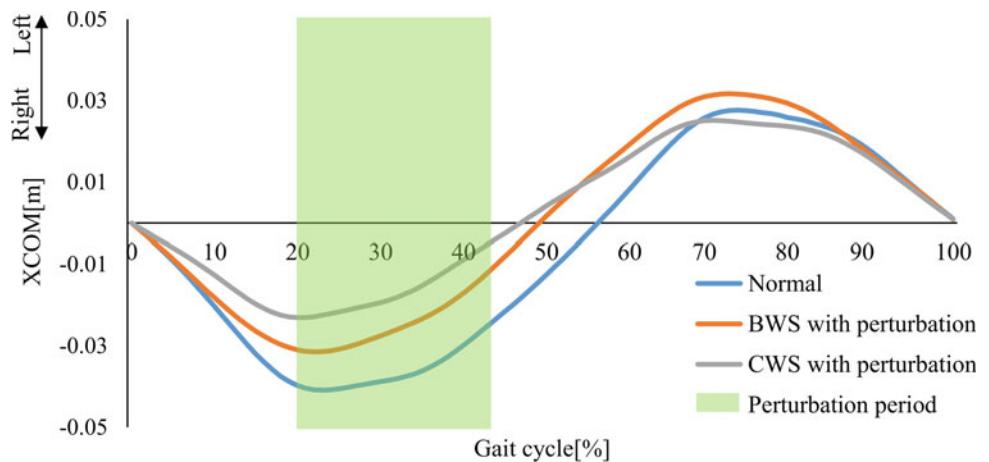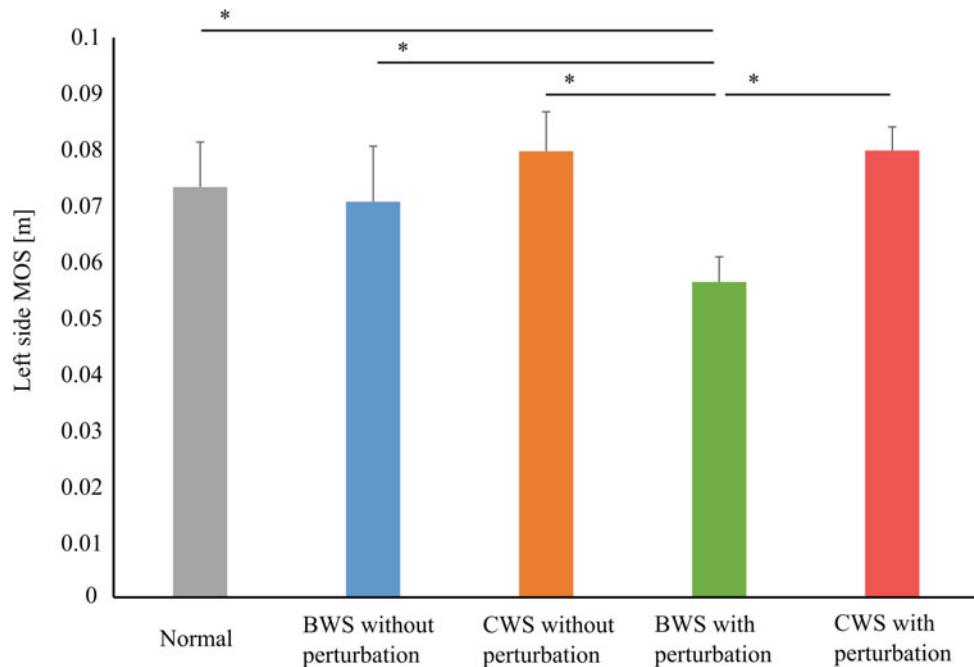
Figure 3 shows the averaged "Extrapolated Center of Mass" (XCOM) for every gait cycles in which the perturbation happened. The perturbation that happened just after left leg toe-on during walking around after 10% of the gait cycle. From the Fig. 3, one could see that the XCOM of the subject in the case of BWS system is closer the normal walking. During perturbation time, the XCOM amplitude of both Counter Weight system and the new BWS system is significantly smaller. The maximum difference between Counter Weight system and normal walking at the peak XCOM is double higher than the difference between BWS and normal case.

Figure 4 shows the comparison the averaged "Margin of Stability" (MOS) on the left side for all subject walking with the conditions: normal walking, BWS system using PAMs without perturbation, Counter Weight system without perturbation, BWS system using PAMs with perturbation and Counter Weight system with perturbation. Form the Fig. 4, the difference MOS between the condition BWS system using PAMs without perturbation and the condition BWS system using PAMs with perturbation perturbation is significant ($p < 0.05$). The MOS of subjects walking under the condition of BWS system with perturbation is smaller than all other

"margin of stability" (MOS) by using MATLAB software (by MathWorks, Inc.). The ANOVA and TuskeyHSD tests were used to investigate the significant difference among cases.

conditions ($p < 0.05$). Meanwhile, no significant difference
from the MOS of subjects walking under the counter-weight
system is found both before and after perturbation ($p > 0.05$).
Comparison the MOS of the normal condition and the BWS
system without perturbation indicated that subject could walk
stably under the BWS system without perturbation. The

reduction of the MOS under the BWS condition suggests that
the perturbation significantly affected to the subjects' balance;
and this condition could be appropriated applying in balance
training. The significant difference among the conditions with
the normal walking, Counter Weight system with and without
perturbation is not found. During walking under the Counter

Fig. 4 Comparison the "margin of stability" (MOS) on the left side averaged for all subject walking with the conditions: normal walking, BWS system using PAMs without perturbation, counter weight system without perturbation, BWS system using PAMs with perturbation and counter weight system with perturbation. * indicates the significant value smaller than 0.05

Weight system, the lateral tension force could restrict the movement on the frontal plane, therefore the effect of perturbation could be small.

Locomotion functionality training of spinal cord injury patient is very essential. Among many criteria to evaluate the training strategy, the stable walking is one of the most important factors which represents the effect of the Locomotion training. There could be two type of reasons that influence to the quality of stable walking: the internal reasons and the external impacts. The internal reasons somewhat belong to the patient such as the locomotion functional mutilations, for example, spinal cord injury (SCI). In contrast, the external impacts come from the walking environmental in which the uncertain events suddenly happen and effect to the patient. Hof, A. L. presented important parameters to quantify the stable walking; they were XCOM and MOS [7]. The varied XCOM and MOS due to the effect of unloading system are very clear in this study. During walking, the lateral force which is a part of unloading force could make changes of the gait parameter, especially, the later parameters such as the XCOM, or MOS. Moreover, the perturbation force, which added in lateral, aggravates the variance of the gait parameters.
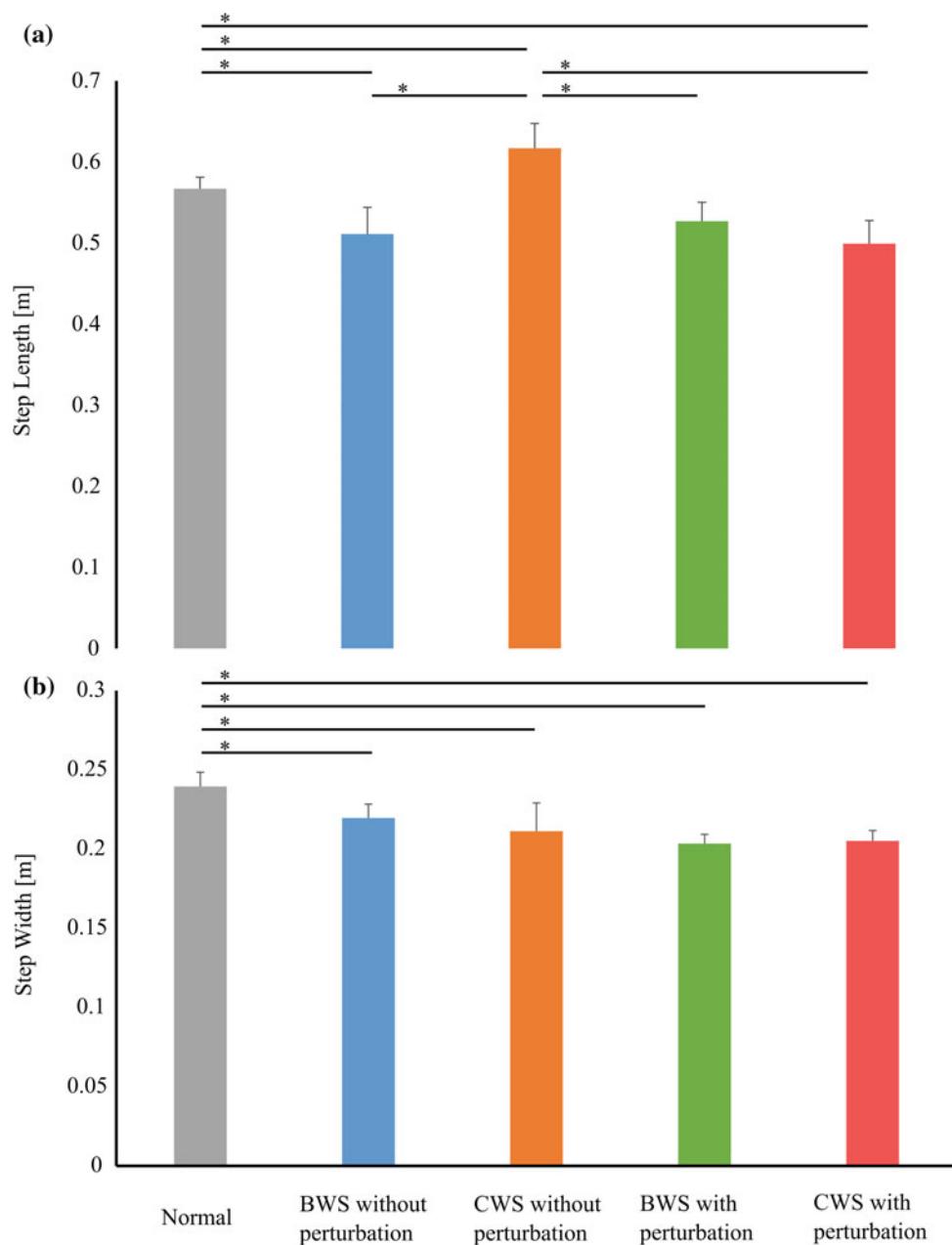
Figure 5a, b represent the quantification of step lengths and step widths, respectively, for all subject with conditions: normal walking, BWS system using PAMs without perturbation, Counter Weight system without perturbation, BWS system using PAMs with perturbation and Counter Weight system with perturbation. The step length and step width in the normal walking case are significantly higher than the case using unloading systems (p < 0.05). The result

consistently agrees with the previous result [10]. Such that the unloading system modified the subject's gait parameters during walking. The smaller step-width and step-length represent the adaptation of subject during walking under the weight support system and the effect of the vertical unloading force. The higher vertical unloading force would impact stronger to the walking parameters such that the step-length and step-width would smaller. Therefore, the higher of the vertical unloading force was applied the vertical center of mass would be in the higher position.

4   Conclusion

In this case study, the validation of the novel BWS system had been done with perturbation in lateral. The stable walking was investigated based on the "extrapolated center of mass" (XCOM) and "margin of stability" (MOS) quantification. The step length and the step width parameters were also calculated. The significant reduction of the MOS under the BWS condition suggests that the perturbation affected to the subjects' balance and this condition could be appropriated applying in balance training. The walking gait result, i.e. step length and step width, consistently agreed with the previous results such that walking gait parameters were modified by the vertical unloading force. In the limitation of this study, the internal mechanism of locomotion, such as energy consumption or human muscle activation, was not presented. Future work, we would analyze the internal mechanism of human locomotion. Several scenarios in the real clinical will be considered to investigate.

Fig. 5 **a** and **b** represent the quantification of step lengths and step widths, respectively, for all subject with conditions: normal walking, BWS system using PAMs without perturbation, counter weight system without perturbation, BWS system using PAMs with perturbation and counter weight system with perturbation. * indicates the significant value smaller than 0.05

References

1. Wernig, A., Muller, S., Nanassy, A., Cagol, E.: Laufband therapy based on rules of spinal locomotion is effective in spinal cord injured persons. Eur. J. Neurosci. 7, 823–829 (1995). https://doi.org/10.1111/j.1460-9568.1995.tb00686.x.

2. Wernig, A., Nanassy, A., Muller, S.: Maintenance of locomotor abilities following laufband (treadmill) therapy in para- and tetraplegic persons: Follow-up studies. Spinal Cord. 36, 744–749 (1998). https://doi.org/10.1038/sj.sc.3100670.

3. G Colombo, M Wirz, V Dietz.: Driven gait orthosis for improvement of locomotor training in paraplegic patients. Spinal Cord. 39, 252–255 (2001). https://doi.org/10.1093/ptj/85.1.52.

4. Hornby TG, Zemon DH, Campbell D.: Robotic-assisted, body-weight-supported treadmill training in individuals following motor incomplete spinal cord injury. Phys Ther. 2005 Jan; 85 (1):52–66. https://doi.org/10.1038/sj.sc.3100670.

5. Franz JR, Riley PO, Dicharry J, Allaire PE, Kerrigan DC.: Gait synchronized force modulation during the stance period of one limb achieved by an active partial body weight support system. J Biomech. 2008 Nov 14; 41(15):3116–20. https://doi.org/10.1016/j.jbiomech.2008.09.007.

6. Bachmann V1, Mller R, van Hedel HJ, Dietz V.: Vertical perturbations of human gait: organisation and adaptation of leg muscle responses. Exp Brain Res. 2008 Mar; 186(1):123–30. https://doi.org/10.1007/s00221-007-1215-6.

7. Hof AL, Vermerris SM, Gjaltema WA.: Balance responses to lateral perturbations in human treadmill walking. J Exp Biol. 2010 Aug 1; 213(Pt 15):2655–64. https://doi.org/10.1242/jeb.042572.

8. Matsubara JH, Wu M, Gordon KE.: Metabolic cost of lateral stabilization during walking in people with incomplete spinal cord injury. Gait Posture. 2015 Feb; 41(2):646–51. https://doi.org/10.1016/j.gaitpost.2015.01.015.

9. Wu M, Brown G, Gordon KE.: Control of locomotor stability in stabilizing and destabilizing environments. Gait Posture. 2017 Jun; 55:191–198. https://doi.org/10.1016/j.gaitpost.2017.04.021.

10. Tran van Thuc, Shin-ichiroh Yamamoto.: Investigation of the Pendulum Effect During Gait Locomotion Under the Novel Body Weight Support System and Counter Weight System. 2nd International Conference for Innovation in Biomedical Engineering and Life Sciences. ICIBEL 2017. IFMBE Proceedings, vol 67. Springer, Singapore. https://doi.org/10.1007/978-981-10-7554-4_15.

11. Tran van Thuc, Shin-ichiroh Yamamoto.: Development of a body weight support system using pneumatic muscle actuators: Controlling and validation. Advances in Mechanical Engineering, 8, 12, 598 (2016). https://doi.org/10.1177/1687814016683598.

Estimation of Postural Control Strategy During Continuous Perturbation

Nur Fatin Fatina bt Mohd Ramli, Ogawa Sho, Ikeda Takehiro, and Yamamoto Shin-ichiroh

Abstract

Stability is an important aspect for every moving object and millions of people spend a good deal of their time on their feet for standing, walking, or running. Compared to static balance, dynamic balance with presence of external perturbation requires more complex strategy. The purpose of this study was to investigate the multi-segment of human postural control strategy organization in continuous perturbation balance task between ankle-hip angle as collective variable. We examined the transition of Center of Mass (COM)-Center of Pressure (COP) and ankle-hip angle pattern in moving platform balance paradigm. Eight healthy young adults stood on a moving platform in the anterior-posterior direction continuously within the frequency range 0.2–0.8 Hz and vice versa with eyes opened. COM, COP, and ankle-hip angle changed from in-phase to anti-phase at a certain point frequency of support surfaces. From the cross-correlation coefficient calculation, higher frequency shows negative correlation between the ankle-hip angle which mean these two variables were moving in the different phase direction. These results indicate that joint angle sway also could be one of the collective variables in order to determine postural strategy determination.

Keywords

Balance • Postural response • Continuous perturbation Transition • Ankle strategy • Hip strategy

1 Introduction

Balance can be defined as an ability to keep equilibrium state by adjusting the center of mass (COM) and center of pressure (COP) which frequently changes due to changes in positions and movements of the body segments [1]. However, as we grow older, the balance control system will be degenerated and this become the main reason of high risk falls among older people. Before new balance training and rehabilitation tools can be developed, a better and deeply understanding of the pastoral strategies used to maintain balance need to be understood first.

Human bipedal stance is inherently unstable due to large body mass located high above the small relative base support. Human are able to select distinct strategies depending on task requirements. Ability to maintain appropriate relationship between the body segments, and between the body and the environment task is defined as postural orientation [2]. Over the past 20 years, research on postural control orientation has been concentrated within two strategies which called ankle and hip strategies.

According to Horak and Nasher, by using an ankle strategy, the postural control orientation was mainly around ankle joint rotation [3], yet including low hip joint rotation. On the other hands, when the high or great frequency perturbation was imposed, anti-phase rotation at both ankle and hip joints is observed [4]. The selection of postural control strategies was influenced by many factors such as the perturbation conditions, experience, adaptation and also fear of falling [5–7]. Besides, the perturbation type and frequency become important factors in investigating postural control strategies. However, there are no details prove in at which frequency the postural control strategy transition occurred. Therefore, there are still room for investigation in order to deeply understand the relationship between postural responses strategy toward frequency perturbation.

Due to the existence a number of postural strategies available to achieve multiple goals, it's believed that

N. F. F. bt Mohd Ramli (✉) · O. Sho · I. Takehiro
Graduate School of Engineering and Science, Shibaura Institute of Technology Saitama, Saitama, Japan
e-mail: nb16106@shibaura-it.ac.jp

Y. Shin-ichiroh
Department of Science and Engineering, Shibaura Institute of Technology, Saitama, Japan

kinematics variable parameters and the cross-correlation analysis may reveal their presence. Therefore, the aim of this paper is to investigate the multi-segment of human postural control strategy organization in translation anterior-posterior continuous perturbation balance task between ankle-hip angle as collective variable. It is believed that perturbation at surface level is sufficient enough to challenge postural control systems. As an addition, the causes of the transition will be discussed in this paper.

2 Methods

2.1 Participants

Eight healthy male were participated voluntarily in this study experiment. Their age, height and body mass were 23.29 ± 3.15 years old, 173.0 ± 4.0 cm, 76.0 ± 4.0 kg (mean $\pm$ SD), respectively. They had no history of neurological history. All participants gave their informed consent to participate in the study experiment after receiving a detailed explanation of the purpose and risk involved.

2.2 Experimental Protocol and Apparatus

Figure 1 shows the experimental setup for this experiment study. The participants were requested to keep a quiet standing (no motion of the platform) with barefoot for 20 s to record quiet standing data for every participant. Then, the participants were imposed with the perturbation which was induced by moving platform. The participants were instructed to maintain their postural balance while the perturbation was given with barefoot, eyes open and focused at a mark that been set at the eye level. The participants placed their feet side by side, with shoulder width, comfortably and kept their arms folded across their chest. A 6-axis movable platform (MB-150, Cosmate, Japan) was used as a moving platform to generate sinusoidal translation along the anterior-posterior direction. There were 31 frequencies of 0.2–0.8 Hz with 0.02 Hz steps of ascending and descending frequencies in 6 cycles for each frequency at the single platform motion with amplitude 50 mm. The perturbation was given randomly with three trials of each perturbation. The total duration of each trial was about 368 s. The participants were given sufficient rest in between the trials. Additional trials were conducted in which case of participant was almost felt or occasional steps occurred.

A 3-D motion capture analysis system with ten high-precision infrared cameras (HWK-200RT camera, Motion Analysis, USA) was used to record the motion of passive marker attached over the joints of the experimental participants. A fix of 16 reflective markers (placed at 3rd metatarsal, lateral malleolus, lateral condyle, trochanter of the femur, iliac crest, acromion of spacula, top of the head and four markers on the force plate) were attached over the participants' joints. Besides, during all experiment trials, both right and left knee joints were locked to prevent bias movement at the knees. A force platform (9286A, Kitsler, Japan) was used to derive the displacement of the body's COP and mounted on the moving platform.

2.3 Data Measurement and Analysis

The COM was calculated from the eight-segment model. The total body COM position was obtained by the weighted summation of the individual segment COM position. The ground reaction force, the horizontal component in y-direction force and the force plate moment at the x-axis, recorded from the force plate with sampling rate 200 Hz and filtered with low pass 2nd order Butterworth filter. Joint movement coordinates obtained from motion analysis systems with 1 kHz sample rate were used to measure joint angle displacement and body segment length for segmental COM location. A comparison of different frequencies and individual participant was compared using Two-way analyses of variance (ANOVA) with significant level of $p < 0.005$. Besides, paired t-test was used to observed different between COM-COP and ankle-hip transition frequency and unpaired t-test for observation between ascending and descending frequency condition. Cross-correlation coefficient function analysis was used to observed the changes transition between COM-COP displacement and ankle-hip angular displacement. All statistical analyses were completed using the MATLAB software.

3 Results

3.1 Displacement of Kinematics Variable

All participants were able to accomplish the task given perfectly. Figure 2 presents time series of mean displacement of the COM, COP, head, ankle angle and hip angle for ascending and descending frequency condition. COM and head displacement gradually decreased as the platform function frequency was increased. On the other hand, the ankle and the hip angular motion displacement increased as the frequency increased. For descending condition, COM, COP and head displacement were increased as a response to decreasing frequency. Ankle and hip angle displacement were decreased along with the decreased of the frequency. By comparing between frequency with individual participant, all kinematic displacements were significantly different between frequencies (COM ($p < 0.005$) ($F_{(30,216)} = 25.76$,
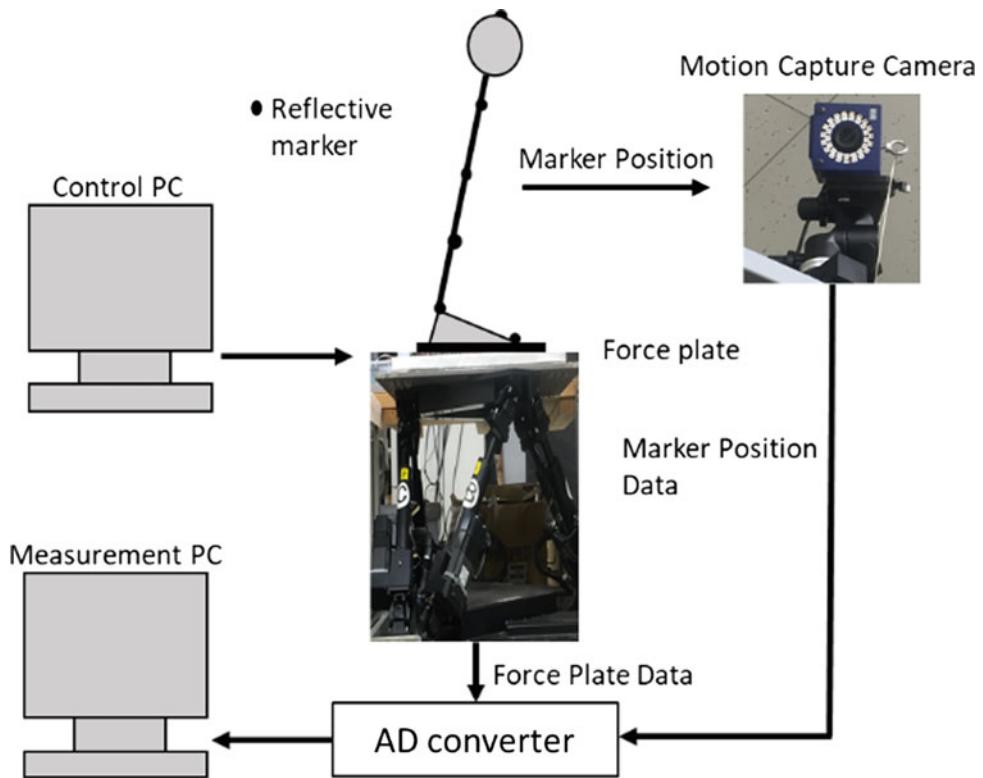
Fig. 1 Experimental setup. The participant rode on the moving platform loaded with force plate in anterior-posterior translation perturbation
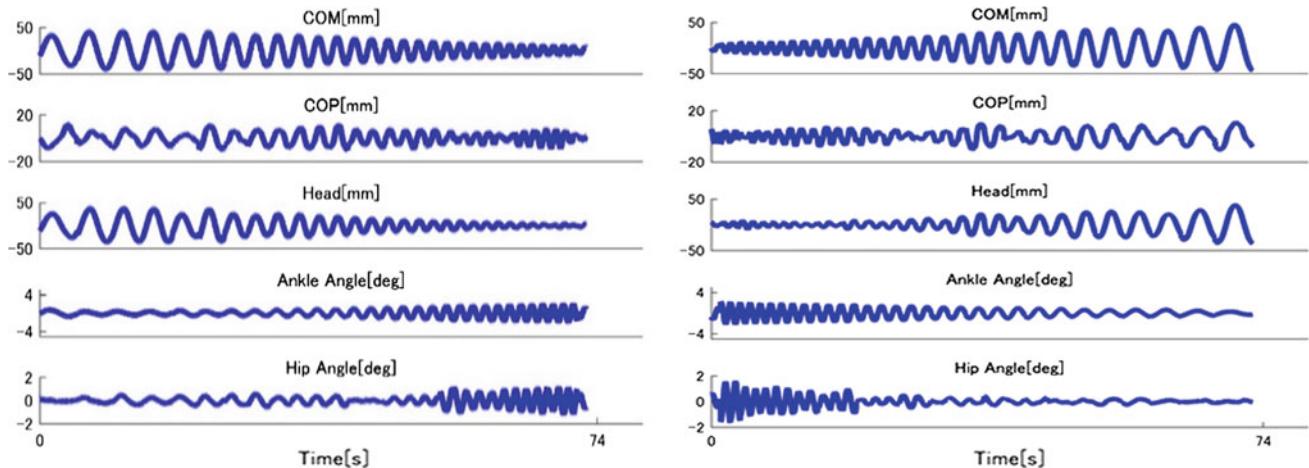

Fig. 2 Time series of mean displacement of kinetic and kinematic variables at the platform frequency 0.2–0.8 Hz for ascending (left) and descending (right) condition

p = 3.18E−50), head (F (30,216) = 10.71, p = 1.6E−26), ankle angle (F (30,216) = 42.57, p = 2.34E−66), hip angle (F (30,216) = 2.35, p = 0.0003), respectively) except COP displacement which show no significant difference in between frequencies during ascending frequency condition.

3.2 Cross Correlation Analysis

Cross correlation function analysis was used to address transition between COM-COP and ankle-hip coordination (see Fig. 3). Even though all participants were free from
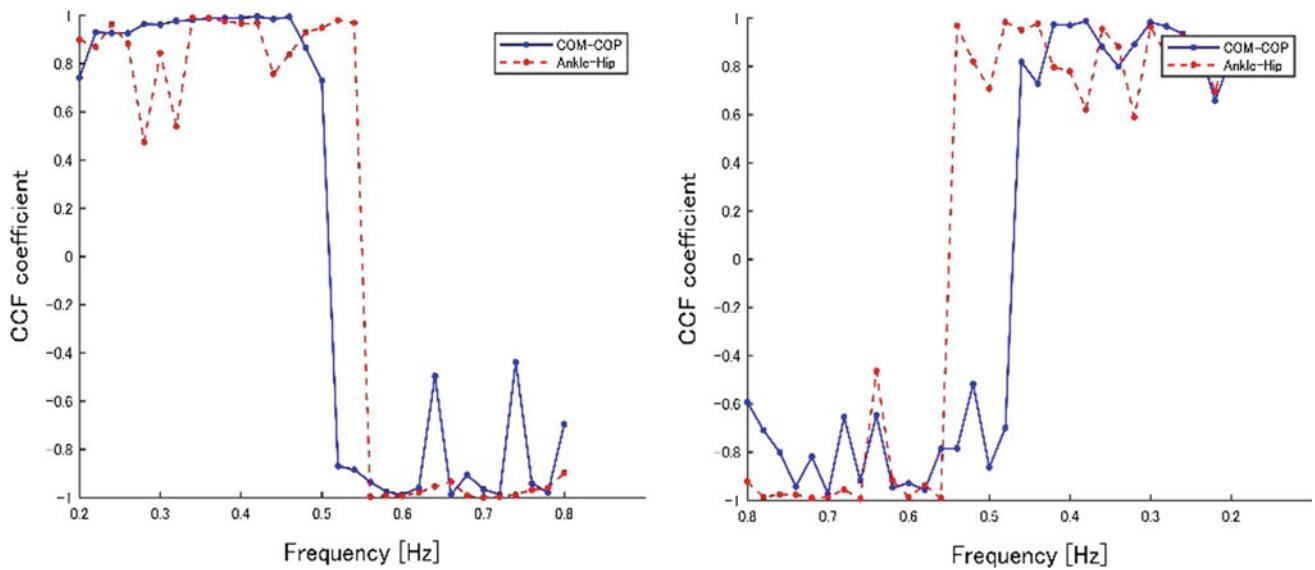
Fig. 3 A typical of cross correlation coefficients between COM-COP and ankle-hip of participant for descending (left) and ascending (right) condition

Table 1 The frequency of the transition for the COM-COP and ankle-hip coordination

Participant	COM-COP		Ankle-hip	
	Ascending	Descending	Ascending	Descending
S1	0.48	0.48	0.48	0.56
S2	0.38	0.62	0.44	0.38
S3	0.38	0.28	0.44	0.44
S4	0.26	0.58	0.48	0.36
S5	–	0.68	–	0.62
S6	0.50	0.78	0.54	0.58
S7	0.26	0.74	0.54	0.68
S8	0.42	–	0.44	–
Mean (SD)	0.38 (0.009)	0.59 (0.03)	0.48 (0.002)	0.52 (0.015)

COM Center of mass, *COP* Center of pressure

neurological diseases, none applied the same transition point between COM-COP and ankle-hip. All participants show the transition between COM-COP and ankle-hip angular except S5 which show no COM-COP transition during ascending frequency condition and ankle-hip transition during descending frequency condition for S8. Figure 3 indicate that all participants show positive correlation coefficient for the lower frequency which demonstrated an in-phase pattern, and a negative correlation coefficient for the higher frequency where the phase pattern was in anti-phase. However, the transition point was different between the participants. A transition point for every participant was shown in Table 1. For COM-COP transition changes, the transition was occurred in the range between 0.26 and 0.50 Hz for ascending frequency condition and in between 0.28 and 0.78 Hz for descending frequency condition. Besides, for ankle-hip transition changes, for ascending condition, the transition was occurred in the range between 0.44 and 0.54 Hz and in between 0.36 and 0.68 Hz for descending condition. A significant difference was observed at COM-COP transition between ascending and descending frequency condition ($p = 0.014$). However, no significant difference was observed in between ankle-hip transition frequency ($p = 0.44$; ns). For comparison between COM-COP and ankle-hip transition frequency in each condition, no significant difference was observed in both conditions ($p = 0.06$ for COM-COP and $p = 0.24$ for ankle-hip; ns).
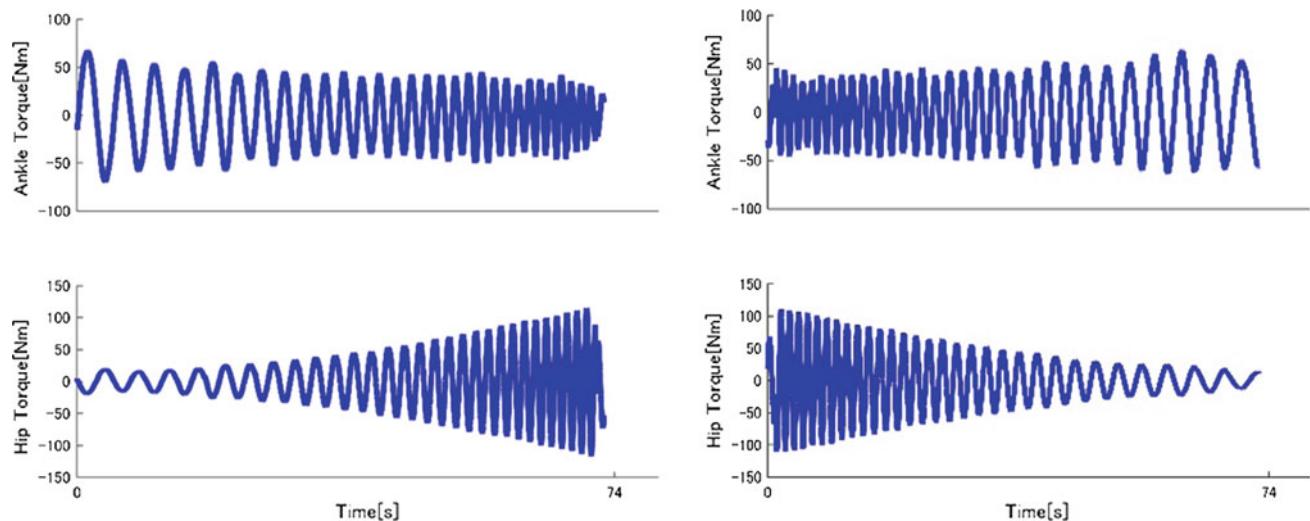
Fig. 4 Mean torque of all subjects towards ascending (left) and descending (right) frequency perturbation

3.3 Ankle and Hip Joint Torques

Postural control strategy formation was pursued with the analysis of ankle joint and hip joint torques. The formation of mean of all participant's ankle and hip joint torques in time series was presented on Fig. 4. In the early perturbation (low frequency), the ankle joint torque was greater than the hip joint torque for ascending frequency condition and vice versa for descending frequency condition. However, as the frequency perturbation increased/decreased, hip joint torque becomes higher/smaller than ankle joint torque. Even though the ankle joint torque was decreased/increased, but the decrease/increase was small compared to hip joint torque where the increased/decreased was seem to be about three times at the higher/lower frequency.

4 Discussion

This study's primary objective was to investigate the multi-segmental of postural control strategies from the kinematic variable in continuous anterior-posterior translation. In quiet standing, it was observed that the hip angle was greater than ankle angle [7]. However, in this study both joint angles were increased in dynamic standing with external continuous perturbation. From these results (Fig. 2), it's shown that ankle and hip were both in function towards maintaining balance in dynamic standing. It was believed that human postural control for every person is different and adapt quickly in order to maintain balance. Based on the results in Fig. 2, it was illustrated that kinematic characteristics were changed towards imbalance. For low anterior-posterior translation frequency, the participants rode the platform which resulted in higher COM displacement,

however, for higher translation frequency, participants fixed head motion in order to remain maintain on the platform. It was believed that in high frequency perturbation, adaptation was not a choice. The Central Nervous Systems (CNS) tend to apply accuracy control to reduce kinematic displacement in order to maintain balance in desired position [8]. Moreover, even the changes of frequency perturbation were not notified to the participants, the human body still can detect the changes of the frequency perturbation and adjust the COM within COP line. This can be seen by the participant gradually adjusting the postural control strategies from ankle strategy to hip strategy and influence the head and COM displacement to be decreased.

As shown in Table 1, the COM-COP transition occurred former than ankle-hip transition was observed in all participants in ascending condition. While the external force was given (perturbation frequency increased), the COM and COP position was moved and caused imbalance to the participants. Therefore, in order to achieve balance condition, postural control strategies were changed according to the pressure of varying task. From these results, when the participants were given external force, thus becomes unbalance and instable, postural control strategies were applied depending on the individual's goal and environment condition. Differences of transition point in between individual participants might be caused by variation of length segment, mass and force [9]. Besides, the transition was found on COM-COP and ankle-hip coordination demonstrated that the participants were able to control their body coordination depends on varying given frequency perturbation. However, for descending condition, the transition of ankle-hip was occurred former than COM-COP transition. In descending frequency, the subjects changed the strategies first in order to keep COM and COP point within balance line.

The result from ankle and hip torque (Fig. 3) proved that human used ankle strategy to maintain balance at the lower frequency. If the ankle cannot exert a sufficient moment on the ground, hip movement will replace the ankle strategy to achieve balance. Besides, ankle and hip strategies were both used at the higher frequency since the torque was higher for both joints. It appears that in constraining situation that limit the effectiveness of ankle torque, the anti-phase mode appears where the hip torque was higher than ankle torque. At the anti-phase mode where hip movement was occurring, without affecting the balance, body coordination was changed as to prevent the heel from lifting from the motion base in order to correct the COM and COP position [4].

5   Conclusion

The aim of this paper is to investigate the multi-segmental of human postural control strategies by using ankle and hip angular displacement as collective variable and discussed the cause of the transition. By manipulating the frequency of the perturbation, the changes in the COM and COP and also the changes in strategy applied can be observed. This study also able to demonstrated that ankle and hip angle parameter can be a collective variable to determine the postural control orientation by inducing simple dynamic balance task. By using cross-correlation analysis, in-phase and anti-phase between ankle and hip angle can be observed. Thus, these results were supported by observation at the ankle and hip joint torque where at the lower frequency greater ankle joint torque was observed. On the contrary, at the higher frequency perturbation, both ankle and hip joint torque were greater indicate that both joints were used to maintain

balance. However, further analysis should be done in order to collect more data and understanding in postural control orientation at continuous condition with visual constraint and increased more participant number.

Conflicts of Interest   The authors declare that they have no conflict of interest.

References

1. Pollock, A. S., Durward, B. R., Rowe, P. J., Paul, J. P., What is balance?. Clinical Rehabilitation. vol. 2000, pp. 6. (2000).
2. Anne, S. C., Marjorie, H. W., Motor control translating research into clinical practice. 3rd edn. Lippincott williams & wilkins, USA (2007).
3. Horak, F., B., and Nashner, L., M., Central programming of postural movements: adaptation to altered support-surface configurations. Journal of Neurophysiology. vol. 55, no. 6, pp. 1369. (1986).
4. Myriam, F., Violaine, C., Luc, M., Postural coordination modes and transitions: dynamical explanations. Exp. Brain Res. vol. 180, pp. 49–57. (2007).
5. Welch, T., D., J., and Ting, L., H., Mechanism of motor adaptation in reactive balance control. PLos One. vol. 9: e96440. (2014).
6. Adkin, A., L., Frank, J., S., Crpenter, M., G., Oeysar, G., W., Postural control is scaled to level of postural threat. Gait Posture. vol. 12, pp. 87–93. (2000).
7. Yu, A., Daichi, N., Kei, M., Takeshi, S., Kimitaka, N., Hideo, Y., Reciprocal angular acceleration of the ankle and hip joints during quiet standing in humans. Exp. Brain Res. Vol 136, pp. 463–473. (2001).
8. Missenard, O., and Fernandez, L., Moving faster while preserving accuracy. Neuroscience. vol. 197, pp. 223–241. (2011).
9. Ji-Hyun, K., John, H., C., Karl, M., N., Transition of COM-COP relative phase in dynamic balance task. Human Movement Science. vol. 38, pp. 1–14. (2014).

Semiportable Manually Actuated System for Measuring Muscle Spasticity

Barbora Adamova, Petr Volf, Jan Hybl, Patrik Kutilek, Jan Hejda,
Slavka Viteckova, Vaclav Krivanek, Radek Doskocil, Jan Farlik,
and Pavel Smrcka

Abstract

In the article, we describe a design of a new system which provides means to quantitatively assess passive resistance of skeletal muscles, also termed muscle spasticity. New design is focused on the measurement of muscle groups which are responsible for movement of elbow joint. The semiportable system is an alternative to expensive motorized isokinetic dynamometers. System is manually actuated dynamometer. The electronic subsystem of the system is used to measure angular velocity and torque in the elbow joint. An incremental encoder is used for the measurement of angular velocity. The angular velocity of the rotational movement in a joint is a result of movement effected by manually controlled lever. The lever is controlled by a physician. During the angular movement of the upper limb segments, the elbow joint torque is measured by a strain gauge subsystem. The output from the system is a graphic dependence between the angular velocity and the torque, which is used to evaluate spasticity. The dependence between the passive moment of force and kinematic angular parameters allows us to study complex motion and force possibilities of the joint. The designed system could be useable and widely applicable in clinical practice, as well as research of diseases and treatment of musculoskeletal system.

B. Adamova · P. Volf (✉) · J. Hybl · P. Kutilek
J. Hejda · S. Viteckova · P. Smrcka
Faculty of Biomedical Engineering, Czech Technical University
in Prague, Sitna sq. 3105, Kladno, Czech Republic
e-mail: petr.volf@fbmi.cvut.cz

B. Adamova
e-mail: adamobar@fbmi.cvut.cz

J. Hybl
e-mail: jan.hybl@fbmi.cvut.cz

P. Kutilek
e-mail: kutilek@fbmi.cvut.cz

J. Hejda
e-mail: jan.hejda@fbmi.cvut.cz

S. Viteckova
e-mail: slavka.viteckova@fbmi.cvut.cz

P. Smrcka
e-mail: smrcka@fbmi.cvut.cz

V. Krivanek · R. Doskocil · J. Farlik
Faculty of Military Technology, University of Defence,
Kounicova 65, Brno, Czech Republic
e-mail: vaclav.krivanek@unob.cz

R. Doskocil
e-mail: radek.doskocil@unob.cz

J. Farlik
e-mail: jan.farlik@unob.cz

1 Introduction

The oldest and most widely used methods for assessing muscle spasticity are qualitative methods of subjective evaluation by the scale of the forces acting against the movement induced by a physician. It is believed, that biggest limitation of currently used assessment techniques is their subjectivity, as the methods rely heavily on individual perception of assessing medical professional, [1]. Given these limitations, qualitative evaluation methodology and systems for measuring physical variables (force or torque) were designed.

Method used to measure muscular force and torque is called dynamometry, [2]. There is wide range of systems and methods measuring muscular force and torque [3], which can be categorized in various manners, but for purposes of this article, dynamometric systems for measurement of joint torque will be considered. Dynamometric methods can be divided into groups based on the type of muscular contraction involved. The groups would then be: isoinertial, isometric, and isokinetic dynamometry, [4, 5]. The isometric

and isokinetic dynamometry are mainly used in medical practice, [6]. Isometric dynamometry measures an isometric contraction of a muscle, which is muscle activity without resulting motion, [7]. Isokinetic dynamometry allows testing of isokinetic contraction, control and maintaining of constant angular velocity, [8, 9].

Above described dynamometers have significant limitations of use in small medical facilities. The main reason for a small extension into practice is their higher cost and technical complexity, especially in the case of isokinetic dynamometers. There is no cheap and portable/semiportable system for a determination of kinematic and dynamics quantities and parameters of a joint movement and their direct use in the field of medical research and practice, [10]. Therefore, the aim of this article is to describe new semiportable system capable of measurement of spastic muscles' passive resistance during angular joint movements.

2 Structure Design and Methods

2.1 Conceptual Design of the System's Structure

System consists of four main sections: manual actuation mechanism, movement measurement subsystem and torque measurement system. Less important parts, but without which the system could not be used to measure subjects are: adjustable table and chair, see Fig. 1. Overcoming the passive resistance of spastic limb is often considered to be the most challenging task during assessment. Therefore, the muscle stiffness measurement system is designed with a manual actuation. This decision was made in order to meet the cost requirements and to avoid the time-consuming

approval process for the use in practice. Proposed manual actuation utilizes a lever, where the assessing healthcare professional pulls on the end of the lever, which creates high torque at the shaft, which is then used to stretch the spastic muscles much easier than by pulling the limb directly. Torque generated on the lever is transmitted through the shaft supported by bearings onto a brace with a body segment.

2.2 Measurement Subsystem

To measure the torque at any joint a torque sensor which fits the design specifications is being used. To avoid under-specifying the system, the highest achievable torque in these joints has to be considered. The highest torque can be found in knee, at 318 ± 35 N m. Using gentle factor of safety at 1.1, the final limit equals 388.1 N m, which the sensor has to be able to measure. In the case of cheapest option, with manual actuation, we use stick strain gauges (1-xy21-3/120 type (max. perm. effective bridge excitation voltage is 6 V), Hottinger Baldwin Messtechnik (HBM) GmbH) arranged to full strain gauge bridge to measure strain caused by torsion in the shaft. For this measurement, A/D converter is also used as a data acquisition system for calibration of the strain gauge bridge, filtering of the measured data, and calculates the torque. The reason for this approach is high cost of commercial torque sensors. The strain gauges are placed on the shaft, between the lever and the brace for measured limb segment, see Fig. 2.

To measure the angular velocity of the angular joint movement, an incremental encoder can be used. Incremental encoder wheel can only be placed on the part of the shaft,
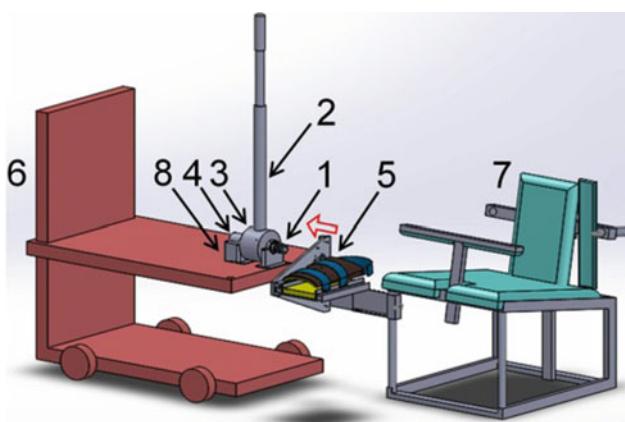
Fig. 1 The concept diagram of semiportable system for measuring muscle spasticity; 1—spline shaft, 2—lever, 3—torque sensor, 4—incremental sensor, 5—brace with support and guideway, 6—adjustable table, 7—adjustable chair, 8—bearing unit
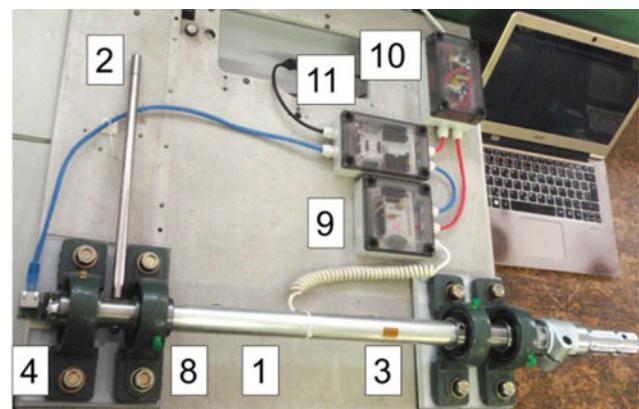
Fig. 2 The semiportable system for measuring muscle spasticity; 1—shaft, 2—lever, 3—torque sensor, 4—incremental sensor, 8—bearing unit, 9—A/D converter, 10—power supply, 11—programmable automation controller

that does not bear the load, i.e. isn't between the actuator and the load. This is fairly simple for the lever-action option. For the manual system, the main shaft is simply narrowed down at the loose end to a suitable diameter and the sensitive assembly of incremental encoder is obscured by a simple casing. Broadcom Limited incremental encoder is used, primarily due to its cost, accessibility and team's experience with its use. It consists of a sensor and a code wheel. System uses dedicated incremental encoder by Broadcom Limited, which consists of code wheel HEDS-5140#A13, see Fig. 2.

2.3 Limb Segment Fixation

Fixation of the rotating limb segment, which in all cases is the distal of the two segments connected by the joint, is solved by bespoke brace. Brace is mounted onto a system, which uses a combination of linear guideways to connect the brace to a socket, which connects this rotating part to the measuring and actuating assembly. To create controlled rotation in any joint, one segment has to be moved in a controlled manner, while the second segment has to remain fixed and stationary. For this purpose, a simple, adjustable chair was designed, with features to which the static segments can be strapped, see Fig. 1.

2.4 Control and Data Processing System

A successive approximation programmable 10-bit A/D converter (based on microcontroller AVR AT Tiny) is used to convert a continuous analog waveform into a discrete digital representation, [11]. Programmable converter also performs calibration of the strain gauge bridge, filtering of the measured data, and calculates the torque experimentally through predefined calibration curve.

Programmable automation controller (PAC) is used for data processing in real time. PAC allows a control of measurement process cyclically. Signals from torque sensor and incremental encoder are synchronized, converted and carried to PAC, where the outputs, such as torque and angular velocity are easily observed. The PAC is based on microcontroller Atmel AVR (AT90). PAC provides several functions: communication with the PC (i.e. data sending), sensor data collection and synchronization, and controlling the measurement process. Calculation of the angular velocity by counting the number of pulses per time is performed and the computational data are synchronized with the values of the torque.

More complex methods are evaluated using a custom-designed program using the MatLab software (MatLab R2010b, Mathworks, Inc., Natick, MA, USA). The
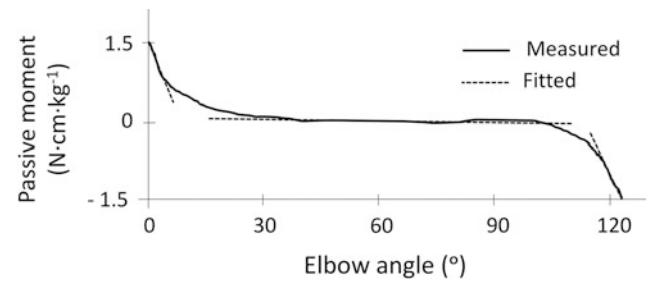
Fig. 3 Method of interpretation of record of passive elastic moment versus elbow angle. The measured torque is normalized to the weight of the subject being measured

main parameter that software allows to determine is joint stiffness. Joint stiffness is determined from plot of normalized, sagittal plane, ankle moment versus sagittal plane, ankle angle for an individual, during the rotation in the joint, see [12]. The joint stiffness is determined from the straight line that that is fitted to the curve parts, Fig. 3.

3 Discussion

In the literature review for design of system it was found that the assessment methods currently used in the clinical practice rely heavily on subjective perception of assessing individual [13, 14]. System described in this article provides objective means of spasticity evaluation. System is dimensioned based on values found during the measurement of certain joints. During the design process, the current clinical practice in the area was researched, while the expected torques at given joints were used as the key design constrains.

During the measurement with the manually actuated system, the electronics have no control over the actuation, but provide feedback to the operator to make sure the injury of a patient is prevented. It is strongly recommended that the system is in clinical practice only operated by an experienced healthcare professional who knows the limits of movement for measured joints. In a simple experiment it was found that untrained woman has very hard time producing a force exceeding 100 N. With 1 m lever and 100 N of force, 100 N m can be produced, which is enough to measure ankle or wrist, in case of slightly stronger assessor, also the elbow joint can be measurable. A claim can be made that the original assignment asked for system for measurement of only the upper extremities, which the designed manual system fulfills, [10].

Among the advantages of the system can be mentioned it's reduced cost, weight and complexity. The maintenance of the manual system does not differ largely from the eventually powered version, but the lack of motor suggests lower risk of breakdown.

4 Conclusion

Aim of this article was to describe new design of a prototype system which would provide means to quantitatively assess passive resistance of muscles, also termed muscle stiffness, muscle tone or spasticity. Muscle stiffness measurement system described in this article, will be used in practice, where the initial request originated from, once the system is assembled. As for the future work, design of the fixation and brace system to allow measurement of stiffness of wrist, knee, ankle neck and back muscles would surely increase the usability of the system.

References

1. Li, F., Wu, Y., Xiong, L.: Reliability of a new scale for measurement of spasticity in stroke patients, J. Rehabil. Med 48 (8), 746–53 (2014).
2. Aquin, C.F., Freire, M.T.F., Neves, N.M., Ferreira, P.C.A., Fonseca, S.T.: Analysis of the reliability of a method for measuring hamstring active peak torque angle, Rev. Bras. Fisioter. 11(2), 169–75 (2007).
3. Kawakami, Y., Fukunaga, T.: New insights into in vivo human skeletal muscle function", Exerc Sport Sci Rev. 34(1), 16–21 (2006).
4. Tatsukawa, D.E., Freitas, S.T., Carvalho Abreu, E.M., Dos Reis, M.C., Cunha, B., Moreira Prianti, T., Pupio Silva Lima, F., Oliveira Lima, M.: Muscle torque of healthy individuals and individuals with spastic hemiparesis after passive static stretching, Acta Bioeng. Biomech. 18(1), 35–9 (2016).
5. Abernethy, P.J., Jürimäe, J.: Cross-sectional and longitudinal uses of isoinertial, isometric, and isokinetic dynamometry, Med. Sci. Sports. Exerc. 28(9), 1180–7 (1996).
6. Menezes Bassan, N., Bertelli Simões, L., Siqueira Cesar, T. E. A., Corrêa Caritá, R. A., Rabello Lima, L. C., Denadai, B., Coelho Greco, C.: Reliability of isometric and isokinetic peak torque of elbow flexors and elbow extensors muscles in trained swimmers, Braz. J. Kinathrop. Hum. Perform., 17(5), 507–16 (2015).
7. Hogrel, J.Y., Ollivier, G., Canal, A.: Isometric dynamometry with a Biodex system for the follow-up of patients suffering from LGMD2A (calpainopathy), Neuromuscul. Disord. 19(8–9), 603 (2009).
8. Sasaki, K., Ishii, N.: Unloaded shortening velocity of voluntarily and electrically activated human dorsiflexor muscles in vivo, PLoS One 5(9), e13043 (2010).
9. Baltzopoulos, V., Brodie, D.A.: Isokinetic dynamometry, applications and limitations, Sports Med. 8(2), 101–16 (1989).
10. Lu, T.W., Hsu, H.C., Chang, L.Y., Chen, H.L.: Enhancing the examiner's resisting force improves the reliability of manual muscle strength measurements: comparison of a new device with hand-held dynamometry, J. Rehab. Med. 39(9), 679–84 (2007).
11. Baker, R. J.: CMOS Circuit Design, Layout, and Simulation, 3rd ed., Wiley IEEE, Hoboken (2010).
12. Quesada, P. M., Pitkin, M., Colvin, J: Biomechanical evaluation of a prototype foot/ankle prosthesis, IEEE Trans Rehabil Eng. 8(1), 156–159 (2000).
13. Lin, Y.C., Lin, I.L., Chou, T.F., Lee, H.M.: Quantitative evaluation for spasticity of calf muscle after botulinum toxin injection in patients with cerebral palsy: a pilot study, J. Neuroeng. Rehabil. 13 (1), 1–11 (2016).
14. Gregson, J.M., Leathley, M., Moore, A.P., Sharma, A.K., Smith, T.L., Watkins, C.L.: Reliability of the tone assessment scale and the modified ashworth scale as clinical tools for assessing poststroke spasticity, Arch. Phys. Med. Rehabil. 80(9), 1013–6 (1999).

Position Estimation of an IMU Placed on Pelvis Through Meta-heuristically Optimised WFLC

Stefano Cardarelli, Federica Verdini, Alessandro Mengarelli,
Annachiara Strazza, Francesco Di Nardo, Laura Burattini,
and Sandro Fioretti

Abstract

The estimation of lower trunk orientation and position during normal walking is relevant in clinical setting in order to improve the assessment of walking disorders. In this paper we introduce a new method for the estimation of the position of an Inertial Measurement Unit (IMU) placed on pelvis, during normal walking on a treadmill. The element of innovation is the use of a meta-heuristic optimisation process to estimate the optimal parameters of a Weighted Fourier Linear Combiner (WFLC) filter, which is designed to efficiently extract periodic/pseudo-periodic components of signals. The estimation of WFLC parameters was performed through an optimisation procedure based on the Artificial Bee Colony (ABC) algorithm, minimising the difference between the WFLC reconstructed position and the data coming from a sterophotogrammetry (SP) system. The WFLC weights obtained from the first set of data (training set), with different walking speeds, were then used to improve the estimation of multiple walking trials with the same measurement setup (test set). This approach allows to obtain useful clinical information using wearable, lightweight and low power consuming devices such as IMUs. This method has been validated through SP data, evaluating the Root Mean Square Error (RMSE) between the two system's position estimations. The results show a global improvement of the position estimation over the three axes both during the training phase and the test phase. A low SD among the RMSEs in the test set, after the filter application, shows a good repeatability of the method over different trials at the same speed.

1 Introduction

The estimation of center of mass (COM) during walking plays an important role in the detection of walking disorders [1–4], which can be also improved by the addition of electromyography signal [5]. In literature it is possible to find several methods to estimate the COM, which can be brought together in three main groups [6]:

1. Methods based on segmental analysis, which require measurements of center of masses of every body segment. These methods are considered to be the gold standard and provide an accurate COM estimation, at the cost of a great amount of computation.
2. Methods based on the double integration of the ground-reaction force data from force plates, also during posture trials [7, 8].
3. Methods based on the position of a single marker placed on the trunk or pelvis.

This last method assumes that the motion of the marker placed on the trunk or pelvis is similar to the one of the COM because of the anatomical proximity [1]. The main advantage of this method is the use of a single marker, thus allowing the use of a lighter hardware setup with respect to the other two methods. It is also remarkable that the use of a single marker gives the subject a great freedom of movement, taking the experiment closer to a normal walking situation. The experimental setup adopted in this study resulted to be compliant with the choice of replacing the

S. Cardarelli (✉) · F. Verdini · A. Mengarelli · A. Strazza · F. Di Nardo · L. Burattini · S. Fioretti
Università Politecnica delle Marche, Ancona, Italy
e-mail: s.cardarelli@pm.univpm.it

marker with an IMU, thus avoiding the use of the stereophotogrammetry (SP) system except for an initial filter tuning that will be introduced later on.

This kind of hardware setup choice requires a reliable software technique to provide a good estimation of the IMU position during time.

In the last ten years, one filtering technique that has proven to be suitable to improve position and orientation estimation performances in the field of human motion analysis is the Weighted Fourier Linear Combiner (WFLC) [9, 10]. This kind of filtering technique allows to extract periodic/pseudo-periodic components from signals. Since an intrinsic characteristic of human movement, and in particular human gait, is the periodicity or pseudo-periodicity of the position and orientation variation [11, 12], this filtering technique allows to remove all the non-periodic components from signals, such as drift introduced by IMUs [9].

However, the WFLC requires an initial parameters tuning in order to optimally perform. The aim of this work is to provide a method to estimate the best set of parameters to be used in the WFLC filter in order to reduce the root mean square distance between the position estimated by an IMU placed on pelvis and the one measured by a SP system, tracking a marker placed directly on the IMU. The novelty of this method is the necessity to estimate a single set of WFLC parameters, for a determined walking speed, in order to properly filter all the data acquired in different sessions at the same speed, to obtain results comparable to the SP system.

In the following work the method is presented as a list of single steps in the introduction of Sect. 2. Steps I and V of the aforementioned algorithm are then fully explained in the following subsections.

2 Materials and Methods

The proposed technique relies on two main phases. The first one consists in the estimation of the optimal WFLC weights and gains to properly reconstruct the device's position during normal walking, and it can be achieved through the following steps:

   I. IMU and SP data acquisition.
  II. Lower trunk pose estimation through a quaternion-based Unscented Kalman Filter (UKF) approach (Sect. 2.2) [13–15].

  III. Double integration of gravity-free acceleration data to obtain position.
  IV. High-pass filtering of position data to remove drift [9].
  V. Estimation of WFLC weights and gains through Artificial Bee Colony (ABC) optimisation algorithm, minimising the Root Mean Square Error (RMSE) between IMU-derived position and SP data (Sect. 2.3). This is performed for each of the three axes.

In the second phase (test) the fifth step is replaced by the following:

  V. Position data is passed through a WFLC filter set up with the weights and gains estimated during the first phase.

In other words, data gathered during the first phase is used as a training dataset to optimally tune the WFLC weights and gains for the next acquisitions.

2.1 Experimental Setup

Data was acquired from one healthy subject (*Gender*: Male, *Age*: 25, *Weight*: 80 kg, *Height*: 177 cm) with no history of neurological disorders, orthopedic surgery, acute/cronic knee-pain or pathology. The subject was asked to walk on a treadmill at different speeds (3 trials of 30 s at 3 km/h and 3 more at 5 km/h for a total of 6 trials) wearing an IMU (NGIMU, x-io Technologies, UK) placed on the lower back, with a sampling rate of 50 Hz. A retro-reflective marker was attached on the IMU device in order to be tracked by a 6-cameras SP system (Elite, BTS Bioengineering, IT, sampling rate 100 Hz).

This study was approved by the local expert committee and the subject gave his written informed consent.

2.2 Unscented Kalman Filter for Orientation Estimation

The followed UKF approach allows to perform a sensor fusion between the IMU's accelerometer and gyroscope [13–15]. Given these measurements, the filter computes an estimate of the state vector which matches the sensor's orientation:

$$\mathbf{x} = \begin{bmatrix} q_0 & q_1 & q_2 & q_3 \end{bmatrix}^T \tag{1}$$

where $\mathbf{q} = \begin{bmatrix} q_0 & q_1 & q_2 & q_3 \end{bmatrix}^T$ is a unit quaternion and $\mathbf{q}_t \equiv \mathbf{x}_t$ is the sensor's estimated orientation at time t.

The model function propagates the state from t to $t+1$ using the information acquired from the gyroscope [16]:

$$\mathbf{x}_{t|t+1} = \mathbf{x}_t + \frac{1}{2} \cdot \mathbf{x}_t \otimes \omega^q \cdot dt \tag{2}$$

where $\otimes$ is the quaternion product, ω^q is a quaternion vector defined as $\omega^q = \begin{bmatrix} 0 & \omega_x & \omega_y & \omega_z \end{bmatrix}^T$, where ω_i are gyroscope samples in the IMU's reference frame and dt is the inverse of the IMU's sampling rate.

The measurement function relates the state vector to the measurement coming from the accelerometer in order for the filter to be able to compute the residual (3) [13, 17]:

$$\mathbf{r} = (\mathbf{z}_t - \hat{\mathbf{z}}_t) \tag{3}$$

$$\hat{\mathbf{z}}_t = \mathbf{x}_t^* \otimes \mathbf{g}^q \otimes \mathbf{x}_t \tag{4}$$

where $\mathbf{x}_t^*$ is the conjugate of $\mathbf{x}_t$, $\mathbf{z}_t$ is the measured gravity field at time t in the sensor's reference frame obtained by low-pass filtering accelerometer data and $\mathbf{g}^q$ is a vector quaternion defined as $\mathbf{g}^q = \begin{bmatrix} 0 & 0 & 0 & g \end{bmatrix}^T$ in the earth reference frame.

The nonlinear nature of the measurement function (4) justifies the use of the UKF approach [13, 14, 18].

Accelerometer and gyroscope data acquired from each session were remotely elaborated through the previously described quaternion based UKF approach. The estimated pose for each time instant ($\mathbf{q}_t$) was then used to properly remove the gravity vector from acceleration data as follows:

$$\mathbf{a}_t = \mathbf{a}_t^{\mathbf{g}} - \mathbf{q}_t^* \otimes \mathbf{g}^q \otimes \mathbf{q}_t \tag{5}$$

where $\mathbf{a}_t^{\mathbf{g}}$ is the acceleration sample at time t which contains the gravity vector bias, $\mathbf{q}_t$ is the state vector estimate at time t with respect to the earth reference frame, $\mathbf{q}_t^*$ is the conjugate of $\mathbf{q}_t$ and $\mathbf{g}^q$ is defined as above.

The result of the quaternion products in (4) and (5) are both vector quaternion changes of reference frame (from earth-fixed to IMU-fixed). However, to compute the subtractions in (3) and (5), the result of the rotation operation must be converted into a (3×1) vector in order to avoid a dimension mismatch.

In order to properly estimate the sensor's position over time in the earth-fixed reference frame, each acceleration sample $\mathbf{a}_t$ was rotated about its relative estimated quaternion $\mathbf{q}_t$ as follows:

$$\mathbf{a}_t^e = \mathbf{q}_t \otimes \mathbf{a}_t \otimes \mathbf{q}_t^*, \quad \forall t \tag{6}$$

The operation showed in (6) is the inverse form of the one displayed in (4) and (5), which is still a vector quaternion change of reference frame but this time from the sensor's reference frame to the earth-fixed one.

At the end of this procedure, it is possible to estimate the IMU position over time by double integrating the acceleration $\mathbf{a}_t^e$ expressed in the earth fixed reference frame (Sect. 2 steps III and IV).

2.3 WFLC Weights and Gains Estimation

Given a periodic or pseudo-periodic signal as input s (where s_k is a sample of s at time k) the WFLC algorithm can estimate the Fourier series coefficients which represent the signal at time $k+1$ evaluating the following difference:

$$\varepsilon_k = s_k - \hat{s}_k \tag{7}$$

where $\hat{s}_k$ is the signal estimated by the WFLC algorithm at time k. The WFLC algorithm is briefly summarised in Algorithm 1.

Algorithm 1 Matlab WFLC pseudocode

1: **procedure** FILTER INITIALISATION
2:     $set: \ k = 1$
3:     $set: \ \mathrm{w}_{0_1}$ ▷ Frequency weight (fundamental pulsation)
4:     $set: \ \mathrm{w}_{b_1}$ ▷ Bias weight
5:     $set: \ \mathbf{w}_1$ ▷ Vector containing the amplitude weights
6:     $set: \ \boldsymbol{\mu} = \begin{bmatrix} \mu_0 \\ \mu_b \\ \mu \end{bmatrix}, \forall k$ ▷ WFLC Gains
7:     $compute: \ \mathcal{X}_1 = \begin{bmatrix} \sin(\sum_{j=1}^{k} \mathrm{w}_{0_j}) \\ \cos(\sum_{j=1}^{k} \mathrm{w}_{0_j}) \end{bmatrix}$ ▷ WFLC State [10]
8:     $compute: \ \hat{s}_1 = \mathbf{w}_1^T \mathcal{X}_1$ ▷ WFLC signal estimate at time $k = 1$
9: **procedure** MAIN LOOP
10:        **for** $k = 1 : length(s)$ **do**
11:            $\varepsilon_k = s_k - \hat{s}_k - \mathrm{w}_{b_k}$ ▷ As in (7) considering also the bias
12:            $\begin{cases} \mathbf{w}_{k+1} = \mathbf{w}_k + 2\mu \mathcal{X}_k \varepsilon_k \\ \mathrm{w}_{0_{k+1}} = \mathrm{w}_{0_k} + 2\mu_0 \varepsilon_k (\mathbf{w}_k(1)\mathcal{X}_k(2) - \mathbf{w}_k(2)\mathcal{X}_k(1)) \\ \mathrm{w}_{b_{k+1}} = \mathrm{w}_{b_k} + 2\mu_b \varepsilon_k \end{cases}$ ▷ LMS [19]
13:            $compute: \ \mathcal{X}_{k+1}$ ▷ As in step 7
14:            $compute: \ \hat{s}_{k+1}$ ▷ As in step 8

In order to apply the algorithm above, a certain number of parameters must be given in advance (steps 2–6) so that the filter can properly estimate the signal $\hat{s}_{k+1}$ when $k = 1$ (i.e. first main loop cycle).

Let us define $\mathcal{H}$ as the set of all the possible combinations of weights (steps 3–5) and gains (step 6) that can be fed to the WFLC algorithm at $k = 1$.

Following the work of Bonnet et al. [10], in which an unreported method is used to minimise a cost function, we managed to set up an optimisation process, using a meta-heuristic technique known as ABC [20], in order to find the set $h \in \mathcal{H}$. which satisfies the following form:

$$\min_{h \in \mathcal{H}} \{\mathrm{RMSE}(\hat{s}(h), s_{SP})\} \qquad (8)$$

where $\hat{s}(h)$ is the output of the WFLC algorithm with a given $h \in \mathcal{H}$ set of weights and gains and s_{SP} is the 3D trajectory of the marker placed on the IMU and recorded by the SP system.

For each walking speed, a single trial (training data) was used to obtain the optimal h-set of weights and gains which satisfies (8) for each of the three axes. Again, for each

walking speed, the optimal h-set was used to filter the remaining data.

The results shown in Sect. 3 are relative to the following ABC setup:

Colony size: 20 bees, *Stopping criteria*: 40 cycles, *Stuck resource trials limit*: 10 trials, *Number of parameters*: 7 (w_{0_1}, w_{b_1}, $\mathbf{w}_{1_{(2 \times 1)}}$ its dimension is bound by the chosen number of harmonics [10], $\boldsymbol{\mu}_{(3 \times 1)}$), *Parameters upper bound*: 0.6 (an higher value results in filter divergence), *Parameters lower bound*: 1e−8.

3 Results

See Fig. 1.

4 Discussion

The main focus of this work was to provide a method to reduce the error in the estimation of the absolute position of an IMU placed on the lower trunk during normal walking on treadmill at different speeds. The proposed experimental
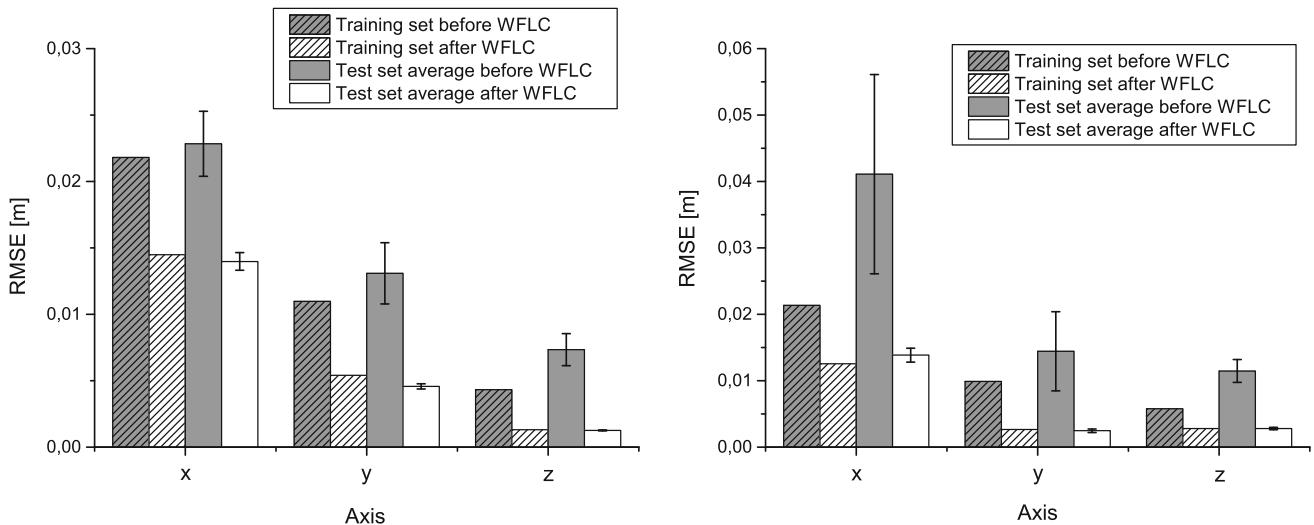
Fig. 1 In each bar graph the first couple of columns, for each axis, shows the ABC plus WFLC optimisation process results on training data. The same WFLC parameters were then used on the other trials, which results are shown as mean ± standard deviation (SD) of the RMSEs in the second couples of bars for each axis. The bar graph on the left refers to data acquired during trials at 3 km/h whilst the one on the right refers to trials at 5 km/h

setup could provide a useful instrument for the COM estimation [1] allowing the use of a single IMU instead of a marker placed on the trunk or pelvis, thus avoiding the need of an SP except for the initial filter's parameters tuning. Also, the use of a single IMU allows the subject to move freely, limiting the discomfort given by body-applied instrumentation.

The WFLC filter is an optimal estimator of periodic and pseudo-periodic signals. The motivation behind the choice of this kind of filter lies in the pseudo-periodic characteristics of signals related to human gait [11, 12]. This filtering choice reduces the effect of all the non-periodic components of the signal, thus increasing the quality of the position estimation.

However the WFLC approach requires a starting set of parameters to work properly. In the work of Bonnet et al. [10], in which the WFLC approach is applied to an orientation problem, this set of parameters is chosen by minimising a cost function. In this work we applied the same principle but minimising the RMSE between the IMU data and the gold standard in 3D tracking, the SP system, hence focusing on a position estimation problem, leaving the orientation estimation to the quaternion-based UKF approach. This minimisation was approached with a robust meta-heuristic technique, the ABC, which, to the knowledge of the authors, has never been applied in this kind of context.

The output of this minimisation was obtained by a number of training sets at different walking speeds and hence used on the test sets of data to improve their 3D position estimations' quality.

The results are shown in Fig. 1. This kind of representation of the RMSEs achieved using the proposed method, aims to focus the attention on the following two main aspects. The first and at the same time the most evident fact is that in both instances, during the training and the testing phase, the RMSEs between the IMU-estimated position and the SP-estimated one significantly decrease among each axis. The second one can be inferred directly comparing the values reached by the RMSEs both during the training and the test phase after the WFLC filtering. In fact, in both instances, the values reached are comparable regardless of the starting RMSE values. This is also pointed out by the SD values' drop in the test sets before and after the WFLC filtering, confirming that, although the initial errors may be much higher than the ones in the training set, and very different from one trial to another, the final error values will be similar among all the trials analysed.

This last point underlines the robustness of the method with respect to the initial error values and the diversity among the trials acquired.

Lastly, the second point highlights also the fact that a single set of parameters got from one trial under certain experimental circumstances (such as same subject walking at a determined speed) well fits the other trials acquired under the same experimental setup.

Further studies will aim to prove the repeatability of this method under different experimental setups (different walking speeds, run, different subjects and multiple terrains), in order to prove that a single set of parameters, under the same experimental conditions, could work on different subjects. It

would then be possible to build a database of WFLC parameters, categorized by kinematic tasks, which could be used to apply the proposed method without the need of a SP system.

Conflict of Interest The authors declare that there is no conflict of interest.

References

1. Kerrigan, D.C., Viramontes, B.E., Corcoran, P.J., LaRaia, P.J.: Measured versus predicted vertical displacement of the sacrum during gait as a tool to measure biomechanical gait performance. American journal of physical medicine & rehabilitation 74(1), 3–8 (1995).
2. Simon, S., Knirk, J., Mansour, J., Koskinen, M.: The dynamics of the center of mass during walking and its clinical applicability [proceedings]. Bulletin of the Hospital for Joint Diseases 38(2), 112 (1977).
3. Iida, H., Yamamuro, T.: Kinetic analysis of the center of gravity of the human body in normal and pathological gaits. Journal of biomechanics 20(10), 987–995 (1987).
4. Inman, V.T., Eberhart, H.D., et al.: The major determinants in normal and pathological gait. JBJS 35(3), 543–558 (1953).
5. Di Nardo, F., Fioretti, S.: Emg-based analysis of treadmill and ground walking in distal leg muscles. In: XIII Mediterranean Conference on Medical and Biological Engineering and Computing 2013. pp. 611–614. Springer (2014).
6. Thirunarayan, M.A., Kerrigan, D.C., Rabuffetti, M., Della Croce, U., Saini, M.: Comparison of three methods for estimating vertical displacement of center of mass during level walking in patients. Gait & Posture 4(4), 306–314 (1996).
7. Cavagna, G.A.: Force platforms as ergometers. Journal of applied physiology 39(1), 174–179 (1975).
8. Fioretti, S., Guidi, M., Ladislao, L., Ghetti, G.: Analysis and reliability of posturographic parameters in parkinson patients at an early stage. In: Engineering in Medicine and Biology Society, 2004. IEMBS'04. 26th Annual International Conference of the IEEE. vol. 1, pp. 651–654. IEEE (2004).
9. Latt, W.T., Veluvolu, K.C., Ang, W.T.: Drift-free position estimation of periodic or quasi-periodic motion using inertial sensors. Sensors 11(6), 5931–5951 (2011).
10. Bonnet, V., Mazzà, C., McCamley, J., Cappozzo, A.: Use of weighted fourier linear combiner filters to estimate lower trunk 3d orientation from gyroscope sensors data. Journal of neuroengineering and rehabilitation 10(1), 29 (2013).
11. Winter, D.A.: Biomechanics of human movement with applications to the study of human locomotion. Critical reviews in biomedical engineering 9(4), 287–314 (1984).
12. Perry, J., Davids, J.R., et al.: Gait analysis: normal and pathological function. Journal of Pediatric Orthopaedics 12(6), 815 (1992).
13. Kraft, E.: A quaternion-based unscented kalman filter for orientation tracking. In: Proceedings of the Sixth International Conference of Information Fusion. vol. 1, pp. 47–54 (2003).
14. Merwe, R.V.D.: Sigma-Point Kalman Filters for Probabilistic Inference in Dynamic State-Space Models. dissertation (2004).
15. Enayati, N., Momi, E.D., Ferrigno, G.: A quaternion-based unscented kalman filter for robust optical/inertial motion tracking in computer-assisted surgery. IEEE Trans. on Instrum. and Measure. 64 (8), 2291–2301 (2015).
16. Sabatini, A.M.: Estimating three-dimensional orientation of human body parts by inertial/magnetic sensing. Sensors 11, 1489–1525 (2011).
17. Jazwinski, A.H.: Stochastic Processes and Filtering Theory. Analytical Mechanics Associates, Inc., Seabrook, Maryland (1970).
18. Terejanu, G., Singh, T., Scott, P.D.: Unscented kalman filter/smoother for a cbrn puff-based dispersion model. In: Information Fusion, 2007 10th International Conference on. pp. 1–8. IEEE (2007).
19. Widrow, B., Stearns, S.D., Burgess, J.C.: Adaptive signal processing edited by bernard widrow and samuel d. stearns. The Journal of the Acoustical Society of America 80(3), 991–992 (1986).
20. Karaboga, D., Basturk, B.: A powerful and efficient algorithm for numerical function optimization: Artificial bee colony (abc) algorithm. Journal of Global Optimization 39 (2007).

Pressure Pulse Wave Velocity and Axial Prestretch in Arteries

Lukáš Horný and Ján Kužma

Abstract

The velocity of the propagation of a pressure pulse wave is considered to be a useful marker of the state of health of the cardiovascular system. Many clinical measurements, laboratory experiments and computational simulations have proved that the pressure pulse velocity correlates with age-related changes in the mechanical properties of arteries. Age-related stiffening of arteries, referred to as arteriosclerosis, leads to the increase in the pressure pulse velocity. However, the stress and strain state of an artery is not given solely by its loading and mechanical properties. Arteries are residually stressed that can be seen when cylindrical segment of an artery is excised from the body. The segment retracts because the axial prestretch is released. This prestretch declines with age, as a consequence of the damage accumulated to elastic lamellae during aging. Previous studies have paid little attention to the effect of axial prestretch on the velocity of the pressure pulse wave. The study presented here is based on a combination of a linearized 1D model of the fluid dynamics and the nonlinear anisotropic response of the human abdominal aorta. The model predicts that the application of axial prestretch can significantly change the velocity of the pressure pulse. To be more specific, preliminary results suggest that within the range of physiological pressures, the model that considers initial axial stretch of the aorta predicts lower pressure pulse velocity in comparison with the model that neglects axial prestrain of the tube.

1 Introduction

The blood ejected into the aorta during heart systole induces a pressure pulse wave, which is transmitted by the arterial wall towards the periphery [1]. As this is a mechanical wave, the pressure pulse travels with finite velocity (PWV), which depends on the mechanical properties of the wall and the blood, and on the geometry of the artery. Due to its direct relation to arterial stiffness, PWV has been established as a useful marker of the state of health of the cardiovascular system [2, 3]. Aged, therefore stiffened, arteries transmit a pressure pulse wave with higher velocity. This has been proven in many clinical measurements, laboratory experiments and computational simulations [4, 5].

The mechanical state of an artery, however, is not dictated merely by its material properties and by the external loading caused by blood pressure. Arteries exhibit stresses and strains induced by their growth and remodeling [6, 7]. When a tubular segment of an artery is excised in an autopsy, the segment retracts because arteries grow axially prestretched [8–10]. This way induced axial residual stress plays an important mechanical role. Under physiologically optimal conditions, axial prestress reduces the variation of axial stress and strain during the pressure cycle, and also contributes to the circumferential distensibility of an artery [11, 12].

The axial prestretch declines with age, and this goes hand-in-hand with the damage accumulated to elastic

L. Horný (✉) · J. Kužma
Faculty of Mechanical Engineering, Czech Technical University in Prague, Technická 4, 16607 Prague, Czech Republic
e-mail: lukas.horny@fs.cvut.cz

J. Kužma
Institute of Rock Structure and Mechanics, Academy of Sciences of the Czech Republic, V Holešovičkách 94, 18209 Prague, Czech Republic

membranes [8, 10, 11]. Our study aims to elucidate the effect of axial prestretch on the pressure pulse wave velocity in the human abdominal aorta. Our computational model for predicting PWV will be based on a 1D linearized model of the fluid dynamics, which will be combined with the nonlinear solid mechanical response of the aorta. It will be shown that axially prestretched artery transmits a pressure wave with a lower velocity than its non-prestretched counterpart.

2 Methods

2.1 Inflation and Extension of the Aortic Wall

The abdominal aorta is modeled as a thin-walled tube with middle radius R, thickness H and length L, which, due to a change in internal pressure or axial force, changes its radius to r, its length to l, and its thickness to h. Thus, the deformation gradient $\mathbf{F}$ expressed in polar cylindrical coordinates takes the form as follows, $\mathbf{F} = diag(\lambda_R, \lambda_\Theta, \lambda_Z) = diag(h/H, r/R, l/L)$. The material of the wall is assumed to be incompressible, $det\mathbf{F} = \lambda_R \lambda_\Theta \lambda_Z = 1$.

It is assumed that the thin-walled tube modeling the abdominal aorta satisfies the balance equations expressed in (1). The radial stress σ_{rr} is considered to be zero, thanks to the thin-walled assumption. The circumferential stress $\sigma_{\theta\theta}$ and the axial stress σ_{zz} correspond to the Laplace law for a closed circular cylindrical tube loaded by internal pressure P and axially prestretched by force F_{red}. The inertial force is neglected due to the small volume of the wall in comparison to the blood.

$$\sigma_{rr} = 0 \quad \sigma_{\theta\theta} = \frac{rP}{h} \quad \sigma_{zz} = \frac{rP}{2h} + \frac{F_{red}}{2\pi rh} \tag{1}$$

2.2 Constitutive Behavior of the Aortic Wall

The abdominal aorta is considered to be an anisotropic and nonlinearly elastic continuum. Its mechanical response is governed by the strain energy density function W, which is expressed in (2). The stored energy is here decoupled into the part related to the isotropic matrix (elastic fibers, passive smooth muscle cells, and other connective proteins), which is represented in (2) by a linear neo-Hookean term, and into the part expressing the contribution of the collagen fibers, which is represented by the sum of two exponential expressions. These two exponential expressions reflect the large strain stiffening of an artery wall due to nonlinear recruitment of collagen fibers into the load-carrying process. I_1 denotes the first principal invariant of the right Cauchy-Green strain tensor $\mathbf{C} = \mathbf{F}^T\mathbf{F}$. K_j (j = 4, 6) denotes

structural invariants arising from the anisotropy of the material, and is expressed in (3). The anisotropy of an artery wall is a consequence of the collagen fibers that reinforce the wall. The collagen fibers are assumed to be arranged into two families of helices, around which a small portion of the fibers is dispersed. The predominant directions of fiber families are inclined from the tangential axis of the tube with angles β and $-\beta$. Under this situation, $I_4 = I_6 = \lambda_\Theta^2 cos^2(\beta) + \lambda_Z^2 sin^2(\beta)$ holds.

$$W = \frac{\mu}{2}(I_1 - 3) + \sum_{j=4,6} \frac{k_1}{2k_2}\left(e^{k_2\left(K_j-1\right)^2} - 1\right) \tag{2}$$

$$K_j = \kappa I_1 + (1 - 3\kappa)I_j \quad j = 4, 6 \tag{3}$$

Strain energy density function W expressed in (2) has been introduced by T. C. Gasser et al. in [13] and has become very popular in the last decade in cardiovascular biomechanics community. Constitutive equations for the hyperelastic incompressible wall of the abdominal aorta are expressed in (4). The Cauchy stress tensor is assumed to be of the form $\boldsymbol{\sigma} = diag(\sigma_{rr}, \sigma_{\theta\theta}, \sigma_{zz})$. In (4), p denotes a Lagrangean multiplier enforcing a hydrostatic stress component, which has to be determined by means of boundary conditions.

$$\sigma_{rr} = \lambda_R \frac{\partial W}{\partial \lambda_R} - p \quad \sigma_{\theta\theta} = \lambda_\Theta \frac{\partial W}{\partial \lambda_\Theta} - p \quad \sigma_{zz} = \lambda_Z \frac{\partial W}{\partial \lambda_Z} - p \tag{4}$$

2.3 Fluid Dynamics Equations

The blood flow in the abdominal aorta is considered to be 1D. Under this condition, the balance of the momentum can be written in the form of (5) and the conservation of mass can be written in the form of (6). Here v is the axial velocity of the flowing blood, A is the cross-section of the pressurized artery, ρ is blood density, and t denotes time.

$$\frac{\partial v}{\partial t} + v\frac{\partial v}{\partial z} + \frac{1}{\rho}\frac{\partial P}{\partial z} = 0 \tag{5}$$

$$\frac{\partial vA}{\partial z} + \frac{\partial A}{\partial t} = 0 \tag{6}$$

Following standard arguments and assumptions (long wave and insignificant $r = r(z)$, insignificant contribution of the convective acceleration), explained in detail for instance in Fung's monograph [14] pp. 140–146, one can arrive to (7). Pulse wave velocity c is in (7) expressed in one of possible forms of the famous Moens-Korteweg equation. Here, in contrast to ordinary linear form, where Young

elastic modulus appears in (7), stiffness is introduced via term $\lambda_\Theta(\partial P/\partial\lambda_\Theta)$ which opens a possibility to combine linear fluid dynamics inside the elastic tube with nonlinear solid mechanics of the tube's wall.

$$c = \sqrt{\frac{\lambda_\Theta}{2\rho}\frac{\partial P}{\partial\lambda_\Theta}} \quad (7)$$

2.4 Differentiation of the Pressure

Equation (7) gives us a simple instrument for estimating how the axial prestretch induced by axial force F_{red} influences the velocity of the propagation of the pressure pulse in the abdominal aorta. What we need here is $P = P(\lambda_\Theta)$ to be able to evaluate $\partial P/\partial\lambda_\Theta$, which appears in (7). This can be done with the help of balance equations (1). The substitution of σ_{rr}, $\sigma_{\theta\theta}$, and σ_{zz} from constitutive equations (4) into (1) and the replacement of the unknown deformed dimensions by means of kinematic equations of the inflated thin-walled cylindrical tube $h = \lambda_R H$, $r = \lambda_\Theta R$, leads to the system of equations (8–10).

$$\lambda_R\frac{\partial W}{\partial\lambda_R} - p = 0 \quad (8)$$

$$\lambda_\Theta\frac{\partial W}{\partial\lambda_\Theta} - p = P\frac{\lambda_\Theta}{\lambda_R}\frac{R}{H} \quad (9)$$

$$\lambda_Z\frac{\partial W}{\partial\lambda_Z} - p = \frac{P}{2}\frac{\lambda_\Theta}{\lambda_R}\frac{R}{H} + \frac{F_{red}}{2\pi\lambda_\Theta\lambda_R RH} \quad (10)$$

Equation (8) determines p. It is substituted to (9) and (10). Simultaneously, the incompressibility condition $\lambda_R\lambda_\Theta\lambda_Z = 1$ is used to replace λ_R. Equation (9) takes the form of (11), and Eq. (10) takes the form of (12).

$$\left[\lambda_\Theta\frac{\partial W}{\partial\lambda_\Theta}\right]_{\lambda_R=\lambda_\Theta^{-1}\lambda_Z^{-1}} - \left[\lambda_R\frac{\partial W}{\partial\lambda_R}\right]_{\lambda_R=\lambda_\Theta^{-1}\lambda_Z^{-1}} = P\lambda_\Theta^2\lambda_Z\frac{R}{H} \quad (11)$$

$$\begin{aligned}\left[\lambda_Z\frac{\partial W}{\partial\lambda_Z}\right]_{\lambda_R=\lambda_\Theta^{-1}\lambda_Z^{-1}} &- \left[\lambda_R\frac{\partial W}{\partial\lambda_R}\right]_{\lambda_R=\lambda_\Theta^{-1}\lambda_Z^{-1}} \\ &= \frac{P}{2}\lambda_\Theta^2\lambda_Z\frac{R}{H} + \frac{F_{red}}{2\pi RH}\lambda_Z\end{aligned} \quad (12)$$

3 Simulation of the Effect of Axial Prestretch on PWV

Computational model based on the system of equations (11–12) and (7) will be used to estimate how axial prestretch affects pressure pulse wave velocity in the human abdominal

aorta. The material parameters and the reference dimensions were adopted from [15].

In the first step of the simulation, neglecting inertial forces for the aortic wall, quasi-static predictions of the simultaneous inflation and extension of the aorta were conducted on the basis of Eqs. (11) and (12). With the parameters adopted form [15], the initial axial stretches were given as λ_Z^{ini} = 1, 1.05, 1.1, 1.15, 1.2, 1.25, 1.3, 1.35, and 1.4. (11) and (12) were used to compute λ_Θ and λ_Z for pressures $P = 0.1(i − 1)$ kPa, where $i = 1 \dots 181$. For $i = 1$, $\lambda_Z = \lambda_Z^{ini}$ and $P = 0$ hold and λ_Θ^{ini} and F_{red} are computed.

When $i > 1$, P and F_{red} are assigned and λ_Θ and λ_Z are obtained from the simulation. This means that when the pressure rises, the tube axially prestressed by F_{red} inflates and, as a consequence, the tube deforms both in circumferential direction (λ_Θ) and in axial direction (λ_Z). Although F_{red} is constant during pressurization, $\sigma_{\theta\theta}$ and σ_{zz} change to satisfy the constitutive equations (4). In the second step of the simulation, $\partial P/\partial\lambda_\Theta$ was computed for specific P, F_{red}, λ_Θ and λ_Z, and all these quantities were substituted into (7) to obtain PWV. For the sake of completeness, blood density ρ was considered to be 1060 kg/m^3 throughout the study. All the computations were performed with the help of Maple 2015.

4 Results and Discussion

The computed results are presented in Figs. 1 and 2. Figure 1 depicts the quasi-static inflation-extension response of 38 years old male individual characterized with the following constitutive parameters μ = 15.90 kPa, k_1 = 78.49 kPa, k_2 = 4.991, β = 41.41°, κ = 0.1875, and referential geometric dimensions R_i = 5.3 mm, H = 1.22 mm. Figure 2 shows the dependence of the pressure pulse wave velocity on the axial prestretch determined in the simulation.

Figure 1 is easy to interpret, when the reader realizes that the $P - \lambda_\Theta$ curves shift to the left for increasing prestretch, and the $P - \lambda_Z$ curves shift monotonically to the right. It is clear that the mechanical response depends substantially on the prestretch. From previous studies [11, 12], it is known that axial prestretch makes the aorta more distensible at in vivo pressures (approx. 10–16 kPa). Detailed exploration of $P - \lambda_\Theta$ dependences in Fig. 1 confirms this statement. One reveals that highly axially prestretched artery (violet curve, λ_Z^{ini} = 1.4) is more deformed when the pressure rises from 10 to 16 kPa than a non-prestretched artery (brown curve, λ_Z^{ini} = 1.0).

Figure 2 shows that axial prestretch also affects pressure pulse velocity. The lowest velocities were computed for the highest axial prestretchces. It suggests that axial prestretch not only makes arteries more distensible, it simultaneously
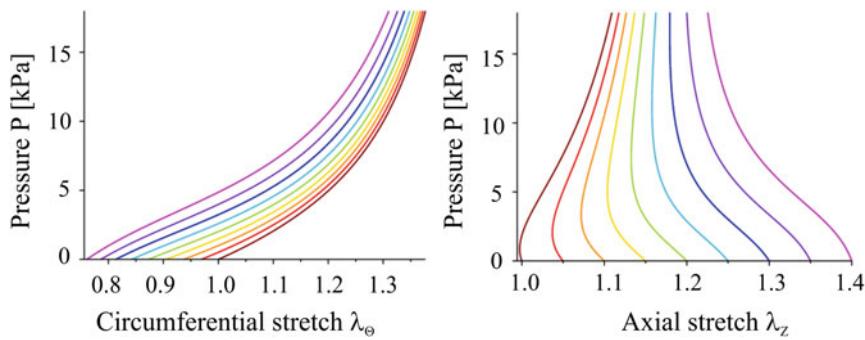
Fig. 1 Quasi-static predictions of the inflation-extension behavior for abdominal aorta obtained from (11–12). Axial prestretch λ_Z^{ini} is the value at which $P - \lambda_Z$ curves begin for $P = 0$. Prestretches are distinguished by the color of the curves (Color figure online)
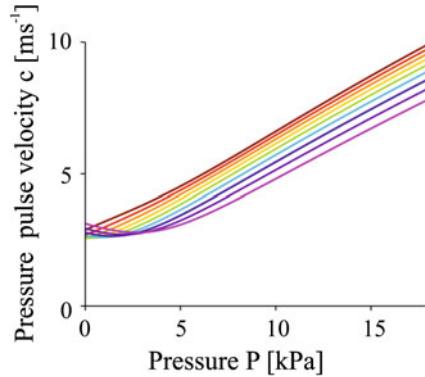

Fig. 2 Dependence of the pressure pulse velocity on the pressure. Prestretches are distinguished by the color of the curves. Color scheme is the same as in Fig. 1. The highest prestretch $\lambda_Z^{ini} = 1.4$ is indicated by the violet color (lowest curve) (Color figure online)

decreases the velocity at which pressure pulse propagates along the aorta. Although this study is based on simplified model of the fluid-structure interaction, it again indicates that initial axial stretch plays very important role in the cardiovascular physiology. Limitations of the study consists in assumptions adopted in the model. The most important limitations are neglected nonlinearity in flow equations and the assumption of inviscid flow.

Conflict of Interest Authors declare that they have no conflict of interest.

References

1. Greenwald, S. E.: Ageing of the conduit arteries. Journal of Pathology 211(2), 157–172 (2007).
2. Hansen, T. W., Staessen, J. A., Torp-Pedersen, C., Rasmussen, S., Thijs, L., Ibsen, H., Jeppesen, J.: Prognostic value of aortic pulse wave velocity as index of arterial stiffness in the general population. Circulation 113(5), 664–670 (2006).
3. Boutouyrie, P., Vermeersch, S. J.: Determinants of pulse wave velocity in healthy people and in the presence of cardiovascular risk factors: Establishing normal and reference values. European Heart Journal 31(19), 2338–2350 (2010).
4. Avolio, A. P., Chen, S. G., Wang, R. P., Zhang, C. L., Li, M. F., O'Rourke, M. F.: Effects of aging on changing arterial compliance and left ventricular load in a northern chinese urban community. Circulation 68(1), 50–58 (1983).
5. McEniery, C. M., Yasmin, Hall, I. R., Qasem, A., Wilkinson, I. B., Cockcroft, J. R.: Normal vascular aging: Differential effects on wave reflection and aortic pulse wave velocity - the anglo-cardiff collaborative trial (ACCT). Journal of the American College of Cardiology 46(9), 1753–1760 (2005).
6. Humphrey, J. D., Eberth, J. F., Dye, W. W., Gleason, R. L.: Fundamental role of axial stress in compensatory adaptations by arteries. Journal of Biomechanics 42(1), 1–8 (2009).
7. Rachev, A., Greenwald, S. E.: Residual strains in conduit arteries. Journal of Biomechanics 36(5), 661–670 (2003).
8. Horny, L., Adamek, T., Kulvajtova, M.: Analysis of axial prestretch in the abdominal aorta with reference to post mortem interval and degree of atherosclerosis. Journal of the Mechanical Behavior of Biomedical Materials 33(1), 93–98 (2014).
9. Horny, L., Adamek, T., Chlup, H., Zitny, R.: Age estimation based on a combined arteriosclerotic index. International Journal of Legal Medicine 126(2), 321–326 (2012).
10. Horný, L., Adámek, T., Kulvajtová, M.: A comparison of age-related changes in axial prestretch in human carotid arteries and in human abdominal aorta. Biomechanics and Modeling in Mechanobiology 16(1), 375–383 (2017).

11. Horný, L., Netušil, M., Voňavková, T.: Axial prestretch and circumferential distensibility in biomechanics of abdominal aorta. Biomechanics and Modeling in Mechanobiology 13(4), 783–799 (2014).

12. Horný, L., Netušil, M.: How does axial prestretching change the mechanical response of nonlinearly elastic incompressible thin-walled tubes. International Journal of Mechanical Sciences 106, 95–106 (2016).

13. Gasser, T. C., Ogden, R. W., Holzapfel, G. A.: Hyperelastic modelling of arterial layers with distributed collagen fibre orientations. Journal of the Royal Society Interface 3(6), 15–35 (2006).

14. Fung, Y. C.: Biomechanics: Circulation. 2nd edn. Springer-Verlag, New York (1997).

15. Horný, L., Netušil, M., Daniel, M.: Limiting extensibility constitutive model with distributed fibre orientations and ageing of abdominal aorta. Journal of the Mechanical Behavior of Biomedical Materials 38, 39–51 (2014).

Biphasic Rheology of Different Artificial Degenerated Intervertebral Discs

Mohammad Nikkhoo, Romina Kargar, and Kinda Khalaf

Abstract

Simulation of the intervertebral disc (IVD) degeneration in animal models is of great interest towards exploration and evaluation of potential regenerative therapeutics. Hence, the objective of this study was to investigate the biphaisc response of the IVD for different artificial degeneration models. Fifty motion segments were dissected from juvenile sheep lumbar spines. The specimens were assigned equally into 5 groups (i.e., (1) intact (I), (2) punctured with a 16-G needle (P), (3) punctured with a 16-G needle combined with fatigue loading (PF), (4) denatured by injecting 0.5 ml 0.25% trypsin solution (T), and (5) denatured by injecting 0.5 ml 0.25% trypsin solution combined with fatigue loading (TF)). Specimens were mounted in a chamber filled with phosphate buffered saline and underwent a stress-relaxation test. Based on linear biphasic theory, the aggregate modulus (H_A) and permeability (k) were extracted. Aggregate modulus decreased in P and T discs but increased in PF discs as compared to intact ones. The difference of the aggregate modulus between TF and intact discs was not significant. Permeability decreased in T, PF and TF discs. The permeability of both PF and TF discs was significantly lower than F and T discs, respectively. It is concluded that proposed artificial degeneration models can be used to investigate potential regenerative therapeutics.

Keywords

Intervertebral disc • Degeneration • Biphasic theory Biomechanics

M. Nikkhoo (✉) · R. Kargar
Department of Biomedical Engineering, Science and Research Branch, Islamic Azad University, Tehran, Iran
e-mail: m_nikkhoo@hotmail.com

K. Khalaf
Department of Biomedical Engineering, Khalifa University of Science and Technology, Abu Dhabi, United Arab Emirates

1 Introduction

The economic cost, activity limitation and human suffering caused by low back pain have been highlighted by many epidemiological studies and have motivated researchers to seek proper therapeutic strategies [1, 2]. Hence, there is a great deal of interest in investigating innovative therapies for treating degeneration of the intervertebral disc. Developing potential therapies, though, requires testing in artificial denatured or degenerated models before being used for patients [2, 3]. An in vivo experiment using large animals is costly and may not be realistic for screening new therapies at a large scale. Hence the in vitro and ex vivo experiments are usually desirable before the conduction of large animal studies [2, 4–6].

Various animal models were employed to mimic disc degeneration using the injection of enzymatic digestion (such as Trypsin, Glycation and Chondroitinase ABC), stab injury, and mechanical loading [3–5, 7]. The underlying mechanisms involved in these human-made degeneration methods, however, may be different from the natural physiological human disc degeneration. Little research addresses the rheological properties of the disc following chemical, physical and mechanical treatments, which result in some similar changes observed in mild and severe degenerative disc disease.

Several experimental and clinical observations suggested that it would be more realistic to model the intervertebral disc using a biphasic model approach [8–11]. These studies suggest that the biphasic nature of the disc is an important factor in load transfer and stress distribution, which could alter during the different grades of degeneration [11–13]. Therefore, the objective of this study was to investigate the biphasic response of the IVD to various artificial disc degeneration models.

2 Materials and Methods

2.1 Experimental in Vitro Tests

Fifty motion segments were dissected from juvenile sheep lumbar spines. For each specimen, the posterior elements, muscle, and articular facet joints were carefully removed. The upper and lower vertebral bodies were cut parallel to warrant pure compressive deformation during the experiments. The specimens were assigned equally to 5 groups (i.e., (1) intact (I), (2) punctured with a 16-G needle (P), (3) punctured with a 16-G needle combined with fatigue loading (PF), (4) denatured by injecting trypsin solution (T), and (5) denatured by injecting trypsin solution combined with fatigue loading (TF)) (Fig. 1).

In the PF and TF groups, 4-h fatigue loading (peak to peak; 190 to 590 N at 2.5 Hz) was applied after needle puncture and Trypsin injection, respectively. All specimens were mounted in a chamber filled with phosphate buffered saline (PBS) and underwent a stress-relaxation test using a mechanical testing apparatus (Zwick/Roell, Ulm-Germany). To avoid swelling of the intervertebral discs, all specimens underwent 10% strain preloading for 10 min. For the stress-relaxation tests, 1-h 20% strain loading was applied and the relevant force was measured.

2.2 Biphasic Modeling

A linear biphasic model [14] was utilized to calculate the hydraulic permeability (k) and aggregate modulus (H_A) of the intervertebral discs. The stress-relaxation solution for the 1 dimensional model is as follows:

$$u(z,t) =$$
$$\begin{cases} \frac{-V_0 tz}{h} - \frac{2V_0 h^2}{H_A k_0 \pi^3} \sum_{n=1}^{\infty} \frac{(-1)^n}{n^3} \left(1 - e^{-n^2 \pi^2 H_A k_0 t/h^2}\right) \sin\frac{n\pi z}{h}, & 0 \le t < t_0 \\ \frac{-V_0 t_0 z}{h} - \frac{2V_0 h^2}{H_A k_0 \pi^3} \sum_{n=1}^{\infty} \frac{(-1)^n}{n^3} \left(e^{\frac{-n^2 \pi^2 H_A k_0 t}{h^2}}\right)\left(e^{\frac{n^2 \pi^2 H_A k_0 t_0}{h^2}} - 1\right) \sin\frac{n\pi z}{h}, & t_0 \le t \end{cases}$$
$$(1)$$

The total stress can then be evaluated at the surface $z = h$ as follows:

$$\sigma(h,t) = H_A \frac{\partial u}{\partial z}\bigg|_{z=h} \qquad (2)$$
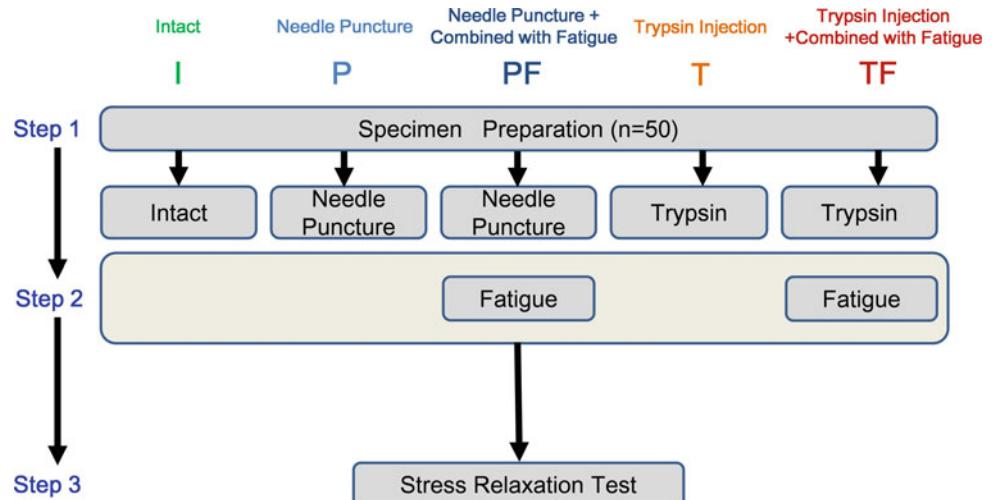
where, $u(z, t)$ is the displacement of intervertebral disc, H_A is the aggregate modoulus, k_0 is the permeability, z is the distance along the disc, t_0 is the time to reach disc strain and t is the loading time. Because symmetry toward the transversal plane was assumed, ½ of disc height is considered and z starts from the center of the disc. V_0 is the rate of displacement and h is the disc height.

Based on linear biphasic theory, a code was developed in MATLAB to calculate the aggregate modulus (H_A) and the permeability (k). One-way ANOVA tests were then used to compare the calculated parameters among different groups. Statistical differences were considered to be significant at a p value less than 0.05.

3 Results

The intervertebral disc deformations during the stress-relaxation tests were well fitted by the linear biphasic solution. The coefficient of determination of curve-fitting (i.e., R^2) ranged from 0.958 to 0.992, confirming the accuracy of the

Fig. 1 Protocol of the in vitro experiments for 5 different intervertebral disc groups
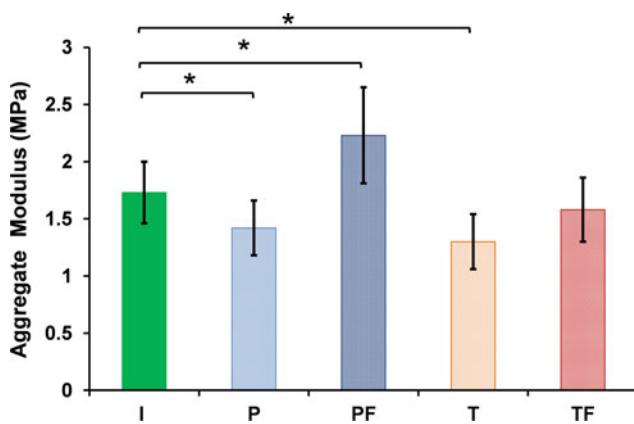
Fig. 2 Effect of different types of degeneration on the intervertebral disc aggregate modulus
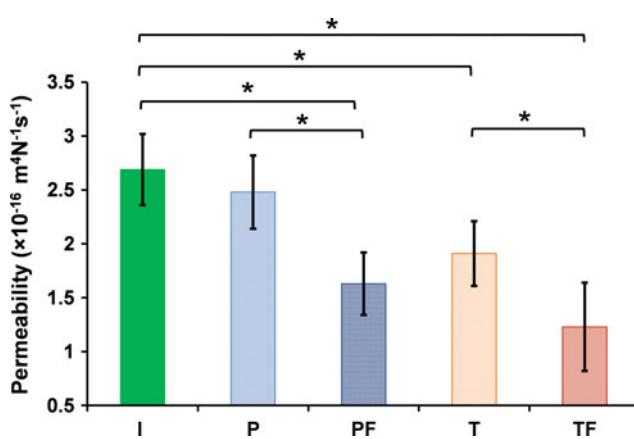
Fig. 3 Effect of different types of artificial degeneration on the intervertebral disc permeability

analytical solution. The averaged calculated aggregate modulus and permeability for the intact group were 1.68 (0.25) MPa and 2.76 (0.38) $\times 10^{-16}$ m^4/Ns, respectively

The results indicate that the aggregate modulus decreased in the P and T discs but increased in the PF discs as compared to intact ones. The difference of the aggregate modulus between the TF and intact discs was not significant (Fig. 2). The permeability decreased in the T, PF and TF discs. The permeability of both the PF and TF discs was significantly lower than the P and T discs, respectively (Fig. 3).

4 Discussion

The current study investigated the biphasic rheology of intervertebral discs for different artificial degeneration model using one intact and four different artificially-degenerated sheep intervertebral disc models. Sheep discs are comparable to human disc in terms of geometry, histology, and

mechanical properties [15]. The biphasic properties of 50 porcine intervertebral discs in five groups were extracted, and were found in alignment with the available reported data in literature [12, 16].

Loss of collagen fiber integrity and looseness of the fibers are hypothesized to occur in punctured and denatured IVDs, which decreases the aggregate modulus. Needle puncture, on the other hand, can lead to leakage of the nucleus pulposus, which reduces the intradiscal pressure and compromises the energy absorption capacity of the disc. Injection of trypsin creates dehydration of the extracellular matrix of both the nucleus pulposus and anulus fibrosus, which may also decrease the aggregate modulus. On the other hand, the fissures, clefts or tears produced by fatigue loading after needle puncture can increase the aggregate modulus. The collapsed disc structure hinders the fluid flow capability; hence, the fluid loss decreases for the T, PF and TF discs, which is reflected as lower permeability.

It is concluded that artificial degeneration models can be successfully used to investigate potential regenerative therapeutics as long as they are implemented and interpreted properly. The aforementioned methodologies are reproducible, convenient, and cost-effective techniques that can be effectively used to simulate the degeneration mechanisms in animal models, such as sheep and porcine.

References

1. Adams, M. A., Stefanakis, M. and Dolan, P., "Healing of a painful intervertebral disc should not be confused with reversing disc degeneration: implications for physical therapies for discogenic back pain". *Clinical Biomechanics,* 25 (10), pp. 961–971 (2010).
2. Chuang, S. Y., Lin, L. C., Tsai, Y. C. and Wang, J. L., "Exogenous crosslinking recovers the functional integrity of intervertebral disc secondary to a stab injury". *Journal of biomedical materials research. Part A,* 92 (1), pp. 297–302 (2010).
3. Roberts, S., Menage, J., Sivan, S. and Urban, J. P., "Bovine explant model of degeneration of the intervertebral disc". *BMC Musculoskelet Disord,* 9, pp. 24 (2008).
4. Chuang, I.-T., Hsu, Y.-C., Lin, J.-H., Nikkhoo, M. and Wang, J.-L., "Disc rheology changes in degenerated disc model by trypsin and glycation". *Journal of biomechanics,* 45, pp. S619 (2012).
5. Hsu, Y.-C., Kuo, Y.-W., Chang, Y.-C., Nikkhoo, M. and Wang, J.-L., "Rheological and dynamic integrity of simulated degenerated disc and consequences after cross-linker augmentation". *Spine (Phila Pa 1976),* 38 (23), pp. E1446–E1453 (2013).
6. Khalaf, K., Nikkhoo, M., Kargar, R. and Najafzadeh, S., "The effect of needle puncture injury on the biomechanical response of intervertebral discs". *Bone and Joint Journal Orthopaedic Proceedings Supplement,* 99-B (SUPP 1), pp. 122–122 (2017).
7. Norcross, J. P., Lester, G. E., Weinhold, P. and Dahners, L. E., "An in vivo model of degenerative disc disease". *J Orthopaed Res,* 21 (1), pp. 183–188 (2003).

8. Simon, B. R., Wu, J. S., Carlton, M. W., Kazarian, L. E., France, E. P., Evans, J. H. and Zienkiewicz, O. C., "Poroelastic dynamic structural models of rhesus spinal motion segments". *Spine (Phila Pa 1976),* 10 (6), pp. 494–507 (1985).

9. Nikkhoo, M., Khalaf, K., Kuo, Y.-W., Hsu, Y.-C., Haghpanahi, M., Parnianpour, M. and Wang, J.-L., "Effect of degeneration on fluid–solid interaction within intervertebral disk under cyclic loading–a meta-model analysis of finite element simulations". *Frontiers in bioengineering and biotechnology,* 3 (2015).

10. Nikkhoo, M., Haghpanahi, M., Wang, J. L. and Parnianpour, M., "A Poroelastic Finite Element Model to Describe the Time-Dependent Response of Lumbar Intervertebral Disc". *Journal of Medical Imaging and Health Informatics,* 1 (3), pp. 246–251 (2011).

11. Natarajan, R. N., Williams, J. R. and Andersson, G. B., "Recent advances in analytical modeling of lumbar disc degeneration". *Spine (Phila Pa 1976),* 29 (23), pp. 2733–2741 (2004).

12. Nikkhoo, M., Hsu, Y.-C., Haghpanahi, M., Parnianpour, M. and Wang, J.-L., "A meta-model analysis of a finite element simulation for defining poroelastic properties of intervertebral discs". *Proceedings of the Institution of Mechanical Engineers, Part H: Journal of Engineering in Medicine,* 227 (6), pp. 672–82 (2013).

13. Nikkhoo, M., Hsu, Y.-C., Chuang, I. T., Lin, J.-H., Haghpanahi, M., Parnianpour, M. and Wang, J.-L., "Effect of Loading Mode and Rate on Time-Dependent Response of Intervertebral Disc". *Journal of biomechanics,* 45, pp. S614 (2012).

14. Soltz, M. A. and Ateshian, G. A., "Experimental verification and theoretical prediction of cartilage interstitial fluid pressurization at an impermeable contact interface in confined compression". *Journal of biomechanics,* 31 (10), pp. 927–934 (1998).

15. Beckstein, J. C., Sen, S., Schaer, T. P., Vresilovic, E. J. and Elliott, D. M., "Comparison of animal discs used in disc research to human lumbar disc: axial compression mechanics and glycosaminoglycan content". *Spine (Phila Pa 1976),* 33 (6), pp. E166–173 (2008).

16. Kuo, Y. W., Wang, J. L., "Rheology of intervertebral disc: an ex vivo study on the effect of loading history, loading magnitude, fatigue loading, and disc degeneration". *Spine (Phila Pa 1976),* 35 (16), pp. E743–E752 (2010).

Accuracy Evaluation of 3D Reconstruction of Transfemoral Residual Limb Model Using Basic Spline Interpolation

Mohd Syahmi Jamaludin and Akihiko Hanafusa

Abstract

In this paper, a study on the accurateness of 3D reconstruction for transfemoral residual limb based on Magnetic Resonance Imaging (MRI) using basic spline (B-Spline) interpolation feature is presented. Many researches have constructed 3D models by using the Non-Uniform Rational B-Spline (NURBS) approach; however, almost none of those studies have elaborated in detail the methodology used in the project and the accuracy of the model's volume against the residual limb volume. This study focuses on the optimization of the residual limb model's volume by investigating the effect of spline points on the volume value. This project is divided into 3 phases, namely pre-segmentation, segmentation, and 3D reconstruction. However, this study focuses on the segmentation phase in which four different spline point numbers are chosen, namely 72, 36, 24, and 12 points; CAD software CREO Parametric (PTC) was used for this process. A higher number of spline points achieved greater accuracy for the model's volume. The volume (mm^3) of the 3D model with the specified number of spline points was evaluated by comparing it with the volume of the 3D model created by using image processing tools from MATLAB (Math Works). The results show the increment in accuracy of the volume value when the number of spline points is increased. The highest accuracy in terms of volume value is achieved when the model is created with 72 and 36 spline points, with an average error percentage of 6.36%, which realized the hypothesis. The results indicate that CAD software, which is a technical drawing tool, can also be used in the biomedical field to design 3D models of the human anatomy with high accuracy, if the software includes a spline interpolation feature.

1 Introduction

Recent technological developments have improved the design of transfemoral prosthesis sockets, by using 3D models of the residual limb created with various type of machines and software, e.g. Rodin 4D (Rodin 4D), Canfit™ (Vorum), and 3D Scanner. These technologies help manufacturers and therapists to develop prosthesis and orthosis devices. However, these technologies are quite complex and involves considerable workload, besides being difficult to apply in practice due to their unclear methodologies, as mentioned by Ngon Dang Thien and Giang Nguyen Truong [1]. For instance, Giorgio Colombo et al. [2] reported the construction of an amputee digital model using LifeMOD™, which is a biomechanical simulation package based on MSC ADAMS solver. The simulator is expensive and is not affordable for general users. Furthermore, the simulator cannot measure the residual model volume for evaluation purposes.

Le Van Tuan et al. [3] mentioned the use of CAD and MATLAB software in constructing the geometry model of a residual limb (shown in Fig. 1); however, the methodology of creating the model was not described clearly. Moreover, the measurements of the created model were not compared with real amputee data, and the model was not evaluated in terms of the volume value.

Arun Dayal Udai and Amarendra Nath Sinha [4] reported the use of a combination of CAD and image processing tools to generate a 3D model. They have also mentioned the use of MATLAB for filtering the Magnetic Resonance Imaging (MRI) image before it was used to construct the model. However, in their paper, the accuracies of the model's

M. S. Jamaludin (✉) · A. Hanafusa
Shibaura Institute of Technology, Saitama 337-8570, Japan
e-mail: nb17107@shibaura-it.ac.jp
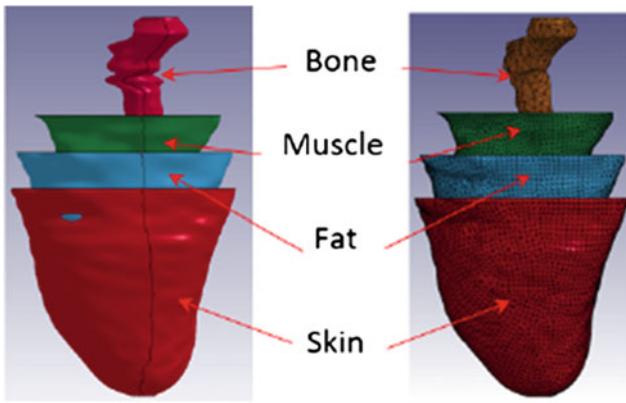
Fig. 1 Geometry model of residual limb [3]

volume, shape, and composition of fat, skin, muscle, and bone were not evaluated.

The above mentioned projects created models of the transfemoral residual limb using various methods; each of these methodologies has its own pros and contras. However, no measurements were made to evaluate the accuracy of the models in terms of the volume value. The accuracy of volume value in a residual limb model is a very crucial factor in the medical field, since it can help researchers to measure the density of residual limbs in future researches and investigate the muscle and fat changes. The objective of this project is to evaluate the accuracy of the created model by comparing its volume value with the measured volume of a model created using image processing tools from MATLAB (Math Work). The model is created with CREO Parametric (PTC) software by using the basic spline (B-spline) interpolation feature with 4 different spline point amounts (72, 36, 24, and 12 points). The volume of each model is compared with the image processing model, as its hypothesized volume has an almost similar value as that of a real residual limb. The methodology to create the model with different spline point amounts is proposed to achieve the objective.

2   Proposed Modeling Methodology

In this section, a method to design a residual limb model is proposed. The proposed method must satisfy the following criteria:

- No extra features in CREO Parametric 3.0 (CREO 3.0) to maintain the novelty of the method.
- Simple and effective to use for physiotherapists and practitioners who are amateur users of CREO 3.0.

A methodology for designing a transfemoral residual limb using CREO 3.0 is proposed by following the above

requirements. This methodology contains 4 phases, namely MRI data collection, pre-segmentation, segmentation, and 3D model construction.

2.1   MRI Data Collection

In this study, MRI data of three (3) local transfemoral amputees are used. Data collection has been conducted ethically following the Declaration of Helsinki (DoH). The details of each amputee is given in Table 1.

MRI was used in order to obtain better images of the soft tissue and muscle boundaries [4]. Moreover, overdoses of Computed Tomography (CT) may prove to be harmful to the human body [5]. The MRI images were obtained using Siemens Magneton Symphony Maestro class 1.5 T. According to Chambers S et al. [6], MRI scanning image can reached 90.5% for the sensitivity, 89.5% for specific and 90.1% for accuracy. The MRI image of each amputee had a slightly different specification, as shown in Table 2.

The MRI images were collected and stored in 3 different folders, indicating the 3 different amputees. Each file contains 30 MRI images of the sliced residual limb viewed from the z-axis.

2.2   Pre-segmentation

In this section, all the procedures are conducted using CREO 3.0 software. CREO 3.0 is a 3D CAD software, which provides the broadest range of powerful and flexible 3D

Table 1 Profile of amputees

Measurement	Amputee		
	A	B	C
Weight (kg)	63	61	80
Height (cm)	169	167	162
Age (years old)	35	47	56
Sex (M/F)	M	M	M
Amputated leg	Left	Right	Right

Table 2 MRI image specifications

MRI specification	Amputee	
	A, C	B
Pixels (mm)	0.78×0.78	0.8×0.8
Matrix size (pixels)	512×512	512×512
Repetition time (ms)	10.7	10.7
Echo train length	1	1

Table 3 CREO 3.0 features
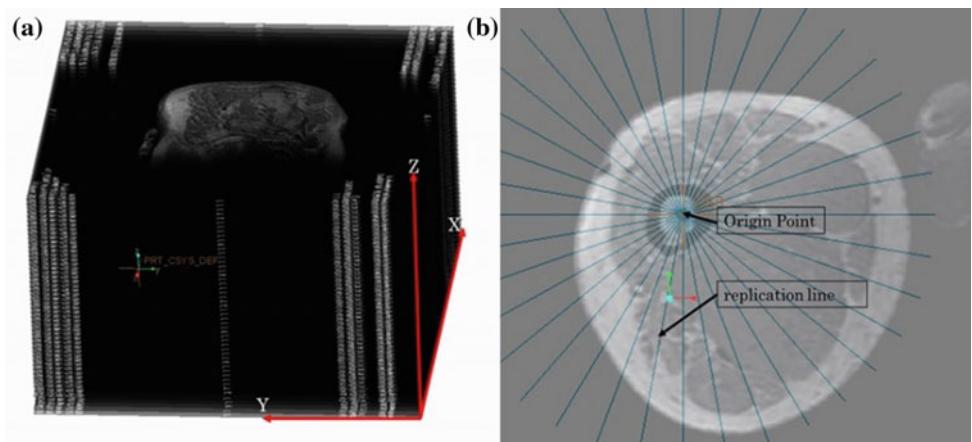
Feature	Function
View/Model Display/Images	Export MRI images into CREO 3.0
Model/Plane	Create a plane where the MRI image will be located
Model/Sketch/Spline	Create a Non-uniform rational B-spline (NURBS) curve
Model/Sketch/Line	Create a horizontal line indicating the length of the model (Trajectory)
Model/Swept blend	Create a 3D model, which is defined by two or more cross sections (Spline Curve) positioned along a trajectory
Model/Shell	Remove material from the inside of a fixed outside volume
Model/Pattern	Create a rotation replica of a line along the z-axis indicating the number of intersection points for spline curves
Model/Sketch/Offset	Offset the selected curve or line

CAD capabilities to accelerate the design of the parts and assemblies [7]. Table 3 shows some features of CREO 3.0 used to construct the 3D model using MRI images.

In the pre-segmentation phase, the first step involves creating thirty planes where each plane is translated 5 mm from each other horizontally. In each plane, the MRI image is placed according to the sequence and scaled according to the pixel size, as shown in Fig. 2a.

Next, the last image is chosen and all the images excluding the chosen one are hidden. In the image, a coordinate system is created at the center of the bone. Then, a 150-mm line is drawn starting from the center point of the coordinate system, and the pattern function is used to replicate the line, rotationally along the z-axis of the coordinate system (with a difference of 10° between each line), as shown in Fig. 2b.

2.3 Segmentation

In the segmentation phase, basic spline interpolation (B-Spline) curves (or spline, as described in CREO 3.0) are used to connect the intersection between the replication line and the edge of each part. In this study, B-spline function is defined as generalization of Be'zier curve which is the combination of flexible line that passes through the number of spline point and create smooth curve for each slice of residual limb's MRI image. B-spline curves and surfaces are used in CAD and computer-aided geometric design (CAGD) not only to describe the mechanical parts but also to determine the offset curves and surfaces [8]. In this phase, the intersection between the replication line and the edge of each part is connected using the spline function. For one slice of residual limb, the estimation time to complete the segmentation for 12 spline point model is 40 s (± 5 s) while 24 spline point model took 60 s (± 5 s), 36 spline point model took 75 s (± 5 s) and 72 spline point required 100 s (± 20 s). The accuracy of the model's volume is investigated by creating the model with different spline point values, as shown in Fig. 3. The volume of each model is measured, and the percentage error for each model is calculated.

2.4 3D Construction

Once a spline curve has been created in every plane, a single line is drawn along the z-axis of the created coordinate system, which acts as the trajectory. For 3D construction, Swept Blend (SB) features are necessary. SB is a function used to create a feature that is defined by two or more cross sections positioned along a trajectory. In this feature, the cross section is defined by a spline curve created previously. In SB, the first section is defined as the first spline curve, and

Fig. 2 **a** Process of stacking MRI images in the z-axis, **b** replication process in one layer of the MRI image

Fig. 3 Process of segmentation in different spline points. **a** 12 spline points, **b** 24 spline points, **c** 36 spline points, **d** 72 spline points

it continues until the thirtieth section, which is defined as the thirtieth spline curve.

3 Evaluation of the Residual Limb Model

In this study, the model is evaluated quantitatively by calculating the total volume of the model (Eq. 1), and it is compared with the total volume of the model obtained from the image processing method. The evaluation is made by assuming that the volume value taken from the image processing tools model is close or equal to the actual value of the residual limb's volume. This assumption is made to ensure the precision of the image processing model calculation.

$$\text{Volume} = \sum_{i=0}^{n} \frac{(A_n + A_{n+1})}{2} h \left(\text{mm}^3 \right) \qquad (1)$$

A   Spline Curve Area (mm^2)
h   Height Between Plane (mm)
n   30 (number of planes)

The volume accuracy is evaluated by measuring the percentage error that occurs during comparison with the volume obtained from the image processing model using the error measurement equation (Eq. 2)

$$error = \left| \frac{Experiment\ Value - Simulation\ Value}{Experiment\ Value} \right| \times 100\% \qquad (2)$$

4 Result of Evaluation

The result of the total volume for each model is shown in Fig. 4. The result shows that each model produced total volumes similar to those produced by the image processing model for each amputee, with a correlation coefficient that is higher than 0.999 for all the models. The result shows that for amputee A, the 24-spline point model generated the
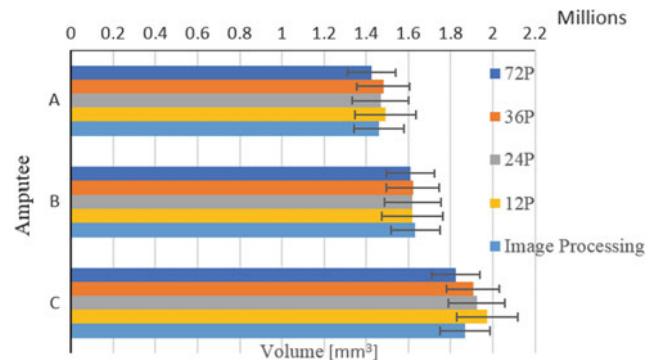
Fig. 4 Comparison of total volume of each model for every amputee
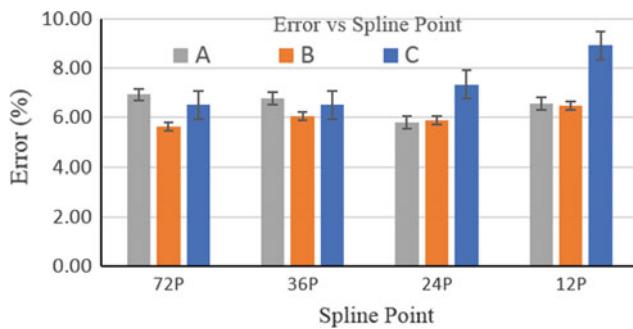
Fig. 5 Average error of volume for each amputee with different spline point models
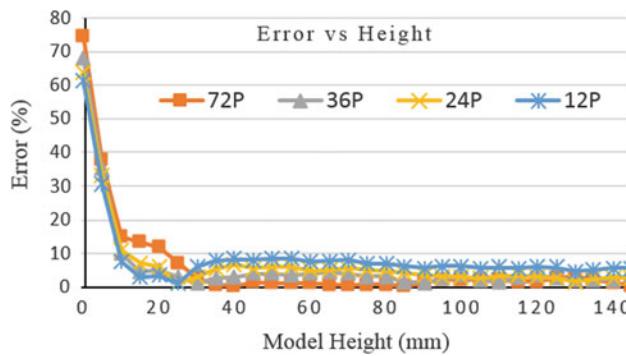
Fig. 6 Error percentage of volume against height for amputee B

smallest error (0.57%), while for amputee B, the 36-spline point model generated the smallest error (0.78%). For amputee C, the 36-spline point model produced an error of 2.1%, which is the smallest among the others.

Figure 5 shows the results of the evaluation done by calculating the error percentage of volume for every 5-mm of the sliced MRI image. The result indicates that the 72-spline point model generated the smallest average error (6.36%), and has an acceptable value of consistency (<0.3).

In order to calculate the difference, statistical tests are necessary. Based on the result, all the models satisfied the correlation coefficient value (>0.9). For the accuracy of the total volume, the 36-spline point model produced smallest error and has the highest accuracy rate. On the other hand, when the accuracy is evaluated for every 5 mm of the model height, the 72-spline point model was found to be the one

with the highest accuracy, with the smallest error percentage and acceptable value of consistency.

5 Discussion

When the volume of every model was evaluated according to its height, the highest error occurred during the beginning of the model (0-mm), as shown in Fig. 6 with amputee B's result taken as an example (the results of all amputees have the same pattern).

From 0 to 10 mm, the errors that occurred were high. It is due to the large difference in volume between the models, because for the calculation of the spline point model, it starts at 0 mm^3, while for the calculation of the image processing model, it starts at 74.22 mm^3. Starting from a height of 15 mm, the error is small (<10%) due to the similarities in volume between the models.

Parallax error could occur during the segmentation process, because the result of the plotting process mainly depends on human vision. Since the MRI image is not filtered due to the novelty of the methodology, some parts of the residual limb image cannot be seen clearly.

6 Conclusion

In this paper, the accuracy of the transfemoral residual limb model was evaluated by comparing the volume value of the model with the volume obtained from the image processing model. The result shows considerably high accuracy of the volume value for all the models with a very small error. To conclude, the model created with CREO 3.0 can be accepted as an alternative way to create a transfemoral residual limb model. The error that occurred for the different spline models (<10%) indicates that the methodology can be used in any of the models (with different number of spline points) tested in this study. It is seen that the most accurate models are the ones with 72 and 36 spline points. The model created is yet to be tested for numerical calculation, but the model can be used for analyzing the surface pressure and force by using Finite Element Methodology (FEM).

This paper also shows that the CAD software with basic spline interpolation can be used an alternative method to

create an anatomy model. In the bioengineering field, a high accuracy model is important for imitating real human anatomy in order to understand its characteristics.

Conflict of Interest There is no conflict of interest in the research.

References

1. Ngon Dang Thien, Giang Nguyen Truong "An Approach to Design a Globoid CAM Using CREO Parametric 3.0" in 2016 3rd International Conference on Green Technology and Sustainable Development pp. 200–205 (2016).
2. Giorgio Colombo et al. "Automatic 3D Reconstruction of Transfemoral Residual Limb from MRI Images" in DHM/HCII 2013, Part II, LNCS 8026, 2013, pp. 324–332.
3. Le Van Tuan et al. "Finite Element Analysis for Quantitative Evaluation of a Transfemoral Prosthesis Socket for Standing Posture" in International Journal of Computer Applications (0975–8887) Vol. 170, No. 1, pp. 1–8, 2017.
4. Arun Dayal Udai, Amarendra Nath Sinha "Processing Magnetic Resonance Image for CAD Model development of Prosthetic Limbs Socket" in IEEE Region 10 Colloqium and the Third ICIIS, paper Id. No. 70, 2008.
5. Mehta B. V, Rajani S., Sinha G., "Comparison of image processing techniques (magnetic resonance imaging, computed tomography scan and ultrasound) for 3D modeling and analysis of the human bones", Int. J. Digit Imaging, Vol. 10(3 Suppl 1), pp. 203–206, Aug. 1997.
6. Chambers S, Cooney A, Caplan N, Dowen D, Kader D. "The accuracy of magnetic resonance imaging (MRI) in detecting meniscal pathology" in J R Nav Med Serv. 2014;100(2):157–160 2014.
7. Creo, PTC Inc, www.ptc-jp.com/cad/creo.
8. Aziguli Wulamu, GOETTING Marc et al. "Approximation of NURBS Curves and Surfaces Using Adaptive Equidistant Parameterization" in Tsinghua Science and Technology, ISSN 1007-0214 07/21 Vol. 10, No. 3, pp. 316–322, 2005.

Gait Asymmetry in Winters Group I Hemiplegic Children: Role of Tibialis Anterior

Francesco Di Nardo, Alessandro Mengarelli, Annachiara Strazza, Marta Malavolta, Federica Verdini, Stefano Cardarelli, Laura Burattini, Alberto Nascimbeni, and Sandro Fioretti

Abstract

Hemiplegia is a neurological disorder that occurs quite often in children, affecting up to one child in one thousand. Typically, only one side of the body is affected by hemiplegia, while the other side is maintaining an apparently normal behavior. Purpose of present analysis was assessing gait asymmetry in group I (W1) hemiplegic children according to Winters classification, where W1 is characterized by presence of drop foot in swing in the hemiplegic side. Asymmetry was quantified by differences between hemiplegic and non-hemiplegic side in terms of foot-floor contact and electromyographic (EMG) activity. Surface EMG from tibialis anterior (TA) and foot-floor contact data were acquired in ten hemiplegic W1 children during walking to fulfill this aim. An exceptional number of strides was analyzed to consider the data variability, expected in W1 (mean $\pm$ SD = 287 ± 62 strides for each child, more than 3000 in total). Statistical gait analysis, a recent methodology performing a statistical characterization of gait, was applied to process EMG data. The research was undertaken in compliance with ethical principles of Helsinki Declaration and approved by institutional expert committee. Results showed that asymmetries were detected in basographic data: W1 children showed a significant decrease ($p < 0.05$) of strides with normal foot-floor contact (HFPS sequence: heel contact, flat-foot contact, push-off, swing) in hemiplegic side with respect to non-hemiplegic side. Also, TA recruitment presented asymmetries during walking, characterized by a curtailed, less frequent activity ($p < 0.05$) during terminal swing and a lack of activity at heel strike in hemiplegic side, with respect to non-hemiplegic side. In conclusion, present study suggested that walking in W1 children is characterized by asymmetries in both foot-floor contact patterns and TA recruitment.

1 Introduction

Hemiplegia is a neurological disorder that occurs quite often in children, affecting up to one child in one thousand. Typically, only one side of the body is affected by hemiplegia, while the other side is maintaining an apparently normal behavior [1]. Asymmetry during walking should be therefore studied in hemiplegic children, in order to describe control strategies and to support specialists in planning treatment approaches. In 1987, Winters et al. analyzed the most common gait patterns in spastic hemiplegic children and young adults, providing an acknowledged classification of spastic hemiplegia [2]. Winters' group I was characterized by the hypo-activation of ankle dorsi-flexors in hemiplegic side, which elicited drop foot during swing. More severe condition was detected in Winters' group II: persistence of equinism all through the gait cycle, associated to a possible knee hyperextension in stance. Hemiplegic side has been investigated also in more recent studies in terms of dynamic EMG activity [3, 4] in Winters' group I and group 2 children; a large variability was revealed within each group and mean differences have been also found with respect to control children. This modified EMG-activity picture detected in the hemiplegic lower limb would be expected to provoke related changes the recruitment of non-hemiplegic-side muscles. However, poor findings were reported about the analysis of the uninvolved limb of

F. Di Nardo · A. Mengarelli (✉) · A. Strazza · M. Malavolta
F. Verdini · S. Cardarelli · L. Burattini · S. Fioretti
Department of Information Engineering, Università Politecnica delle Marche, Ancona, Italy
e-mail: a.mengarelli@univpm.it

A. Nascimbeni
Rehabilitation Unit, Ospedale S. Croce, A.S.L. TO5, Moncalieri (TO), Torino, Italy

hemiplegic children. Recently, the present group of researchers investigated on ankle-muscle activity of non-hemiplegic limb, focusing only on gastrocnemius lateralis [5].

The purpose of current analysis was assessing gait asymmetry in group I (W1) hemiplegic children according to Winters classification. Asymmetry was quantified by differences between hemiplegic and non-hemiplegic side in terms of foot-floor contact and surface EMG (sEMG) from tibialis anterior (TA). It was shown [3] that a curtailed activity of TA during terminal swing and a lack of activity at loading response were detected in hemiplegic side of pathological children (Winters' group I and II), with respect to typically-developing subjects. In the present work TA muscle has been analyzed to prove alterations of TA activity also in non-hemiplegic side.

2 Materials and Methods

2.1 Subjects

Surface EMG from tibialis anterior (TA) and foot-floor contact data in ten hemiplegic children (Winters' group I, W1, age-range: 5–13 years, male/female ratio: 5/5) have been taken from a retrospective study performed at Gait Analysis Laboratory, Ospedale Santa Croce, Moncalieri (TO), Italy [3]. Exclusion criteria: lower-limb orthopedic surgery or botulinum-toxin injections during 6 months prior to gait test. The present research has been undertaken following the ethical principles of the Helsinki Declaration and was approved by local ethical committee.

2.2 Signal Acquisition and Processing

Children were instrumented bilaterally with bipolar electrodes for sEMG measurement following Winter's guidelines [6]. Three foot-switches were also applied under the heel, the first and the fifth metatarsal heads of each foot. Participants were asked to walk barefoot back and forth over a 10-m straight path at their self-selected speed and cadence, for around 2 min and 30 s.

sEMG signals were acquired (sampling rate: 2 kHz; resolution: 12 bit), band-pass filtered (20–450 Hz) and treated by a double-threshold statistical detector, in order to identify myoelectric activation intervals. Briefly, this detector is based on the observation of m successive samples once the signal exceeded the first threshold §; if at least r_0 (second threshold) out of successive m samples are still above §, activation is acknowledged. Detailed algorithm description is reported by Bonato et al. [7]. Foot-switch signals were converted into four different levels, corresponding to four different gait phases: the heel strike (H), foot-contact (F), push-off (P) and swing (S). Then, foot-switch signals were processed to identify each gait cycle (GC) [8]. Further detail on signal acquisition and processing can be found in [3].

2.3 Statistical Gait Analysis

sEMG pattern analysis was performed through a recently developed methodology [9] characterizing human walking on the basis of spatial-temporal and sEMG parameters, considered hundreds of consecutive strides. This methodology relies on the cycle-dependency of muscle-activation during walking. Thus, sEMG parameters are averaged only over those cycles including the same number of activations, i.e. over each single activation modality. The activation modality defines the number of times a muscle activates during a single gait cycle: the n-activation modality consists of n active intervals for the considered muscle during a single gait cycle. To get mean activation intervals for each activation modality, muscle activations relative to every gait cycle were identified, computing onset/offset instants in temporal space. Then muscle activations were grouped according to the number of active intervals, i.e. relative to their activation modality and onset/offset time instants of each activation modality were averaged over the entire population. Averaged onset/offset percentage time instants were normalized, providing mean activation intervals in percentage of gait cycle. This kind of analysis, performed on numerous strides, allowed quantifying muscles co-contractions not only in terms of the onset-offset muscular activation, but also in terms of the occurrence frequency. The occurrence frequency is quantified by the number (%) of strides where the muscle is recruited with each specific activation modality, with respect to the total number of strides [10, 11].

2.4 Statistics

Data were reported as mean $\pm$ standard error (SE). Shapiro-Wilk test was used to evaluate the normality of each distribution. ANOVA test and Kruskal-Wallis test were used to compare normally and not normally distributed samples, respectively. Statistical significance was set at 5%.

3 Results and Discussion

Mean relative percentages of HFPS and PFPS foot-floor contacts are quantified in Table 1, for hemiplegic and non-hemiplegic lower limb.

Table 1 Percentage frequency of foot-floor contact patterns

Wl	Hemiplegic side (%)	Non-hemiplegic side (%)
HFPS	28.1 ± 9.8	78.7 ± 4.0
PFPS	47.4 ± 9.6	7.6 ± 1.1

Data are reported in mean ± standard error (SE). * $p < 0.05$
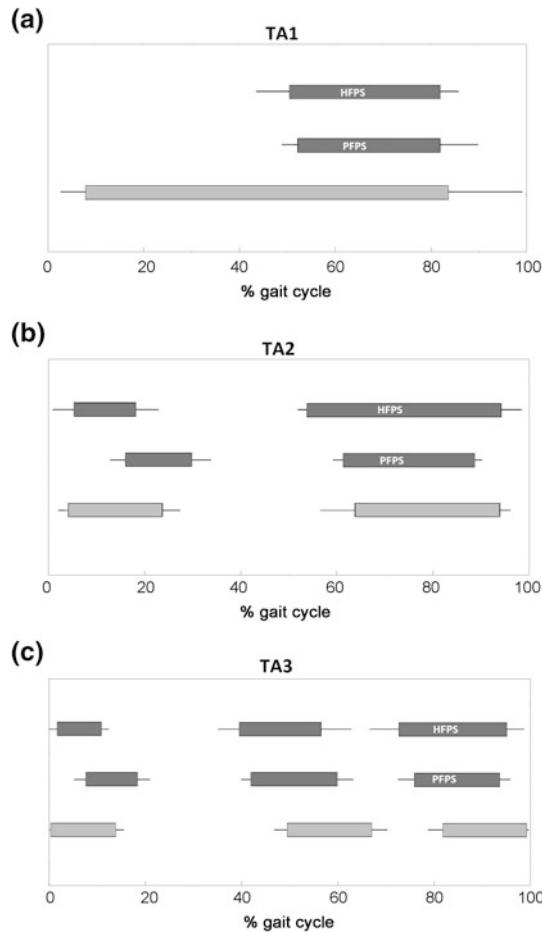
Fig. 1 Mean (+SE) activation intervals versus percentage of gait cycle for tibialis anterior in non-hemiplegic side (light gray) and for hemiplegic side (dark gray) of W1 children. Cycles where TA showed 1 (TA1), 2 (TA2) or 3 (TA3) activations during gait cycle were reported in Panel **a**, **b**, and **c**, respectively

$(7.6 \pm 1.1\%)$; thus, sEMG analysis was not computed in these strides.

Figure 1 shows mean muscle-activation patterns. TAi (i = 1−3) are the modality of TA activation with one activation (TA1, Fig. 1a), two activations (TA2, Fig. 1b), or three activations (TA3, Fig. 1c) during a single gait cycle. In the present study, it has been reported only gait cycles with HFPS sequence for non-hemiplegic side (light gray) and HFPS and PFPS sequences for hemiplegic side of W1 (dark gray). In both hemiplegic and non-hemiplegic side, muscles showed different modalities in number of activations and timing of signal onset/offset, in different strides of the same walking, as reported for healthy children [9]. Differences were observed between the two lower limbs in terms of TA activation intervals: a curtailed activity during terminal swing and a concomitant lack of activity at heel strike, especially in PFPS foot-floor contact sequence of hemiplegic side (Fig. 1). Also the occurrence frequencies of each activation modality changed between sides. This led to an
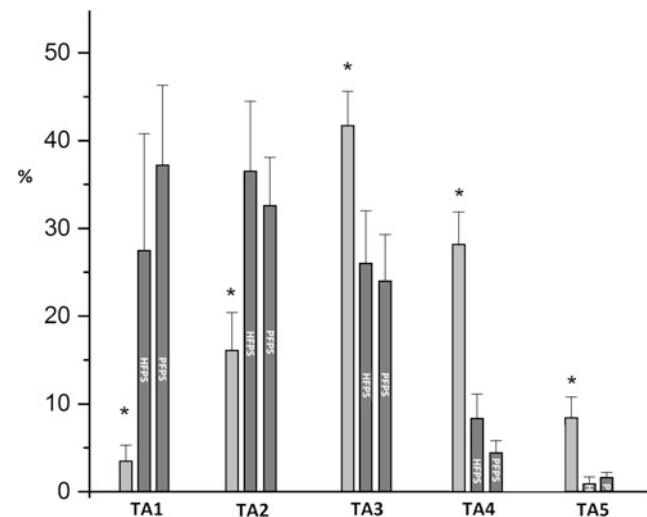
Fig. 2 Mean (+SE) occurrence frequency of tibialis anterior in non-hemiplegic (light gray) and hemiplegic side (dark gray) of W1children. Data were reported for all the modalities of TA activation (TA1, TA2, TA3, TA4, and TA5). * means $p < 0.05$ with respect to the other bars of the same activation modality

HFPS foot-floor-contact percentage was significantly ($p < 0.05$) lower in hemiplegic side than in non-hemiplegic one. Concomitantly, PFPS sequence increased significantly ($p < 0.05$) in non-hemiplegic side. These findings suggested that modified foot-floor contact pattern detected in W1 children involved mainly the hemiplegic limb. Percentage of PFPS strides in non-hemiplegic side is not relevant

increased number of strides where the lack of activity at heel strike is more evident ($p < 0.05$, 1-activation and 2-activation modalities, Fig. 2), a decreased number of strides where the typical 3-activation modality and the 4-activation modality of TA occurred (Fig. 2, $p < 0.05$) in the hemiplegic side.

The present findings highlighted that the recruitment of tibialis anterior in W1-children walking was differ between the two lower limbs. In particular, the reported impairment of anti-phase eccentric control of the dorsi-flexors [3] is confirmed only in hemiplegic side of W1 while non-hemiplegic leg seems not to be (or only slightly) involved in this impairment process.

4 Conclusion

The present study showed clear asymmetries in foot-floor contact patterns in Winters' group I hemiplegic children, represented by a significant increase in hemiplegic side of strides characterized by PFPS sequence. Also the recruitment of tibialis anterior presented asymmetries both in terms of activation intervals and related occurrence frequencies, i.e. a curtailed and less frequent activity during terminal swing and a lack of activity at heel strike in hemiplegic side, especially in PFPS foot-floor contact sequence.

Conflict of Interest Statement The authors declare that they have no conflict of interest.

References

1. Ostensjø S, Carlberg EB, Vøllestad NK (2004) Motor impairments in young children with cerebral palsy: relationship to gross motor function and everyday activities. Dev Med Child Neurol 46: 580–589.
2. Winters TF, Gage JR, Hicks R (1987) Gait patterns in spastic hemiplegiain children and young adults. J. Bone and Joint Surg 69: 437–441.
3. Agostini V, Nascimbeni A, Gaffuri A, Knaflitz M (2015) Multiple gait patterns within the same Winters class in children with hemiplegic cerebral palsy. Clin Biomech 30: 908–914.
4. Patikas D, Wolf S, Döderlein L (2005) Electromyographic evaluation of the sound and involved side during gait of spastic hemiplegic children with cerebral palsy. Eur J Neurol 12: 691–699.
5. Di Nardo F, Agostini V, Strazza A, Nascimbeni A, Knaflitz M, Burattini L, Fioretti S (2017) Gait asymmetry in Winters' group I hemiplegic children.. IFMBE Proceedings 65: 976–979.
6. Winter DA (1990) "Biomechanics and motor control of human movement", 2nd ed., Wiley, New York.
7. Bonato P, D'Alessio T, Knaflitz M (1998) A statistical method for the measurement of muscle activation intervals from surface myoelectric signal during gait. IEEE Trans Biomed Eng 45: 287–299.
8. Agostini V, Balestra G, Knaflitz M (2014) Segmentation and classification of gait cycles. IEEE Trans Neural Syst Rehabil Eng 22: 946–952.
9. Agostini V, Nascimbeni A, Gaffuri A, Imazio P, Benedetti MG, Knaflitz M (2010) Normative EMG activation patterns of school-age children during gait. Gait Posture 32: 285–289.
10. Di Nardo F, Mengarelli A, Strazza A, Agostini V, Knaflitz M, Burattini L, Fioretti S (2017) A new parameter for quantifying the variability of surface electromyographic signals during gait: The occurrence frequency. J. Electromyogr. Kinesiol 36: 25–33.
11. Di Nardo F, Fioretti S (2014) Emg-based analysis of treadmill and ground walking in distal leg muscles. IFMBE Proceedings 41: 611–614.

Role of the Visual Feedback on Balance Responses to Upright Stance Perturbations

Alessandro Mengarelli, Stefano Cardarelli, Sandro Fioretti,
Annachiara Strazza, Andrea Tigrini, Francesco Di Nardo,
Laura Burattini, and Federica Verdini

Abstract

In this study an evaluation of visual feedback on the balance response to upright stance perturbations is proposed. Subjects underwent to base of support translations in backward direction at fixed velocity in an eye-open (EO) and eye-closed (EC) condition. Center of pressure (COP) and center of mass (COM) were acquired, showing a repeatable double-peak shape which mirrors two different response periods: a destabilizing phase and a counterbalancing phase. Thus, COP and COM were analyzed on the basis of their temporal and spatial features. Further, also the angular displacement of lower limb joints, trunk and head were considered and lower limb muscular activity in terms of myoelectric latencies. Results showed several differences in COP and COM based parameters between EO and EC condition. Moreover, angular range variations seemed to indicate a different role of each joint in the two considered sensory conditions, highlighting the switch from an ankle-based strategy (EO condition) to a more complex kinematic strategy (EC condition). Outcomes of this study could add information about: (A) the suitability of considering COP displacement in perturbed posture analyses with sensory deprivation and (B) the significant role of the visual feedback in balance maintenance when a sudden and quasi-impulsive disruption is employed.

Keywords

Dynamic posturography • Sensory deprivation
Visual feedback

A. Mengarelli (✉) · S. Cardarelli · S. Fioretti · A. Strazza
A. Tigrini · F. Di Nardo · L. Burattini · F. Verdini
Department of Information Engineering, Università Politecnica della Marche, Ancona, Italy
e-mail: a.mengarelli@univpm.it

1 Introduction

Balance maintenance represents a particularly challenging task for a subject when an external perturbation is imposed, requiring the integration of information from visual, somatosensory and vestibular systems [1]. Perturbed posturography has been applied to subjects suffering from balance impairments caused by diseases affecting one or more of the abovementioned physiological systems [2], in order to assess treatments effects, disease severity and risk of falling [1]. Nevertheless, the evaluation of external disruption withstanding and upright stance recovery is valuable also for non-pathological subjects, intended to gain information about neurological pathways and sensory-motor integration [2].

A number of manipulations can be adopted to make the balance maintenance more challenging. They involve the application of further assignments while subject have to maintain balance [1] or regard the perturbation characteristics, i.e. acceleration, speed, duration, or disturbance direction and waveform [3], as well as the reduction of the base of support and the decrease of proprioceptive feedbacks [1]. The weight of each sensory system in maintaining upright stance is often addressed reducing or conflicting visual, vestibular and somatosensory inputs [4]; this provides information also on the subject ability to arrange the available sensory data in order to keep upright stance position after an external disruption [1]. In particular, vision is well acknowledged as a fundamental factor heavily influencing both static and dynamic balance, enhancing postural stability whether vestibular or somatosensory systems are impaired [5]. Furthermore, when continuous, sinusoidal-like stimuli are applied, visual feedback appeared to have a significant role in the stabilization of head and trunk [6] and in controlling center of mass (COM) displacement [7], driving the selection of the body segment used as the reference [3]. However, despite its central role in maintaining postural stability under long-lasting perturbations, poor information

is available about balance maintenance in a visual deprivation scenario after a sudden and quasi-impulsive base of support translation. The latter represents one of the most used type of disruption, being able to elicit well-known features of balance response after unexpected disturbances, i.e. the first trial effect and the habituation rate [8]. Further, the importance of considering this kind of perturbation lies also in being similar to those a subject can experiment in daily life, considering that falling usually occurs after unpredictable and sudden disruptions [1].

The analysis of balance maintenance after external stimuli is usually performed evaluating kinematic and electromyography measures, which provide body segment displacements and the extent of muscular response, based on myoelectric latencies [9]. Despite its importance in unperturbed standing balance, center of pressure (COP) is seldom considered in dynamic posturography, in particular when an impulsive disruption is employed [8, 9]. However, previous studies suggested the opportunity to examine this quantity [10], which seemed to provide useful information to characterize balance also in dynamic conditions. Thus, this study aimed at comparing postural responses after a sudden and quasi-impulsive external disruption of quiet standing when vision is denied, by a direct comparison of the same response in a visual allowed condition. To this aim, electromyography, kinematic and dynamic measures have been considered.

2 Methods

Seven healthy subjects were recruited for this study. Average values for age, weight and height were 23.3 ± 1.5 years, 60.5 ± 8.8 kg and 159 ± 11 cm. None of the subjects reported neurological or musculoskeletal impairments which can affect upright posture or balance maintenance. Present research was undertaken following the ethical principles of the Helsinki Declaration and was approved by the local ethics committee. All volunteers gave their written informed consent prior the beginning of the tests.

Participants stood on a servo-controlled movable platform with their feet on an embedded force plate (sampling rate 500 Hz) which measured the anterior-posterior and medial-lateral COP displacement. Each subject underwent to five randomly selected perturbations, consisting in sudden platform translations in eyes open (EO) and eyes closed (EC) conditions. A speed of 20 cm/s and a backward platform displacement of 5 cm were chosen (duration 250 ms). Participants were asked to assume their natural standing position, avoiding stepping during perturbation, unless it was necessary to prevent fall. Subjects had no prior knowledge of the perturbation characteristics and the

experiment started without any preceding trial. Prior the beginning of each trial, knee position was checked by the examiner in order to ensure a complete extended joint.

Subjects were instrumented with 26 reflective markers, to collect the full body kinematics (sampling rate 100 Hz) through a six cameras optical motion analysis system (BTS Elite, Italy). Four additional markers were placed on the platform corners, to track translational movement. Muscular activity from tibialis anterior (TBA), gastrocnemius medialis (GAS), rectus femoris (RCF), vastus medialis (VST), biceps femoris (BCF) and erector spinae longus (ERSL) was also bilaterally acquired (sampling rate 1 kHz). Signal were band-pass filtered (20–450 Hz) and then activation periods, i.e. onset-offset time instants [11, 12], were extracted using a custom developed software [13].

2.1 Data Extraction

All data were acquired from 1 s before the perturbation onset to 3 s after the perturbation offset. Dynamic and kinematic data were low-pass filtered at 10 and 5 Hz respectively. COM displacement was referred to the force plate reference frame [2], allowing a direct comparison with the COP displacement.

A series of temporal and spatial parameters were extracted from the anterior-posterior component of COP and COM. The first peak time (FPT) defines the temporal delay between the perturbation onset and the maximum COP/COM value, while the first peak amplitude (FPA) is the maximum amplitude value referred to the average value computed on 1 s before the perturbation onset. The inter-peaks time (IPT) represents the temporal interval between the maximum and the minimum value of COP/COM. The second peak amplitude (SPA) is the amplitude of the minimum COP/COM value with respect to the FPA. Eventually, the steady state time (SST) represents the temporal interval between the perturbation offset and the reaching of a steady state, defined as the instant when COP entered an interval equal to its mean value computed in the last 1 s plus two standard deviation. The COM distance (COMD) was computed as the distance between the initial (perturbation onset) and final (steady state reaching) COM position All spatial parameters were normalized with respect to the foot length (%FL).

From kinematic data, angular range variations from the perturbation onset and the reaching of the steady state was computed for the following joints/segments: ankle, knee, thigh, hip, trunk and head. From sEMG data, temporal latencies for each muscle were computed as the time interval between perturbation start and the onset of the muscular response [9].

3 Results

COP and COM showed a repeatable, double peak shape (Fig. 1), which allowed to define two different periods: a destabilizing phase, which lasted until the first peak and a counterbalancing phase, which ended in correspondence with the second peak. COMD resulted 18.6 ± 6.1 mm (EO) and 40.4 ± 21.7 mm (EC). SST showed a marked difference between the two sensorial conditions with a value of 153.0 ± 39.4 ms (EO) and 170.8 ± 18.9 ms (EC). Spatial and temporal parameter of COP and COM are reported in Table 1. Angular range variations and muscles activation latencies are reported in Fig. 2.

4 Discussion

In this study, an evaluation of the postural response to quasi-impulsive perturbations in EO and EC conditions was performed. In both sensorial settings, COP and COM exhibited a characteristic double peak shape (Fig. 1), already reported in [10]. The first peak appeared directly linked to the perturbation, being in the opposite direction of the platform translation, while the second one resulted in the same direction, thus highlighting the counterbalancing effort of the subject. The double balance challenging configuration suggested by the COP and COM shape seemed to be linked also to a different kind of response. The higher total COMD
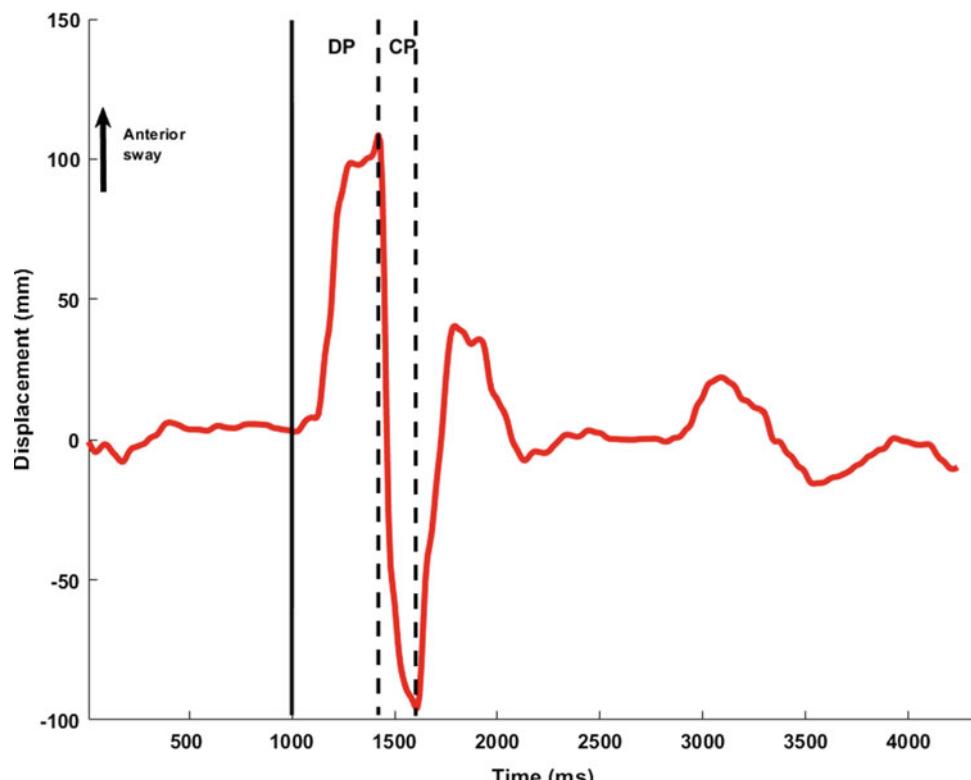
Fig. 1 COP displacement (red trace) in a representative trial. Vertical solid line marks the perturbation onset. Dashed lines mark the end of the destabilizing (DP) and counterbalancing (CP) phase (Color figure online)

Table 1 COP and COM spatial and temporal parameters in EO and EC conditions

Parameter	COP		COM	
	EO	EC	EO	EC
FPT (ms)	380.0 ± 42	365.7 ± 90.3	291.4 ± 89.5	271.4 ± 23.4
FPA (%FL)	0.50 ± 0.05	0.49 ± 0.05	0.23 ± 0.05	0.20 ± 0.03
IPT (ms)	326.7 ± 186.4	358.0 ± 248	1094 ± 576.0	822.9 ± 316.3
SPA (%FL)	0.75 ± 0.14	0.76 ± 0.13	0.26 ± 0.09	0.24 ± 0.08
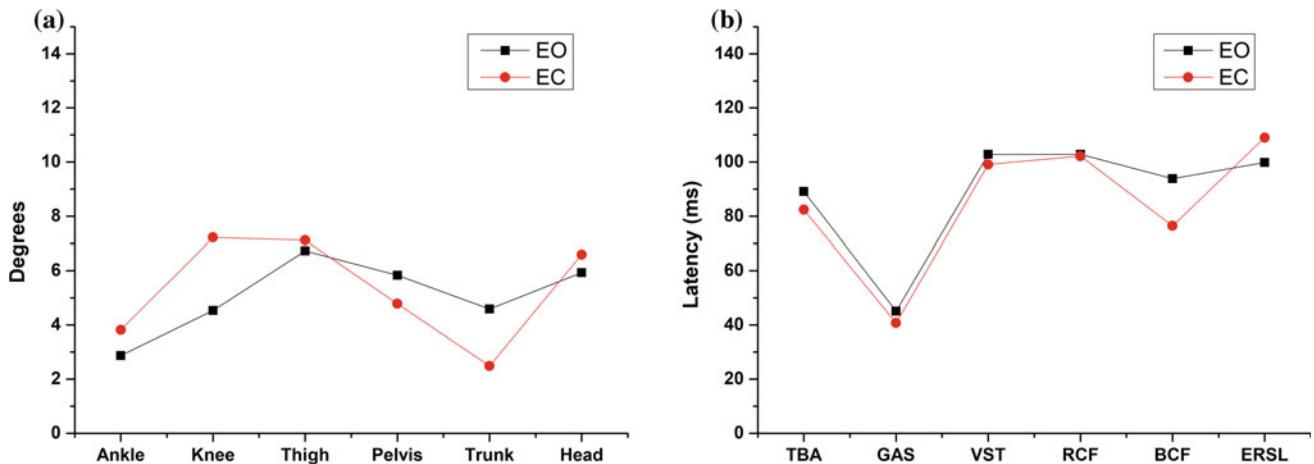
Fig. 2 Angular range variations for each considered joint (**a**) and muscular latencies for each considered muscle (**b**) in EO and EC conditions

in the EC condition supports the more challenging balance recovery when the visual information is absent, according with its significant role in keeping COM away from the limits of foot support [7].

The latter feature is reflected also by the COP, with a slower return to an initial, stable condition, highlighted by the higher SST in EC condition (153 ± 39 ms versus 171 ± 19 ms). SST has been reported as a possible indicator of the habituation rate [10], a well-known feature of balance response after unexpected perturbations [8]. Therefore, a higher SST in EC condition seems to indicate that the lack of the visual feedback prevents an optimal return to the upright position, remaining in an unstable configuration for a higher temporal interval respect to the EO condition. The more challenging characteristics of the EC trials and thus the importance of the visual cue for balance maintenance is suggested also by examining the temporal features of both COP and COM. FPT and IPT showed a mirrored behavior, with a faster reaching of the first, destabilizing peak in EC condition. Despite the limited difference with the EO FPT, this feature could indicate that the lack of the visual feedback provides a more difficult perturbation withstanding, leading to a faster, less controlled and potentially more dangerous reaching of the first, destabilizing peak.

As noted above, visual deprivation appeared to affect the control of the counterbalancing phase in an opposite way, increasing the temporal delay between the first and second peak (higher IPT in the EC condition for both COP and COM). Thus, visual feedback seems to affect also the return to the upright position, retarding the achievement of the second, counterbalancing peak in EC condition and delaying the return to the initial upright stance position. It is noteworthy that the different sensory conditions appeared to not affect COP and COM spatial characteristics. This is partially in contrast with what has been observed for repeated perturbations of balance without the lack of the visual cue [10],

where the SPA of COP showed a decreasing trend throughout the trials. These aspects highlight that: (A) the availability of visual information appeared to have a predominant role on the temporal characteristic of COP and COM based responses rather than on their spatial magnitude; (B) the importance of taking into account also the counterbalancing phase (Fig. 1) when considering postural responses to sudden balance perturbations. Further, a temporal rather than an amplitude-based control of the destabilizing phase was reported with forward-directed perturbations [10], which are considered particularly challenging respect to the backward ones, due to the induced posteriorly directed sway [2]. Thus, the lack of visual feedbacks seems to evoke postural responses similar to those elicited in more challenging configurations, showing once again a significant role in tuning balance response not only when continuous, sinusoidal-like translation of the base of support are applied [3, 7] but also for a sudden and quasi-impulsive perturbation.

EO and EC conditions could reflect also different postural strategies: the absence of visual information seems to lead to a more complex kinematic strategy, as suggested by the higher angular range for the knee in EC condition (Fig. 2a). The latter highlights an enhanced role of this joint when visual information is absent, supporting the observation that the more the perturbation is challenging, the more the deployed strategy is complex [8] and matching with a knee role in controlling upright stance when a rapid balance restoration is needed [14]. Incidentally, the role of the ankle joint, which is predominant for balance maintenance after external stimuli [15], appeared to have the same weight in the two sensory conditions, strengthening the different kinematic response in EC condition, based on a greater knee joint activity and on an almost equal role of the ankle. The enhanced weight of the knee when visual input is not at subject disposal seems to be supported also by muscular activity. BCF, a knee flexor muscle, showed a significantly

lower latency in EC condition (Fig. 2b), underlining the need for a faster knee joint activity. The difference between EO and EC latency for the BCF resulted also the highest with respect to the other muscles (17.4 ms), indirectly confirming the role of the knee when visual information is missing. Incidentally, the limited change in thigh and pelvis angular variations could relate to the low magnitude of the disruption, likely indicating that a clear arising of the hip strategy [15] heavily depends on the nature of the stimulus rather than on the available sensory information.

Previous studies [6, 7] highlighted the importance of controlling head and trunk during balance perturbations; in particular head is used as the reference frame when vision is allowed [3]. Further, the control of the trunk drift was reported as an important feature for keeping the COM away from the limits of stability [7] and when vision is available both head and trunk are kept almost still, while in EC condition they exhibited a higher level of sway [6]. However, present data appear to not completely agree with these observations: head presented almost the same angular range and the trunk resulted with a lower value in EC condition (Fig. 2a), which is supported by a higher ERSL latency in EC condition (Fig. 2b). These seeming discrepancies could be related to the different kind of perturbation: a continuous, spherical perturbation or a sinusoidal displacement at several frequencies were used in [3, 6, 7], while in the present study a quasi-impulsive base of support translation was adopted. Therefore, head and trunk stabilization mechanism could be linked to a long-lasting adaptation rather than to an impulsive perturbation withstanding, underlining the significant role played by the disruption shape in evoking different responses also in the same sensorial conditions.

In conclusion, COP appeared able to provide evidences of the visual information role in withstanding balance perturbations, exhibiting clear differences between EO and EC conditions. This could help to provide further insight about the physical quantity which directly control body sway and mass displacement [16]. Visual deprivation appeared to affect balance response also to sudden and quasi-impulsive disruptions, providing evidences of a role of the vision not limited in withstanding long-lasting perturbation at increased frequencies [7]. Furthermore, results suggested to consider, in addition to the destabilizing phase, also the counterbalancing phase of postural response, which showed a different kind of temporal control, depending on whether visual information is allowed or prevented.

Conflict of Interest Statement The authors declare that they have no conflict of interest.

References

1. Visser, J.E., Carpenter, M.G., van der Kooij, H., Bloem, B.R.: The clinical utility of posturography. Clinical Neurophysiology 119 (11), 2424–2436 (2008).
2. Nonnekes, J., Scotti, A., Nijhuis, L.O., Smulders, K., Queralt, A., Geurts, A., Bloem, B., Weerdesteyn, V.: Are postural responses to backward and forward perturbations processed by different neural circuits? Neuroscience 245, 109–120 (2013).
3. Amori, V., Petrarca, M., Patané, F., Castelli, E., Cappa, P.: Upper body balance control strategy during continuous 3d postural perturbation in young adults. Gait & posture 41(1), 19–25 (2015).
4. Cappa, P., Patané, F., Rossi, S., Petrarca, M., Castelli, E., Berthoz, A.: Effect of changing visual condition and frequency of horizontal oscillations on postural balance of standing healthy subjects. Gait & posture 28(4), 615–626 (2008).
5. Guerraz, M., Bronstein, A.: Ocular versus extraocular control of posture and equilibrium. Neurophysiologie Clinique/Clinical Neurophysiology 38(6), 391–398 (2008).
6. Corna, S., Tarantola, J., Nardone, A., Giordano, A., Schieppati, M.: Standing on a continuously moving platform: is body inertia counteracted or exploited? Experimental Brain Research 124(3), 331–341 (1999).
7. Buchanan, J.J., Horak, F.B.: Emergence of postural patterns as a function of vision and translation frequency. Journal of Neurophysiology 81(5), 2325–2339 (1999).
8. Nanhoe-Mahabier, W., Allum, J., Overeem, S., Borm, G., Nijhuis, L.O., Bloem, B.: First trial reactions and habituation rates over successive balance perturbations in parkinson's disease. Neuroscience 217, 123–129 (2012).
9. Nardone, A., Galante, M., Pareyson, D., Schieppati, M.: Balance control in sensory neuron disease. Clinical neurophysiology 118 (3), 538–550 (2007).
10. Mengarelli, A., Cardarelli, S., Fioretti, S., Burattini, L., Di Nardo, F., Verdini, F.: Center of pressure based assessment of balance responses to repeated perturbations of upright stance. In: EMBEC & NBC 2017, pp. 262–265. Springer (2017).
11. Di Nardo, F., Laureati, G., Strazza, A., Mengarelli, A., Burattini, L., Agostini, V., Nascimbeni, A., Knaflitz, M., Fioretti, S.: Is child walking conditioned by gender? surface emg patterns in female and male children. Gait & posture 53, 254–259 (2017).
12. Di Nardo, F., Fioretti, S.: Emg-based analysis of treadmill and ground walking in distal leg muscles. In: XIII Mediterranean Conference on Medical and Biological Engineering and Computing 2013. pp. 611–614. Springer (2014).
13. Mengarelli, A., Cardarelli, S., Verdini, F., Burattini, L., Fioretti, S., Di Nardo, F.: A matlab-based graphical user interface for the identification of muscular activations from surface electromyography signals. In: Engineering in Medicine and Biology Society (EMBC), 2016 IEEE 38th Annual International Conference of the. pp. 3646–3649. IEEE (2016).
14. Cheng, K.B.: Does knee motion contribute to feet-in-place balance recovery? Journal of biomechanics 49(9), 1873–1880 (2016).
15. Horak, F.B., Nashner, L.M.: Central programming of postural movements: adaptation to altered support-surface configurations. Journal of neurophysiology 55(6), 1369–1381 (1986).
16. Fioretti, S., Guidi, M., Ladislao, L., Ghetti, G.: Analysis and reliability of posturographic parameters in parkinson patients at an early stage. In: Engineering in Medicine and Biology Society, 2004. IEMBS'04. 26th Annual International Conference of the IEEE. vol. 1, pp. 651–654. IEEE (2004).

Biomechanical Evaluation of the Impact of Different Weight Loading Conditions on the Mechanical Environment of the Hip Joint Endoprosthesis

Ioannis-Ilias K. Farmakis, Vassiliki T. Potsika, Emilios Pakos, and Dimitrios I. Fotiadis

Abstract

Total hip arthroplasty (THA) is a reconstructive procedure which restores mobility and relieves pain related to several types of hip arthritis. Obesity is associated with a higher rate of postoperative complications after THA, including poor wound healing, periprosthetic joint infection, instability, and aseptic loosening. The proposed biomechanical study evaluates the effect of different weight loading conditions on the mechanical environment of the hip joint endoprosthesis. The bones were osteotomized and specifically machined for the experiments by an orthopaedic surgeon. Load cycles were programmed to simulate single-leg stance of gait of a normal-weight individual (70 kg) and an overweight individual (100 kg). The discrimination between normal and overweight subjects was based on the standards of the World Health Organization. To measure the micro strains on the femur during single-leg stance of gait, 14 strain gages were positioned on critical stress points of the femur based on the Gruen femoral zones. For all the examined zones, the micro strain values were found to increase with increasing the weight. This indicates that the displacement in the hip joint endoprosthesis is higher for overweight subjects increasing the risk of failure. Also, the mean micro strain difference was higher on the greater trochanter compared to other zones. To our knowledge, this is the first biomechanical study which quantifies the impact of weight loading conditions on the mechanical environment of the hip joint endoprosthesis and for different measurement positions.

1 Introduction

Total Hip Arthroplasty (THA) is a safe and cost-effective surgical intervention which alleviates pain from most kinds of hip arthritis improving the quality of patient's life. Osteoarthritis (OA) is the primary indication for 94% of THA [1]. The association between OA and obesity is well established, while obesity also has a negative influence on disease outcomes such as the need for surgery [2]. According to [3], worldwide, about 2 billion people are overweight and one third of them obese implying that excessive body weight could be a potential factor of implant failure. Obesity is associated with a higher rate of postoperative complications after THA, including poor wound healing, periprosthetic joint infection, instability, and aseptic loosening [4], which may lead to revision THA. Compared to primary THA, revision THA is also potentially morbid, with higher risks of mortality and major complications.

THA causes the alteration of the physiological stress pattern in the proximal femur. The implant carries a portion of the total load yielding a reduction of stress in the femoral bone. As a result, the femoral bone adapts to a new stress distribution, according to Wolff's law [5], implying that the region which receives less stress will become less dense (stress shielded). The body will respond to this by increasing osteoclast activity, causing bone resorption. Stress shielding

I.-I.K. Farmakis · V. T. Potsika (✉) · D. I. Fotiadis
Unit of Medical Technology and Intelligent Information Systems, Department of Materials Science and Engineering, University of Ioannina, 45110 Ioannina, Greece
e-mail: vpotsika@gmail.com

D. I. Fotiadis
e-mail: fotiadis@cc.uoi.gr

E. Pakos
Laboratory of Biomechanics, School of Medicine, University of Ioannina, 45110 Ioannina, Greece

D. I. Fotiadis
Foundation for Research and Technology–Hellas, Department of Biomedical Research, Institute of Molecular Biology and Biotechnology, 45110 Ioannina, Greece

provokes the loosening of endoprosthesis which is the most common THA mechanical failure.

In the literature, several clinical, experimental and numerical studies have been presented for the assessment of the implant status after a THA and the risk of failure focusing on various parameters such as implant design and orientation, different loading conditions, patient characteristics and needs, as well as the effect of exercise. More specifically, the impact of different loading conditions on the implant was investigated in [6]. Contact forces and friction moments in total hip joint prosthesis were measured in vivo during walking. In vivo measurements were taken 3 months post-operatively in 8 subjects. The coefficient of friction was calculated throughout the whole gait cycle, and average values of the friction induced power dissipation in the joint were determined. It was shown that the friction moment increased during the extension phase of the joint. However, contact forces and friction moments varied greatly between individuals. The effect of an exercise program on patients after a THA concerning parameters such as muscle strength and postural stability was examined in [7]. The effects of a late-phase exercise program for patients who underwent THA 4–12 months earlier were investigated. An 8-week, hip-exercise intervention was applied, during which the control group received basic isometric and active range of motion exercises, while the experimental group received strength and postural stability exercises. A statistically significant improvement in all measures of self-perceived function, muscle strength and postural stability was detected in the experimental group and no significant change in the control group. A post-surgery exercise program was also implemented in [8], to investigate the effect on functional recovery compared with control subjects who received no additional exercise apart from routine in-hospital physical therapy. Strength, range of motion, and physical function tests were completed for 57 patients at weeks 8, 1 before surgery, as well as at weeks 3, 12, and 24 postoperatively. It was observed that customized perioperative exercise programs are well tolerated by patients with end-stage hip arthritis, and are effective in improving early recovery of physical function after THA. The friction of THA with different bearings and loading conditions was also examined in [9] considering different material properties of the implant and different lubricants. A range of 28 mm diameter bearings were investigated using a hip friction simulator, including conventional material combinations such as Metal-on-ultra-high molecular weight polyethylene (metal-on-UHWMPE), ceramic-on-ceramic (CoC), metal-on metal (MoM), as well as novel ceramic-on-metal (CoM) pairings. Different swing-phase load and lubricant conditions were examined. It was shown that the friction factors were lowest in the ceramic bearings, with the CoC bearing having the lowest friction factor in all conditions.

CoM bearings also had low friction factors compared with MoM, and the trends were similar to CoC bearings for all test conditions. This study showed that test conditions, such as swing phase load and lubricant, may have a substantial effect upon the outcome of the friction study, hence it is important to evaluate this information when comparing materials or implant design. In a more recent study [4], the impact of bone mass index (BMI) on: (a) the duration of primary THA implant survival before revision THA, and (b) indication for revision THA was examined. It was observed that there was a significant increase in early revision THA with obese patients for aseptic loosening/osteolysis when compared to the non-obese patients.

Moving forward the state of the art in this research field, this is the first biomechanical study which quantifies the impact of normal and overweight subjects on the mechanical environment of the hip joint endoprosthesis. Medium left, fourth generation, composite femoral models and a stem of alpha-beta titanium alloy (Ti6Al4V) were used. Load cycles were programmed to simulate single-leg stance of gait of a normal-weight individual (70 kg) and an overweight individual (100 kg). The discrimination between normal and overweight subjects was based on the calculation of BMI according to the standards of the World Health Organization.

2 Materials and Methods

Custom-made, commercially available, medium left, fourth generation, composite femoral models were used for biomechanical testing (Sawbones, Pacific Research Laboratories, Vashon Island, WA, USA). The bones were osteotomized and specifically machined for use by an orthopaedic surgeon according to the procedure recommended by the manufacturer. A PROFEMUR-E® stem (Wright Medical Technology Inc., Arlington, TN) was incorporated in the femoral models which is composed of Ti6Al4V featuring high strength, low weight ratio and excellent corrosion resistance.

Figure 1 presents the experimental setup based on [10]. A custom-made fixture designed to reproduce loading conditions during the single-leg stance phase of walking was attached to the load cell of a computer-controlled hydraulic testing machine (MTS 858 Mini Bionix, MTS Systems Corp, Eden Prairie, MN, USA) according to [11, 12]. The femur was tilted into 12° of valgus and was positioned neutral on the sagittal plane. Hip abductors were simulated by a small chain attached to a custom-made base that was fixed to the lateral aspect of the greater trochanter. The abductor force simulation applied the load at an angle of abduction 15° to the sagittal plane. The distal end of the femur was embedded in a steel pot with an appropriate

polymer (polyester). A modified universal ball joint was mounted between the distal construct and the base of the machine.

Load cycles were programmed to simulate single-leg stance of a normal-weight individual (70 kg) and an over-weight individual (100 kg). Applying a vertical force 5-sixths of the body weight, with the weight of the lower extremity subtracted, would yield a physiological resultant hip joint force in the hip simulator [13]. A 3-step testing sequence was used as follows: (1) Ramp-up to −300 N (rate 100 N/s), (2) Sinusoidal axial loading between −100 and −572 N (70 kg) or −817 N (100 kg) applied at a frequency of 1 Hz for 200 cycles, (3) Ramp-down to −50 N (rate 500 N/s). The time of recording was set to 5 ms.

To measure the micro strains on the femur during single-leg stance of gait, 14 uni-axial 120-Ω strain gages (KYOWA, KFG-5-120-C1-11L1M2R, Kyowa Electronic Instrument, Tokyo, Japan) were positioned on critical stress points of the femur. The concept of Gruen femoral zones was used which have been defined for the evaluation of radiographs for signs of loosening [14, 15]. The strain gages were placed on predefined positions in each one of the seven Gruen zones (Fig. 1).

The leads of the gages were connected to a Wheatstone bridge configuration (KYOWA SS-24R Switching and Balancing Box, Kyowa Electronic Instrument, Tokyo, Japan). The gage outputs were transferred to a signal amplifier module and consequently to a data acquisition system (MTS TestStar II®, MTS Systems Corp, Eden Prairie, MN, USA). During the simulation of gait, a computer connected to the acquisition system recorded all the micro strain measured data on 5 ms intervals. Prior to testing, the abductor chain was pre-tensioned until the level arm was balanced at the horizontal plane in the beginning of every load cycle. Each experiment was repeated five times to

obtain the average values for all measurements and calculate the standard errors for the examined zones of interest. The average value of the sinusoidal strain over time was computed for each receiving position.

3 Results

Figure 2 shows the results derived from the different measurement positions on the femoral models illustrated in Fig. 1. The results are presented as the median of micro strain values derived from 5 measurements ± standard error. SGi denotes the strain gage which is placed in Gruen zone i (the variable i varies from 1 to 14).

More specifically, for a normal-weight individual (70 kg) the average measured micro strains were 1052 for SG1, 1021 for SG2, 1029 for SG3, 1012 for SG4, 1025 for SG5, 1021 for SG6, 1016 for SG7, 1010 for SG8, 1009 for SG9, 1015 for SG10, 1030 for SG11, 1011 for SG12, 1007 for SG13 and 1011 for SG14.

Considering an overweight individual, higher micro strain values were measured compared to a normal-weight individual for all the measurement positions. In particular, the corresponding average measured micro strain values were 1095 for SG1, 1035 for SG2, 1051 for SG3, 1017 for SG4, 1037 for SG5, 1030 for SG6, 1023 for SG7, 1015 for SG8, 1012 for SG9, 1023 for SG10, 1044 for SG11, 1015 for SG12, 1010 for SG13, 1016 for SG14.

In addition, the highest micro strains were observed in Gruen zone 1 for both normal and overweight individuals, corresponding to measurements performed on the greater trochanter. Table 1 summarizes the measured micro strains, as well as the standard error values for all the examined cases. All the calculated standard errors were lower than ±0.1% except for SG1 and SG3 for the weight 100 kg.

Fig. 1 a Experimental setup, b Gruen zones and measurement positions (with red arrow) (Color figure online)
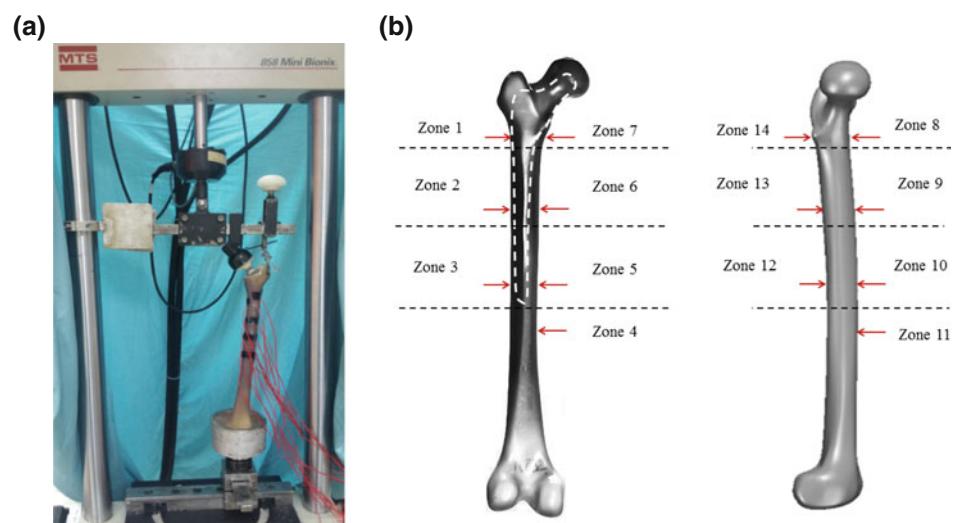
Fig. 2 Micro strain values derived from the 14 Gruen zones. SG denotes strain gage and the numbering corresponds to the number of Gruen zone as illustrated in Fig. 1
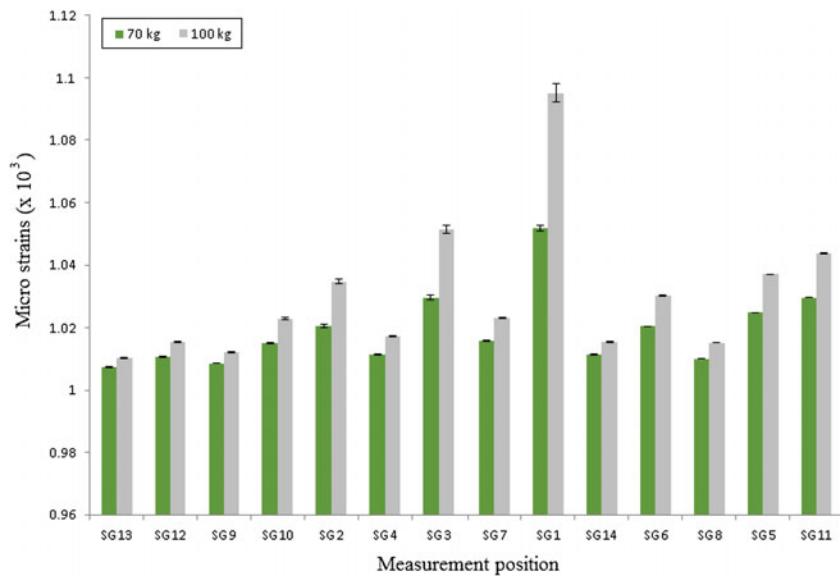
Table 1 Micro strain values and standard errors (%) for SG1–SG14

Gruen zone	Micro strains	
	Normal-weight individual (70 kg)	Overweight individual (100 kg)
1	1052 (±0.089)	1095 (±0.278)
2	1021 (±0.044)	1035 (±0.083)
3	1029 (±0.066)	1051 (±0.121)
4	1012 (±0.015)	1017 (±0.024)
5	1025 (±0.005)	1037 (±0.013)
6	1021 (±0.006)	1030 (±0.007)
7	1016 (±0.013)	1023 (±0.011)
8	1010 (±0.008)	1015 (±0.005)
9	1009 (±0.011)	1012 (±0.014)
10	1015 (±0.024)	1023 (±0.029)
11	1030 (±0.009)	1044 (±0.019)
12	1011 (±0.013)	1015 (±0.019)
13	1007 (±0.013)	1010 (±0.014)
14	1011 (±0.011)	1016 (±0.024)

4 Discussion

This work presented a biomechanical study on the impact of different weight loading conditions on the mechanical environment of the hip joint endoprosthesis aiming to provide insight to the risk of implant failure. More specifically, the single-leg stance was simulated for a normal-weight individual and an overweight individual. To measure the micro strains on the femur during single-leg stance of gait, strain gages were positioned on critical stress points of the femur based on the Gruen femoral zones. To our knowledge, this is the first biomechanical study which quantifies the impact of different weight loading conditions on the mechanical environment of the hip joint endoprosthesis considering different measurement positions.

It was found that with increasing the weight of the subject from 70 to 100 kg the micro strain values increase for all the measured positions reflecting the deformation in the implant area. This indicates that the risk for implant failure increases with increasing the weight and more specifically the occurrence of aseptic loosening. According to [4], the reason for increased rate of early failure due to aseptic loosening/osteolysis in the obese may be related to the higher mechanical stresses at the bone implant interface, and the joint reaction forces proportional to the body weight of

the individual. The negative impact of obese on the longevity of the implant was also reported in [16]. It was shown that patients who have a higher BMI needed endoprosthetic joint replacement at a younger age. Also, the time of primary implantation of a total hip or total knee arthroplasty was significantly influenced by the stage of obesity. A more recent study [17] in patients with a failed THA revealed that comorbidities may account for the risk of revision due to infection in obese patients. Moreover, obesity was independently associated with early primary THA failure for aseptic loosening. On the other hand, there are multiple studies that have shown no association between patient obesity and aseptic loosening rates [18].

In addition, the highest micro strain values were calculated in Gruen zone 1 reflecting that the great trochanter is subjected to higher deformation increasing thus the risk for stem revision for aseptic loosening or the occurrence of a greater trochanteric fracture. Also, the increase in weight loading conditions may lead to trochanteric bursitis or greater trochanteric pain syndrome which results from repetitive movements at the hip joint and according to [19] is more prevalent in women, frequently associated with mechanical back strain and obesity.

This work is subject to certain limitations. One constraint is that only 2 different weights were examined, while our ongoing study will consider subjects with different values of BMI for normal, pre-obese and obese subjects. Also, this study has the advantage of measuring the strain values in ideal conditions, changing only the weight every time, while this is not possible in clinical practice.

5 Conclusions

This paper presented a biomechanical study aiming to investigate the effect of obesity on the mechanical environment of the hip joint endoprosthesis and the risk of aseptic loosening. The micro strains were measured at predefined receiving positions of the femur keeping constant other material and structural features of the femoral model and stem. It was shown that the micro strain values increase with increasing the weight which may increase the risk of complications after a total hip arthroplasty and influence the longevity of the prosthesis.

Conflict of Interest The authors declare that they have no conflict of interest.

References

1. Katz J. N., Wright J., Wright E. A., Losina, E. Failures of Total Hip replacement: A Population-Based Perspective 9, Orthop. J. Harvard Med. Sch., 101–106 (2009).
2. Bliddal H., Leeds A. R., Christensen R. Osteoarthritis, obesity and weight loss: evidence, hypotheses and horizons 15(7), Obes Rev., 578–586 (2014).
3. Seidell J.C., Halberstadt J. The global burden of obesity and the challenges of prevention, Ann Nutr Metab 66, 7–12 (2015).
4. Electricwala A. J., Narkbunnam R., Huddleston J. I., Maloney W. J., Goodman S. B., Amanatullah D. F., Obesity is Associated With Early Total Hip Revision for Aseptic Loosening, The Journal of Arthroplasty 31, 217–220 (2016).
5. Wolff J. Das Gaesetz der Transformation der Knochen, Hirchwild, Berlin (1982).
6. Damm P., Dymke J., Ackermann R., Bender A., Graichen F., Halder A., Beier A., Bergmann G. Friction in Total Hip Joint Prosthesis Measured In Vivo during Walking, Plos One 8 (2013).
7. Trudelle-Jackson E., Smith S.S. Effects of a Late-Phase Exercise Program After Total Hip Arthroplasty: A Randomized Controlled Trial, Arch Phys Med Rehabil 85, 1056–1062 (2004).
8. Gilbey H. J., Ackland T. R., Wang A. W., Morton A. R., Trouchet T., Tapper J. Exercise Improves Early Functional Recovery After Total Hip Arthroplasty, Clinical Orthopaedics and related research 408, 193–200 (2002).
9. Brockett C., Williams S., Jin Z., Isaac G., Fisher J. Friction of Total Hip Replacements with Different Bearings and Loading Conditions, Wiley InterScience (2006).
10. Politis A. N., Siogkas K. G., Gelalis I.D., Xenakis T.A. Patterns of stress distribution at the proximal femur a of a modular neck prosthesis. A biomechanical study, Hip Pelvis 28(2), 65–75 (2013).
11. McLeish R.D., Charnley J. Abduction forces in the one-legged stance, J Biomech 3, 191–209 (1970).
12. Finlay J.B., Rorabeck C.H., Bourne R.B., Tew W.M. *In vitro* analysis of proximal femoral strains using PCA femoral implants and a hip-abductor muscle simulator, J Arthroplasty 4, 335–345 (1989).
13. Wik TS, Enoksen C, Klaksvik J, Østbyhaug PO, Foss OA, Ludvigsen J, Aamodt, A. *In vitro* testing of the deformation pattern and initial stability of a cementless stem coupled to an experimental femoral head, with increased offset and altered femoral neck angles, Proc Inst Mech Eng 225f, 797–808 (2011).
14. Gruen TA, McNeice GM, Amstutz HC. Modes of Failure of cemented stem-type femoral components. A radiographic analysis of loosening. Clin Orthop Relat Res 141, 17–27 (1979).
15. Park Y., Choi D., Hwang D.S., Yoon Y.S. Statistical Analysis of Interfacial Gap in a Cementless Stem FE Model. Journal of Biomechanical Engineering 131, 1–8 (2009).
16. Guenther D., Schmidl S., Klatte T., Widhalm H. K., Omar M., Krettek C., Gehrke T., Kendoff D., Haasper C. Overweight and obesity in hip and knee arthroplasty: Evaluation of 6078 cases, World J Orthop 18 (1), 137–144 (2015).
17. Goodnough L. H., Finlay A. K., Huddleston J. I., Goodman S. B., Maloney W. J., Amanatullah D. F. Obesity is Independently Associated With Early Aseptic Loosening in Primary Total Hip

Arthroplasty. The Journal of Arthroplasty, https://doi.org/10.1016/j.arth.2017.09.069 (2017).

18. Cherian J. J., Jauregui J. J., Banerjee S., Pierce T., Mont M. A. What Host Factors Affect Aseptic Loosening After THA and TKA? Clin Orthop Relat Res 473, 2700–2709 (2015).

19. Segal N. A., Felson D. T., Torner J. C., Zhu Y., Curtis J. R., Niu J., Nevitt M. C. Greater Trochanteric Pain Syndrome: Epidemiology and Associated Factors, Arch Phys Med Rehabil. 88(8), 988–992 (2007).

Assessment of Postural Stability Using the Method of Postural Somatooscilography

Roman Melecky, Eugen Rasev, Patrik Kutilek, Jaroslav Jerabek, Marketa Janatova, Karel Hana, Jan Muzik, Pavel Smrcka, and Jan Kaspar

Abstract

The aim of article is to present new method for evaluating the postural stability using oscillating platform. Proposed methods are alternative to basic methods which are usually parts of the commercial posturography systems. The methods for calculating the postural parameters have been designed in order to objectively quantify and classify the ability of postural stabilization on a standardized oscillatory platform, and determine differences in the postural stabilization of motor function in healthy people and in people with postural instability. The Posturomed (Haider Bioswing GmbH) and biaxial accelerometer sensor were used for measurement the body acceleration during single leg stance provocation test. The postural somatooscilogram has been defined, which shows accelerations of platform, in horizontal plane in both anteroposterior and mediolateral directions over time. Two parameters, Average Damping Coefficient (ADC) and Average Coefficient of Damped Energy (ACDE), were used to evaluate postural stability. The proposed method was implemented in MatLab sw. Patients with postural disorders and control group of healthy subjects were measured. Statistically significant differences have been observed in postural stability between independent postural stable group and postural unstable groups. Based on the findings, we can say that the presented method allows a complex analysis of the single leg stance in patients with postural balance disorders in clinical practice.

R. Melecky · P. Kutilek (✉) · J. Jerabek · M. Janatova
K. Hana · J. Muzik · P. Smrcka · J. Kaspar
Faculty of Biomedical Engineering, Czech Technical University in Prague, Sitna sq., 3105 Kladno, Czech Republic
e-mail: kutilek@fbmi.cvut.cz

R. Melecky
e-mail: roman.melecky@fbmi.cvut.cz

J. Jerabek
e-mail: jerabek@fbmi.cvut.cz

M. Janatova
e-mail: marketa.janatova@fbmi.cvut.cz

K. Hana
e-mail: hana@fbmi.cvut.cz

J. Muzik
e-mail: muzik@fbmi.cvut.cz

P. Smrcka
e-mail: smrcka@fbmi.cvut.cz

J. Kaspar
e-mail: kaspar@fbmi.cvut.cz

E. Rasev
Faculty of Physical Education and Sport, Charles University, Jose Martiho 31, Prague, Czech Republic
e-mail: eugen.rasev@t-online.de

1 Introduction

In clinical practice, static and dynamic posturography [1] are used for objective quantification of postural stability disorders. Dynamic posturography provides functional, selective testing of three sensory modalities for maintenance of balance: vestibular, visual, and somatosensory [1]. Dynamic force platforms are sensitive to small changes in subject's ability to balance and can successfully simulate dynamic situations through which the identification of most balance disorders can be made.

The majority of scientific and clinical investigations in postural control have directed their attention to examine postural responses of the human body to various externally controlled perturbations [2]. Postural perturbation (or provocation) tests should attempt to simulate dynamic conditions in order to load the postural control system fully and reveal a measurable presence of a balance disorder.

Several research studies have examined responses to continuous, externally-imposed disturbances by exposing probands to constant amplitude, sinusoidal movements of the platform [2]. Results have demonstrated that these conditions can provide an opportunity for the CNS to integrate predictive postural adjustments with automatic responses [3], and that this predictive control occurs in as few as three to five oscillations [4].

In the presented method, an externally controlled perturbation on a dynamic unstable oscillatory platform Posturomed [5] equipped with two axis accelerometer sensor is being examined in order to measure participant's postural perturbation response. Accelerometry (ACC) shows promising as an easily implemented clinical measure of balance. The use of ACC may have value in estimating the balance function and minimizing clinical evaluation time [5]. The aim of the article is to introduce new methods of data evaluation in these postural stability tests. A defined provocation test has been used consisting of three steps on the spot, which induces the platform to oscillate, disturbs participant's posture and forces him to maintain balance during following one-leg stance. To verify the proposed methods, the damped oscillations of the system on a training group of postural healthy people and people with postural imbalance have been investigated in order to extract stabilometric parameters related to the inverted pendulum model. Extracted parameters were further tested on an independent testing group in order to find differences in the measured postural stabilization responses in healthy people and in people with postural instability. Differences between healthy and pathological subjects were evaluated statistically. The presented data are part of a larger experiment investigating clinical groups with different postural disorders with the presented method.

2 Methods

2.1 Participants

We have separated participants into three groups: stable subgroup (consisted of postural healthy (PH) individuals),

slightly unstable (SU) and highly unstable subgroup (HU). In the preliminary study were 6 subjects in the postural healthy group, 6 subjects in the slightly unstable group, and 6 subjects in the highly unstable group. Among the known pathology diagnoses in the unstable groups were the following: pseudoradicular syndrome of the lumbar spine, pseudoradicular syndrome of the cervical spine, whiplash injury and instability of the knee joint. The average age for groups was very close, in the group of patients the average age had a value of 41.11 ± 8.8 years while in the healthy group the average age was 40.6 ± 8.1. The diagnostic evaluation of the subjects included a detailed disease history, a neurologic examination and routine laboratory testing. The subjects were chosen for measurement randomly, and on different days. The study was performed in accordance with the Helsinki Declaration. The study protocol was approved by the local Ethical Committee, and informed consent was obtained from all subjects.

2.2 Measurement Equipment

The Posturomed © (Haider-Bioswing, Pullenreuth, Germany) platform was used to evaluate stance ability and characterise the patterns of one legged stance during perturbations. The structure consists of a rigid frame connected to a rigid platform (60 cm × 60 cm, 12 kg) using 15 cm steel springs of identical strength. This realization allows the platform to oscillate in a horizontal plane. The number of working springs (4, 6, or 8 springs) can be engaged or disengaged using two brakes in order to setup the oscillation adjustment. The easiest mode is when all 8 springs are engaged and it is used for testing and rehearsal of postural stability. In our method, the most difficult disengaged adjustment mode (all 8 springs are disengaged) of the platform has been used in all measurements, as controlled perturbation a provocation test and accelerometer sensory measuring system have been used, see Fig. 1. The actual movement of the platform is registered by a biaxial accelerometer sensor of the diagnostic system Microswing 6 for Posturomed placed on the underside of the platform with sampling frequency 100 Hz. The position is directly in the
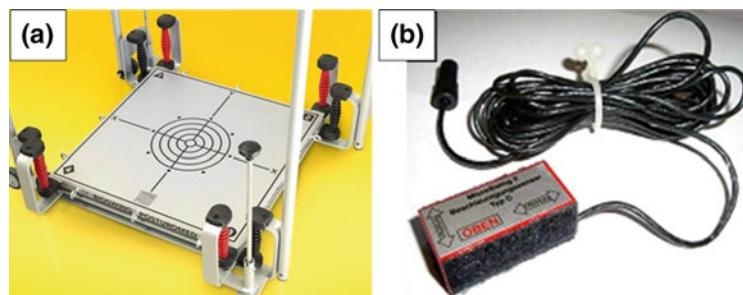
Fig. 1 Measurement equipment; **a** Posturomed platform; **b** 2-D accelerometer microswing for Posturomed platform

middle, in a way that deflections in the anteroposterior (AP) plane represented with the Y axis and deflections in the mediolateral (ML) plane were represented on the axis X.

2.3 Test Procedure

The recovery of equilibrium depends on the balancing ability of the subject. The participant has to use his compensatory equilibrium reactions to maintain balance on the platform after execution the test. The test is called provocation test and models the standing balance after a sudden change in direction [5, 6]. On Posturomed the single leg stance was performed. The test consists of a single leg stance for 8 s, after that the measuring stops, the lower limb alternates and another preparatory part starts for the alternate lower limb. This technique is executed ten times in a row so it investigates five left leg stances and five right leg stances. The provocative part of the test is the walking on the spot on Posturomed with strictly defined limb movement (with the three steps) before each single leg stance.

2.4 Method of Data Processing

For each subject, measurement data files contain 2D accelerometer data, namely 10 measurements in X and 10 Y-axis measurements in a total of twenty signals of 8 s duration in one file, see Fig. 2. Processing of data was performed in custom made program, which was developed specifically for our purpose.

The parameters to quantify a short term damped oscillation in signal have been designed and used. Before calculation of parameters, the cover of each signal has been separated, local extremes were detected and damped oscillation localized. Then we used two parameters. Average Damping Coefficient (ADC) characterizes amplitude decay. It is computed from the logarithmic decrement [7] of a harmonic motion as the logarithm of the ratio of two successive amplitudes one period apart. In our experiment the

logarithmic decrement was improved and the third amplitude was added into the formula. The exponential function steepness after this improvement became more like in the case of disengaged Posturomed platform. Improved damping coefficient is calculated for each signal and the ADC is the average value for all signals.

$$ADC = \frac{1}{N}\sum_{i=1}^{N}\frac{1}{T_i}\cdot\ln\frac{A_{\max i}}{0.5\cdot(A_{\max i+1}+A_{\max i+2})}, \quad (1)$$

where T_i means the average period of each signal, $A_{\max i}$ is the maximum of detected damped oscillation, $A_{\max i+1}$, $A_{\max i+2}$ are amplitudes following after the first maximum amplitude. N is the number of averaged signals.

Average Coefficient of Damped Energy (ACDE) indicates the ratio of oscillator energy to the average value of energy lost during one period. ACDE value determines how quickly the Posturomed platform loses its energy (i.e. how fast the vibrations are completely dampened):

$$ACDE = \frac{2\pi}{N}\sum_{i=1}^{N}\frac{1}{T_i}\frac{\omega_{0i}}{ADCi}, \quad (2)$$

where ω_{0i} is frequency of undamped angular oscillations, N is number of signals.

2.5 Statistical Analysis

The data were subjectively divided into three groups according to their overall stabilization performance on the Posturomed platform. When examining the independence of the parameters, the Kruskal-Wallis test (the non-parametric equivalent of a one-way ANOVA method) was used to assess the significance of the differences between three groups of subjects. The significance level was set at $\alpha = 0.05$. The median (Mdn), minimum (Min), maximum (Max), the first quartile (Q1) and the third quartile (Q3) of the biomedical data were calculated and plotted into a box diagram. The statistical analysis was performed using MatLab software.
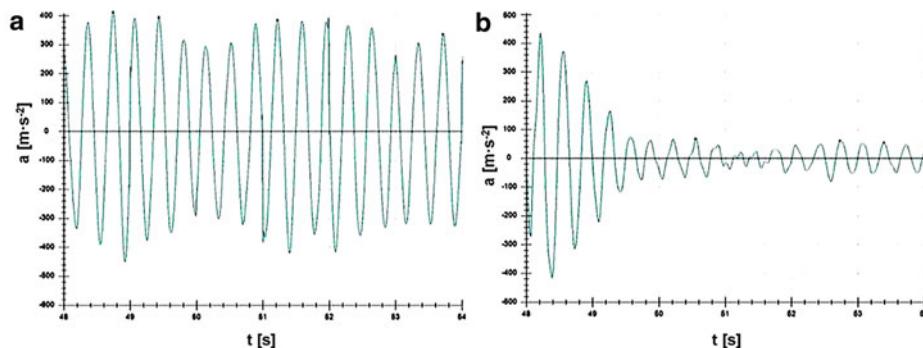
Fig. 2 Raw accelerometric signals measured by Posturomed; **a** signal with high amplitudes of oscillations of highly unstable class; **b** example of relatively stable signal assigned to postural stable class
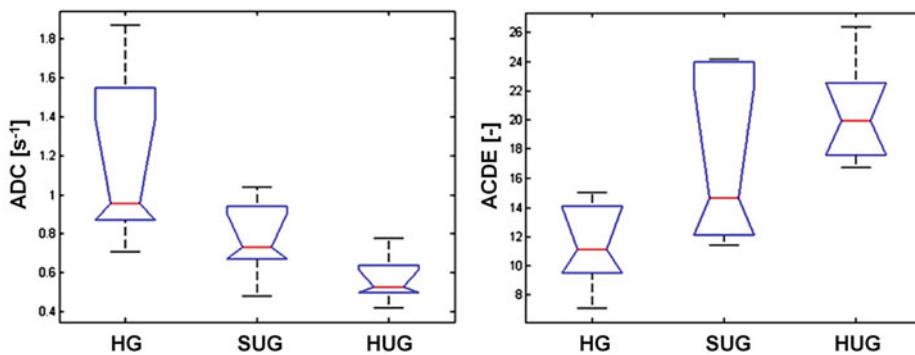
Fig. 3 One-way ANOVA results of extracted parameters on three groups. One-way ANOVA box plots provide a test of group medians for each parameter for the groups: postural healthy group (HG) (i.e. stable), slightly unstable group (SUG), highly unstable group (HUG)

3 Results

A statistically significant result for the parameters has been found. There was a significant difference among the postural groups in the parameter ADC ($p < 0.05$) and very significant differences among the postural groups in the parameter ACDE ($p < 0.001$). The following Fig. 3 displays the Min, Max, Mdn, Q1, and Q3 for the calculated parameter values.

4 Discussion

Two parameters describing the damped oscillations have been defined in order to objectively quantify and classify the patient's ability of postural stabilization on the Posturomed platform after passing the provocation test. There are statistically significant differences in motoric behavior between the independent postural stable group and the postural unstable groups. Examination of the oscillatory behaviour of the platform revealed the path signal to be a suitable parameter for analyzing the platform movements. Postural healthy subjects showed in the most cases a presence of damped oscillation as seen in (Fig. 2). In opposite, subjects with postural disorder showed often more sinusoidal waveforms in the signal. The ADC allows us to predict the ideal damping path depending on the first three amplitudes. ADC showed significant difference among the stability classes of the groups. It can be seen, that the higher the ADC value is, the better is the damping. To validate the ADC, differences were investigated on an independent testing groups.

The ACDE is an analogue to Q-factor, which describes how under-damped an oscillator is [7]. ACDE is an improved Q-factor for Posturomed since it is computed from the improved damping coefficient ADC. It gives the opposite information as the ADC and shows the same statistically significant differences between the groups. In comparison with the ADC, signals with higher ACDE were oscillating with greater amplitudes, so unstable participants have its value higher than stable. The ACDE is often used to quantify oscillator's frequency bandwidth relative to its center frequency [7], it could be assumed that this parameter will be useful in a future spectral analysis. The ADC and AICD describe the postural stability ability to damp a one-leg stand immediately after locomotion stops in short term and the exponential function steepness is depending on.

The results of the comparison of groups indicate that the new methods identified deterioration in postural control and strong differences between the patients and healthy subjects. There are limitations to our study. The most important one is that the sample of the subjects was small and probably not representative of the larger population. However, to test the basic attributes of the method proposed for the study of postural stability in this preliminary study, a sample of subjects is sufficient, just as it was in similar works [8].

5 Conclusion

The article presented application of new parameters describing the damped oscillations. The new technique has never been used before. The results pointed to significant differences between the postural healthy group, slightly unstable group and highly unstable group. Described findings demonstrate the ability of the proposed methods to identify differences in the states of subjects. The method can be used for quantifying progress in postural control in people with postural disorder.

Conflict of Interest The authors declare that they have no conflict of interest.

References

1. Faraldo-García, A., Santos-Pérez, S., Crujeiras, R., Labella-Caballero, T., Soto-Varela, A.: Comparative study of computerized dynamic posturography and the SwayStar system in healthy subjects. Acta Otolaryngol 132(3), 271–6 (2012).
2. Horak, F.B., Henry, S.M., Shumway-Cook, A.: Postural perturbations: new insights for treatment of balance disorders. Phys Ther 77 (5), 517–33 (1997).
3. Dietz, V., Trippel, M., Ibrahim, I.K., Berger, W.: Human stance on a sinusoidally translating platform: balance control by feedforward and feedback mechanisms. Exp Brain Res, 93(2), 352–62 (1993).
4. Bugnariu, N., Sveistrup, H.: Age-related changes in postural responses to externally- and self-triggered continuous perturbations. Arch Gerontol Geriatr 42(1), 73–89 (2006).
5. Müller, O., Günther, M., Krauss, I., Horstmann, T.: Physical characterization of the therapeutic device Posturomed as a measuring device–presentation of a procedure to characterize balancing ability. Biomed Tech (Berl), 49(3), 56–60 (2004).
6. Kiss, R.M.: A new parameter for characterizing balancing ability on an unstable oscillatory platform. Med Eng Phys 33(9), 1160–6 (2011).
7. Pain, H.: The physics of vibrations and waves. John Wiley, Hoboken (2005).
8. Diener, H.C., Dichgans, J., Guschlbauer, B., Bacher, M., Rapp, H., Klockgether, T.: The coordination of posture and voluntary movement in patients with cerebellar dysfunction. Mov Disord. 7 (1) 14–22 (1992).
9. Van Ooteghem, K., Frank, J.S., Allard, F., Buchanan, J.J., Oates, A.R., Horak, F.B.: Compensatory postural adaptations during continuous, variable amplitude perturbations reveal generalized rather than sequence-specific learning. Exp Brain Res, 187(4), 603–11 (2008).

Quantitative Assessment of Osteoarthritic Knee Instability: Comparison with Conventional Imaging Modalities

V. K. O. Virtanen, J. Thevenot, A. Tiulpin, J. Hirvasniemi, J. Niinimäki, M. Nevalainen, and S. Saarakkala

Abstract

Knee osteoarthritis (OA) is the most common musculoskeletal disorder affecting all populations. One common knee OA symptom is instability; thus its assessment could allow diagnosing and following-up of the disease without using conventional imaging techniques, such as plain radiography or magnetic resonance imaging (MRI). Knee kinematic measurements using accelerometers could provide a low-cost and non-invasive option to quantify knee instability. The aim of this study was to assess the relationships between kinematic data, instability parameters derived from the imaging techniques, goniometer-based measurements, and radiological OA stage. The right knees of 66 females (44–67 years) were examined using MRI, plain radiography, and goniometer-based angle measurement. Kellgren–Lawrence (KL) grade and the joint line convergence angle (JLCA) were determined from the radiographs. Cartilage thickness and OA score (MOAKS) were derived from the MRI. A ratio between lateral and medial cartilage thicknesses was calculated from the average thickness of segmented cartilage over the weight bearing area (MRI_{ratio}). Accelerometers attached to thigh and shank were used to record kinematic signals during a one-leg-stand test. Power of the accelerometer signals along the anatomical longitudinal axis (P_{acc}) was used as a measure of knee instability. Finally, Spearman's correlations between the acquired parameters and KL grade/MOAKS scores were calculated. Leave-one-out cross-validation and logistic regression were used to discriminate OA subjects ($KL \geq 2$). All the instability parameters (P_{acc}, JLCA and MRI_{ratio}), except the goniometer angle, showed significant correlations with KL grading (rho = 0.32–0.64, $p < 0.01$) and MOAKS composite score (rho = 0.35–0.56, $p < 0.01$). Both P_{acc} and JLCA showed higher areas under the ROC curve to discriminate OA (AUC = 0.76 and AUC = 0.78) than MRI_{ratio} and goniometer angle (AUC = 0.55 and AUC = 0.56). Our results demonstrate the clinical potential of kinematic knee instability measurements using low-cost accelerometers. Such approach could become a potential new tool in OA diagnostics.

Keywords

Osteoarthritis • Knee • Instability • MRI Radiography • Accelerometer • Kinematics

1 Introduction

Osteoarthritis (OA) is a degenerative joint disease affecting various tissues, such as bone, cartilage and ligaments. It can occur in any joint, but most typically it affects knee, hand and hip joints. OA is one of the leading causes of disability and pain [1], and its impact on healthcare costs are significant [2, 3]. Currently used tools for diagnosing OA are conventional radiography and magnetic resonance imaging (MRI) combined with clinical assessment. It is well known that radiography is not sensitive to early OA changes [4]. MRI provides full 3D imaging of all soft tissues of the joint and can detect OA changes earlier than radiography, but its availability is limited in routine healthcare. Consequently, there is a need for novel low cost, non-invasive and sensitive diagnostic tools to assess joint health.

OA progression is associated with biomechanical changes in the affected joints [5, 6]. One of the most clinically relevant change occurring within the knee joint is the increase

V. K. O. Virtanen (✉) · J. Thevenot · A. Tiulpin · J. Hirvasniemi
J. Niinimäki · M. Nevalainen · S. Saarakkala
Research Unit of Medical Imaging, Physics and Technology,
University of Oulu, Aapistie 5A, 90014 Oulu, Finland
e-mail: vesa.k.virtanen@oulu.fi

J. Niinimäki · M. Nevalainen · S. Saarakkala
Department of Diagnostic Radiology, Oulu University Hospital,
Oulu, Finland

J. Hirvasniemi
Center for Machine Vision and Signal Analysis,
University of Oulu, Oulu, Finland

of instability, which is caused by the wear and tear of the soft tissues, such as cartilage, menisci and ligaments [7]. Eventually, this will cause greater deviation from normal varus-valgus angle of the knee joint [8].

Gait analysis has been used in multiple studies to assess lower limb movement in subjects with knee OA, however the reported findings have been conflicting. For example, the review article by Ornetti et al. [9] concluded that kinematic parameters were mostly insufficient to be considered as valuable outcome measures. Yet, the recent study by van der Straaten et al. [10] found that differences in knee flexion range of motion, stride and gait cycle duration were distinct in subjects with knee OA when compared to healthy subjects.

Development of accurate and sensitive novel tools for clinical purpose is crucial. For instance, kinematic systems with low accuracy might fail to detect symptomatic changes during movements. Recent progress in electronics enables high accuracy inertial measurement unit (IMU) sensors to be accessible even to the general public. In principle, the kinematic data obtained from these sensor units can provide new insights of the alterations within the knee joints of OA subjects when compared to subjects with healthy knees.

The aim of this study was to assess the feasibility of using low-cost accelerometer-based measurements from thigh and shank to extract information on knee instability, and compare it with currently used clinical modalities, i.e., conventional radiography and MRI. Our study has the following novelties: (1) utilizing the power of accelerometer signal as a parameter for assessing knee instability, and (2) high number of subjects and data from clinical assessment, radiographs and MRI scans to provide a reliable comparison.

2 Materials and Methods

2.1 Data Acquisition Protocol and OA Staging

Sixty-six females (57.8 ± 6.2 years old, range 44–67 years) with body mass index (BMI) of 27.4 ± 4.8 kg/m^2 underwent a clinical trial at Oulu University Hospital, Finland (clinicaltrials.gov study identifier: NCT02937064). The first part of the trial included a background questionnaire, physical examination and varus-valgus angle assessment using a goniometer. For the goniometer measurements, the subjects stood up with legs rotated 10° out. The second part of the trial protocol consisted of knee MRI, anthropometric measurements (weight, height), inertial measurements using kinematic modules (accelerometer and gyroscope), and a weight bearing knee radiograph acquisition. The OA stage was assessed from the radiographs using the Kellgren–Lawrence (KL) grading scale [11], and from the MRI data using the MRI OA knee scoring (MOAKS) system [12]. A composite MOAKS score was calculated by combining
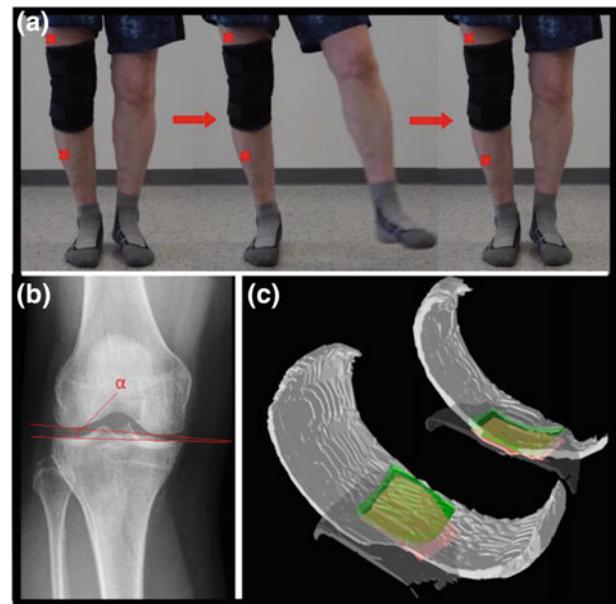
Fig. 1 Visualization of the knee instability parameters' acquisition methods. **a** Kinematic power of signal was recorded during one leg stand. Red crosses are marking roughly the placement of sensors; **b** method for calculating JLCA angle (α) from plain radiograph; **c** 3D cartilage masks with colored areas (green: femur, red: tibia) used in weight bearing area thickness calculations (Color figure online)

full-thickness and non-full-thickness cartilage degeneration parameters from medial and lateral sides of both femur and tibia, which resulted in a total score between 0 and 24.

2.2 Accelerometer Analysis

The accelerometer measurements were performed using a custom-made prototype device with the sensors attached to the thigh and shank as indicated by red marks in Fig. 1a. One-leg-stand movement was repeated twice. Acceleration in anatomical longitudinal axis was used as a measure of knee instability and the power of the signal (P_{acc}) over the two repeated movements was calculated according to Eq. 1:

$$P_{acc} = \frac{1}{n} \sum_{i=1}^{n} a_i^2, \tag{1}$$

where: P_{acc} = power of the accelerometer signal, n = total number of signal samples, i = signal sample number, a = acceleration in anatomical longitudinal axis.

2.3 Radiograph Analysis

Knee radiographs were acquired using Digital Diagnost (Philips Medical Systems) X-ray device with 60 kVp voltage, automatic exposure and pixel size of 0.148 mm

0.148 mm. The subjects were instructed to stand on pre-determined feet markers and were leaning their legs against a plate to standardize the degree of knee bending. Joint line convergence angle (JLCA) [13] was calculated from the radiographs (Fig. 1b). The required anatomical reference points were manually marked and the angle was calculated with an ad hoc MATLAB-based (MATLAB R2017B, version 9.2.0.518641, The MathWorks, Inc., Natick, Massachusetts, United States) script. The markings were repeated twice, and the average of both calculated angles was used as the final JLCA value.

2.4 MRI Analysis of Cartilage Thickness

MRI images were acquired using Siemens Skyra 3-Tesla scanner using 3D Double Echo Steady State sequence with water excitation (3D-DESS-WE): repetition time of 14.1 ms, echo time of 5 ms, and echo train length of 2. Slices were oriented in sagittal plane, and both the pixel spacing and slice thickness were 0.6 mm. The cartilage was then semi-automatically segmented from the slices using the Mimics software (version 17.0.0.435, Materialise NV, Leuven, Belgium). Lateral and medial compartments of tibial and femoral cartilage was segmented using the following method: the start and end slices were determined by the first slices in which the ligaments were not interfering with cartilage segmentation, except on last slices of medial side where the last slice was determined by visually assessing that enough of the tibial cartilage was still visible in the slice.

To reach high accuracy of the segmentation, a preliminary mask was carefully drawn following the cartilage surface, to solely include cartilage and bone. Subsequently, a thresholding value was manually selected to provide the best compromise to separate cartilage from bone. All the segmented slices were visually checked by the user and corrected if necessary. The end result consisted of four distinct masks corresponding to medial and lateral compartments of the femur and tibia (Fig. 1c). The average thickness over the weight-bearing area from the segmented masks for each subject was calculated with a custom-made MATLAB script. The area used for calculations is illustrated in Fig. 1c.

2.5 Statistical Methods

As a measure of instability, we normalized the data by assessing the relative deviation between medial and lateral sides for all modalities. Briefly, MRI_{ratio} was calculated by dividing higher (between medial and lateral) cartilage thickness by the lower one. Similarly, the absolute value of JLCA was used as a measure of deviation. For the goniometer data, the absolute values of the measured varus or valgus angles were used.

Spearman's correlations were calculated between kinematic instability parameters and OA stages (KL grades and MOAKS-derived composite scores). We also used leave-one-out cross-validation (LOOCV) with logistic regression and performed receiver operating characteristic (ROC) analysis by calculating area under the curve (AUC) to discriminate OA cases (KL $\geq$ 2) from controls.

3 Results

The KL assessment of the knees yielded the following results: KL0: 7, KL1: 25, KL2: 16, KL3: 16, KL4: 2, which corresponds to 32 controls and 34 OA cases. The relation between KL grade and composite MOAKS scores can be seen from the Fig. 2.
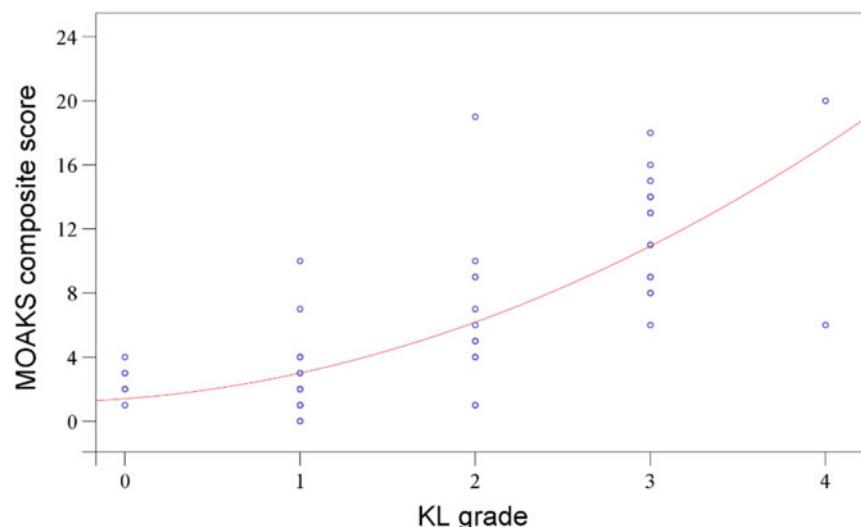
Fig. 2 MOAKS composite score compared to KL grade. The subjects are shown in blue and the second order polynomial fit in red ($r^2 = 0.57$) (Color figure online)

Table 1 Comparison between measured kinematic parameters and radiological findings (Kellgren–Lawrence (KL) grades and composite MOAKS scores), using Spearman correlation and area under the ROC-curve (AUC) for leave-one-out cross validation (LOOCV). P_{acc}: power of acceleration signal; JLCA: joint line convergence angle; MRI_{ratio}: ratio between medial and lateral side knee cartilage thickness

Parameter	Spearman rho (KL)	Spearman rho (MOAKS)	AUC (LOOCV)
P_{acc}	0.48**	0.56**	0.76
JLCA	0.64**	0.56**	0.77
MRI_{ratio}	0.32**	0.35**	0.55
Goniometer angle	0.20	0.12	0.54

*$p < 0.05$, **$p < 0.01$

Statistically significant correlations ($p < 0.01$) were found for P_{acc}, JLCA and MRI_{ratio} when compared against KL grades or MOAKS composite scores, as shown in Table 1. Compared to KL grade, JLCA achieved a rho of 0.64, while P_{acc} had rho of 0.48 and MRI_{ratio} had rho of 0.32. When assessing correlations with MOAKS composite score, P_{acc} and JLCA achieved similar correlations (rho of 0.56) while MRI_{ratio} had the lowest (rho of 0.35).

Logistic regression with LOOCV yielded AUC of 0.76 (95% CI: 0.64–0.88) for P_{acc} and AUC of 0.77 (95% CI: 0.66–0.89) for JLCA. MRI_{ratio} and goniometer parameters had poor AUC close to 0.5.

4 Discussion

Knee instability is known to be associated with OA [6]. As the disease progresses, the alteration of the soft tissues within the joint can result in a knee misalignment and an increased shear and motion during bending. The aim of this study was to assess the feasibility of using low-cost accelerometer-based measurements from thigh and shank to extract information on knee instability and compare it with OA severity evaluated from both conventional radiography and MRI.

Changes in varus-valgus angle have been shown to be associated with OA progression [8, 14, 15]. The greater deviation from a normal angle can be considered as a measure of instability. In the current study, the misalignment of the knee was assessed from two different clinical imaging modalities as well as using a traditional goniometer device. Goniometer is widely used in clinical practice and has been applied in OA studies [16], however despite the measurement being fast and easy to perform, its reliability to define the varus-valgus angle is low [17]. Conventional knee radiography allows to determine the actual anatomical angle between the femur and the tibia (an angle close to the one assessed by goniometer), but here we decided to focus on the

JLCA as it is more representative of the difference in cartilage thicknesses between medial and lateral sides. We also measured the ratio between medial and lateral cartilage thicknesses segmented volumetrically from MRI scans of unloaded knees, as an analogic evaluation of the joint space width difference between sides, comparable to the JLCA information obtained from the radiographs.

Accelerometers and IMUs have been used in studies related to knee OA, but those have focused on knee range of motion and knee angle during both stance and swing phase of gait, as well as temporal parameters of gait during level walking [10]. In our study, we wanted to assess knee instability and hypothesized a one-leg-stand test as a potential experiment to evaluate instability. Due to the age of subjects, lifting of the leg was only done conservatively as shown in the Fig. 1a, which allowed all of the subjects to perform the test. The test only takes a few seconds to perform and the results can be obtained instantly and objectively, unlike with current clinical modalities which require subjective assessment from the data. The results show that the P_{acc} signal during one-leg-stand test correlates significantly with OA stage and can discriminate OA patients from control subjects with similar AUC as JLCA.

While both JLCA and MRI_{ratio} are estimations of the difference between the lateral and medial side, the obtained results showed that JLCA outperformed the MRI_{ratio} in assessing OA. One reason of this finding could be that the joint is loaded during radiography and that the compression of the cartilage might be directly affected not only by its original thickness, but also by its composition changing with OA [18]. Furthermore, JLCA is more representative of the overall current joint condition (the surfaces of the bones are used as references), whereas menisci and ligaments were totally ignored in the MRI_{ratio} assessment (only cartilage thicknesses were used). While JLCA and P_{acc} provided similar correlations with MOAKS composite score, the higher correlation obtained between JLCA and KL grading is most likely because both of those parameters were

evaluated from the same radiographs. Moreover, the standardized standing position required during the knee radiography might have accentuated the medial-lateral difference—especially in subjects with high knee joint laxity—resulting in higher correlations with KL grading.

The angles measured by the goniometer did not show any statistically significant association with OA severity. One explanation for the poor performance of this measurement could be that multiple subjects were overweight and/or had knees with inflammation, affecting the accuracy of the measurements as locating the anatomical references can be challenging in these cases. Goniometer measurements were performed by experienced clinicians using established measurement protocols, but the reliability of the method, unfortunately, could not be assessed since only a single measurement per subject was conducted. The results reported here suggest that goniometer measurements may not be an appropriate modality to be used in clinical OA trials.

As a limitation of this study, the protocol for kinematic acquisition had some variation among the subjects: due to anatomical differences, the location of the sensors was not constant between the subjects. We tried to diminish this variation to a minimum by attaching a rigid 3D printed frames with straps to both thigh and shank. This arrangement reduced the artefacts related to loose tissues and skin movements, which are common when sensors are directly taped onto the skin. From this point of view, one-leg-stand test is a good candidate for assessing knee joint instability with accelerometers as it involves minimal movement. A second limitation of the study is related to the cartilage thickness measurements from MRI: while the method we proposed here should provide an accurate segmentation of the tissue, it cannot overcome the low resolution of the modality. Finally, in this study we had only two patients with KL grading of 4, corresponding to severe OA. While a more even distribution could have provided better correlations with the disease, in this clinical trial we recruited subjects with early to mild osteoarthritis, as the diagnosis at those stages is more challenging than at later phases. Eventually, the ability of this kinematic approach to discriminate earlier stages of OA further supports the potential of this method in clinical applications.

As a conclusion, the kinematic approach presented in this study provides a simple, low-cost and non-invasive solution to obtain information on the knee joint instability. The preliminary validation of this method suggests the feasibility of using simple kinematics as a potential diagnostic tool for OA. The combination of this instability information with other parameters known to be associated with the condition should be considered in the future to improve the accuracy of the models to discriminate OA in clinical practice.

References

1. Chu CR, Millis MB, Olson SA. Osteoarthritis: From Palliation to Prevention: AOA Critical Issues. J Bone Joint Surg Am 96:e130. (2014)
2. Neogi T. The epidemiology and impact of pain in osteoarthritis. Osteoarthritis Cartilage 21:1145–1153. (2013)
3. Hiligsmann M, Cooper C, Arden N, Boers M, Branco JC, Luisa Brandi M, Bruyere O, Guillemin F, Hochberg MC, Hunter DJ, Kanis JA, Kvien TK, Laslop A, Pelletier JP, Pinto D, Reiter-Niesert S, Rizzoli R, Rovati LC, Severens JL, Silverman S, Tsouderos Y, Tugwell P, Reginster JY. Health economics in the field of osteoarthritis: an expert's consensus paper from the European Society for Clinical and Economic Aspects of Osteoporosis and Osteoarthritis (ESCEO). Semin Arthritis Rheum 43:303–313. (2013)
4. Guermazi A, Roemer FW, Burstein D, Hayashi D. Why radiography should no longer be considered a surrogate outcome measure for longitudinal assessment of cartilage in knee osteoarthritis. Arthritis Res Ther 13:247. (2011)
5. Heijink A, Gomoll AH, Madry H, Drobnic M, Filardo G, Espregueira-Mendes J, Van Dijk CN. Biomechanical considerations in the pathogenesis of osteoarthritis of the knee. Knee Surg Sports Traumatol Arthrosc 20:423–435. (2012)
6. Blalock D, Miller A, Tilley M, Wang J. Joint instability and osteoarthritis. Clin Med Insights Arthritis Musculoskelet Disord 8:15–23. (2015)
7. Lohmander LS, Englund PM, Dahl LL, Roos EM. The long-term consequence of anterior cruciate ligament and meniscus injuries: osteoarthritis. Am J Sports Med 35:1756–1769. (2007)
8. Freisinger GM, Schmitt LC, Wanamaker AB, Siston RA, Chaudhari AMW. Tibiofemoral Osteoarthritis and Varus-Valgus Laxity. J Knee Surg 30:440–451. (2017)
9. Ornetti P, Maillefert JF, Laroche D, Morisset C, Dougados M, Gossec L. Gait analysis as a quantifiable outcome measure in hip or knee osteoarthritis: a systematic review. Joint Bone Spine 77:421–425. (2010)
10. van der Straaten R, De Baets L, Jonkers I, Timmermans A. Mobile assessment of the lower limb kinematics in healthy persons and in persons with degenerative knee disorders: A systematic review. Gait Posture 59:229–241. (2017)
11. Kellgren JH, Lawrence JS. Radiological assessment of osteo-arthrosis. Ann Rheum Dis 16:494–502. (1957)
12. Hunter DJ, Guermazi A, Lo GH, Grainger AJ, Conaghan PG, Boudreau RM, Roemer FW. Evolution of semi-quantitative whole joint assessment of knee OA: MOAKS (MRI Osteoarthritis Knee Score). Osteoarthritis Cartilage 19:990–1002. (2011)
13. Kleeblad LJ, van der List JP, Pearle AD, Fragomen AT, Rozbruch SR. Predicting the Feasibility of Correcting Mechanical Axis in Large Varus Deformities With Unicompartmental Knee Arthroplasty. J Arthroplasty. (2017)
14. Sharma L, Chmiel JS, Almagor O, Felson D, Guermazi A, Roemer F, Lewis CE, Segal N, Torner J, Cooke TD, Hietpas J,

Lynch J, Nevitt M. The role of varus and valgus alignment in the initial development of knee cartilage damage by MRI: the MOST study. Ann Rheum Dis 72:235–240. (2013)

15. Bastick AN, Belo JN, Runhaar J, Bierma-Zeinstra SM. What Are the Prognostic Factors for Radiographic Progression of Knee Osteoarthritis? A Meta-analysis. Clin Orthop Relat Res 473:2969–2989. (2015)

16. Amaratunga HA, Adikari SB, Dassanayake TL, Gamage J, Suraweera HJ. Relationship between the goniometric alignment and articular cartilage damage in knee osteoarthritis. Ceylon Med J 62:167–174. (2017)

17. van Trijffel E, van de Pol RJ, Oostendorp RA, Lucas C. Inter-rater reliability for measurement of passive physiological movements in lower extremity joints is generally low: a systematic review. J Physiother 56:223–235. (2010)

18. Julkunen P, Jurvelin JS, Isaksson H. Contribution of tissue composition and structure to mechanical response of articular cartilage under different loading geometries and strain rates. Biomech Model Mechanobiol 9:237–245. (2010)

Recent Progress on Preferential Covered Stent Development

Fangsen Cui, Gideon Praveen Kumar, Li Buay Koh, Keping Zuo, Hwa Liang Leo, and Jackie Pei Ho

Abstract

Carotid artery stenosis can be treated by carotid endarterectomy operations (CEA) and carotid artery stenting procedures (CAS). Unlike other artery stents, the effectiveness and safety of carotid artery stenting is not prevailing though it has many advantages. Our group has been developing new generation carotid artery stent since 2011. The innovative carotid stent was named as preferential covered stent (PCS) as it could prevent both emboli release at internal carotid artery (ICA) and provide perfusion to external carotid artery (ECA). A series of studies have been carried out to verify the carotid stent design through modeling and simulation, in vitro loop testing, and in vivo pilot animal testing in our previous proof of concept (POC) stage. Here we report some recent findings on PCS development, including simulation and experimental work on stent crimpability, membrane material characterization, and the flow response for different slit designs in vitro.

Keywords

Carotid artery stent • Preferential covered stent
Modeling and simulation • In vitro testing
In vivo study

F. Cui (✉) · G. P. Kumar
Institute of High Performance Computing, A*STAR, Singapore, Singapore
e-mail: cuifs@ihpc.a-star.edu.sg

L. B. Koh · K. Zuo · J. P. Ho
Department of Surgery, National University of Singapore, Singapore, Singapore

H. L. Leo
Department of Biomedical Engineering, National University of Singapore, Singapore, Singapore

1 Introduction

Usually vascular stents for cardiovascular diseases are a better choice than those surgery treatments, as they are less invasive, faster recovery, not expensive, and good clinical results. However, the development for carotid artery stent does not prove this. The carotid artery stenting (CAS) is not superior to carotid endarterectomy (CEA) in many ways, especially its peri-procedural risk of stroke is higher than conventional endarterectomy, mainly because bare metal stents used in CAS fail to constrain small fragments detached from atherosclerotic plaques, resulting in stroke after stenting. Because the common carotid artery (CCA) bifurcates into internal carotid artery (ICA) and external carotid artery (ECA), the covered stent is not a good solution, as it will compromise the perfusion of the external carotid artery branch. Besides, embolic protection devices (EPDs) in the market can only offer protection during the stenting procedure and not afterwards.

Hence, to address this unmet clinical need and to fill this crucial gap of medical devices, our research team has designed and prototyped a novel covered stent (Fig. 1) that can prevent emboli occurrence while preserving the side-branch flow [1, 2]. The concept was well proofed and study was moved to new cover material development, fabricating membrane cover on bare stent, delivery system, in vitro testing, and in vivo testing. The modeling and simulation has been extensively used in design, evaluation, and optimization of prototypes. In following sections, the modeling and simulation work for a better stent design, stent cover, and in vivo testing results are briefly introduced.

2 In Vitro Testing

PCS were made and tested in 3 different diameter and branch angle vessel models for current study (Fig. 2). Previous flow testing and PIV measurement results were reported in [3, 4].
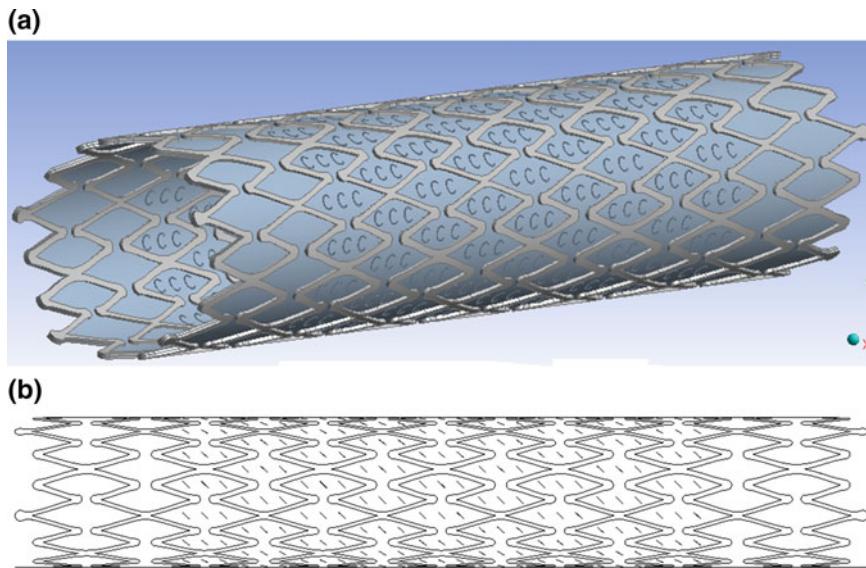
Fig. 1 New preferential covered stent designs, **a** design with flaps, **b** design with slits

Fig. 2 Flow loop testing for three configurations (Y-shape, Curve, and straight bifurcation. From left to right)

Table 1 Side-branch flow preservation tests for various stents in different arterial geometric models

Designs	Y-shape	Curved	Straight
Flow ratio	ICA–ECA	ICA–ECA	ICA–ECA
Control (%)	70–30	70–30	70–30
Slit 60° (%)	78–22	78–22	82–18
Slit 90° (%)	77–23	81–19	85–15
S-slit 45° (%)	74–26	73–27	81–19

Here similar experimental setup was used to measure the flow rate.

Table 1 listed the flow testing results.

3 Modeling and Simulation

Side branch flow preservation tests were conducted for different configurations with varied bifurcation angels. It was found that the flow in the straight arterial model was considerably lower than that observed in Y-shaped model. This is mainly due to the Y-shaped bifurcation model has more area facing the side-branch opening than that in the straight model. Besides, the number of slit openings of the stent

membrane in each stent cell plays a key role in side branch flow preservation, as the stent struts could block the passage. One way to realize higher ECA flow rates is to design new bare metal stents with bigger cell size which can accommodate more number of slits so that better perfusion to the side-branch is envisaged. We [5] designed a few types of stent with big cells and simulated their performance through finite element analysis (FEA). We showed that the mechanical performance of the new design is not inferior to commercial ones. The effect of crown numbers on radial stiffness was also recently studied. We showed that (Fig. 3) less crown number could lead to stiffer stents for open-cell designs, which is contrary to the usually thinking that less crowns result in soft stent. This effect was further confirmed

Fig. 3 FEA study on the effect of crown number on stent stiffness, **a** fabricated stent designs with different crown number; **b** displacement of different designs with a load of 0.5 N. The 6 crown design shows least displacement which is the stiffest
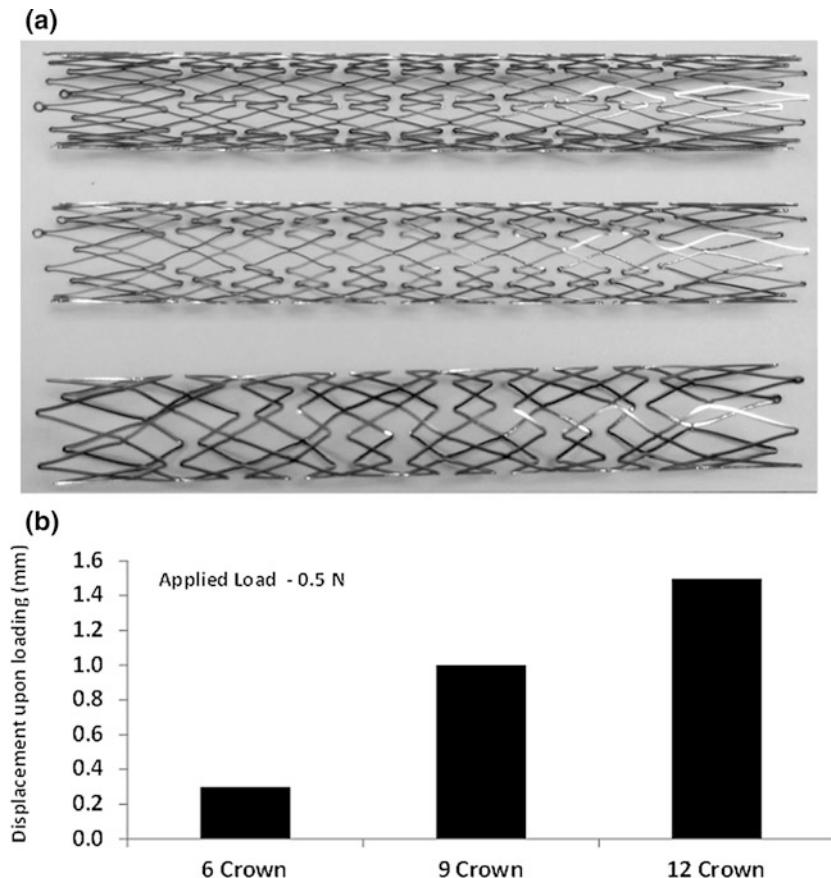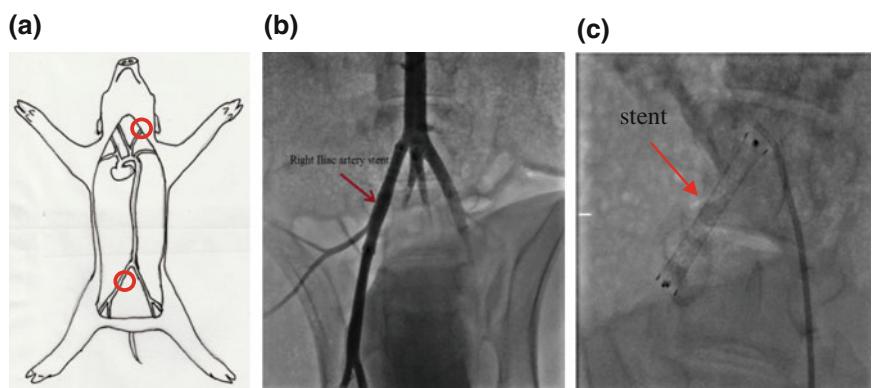
Fig. 4 Pig model. **a** Red circles show the left carotid artery and right Iliac artery. **b** Day 0—patent flow at right iliac. **c** Day 30 partial occlusion of right iliac (Color figure online)

by experimental testing with fabricated stents and analytical method. This finding is important for stent design and development, especially for peripheral stents which are usually subjected to more loading during daily activities.

4 In Vivo Testing

Pigs were used to test the patency of developed preferential covered stents (approved by Institutional Animal Care and Use Committee (IACUC) prior to testing). Usually the

implantation with good patent flow but some occlusions were observed after 30 days. Figure 4 showed one pig patency testing result. The right iliac artery was chosen for PCS stent implantation (Fig. 4c).

5 Conclusions

We have invented a preferential covered stent (PCS) for the treatment of carotid artery stenosis. Many efforts have been made to overcome issues such side branch flow preservation

by different slits designs, large open cell designs. The biocompatible of membrane materials, different coating methods and stent fabrications were studied. The in vitro testing and animal testing results showed the new design is promising but partial occlusions are still observed. More work is required before this stent can be evaluated in clinic.

Conflict of Interest The authors declare that they have no conflict of interest.

References

1. Ho, P., Leo, H. L., Ng. S. H., Cui, F. S., Kabinejadian, F.: Membrane for covering a peripheral surface of a stent, Singapore patent No:11201401358V, PCT patent No: WO2013055293 A1.
2. Kabinejadian F., Cui F., Zhang Z., Ho P., Leo H. L.: A novel carotid covered stent design: in vitro evaluation of mechanical performance and influence on the blood flow regime at the carotid artery bifurcation. Annals of Biomedical Engineering, 41(9), 1990–2002 (2013).
3. Kabinejadian F., Cui F., Leo H. L., Ho P.: Covered stent membrane design for treatment of atheroembolic disease at carotid artery bifurcation and prevention of thromboembolic stroke: an in vitro experimental study, Artificial Organs 40(2), 159–168 (2016).
4. Kabinejadian F., Cui F. S., Su B., Danpinid A., Ho P., Leo H. L.: Effects of a novel carotid covered stent on blood flow regime and hemodynamic parameters distribution at the carotid artery bifurcation, Medical & Biological Engineering & Computing, 53(2), 165–77 (2015).
5. Kumar G. P., Kabinejadian F., Liu J. F., Leo H. L., Ho P., Cui F.: Simulated bench testing to evaluate the mechanical performance of new carotid stents, Artificial Organs, 41(3), 267–272 (2017).

Photoelastic Analysis of Shoulder Arthroplasty: Current Descriptive Analysis of Research in Scientific Journals

D. A. Almeida-Galárraga, A. Ros Felip, F. Marco Martínez, and Laura Serrano-Mateo

Abstract

Shoulder joint complex poses a biomechanical challenge due to its complexity and the number of structures involved. Shoulder pain is one of the most prevalent reasons for consultation in primary health. The main chosen surgical treatments for joint degeneration, as a consequence of the chronic injury of the rotator cuff, is reverse arthroplasty. Photoelasticity is an experimental method used to evaluate the strain environment under mechanical loading. The aim of this study is to present a systematic revision of the literature in academic journals for the period 2000–2017 related to the study of stresses and deformations in the shoulder joint with arthroplasty through photoelasticity technique. To obtain the data, specialised search engines were used: Google Scholar, Scopus, Web of Science and PubMed. Descriptive investigation was performed through a combination of values and boolean algebra. A total of 13 articles were selected, which were reviewed and classified in two categories (photoelasticity analysis in the shoulder joint without prosthesis and study of photoelasticity in the shoulder with arthroplasty). There distribution of articles by year, journal and investigation method was also described. The photoelasticity by stress freezing allows the study of internal zones, something that is not possible with other techniques. The analysis is frequently performed with prosthetic components of total anatomical shoulder arthroplasty, but there are barely any precedents in reverse shoulder arthroplasty. Therefore, new investigations that show the effect of reverse arthroplasty are suggested, since it is present in the treatment of many other prevalent pathologies.

1 Introduction

The shoulder joint complex is composed of three bones (scapula, clavicle, and humerus), and four joints (Gleno-humeral, acromio-clavicle, scapulo-toracic, esterno-clavicle) and it has 12 degrees of freedom [1, 2]. The pathology of the shoulder is one of the most prevalent causes of medical consult [3]. Total shoulder arthroplasty is a surgical procedure whereby the glenohumeral joint is replaced by a prosthetic implant. There are two main types of total shoulder arthroplasty: anatomical and reverse. Due to the aging of the population, the degeneration of the gleno-humeral joint because of the pathology of the rotator cuff is increasing. The reverse shoulder arthroplasty (RSA) has surpassed the anatomical shoulder prosthesis design in the treatment of this kind of pathology. RSA has also begun to be used in other highly prevalent shoulder pathologies (proximal humeral fracture, post-traumatic sequelae, revision of anatomical shoulder prosthesis, and so on) [4]. The increase of indications of RSA makes more important to know how RSA interact with the bone and its possible biomechanical complication, that is why stress analysis should be studied.

The different experimental methods for stress analysis provide information about the interaction of bones with the prosthesis and allow the visualization of stress distribution patterns in specific points or throughout the joint [1]. Photoelastic analysis is a method of two and three dimensional

D. A. Almeida-Galárraga (✉) · A. Ros Felip
Department of Mechanical, Universidad Politécnica de Madrid, José Gutiérrez Abascal 2, Madrid 28006, Spain
e-mail: diego_almeidag@hotmail.com

F. Marco Martínez · L. Serrano-Mateo
Department of Orthopaedic Surgery and Traumatology, San Carlos Clinical Hospital, Profesor Martín Lagos s/n, Madrid 28040, Spain

D. A. Almeida-Galárraga
Department of Engineering, Universidad de las Fuerzas Armadas, Av. General Rumiñahui s/n, Sangolquí 171103, Ecuador

full field stress analysis that can be applied to highly complex statically or dynamically loaded models [5]. When photoelastic materials are observed under crossed polarized light, a series of continuous colored bands or fringes are seen. Each fringe corresponds to areas within the test material with similar strain conditions [6]. Several authors [5–16] have employed photoelastic models to study the biomechanics of shoulder joint complex.

Photoelasticity allows for the analysis of the stress distribution in the bones. The bones that compose the shoulder joint complex absorb the force of tension in the muscle. In the case of exceeding the stress threshold, forces cause structural modifications in the bone, causing dislocations or other conditions. Stress-freezing is an experimental technique of photoelasticity for accurately measuring internal strains in a threedimensional photoelastic model to determine the stresses during static testing [11]. Photoplastic models of a real size were molded using two different techniques: by modeling the whole bone (replica) and coating the bone with a photoelastic material.

Numerical methods contribute a great amount of information for analysis, but runs the risk of idealizing and making generalizations that do not accurately reflect reality [17]. For this reason, it is necessary to use alternative techniques, like photoelasticity, to validate and complement numerical results.

The aim of this study is to present a systematic review of the literature in academic journals during 2000–2017 related to the study of stress and deformations in the shoulder joint with arthroplasty using the photoelasticity technique. In this research, anatomy of the shoulder, biomechanics of the shoulder joint complex [2], experimental models with photoelasticity [1, 5, 6], the fabrication of photoelastic synthetic bones [7, 8] and stress-freezing studies are analyzed in the glenohumeral joint with arthroplasty [1, 9].

2 Materials y Methods

To obtain the data, the specialized search engines Google Scholar Advanced, Scopus, Web of Science and PubMed were used. Descriptive research was carried out through a combination of descriptors and Boolean algebra.

This review is descriptive and systematic, experimental studies are described as a comparative analysis between authors, a rigorous process is used (to minimize biases) that identifies, evaluates and synthesizes scientific articles to show the evolution of photoelasticity and the shoulder to finally draw conclusions about the collected data.

A bibliographic search was carried out from the year 2000 to the present date using the descriptors: shoulder, glenoid, humeral, photoelasticity, stress freezing, arthroplasty, prosthesis, reverse, anatomic. 78 search combinations

were obtained after the application of Boolean algebra. The records obtained ranged between 2 and 176 records after the combination of the different keywords.

Documents were selected to report on studies of photoleasticity in the shoulder joint or in bones in general and the manufacture of photoelastic models of bones and stress analysis with experimental optomechanical techniques in the glenohumeral joint with arthroplasty. Subsequently, a total of 13 articles were reviewed and classified into two categories, those focused on the analysis of deformations in the shoulder joint with experimental optomechanical techniques and another on the study of photoelasticity in models with shoulder arthroplasty. The distribution of articles per year, journal and research method were also described. Finally, an analysis of the variability, reliability and validity of the articles is carried out.

The 176 records obtained consist of experimental studies with quantitative and qualitative results that are mostly about studies on other bones. After selecting a certain number of articles, they were generally grouped by the sense of their results and the methodological characteristics of each study investigated to derive a general conclusion after their analysis.

3 Results

Most publications were made in the first five years, 69.24% (n = 9) from 2000 to 2005 and 15.38% (n = 2) in the following five years (Fig. 1). No research was carried out from 2010 until 2016 but last year in 2017 new studies were carried out in relation to photoelasticity techniques in the shoulder, 15.38% (n = 2).

The analysis of tensions and deformations with the photoelasticity technique, although well studied in hip and jaw arthroplasty, has received less attention in shoulder arthroplasty due to the biomechanical complexity that creates many design challenges. For this reason, of the 176 records obtained, 68% had a relationship with the hip, knee and jaw.

Only, 7.69% (n = 1) of the sample uses a descriptive methodology design [10], while the rest 92.31% (n = 12) use an experimental design. 76.92% (n = 10) apply stress freezing as a technique of photoelasticity to analyze the stress distribution in the bone (Table 1).

The construction of photoelastic bones is designed in two different ways: by coating the bone with a photoelastic material or by making a replica of the whole bone. There are fewer publications with the first technique [6, 13], 15.38% (n = 2), while 76.92 (n = 10) are replicas of the humerus and scapula.

Experimental studies with synthetic bone models are very limited by their difficulty, only 15.38% (n = 2) are publications of fabrication of photoelastic models [7, 8], one of
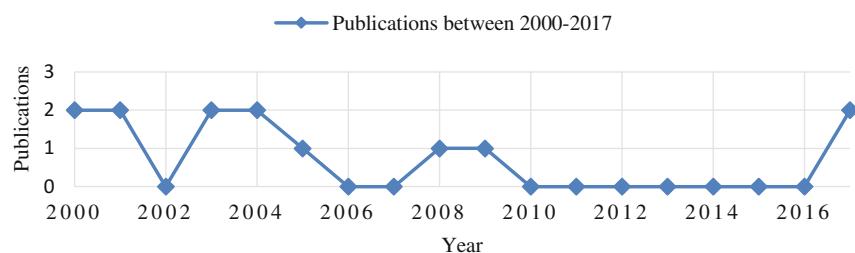
Table 1 Revision of the literature in academic journals for the period 2000–2017 related to the study of photoelasticity in the shoulder joint

Year	Reference	Research type: Manufacturing of bones/Analysis of photoelasticity	Analysis of: Scapula/Humerus/Both	Research method: Descriptive/Experimental	Technique: Replica/Coating of the bone	Shoulder prosthesis: Yes/No
2000	[11]	Analysis	Scapula	Experimental	Replica	Yes
2000	[12]	Analysis	Scapula	Experimental	Replica	Yes
2001	[7]	Manufacturing	Both	Experimental	Replica	No
2001	[13]	Analysis	Scapula	Experimental	Coating	No
2003	[14]	Analysis	Scapula	Experimental	Replica	Yes
2003	[15]	Analysis	Humerus	Experimental	Replica	No
2004	[9]	Analysis	Scapula	Experimental	Replica	Yes
2004	[16]	Analysis	Humerus	Experimental	Replica	No
2005	[5]	Analysis	Scapula	Experimental	Replica	Yes
2008	[6]	Analysis	Scapula	Experimental	Coating	Yes
2009	[10]	Analysis	Both	Descriptive		No
2017	[8]	Manufacturing	Both	Experimental	Replica	Yes
2017	[1]	Analysis	Both	Experimental	Replica	No

these articles compares two methods of photoelastic bone manufacture for the joint with two types of reversed prostheses: Delta (Depuy Sinthes) and SMR (Lima) [8].
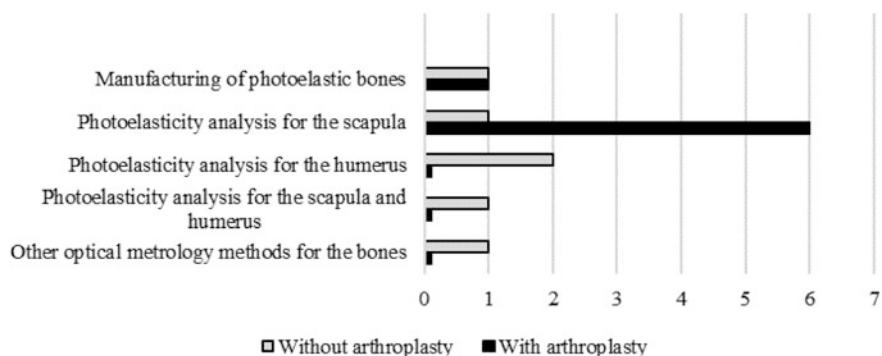
The articles that focused on the analysis of stresses and deformations in the shoulder joint without arthroplasty with experimental optomechanical techniques form 46.16% of the total sample (n = 6), while 53.84% (n = 7) are studies of photoelasticity in models with shoulder arthroplasty (Fig. 2).

There is less research on stress analysis with photoelasticity for the humerus than for the scapula, 23.08% (n = 3)

and 61.54% (n = 8), respectively. Only one article presents a model based on photoelasticity techniques in the complete glenohumeral joint (humerus and scapula) without shoulder arthroplasty [1]. The percentage is higher in the scapula because there are more problems in the glenoid cavity [11–14] with respect to the humerus [1, 15, 16].

Photoelasticity is used to obtain experimental data to be compared with the results of finite element analysis and confirm the structural behavior of the numerical model. 23.08% (n = 3) use finite element analysis and

photoelasticity [5, 15, 16], while 53.85% (n = 7) base their experimental design solely on optical metrology to validate the numerical results.

4 Discussion of Results

Stress freezing [1, 9] continues to be the main method to evaluate the internal stresses with photoelastic biomechanical models. The resulting deformations were observed using a reflection polariscope [1, 5]. When the tensions are correctly displayed, the photograph is taken and the data is studied using image analysis software [1, 13]. Experimental models easily transmit information to doctors and other non-engineering professionals, provide valuable and intuitive visual data, and are versatile and suitable for didactic applications in shoulder anatomy and biomechanics [2].

Despite the attractiveness of photoelasticity as a method capable of mapping distributions of surface tensions, it also has several inherent weaknesses. When a sample is coated with a photoelastic material, potential errors include a mismatch of the Poisson's ratio between the coating material and the structure under investigation, incorrect light incidence, uneven coating thickness, and the potential reinforcing effect of the photoelastic material [6, 13]. When a replica is used, only the geometry is simulated homogenously but not the different layers of the sample and the complex properties of the materials are not taken into account [7, 9, 11]. The homogeneity of the material is a disadvantage because not all bone layers are modeled with different photoelastic materials, for example, the humerus and scapula are composed of a hard outer layer (cortical bone) with a softer nucleus (cancellous bone) and are not analyzed separately [7, 14].

In this review several articles have used optical metrology to investigate the mechanical behavior of bones [1] and bone implants [9, 12, 14]. However, the results only showed estimations because the material analyzed (replicas of photoelastic resin) was homogeneous and isotropic [5]. To improve these results, replicas should be constructed with several layers of photoelastic material, which model the complex and anisotropic bone material with structures similar to cancellous bone [7] and cortical bone [10]. Future work is aimed at using replica models of the actual structure of the bone to determine the transmission of forces through cancellous and cortical bone [14].

Stress and deformations produced in the shoulder with arthroplasty and in a healthy shoulder were evaluated. The stress produced by the prosthesis after a shoulder arthroplasty leads to loosening of the implant and subsequently deformations in the glenoid cavity [6] and the acromion [5].

Peindl et al. evaluated the stresses of the cortical cortex on the anatomically normal glenoid loaded through the humeral head versus the glenoid with a hemiarthroplasty component (keeled and pegged) using a photoelastic analysis approach. Models with a hemiarthroplasty component reduced maximal tensions to almost anatomical levels at the base of the glenoid cavity for various loading conditions [14].

The results of the photoelasticity analysis in the glenoid cavity show that, when prostheses are implanted in healthy bones, the stresses in the neck of the glenoid cavity increase [9, 11] and cortical stresses [6, 9, 11, 14] and uncemented keeled with metal-backed implants produce some areas of significantly higher cortical shear stresses with static loading compared to a cemented polyethylene design [6]. Due to increased load transfer through the keeled complement, stress in the glenoid cavity was more evident with the keel components versus the cemented pegged design [9, 11].

Murphy et al. used a finite element analysis to investigate whether acromion fixation is a significant advantage for the glenoid components. The union of the glenoid prosthetic component to the acromion may seem simple and beneficial but does not create any advantage for fixation. When implanted with a prosthesis fixed by acromion, it is found that strong non-physiological stresses occur in the scapula, and that the stresses in the fixation are not reduced [5].

The humerus generally suffers fewer injuries, which is why the vast majority of studies of photoelasticity are performed in the glenoid cavity. The studies of photoelasticity of the humerus [6, 8] were not related to total shoulder arthroplasty. Yu et al. analyzed the distribution of tension in the humeral ectocondyle by means of an experimental continuous field technique and finite element method [6, 8].

The application of advanced photoelasticity techniques for the study of complete bones has lots of potential. In the future, development of an experimental analysis to study at a qualitative level the internal stress with 3D photoelasticity in the bones of the shoulder with arthroplasty should be
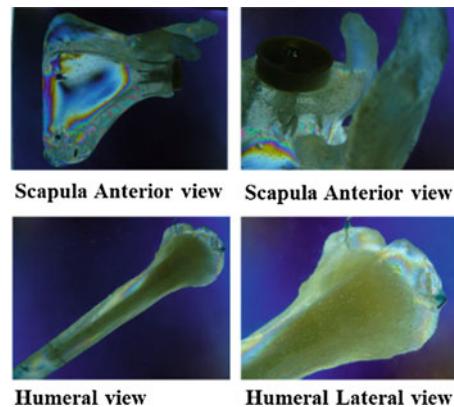
Fig. 3 Analysis of 3D photoelasticity in the shoulder joint with total arthroplasty

investigated. Additionally, the effects of the implantation of joint prostheses with the bones should be researched. Overall, this method could be applied to other joint complexes (Fig. 3).

5　Conclusion

Photoelasticity gives a global vision of the internal forces in the whole structure (scapula and humerus). The results are very visual, allowing an immediate and intuitive interpretation without the need for calculations, which makes it especially attractive in multidisciplinary problems. In addition, stress freezing allows the study of internal zones, far from the contour, which is not possible with other techniques.

The main disadvantage of models that replicate bones with photoelastic materials is that the bone is designed as a homogeneous isotropic material. However, are that they use precise three-dimensional geometry of the solid model and adequately represent the load and strain interactions between the bone and the prostheses for the actual applications of compound component loading. As a result, the model provides a complementary three-dimensional experimental analysis to validate finite element analysis techniques.

While there is currently more research on stress and strain analysis in the hip, knee and jaw, it is necessary to develop new numerical and experimental techniques to study the glenohumeral joint and improve implants in total arthroplasty of the shoulder.

Conflict of Interest Statement　The authors declare that they have no conflict of interest.

References

1. Almeida-Galárraga, D., Ros-Felip, Serrano-Mateo, L., & Marco-Martinez, F. (2017). Estudio de deformaciones en la articulación del hombro con técnicas experimentales optomecánicas. In CASEIB 2017: XXXV Congreso Anual de la Sociedad Española de Ingeniería Biomédica: libro de actas: Bilbao, 29 Nov–1 Dec, 2017 (pp. 447–450).
2. Almeida-Galárraga, D., Ros-Felip, A., Álvarez-Sánchez, V., Marco-Martinez, F., & Serrano-Mateo, L. (2017). Kinematics based physical modelling and experimental analysis of the shoulder joint complex. Ingeniería e Investigación, 37(3), 115–123.
3. Greving, K., Dorrestijn, O., Winters, J. C., Groenhof, F., Van der Meer, K., Stevens, M., & Diercks, R. L. (2012). Incidence, prevalence, and consultation rates of shoulder complaints in general practice. Scandinavian journal of rheumatology, 41(2), 150–155.
4. Brolin TJ, Throckmorton TW. (2018). Emerging indications for reverse shoulder arthroplasty. En: Dines DM. Reverse shoulder arthroplasty. Edición 1. (p 35–39). New York.
5. Murphy, L. A., & Prendergast, P. J. (2005). Acromion-fixation of glenoid components in total shoulder arthroplasty. Journal of biomechanics, 38(8), 1702–1711.
6. Pelletier, M. H., Langdown, A., Gillies, R. M., Sonnabend, D. H., & Walsh, W. R. (2008). Photoelastic comparison of strains in the underlying glenoid with metal-backed and all-polyethylene implants. Journal of Shoulder and Elbow Surgery, 17(5), 779–783.
7. Mushipe, M. T., & Orr, J. F. (2001). Fabrication of Life-size Photoelastic Cancellous Bone Models. Strain, 37(3), 123–126.
8. Bel P, Dalmau A (Eds). Actas del XL Congreso de la Sociedad Ibérica de Biomecánica y Biomateriales. Barcelona 2017.
9. Peindl, R. D., Harrow, M. E., Connor, P. M., Banks, D. M., & D'Alessandro, D. F. (2004). Photoelastic stress freezing analysis of total shoulder replacement systems. Experimental mechanics, 44(3), 228–234.
10. Barak, M. M., Sharir, A., & Shahar, R. (2009). Optical metrology methods for mechanical testing of whole bones. The Veterinary Journal, 180(1), 7–14.
11. Harrow, M. E. (1999). An interactive computer graphics tool for visualization of three-dimensional photoelastic stress frozen models: a study of total shoulder arthroplasty glenoid components (Master's thesis, University of North Carolina at Charlotte).
12. Peindl, R., Harrow, M., Banks, D., Connor, P. M., & D'Alessandro, D. (2000). Glenoid stress distributions in total shoulder arthroplasty: analysis of keeled versus pegged implants. In Proceedings of the 46th Annual Meeting of Orthopaedic Research Society (p. 117).
13. Malicky, D. M., Soslowsky, L. J., Kuhn, J. E., Bey, M. J., Mouro, C. M., Raz, J. A., & Liu, C. A. (2001). Total strain fields of the antero-inferior shoulder capsule under subluxation: a stereoradiogrammetric study. Journal of biomechanical engineering, 123(5), 425–431.
14. Peindl, R. D., Connor, P. M., Coley, E. R., Stull, D. E., & D'Allesandro, D. F. (2003). Glenoid stress distribution patterns for anatomic and posterior-deficient shoulders managed by hemiarthroplasty and TSR. In 49th Annual Meeting of the Orthopaedic Research Society: libro de actas.
15. Yu, L., Chen, R. Q., & Zhang, J. X. (2003). Analysis of the Mechanism of Extensor Tractive Force on Humeral Ectocondylar Fracture.
16. Yu, L., Chen, R., & Zhang, J. (2004). Analysis of the stress distribution on humeral ectocondyle in different postures. Jiangsu Medical Journal, 30(2), 98–100.
17. Schmidutz, F., Agarwal, Y., Müller, P. E., Gueorguiev, B., Richards, R. G., & Sprecher, C. M. (2014). Stress-shielding induced bone remodeling in cementless shoulder resurfacing arthroplasty: a finite element analysis and in vivo results. Journal of biomechanics, 47(14), 3509–3516.

A Sliding Mode Control Model for Perturbed Upright Stance in Healthy Subjects

Alessandro Mengarelli, Sandro Fioretti, Giuseppe Orlando,
Stefano Cardarelli, Ismaele Fioretti, Gian Marco Paci, Laura Burattini,
Francesco Di Nardo, Annachiara Strazza, and Federica Verdini

Abstract

Human upright stance and balance maintenance in quiet conditions have been extensively evaluated throughout the years. However, relatively less information is available on how the central nervous system (CNS) acts to maintain balance after sudden perturbations of stance. Here, a sliding mode control (SMC) model for the characterization of balance maintenance after external perturbations is proposed. Human stance was modeled as an inverted pendulum (IP), which describes kinematics in the sagittal plane; the choice of a SMC allowed to avoid model linearization, commonly employed when using a single-link IP for bipedal stance modeling, thus providing a more accurate description of the human-stance system dynamics. Model was applied on experimental data obtained from perturbed stance trials consisting of a series of disruptions of the same magnitude. This experimental condition was able to elicit a well-known feature called "habituation rate", which refers to the subject capacity to self-adapt his/her responses to identical perturbations. SMC parameters were identified through a robust optimization procedure. Results showed limited tracking errors for center of mass displacement. One of the SMC parameters exhibited a clear trend from the first to the last trial, appearing able to quantify the habituation rate effect. The application of such a control model to the non-quiet stance can provide additional information in understanding how the CNS tailors balance responses in different conditions.

Keywords

Sliding mode control • Balance maintenance
External perturbation • Inverted pendulum
Optimization procedure

1 Introduction

Despite its apparent steadiness, human upright stance requires continuous control in order to be maintained and this is clearly displayed by observing the center of pressure sway, measurable during balance maintenance tasks [1, 2]. The inherent instability of the bipedal stance is caused by the gravitational torque, which, if not opposed, would lead the center of gravity, i.e. the projection of the body center of mass (COM) on the ground, outside the base of support, thus inducing fall. Therefore, balance is maintained through the application of control torques to the ankle joint. Despite the role of the passive and active component of the control torque has been object of debate [3, 4], nowadays it is acknowledged that passive torque alone, linked to the viscoelasticity properties of the joints, is not able to control balance and thus the presence of an active torque implies an active neural control [5].

Bipedal human stance has been often modeled as an inverted pendulum (IP) [3, 6], which is a simple and nonlinear model, able to mirror the upright stance due to its inherently instability. Throughout the years, many control models able to simulate central nervous system (CNS) activity in maintaining balance have been proposed, depending also by the type of stability the CNS is supposed to seek, e.g. asymptotic versus bounded [7], or if the CNS tries to minimize the postural sway rather than to achieve the upright stance stability [8]. One of the most used control model for quiet upright stance is the proportional plus derivative (PD), and proportional plus integral plus derivative (PID) control, which are relatively easy to design and able to provide asymptotic stability, also with simulation postural measures

A. Mengarelli (✉) · S. Fioretti · G. Orlando · S. Cardarelli
I. Fioretti · G. M. Paci · L. Burattini · F. Di Nardo · A. Strazza
F. Verdini
Department of Information Engineering, Università Politecnica
della Marche, Ancona, Italy
e-mail: a.mengarelli@univpm.it

in line with physiological values [9]. However, this kind of control requires the linearization of the plant and thus can be applied only under the hypothesis of small perturbations, which lead to small angular variation of the IP. Further, the use of more complex models for upright posture, as multi-link inverted pendulums, is prevented because PID-like controllers are not able to handle multi-joints angles coupling. Therefore, throughout the years, several different kind of control models have been proposed in order to provide an accurate description of CNS strategies for static upright posture maintenance, involving continuous rather than intermittent feedback laws [7–9].

Despite the high interest in static balance modeling and control, relatively less information is available about the control of upright stance when external, destabilizing stimuli are applied. Perturbed posturography had received growing interest throughout the years [9] and the analysis of human response to an external perturbation of balance appeared valuable to gain insights into adaptation mechanisms, neural pathways involved in balance maintenance and sensory integration degree [10]. Depending on the applied external stimulus, different strategies have been reported for perturbation withstanding and balance recovery and thus perturbed upright stance represents a more complex process to be modeled than quiet stance, despite some control model approaches have been yet proposed for the description of perturbed balance [9, 11].

Here, a sliding mode control (SMC) for the perturbed stance is proposed, in order to assess whether such kind of control, already applied to static balance [12], is able to provide an adequate COM kinematics tracking in non static conditions. Further, SMC was applied to a series of repeated trials with the same perturbative conditions, in order to observe if SMC parameters values, selected through an optimization procedure, are able to identify characteristic features of this kind of perturbative trials.

2 Methods

Data of three subjects from a previous study were retrospectively analyzed [13]. Subjects were asked to stand on a servo-controlled moveable platform, able to translate in backward and forward direction, thus providing a translational perturbation. Each subject underwent to five consecutive backward directed perturbations, with the same disruption parameters: for this study a speed of 15 cm/s and a displacement of 5 cm were chosen, with an acceleration equal to 3 m/s^2. Subjects have no prior knowledge of the disruption characteristics and experiments started without any preceding trial, allowing to analyze an unpracticed response to the stimulus.

Full body kinematics was collected through a six cameras optical motion analysis system (sampling rate 100 Hz,

BTSBioengineering, Italy) and a total of 26 reflective markers were placed on subjects anatomical landmarks, as reported in [13]. Markers position was then low-pass filtered at 5 Hz and sagittal COM displacement was estimated following the procedure reported in [3].

2.1 Sliding Mode Control Model

Human stance was modeled as an IP, which described kinematics and dynamics of balance in the sagittal plane [3]. The choice of a single-link model is justified by considering that for moderate perturbations balance maintenance is achieved controlling only the torque around the ankle, while knee and hip joint are kept rigid [3, 7]. Thus, the experimental setup supported the use of this simplified model and the body dynamics can be efficiently described by the plantar/dorsiflexion ankle torque T_a, given by:

$$T_a = -\ddot{\theta}\left(I_b + M_b h_b^2\right) - B\dot{\theta} - K\theta + M_b g h_b \sin \theta. \quad (1)$$

where θ is the COM angle with respect to the vertical, $\ddot{\theta}$ the COM angular acceleration, I_b is the human body moment of inertia computed with respect to COM, M_b indicates the body mass, g is the gravitational acceleration and h_b is the height of the COM with respect to the ankle joint. Finally, K and B are the passive ankle stiffness and damping and their value was chosen according with [11]. The SMC will provide the torque in Eq. (1) required to maintain the plant, i.e. the IP, balanced; the SMC development involves two main steps: first, the definition of a suitable sliding surface and second the definition of the control law.

The control error between the predicted COM angle θ and the reference COM angle θ_m is defined as follows:

$$e = \theta - \theta_m \quad (2)$$

where $\theta_m = 0$. The sliding surface was then defined as:

$$s = \dot{e} + \lambda e \quad (3)$$

where λ is a positive value affecting the state convergence [14]. In order to ensure that the state trajectory points towards the sliding surface, the Lyapunov stability condition must be satisfied [14]. Thus, choosing as Lyapunov function:

$$V(s) = \frac{1}{2} s^T s \quad (4)$$

then the following condition holds:

$$\dot{V}(s) = s^T \dot{s} < 0 \quad (5)$$

The optimal SMC ensures that from any initial position the state trajectory will converge to the desired trajectory, satisfying the following condition:

$$\dot{s} = 0 \tag{6}$$

In the present case, condition (6) means:

$$\dot{s} = \ddot{e} + \lambda \dot{e} = \ddot{\theta} - \ddot{\theta}_m + \lambda(\dot{\theta} - \dot{\theta}_m) = 0 \tag{7}$$

Substituting $\ddot{\theta}$ given by Eq. (1) in Eq. (7):

$$\dot{s} = \frac{-T_a - B\dot{\theta} - K\theta + M_b g h_b \sin \theta}{(I_b + M_b h_b^2)} - \ddot{\theta}_m + \lambda(\dot{\theta} - \dot{\theta}_m) \tag{8}$$

Condition (6) provides the ideal continuos control, i.e. the equivalent control torque T_{eq}:

$$T_{eq} = (-B + \lambda I_b + \lambda M_b h_b^2)\dot{\theta} - K\theta + M_b h_b g \sin \theta \\ - (I_b + M_b h_b^2)(\ddot{\theta}_m + \lambda \dot{\theta}_m) \tag{9}$$

The control law is discontinuous across the sliding surface $s = 0$ [12] and $sign(s)$ function is introduced to describe the phenomenon. The ideal sliding movement is actually affected by fluctuations around the surface $s = 0$, due to non ideal characteristics of the switching, which clearly does not present an infinite frequency. Thus, this chattering phenomenon [14] is addressed requiring the state to move in a bounded interval of the sliding surface, thus introducing a less strict condition:

$$|s| \leq \epsilon \tag{10}$$

where ϵ defines a boundary layer region around the sliding surface. In this study, ϵ was selected equal to 0.1. Then, the switching control torque T_{sw} resulted:

$$T_{sw} = \begin{cases} -Jsign(s) & |s| > \epsilon \\ -J \cdot \frac{s}{\epsilon} & |s| \leq \epsilon \end{cases} \tag{11}$$

The total control torque is thus:

$$T = T_{eq} + T_{sw} \tag{12}$$

Experimental COM angles for each subject and for each of the five trials were used for the SMC parameters identification, i.e. λ and J, performed through an optimization procedure based on a meta-heuristic algorithm [15], which provided SMC parameters satisfying:

$$\min\{\text{RMSE}(d, d_m)\} \tag{13}$$

where d and d_m refer to the modeled and experimental COM displacement in the sagittal plane, respectively. For each considered trial, a total of 10 cycles of the optimization procedure were performed.

3 Results and Discussion

For all the considered subjects and for all trials, SMC appeared able to provide a very low tracking error between experimental and modeled COM (Fig. 1).

For the first trial, a mean RMSE error of 0.80 ± 0.15 mm was obtained, while from the second to the last one mean RMSE resulted 0.71 ± 0.19, 0.67 ± 0.21, 0.68 ± 0.23 and 0.67 ± 0.18 mm, respectively. Thus, from this viewpoint, the application of a SMC to perturbed upright stance seems

Fig. 1 Experimental (blue trace) and modeled (red trace) COM displacement for a representative subject in the first (top panel) and last (bottom panel) trial. COM exhibited a quite different displacement, with the attenuation of the second peak (Color figure online)
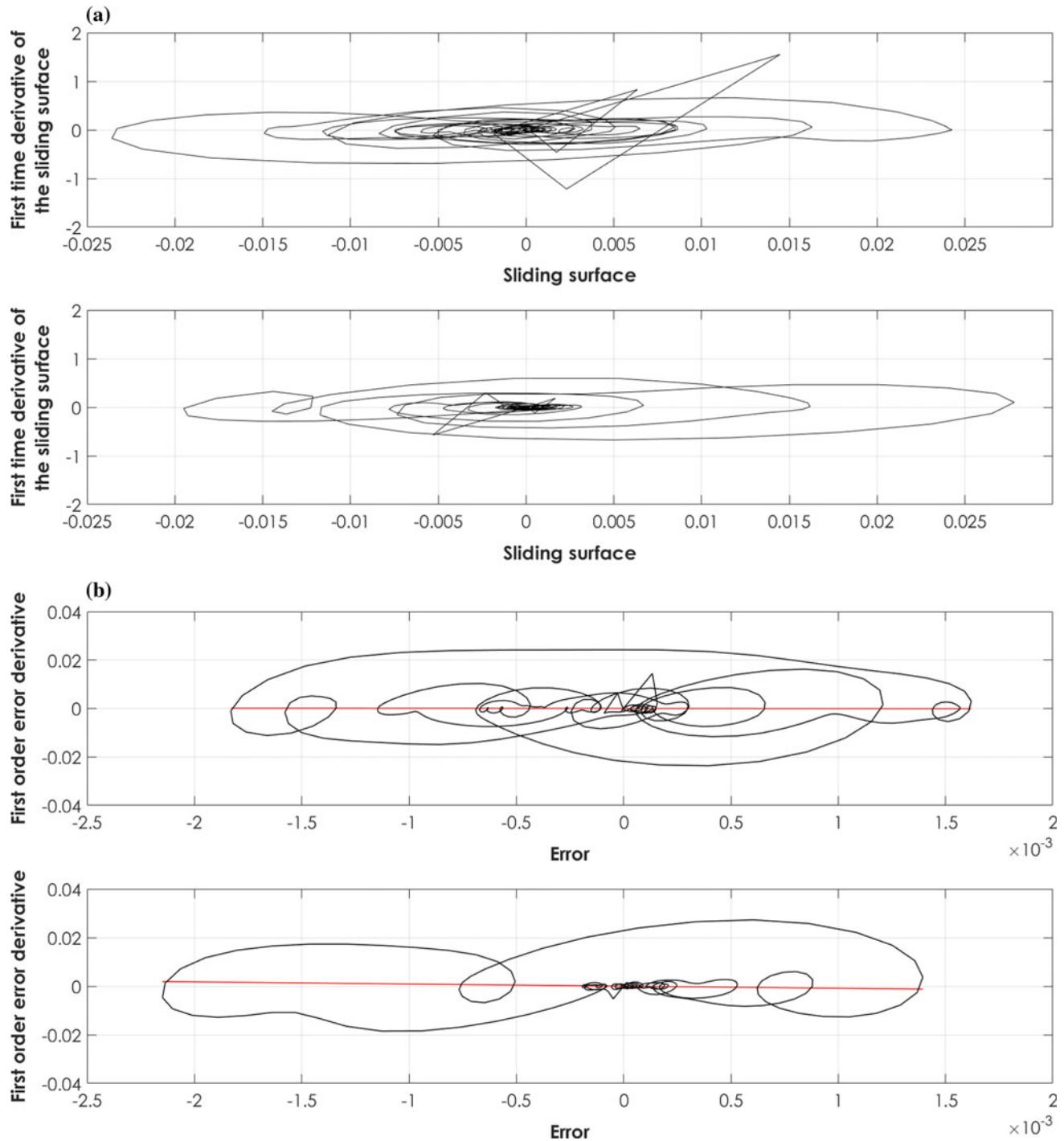
Fig. 2 Phase plot of the first order derivative of the sliding surface versus sliding surface (**a**) and phase plane diagram of the closed-loop system (**b**) for the first (top panels) and last (bottom panel) trial

to provide good results, comparable with those obtained when a similar control model has been applied to the static and unperturbed balance [12].

Sliding surface and its derivative (Fig. 2a, b) appeared without the initial, large overshoot reported for static balance task [12], with values close to 0 throughout the remaining

simulation, highlighting the robustness of the applied control.

The higher range variation of $\dot{s}$ with respect to that reported in [12] is probably related to the different kind of considered motor task. Indeed, Zhang and colleagues reported results relative to the quiet upright stance, where
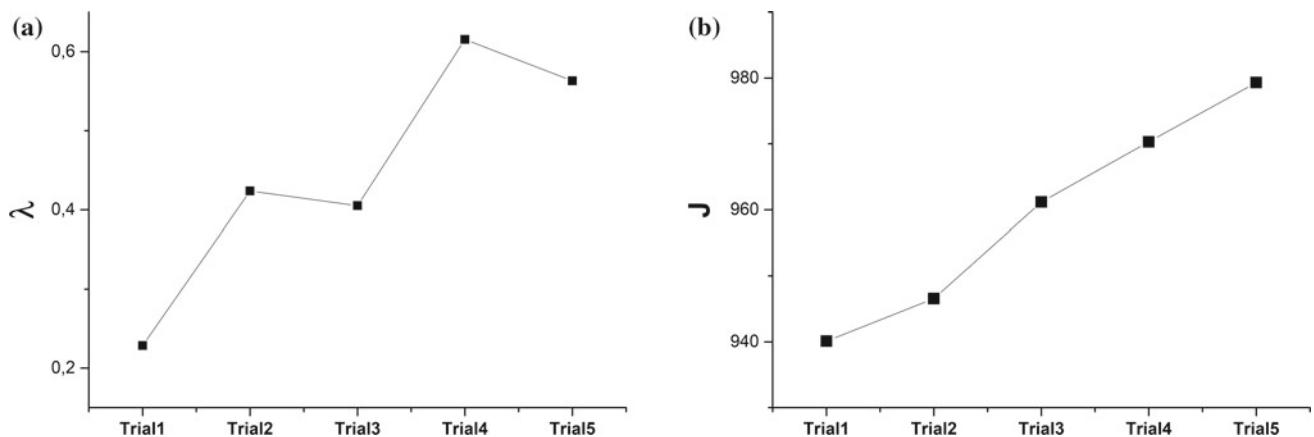
Fig. 3 SMC optimized parameters obtained for each posturographic trial. Values are averaged over the three considered subjects. J exhibits a clear increasing trend from the first to the last trial

COM presented an angular range up to 1.5°, while in this study COM resulted with an angular variation almost three times higher ($\simeq 5°$), corresponding to the displacement reported in Fig. 1, and with an angular velocity more than twice (approximately 0.8 °/s vs. 2 °/s). Thus, the marked oscillations showed in Fig. 2a could be explained considering that, despite the low RMSE error, COM movement is probably more difficult to track for the SMC in a perturbed scenario like that considered in the present study, leading to a challenging convergence to zero. As mentioned above, a meta-heuristic algorithm was applied to obtain the optimal values for the SMC parameters, i.e. λ and J, and their mean value for each trial, averaged over the three subjects, are reported in Fig. 3. It is well acknowledged that the considered postural task, i.e. a series of repeated perturbations of stance with the same magnitude, is able to elicit some characteristic feature of the balance maintenance process, such as the habituation rate and the first trial effect [13, 16]. The first is characterized by a gradual change in balance responses throughout the posturography trials, while the second consists in higher responses to the first trial respect to the subsequent ones.

Thus, this kind of different behaviors related to the trial sequence appear to mirror a change in how CNS manages loss of balance and disruption withstanding, tuning the stance control with a learning-based mechanism. Results of this study seem to confirm the presence of these features and in particular the increasing trend of the SMC parameters (Fig. 3) appears to support the presence of a subject capacity to self-adapt the postural response, underlining a progressive learning effect. The habituation process appeared related to the optimal J parameter value 3B, which presented a quasi-linear increase from the first to the last trial. Conversely, despite an increasing trend, λ parameter showed a less clear development throughout the trials (Fig. 3a). The J parameter is relative to the switching control (Eq. (11) and

governs the reaching of the sliding surface; thus, a habituation rate, linked to an improved perturbation withstanding could be reflected by a more efficient reaching of the sliding surface, as showed by the phase plane diagram of the closed loop system (Fig. 2b).

In conclusion, SMC appeared able to properly track COM in perturbed conditions, with limited errors for all the considered subjects. Further, SMC showed a promising relationship between at least one of its setting parameter and the perturbed stance trial sequence, showing a possible, direct relationship with a learning effect which tailors the postural response through a habituation mechanism. Further studies are needed to confirm present results on an enlarged population, also with the expansion to multi-link IP models and different experimental conditions, e.g. sensory deprivation and progressively higher disruptions.

Conflict of Interest Statement The authors declare that they have no conflict of interest.

References

1. Prieto, T.E., Myklebust, J., Hoffmann, R., Lovett, E., Myklebust, B.: Measures of postural steadiness: differences between healthy young and elderly adults. IEEE Transactions on biomedical engineering 43(9), 956–966 (1996).
2. Fioretti, S., Guidi, M., Ladislao, L., Ghetti, G.: Analysis and reliability of posturographic parameters in parkinson patients at an early stage. In: Engineering in Medicine and Biology Society, 2004. IEMBS'04. 26th Annual International Conference of the IEEE. vol. 1, pp. 651–654. IEEE (2004).
3. Winter, D.A., Patla, A.E., Prince, F., Ishac, M., Gielo-Perczak, K.: Stiffness control of balance in quiet standing. Journal of neurophysiology 80(3), 1211–1221 (1998).
4. Morasso, P.G., Sanguineti, V.: Ankle muscle stiffness alone cannot stabilize balance during quiet standing. Journal of Neurophysiology 88(4), 2157–2162 (2002).

5. Casadio, M., Morasso, P.G., Sanguineti, V.: Direct measurement of ankle stiffness during quiet standing: implications for control modelling and clinical application. Gait & posture 21(4), 410–424 (2005).

6. Pepa, L., Verdini, F., Spalazzi, L.: Gait parameter and event estimation using smartphones. Gait & posture 57, 217–223 (2017).

7. Bottaro, A., Yasutake, Y., Nomura, T., Casadio, M., Morasso, P.: Bounded stability of the quiet standing posture: an intermittent control model. Human movement science 27(3), 473–495 (2008).

8. Kiemel, T., Zhang, Y., Jeka, J.J.: Identification of neural feedback for upright stance in humans: stabilization rather than sway minimization. Journal of Neuroscience 31(42), 15144–15153 (2011).

9. Peterka, R.: Sensorimotor integration in human postural control. Journal of neurophysiology 88(3), 1097–1118 (2002).

10. Visser, J.E., Carpenter, M.G., van der Kooij, H., Bloem, B.R.: The clinical utility of posturography. Clinical Neurophysiology 119 (11), 2424–2436 (2008).

11. Davidson, B.S., Madigan, M.L., Southward, S.C., Nussbaum, M. A.: Neural control of posture during small magnitude perturbations: effects of aging and localized muscle fatigue. IEEE Transactions on Biomedical Engineering 58(6), 1546–1554 (2011).

12. Zhang, H., Nussbaum, M.A., Agnew, M.J.: Development of a sliding mode control model for quiet upright stance. Medical Engineering and Physics 38(2), 204–208 (2016).

13. Mengarelli, A., Cardarelli, S., Fioretti, S., Burattini, L., Di Nardo, F., Verdini, F.: Center of pressure based assessment of balance responses to repeated perturbations of upright stance. In: EMBEC & NBC 2017, pp. 262–265. Springer (2017).

14. Slotine, J.J.E., Li, W., et al.: Applied nonlinear control, vol. 199. Prentice hall Englewood Cliffs, NJ (1991).

15. Karaboga, D., Basturk, B.: A powerful and efficient algorithm for numerical function optimization: artificial bee colony (abc) algorithm. Journal of global optimization 39(3), 459–471 (2007).

16. Nanhoe-Mahabier, W., Allum, J., Overeem, S., Borm, G., Nijhuis, L.O., Bloem, B.: First trial reactions and habituation rates over successive balance perturbations in parkinson's disease. Neuroscience 217, 123–129 (2012).

Could Postural Strategies Be Assessed with the Microsoft Kinect v2?

Diego Gonzalez, Luis Imbiriba, and Frederico Jandre

Abstract

Quantification of body movement strategies to maintain balance may be useful to understand changes in postural control. Some methods for this purpose require special preparations, such as placement of inertial sensors, goniometers or EMG electrodes. In this study, the capability of the Microsoft Kinect v2, a markerless motion sensor, to assess postural control strategies was tested. Forty-six young healthy subjects had the trajectories of 25 "joints", provided by a Kinect v2, recorded during upright stance with eyes open or close, on rigid (force platform) and soft (foam pad) surfaces. Postural strategies were characterized by a strategy index (SI) based on the phase difference between the accelerations of upper (trunk) and lower (hip) segments of the body, measured by the Kinect in anterior-posterior and medial-lateral direction. Ankle and hip strategies were identified by in-phase or counterphase accelerations respectively, the phase being estimated from the covariance between 2-s sliding windows of the two signals. The trajectories of center of mass (COM) and center of pressure (COP) were also computed from the Kinect and the force plate, respectively. The SI and the velocities of COP and COM were significantly different between conditions (Friedman $p < 0.001$ for SI), suggesting effects of sensory information. These results are in line with other studies, showing coexistence of both strategies during stance and the predominance of ankle rather than hip strategy on foam or with closed eyes instead of on rigid surface with open eyes. These results support using the Kinect v2 to assess postural strategies.

1 Introduction

Different methods have been employed to attain a quantitative measure of balance [1], among which is the measure of center of pressure (COP) and center of mass (COM) sway [2]. However, univariate measures such as the displacement of COP or COM may be insufficient to describe changes in postural control, which involve the coordination of many body segments [3]. The study of individual body segment movements may help understanding postural instability in some disorders [1]. Two main strategies are usually considered, one in which primary forces to maintain balance occur at the ankle (ankle strategy) and one that involves corrective movements primarily about the hip (hip strategy) [4]. Recent research showed that, in general, those strategies coexist and the predominance of some strategy depends on the sensory information [5], which can be affected for instance by aging or the presence of neurological or vestibular diseases [4, 6].

Some physiological variables have been used to identify these strategies, such as muscular activity in the legs and trunk, joint angles, displacement and acceleration of individual body segments [6–8]. However, the methods to obtain these variables require special preparations, such as the placement of reflective markers, inertial sensors, goniometers or EMG electrodes, which may limit their use. The Microsoft Kinect v2 (Microsoft, US), a portable, markerless motion sensor initially developed for video-games, has been used to assess balance since it can detect movements of several body segments [9, 10]. The purpose of this study is to evaluate the capability of Microsoft Kinect v2 to distinguish postural strategies under different sensory disturbance, using a recent method based on the coordination of movement of upper and lower body segments.

D. Gonzalez (✉) · F. Jandre
Biomedical Engineering Program, Federal University
of Rio de Janeiro, Rio de Janeiro, Brazil
e-mail: diegorgg@peb.ufrj.br

L. Imbiriba
School of Physical Education and Sports, Federal University
of Rio de Janeiro, Rio de Janeiro, Brazil

2 Materials and Methods

2.1 Experimental Protocol

Forty-six young subjects (twenty-seven males, age 22 ± 2 years, height 1.72 ± 0.09 m, weight 67.5 ± 10.7 kg) participated in the experiment. They reported no neurological or musculoskeletal impairments, illnesses or injuries that could affect balance. The experimental protocol was approved by the Ethics Committee of the Federal Institute of Education, Science and Technology of Rio de Janeiro (IFRJ). All subjects informed written consent. The test consisted of four 60-s tasks in upright stance on a force plate: quiet standing with eyes open (EO) or closed (EC), and quiet standing with a foam pad (Balance Pad, AIREX, Switzerland) between feet and force plate, with eyes either open (EOf) or closed (ECf). Task order was randomized, with 60-s rest periods between successive tasks. Subjects were instructed to stand barefoot, with feet parallel and 12 cm apart, avoiding any voluntary movements. During the tasks with eyes open, the subjects were instructed to look at a marker (a 10-cm wide blue cross) fixed at eye level on a wall, 2 m ahead of the force plate. The Microsoft Kinect v2 was placed 2 m away from the force plate and 1 m above the floor.

2.2 Data Acquisition

The Microsoft Kinect v2 was used to acquire the positions of 25 specific points of the body, called "joints", in 3 dimensions and at a sampling frequency around 30 Hz, during each task. A customized interface was written in LabVIEW 2013 (National Instruments, US) using a Kinect v2 toolkit (Haro3D, HaroTek, US) to record the joint positions and the corresponding system timestamp. The joint displacements were used to compute the COM of the body, using the segmental method [9, 11], in medial-lateral (ML) and anterior-posterior (AP) direction. In short, the body was divided into 15 segments and its COM was calculated as the weighted average of the individual COM of these segments. The positions of the individual COMs were given by their respective endpoint joints, and the respective weights of each segment were obtained from a table of anthropometric data [12]. COP displacement was measured in ML and AP direction using an AccuSway Optimized (AMTI, US) force platform and the software Balance Clinic (AMTI, US), with sampling frequency of 50 Hz and resolution of 10^{-5} m. Data from the Kinect and the force plate were acquired by different computers, and the systems were synchronized by a

trigger pulse generated by a Labjack U12 (Labjack, US) data acquisition board controlled by the Kinect interface and connected to the synchronism input of the force plate.

The COM trajectory from the Kinect v2 was interpolated to match the sampling frequency of the force plate. The COP and COM signals were aligned by the point of maximal cross-correlation, seeking to minimize the lag between them [10], since both signals are almost in phase [13]. They were filtered using a 4th order Butterworth filter and with a cut-off frequency of 2 Hz. The acceleration of the upper and lower segments, defined respectively as the joint midway between the shoulders and the joint at the center of the hip, were computed in ML and AP directions, by double numerical differentiation of the filtered (4th order Butterworth, cut-off at 0.5 Hz) positions. These two joints have shown a high correlation ($r > 0.9$) when compared with a gold standard motion capture system [10]. The signal averages were subtracted and the first and last 5 s of each signals were removed to avoid filter transient effects.

2.3 Data Analysis

COP and COM Mean Velocity. The mean velocities [2, 9] of displacement of COP and COM were calculated as the average velocity given by the ratio of the total displacement and time in the horizontal plane (Vel_{COP} and Vel_{COM}, respectively), as shown in Eq. 1. The variable x_i is the position of COP (or COM) at ML direction and y_i the position at AP direction, at time i. The variable T is the duration of the signal

$$Vel = \frac{\sum \sqrt{(x_i - x_{i-1})^2 + (y_i - y_{i-1})^2}}{T} \qquad (1)$$

Strategy Index. The contributions of ankle strategy and hip strategy in the postural control were quantified by a strategy index (SI) proposed by Baston et al. [6], and is described below. First, a covariance index (CI), defined as the covariance between the acceleration of upper and lower segments, normalized by the standard deviation of both signals, was computed. This CI was calculated using a 2-s sliding window with a step of 0.1 s between consecutive windows. A value of CI close to 1 indicates that the signals are in-phase and can be associated to a postural ankle strategy, and a value of CI close to -1 indicates a counter-phase pattern and can be associated to a postural hip strategy. The percentage of the total signal time spent in-phase (T_{IP}) and counter-phase (T_{CP}) was computed and was defined by the intervals when $0.4 < CI < 1$ and

$-1 < CI < -0.4$, respectively. The values of CI when $-0.4 < CI < 0.4$ were not used for calculation since they represent a transitional, undefined phase. The SI was calculated as a function of the time spent in-phase and counter-phase, defined as

$$SI = \left(\frac{T_{IP} - T_{CP}}{T_{IP} + T_{CP}}\right)W \qquad (2)$$

W is applied in order to weigh only the time when the strategy pattern is defined, $W = (T_{IP} + T_{CP})/100$. The interpretations of SI values, between -1 and 1, is similar to that of the abovementioned CI. The SI was computed for both directions ML and AP.

Statistical Analysis. The normality of the variables SI and Vel was analyzed by the Shapiro-Wilk test. Since the variables at some tasks do not show a normal distribution and/or homoscedasticity, the Friedman test was used to verify the difference between the four tasks, and the post hoc analysis was done by a pairwise comparison of all tasks with the Wilcoxon Signed Rank test, at the significance level of $\alpha = 0.008$, including Bonferroni correction for 6 comparisons.

3 Results

The Vel calculated for COP and COM and the SI at ML and AP direction are presented in Table 1 for each task. The mean value of each variable increased with changes in sensory information. The Vel_{COP} values were higher than the Vel_{COM} values for all tasks, since the COP displacement always exceeds the COM trajectories [13].

For all variables, the Friedman test indicated that the results of at least one task differs from the others ($p < 0.001$). In post hoc analysis, all pairwise comparison between tasks of Vel_{COP} and Vel_{COM} showed significant difference ($p < 0.001$). The values of SI between tasks were significantly different for all pairwise comparison ($p < 0.003$), except when the values of SI_{AP} were compared between EO and EC ($p = 0.011$). Figure 1 presents representative plots of COP and COM displacement at AP direction and Fig. 2 presents CI, for one subject at EO and ECf tasks.

4 Discussion

The resulting values from the analysis of the differences between the movements of upper and lower segments to assess postural strategies, as identified by the SI index calculated with data from the Microsoft Kinect v2, were sensitive to changes in sensory information. As seen in Fig. 2, the coexistence of both in-phase and counter-phase pattern was expected during upright stance. The contribution of each strategy seems dependent on the sensory information, although the ankle strategy prevailed in all tasks [5, 6]. Both absence of vision and presence of foam changed the pattern of multi-segmented movement in upright stance [8]. These effects are also reflected in Vel parameter considered sensitive to sensory disturbances [2]. The results in the present study seem to agree with those in another study in which the disruption of visual information may have increased the use of ankle strategy (in-phase pattern) in healthy subjects [6]. In that study, the authors compared the 6 conditions of the Sensory Organization Test, but did not make pairwise comparisons between open and closed eyes tasks.

Only the comparison of SI_{AP} between EO and EC failed to show a significant difference. However, the Bonferroni correction is conservative and this has to be taken into account in face of the small observed p-value ($p = 0.011$) in this statistical test. The introduction of disturbances in somatosensory information also changes the adopted postural strategies, but those changes depend on how this sensory system is affected. Other studies have shown that the use of a sway-referenced platform increases the contribution of hip strategy (counter-phase pattern) in postural control for healthy subjects [3, 6]. However, another study showed that the behavior of phase when the foam was present is more similar to the phase at quiet standing than on a sway-referenced platform [5]. This may explain why ankle, and not hip strategy, contribution increased with the foam in the present study.

Some limitations should be considered in this study. Although the methods employed in this study were used before, characterization of ankle and hip strategy may differ when sources of information other than the phase difference between upper and lower segments acceleration are used,

Table 1 Mean ± standard deviation of Vel_{COP}, Vel_{COM}, SI_{ML} and SI_{AP} at all tasks

Parameter	EO	EC	EOf	ECf
Vel_{COP}	7.49 ± 2.20	8.93 ± 2.95	18.17 ± 3.87	33.84 ± 9.43
Vel_{COM}	2.51 ± 0.85	3.02 ± 1.02	5.87 ± 1.79	11.28 ± 3.68
SI_{ML}	0.76 ± 0.14	0.83 ± 0.11	0.95 ± 0.04	0.99 ± 0.02
SI_{AP}	0.81 ± 0.11	0.85 ± 0.08	0.94 ± 0.05	0.98 ± 0.02

Fig. 1 COP and COM
displacement in AP direction at
EO and ECf tasks, respectively
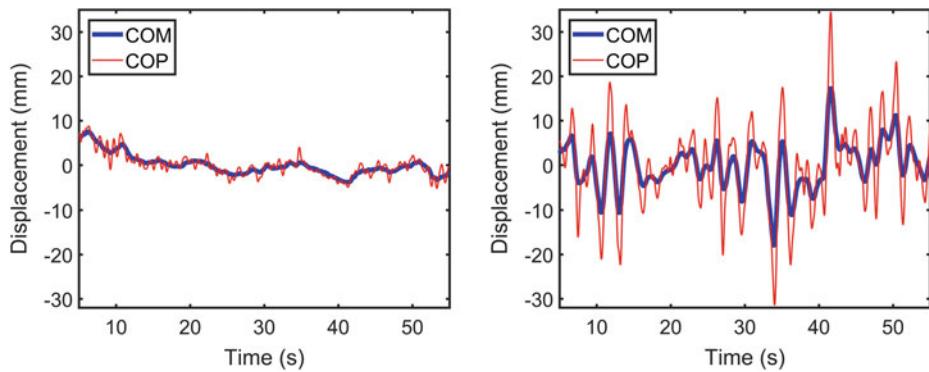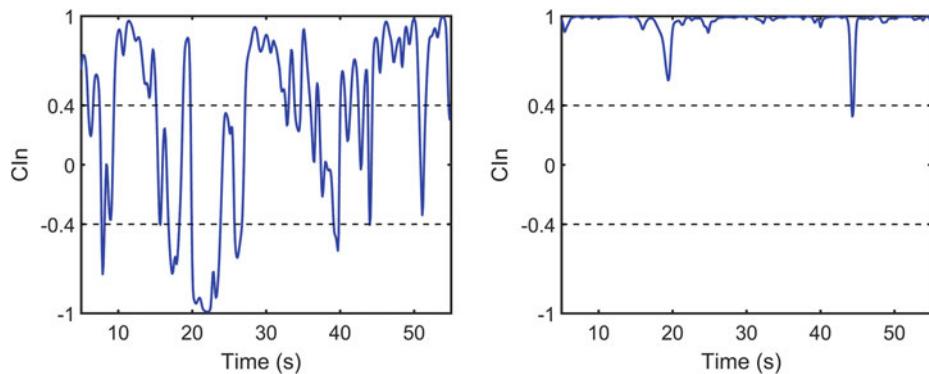
Fig. 2 CI in AP direction at EO
and ECf tasks, respectively

such as the variance of linear sway of body segments, joint angles or EMG signals [3, 7, 8]. The anatomic points chosen to identify segmental movements in the present study, even at the segments corresponding to the double pendulum, differ from those used in the original work [6]. The results of the present study encourage further research on the capability and limitations of devices such as the Microsoft Kinect v2 to evaluate postural control and balance, especially with respect to the assessment of postural strategies.

Conflict of Interest The authors declare that they have no conflict of interest.

References

1. Visser, J.E., Carpenter, M.G., van der Kooij, H., Bloem, B.R.: The clinical utility of posturography. Clin. Neurophysiol. 119, 2424–2436 (2008).
2. Raymakers, J.A., Samson, M.M., Verhaar, H.J.J.: The assessment of body sway and the choice of the stability parameter(s). Gait Posture. 21, 48–58 (2005).
3. Kuo, A.D., Speers, R.A., Peterka, R.J., Horak, F.B.: Effect of altered sensory conditions on multivariate descriptors of human postural sway. Exp. Brain Res. 122, 185–195 (1998).
4. Horak, F.B., Nashner, L.M., Diener, H.C.: Postural strategies associated with somatosensory and vestibular loss. Exp. Brain Res. 82, 167–177 (1990).
5. Creath, R., Kiemel, T., Horak, F., Peterka, R., Jeka, J.: A unified view of quiet and perturbed stance: simultaneous co-existing excitable modes. Neurosci. Lett. 377, 75–80 (2005).
6. Baston, C., Mancini, M., Schoneburg, B., Horak, F., Rocchi, L.: Postural strategies assessed with inertial sensors in healthy and parkinsonian subjects. Gait Posture. 40, 70–75 (2014).
7. Runge, C.F., Shupert, C.L., Horak, F.B., Zajac, F.E.: Ankle and hip postural strategies defined by joint torques. Gait Posture. 10, 161–170 (1999).
8. Fransson, P.A., Gomez, S., Patel, M., Johansson, L.: Changes in multi-segmented body movements and EMG activity while standing on firm and foam support surfaces. Eur. J. Appl. Physiol. 101, 81–89 (2007).
9. Eltoukhy, M., Kuenze, C., Oh, J., Signorile, J.: Validation of Static and Dynamic Balance Assessment using Microsoft Kinect for Young and Elderly Populations. IEEE J. Biomed. Health Inform. PP, 1–1 (2017).
10. Otte, K., Kayser, B., Mansow-Model, S., Verrel, J., Paul, F., Brandt, A.U., Schmitz-Hübsch, T.: Accuracy and Reliability of the Kinect Version 2 for Clinical Measurement of Motor Function. PloS One. 11, e0166532 (2016).
11. Yeung, L.F., Cheng, K.C., Fong, C.H., Lee, W.C.C., Tong, K.-Y.: Evaluation of the Microsoft Kinect as a clinical assessment tool of body sway. Gait Posture. 40, 532–538 (2014).
12. Winter, D.A.: Biomechanics and Motor Control of Movement. John Wiley & Sons, Upper Saddle River (2004).
13. Winter, D.A., Patla, A.E., Prince, F., Ishac, M., Gielo-Perczak, K.: Stiffness control of balance in quiet standing. J. Neurophysiol. 80, 1211–1221 (1998).

The Elbow and Forearm Portable Rehabilitation Device

Sergei Sokolov, Sergei Krivosheev, Maria Aleksandrova, Roman Iutsis, Roman Olejnik, and Stanislav Reznikov

Abstract

In this paper the design of a new rehabilitation device for the elbow joint and forearm will be presented. In the beginning of the article key requirements (such as mass of the device, movement amplitude, degrees of freedom etc.) will be discussed and established. Then, the design concept of the rehabilitation device will be presented. The main functional and design features, such as two degrees of freedom or placement of bidirectional load cells, will be highlighted and discussed. Key equations connected to the design requirements will be reported. Then, the control system, which included active and passive control mode, will be presented. Finally, an overview of the whole device with full functionality and the plan of further improvements will be given.

Keywords

Elbow and forearm orthosis • Mechanotherapy Motor relearning

1 Introduction

There are a large number of people with motor disabilities throughout the world. Insult is the most common reason of such disability, with a 15 million cases per year, according to the World Health Organization [1], for example, every year more than 795,000 people in the United States have a stroke [2]. This number will be growing with the population ageing in next 20 years [3]. Rehabilitation process should begin as soon as possible to ensure the effective restoration [4]. Rehabilitation, as patient's condition stabilizes, includes

S. Sokolov · S. Krivosheev · M. Aleksandrova · R. Iutsis (✉)
R. Olejnik · S. Reznikov
ITMO University, St. Petersburg, 197101, Russia
e-mail: yutsis5@gmail.com

S. Krivosheev
e-mail: krivosheev.sergey89@gmail.com

massage therapy, passive and active gymnastics and psychotherapy. In recent years, the direction of robotic mechanotherapy has been actively developed; this is confirmed by a large number of articles on this topic. Research indicates that robotic therapy is an effective method of motor rehabilitation [5]. But there is still some limitations of wide expansion of this approach. Development of the device which will overcome some of them will be shown and discussed further. The aim of the work is to produce a robotic rehabilitation device for elbow joint.

2 State of the Art Analysis

At this moment, robotic rehabilitation systems could be divided in two groups [6]: stationary therapeutic systems and home-use systems that assist in activity of daily living. Stationary systems, in most cases, are pretty costly, heavy and could be used only in medical centers which reduce the number of people who can use them. But they showed a positive effect as an additional therapy during traditional rehabilitation. One of the key approaches to increase level of involvement of patient is use human-machine interface and force user to impose user completing task during the game or the interactive exercises.

The rehabilitation systems which could be used at home are traditionally driven by one or two DC motors. Some of them [7] include only elbow flexion/extension, while other [8] proposes also wrist rotation and change of resistance level. Some works [9, 10] propose use hydraulic actuators to move joints. The most common way to obtain control signals for these devices is surface electromyography (sEMG).

3 Design Requirements

The aim of the work was to develop a robotic rehabilitation device for elbow joint. An analysis of analogs was conducted and it has been decided to make a device, which

combines flexion/extension of elbow joint with pronation/supination (rotation) of forearm.

Maximum training effectiveness is achieved through training with usage of different forearm position angle. Studies indicate the possibility of flexion/extension of the elbow in the range of 15°–165° [11], the recommended operating range is 30°–130° [12]. However, the muscles involved in the movement should be slightly stretched, so we chose the working range from 45° to 180°. The pronation/supination movements of the forearm are available within 180°. These anatomic limits were taken into account in the design of the device.

Weight, possibility to adjust the elements of the device for different sizes of hands, different training modes and battery life time, were identified as key features of developed device. To increase the effectiveness of the training process, it was necessary to develop a control system, which includes a change in the speed of the exercise and set angles of movement. Also, it was decided to use the pluses of active and passive training mode, this was also included in the requirements for the device.

4 Design of the Device, Equations and Control System

After creating the structure scheme, a three-dimensional model of the developed device was made in CAD environment (see Fig. 1). It was decided to use miniature linear actuators for flexion/extension of forearm.

For pronation/supination of the forearm were suggested to use a system with servo motor and gear system, for tough fixation of the forearm and the implementation of pronation/supination, a silicone cushion is embedded in the structure, the part with the cushion rotates inside the rigid part with the sleeve. Taking into account a necessity to facilitate the weight of the device and reducing the cost there were used lightweight aluminum components. Also most of the parts with complex geometry have been designed taking into account opportunities of 3D printing from ABS plastic.

The next step was calculation and selection of control and performing devices. To perform the calculations we needed to find the masses of the segments, as well as the centers of mass. As input data formulas were used to calculate the mass of the body's segments and the location of segments' center of mass [13]. To calculate the location of the segments' center of mass was applied the percentage ratio to the total length.

On the basis of the performed calculations, a scheme for the application of forces was drawn up and an equation was derived for finding the force necessary for lifting the arm with an orthosis:

$$F_{fa} \cdot \cos\alpha \cdot l_{fa} = F_{go} \cdot l_{ocm.} + F_g \cdot (l_{fcm.} + l_d) + F_{pg} \cdot (l_{pcm} + l_d) \tag{1}$$

where F_{fa}—the force required to lift the forearm, l_{fa}—the distance from hinge to attachment of the actuator, F_{go}—gravity forearm part of the orthosis, l_{ocm}—distance from hinge to the orthosis' center of mass, l_d—the distance between the hands and bend the hinge, F_g—gravity of the forearm, l_{fcm}—the distance from hinge to the forearm's center of mass, F_{pg}—gravity force of the palm, l_{pcm}—distance from the hinge to the palm's mass center.

This equation was obtained the necessary force to lift the forearm. Thereafter this value was multiplied by the safety coefficient $k = 2$.

The principle of operation of the small-size linear actuators based on the transformation of rotational movement into linear translational, in our case, by the screw-nut

Fig. 1 A three-dimensional model of a device

transmission. For rotation of the forearm, it was decided to use a gear system. To calculate the static moment (torque) it was necessary to multiply the traction force on the radius of the working body. The traction force depends on friction and the load, in this case the load was the gravity force. Calculating the dynamic moment required the calculation of acceleration and moment of inertia. The arm consists of segments that form the open kinetic chain segments can be represented by simple cylindrical or prismatic bodies. It should be taken into account, that the forearm rotates partially, so take 2/3 parts of the total weight. The formula for finding the moment of inertia:

$$I_x = \frac{m_p}{12} \cdot (b^2 + c^2) + \frac{1}{2} \cdot \left(\frac{2}{3} \cdot m_{fore} \cdot r_{fore}^2 \right) + \frac{1}{2} \cdot m_{ort} \cdot r_{ort}^2 \tag{2}$$

where m_p—the mass of the palm, b, c—the dimensions of the parallelepiped model of the fist, m_{fore}—the mass of the forearm, r_{fore}—the radius of the forearm, m_{ort}—weight of the rotating part of the orthosis, r_{ort}—the radius of the rotating part of an orthosis.

Find the dynamic moment (torque) on the motor shaft:

$$T_{dm} = \frac{2\pi n_{nom}}{60t} \cdot I_x \tag{3}$$

where t is the time required acceleration, we take t = 0.3 s; n_{nom}—rated speed.

As a result of the calculations by formulas 1–3 were obtained the following values F_{fa} = 82,14 N, I_x = 0.000934 kg m^2, T_{dm} = 0.22 N m. From this was calculated the total moment and the moment on the engine with the safety coefficient k = 2.

$$T_{common} = T_{shaft} + T_{dm} = 0.433 + 0.022 = 0.455 \, \text{N m} \tag{4}$$

$$T_{actu} = T_{common} \cdot k = 0.91 \, \text{N m} \tag{5}$$

According to the found values, were selected linear actuators and the servo with the drive pinion set on the output shaft. The linear actuators have the following technical characteristics: the maximum load is 100 N; the maximum speed is 8 mm/s; stroke length is 100 mm. And the servo motor has following technical characteristics: torque 18 kg cm with power supply 6 V; rotation speed 60° in 0.14 s with 6 V power supply.

The common algorithm of the patient's standard training is shown in Fig. 2. In the current version of the control program, two training modes were implemented. In the passive mode a device forced user to move elbow and forearm in limited range. An active training mode was based on the idea of motor relearning and increasing of the
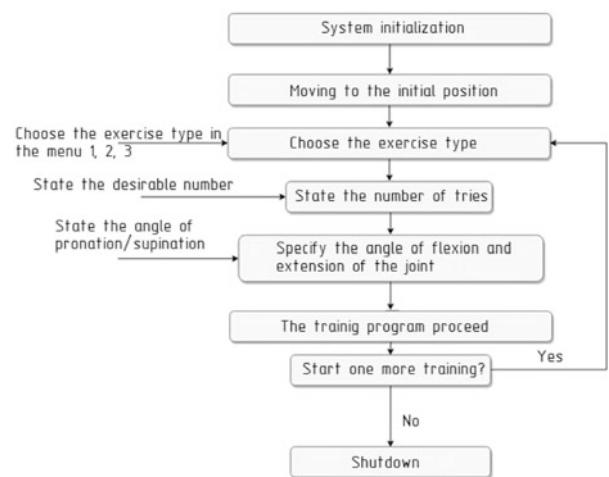
Fig. 2 Algorithm of training for active and passive modes

involvement of patient into the rehabilitation process. It means that patient should use specified muscles to send signal to control system which would start movement of the device. The contraction of the muscle and further movement builds up new neural connections or updates the old ones. Also, during the training in active mode user will observe hand movement, which was immobilized, which will give an emotional rise, which also positively effects on the motivation and effectiveness of the rehabilitation. The surface electromyography was used to recognize signals. In order to track the force produced by the device, as well as the force exerted by the patient for resistance, miniature strain gauges of bi-directional action are located at the ends of the rods of linear actuators. Several key training parameters, such as number of movement repetitions or angle of flexion/extension, could be adjusted by the user or medical specialist during the process of rehabilitation for current. The current version of the device used a button interface with an LSD display connected to the Arduino board. Using it, the modes of operation were selected and the key parameters of the training were adjusted.

5 Conclusion

The development of the device was carried out in accordance with the highlighted key design features. First of all, the device should have a reduced weight, as well as the ability to adjust to different sizes of the hands. The weight of the device without battery was 1450 g. The design provides the possibility of adjusting the elements relative to each other, which makes it possible to use devices for people with different anthropomorphic data. Several training modes have

also been developed. To reduce costs, widespread electronic components are used, tied to a control system based on the microcontroller Arduino Uno.

However, it should be noted that all the work done at the moment is of a purely theoretical nature, since the device itself is in the production stage. Therefore, further plans will be: approbation of the developed device on patients, receiving feedback and removing remarks from their side. Also, it is necessary to fill the system with a number of sensors to implement more precise movements, as well as to avoid emergency situations that may arise during training process.

Conflict of Interest The authors declare that they have no conflict of interest.

References

1. The World Health Report 2002, http://www.who.int/whr/2002/en/whr02_en.pdf?ua=1, last accessed 2018/01/30.
2. Benjamin, E.J., Blaha, M.J., Chiuve, S.E., et al. on behalf of the American Heart Association Statistics Committee and Stroke Statistics Subcommittee. Heart disease and stroke statistics—2017 update: a report from the American Heart Association. Circulation. 2017;135:e229–e445.
3. Wissel, J., Olver, J., Sunnerhagen, S. K.: Navigating the Poststroke Continuum of Care. Journal of Stroke and Cerebrovascular Diseases 22(1), 1–8 (2013).
4. Nijland, R.H., van Wegen, E.E., Harmeling-van der Wel, B.C., Kwakkel, G.: Presence of finger extension and houlder abduction within 72 hours after stroke predicts functional recovery: early prediction of functional outcome after stroke: the EPOS cohort study. Stroke 41(4), 745–50 (2010).
5. Susanto, E, Tong, R, Ockenfeld, C., Newmen, S.K.: Efficacy of robot-assisted fingers training in chronic stroke survivors: a pilot randomized-controlled trial. Journal of Neuro Engineering and Rehabilitation 12:42 (2015).
6. Riener, R., Nef, T., Colombo, G.: Robot-aided neurorehabilitation of the upper extremities. Med. Biol. Eng. Comput. 43(1), 2–10 (2005).
7. Vanderniepen, I., Van Ham, R., Van Damme, M., Lefeber, D.: Design of a powered elbow orthosis for orthopaedic rehabilitation using compliant actuation. In: Proceedings of the IEEE International Conference on Biomedical Robotics and Biomechatronics, pp. 801–806. IEEE, Scottsdale, AZ, USA (2008).
8. Andreasen, D.S., Allen, S.K., Backus, D.A.: Exoskeleton with EMG Based Active Assistance for Rehabilitation. In: Proceedings of the 9th IEEE International Conference on Rehabilitation Robotics (ICORR 2005), pp. 333–336. IEEE, Chicago, IL, USA (2005).
9. Landkammer, S., Valek, R., Hornfeck, R.: A Novel Bio-Inspired Fluidic Actuator for Robotic Applications. In: Proceedings of 25nd International Conference on Adaptive Structures and Technologies. ETH Zurich, Hague, Netherlands (2014).
10. Pylatiuk, C., Kargov, A., Gaiser, I., Schulz, S., Bretthauer, G.: Design of a Flexible Fluidic Actuation System for a Hybrid Elbow Orthosis. In: Proceedings of 11th International Conference of Rehabilitation Robotics. IEEE, Kyoto, Japan (2009).
11. Murray, I.A., Johnson, G.R.: A study of the external forces and moments at the shoulder and elbow while performing everyday tasks. ClinBiomech 19(6), 586–594 (2004).
12. Bruno, R.J., Lee, M.L., Strauch, R.J., Rosenwasser, M.P.: Posttraumatic Elbow Stiffness: Evaluation and Management. Journal of the American Academy of Orthopaedic Surgeons 10 (2), 106–116 (2002).
13. Miroslav, D.: Models and Modelling of Dynamic Moments of Inertia of Human Body. International Journal of Sports Science 6, 249–256 (2016).

Can Be Minimization of Membrane Bending Energy Used for Simulation of the Nanoparticle-Cell Interaction?

Martin Otáhal, Jitka Řezníčková, and Matej Daniel

Abstract

In addition to size, shape plays an important role when nanoparticle interacts with a cell. Mathematical model was formulated to predict membrane elastic energy in the presence of hydrophobic cylindrical nanoparticle. Two states of nanoparticle-phosholipid complexes were studied: the micellar complex with a nanoparticle encapsulated in the phospholipid monolayer and the lamellar complex where a nanoparticle is trapped inside the lipid bilayer. It was shown that there exists a critical size for the cylindrical nanoparticle below which the lamellar state is energetically more favorable. However, the critical size of cylindrical nanoparticle is considerably lower than the one of spherical nanoparticle. It might be concluded, that biological activity of cylindrical nanoparticle in comparison to spherical nanoparticles might be attributed not only to its higher area to volume ratio, but also to lower critical size. Lower critical size prevents a nanoparticle to be trapped inside the lipid bilayer and facilitates its translocation through phosholipid bilayer.

Keywords

Helfrich energy • Nanoparticle • Biological membrane

1 Introduction

Nanoparticles (NP) and nanotechnologies are being used in an increasing number of diverse industries. Unfortunately, there is still insufficient knowledge about the impact of NP on the environment as well as on the human body and its soft tissues [1]. The cell is the cornerstone of any living organism, and in order to determine the impact of NP on the living organisms, it is necessary to study the interactions between the NP and the cells [8]. The penetration of the cell membrane by nanoparticle is fundamental and very important in NP-cell interaction.

NP types of different size and shape are used in biomedicine. Most NPs developed for drug delivery have a spherical shape, although different shapes, like cylindrical or disc and other, are studied [5]. Most of studies [1, 2, 9, 10] are focused on interaction spherical NP with lipid membrane. It has been shown that the size of spherical NP affects its membrane interactions [10]. NPs with diameters smaller than 5 nm stay in the bilayer core, whereas NPs with diameters larger than 5 nm open pores in the bilayer [2]. In addition to size, shape plays an important role. Cylindrical NPs interact with cells very differently to spherical ones [11]. Therefore, the aim of this study is to study the interaction between the cell membrane and cylindrical nanoparticle (CNP) of various geometry. A theoretical model developed for spherical nanoparticle [10] was adopted in this study. The lipid bilayer composed exclusively of phospholipids is considered.

There are two important states of interaction between the cell membrane and CNP. The first state is the CNP micellar complex (M-CNP) and represents situation when the CNP is encapsulated by lipid monolayer whereas the CNP is trapped inside the lipid bilayer (L-CNP) in the second state. The model predict the dependence between the size and shape particle and the elastic energy of the membrane.

M. Otáhal (✉)
Faculty of Biomedical Engineering, Czech Technical University in Prague, Sítná square 3105, 27201 Kladno, Czech Republic
e-mail: Otahal.Martin.Otto@gmail.com
URL: https://kpo.fbmi.cvut.cz/

J. Řezníčková · M. Daniel
Faculty of Mechanical Engineering, Czech Technical University in Prague, Technická 4, 16607 Prague, Czech Republic

2 Methods

Analysis of CNP-biomembrane interaction is based on the model of Sub Wi et al. [10] (see the original model for assumptions). The deformation of the membrane by inclusion is described by free energy which is increased by

intercollation of CNP into hydrophobic moiety of membrane [7]. Two key modes of membrane deformation caused by hydrophobic CNP are the hydrophobic mismatch causing deformation of hydroxycarbon chains and the membrane bending (Fig. 1). The equilibrium shape is determined as a shape with minimal free energy of the membrane in the deformed state.

Bending energy of monolayer is expressed using the Helfrich formula [3]

$$E_{bend} = \frac{1}{2}\kappa \int_A (C_1 + C_2 - C_0)dA \qquad (1)$$

where κ is the bending modulus of monolayer, C_1 and C_2 are the first and the second principal curvature, respectively and C_0 is the monolayer spontaneous curvature. The integration is performed over a membrane area affected by the nanoparticle.

A length mismatch u between the length of the lipid tails of an unperturbed monoloayer h (Fig. 1) and the thickness of the deformed monolayer in the vicinity of the CNP describes the deformation of the hydrophobic core. It is considered that the hydrophobic binding is strong enough to prevent the exposure of hydrophobic moiety to the water [4]. The corresponding deformation energy of hydroxycarbon tails is expressed as [6].

$$E_{stretch} = \frac{1}{2}K \int_A \left(\frac{u}{h}\right)^2 dA \qquad (2)$$

where K is the compression-expansion modulus of the lipid bilayer. The sum of bending and stretching energy is expressed relative to the reference state of planar lipid bilayer ΔE of corresponding area A. The reference planar bilayer has zero principal curvatures with the unstretched lipid core.

It is assumed that the CNP has capsule geometry consisting of a cylinder with two hemispherical caps. The CNP geometry is defined by two parameters: the cylinder length and radius, l and r respectively (Fig. 1).

The energy of hydroxycarbon chain stretching is negligible for the M-CNP phase [10] and the free energy of lipid bilayer is expressed as

$$\Delta E = 2\pi r^2 \left(\frac{2}{r} - C_0\right)^2 + \pi r l \left(\frac{1}{r} - C_0\right)^2 - \pi r(2r + l)C_0^2 \qquad (3)$$

For the sake of simplicity, the energy of L-CNP phase is expressed for spherical cups and cylinder. The influence of spherical cups is taken as the energy of spherical nanoparticle of radius r incorporated into the lipid bilayer, i.e. the spherical symmetry is considered. The cylindrical segment has cylindrical symmetry with the zero second principal curvature. It is assumed that CNP is placed in the middle of lipid bilayer, i.e. both monolayers are deformed symmetrically.

Sub Wi et al. [10] suggested an analytical model describing deformation of lipid bilayer in the presence of hydrophobic nanoparticle by assuming a simple parametric geometry. The monolayer profile is represented by two circular arcs with angular distance ϑ (Fig. 2b). The radius of the arc in the non-stretched monolayer is $r + h$, which is the radius of the two identical principal curvatures (part I in Fig. 2a). The radius of the second; arc defined by angle (part II and III) ϑ is R_1.

$$R_1 = \frac{r\cos\vartheta}{1 - \cos\vartheta} - h \qquad (4)$$

The hydroxycarbon chains are perpendicular to the membrane. The hydroxycarbon chains in the part I are undeformed, while they are in stretched in part II and III in order to prevent void formation around the CNP. The deformation u is determined from the distance between the membrane surface, CNP and bilayer central plane in the part II and III, respectively. The membrane stretching energy is obtained from Eq. (2).

A shape of optimal θ that minimizes total energy is estimated by minimization of the total energy from Eqs. (1) and (2). To prevent shape discontinuity, the identical ϑ is
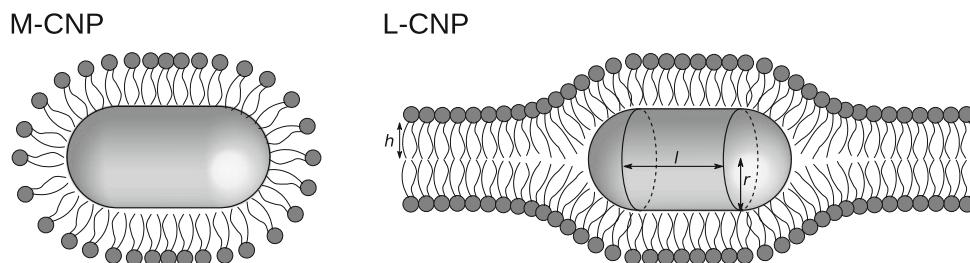
Fig. 1 Geometry of cylindrical nanoparticle embedded with the lipd membrane. M-CNP and L-CNP denotes micellar and lamellar complex of phosholipids and nanoparticles, respectively

Fig. 2 a Micellar phase and **b** Lamellar phase of the cylindrical nanoparticle (CNP) and phosholipids. Cross-section is perpendicular to the longitudinal axis in the cylinder region of the CNP
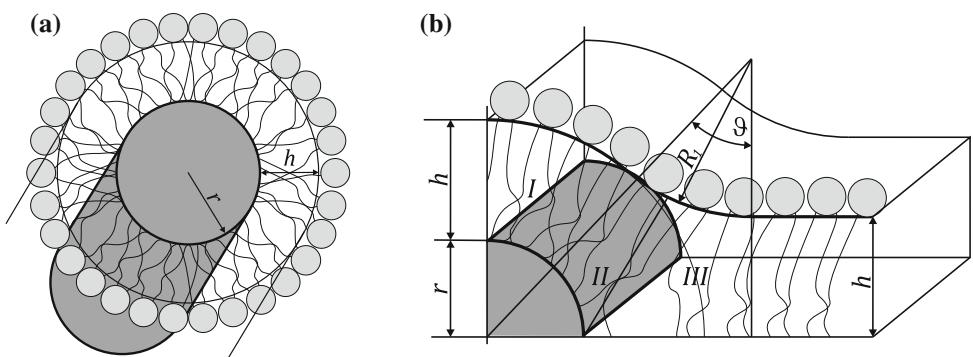
Table 1 DOPC parameters

Parameters	Value	Unit
Bending modulus, κ	9	k_BT
Monolayer thickness, h	1.3	nm
Area stretching modulus, K	23	$k_BT\ nm^{-2}$
Monolayer spontaneous curvature C_0	$-1/16$	nm^{-1}

assumed in the whole cylindrical and the spherical CNP sections. The calculation was performed for parameters listed in Table 1 that represents DOPC monolayer [10].

3 Results and Discussion

The energy of embedding CNP into the membrane bilayer (L-CNP) is increased with the size of the CNP. The effect of CNP size on bending energy is less pronounced in the micellar phase (M-CNP) (Figs. 3 and 4). The insensitivity of

the M-CNP complex radius on the change in energy might be explained by Eq. (3). Equation (1) shows that the energy is proportional to the second root of curvature and area. The curvature is decreased with increasing radius of CNP, while the area is increased in the M-CNP phase in Eq. (3) and these two effects cancel each other. The interaction between phospholipid bilayer and CNP is more complex as the interstitial energy of hydroxycarbon chain deformation must be considered.

We may identify a critical size of CNP that induces micellar to lamellar phase transition. Below the critical size, the energy of L-CNP is lower than the energy of M-CNP and the nanoparticle is more likely to be in lamellar phase (Table 2). If the size of the particle is higher than critical, the particle is separated from membrane and may penetrate the membrane into the cell.

The spherical hydrophobic particle ($l = 0$ nm) has critical radius around 3.2 nm as also reported by model of Sub Wi et al. [10]. Cylindrical nanoparticles has considerably lower

Fig. 3 Dependency of deformation energy of lipid layer on radius of cylindrical nanoparticle with different length. Solid line represents situation that the nanoparticle is inside lipid bilayer, and dashed line represents situation, that the nanoparticle is fully covered by lipid monolayer (micelle)
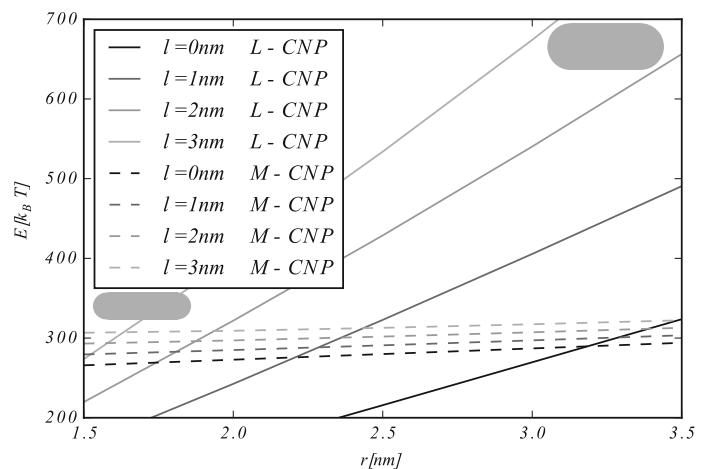
Fig. 4 Dependency of deformation energy of lipid layer on length of cylindrical nanoparticle with different radius. Solid line represents situation that the nanoparticle is inside lipid bilayer, and dashed line represents situation, that the nanoparticle is fully covered by lipid monolayer (micelle)
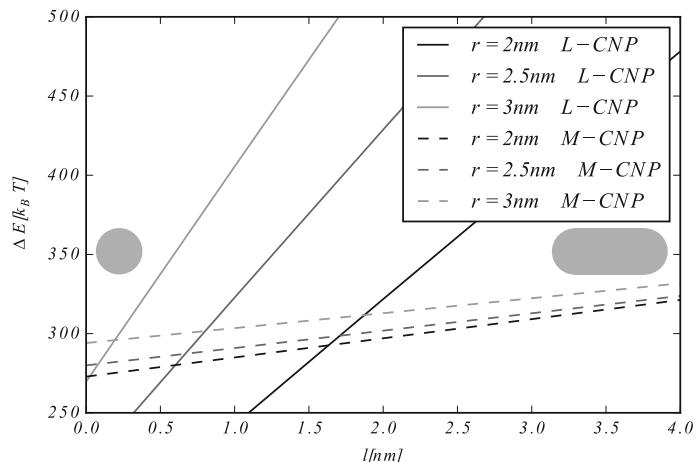
Table 2 Estimated values of critical radius and length for different cylindrical nanoparticle length and radius, respectively

Length l (nm)	Critical radius r_{crit} (nm)	Radius r (nm)	Critical length l_{crit} (nm)
0	3.2		
1	2.3	2	1.6
2	1.9	2.5	0.6
3	1.6	3	0.2

critical radius than spherical ones. For example, small cylindrical nanoparticle of length 1 nm has critical radius below 2.3 nm. In the same manner, a critical length can be estimated for the CNP of given radius. Critical length gives similar information to critical radius. Nanoparticles shorter, than l_{crit} will be stable inside lipid bilayer, while longer nanoparticles will form micellar structures.

The critical CNP size might explain different biological behavior of cylindrical and spherical nanoparticles [12]. The nanoparticle biological activity depends on the surface area. It is shown, that if we take spherical nanoparticle of radius 3 nm, it will not penetrate the membrane and stays trapped inside. However, the cylindrical nanoparticle of the length $l = 1$ nm and the same area as spherical nanoparticle has radius of 2.76 nm. It is above critical radius and it indicates that CNP penetrates cell membrane more likely than spherical nanoparticles.

The present study employs the number of assumptions to intentionally keep the model simple. We have used a continuum approach although the studied length scale is at molecular dimensions. Describing the biomembrane as elastic continuum is certainly an approximation. Further approximation arises from simplified prescribed geometry. The more appropriate approach would be to optimize arbitrary membrane shape. The more accurate description would

probably affect the values of membrane energy, but it will not considerably change the main conclusions of the study.

4 Conclusion

Mathematical model was formulated to predict membrane elastic energy in the presence of hydrophobic cylindrical nanoparticle. It was shown that there exists a critical size for the CNP that allow its incorporation into lipid bilayer. However, the critical radius of CNP is considerably lower than critical radius of spherical nanoparticle. It might be concluded, that higher biological activity of CNP in comparison to spherical nanoparticles might be attributed not only to its higher area to volume ratio, but also to low critical size that allows membrane penetration.

Conflict of Interests The authors declare that they have no conflict of interest.

References

1. Contini, C., Schneemilch, M., Gaisford, S., Quirke, N.: Nanoparticle membrane interactions. J. Exp. Nanosci. (December), 1–20 (2017).
2. Guo, Y., Terazzi, E., Seemann, R., Fleury, J.B., Baulin, V.A.: Direct proof of spontaneous translocation of lipid-covered hydrophobic nanoparticles through a phospholipid bilayer. Sci. Adv. 2(11), e1600261–e1600261 (2016).
3. Helfrich, W.: Elastic properties of lipid bilayers: theory and possible experiments. Zeitschrift für Naturforschung. Tl. C. Biochem. Biophys. Biol. Virol. 11(28), 693–703 (1973).

4. Nielsen, C., Andersen, O.S.: Inclusion-induced bilayer deformations: effects of monolayer equilibrium curvature. Biophys. J. 79 (5), 2583–604 (2000).

5. Panariti, A., Miserocchi, G., Rivolta, I.: The effect of nanoparticle uptake on cellular behavior: Disrupting or enabling functions? Nanotechnol. Sci. Appl. 5(1), 87–100 (2012).

6. Perutková, Š., Daniel, M., Rappolt, M., Pabst, G., Dolinar, G., Kralj-Iglič, V., Iglič, A.: Elastic deformations in hexagonal phases studied by small-angle X-ray diffraction and simulations. Phys. Chem. Chem. Phys. 13(8), 3100–7 (Feb 2011).

7. Phillips, R., Ursell, T., Wiggins, P., Sens, P.: Emerging roles for lipids in shaping membrane-protein function. Nature 459(7245), 379–385 (May 2009).

8. Robertson, J.D., Rizzello, L., Avila-Olias, M., Gaitzsch, J., Contini, C., Magoǎ, M.S., Renshaw, S.A., Battaglia, G.: Purification of Nanoparticles by Size and Shape. Sci. Rep. 6, 1–9 (2016).

9. Rossi, G., Monticelli, L.: Gold nanoparticles in model biological membranes: A computational perspective. Biochim. Biophys. Acta - Biomembr. 1858(10), 2380–2389 (Oct 2016).

10. Sub Wi, H., Lee, K., Kyu Pak, H.: Interfacial energy consideration in the organization of a quantum dotlipid mixed system. J. Phys. Condens. Matter 20(49), 494211 (Dec 2008).

11. Yoo, J.W., Mitragotri, S.: Polymer particles that switch shape in response to a stimulus. Proc. Natl. Acad. Sci. 107(25), 11205–11210 (2010).

12. Yoo, J., Cui, Q.: Three-dimensional stress field around a membrane protein: Atomistic and coarse-grained simulation analysis of gramicidin A. Biophys. J. 104(1), 117–127 (2013).

Fundamental Study of a Simple Walking Support System Using Smart Devices

Nobuyuki Toya, Yutaro Sakamoto, Yu Taguchi, and Kodai Kitagawa

Abstract

Accidents involving falling frequently occur and are a particularly serious problem for the elderly. Therefore, prompting and training people to maintain a form of gait with appropriate stride length and foot-ground clearance in daily life are essential to mitigate the danger of such accidents. Herein, we propose a simple walking assistance system designed to prevent falls using a smart device that is worn on the arm. This system can be used in daily life. The smart device is equipped acceleration sensors, which are used for gait decision. When the risk of falling becomes high, the device prompts the user to adjust their gait using notifications such as alarms, vibrations, and flashing lights. To increase the accuracy of decision making of the smart device, we have introduced a decision tree approach. This method was found to accurately classify gait patterns in all but a small number of test participants. Furthermore, we analyzed arm acceleration data during walking and found that significant arm swing is necessary for the users of our proposed system. Taking these considerations, we reconstructed the experimental system using a Microsoft Kinect® v2 sensor to analyze the motion of the test participants in more detail, and preliminary tests of the device were conducted. The system was successful in recording gait and in providing a foot height feedback system for the user.

N. Toya (✉) · Y. Sakamoto · Y. Taguchi · K. Kitagawa
National Institute of Technology, Kushiro College, 2-32-1, Otanoshike-Nishi, Kushiro, Hokkaido, 084-0916, Japan
e-mail: toya@kushiro-ct.ac.jp

1 Introduction

Falling accidents involving elderly people are increasingly common and often result in serious injury [1], severely limiting quality of life. For elderly people, the cause of falling accidents is usually tripping [2, 3], which seems to be related to an inability to accurately detect the position of the feet [4–6]. Therefore, to improve the mobility of elderly people, assisting them in walking by training them is essential to maintain an appropriate stride length and foot-ground clearance.

A number of automated systems for detecting falls have been proposed, however, little research has been conducted on prevention of falls. In addition, such systems usually require the use of multiple sensors or cameras, thus limiting the locations in which they can be easily used and the clothes that can be worn by the user [7]. We have developed a fall prevention system controlled by a smart device equipped with acceleration sensors [8]. This smart device is worn on the arm, therefore, its use is not limited to specific environments. Previous studies have been conducted on the relation between the movement of the arm and upper body rotation, energy expenditure, and other dynamic parameters. We therefore take arm movement as being influenced by the gait [9–11] and providing a way of tracking it.

The operation of our proposed system is as follows: (1) when the system is started, it performs an initial configuration for individual users using the few points of arm acceleration data corresponding to different patterns of gait (such as "normal step" and "high step"), which can then be used to identify the user's gait; (2) continuous gait monitoring begins, and gait patterns are identified to estimate the risk of falling; and (3) whenever the risk of falling is high, the system prompts the user to modify their gait with alerts such as sounds, vibrations, and flashing lights.

Recent studies have shown that the time waveforms of arm acceleration are influenced by the step length and foot-ground clearance [8]. Furthermore, to improve the decision accuracy

of gait patterns, we have introduced a method of gait classification in which a decision tree is built using arm acceleration data as feature quantities [12]. This method was able to accurately classify gait patterns. However, the classification did not work well for a few test participants.

To improve the accuracy of decision of gait, we analyzed the cause of the decision error and modified the experimental system using a Kinect sensor with the objective of developing a practical walking support system.

2 Improvement of Practicality

2.1 Improvement of Decision Accuracy

In a recent study conducted by us [12], ten male students were selected as participants in gait experiments on a treadmill. We tested the performance of a smart device-controlled walking support system while classifying the following three gait patterns: normal step, high step, and long step. Figure 1 shows the experimental setup; the smart device is worn on the wrist of the test participant and a digital camera records the participant's gait. An infrared sensor detected the high step gait and triggered a buzzer when the foot-ground clearance exceeded 15 cm (Fig. 2). Complementary arm acceleration data were obtained for each step using the proximity sensor
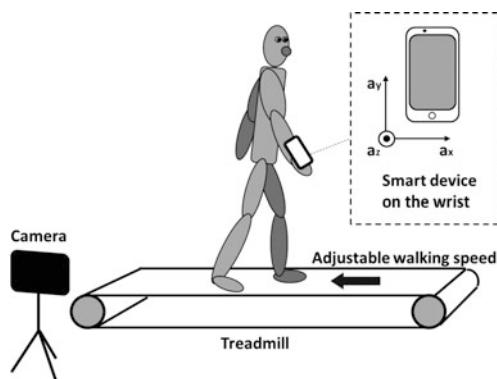
Fig. 1 Experimental system
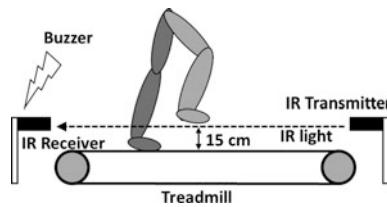
Fig. 2 Foot height detection
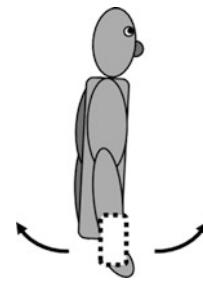
Fig. 3 Timing detection by proximity sensor

of the smart device, which timed the moment of passage of the forearm across the side of the body (Fig. 3). Table 1 shows the accuracy of gait classification obtained in our experiment [12], in which a decision tree is built using the arm acceleration data in the x-, y-, z-, and composite directions as feature quantities. The accuracy functions as an evaluation index and indicates the reliability of the method of gait classification. We used Weka and J48 algorithms to evaluate the accuracy of gait classification and introduced a 5-fold cross-validation method for each subject. Of the ten test participants, the gait classification accuracies of two (E and H) were low.

To improve the accuracy of gait classification, we analyzed arm acceleration data (Table 2). In this data, participants E and H exhibited relatively low differences in acceleration between normal step and high step. Furthermore, the standard deviation in the case of participant E was relatively large (Table 2). To raise the classification accuracy of the system, making a significant arm swing during the walk seems to be necessary. Although previous studies have suggested that arm swing is influenced by the gait [9–11], it is also possible for people to walk without arm swing. Therefore, for the successful functioning of our system, detecting the lowness of arm swing and prompting the user are essential to enhance the significance of arm swing during normal walking.

2.2 Necessity of Low Foot Analysis

In our recent studies, we judged that a foot-ground clearance below 15 cm constituted normal (relatively low) step. However, for elderly people, a foot-ground clearance below 10 cm can pose a more critical problem; this low clearance, as in the case of dragging the foot, can increase the chances of falling. Therefore, it was necessary to modify our experimental system for it to be used for analysis of the gait with low foot-ground clearance, i.e., the setup of the experiment must be capable of detecting a plurality of foot-ground clearance levels.

Table 1 Accuracy of gait determination and arm acceleration data

Test participant	Accuracy	Acceleration of composite direction (m/s^2)	
		Normal step height	High step
A	0.77	11.55 ± 1.16	18.98 ± 2.82
B	0.59	12.57 ± 2.02	15.53 ± 3.43
C	0.69	10.56 ± 1.04	12.78 ± 2.21
D	0.70	11.77 ± 1.26	14.09 ± 2.19
E	0.58	10.70 ± 1.23	11.28 ± 1.91
F	0.72	10.19 ± 0.79	13.57 ± 2.66
G	0.74	10.16 ± 1.29	11.85 ± 1.78
H	0.38	11.59 ± 1.51	12.59 ± 2.74
I	0.66	10.72 ± 1.22	9.875 ± 1.99
J	0.67	11.73 ± 0.86	13.13 ± 1.90

Table 2 Difference of arm acceleration and sum of standard deviation

Test participant	Difference of acceleration in (m/s^2)	Sum of SD (m/s^2)
A	7.43	3.98
B	2.96	5.45
C	2.22	3.25
D	2.32	3.45
E	0.58	3.14
F	3.38	3.45
G	1.69	3.07
H	1.00	4.25
I	−0.85	3.21
J	1.40	2.76

3 Reconstruction of Experimental System

3.1 Introduction of Kinect Sensor

We modified our experimental system in response to the investigation described in Sect. 2. Specifically, a Microsoft Kinect® v2 sensor was added since it has the potential to improve our gait experiment because of the following capabilities:

- Detection of a plurality of foot-ground clearance levels.
- Ability to give appropriate feedback of foot-ground clearance to the test participant by means of alarm sounds or displays during the experiment.
- Objective measurement of arm movement for signal analysis.

On account of these advantageous facilities, we introduced a Kinect sensor into our experimental system.

3.2 Experimental System Including Kinect Sensor

The Kinect sensor was fixed to observe the gait of the test participant by side-view. The foot-ground clearance was measured using the corresponding length between the bottom of the image and the foot of the participant. Figure 4 shows the Kinect sensor side-view image of a test participant walking on the treadmill. Lines and dots in this photograph indicate the body elements recognized by the Kinect sensor. Using Kinect for Windows SDK 2.0, we designed our experimental system as follows:

- An alarm sounds when the foot-ground clearance exceeds an arbitrary height threshold, and the participant is informed that their foot is at an appropriate height.
- Foot-ground clearance measurements and joint angles are indicated on the display with respect to the recognized body elements during the experiment.

Fig. 4 Recognition of body elements
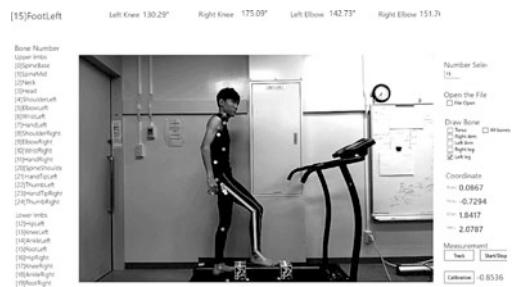
Fig. 5 Indicated participant and recognized parameters on the display

- The experimental video is recorded with the recognized body elements at 30 frames per second for detailed gait analyses.

3.3 Preliminary Test

A preliminary test was conducted using the reconstructed system. The system successfully recognized body elements and sounded the alarm when the foot-ground clearance exceeded the 5 cm threshold. Tracking errors were

occasionally observed. Figure 5 shows a sample preliminary test picture that was displayed on the experimental system. In this picture, the participant is standing with their left foot on a 10 cm high acryl bridge with obtained parameters of the foot element height, the knee joint angle and the elbow joint angle. Figure 6 shows the height of the recognized foot element while the participant holding the foot on a footrest of 10 cm high for 5 s. This result shows that the error of the estimated foot height is less than 1 cm. Furthermore when the experiment was performed five times repeatedly, the result showed a similar trend and the mean value of the estimated foot height was 9.8 cm. The system was successful as a feedback system for foot height reference and detailed gait analysis.

4 Conclusion

In a previous study, we introduced a fall prevention walking support system controlled by a smart device. In this study, we furthered our experiments by analyzing arm acceleration data obtained from recent experiments and found that significant arm swing is necessary to improve the accuracy of the classification of gait by our proposed walking support system. With this consideration in mind, we reconstructed our experimental system using a Microsoft Kinect® v2 sensor to analyze the motion of the test participant in more detail. A preliminary test showed that the system was successful in classifying gait using a foot-ground clearance height feedback system which alerts the participant using an alarm, thus assisting in training the participant in a style of walking that limits the chance of falling. Such technology has applications to training the elderly in such styles of walking, which is critical since they are particularly susceptible to accidents involving falls.
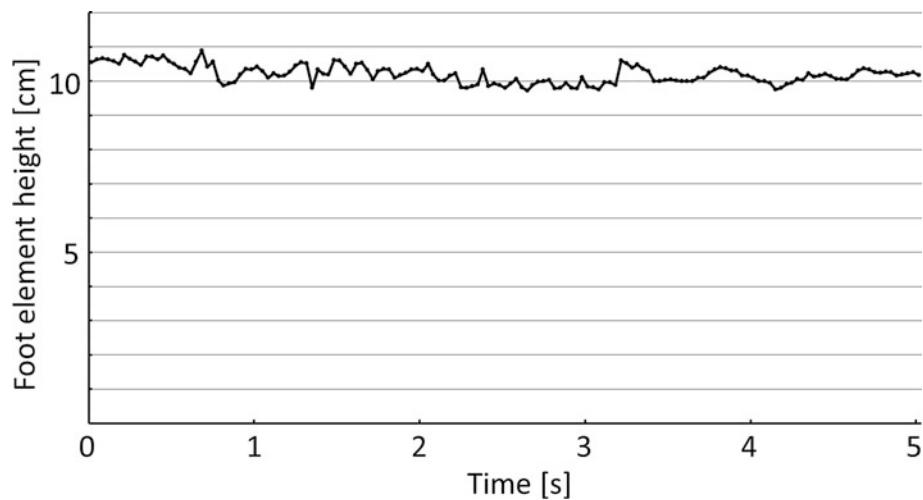
Fig. 6 Obtained foot element height by the experimental system

References

1. Yukimasa T., et. al: "The investigation of risk factor of injury caused by falling," Journal of Biomedical Fuzzy System Association (in Japanese), Vol. 13, No. 2, pp. 109–114 (2011).
2. Kim H., et. al: "The relationship between fall-related activity restriction and functional fitness in elderly women," Japanese Journal of Geriatrics (in Japanese), Vol. 38, No. 6, pp. 805–811 (2001).
3. Overstall P.W., et. al: "Falls in the elderly related to postural imbalance," British Medical Journal, Vol. 29, No. 1, pp. 261–264 (1977).
4. Saito S., Muraki S.: "Study on tracks and sense of feet position while stepping over an obstacle in the elderly," The Japanese Journal of Ergonomics (in Japanese), Vol. 46, No. 2, pp. 172–179 (2010).
5. Kobayashi Y., et. al.: "Foot position tends to be sensed as more medial than the actual foot position," Journal of Motor Behavior, Vol. 41, No. 5, pp. 437–443 (2009).
6. Shin S., et. al.: "Relationship between the obstacle height cognition and step movement in the elderly," Journal of Physiological Anthropology, Vol. 31, No. 1, pp. 172–179 (2010).
7. Delahoz Y.S., Labrador M.A.: "Survey on fall detection and fall prevention using wearable and external sensors," Sensors, Vol. 14, No. 10, pp. 19806–19842 (2014).
8. Kitagawa K., Go K., Toya N.: "Some discussions of walking state estimation using miniaturized sensors for fall prevention," Research Reports: Kushiro National College of Technology (in Japanese), Vol. 49, pp. 27–30 (2016).
9. Pontzer H., et. al: "Control and function of arm swing in human walking and running," The Journal of Experimental Biology, Vol. 212, pp. 523–534 (2009).
10. Yizhar Z., et. al.: "The effect of restricted arm swing on energy expenditure in healthy men," International Journal of Re-habilitation Research, Vol. 32, No. 2, pp. 115–123(2009).
11. Sutherland D.H., et. al.: "The development of mature gait," The Journal of Bone and Joint Surgery, Vol. 62, No. 3, pp. 336–353 (1980).
12. Kitagawa K., Taguchi Y., Toya N.: "Proposal and evaluation of the gait classification method using arm acceleration data and decision tree," Proceedings of The 2017 International Conference on Artificial Life and Robotics, pp. 104–107 (2017).

Experimental Analysis of Cellular Membrane Mechanical Properties

Bohumil Hornát, Martin Otáhal, and Jana Turňová

Abstract

The study of cell-environment can reveal the possibilities of using nanoparticles in biomedicine. The condition of the cell membrane reflects the mood of whole cell. The membranes as the outer envelope of the cell have a semi-fluid character, and the proteins and lipid molecules are in constant motion. Our aim is to develop methodology for measuring of cell mechanical properties. Atomic force microscopy and force spectroscopy were selected for contact between a tip of cantilever and a cell. This work presents the results of comparison using different tips of cantilevers and verification on several types of cells. Dependence between Young's modulus of a cell membrane and surface attachment is next part of this work. Different surfaces are creating by coating of glass. Working with living cells claims specific approach in all parts of the research. The results compare the properties of the same cells on different surfaces.

Keywords

Atomic force microscopy • Force spectroscopy
Membrane properties

1 Introduction

Epilepsy affects the lives of millions of people around the world. Understanding of the effect of disease on mechanical properties on neuron can help us to understand the epilepsy from another point of view. The neuron membrane can be monitored by atomic force spectroscopy (AFM) and the dynamics of the processes triggering the individual states could be clarified [1]. Membrane properties also play an important role in cancer cells, where changes in plasticity and adhesion have been observed [2]. Generally, can be said that the mechanical properties, like Young's modulus, are useful as marker a marker for observing some cellular processes during different diseases.

1.1 Cell Membrane

Each cell has a cell membrane, which protects the cell from the external environment, and at the same time enables it to receive the necessary nutrients from the outside, as well as emit the waste out. In principle, the membrane consists of a lipid bilayer that is full of other proteins. A selectively permeable property is important for proper regulation of the internal environment (cytoplasm) and for maintaining stable concentrations of ions and other organic molecules [3].

1.2 Atomic Force Microscopy

The AFM principle is based on the deformation of the cantilever upon contact with the sample [4]. Cantilever is equipped with a tip defined by the supplier. For a given task, a specific combination of tip and cantilever is required. Cantilever deforms as soon as the tip approaches the surface. Deformation of the cantilever is monitored by a laser beam, which is scanned after the reflection. The position of the laser is scanned during sample scanning pixel by pixel. That calls contact mode.

1.3 Force Spectroscopy

When the tip and cantilever parameters are known, it is possible calculate the mechanical properties of the sample

B. Hornát (✉)
Faculty of Biomedical Engineering, Czech Technical University in Prague, Kladno, Czech Republic
e-mail: hornatb@gmail.com

M. Otáhal · J. Turňová
Faculty of Biomedical Engineering, Department of Natural Sciences, Czech Technical University in Prague, Kladno, Czech Republic

using force spectroscopy curves. Force spectroscopy curves describe the dependence of the force acting on the cantilever on the position of the cantilever. The measurement has the following stages. First approach should be free of force and there is a horizontal line on the chart. Second extend is contact between tip and sample. In the next phase, the cantilever will remain in a certain position for a given time. It is possible definite a remain phase by constant force. Adhesion can be calculated from retract phase as shown in the Fig. 1.

2 Equipment and Methods

2.1 Experimental Setup

All data was measured on the JPK NanoWizard 3 AFM device.

Imaging and Force spectroscopy were carried out in contact mode. Living cells were measured in Phosphate-buffered saline (PBS). Fixed non-living cells were measured in Ethanol or PBS and empty glass was measured on air or in distilled water.

For measuring were used different shape cantilevers and tip from Applied Nanostructures Inc. Parameters specified by the manufacturer are entered in the Table 1 where k is spring constant.

HYDRA2R-100N. This cantilever is universal probe for STM and AFM. It can be use in liquid and that allow for high resolution imaging. Cantilever is without reflex counting. Tip has shape of irregular quadrangular pyramid. For calculating was used an approximation of a regular triangular pyramid with half-angle to edge 31°. Because this probe is commercially available, it was also the most affordable.

Fig. 1 Characterization of force spectroscopy curve [5]

SHOCONA-B20. This probe is specific with small ball on the top of pyramid. This cantilever is reflex coated by aluminum.

HYDRA6R-200NG. For this cantilever without tip was ordered special tip. Sphere with diameter 5–7 μm was attached on the end of cantilever.

2.2 Hertz Model

Hertz model is mathematical model for calculating Young modulus of the sample [7]. The original Hertz model was defined for two spheres. For force spectroscopy, the equations were adapted to the shape of the tip [8], and in present are defined Hertz models for various combination of surfaces. In our work we are using spherical and pyramidal tips. Relationship between F force, R tip radius and E Young modulus for combination of sphere and plain field is defined by equation

$$F = \frac{E}{1 - v^2} \left[\frac{a^2 + R^2}{2} \ln \frac{R + a}{R - a} - aR \right] \tag{1}$$

where v is Poisson ratio. Poisson ratio is default set to 0.5 in biological application. If we define same relationship for pyramidal tip on plain field, we obtain next equation

$$F = \frac{E}{1 - v^2} \frac{\tan \alpha}{\sqrt{2}} \delta^2 \tag{2}$$

where

$$a = \frac{\tan \alpha}{\sqrt{2}} \delta \tag{3}$$

where α is face angle of pyramid.

2.3 Biological Samples

For our first experiments and apparatus calibrating we chose durable cells.

Non-living CT26.WT mice colon cancer cells have been used for the first measurement. It is necessary to learn how to measure in liquid and these cells are good for their endurance and ability to attach to the cover glass.

Living NIH/3T3 fibroblast from mouse embryo were used. These cells were prepared multiple ways. There were prepared fixed non-living cells in ethanol, living cells on glass (collagen coated) and last living cells on glass (PEI 2000 coated).

Table 1 AppNano probes—specification [6]

Name	k (N/m)	Tip shape	Diameter	Half-angle to edge
HYDRA2R-100N	0.011	Pyramidal	–	31°
SHOCONA-B20	0140	Ball	20 nm	–
HYDRA6R-200NG with SiO2 sphere 5–9 μm	0.035	Sphere	7 μm	–

3 Results and Discussion

3.1 Imaging

Imaging in contact mode is simple but it is necessary take care about gain and error signal. These two parameters have to be balanced for the best resolution and unsupported sample. The Fig. 2 shows imaging cells in liquid.

For better pictures can be extended measuring time and increased resolution (see Fig. 3).

These pictures show morphology but there is no information about mechanical properties.

3.2 Force Spectroscopy

Fitting method. Using the right mathematical model is a prerequisite for qualitative results. There is comparison on of two mathematical models on the same dates (100 force spectroscopy curves) in the Table 2.

The fact that sphere fitting has smaller standard deviation is predictable, because only the cantilever deforms in contact hard tip with hard glass. A contact flat will be very small and comparable with a radius of curvature (ROC). Furthermore, it is only counted with the triangular pyramid fit at HYDRA2R-100N.

Different surface. The comparison of the same cells on different surfaces is reported in the Table 3. All data in Table 3 were measured with the same tip HYDRA6R-200NG with SiO2 sphere 5–9 μm and fitting as sphere (7 μm). The cells are 72 h old.

For cells as inhomogeneous material, values vary greatly from one another. The largest statistic value difference in cell elasticity is observed between cells on collagen and PEI cells. This corresponds to the measurement experience and that it was easier to pull down the cell by measuring. For full comparison, you need to measure several identical cells with the same tip.

4 Conclusion

The imaging of living cells in contact mode is possible in certain cases. First it must be used captured cells on the substrate. This will help us to coat the glass for better cell attachments. Secondly it is necessary use a cantilever with a tip with height greater than the size observed cells. Failure to observe this rule will result in tearing the cell. Last but not least scanning itself can damage the cell and therefore it is necessary to track the measuring in the course.

Force spectroscopy at any point can be measured and evaluated. There are several issues here. The cantilever manufacturer is unable to produce two identical ones. For a

Fig. 2 Mouse (Mus musculus) fibroblast—CT26.WT (ATCC® CRL-2638™) non-living cancer cell in PBS (Phosphate-buffered saline) 512 × 512 pixels imaged by AFM
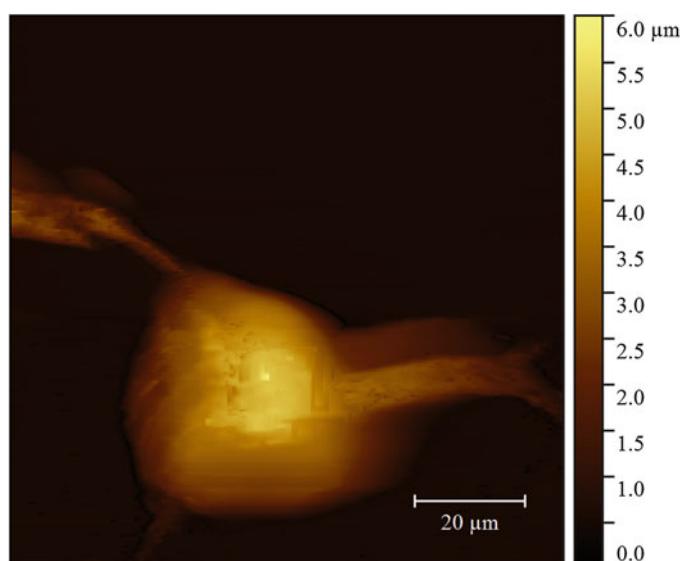
Fig. 3 Mouse (Mus musculus) fibroblast—CT26.WT (ATCC® CRL-2638™) non-living cancer cell in PBS 1024 × 1024 pixels imaged by AFM
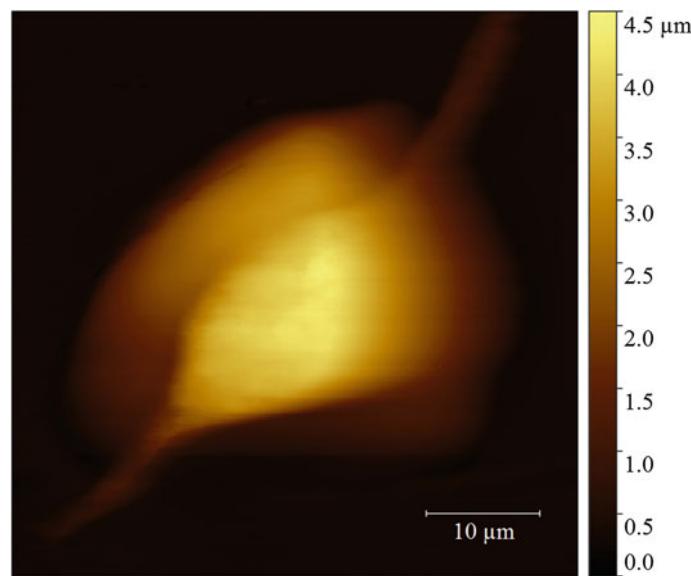
Table 2 Comparison two methods of fitting

Young modulus of cover glass	Fit as sphere (10 nm)	Fit as triangular (31°)
1st quartile (lower quartile) (Pa)	655,109	648,857
2nd quartile (median) (Pa)	685,401	711,967
3rd quartile (upper quartile) (Pa)	702,453	743,012
Standard deviation (Pa)	33,326	63,532

Table 3 Comparison the same cells on different surfaces. NIH/3T3 (ATCC® CRL-1658™)

Young modulus	Fixed (non-living)	Collagen	PEI
1st quartile (lower quartile) (Pa)	58.00	30.85	147.31
2nd quartile (median) (Pa)	130.97	58.69	201.95
3rd quartile (upper quartile) (Pa)	289.25	143.54	268.66
Standard deviation (Pa)	184.57	86.08	126.70

quite homogeneous material, such as clear glass, we can observe a standard deviation of elasticity values up to 5% using one tip. It is therefore impossible to simply determine the elasticity of the sample.

Adhesion is another parameter that can be evaluated from force spectroscopy curves. The standard deviation is 5% for the value of the force needed to pull the tip out of the glass. The standard deviation is 7% for the work needed to pull the tip off the glass. There is a high risk of pinching impurities and affecting the results.

While measuring complex samples, membranes full of protein, which may change over time depending on various factors, the results should be treated with caution.

References

1. Wu, X., Muthuchamy, M., Reddy, D. S.: Atomic force microscopy protocol for measurement of membrane plasticity and extracellular interactions in single neurons in epilepsy. Frontiers Aging Neuroscience 8(88), (2016).
2. Friedl, P., Alexander, S.: Cancer invasion and the microenvironment: plasticity and reciprocity. Cell 147, 992–1009 (2011).
3. Alberts, Bruce.: Molecular biology of the cell. 4th edn. Garland Science, New York (2002).
4. Binnig, G., Quate, C. F., Gerber, C.: Atomic force microscope. Phys. Rev. Lett. 56, 930–933 (1986).
5. Maver, U., Maver, T., Peršin, Z., Mozetič, M., Vesel, A., Gaberšček, M., Stana-Kleinschek, K.: Polymer characterization with the atomic force microscope. Polymer Science 4 (2013).

6. Silicon AFM probes, Silicon nitride (SiN) AFM probes, http://www.appnano.com/product/category/spmprobes, last accessed 2018/01/31.

7. Hertz, H.: Über die berührung fester elastischer Körper. Journal für die reine und angewandte Mathematik 92, 156–171 (1881).

8. Lin, D. C., Dimitridas, E. K., Horkay, F.: Robust strategies for automated AFM force curve analysis-I. Non-adhesive indentation of soft, inhomogeneous materials. ASME 129, 430–440 (2007).

Development of a Modular Bionic Prototype Arm Prosthesis Integrating a Closed-Loop Control System

Christoph Kast, Bernhard Rosenauer, Helmut Meissner,
Weerayot Aramphianlert, Matthias Krenn, Christian Hofer,
Oskar C. Aszmann, and Winfried Mayr

Abstract

An active prosthetic arm is not only dependent on critical factors for clinical use, such as weight or bulk but also needs reliable control inputs for accurate and safe positioning. Particularly with a high level of amputation, light but robust devices are essential. Our concept is composed of a modular system, based on bionic design principles, that is adaptable to the specific level of amputation of an arm. By following three basic rules: proximal weight, flexibility and lightweight but silent operation, it is possible to mimic the weight distribution of a human arm. A custom developed control hardware attached on top (HAT) is based on a Raspberry Pi 3 (RPi3) and holds the ADS1299 that is capable of acquiring sensor and other bioelectrical signals. The motion and position data is gathered using a 9-axis inertial measurement unit. Based on the processed data a control signal is sent to the independent actuator control unit. The use of the RPi3 allows performing complex decisions and control algorithms fast enough for real-time control of the prosthesis actuators. The resulting ranges of motion are 120° for the elbow joint and 270° for the wrist joint. The elbow joint can lift a weight of maximal 3.3 kg with a lever of 30 cm through the entire range of motion within two seconds. The system provides a novel bionic design that allows usage not only for transradial but also transhumeral amputation. The proximal weight distribution and the used materials increase the wearing comfort in daily tasks and mimic to a high extent physiological conditions. Furthermore, the speed of the control system is within the range of the electromechanical delay in the human body which not only is beneficial for control purposes but also increases the acceptance of the prosthesis.

1 Introduction

To design an arm prosthesis, there are several factors that need to be taken into account, e.g., weight, ease of use, noise, price, ease of maintenance, etc. However, the most two essential factors are functions and cosmetic appearance of the device. A proper arm prosthesis should be able to make the wearer feel like the device is a part of their body and be confident to wear it and benefit from it [1]. However, motors, batteries, and other mechanical and electronic components increase weight and cost of the device. Another factor that strongly influences the acceptance of the prosthesis is the delay created by multifunctional prosthesis controller. Large controller delays maximize the amount of time available for EMG signal processing and analysis. However, significant delays also degrade prosthesis performance by decreasing the responsiveness of the prosthesis. A delay greater than 100 ms causes a decrease in performance, whereas a delay between 50–100 ms is felt like the user is operating their prosthesis 'in molasses' [2].

Studies show that individuals with upper limb amputation are not satisfied with available technology. Factors like the proximal level of amputation, type of device, inadequate

C. Kast (✉) · B. Rosenauer · H. Meissner · W. Aramphianlert
M. Krenn · W. Mayr
Center for Medical Physics and Biomedical Engineering, Medical
University of Vienna, Vienna, Austria
e-mail: christoph.kast@meduniwien.ac.at

C. Kast · W. Aramphianlert · C. Hofer · O. C. Aszmann · W. Mayr
Christian Doppler Laboratory for Restoration of Extremity
Function, Division of Plastic and Reconstructive Surgery,
Department of Surgery, Medical University of Vienna, Vienna,
Austria

M. Krenn
Department of Neurobiology and Anatomical Sciences, University
of Mississippi Medical Center, Jackson, MS, USA

C. Hofer
Otto Bock Healthcare Products GmbH, Vienna, Austria
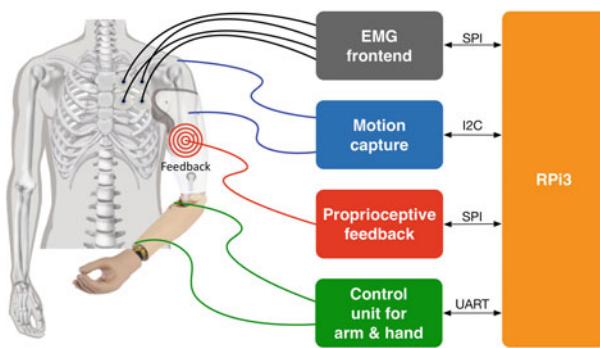
Fig. 1 This system configuration contains recording units for electromyography (EMG) and motion capture. A Raspberry Pi 3 analyzes the input data and controls the prosthetic arm. Proprioceptive feedback closes the loop

training, late fitting, limited functionality of devices, or cost for maintenance and repairs can lead to little or non-use of prosthetic devices. Despite a high rate of dissatisfaction with prostheses, proper use of prosthetic devices can provide highly beneficial support for activities of daily living, support of body hygiene, grooming, and dressing [3].

Our concept of a lightweight, modular arm prosthesis prototype is based on bionic design principles that can be adapted to the level of amputation. Additionally, the prosthetic arm mimics the weight distribution of a human arm. The control solution is a portable, fast, and reliable system (Fig. 1). A Raspberry Pi 3 (Raspberry Pi Foundation, Caldecote, United Kingdom) is not only used to process the data and to generate control signals for the actuator control unit but also delivers proprioceptive feedback to close the control loop.

2 Methods

The design concept of the prototype arm prosthesis follows three basic rules.

- **Proximal weight**: to mimic the weight distribution of a human arm, the actuators are driving the joints using Bowden cables, which allows placement of the driving components within the prosthetic shaft or on other comfortable body areas outside of the artificial arm. This ensures a relief of contact pressure on the stump and potential side effects. The weight distribution of the prosthesis can be arranged as proximal as possible.
- **Flexibility**: the prosthesis is designed to fit transradial and transhumeral amputees. Depending on the level of amputation, driving components, artificial joints and frame material can be trimmed which again reduces the overall weight. In the case of a transradial application, only the artificial wrist joint is used.

- **Lightweight and silent operation**: by using AlCu4Mg1, Titan Grade 5, and carbon fiber enforced epoxy the weight is kept low while load capacities are similar to stainless steel. The custom developed cam belt gear and low noise servo motors with optimized control patterns ensure low movement associated noise levels.

The control electronics is based on a Fubarino™ Mini (Schmalz Haus LLC and Fubar Labs), which uses a PIC32MX microcontroller. It controls the motors, reads the encoder values and monitors position sensors. Control input signals are processed in a control algorithm and provide pulse-width modulated (PWM) signals to integrated servo motor controller units (ESCON Module 50/5, Maxon motor, Sachseln, Switzerland and SC5008, Faulhaber Group, Germany) that drive the prosthesis movements.

A Raspberry Pi 3 acts as the central command and processing unit. It reads different sensors like an analog frontend, inertial measurement units, pressure sensors and ultrasound sensors. Depending on the processed EMG data, a control signal is sent to the control unit. A custom developed hardware attached on top (HAT) holds the analog frontend, the ADS1299 (Texas Instruments Inc., Dallas, TX, USA) that is capable of acquiring sensor and other bioelectrical signals simultaneously on eight channels. The motion and position data is gathered using a 9-axis inertial measurement unit (MPU9250, InvenSense Inc., San Jose CA, USA). It will be used for predictive algorithms that improve the control dynamics and accuracy of the prosthesis. Pressure and ultrasound data is used to refine the arm position.

To close the loop, we use electrical stimulation to provide sensory feedback. An additional HAT is under development, to integrate the stimulator into the portable system. With the focus on the elbow joint, the feedback will help to implement more natural movement patterns and intuitive control.

3 Results

The elbow joint can lift a weight of maximal 3.3 kg with a lever of 30 cm through the entire range of motion within 2 s. This results in traction on the wire rope of 437 N. The ranges of motion are 120° for the elbow joint and 270° for the wrist joint. Nevertheless, in a target reach test of the elbow joint with 100 repetitions, the reproducible movement to an end-position of the fingertips had an accuracy of 3.4 mm.

Due to the different construction materials, we could manage to keep the weight of the whole arm around 600 g in the transhumeral case, where two degrees of freedom are needed. The weight will even decrease with a lower level of amputation.
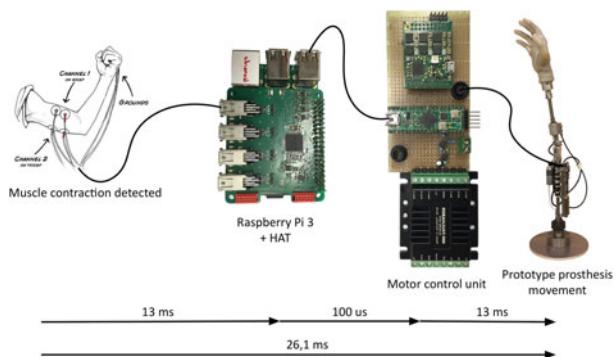
Fig. 2 System delay [5]

The driving components that consist of the motors and the corresponding gearboxes have a maximum weight of around 1.1 kg which also decreases if only one degree of freedom is used.

Assuming a full load of 3.3 kg, the average power consumption to lift the arm is equal to 95 W. By using a 24 V battery with a capacity of 2200 mAh, 1000 lifting operations would be feasible.

Electromechanical Delay: In the physiological pathway of humans, the time from the activation of the muscle to the actual stretch of the tendon respectively to force production takes 20–100 ms [4].

Our system (Fig. 2) needs 7 ms to detect the muscle contraction, process the EMG signal and calculate the corresponding control signal if a predefined threshold of the EMG signal is exceeded. Within this 7 ms, the data is also stored via HDF5 file format to the internal memory of the RPi3 for post-processing.

The system requires additionally 100 us to send the control signal to the control unit via UART. This signal is processed, the corresponding PWM is generated with a PIC32 microcontroller and sent to the motor drivers which again drive the actuators and consequently the prosthesis. The control signal codes which actuator to choose and its intensity. This takes another 13 ms which sums up to a resulting delay of 20.1 ms from the muscle contraction to the movement of the prosthesis. This means that our system can compete with the natural activation of muscles in the matter of speed and the controller delay is too small to influence the responsiveness of the prosthesis.

4 Discussion

The system provides a novel bionic design that allows usage not only for transradial but also transhumeral amputation. The proximal weight distribution and the used materials increase the wearing comfort in daily tasks and mimic to a high extent physiological conditions. The control system reads multiple sensors which improve the accuracy of the position data and with the given sensory feedback ultimately increases the control accuracy of the prosthesis. The short system delay will not only be beneficial for control purposes but also increase the acceptance of the prosthesis in daily tasks.

References

1. E. A. Biddiss and T. T. Chau, "Upper limb prosthesis use and abandonment: a survey of the last 25 years," *Prosthet. Orthot. Int.*, vol. 31, no. 3, pp. 236–257, Sep. 2007.
2. T. R. Farrell and R. F. Weir, "The optimal controller delay for myoelectric prostheses," *IEEE Trans. neural Syst. Rehabil. Eng. a Publ. IEEE Eng. Med. Biol. Soc.*, vol. 15, no. 1, pp. 111–118, Mar. 2007.
3. L. Resnik, M. R. Meucci, and S. Lieberman-klinger, "Advanced Upper Limb Prosthetic Devices: Implications for," *YAPMR*, vol. 93, no. 4, pp. 710–717, 2012.
4. G. Johns, E. Morin, and K. Hashtrudi-Zaad, "The role of electromechanical delay in modelling the EMG-force relationship during quasi-dynamic contractions of the upper-limb," *Proc. Annu. Int. Conf. IEEE Eng. Med. Biol. Soc. EMBS*, vol. 2016–Oct, pp. 3634–3637, 2016.
5. Adapted from https://backyardbrains.com/experiments/img/bicep_tricep.jpg licensed under CC BY-SA 3.0 [Accessed: 17-Jan-2018].

A Wearable Gait Assessment System for Evaluating Post-stroke Patients' Rehabilitation

C. Y. Wu and Tainsong Chen

Abstract

Most of the post stroke patients are common with walking difficulty. The gait pattern could be taken as the severity of the patients. About 88% of stroke patients have certain degrees of hemiparesis. Hemiparesis will attribute to weakness of one side of the body. For post-stroke patients, the rehabilitation is a tedious and long term process. It needs tremendous medical cost and care manpower. Therefore, how to develop a simple wearable device for evaluating the rehabilitation outcome becomes a needful clinical issue. In this study, two wearable devices with accelerometer and gyroscope are placed in both sides of foot. Therefore, the gait patterns can be obtained from the information of both side accelerometer and gyroscope. The gait pattern is also shown in smartphone through wireless techniques. This device can be used to evaluate the rehabilitation outcome and as biofeedback training for stroke patients. The system was tested when normal subject was asked to walk straight in comfortable or self-selected walking speed, but the stride length was limited to 1.2 m. The results indicated stride length closed to 1.2 m. And the symmetry ratio of various spatiotemporal parameters between both feet is around 1.0 which means normal.

C. Y. Wu (✉) · T. Chen
Department of Biomedical Engineering, National Cheng Kung University, Tainan, 70101, Taiwan, China
e-mail: p86054161@mail.ncku.edu.tw

1 Introduction

The cerebrovascular and related diseases ranked the fourth according to the 2016 statistics of causes of death from the Taiwanese Ministry of Health and Welfare [1]. The cerebrovascular accident or the stroke is a type of cerebrovascular diseases, the prevalence rate of stroke for Taiwanese people aged 36 and older about 16.42‰ [2]. Hyperglycemia, hyperlipidemia and hypertension can cause higher probability of stroke. As the most common type of nervous system disease, the condition and severity of outcome after stroke may vary based on the location of brain lesion [3].

Based on so many types of conditions which may develop after a stroke, the National Stroke Association classified the post-stroke conditions into three type: physical, emotional and cognition [4], and many post-stroke conditions are physical ones. About 50% of patients performed disability on walking initially and 12% depended on assistance to walk [5], and the presentation of hemiplegic gait is as the most common type of the abnormal gait [6]. Hemiparesis will weaken one side of the body, about 88% of stroke patients have certain degrees of hemiparesis [7].

The characteristic of a normal gait is supporting and propelling body by continuous and repeat swinging lower limbs. Hence, there is the largest stability between both feet for health people ideally. And the asymmetric walking pattern that the stability was reduced as a most common characteristic after suffering hemiparesis [8]. Hemiplegic gait will affect spatial, temporal, kinematic and dynamic performance of gait characteristics, including stance time, swing time, single support time, double support time, speed, cadence, step length and stride length.

The Performance of gait and walking can be considered as a factor to assess whether health. There are a lot of methods which are from requiring no equipment at all to expensive and complex system to assess gait. Even though as a common rule, those elaborate systems will provide higher quality of objective data more than simpler devices or

equipment, it doesn't mean that those simpler techniques are unworthy of being used. The elaborate systems have been verified that they aren't suitable for clinical applications based on some characteristics such as expensive, requirement of large space and time-consuming. So let alone using at home.

In the study, inertial measurement units are used in extraction of gait characteristics from walking. As a technique is used in aircrafts, helicopters and unmanned aircraft system originally [9], its size has been progressively minimized and then it can be used in other applications due to development of microelectromechanical systems. It isn't limited by large space or laboratory environment. A lot of studies used inertial measurement units for their experiments because they are wearable and cheaper than optical motion capture system or other instrument. Inertial measurement units consist of accelerometer and gyroscope, they can measure acceleration and angular velocity. The gait patterns can be obtained from the information of accelerometer and gyroscope.

2 Methods and Material

2.1 Experimental Design

The system was tested when normal subject was asked to walk straight in comfortable or self-selected walking speed, but the stride length was limited to 1.2 m.

2.2 Inertial Measurement Units

In the study, two wearable inertial sensors which contains MPU-9250 are placed in both sides of foot (Fig. 1). MPU-9250 which contains 3-axis accelerometer, 3-axis gyroscope and magnetometer is a 9-axis inertial measurement unit. The measurement range, accuracy and precision are affected by specification of each element, including gyroscope full scale range, gyroscope sensitivity, gyroscope rate noise, accelerometer full scale range and accelerometer sensitivity. There is a list that contains the setting of inertial measurement in the study (Table 1).

Fig. 1 The sensor placement

2.3 Bluetooth Low Energy

The sensor's way of communication is Bluetooth Low Energy, that is Bluetooth 4.0. This protocol has a lot of advantages which are better than Classic Bluetooth such as high reliability, low cost and low power consumption, quick start and instant connection, increased transmission distance and high security.

For two Bluetooth devices which are communicating each other can be divided into peripheral and central device. The peripheral device would transmit data to central device. In the system, Bluetooth module would transmit packet which contains all 12 bytes of data after receiving measurement results from accelerometer and gyroscope (Fig. 2). That is the measurement of each axis is 2 bytes. The sensor would generate 600 bytes of data per second due to the sampling rate of analog-to-digital converter is 50 Hz. Based on every packet only includes current measurement, it can prevent error that different sampling is mistaken for same sampling.

2.4 Smartphone Application

Android platform gained the highest market share so far, therefore the system was developing on android by JAVA. The smartphone would receive packet from inertial sensor by Bluetooth Low Energy. The development of smartphone application not only need to consummate function but also consider design of user interface and user experience. In order to prevent the mistake operation from users, they must follow the state machine that we design. And finally, the application would visualize the data that inertial sensor measured and display some analysis result (Fig. 3).

2.5 Feature Extraction Algorithm
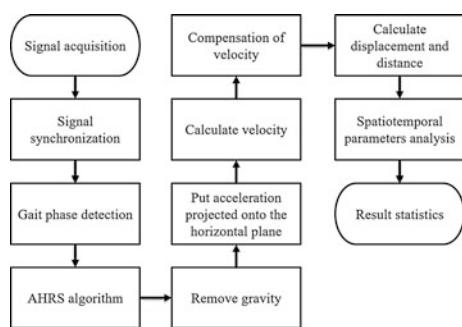
There is a flow chart which describe algorithm in the system (Fig. 4). First, even though both sensors were 50 Hz of sampling rate, they weren't synchronization on sampling. Hence, the system would record the time stamp when it received any packet and then it can calculate the data at a certain time by means of interpolation.

Theoretically, the inertial technology is able to achieve autonomous control and measurement which doesn't rely on external information. But in fact, there are a lot of error in the measurement result based on the characteristics of accelerometer and gyroscope. Acceleration which was measured by accelerometer is consist of linear acceleration and gravitational acceleration. If object which is measured is moving, it is hard to be separated for two types of acceleration. Furthermore, the simple integration of acceleration

Table 1 MPU-9250 specifications

Gyroscope full scale range	±250 °/s
Gyroscope sensitivity	131 LSB/°/s
Gyroscope rate noise	0.01 dps/√Hz
Accelerometer full scale range	±2 g
Accelerometer sensitivity	16384 LSB/g

x-axis Acc	y-axis Acc	z-axis Acc	x-axis Gyr	y-axis Gyr	z-axis Gyr
2 bytes	2 bytes	2 bytes	2 bytes	2 bytes	2 bytes

Fig. 2 Packet architecture

Fig. 3 User interface

Fig. 4 Flowchart of algorithm

would only result in useless data due to baseline drift. And drift effect would certainly exist in gyroscope. The effect may result in angular velocity not zero even if the object is static. In summary, it is necessary to use some methods for inertial signal processing.

The attitude and heading reference system can provide attitude information by inertial measurement units. There is a famous algorithm that it was named Madgwick method, it fuses gyroscope, accelerometer and magnetometer information to estimate correct attitude of object. In the study, we adjust the algorithm to fit the people's gait, and try to estimate attitude, velocity and displacement.

The first, in order to minimize accumulation of error, the system would correct repeatedly signal integration based on temporary stance phase [10]. The stance phase was defined by signal pattern on pitch rotation when walking. The second, both signal would be restructured by Madgwick method. The 3-axis angular velocity was corrected by PID controller. The third, indirect estimation of linear-acceleration by definition of attitude of the wearable sensors at present. The last, putting acceleration projected onto the horizontal plane so as to calculate the moving distance of something. But unfortunately, everything has own coordinate, the linear-acceleration exists in the something itself. The linear-acceleration which is in plane frame of reference must be transformed into ground frame of reference.

2.6 Assessment of Symmetry

The direct and indirect information which is from inertial sensor can be treated as a characteristic of 3 dimensions of individual. And because the gait pattern could be taken as the severity of the patients, especially gait symmetry which have been widely used to evaluate post-stroke gait [11]. The following is the equation of symmetry ratio.

$$Symmetry\ ratio = V_{paretic}/V_{non-paretic} \tag{1}$$

There are some spatiotemporal parameters can be taken to analyze symmetry of gait pattern. Including walking speed, stride length, proportion of single support time to double support time, cadence, step length and proportion of stance time to swing time.
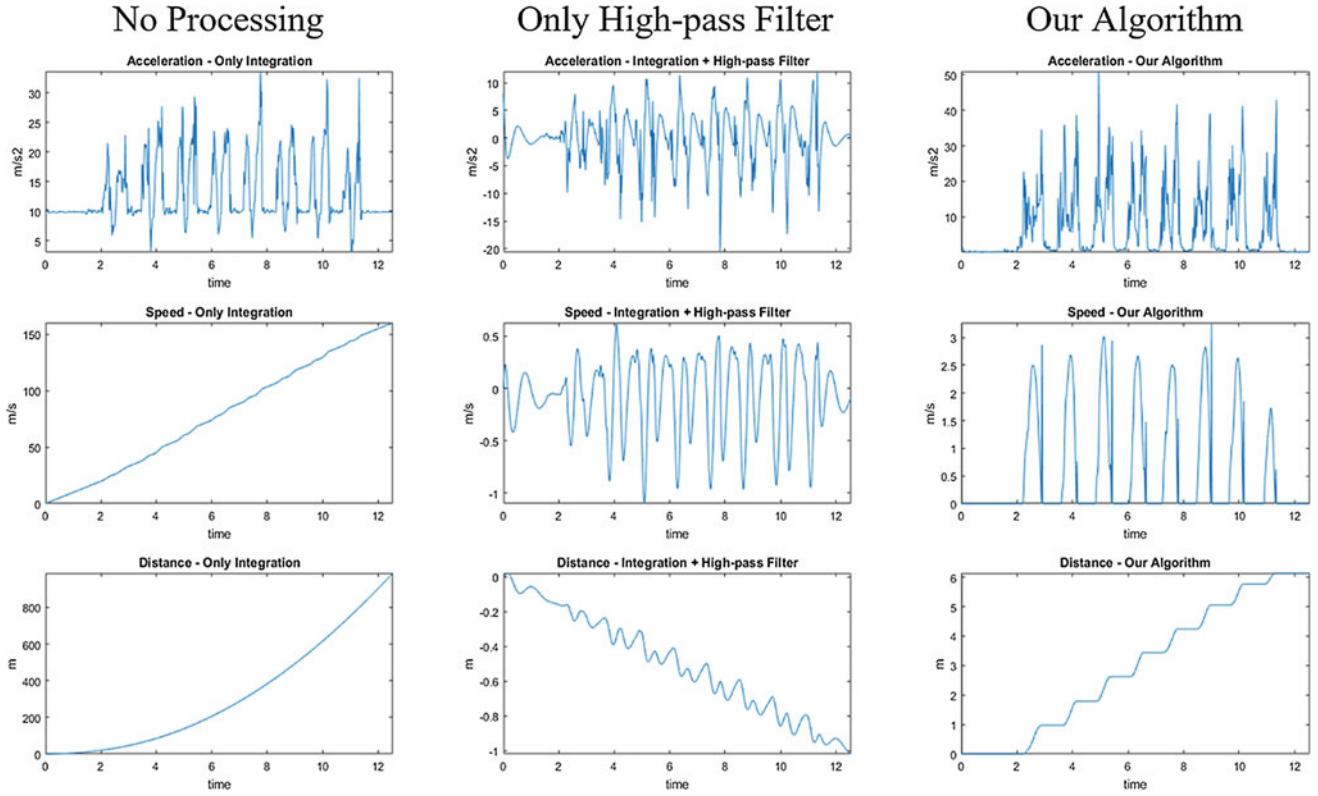
Fig. 5 Comparison among different processing

3 Results

The results after different processing algorithm for same data are shown in Fig. 5. According to common knowledge, the relationship among acceleration, velocity and displacement is differentiation and integration, like first column. But the results will be not consistent actually. Now consider the effect of gravity, a simple method was used to eliminate gravity which is a DC component. Just only using a high-pass filter, the result was still not good enough. The final column was the results after our developed algorithm. The results are much better than other processing.

And then, the system was used to analyze two subjects gait (Tables 2 and 3). The theoretical proportion of gait cycle could be used in the preliminary test for evaluation of spatial characteristics. For distance, it could be assessed based on the experimental design, too.

4 Discussion

According to the mentioned limitations above on accelerometer and gyroscope, it is impossible to define stance phase and swing phase only by raw data. But unfortunately, it is required to process raw data based on definition of stance phase and swing phase.

In order to resolve the problem, there are a lot of papers indicated that the stance phase and swing phase could be recognized by pattern of pitch signal of gyroscope. But the study considered that it is only suitable for normal subjects. It is difficult even impossible to define all abnormal gait pattern by normal subject's gait pattern. In this study, a suggestion is that using signal magnitude vector to detect and define the stance phase and swing phase for paretic lower limb. No matter what the performance of people's gait, the system can detect it successfully.

Table 2 Preliminary system testing: a normal gait 1

	Left	Right	Ratio (L/R)
Speed	1.67 ± 0.05 m/s	1.96 ± 0.11 m/s	0.86 ± 0.04
Distance	0.83 ± 0.05 m	0.89 ± 0.07 m	0.93 ± 0.06
Theoretical value	1.10–1.30 m	1.10–1.30 m	1.00
Stance time/swing time	1.27 ± 0.17	1.53 ± 0.05	0.83 ± 0.10
Theoretical value	1.50	1.50	1.00
Single support time/double support time	3.23 ± 0.47	3.63 ± 0.63	0.89 ± 0.04
Theoretical value	2.00	2.00	1.00

Table 3 Preliminary system testing: a normal gait 2

	Left	Right	Ratio (L/R)
Speed	1.83 ± 0.13 m/s	1.51 ± 0.12 m/s	1.22 ± 0.12
Distance	0.85 ± 0.05 m	0.80 ± 0.08 m	1.07 ± 0.11
Theoretical value	1.10–1.30 m	1.10–1.30 m	1.00
Stance time/swing time	1.65 ± 0.12	1.23 ± 0.10	1.36 ± 0.17
Theoretical value	1.50	1.50	1.00
Single support time/double support time	3.33 ± 0.51	2.81 ± 0.40	1.19 ± 0.07
Theoretical value	2.00	2.00	1.00

5 Conclusion

A wearable gait assessment system based on smartphone has been implemented. This system can be used as a rehabilitation assessment and biofeedback training tool for post-stroke patients.

Conflict of Interest I declare that we have no conflict of interest, financial or otherwise.

References

1. Ministry of Health and Welfare, "2016 Statistics of Causes of Death," 2017.
2. B.-S. Yip, "Cerebrovascular disorder in recent Taiwan and treatment strategy in acute ischemic stroke," Journal of the Chinese Statistical Association, vol. 55, pp. 63–66, 2017.
3. C.-L. Chen, F.-T. Tang, H.-C. Chen, C.-Y. Chung, and M.-K. Wong, "Brain lesion size and location: effects on motor recovery and functional outcome in stroke patients," Archives of physical medicine and rehabilitation, vol. 81, pp. 447–452, 2000.
4. National Stroke Association. (2014). Post-stroke conditions. Available: http://www.stroke.org/we-can-help/survivors/stroke-recovery/post-stroke-conditions.
5. B. Balaban and F. Tok, "Gait disturbances in patients with stroke," PM&R, vol. 6, pp. 635–642, 2014.
6. A. Armitage, Advanced Practice Nursing Guide to the Neurological Exam: Springer Publishing Company, 2015.
7. S. J. Cuccurullo, Physical medicine and rehabilitation board review: Demos Medical Publishing, 2014.
8. K. K. Patterson, W. H. Gage, D. Brooks, S. E. Black, and W. E. McIlroy, "Evaluation of gait symmetry after stroke: a comparison of current methods and recommendations for standardization," Gait & posture, vol. 31, pp. 241–246, 2010.
9. Z.-L. Deng, "Inertial Technology", Hyweb Technology Co. Ltd., 2011.
10. Y.-S. Lee, C.-S. Ho, Y. Shih, S.-Y. Chang, F. J. Róbert, and T.-Y. Shiang, "Assessment of walking, running, and jumping movement features by using the inertial measurement unit," *Gait & posture*, vol. 41, pp. 877–881, 2015.
11. K. K. Patterson, W. H. Gage, D. Brooks, S. E. Black, and W. E. McIlroy, "Evaluation of gait symmetry after stroke: a comparison of current methods and recommendations for standardization," *Gait & posture*, vol. 31, pp. 241–246, 2010.

Spherical Angular Analysis for Pelvis Coordination Assessment on Modified Gait

Carlos Rodrigues, Miguel Correia, João Abrantes, Jurandir Nadal, and Marco Benedetti

Abstract

This study presents and applies 3D spherical angular analysis in relation with 2D polar coordinates to assess anatomic pelvic movement on modified gait, namely stiff knee (SKG) gait and slow running (SR) comparing with normal gait (NG). Subject specific analysis was performed of an adult healthy male based on inverse kinematics from in vivo and noninvasive capture at human movement lab of reflective markers position from pelvis anatomical selected points with Qualisys camera system during a complete stride of NG, SKG and SR. Radial distance (R), pitch (ψ) and azimuth (λ) angular phases were computed from pelvic angle-angle diagrams (θ_T, θ_C, θ_S) at transverse (T), coronal (C) and sagittal (S) planes, and angular phase (ϕ) and planar radial distance (r) polar coordinates computed from pelvic angle-angle diagrams projections at cartesian planes (θ_T, θ_C), (θ_T, θ_S), (θ_C, θ_S). Average radial distances and phase standard deviation were assessed on spherical and polar coordinates.

Keywords

Pelvis coordination • Angular analysis • Spherical coordinates

C. Rodrigues (✉) · M. Correia
FEUP, Faculty of Engineering University of Porto, Porto, Portugal
e-mail: c.rodrigues@fe.up.pt

C. Rodrigues · M. Correia
INESC TEC, Institute for Systems and Computer Engineering, Technology and Science, Porto, Portugal

J. Abrantes
MovLab, Interactions and Interfaces Laboratory, Lisbon, Portugal

J. Nadal
UFRJ, Federal University of Rio de Janeiro, Rio de Janeiro, Brazil

M. Benedetti
UFPE, Federal University of Pernambuco, Recife, Brazil

1 Introduction

Pelvic coordination is a determinant factor in human gait due to its unique role on lower limbs interconnection and HAT (head, arms, trunk) support. People walk at lower velocities and run for higher velocities. Although at gait and running the movement of the legs occurs alternately, gait and running are different in many other aspects. As a result of injury or pathology, people often adopt modified gait (MG) such as stiff knee gait (SKG) and slow running (SR) as an alternative to normal gait (NG). Stiff knee is characterized by decreased range of motion of the knee in patients with cerebral palsy or after stroke [1, 2] with impact at other joints and segments kinematics, namely on pelvic coordination due to integrated nature of human body movement [3]. While lower limbs dominant flexion-extension movement during gait occurs mainly at sagittal plane, gait pelvic movement presents higher displacement amplitudes at transverse (T) and coronal (C) planes with lower amplitude at sagittal (P) plane. Although most frequent study in human gait corresponds to 2D planar analysis, the study of pelvic movement in NG and in particular MG requires the use of 3D aggregated analysis. While most so-called 3D analysis on human movement consist of three 2D analysis, proposed method corresponds to a single analysis of the three considered dimensions. The purpose of this work is to apply 3D spherical coordinates in relation with 2D polar coordinates to analyze pelvic angular movement coordination at T-C-S planes in SKG and SR for comparison with NG.

2 Materials and Methods

2.1 Experimental Tests

According to the interest on specific subject study and difficulty on average sample in representing individual subject, attention was focused on case study of one adult healthy

male subject 70 kg mass and 1.86 m height during NG, SKG and SR at motion capture laboratory. The experiment was performed in accordance with the ethical guidelines of the North Denmark Region Committee on Health Research Ethics (N-20130014) and the participant provided full written informed consent prior to the experiment. Adhesive reflective markers were attached to subject palpable skin surface including right and left anterior and posterior superior iliac spines (rasis/lasis/rpsis/lpsis). 3D cartesian coordinates of reflective markers were obtained from direct linear transformation (DLT) of acquired image motion with calibrated eight camera Qualisys system at 100 Hz. Inverse kinematics was performed with generation of stick-figure model based on static trial, with over-determinate kinematic analysis over the dynamic trial and joint angles, morphing Twente Lower Extremity Model (TLEM) to match the size and joint morphology of the stick-figure model obtaining scaled subject dimension of the coronal (C), sagittal (S) and transverse (T) planes.

2.2 Data Analysis

3D spherical coordinates of pelvic angle-angle diagrams (θ_T, θ_C, θ_S) at T, C, S planes were considered for calculation of radial distance (R), pitch (ψ) and azimuth (λ) angular phases. Pelvic angle-angle diagrams were projected at the cartesian planes (θ_T, θ_C), (θ_T, θ_S), (θ_C, θ_S) and polar coordinates considered for calculation of angular phase (ϕ) and planar radial distance (r). Average radial distance and phase standard deviation on entire stride of NG, SKG and SR were calculated for the spherical and polar coordinate systems. Angular displacements were analyzed at angular phase (ϕ) and radial distance (r) in polar coordinates (r, ϕ) at (θ_x, θ_y) for T-C, T-S and C-S, as well as in spherical coordinates at azimuth (λ), pitch (ψ) angular phases and radial distance (R) of the T-C-S angular displacements (θ_x, θ_y, θ_z) as defined by Eqs. (1) and (2),

$$\phi = \text{atan2}(\theta_y/\theta_x); r = (\theta_x^2 + \theta_y^2)^{1/2}, \tag{1}$$

$$\lambda = \text{atan2}(\theta_y/\theta_x); \quad \psi = \text{atan}(\theta_z/(\theta_x^2 + \theta_y^2)^{1/2}); \\ R = (\theta_x^2 + \theta_y^2 + \theta_z^2)^{1/2}. \tag{2}$$

3 Results

Figure 1 presents spherical plots of pelvic angle-angle diagrams (θ_T, θ_C, θ_S) at transverse (T), coronal (C) and sagittal (S) planes with solid circles corresponding to visible and open circles to occluded points for spherical coordinates

calculation azimuth (λ), pitch (ψ) angular phases and radial distance (R) including entire stride of NG, SKG and SR.

Figure 2 presents projected pelvic angle-angle diagrams at the cartesian planes (θ_T, θ_C), (θ_T, θ_S), (θ_C, θ_S) including entire stride of NG, SKG and SR, with polar coordinates considered for calculation of angular phase (ϕ) and planar radial distance (r).

Figure 3 presents rose diagrams of the pelvic angle-angle at the cartesian planes (θ_T, θ_C), (θ_T, θ_S), (θ_C, θ_S) with polar
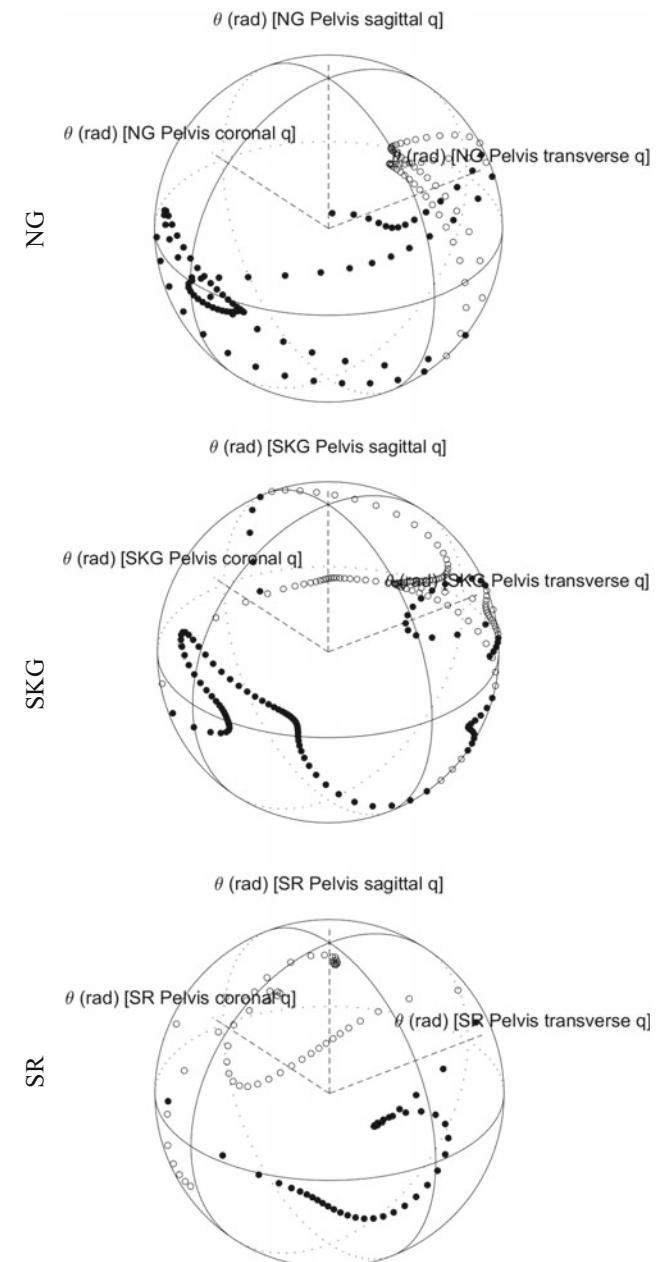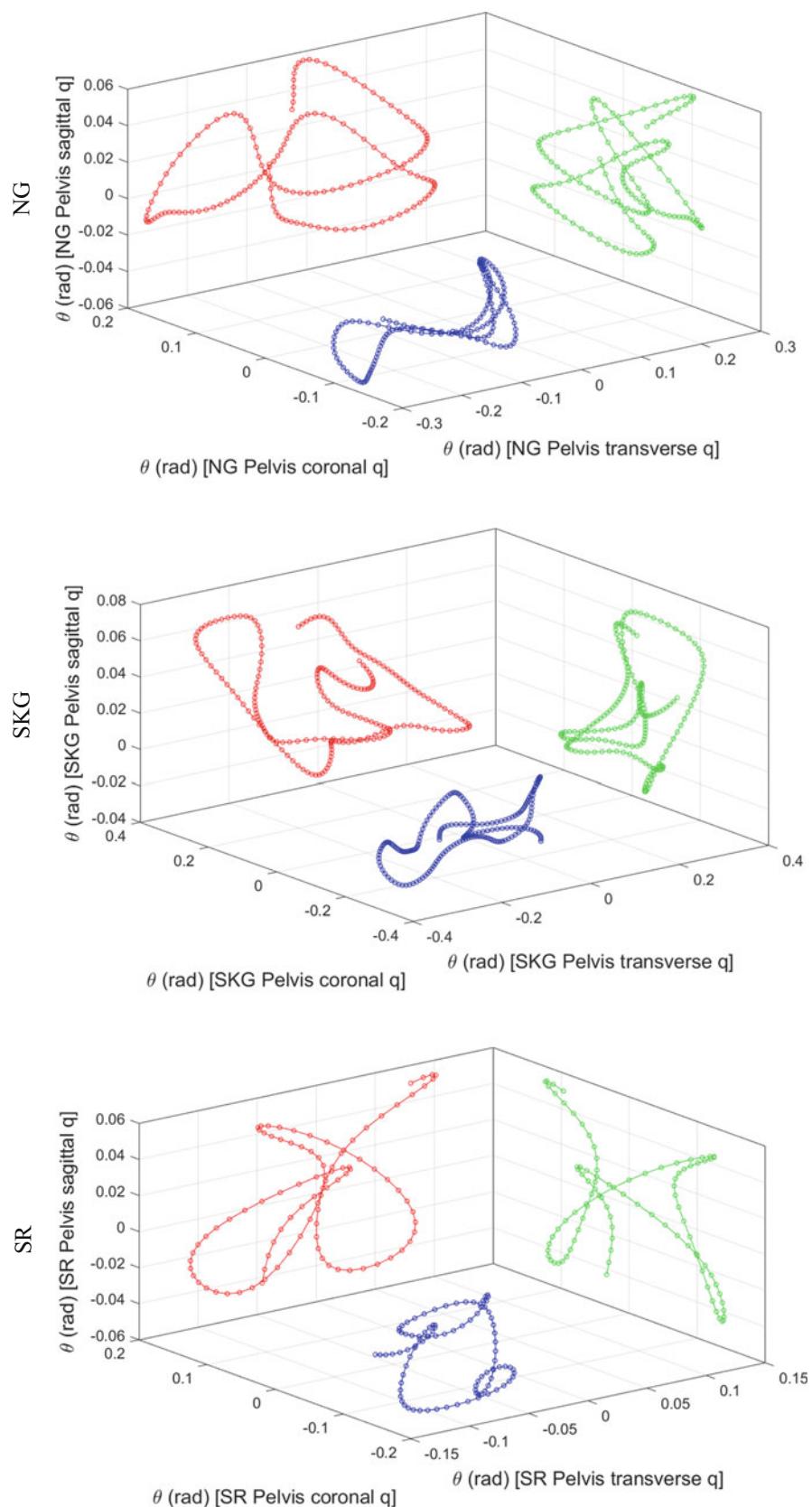
Fig. 1 Spherical plots of pelvic angle-angle diagrams (θ_T, θ_C, θ_S) at transverse (T), coronal (C) and sagittal (S) planes on entire stride of NG, SKG and SR

Fig. 2 Projected pelvic angle-angle diagrams at the cartesian planes (θ_T, θ_C), (θ_T, θ_S), (θ_C, θ_S) of transverse (T), coronal (C) and sagittal (S) planes on entire stride of NG, SKG and SR
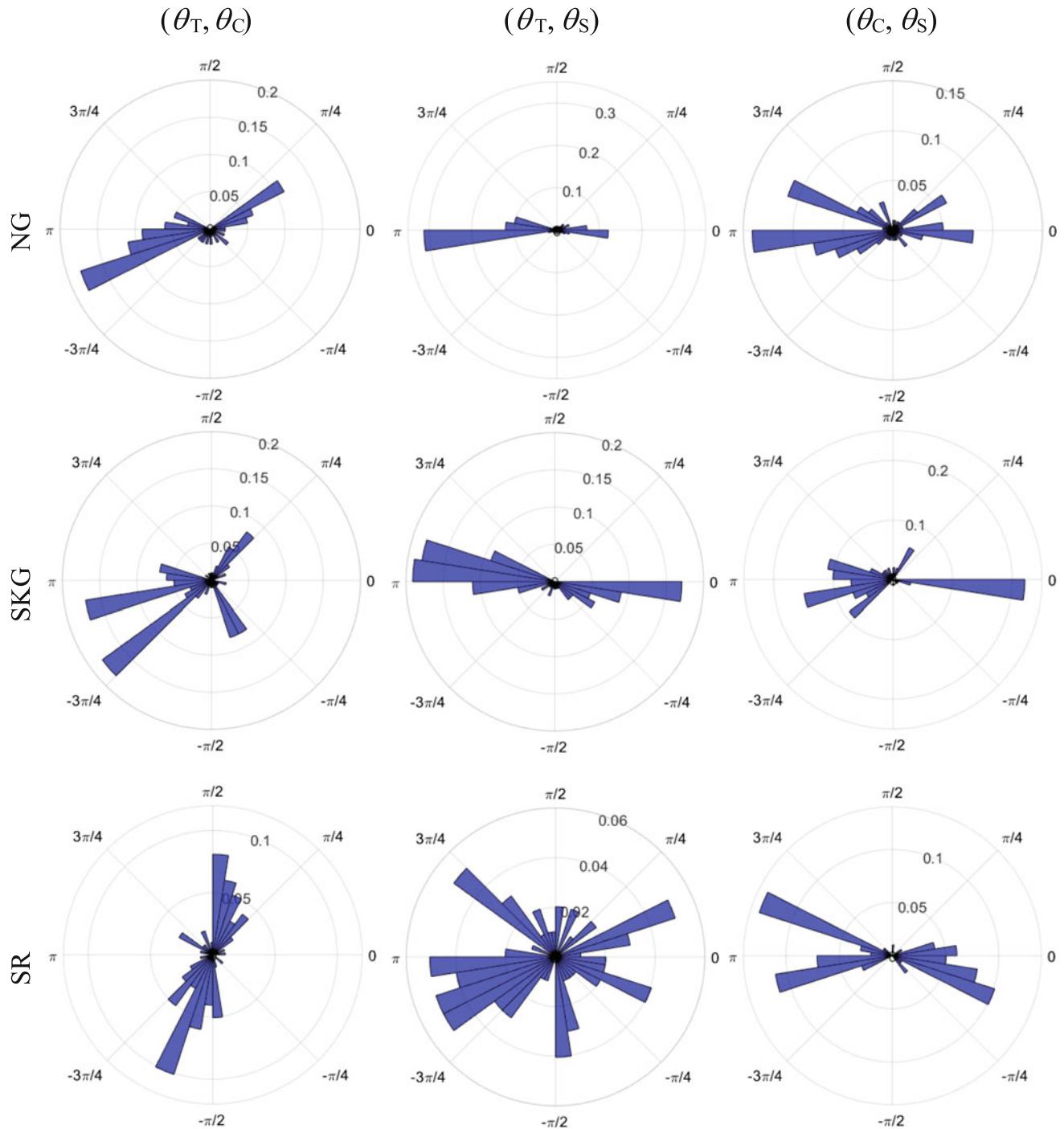
Fig. 3 Rose diagrams of the pelvic angle-angle at cartesian planes (θ_T, θ_C), (θ_T, θ_S), (θ_C, θ_S) of transverse (T), coronal (C) and sagittal (S) planes on entire stride of NG, SKG and SR

coordinates considered for calculation of angular phase (ϕ) and planar radial distance (r) on entire stride of NG, SKG and SR.

SKG presents higher average radial distance (R) than NG ($p \geq 0.05$) both higher than SR ($p < 0.05$), with NG presenting higher standard deviation of angular phases azimuth (λ) at NG than SKG ($p \geq 0.05$) both higher than SR (p 0.05), and the opposite at pitch (ψ) angular phases presenting lower standard deviation at NG than SKG (p 0.05) both lower than SR ($p < 0.05$), Table 1.

As regards to polar coordinates analysis of pelvic angle-angle diagrams, Table 2, several statistical

Table 1 Average radial distance (R) and standard deviation of angular phases azimuth (λ) and pitch (ψ) at spherical coordinates of pelvic angle-angle diagrams (θ_T, θ_C, θ_S)

	NG	SKG	SR
R avg. (rad)	0.147	0.158	0.099
λ std. dev. (rad)	2.055	2.000	1.762
ψ std. dev. (rad)	0.211	0.255	0.278

Table 2 Average planar distances (r) and standard deviation of the angular phases (ϕ) at polar coordinates of pelvic angle-angle diagrams (θ_T, θ_C), (θ_T, θ_S) and (θ_C, θ_S)

	NG	SKG	SR		NG	SKG	SR
r_{TC} avg. (rad)	0.145	0.155	0.095	ϕ_{TC} std. dev. (rad)	2.055	2.000	1.762
r_{TS} avg. (rad)	0.134	0.123	0.050	ϕ_{TS} std. dev. (rad)	2.370	2.238	1.918
r_{CS} avg. (rad)	0.057	0.094	0.086	ϕ_{CS} std. dev. (rad)	2.161	2.308	2.088

significative differences were detected on average planar distances (r) and angular phases (ϕ) standard deviation at 0.05 significant level.

4 Discussion and Conclusion

Applied spherical analysis presented more adequate to pelvic movement assessment due to its ability to consider at a single step 3D coordinate of natural pelvic movement in contrast with the three 2D polar coordinates. Advantage of one 3D spherical analysis in relation to three 2D polar analysis is also associated with the reduction of the number of necessary parameters to assess pelvic movement, without loss of determinant information. Nevertheless the circular nature of spherical and polar coordinates requires the use of directional statistics to assess distribution concentration and mean direction. Variation of these parameters along gait cycle time present as key issues regarding information on pelvic movement coordination at each anatomical geometrical plane and gait phase. The authors declare that they have no conflict of interest.

References

1. Böhm, H., Hösl, M, Schwameder, H., Döderlein, L.: Stiff-knee gait in cerebral palsy: how do patients adapt to uneven ground? Gait Posture 39(4), 1028–1033 (2014).
2. Campanini, I., Merlo, A, Damiano, B.: A method to differentiate the causes of stiff-knee gait in stroke patients. Gait Posture 38(2), 165–169 (2013).
3. Perry, J., Burnfield, J. M.: Gait Analysis: Normal and Pathological Function. 2nd edn. SLACK Incorporated, Thorofare, NJ (2010).

Basic Study for 3D Kinematic Measurement of Patella from Single-Plane Fluoroscopic Image Using Intensity-Based 2D/3D Registration

Takaharu Yamazaki, Yuichi Hayashi, Tetsuya Tomita, Kenichi Kono, Yoshinobu Sato, and Kazuomi Sugamoto

Abstract

The 3D measurement of dynamic knee kinematics under in vivo conditions is highly valuable for understanding the effects of joint diseases, dysfunction and for evaluating the outcome of surgical procedures. For artificial knee implants, to achieve 3D measurement of the dynamic kinematics, 2D/3D registration techniques which use X-ray fluoroscopic images and computer-aided design model of the implants have been applied to clinical cases. These fluoroscopic techniques have also been applied for motion measurement in joints without implants in recent years, where 3D bone models created from CT or MRI images are utilized. In previous studies, however, the pose estimation accuracy for patella was not sufficient for analyzing 3D knee kinematics, particularly out-of-plane rotation error was relatively large because of small shape and poor geometrical feature of patella. Therefore, this study presents a method to determine 3D kinematics of patella using single-plane fluoroscopic image. The 3D pose of patella is estimated using an intensity-based 2D/3D registration technique, which uses a digitally reconstructed radiography (DRR) image created from 3D bone volume model. The 3D bone volume model for patella was created using CT scan data from a single subject. The 3D pose of the patella model is estimating by maximizing similarity measures between the DRR and fluoroscopic images iteratively with an optimization technique. In order to validate the pose estimation accuracy of patella including femur and tibia/fibura using the intensity-based 2D/3D registration, computer simulation test was performed. A set of synthetic silhouette images was created for each knee model in known typical orientations, and the test was carried out using three similarity measure methods. The result of computer simulation test showed that the root mean square errors were around 1.0 mm, 1.0° except for out-of-plane translation, and the reliability and feasibility of present method was demonstrated.

Keywords

Patella • 3D kinematics • 2D/3D registration

1 Introduction

Quantitative assessment of 3D dynamic knee kinematics under in vivo conditions is very important for understanding the effects of joint diseases, dysfunction and for evaluating the outcome of surgical procedures. For artificial knee implants, to achieve 3D measurement of the dynamic kinematics, feature-based 2D/3D registration techniques which use X-ray fluoroscopic images and computer-aided design model of the implants have been applied to clinical cases [1–6]. These fluoroscopic techniques have also been applied for motion measurement in joints without implants in recent years, where 3D bone models created from CT or MRI images are utilized [7, 8].

In previous studies, however, the pose estimation accuracy for patella was not sufficient for analyzing 3D knee kinematics, particularly out-of-plane rotation error was relatively large because of small shape and poor geometrical feature of patella. To overcome this problem, some researchers have reported a system using biplane fluoroscopic images [9, 10]. However, with biplane fluoroscopy, a

T. Yamazaki (✉) · Y. Hayashi
Department of Information Systems, Saitama Institute of Technology, Fukaya, Japan
e-mail: yamazaki@sit.ac.jp

T. Tomita · K. Sugamoto
Division of Orthopaedic Biomaterial Science, Osaka University Graduate School of Medicine, Suita, Japan

K. Kono
Department of Orthopaedic Surgery, Graduate School of Medicine, The University of Tokyo, Tokyo, Japan

Y. Sato
Graduate School of Information Science, Nara Institute of Science and Technology, Ikoma, Japan

sufficient amount of space for testing cannot be ensured for knee joint undergoing dynamic motion, and it is difficult to analyze the knee motion for daily activities such as a walking and rising from chair. Problems such as limited space for testing, system complexity and increased radiation exposure remain unresolved. In this study, therefore, we present a method to determine 3D kinematics of patella using single-plane fluoroscopic image.

2 Methods

2.1 Condition and Requirement

To achieve pose estimation of patella including femur and tibia/fibura using single-plane fluoroscopic image, it is necessary to have an accurate geometrical model of the knee bone (patella, femur and tibia/fibura) and to know the geometrical parameters of the X-ray imaging system.

The 3D geometry of the knee bone is taken from CT scan data. Multidetector computed tomography (MDCT) data, the 2 mm axial slice with 512×512 image matrix was used to create 3D bone volume models of patella, femur and tibia/fibula. Segmentation of the bone was performed by applying a thresholding filter.

The geometrical parameters of the imaging system are determined with a 3D calibration cube and a non-linear calibration technique [11]. The calibration cube has evenly spaced 129 metallic markers, which are employed as calibration markers.

2.2 Intensity-Based 2D/3D Registration

The 3D poses of patella including femur and tibia/fibura are estimated using an intensity-based 2D/3D registration technique [12], which uses a digitally reconstructed radiography (DRR) image created from 3D bone volume model (described in Sect. 2.1). The DRR image is created by using a ray-sum method [13], which is the most basic projection technique. That is, the DRR is generated by casting a virtual X-ray through the 3D bone volume model to each pixel of the virtual image and integrating the 3D voxel value (CT value) along the virtual X-ray. The CT values on the virtual X-ray are also interpolated by using a trilinear interpolation technique, because the coordinate of the sampling position on the ray is not always integer number.

Thus, the 3D pose of the patella model is estimating by maximizing similarity measures between the DRR and actual fluoroscopic images iteratively with an optimization technique as shown in Fig. 1.
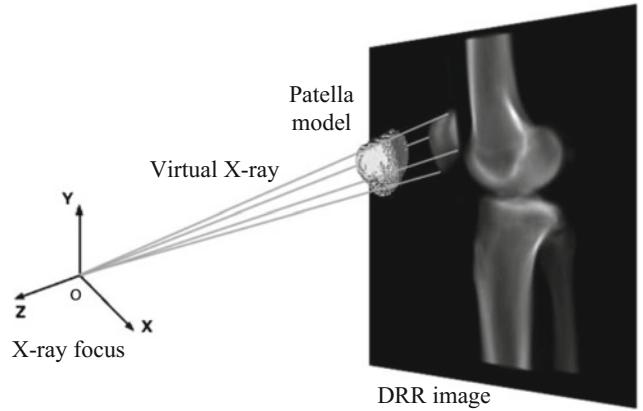
Fig. 1 Intensity-based 2D/3D registration utilizing DRR image

In this study, we used the following three similarity measure methods (NCC, GD and MI) for the intensity-based 2D/3D registration.

Normalized Cross Correlation (NCC) NCC is given by the following equation.

$$R = \frac{\sum_i \sum_j \left(I(i,j) - \overline{I}\right)\left(I_{drr}(i,j) - \overline{I}_{drr}\right)}{\sqrt{\sum_i \sum_j \left(I(i,j) - \overline{I}\right)^2} \sqrt{\sum_i \sum_j \left(I_{drr}(i,j) - \overline{I}_{drr}\right)^2}} \quad (1)$$

where $I(i, j)$ and $I_{drr}(i, j)$ are pixel values at coordinates (i, j) in the fluoroscopic image and DRR image, respectively.

Gradient Difference (GD) GD is given by the following equation.
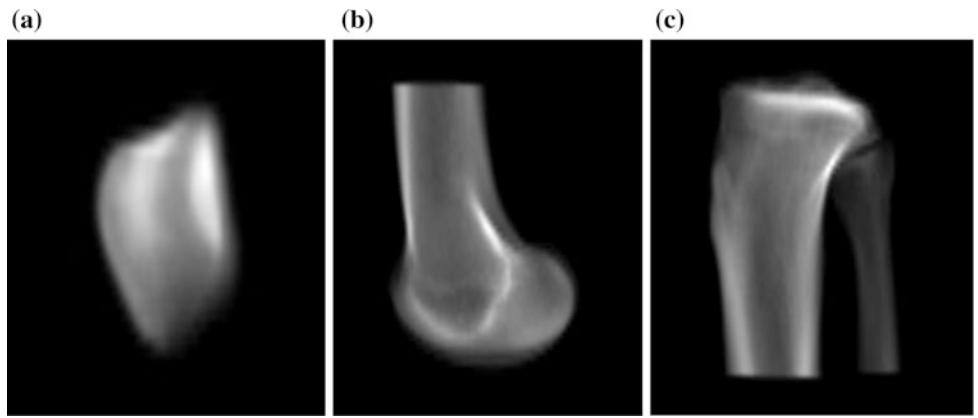
$$G(s) = \sum_i \sum_j \frac{A_v}{A_v + \left(I_{diffV}(i,j)\right)^2} + \sum_i \sum_j \frac{A_h}{A_h + \left(I_{diffH}(i,j)\right)^2} \quad (2)$$

$$I_{diffV}(i,j) = \frac{dI}{di} - s\frac{dI_{drr}}{di} \quad (3)$$

$$I_{diffH}(i,j) = \frac{dI}{dj} - s\frac{dI_{drr}}{dj} \quad (4)$$

where $I_{diffV}(i, j)$ and $I_{diffH}(i, j)$ are differences of vertical and horizontal differential image in the fluoroscopic image and DRR image, respectively. A_v and A_h are constants, which are the variance of the respective gradient fluoroscopy image. In this study, to create differential image, Sobel filter was used as differential filter.

Fig. 2 Representative DRR images used for computer simulation. **a** Patella, **b** Femur, **c** Tibia/Fibula

Mutual Information (MI) MI is given by the following equation.

$$S = \sum_a \sum_b p(a,b) \log_2 \frac{p(a,b)}{p(a)p(b)} \qquad (5)$$

where $p(a)$ and $p(b)$ are the probability distributions in the fluoroscopic image and DRR image, respectively, and $p(a, b)$ is the knee joint (patella, femur or tibia/fibura) probability distribution.

2.3 High-Speed Processing for Intensity-Based 2D/3D Registration

Generally, the computational cost for the intensity-based 2D/3D registration compared to the feature-based 2D/3D registration becomes higher because the amount of information increases by using the 3D bone volume model. In this study, we implemented parallel processing for the DRR generation using the Compute Unified Device Architecture (CUDA) [14] as one of the techniques for general-purpose computing on graphics processing units (GPGPU). Therefore, the calculation for the intensity-based 2D/3D registration can be performed faster.

3 Experimental Results

3.1 Computer Simulation Test

In order to validate the pose estimation accuracy of patella, femur and tibia/fibura using the intensity-based 2D/3D registration, computer simulation test was performed. A set of three synthetic silhouette images was created for each knee model in known typical orientations, and the test was carried out using three similarity measure methods (described in Sect. 2.2). Initial guess poses of each bone model were randomly given from within ±3 mm and ±3° of the correct value. Errors in the 3D pose of the model were determined by comparing the estimated pose to the known pose. Figure 2 shows representative DRR knee images used for computer simulation test.

The results of the computer simulation test are summarized in Tables 1, 2 and 3. The root-mean-square errors (RMSE) are given for each bone model (patella, femur and tibia/fibula). For each bone model, large RMSE was presented in the Z (out-of-plane) translation, but the Z translation error was relatively small (about 1 mm) for femur and tibia/fibula (Tables 2 and 3). The rotation error (Z (in-plane) and X, Y (out-of-plane) rotation error) was within 1° for all bone models including patella. In addition, the large

Table 1 RMS errors of 3D pose estimation for patella using three similarity measure methods (NCC, GD and MI)

	Translation (mm)			Rotation (°)		
	X	Y	Z	X	Y	Z
NCC	0.23	0.14	2.03	0.29	0.16	0.18
GD	0.22	0.13	2.10	0.25	0.10	0.16
MI	0.44	0.21	2.11	0.30	0.46	0.31

Table 2 RMS errors of 3D pose estimation for femur using three similarity measure methods (NCC, GD and MI)

	Translation (mm)			Rotation (°)		
	X	Y	Z	X	Y	Z
NCC	0.33	0.11	0.80	0.17	0.13	0.13
GD	0.30	0.12	0.91	0.16	0.10	0.13
MI	0.49	0.17	1.20	0.27	0.16	0.21

Table 3 RMS errors of 3D pose estimation for tibia/fibula using three similarity measure methods (NCC, GD and MI)

	Translation (mm)			Rotation (°)		
	X	Y	Z	X	Y	Z
NCC	0.30	0.12	0.67	0.59	0.23	0.36
GD	0.28	0.14	0.68	0.68	0.16	0.41
MI	0.43	0.16	0.95	0.54	0.12	0.32

difference of RMSE depended on similarity measure methods were not founded.

3.2 Convergence Time

In order to investigate convergence time (computation time) for the pose estimation of patella, femur and tibia/fibura using the intensity-based 2D/3D registration, we compared GPU parallel processing time using CUDA with CPU serial processing time. In this experiment, we performed the convergence test, with performance of CPU: Intel Core i5 2.70 GHz 4core, RAM: 8.00 GB, GPU: NVIDIA GeForce GTX 1070 1.68 GHz installed in a personal computer (OS: Windows 10 Home edition).

The results of the convergence time are summarized in Tables 4 and 5. By GPU parallel processing using CUDA, the computation time was dramatically improved (about tens

of times), and the computation time for patella was about 30 s.

4 Discussion and Conclusions

The intensity-based 2D/3D registration for 3D kinematic measurement of patella including femur and tibia/fibura using single-plane fluoroscopic image was performed successfully.

In computer simulation test, the RSME of the five variables except for Z (out-of-plane) translation were sufficiently within 1.0 mm and 1.0° for patella, femur and tibia/fibula, and also the Z translation error was relatively small (about 1 mm) for femur and tibia/fibula (Tables 2 and 3). The reason for this can be explained by large silhouette size and intensity information of femur and tibia/fibula compared to patella. The rotation error (Z (in-plane) and X, Y

Table 4 Convergence time by CPU serial processing for three similarity measure methods (NCC, GD and MI)

Computation time (s)			
	Patella	Femur	Tibia/Fibula
NCC	1052.3	2200.1	2373.9
GD	1312.6	2183.4	2547.3
MI	962.7	2170.5	2402.3

Table 5 Convergence time by GPU parallel processing using CUDA for three similarity measure methods (NCC, GD and MI)

Computation time (s)			
	Patella	Femur	Tibia/Fibula
NCC	32.6	51.5	53.7
GD	34.8	52.7	56.3
MI	28.0	50.1	53.5

(out-of-plane) rotation error) was within 1° for all bone models including patella. Therefore, out-of-plane rotation accuracy for patella was improved by using the intensity-based 2D/3D registration, and the present method suggested a possibility for analyzing 3D knee kinematics including patella. In addition, the large difference of RMSE depended on similarity measure methods were not founded in this study.

In the experiment of the convergence time, by GPU parallel processing using CUDA, the computation time was dramatically improved (Tables 4 and 5), and the feasibility of present method for clinical application was demonstrated.

Disclosure Statement   The authors declare that they have no conflict of interest.

References

1. Banks, SA., Hodge, WA.: Accurate measurement of three-dimensional knee replacement kinematics using single-plane fluoroscopy. IEEE Trans Biomed Eng 43(6), 638–649 (1996).
2. Zuffi, S., Leardini, A., Catani, F., et al.: A model-based method for the reconstruction of total knee replacement kinematics. IEEE Trans Meg Imag 18(10), 981–991 (1999).
3. Yamazaki, T., Watanabe, T., Nakajima, Y., et al.: Improvement of depth position in 2-D/3-D registration of knee implants using single-plane fluoroscopy. IEEE Trans Meg Imag 23(5), 602–612 (2004).
4. Kobashi, S., Tomosada, T., Shibanuma, N., et al.: Fuzzy image matching for pose recognition of occluded knee implants using fluoroscopy images. J Advanced Computational Intelligence and Intelligent Informatics 9(2), 181–195 (2005).
5. Bingham, J., Li, G.: An optimized image matching method for determining in-vivo TKA kinematics with a dual-orthogonal fluoroscopic imaging system. J Biomech Eng 128(4), 588–595 (2006).
6. Hirokawa, S., Abrar Hossain, M., Kihara, Y., et al.: A 3D kinematic estimation of knee prosthesis using X-ray projection images: Clinical assessment of the improved algorithm for fluoroscopy images. Medical Biological Engineering and Computing 46(12), 1253–1262 (2008).
7. Komistek, RD., Dennis, DA., Mahfouz, MR.: In vivo fluoroscopic analysis of the normal human knee. Clinical Orthopaedics & Related Research 410, 69–81 (2003).
8. Moro-oka, T., Hamai, S., Miura, H., et al.: Dynamic activity dependence of in vivo normal knee kinematics. Journal of Orthopaedic Research 26(4), 428–434 (2008).
9. Li, G., Papannagari, R., Kyung, WN., DeFrate, LE., Gill, TJ., Rubash, HE.: The coupled motion of the femur and patella during in vivo weight bearing knee flexion. J Biomech Eng 129(6), 937–943 (2007).
10. Ohnishi, T., Suzuki, M., Nawata, A., et al.: Three-dimensional motion study of femur, tibia, and patella at the knee joint from bi-plane fluoroscopy and CT images. Radiological Physics and Technology 3, 151–158 (2010).
11. Weng, J., Cohen, P., Herniou, M.: Camera calibration with distortion models and accuracy evaluation. IEEE Trans Pattern Anal Mach Intell 14, 965–980 (1992).
12. Penney, GP., Weese, J., Little, JA., et al.: A comparison of similarity measures for use in 2-D-3-D medical image registration. IEEE Trans Meg Imag 17, 586–595 (1998).
13. Lacroute, P., Levey, M.: Fast volume rendering using a shear-warp factorization of the viewing transformation. Proc. SIGGRAPH, 451–458 (1994).
14. NVIDIA Corp. CUDA download webpage, https://developer.nvidia.com/cuda-toolkit, last accessed 2018/2/5.

Design of Smart Orthosis of Upper Limb for Rehabilitation

Ana Carolina D´Angeles Mendes de Brito, Patrik Kutilek, Jan Hejda, Pavel Smrcka, and Vojtech Havlas

Abstract

Movement problems of the upper limb are a common consequence of many diseases and can drastically affect the daily life impairing normal activities. To regain motor function and muscle power is necessary to treat these diseases with an intense physical therapy. The smart orthosis is an effective and modern method used in the process of muscle rehabilitation. We propose a design of motorized orthosis subsystems for the upper limbs. The orthosis is a motor assist robotic system that, with the help of actuators, will allow the movement of selected parts of the upper limb. The main point is to offer a reliable low weighted exoskeleton with selected sensors to move and control the upper limbs covering 6 motions: shoulder adduction and abduction, shoulder flexion and extension and elbow flexion and extension. The device is a junction of a hard orthosis with a soft orthosis in order to perform passive physical therapist exercises in clinical practice. The actuation is made by Bowden cables connected in one end to the limb and another to a stepper motor located at a backpack carried by the patient decreasing the apparatus weight substantially. The project also includes a selection of sensors comprising accelerometers, strain gages, thermostats, oximeters, that can provide the necessary information to move the limbs quantifying the muscle activity and physical condition through time. Also, a cooling subsystem based on Peltier thermoelectric modules was implemented to control the muscle temperature in case of an inflammatory reaction. The design was certified by kinematic and structural strength simulation using SolidWorks software.

1 Introduction

Many people have severe problems with muscle degeneration and muscle atrophy. Several neural diseases have muscle impairment as consequence and can drastically affect the daily life impairing normal [1]. To regain motor function and muscle power is necessary to treat these diseases with an intense physical therapy which can demand a dedicated physical therapist. The manual treatment has several disadvantages including staff exhaustion, price [2], and the distress caused by shifting the physically impaired to the clinic [3]. The motor assist robotic systems offer a useful tool around these problems [1] since this they can generate a precise and reproducible path and can quantify the muscle recovery obtaining better image of the patient condition through time [2]. There are 2 types of orthosis, hard and soft. The first is usually a rigid-framed high weighted device supporting the specific limbs with actuators attached directly to the frame in body (intelligent hard orthosis) [17]. The soft ones on the other hand, takes advantage of natural anatomic structure such as bones and joints for the device structure. The conventional rigid robots frame can be disregarded, and its function is performed by the user bones, and the actuation is performed by mechanical tendons or other soft actuators

A. C. D´Angeles Mendes de Brito (✉) · P. Kutilek · J. Hejda
P. Smrcka
Faculty of Biomedical Engineering, Czech Technical University
in Prague, Sitna sq. 3105, Kladno, Czech Republic
e-mail: ana-carolina.dangeles-mendes-de-brito@fbmi.cvut.cz

P. Kutilek
e-mail: kutilek@fbmi.cvut.cz

J. Hejda
e-mail: jan.hejda@fbmi.cvut.cz; petr.volf@fbmi.cvut.cz

P. Smrcka
e-mail: smrcka@fbmi.cvut.cz

V. Havlas
2nd Faculty of Medicine, Department of Orthopaedics, Charles
University in Prague and Motol University Hospital, V Uvalu 84,
Prague, Czech Republic
e-mail: vojtech.havlas@fnmotol.cz

that will apply shear forces to its attachment points in the body [4].

This study proposes a design of an intelligent orthosis for the upper limbs in order assist the physically weak patients in the rehabilitation process performing passive exercises. The actuation is made by Bowden cables connected in one end to the limb and another to a stepper motor located at a backpack carried by the patient. The main point was to offer a reliable low weighted exoskeleton with selected sensors to move and control the upper limbs covering 6 motions: shoulder adduction and abduction, shoulder flexion and extension and elbow flexion and extension.

2 Design

We designed a light weight orthosis, Fig. 1, in order to move and control the upper limbs. The motions to be controlled were defined focusing on physical therapy so that would allow the execution of the most frequently recommended rehabilitation exercises. The structure of the orthosis comprises mainly 4 main parts: the upper-arm support, the forearm support, the shoulder support and the actuation system. The dimension of the orthosis was determined by the anthropometric studies carried out by Henry Dreyfuss [5, 6] and by De Leva studies [7].

The upper-arm support, Fig. 2a, is formed a 2 mm thickness rectangular aluminum alloy covering the upper-arm length followed by an 8 mm thickness cylinder covering the elbow joint, Fig. 2c. The cylinder was necessary to support the rotational movement of the elbow with and for the fixation of the encoder responsible for the angle control of the elbow. Furthermore, the forearm support, Fig. 2b, was designed with a 1.5 mm thickness aluminum

rectangular alloy covering the forearm from the elbow joint to the wrist joint followed by a circular part covering the elbow joint with a shaft located at the middle, Fig. 2d that was instrumental to the fixation of the 2 parts together. The shoulder support was designed mainly to fix the upper-arm support to the body and organize the sensors wires through the arm. This part resembles a shirt and the fabric chosen was neoprene. The wires connecting the sensors to the electronic board as well as the cables connecting the orthosis to the motor are threaded to a hem (continuous tube) formed in the fabric, using the same concept used on drawstrings. To decrease the force needed by the motor a shoulder pad located at the shoulder, Fig. 4b; and a disk, Fig. 4e, located at the elbow were used to define the route of the Bowden cables. The shoulder pad increases the distance between the actuation point of the cables and the arm and the disk increases the distance between the actuation point of the cables and the elbow joint, both decreasing the needed torque, and thus the motor weight.

All limbs are driven by Bowden cables being manipulated by a motor and 2 sets of gears located in a backpack carried by the patient. This actuation system was chosen considering the weight of the device, which is concentrated on the backpack and not at the injured limb. To be able to perform all those movements with only one motor was necessary to design a gear box with 2 separated gears, Fig. 3a, b. Each gear is attached to a spool to wind the cable that will activate a specific subpart of the exoskeleton performing one specific joint motion per time. An electromagnetic pin located in the motor shaft will activate the gear
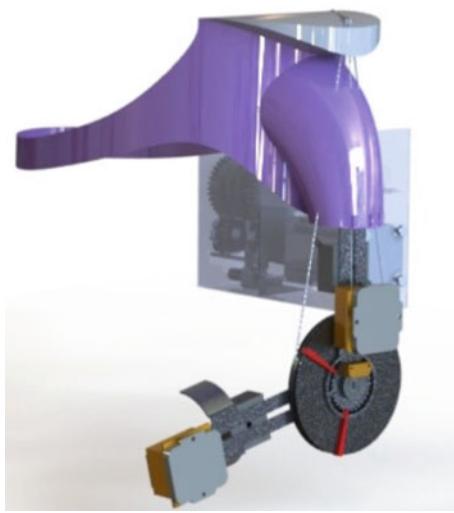
Fig. 1 Complete orthosis
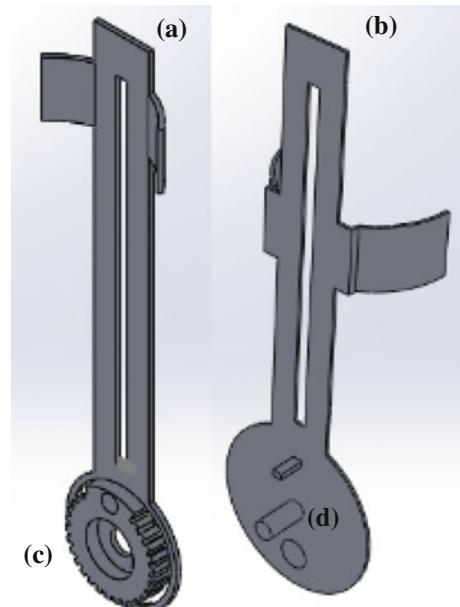
Fig. 2 **a** Upper-arm support; **b** forearm support; **c** 8 mm thickness cylinder; **d** shaft
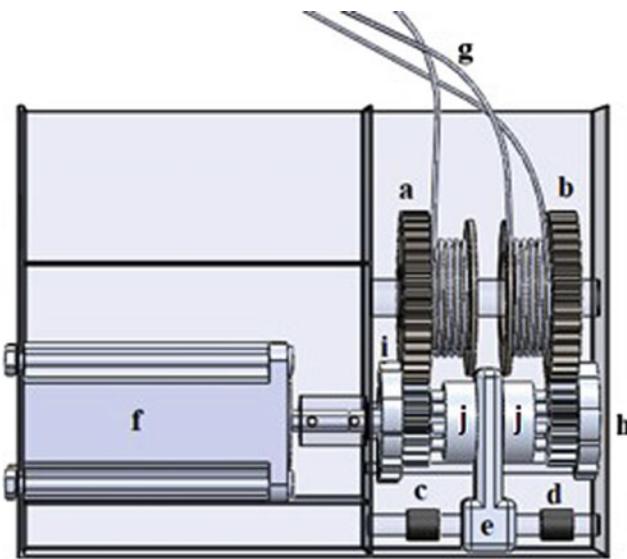
Fig. 3 **a** Gear 1; **b** gear 2; **c** electromagnetic pin 1; **d** electromagnetic pin 2; **e** gear wheel; **f** motor; **g** cable; **h** locking system 1; **i** locking system 2; **j** gear wheel cylinder

wheel, Fig. 3e, which will select each mechanism according to the movement being made, Fig. 3c, d. It was considered to trigger the spools directly by the motor shaft, however this piece would need a larger radius to allow the connection of the spool to the gear wheel, and that would decrease the tangential force supplied by the motors at the cables. The gears were designed according to the DIN 862 and DIN 867 standards.

- Gears set 1: Shoulder Flexion/extension motion, Fig. 4c; Elbow flexion/extension motion Fig. 4d

- Gears set 2: Shoulder Adduction/abduction motion, Fig. 4a.

Considering that the motor can move the arm breaking the entire movement in simple joints motions (shoulder adduction and abduction, shoulder flexion and extension and elbow flexion and extension) per time. A locking system had to be developed using a ratchet, a pawl and a spring to avoid the uncontrolled spin of the gears once the pinion is released. The ratchet is fixed at the pinion and locks the mechanism when the counterweight of the loose arm pushes it against the pawl, Fig. 3h, i. To release the mechanism an electro-magnetic pin pushes the pawl back and the gear can rotate free in the other direction. The motor selection was made according to static computations considering all the positions of the upper limbs inside the 6 motions allowed by the orthosis. The main point was to discover the highest power required from the motor to sustain the arm in a determined position at the threshold of movement. The highest force necessary for the limb sustainability was with the arm in an extended position in front of the body in a 90° angle. Was necessary a torque of 3.8 Nm, thus any motor achieving a higher torque would be able to move the body. The speed of the movement was not taken into consideration.

2.1 Sensing

Two accelerometers XSense with an integrated GPS and MEMS [8], placed at the forearm near the wrist joint and at the upper-arm near the elbow joint, in addition to an HEDS-9040/9140 encoder from Avago Technologies [9] placed on the elbow joint will provide the information to
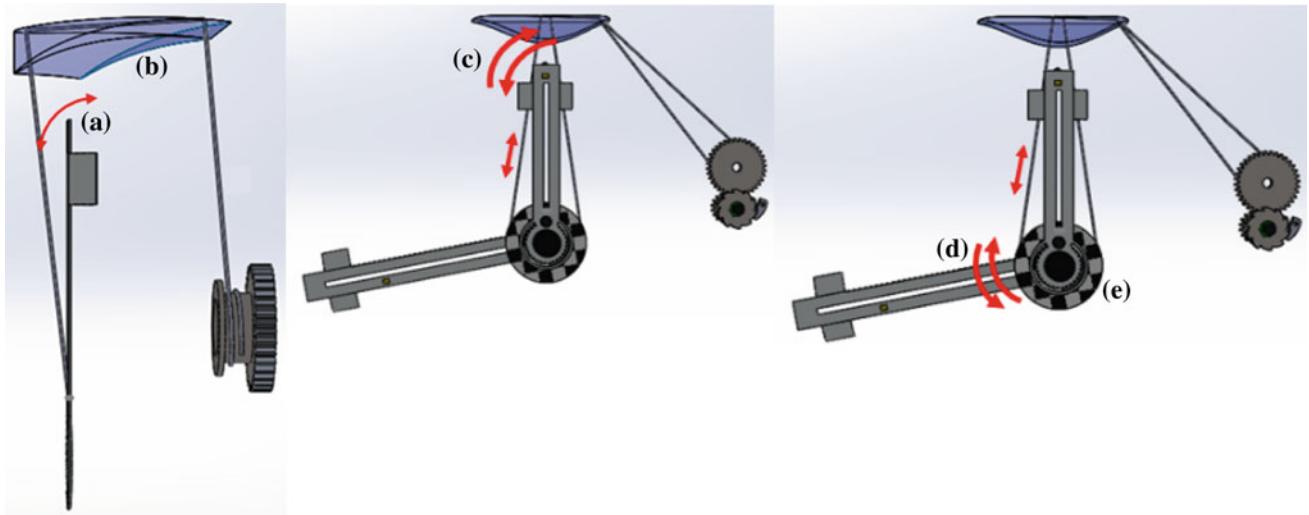
Fig. 4 **a** Shoulder adduction/abduction; **b** shoulder pad; **c** shoulder flexion/extension; **d** elbow flexion/extension; **e** disk

acquire the position of the arm through time. The patient muscle recovery can be quantified with the help of two SGK-L3A-K350U-PC11-E strain-gages from OMEGA [10] located at the upper-arm near the shoulder extremity and at the forearm near the wrist extremity. Both sensors will inform the value of the force made by the patient. Ten 3 leads MyoWare™ Muscle Sensor (AT-04-001) from Advanced Technologies will be attached to the patient skin in order to detect muscle activity of 10 designated muscles (deltoid anterior, deltoid posterior, pectoralis major, teres major, biceps brachi, brachalis, anconeus, triceps brachii, pectoralis major, latissimus dorsi). The different combinations of active muscles detected by the sensor will define the motion to be performed by the device. In addition, this project includes a muscle cooler module in which two thermometers MAX30205 from Maxim Integrated [11] placed at the skin will detect a temperature increase activating a Peltier module [12] in order to cool the area lowering the chances of an inflammatory reaction. The pulse oximeter TL-101S from the company Nihon Kohden [13] will monitor the patient oxygen saturation—$SpO2$ during the exercises using the orthosis as well as the heart rate. Two electromagnetic pins are used to select which of the gear set will be activated by the gear wheel and a 3rd one is placed at the elbow joint position of the orthosis. This position is exactly the union of the forearm orthosis part with the upper-arm orthosis part and the disk. When there is no energy passing through the pin the elbow joint is free to move enabling the elbow flexion/extension movement, Fig. 4d. When there is energy passing through the pin the magnetic lock will fix the upper-arm orthosis part to the forearm orthosis part making the whole system (upper-arm + forearm + disk) a rigid piece that will move together executing the motion of shoulder flexion/extension, Fig. 4c.

The whole system electrical energy will be supplied by the battery Li-ion 11, Acer Aspire One A110/A150, D150/250, P531 series. It has 7800 mAh and 87 Wh. This battery may be more expensive, however will last longer considering all the electronics components that has to supply. The whole design together has power of 30 watts, thus this battery will be able to supply the system for almost 3 h. After that is necessary a recharge.

The control proposed on this project is made by using 6 different modules, each one controlled by a PAC [14]. The EMG controller (DKE-IOPE-16), the cooler controller (DKE-IOPE-16), the oxi controller (DKE-IOPE-16), the motor controller (DKE-IOPE-16), the power controller (DKE-IOPE-16), and the main controller (DKE-PAC-AT90).

3 Tests

To certify the mechanical functionality of the device was necessary to verify the structural elements of the design, and also its geometry taking into consideration the dynamics and kinematics, ensuring that the placement of all pieces together do not restrain any necessary movement. SolidWorks was the main tool used to validate the motion system, taken that the software offers the motion study feature, mechanical tests and finite element analysis. Unfortunately, was not possible to analyze the system kinematics including all the parts at the same time. The program is not able to simulate the actuation of cables and thus couldn't predict the behavior of the proposed prototype. However, the test was possible if separating the exoskeleton in 2 different parts: the actuation system and the orthotic system. The first is comprised by the 2 gears sets, the locking system, the electromagnetic pin selector, the 2 gear shift wheels and all the fixating components. The second is comprised by the upper-arm support, forearm support, the Bowden disk, the motion range limiting pin and the fixating components. The kinematic test of the actuation system aimed to certify the gears and pinon relationship, as well as the torque transferred by the gear shift wheel to the gear sets. The evaluation was carried out with the application of different forces in selected components at different instances. At the beginning of the test the teeth of the gear shift wheel were already aligned with the pinion orifices. At the first instance a torque was applied at one of the gear wheel cylinder, Fig. 3j, causing the wheel to rotate around its shaft. The teeth of the wheel triggered the rotational motion of the pinion that triggered the rotational motion of the gear. At the second moment of the test a linear force was applied at the gear wheel, Fig. 3j, and the whole gear selection system (wheels + electromagnetic pin) dislocated in direction of the pinion 2. Because there was no actuator acting on the gear set 1 the pair stopped rotating. At the third moment the gear shift wheel was connected and aligned to the pinion 2 orifices. Another torque was applied to the wheel 2 which caused the gear set 2 to rotate until the end of the test.

The simulation of the orthotic system was simpler. The main point is to evaluate if the design contains any constrains of movement. All the mechanical parts that can interfere at the orthotic system motion are located and assembled at elbow joint. After assembling all parts aligned with the forearm support shaft an oscillating torque was applied at the Bowden disk. During this moment, the forearm support oscillated in a range of 90° simulating the elbow flexion and extension motion.

On the mechanical structural analysis, in all the parts to be tested, was considering the worst-case scenario to cover all the hypothesis of fracture and deformation. The situation that put the design at the highest level of stress was when the motor is actuating with the highest torque. Using the SolidWorks software was possible to conduct a finite element analysis of all arts involved in the design.

4 Results Analysis

The mechanical design here proposed were submitted to a material resistance evaluation. The 2 gears, the 2 pinions, the ratchet and the gear wheel were tested using the mechanical properties of the aluminum alloy 6061—T4 SS due to its stronger resistance characteristics, and the other components were tested with the aluminum alloy 7050-T7350, a lighter material in weight terms. The highest distress calculated on this design was on the pinion teeth with the value of $9.80 * 10^7$ Pa. This was expected because thee piece is directly connected to the motor shaft. However, the high tension did not impair the design in any way taken that the value is still under the yield strength, therefore the part did not present ant deformations that would interfere with the orthosis functionality. Considering the components tested with the aluminum 7050-T7350, the higher distress was applied on forearm support with the value of $5.52 * 10^7$ Pa. As well as the pinion the high tension was still under the yield strength of the material and did not caused any plastic deformation.

The kinematics designs made by this study proved that the geometry does not interfere in the motion range of the exoskeleton and indicated that the system behaves according to the expected. On the actuation system the gear shift wheel was able to trigger each one of the pinions. The test made with the orthotic system showed that the joint between the pieces has good articulation. The forearm managed to move without obstacles and the geometry of the parts are adequate to the objective of this design.

One of the focus of the study was the weight of the whole device. The orthotic device being carried by the injured arm had a weight of 387 g considering all sensors and mechanical parts, and the weight placed on the backpack had a value of 2085 g.

5 Conclusion

The main goal of this work was to create a construction design on SolidWorks and select sensors of subsystems of an intelligent orthosis for the upper limbs of patients to assist on the process of rehabilitation. The device is only able to perform one motion of the time creating the need to break

the movement is several basic movements. However, physical therapy exercises are usually basic in order to facilitate its execution. The sensors suggested on the design will inform about of the limb movement, position, temperature, strength, patient oxygenation and heartbeat to allow the tracking of the patient conditions and development through time. The orthosis actuation is made by the change of size of Bowden cables connected in one end to a motor and the other end to the orthosis.

The tests carried out showed that the limits of the material were not reached, and all the parts were working inside their elastic parameters. Thereby, permanent deformations won't occur. The kinematics analysis showed that the system will behave as expected.

The mechanical design was made using only software and was not yet constructed. The selection of sensors and electronic components was made taking into consideration the design requisites and demands but was not yet tested or simulated. For future projects this simulation can be done and implemented at the mechanical project.

Conflict of Interest The authors declare that they have no conflict of interest.

References

1. Sandri, M.: Signaling in Muscle Atrophy and Hypertrophy. Physiology, p. 160–170, (2008)
2. Viteckova, S., Kutilek, P., Jirina M.: Wearable Lower Limb Robotics: A Review, Biocybernetics and Biomedical Engineering, p. 96–105, (2013)
3. Kesner, S. B., Jentoft, L., Hammond, F. L., Howe, R. D., Popovic, M,; Design Considerations for An Active Soft Orthotic System for Shoulder Rehabilitation. 33nd ANNUAL INTERNATIONAL IEEE EMBS CONFERENCE, Boston USA, (2011)
4. In, H., Kang, B. B., Sin, M., Cho, K. J.: Exo-Glove: A Wearable Robot for the Hand with a Soft Tendon Routing System. IEEE Robotics & Automation Magazine, vol. 22, no. 1, p. 97–105, (2015)
5. Tilley, A. R., H. Dreyfuss, The Measure of Man and Woman. Whitney Library of Design, Watson-Guptill Publications, New York, (1993)
6. Leva D., Adjustments to Zatisiorsky-Seluyanoy's Segment Inertia Parameter. Elsevier Science, (1996)
7. Omega Pressure Strain and Force Group homepage, Introduction to Strain Gages, http://www.omega.com/prodinfo/straingages, last accessed: 06/04/2017
8. Avago Technologies, Three Channel Optical Incremental Encoder Modules, Heds-9040/9140 Datasheet, March 17th (2014)
9. Cui Inc, Peltier Application Note, (2016)
10. X Sens homepage, IMU Inertial Measurement Unit, https://www.xsens.com/tags/imu, last accessed: 06/04/2017
11. Opto 22, Understanding Programmable Automation Controllers (Pacs) In Industrial Automation, Pacs In Industrial Automation, White Paper, Form 1634–070228, (2016)
12. Maxim Integrated, Human Body Temperature Sensor, Max30205 Datasheet, (2016)

13. Park, Y., Santos, J., Galloway, K. G,. Goldfield,. C., Wood, R. J.: A Soft Wearable Robotic Device for Active Knee Motions Using Flat Pneumatic Artificial Muscles", IEEE INTERNATIONAL CONFERENCE ON ROBOTICS & AUTOMATION, Hong Kong, (2014)

14. Nihon Kohden, Accessories Patient Monitoring, Product Catalog (2013)

15. Giangregorio, L., Mccartney, N.: Bone Loss and Muscle Atrophy in Spinal Cord Injury: Epidemiology, Fracture Prediction, and Rehabilitation Strategies. J Spinal Cord Med, 29(5): 489–500, (2006)

16. Goldman, L., Chinnery, P. F.: Muscles Diseases. Cecil's Textbook of Medicine 24th Edition. Saunders, p. 2409–2420, (2012)

Methods of Motion Assessment of Smart Orthosis of Upper Limb for Rehabilitation at the Clinic and at Home

Ana Carolina D´Angeles Mendes de Brito, Patrik Kutilek, Jan Hejda, Veronika Kotolova, and Vojtech Havlas

Abstract

The aim of this work is to describe proposed and tested methods for evaluation of short-term and long-term movement activity of a smart orthosis for the upper limbs during a rehabilitation process carried out at a clinic or at home. To quantify the description of motion we used methods of evaluation of the time domain data. To test the functionality of the methods, we compared the movement of the dominant and non-dominant limbs, assuming cyclical and acyclic movement, to obtain the expected values for a healthy population. In accordance with the goal, a group of cyclic and non-cyclic movements common to the home environment were proposed. The movements were divided according to the activities performed during sitting, standing and walking. It was: pen writing, typing on the keyboard/using the mouse, eating with a spoon and eating a croissant combing, lifting weights, reading a book, etc. Twenty healthy subjects participated in the study. Four gyro-accelerometers (Xsens Technologies B.V.) attached to the forearms and upper arms of both upper limbs were used to record the upper limb movements. The results show that the calculated values of dominant and non-dominant limb parameters differ significantly in acyclic movements. The smart orthosis which uses the proposed methods can be used to evaluate the physical activity, quantify the evaluation of the rehabilitation process, and thus, it finds use in clinical practice.

1 Introduction

Today, smart orthosis of upper limb for evaluation of short-term and long-term movement activity are not used in clinical practice. There are several projects, but there is no such thing as a detailed description of the sensor system of the smart orthosis and the measured data. Only preliminary designs were mentioned, [1, 2]. The methods for calculating the parameters for the assessment and evaluation of short-term and long-term movement activity in relation to the use in the orthosis have not been described.

The aim of this article is to describe proposed methods for evaluation of short-term and long-term physical activity by sensors suitable for use in the orthosis construction. Methods were tested and used to compare the movement of dominant and non-dominant limbs, assuming cyclical and a cyclical movement.

2 Methods and Materials

Based on the above mentioned drawbacks, methods of motion assessment are designed. Method provides movement evaluation and the evaluation of kinematic data of the movement of healthy subjects was tested.

A. C. D´Angeles Mendes de Brito (✉) · P. Kutilek · J. Hejda
V. Kotolova
Faculty of Biomedical Engineering, Czech Technical University in Prague, Sitna sq. 3105, Kladno, Czech Republic
e-mail: ana-carolina.dangeles-mendes-de-brito@fbmi.cvut.cz

P. Kutilek
e-mail: kutilek@fbmi.cvut.cz

J. Hejda
e-mail: jan.hejda@fbmi.cvut.cz

V. Kotolova
e-mail: kotolver@fbmi.cvut.cz; petr.volf@fbmi.cvut.cz

V. Havlas
2nd Faculty of Medicine, Department of Orthopaedics, Charles University in Prague and Motol University Hospital, V Uvalu 84, Prague, Czech Republic
e-mail: vojtech.havlas@fnmotol.cz

2.1 Participants

Twenty healthy subjects (age of 22.3 (SD 1.0) years), 8 women and 12 men, were recruited from the students at The Czech Technical University in Prague. The Edinburgh Handedness Inventory was used to assess the dominance of a person's right or left upper limb (e.g. [3]). In the study, there were three left-handers and rest of the subjects was right-handers. The diagnostic evaluation included a detailed disease history, and an informed consent was obtained from each subject. The study was performed in accordance with the Helsinki Declaration. The study protocol was approved by the local Ethics Committee of the Faculty of Biomedical Engineering of the Czech Technical University (CTU) in Prague. The subjects were chosen for measurement randomly, and on different days. Each subject was measured only once, but each subject's physical activity was performed at least twice in the measurement.

2.2 Motion Capture Equipment

In order to record the movement of body segments is instrumental the use of sensors that will be implemented into smart orthosis. Because inertial measurement units (IMU) offer a record of kinematic variables of angular and translational motion, we assume IMU sensors in the construction of a smart orthosis. Although gyro-accelerometer sensors are presumed for the construction of a smart orthosis, we need to apply motion sensors not only to the upper limbs, but also to other parts of the body segments. For this reason, the Xsens system with seven gyro-accelerometer MTx sensors has been configured to measure body segment movements. The Xbus Master Motion capture system, which is a lightweight (330 g) device, uses MTx units for the orientation and translation measurement of the segments [4]. The MTx unit with an embedded accelerometer and gyroscope represents an accurate IMU measurement of the drift-free 3-D orientation and 3-D acceleration [5]. The data, i.e. the three Euler angles (roll (φ), yaw (ψ), pitch (θ)) and three accelerations measured by each MTx unit are described in detail by [6, 7].

2.3 Application of Sensors

The Xsens motion sensors were placed in accordance with the recommendations of the Xsens manufacturer and similar studies [8, 9]. The sensors were placed on body segments to record useful signals to assess the movement of the upper limbs. The exact placement of the sensors was as follows:

Sensor 1—Right Upper Arm: point between the dorsal and lateral sides of the upper arm close to the caput lateral abdomen in the distal third of the forearm bone (at the site of the smallest deformation of the tissue during flexion in the elbow). The X axis of the sensor is parallel to the bone, its positive direction is oriented distally. The Z axis is in the positive direction in dorsolar, the Y axis in the positive direction in ventrolateral, both are approximately 45° laterally.

Sensor 2—Right forearm: Dorsal forearm, 20 mm proximal to the center line of the radial and ulnar styloid. The sensor is oriented so that its Z-axis extends vertically from the dorsal surface of the forearm. Direction of the X axis parallel to the elbow bone, its positive direction is oriented distally. The positive direction of the Y axis is the same as the lateral direction.

Sensor 3—Left Upper Arm: The specific point is determined as for sensor 1.

Sensor 4—Left forearm: The specific point is determined as for sensor 2.

2.4 Methods of Data Processing

For the quantitative description of motion, parameters that by their value can characterize a certain motion property. Various methods are used to determine parameters. These methods can be further divided into:

- Methods of evaluation of time domain data,
- Methods of evaluation of frequency domain data [10],
- Methods of evaluation of the relationship between measured variables [11],
- Non-linear methods of data evaluation [12].

On the basis of previous experiments and consultations with the Orthopedic and Traumatology Clinic, Hospital Motol, Charles University, and with respect to the length of time window 1 s used, we selected parameters based on time domain analysis. The data recording frequency was 50 Hz. The parameters were determined for the 1 s window of the measured data, as some motion activities may take only about 1 s. For methods of analysis in the time domain, common statistical characteristics such as max(v) or min(v) can be used, where v is the measured variable i.e. angle (α) or acceleration (a) in the x and y directions of the sensor coordinate system. If we take into account more complex

parameters implemented in custom made software, the first is the average of movement intensity (AI), calculated by [13]:

$$AI = \frac{1}{k} \cdot \sum_{i=1}^{k} \sqrt{v_{x,i}^2 + v_{y,i}^2 + v_{z,i}^2}. \tag{1}$$

Another parameter used is the Variance of movement intensity (VI), which is calculated by [13]:

$$VI = \frac{1}{k} \cdot \sum_{i=1}^{k} \left(\sqrt{v_{x,i}^2 + v_{y,i}^2 + v_{z,i}^2} - AI \right)^2. \tag{2}$$

We also used the signal magnitude area (SMA) according to [14]:

$$SMA = \frac{1}{k} \cdot \sum_{i=1}^{k} \left(|v_{x,i}| + |v_{y,i}| + |v_{z,i}| \right). \tag{3}$$

2.5 Test Procedure

A group of cyclical and non-cyclical movements common to the home environment were proposed. The division of movements was according to the activity of during sitting, standing and walking. The list of selected activities is shown in Table 1.

The motion sensor was placed on the subject prior to measurement in accordance with the description above. Each subject was instructed to perform a sequence of activities at the Table 1. During the movements the motion data were recorded. After performing all of the movements activities, the data for each activity was processed separately to compare activities.

2.6 Statistical Analysis

After calculating the values for the individual movement activities of each subject, the statistical analysis was performed with the use of MatLab sw. The movement of the dominant and non-dominant limb was compared. The Jarque-Bera test was used to test the normal distribution of all parameters (significance level was 5%). The Wilcoxon Test was used to assess the significance of the differences between dominant and non-dominant limbs. The significance level was set at was 5%.

3 Results Analysis

The Jarque-Bera test in some cases did not confirm the hypothesis of normal distribution of data, thus, the Wilcoxon test was used for analysis. Using the Wilcox test, the parameters for the dominant and non-dominant limb was compared. Table 2 shows an overview of differences in result with statistically significant differences, i.e. p < 0.05.

4 Discussion

For asynchronous movements, it is assumed that a significant difference will be found for paired segments, i.e. combing when the subject uses only one hand. The tests confirmed this assumption on the three methods of the experiment; when sitting down the subjects had divergences of movement of the forearm and upper-arm when writing a pen, typing keyboard and using mouse. In the same way, the subjects shown high statistically differences when brushing teeth in standing position and when walking while lifting the weight in the middle of the path. The latter had high incompatibilities when analyzing both the angle and acceleration on the forearm and on the upper-arm. At waving at head level movement there was discrepancies on the upper-arm angle while sitting down and on the acceleration of the upper-arm while standing. Only while slow walking the forearm had nonconformities on the result. For synchronous data, this was not expected, yet there was a divergence on the forearm movements while walking and on the upper-arm movements while running.

The aim of this work was to present the methods of measurement for the identification of movement on determined activities. It was used 4 gyro-accelerometers placed at the upper limbs. The sensors selected from X-Sens presented good repeatability of results which allowed the statistically analysis of the three parameters (average of movement intensity, variance of movement intensity and signal magnitude area) selected on this study. The AI parameter shown higher levels of contrast on the results of each movement

Table 1 Cyclical and non-cyclical movements used to test methods of data processing

Method	Activity
Sitting	Writing with a pen; typing on the keyboard/using the mouse; eating with a cutlery; waving at head level; combing; lifting weight
Standing	Waving at head level; combing; tooth brushing; lifting weight; reading a book
Walking	Slow walking; running; waving at head level; lifting the weight in the middle of the path; throw a ball in the middle of the path

Table 2 Statistically significant differences in parameters when comparing dominant and non-dominant arm

Method	Activity	Variable	Segment	Parameter
Sitting	Writing with a pen	Angle	Forearm	VI, AI
		Acceleration	Upper arm	SMA
	Typing on the keyboard/using the mouse	Angle	Forearm	VI, AI
		Acceleration	Upper arm	SMA
	Eating with a cutlery	Acceleration	Upper arm	SMA
	Waving at head level	Angle	Upper arm	AI
	Combing	Angle	Forearm	SMA, VI, AI
Standing	Waving at head level	Acceleration	Upper arm	AI
	Combing	Angle	Forearm	AI
	Tooth brushing	Angle	Forearm	VI, AI
		Acceleration	Upper arm	AI
	Lifting weight	Angle	Forearm	AI
Walking	Slow walking	Angle	Forearm	AI
	Running	Acceleration	Upper arm	SMA
	Lifting the weight in the middle of the path	Angle	Upper arm	VI, AI
			Forearm	VI
		Acceleration	Upper arm	SMA
			Forearm	SMA
	Throw a ball in the middle of the path	Angle	Upper arm	VI, AI

when comparing the dominant arm with the nondominant one.

There are limitations to our study. The most important one is that the sample of the subjects was small and probably not representative of the larger population. However, to test the basic attributes of the method proposed for the study of operational preparedness in this preliminary study, a sample of subjects is sufficient.

5 Conclusion

In this work was described new proposed methods for evaluation of short-term and long-term physical activity. The main benefit of this work is the selection of sensors to be used on the creation of an orthosis for the upper limbs in order to evaluate and move the arm. According to the requirements of the clinical practice, the sensors selected were able to acquire information to evaluate the upper-limbs movements of determined daily life activities and compare the behavior of the dominant and non-dominant limb. The average of movement intensity method showed parameters able to reveal the highest differences between the two limbs.

The applicability of sensors and methods for calculating the parameters of the evaluation of physical activity was tested on younger subjects, however, we expect follow-up measurement and testing also for elder subjects and patients.

The reason for use is, for example, application of methods for the identification and evaluation of movement activity to judge typical stroke patient recovery progress. The method here proposed can be used in future construction of orthosis for the upper-limbs to evaluate and move the body of a patient.

Conflict of Interest The authors declare that they have no conflict of interest.

References

1. Romilly, D. P., Anglin, C., Gosine, R. G., Hershler, C., Raschke, S. U.: A Functional Task Analysis and Motion Simulation for the Development of a Powered Upper-Limb Orthosis. IEEE Transactions on Rehabilitation Engineering, 2(3), 119–129, (1994)
2. Rupp, R., Rohm, M., Schneiders, M., Kreilinger, A., & Müller-Putz, G. R. Functional rehabilitation of the paralyzed upper extremity after spinal cord injury by noninvasive hybrid neuroprostheses. Proceedings of the IEEE, 103(6), 954–968, (2015)
3. Oldfield, R. C. The assessment and analysis of handedness: The Edinburgh inventory. Neuropsychologia, 9, 97–113, (1971)
4. Kutilek, P., Cakrt, O., Hejda, J., Cerny, R.: Comparative measurement of the head orientation using camera system and

gyroscope system, 2013 13th MEDITERRANEAN CONFERENCE ON MEDICAL AND BIOLOGICAL ENGINEERING AND COMPUTING, Seville, Spain, IFMBE Proceedings, Volume 41, p. 1519–1522 (2014)

5. Kutilek, P., Socha, V., Cakrt, O., Schlenker, J., Bizovska, L.: Trajectory length of pitch vs. roll: Technique for assessment of postural stability. Acta Gymnica, 45(2), 85–92, (2015)

6. Allum, J. H., Nijhuis, L. B. O., & Carpenter, M. G. Differences in coding provided by proprioceptive and vestibular sensory signals may con-tribute to lateral instability in vestibular loss subjects. Experimental brain research, 184(3), 391–410, (2008)

7. Gil-Agudo, Á., Reyes-Guzman, L. A., Dimbwadyo-Terrer, I., Peñasco-Martín, B., Bernal-Sahún, A., López-Monteagudo, P., Ama-Espinosa, A., Pons, J. L.: A novel motion tracking system for evaluation of functional rehabilitation of the upper limbs. Neural regeneration research, 8(19), p. 1773–1782, (2013)

8. Stirling, D., Hesami, A., Ritz, C., Kdistambha, K., Naghdy, F.: Symbolic Modelling of Dynamic Human Motions. Biosensors. Pier Andrea Serra (Ed.), InTech, https://doi.org/10.5772/7215, (2013)

9. Lorussi, F., Carbonaro, N., Rossi, D. D., Tognetti, A.: A bi-articular model for scapular-humeral rhythm reconstruction through data from wearable sensors. J Neuroeng Rehabil. 2016; 13: 40, (2016)

10. Winter, D.: Stiffness Control of Balance in Quiet Standing. Journal of Neurophysiology, p. 1211–1221, (1998)

11. Kutilek, P., Farkasova, B.: Prediction of Lower Extremities' Motion by Angle-angle Diagrams and Neural Networks. Acta of Bioengineering and Biomechanics, 13.2: 57–65, (2011)

12. Bruijn, S. M.: Assessing Stability of Human Locomotion: a review of current measures. Journal of the Royal Society Interface, 10.83: 20120999, (2013)

13. Garcia-Ceja, E., Brena, R.: Long-Term Activity Recognition from Accelerometer Data; IBEROAMERICAN CONFERENCE ON ELECTRONICS ENGINEERING AND COMPUTER SCIENCE, Procedia Technology 7, p. 248 – 256, (2013)

14. Khusainov, R., Azzi, D., Achumba, I. E., Bersch, S. D.: Real-Time Human Ambulation, Activity, and Physiological Monitoring: Taxonomy of Issues, Techniques, Applications, Challenges and Limitations, Review, Sensors 2013, (2013)

Inertial Measurement System for Upper Limb Joints Tracking

Elisa Perez, Natalia López, Marcos Dominguez, and Eugenio Orosco

Abstract

This work presents a system for tracking and analysis of upper limb movement through the use of inertial sensors. The designed system uses four inertial sensors, which are placed at the midpoint of the corresponding segments, that is, hand, forearm, arm, and the last one is located between the scapulae and the spine, and between vertebrae T5 and T6 (Thoracic 5 and Thoracic 6). This last sensor is used as a reference point. The information of the four sensors is preprocessed by a microcontroller and sent wirelessly to a computer. The data of each sensor is processed in order to calculate the angular position of each joint. In this work the concept of quaternions is used to avoid the singularities that occur when the reference axes are aligned with the Earth's gravity axis, instead of working directly with the representation through Euler angles. In addition, a descending gradient filter is implemented to merge the accelerometer and gyroscope data in order to compensate drift errors. To visualize the movement, a simple virtual environment is implemented with SimMechanics®. The designed system is evaluated with 10 volunteers, in flexo-extension and abduction-adduction movements, at different velocities and compared with goniometer measures. The system demonstrates good repeatability and the computed error was less than 3°.

Keywords

Inertial sensors • Upper limb • Tracking joints

E. Perez · N. López (✉) · M. Dominguez
Facultad de Ingeniería, GATEME, Universidad Nacional de San Juan, Av. Libertador San Martín, 1109(O), San Juan, Argentina
e-mail: nlopez@gateme.unsj.edu.ar

E. Perez
e-mail: eperez@gateme.unsj.edu.ar

E. Orosco
Facultad de Ingeniería, INAUT, Universidad Nacional de San Juan, Av. Libertador San Martín, 1109(O), San Juan, Argentina

1 Introduction

There are several neurological, motors or neuromotors pathologies that affect the upper limb movements. One of these pathologies is the stroke, that according to WHO is the most important cause of disability in the adult population [1]. Stroke causes a greater range of disabilities than any other condition and it can affect walking, prehensing, grasping, speech, balance, co-ordination, vision, spatial awareness, swallowing, bladder control and bowel control. About 41% of stroke survivors are discharged from hospital requiring help with activities of daily living. Therefore, these people should receive integral neurorehabilitation [2, 3] as soon as possible and this neurorehabilitation should be coordinate and planning in a multidisciplinary way. When the person has affect the upper limb, he cannot carried out the most of activities of daily living, producing a negative impact in familiar and social life. Then, the neurorehabilitation is very important because this way the person can recover the functionality of the upper limb through the neuroplasticity and achieving autonomy. For the neurorehabilitation planning, physiotherapist requires quantification tools. The measurements with goniometer are more subjective than the other measurement systems, such as [4, 5]. Research works related to the quantification of movements and joints position of upper limb have increased in last years. For example, in [6] authors present a method for joint angle measurement, combining inertial sensors (accelerometers and gyroscopes) and magnetic sensors. This method estimates wrist flexion, wrist lateral deviation, elbow flexion, elbow pronation, shoulder flexion, shoulder abduction and shoulder internal rotation. In [7] is presented a pilot study that aimed to improve the quality of a specific movement, the forearm supination. The participants wore the BiMU system and they played a series of virtual reality (VR) games that recorded their performance. BiMU's peripheral consists of two wireless inertial measurement units that are attached to the forearm and upper arm and measure their movement.

This information is used to control the movement of the cursor and perform click actions. Other works such as [8–10] have carried out studies, analysis and comparison of measurement with inertial sensors.

In this work we develop a system for sensing the joint angles of the upper limb by using inertial sensors (accelerometer and gyroscope). The angles are estimated by using the quaternions method. In addition, to visualize the movement, a simple virtual environment is implemented in SimMechanics®.

2 Materials and Methods

The designed system have four inertial sensors (IMU's), which are placed at the midpoint of the segments, that is, hand, forearm, arm, and the last one is located between the scapulae and the spine, and between vertebrae T5 and T6 (Thoracic 5 and Thoracic 6). This last sensor is used as a reference point (see Fig. 1). Firstly, the IMU's data are sent to the microcontroller, and then these data are sent to the computer for the information processing. In this section the electronic circuit and data processing are described.

2.1 Inertial Sensors

An IMU consists of gyroscopes and accelerometers enabling the tracking of rotational and translational movements. In order to measure in three dimensions, tri-axis sensors consisting of 3 mutually orthogonal sensitive axes are required. A gyroscope measures angular velocity which, if initial conditions are known, may be integrated over time to compute the sensor's orientation. The integration of gyroscope measurement errors will lead to an accumulative error in the calculated orientation. Therefore, gyroscopes cannot

Fig. 1 Sensors position: each one is placed at the midpoint of the segments by hand, forearm, arm, and the fourth is between the scapulae at the height between vertebrae T5 and T6

provide an absolute measurement of orientation by itself. An accelerometer will measure the earth's gravitational so provide an absolute reference of orientation. However, he is likely to be subject to high levels of noise. Therefore a filter should be used for computing a single estimate of orientation through the optimal fusion of gyroscope and accelerometer measurements.

The IMU used in this work is GY-80, this IMU contains a gyroscope L3GD4200D of 3 axes, an accelerometer ADXL345 of 3 axes, a magnetometer HMC5883L and BMP085 that measures pressure and temperature. The communication protocol of sensor data with the Arduino One R3 microcontroller is established through out of pinout SDA and SCL using I2C protocol. The Arduino is the master and it begins the communication and generates the clock signal. The identification of each IMU sensor a multiplexer TCA9548A is used and this way each IMU sensors is configured as slave with a predetermined order (see Fig. 2). The wireless data transmission to the computer is carried out by using a Pololu® Wixel.

2.2 Angular Position of the Joints

The data of the IMU's should be processed in order to obtaining the angular position. In this work the orientation filter proposed in [11] is used. The filter employs a quaternion representation of orientation to describe the coupled nature of orientations in three-dimensions and is not subject to the problematic singularities associated with an Euler angle representation. The data of the gyroscope and accelerometer of each IMU's are introduced in the filter and the quaternion of the output is converted in Euler angles. This way the Euler angles can be obtained starting from the quaternion, with the advantage that singularities are avoided.

2.3 Experimental Protocol

The experimental protocol was carried out with 10 adults 35 ± 3.8 years old, 1.69 ± 0.11 m high), 4 females and 6 males, without clinical history of neurological and/or muscular disorders. After signing the informed consent, the volunteers were asked to carry out the suggested tasks at a comfortable speed. The volunteers performed the following movements: flexion and extension the arm to 90°, abduction and adductions to 90°, flexion and extension of elbow. An expert physiotherapist measures the angular position at the end of the movement by using a goniometer. This measurement is compared with the measurement obtained by IMU sensor.
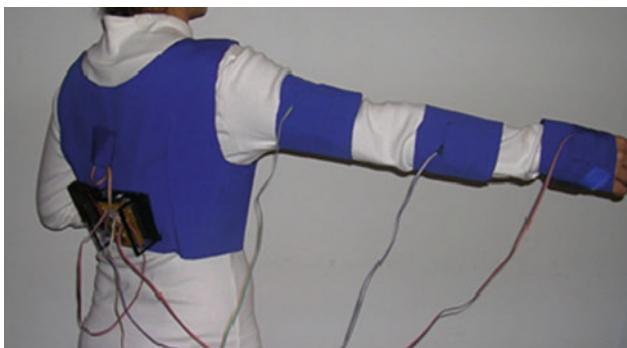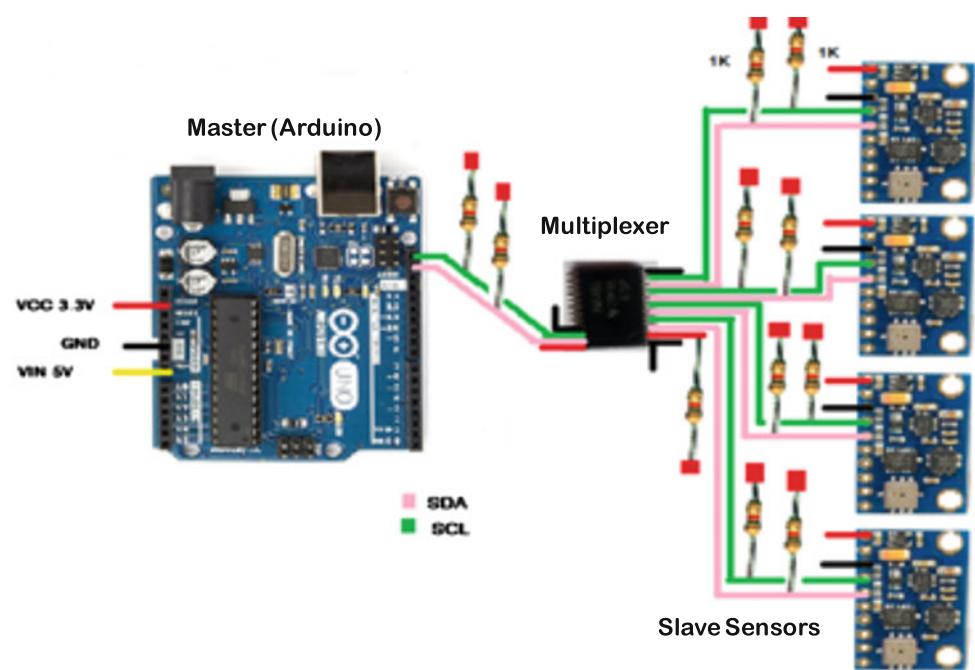
Fig. 2 Electronic configuration: The four IMU sensor are connected with multiplexer and this is connected with microcontroller (master)

2.4 Virtual Reality

The movements carried out by upper limb of the participants can be observed in a simple Virtual reality (VR) environment. These movements in VR were designed using the SimMechanics® toolbox. SimMechanics is a block diagram based modeling environment for the engineering design and simulation of rigid body machines and their motions, using the standard Newtonian dynamics of forces and torques. Then, the software Virtual Reality Toolbox (Simulink 3D Animation®) is used according to [12], for generating the VR (see Fig. 3).
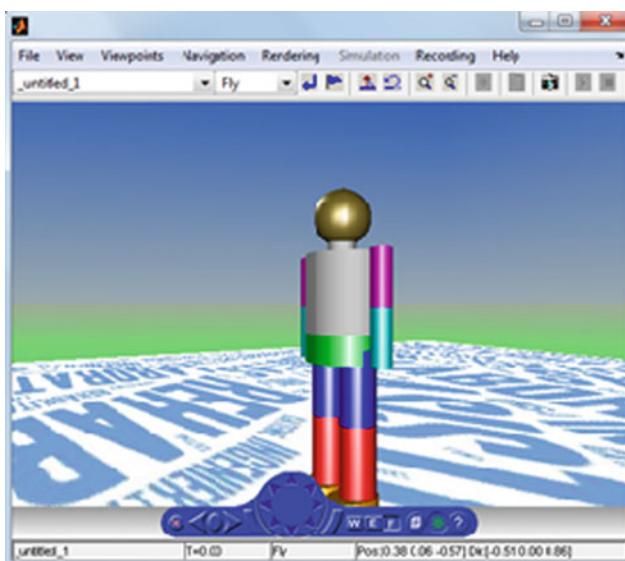
Fig. 3 Graphic interface of the VR designed in SimMechanics

3 Experimental Results

The measurement of the angular position joints obtained with the IMU's and goniometer for each movement explained in Sect. 2.3 is presented in Table 1. The average error measurement of the IMU's is 3%, which represents a low error for the application. In addition the measurement with goniometer is subjective because depend of the physiotherapist, therefore

Table 1 Measurements of the angular position obtained with the IMU's and goniometer. In the last rows the average and error in the measurement with the IMU's sensor comparing with de goniometer is presented

Volunteer	Abduction of the arm	Flexion of the arm	Flexion of the elbow
Goniometer	90	90	90
1	87	88	85
2	80	86	87
3	89	87	90
4	82	95	89
5	98	102	94
6	85	93	89
7	83	87	86
8	91	92	95
9	88	93	95
10	96	104	98
Average	87.9	92.7	90.8
Error	2.1	−2.7	−0.8
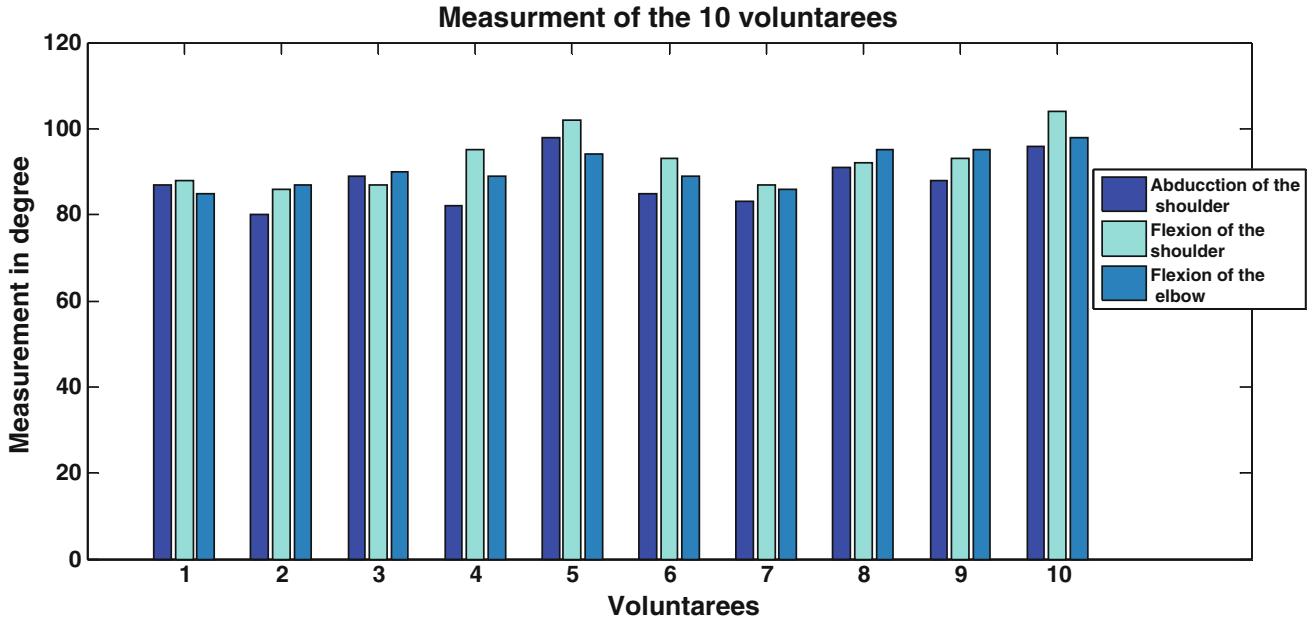
Fig. 4 Measurements obtained with IMU's of ten volunteers
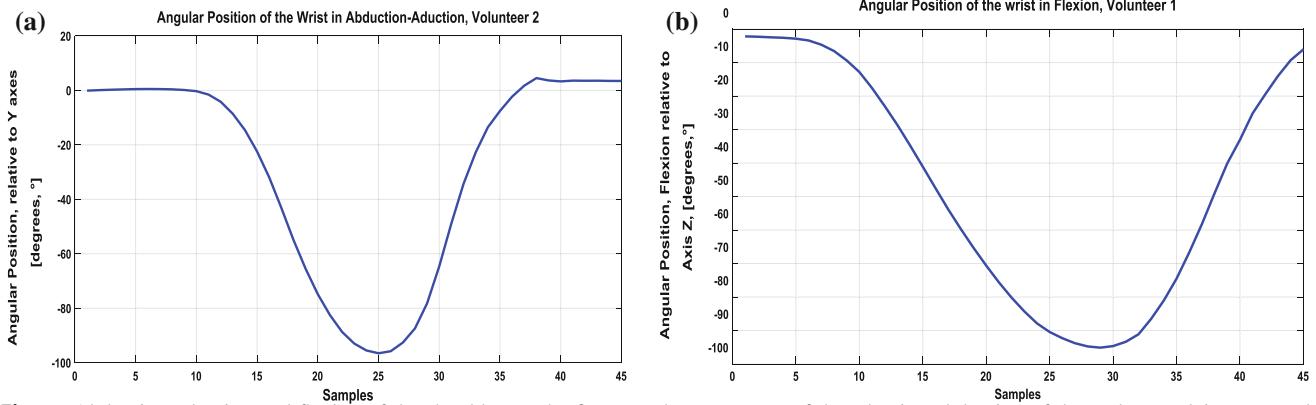
Fig. 5 Abduction-aduction and flexion of the shoulder. In the figure **a**, the movement of the aduction-abduction of the Volunteer 2 is presented, and the measurement is very accurate such as can be observed. In figure **b** the flexion movement of the Volunteer 1 is presented, as accurate than figure (**a**)

we consider that measurements obtained with the IMU's sensor are acceptable. Measurements can be observed in Fig. 4 in a graphics bar, for 10 volunteers. The angular position when two volunteers carried out a flexion-extension and abduction-adduction of the arm can be observed in Fig. 5. The signal obtained does not present noise, is smooth and presents accuracy in the angular position.

4 Conclusions

In this work a measurement system of the angular position of the arm joints has been developed. This system is low cost and presents a good performance regarding the measurement in angular position, even when it is necessary a complete validation of the system with a gold standard method. In

addition is the easy assembly and used. We think the measurement obtained can be used for analysis and study in movements of person with disabilities in the upper limb. This way the professional of health can save the measurement obtained by IMU's and then compare it, obtaining information of the evolution in the movement carried out by patient. The VR development helps the person to visualize the movement performed, therefore this provides the visual feedback which improves the neuroplasticity in person with disability.

References

1. World Health Organization; World Report on Disability, 325 pp; ISBN: 978-92-4-068636-6 (ePUB); see, 2011.
2. R. Cano de la Cuerda, S. Collado Vázquez, "Neurorrehabilitación: Métodos específicos de valoración y tratamiento," 1er ed., Ed. Médica Panamericana: 2015.
3. Lopez N, Perez E, Berjano R, Rizo V, Quiroga J, Abelin C, Tello E, Rodrigo A: Technology Assisted Neurorehabilitation as colaborative project. Proceedings CONFERENCE SCHOOL AND SYMPOSIUM ON ADVANCED NEUROREHABILITATION (SSNR2017). September 17–22, 2017. Baiona (Spain).
4. https://www.vicon.com/motion-capture Accessed 03-30th-2017.
5. Lopez N, Perez E, Tello E, Rodrigo A, Valentinuzzi M: Statistical Validation For Clinical Measures: Repeatability And Agreement Of A Kinect Based Software. BioMed Research International, Hindawi Ed. (in Press).
6. Álvarez, Diego, Alvarez, Juan C., González, Rafael C., López, Antonio M. Upper limb joint angle measurement in occupational health. 2016. Computer Methods in Biomechanics and Biomedical Engineering, 159–170, vol 19, 2. Taylor & Francis.
7. Velasco M.A. et al. (2017) BiMU—Inertial Sensors and Virtual Reality Games for the Rehabilitation of the Upper Limb in Cerebral Palsy. In: Ibáñez J., González-Vargas J., Azorín J., Akay M., Pons J. (eds) Converging Clinical and Engineering Research on Neurorehabilitation II. Biosystems & Biorobotics, vol 15. Springer, Cham.
8. Xavier Robert-Lachaine, Hakim Mecheri, Christian Larue, André Plamondon, Accuracy and repeatability of single-pose calibration of inertial measurement units for whole-body motion analysis, Gait & Posture, Volume 54, 2017, Pages 80–86, ISSN: 0966-6362.
9. Liyun Yang, Wilhelmus J.A. Grooten, Mikael Forsman. An iPhone application for upper arm posture and movement measurements. Applied Ergonomics, Volume 65, 2017, Pages 492–500, ISSN: 0003-6870, https://doi.org/10.1016/j.apergo.2017.02.012.
10. Filippeschi, Alessandro, Schmitz, Norbert, Miezal, Markus, Bleser, Gabriele, Ruffaldi, Emanuele and Stricker, Didier. Survey of Motion Tracking Methods Based on Inertial Sensors: A Focus on Upper Limb Human Motion. Sensors. 2017. Vol 17. Pp: 1424–8220.
11. http://www.x-io.co.uk/res/doc/madgwick_internal_report.pdf.
12. Muri F., Carbajal C., Perez E., Fernandez H, Echenique A.M. and Lopez N. Diseño de un sistema de rehabilitación para miembro superior en entorno de realidad virtual. Revista Ingeniería Biomédica, 2013, 7(1):81–89; ISSN: 1909-9762.

Estimation of Spinal Loads Using a Detailed Finite Element Model of the L4-L5 Lumbar Segment Derived by Medical Imaging Kinematics; A Feasibility Study

Mohammad Saber Hashemi and Navid Arjmand

Abstract

Low back pain is the most prevalent orthopedic disorder and the first main cause of poor working functionality in developed as wells as many developing countries. In Absence of noninvasive in vivo measurement approaches, biomechanical models are used to estimate mechanical loads on human joints during physical activities. To estimate joint loads via musculoskeletal models, the calculation of muscle forces are of importance. It is however difficult to estimate muscle forces as the number of muscles, i.e. unknown parameters, is far more than the existing degrees of freedom; the system is highly redundant. Therefore, in this study, instead of muscle forces estimation, their effects (i.e., rotations and displacements) is measured by medical imaging techniques and prescribed to a detailed finite element model of the L4-L5 spine segment to determine intervertebral disc pressure as a representative of compressive forces acting on the joint. A previously validated geometrically-detailed passive finite element model of the L4-L5 segment was used. Disc, facet joints, vertebrae, and ligaments were simulated with appropriate elements/material properties. Rotations and displacements of the L4 and L5 vertebrae from supine to upright and from upright to trunk flexion of 10° were measured via x-ray imaging. The kinematics were prescribed to the L4 and L5 centroids. Maximal intradiscal pressure of ~ 0.45 MPa was predicted for the simulated tasks that was in agreement with in vivo data in the literature. Preliminary results indicate feasibility of this kinematics-based approach to predict in vivo spine loads.

M. S. Hashemi (✉)
School of Mechanical Engineering, College 2 of Engineering Schools, University of Tehran, Tehran, Iran
e-mail: ms.hashemi@ut.ac.ir; ms.hashemi92@gmail.com

N. Arjmand
School of Mechanical Engineering, Sharif University of Technology, Tehran, Iran
e-mail: arjmand@sharif.edu

1 Introduction

Backache is known as the most prevalent musculoskeletal disorder and the second agent of disability in Iran impressing 14 millions of mature people [1]. Backaches caused by job tasks are the most significant industrial musculoskeletal disorder. Preventing these difficulties is impossible due to their very high prevalence, though considering Health and Safety Executives (HSE) guidelines and ergonomics requirements could lead us to less potentially harmful ways and designs [2]. Researchers have been encouraged to use computer models in various branches of orthopedic biomechanics. Due to precise simulation of human body's anatomy, repetitiveness, and possibility of accurately imposing loads and boundary conditions as well as calculating desired mechanical parameters in every point of models, finite element models in biomechanics are among the most useful methods of studying body performance in different conditions.

There are diverse experimental and modeling methods for spine load estimation during physical activities. In vivo experimental methods are usually invasive and without practical usability in alive healthy humans. For instance, in a study using such methods, intervertebral disc pressure has been quantified by special sensors placed in the disc for different activities [3]. Then, based on the obtained disc pressure, compressive force acting on the joint equal to the multiplication of pressure and surface area has been readily calculated. However, spine modeling based on the moment and force equilibrium equations has more unknown parameters (including muscle forces) than equations. Therefore, solving such equations is very difficult and is usually handled by approximate methods of optimization or

Table 1 Vertebrae positions in standing posture with respect to relaxing one (positive direction of rotation and displacement are in extension and compression, respectively)

Vertebra	Bending rotation (°)	Superior-Inferior disp. (mm)
L4	1.84	0.714
L5	3.46	0.996

Table 2 Vertebrae positions in 10° free flexion with respect to relaxing posture

Vertebra	Bending rotation (°)	Superior-Inferior disp. (mm)
L4	−1.17	0.714
L5	−4.38	0.996

electromyography. In this study, instead of muscle forces estimation by equilibrium equations, their effects or rotations and displacements gauged by medical imaging of a physical activity is imposed on a finite element model of L4-L5 spine segment to determine intervertebral disc pressure as a representative of compressive forces acting on the joint. For this purpose, first the displacement of L4 with respect to L5 vertebra from resting posture to the desired physical activity's one is measured by a medical imaging modality. Then, these displacements should be imposed on a finite element model of spine's L4-L5 segment and the disc (more precisely, disc's nucleus) pressure would be readily calculated and compared with available experimental data [3].

2 Method

In the studied model [4], CT-scan images of a carefully selected sample taken from a research [5] have been converted to cloud points via Mimics 17 image processing software. Then, the points have been transferred to Shape Design module of CATIA V5R20 for achieving the best mesh structure on vertebrae surface. Based on existing literature [4], vertebrae were divided to three sections for three material properties. Facet joints have been modeled according to anatomical data available in the literature [4]. The disc and its end plates cannot be obtained from CT-scan because of its softness; thereby it has been constructed based on the existing literature information and available geometrical boundaries. For collagen fibers of each of 8 disc annulus membranes, Rebar reinforcing elements were defined by angle alternating between +30 and −30° to the horizon. In total, 31 axial basic connector elements have been modeled for 7 lumbar spine ligaments in the Interaction module. The vertebrae have been tied to the intervertebral disc part to avoid over-complexity while maintaining

resemblance to the actual physics of problem. The contact between the facet joints has been modeled by Surface to Surface Frictionless Contact [4]. The vertebrae have been considered as rigid bodies, because when a body is in contact with another body which is above 100 times softer than the former, it is reasonable to assume the harder one as rigid.

ABAQUS 6.13 was used for finite element analysis. The disc and both vertebrae have been respectively modeled with 56,602 and 78,234 C3D10H elements, but facet cartilage layers have been modeled with 60 C3D20RH elements.

Based on the imaging data, when a person changes posture from relaxing to standing, resulting vertebrae displacements are as shown in Table 1. Furthermore, physical activity of 10° flexion without any other loads, leads to the rotations and displacements illustrated in Table 2. The rotations and displacements were imposed on the finite element model and the results for the disc's nucleus pressure were calculated.

Since many studies concerning finite element models of spine segments have used a range of motion for verification, flexion and extension range of motion were utilized for verification. Pure moment of flexion and extension to the reference point of L4 with the boundary condition of fixing L5 results in a trend of moment against angle of rotation which resembles the ones reported in the literature [6, 7]. In addition, extension stiffness was a little higher than flexion one. Indirect loading were imposed by boundary condition determination having vertebrae positions from the appropriate medical imaging data. Due to unprepared experimental results of a parallel research, imaging data were obtained from the musculoskeletal model of a previous study [5] wherein global and local muscles have been modeled comprehensively.

3 Results and Discussions

By enforcing just relative rotation angle of L4 in flexion direction for standing posture, average Von-Mises stress at integration points reaches 0.044 MPa for the disc's nucleus, but it assumes a diverse range of 0.002–0.160 MPa for different elements of the region. Adding positive relative displacement in vertical direction increases the average one to 0.083 MPa while the range changes to 0.004–0.359 MPa. Considering empirical data of 0.43–0.5 MPa for the disc's nucleus pressure in standing posture [3], one can argue that the maximum stresses resulted from this study's simulations are more correlated with the experimental measures compared with the average ones. It is due to the fact of intrinsic statistical stress variations for the type of element used for the disc's nucleus. Another useful stress measure is the pressure or the minus of one third of stress tensor's trace.
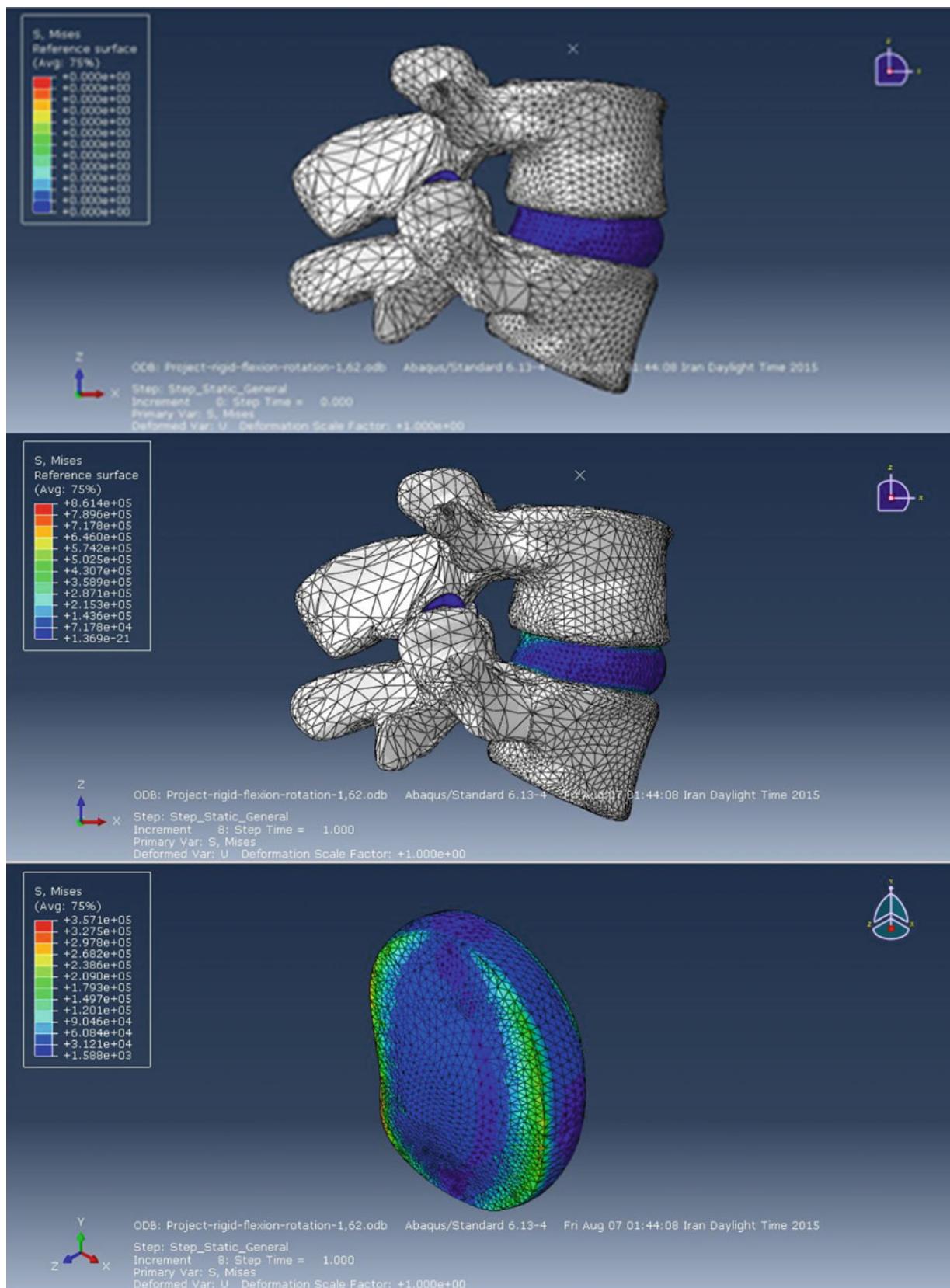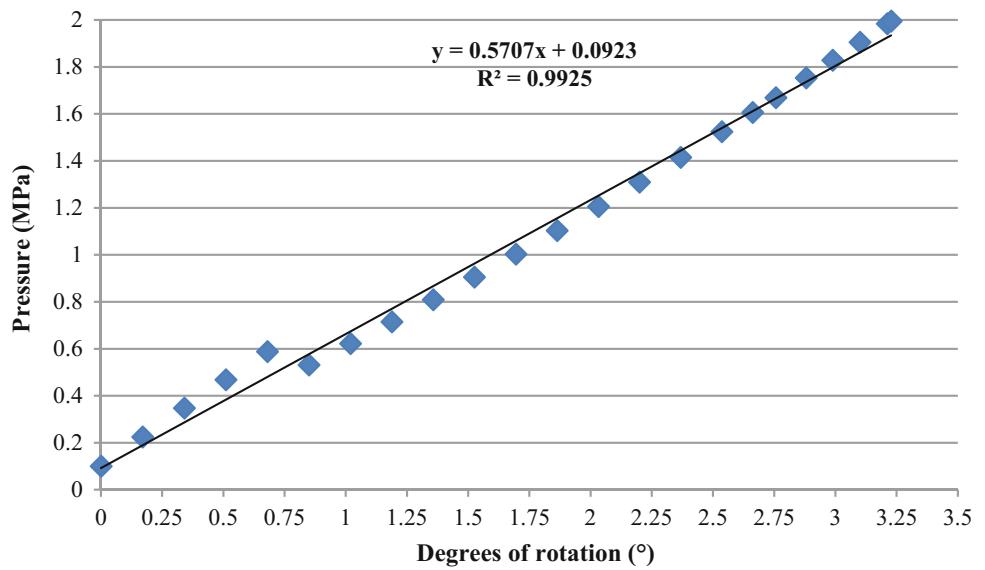
Fig. 1 A sample of simulation results in FE software showing (top) relaxing or initial posture, (middle) deformed state of model, and (bottom) the disc's (including both annulus and nucleus elements) Mises stress distribution

Fig. 2 Pressure measured by maximum Mises stress (in MPa) versus degrees of rotation (flexion direction)

In the physical activity of 10° free-load flexion, the relative rotation would be doubled to 3.2°, but the relative axial displacement would dwarf to −0.006 mm according to the aforementioned data. The average Von-Mises stress is 0.086 and 0.084 MPa for rotation-only and rotation-displacement analyses, respectively. Nonetheless, the maximum ones are 0.316 and 0.359 MPa, respectively. Thus, it is clear that compression represented by the axial displacement increased the simulated pressure which is a better representation of actual phenomenon. It is relatively close to the reported experimental data of this activity [3] (about 0.5 MPa) considering that reported prone pressure is 0.1 MPa, but it is simulated by initial state of simulation or 0 in this study.

Figure 1 shows a schematic of FE simulation results for relaxing or initial posture on the top section, deformed state of model on the middle section, as well as Mises stress distribution of the disc (including both annulus and nucleus elements) on the bottom section. Clearly, the stress distribution is uneven throughout the elements of disc.

Figure 2 illustrates the relationship between the maximum Mises stress and imposed boundary condition of degrees of rotation in flexion direction. It is inferred that the stress has an increasing linear trend with the degrees of rotation. Furthermore, the posterior parts of both of the disc and the nucleus experience tension, but their anterior parts are in compression. Nevertheless, the stresses–especially the maximum values–in nucleus are smaller than those of the whole disc.

4 Conclusion

To date, biomechanical models mostly rely on the optimization or electromyography methods for the calculation of muscle forces accompanied with error, uncertainty, and practical limitations due to the lack of awareness about the central nervous system in functioning and activating different muscles for physical tasks. This issue necessitates inventing and validating new techniques for spine load estimation (especially the disc's nucleus pressure and facet joints' pressure as important mechanical parameters in critical parts of spine like the segment studied here) without any dependency on muscle forces data. Results show that our developed hybrid method of an imaging modality and the finite element model is feasible for the load estimation. More developmental studies may consider more diverse imaging information for different physical activities, more precise imaging data, and better elements instead of the solid cubic ones for the disc's nucleus as used in our study.

References

1. Davatchi, F. et al.: The prevalence of musculoskeletal complaints in a rural area in Iran: a WHO-ILAR COPCORD study (stage 1, rural study) in Iran. Clin Rheumatol, 28, 1267–74 (2009).
2. Shirazi-Adl A. and Parnianpour, M.: Finite Element Model Studies in Lumbar Spine Biomechanics. Biomechanical Systems, ed: CRC Press (2000).
3. Wilke, H. et al.: Intradiscal pressure together with anthropometric data–a data set for the validation of models. Clin Biomech (Bristol, Avon), 16, S111–26 (2001).
4. Rahimi Moghaddam T.: A detailed Finite Element Model of theL4-L5 Motion Segment while Considering Trunk Muscle Forces, M.Sc. thesis in Applied Mechanics. Sharif University of Technology, Tehran, Iran (2014).
5. Arjmand, N. and Shirazi-Adl, A.: Model and in vivo studies on human trunk load partitioning and stability in isometric forward flexions. Journal of Biomechanics, 39, 510–521 (2006).
6. B. Weisse, et al.: Determination of the translational and rotational stiffnesses of an L4-L5 functional spinal unit using a specimen-specific finite element model. Journal of the mechanical behavior of biomedical materials, vol. 13, pp. 45–61 (2012).
7. H. Schmidt, et al.: Application of a new calibration method for a three-dimensional finite element model of a human lumbar annulus fibrosus. Clinical Biomechanics, vol. 21, pp. 337–344 (2006).

Upper Limb Motions Analysis for Development of an Upper Limb Rehabilitation Robotic System

Dorin Popescu, Cristian Petre Copilusi, Horatiu Roibu, Mihnea Ion Marin, Ligia Rusu, and Livia Carmen Popescu

Abstract

The therapists from Prokinetic Rehabilitation Clinic identified the need of a passive rehabilitation robotic system with 3 degrees of freedom for the upper limb. This paper presents the work for the design and development of this kind of rehabilitation robotic system. This project aims to use a user-centered design process to create an upper limb rehabilitation robotic system for patients and therapists from Prokinetic Rehabilitation Clinic. The end-users are and will be involved actively, continuously throughout the system design, development and testing. Upper limb motion analysis has been done using the Vicon system, for simple motions and for functional motions. The positions, velocities and accelerations of each interest joint were obtained. We used this analysis in order to implement the control algorithms for the rehabilitation procedures with an upper limb rehabilitation robotic system. We designed the mechanical, actuation and control systems for this upper limb rehabilitation robotic system.

1 Introduction

World Health Organization (WHO) presented in 2013 some projections of mortality for 2015 and 2030. The stroke is the second cause of death, with 11.7% of deaths in 2015 and 12.2% of deaths in 2030, at global level [1]. Also, WHO presented the latest estimates of cause-specific disability-adjusted life year (DALY), years of life lost and years lost due to disability for the year 2015, where the stroke is the third cause (5.2% DALYs) at global level, and the second cause (6.8% DALYs) at European level [1].

For Romania, WHO estimated that in 2015 the Years Lost due to Disability (YLD) for people living with the health condition or its consequences (due to stroke) is 37.9. In Romania, in the last two decades an important progress has been made for stroke prevention and rehabilitation.

Daily activities of persons with neuromuscular disorders (including stroke or different types of injuries with traumatic or non-traumatic causes) are dramatically changed due to these injuries consequences.

The lower limbs have the main role of human locomotion, but when a person sits down, the upper limbs have the main role for daily activities (eating, drinking, writing etc.). Daily activities require coordination of multiple joints of the upper limbs. This coordination involves both the musculoskeletal and the neural systems.

The most common consequence for central nervous system diseases represents the impairment of the upper limbs, which is also frequently seen at patients with musculoskeletal impairments. The stroke, at the beginning of this century, was a leading cause of movement deficits in Europe and USA [2].

The most common outcomes of stroke are hemiparesis and hemiplegia, which lead to movement deficits in the limbs. Hemiparetic patients present lack of mobility, weakness of specific muscles, abnormal muscle tone, abnormal postural adjustments, loss of sensation etc. [3]. All of these dysfunctions for the upper limbs limit a person's activity and participation in their daily life.

In order to obtain independence and reintegration into normal life, the hemiplegic/hemiparetic patients have to participate to rehabilitation. The rehabilitation aim for this type of patients is to promote recovery of lost functions.

Traditional rehabilitation treatment is based on the use of physiotherapy and it is more effective if it is used early and consists of intensive multisensory stimulation.

D. Popescu (✉) · C. P. Copilusi · H. Roibu · M. I. Marin · L. Rusu
L. C. Popescu
University of Craiova, 13 A.I. Cuza Street, Craiova, Romania
e-mail: dorinp@robotics.ucv.ro

In the last two decades a novel approach of rehabilitation therapy has appeared: rehabilitation robotics. Rehabilitation robotics relies on using robotic systems to assist persons with disabilities. In this way rehabilitation robotics helps therapists to increase the intensity of therapies and to decrease the time of patients' rehabilitation.

Five years ago, Poli et al. reviewed the specific literature and presented the state-of-the-art and the possible future role of robotics in post-stroke rehabilitation, for both upper and lower limbs [4]. Nine years ago, Masiero et al. stated that robots used to assist in repetitive movement practice following neurological injury provide a significant improvement in terms of movement recovery. Their paper presents some key issues in the future perspective of upper limb robotic rehabilitation after stroke [5].

Mazozoleni et al. suggested that combination-therapies may be more effective than individual treatment techniques. Their paper highlights the potential benefits of combining upper limb movement-based robotic therapy with other approaches [6]. Qian et al. designed an electromyography-driven neuromuscular electrical stimulation-robot arm for the multi-joint physical training on the elbow, the wrist, and the fingers [7]. Calabrò et al. stated that it could be possible to strengthen the effects of robotic rehabilitation by coupling focal muscle vibration [8]. Some researchers observed that one third of evaluated post-stroke physical-rehabilitation systems offered via the Internet had a randomized controlled trial that proved efficacy [9]. Sailer et al. presented an overview of technological aspects and differential use of systems for upper limb rehabilitation and they made a review of relevant clinical studies [10].

2 Upper Limb Motions Analysis

Monitoring and assessing movements of the upper limb could improve the quality of robotic rehabilitation procedures. The study of upper limb motion could give important data about shoulder, elbow and wrist kinematics (positions, velocities and accelerations) that can be used in the design and development of a robotic rehabilitation system.

The limbs motions evaluation can be performed with high-end equipment based on:

- Sensors applied on the body, for example the system consists of wearable inertial measurement unit.
- Sensors attached to the patient's limbs.
- Motion analysis equipment such as VICON [11], SIMI [12], CONTEMPLAS [13].

Analyses of upper limb movements are generally performed by measuring kinematic variables of the links and joints with accelerometers, electrogoniometers, or video cameras. Yang and colleagues proposed a decision support system for optical motion analysis [14]. Richards presented a comparison of commercially optical motion analysis systems [15]. There are some systems with high accuracy and real-time tracking features. These systems using multiple infrared cameras capture human motion, by tracking reflective markers fixed to the skin (anatomical landmarks of the subject) [16].

Murphy et al. performed a three-dimensional motion analysis with a ProReflex Motion Capture System (Qualisys, Sweden), during subjects performed the drinking movement with their right arm. Their study provides a detailed three-dimensional kinematic analysis of the drinking task in control subjects [17].

Fitoussi et al. used a VICON optoelectronic system in order to measure the trunk, arm, forearm and hand motions, during the subjects performed two tasks ("to drink" and "to move an object"). Pre- and post-operative kinematic analysis (upper limb evaluation in children with cerebral palsy) were done. Upper limb kinematic evaluation in a group of children with mild hemiplegia involvement showed significant differences when compared to a control group [18].

Rammer et al. used upper limb markerless motion analysis system based on the Microsoft Kinect. They showed this system has potential for improving functional assessment of patients with hemiplegic cerebral palsy [19]. Scallon and Van Heest showed that assessment of dynamic motion is crucial to management of upper limb involvement in children with cerebral palsy [20]. Prat et al. used a six-camera optoelectronic system BTS SMART-Dw for 3D motion recording. The trials were used to carry out the kinematic, inverse dynamic and energetic analyses [21].

Pérez et al. used an inertial sensor-based monitoring system for measuring and analyzing upper limb movements. Their goal was the integration of this motion-tracking device within a portable rehabilitation system for brain injury patients [22].

Our partner in this project (Prokinetic Rehabilitation Clinic) identified the need of a passive rehabilitation robotic system (RRS) with 3 degrees of freedom for upper limb. Our research was based on user-centered design. This was reason to use several tools such as participant observation, interviews and questionnaires to understand therapists/patients in their work/rehabilitation environment. Observation sessions and interviews were limited to observing therapists' interactions with their patients at Prokinetic Rehabilitation Clinic. For engineers it is important to guide the design and integration of robotic systems in clinical practice after they understood the treatment methods and the rehabilitation aims used by therapists.

Kinematic analysis of the upper limb could be conducted using a wide variety of techniques, and methods. We used a marker-based 3D video technique that borrows concepts

from lower limb kinematic analysis. The motion video analysis gave us the information about joint trajectories and range of motion of an upper limb. An experimental motion analysis was performed using a modern equipment (Vicon system with 14 Vicon T10 video cameras and Vicon Nexus software) and the tracking joints were elbow and wrist. The obtained results are used for the implementation the rehabilitation procedures with an upper limb RRS (an exoskeleton with 3 DoF).

The assessment of the impairment of the upper limb following injuries uses:

- Measuring physical attributes, for example range of motion, motion speed, strength and coordination.
- Quantitatively assessing the ability to carry out a functional task.

The subject must wear a special black suit on which reflective markers are attached. These markers could adhered to the skin, too, and have to overlay anthropometric points of the shoulder, elbow, and wrist of the human subject (Fig. 1, left). The VICON system records frame by frame (100 frames/s), it identifies each marker from each frame, and then the Vicon software calculates the joint angles, velocities and accelerations. Using Vicon Nexus software a virtual upper limb skeleton was elaborated in accordance with the person anthropometric parameters (Fig. 1, right).

The VICON equipment records on an infrared technique which needs special attention to the reflective objects inside work environment.

Using the Vicon equipment for experimental human motion analysis, a motion will be analyzed by performing some types of movements. With this equipment the human upper limb joints angular variations, and trajectories will be evaluated in a 3D space. This could be used in rehabilitation robotics for programming a human upper limb exoskeleton in terms of complex motions (at high speeds and combined motions for elbow and wrist joints).

The study group included the members of research teams from both institutions/partners. This means 18 control subjects (9 male and 9 female). The mean age was 38.7 years (from 22 to 63). The subject's height were between 1.50 and 1.86 m, and the weight between 50 and 95 kg. The length of the right arm was measured (from 54 to 69 cm). The subjects (with right dominant hand) were in good health, without musculoskeletal or neurological problems that could affect the arm motion.

All subjects knew information about the study and gave their consent before entering the study. The chosen healthy human subjects have the anthropometric data known and these served as input data for equipment calibration.

The therapists from the Prokinetic Clinic asked that analysed motions to be:

- Each joint movements: flexion/extension of elbow, pronation/supination of forearm and flexion/extension of wrist. For first type of movements, we asked subjects to try not to move the rest of the joints.
- Functional motions (as feeding: "to eat", "to drink"; or "to pick and place an object", "to see what time is it, at hand watch", "to sew").

According to the equipment setup, the movements of the reflective markers were analyzed. The collected data were acquired for both types of analysed motions and these consist in joint center trajectories expressed in angular amplitudes. A movement was repeatedly recorded, for the same person, for several seconds. The acquired data were
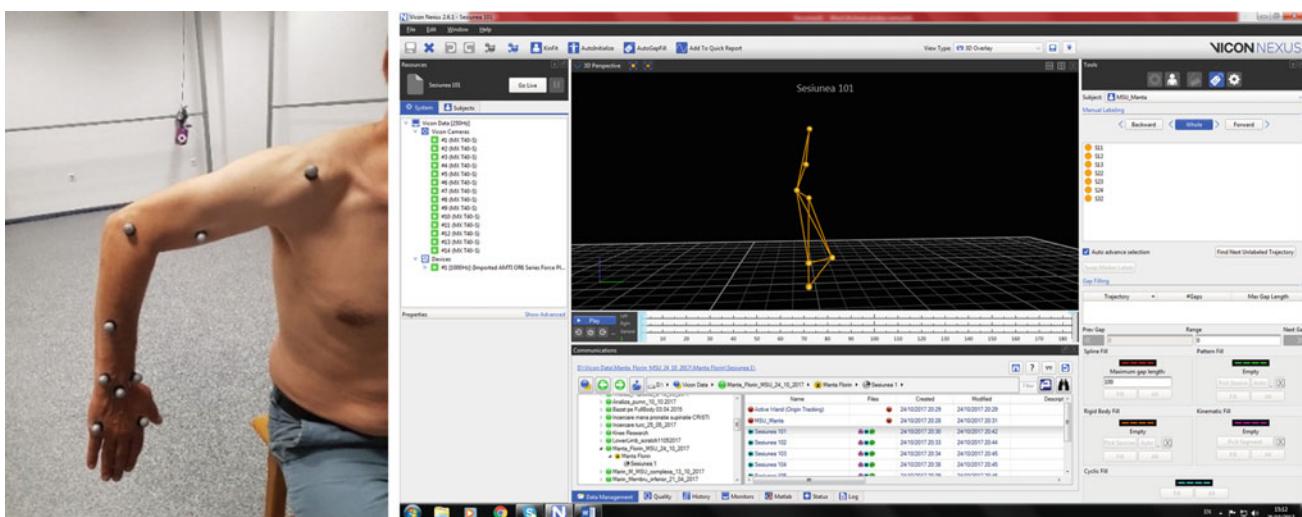
Fig. 1 The reflective markers adhered to the skin (left). Upper limb skeleton definition (right)
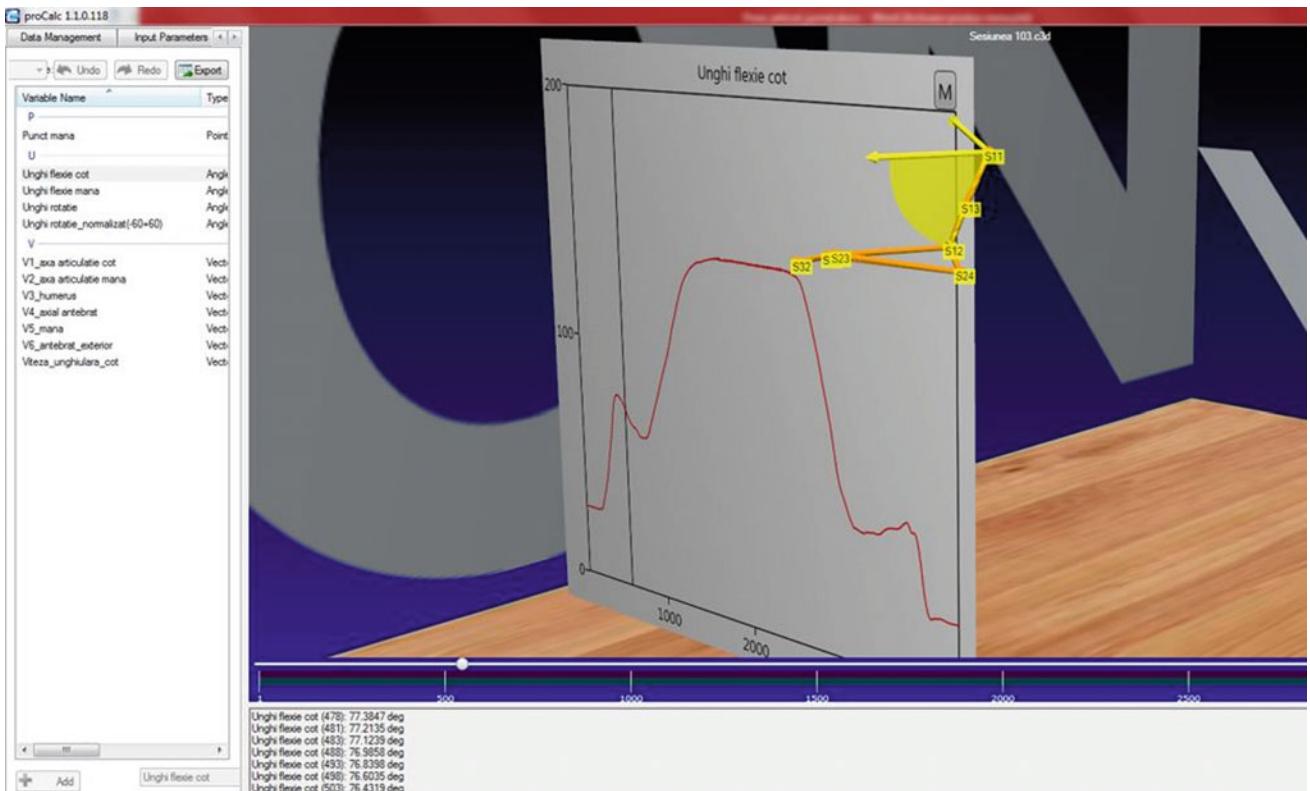
Fig. 2 Flexion/extension of elbow for a functional task (eating)

processed in real-time. A kinematic model was built to estimate 3D upper limb motion. The obtained results for one subject are shown in Figs. 2, 3 and 4 represents angular amplitudes and upper limb trajectory for the acquired motion of the subject.

In this way we obtained a database with these 3 types of variables (angular positions for each joint), and with the corresponding velocities and accelerations for each one, for men and women, youth or adult, which can help us to implement a recovery procedure with a RRS. There were no significant differences between the subjects (obtained results). With these results we established the motion laws for programming of the control system of human upper limb RRS. This information can be used as reference for human recovery after injuries.

3 Upper Limb Rehabilitation Robotic System

Based on technical requirements (obtained from therapists' observation, interviews and questionnaires) and upper limb motion video analysis, we designed the mechanical (by SolidWorks; Fig. 5, left), actuation and control systems for a RRS.

One of the questions of therapists' questionnaire asked about costs of a RRS of the upper limb. At this question, majority of respondents considered that the cost of RRS should not be expensive: to be less than €5,000 (64.7%), or between 5,000 and 10,000 Euro (11.8%). From this reason we tried to find good technical solutions which fulfill technical requirements, but in the same time are not expensive. Therefore, we decided to fabricate many of components of our RRS using our 3D printer (Fig. 5, right).

The RRS will allow flexion/extension of elbow, supination/pronation for forearm and flexion/extension for wrist. The virtual model developed on the basis of the conceptual solution, totals a number of 112 components structured in the final assembly. The subassemblies comprise the main segments of the exoskeleton, the drive units (actuator-planetary gear group), mechanical transmissions and fasteners—screws for assembling the demountable elements.

The mechanical structure of the robotic system is made up of two parts: the fixed part, the support of the exoskeleton and the movable part made up of 3 parts of the upper human arm (arm, forearm and hand). They are connected to each other by means of three rotation kinematic joints equivalent to the main joints for which the conceptual solution has been developed.
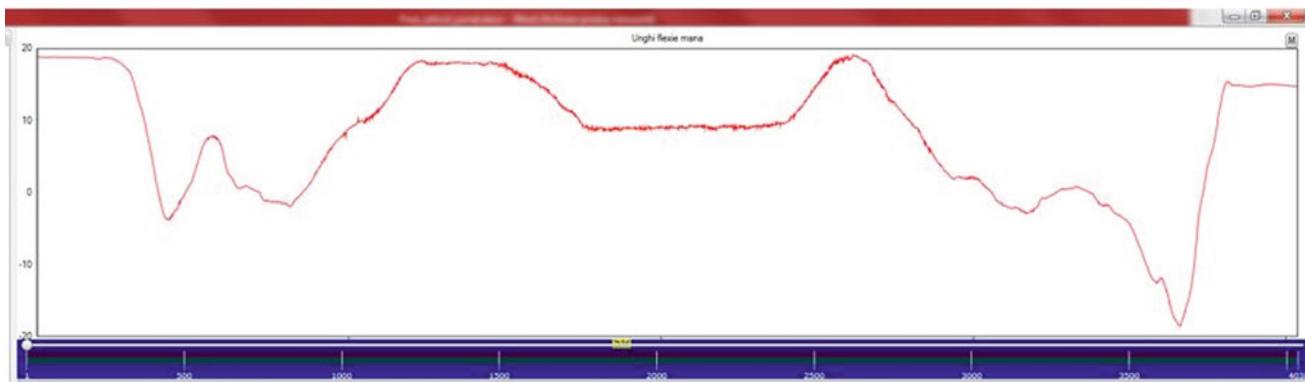
Fig. 3 Flexion/extension of wrist for a functional task (eating)
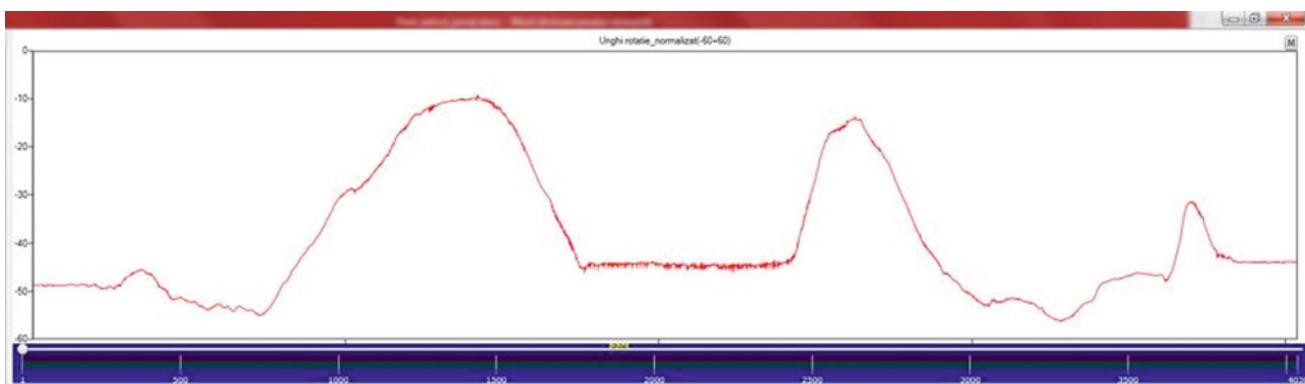
Fig. 4 Pronation/supination of forearm for a functional task (eating)
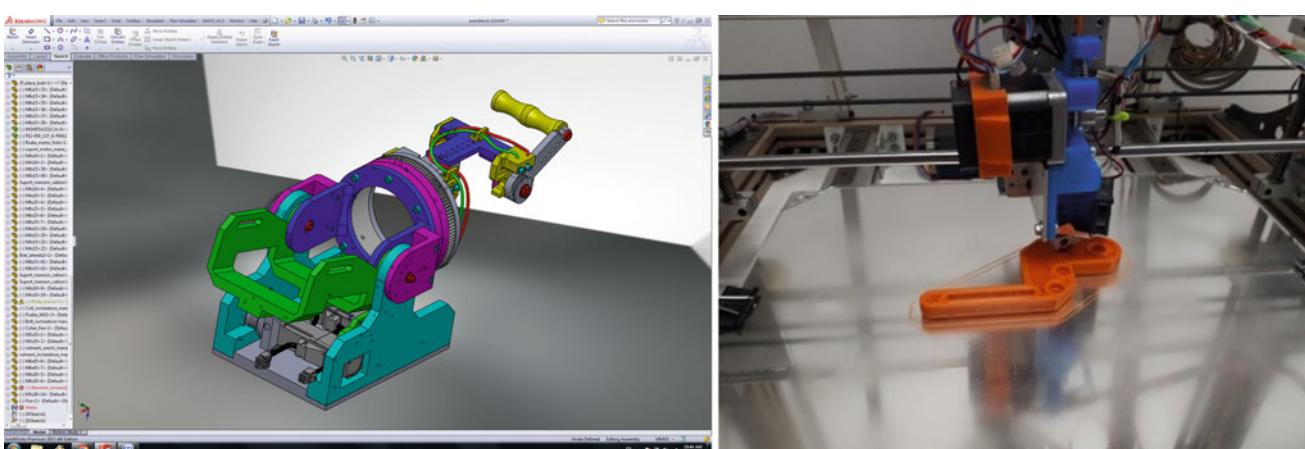
Fig. 5 The virtual model (left). 3D printer fabricates a component (right)

The support of the exoskeleton is the basis of both the exoskeleton itself and the actuators for its operation. The actuation is done by 3 actuators, namely: one for the elbow joint flexion/extension movement, the second for the forearm pronation/supination movement and the third for the wrist flexion/extension movement.

4 Conclusions

A high resolution optical system could be used to record 3D kinematics of the upper limb and to detect the upper limb segments postures and movements. A video motion analysis

system is technically sound and could be applied to standardized task-based upper limb evaluation but their disadvantages (the cost, space, and portability) make them hard to use in clinical analysis.

This paper presents the work for the design and development of rehabilitation robotic system. This project aims to use a user-centered design process to create an upper limb rehabilitation robotic system for patients and therapists from Prokinetic Rehabilitation Clinic. The end-users are and will be involved actively, continuously throughout the system design, development and testing. Upper limb motion analysis has been done using the Vicon system, for simple motions and for functional motions. The positions, velocities and accelerations of each interest joint were obtained. We create a database with motions performed by humans when they are in good health conditions. We used this analysis in order to implement the control algorithms for the rehabilitation procedures with an upper limb rehabilitation robotic system. We designed the mechanical, actuation and control systems for this upper limb rehabilitation robotic system.

Conflicts of Interest The authors declare that they have no conflicts of interest.

References

1. WHO Homepage, http://www.who.int, last accessed 2018/01/29.
2. Rosamond, W., Flegal, K., Friday, G., Furie, K., Go, A., Greenlund, K.: Heart disease and stroke statistics-2007 update: a report from the American heart association statistics committee and stroke statistics subcommittee. Circulation, 115: 69–171 (2007).
3. Cirstea, M.C., Levin, M.F.: Compensatory strategies for reaching in stroke. Brain, 123: 940–953 (2000).
4. Poli, P., Morone, G., Rosati, G., Masiero, S.: Robotic Technologies and Rehabilitation: New Tools for Stroke Patients' Therapy. Hindawi Publishing Corporation, BioMed Research International, Volume 2013, Article ID 153872, 1–8 (2013).
5. Masiero, S., Carraro, E., Ferraro, C., Gallina, P., Rossi, A., Rosati, G.: Upper Limb Rehabilitation Robotics after Stroke: A Perspective From the University of Padua, Italy. J. Rehabil. Med.; 41: 981–985 (2009).
6. Mazzoleni, S., Duret, C., Grosmaire, A.G., Battini, E.: Combining Upper Limb Robotic Rehabilitation with Other Therapeutic Approaches after Stroke: Current Status, Rationale, and Challenges. Biomed Res Int., 2017: 8905637 (2017).
7. Qian, Q., Hu, X., Lai, Q., Ng, S.C., Zheng, Y., Poon, W.: Early Stroke Rehabilitation of the Upper Limb Assisted with an Electromyography-Driven Neuromuscular Electrical Stimulation-Robotic Arm. Front. Neurol. 8:447 (2017).
8. Calabrò, R.S., Naro, A., Russo, M., Milardi, D., Leo, A., Filoni, S.: Is two better than one? Muscle vibration plus robotic rehabilitation to improve upper limb spasticity and function: A pilot randomized controlled trial. PLoS ONE 12(10): e0185936 (2017).
9. Aguirrea, L.G., Urrunaga-Pastora, D., Lazo-Porrasb, M., Taype-Rondan, A.: Post-stroke rehabilitation devices offered via the Internet: Based on randomized controlled evidence?, Annals of Physical and Rehabilitation Medicine 61, 54–55 (2018).
10. Sailer, M., Sweeney-Reed, C.M., Lamprecht, J.: Robot-Assisted and Device-Based Rehabilitation of the Upper Extremity. Neurology International Open 2017; 1: E242–E246, Georg Thieme Verlag KG Stuttgart, New York (2017).
11. Vicon Motion Analysis Equipment User Manual (2014).
12. SIMI Homepage, http://www.simi.com/en, last accessed 2018/01/22.
13. CONTEMPLAS Homepage, https://www.contemplas.com, last accessed 2018/01/22.
14. Yang, C., Kerr, A., Stankovic, V., Stankovic, L., Rowe, P., Cheng, S.: Human Upper Limb Motion Analysis for Post-Stroke Impairment Assessment Using Video Analytics. IEEE Access (Volume: 4), pp. 650–659 (2016).
15. Richards, J.G.: The measurement of human motion: A comparison of commercially available systems. Human Movement Sci., vol. 18, pp. 589–602 (1999).
16. Poppe, R.: Vision-based human motion analysis: An overview. Comput. Vis. Image Understand., vol. 108, nos. 1–2, pp. 4–18 (2007).
17. Murphy, M.A., Sunnerhagen, K.S., Johnels, B., Willén, C.: Three-dimensional kinematic motion analysis of a daily activity drinking from a glass: a pilot study. Journal of NeuroEngineering and Rehabilitation, 3:18 (2006).
18. Fitoussi, F., Diop, A., Maurel, N., Laasel, E.M, Ilharreborde, B., Pennecot, G.F.: Upper limb motion analysis in children with hemiplegic cerebral palsy: proximal kinematic changes after distal botulinum toxin or surgical treatments. J. Child. Orthop. 5:363–370 (2011).
19. Rammer, J.R., Krzak, J.J., Riedel, S.A.,: Evaluation of Upper Extremity Movement Characteristics during Standardized Pediatric Functional Assessment with a Kinect-Based Markerless Motion Analysis System. In: Conf Proc IEEE Eng Med Biol Soc., 2525–2528 (2014).
20. Scallon, G., Van Heest, A.: Kinematic Motion Analysis in Upper Extremity Cerebral Palsy. Phys Med Rehabil Int. 3(5): 1097 (2016).
21. Prat, J.L., Llagunes, J.M.F., Gómez-Pérez, C., Medina-Casanovas, J., Angulo-Barroso, R.M.: New biomechanical model for clinical evaluation of the upper extremity motion in subjects with neurological disorders: an application case. Computer Methods in Biomechanics and Biomedical Engineering (2012).
22. Pérez, R., Costa, U., Torrent, M., Solana, J., Opisso, E., Cáceres, C., Tormos, J.M., Medina, J., Gómez, E.J.: Upper Limb Portable Motion Analysis System Based on Inertial Technology for Neurorehabilitation Purposes. Sensors, 10, pp. 10733–10751 (2010).

Virtual Biopsies with Handheld Dual-Axis Confocal Microscope

Wibool Piyawattanametha

Abstract

We demonstrate a novel microelectromechanical system (MEMS) based Dual-Axes confocal (DAC) microscope in a 10-mm diameter handheld package. Miniaturization is achieved by using a barbell-shaped, gimbaled, two-dimensional (2-D) MEMS scanner that is actuated by self-aligned vertical comb actuators. The maximum DC optical scan angles are $\pm 4.25°$ on the inner axis and $\pm 1.5°$ on the outer axis, and the corresponding resonance frequencies are 3.4 and 1.2 kHz. The maximum imaging rate is 5 frames/s. The miniature DAC microscope operating at 785-nm-wavelength achieves full-width-half-maximum (FWHM) transverse and axial resolutions of 4.5 μm and 5 μm, respectively.

Keywords

Confocal microscope • 2-D MEMS scanner
Imaging • High resolution image • 3-D image

1 Introduction

Conventional single-axis confocal (SAC) microscopes are very attractive for imaging biological microstructures in biomedical research. This is due to its sub-cellular imaging capability from a high numerical aperture (NA) lens to achieve high lateral resolution, and its optical sectioning property from a confocal pinhole to reject out of focus light. Therefore, a high resolution three-dimensional (3-D) image from highly scattering media can be reconstructed by successively scanning each 2-D focal imaging plane. Furthermore, the combination of confocal and fluorescence microscopy, by fusing fluorescent molecules to proteins and enzymes to study cellular processes, heralds a new in vivo imaging era. As a result, in vivo functional images obtained from the combined techniques are unmatched by other imaging modalities. SAC microscopes have a tradeoff between resolution, field of view (FOV), and objective lens size, since a high numerical NA lens is needed for sufficient resolution, and a long focal length is needed for a large FOV and working distance (WD). The DAC microscope architecture has been proposed utilizing two overlapping low NA beams, which effectively decouples these tradeoffs [1, 2]. The DAC architecture shown schematically in Fig. 1, utilizes two low NA objectives with the input illumination and output collection beams crossed at a half angle, θ, from the midline.

This DAC design offers several advantages over the SAC design. First, the higher NA required by the SAC design implies a smaller WD and smaller FOV. In contrast, the DAC design has a long WD (due to its utilization of low NA lenses), providing room for post-objective scanning by using a MEMS scanner. An additional advantage of post-objective scanning is an aberration-free scanning beam. Second, in the SAC design, the axial resolution is substantially worse than the transverse resolution, while the DAC design provides balanced resolutions in all spatial dimensions. Third, the DAC design has superior optical sectioning because light scattered along the illumination path outside the focal volume couples to the output fiber with very low efficiency, enhancing both detection sensitivity and dynamic range [3]. Previously, MEMS-scanner-based DAC microscopes have been demonstrated in a tabletop setup [4, 5], and then in the first miniaturized prototype system on a V-block [6, 7]. In this paper, we present the first fully-packaged miniature MEMS-scanner-based DAC microscope capable of 3-D in vivo real-time imaging at 785-nm-wavelength.

W. Piyawattanametha (✉)
Departments of Biomedical and Electronics Engineering, King Mongkut's Institute of Technology Ladkrabang, Bangkok, 10520, Thailand
e-mail: wibool@gmail.com
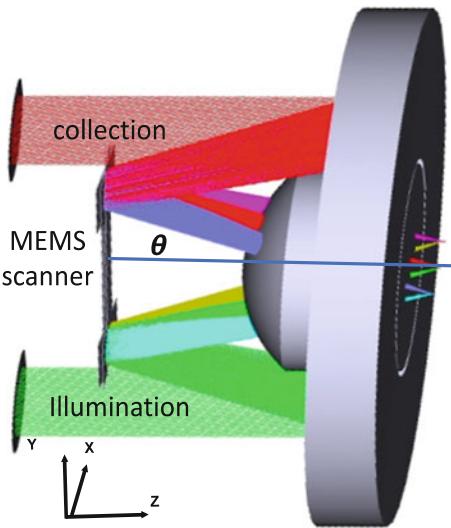
Fig. 1 Dual-axes confocal microscope architecture
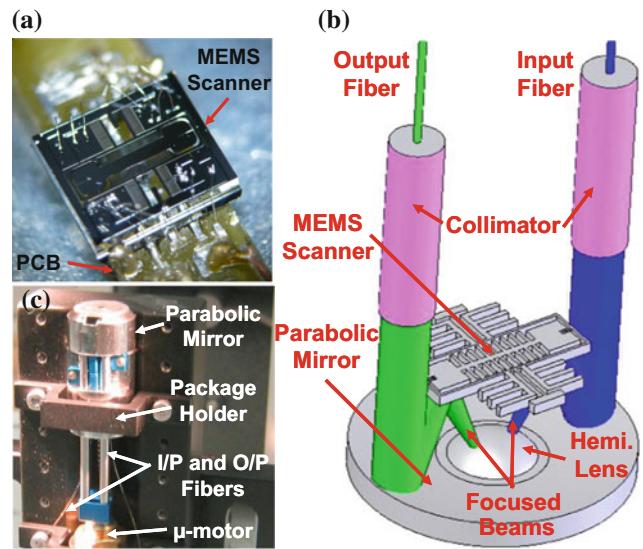
Fig. 2 **a** A MEMS scanner on a PCB. **b** Schematic drawing of the scan head. **c** A 10-mm diameter scan head held on a V-block during assembly

2 MEMS Based Imaging Head Design

Figure 2a shows an optical image of a scanner (die size = 3.2 × 2.9 mm^2) on a printed circuit board. The scan head (Fig. 2b) consists of two optical fiber collimators for illumination and collection beams, a parabolic mirror (PM), and a fused-silica hemispherical lens (HL) to reduce beam aberrations. Figure 2c shows a photograph of the 10-mm diameter scan head. The 2-D MEMS scanner is actuated by electrostatic vertical comb actuators. The scanners are batch fabricated on silicon-on-insulator wafers that have two single-crystalline silicon device layers (30 μm each). The mirror, movable comb teeth, and inner torsional springs reside in the upper device layer. The frame, outer torsional springs, and fixed comb teeth are fabricated within both device layers. Fabrication involves four deep-reactive-ion-etching steps. The first three steps self-align the comb fingers in the device layers by transferring mask features sequentially from upper to lower layers. The last step removes the backside of the substrate behind the mirror, releasing the gimbal for rotation [4, 8]. The scanner has a barbell shape to accommodate both the illumination and collection beams. By using the same scanning surface for both beams, the two overlapping focal regions stay aligned throughout the scan. The scanner is metallized with 10-nm thick aluminum (reflectivity = 67% at 785-nm-wavelength) to increase reflectivity. The mirror radius of curvature is greater than 60 cm. Static optical deflections of ±1.5° and ±4.25° are achieved for the outer and inner axis, respectively. The resonant frequencies are 1.22 kHz for the outer axis, and 3.41 kHz for the inner axis.

3 DAC Microscope Imaging Setup

A schematic of the optical imaging setup is shown in Fig. 3a. The optical power from an 11-mW CW laser source (λ_0 = 785 nm) is coupled into the illumination collimator (θ = 24.3°). The illumination beam is focused by a parabolic mirror (PM) and reflected off the first mirror surface of MEMS scanner. The focused beam continues through a HL until it reaches the focal plane within the sample. Scattered light from the overlapping foci is collected through the HL and reflected to the other mirror surface. The light is collimated by the PM before being focused onto the output fiber and detected by a photomultiplier tube (PMT). The signal is digitized by a frame grabber and displayed on a monitor. A 790-nm long pass filter is used for fluorescence imaging. The NA of focused beams is 0.2. The output laser power on the sample is 1.8 mW. A photograph of a fully-packaged miniature DAC microscope is shown in Fig. 3b.

4 Imaging Results and Discussions

Each image is acquired by the MEMS scanner performing a 2-D raster scan on the image plane. Both the inner axis (slow-axis) and the outer axis (fast-axis) have their opposing comb actuator banks driven 180° out of phase. This is done
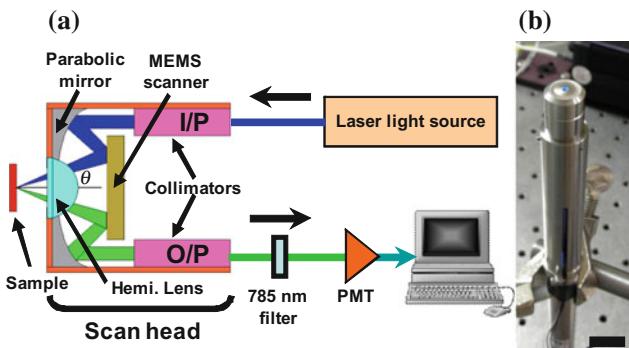
Fig. 3 a DAC microscope imaging setup. **b** A full–packaged miniature DAC microscope. The scale bare is 10 cm

to maximize the linear region of the angular deflection [6, 8]. However, small image distortions can still be observed on acquired images because higher order voltage dependent terms of the actuators still remain. The voltage on each axis is tuned to have similar deflection angles. The fast-axis is driven at resonance by a unipolar sinusoidal waveform (V_{pp} = 70 V). The slow-axis is driven in a DC driving mode (1–5 Hz depending on required imaging frame rate) with smooth-turn-around sawtooth waveforms (V_{pp} = 200 V) to avoid MEMS scanner oscillating.

All acquired images have 548 × 255 pixels and are captured at 5 frames/s. The maximum FOV is 800 × 450 μm^2. The first imaging demonstration from the miniature DAC microscope in Fig. 4 is performed on a US Air Force (USAF) resolution target. It is also used as a sample to measure the image resolutions and FOV. The FWHM

Fig. 4 A cropped reflection image (no frame averaging) shows group 7 of USAF resolution target. The scale bar is 20 μm
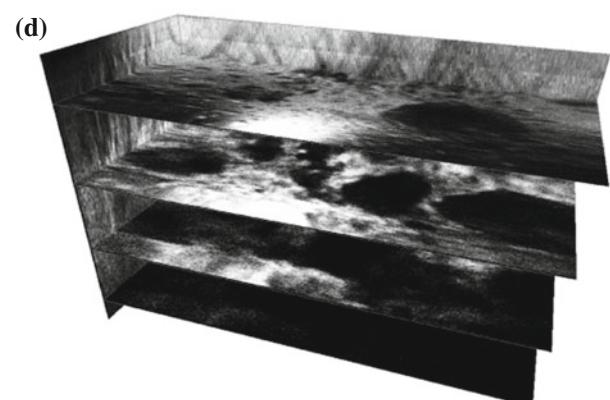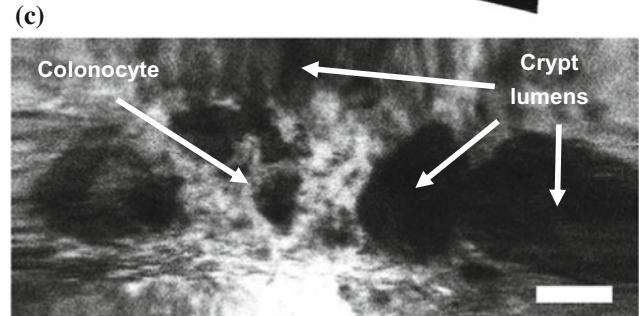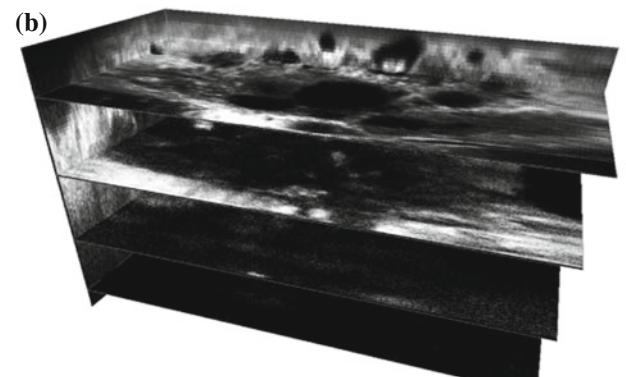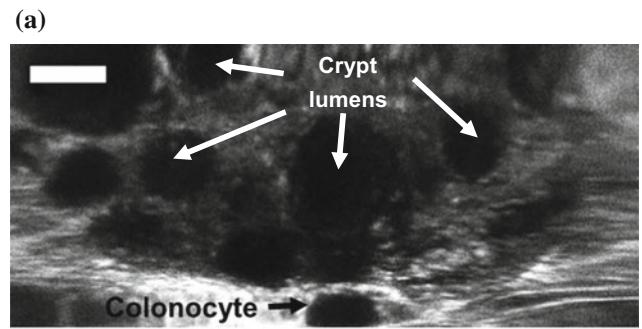
Fig. 5 Ex vivo fluorescence images of normal human colon tissue (**a** and **b**) and pre-cancerous polyps (**c** and **d**). The scale bars are 100 μm

transverse resolution is 4.2 μm. The FWHM axial resolution measured by translating a plane mirror in the *z*-direction is 7 μm. Both the transverse and axial resolutions match well with theory.

Figure 5 shows fluorescence images obtained with Li-Cor IRDye 800CW and Indocyanine Green (ICG), respectively. Both dyes are near-infrared fluorescent dyes. Freshly excised colon tissues are soaked in the fluorescent dyes solution for 1 min before being irrigated with water to remove excess dye. All scale bars are 100 μm. Each fluorescence image is an average of 4 frames. The maximum fluorescence imaging depth in tissue is 410 μm at 785-nm-wavelength. Figure 5a–d show ex vivo fluorescence images of freshly excised (<2 h) normal human colon tissue (a and b) and pre-cancerous polyps (c and d). Rings of colonocytes and crypt lumens are clearly resolved. Figure 5b, d are cross-sections and serial *en face* planes extracted from a 3-D volume rendering of normal colons and pre-cancerous polyps, respectively.

5 Conclusions

We have successfully demonstrated 3-D high-resolution real-time in vivo and ex vivo imaging by the miniature MEMS-scanner-based DAC microscope in both reflectance and fluorescence imaging modes. Our ultimate goal is to further miniaturize the outer diameter of the microscope package while using the same MEMS scanner and electro-optical-mechanical components in order to guide it into a standard endoscope instrument channel (<6 mm in diameter). From our high-quality images, the DAC microscope shows great potential to substantially enhance endoscopic imaging practice by permitting 3-D in vivo real-time imaging. When coupled with fluorescence markers targeted against a variety of diseases, the microscope will enable in vivo optical biopsy for early and accurate detection of cancer and for precise surgical resection.

References

1. T. D. Wang, M. J. Mandella, C. H. Contag, and G. S. Kino, "Dual-axis confocal microscope for high-resolution *in vivo* imaging," *Opt. Lett.,* vol. 28, pp. 414–416, 2003.
2. T. D. Wang, C. H. Contag, M. J. Mandella, N. Y. Chan, and G. S. Kino, "Dual-Axes confocal microscopy with post-objective scanning and low coherence heterodyne detection," *Opt. Lett.,* vol. 28, pp. 1915–1917, 2003.
3. Z. Qiu and W. Piyawattanametha, "MEMS-Based Medical Endomicroscopes," Journal of Selected Topics in Quantum Electronics (JSTQE), Vol. 21, No. 4, August 16, 2015, https://doi.org/10.1109/jstqe.2015.2389530.
4. H. Ra, Y. Taguchi, D. Lee, W. Piyawattanametha, and O. Solgaard, "Two-Dimensional MEMS scanner for Dual-Axes Confocal *In Vivo* Microscopy," *MEMS 2006, IEEE Int. Conf. on Micro Electro Mechanical Systems*, Turkey, 2006, pp. 862–865.
5. H. Ra, W. Piyawattanametha, Y. Taguchi, and O. Solgaard, "Dual-Axes Confocal Fluorescence Microscopy with a Two-Dimensional MEMS Scanner," *IEEE Int. Conf. on Opt. Micro. Electro. Mech. Syt.*, Montana, Aug 21–24, 2006, pp. 166–167.
6. W. Piyawattanametha, J. T. C. Liu, M. J. Mandella, H. Ra, L. K. Wong, P. Hsiung, T. D. Wang, G. S. Kino, and O. Solgaard, "MEMS Based Dual-Axes Confocal Reflectance Handheld Microscope for *in vivo* Imaging," in *IEEE Int. Conf. on Opt. Micro. Electro. Mech. Sys.*, Montana, Aug 21–24, 2006, pp. 164-165.
7. W. Piyawattanametha, H. Ra, Z. Qiu, S. Friedland, J. T. C. Liu, K. Loewke, G. S. Kino, O. Solgaard, T. D. Wang, M. J. Mandella, and C. H. Contag, "*In Vivo* Near-infrared Dual-Axis Confocal Microendoscopy in the Human Lower Gastrointestinal Tract," Journal of Biomedical Optics 17(2), February 2012, 021102:1–4.
8. W. Piyawattanametha, R. P. J. Barretto, T. H. Ko, B. A. Flusberg, E. D. Cocker, H. Ra, D. Lee, O. Solgaard, and M. J. Schnitzer, "Fast-scanning two-photon fluorescence imaging based on a microelectromechanical systems two- dimensional scanning mirror," *Opt. Lett*., vol. 31, no. 13, July 1, 2006, pp. 2018–2020.

Augmented-Reality Surgical Navigation System for Better Healthcare Visualization

Boyu Zhang, Longfei Ma, Xiaofeng Qu, Xinran Zhang, and Hongen Liao

Abstract

Nowadays, good medical services are located in the high-level hospitals. The uneven regional distribution and the unbalanced medical quality between different hospitals bring obstacles to patients for better healthcare. In the community hospital, surgeons may lack advanced surgical skills. Considering the clinical needs, we present an augmented-reality (AR) navigation system using 3-D image overlay technology for better healthcare visualization. Autostereoscopic 3-D images of anatomic structures, which are reproduced by employing integral videography technology, are superimposed on the patient via a half-silvered mirror to form an AR navigation scene. The proposed system can generate the vivid autostereoscopic 3-D medical images and realize in situ image overlay, which eliminates the hand-eye coordination problem. By using our system, surgeons can intuitively observe the operative area, the marked high-risky tissue, surgical tools and surgical planning pathway, which make the surgical operation more convenient and intuitive. To consider the demands of clinical applications, we design a new semi-streamlined prototype combining adjustment mechanism and servomotors, which can broaden the visual field. Results illustrate that the navigation system can enhance the surgeons' operation of the facilitation, as well as the design is more integrated and commercialized, which are more suitable for clinical applications. It is advanced to realize remote visual display and intuitive guidance to solve the uneven distribution of medical resources. What's more, the system can be used for surgical skill training under the guidance of the 3-D images. Thus, the AR system is beneficial to healthcare, especially in the resource-scare communities.

1 Introduction

Image-guided surgeries indicate the location of surgical instruments and the information of the patient's lesion area with 2-D or 3-D reconstructed data obtained from medical imaging devices, like computed tomography (CT) and magnetic resonance images (MRI) [1, 2]. In conventional image-guided surgery, hand-eye coordination problem is often existed during the operation because surgeons perform surgery guided by the non-intuitive images on the computer screen, which is away from the surgical site. To solve this problem, several researchers have proposed relative techniques to merge images into real world view in a more natural and unconstrained manner by using augmented-reality (AR) visualization with microscopes [3], head-mounted displays [4], and half-silvered mirrors [1].

What we interested in medical image display technology is naked-eye autostereoscopic 3-D display without tracking observer's head/eye or wearing stereo glasses for 3-D vision. In the past years, our group has proposed a unique autostereoscopic 3-D image overlay technology based on the integral videography (IV) technology. This technology has been applied in the image-guided surgery. The autostereoscopic 3-D image overlay technology that can be integrated into a surgical navigation system by superimposing an autostereoscopic 3-D image onto the patient in situ using a half-silvered mirror [1–3]. In addition, several prototype systems have been developed to evaluate the feasibility. The surgical navigation system using 3-D image overlay has been evaluated in several clinical areas, such as the neurosurgery [1], oral and maxillofacial surgery [2], as well as the orthopaedic surgery [5].

B. Zhang (✉) · L. Ma · X. Qu · X. Zhang · H. Liao (✉)
Department of Biomedical Engineering, School of Medicine, Tsinghua University, Beijing, 100084, China
e-mail: zhangby14@mails.tsinghua.edu.cn

H. Liao
e-mail: liao@tsinghua.edu.cn

However, there are still some problems in the overlay system need to be solved. Firstly, the depth of the overlaid scene is limited because of the limited depth of IV image, for example, we cannot clearly display both the skin and the spine because they are located in the different depths. Secondly, the lack of user-friendly design from the perspective of clinical needs and poor interactive interface are the factors that limit the clinical translation. Considering the needs of clinical application and economic cost, we developed a new AR-guided surgical navigation system, which combines automatic adjusting mechanism and low-cost tracking modules. The new navigation system could broaden the visual field of the surgical site and realize clear display of the overlaid scene at different depths.

2   Materials and Methods

2.1   Clinical Requirements and Design Strategies

The translation of the AR-guided surgical navigation system from laboratory research to clinical application should consider both technical and clinical requirements:

1. The 3-D image should have a high resolution and a broad visual field.
2. The device and the 3-D image should be tracked accurately.
3. The device should be easily assembled, disassembled and repaired.
4. The device should be protective, user-friendly, and have a better human-interactive interface as well as operating process.
5. Surgeons can adjust the contrast of the 3-D image and the patient's body according to their needs. Generally, they need a brighter view of the patient's body.

Thus, this novel design has considered the clinical requirements based on the discussion with clinical doctors. The novel AR navigation prototype using the 3-D image overlay technology and the automatic adjustment mechanism will make our surgical navigation a safe, accurate, convenient and user-friendly process and provide a better prospect of clinical applications.

2.2   Principle of 3-D Image and AR Overlay

The proposed AR navigation system contains six parts: a 3-D image display module, an automatic adjustment mechanism, a tracking module using stereo camera, a half-silvered mirror for image overlay, a semi-streamlined shell for support and an LED lighting module at the bottom. The whole AR navigation system is mounted on a passive support arm or a robotic arm to reach the required location and posture. In addition, the mechanism for adjusting the 3-D image display module has one translational degree and a rotational degree of freedom to broaden the depth of visual field. As mentioned earlier, the surgeons can see the surface of the patient's lesion as well as the 3-D internal anatomical structures reconstructed by data source equipment through the observing window, as illustrated in Fig. 1.

The patient's data obtained from medical imaging devices are processed using our IV technology [2]. The 3-D image display module including a micro-lens array and a high-resolution high-pixel-density flat display can reproduce autostereoscopic 3-D images along with a fast image-rendering algorithm based on IV technology. The computer-generated graphical 3-D images through a micro-lens array can accurately reproduce the same geometric shape as the original object. For AR surgical navigation system, the autostereoscopic 3-D image is properly superimposed onto the patient by adjusting the external passive support arm before the operation. Surgeons could determine the incised location and operative path more intuitively with the assistant information of displaying the anatomical structure and marking function regions as well as observing the patient's skin.

2.3   Automatic and Precise Adjustment Mechanism

By using the stereo camera, the overlay device, surgical instruments and patient's posture are tracked and adjusted to superimpose the 3-D virtual image on the proper position in the surgical process. This new prototype uses one linear motor and a servo with integrated sensors, which has the fixed parameter and precise position and angle feedback. The 3-D image display module can move the parameter D within 100 mm along the linear guide-way which is 45° to the mirror plane and rotate θ within ±15° around the axis, as illustrated in Fig. 2. More importantly, we can always ensure the suitable fused image is in situ onto the patient according to the patient's posture and the overlay device position. In clinical application, the patient and the overlay device should keep static during operation after registration. However, the depth of the 3-D virtual image and the visual field are limited by the display flat and the lens array. On this occasion, the cooperation of adjustment mechanism and display image could superimpose a proper image on a dynamic position of the human body, which improve the depth of IV image and broaden the visual field.
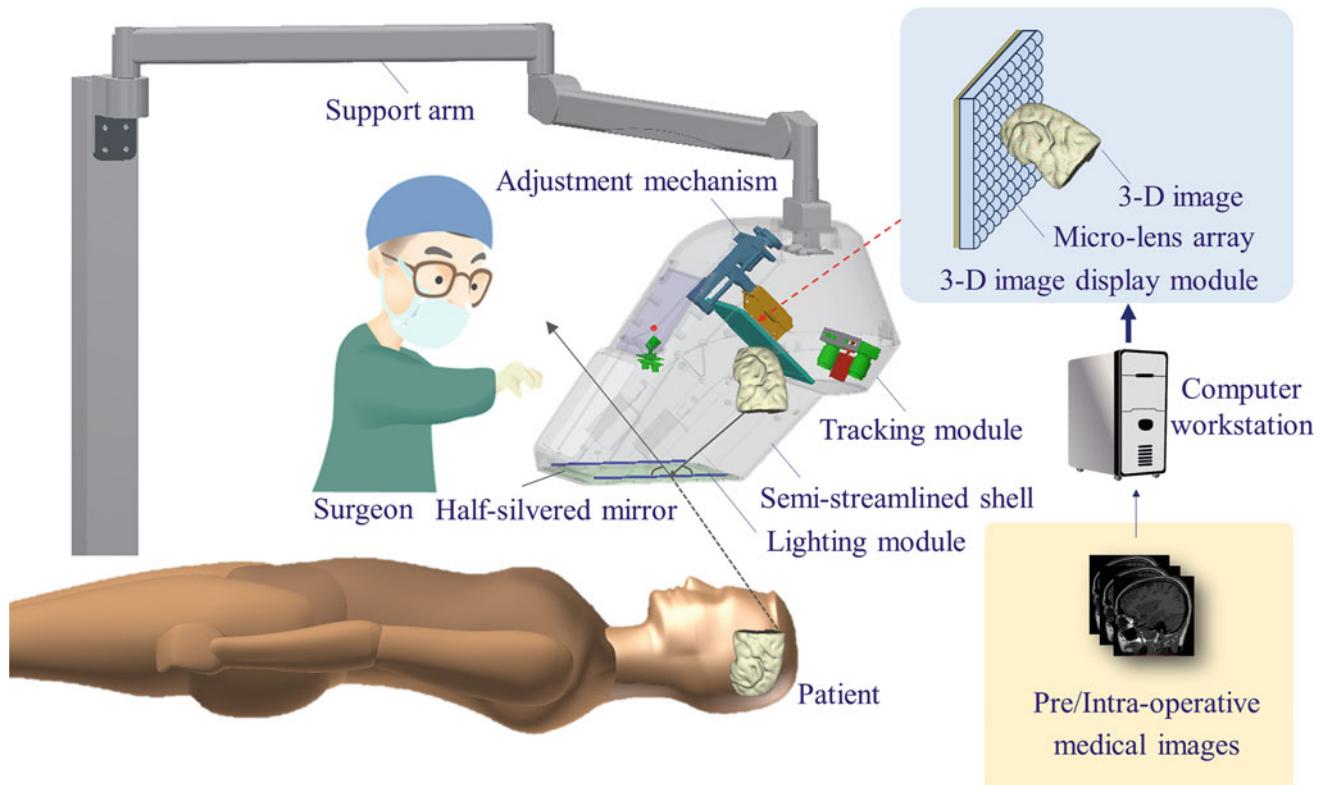
Fig. 1 Principle of the 3-D image and the AR overlay
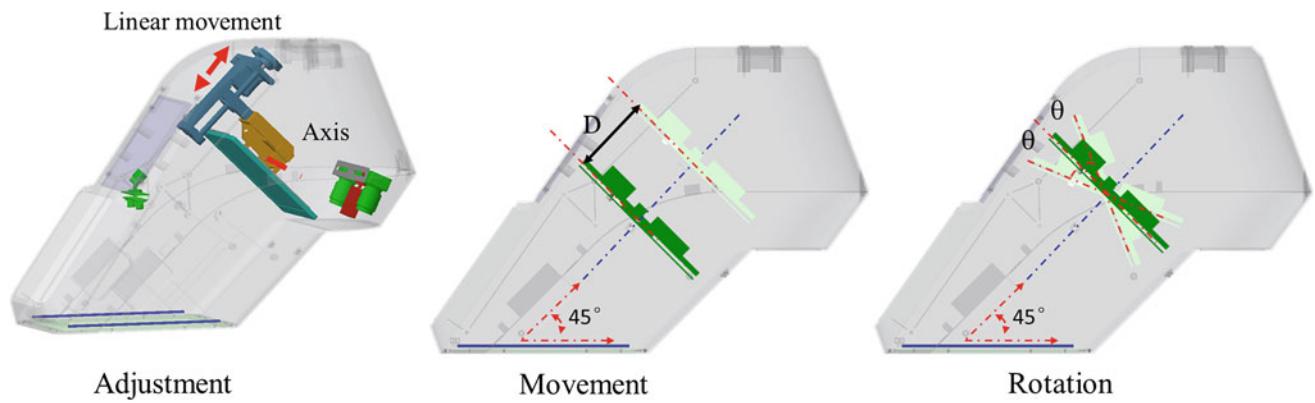
Fig. 2 Adjustment mechanism with two degrees of freedom
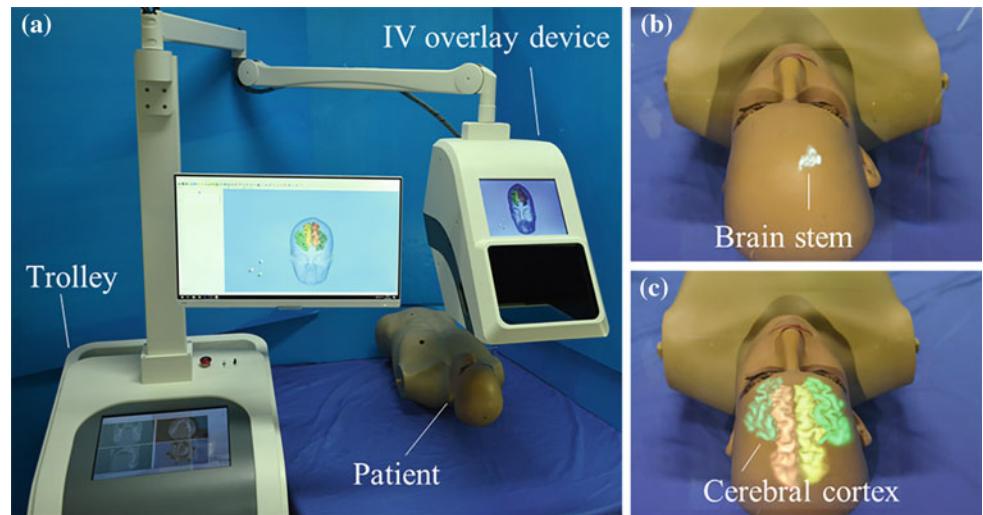
3 System Prototype and Device Evaluation

3.1 System Configuration

The navigation system consists of a trolley, a support arm, and an IV overlay device, as shown in Fig. 3a. The IV overlay device shell is manufactured using ABS plastic considering the weight and strength, and painted with medical white. The results illustrate that the IV overlay device has a good operating experience and could realize the basic adjustment, which is suitable for clinical applications. The IV overlay device consists of the 3-D image display module (includes a 9.7 in. LCD with a resolution of 1536×2048 pixels, micro-lens array with a lens pitch of 1.016 mm and a focal length of 3.0 mm), a half-silvered mirror for image overlay, the computer inside the trolley was equipped with a high-performance GPU, and we have implemented a rendering pipeline using the GPU to accelerate IV rendering for real-time medical imaging.

Fig. 3 a Experimental setup of the AR surgical navigation system. b The 3-D overlaid scene of the brain stem. c The 3-D overlaid scene of the cerebral cortex

3.2 Feasibility in Clinic and Future Application

To simulate the real clinical environment, the phantom experiments were respectively performed in the fields of neurosurgery and knee surgery. The experimental setup of the developed navigation system is shown in Fig. 3a. The experiments proved that the system can provide surgeons in situ visualization of anatomy with motion parallax. The 3-D overlay device was placed at about 15–25 cm above the surgical area, giving the surgeon a sufficient working space. Figure 3b, c show the 3-D overlaid scenes of the brain's anatomical structures of different depths in the phantom experiment.

As shown in Fig. 4, there are overlaid scenes of the knee's anatomies of different depths. The IV overlay device and the models are relatively fixated. The experiments demonstrated that the 3-D display of the anatomical structures at different depths were realized by moving the display fat inside the IV overlay device. The limited depth of the 3-D virtual image and the visual field can be overcome by automatically adjusting the position and angle of the display flat with the lens array to ensure the suitable fused image. The 100-mm moving distance and the 30° rotate angle of the 3-D display device can present a high resolution display of anatomical structures at different depths, it is very useful for clinic.

The AR navigation system could receive further evaluation in clinical studies and have wide prospect in the clinical application. This AR system can potentially assist to transfer the decision of the experienced surgeons to inexperienced surgeons in the less developed areas through internet. It is advanced to realize remote visual display and intuitive guidance to solve the uneven distribution of medical resources. With the assistance of the proposed AR system, even the inexperienced surgeons can easily perform a high

Fig. 4 The 3D overlay scenes of the anatomical structures of the different depths. a The overlaid scene of the knee's skin. b The overlaid scene of the knee bone. c The overlaid scene of the knee bone and blood vessels

quality surgery. What's more, the system can be used for surgical skill training under the guidance of the 3-D image. Thus, the AR system is beneficial to healthcare, especially in the resource-scare communities.

4 Conclusion

According to the requirements of clinical application, we propose the novel AR surgical navigation system, which is more integrated and lower cost. In addition, we will improve the performance of the navigation system and promote clinical translation. Our system implies comprising advances according the following four aspects:

1. **Innovativeness**: We applied the AR technology for surgical navigation and the IV technology to realize a 3-D image visualization. What's more, for realizing the broad visual field and dynamically tracking, we proposed the automatic adjustment mechanism and low-cost stereo camera tracking method.
2. **Potential benefits to healthcare**: The AR system can generate the vivid, true 3-D medical image and realize in situ image guidance, which eliminate the hand-eye coordination problem. The system realizes a high quality surgery for surgeons even such unskilled surgeons, which are beneficial to healthcare.
3. **Low cost**: This system adopted the stereo camera for tracking, which is low-cost and more integrated.
4. **Great potential to reach the market**: In the system design, we considered the clinical needs, operating space, disinfection and the workflow of our system. The AR

surgical navigation system is user-friendly and integrated. Thus, our system implies a high potential to reach the market.

Conflict of Interest The authors declare that they have no conflict of interest.

References

1. H. Liao, et al.: 3-D Augmented Reality for MRI-guided Surgery using Integral Videography Autostereoscopic-image Overlay, IEEE Transactions on Biomedical Engineering, 57(6), pp. 1476–1486 (2010).
2. J. Wang, et al.: Augmented Reality Navigation With Automatic Marker-Free Image Registration Using 3D Image Overlay for Dental Surgery, IEEE Transactions on Biomedical Engineering, 61 (4), 1295–1304 (2014).
3. A. P. King, et al. Stereo Augmented Reality in the Surgical Microscope, Teleoperators and Virtual Environments, 9(4), 360–368 (2000).
4. K. Keller et al.: Head Mounted Displays for Medical Use, Journal of Display Technology, 4(4), 468–472 (2008).
5. L. Ma, et al. Augmented reality surgical navigation with ultrasound-assisted registration for pedicle screw placement: a pilot study, International Journal of Computer Assisted Radiology and Surgery, 1–11 (2017).

An Automatic Preoperative Path-Planning Algorithm for Neurosurgery Using Combined MRI and DTI

Jia Liu, Miao Li, Fang Chen, Changcun Pan, Xinran Zhang, Liwei Zhang, and Hongen Liao

Abstract

Background: The structure of brainstem is very complex, and the surgical path planning for surgical navigation system can reduce the damage of the important tissue. We proposed an automatic preoperative path planning method based on combined magnetic resonance imaging (MRI) and diffusion tensor imaging (DTI) for determining optimal surgical paths in brain stem tumor surgery. *Methods*: First, we register the DTI into the MRI by comprehensive considering three type's information of trace, fractional anisotropy and relative anisotropy to achieve more accurate DTI location information. After that, the optimal solution model of the preoperative path which computes a cost function associated with each point on the outer brain boundary and instrument entry path, is constructed by the gravitational repulsion model and spline interpolation using the segmented model of brainstem and fiber bundle. Furthermore, the preoperative path can be achieved automatically by optimizing the solution of the cost function, and the results are evaluated by comparing the cost of a particular path associated with each critical structure, as well as the total number of examining all the cross-sectional images orthogonal to this path. *Results*: Our method could complete automatic preoperative path planning and avoid important tissue damage with less cross-sectional images orthogonal to the planning path.

1 Introduction

Brain injury and intracranial disease is a common critical disease and neurological surgery is an important means of treatment [1]. Many doctors hope to have a system that will enable them to see the internal structure of the brain and surgical path in real time during the operation, and provide help to the operation. Surgical navigation system has significant effect on neurological surgery, which has experienced tremendous development over the past decades for minimizing the risks and improving the precision of the surgery [2]. Preoperative path-planning is a very important part in surgical navigation system. Path-planning method for surgical navigation system can visualization of proposed needle trajectories to avoid passage through critical structures [3].

There are some research on the path planning. For example, the commonly used method in preoperative path-planning is point-governed region [4]. Although this method considers the influence of some key structures on operative path during operation, the key area still needs to be delineated manually and selected by doctor. According to the literature, path planning can be automatic learned from a number of doctor's experience based on machine learning [5], but this way often requires a large number of sample data to maintain accuracy. A fast adaptive fractal tree is proposed for preoperative path planning in three-dimensional space [6]. This method can achieve the real-time performance by hardware acceleration, but it only used Magnetic Resonance Imaging (MRI) without functional image function. For neurological surgery, it is vital to protect and minimize the injury of brain nerve and function.

Therefore, in this study, we proposed an automatic preoperative path planning method based on combined MRI

J. Liu (✉) · M. Li · F. Chen · X. Zhang · H. Liao (✉)
Department of Biomedical Engineering, School of Medicine,
Tsinghua University, Beijing, China
e-mail: liu-j15@mails.tsinghu.edu.cn

H. Liao
e-mail: liao@tsinghua.edu.cn

C. Pan · L. Zhang
Department of Neurosurgery, Beijing Tiantan Hospital, Capital
Medical University, Beijing, China

and Diffusion tensor imaging (DTI) for determining optimal surgical paths in neurological surgery. We devote on solving the problem of finding a minor injury path from the outer boundary of the brain to a target outlined in a fusion MR and DTI image of patient.

2   Material and Method

Our proposed network consists of three parts: preoperative DTI image distortion correction and image registration with MRI structure; the establishment of spatial location information of important tissue; and automatic acquisition of preoperative path planning, as illustrated in Fig. 1.

2.1   DTI Image Distortion Correction and Image Registration with MRI Structure

DTI imaging is prone to produce severe geometric deformation at the boundary with large magnetic susceptibility. The geometric distortion can reduce the quality of the image, and seriously affects the measurement of the lesion size, lesion location and the precision of surgical plan. We register the DTI into the MRI by comprehensive considering three types information of trace, fractional anisotropy and relative anisotropy to remove the geometric distortion of DTI.

First, we need to transform DTI image into scalar image by extracting the characteristic value of anisotropic information that can be extracted from tensor information. The extracted characteristic value including the trace of the diffusion tensor (Trace), Fractional Anisotropy (FA) and Relative Anisotropy (RA) are used. After that, we used these three kind characteristic value of DTI to register with MRI.

The non-rigid registration method combining affine transformation and B-spline [7] is used, and mutual information is used as the similarity measure.
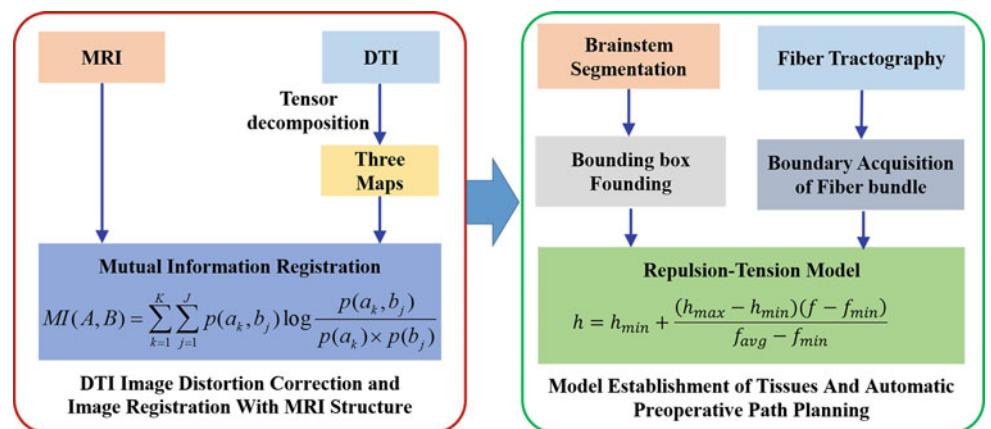
2.2   Spatial-Model Establishment of Important Tissues and Automatic Acquisition of Preoperative Path Planning

The spatial-model establishment of important tissues mainly aimed at protect normal brain tissue, especially for brainstem region and fiber bundle. First, the brain tissue structure is segmented by multi-atlas brain MRI segmentation method [8], and the spatial location information of different brain tissues is obtained. Fiber tractography of DTI can be completed using 3D slicer. We transform these important tissues to some very simple bounding box model which can be used to rapidly and accurately detect of the collision relationship between surgical instruments and important tissues. Hierarchical bounding box method [9] is a commonly used method in collision detection algorithm. This method is used to realize fast test operation path and important areas, to avoid important areas the injury.

2.3   Automatic Acquisition of Preoperative Path Planning

Due to the operation of human body in department of cerebral surgery, the damage of surgical instruments to brain tissue is divided into two parts, one is structural damage (brain stem structure), and the other is functional damage (fiber bundle). Therefore, the two important organs to be considered in cerebral surgery are the brain stem and fiber bundle. Surgical instruments are closer to these tissues, the

Fig. 1 Illustration of the proposed framework

risk is higher, and surgical instruments are farther from these organs, the risk is lower. The mathematical model is established by quantifying this relationship.

In the process of path planning, there are two important factors: one is the distance of path, and another is the important structural damage caused by the surgical path. Therefore, we design preoperative path planning according to these two factors. We use the gravitational force in traditional physics to represent the distance of surgical path, and the repulsive force represents the important structural damage caused by the surgical path.

The quantitative formula of gravitational force is as follows:

$$f_g = \frac{1}{1 + e^{kd}} \qquad (1)$$

d is the distance from the operative start point to the target point, k is set as a coefficient, and it is used to adjust the degree of correlation between d and gravitational force.

The quantitative formula of repulsive force is as follows:

$$f_r = e^{-\frac{s}{\lambda_1 + \lambda_2}} \qquad (2)$$

s is the distance from the surgical path to the important tissue structure. λ_1 and λ_2 represent the influence coefficient of two important tissues for repulsive force. In our paper, two important tissue are brainstem and fiber bundle.

The overall preoperative-path-planning design is:

$$F_{best} = \max\left(h_g f_g - h_r f_r\right) \qquad (3)$$

h_g and h_r represent the impact of two forces on path design, respectively. F_{best} represent the process of finding the extreme value of the difference between the gravitational force and the repulsive force. Furthermore, preoperative-path-planning design can be converted to the influence of the coefficient $h(h_g$ and $h_r)$ for two forces. According to an improved particle swarm optimization (PSO), the influence of the coefficient h_g and h_r for two forces can be established:

$$h = h_{min} + \frac{(h_{max} - h_{min})(f - f_{min})}{f_{avg} - f_{min}} \qquad (4)$$

h_{min} and h_{max} are the minimum and maximum of the coefficient h, respectively. f_{min} and f_{avg} are the minimum and average of the current force (f_g or f_r), respectively. We can get the optimal solution of the distance from the operative start point to the target point and the distance between surgical path and important tissue structure by estimating the h value.

3 Experiments and Results

The research-ethics committee of Beijing Tiantan Hospital approved this study. The clinical and radiological data were collected from medical charts. In the hospital, five patients having brain tumors were scanned. The scanning device is a Philips Achieva 3.0T TX magnetic resonance imaging system. The scanning parameters of T1 sequence are TR = 7.6 ms, TE = 3.7 ms, Matrix = 256 × 256, Thickness = 2 mm, PixelSpacing = 0.9 × 0.9 mm, and the scanning parameters of DTI sequence are: TR = 8464.6 ms, TE = 70.1 ms, Matrix = 256 × 256, Thickness = 2 mm, b = 1000 s/mm^2.

Some experimental results were achieved to evaluate our method. First, the DTI image is decomposed to trace FA and RA maps, and these three maps were used to register with the MRI structure image (shown in Fig. 2). Second, the spatial structure information of brain tissue was segmented from MR images and the fiber tractography of DTI was completed. Finally, the preoperative-path-planning was automatically designed, shown in Fig. 3.

Figure 3 is a comparison result of one patient using the traditional surgical path and the automatic planning path. Traditional path panning is that doctors observe the position of the important organization on the MRI structure image, and then mark the starting point and the target point by themselves. However, it does not take into account fiber bundles connected to the upper and lower regions of the brain in DTI images. In addition, doctors are also prone to subjective errors in path design due to visual errors. Through casting the operation path onto two-dimensional plane, we calculated the number of two-dimension cross plane
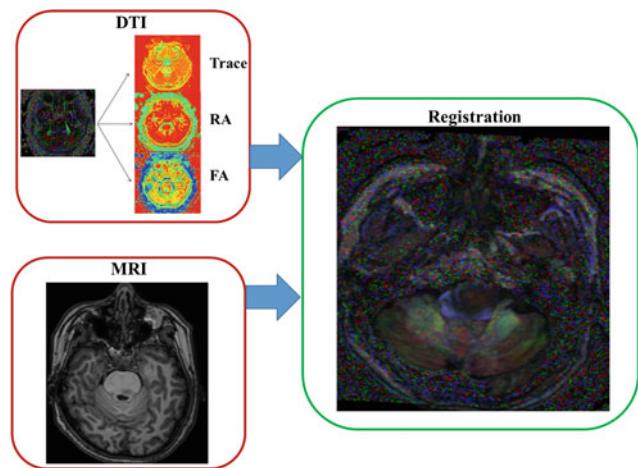
Fig. 2 Registration results between DTI and MRI

Fig. 3 Automatic path planning results based on DTI-MRI fusion information
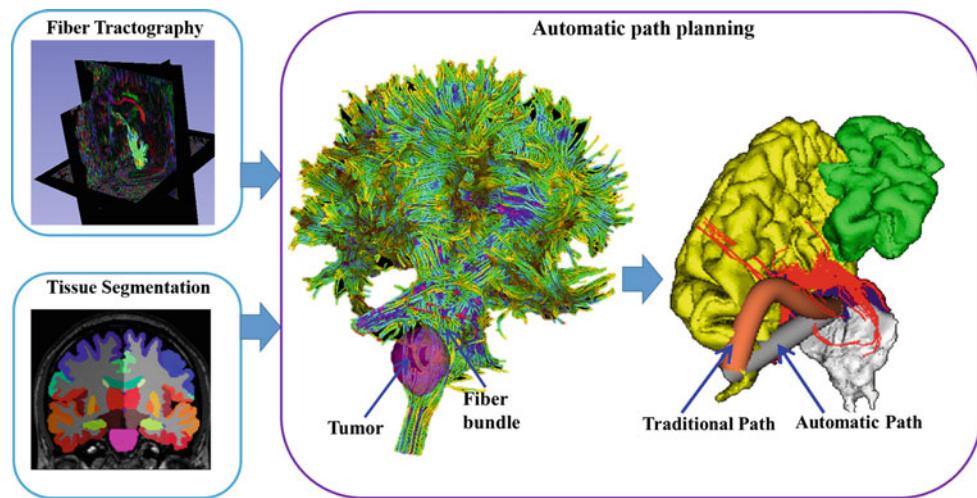
Table 1 The number of collision slices using traditional path and our preoperative path

Patients	Types	Methods	Axial	Sagittal	Coronal
Patient 1	Age: 36	Traditional	5	13	11
	Brainstem glioma	Proposed	1	3	2
Patient 2	Age: 58	Traditional	4	11	9
	Brainstem glioma	Proposed	2	3	1
Patient 3	Age: 22	Traditional	3	8	7
	Brainstem glioma	Proposed	1	3	2
Patient 4	Age: 57	Traditional	3	6	6
	Acoustic neuroma	Proposed	2	2	1
Patient 5	Age: 37	Traditional	2	7	5
	Angiocavernoma	Proposed	1	3	2

occupied by the collision between the surgical path and tissues (brainstem and fiber bundle), as shown in Table 1. We can see that, our proposed automatic path planning method can obtain less number of collision slices.

4   Conclusions

In this paper, we presented an automatic preoperative path planning method based on combined MRI and DTI for determining optimal surgical paths in brain stem tumor surgery, which can effectively circumvent the important tissues and reduce the disability rate. The distortion of DTI images was corrected and registered with MRI. Then, according to the structural information of important tissue in MRI and fiber bundle information in DTI, we finish the automatic preoperative path planning based on the bounding box method and repulsion-tension model. Compared with the traditional shortest path method by doctors' visual observing to determine, automatic preoperative path

planning can overcome the subjectivity of the doctor observed and the visual error. It is helpful for doctors to avoid to damage important tissue in the operation and improve the quality of operation.

References

1. Abbott, N. J., Patabendige, A. A., Dolman, D. E., et al: Structure and function of the blood–brain barrier. Neurobiology of disease, 37 (1), 13–25 (2010).

2. Liao, H.: Integrated diagnostic and therapeutic techniques: Toward an intelligent medical system. Computerized Medical Imaging & Graphics 38(5):421–422(2014).

3. Liao H., Noguchi M, Maruyama T, *et al*.: An integrated diagnosis and therapeutic system using intra-operative 5-aminolevulinic-acid-induced fluorescence guided robotic laser ablation for precision neurosurgery. Medical Image Analysis, 16 (3):754–766(2012).

4. Liu, Y., Dawant, B. M., Pallavaram, S., *et al*.: A surgeon specific automatic path planning algorithm for deep brain stimulation. Medical Imaging 2012: Image-Guided Procedures, Robotic Interventions, and Modeling, 8316:83161D (2012).

5. Dorileo E, Albakri A, Zemiti N, *et al*.: Simplified adaptive path planning for percutaneous needle insertions. Robotics and Automation (ICRA), 2015 IEEE International Conference on.: 1782–1788 (2015).

6. Liu, F., Garriga-Casanovas, A., Secoli, R., *et al*.: Fast and Adaptive Fractal Tree-Based Path Planning for Programmable Bevel Tip Steerable Needles. IEEE Robotics and Automation Letters, 1(2), 601–608(2016).

7. Oguro, S., Tokuda, J., Elhawary, H., *et al*.: MRI signal intensity based B-Spline nonrigid registration for pre- and intraoperative imaging during prostate brachytherapy. Journal of magnetic resonance imaging, 30(5), 1052–1058 (2009).

8. Koch, L. M., Rajchl, M., Tong, T., *et al*. Multi-atlas segmentation as a graph labelling problem: Application to partially annotated atlas data. In International Conference on Information Processing in Medical Imaging (pp. 221–232). Springer, Cham (2015).

9. Liu, J., Chen, J.: 3D Collision Detection Algorithm based on Composite Balanced Binary Bounding Box Tree. International Conference on Education, Management, Computer and Medicine (2017).

A Low-Cost Pedagogical Environment for Training on Technologies for Image-Guided Robotic Surgery

B. Rodríguez-Vila, A. Gutiérrez, M. Peral-Boiza, H. Ying,
T. Gómez-Fernández, E. J. Gómez, and P. Sánchez-González

Abstract

This research presents a novel low-cost pedagogical environment oriented to ease the use experiential learning methods for training on image-guided robotic surgery technologies. The environment proposes a simplified surgical simulation use case: the movement of insertion and extraction of a needle, similar to an image-guided biopsy situation. The training environment is composed of a 3D-printed phantom, a CT scan of the phantom, a virtual reality environment that includes haptic information, an ad hoc 1 degree of freedom (DOF) robotic system for insertion/extraction and a Novint Falcon, a low cost 3 DOF manipulator that allows achieving haptic feedback. A first pilot experience has been carried out in the "Surgical Simulation and Planning" course of the Bachelor of Biomedical Engineering at Universidad Politécnica de Madrid (UPM). Results of the surveys carried out (by teachers and learners) show that the new project-based methodology improves in all cases the values of student's satisfaction obtained using the classical methodology based on master classes and practices.

1 Motivation

Image-guided surgery (IGS) is any surgical procedure where the surgeon uses tracked surgical instruments in conjunction with preoperative or intraoperative images and virtual models in order to indirectly guide the procedure. Robotic surgery or robot-assisted surgery (RAS) are terms for technological developments that use robotic systems to aid in surgical procedures. In case of RAS, instead of directly moving the surgical instruments the surgeon uses a tele-manipulator for remotely controlling them.

Courses related to IGS and RAS taught in the degrees and masters of biomedical engineering of the Universidad Politécnica de Madrid (UPM) have had a theoretical approach until now. Pedagogical methodologies applied involved theoretical sessions and master classes in which the knowledge that the learners have to acquire is presented. In the best scenario, guided practical sessions are carried out in which learners can observe the results of applying that theoretical knowledge to a specific simulated case. On the contrary, experiential learning [1] allows the students to direct their own learning process, increasing their commitment and motivation through a team-based research methodology.

However, the high cost of real IGS and RAS environments makes them inaccessible for biomedical engineering training. Thus, this research presents a new methodology and a novel low-cost pedagogical environment for increasing learners' motivation and autonomy, giving them an active role during their didactic process and based on experiential training methods. The environment proposes a simplified

B. Rodríguez-Vila · H. Ying · E. J. Gómez
P. Sánchez-González (✉)
Biomedical Engineering and Telemedicine Centre, ETSI de Telecomunicación, Universidad Politécnica de Madrid, 28040 Madrid, Spain
e-mail: psanchez@gbt.tfo.upm.es

B. Rodríguez-Vila
e-mail: brvila@gbt.tfo.upm.es

E. J. Gómez
e-mail: egomez@gbt.tfo.upm.es

B. Rodríguez-Vila · M. Peral-Boiza
T. Gómez-Fernández · E. J. Gómez · P. Sánchez-González
Center for Biomedical Technology, Universidad Politécnica de Madrid, Madrid, Spain

A. Gutiérrez · M. Peral-Boiza · T. Gómez-Fernández
E.T.S. Ingenieros de Telecomunicación, Universidad Politécnica de Madrid, Madrid, Spain
e-mail: aguti@etsit.upm.es

E. J. Gómez · P. Sánchez-González
Biomedical Research Networking Center in Bioengineering, Biomaterials and Nanomedicine, Madrid, Spain

surgical simulation use case: the movement of insertion and extraction of a needle, similar to an image-guided biopsy situation.

2 Design of the Pedagogical Environment

The training environment is composed of the following systems:

- **3D-printed physical phantom** from which CT medical images are obtained and serves as the basis for creating 3D virtual models. This helps students understand the role of medical images, as well as their processing and analysis, in IGS and RAS.

  The material of the phantom has to be suitable for the selected medical imaging modality, CT in our case. Furthermore, the 3D-printed phantom: (1) must have holes through which the instruments are inserted; (2) inside the phantom, there should be objects with different mechanical properties to understand the role of haptic information in the surgical intervention; (3) it should be filled with a viscous medium that simulates tissue and interstitial fluid and (4) it can have a simple geometry, since the aim is not to achieve a realistic model of the human body but to transmit the basic concepts of a simulation to engineering learners.
- **A virtual reality software tool** in which virtual models are presented (tissues and surgical tools). The software tool must fulfill several features to cover the needs of the final environment: (1) loading and viewing of medical images; (2) image processing, more specifically segmentation; (3) creation and visualization of virtual models; (4) user interaction with the models; (5) collision detection; and (6) haptic feedback.
- **Robotic system** which allows learners to connect the virtual events in the software tool to the physical world, so they can learn the key issues of the RAS. The EDUCIR robotic system is a 1 DOF robot for insertion/extraction of the needle. User interaction must be done through a haptic device with at least 1 DOF. This device must be compatible with the virtual reality system that will broadcast the information about forces.

3 Results and Discussion

The phantom is formed by an assembled rectangular box built by 3D printing using PLA. Dimensions are $140 \times 210 \times 140$ mm (width, depth and height). In addition, inside the phantom, circular notches of 10 mm diameter are available every 30 mm, where the objects that are inserted inside the

box are fitted. As objects, there are different geometric shapes (cube, sphere and cylinder) and materials (PLA, cork, wood and polypropylene) and (see Fig. 1, left) visible in the CT image as different Hounsfield levels.

There are different software tools that cover the needs of medical image visualization and processing, including the creation and visualization of virtual models. Some of them allow user interactions beyond a simple change of perspective in the visualization of objects. However, the authors have not found any software tools that include the above features and the collisions detection and haptic feedback. For this reason, two independent tools have been selected, one associated with the visualization and processing of medical images and another associated with the simulation of virtual reality. For acquiring the virtual models 3DSlicer [2, 3] is used and the virtual reality simulation is developed using Chai3D [4, 5], an open-source and multiplatform programming environment designed to integrate real-time tactile sensing, visualization and interactive simulation. This environment, developed in C++, allows the student to understand the basic concepts related to visualization (cameras use, lights, textures, etc.), simulation and collision management, haptic feedback and interaction (using keyboard, mouse or haptic devices).

The 1 DOF robotic system is formed by a motor that moves a needle along a single axis. The motor is controlled by an Arduino microcontroller connected to the simulation environment. In this way, the movement of the haptic device results in insertion/extraction of the needle. The base of the robot is fixed in the environment, while the phantom can be manually moved so the needle is inserted through one of the nine access points (see Fig. 2).

As a haptic feedback device, a low-cost commercial system, Novint Falcon (Novint Technologies, Inc.) has been selected (see Fig. 3). Novint Falcon is compatible with Chai3D and its integration with it does not require any additional development. This device has 3 DOF, so the associated Chai3D controller has been modified so that only movements on the insertion axis are transmitted.
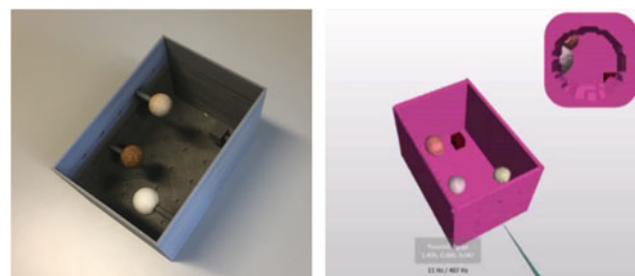
Fig. 1 (Left) Phantom and (Right) visualization example of the virtual models
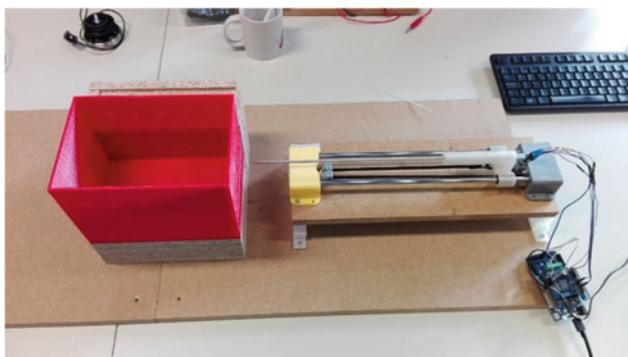
Fig. 2 EDUCIR robotic system and its integration within the training environment

Fig. 3 Novint Falcon, in foreground, with the robotic system and the phantom in background

A proof of concept has been carried out in the "Surgical Simulation and Planning" course of the fourth year of the Bachelor in Biomedical Engineering of the UPM. The course has been designed following the concept of project-based learning (PBL), where learners have worked in small groups (four members) over a semester in the realization of their own simulator.

Learners initially received the DICOM images of the phantom with an unknown distribution of the internal elements. Students created the 3D models and exported them to their own application made in Chai3D. Later, students need to reconstruct the phantom distribution in order to create the experimental stet-up. After this, a Novint Falcon was given to each group. A robotic system was also given but it did not respond to the movements of the haptic device. The learners had to relate the movements of the Novint Falcon with the behaviour of the motor and make the registration between the virtual world and the real one. All the groups were able to deliver an original and unique functional simulation application that integrated all the necessary components.

In order to have a first evaluation of the proof of concept, the survey of the teaching activity was used. Table 1 shows the average values of some of the questions analyzed. In general, the values obtained by the new methodology improve in all cases the results using the classical methodology based on master classes and practices. This improvement is significantly increased if we compare the first edition of the course in which each of the methodologies was applied.

As shown in the table, students support the change made regarding tasks and learning outcomes, the evaluation methodology, the skills acquired and the learner's participation in the development of the subject. In most cases, the difference is near the half a point on a scale of 1–5.

4 Conclusions

Traditional methodologies based on master classes and practices for training IGS and RAS concepts are being replaced by others that encourage learners' motivation and autonomy. This work presents a new methodology and a novel low-cost pedagogical environment based on experiential learning methods for training on technologies for both surgical concepts. A proof of concept has been carried out in the Bachelor in Biomedical Engineering of UPM. Results of the surveys carried out (by teachers and learners) show that the new project-based methodology improves in all cases the

Table 1 Results of the survey (max. score 5)

Question	Classical methodology		PBL
	First edition	Last edition	First edition
The planned tasks are aligned with the learning guide	3.36	3.36	4.23
Evaluation methods are well aligned with the type of tasks	2.95	3.60	4.20
I have improved my starting level, in relation to the competences foreseen in the program	3.59	3.79	4.24
The teacher incentives the participation of the learner during the lessons	3.45	3.68	4.16
In general, I am satisfied with the teaching activity of the teacher	3.50	3.78	4.10

values of student's satisfaction obtained using the classical methodology based on master classes and practices.

References

1. Kolb AY., Kolb DA. Learning styles and learning spaces: Enhancing experiential learning in higher education. Academy of management learning & education. 2005 Jun; 4(2):193:212.

2. Fedorov A., Beichel R., Kalpathy-Cramer J., Finet J., Fillion-Robin J-C., Pujol S., Bauer C., Jennings D., Fennessy F., Sonka M., Buatti J., Aylward S.R., Miller J.V., Pieper S., Kikinis R. 3D Slicer as an Image Computing Platform for the Quantitative Imaging Network. Magnetic Resonance Imaging. 2012 Nov; 30(9):1323-41. PMID: 22770690.

3. 3D Slicer Homepage, www.slicer.org, last accessed 2018/01/30.

4. Conti, F. and Barbagli, F. and Balaniuk, R. Halg, M. and Lu, C. and Morris, D. Sentis, L. Warren, J. and Khatib, O. Salisbury, K. The CHAI libraries. Proceedings of Eurohaptics 2003, Dublin, Ireland, 496–500.

5. Chai3D Homepage, www.chai3d.org,, last accessed 2018/01/30.

Analyzing Rheoophthalmic Signals in Glaucoma by Nonlinear Dynamics Methods

P. V. Luzhnov, D. M. Shamaev, A. A. Kiseleva, E. N. Iomdina, D. D. Khoziev, O. A. Kiseleva, and A. P. Nikolaev

Abstract

We assess the possibility to analyze signals of transpalpebral rheoophthalmography (TP ROG) by methods of nonlinear dynamics and find out how informative this technique is in examining patients with various stages of primary open-angle glaucoma (POAG). The technique was verified on the basis of TP ROG signals obtained in examining 4 groups of subjects: (1) control group (10 eyes with no ocular pathology), (2) stage I of POAG (15 non-operated eyes), (3) stage II of POAG (7 eyes), and (4) stage III of POAG (4 eyes). In all, 36 eyes of 28 subjects aged 25–84 (average age 62.1 ± 7.1 years) were examined. The analysis of TP ROG signals included determining the rheographic index (RI), calculating the RI average in each group, and finding out how RI depends on POAG stage. Alternatively, we used the nonlinear dynamics method with the signal's attractor reconstruction, where we chose the time delay, determined the embedding dimension, and constructed the attractor in the space of the chosen coordinates. After the barycenters of each reconstructed attractor were found, we analyzed TP ROG signals graphically in the attractors' representation plane. The analysis of TP ROG signals by nonlinear dynamics methods demonstrated that a more distinct differentiation of POAG stages as compared to traditional signal processing becomes possible. As the stage of the diseases advances, the location of the barycenter of the reconstructed attractor is changing significantly. It shifts rightward and upward in the space of the chosen coordinates. Due to this fact, it becomes possible to separate TP ROG signals into POAG stages by simple geometric figures and to increase the accuracy of the diagnosis at early stages of the disease, which may be used for further study of the link between the hemodynamic state of the eye and glaucoma stages.

1 Introduction

In recent years, clinics and prophylactic centers display a growing demand for innovative systems of diagnosis, adjustment of treatment plans, and prognostication of the course and outcome of diseases. Being introduced into medical practice, new diagnostic equipment and algorithms able to determine any required number of parameters of the patient's body and organs increases the volume of information available to the doctor, but does not always facilitates the diagnosis. The difficulties encountered in the analysis of information flow by traditional techniques encourage the search for new methods of information processing.

The variety of specific situations, supplemented be the presence of noises and non-stationary of biological signals gave rise to a multitude of approaches to information registration and processing. A growing interest has been observed recently in the study of time series of diagnostic data by nonlinear dynamics methods [1]. It has been proven that functioning manifestations of various body systems are deterministically chaotic processes. Nonlinear dynamics methods provide new data on biological systems, in particular, on the blood circulatory system of human organs or tissues [2].

The normal functioning of the eye, as well as any other organ of the human body, is primarily determined by the adequate level of trophicity of its tissues, which is detected by the relevant blood flow parameters during diagnostic

P. V. Luzhnov (✉) · D. M. Shamaev · A. A. Kiseleva · A. P. Nikolaev
Bauman Moscow State Technical University, 2-Nd Baumanskaya 5, 105005 Moscow, Russia
e-mail: peterl@hotmail.ru

E. N. Iomdina · D. D. Khoziev · O. A. Kiseleva
Moscow Helmholtz Research Institute of Eye Diseases, Sadovaya-Chernogryazskaya 14/19, 105062 Moscow, Russia

procedures. In eye pathologies like myopia, diabetic retinopathy, glaucoma, retinal vascular occlusion and others, hemodynamic tests of the eye provide the ophthalmologist with additional data on the pathogenesis of the disease, ensure prospects of early diagnosis, and enable the evaluation of treatment efficiency. The importance of the research in this field is explained by high incidence of these diseases. For example, glaucoma claims a stable 1st or 2nd place in the overall structure of vision disability in Russia while complicated myopia claims the 3rd place (2nd place for children's disability). For this reason, diagnostic equipment able to determine intraocular blood supply and to evaluate the efficiency of the treatment offered to patients with visual impairment could be very helpful [3, 4]. Possibilities of assessing the changes of diagnostic parameters depending on the stage of the disease and prospect of using these parameters for early diagnosis of eye diseases make the reported study all the more important.

This paper presents the methods of quantitative comparison of signals based on the location of attractor center in the space of the chosen coordinates. The use of these methods is demonstrated by examples of analysis of transpalpebral rheoophthalmography (TP ROG) signals in patients with various stages of primary open-angle glaucoma (POAG).

2   Materials and Methods

The method was verified using TP ROG signals. Rheoophthalmography can evaluate blood flow in the uveal tract. The method is based on the registration of total resistance (impedance) change when the low amplitude probe current flows through eye tissues. The classic arrangement of rheoophthalmography includes the installation of electrodes, e.g. of I. Chibirene design, whereby the electrodes are positioned directly on the surface of the eye near the limbus [5, 6], which necessitates anesthesia of the conjunctiva during the test, may distort the hemodynamic parameters and increases the risk of infection or eyeball damage. Papers [7, 8] describe the currently used TP ROG procedure, in which the electrodes are placed transpalpebrally (on the closed eyelid). To increase test accuracy, the electrodes are placed according to the tetrapolar technique [8] instead of the existing bipolar technique in which Chibirene-designed electrodes are used. The tetrapolar technique has an additional advantage as it permits to make a mathematical model and take into account the characteristics of the anatomical structure of the vascular bed of the eye, which additionally increases measurement precision [9].

Rheoophthalmograpic signals were registered using a rheograph and a tetrapolar lead system whose design allows for transpalpebral use. To ensure the force required to press the electrodes against the eyelid, a specially designed knitted helmet was used, whose geometry can be adjusted to individual anatomical features of the patient. During the test the patient was in a recumbent position, with eyes closed; the lead system was positioned on the examined eye and fixed by the knitted helmet.

The study, which took 7 months, was carried out in the glaucoma department of the Moscow Helmholtz Institute of Eye Diseases. TP ROG signals of 36 eyes of 28 subjects aged 25–84 (average age 62.1 ± 7.1 years) were analyzed. Of these, 15 non-operated eyes had stage I of POAG, 7 eyes had stage II, 4 eyes had stage III of POAG, and 10 eyes belonged to subjects with no eye pathology, who formed the control group.

In the first phase of the experiment, the rheographic index (RI) was determined for the groups considered, and the average RI for each group was calculated. The graph showing the RI dependence on the POAG stage produced controversial results. In stage I of POAG, RI shows a slight increase, after which it falls lower than that of the control group as the disease advances to a more severe stage. This fact impedes the used of RI alone for POAG stage differentiation and gives rise to additional questions regarding fundamental regularities of ocular blood flow changes in POAG registered in TP ROG diagnostic procedures. The changes of blood flow parameters registered on rheographic signals reflect the biophysical, biomechanical and hydrodynamic factors affecting the tone and innervation of blood vessels in the area examined during the diagnostic procedure. The structure of the rheographic signal [10] and the hemodynamic content of signal elements in the cardio interval are shown in Fig. 1.

The cardio interval on the rheographic signals starts (S_{wr}) with a steep rise which passes to the peak of the systolic wave. After that, the level of the signal falls until the next cardio interval ($S_{wr}[i + 1]$). The interval of the ascending part of the signal is called anacrotic limb (T_a) while the descending part of the signal is catacrotic limb (T_d). As the signal level increases, the steepness of the anacrotic limb does not remain the same. It is divided into two parts: the rapid blood filling phase (T_{rf}), which lasts until the maximum derivative of the signal is reached and the slow blood filling phase which continues until the systolic peak of the signal. The systolic peak determines the amplitude of the total rheographic signal ($R_s = RI$) and forms a systolic wave on the signal which is hydrodynamically determined by the heart systole. The systolic wave is followed by a local minimum of the signal, called the incisures (R_{in}). In normal conditions, the incisure is followed by a diastolic wave (R_d). As a rule, the amplitude of the diastolic wave is more pronounced on peripheral rheograms. The amplitude and the form of the rheographic signal is affected by the character of blood flow and the state of viscoelastic properties of blood vessel walls directly in the examination area and in the neighboring areas of the vascular bed at different levels. The
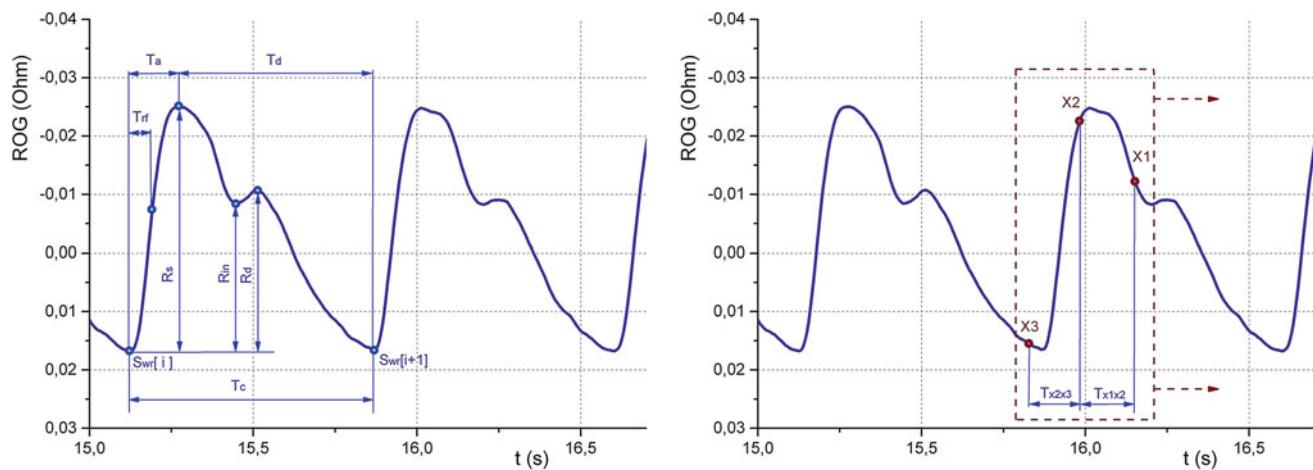
Fig. 1 The analyzing TP ROG signals: structural elements of the rheographic signal and determining the coordinate space

main hemodynamic content of the anacrotic and the catacrotic limbs is the difference between blood inflow and outflow in the examined area. In the anacrotic interval, the volume rate of blood filling prevails over the outflow in the examined area, whereas during the catacrotic interval the rate of blood volume reduction is greater than the inflow rate. The period of rapid blood filling may be considered, on the one hand, as a manifestation of physiological heterogeneity of the left ventricular ejection period, when up to 80% of the stroke volume of the heart is ejected during the rapid ejection phase, and on the other hand, as a reflection of hemodynamic properties of large-bore arterial vessels. The period of slow blood filling falls upon the phase of reduced left ventricle ejection. The catacrotic limb and the diastolic wave are determined by the rate of blood advancement through arterioles and precapillaries into the eye capillary system and by the viscoelastic features of the vessels of the examined area and the vessels located distally. The main temporal and amplitude parameters of the rheographic signal are given in Fig. 1.

Since the evaluation of TP ROG signals of glaucoma patient groups by amplitude parameters alone was ambivalent, we tried to analyze these signals in the temporal area by the methods of nonlinear dynamics. In this case, the diagnostic signal obtained as a result is represented in the coordinate space in accordance with the chosen processing algorithm. While this algorithm has to take into account the main time and amplitude parameters of the rheographic signal, it must manage no less than three parameters. Accordingly, the results of TP ROG signal processing are represented in a three-dimensional coordinate space.

In studying any systems, including biological ones, nonlinear dynamics uses nonlinear models. As a rule, these models are differential equations and discrete mappings [1, 11]. Nonlinear dynamics methods are based on a fundamental mathematical theory which describes nonlinear autoregressive processes and proves that an attractor can be reconstructed from the time series. To restore an attractor, the time series is used, which is represented in our research by a time-sampled TP ROG signal. This time series is analyzed by the delay coordinate method, which means that a sequence of reconstructed vectors [11] obtained from the time series elements is built in the phase space.

Signal attractor reconstruction has three principal stages: choosing the time delay, determining the embedding dimension, building the attractor in the chosen coordinate space.

At the first stage, we choose the time delay in such a way that the correlation between the adjacent units is minimal. To choose this delay, we calculate the autocorrelation function of the TP ROG signal. The time delay will be equal to the time of the first crossing of the zero level by the autocorrelation function. The obtained delay value is 0.5 s.

At the second stage, we determine the embedding dimension. We choose two neighboring points belonging to the reconstruction of the attractor. We determine the distance between them and the distance between the two following points and calculate the ratio between the values (see Fig. 1), $T_{X1X2} = T_{X2X3} = 0.25$ s.

At the third stage, we use the obtained values of the time delay and embedding dimension to reconstruct the attractors of all signal groups considered. The space attractors built for the TP ROG signal are shown in Fig. 2.

The results of the obtained reconstructions are used to compare the shape of the attractors based on the calculation of maximum and minimum averaged vectors.
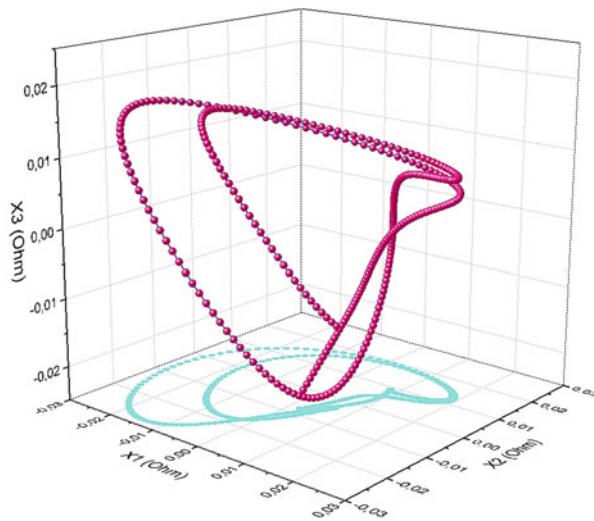
Fig. 2 The building TP ROG signal attractor in the chosen coordinate space

3 Compliance with Ethical Requirements

This study was performed in accordance with the Declaration of Helsinki and was approved by the Local Committee of Biomedical Ethics of the Moscow Helmholtz Research Institute of Eye Diseases. A written informed consent was obtained from all participants.

4 Results

We calculate three attractor reconstruction vectors. The results are shown in Fig. 3. It follows from Fig. 3 that the attractors have a shape of a triangle whose position and form changes depending on the stage of the disease. On the basis of these dependence, a new feature has been proposed, which characterizes the stage of the disease depending on the position of the barycenter of the obtained attractor in the coordinate plane. The barycenter of the triangle is determined geometrically as the intersection point of its medians. After the barycenters of all reconstructed attractors have been calculated, we can analyze TP ROG signals graphically in the plane of attractor representations.

Figure 3 shows the obtained positions of barycenters for each one of the four cases considered. To compare the obtained results quantitatively, let us represent the mappings of the barycenters in a unified coordinate system. Figure 4 shows the diagrams of barycenter position changes depending on the POAG stage, from healthy subject TP ROG signal (M0) to stage III of POAG TP ROG signal (M3).
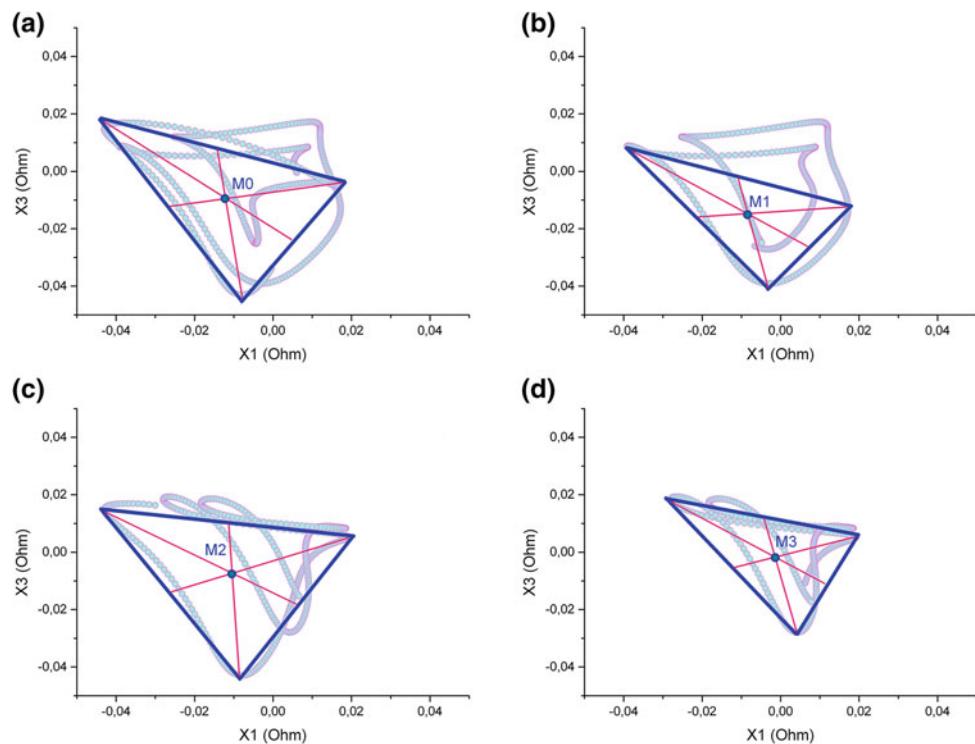
Fig. 3 The barycenters of reconstructed attractors of TP ROG signals: **a** healthy subject, **b** stage I of POAG, **c** stage II of POAG, **d** stage III of POAG
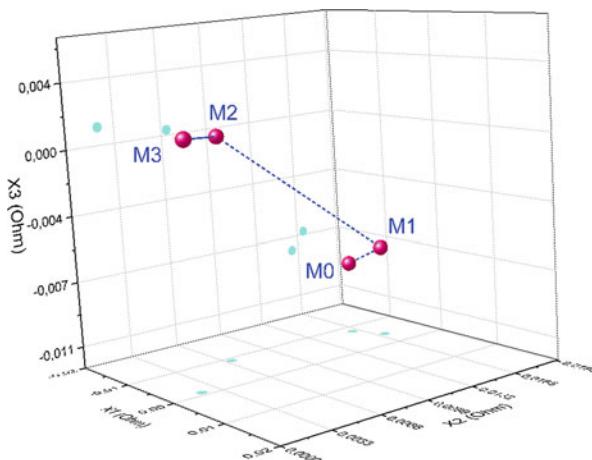
Fig. 4 The barycenter diagram depending on the stage of the disease

5 Conclusions

Our analysis shows that as the stage of the disease advances, the position of the barycenter of the reconstructed attractor changes significantly: it shifts rightwards and upwards in the space of the chosen coordinates. Due to this fact, it becomes possible to discriminate between TP ROG signals in accordance with POAG stages by simple geometrical figures, which makes the diagnosis at early stages of the diseases more precise and creates ground for a further study of the connection between the state of eye hemodynamics and stages of glaucoma and other eye diseases.

References

1. Goldberger, A.L.: Non-linear dynamics for clinicians. Lancet 347 (9011), 1312–1314 (1996). https://doi.org/10.1016/s0140-6736(96)90948-4
2. Ishbulatov, Y.M., Karavaev, A.S., Ponomarenko, V.I. et al.: Phase synchronization of elements of autonomic control in mathematical model of cardiovascular system. Rus. J. Nonlin. Dyn. 13(3), 381–397 (2017). https://doi.org/10.20537/nd1703006
3. Cherecheanu, A.P., Garhofer, G., Schmidl, D. et al.: Ocular perfusion pressure and ocular blood flow in glaucoma. Curr Opin Pharmacol 13(1), 36–42 (2013)
4. Kunin, V.D.: Autoregulation of ocular vessels in health and in primary open-angle glaucoma. Vestnik Oftal'mologii 118(4), 43–47 (2002)
5. Lazarenko, V.I., Kornilovsky, I.M., Il'enkov, S.S. et al.: Our method of functional rheography of eye. Vestnik Oftal'mologii 115(4), 33–37 (1999)
6. Lazarenko, V.I., Komarovskikh, E.N.: Results of the examination of hemodynamics of the eye and brain in patients with primary open-angle glaucoma. Vestnik Oftal'mologii 120(1), 32–36 (2004)
7. Luzhnov, P.V., Shamaev, D.M., Iomdina, E.N. et al.: Transpalpebral tetrapolar reoophtalmography in the assessment of parameters of the eye blood circulatory system. Vestn Ross Akad Med Nauk 70(3), 372–377 (2015). https://doi.org/10.15690/vramn.v70i3.1336
8. Luzhnov, P.V., Shamaev, D.M., Iomdina, E.N. et al.: Using quantitative parameters of ocular blood filling with transpalpebral rheoophthalmography. IFMBE Proceedings 65, 37–40 (2017). https://doi.org/10.1007/978-981-10-5122-7_10
9. Shamaev, D.M., Luzhnov, P.V., Iomdina, E.N.: Modeling of ocular and eyelid pulse blood filling in diagnosing using transpalpebral rheoophthalmography. IFMBE Proceedings 65, 1000–1003 (2017). https://doi.org/10.1007/978-981-10-5122-7_250
10. Avetisov, E.S., Katsnel'son, L.A., Savitskaia, N.F.: Rheocyclographic examinations in myopia. Vestnik Oftal'mologii 80(3), 3–7 (1967)
11. Gracia, J. et al.: Nonlinear Local Projection Filter for Impedance Pneumography (2017) IFMBE Proceedings 65, 306–309 (2017). https://doi.org/10.1007/978-981-10-5122-7_77

Validation of a Wireless and Portable EEG Acquisition System with Dry Electrodes

G. E. Cañadas, C. R. Dell'Aquila, A. Garces, and E. Laciar

Abstract

The Electroencephalogram (EEG) is the non-invasive record of electrical cerebral activity. It is used commonly in sleep studies and in the diagnosis of brain diseases and injuries. In order to reduce noise in the acquisition process and enable new EEG applications such as BCI and home polysomnography studies, we carry out the design and manufacture of a portable wireless system for acquisition of EEG signals. In this paper, we carried out the validation of the system designed by comparing signals acquired with commercial EEG equipment from the AKONIC company. Different EEG recordings were obtained in 4 healthy adult subjects using standard Ag/AgCl cup electrodes and dry electrodes TDE-200 from Florida Research Instruments. Also, we performed the analysis of the acquired signals in eyes-closed and eyes-open resting condition. We conclude that the designed system has low noise levels (0.147 µVRMS and 0.984 µVp-p) and a signal quality comparable to that of commercial equipment, which allows its use in research tasks and portable studies. On the other hand, we observe that the quality of the signal obtained with the dry electrodes is worse, due to the high skin-electrode impedance, but even so it is good enough to detect the eyes-closed and eyes-open resting condition, allowing a more comfortable use of the system.

G. E. Cañadas · C. R. Dell'Aquila · A. Garces · E. Laciar (✉)
Facultad de Ingeniería, Gabinete de Tecnología Médica,
Universidad Nacional de San Juan, San Juan, Argentina
e-mail: laciar@gateme.unsj.ed.ar

G. E. Cañadas
e-mail: gcanadas@unsj.edu.ar

G. E. Cañadas · C. R. Dell'Aquila · A. Garces · E. Laciar
Consejo Nacional de Investigaciones Científicas y Técnicas
(CONICET), Buenos Aires, Argentina

1 Introduction

The Electroencephalogram (EEG) is a record of electrical cerebral activity from different regions of the brain. It's a completely non-invasive procedure that can be applied repeatedly to patients, normal adults, and children with virtually no risk or limitation.

When brain cells (neurons) are activated, local current flows are produced. EEG measures mostly the currents that flow during synaptic excitations of the dendrites of many pyramidal neurons in the cerebral cortex. Differences of electrical potentials are caused by summed postsynaptic graded potentials from pyramidal cells that create electrical dipoles between soma (body of neuron) and apical dendrites (neural branches) [1].

The amplitude of EEG signal may vary from 10 to 100 µV with a bandwidth of 1–100 Hz [2]. It can be decomposed into distinct frequency bands (delta: 1–4 Hz, theta: 4–8 Hz, alpha: 8–12 Hz, beta: 12–30 Hz, gamma: 30–70 Hz) [3]. These characteristics make the EEG very susceptible to the noise produced by the electrode-skin interface and electromagnetic interference (EMI), mainly line power interference. It is also very affected by the artifacts introduced by other biosignals (EOG, ECG, EMG, respiration, etc.) of the studied subject.

EEG is very important in the clinical field. It is used commonly in sleep studies and in the diagnosis of brain diseases and injuries. In research area, it is applied in brain computer interfaces (BCI), detection of drowsiness and fatigue, neurobotics, etc.

The recording of EEG signals is simply done by placing electrodes on the scalp of the subject.

Electrodes for EEG are classified in wet and dry. Wet electrodes are considered the gold standard; these are impregnated with an electrolyte gel that facilitates the transduction of the ionic currents, which freely move through brain tissues and the cerebrospinal fluid, into electric currents (decreases skin impedance) [4]. An acceptable

contact impedance value is typically in the 5–20 KΩ range [5]. However, wet electrodes are not suitable for long-term recordings due to desiccation of the conductive gel that in turn decreases signal-to-noise ratio and increases contact impedance together with sweat and gel leakage that can cause electrical short circuits between adjacent sites [6].

Dry electrodes do not require conductive gel between the skin and the electrode surface to acquire a signal. Their main disadvantage is that they have higher contact impedance than wet electrodes, which makes it necessary to have acquisition systems with high input impedance and an adequate shielding to obtain good quality EEG signals.

In order to reduce noise in the acquisition process and enable new EEG applications such as driver control and home polysomnography studies, in this paper we design and manufacture of a portable wireless system for acquisition of EEG signals.

The validation of the system designed by comparing signals acquired with commercial EEG equipment is also carried out. The signals are registered in subjects using wet and dry electrodes, to make the comparison between both.

2   EEG Acquisition System

To conduct studies of drowsiness in drivers and polysomnography in the home, it was necessary to design a portable system that would allow us to acquire wireless EEG signals with a similar quality to that of commercial research and diagnostic equipment.

Figure 1 shows a general block diagram of the designed system. It has eight channels of EEG signal input. The acquired data are sent through Bluetooth 4.0 wireless communication protocol to a receiver system. It is also allowed to store the data in a microSD memory card for cases in which the device is not connected to any wireless receiver. The whole system is powered by batteries, which provides greater electrical safety in the patient and allows the portability of the equipment.

An ADS1299 analog front-end integrated circuit from the Texas instrument firm was used to design the equipment. This chip performs the conditioning and digitalization of the EEG channels. Once digitized, the signals are sent to a PIC32 microcontroller (MCU) which sends the signals through a serial communication to a Bluetooth 4.0 transmitter and also stores them in the microSD memory. Finally, the transmitter sends the data wirelessly to any compatible device (computer, cell phone, tablet, etc.) for further analysis and processing.

3   Validation of the EEG System

3.1   Input-Referred Noise Analysis

Internal circuit noise and drift are additional unwanted signals that contaminate a biopotential signal under measurement. Both are generated within the amplifier circuitry. The former generally refers to undesirable signals with spectral components above 0.1 Hz, while the latter generally refers to slow changes in the baseline at frequencies below 0.1 Hz. The noise produced within amplifier circuitry is usually measured either in microvolts peak to peak (µVp-p) or microvolts root mean square (µVRMS), and applies as if it were a differential input voltage [7]. Because the frequency range of interest of the EEG is above 0.1 Hz, the drift in our system can be quickly eliminated using a digital high-pass filter. The noise generated by the system needs to be measured and quantified, because its frequency components overlap with those of the EEG. To measure the Input-Referred Noise of our equipment, the input and reference channels were connected to ground. Then, records of 60 s were acquired with a sampling rate of 250 Hz. Using the Matlab software, a fraction of 10 s was extracted and a butterworth bandpass filter of order 10 was applied with cutoff frequencies in 0.1 and 65 Hz. This frequency range was established to be able to compare the results with the ADS1299 datasheet. The input referred noise was also obtained from an EEG commercial equipment AKONIC S.A. model MINI-PC. In Fig. 2 the results obtained for the two equipment are shown. As can be seen, the noise of the designed system is much lower than that of the commercial system.

Table 1 shows the peak-to-peak and RMS noise values of both pieces of equipment in the frequency range of 0.1–65 Hz and 0.5–100 Hz. In the ADS1299 datasheet, it is

Fig. 1 Block diagram of the acquisition system
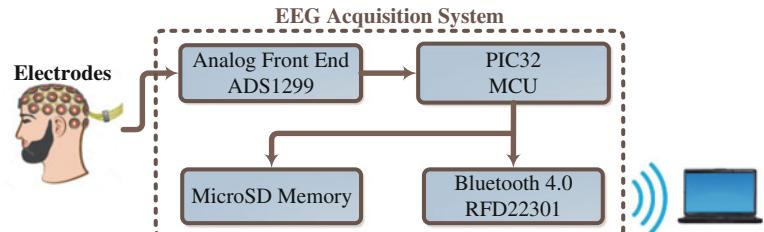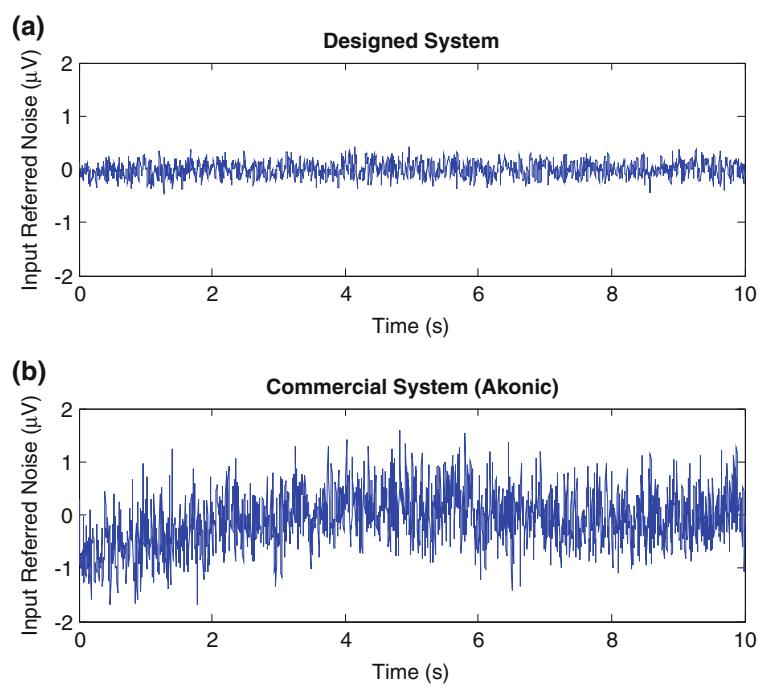
Fig. 2 Input-referred noise.
a Designed system.
b Commercial system (AKONIC)

(a)

Designed System

(b)

Commercial System (Akonic)

Table 1 Input-referred noise (µVRMS, µVp-p)

	Bandpass filter [0.1–65 Hz]		Bandpass filter [0.5–100 Hz]	
	µVRMS	µVp-p	µVRMS	µVp-p
Designed system	0.147	0.984	0.157	1.001
Commercial system	0.516	3.273	0.577	3.799

established that for a sampling rate of 250 Hz the noise value is 0.14 µVRMS and 0.98 µVp-p, practically equal to the values obtained. Therefore the conclusion is reached that the system works correctly and that the noise of it depends only on the analog front end. On the other hand, according to the American Clinical Neurophysiology Society, the acceptable noise in a commercial equipment record must be less than 1 µVp-p in the frequency range of 0.5–100 Hz [8]. According to the data obtained, our system meets this requirement tightly. Therefore we can conclude that the noise level is acceptable for clinical EEG acquisitions.

Comparing the data in Table 1 confirms that the noise level of our system is much lower than that of the commercial system.

3.2 Acquisition with Wet and Dry Electrodes
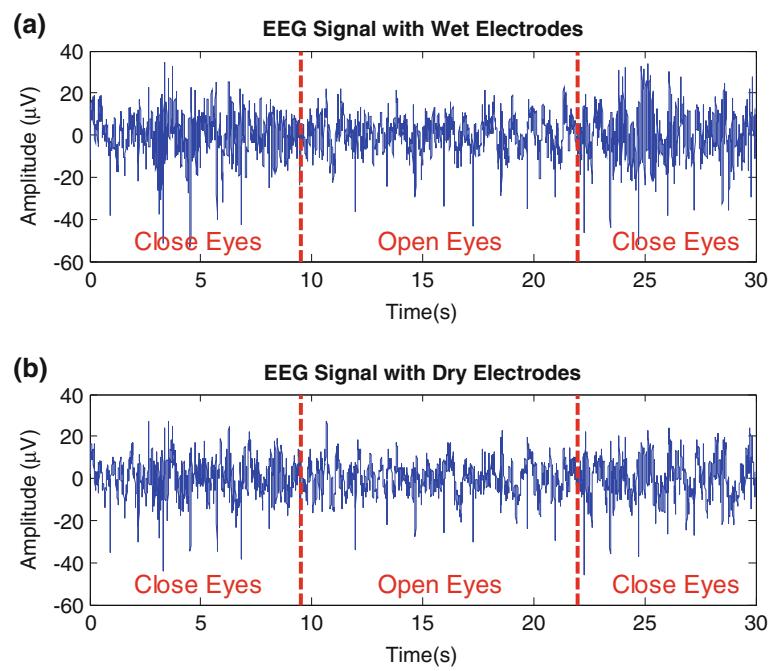
As it was already demonstrated that the designed equipment does not introduce significant noise to the EEG signal, now we proceed to acquire EEG signals with wet and dry

electrodes to compare the quality of the signals obtained with this system.

To perform the acquisitions, Ag/AgCl electrodes were used with Ten20 conductive gel and TDE-200 dry electrodes, both from Florida Research Instruments. Two EEG channels were acquired, in one a dry electrode was placed in the O2 position and in the other a wet electrode in Oz, according to the 10–20 system. The records were acquired during 4 min in 4 healthy subjects of 35 ± 5 years. A Butterworth bandpass filter of order 10 with cutoff frequencies in 0.5 and 30 Hz was applied to the signals. This bandwidth was selected because it contains the highest energy components of the EEG signal. Figure 3 shows a fraction of 30 s of one of the acquisitions. In spite of using a notch filter, it is observed that both signals have a lot of noise due mainly to the 50 Hz of the line, but even so, both signals can be observed correctly. In the graph, it can be seen that the quality of both signals is very similar.

In the acquisitions, tests were performed with open and closed eyes. With both electrodes, the change of frequency in the signal is easily appreciated by the appearance of the

Fig. 3 Acquisition of data in a subject. **a** With wet electrode. **b** With dry electrode

(a) EEG Signal with Wet Electrodes

(b) EEG Signal with Dry Electrodes

alpha rhythm that indicate the opening and closing of the eyes, as shown in Fig. 3. In this way we can demonstrate that using dry electrodes in our system, we can obtain an EEG signal of an acceptable quality, which will allow us to use them in future research work.

4 Conclusions

In this work, a self-developed EEG signal acquisition system was tested. Due to the low input-referred noise levels obtained (shown in Table 1) and comparisons made with a commercial EEG equipment of the AKONIC®, it is concluded that the system performs correctly without introducing a significant noise level in the records.

On the other hand, from the records acquired in subjects, we can conclude that the quality of the signal obtained with dry electrodes is almost as good as that of the wet electrodes with the advantage that they are more stable for long-term recordings. It should also be noted that despite the high level of noise in the records due mainly to the line interference (50 Hz) that is introduced in the EEG cables, the signal is of sufficient quality to detect actions such as opening and closing eyes by varying of the alpha rhythm. We conclude that the developed system could be used in research tasks and portable studies.

In future work, tests will be made with different types of shield cables to try to reduce as much as possible the interferences that are introduced into the EEG. Tests will also be carried out in a greater number of subjects and performing different types of tasks.

Conflict of Interest The authors declare that they have no conflict of interest.

References

1. M. Teplan, "Fundamentals of EEG measurement," *Meas. Sci. Rev.*, vol. 2, no. 2, pp. 1–11, 2002.
2. J. Kaur and A. Kaur, "A review on analysis of EEG signals," *2nd Int. Conf. Adv. Comput. Eng. Appl. ICACEA 2015*, pp. 957–960, 2015.
3. O. David and K. J. Friston, "A neural mass model for MEG/EEG: Coupling and neuronal dynamics," *Neuroimage*, vol. 20, no. 3, pp. 1743–1755, 2003.
4. M. A. Lopez-Gordo, D. Sanchez Morillo, and F. Pelayo Valle, "Dry EEG electrodes," *Sensors (Switzerland)*, vol. 14, no. 7, pp. 12847–12870, 2014.
5. P. L. Nunez and R. Srinivasan, *Electric Fields of the Brain*, 2nd ed. Oxford University Press, 2005.
6. G. Gargiulo *et al.*, "A new EEG recording system for passive dry electrodes," *Clin. Neurophysiol.*, vol. 121, no. 5, pp. 686–693, 2010.

7. D. Prutchi and M. Norris, *Design and Development of Medical Electronic Instrumentation: A Practical Perspective of the Design, Construction, and Test of Medical Devices*. Wiley, 2005.

8. J. J. Halford, D. Sabau, F. W. Drislane, T. N. Tsuchida, and S. R. Sinha, "American Clinical Neurophysiology Society Guideline 4: Recording Clinical EEG on Digital Media," *Neurodiagn. J.*, vol. 56, no. 4, pp. 261–265, 2016.

A Bioimpedance-Based Cardiovascular Measurement System

Roman Kusche, Sebastian Hauschild, and Martin Ryschka

Abstract

Bioimpedance measurement is a biomedical technique to determine the electrical behavior of living tissue. It is well known for estimating the body composition or for the electrical impedance tomography. Additionally to these major research topics, there are applications with completely different system requirements for the signal acquisition. These applications are for example respiration monitoring or heart rate measurements. In these cases, very high resolution bioimpedance measurements with high sample rates are necessary. Additionally, simultaneous multi-channel measurements are desirable. This work is about the hardware and software development of a 4-channel bio-impedance measurement system, whereat all channels are galvanically decoupled from each other. It is capable of measuring 1000 impedance magnitudes per second and per channel. Depending on the chosen measurement configuration, impedance changes down to mΩ ranges are feasible to be detected. To enable the usage in a variety of different research applications, further biosignals like photoplethysmography, electrocardiography or heart sounds can be acquired simultaneously. For electrical safety purposes, an implemented galvanically isolated USB interface transmits the data to a host PC. The impedance measurements can be analyzed in real-time with a graphical user interface. Additionally, the measurement configuration can easily be changed via this GUI. To demonstrate the system's usability, exemplary measurements from human subjects are presented.

1 Introduction

Measuring the electrical bioimpedance has been proven to be a useful method to determine the electrical behavior of living tissue [1]. It is mostly used to estimate the composition of the human body. Further applications are monitoring of the respiration and the cardiac output as well as the detection of arterial pulse waves and muscle contractions [2–6]. For these purposes, several specific bioimpedance measurement systems have been developed and published in the past [3, 5, 7].

It is conceivable that the additional acquisition of further biosignals like the electrocardiogram (ECG), the photoplethysmogram (PPG) or phonocardiogram (PCG) enables a variety of biomedical measurement setups. A challenge of implementing a multi-channel bioimpedance setup is the electrical decoupling of the different measurement channels from each other and from the ECG, as well as the synchronized data acquisition.

This work proposes the design of a measurement system capable of acquiring up to four bioimpedances simultaneously using galvanically decoupled current sources. Additionally, the synchronized measurement of ECG, PPG, PCG and pressure signals is possible. The microcontroller based device acquires 1000 bioimpedance magnitudes per second and per channel as well as the other mentioned signals with a sampling rate of 1000 samples per second (SPS). The digitized data is transmitted, via an isolated USB port to comply with electrical safety requirements according to IEC 60601-1.

After explaining the respective biosignals, the development of the measurement system is described. Finally, an exemplary measurement setup is proposed to analyze the

R. Kusche (✉) · S. Hauschild · M. Ryschka
Laboratory of Medical Electronics, Luebeck University of Applied Sciences, 23562 Luebeck, Germany
e-mail: roman.kusche@fh-luebeck.de

M. Ryschka
e-mail: martin.ryschka@fh-luebeck.de

timing relationship between the ECG, the PCG and the actual blood ejection of the heart.

2 Materials and Methods

2.1 Measurement Methods

Bioimpedance Measurement

To determine the electrical impedance of tissue, a small known AC current ($I_{Meas.}$) in mA ranges is applied via electrodes (Z_{ESI1}, Z_{ESI2}) to the bioimpedance (Z_{Bio}) under test, as shown in Fig. 1. Typical excitation frequencies are in the range of tens to hundreds of kHz [1]. The occurring voltage drop is measured utilizing two additional electrodes (Z_{ESI3}, Z_{ESI4}).

Since the inner impedance of the used voltage measurement circuit ($V_{Meas.}$) is supposed to be extremely high, the voltage drop over Z_{ESI3} and Z_{ESI4} can be neglected and the measured voltage together with the known current $I_{Meas.}$ can be used to calculate the bioimpedance under test.

Electrocardiography

The electrocardiography is the measurement of the electrical heart activities. Its morphology can be analyzed to gather information about the heart. Additionally, it can be used as time reference in several applications such as pulse wave velocity measurements [8]. The frequency range of a typical ECG signal is from 0.5–100 Hz and the signal's amplitude is between 100 µV and 10 mV [9].

Phonocardiography

Phonocardiography is the measurement of the heart sounds, which occur due to the mechanical activity of the heart. Especially the characteristic sounds S_1 and S_2, caused by the closing of the mitral and aortic valve, are of interest [8].

Photoplethysmography

The photoplethysmography is an optical method to acquire the arterial pulse wave. It is based on the measurement of the
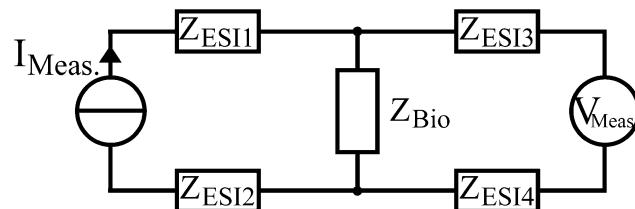
optical reflection/absorption of light in tissue over time. By performing this measurement using two light sources of different wave lengths, the blood oxygenation can be determined [8].

In-Ear Pressure

In-Ear pressure measurements have been proven to be a useful method for detecting the arterial pulse wave [10]. By sealing the ear canal and measuring the occurring pressure changes inside, the pulse wave can be acquired [11].

2.2 System Design

To enable the simultaneous measurement of all proposed methods, a specific microcontroller based measurement system has been developed. As it can be seen from the block diagram, illustrated in Fig. 2, the system consists of four voltage-controlled current source (VCCS) modules [12] in combination with a data acquisition (DAQ) module.

The ECG block of the DAQ module is realized by an instrumentational amplifier (INA, INA126 from Texas Instruments) in combination with a driven right leg circuit to attenuate the occurring common mode interferences. To reduce the signal drifting, the output signal of the INA is integrated and fed back to its reference input. In order to remove the high frequency voltages, caused by simultaneous bioimpedance measurements, the ECG signal is filtered by a passive 1st order low pass filter with a cut-off-frequency of f_c = 600 Hz.
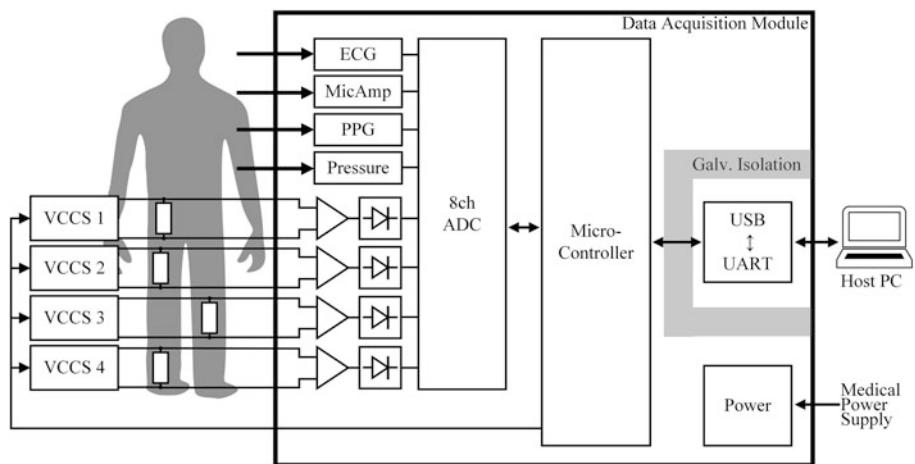
To acquire a phonocardiogram via an electret microphone, a microphone amplifier block (MicAmp) is implemented. For extracting just the useful frequency components of the signal, a 1st order high pass filter (f_c = 16 Hz) and a 1st order low pass filter (f_c = 3.6 kHz) are implemented. Additionally, the signal is amplified with a gain of G = 20.

The circuitry of the PPG block is split into two parts. The light transmitting part is realized by an infrared LED (VSMB3940X01 from Vishay), whose current is limited to 17 mA. To convert the received light into a voltage signal, a photo diode (VBPW34S from Vishay) in combination with a transimpedance amplifier circuit is provided.

As in-ear sensor, a miniature pressure sensor (HCEM010DBE8P3 from Sensortechnics) is used. It converts the measured differential pressure in a range of ±10 mbar into a corresponding DC voltage between 0.25 and 2.25 V.

To measure up to four bioimpedances, the data acquisition module controls the four external current source modules. In order to avoid coupling effects, these modules are galvanically isolated from each other, regarding their power supplies as well as the data transmission paths [12]. The

Fig. 1 Equivalent circuit of a bioimpedance measurement

Fig. 2 Block diagram of the developed cardiovascular measurement system. The system consists of four galvanically decoupled current source modules (VCCS) and a data acquisition module

configured current sources apply AC currents in the range from 0.12 to 1.5 mA with frequencies between 12 and 250 kHz into the tissue under observation. The occurring differential voltage drops over the bioimpedances are amplified by the differential programmable gain amplifiers (AD8250 from Analog Devices) of the data acquisition board. Since the useful information of these AC signals is their envelope, caused by the bioimpedance magnitude, analog amplitude demodulation circuits are implemented. These circuits are based on analog rectifiers in combination with 6th order active low pass filters (f_c = 1 kHz).

The resulting eight analog signals are simultaneously digitized by an 8 channels analog-to-digital converter (ADC, ADS131E08 from Texas Instruments) and transmitted to the implemented 32 bits microcontroller (ATSAM4S16C from Microchip). This controller communicates via a galvanically isolated (ISO7721 from Texas Instruments) USB-UART interface with a host PC. The usage of this isolator as well as the usage of a medical power supply is intended to comply with the standard for medical electrical equipment (IEC 60601-1).

In Fig. 3 a photograph of the developed measurement system, consisting of the data acquisition module and the

Fig. 3 Photograph of the cardiovascular measurement system. The current source modules are mounted on the data acquisition module with a metal sheet for shielding in between

four decoupled current sources, is depicted. The 4-layers printed circuit board (PCB) of the data acquisition module has dimensions of 161×97 mm^2 and contains more than 600 electronic components.

A graphical user interface, written in C# language, enables the configuration of the decoupled current sources and the programmable gain amplifiers in real-time. Additionally, all acquired signals can be plotted and exported to Matlab (from MathWorks).

3   Results

To demonstrate the system's usability, an exemplary measurement setup as shown in Fig. 4a has been used for analyzing the timing behavior of the blood ejection of the heart. Therefore, the measurements of an ECG, the heart sounds and the bioimpedance have been performed on a young male subject simultaneously. To acquire the ECG and the bioimpedance signals, Ag/AgCl electrodes were used. In Fig. 4b the acquired signals are plotted for a time duration of 3.5 s.
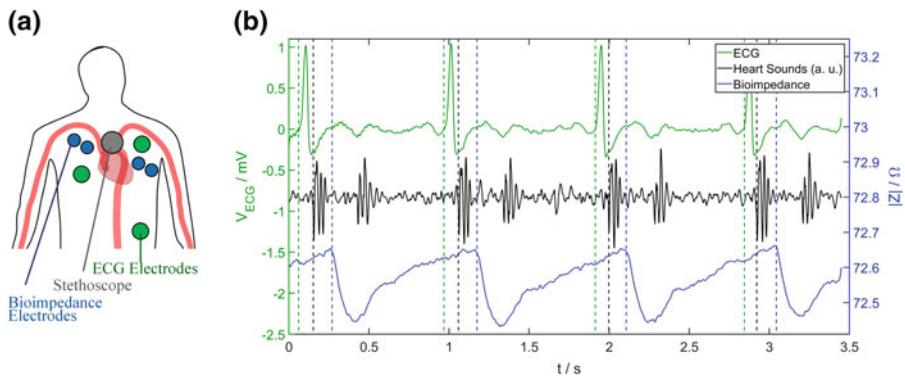
To remove the 50 Hz noise, caused by the mains, a digital notch filter was applied to the ECG signal (green). To attenuate high frequency noise, the signal has also been filtered by a 1st order low pass (f_c = 20 Hz). The same low pass is also applied to the bioimpedance signal (blue). The heart sounds signal from the stethoscope (black) has not been digitally filtered, but normalized for better display. To remove the effect of the filters' delays, only zero-phase filters have been used.

The vertical dashed lines indicate the corresponding cardiovascular events. In the ECG plot this represents the beginning of electrical stimulation. Afterwards, the first heart sound occurs, which is caused by the closing of the mitral valve. Finally, the bioimpedance decreases abruptly. This

time point represents the sudden increase of blood volume in the aortic arch, caused by the opening of the aortic valve.

The acquired signals can be used to determine cardiovascular parameters like heart rate, heart rate variability and pre-ejection period.

4 Summary and Outlook

In this work, the development of a cardiovascular measurement system has been presented. The system is capable of acquiring up to four bioimpedances, ECG, heart sounds, PPG and In-Ear pressure signals, simultaneously.

A measurement setup to analyze the timing behavior of the heart's blood ejection has been proposed and an exemplary measurement was shown. Further analysis of the resulting ECG, heart sound and bioimpedance signals could be used to measure the pre-ejection period, the heart rate or the ejection duration of the heart.

In the future, algorithms have to be developed to extract the information from the signals automatically. Furthermore, the PPG and the In-Ear pressure signals could be used to measure a variety of other parameters, such as the pulse wave velocity.

Conflicts of Interest The authors declare that they have no conflict of interest.

References

1. Grimnes, S. Martinsen, O.G.: Bioelectricity and Bioimpedance Basics. 2nd edn. Academic Press: Cambridge, MA, USA, (2008).
2. Matthie, J.R.: Bioimpedance measurements of human body composition: critical analysis and outlook. Expert Rev Med Devices 5(2), 239–61 (2008).
3. Kusche, R., et al.: A FPGA-Based Broadband EIT System for Complex Bioimpedance Measurement - Design and Performance Estimation. Electronics 4(3), 507–25 (2015).
4. Northridge, D. B. et al.: Non-Invasive Determination of Cardiac Output by Doppler Echocardiography and Electrical Bioimpedance. British Heart Journal 63(2), 93–97 (1990).
5. Kaufmann, S., Malhotra, A., Ardelt, G., Ryschka, M.: A high accuracy broadband measurement system for time resolved complex bioimpedance measurements. Physiol Meas. 35(6), 1163–80 (2014).
6. Nyboer, J.: Electrical impedance plethysmography; a physical and physiologic approach to peripheral vascular study. Circulation 2 (6), 811–21 (1950).
7. Kusche, R., Adornetto, T. D., Klimach, P., Ryschka, M.: A Bioimpedance Measurement System for Pulse Wave Analysis. In: 8th International Workshop on Impedance Spectroscopy, Chemnitz (2015).
8. Akay, M.: Wiley Encyclopedia of Biomedical Engineering. 1st edn. John Wiley & Sons Inc., Hoboken, New Jersey (2006).
9. Yazicioglu, R.F., van Hoof, C., Puers, R.: Biopotential Readout Circuits for Portable Acquisition Systems. 1st edn. Springer Netherlands (2009).
10. Park, J.H., Jang, D.G., Park, J. W., Youm, S.K.: Wearable Sensing of In-Ear Pressure for Heart Rate Monitoring with a Piezoelectric Sensor. Sensors 15(9), 23402–17 (2015).
11. Kusche, R., et al.: An in-ear pulse wave velocity measurement system using heart sounds as time reference. Current Directions in Biomedical Engineering, 1(1), 366–70 (2015).
12. Kusche, R., Hauschild, S., Ryschka, M.: Galvanically Decoupled Current Source Modules for Multi-Channel Bioimpedance Measurement Systems. Electronics 6, 90 (2017).

Aortic Pulse Wave Velocity Measurement via Heart Sounds and Impedance Plethysmography

Roman Kusche , Arthur-Vincent Lindenberg, Sebastian Hauschild, and Martin Ryschka

Abstract

The determination of the physical characteristic of the human arterial system, especially the stiffness of the aorta, is of major interest for estimating the risk of cardiovascular diseases. The most common measurement technique to get information about the state of the arterial system is the pulse wave analysis. It includes the measurement of the pulse wave velocity inside the arteries as well as its morphologically changes when propagating through the arteries. Since it is difficult to detect the pulse wave directly at the aorta, most available devices acquire the pulse wave at the extremities instead. Afterwards, complex models and algorithms are often utilized to estimate the original behavior of the pulse wave inside the aorta. This work presents an impedance plethysmography based technique to determine the aortic pulse wave velocity. By measuring the starting time of the pulse wave directly at its origin by the acquisition of heart sounds and the arrival time at the end of the aorta non-invasively via skin electrodes, unreliable complex models or algorithms aren't necessary anymore to determine the pulse wave velocity. After describing the measurement setup and the problem-specific hardware system, first measurements from a human subject are analyzed and discussed.

Keywords

Pulse wave analysis • Pulse wave velocity
Aorta • Bioimpedance • Impedance plethysmography
Heart sounds

1 Introduction

Arterial pulse wave analysis has become a useful technique in biomedical engineering in the past several years [1]. It comprises different methods like the determination of the pulse wave velocity within the arteries or the analysis of the pulse wave morphology [2]. The overall goal of all methods is to obtain information about the physical behavior of the aorta, preferable non-invasively [1].

Therefore, several measurement setups and devices have been developed in the past. Since it is difficult to measure the pressure pulse wave directly at two positions of the aorta to obtain its velocity, more practical measurement methods have been developed. Nowadays, a common method is the acquisition of the pulse wave at only one single point of the body which is easily accessible, like the radial artery or the brachial artery [3]. The morphology of the pulse wave within this vessel is then acquired by the usage of pressure sensors in various specific measurement setups, e.g. by applying a blood pressure cuff to the upper arm. The actual interesting information, the pulse wave velocity within the aorta, is then estimated by complex algorithms and models [4].

One problem of this procedure is to find a reliable model since the physical behavior of the aorta and of other arteries are very different [5]. Additionally, this model has to fit to the individual subject's anatomy. Furthermore, the measurement of the pulse wave by applying a pressure to the arteries, as performed by cuff-based systems, influences the behavior of the measured vessel itself.

The approach of this work is to measure directly the arterial pulse wave velocity within the aorta. Therefore, the starting time of the pulse wave is determined via the acquisition of the heart sounds. The arrival time is detected by performing a bioimpedance measurement at the lower leg.

In this work the acquired biosignals are introduced and the measurement approach is explained in detail. Afterwards, the developed measurement system is described with

R. Kusche (✉) · A.-V. Lindenberg · S. Hauschild · M. Ryschka
Laboratory of Medical Electronics, Luebeck University of Applied Sciences, 23562 Luebeck, Germany
e-mail: roman.kusche@fh-luebeck.de

M. Ryschka
e-mail: martin.ryschka@fh-luebeck.de

a focus on the signal processing. Finally, first measurements from a human subject are presented and discussed.

2 Materials and Methods

2.1 Phonocardiography

Phonocardiography is the measurement of the heart sounds from a subject. Therefore, a microphone or a stethoscope can be used. The most conspicuous characteristics of this signal are the 1st and the 2nd heart sound. These sounds occur, when the mitral valve, respectively the aortic valve, is closing. Although the 1st heart sound does not exactly represent the opening of the aortic valve, it occurs directly before the actual pulse wave starting time and is therefore a useful information [6]. Furthermore, this signal is related to the actual heart muscle contraction in contrast to an ECG signal, which just represents the electrical stimulation of the heart.

2.2 Impedance Plethysmography
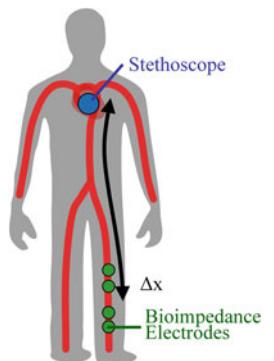
Impedance plethysmography is the acquisition of arterial pulse waves by performing electrical bioimpedance measurements. This technique is based on the fact, that the pressure pulse wave provokes also changes in the diameter of the arteries and therefore affects the amount of blood volume within the tissue under test. Since the conductivity of blood is significantly higher than that of other tissue, these minuscule volume changes can be detected by performing a continuous bioimpedance measurement [7]. Assumable impedance magnitude changes are in the range of Milliohms, when performing bioimpedance measurements at the extremities [8].

2.3 Measurement Approach

The overall goal of this approach is the determination of the pulse wave velocity (PWV), especially within the aorta. Therefore, the pulse wave is detected at two different points, as illustrated in Fig. 1. As starting point, the heart is chosen and the pulse wave starting time is defined by the 1st heart sound, which is detected via phonocardiography with a digital stethoscope.

The pulse wave arrival time is detected at the lower leg of the subject by performing a continuous bioimpedance measurement. Obviously, the arrived wave has passed the aorta but also a piece of the femoral artery. However, the measurement setup avoids discomfort for the subject. This compromise is accepted in this approach.

Fig. 1 Measurement setup to detect the starting time and the arrival time of the pulse wave for calculating the average pulse wave velocity

With the obtained information about the starting time (t_{Heart}) and the arrival time (t_{Leg}) of the pulse wave and the additional knowledge about the covered distance Δx, the average pulse wave velocity (PWV) can be calculated with Formula 1.

$$PWV = \frac{\Delta x}{t_{Leg} - t_{Heart}} \qquad (1)$$

2.4 System Development

To implement the proposed measurement approach, a measurement system has been developed. As shown in Fig. 2, this system consists of an analog part (yellow), which includes sensors and electronic circuits, and a digital (green) part, implemented in Matlab (from Mathworks). The upper signal path represents the extraction and detection of the 1st heart sound to determine the pulse wave starting time. The lower path is intended to determine the pulse wave arrival time at the lower leg.

The heart sounds are acquired via a digital stethoscope, realized by an electret microphone capsule. To remove the undesired DC offset in the microphone signal, the heart sounds are high pass filtered. Afterwards, the signal is amplified and digitized with a sampling rate of 1000 SPS. To determine the maxima of the heart sounds, the signal is enveloped on the digital signal processing side and a peak
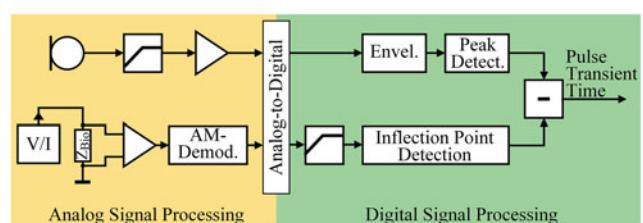
Fig. 2 Block diagram of the developed pulse wave velocity measurement system, consisting of an analog and a digital signal processing part (Color figure online)
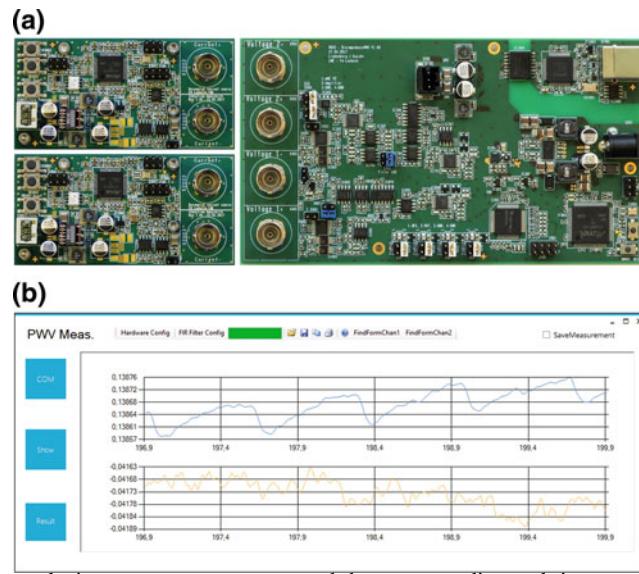
Fig. 3 Photograph of the pulse wave velocity measurement system and the corresponding real-time user interface

detection is performed. The corresponding points in time, which represent the 1st heart sounds are stored as pulse wave starting times.

To determine the pulse arrival times at the leg, the bioimpedance is measured via surface electrodes. A small known AC current is applied via a voltage controlled current source (V/I) into the tissue under observation (Z_{Bio}). The occurring voltage drop is amplified and afterwards an amplitude modulation (AM) demodulator extracts the actual information about the impedance magnitude. This information is digitized via a second, synchronized ADC channel and for attenuating high frequency noise low pass filtered. In order to extract the pulse arrival time, the inflection point before the actual pulse wave is determined by differentiating the signal twice [9]. This point indicates the beginning of the pulse wave morphology change and therefore the beginning of the arriving pulse wave.

Finally, the obtained pulse wave starting times are subtracted from the corresponding arrival times to get the pulse transient times.

The analog signal path was implemented as an application specific printed circuit board (PCB), as shown in Fig. 3a. The PCB has a size of 152×84 mm^2 and contains more than 450 components. It is capable of acquiring the heart sounds as well as two independent bioimpedance channels, using two additional current source boards, which are also depicted in the photograph. To fulfill the electrical safety requirements of the standard for medical electrical equipment (IEC 60601-1), medical power supplies, as well as a galvanically isolated USB interface were implemented.

In Fig. 3b a screenshot of the developed real-time data acquisition software, programmed in C# language is shown. It can be utilized to configure the hardware system and to monitor the acquired signals during a measurement procedure. Afterwards, the data can be exported to Matlab-compatible file format.

3 Results

An exemplary measurement on a human subject for a duration of 8 s has been performed, using the developed hardware system as well as the proposed digital signal processing steps. In Fig. 4 the resulting envelope (blue) of the heart sound signal is plotted and the detected peaks, caused by the 1st heart sounds, are marked (orange).

In the plot below, the measured and filtered bioimpedance signal is presented. For better display, this signal has been inverted. It shows the typical pulse wave morphologies. The obtained pulse wave arrival times at the leg are marked (purple) as well.

Subtracting of the corresponding detected points in time from each other leads to the pulse transient times. Averaging the calculated pulse transient times of these 10 pulse waves and assuming the distance Δx to be 1.35 m leads to a mean pulse wave velocity of 10.3 m/s (SD = ± 0.6 m/s), using Formula 1. An additional system characterization has proven that time delays, generated by the measurement system, are lower than 5 ms in the relevant frequency range.

4 Discussion

A first measurement from a human subject has demonstrated the usability of the proposed measurement approach. Due to the influence of the femoral artery to the measured average
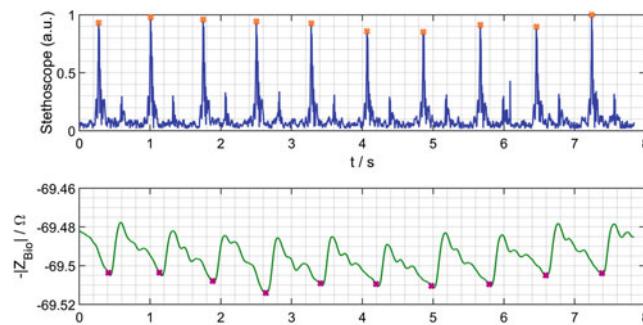
Fig. 4 Envelope of the acquired heart sounds (blue), and the measured bioimpedance (green). The crosses in the plots indicate the obtained points in time, in which the pulse wave starts and arrives, respectively (Color figure online)

pulse wave velocity, the obtained value does not only represent the velocity inside the aorta. It is assumed, that this issue can easily be solved by performing a second bioimpedance plethysmography at the same leg. Thereby, the velocity inside the femoral artery could be determined and with the knowledge about the length of the aorta, both the velocities can be separated from each other.

Another point of uncertainty is the usage of the heart sounds. As described before, this event does not physically correspond to the actual opening of the aortic valve. Implementing empirical values of this time delay to the proposed algorithm could improve the results.

A common problem of detecting the pulse wave at specific points, like the minimum, the maximum or the inflection point of the propagating wave, is that these points are based on the phase delay. However, the group delay is the actual value of interest.

Conflicts of Interest The authors declare that they have no conflict of interest.

References

1. Laurent, S., et al.: Expert consensus document on arterial stiffness: methodological issues and clinical applications. Eur Heart J. 27(21), 2588–605 (2006).
2. Wilkinson, I.B., et al.: Reproducibility of pulse wave velocity and augmentation index measured by pulse wave analysis. J Hypertens. 16(12), 2079–84 (1998).
3. O'Rourke, M.F., Pauca, A., Jiang, X.J. Pulse wave analysis. British Journal of Clinical Pharmacology 51(6), 507–22 (2001).
4. Rajzer, M.W., et al.: Comparison of aortic pulse wave velocity measured by three techniques: Complior, SphygmoCor and Arteriograph. J Hypertens. 26(10), 2001–7 (2008).
5. Belz, G.G.: Elastic Properties and Windkessel Function of the Human Aorta. Cardiovasc Drugs Ther. 9(1), 73–83 (1995).
6. Akay, M.: Wiley Encyclopedia of Biomedical Engineering. 1st edn. John Wiley & Sons Inc., Hoboken, New Jersey (2006).
7. Nyboer, J.: Electrical impedance plethysmography; a physical and physiologic approach to peripheral vascular study. Circulation 2(6), 811–21 (1950).
8. Kusche, R., Adornetto, T. D., Klimach, P., Ryschka, M.: A Bioimpedance Measurement System for Pulse Wave Analysis. In: 8th International Workshop on Impedance Spectroscopy, Chemnitz (2015).
9. Kazanavicius, E., Gircys, R., Vrubliauskas, A.: Mathematical Methods for Determining the Foot Point of the Arterial Pulse Wave and Evaluation of Proposed Methods. Information Technology and Control 34(1), 29–36 (2005).

Respiration Monitoring by Combining EMG and Bioimpedance Measurements

Roman Kusche and Martin Ryschka

Abstract

A common technique to measure diaphragm electrical activation is the acquisition of the occurring electromyography signals using surface electrodes. A significant problem of this technique is its sensitivity against motion artifacts. Forces or vibrations can influence the electrode skin contacts, which generate changes of the electrodes' half-cell voltages as well as the electrode skin impedance. Both effects result in noise in the same frequency range as the typical electromyography signal and therefore it's hard to separate these distortions from the desired signal. Another technique to detect muscle contractions is the electrical impedance myography. By applying a small alternating current to the tissue of interest and measuring the occurring voltage drop, the bioimpedance is determined. It contains the information about muscle contractions and relaxations. The major advantage of this technique is, that the impedance information is coded as the amplitude modulation of that voltage drop. The frequency of the excitation current is typically chosen in the range of tens of kHz and thus can easily be separated from the above mentioned artefacts. This work describes a measurement setup which is capable of acquiring electromyography as well as bioimpedance signals simultaneously, sharing the same electrodes. An analog circuit is presented which combines the information of both measurement techniques, allowing their common analog-to-digital conversion by a single converter. The system is capable to acquire 1000 bioimpedances/electromyography samples per second with a resolution of 24 bits. First measurements show that signal distortions, caused by vibrations at the electrodes, are attenuated significantly in bioimpedance measurements.

R. Kusche (✉) · M. Ryschka
Laboratory of Medical Electronics, Luebeck University of Applied Sciences, 23562 Luebeck, Germany
e-mail: roman.kusche@fh-luebeck.de

M. Ryschka
e-mail: martin.ryschka@fh-luebeck.de

1 Introduction

Each respiration cycle is controlled by the contraction of the diaphragm [1]. Therefore, monitoring of this muscle is of interest in many biomedical applications, which are focused on respiration. A well-known method is acquiring the electrical activation of the diaphragm (EAdi) [2]. This specific electromyography (EMGdi) application can be performed by attaching needle or surface electrodes on the thorax, whereas this work focusses on the usage of surface electrodes.

There are two major challenges regarding EMGdi measurements. First, the heart of the subject is close to the diaphragm. Therefore, there is a superposition of the actual EMGdi voltage signal and the ECG signal. Unfortunately, the high frequency components of the ECG are in the same frequency range as the EMGdi signal [1].

The second problem are the electrode-skin interfaces. The occurring half-cell voltages, which depend on the chosen kind of electrode, vary when mechanical forces occur [3]. Especially vibrations in the frequency range of the EMGdi signal can consequently lead to misinterpretations of the acquired signals.

The approach of this work is to modulate the information about the muscle contraction to a much higher frequency range, by performing bioimpedance measurements. Since the origin of the bioimpedance signal differs from the EMGdi's origin, both signals do not exactly contain the same kind of information [4]. Furthermore, present signal processing algorithms are commonly focused on EMG signals. Due to these facts, it is desirable to measure the EMGdi and the bioimpedance simultaneously.

In this work we propose a measurement approach to monitor respiration via the simultaneous acquisition of the diaphragm's EMG as well as its bioimpedance. Afterwards, the technical implementation and a first measurement from a human subject are presented.

2 Materials and Methods

2.1 Electromyography

Electromyography is the acquisition of the action potentials of muscles. Therefore, surface electrodes can be used to acquire the occurring differential voltages. Commonly, this signal is in millivolt ranges and has its major frequency components between 10 and 500 Hz [5].

2.2 Impedance Myography

Impedance myography is the measurement of changes in the electrical bioimpedance of muscles, caused by geometrical changes. Therefore, a small AC current in a frequency range of several kHz is applied to the tissue under observation via electrodes. The occurring voltage drop over the muscle is amplitude modulated (AM) by the impedance changes within the tissue [4].

2.3 Measurement Approach

Both signals, the EMG as well as the bioimpedance signal are electrical signals, which can be acquired by using surface electrodes. Therefore, this approach is based on the usage of a common set of electrodes.

As described above, the frequency ranges of the EMG signal and of the bioimpedance signal are very different. The interesting frequency range of the EMG signal is marked in Fig. 1 (red). The lower end of this range ($f_{EMG,l}$) is typically about 10 Hz, whereas the higher end ($f_{EMG,h}$) can reach up to hundreds of Hz [5]. The carrier frequency of the bioimpedance measurement (f_c) is about three decades higher, respectively in ranges of tens or hundreds of kHz. However,

the modulating frequency (f_m), corresponding to the respiration related impedance changes, is typically below 1 Hz. Therefore, the depicted frequency band of the bioimpedance measurement (blue) is very small in the real application.

To avoid a very high analog-to-digital (ADC) sampling rate and the entailing high computational effort for the AM demodulation, the acquired voltage signal is pre-processed. Since the frequency range of the signal below $f_{EMG,l}$ is unused so far, the narrowband signal of the bioimpedance can be shifted, as shown in Fig. 1. Obviously, this procedure is only applicable when the condition $f_m < f_{EMG,l}$ is fulfilled.

The resulting required sampling frequency can consequently be reduced to $f_s > 2 \cdot f_{EMG,h}$.

2.4 Implementation

The proposed approach has been implemented as a mixed signal system. The corresponding block diagram is shown in Fig. 2.

On the left side of the illustration, the tissue under observation is modelled as a series circuit consisting of the bioimpedance Z_{Bio} and an EMG generating voltage source V_{EMG}. To measure the bioimpedance, a current source applies a current of 800 µA with a frequency of 143 kHz to the area of interest. These current values comply with the limitations, given by the standard for medical electrical equipment (IEC 60601-1). The superposition of the occurring voltage over the bioimpedance and the EMG voltage is amplified by an analog differential amplifier. Afterwards, the high frequency components of the bioimpedance measurement are shifted down, as described before. Therefore, an AM demodulation circuit is realized by combining an analog rectifier and a low pass filter (LP_1). To avoid the disappearance of the low EMG frequencies, a half-wave rectifier is used.

The low pass filtered signal is digitized with a sampling rate of 1 kSPS and a resolution of 24 bits. Afterwards, a digital notch filter is used to remove the 50 Hz interference, caused by the mains. In a final step, the EMG signal and the bioimpedance signal are separated from each other. Therefore, a digital high pass filter is used for extracting the EMG signal and a low pass filter to obtain the bioimpedance magnitude information.

3 Results

The described measurement instrumentation has been used to perform first measurements on a human subject. In the first experiment, the relationship between the EMG signal and the bioimpedance magnitude is analyzed. Therefore, the measurement setup, shown in Fig. 3, was used. Using a
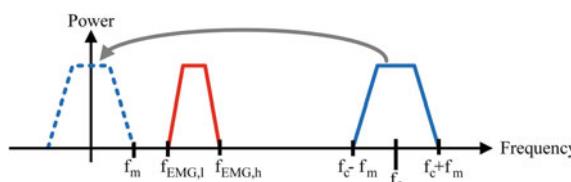
Fig. 1 Signal spectrum of the superposition of the EMG signal and the corresponding bioimpedance measurement signal (Color figure online)

Fig. 2 Block diagram of the technical implementation
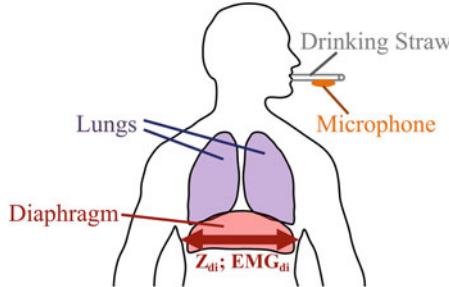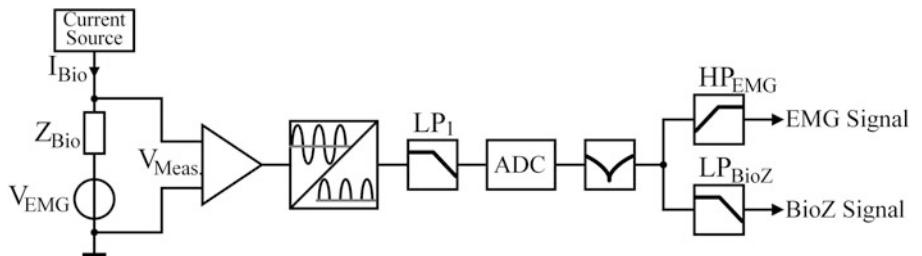
Fig. 3 Setup to acquire the respiration via EMG and bioimpedance measurements of the diaphragm. As a time reference, a microphone, mounted on a drinking straw, detects the breathing sounds

common set of surface electrodes, positioned at the thorax, the bioimpedance Z_{di} and the electromyography signal EMG_{di} have been acquired.

To provide a time reference, the respiration was also detected by an additional microphone, positioned on a drinking straw. The subject was asked to inhale through this drinking straw for three times.

In Fig. 4a the resulting signals are depicted. The first plot shows the microphone signal from the drinking straw and therefore indicates the time periods of inhaling. In the
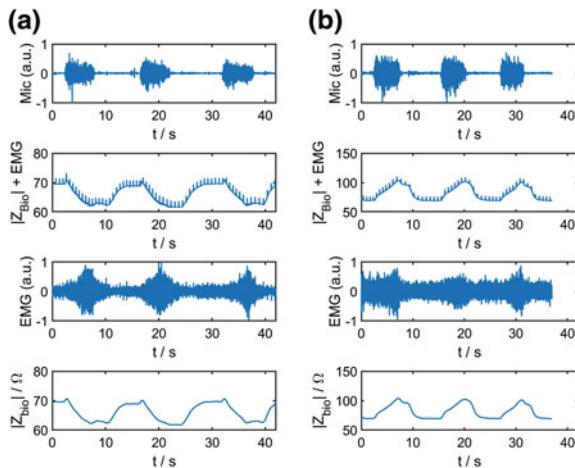
second plot, the acquired signal, consisting of the EMG and the bioimpedance component is shown. Since the amplitude of the EMG component is much lower than that of the bioimpedance, it is hard to recognize in this plot. Below this plot, the separated signal components are displayed.

It can be seen, that during inhaling, when the diaphragm muscle is contracting, the EMG signal increases, whereas the bioimpedance magnitude decreases. This impedance behavior indicates, that actually a muscle contraction is measured [4]. To compare this result with a measurement, more focused on the lungs' impedance changes, the procedure has been repeated with electrodes, attached about 10 cm above the previous position. The results are shown in Fig. 4b. It is distinguishable, that the EMG signal is reduced and therefore closer to the noise level. Additionally, now the bioimpedance magnitude increases during inhaling, which corresponds to the typical impedance behavior of the lungs [6].

To compare the robustness against electrode motion artifacts, the experiment has been repeated. The subject was asked to inhale and exhale again. During this cycle, one of the voltage electrodes has been tapped gently. In Fig. 5 the resulting processed signals of the EMG and the bioimpedance are shown for a time span of 7 s. Since the occurring frequency of this kind of interference is much higher than the frequency range of the bioimpedance changes, it can easily be filtered out. However, the EMG signal is disturbed significantly. Some occurring peaks, e.g. at t = 3 s or t = 5 s, are much higher than the original EMG signal, which can hardly be recognized in this plot. Since the frequency range of the actual EMG signal contains the frequencies of these motion artifacts, common filter techniques are not effective.

4 Discussion

The proposed measurement method has proven to be useful for gathering additional respiration information.

A first experiment has demonstrated the significant influence of the exact electrodes positioning on the measurement results. Therefore, the electrodes positioning has to

Fig. 4 Measured signals, acquired via surface electrodes attached on the thorax, close to the diaphragm (**a**). The signals in (**b**) have been acquired after relocating the electrodes about 10 cm more upwards
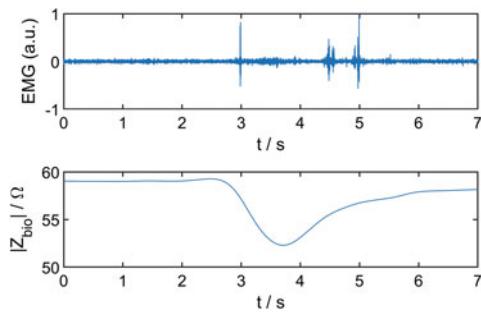
Fig. 5 Measurement result of one respiration cycle. To simulate motion artifacts, the positive voltage electrode has been tapped gently at t = 3, t = 4.5 and t = 5 s

be performed precisely. Even in the proposed measurement results it is difficult to evaluate the influence of the lungs or other tissue, which changes its geometry during respiration.

The major advantage of performing a bioimpedance measurement is the robustness against disturbances. By using a known modulation frequency, much higher than the expected motion artifacts, and demodulating it to a frequency range below these artifacts, this technique is capable of bypassing the critical frequency band. This beneficial effect has been demonstrated in the second experiment. However, even when distortions in much higher frequency ranges than the respiration cycles are attenuated reliably, there could be additionally distortions in lower frequency ranges, e.g. caused by motion artifacts or drifting effects. These conditions have to be examined in the future.

References

1. Alty, S.R., Man, W.D., Moxham, J., Lee K.C.: Denoising of diaphragmatic electromyogram signals for respiratory control and diagnostic purposes. In: 30th Annual International Conference of the IEEE Engineering in Medicine and Biology Society, pp. 5560–3., Vancouver, BC, Canada (2008).
2. Estrada, L., Torres-Cebrian, A., Sarlabous, L., Jane, R.: Onset and Offset Estimation of the Neural Inspiratory Time in Surface Diaphragm Electromyography: A Pilot Study in Healthy Subjects. IEEE J Biomed Health Inform. PP(99), (2017).
3. De Luca, C.J., Gilmore, L.D., Kuznetsov, M., Roy, S.H.: Filtering the surface EMG signal: Movement artifact and baseline noise contamination. J Biomech. 43(8), 1573–9 (2010).
4. Rutkove, S.B.: Electrical Impedance Myography: Background, Current State, and Future Directions. Muscle Nerve 40(6), 936–946 (2009).
5. Akay, M.: Wiley Encyclopedia of Biomedical Engineering. 1st edn. John Wiley & Sons Inc., Hoboken, New Jersey (2006).
6. Kaufmann, S., Malhotra, A., Ardelt, G., Ryschka, M.: A high accuracy broadband measurement system for time resolved complex bioimpedance measurements. Physiol Meas. 35(6), 1163–80 (2014).

Investigation of a Possibility of ECG and PPG Common Measurement

Lukas Peter, Antonino Proto, and Martin Cerny

Abstract

Electrocardiography and Photoplethysmography are basic investigative methods used in healthcare. As the ECG and the PPG are non-invasive methods. The principle consists in ECG recording of electrical activity of the heart and the result of this sensing is a graph plotting—electrocardiogram. PPG is one of the main methods of measurement plethysmography when the result is a graphic record of pulse wave. The main function of PPG is the volumetric flow measurement of blood (e.g. in atherosclerosis, which is possible by vascular permeability derive their rigidity). Both of these methods are used for monitoring of cardiovascular system. It would be advantageous to have possibility to measure ECG and PPG from one place on human body. It would be also advantageous to have only one device and reduce number or size of sensors or electrodes. In this paper we describe developing such system and also investigation the ideal place for placing of sensors for satisfactory measurement.

Keywords

ECG • PPG • Two electrodes • PTT • Common electrode

1 Introduction

Electrocardiography *ECG* is a frequently used method in cardiology, measurement and analysis function of the heart. It is used not only in a clinical setting, but also in long-term monitoring of cardiac activity using heart monitors.

ECG signal is measured between pairs of electrodes located at different parts of the human body. Theoretically is possible to capture ECG from any part of the body. However, these signals can have different shapes and sizes of voltage amplitudes, depending on exactly where the electrodes are placed. This is also influenced by the formation of artefacts in the measurement [1].

Photoplethysmography *PPG* is the method for measurement right function of blood flow. It is measurement pulse wave which is display of changes of volume blood vessels based on pulse blood flow. From PPG measurement is possible to evaluate heart rate. The measured curves can be compared with ECG, for better analysis of activity of the heart [2].

The principle of the method is based on light which pass through the capillary bed. Thanks to the elasticity of the arterial system and heart activity varies volumes capillaries, causing a change in absorption, reflection and scattering of light. Optoelectronic sensor could be also sensitive to changes in blood oxygen saturation. Way to suppress this effect is to use a light source which operates in the infrared and red region simultaneously. and red, it moves in the vicinity of wavelength 940 nm. The detector must include elements as phototransistors or photodiodes [3].

2 Problem Definition

Experts are constantly trying to develop the most appropriate materials for the electrodes and sensors. The combination of the ECG and PPG measurement could arise a sophisticated measurement system.

The big question is the types electrodes and sensors should be use. There is a quite problem, whether dry electrodes that do not need to implement a conductive gel, can capture the signal as accurately as standard electrodes, and if not, how to achieve this goal. For long-term measurement are dry electrodes much better. Of course it would be the best to use a wireless electrodes, unfortunately it isn't still at such a level as would be required [4].

L. Peter (✉) · A. Proto · M. Cerny
Department of Cybernetics and Biomedical Engineering,
VSB-Technical University of Ostrava, 70800 Ostrava, Czech Republic
e-mail: lukas.peter@vsb.cz

Sensing blood volume using PPG sensor is becoming a very popular method that can determine the width of the vessel, volume changes of organs and heart rate. Scientists are still working on a reflective types of sensors which are currently unable to penetrate deep into the tissue. Some results have shown that in this situation there is a way in the form of changes in intensity of light emitted from the LEDs. The important issue is the contact force which acts on the skin surface after attachment of the sensor which can greatly affect the value of the signal [5].

3 Implementation of New Solution

The aim of this work was to design and develop a common ECG/PPG measurement from same place. The uniqueness of this method consists mainly in conjunction conventional ECG electrodes and reflective photoplethysmography sensor, and also in the method of sensing an ECG, which is accomplished with only two electrodes.

The combination of these methods allow the scan of a small area on the body of the electrical activity of the heart and at the same time investigate volume changes, activity and reactivity of the blood vessels. These parameters are important values for human health. This scanning method is intended primarily for long-term monitoring, which is a major requirement for patient comfort.

3.1 Hardware Solution

The circuit for ECG measurement was developed as two electrodes circuit. With this circuit was not used the third electrode which determines zero potential for circuit and it is called *an active ground*.

Circuit for ECG measurement consists of two basic blocks.

The first block is the circuit for analogue processing of differential measured signal. This block consist from

differential amplifier which adjust the signal, which is result of difference voltage between two electrodes, to other analogue preprocessing [6].

The second block is the circuit for analogue filtering and attenuating of measured signal. It consist from active and passive high pass and low pass filters.

The signal of PPG is measured by optical method. It was used reflective principle of measurement. One infra LED emits light which properties are changed by change in tissue volume. The changed light is received by photodiode. It was necessary to set offset level of voltage to 500 mV because of possibility to measure whole pulse wave.

The whole circuit was powered asymmetrically 0–5 V. It was used standard 9 V battery which was stabilized to 5 V.

3.2 The Measurement Belt

For satisfactory measurement it was necessary to choose the right material in which the sensors could be placed. Because of the different widths of the chest of every man it was the best solution to use material from the rubber. Rubber strip is sufficiently flexible to adjust to various sizes and is secured with Velcro which is very advantageous in setting the required length for attachment. Into this belt were placed metal electrodes for ECG measurement and LED and photodiode for PPG measurement (Fig. 1).

4 Testing of the Measurement Hardware

Because of using two ECG electrodes it was need to investigate their relative positions. Although the voltage spread from the cardiac muscle of the heart to the whole body it isn't possible to measure all places equally large voltage. Therefore the distance from the heart determines the size and stability of measured ECG signal. This analysis was made to find the most suitable place for placing of two electrodes for ECG measurement and sensors for PPG

Fig. 1 The rubber belt where were placed measurement parts which are connected directly to the human body and placing of the belt with electrodes and sensors
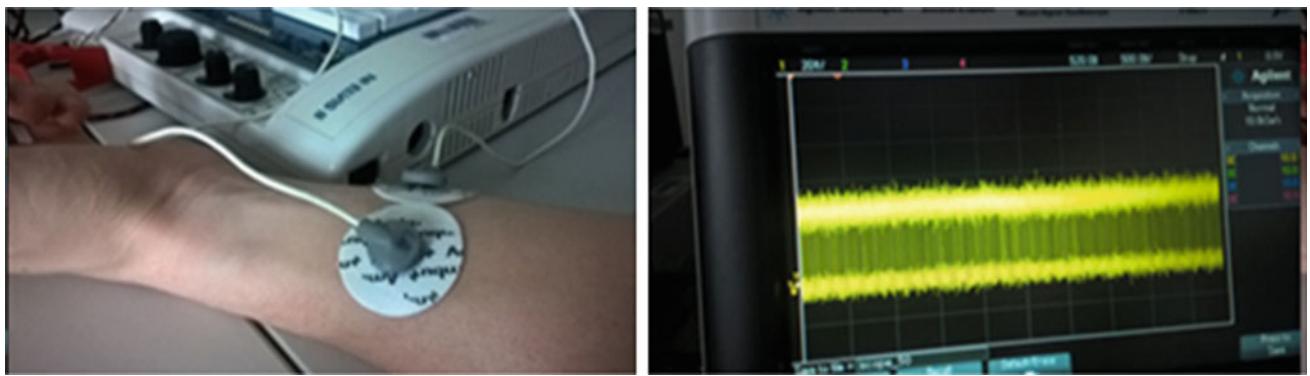
Fig. 2 Left side, the placing of electrode, right side, measured ECG signal
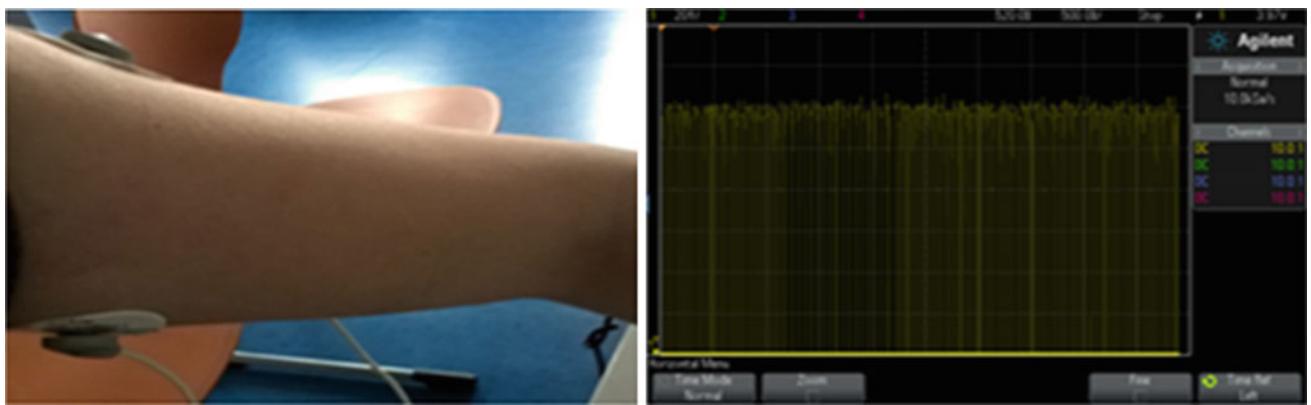
Fig. 3 Left side, the placing of electrode, right side, measured ECG signal

measurements. The analysis ass shown that these afore-mentioned factors for the location of the electrodes is very important.

4.1 The Measurement on the Hand

The first method was the location sensing electrodes on the wrist, in various ways, next to each other vertically, horizontally, below the one electrode disposed on the front side of the wrist and the other on the back. All of these options were tested at different distances. Because of minimal difference between ECG vectors and big distance between the heart and measured place the measurement wasn't work (Fig. 2).

Another possible place for sensing appeared upper side of the left arm as it is closer to the heart. The measured voltage amplitude should be higher than on the right hand. Testing was conducted again at a different location options, electrodes were applied horizontally, vertically, again at different

distances. Unfortunately, even in this case wasn't measured ECG signal clearly (Fig. 3).

PPG measurement was tested similar way. As control measurement was used measurement from the finger. There are a large number of capillaries. The sensor was tested also on the wrist. It was positioned over the artery (Fig. 4).

4.2 The Measurement on the Chest

It was tried to capture the signal from the chest. From theoretical knowledge there should be obtain signal with better results. The electrode location was again tested in a variety of possibilities, both vertically and horizontally apart at different distances. The best option was the vertical spacing of the electrodes at an approximate distance of 10 cm.

PPG signal from the chest had amplitude a much lower than from finger or wrist. When properly positioned, however, it was possible to measure the signal for further analysis and processing.

Fig. 4 Left side, signal from the finger, right side, signal from the wrist

5 Analysis of Measured Signal

From the measured signals it was possible to analyse the recorded curves. Analysis of these curves allowed the detection of heart rate, then the curves mutually compared.

To determine heart rate from the ECG was important to detect individual R waves. The interval between these waves is the time period between two ventricular complexes. In the case of pulse wave, for evaluating the heart rate was used the intervals between the peak.

Thanks this common measurement is possible to evaluate pulse transit time which can be use for non invasive blood pressure measurement. Pulse transit time which is the difference between the distance from the top of the R wave and the following peak of pulse wave.

It were performed 8 measurements when the four experiments were measured at the rest and 4 attempts after physical exertion. ECG sensors were spaced 10 cm away. PPG sensor was placed about 1 cm vertically. This measurement method has enabled scan curves of sufficient quality for subsequent comparison and evaluation of heart rate.

The analysis of the signals shows that ECG signals and PPG scan from the chest are very good indicator for the heart rate, the intervals between the R wave peaks and peaks of the pulse wave are almost identical (Fig. 5).
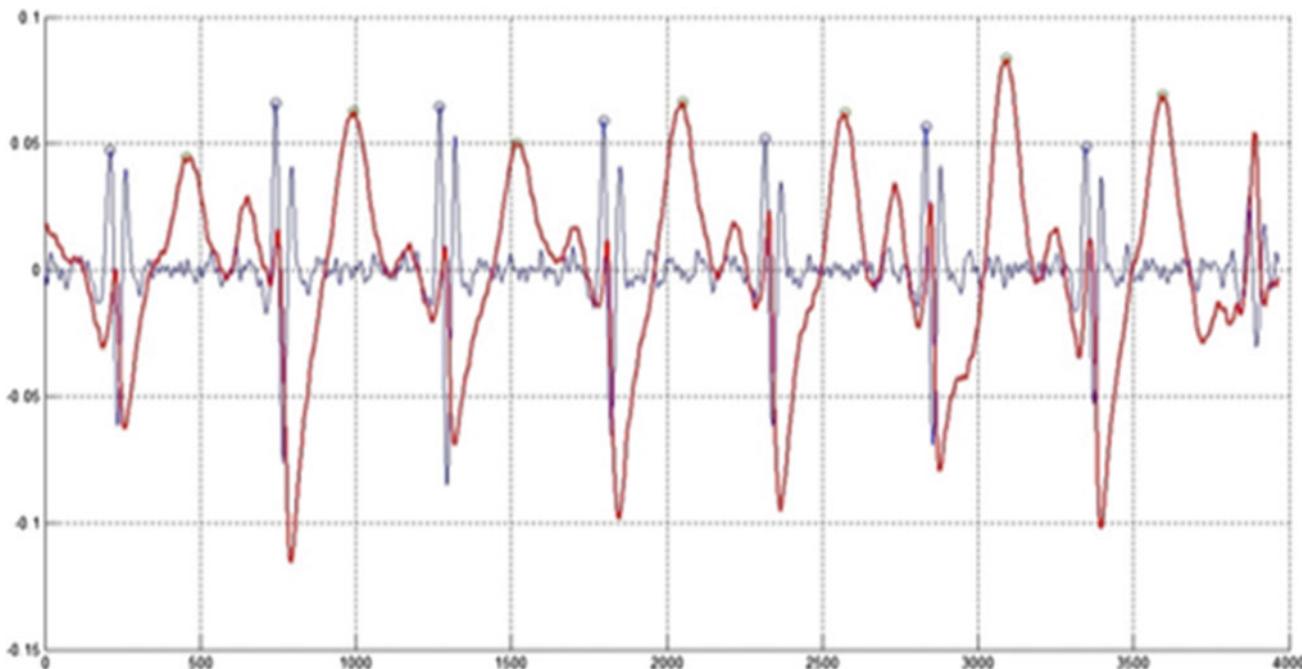
Fig. 5 Measured signals. ECG signal blue curve, PPG signal red curve (Color figure online)

6 Conclusion

The aim of this work was to combine the two relevant measurement methods electrocardiography and photo-plethysmography. These methods are now used not only for clinical purposes but also for diagnosis during long-term monitoring. Due to common production prototype ECG/PPG electrode allow to scan and compare two different signals and the electrical activity of the heart and volume changes in the tissues. It was investigated the best place for placing electrodes and sensors.

This kind of method is very promising. It would be advantageous for a medical doctors and and more comfortable for patient.

References

1. BORIK, Stefan; CAP, Ivo. Measurement and analysis possibilities of pulse wave signals. Advances in Electrical and Electronic Engineering, 2013, 11.6: 514–521.
2. HOFFMANN, Klaus-Peter; RUFF, Roman. Flexible dry surface-electrodes for ECG long-term monitoring. In: 2007 29th Annual International Conference of the IEEE Engineering in Medicine and Biology Society. IEEE, 2007. p. 5739–5742.
3. PENG, Fulai; WANG, Weidong; LIU, Hongyun. Development of a reflective PPG signal sensor. In: 2014 7th International Conference on Biomedical Engineering and Informatics. IEEE, 2014. p. 612–616.
4. RATTFLT, Linda. Smartware electrodes for ECG measurements: Design, evaluation and signal processing. 2013.
5. LEE, Yunjoo; HAN, Hyonyoung; KIM, Jung. Influence of motion artifacts on photoplethysmographic signals for measurement pulse rates. In: Control, Automation and Systems, 2008. ICCAS 2008. International Conference on. IEEE, 2008. p. 962–965.
6. KURONEN, Esa, et al. Epic Sensors in electrocardiogram measurement. 2013.

Wearable Pulse Wave Monitor Resistant to Motion Artifacts

A. A. Fedotov and S. A. Akulov

Abstract

The aim of this study is to create a wearable device for long-term pulse wave monitoring as well as to investigate the possibility of using adaptive noise cancellation approach for reducing motion artifacts occurred during the real-life recording. In our study wearable monitoring device have acquired pulse wave by using photoplethysmography approach and human movement with triaxial accelerometer. The electrical design of wearable device was based on synchronous demodulation and using 24 bits sigma-delta analog-to-digital converter. To achieve effective and robust motion artifacts reduction we create the pulse wave signal processing method based on band-pass filtering and adaptive noise cancellation. Pulse wave signals were initially pass-band filtered at 0.5–10 Hz to remove noise, electrical and physiological interferences, using a zero-phase forward and reverse digital filter, which first filtered the raw signal in the forward direction, and subsequently filtered the reversed signal, thus the resultant signal has zero-phase distortion. Adaptive noise cancellation was implemented by using a recursive least squares algorithm based on the solution of the Wiener-Hopf equation. Our studies have shown that the best results of pulse wave signal processing are achieved for the following parameters of the algorithm: the forgetting factor of 0.99; filter order of 16. Performance of proposed processing technique was evaluated by assessing signal-to-noise ratio (SNR) of the filtered signal and compared with other approaches such as wavelet multiresolution decomposition and moving average filtering. For correct estimation of SNR we used robust approach based on the eigenvalues of signal autocorrelation matrix. This study indicates that designed wearable device based on principles of photoplethysmography for unobtrusive and noninvasive recording of pulse waves and using advanced digital processing technique for removing motion artifacts could provide an effective and performance tools for improving the long-term healthcare monitoring of human vital signs.

1 Introduction

One of the leading trends in modern biomedical engineering is the long-term personal healthcare monitoring of human's vital signs during his daily activity. Recording and processing important physiological signals, e.g. pulse wave, respiration, heart rate, by using unobtrusive wearable devices can enable early detection of cardiovascular and respiratory diseases in the preclinical stage, drastically reduce the cost of medical services, bring quality healthcare to remote locations and improve the effectiveness of treatment [1, 2].

The arterial pulse wave monitoring in order to control the heart rate variability, oxygen saturation, arterial stiffness, pulsatile perfusion plays a central role in the modern clinical diagnostics of many severe diseases. Distal pulse waves are available for noninvasive and long-term monitoring, highly informative about the general state of autonomic nervous system, arterial vessels and peripheral hemodynamics, while the importance and urgency of early diagnosis of cardiovascular pathologies can hardly be overestimated.

For long-term pulse wave monitoring the most valuable approach is photoplethysmography (PPG)—simple and low-cost electro-optic method for detecting the cardiovascular arterial pulsations generated by the elastic nature of the peripheral vascular arteries and heart contractions [3].

The main aim of this study is to develop the wearable device for long-term pulse wave monitoring as well as robust

A. A. Fedotov (✉) · S. A. Akulov
Department of Laser Systems and Biomedical Engineering,
Samara National Research University, Samara, Russia
e-mail: fedoaleks@yandex.ru

and effective digital processing method for filtering motion artifacts and compare the proposed method with exist widespread approaches using for motion artifacts reduction that based on wavelet transforms and moving average filtering [4, 5].

2 Theory

The basic form of PPG technology requires only a few optical components: a light source to illuminate the tissue, often operated at a red or a near infrared wavelength, and a photodetector to measure the small variations in absorbed or reflected light intensity associated with changes in pulsatile oscillations [3].

Despite its simplicity and availability, the PPG signal is easily corrupted by motion artifacts, especially in continuous mobile monitoring during real-life human activities. Pulse wave signal processing contaminated by motion artifacts is nontrivial task because of their random origin and spectral overlapping between motion artifacts and pulse wave [4, 5].

The main challenge for designing wearable pulse wave monitors is to overcome the problem of occurring unavoidable motion artifacts, which significantly contaminate the pulse wave and lead to errors in measuring pulse amplitude and beat-to-beat intervals. One of the possible solutions proposed in this study is to develop new approach for effective reducing of motion artifacts by using joint hardware and software implementations in wearable devices for long-term monitoring.

3 Materials and Methods

For noninvasive and unobtrusive recording of pulse wave we have used PPG sensor placed on human wrist in a special bangle that contains electronic circuit for biosignal analog and digital processing as well as Bluetooth module for transmitting data to the smartphone or tablet PC with Android OS. In this type of sensors the reflectance light intensity is measured by broadband photodiode with low noise and dark current level.

Due to the fact that the light variations associated with pulse waves have a small value of the total DC component caused by light reflection from non-pulsatile tissue (about 0.1–5%) we used alternating electric current for powering infrared light emitting diode (LED), pulse-amplitude modulation with further synchronous demodulation and high-resolution analog-to-digital converter (ADC) to improve the signal-to-noise ratio [6, 7].

Figure 1 shows block diagram of the recording channel of designed wearable device consisting of PPG transducer, movement recorder, and the computing unit; 1—current generator; 2—LED with 940 nm wavelength; 3—photodiode; 4—triaxial accelerometer with measuring range of ± 2 g; 5—current-to-voltage convertor; 6—synchronous demodulator; 7—two-channel delta-sigma ADC; 8—microcontroller; 9—Bluetooth transmitter. The dotted line shows the PPG sensor and accelerometer placed in a single package.

Rectangular current generator 1 was used to supply infrared LED. To obtain an acceptable sensitivity for quality recording of pulse waves the amplitude of the alternating current was selected at 20 mA, the duty cycle was 10 and frequency was 5 kHz. The photocurrent from photodiode was converted to voltage by using photoconductive circuit on the basis of precision operational amplifier with extremely low input currents (few pA). Then the voltage signal is supplied to a synchronous demodulator 6, where the envelope of the modulated signal proportional to pulse wave is extracted.

The resultant voltage demodulated signal, containing both AC and DC components, was digitized by using 24-bit delta-sigma ADC 7 with sampling frequency of 250 Hz, and then pulse wave samples were written to the RAM memory of microcontroller 8 for further digital processing, filtering and transmitting to the Bluetooth module 9.

To reduce the motion artifacts, we used joint hardware and software solution that includes triaxial accelerometer sensor 4 located into the wrist bangle, and software implementation of adaptive noise cancellation (ANC) for microcontroller's firmware. Figure 2 shows the block diagram of adaptive noise canceler [8].

The observed raw signal on the "Primary input" $x(n)$ is a mixture of the pulse wave signal $v(n)$ and the "primary noise" (motion artifact) $m(n)$:

$$x(n) = v(n) + m(n)$$

It is desired that the motion artifact $m(n)$ should be estimated and removed from $x(n)$ in order to obtain the filtered pulse wave signal $v(n)$. It is assumed that $v(n)$ and $m(n)$ are uncorrelated. ANC requires a second input: "reference input" $r(n)$, uncorrelated with the pulse wave signal $v(n)$, but closely related to the motion artifact $m(n)$.

The ANC modifies the reference input $r(n)$ e.g. the movement signal in order to obtain a signal $y(n)$ as close to
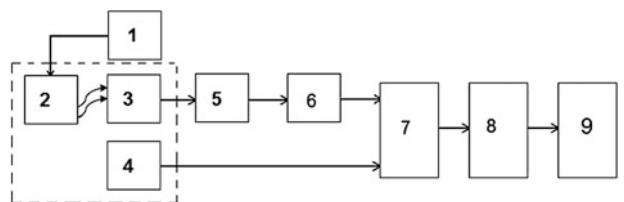
Fig. 1 Block diagram of PPG recording channel
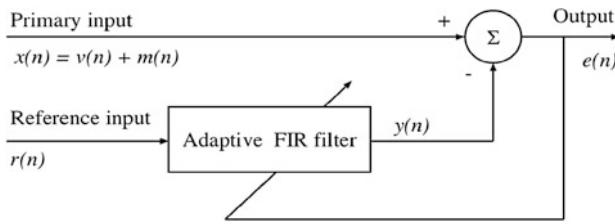
Fig. 2 Block diagram of adaptive noise canceler [8]

motion artifact $m(n)$ as possible; then $y(n)$ is subtracted from primary input to estimate pulse wave signal:

$$v * (n) = e(n) = x(n) - y(n)$$

The output signal of adaptive filter $y(n)$:

$$y(n) = \sum_{k=0}^{N-1} w_k \cdot r(n - k)$$

where N is the filter's order; w_k are the tap-weights of the adaptive filter.

The main objective is to obtain an output $e(n)$ that is a least-squares fit to the desired pulse wave signal $v(n)$. This aim could be achieved by feeding the output back to the adaptive filter and adjusting the filter to minimize the total output power. System output $e(n)$ is an error signal for the adaptive process.

Pulse wave signals were initially pass-band filtered at 0.5–10 Hz to remove noise, as well as electrical and physiological interferences, using a zero-phase forward and reverse digital filter, which first filtered the raw signal in the forward direction by means of 4th order Butterworth filter, and subsequently filtered the reversed signal, thus the resultant signal has zero-phase distortion [8].

For a software implementation of ANC we used a recursive least squares algorithm based on the solution of the Wiener-Hopf equation [8, 9]. To achieve the trade-off between computational cost and quality of processing we downsampled the recorded pulse wave from initial 250 Hz to the 100 Hz in order to decrease the optimal order of adaptive filter, the movement signal was sampled at 100 Hz as well. Our studies have shown that the best results of pulse wave signal processing are achieved for the following parameters of the algorithm: the forgetting factor of 0.99; filter order N of 16.

To evaluate quality of recording and processing of pulse waves contaminated by motion artifacts in real-life situations we performed an experiment with wearable wristband sensor placed on the left arm of volunteer who gave prior and informed consent to participate in the trial.

To assess the performance of the proposed method against pure software approaches of motion artifacts reduction such as wavelet multiresolution analysis (WMRA) and

moving average filtering (MAF), signal-to-noise ratio (SNR) was computed before and after processing. De-noising pulse waves from motion artifacts by using WMRA is based on classic Mallat pyramid algorithm and adaptive soft-thresholding of detailed coefficients at appropriate levels of wavelet decomposition according to Donoho approach [10].

For correct estimation of SNR we used robust approach based on the eigenvalues of signal autocorrelation matrix. The largest eigenvalue of the matrix corresponds to the pulse wave signal power, whereas the sum of the remaining eigenvalues represents the noise power [11].

To find the eigenvalues, the pulse wave recording was divided into M pieces of L samples, where each piece contains one pulse wave complex. For separating several pulse waves from the recording, we used amplitude-time detector based on pass-band filtering, non-linear operations and adaptive thresholding [12].

After separating pulse waves, a matrix X of size $M \times L$ is composed and then M eigenvalues of appropriate autocorrelation matrix $D = X \cdot X^{\mathrm{T}}$ are calculated to find the SNR as follows:

$$SNR = 10 \log \left(\frac{\lambda_{\max}}{\sum_{i=1}^{M} \lambda_i - \lambda_{\max}} \right)$$

where $\lambda_{\max}$ is the largest eigenvalue of the autocorrelation matrix D; λ_i is the i-th eigenvalue of the autocorrelation matrix D.

4 Results

Figures 3, 4, 5 and 6 illustrate the different noisy pulse wave recordings (the upper trace) and pulse waves after digital processing by using consecutive pass-band filtering and
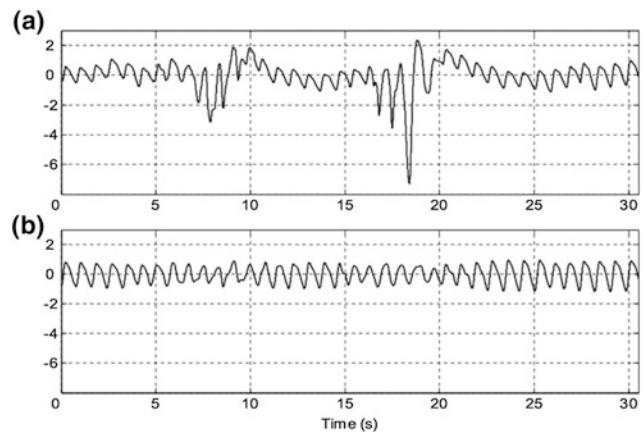
Fig. 3 Processing of PPG signal corrupted by arm bending and waving
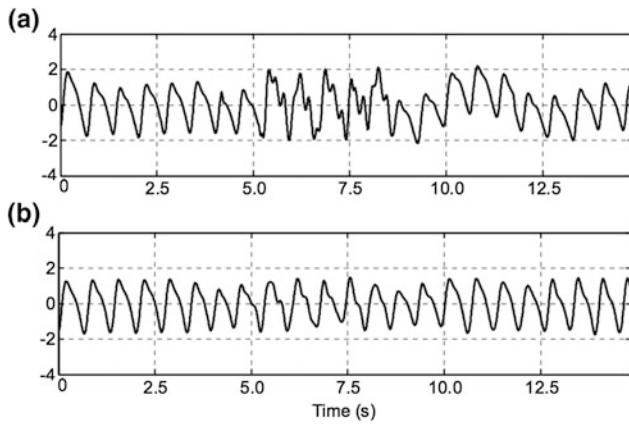
Fig. 4 Processing of PPG signal corrupted by arm's horizontal motion
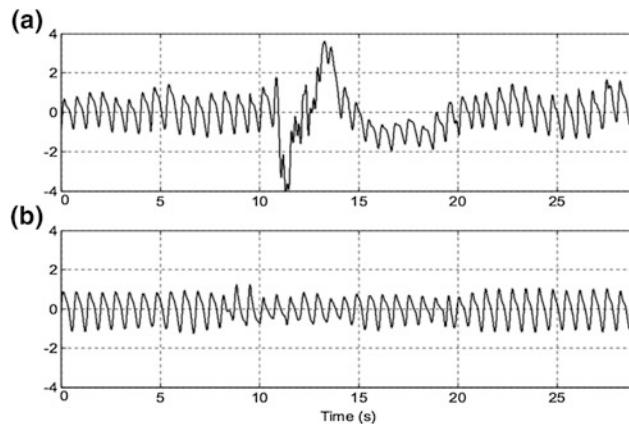
Fig. 5 Processing of PPG signal corrupted by arm's vertical motion
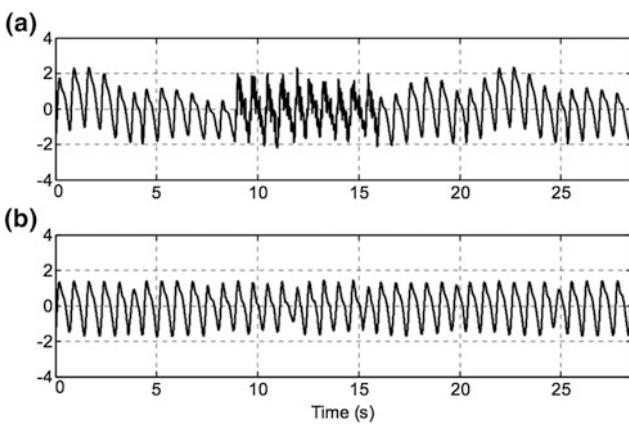
Fig. 6 Processing of PPG signal corrupted by pressurizing the probe

adaptive noise cancellation proposed in this study (bottom trace).

Table 1 contains the *SNR* values, calculated for the raw pulse wave signals, contaminated by different types of

Table 1 *SNR* for different methods of motion artifacts reduction during various types of activity

Activity	Raw signal (db)	Proposed method (db)	WMRA (db)	MAF (db)
Horizontal hand motions	1.9	9.6	**9.8**	7.5
Vertical hand motions	0.9	**7.8**	7.1	5.2
Waving hand	0.1	**6.9**	6.6	4.8
Gesticulation	−1.5	**5.8**	5.1	2.3
Walking	0.8	**7.4**	7	4.6
Jogging	−0.6	**6.3**	5.2	1.9

motion artifacts, as well as for the filtered signals, obtained by different processing methods.

5 Conclusion

Visual analysis of the processed PPG signals shows that the proposed de-noising method based on application of the band-pass filtering and adaptive noise cancellation provides good quality of restored signal during casual activities, which is crucial for long-term real-life monitoring.

Adaptive noise cancellation provides better signal-to-noise ratios of processed pulse wave recordings in comparison with highly usable in modern signal processing multiresolution wavelet analysis and especially with moving average filtering. However, the latter two approaches are pure software solutions and thus universal, because for their successful implementation there is no need in additional hardware modules for recording motion signals.

This study indicates that designed wearable device based on principles of photoplethysmography for unobtrusive and noninvasive recording of human pulse waves and using advanced digital processing technique for removing motion artifacts could provide an effective and performance tools for improving the long-term healthcare monitoring of human vital signs.

It should also be noted that the proposed approach for motion artifacts reduction based on joint hardware and software implementation of the adaptive filtering used in this study could be extended to other biomedical signals acquired in conditions of long-term telemonitoring, such as ECG signals, respiratory signals, as well as arterial pulse waves acquired by other techniques: impedance plethysmography, sphygmography.

Conflict of Interest The authors declare that they have no conflict of interest.

References

1. A.G. Ekeland et al, Effectiveness of telemedicine: A systematic review of reviews, *International Journal of Medical Informatics, 79*(11), 2010, 736–771.
2. G. Pare et al, Comparing the costs of home telemonitoring and usual care of chronic obstructive pulmonary disease patients: A randomized controlled trial, *European Research in Telemedicine, 2* (2), 2013, 35–47.
3. J. Allen, Photoplethysmography and its application in clinical physiological measurement, *Physiological Measurement, 28,* 2007, 1–39.
4. T.H. Fu, Heart rate extraction from photoplethysmogram waveform using wavelet multi-resolution analysis, *Journal of medical and biological engineering, 28*(4), 2008, 229–232.
5. A.A. Fedotov Selection of parameters for filtering distal arterial pulse signal using multi-resolution wavelet transforms, *Springer: Biomedical Engineering, 47*(3). 2013, 146–149.
6. A.A. Fedotov, S.A. Akulov, Structure of arterial pulse signal transducers, *Springer: Biomedical Engineering, 48*(3), 2014, 160–163.
7. J.G. Webster *Design of Pulse Oximeters* (Taylor & Francis, Bristol, 1997).
8. R.M. Rangayyan, *Biomedical Signal Analysis: A Case-Study Approach* (IEEE Press and Wiley, New York, 2002).
9. F.J. Theis, A. Meyer-Base, *Biomedical signal analysis. Contemporary methods and applications* (The MIT Press, 2010).
10. D.L. Donoho (1995) De-Noising by Soft-Thresholding, *IEEE Transactions on Information Theory, 41*(3), 1995, 613–627.
11. W.Y. Shen et al, Research of fetal ECG extraction using wavelet analysis and adaptive filtering, *Computers in Biology and Medicine, 10*, 2013, 1622–1627.
12. A.A. Fedotov, Amplitude–time method for detecting characteristic pulse wave points, *Springer: Biomedical Engineering, 46*(6), 2013, 241–245.

Restricted Interest-Based Adaptation of Avatar for Interaction with Children with Autism Spectrum Disorder

Luis Fernando Guerrero-Vasquez, Dennys Landy-Rivera, Geanina Ávila, Jack F. Bravo-Torres, and Martín López-Nores

Abstract

This article presents a systematic process to develop technological supports for children with Autism Spectrum Disorder (ASD), based on restricted interests. With the information generated from the diagnostic evaluations applied to a group of children with this disorder, were selected avatars that match their preferences. To do this, mobility was added with the aim of being used as a base in the development of therapies that promote the interaction and learning processes of children with ASD. This adaptation increases the children's acceptance of the avatar, unlike other empirical processes that require an intermediate stage of acceptance.

L. F. Guerrero-Vasquez (✉) · D. Landy-Rivera
J. F. Bravo-Torres
Universidad Politecnica Salesiana, Cuenca, Ecuador
e-mail: lguerrero@ups.edu.ec

D. Landy-Rivera
e-mail: dlandy@ups.edu.ec

J. F. Bravo-Torres
e-mail: jbravo@ups.edu.ec

G. Ávila
Fundación Centro de Intervención Multidisciplinaria para el Autismo (CIMA), Cuenca, Ecuador
e-mail: geanina_avila@yahoo.es

L. F. Guerrero-Vasquez · M. López-Nores
AtlantTIC Research Center, University of Vigo, Vigo, España
e-mail: mlnores@det.uvigo.es

1 Introduction

Autism Spectrum Disorder (ASD) is a neurodevelopmental disorder that mainly has two characteristics: presence of fixed interests and repetitive behavior; and social and communication deficit [1, 2]. The Autism Society of American (ASA) mentions that ASD is a neurodevelopmental disability that appears early in childhood and disrupts the functioning of the central nervous system [3]. In addition, the disorder is presented with a lack of mental flexibility, with restricted, repetitive and stereotyped behaviors of interest and activities [4]. The consequence of greater impact on people with ASD are the difficulties in social communication. This does not allow children to develop the social skills necessary to acquire new skills and empower them. It is necessary to attend promptly these deficiencies in the first years of life to improve the acquisition of skills necessary to reach an adult life as a socially functional person.

Currently, according to the World Health Organization (WHO), about 1 in 160 children in the world has been identified with ASD [5]. In this context, the constant generation of support tools for the development of people diagnosed with ASD, is necessary. In the technological aspect, several contributions have been made to help identify and treat ASD. Considering the difficulties in social communication, researchers generate tools based on Information and Communication Technologies (ICT) to promote the social interaction of children with ASD. Using solutions focused on robots, virtual reality and intelligent environments, encouraging results have been observed [6, 7], which motivate to continue using ICT in the treatment of ASD.

Despite the deficient development of social skills such as communication, imagination and empathy in people with ASD, there is a widespread acceptance of technological tools. However, in order for tools to influence and be used as support in therapies, it is necessary to personalize the solutions, seeking greater acceptance by the people for whom they were designed. The project "*Adaptive Robot-Mediated*

Intervention Architecture" (ARIA), focuses on designing individualized interventions for children with ASD based on quantitative measures [8]. It consists of a humanoid robot equipped with artificial vision that reacts to the movements of children heads and adapts to generate messages as required by the interaction. Like ARIA, there are other projects aimed at personalization [9–11], which show encouraging results when working with children with ASD in therapy sessions. However, work with robots allows little customization, since it can only be done based on the "*personality*" of the robot and not on its physical form. Robots are still a generalized solution and there is a risk of not being completely accepted by children with ASD for their use in therapies. The project *Autism*: *Virtual Agents to Augment Relationships in Children* (AVATAR) [12], raises the use of semi-personal virtual agents that combine human intelligence with artificial intelligence algorithms to generate interventions that improve the processes of social interaction in children with ASD. Like AVATAR, there are other developed projects that demonstrate the acceptance of virtual agents and the possibility of customizing them according to the needs [13–15].

This article presents a contribution to the AVATAR project in the process of personalization of virtual agents. In the second section, Restricted and Repetitive Behaviors (RRBs) are analyzed to detect the restricted interests of a group of children from the Multidisciplinary Intervention Center for Autism (CIMA) of Cuenca, Ecuador. This will guide the customization and also ensure that the avatars will be accepted by the children. Then, in the third section, the methodology used to adapt the avatars in the Blender software is presented, generating as a result virtual agents ready to be used in automation processes or generation of therapies.

2 Restricted and Repetitive Behaviors (RRBs)

The first observations about ASD were made in 1943, when Leo Kanner published an article entitled "*Autistic disturbances of affective contact*" [16]. In this article, Kanner presented a complete study to 11 children (8 boys and 3 girls), in which he details that each child shows individual differences in their "*disturbance*", but all of them with an essential number of similar characteristics, that allowed to define for the first time the Autism Spectrum Disorder. Mainly, there are two distinctive features of autistic behavior that the author emphasizes by his presence in all the cases analyzed and are the "*autistic aloneness*" and the "*obsessive insistence on sameness*". Based on "*obsessive insistence on similarity*" of Kanner, Restricted and Repetitive Behaviors (RRBs) are defined [17]. RRBs, although a feature of ASD, are present in other developmental or psychiatric disorders,

such as Obsessive-Compulsive Disorder, schizophrenia, Tourette's syndrome, hyperactive disorder and attention deficit, and anxiety and humor disorders [18]. Subsequently, other authors observed that executive functions, i.e., planning skills, mental and cognitive flexibility, generativity, inhibition of responses, mentalist abilities and sense of activity, are altered in people with ASD and relate these characteristics to the presence of repetitive and stereotyped behaviors [19]. In general, it is necessary for a person to present a particular number of symptoms in a specific order to be diagnosed with ASD [20]. The Diagnostic and Statistical Manual of Mental Disorders (DSM-5) [1], considers the RRBs as a domain of the behavior required for the diagnosis of ASD.

Included in the RRBs are the repetitive motor mannerisms, the persistent occupation in parts of objects, restricted interest patterns and the inflexible adherence to non-functional rituals or routines [17]. In the next section, restricted interest patterns are analyzed to establish the preferences that children have regarding the characteristics of the avatar.

3 Avatar Selection and Adaptation According to RRBs

The process of selection of the avatars begins with the evaluation of the presence of RRBs is evaluated. The detection of RRBs is done during the diagnostic process and the tools used are the *Autism Diagnostic Interview—Review* (ADI-R) [21], and the *Autism Diagnostic Observation Schedule* (ADOS) [22]. Both are widely used diagnostic tests that allow the evaluation of restricted, repetitive or stereotyped behavior patterns. Based on the results provided by the diagnostic tests, the preferences of the children evaluated are defined. These preferences can be classified within the themes presented in Table 1. After knowing the preferences of the children, the next step is to obtain the avatars. The main source consulted was blend swap (https://www.blendswap.com), which consists of a website where several collaborators upload models developed in the Blender with Creative Commons License. This source was chosen because Blender is an open software integrated with

Table 1 General and specific preferences based on restricted interest

General preferences	Specific preferences
Superheros	Ironman, spiderman, batman
Animals	Dog, rabbit, cat, dinosaurs
Cartoons	Mickey mouse, Goku
Robots	Humanoid robots
Famous people	Scarlett Johansson, Zac Efron
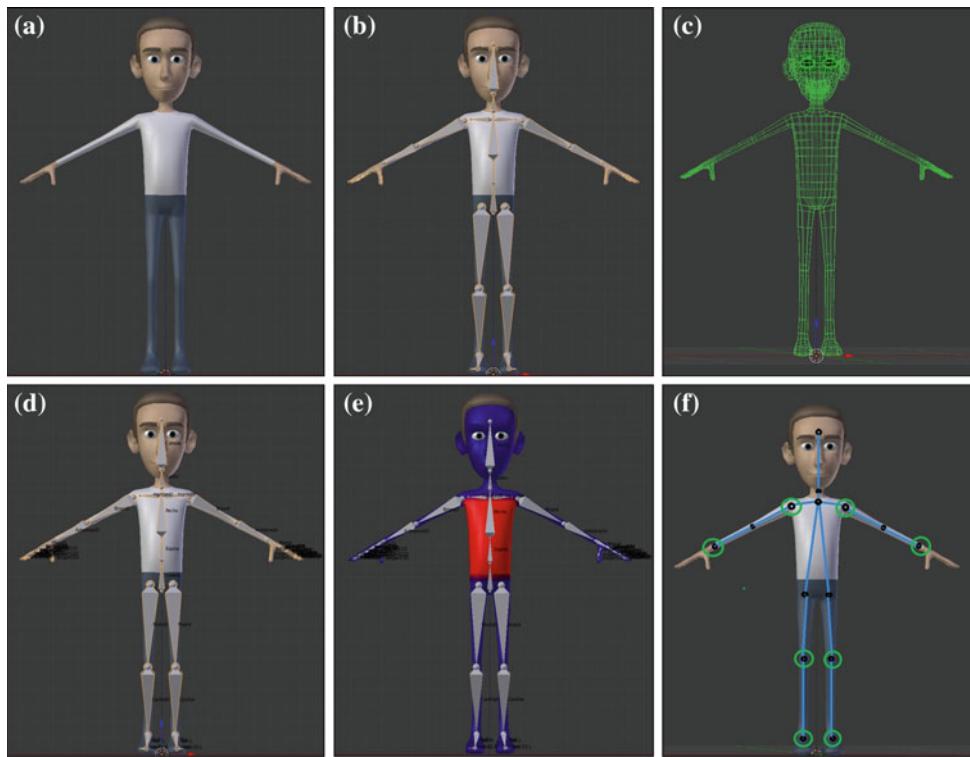
Fig. 1 Avatar adaptation process. **a** Avatar obtained from the website. **b** Skeleton creation. **c** Coupling in the mesh. **d** Dependencies creation. **e** Automatic weights definition. **f** Modifiers placement

Python. At a later stage of development, the use of Phyton in the avatars automation process will be very useful. Finally, with the chosen avatars we proceeded to adapt them so that they can be animated and later used in therapies that promote interaction. The adaptation process of the avatars prior to the animation is shown in Fig. 1.

In Fig. 1a the selected avatar is shown before the adaptation process. After obtaining the avatar, a skeleton is created where each bone must be properly labeled (Fig. 1b). This process is known as Rigging. The skeleton is then attached to the avatar's mesh to relate its movement (Fig. 1c). Dependencies are created between the parts of the body to make everything move as a whole (Fig. 1d). The dependencies prevent that when moving the head the eyes do not move being outside their basins. In order to have natural movements it is necessary to define automatic weights (Fig. 1e). These weights allow to differentiate the intensity of movement of each part of the body. Finally, modifiers that establish movement patterns are added (Fig. 1f). The modifiers allow deformation of the reinforcement together with the mesh. By completing the whole process, the avatars are ready to be animated. The main characteristic of the resulting avatar are its natural and ergonomic movements, without modifying its design features. The points located in the last figure can be loaded as Cartesian coordinates in lines of code

or can be obtained from a digital camera that captures the movement of a person.

4   Conclusions and Future Works

The use of avatars previously developed by experts in the subject, greatly facilitates the process of adaptation. The developers concentrate their efforts solely on the aesthetic aspect and generate a quality and quite detailed products. These characteristics will serve to improve the acceptance of children towards the avatar. For this reason it is very important to start the adaptation process from detailed models.

The avatars obtained have therapeutic characteristics based on Restricted Interest Patterns and thanks to the generalized process of automation, they can be used in any type of avatars-based intervention. It is possible to expand the number of avatars for a larger population with different restricted interests and reduce the adaptation time using basic knowledge about Blender and emulating the proposed process.

It is necessary to have an interdisciplinary team for the development of tools that serve as support in the treatment of children with ASD. Technological developments represent

an excellent alternative as long as they are directed by a psychologist, pediatrician or therapist who masters the subject of ASD. If the result is not an orderly convergence of the contributions of all the experts, the final product could not be considered a useful and integral solution. In the next stage of the present work, we intend to use automatic learning methods to train the avatars with movements of natural and ergonomic characteristics. With programmed sequences of movement will be analyzed the different reactions of children against their avatars. It will also equip the avatars with artificial intelligence algorithms to generate interaction processes driven by a combination of artificial intelligence and human intelligence and analyze the results when they are used in social communication therapy processes in children with ASD.

Conflict of Interest　The authors declare that there is no conflict of interest regarding the publication of this paper.

References

1. D.C., W.: Diagnostic and Statistical Manual of Mental Disorders (DSM-5®). American Psychiatric Pub (2013)
2. Martos, J.: Autismo y trastornos del espectro autista. Definición, génesis del trastorno y explicaciones psicológicas. Autismo del diagnóstico al tratamiento pp. 19–45 (2011)
3. ASA: Autism Society of America. URL https://www.autism-society.org/what-is/
4. Ruiz-Lázaro, P., Posada de la Paz, M., Hijano Bandera, F.: Trastornos del espectro autista: Detección precoz, herramientas de cribado **11**, 381–397
5. WHO: Worl Health Organization. URL http://www.who.int/mediacentre/factsheets/autism-spectrum-disorders/en/
6. Fteiha, M.A.: Effectiveness of assistive technology in enhancing language skills for children with autism **63**(1), 36–44
7. Kouo, J.L., Egel, A.L.: The Effectiveness of Interventions in Teaching Emotion Recognition to Children with Autism Spectrum Disorder **3**(3), 254–265
8. Bekele, E.T., Lahiri, U., Swanson, A.R., Crittendon, J.A., Warren, Z.E., Sarkar, N.: A Step Towards Developing Adaptive Robot-Mediated Intervention Architecture (ARIA) for Children With Autism **21**(2), 289–299
9. Kuriakose, S., Lahiri, U.: Design of a Physiology-sensitive VR-based Social Communication Platform for Children with Autism pp. 1–1
10. Hughes, D.E., Vasquez, E., Nicsinger, E.: Improving perspective taking and empathy in children with autism spectrum disorder. pp. 1–5. IEEE
11. Peca, A.: Robot Enhanced Therapy for Children with Autism Disorders: Measuring Ethical Acceptability **35**(2), 54–66
12. Guerrero-Vasquez, L.F., Bravo-Torres, J.F., Lopez-Nores, M.: AVATAR "autism: Virtual agents to augment relationships in children". pp. 1–4. IEEE
13. Ying, K.T., Sah, S.B.M., Abdullah, M.H.L.: Personalised avatar on social stories and digital storytelling: Fostering positive behavioural skills for children with autism spectrum disorder. pp. 253–258. IEEE
14. Milne, M., Luerssen, M.H., Lewis, T.W., Leibbrandt, R.E., Powers, D.M.W.: Development of a virtual agent based social tutor for children with autism spectrum disorders. pp. 1–9. IEEE
15. Tanaka, H., Sakriani, S., Neubig, G., Toda, T., Negoro, H., Iwasaka, H., Nakamura, S.: Teaching Social Communication Skills Through Human-Agent Interaction **6**(2), 1–26
16. Kanner, L., others: Autistic disturbances of affective contact. Nervous child 2.3 **2**(3), 217–250 (1943)
17. Richler, J., Bishop, S.L., Kleinke, J.R., Lord, C.: Restricted and Repetitive Behaviors in Young Children with Autism Spectrum Disorders **37**(1), 73–85
18. Mahone, E.M., Bridges, D., Prahme, C., Singer, H.S.: Repetitive arm and hand movements (complex motor stereotypies) in children **145**(3), 391–395
19. Martos-Pérez, J., Paula-Pérez, I.: Una aproximación a las funciones ejecutivas en el trastorno del espectro autista **52**(1), 147–153
20. Burack, J., Charman, T., Yirmiya, N., Zelazo, P.: The Development of Autism: Perspectives From Theory and Research. Taylor & Francis (2001)
21. Le Couteur, A., Lord, C., Rutter, M., others: The autism diagnostic interview-revised (ADI-R). Journal of autism and developmental disorders (1994)
22. Lord, C., Rutter, M., Le Couteur, A.: Autism Diagnostic Interview-Revised: A revised version of a diagnostic interview for caregivers of individuals with possible pervasive developmental disorders **24**(5), 659–685

Design and Implementation of Digital Tele Stethoscope

Ijlal Shahrukh Ateeq, Kamran Hameed, Malik Khowaja, and Sana Hyder Khan

Abstract

Our project relates to Tele-stethoscope which is specially designed to provide state of art technology to medical and health professionals to provide best possible practices to the seniors, people with disabilities, and people in distant areas who may have difficulties to grab a proper health care facility. Initial stage of this project was to consult our professors, health professionals and sketch a concept design. Even though, electronic stethoscopes are available in market but they are out of reach of a common man. We revisited the cost and put up a cost analysis which has turned this instrument more economical. Research was completed to identity the frequencies of head sound which stethoscope needed to filter. The concept includes all the attributes that a Tele-stethoscope should include. Next step was to design analog circuit which comprises pre-amp and post amp stages and then the interfaced to Pc via a free open source. Project was then tested with the help of Skype voice call messenger and we successfully transmitted cardiac sounds with such high quality and precision.

Keywords

Tele-stethoscope • Health care • Transmission

I. S. Ateeq (✉) · K. Hameed · S. H. Khan
Imam Abdulrahman Bin Faisal University, Dammam, KSA, Saudi Arabia
e-mail: ishahrukh@yahoo.com; Lsateeq@iau.edu.sa

K. Hameed
e-mail: kamranhameed@live.com

M. Khowaja
Sir Syed University of Engineering and Technology, Karachi, Pakistan

1 Introduction

For past many years, doctors and medical practitioners used Stethoscopes to diagnose the diseases (from heart to lungs) and still experienced physicians can diagnose a large number of clinical conditions just from the use of Stethoscopes. Cardiac auscultation is considered to be hardest task due to number of reasons and as heart sounds are of low frequency and the intervals between the sounds are short. This certainly gives a hard task to examine and get the accurate cardiac sounds to diagnose. For the same reasons, numerous methods and instruments were designed to achieve precise cardiac sounds such as Phono-echocardiograms, Doppler echocardiography. Several attempts were made to develop special Stethoscopes in 1960s and gathered some remarkable achievements which allows group of people to hear heart sounds but still there were disadvantages of getting the desired output due to requiring the plugging of many tubes to a single machine that disperses and makes sound less intense.

In 1980s electronic stethoscopes were developed which had extra functions in comparison to the conventional acoustic stethoscopes by the use of amplifiers and analog filters.

Our objective is to follow the same trend and develop an electronic stethoscope with modifications and alterations which provides us to send cardiac sounds live on internet to the mobile receiver (Synchronization).

In This Project we Introduce a Modern technology electronic stethoscopes, take ad- vantage of modern technologies to reduce these disadvantages. They allow to adjust the volume of auscultations and to store them on a PC. Also, top level devices are mechanically designed to reject most of the environmental noise. Software tools for the record, display and replay of acquired sounds. We provide online web streaming for emergency condition.

1.1 Historical Background

Stethoscope is one of the basic symbols of bio and medical sciences. It is one of the revolutions in the field of medicine. It is the first ever tool which able the world to get the auscultation of the body.

In 56 BC, one of the Chinese invented a tool called "Meng" which believes to be the predecessor of modern stethoscope. The first stethoscope was invented in Paris, France. It comprises of a wooden tube and was monaural. The devices were almost identical to the historical hearing aid; though this tool was identical to ear trumpet which we called a "Microphone".

Continuous developments were made since then and finally we get a commercial stethoscope which is now most common and basic part of medicine.

1.2 Theoretical Investigations

The human body sound signals which have relatively low amplitudes can be amplified by an electronic stethoscope. It creates a window which discards high and low level frequency range sounds and only amplifies mid-range sounds. This attenuation helps to cut off the distortions and noise which are unwanted. As the signal is captured through a human body, it's needed to be transformed from the acoustic signals into electrical signals which can further be amplified and processed for better listening as compared to the acoustic stethoscopes which are all depended upon the same entities. The method of setting up a microphone within the chest piece to detect sound is considered the least favorable method due to the impact of the surrounding noise on the sound signals which directly affects the sound quality.

Another mechanism is used in replacement to the microphone is setting up a piezoelectric crystal on top of a metal shaft, while the base of the shaft is attached to a diaphragm. Another alteration is the use of Electromagnetic diaphragm which contains a conductive inner body to create a capacitive sensor. It responds to sound waves similarly as an acoustic stethoscope does, with the variation in the electric field which works similarly as the change in the air pressure in an acoustic stethoscope. This provides the amplification of the signals and also protects the sound quality.

An electronic stethoscope may as well be used as a sound recording device or a wireless device minimizing the surrounding noise disturbance and enhancing the quality of the signal. Nowadays, computer based software are used for targeting the telemedicine studies and analysis.

1.3 Health Consequences

People suffered from heart diseases are in danger of heart failure at any time which can cause sudden death. The Tele-stethoscope provide instant contact with their doctor if they suffer sudden heart illness and doctor can diagnose the actual disease and save their life before they hospitalized.

1.4 Working Principle

This electronic stethoscope has the feature of clear sound; it can replace the ordinary stethoscope without amplification function. The working principle of this circuit is that this electronic stethoscope circuit is composed of microphone pre-amplifier; it is shown in the Fig. 1. The preamplifier circuit is made of capacitors and resistors. The pin number 1 of the Pre-amp is then connected to the low pass filter. Another leg of the filter is connected to capacitor (1 mf) which is connected to a switch. Switch allows us to either connect the circuit to a PC interface (Sound card) or to the headphone. In between switch and headphone, power amplifier (post amplifier) is connected. This enables us to provide required power to the headphone and can control the volume (Gain is 20) [1].

1.5 Main Features

(1) Amplification of heart sound.
(2) Filtered and Background Noise Free Signal.
(3) Signal Recording and Visualizing software.
(4) Low Cost and Low Power.
(5) Online live transmission of signals.
(6) Portable.

1st Phase
Preparation of feasibility report

2nd Phase
Searching for the components availability

3rd Phase
Working on the design of the project

4th Phase
Preparation of Presentation and Final Re-
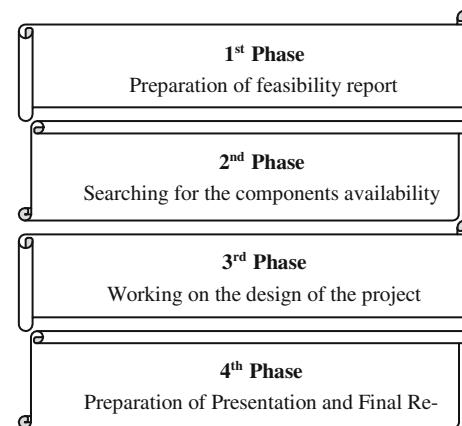
Fig. 1 Phases and projects

2 Applications in Biomedical Engineering

The evolution and applications of the electronic stethoscope with telemedicine initiatives has been intertwined and right hardware/software product are being introduced. Through the Electronic Health Record, service readings could be taken from the comfort of your home and automatically uploaded to the central server for medical practitioners to review. This would be extremely advantageous for seniors, people with disabilities, and people in remote areas who may have difficulties reaching a proper health care facility. The application of Tele-stethoscope can be immense and it would certainly revolutionize the acceptance of Bioengineering to a different level [1, 2].

3 Design Methodology

3.1 Project Design

3.1.1 Phases
See Figs. 1 and 2.

4 Materials and Methods

4.1 Materials

See Table 1.

4.1.1 Techniques and Equipments Used to Implement
Equipments and technology use to demonstrate our project are

(1) Skype to Skype (Through internet)
(2) Source free software Audacity
(3) Computers/Laptops.
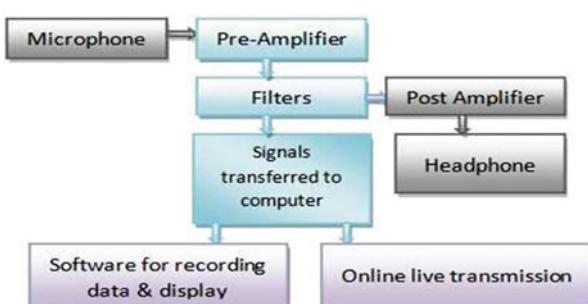
Fig. 2 Block diagram of tele-stethoscope

4.2 Methods

The third phase of this project comprise of three sub stages

(1) The Modification of the prototype to obtain, filter and amplify the cardiac sounds.
(2) The Introduction of a software Program to record, reproduce and visualize them.
(3) The testing of the prototype [3, 2].

4.2.1 Tasks Performed
After all the theoretical work, we were set to build up a prototype (Stage 1), a device similar to conventional stethoscope which filters and acquire sound. The stethoscope was designed with following components Condenser Microphone, Pre-amp and Post-amp, Low Pass Filter, Head-Phones, Switch and Batteries.

This device filtered out high frequencies without losing the actual heart sound and attenuates the noises and distortion. Our Electronic Stethoscope's frequency range is 20–500 Hz. In a standard mechanical stethoscope, there are two settings, or sides, that can be used to listen to internal sounds. The bell has a detection range of 20–500 Hz and is designed to be able to hear the sound of the heart and blood vessels pumping. The other side of the mechanical stethoscope is the diaphragm. The diaphragm has a range of 200–1000 Hz and is used to listen to the higher frequency respiratory sounds [4]. By utilizing Electret condenser microphone capable of picking up sounds with a frequency as low as 20 Hz and a low pass filter designed to eliminate sounds above 500 Hz, the desired frequency range was achieved for the Electronic Stethoscope. The output of this device was then interfaced with the microphone in of sound card which then record and visualize the sound into the computer through software. Also for flexibility and acquire more options, I had connected Post Amplification circuit to Headphones as well. So if user wants to use this device conventionally, they can do so. We have done the audio acquisition, analog design to amplify the signal from the condenser microphone and how I interfaced with the headphone and Audacity. We have used Electret Condenser Microphone by keeping the following parameters under consideration Impedance 2.2 KΩ, Signal to noise ratio (S/N) Ratio 58 dB, Sensitivity 45 dB $\pm$ 4 dB and frequency range from 20 Hz–20 kHz.

Electret material is a stable dielectric with embedded charge. As sound waves are incident against the microphone's diaphragm, the capacitance of the microphone can change dynamically [5]. These microphones are low cost devices that were once considered low quality. Current Electret microphones are comparable with capacitor microphones except that they carry more noise. The main problem

Table 1 Components and total cost

S#	Component	Value	Quantity	Cost in Rupee
1	Stethoscope		1	1000
2	Microphone	High input impedance (2.2 KΩ)	1	50
3	Pre-amp	LM358P	1	25
4	Power amp	LM386 N	1	25
5	Headphone	1	500	
6	Potentiometer	20 k	1	20
7	Switch	2 pin and 3 pin	2	26
8	(Female) Jack	Stereo and mono	3	30
9	Resistors	Resistor Pack	1	70
10	Capacitors	220 uf, 2.2 uf, 1 uf, 33 uf, 47 nf	6	12
11	LED	Green	1	2
12	(Male) Jack	Stereo and mono	2	30
13	(Male) Cable	Stereo	1	40
14	Assembly	Plastic fabric casing box	1	1300
15	Battery (3v)	1.5 AAA cells	2	70
Total cost 3200/-Rs				

with implementing an Electret microphone in a stethoscope amplifier circuit is that it will pick up background noise that may be difficult to filter out. The advantages with an Electret microphone are that relatively simplistic amplification circuits can be utilized in order to produce a waveform and that Electret microphones are simple to manufacture.

The main objectives of the analog circuit were to amplify the signal from the condenser microphone with a reasonable signal-to-noise ratio, maintain low power consumption, and be cost effective. Frequency response, gain, noise, and harmonic distortion also must be taken into account when designing the analog circuit. The circuit was separated into four main stages: preamplifier, amplifier, low-pass filter, and voltage buffer.

The preamplifier was created to increase the low-signal from the condenser microphone to line-level for further amplification. This was accomplished by providing a voltage gain from the microphone to the circuit. The LM358 is an operational amplifier (op-amp) that is used in the preamplifier circuit to achieve a voltage gain of 3. The gain can be varied by increasing or decreasing the resistor between pin 1 and pin 2 or the resistor between the microphone and pin 2. The LM358 was chosen be- because it is a low-power device that draws a small amount of current. It can be powered by a 1.5 AAA × 2 Battery. There are other various op-amps that can be used in this circuit; however, the LM358 is very inexpensive.

A low-pass RC filter was used to limit the audible frequency. The filter has a characteristic of 500 Hz cut-off frequency; this was achieved by using a 150 Ω resistor and a 2.2 μF capacitor. For future improvement, two filters can be

implemented to simulate the bell and diaphragm. A typical bell has the detection range of 20–500 Hz for sounds of the heart and blood vessels; this can be implemented using a low-pass filter. These filters would be used by the physicians to focus on heart. A switch is applied to determine which mode would be used.

The amplifier is used to supply the necessary power to drive the headphones. The LM386 is a low voltage audio power amplifier that is used to achieve a gain of 20. In addition to the gain in this stage, the volume control was implemented. The volume was controlled by varying the 20 KΩ variable resistor. From the amplifier stage, the signal travels to headphone.

In the second stage I had introduced free open source software "Audacity" for recording and editing sounds. This software is widely used to record live audio and have many other features which are the best fit for our project [1–3].
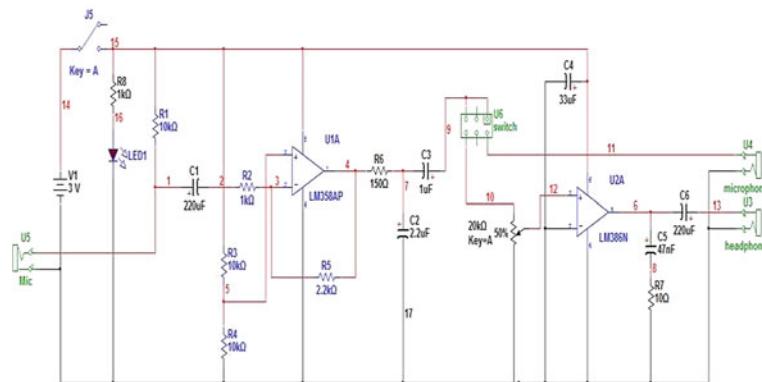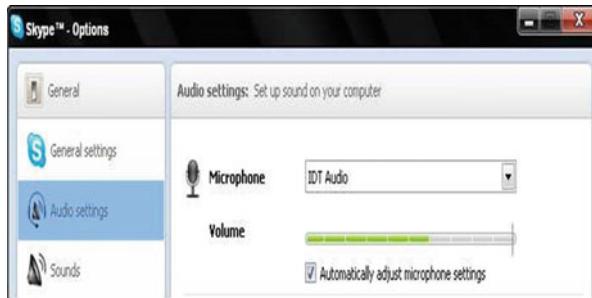
4.3 Final Implementation

See Fig. 3.

5 Results

5.1 Figures and Findings

From Figs. 4 and 5 we can clearly see that without the chest piece being placed on the chest, only gives some background voice with a very low negligible magnitude as the air

Fig. 3 Circuit diagram

Fig. 5 Chest piece placed on chest

Fig. 4 Chest piece without placing on chest

continuously strikes on the diaphragm. However, as we place it on the chest it ultimately gives a clear heart sounds with good magnitude.

Similarly, as shown in Figs. 6 and 7, It clearly shows that when the chest piece is free and not being placed on the chest, it only passes the signal of negligible magnitude which is caused due to continuous air pressure on the diaphragm of the chest piece whereas as in figure, when the chest piece is placed on the chest gives the heart signals that are smooth and optimal. The software is then able to apply various operations as per need for further analysis of the patient's heart signals.

5.2 Basic Algorithms/Software Coding Information

We have used free open source software "Audacity" for recording and editing sounds.

5.3 Calculations

5.3.1 Filter Calculation

Low Pass Filter

$$Fc = 1/2\pi RC \tag{1}$$

Let, Fc = 500 Hz and R = 150 Ω
So, C = 1/(2 * π * Fc * R)
C = 1/(2 * 500 Hz * 150 Ω)
C = 2.12 uf
C = Approx. 2.2 uf (standard value)

5.3.2 Gain Calculation

Preamplifier Gain

$$Av = 1 + Rf/Ri \tag{2}$$

Rf = R_5 = 2.2 kΩ and Ri = R2 = 1 kΩ
So,
Av = 1+R_5/R_2 = 1 + (2.2 kΩ)/(1 kΩ) = 3.2 which is approximated to 3.

Power Amplifier Gain
Av = 20 (set by leaving pin 1, 8 and 7 open)

Fig. 6 Audacity recording without placing chest piece on chest
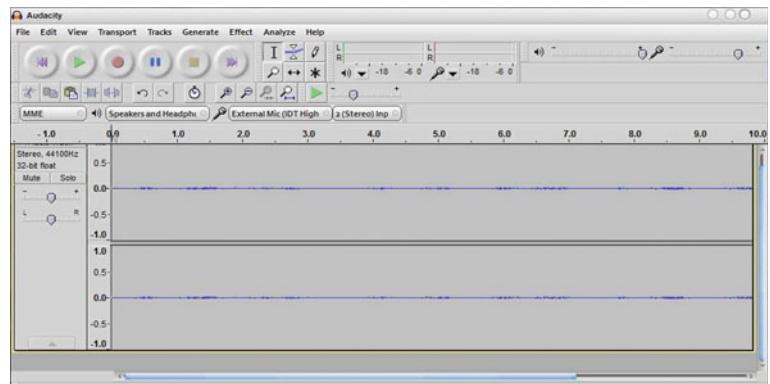
Fig. 7 Audacity recording with chest piece placed on chest

6 Discussion

6.1 Old Studies/Work Related to Project

There have been numerous studies on Tele-stethoscope since few decades and enormous developments have been made. The two studies from which we have taken the references to our project have enlightened us. Old studies have shown to get a graphical output of the heart sound through a source free software i.e. SONY which filters out the signals up till 100 Hz. They have designed their circuitry with the help of transistors and other filters. The circuit operates at a voltage of 1.5 V. Their main purpose was to record the graphical studies of the heart sound for further analysis by medics. They have also tried the usage of SKYPE for live transmission with hundreds of recordings for testing [6].

Other studies have shown that they initially recorded the signals into a microcontroller based storage device and then transferred the recorded data into the computer. They did this for recording purpose. They used Op-amps for amplification and buffers for isolation.

So far till now, there has only been some work done in the Bio-medical department of SSUET regarding digital stethoscope. Their designed digital stethoscope prototype circuitry was much more complex and took a very large

space for the setup and thus could not be used as a portable device. Moreover, they did not even interface it with the computer. Their main focus was to record the signals into the microcontroller based storage device.

We have reviewed all the past contributions and references which were dedicated to that project and designed our very own Stethoscope with a much more integrated and easy circuitry making it occupy a very small space and can be used portably like traditional stethoscopes. It can also be used to interface directly with the computer through a soundcard's 'mic in' jack without the need of any storage device to record the signals. We have tested this device to work exceptionally well and smoothly over SKYPE for live transmission as well, which has never been done before within SSUET. As shown in Figs. 4 and 5, we've also recorded the filtered heart signals through the source free software "AUDACITY" for further studies of heart sound by the medics.

6.2 Suggested Improvements for Future

There are other various op-amps that can be used in this circuit as preamplifier which gives fine output; however, the LM358 is very inexpensive.

In future development, the first thing that needs to be considered is noise reduction. One option would be the

LM1984 which is called the Dynamic Noise Reduction System; unfortunately, our time constraint did not allow us to implement this stage. Therefore, the signal from this stage travels to the amplifier stage.

If low pass (0.5 kHz) and band pass (0.2–1 kHz) filters can be used separately, we can get clear heart as well as respiratory lungs sounds.

7 Conclusion

The design of our tele-stethoscope consists of two major sections; the analog and the other computer interface. Electret Condenser microphone was used in the project. This microphone has attributes to detect cardiac sounds but was effective to surrounding noise. Another option was piezo-electric microphone which could have easily used and better option to get cardiac sounds but the size and ergonomics was not up to our preference as we have to fit it into chest piece.

The prototype Tele-stethoscope analog circuit comprised of a headphone, pre-amp, post-amp, low pass filter and switch. The pre-amp and amplifier increased the voltage to levels that could drive the headphone. A low pass filter was then used to limit signals frequency to 20–500 Hz.

The filter is then connected to a switch. Switch allows us to either connect the circuit to a PC interface through Sound card or to the headphone. Open source "Audacity" software is used to record the desired cardiac sounds. The Skype messenger is then used to transmit sound signals from one laptop to another. Skype is world renowned voice call messenger and known for his high quality audio transmission.

Results show that the signal is transmitting very clearly and shapely on Skype to Skype conferencing.

References

1. K. Hameed, F. Azhar, I. Shahrukh, M. Muzammil, M. Aamair and D. Mujeeb (2010) "Telemetric Epilepsy Monitoring and Seizures Aid", Springer, IFBME Pro- ceeding Volume 32, 278–281.
2. M. Zeeshan-Ul-Haque*, I. Shahrukh Ateeq, S. Manazir Hussain, Murtaza Halai, M. Faraz Shaikh, Kamran Hameed (2009) "Real Time Monitoring and Analysis of Non Invasive Blood Pressure using Lab Windows/CVI 8.0", Northeast American Society of Engineering Education Conference ASEE, University of Bridge-port, USA.
3. Ijlal Shahrukh Ateeq, Kamran Hameed, Muzammil Khan, Junaid Khalid and Muhammad Ali," PROPOSED IMPLEMENTABLE MODEL OF COMPUTER INTERFACED ELECTROCARDIO-GRAM (ECG) MODULE", *Springer, IFMBE Proceedings, Volume 40, 2013, pp 229–232.*
4. Abbruscato, Richard C. (Burnsville, MN), "Remote stethoscope signal processing system," United States Patent 5550902, 08-27-1996.
5. Projects Unlimited Inc., "Electret Condenser Microphone Basics," [Online]. Available: http://www.digikey.com/Web%20Export/Supplier%20Content/PUI_668/PDF/PUI_ElectretCon denserMicro-phone%20Basics.pdf.
6. F L Hedayioglyu et al. "Development of a Tele-stethoscope and its application in pediatric cardiology," in Indian Journal Exp Biology, Vol. 45, pp. 86–92, Jan 2007.

Impedance Spectroscopy Method to Detect Pelvic Floor Muscle Damage—A Feasibility Study

Marcel Młyńczak⬤, Katarzyna Borycka-Kiciak⬤, Małgorzata Uchman-Musielak⬤, and Adam Dziki⬤

Abstract

Impairment of the pelvic floor muscles and fecal incontinence affect 5–10% of the adult populations of European states. The most common cause is perinatal obstetrical anal sphincter injury (OASI) resulting from vaginal delivery. There is no method for screening in the period immediately after delivery. Diagnosis is limited to physical examination. The gold standard, transanal ultrasonography and manometry, can be performed after a few weeks, whereas clinical practice requires that injury be detected as early as possible for optimal treatment. Therefore, we would like to validate an alternative technique, impedance spectroscopy. The aim of the study is to analyze the accuracy of problem detection within the 3–1000 kHz frequency range in 3 radial positions. 22 females (10 issued and 12 included in a control group) were engaged. Impedance moduli and phase shifts were estimated using a bipolar impedance spectrometer along with a specific anal probe. We calculated parameters assessing different subranges of analyzed frequencies and treated them as input vectors for detection. Accuracies were estimated for Naïve Bayes, Random Forest, Support Vector Machine and Quinlay's C5.0 models. We performed recursive feature elimination to find the most significant subranges of frequencies. An accuracy of 86.4% was observed for the Random Forest technique and entire set of considered parameters. It appears that impedance spectroscopy allows assessment of problems with pelvic floor muscle (particularly OASI), directly after vaginal delivery and faster and easier than gold standard methods.

1 Introduction

Fecal incontinence is a clinical symptom of insufficiency of the closing mechanism of the anus [1, 2]. The problem of anal sphincter insufficiency affects about 5–10% of the adult population of European states [1, 3, 4]. The most frequent cause is perinatal damage to the pelvic floor muscles. Symptoms of sphincter damage (with different degrees) are observed in 13–25% subjects after vaginal delivery. Resulting fecal incontinence signs may appear immediately, but they can also develop gradually with age and exacerbate after menopause [5, 6].

The most common type of perinatal damage is partial injury of the external anal sphincter, usually undetected during labor and often asymptomatic. In endosonographic examinations, lesions of one or both anal sphincters are detected following 35% of first deliveries and 44% of later ones.

The basic prevention technique is the controlled episiotomy. The decision is based mainly on the intuition and experience of a doctor, or results from the rules adopted in a given region. However, after the intervention, further damage may occur—the incision line may expand. Therefore, the value of such procedure is controversial. No associated reduction in the risk of gas and stool incontinence has been

M. Młyńczak (✉)
Faculty of Mechatronics, Institute of Metrology and Biomedical Engineering, Warsaw University of Technology, Warsaw, Poland
e-mail: mlynczak@mchtr.pw.edu.pl

K. Borycka-Kiciak
Department of General, Oncological and Gastrointestinal Surgery, Orlowski Hospital, Centre of Postgraduate Medical Education, Warsaw, Poland

M. Uchman-Musielak
Department of Obstetrics and Gynecology, Solec Hospital, Warsaw, Poland

A. Dziki
Department of General and Colorectal Surgery, Medical University of Łódź, Łódź, Poland

demonstrated [7]. A study on pelvic floor muscle dysfunction observed four years after delivery also confirmed that routine episiotomy does not protect against symptoms of fecal incontinence [8].

Available diagnostics (imaging—transrectal ultrasonography, MRI or defecography—or functional examination—manometry) are limited, in terms of both time (they cannot be performed until a few weeks after delivery) and availability (they require specialized equipment and, especially, highly qualified staff to interpret results). Sometimes both types of diagnostics should be performed.

Therefore, new diagnostic methods are sought. One proposal is to register electrical impedance, particularly its module and phase shift, in a specific part of the pelvic floor muscles, using a special probe—impedance spectroscopy.

The aim of the study is to analyze the accuracy of problem detection within the chosen frequency range (3–1000 kHz) in 3 radial positions.

2 Materials and Methods

A group of 22 females (10 issued, with detected sphincter damage, aged 30.9 ± 3.7; 12 healthy, included in a control group, aged 40.8 ± 11.0; 36.3 ± 9.8 overall, all ages expressed as mean $\pm$ standard deviation) was engaged. All were informed about the aim of the study and signed forms indicating informed consent. The study was accepted by the Bioethics Commission of the Medical Chamber in Warsaw (KB/977/15).

All participants were first examined and assigned to a group (issued or control). Then, the main registrations were carried out by placing a special anal probe (Periprobe RU/AAnalis, manufactured by BeacMed, Italy, commonly used for electrostimulation and biofeedback applications) in the anal canal. 2 gold electrodes were positioned on opposite sides. We tested 3 radial positions:

- along the main axis (front-to-back),
- with a 60-degree shift to the right in relation to the main axis, and
- with a 60-degree shift to the left in relation to the main axis.

Bioimpedance was measured using an Impedimed SFB7 spectrometer (developed by Impedimed, Australia QLD), which enables measurement of resistance and reactance in the frequency range of 3–1000 kHz (256 points, unevenly distributed) using the current method (injecting current to the tissue and measuring the modulated voltage signal).

From resistance and reactance, one can calculate impedance moduli and phase shifts, which were used during the analysis. The SFB7 is designed to operate with a tetrapolar

electrode configuration, but the anal probe had only 2 electrode contacts. We therefore used the bipolar technique, connecting two pairs of electrodes (with single application and receiving channel in each pair). Finally, from each participant, we acquired 3 impedance modulus curves for the 3 radial positions, and the corresponding 3 phase-shift curves.

We calculated the set of input parameters by averaging the values of impedance moduli and phase shifts (for all radial positions) within 8 frequency subranges (equal in terms of logarithmic transformation of frequency range):

- 3.0–6.2 kHz (31 points)
- 6.2–12.8 kHz (32 points)
- 12.8–25.6 kHz (31 points)
- 25.6–54.8 kHz (34 points)
- 54.8–113.2 kHz (31 points)
- 113.2–234.0 kHz (33 points)
- 234.0–483.8 kHz (32 points)
- 483.8–1000.0 kHz (32 points)

Therefore, for each subject, we had 48 parameters, and treated them as input vectors for problem detection. Several classification methods were taken into account (tuning parameters determined experimentally):

- Naïve Bayes algorithm (NB),
- Support Vector Machines (SVM; with linear kernel),
- Random Forests (RF; with 300 trees), and
- Classification tree model using Quinlan's C5.0 algorithm (C5.0; 10 trials).

For each case, we divided the data into 2 subsets, training (50%) and testing (50%). 10-fold cross-validation was assumed. Accuracy, sensitivity and specificity were calculated; we estimated them for 2 conditions, considering:

- the entire set of 48 parameters, and
- the "optimal" set, the set obtained with the objective recursive feature elimination (RFE) method.

All calculations and analyses were performed in R.

3 Results

The curves of impedance moduli and phase shifts, obtained for all participants, are presented in Fig. 1 (left and right), for the main radial position, and Fig. 2 (left and right), with a 60-degree shift to the right in relation to the main axis. Groups were distinguished by marker color and shape.

Visual inspection of the data showed that the main differences can be seen in the whole frequency range for
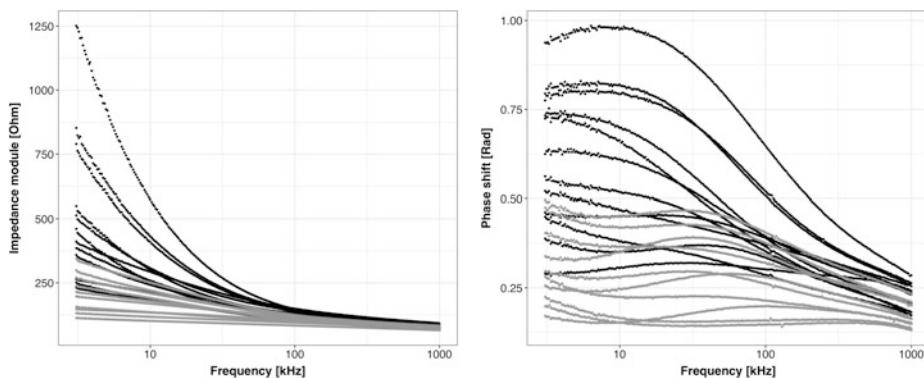
Fig. 1 Left—the graph of impedance moduli across the considered frequencies. Right—the corresponding graph of phase shifts. Both were calculated for the main radial position. Black circles correspond to control group, grey triangles to issued one
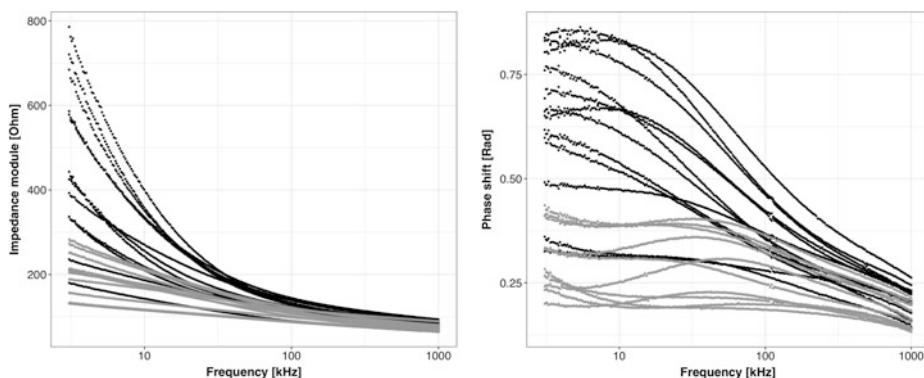
Fig. 2 Left—the graph of impedance moduli across the considered frequencies. Right—the graph of the corresponding phase shifts. Both were calculated for the position with a 60-degree shift to the right in relation to the main axis. Black circles correspond to control group, and grey triangles to issued one

impedance moduli and for smaller frequencies for phase shifts. This was confirmed with objective testing using the RFE method. Therefore, as a reduced set of parameters, we chose the 3–234 kHz range for impedance moduli and 3–54.8 kHz for phase shifts.

Table 1 summarizes the accuracies obtained for all the considered classification techniques and for the full and reduced (RFE-selected) sets of impedance parameters. The results are presented for comparison. The full set seems better in terms of all analyzed features. Overall, random forests provided the best accuracy. However, it is worth

noting that the C5.0 algorithm had the highest sensitivity (about 83%).

4 Discussion and Conclusions

Clinicians face a lack of screening methods that can be used to detect pelvic floor muscles just after delivery. Transanal ultrasonography and manometry may be performed after a few weeks and manual examination seems limited in terms of quantitative and reproducible inference. On the other

Table 1 The summary of the accuracies obtained for all considered classification methods for the full and reduced sets of impedance parameters; abbreviations: Acc.—accuracy, Sens.—sensitivity, Spec.—specificity

Classification technique	Full			Reduced		
	Acc. (%)	Sens. (%)	Spec. (%)	Acc. (%)	Sens. (%)	Spec. (%)
NB	85.5	80.0	92.0	**82.7**	75.0	**92.0**
RF	**86.4**	80.0	**94.0**	80.9	73.3	90.0
SVM	77.3	66.7	90.0	74.5	68.3	82.0
C5.0	85.5	**83.3**	88.0	**82.7**	**80.0**	86.0

hand, diagnostic and therapeutic algorithms are constantly modified [1, 3, 4, 7].

The treatment depends particularly on the speed with which damage is detected. Simple surgical sphincter stapling is possible only up to 24 h from the injury (later reconstruction is done after a few months and using the loop stoma). Moreover, even if the damage consists only of the sphincter and/or neurogenic injury, rehabilitation should be started in the first days after delivery.

The main problem is that few of these injuries (only about 20%) are detected in the early post-delivery period. That is why few patients are referred for further, more specialized diagnostics. Our aim is to deliver a method that allows not only increased clinical symptoms, but also simple, non-invasive examination that almost anyone can perform. From that, we assumed that both anatomical and physiological (functional) information, can be revealed in electrical bioimpedance when considering a wide frequency range. Impedance spectroscopy has been used in many similar applications, e.g., the detection of interstitial cancers of the cervix, colon cancer, bladder pathology, or neuromuscular diseases [9–12].

An impedance spectroscopy method with a specific anal probe was used to preliminarily evaluate the possibility of using impedance-related information and to check the reliability with which participants exhibiting the condition could be distinguished from the healthy control group. Relatively high accuracy (above 85% for 3 different methods, cross-validated) was observed, despite the use of bipolar impedance measurement and a simple set of parameters. This allows us to state that the proposed method seems to enable assessment of problems with pelvic floor muscle (particularly OASI) directly after vaginal delivery and faster and easier than gold standard methods.

There are several limitations. Only 22 participants were tested, each only once and only with a very simple probe, which forced the use of the bipolar technique. The "issued" group represents a range of conditions rather than a specific problem.

We will continue analyses in this field, with tetrapolar electrode configuration provided by a target anal probe (compatible with patent application WO 216/190763 A1), more sophisticated impedance-related parameters, more states and diseases to recognize, and reproducibility and progress analyses. Moreover, we plan to determine what affects the level of impedance modulus and phase shift in the presented application and to what extent.

Conflict of Interest The authors declare that they have no conflict of interest.

References

1. Nelson, R., Norton, N., Cautley, E., Furner, S.: Community-based prevalence of anal incontinence. JAMA 274, 559–561 (1995).
2. Mavrantonis, C., Wexner, S.D.: A clinical approach to fecal incontinence. J Clin Gastroenterol 27, 108–121 (1998).
3. Whitehead, W.E. et al.: Treatment options of fecal incontinence. Dis Colon Rectum 44, 131–144 (2001).
4. Norton, N.: Advancing the Treatment of Fecal and Urinary Incontinence Through Research: trial design, outcome measures and research priorities. Milwaukee, USA (2002).
5. Abramowitz, L. et al.: Are sphincter defects the cause of anal incontinence after vaginal delivery? Results of a prospective study. Dis Colon Rectum 43, 590–596 (2000).
6. McArthur, C. et al.: Obstetric practice and fecal incontinence 3 months after delivery. Br J Obstet Gynecol 108, 6798–683 (2001).
7. Hartmann, K. et al.: Outcomes of routine episiotomy. A systematic review. JAMA, 293(17), 2141–2148 (2005).
8. Fritel, X. et al.: Plevic floor disorders 4 years after first delivery: a comparative study of restrictive versus systematic episiotomy. BJOG 115(2), 247–252 (2007).
9. Miranda, D. A. et al.: Early Detection of Cervical Intraepitelial Neoplasia in a Heterogeneos Group of Colombian Women Using Electrical Impedance Spectroscopy and the Miranda-López Algorithm. J Phys Conf Ser 407, 012010 (2012).
10. Pathiraja, A., Ziprin, P., Shiraz, A., Mirnezami, R., Tizzard, A., Brown, B., Demosthenous, A., Bayford, R.: Detecting colorectal cancer using electrical impedance spectroscopy: an ex vivo feasibility study. Physiol Meas 38, 1278–1288 (2017).
11. Keshtkar, A. et al.: Electrical impedance spectroscopy and the diagnosis of bladder pathology. Physiol Meas 27, 585 (2006).
12. Rutkove, S.B., Aaron, R., Shiffman, C.A.: Localized bioimpedance analysis in the evaluation of neuromuscular disease. Muscle & nerve 25(3), 390–397 (2002).

Behavior of Electrical Resistance in Gastrocnemius Muscle of Rats During Contractions with Different Intensities

A. B. B. Coutinho, J. P. Wereneck-de-Castro, A. V. Pino, and M. N. Souza

Abstract

Changes in skeletal muscle electrical resistance during muscle contraction may be associated to two main factors. Changes at muscle morphology e.g. length, volume or cross-sectional area; and changes in its impeditivity, related to changes of biochemical and physiological processes during muscle activity. However, the mechanisms by both morphological or metabolic parameters and, more importantly, if they increase or decrease electrical impedance parameters is yet controversial. The present study aimed to investigate the behavior of the muscular electrical resistance of the gastrocnemius muscle of Wistar rats during muscle contraction at different levels of force. To address that, tetrapolar invasive needle electrodes were placed in the animal muscle for impedance measurement, while two other needles electrodes were placed on muscle ends to electrical stimulate the muscle and evoke contraction. The experimental protocol consisted of ten pulse trains with 1 s duration with 40 s rest using randomized frequencies. All the procedures were approved by the Institutional Ethics Committee for Research with Animals under the decision number 019/15. Results show a decrease on muscle resistance during contraction. It was observed a correlation of $r = -0.76$ between the intensity of muscle contraction and resistance changes. Our findings suggest that resistance decrease is expected for invasive measurements in healthy muscles. Also, indicates that different changes at resistance amplitudes can be linked with metabolic processes. However, morphological influences cannot be neglected.

Keywords

Muscle contraction • Electrical resistance • Muscle impedance

1 Introduction

Skeletal muscle electrical resistance is related to changes in muscles' morphological and metabolic features and both vary during a muscle contraction/activation [1]. Examples of morphological parameters are muscle length, cross sectional area and volume [1]; while changes in muscle biochemistry are associated with energy pathways, e.g. phosphocreatine system, cytoplasmic glycolysis, and mitochondrial tricarboxylic acid cycle, which may affect directly the muscle impeditivity [1, 2].

Even the studies reporting that both above-mentioned features contribute for changes on electrical impedance, they did not discuss deeply how these features may influence the muscle impedance. Also, there is contradiction in literature about the direction of muscle impedance changes during contraction, i.e., some studies point out increases [1, 3, 4], while other ones decreases [2, 5, 6] on electrical impedance signal. However, it must be mentioned that those works did not assess the same muscles; thus, effects as anisotropy and muscle geometry could be influenced the results in different manner. Moreover, many differences on such studied must be considered, i.e.; measurements techniques (multifrequency [5], monofrequency [1, 2], time domain [3]); electrode arrays (bipolar [4] or tetrapolar arrangement [2, 3]); data collected in humans [1, 2, 5] or animals [3, 6]; differences in experimental protocols; among others factors. Considering all together, it is difficult currently to affirm which is the expected behavior for the muscular electrical resistance during a muscle contraction.

The present study aimed to define the behavior of one electrical impedance component, i.e. the resistance, of the gastrocnemius muscle of Wistar rats during muscle

A. B. B. Coutinho (✉) · A. V. Pino · M. N. Souza
Biomedical Engineering Program, Universidade Federal do Rio de Janeiro, COPPE, Rio de Janeiro, Brazil
e-mail: andrebrand1@hotmail.com

J. P. Wereneck-de-Castro
Exercise Biology Laboratory, Universidade Federal do Rio de Janeiro, Rio de Janeiro, Brazil

contraction at different levels of force, using a tetrapolar electrode arrangement with monofrequency sinusoidal excitation, and the muscles contractions evoked by means of neuromuscular electrical stimulation.

2 Methods

2.1 Sample

The experiments were realized in nineteen male wistar rats, weighting between 250 and 400 g, and aging between 2 and 4 months. The animals were exposed to a 12 h light-dark cycle and were feed ad libitum. Because it is an in vivo experiment, the rats were kept anesthetized with 3% isoflurane throughout the experimental procedure and the surgical procedure, which consisted on gastrocnemius expose. The experimental protocol was submitted and approved by the Institutional Ethics Committee for Research with Animals under the number 019/15.

2.2 Instrumentation

Electrode Placement. To measure bioimpedance signal, four needles electrodes were placed in the rat gastrocnemius belly transversally to the muscle shortening direction. The needles, made of stainless steel, were equally and fixed spaced with 0.8 cm distance between the first and the forth needle and fixed on an insulated material. Two others stainless steel needles were fixed in muscle ends (proximal and distal) and used for electrical stimulation. Figure 1

illustrates, on a simple way, the electrodes placements on rat gastrocnemius (top and side view).

Devices. For force (F) data acquisition we used a calibrated load cell (MLB 50, HMB, USA) and a signal conditioning system specially developed for this purpose with a sensitivity of 379 mV/N. This system provides a DC signal proportional to the force applied to the load cell, which was attached to the gastrocnemius tendon by an inextensible fine cord. To perform the electrical stimulation, we used a buffer amplifier connected to one of the D/A outputs of a NI6252 board (National Instruments, USA) updated at a rate of 2.86 Ms/s and controlled by a LABView software specially developed for this purpose. The system is capable to generate a -2.5 to 2.5 V biphasic voltage square waveform, with minimum pulse width of 500 µs and the longest duty cycle of 2 s. These characteristics are enough to provide the electrical stimulus needed in this work. For impedance measurements, a prototype developed on our laboratory was used to measure resistance in real time. This prototype is basically a single frequency system (50 kHz) with a 1 mA amplitude current sinusoidal excitation. Figure 2 shows a block diagram of such system where one can see that the resistance signal is obtained at the output of a quadrature demodulator that receives as reference signals a square wave in-phase with current excitation signal. Thus, such output is a DC signal proportional to resistance, that was calibrated for the range of resistances between 0 and 300 Ω.

The resistance signal (R), electrical stimulation pulses and load cell signal were sampled and digitalized with rate of 4 kS/s by NI 6009 data acquisition board (National Instruments, USA). The communication between board and computer was via USB interface and a LabVIEW (National
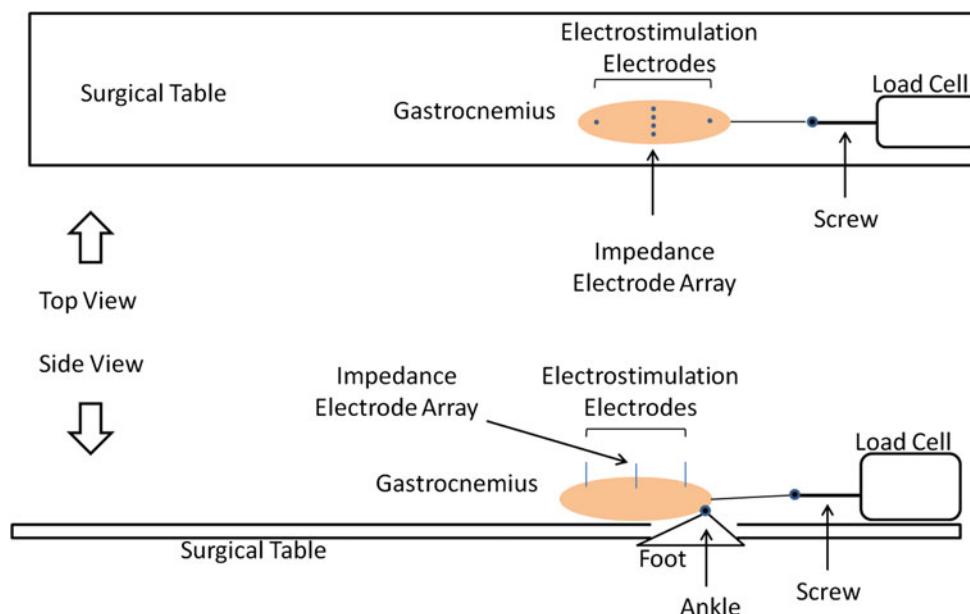
Fig. 1 Simplified schematic of sensors placement on rat's gastrocnemius muscle
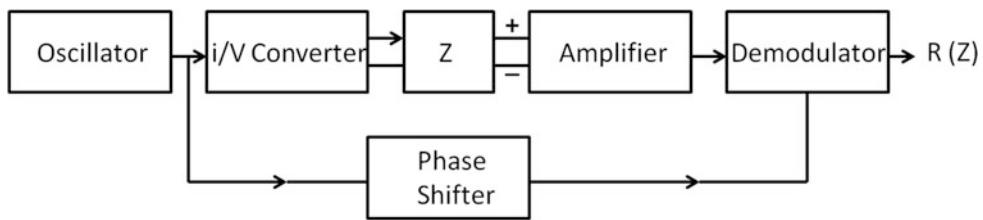
Fig. 2 Block diagram of impedance measurement system

Table 1 Electrical stimulation parameters used on experimental protocol

Pulse duration	Frequencies	Pulse train duration	Pulse train interval
500 μs	2, 10, 20, 30, 40, 50, 60, 75, 100, 150	1 s	40 s

Instruments, USA) program was designed to data acquisition and data visualization in real-time.

2.3 Experimental Protocol

Frequency × Force ($f \times F$) curve for each rat was provide through neuromuscular electrical stimulation based on a previous study [7]. The electrical stimulation parameters can be seen at Table 1.

Briefly, ten pulse trains were applied on gastrocnemius muscle during 1 s with 40-s rest between each stimulus. The frequency of each pulse train was randomized (see frequencies on Table 1). R, and F signals were acquired and recorded during all experiment.

2.4 Analysis and Data Processing

R signal passed through a low-pass filter (Butterworth, second order) with 30 Hz cutoff frequency to remove high frequency interferences. Considering the impedance baseline normally varies along the experiment, a high-pass filter (Butterworth, second order) with 0.01 Hz cutoff frequency was also applied to the resistance data. Peak of R and F, during pulse train stimulation were determined and the variations of R, and F were calculated as a difference between the peaks and baseline as Eq. 1 shows.

$$\Delta S = S_p - S_b \qquad (1)$$

where, ΔS is the variation of the signal, S_p is the signal peak and S_b is signal baseline. For instance, S can be F or R.

As each animal has its range of force and resistance, the processed data were normalized by the highest value of variation modulus ($|\Delta S_{max}|$) and them multiplied per 100%. Then, all the results are values relative to $|\Delta S_{max}|$ ranging between 0 and 100%. See Eq. 2.

$$\Delta S_{rel} = \frac{\Delta S}{|\Delta S_{max}|} \times 100\% \qquad (2)$$

where, ΔS_{rel} is the variation of signal relative to maximum variation, ΔS is the variation of the signal and $|\Delta S_{max}|$ is the magnitude of the maximum signal variation.

Box plots were used to analysis ΔS and ΔS_{rel} as a function of frequencies; and a scatter plot was used to analysis ΔF_{rel} and ΔR_{rel}. The linear correlation of Pearson and a linear regression were calculated to assess correlations between ΔF_{rel} and ΔR_{rel}. The signals processing were made in MATLAB R2017a (Mathworks, USA) and statistical analysis through R 2.13.

3 Results

The results show an increase in the muscle strength related to frequencies increase (Fig. 3), as expected. Then, the used electrical stimulation protocol was able to improve different intensities of muscular contraction. The peaks of the R signal presented an opposite behavior of F, i.e., a decrease as frequencies increase (Fig. 3, right). After normalization the ΔR_{rel} data was at the same range for every animal and seemed to be more informative than ΔR (Fig. 4, left). The scatter plot of ΔR_{rel} versus ΔF_{rel} (Fig. 4, right) shows the negative tendency between variables and a Pearson coefficient $r = -0.76$.

4 Discussion

The electrical stimulation technique allowed muscle contraction at different intensities (Fig. 3 left), showing that frequencies 60–75 Hz were associated to the maximum tetanic force.

Our study analyzed the muscular electrical resistance with a single frequency of 50 kHz, which is the most used
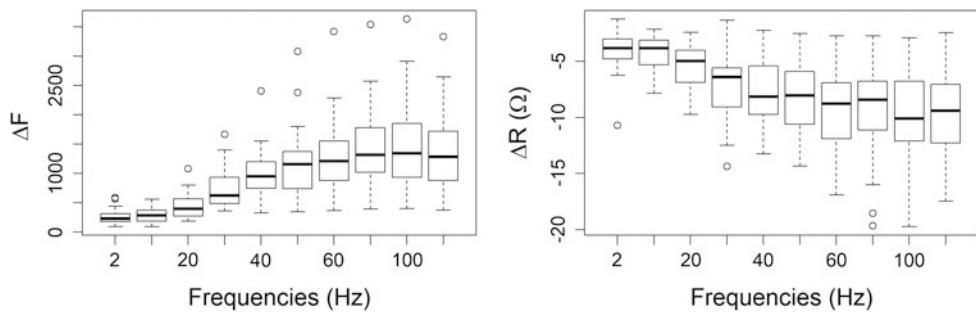
Fig. 3 Boxplot of force changes (left) and resistance changes (right) as function of frequencies
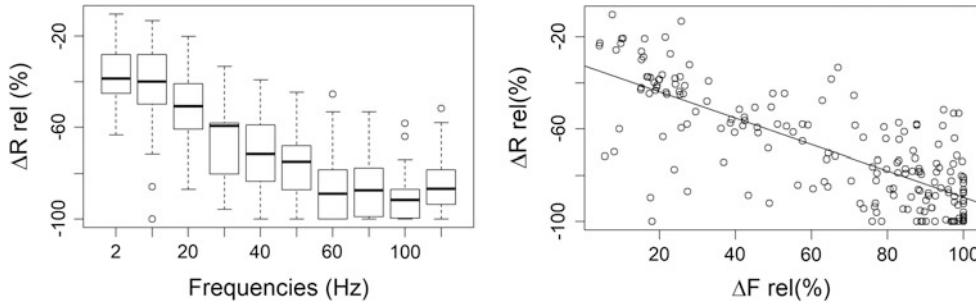
Fig. 4 Boxplot of percentile changes of resistance as function of frequencies (left) and scatter plot between percentile changes of resistance and percentile changes of force (right)

frequency at literature [2], despite some works have used multifrequency [5] or spectroscopy [3] devices.

The used experimental protocol measured electrical resistance directly in the healthy muscle, avoiding external influences, e.g., connective tissue and skin-fat layer, enabling a more reliable study of muscle passive electrical features. However, some factors cannot to be avoided in a live animal, as blood perfusion, and bone.

Results showed a strong negative correlation between electrical resistance and muscle strength changes (Fig. 4 right), corroborating some previous studies [2, 5, 6] and against with other ones [1, 3, 4]. When muscle contracts, its length decrease and its cross sectional area increases, both events induce resistance decrease of any conductor volume [8]. Then, the resistance decrease was expected due changes at muscles morphology. However, morphology changes are not proportional to muscle intensities. From around 30% of maximum muscle strength the muscle morphology is basically the same [9]. So, it indicates that resistance changes were also influenced by contraction intensity, which refers to

biochemical and physiological aspects. Corroborating this hypothesis, the correlation between force and resistance changes was $r = -0.76$.

5 Conclusion

Our findings show a decrease in muscular electrical resistance, and this behavior seems to be reproducible if the measurement is performed directly at healthy muscle. Factors as, different tissues, surface measurement and muscle healthy may interfere on electrical resistance patterns. We also, conclude that morphological changes during muscle contraction exert high influence on impedance changes, but they not linked directly with various amplitude changes of resistance. Intensity of muscular contraction, in other words, biochemical features seems to be directly related with resistance amplitude changes. But which biochemical mechanism may explain the resistance change still need to be studied.

Conflict of Interests The authors declare that they have no conflict of interest.

References

1. Shiffman CA, Aaron R, Rutkove SB. Electrical impedance of muscle during isometric contraction. Physiol Meas. 2003 Feb;24 (1):213–34.
2. Rutkove SB. Electrical impedance myography: Background, current state, and future directions. Muscle Nerve. 2009 Dec;40(6):936–46.
3. Sanchez B, Li J, Geisbush T, Bragos R, Rutkove S. Impedance alterations in healthy and diseased mice during electrically-induced muscle contraction. IEEE Trans Biomed Eng. 2014 Apr 24.
4. Liao TJ, Nishikawa H. The variation of action potential and impedance in human skeletal muscle during voluntary contraction. Tohoku J Exp Med. 1994 Jul;173(3):303–9.
5. Zagar T, Krizaj D. Multivariate analysis of electrical impedance spectra for relaxed and contracted skeletal muscle. Physiol Meas. 2008 Jun;29(6):S365–372.
6. Li J, Yim S, Pacheck A, Sanchez B, Rutkove SB. Electrical Impedance Myography to Detect the Effects of Electrical Muscle Stimulation in Wild Type and Mdx Mice. PLoS ONE. 2016;11(3): e0151415.
7. Mrówczyński W, Celichowski J, Krutki P, Cabaj A, Slawińska U, Majczyński H. Changes of the force-frequency relationship in the rat medial gastrocnemius muscle after total transection and hemi-section of the spinal cord. J Neurophysiol. 2011 Jun;105(6):2943–50.
8. Grimnes S, Martinsen ØG. Bioimpedance and bioelectricity basics. London: Academic; 2008.
9. Hodges PW, Pengel LHM, Herbert RD, Gandevia SC. Measurement of muscle contraction with ultrasound imaging. Muscle Nerve. 2003 Jun;27(6):682–92.

Personalization of the Oscillometric Blood-Pressure Measurement

P. Nagy and Á. Jobbágy

Abstract

Oscillometric blood-pressure (BP) measurement can result in substantial error depending on the physiological parameters of the tested person. Especially the rigidity of the arteries can influence the oscillometric amplitudes. Personalization can greatly improve the accuracy and reproducibility of the measurement. The personalization process requires several measurements taken from a person applying special cuff pressure (CP)—time functions. A BP measuring device was developed to generate different CP—time functions. It is able to sustain the CP at a constant value during both inflation and deflation. The device also measures ECG in Einthoven I lead and photoplethysmographic (PPG) signal at the fingertip. This makes possible to calculate the pulse wave transit time (PWTT). The sampling frequency is 1 ksample/s thus PWTT values are calculated with 1 ms resolution. Recordings were taken from ten healthy subjects, both senior and young ones. The deflation was stopped and the CP was held constant at 90 mmHg and then at 60 mmHg for 60 s each. The subjects were at rest. Pulse wave transit times were determined from the heart to the cuff (PWTTHC) and to the fingertip (PWTTHF). Mean value as well as the trend of change of PWTTHC and PWTTHF over the 60 s intervals with constant CP are person specific, not age-group specific. The change in PPG signal amplitude resulting from cuff occlusion was found to be substantially smaller for senior than for young persons. As a result of the personalization it is possible to define a specific CP—time function providing information not only on actual BP but also on the rigidity of the brachial artery. The recordings taken with constant CP parts help also compensate the effect of breathing.

1 Introduction

High BP is a major cardiovascular risk factor. Undetected high BP can lead to heart attack, stroke, and renal disease. Accurate BP measurement is essential for optimal diagnosis and treatment of hypertension [1]. Oscillometric BP measurement is a widely used technique to determine systolic and diastolic BP. The method basically estimates the mean arterial pressure, systolic and diastolic pressure are calculated. Arterial stiffness can have great impact on the accuracy of the calculated values, thus reliability of the method is questionable for those with cardiovascular diseases [2]. Oscillometric BP measurement is based on fast inflation and slow deflation of the cuff, typically placed on the left upper arm [3]. Influence of physiological factors can be reduced and accuracy of oscillometric BP measurement can be improved if the CP profile is personalized.

2 Materials and Methods

2.1 Pulse Wave Transit Time

A novel method for the examination of the state of the cardiovascular system is PWTT, which is the time while the pressure wave generated by the heart propagates from the aortic valve to a peripheral part of the body (typically the fingertip). Opening of the aortic valve is difficult the detect, therefore the R-peak in the ECG signal is usually used as start time for PWTT calculation. Arrival of the pulse wave to

P. Nagy (✉) · Á. Jobbágy
Department Measurement and Information Systems, Budapest University of Technology and Economics, Magyar Tudósok Krt. 2, Budapest, 1117, Hungary
e-mail: nagy@mit.bme.hu

Á. Jobbágy
e-mail: jobbagy@mit.bme.hu

a body part is typically detected by a photoplethysmographic sensor, placed onto the specific body part.

2.2 Measurement Method

Occlusion of the brachial artery during oscillometric BP measurement changes the diameter of the artery and the strain in the arterial wall. These changes can be considered as an excitation to which the cardiovascular system reacts [4]. We have defined a CP profile, which can help observe the reaction of the cardiovascular system to different kinds of excitation. A BP measuring device was developed to generate the defined CP—time function. The device is able to sustain the CP at a constant value during both inflation and deflation. It also measures ECG in Einthoven I lead and PPG signal at the fingertip, the sampling frequency is 1 ksample/s. In the first 24 s of the measurement, the cuff is not inflated, only ECG and PPG signals are recorded. After 24 s, inflation starts with approximately 6 mmHg/s speed, until 150 mmHg is reached. If 150 mmHg is reached, inflation stops and deflation starts immediately, approximately with the same speed as inflation. With constantly changing cuff pressure, the effect of the occlusion is difficult to be separated from the effect of changes in other physiological parameters influencing BP (e.g. stress level or respiration). Therefore, deflation is stopped at 90 mmHg for 1 min and at 60 mmHg for 1 min. It helps observe the reaction of the cardiovascular system to constant triggers. When 40 mmHg is reached during deflation, CP changes abruptly to 0 mmHg.

After complete deflation, ECG and PPG signals are recorded for further 24 s. This period can be compared to the first 24 s, before inflation started. After this 24 s long period following complete deflation, the measurement ends. Figure 1 shows the CP signal as a function of time during the measurement.
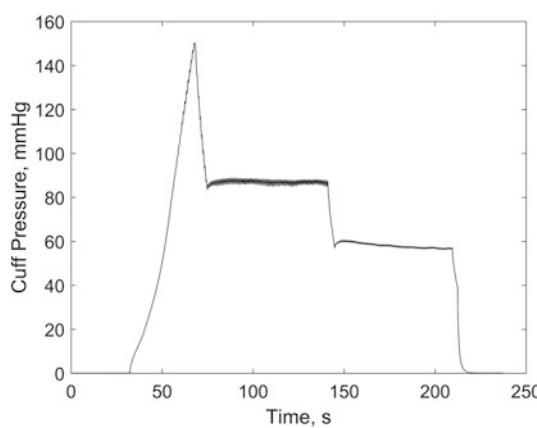
Fig. 1 Cuff pressure as a function of time during the measurement

2.3 Tested Persons

Ten healthy test subjects (6 male, 4 female) volunteered for the study, two seniors (age between 66 and 67 years), four middle aged persons (age between 39 and 57 years) and four young adults (age between 22 and 26 years).

2.4 Characterizing the Effect of Occlusion by PWTT

PWTT was calculated using ECG and PPG signals from the heart to the fingertip, therefore we denote it by PWTTHF. We calculated PWTTHF as the time difference between the R-peak in ECG and the local minimum in the PPG signal, corresponding to the same heart cycle. Using the CP signal, the time of the propagation of the pulse wave from the heart to the cuff can also be determined. Thus, PWTTHF can be cut into two parts, the propagation time from the heart to the cuff (PWTTHC) and from the cuff to the fingertip (PWTTCF) [5]. According to the model suggested by Forouzanfar et al. [6], PWTTHC has a maximum value near the diastolic pressure. According to our previous experiences, PWTTHF increases with increased CP, however, it can be calculated only until CP is lower than SBP. At higher CP values the brachial artery is completely occluded and pulsation in PPG at the fingertip ceases [7]. Mean value and standard deviation as well as the trend of change of PWTTHC and PWTTHF over the 60 s intervals with constant CP were calculated for the tested persons. To quantify the trend of change over the 60 s intervals, mean values of PWTTHC and PWTTHF were calculated. We denote mean PWTTHC value while CP equals 90 mmHg as *PWTTHC*_90 and the mean PWTTHC value while CP equals 60 mmHg as *PWTTHC*_60. Ratio of these mean values is denoted by *PWTTHC*_90_60 and defined in (1).

$$PWTTHC\_90\_60 = PWTTHC\_90/PWTTHC\_60 \quad (1)$$

Similarly, *PWTTHF*_90, *PWTTHF*_60 and *PWTTHF*_90_60 can be defined.

2.5 Characterizing the Effect of Occlusion by the PPG

In the past few years, the PPG signal has been used by several authors as a basis for cuffless BP estimation [8–11]. Most of these methods extract features of the PPG waveform (amplitude, phase, slope, upstroke time, etc.) to estimate BP. In the present study, we investigated the effect of CP changes on the amplitude and slope of the PPG signal. The PPG signal has a descending and an ascending part in
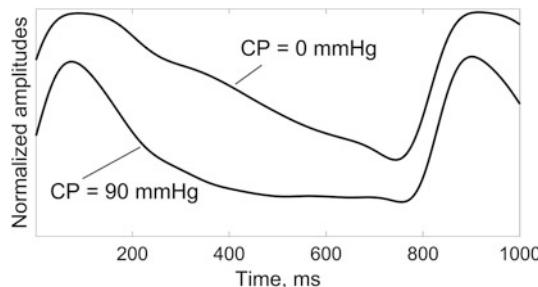
Fig. 2 Normalized PPG signals at the fingertip of a healthy middle aged female. CP = 90 mmHg has a low-pass filtering effect

each heart cycle. Average slope of both parts decreases with increasing CP as a result of decreased PPG amplitude. Shape of the PPG waveform also changes when CP increases, as illustrated in Fig. 2. We used the following approach to characterize the change of the PPG signal shape as a result of CP change: descending part of the PPG signal is cut into only two subparts at 50% of the descending time. Average slope of these two subparts is calculated and the ratio of the averages is used. We denote this ratio as RAS (Ratio of Average Slopes). RAS was calculated for each heart cycle, then the average of the parameter was calculated for heart cycles corresponding to CP = 90 mmHg and CP = 60 mmHg. We denote the calculated averaged RAS parameters as *RAS*_90 and *RAS*_60. Ratio of these parameters is denoted by *RAS*_90_60. It is defined in (2).

$$RAS\_90\_60 = RAS\_90/RAS\_60 \qquad (2)$$

CP decreasing from 90 to 60 mmHg induces increase in the PPG amplitude. The ratio of PPG amplitudes corresponding to different CP values contains information about vascular elasticity. Kuvin et al. [12] found that increase of blood flow rate during reactive hyperemia is impaired in patients with cardiac risk factors. Denoting the mean PPG amplitude while CP equals 90 mmHg as PPG_90 and mean PPG amplitude while CP equals 60 mmHg as PPG_60, ratio of these mean values was defined. The ratio was denoted by *PPG*_90_60 as defined in (3).

$$PPG\_90\_60 = PPG\_90/PPG\_60 \qquad (3)$$

3 Results

Mean value and the trend of change of PWTTHC and PWTTHF over the 60 s intervals with constant CP were found to be person specific, but not age-group specific.
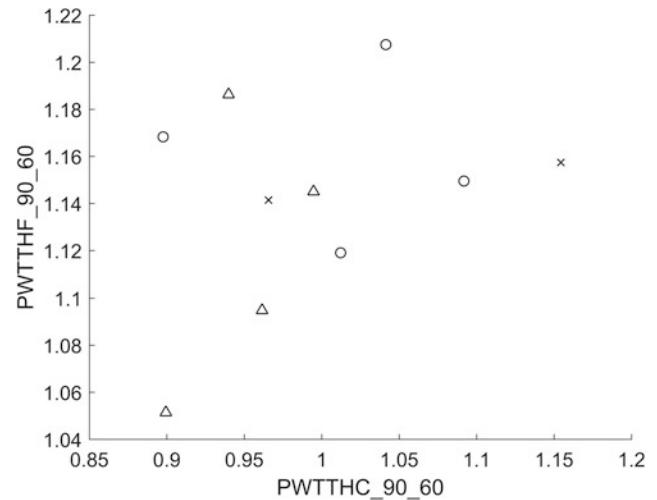
Fig. 3 *PWTTHC*_90_60 and *PWTTHF*_90_60 parameters for each tested person. x: healthy seniors, o: healthy middle aged persons, Δ: healthy young adults
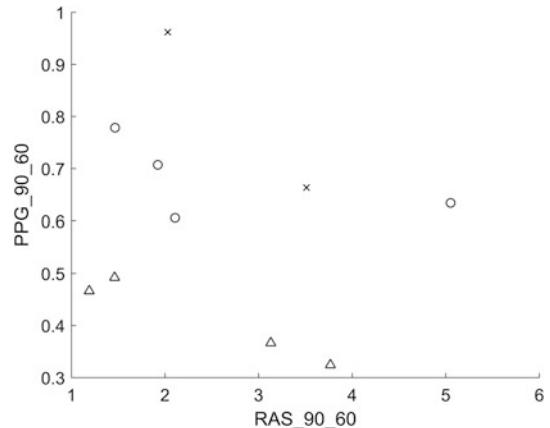
Fig. 4 *RAS*_90_60 and *PPG*_90_60 parameters for each tested person. x: healthy seniors, o: healthy middle aged persons, Δ: healthy young adults

Figure 3 shows the values of the *PWTTHC*_90_60 and *PWTTHF*_90_60 parameters for each tested person.

The change in the RAS parameter as a result of CP change shows large between-subject variability, but values are not age-group specific.

However, PPG amplitude exhibited a larger change as a result of changes in CP for healthy young persons than for healthy middle aged and senior individuals. Age group specific difference was found in the *PPG*_90_60 parameter. Figure 4 shows the values of the *RAS*_90_60 and *PPG*_90_60 parameters for each tested person.

4   Discussion

For all tested subjects PPG_90_60 was less than 1 and RAS_90_60 was greater than 1. PPG_90_60 was found to be smaller for young adults than for middle aged and senior individuals. This indicates age related increase in the rigidity of arteries. The Pearson correlation coefficient value between the *PWTTHC*_90_60 and PPG_90_60 parameters was 0.79, between the *PWTTHF*_90_60 and PPG_90_60 parameters was 0.56 in the present study. The high correlation value between *PWTTHC*_90_60 and PPG_90_60 suggests that both parameters are influenced by the state of the brachial artery.

The large between-subject variability of the *RAS*_90_60 parameter suggests that decreasing CP from 90 to 60 mmHg changed the PPG signal shape differently in case of different persons. It can be supposed, that for persons with low value of the *RAS*_90_60 parameter, a measurement would be more informative about their cardiovascular state, where the difference between constant CP values is larger than 30 mmHg.

Breathing modulates both BP and PWTT. This modulation is superimposed on the changes caused by cuff occlusion and if CP is changing constantly, the effect of breathing is difficult to analyze separately. Johansson [13] proposed a neural network-based method to estimate respiratory rate using PPG. For time intervals, where CP is kept at a constant value, the method described in [13] or similar approaches may help compensate the effect of breathing.

5   Conclusions

Continuous change of CP during oscillometric BP measurement affects the accuracy of the assessment of the state of the cardiovascular system in several ways. In this paper we described a CP profile with two intervals, where CP is kept at a constant value, each for one minute. We introduced parameters characterizing changes in the shape of the PPG waveform, PPG amplitudes and PWTT values as a result of change in CP. Age-group specific difference was found only for the change in the PPG amplitude.

Using the results of the present study, a new measurement series is scheduled with more participants in hospitals.

References

1. Kaczorowski, J., Dawes, M., Gelfer, M., Kapse, C.D., Patil, B.R.: Measurement of blood pressure: New developments and challenges. British Columbia Medical Journal 54(8), 399–403 (2012).
2. van Popele, N.M., Bos, W.J.W., de Beer, N.A.M., van der Kuip, D.A.M., Hofman, A., Grobbee, D.E., Witteman, J.C.M.: Arterial Stiffness as Underlying Mechanism of Disagreement Between an Oscillometric Blood Pressure Monitor and a Sphygmomanometer. Hypertension 36 (4), 484–488 (2000).
3. Kapse, C.D., Patil, B.R.: Auscultatory and Oscillometric methods of Blood pressure measurement: a Survey. International Journal of Engineering Research and Applications 3(2), 528–533 (2013).
4. Fonyó, A.: Az orvosi élettan tankönyve. 5th edn. pp. 306. Medicina Könyvkiadó Rt., Budapest (2011).
5. Jobbágy Á., Nagy P.: The Effect of Occlusion with the Cuff. In: Eskola, H., Väisänen, O., Viik, J., Hyttinen, J. (Eds.) EMBEC & NBC 2017, IFMBE Proceedings, vol. 65, pp. 9–12. Springer, Singapore (2017).
6. Forouzanfar, M., Ahmad, S., Batkin, I., Dajani, H.R., Groza, V.Z., Bolic, M.: Coefficient-free blood pressure estimation based on pulse transit time-cuff pressure dependence. IEEE Transactions on Biomedical Engineering 60(7), 1814–1824 (2013).
7. Jobbágy, Á., Nagy, P.: Pulse Wave Velocity as a Function of Cuff Pressure – Extra Information About the Cardiovascular System. In: Jaffray D. (Eds.) World Congress on Medical Physics and Biomedical Engineering, June 7–12, 2015, Toronto, Canada, IFMBE Proceedings, vol. 51, pp. 1279–1282. Springer, Cham (2015).
8. Xing, X., Sun, M.: Optical blood pressure estimation with photoplethysmography and FFT-based neural networks. Biomedical Optics Express 7(8), 3007–3020 (2016).
9. Jeong, I., Jun, S., Um, D., Oh, J., Yoon, H.: Non-Invasive Estimation of Systolic Blood Pressure and Diastolic Blood Pressure Using Photoplethysmograph Components. Yonsei Medical Journal 51(3), 345–353 (2010).
10. Monte-Moreno, E.: Non-invasive estimate of blood glucose and blood pressure from a photoplethysmograph by means of machine learning techniques. Artificial Intelligence in Medicine 53(2), 127–138 (2011).
11. Ruiz-Rodríguez, J.C., et al.: Innovative continuous non-invasive cuffless blood pressure monitoring based on photoplethysmography technology. Intensive Care Medicine 39(9), 1618–1625 (2013).
12. Kuvin, J.T., Mammen, A., Mooney, P., Alsheikh-Ali, A.A., Karas, R.H.: Assessment of peripheral vascular endothelial function in the ambulatory setting. Vascular Medicine 12(1), 13–16 (2007).
13. Johansson, A.: Neural network for photoplethysmographic respiratory rate monitoring. Medical and Biological Engineering and Computing 41(3), 242–248 (2003).

Presence of Stochastic Resonance in Isolated Mouse Heart

Alberto Peña-Romo, Amelia Ríos-Rodríguez, Bruno Escalante-Acosta, and Jesús Rodríguez-González

Abstract

The heart is an organ with a continuous activity whose heart rate and strength contractions are modulated by several mechanisms including the autonomic nervous system, the renin–angiotensin system, vasopressin, among others. In particular, the nervous system transmits electrical signals to the heart through neurons. Neurons are essentially noisy. During the past years, several researchers have suggested that the nervous and cardio-vascular systems appear to leverage the noise to improve information transfer. Stochastic resonance (SR) is a phenomenon observed when increases in levels of noise cause an increase in any metric of the quality of signal transmission or detection performance, rather than a decrease. In the cardiovascular system, some researchers have suggested that SR could enhance the homeostatic function of the human blood pressure regulatory system, and also SR is present within the baroreflex human center. However, few researchers have addressed in the fact that the noise can enhance contractile response in the whole heart. This study focuses on the electrical stimulation-contractile response coupling and demonstrates experimentally that the noise can enhance the contractile response in the whole heart. Experiments were conducted in isolated mouse hearts (0.040 kg, n = 7) where the contractile response due to an electrical stimulation (3–6 V, 6–17 Hz) perturbed with Gaussian noise was recorded. A Langendorff preparation was used to obtain two variables: the heart rate driven by the pacemaker in the sinoatrial node, and the contraction force, since the force is measured through a suture and a force-transducer placed at the apex of the heart. To the best of our knowledge, this is the first experimental test in whole heart focused on analyzing the contractile response due to electrical stimulation perturbed with Gaussian white noise. We found that the best performance was obtained with 10% induced noise. We have experimentally demonstrated the SR in isolated mouse heart.

1 Introduction

All process in Nature are shaped by noise. Researchers are finding more and more evidence that noise is not always detrimental for a biological function. This phenomenon, termed Stochastic Resonance (SR) does find useful applications in physical, biological and biomedical context [1].

The presence of noise sources can significantly alter the firing pattern of any periodically driven cell [2]. Internal noise (IN) can be interpreted in single-cell models, potentially improving sensory information processing by SR. Noise sources can be observed in nerve terminals, activated postsynaptic receptors, ion concentrations, or membrane conductance, among others [3]. Interestingly, SR promotes synchronization in neuronal systems, according to experimental and stimulation studies [3–5] for large stimulus amplitudes and frequencies [2]. Electrophysiological techniques could therefore provide interesting approaches to the investigation of SR in the heart.

This work is motivated by recent findings in our laboratory, where at whole organ level, the external noise (EN) induced in the sinoatrial node increases the 1:1 synchronization bandwidth in the electrical stimulation-contractile response coupling in the isolated mouse heart. The presence of 1:1

A. Peña-Romo (✉) · A. Ríos-Rodríguez · B. Escalante-Acosta · J. Rodríguez-González
Centro de Investigación y de Estudios Avanzados del Instituto Politécnico Nacional (IPN), Unidad Monterrey, Vía del Conocimiento 201, Parque de Investigación e Innovación Tecnológica, 66600 Apodaca, NL, Mexico
e-mail: mapr1202@gmail.com

J. Rodríguez-González
e-mail: jrodriguez@cinvestav.mx

synchronization pattern is a measurement of the healthy heart performance. Here, we present an experimental test in whole heart focused on analyzing the cardiac mechanical response due to electrical stimulation perturbed with Gaussian white noise.

2 Methods

A Langendorff heart preparation is used to obtain two variables: intensity of contractile force (ICF) and heart rate (HR) in isolated mouse heart. The heart was paced in the right atrium from spontaneous heart rate 6–17 Hz [6]. All animal procedures were conducted in accordance with Federal Regulations for Animal Experimentation and Care and were approved by the Animal Care Committee of CINVESTAV (CINVESTAV Zacatenco, D.F., Mexico).

2.1 Isolated and Perfused Heart Preparation

Male CD1 mice (30–40 g weight) were obtained from the Experimental Animal Care Center from CINVESTAV-IPN, Mexico. Mice were acclimated for one week before experiments in metabolic cages (Nalgene, USA) and they were maintained in a temperature controlled room (22 °C) on a 12-h light-dark cycle. Mice were anesthetized with a mixture of ketamine/xylacine (50:2.5 mg/kg) intraperitoneal [7], and then injected with heparin (100 IU) to avoid intracoronary thrombi. Once deeply anesthetized, mice were intubated and ventilated with room air (Ugo Basile, Italy) with a tidal volume of 0.6 ml and frequency of 110 beats per minute (bpm) [6, 8]. Hearts were excised and placed directly into an ice-cold Krebs-Henseleit bicarbonate solution containing (in mM): 118 NaCl, 25 $NaHCO_3$, 4.7 KCl, 1.2 $MgSO_4$, 1.2 KH_2PO_4, 2.25 $CaCl_2$, 0.5 EDTA and 11.1 glucose, oxygenated with 95% O2–5% CO_2 (pH 7.4) [7, 8]. Under a stereoscopic microscope, the aorta was localized and cannulated with a circular 20-gauge needle. Rapidly, the hearts were placed in a Langendorff system and retrogradely perfused with the Krebs solution at 37 °C infused through a peristaltic pump at 3 mL/min [6–9]. The isolated perfused mouse heart has a rate of 380–420 bpm compared to 580–600 bpm in vivo [6]. In spite of the fact that hearts are isolated from the body, the method remains suitable and reasonably physiological in accordance with our hypotheses [7]. All the experiments were carried out carefully, ensuring that tissue temperature was maintained at 37 °C.

2.2 External Electrical Stimulation

Hearts were allowed to beat spontaneously (380 beats min-1) (6.33 Hz) for 30 min [6]. Then, two platinum stimulation electrodes (Aldrich Chemistry, 0.25 mm diameter) connected to a data acquisition card (NI SCB-68) were superficially attached to the high right atrium to alter the heart rate, avoiding cardiac tissue damage. The pacing frequency was set in a range 6–17 Hz range with increases of 1 Hz, using a square wave of 4.0 ms duration and voltage amplitude between 3 and 6 V [10]. The stimulus amplitude was achieved using a function generator developed in LabVIEW. The mouse heart pacing was performed for 30 s intervals followed by a recovery period of 10 s. In the absence of pacing protocols, the heart will return to sinus rhythm immediately [7]. The upper frequency was selected above the maximum heart rate (12 Hz) [11]. Furthermore, for experiments with a noisy stimulus, a Gaussian white noise signal developed in LabVIEW was added to the stimulus protocol described above. Different noise amplitude values were added to the signal (10–30% with increases of 10%, (300–900 mV)).

2.3 Myocardial Contractile Function

To measure the ICF and HR, a force-displacement transducer (Kent, USA) was attached to the apex of mice heart through a 6-0 silk suture (Johnson & Johnson, Brazil) and a low resistance pulley. The resting tension was adjusted at 0.5 gf to the hearts. All the records were processed by the same data acquisition interface (Lab-Trax-4/24T, WPI) and subsequently analyzed with the Data-Trax2 software with a sample rate of 500 data/s. No significant effect of friction between the silk suture and the pulley was found. The ICF was calculated as the difference between the mean of all maximum and minimum peak values of the recordings, and for statistics, the data were normalized against the maximum value. Additionally, to calculate the HR value due to the electrical stimulation, the characteristic frequency in power spectra of the recording signals at each stimulation frequency was obtained using the Fast Furier Transform.

2.4 Statistical Methods

Values are reported as mean ± standard deviation. Statistical comparisons were made using two-way ANOVA followed by the Tukey's post hoc test. A $P < 0.05$ was

considered significant. Standard signal processing techniques were used to study the spectral content of the contractile force [12].

3 Results and Discussion

It is known that an isolated heart preserves the ability to perform a rhythmic contraction. As the de-innervated heart is perfused, the activity of the pacemaker continues to trigger the beats [9]. The heart is removed from the body and in the absence of preload and afterload of blood, the heart does not lose its contractile property. The ICF and HR signals bring enough information to analyze the mechanical response due to an external electrical stimulation either with and without induced white noise. This study, however, does not take into account the possible frequency dependence of the response of single cells, nor the intracellular mechanisms and the refractory properties that come into play for higher pacing rate frequencies. The perspective in this study is only for the mechanical response at whole organ.

Representative recordings of the mechanical response of an isolated heart at different pacing rates for the minimum electro-stimulation value (3 V) without noise are shown in Fig. 1. The amplitude of the signals is maintained constant during the period of stimulation (Fig. 1a–d), and this amplitude tends to decrease as the frequency of the pacing rate increases. However, for higher pacing rate values

(>12 Hz), an irregular and non-periodic behavior (Fig. 1e) was obtained. It might be associated with a pathological condition. Regardless the frequency of stimulation, after the pacing rate was turned off, the mechanical response was restored to its spontaneous rate.

In an attempt to test the feasibility of the experimental setup, a set of measurements of the contractile response due to an external electrical stimulation without induced noise were recorded. Figure 2 shows the ICF results normalized for seven different isolated hearts. For all the stimulation intensities (3–6 V) without induced noise (Fig. 2a), it can be seen that the ICF tends to decrease as the pacing rate increases (6–17 Hz). The relationship between the contraction force and the heart rate is well known: the amplitude of the cardiac response tends to decrease as the heart rate increases, and our results agree with Slabaugh experiments for isolated mouse heart [13]. There is no statistical difference ($P < 0.05$) between 3 and 6 V for results without noise induced.

Results for heart rate due to ascending pacing rate values at critical electro-stimulation intensities can be seen in Fig. 3. For experiments with seven isolated hearts stimulated at 3 V without noise (Fig. 3a), at some values of pacing rate, the hearts adequately responded to the frequency of stimulation (9, 10, 12–14 Hz). Furthermore, by analyzing results with 6 V, almost all the hearts failed to obtain the 1:1 synchronization as the pacing rate is increased. The isolated perfused mouse heart has a basal frequency of 380 bpm
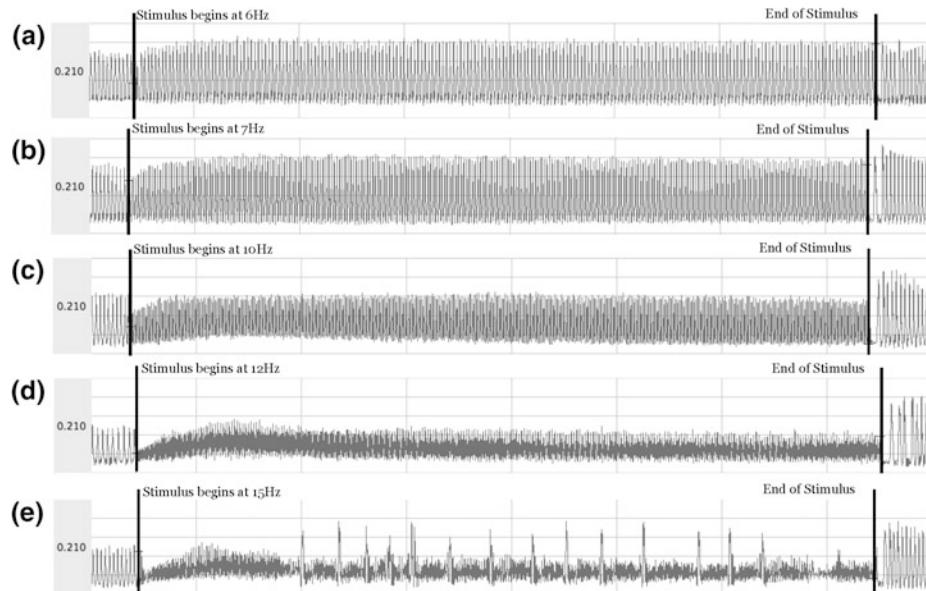
Fig. 1 Contractile response in isolated heart without noise. Recordings of the mechanical response to external stimulation at 3 V for lower pacing rate values (<12 Hz), **a** 6 Hz, **b** 7 Hz, **c** 10 Hz and **d** 12 Hz are presented. The amplitude of the cardiac response remains constant, whereas for higher pacing rate values (>12 Hz), **e** 15 Hz, a non-ordinary dynamic response is presented with non-periodic overshoots and were presumably the synchronization is lost. The hearts recovered their basal behavior after the external stimulation was over; this recovery was achieved after few seconds
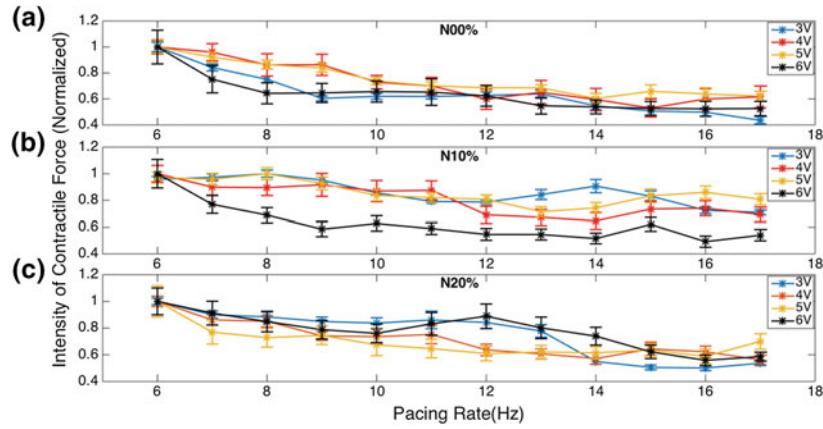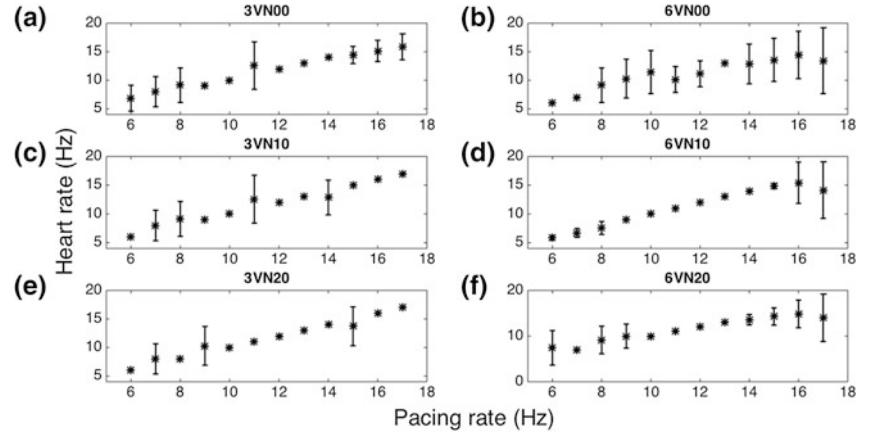
Fig. 2 Intensity of contractile force (ICF) normalized with respect to basal response. As the pacing rate increases, the amplitude of the cardiac response tends to decrease for all stimulation intensities. **a** Experiments carried out without induced noise (3 V vs. 4 V P = 0.66, 3 V vs. 5 V 0.41, 3 V vs. 6 V P = 1.00, 4 V vs. 5 V P = 0.99, 4 V vs. 6 V P = 0.61, 5 V vs. 6 V P = 0.36). **b** Experiments with 10% noise (3 V vs. 4 V P = 0.32, 3 V vs. 5 V 0.99, 3 V vs. 6 V P = 0.00, 4 V vs.

5 V P = 0.49, 4 V vs. 6 V P = 0.01, 5 V vs. 6 V P = 0.00). **c** Experiments with 20% noise (3 V vs. 4 V P = 0.90, 3 V vs. 5 V 0.72, 3 V vs. 6 V P = 0.97, 4 V vs. 5 V P = 0.98, 4 V vs. 6 V P = 0.69, 5 V vs. 6 V P = 0.45). Data are presented as mean values ± standard deviation of the mean (n = 7). Statistical analysis performed using two-way ANOVA followed by Tukey's test

Fig. 3 Heart rate response at critical electro-stimulation values without noise. **a**, **c**, **e** Results for heart rate response at 3 V with 0, 10 and 20% noise, respectively. **b**, **d**, **f** Heart rate at 6 V with 0, 10 and 20% noise, respectively). Data are presented as mean values ± standard deviation of the mean (n = 7)

(6.33 Hz) [6]. Our experimental results show that in some cases it is impossible to obtain a synchronization when stimuli were performed with lower frequencies than basal rate.
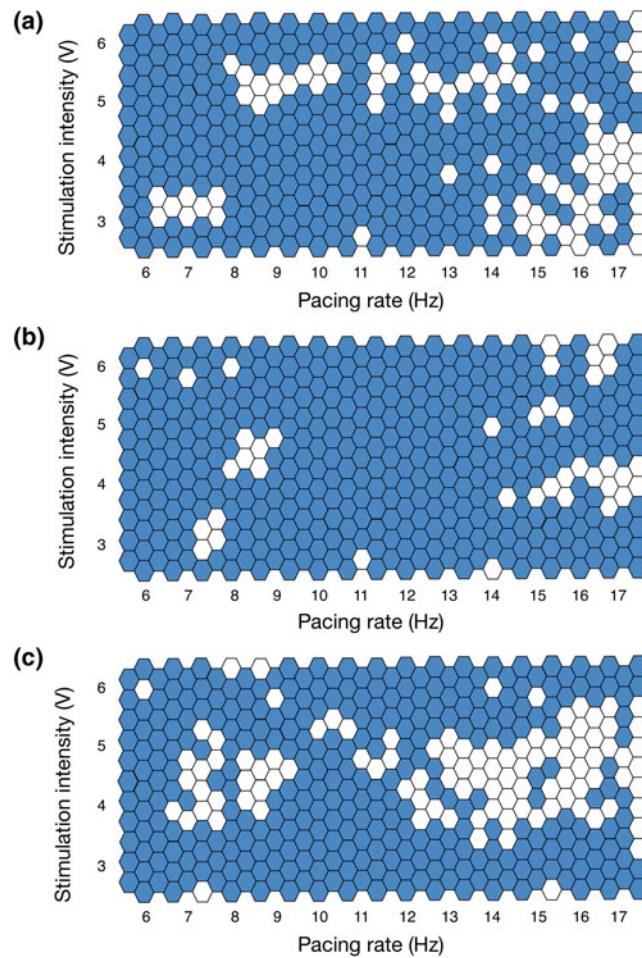
To analyze the heart rate, all the experimental results were organized as clusters in order to quantify the 1:1 synchronization. Results are shown in a seven-hexagon array to each stimulation intensity and each pacing rate value. One hexagon corresponds to one experiment from a different heart. Blue hexagons represent the presence of synchronization between the electrical stimulation and the cardiac response whereas white hexagons represent the lack of it. Then, all hexagonal sets were grouped to form interaction maps and where the presence of synchronization for all pacing rate and stimulation intensities values is clearly seen. The interaction map corresponding to control experiments is

presented in Fig. 4a. Additional experiments at the edges of the maps were carried out.

The influence of noisy stimuli on the contractile response was analyzed once the experimental set up was suitable enough to validate the presence of synchronization in the isolated heart model based on Langendorff technique. A white Gaussian noise signal was added to stimuli and a set of measurements of ICF and HR with different noise levels were obtained, n = 7. The ICF results for noisy stimuli are shown in Fig. 2b, c. As can be seen, as the pacing rate increases, the ICF tends to decrease. However, comparing with control experiments, the IFC for 10% noise do not decay substantially at higher frequencies for 3–5 V.

Results for heart rate due to ascending pacing rate values at critical electro-stimulation intensities can be seen in Fig. 3c, d for 10% noise and Fig. 3e, f for 20% noise. These

Fig. 4 Interaction maps between pacing rate and electro-stimulation intensity. **a** Results for experiments performed without noise induced, **b** 10% noise and **c** 20% noise. One blue hexagon represents the presence of synchronization for one repetition whereas the white hexagons represent the lack of it

plots illustrate how noise induces 1:1 synchronization for more values of pacing rate compared with control experiments (Fig. 3a, b). It can be seen that, in the control experiments, for the lower value of electro-stimulation (3 V), a higher standard deviation at 6 Hz is presented because not all hearts followed the applied stimuli appropriately (Fig. 3a). However, this was improved with a little noise intensity applied to the stimulus (10%) and, on the other hand, for higher pacing rate values (15–17 Hz, 3 V), the synchronization was obtained with 10% noise in all hearts. Moreover, for 6 V and 10% noise, a linear response is observed between 6 and 15 Hz. The interaction map corresponding to experiments with noise added to stimuli are shown in Fig. 4b, c. As can be seen in Fig. 4b, more 1:1 synchronization results are observed with 10% noise, compared with control experiments. On the other hand, the lack of synchronization is frequently found at 20% noise (Fig. 4c).

Because 1:1 synchronization pattern is associated with a normal excitation-contraction coupling, the percentage of these events for each interaction map was calculated as a measurement of the healthy heart performance. Figure 5 shows the heart performance for each noise intensity. As can be seen, the best performance is achieved with 10% noise (90.57% vs. control 79.71%), whereas for 20% noise, the performance is lower than control (75.60%).

Noise has recently emerged as a key component of a wide range of biological systems, from gene expressions to neuronal activity [4]. However, little attention has been shown to the fact that noise can affect the mechanical response in the whole heart. Prior work has demonstrated that abnormal contractions of the heart are a focus of research not only because of their relevance to arrhythmias but also because of the important mathematical and physical concepts raised by their dynamics [14, 15]. Conventional studies of periodically perturbed oscillators involve analyzing the stimulation-response coupling as a function of the parameters of the driving force, specifically the amplitude and the period [2]. This is the approach used in this study, but with the implication of noise as a driving parameter as well.
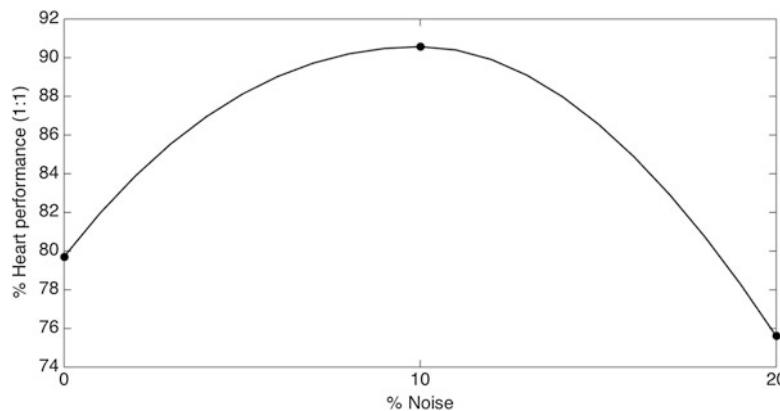
Fig. 5 Presence of stochastic resonance in isolated heart affected by external noise. The percentage of 1:1 synchronization for each interaction map in Fig. 4 was obtained as a measurement of heart performance. The best performance was achieved with 10% noise, whereas for higher noise intensities (20% noise), the performance was lower compared with control. Control: 79.71, 10% noise 90.57 and 20% noise 75.60%

Synchronization due to a lower noise intensity is observed in plot 4B for 10% noise. It can be clearly seen the beneficial role of noise maintaining the 1:1 synchronization comparing with control experiments. However, higher noise intensities (20% noise) cause several irregularities in the cardiac response. In Fig. 4c can be seen the lack of synchronization in most of the experiments performed. Our results for isolated heart imply that the synchronization depends not only on the amplitude or frequency of the stimulus, but external noise as another parameter to be taken into account. This is meant to give a concrete example where the notions of synchronization and noise tuning in excitable cells may be applied to whole organ as well. We use the term 'may' on purpose because the mechanisms involved in the internal noise conception were not considered in this study (no intracellular recordings have yet been possible) and small biochemical and electrochemical fluctuations can significantly alter whole-cell responses [4]. Interestingly, a complex synchronization pattern (2:1, two electrical events that lead to one mechanical contraction) in some harts, due to noise, was observed (plot not shown). A cardiac arrhythmia is a phenomenon due to a loss of synchronization in the excitation-contraction coupling. Thus, to connect our results with preventive and clinic medicine, this study opens the option to research some specific arrhythmias produced by noise, and could be analized as the tunning between the electrical pacing and noise signals. However, we drew this conclusion with reservations. More analysis has to be done in order to characterize this pathological condition. Furthermore, it remains unanswered how the coupling strength, noise and frequency can participate in the development of abnormal synchronization patterns.

4 Conclusion

In this study, the effect of noise that leads to synchronization in the electrical stimulation-contractile response coupling in isolated mouse heart was analyzed. A lower value of external noise effectively induces the 1:1 synchronization in more experiments than control. Stochastic resonance (SR) is said to be observed when increases in noise levels cause an increase in the performance of a system rather than a decrease. Because for some intermediate nonzero noise level (10% noise) provides an optimal performance (compared with control experiments) whereas for large noise levels (20% noise) the response is dominated by the noise, we can conclude that SR can be observed in the isolated heart model. This opens exciting possibilities for the role of noise in the analysis and prevention of abnormal rhythms of the heart.

5 Study Limitations

For experimental systems, it is hard to perform fine variations of parameters because the physiological limitations. Although this study presents an experimental protocol to identify the mechanical response in the whole heart due to external stimulation, the responses obtained are just a physiological approximation. We strongly suggest that further experiments to measure intraventricular pressure and ECG recordings have to be done to characterize commonly known arrhythmias. Furthermore, theoretical analysis could better elucidate the extraordinary dynamics of cardiac

rhythms, exploiting the beneficial role of noise in biological systems.

Conflict of Interest The authors report no relationships that could be construed as a conflict of interest.

References

1. Hänggi, P.: Stochastic resonance in biology: How noise can enhance detection of weak signals and help improve biological information processing. ChemPhysChem 3, 285–290 (2002).
2. Longtin, A.: Effect of noise on the tuning properties of excitable systems. Chaos, solitons and fractals 11, 1835–1848 (2000).
3. Moss, F.: Stochastic resonance and sensory information processing: a tutorial and review of application. Clin. Neurophysiol. 115, 267–281 (2004).
4. Faisal, A. A., Selen, L. P. J., and Wolpert, D. M.: Noise in the nervous system. Nat. Rev. Neurosci. 9, 292–303 (2008).
5. McDonnell, M. D., and Ward, L. M.: The benefits of noise in neural systems: bridging theory and experiment. Nat. Rev. 12, 415–425 (2011).
6. Bell, R. M., Mocanu, M. M., and Yellon, D. M.: Retrograde heart perfusion: The Langendorff technique of isolated heart perfusion. J. Mol. Cell. Cardiol. 50, 940–950 (2011).
7. Skrzypiec-Spring, M., Grotthus, B., Szelag, A., and Schulz, R.: Isolated heart perfusion according to Langendorff-Still viable in the new millennium. J. Pharmacol. Toxicol. Methods 55, 113–126 (2007).
8. Broadley, K. J.: The Langendorff heart preparation-Reappraisal of its role as a research and teaching model for coronary vasoactive drugs. J. Pharmacol. Methods (1979).
9. Sutherland, F. J., and Hearse, D. J.: The Isolated Blood and Perfusion Fluid Perfused Heart. Pharmacol. Res. 41, 613–627 (2000).
10. Larsen, T. S., Belke, D. D., Sas, R., Giles, W. R., Severson, D. L., Lopaschuk, G. D., et al.: The isolated working mouse heart: Methodological considerations. Pflugers Arch. Eur. J. Physiol. 437, 979–985 (1999).
11. Kass, D. A., Hare, J. M., and Georgakopoulos, D.: Murine Cardiac Function. Circ. Res. 82, 519–522 (1998).
12. Herbshleb, J. N., Heethaar, R. M., Tweel, I. Van der, and Meijler, F.: Frequency analysis of the ECG before and during ventricular fibrillation. IEE Comput Cardiol 365–368 (1980).
13. Slabaugh, J. L., Brunello, L., Gyorke, S., and Janssen, P. M. L.: Contractile parameters and occurrence of alternans in isolated rat myocardium at supra-physiological stimulation frequency. AJP Hear. Circ. Physiol. 302, H2267–H2275 (2012).
14. Franz, M. R.: Method and theory of monophasic action potential recording. Prog. Cardiovasc. Dis. 33, 347–368 (1991).
15. Glass, L.: Synchronization and rhythmic processes in physiology. Nature 410, 277–284 (2001).

Feasibility Study of Evaluation of Therapeutic Effect for Sleep Apnea Syndrome Using Mental Healthiness Evaluated from Voice

Mitsuteru Nakamura, Shuji Shinohara, Yasuhiro Omiya,
Shunji Mitsuyoshi, Masakazu Higuchi, Naoki Hagiwara,
Takeshi Takano, Hirosuke Danno, Shun-ichi Tanaka,
and Shinichi Tokuno

Abstract

Dealing with sleep apnea syndrome (SAS) is important because of its social burden, however current standard diagnosis requires a costly examination (polysomnography, PSG). Therefore, strong demand for easy screening methods for SAS exists. There is also a need for evaluation of therapeutic effect by continuous positive airway pressure (CPAP). Because CPAP requires adjustment of parameters (titration), or CPAP used inadequately will not improve a patient's symptom. Considering quality of life, evaluation of therapeutic effect requires monitoring of mental and physical conditions in daytime. We already reported that mental healthiness evaluated from voice, called "vitality," showed some correlation with severity of SAS. In this study we examined feasibility of vitality as an index of therapeutic effect by CPAP. We recorded voices from subjects when they were examined by PSG for first diagnosis and titration, before and after each examination. Then we evaluated vitality of the subjects at the recording. The subjects were categorized into two groups; subjects of a group started using CPAP after titration, and subjects of another group started using CPAP before titration. As results, direction of change in vitality in the former group varied by subjects at titration, while vitality in the latter group showed tendency of improvement. Within the latter group, the change in vitality tends to get larger as usage rate of CPAP before titration is higher. This result suggests that vitality has a potential for an easy method to evaluate therapeutic effect for SAS, and that diligence of CPAP usage is important for effective treatment.

1 Introduction

Sleep apnea syndrome (SAS) is a disease marked by frequent shallow breathing or interrupted breathing during sleep. Insufficient respiration while sleep requires brain activity to restore breathing activity therefore quality of sleep deteriorates. As a result, the person will be prone to feeling sleepy during the day, resulting in reduced productivity or accidents [1]. Also it is known that the load imposed on tissue by intermittent oxygen deprivation during sleep [2] or the increased load placed on the circulatory system as it recovers from a state of oxygen deprivation increases the risk of life-style related diseases such as diabetes [3] and hypertension [4]. It is reported that the rate of coincidence with depression is also increased [5].

And because on one hand, it appears that the incidence rate of SAS is high and there are many latent patients [6], it is believed that the cost to society of SAS is too high to be ignored and that treating SAS patients is an important issue for society.

Currently, polysomnography (PSG) is used as the standard method of diagnosing SAS. PSG is a costly examination using many sensors and requiring laborious effort. If the patient is diagnosed as severe SAS, the patient should be treated to reduce burden by SAS. Respiratory support by continuous positive airway pressure (CPAP) equipment is the only practical and effective treatment for most cases. For effective treatment using CPAP, adjusting operational

M. Nakamura (✉) · S. Shinohara · S. Mitsuyoshi · M. Higuchi
S. Tokuno
The University of Tokyo, Hongo 7-3-1, Bunkyo Tokyo,
113-8655, Japan
e-mail: m-nakamura@m.u-tokyo.ac.jp

Y. Omiya · N. Hagiwara · T. Takano
PST Inc, Yamashita-cho 2, Yokohama Kanagawa, 231-0023,
Japan

H. Danno · S. Tanaka
Minatomirai Clinic, Minatomirai 3-6-3, Yokohama Kanagawa,
220-0012, Japan

parameters of CPAP called "titration" is required. While titration, sleep status of a patient is continuously monitored by an engineer using PSG to examine whether parameters of CPAP is adequate or not.

A simple and low-cost evaluation method for respiratory condition while sleeping will help to dissolve the burden by SAS, in finding latent patients to be treated and monitoring efficacy of CPAP. Currently simple measurement machines such as pulse oximeters that measure limited examination items are used as simple examination machines. But simple measurement machines are also specialized hardware, so they are not mass produced. If it were possible to evaluate respiratory condition while sleeping using smartphones or other devices that are in wide use, this would definitely contribute greatly to discovering and treating latent SAS patients.

As we know from the fact that SAS patients are susceptible to concurrent depression, people's mental state is also impacted by inadequate rest during sleep, so it is thought a person's mental state immediately after waking up reflects the quality of the sleep to some degree. Technology to measure emotions and other aspects of mental state from a voice recorded on a smartphone has been developed [7–9], and it is predicted that if this were used to measure a person's mental state immediately after waking up, it would be possible to also measure the quality of the person's sleep.

We already reported that mental status index based on voice analysis called "vitality" shows feasibility as an easy screening tool of SAS [10]. In this study we examined the vitality as an evaluation tool of therapeutic efficacy by CPAP. For the purpose we obtained the voices of patients who started using CPAP at their first examination by PSG and titration, then evaluated the vitality and compared to usage of CPAP. From the results of the comparison, the change of the vitality was affected by the usage of CPAP. This result shows the possibility of a voice based evaluation of therapeutic effect by CPAP.

2 Materials and Methods

2.1 Subjects

Subjects were recruited from among people who had a PSG examination at the Minatomirai Clinic (Yokohama, Japan). They were 83 men and 18 women ranging in age from 22 to 84. As stipulated by the Declaration of Helsinki and ethical guidelines enacted by the Ministry of Health, Labour and Welfare of Japan, the clinic staff explained the test to the candidate subjects and only those who gave written consent were selected as test subjects. The test protocol was examined and approved by the Ethics Committee of the Minatomirai Clinic.

2.2 Data Acquisition

The PSG test measured the same items as those measured under clinical practice conducted at the Minatomirai Clinic. Voices of the subjects were recorded four times: immediately before the start of first PSG measurements, immediately after the completion of the first PSG measurements, immediately before the start of titration and immediately after the completion of the titration. Figure 1 shows timing of the voice recording. The recordings were made by instructing each subject to read 17 pre-determined sentences aloud twice. The recorder used was an R-26 (Roland, Hamamatsu, Japan), and the microphone used was an ME52W (Olympus, Tokyo, Japan). Audio format of the recorded voices was linear pulse code modulation (LPCM) with a sampling rate of 96,000 Hz and 24-bits quantization.

2.3 Data Analysis

After the first PSG tests, the subjects were evaluated their severity of SAS same as the clinical practice conducted at the Minatomirai Clinic based on the apnea hypopnea index (AHI). AHI indicates the frequency per hour of the total numbers of hypopnea (shallow breathing) and apnea (interrupted breathing) events. The subjects decided whether to use CPAP and when they would start using CPAP, immediate (before titration) or after titration, according to suggestion by the doctors.

As for the voice, the format was converted into LPCM with a sampling rate of 11,025 Hz and 16-bits quantization. Emotion-recognition was done for each sentence using ST SDK (PST, Yokohama, Japan) depending on attack and decay of the voice [7, 8], and based on the results, "vitality," the index of mental health was calculated using MIMOSYS (PST, Yokohama, Japan) [9]. Vitality calculated by sentence in each recording occasion was averaged and the average was used as vitality for the recording occasion. The vitality is a dimensionless quantity, ranging from 0 to 1.

3 Results

In this study, 47 subjects chose to use CPAP therefore they had a titration. Within the 47 subjects, 27 subjects started using CPAP after titration, categorized as group (A). Other 20 subjects started using CPAP before titration, categorized as group (B).

Figure 2 shows distribution of vitality at each recording occasion, and difference of vitality between the first PSG and the titration, discriminating two groups of subjects by usage of CPAP before the titration. Timings in Fig. 2 resembles those in Fig. 1. Though there is no significant difference,
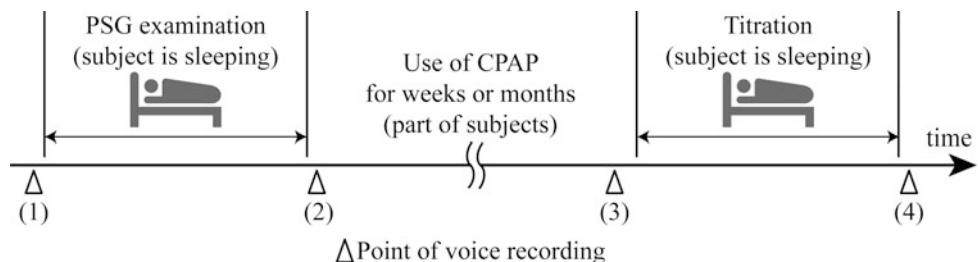
Fig. 1 Timing of voice recordings. Recordings were carried out for four times; (1) immediately before the start of the first PSG (before PSG), (2) immediately after the completion of the first PSG (after PSG), (3) immediately before the start of the titration (before TR), (4) immediately after the completion of the titration (after TR)

vitality of group (B) at awakening tends to become higher at the titration than that at the first PSG (Fig. 2a). This results in shrinkage of distribution for negative direction at the titration in group (B) (Fig. 2b).

Figure 3a shows scatter plot for subjects of group (B) between usage rate of CPAP and change in vitality between the first PSG and the titration. The number of the subjects in Fig. 3a is 15, because of partial lack in required data. The usage rate of CPAP is defined as the ratio of days the subject used CPAP to whole days since the start of using CPAP until the day just before the titration. These data were recorded automatically by the CPAP equipment the subject used. The change in vitality is calculated by subtracting the difference of vitality between the first PSG from the difference of vitality between the titration. Correlation coefficient between the usage rate of CPAP and change in vitality is 0.342.
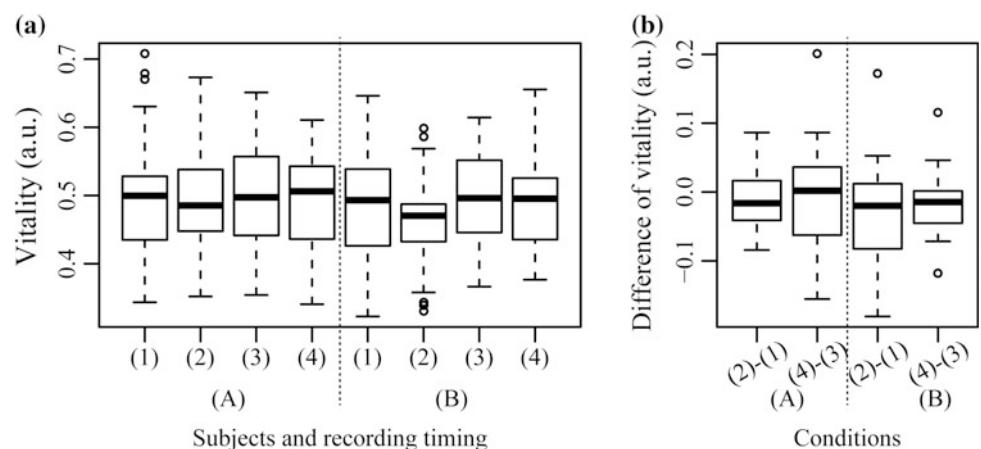
Then we split group (B) into two subgroups based on usage rate of CPAP. The threshold was set at 0.9. Figure 3b shows distribution of change in vitality of each group. The distribution shows significant difference at level 0.05 between two subgroups of (B), and the subgroup of the subjects whose usage rate of CPAP is over 0.9 shows significant difference at level 0.1 compared to (A).

4 Discussions

Vitality surmised from the voices is an indicator that suggests the overall health of an individual, so it is of course impacted by factors other than sleep. This varies widely between people, so it is difficult to equalize all factors other than sleep and the differences between groups and conditions are not significant. But looking at the difference between the values obtained by measuring twice—immediately before and after sleep—presumably shows that sleep is the principal factor impacting vitality.

In this study, difference between two subject groups is whether the subjects had already used CPAP or not before the titration. Therefore, it is assumed that difference of vitality between the two groups reflects the therapeutic effect of CPAP. Though no significant difference is found, the tendency of change shown in Fig. 2b infers possibility of vitality as evaluator of CPAP treatment. In addition, the result shown in Fig. 3 suggests that diligence of CPAP usage also may affect the therapeutic efficacy. The number of the subjects was limited because of prospective approach in this study, therefore further verification in much more subjects will be required.

Fig. 2 **a** Distribution of vitality at each timing. (1)–(4) shows the timing same as Fig. 1; (1) before PSG, (2) after PSG, (3) before TR, (4) after TR. (A) and (B) indicate groups of subjects. **b** Distribution of difference of vitality at the first PSG ((2)–(1)) and the titration ((4)–(3))
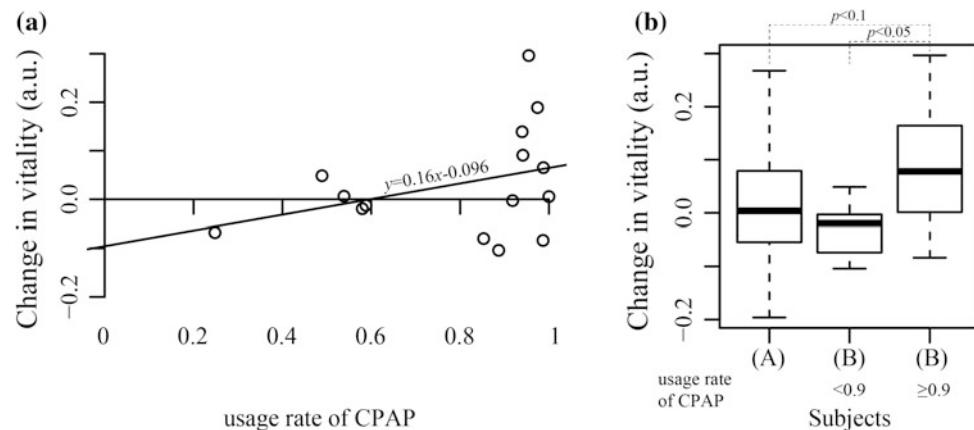
Fig. 3 a Scatterplot for group (B) (n = 15) between usage rate of CPAP and change in vitality between the first PSG and the titration. The usage rate of CPAP is calculated by date, ignoring duration of using CPAP in a night. Change in vitality is calculated as "difference between the first PSG; (2)–(1) in Fig. 1"—"difference between the titration; (4)–(3) in Fig. 1." Line in the plot shows regression line. **b** Distributions of change in vitality for each group. Group (B) is divided into two subgroups, based on usage rate of CPAP. Threshold of usage rate was set at 0.9

Vitality is not specialized for sleep as mentioned above. We believe that it is possible to provide a more useful index specialized for sleep by using feature values of voice showing a better correlation with indices concerning the state of sleep.

5 Conclusion

In this study we investigate the relation between usage of CPAP, one of popular treatment method for SAS, and index of mental health called vitality surmised from voices recorded before and after sleeping. As a result, by measuring vitality several times and evaluating the change between two times, we can remove to a certain degree the impact of factors other than sleep which impact mental health, to indicate the therapeutic effect of CPAP for SAS. The result suggests that the diligence of CPAP usage modifies the therapeutic efficacy.

This study has demonstrated possibility of a low cost and easily performed monitoring of CPAP efficacy by evaluating vitality acquired from voice.

References

1. Findley, L.J., Unverzagt, M.E., Suratt, P.M.: Automobile Accidents Involving Patients with Obstructive Sleep Apnea. Am. Rev. of Respiratory Disease 138, 337–340 (1998).
2. Ryan, S., Taylor, C.T., McNicholas, W.T.: Selective Activation of Inflammatory Pathways by Intermittent Hypoxia in Obstructive Sleep Apnea Syndrome. Circulation 112, 2660–2667 (2005).
3. Tasali, E., Mokhlesi, B., Cauter, E.V.: Obstructive Sleep Apnea and Type 2 Diabetes. Chest 133, 496–506 (2008).
4. Lavie, P., Herer, P., Hoffstein, V.: Obstructive sleep apnoea syndrome as a risk factor for hyper-tension: population study. BMJ 320, 479–482 (2000).
5. Sharafkhaneh, A., Giray, N., Richardson, P., Young, T.: Association of Psychiatric Disorders and Sleep Apnea in a Large Cohort. SLEEP 28, 1405–1411 (2005).
6. Young, T., Palta, M., Dempsey, J., Skatrud, J., Weber, S., Badr, S.: The occurrence of sleep-disordered breathing among middle-aged adults. The New England J. of Medicine 328, 1230–1235 (1993).
7. Mitsuyoshi, S., Ren, F., Kuroiwa, S., Tanaka, Y.: Non-verbal voice emotion analysis system. Intl. J. of Innovative Computing, Information and Control 2, 819–830 (2006).
8. Tokuno, S.: Stress Evaluation by Voice: From Prevention to Treatment in Mental Health Care. Econophysics, Sociophysics & Other Multidisciplinary Sciences J. 5, 30–35 (2015).
9. Omiya, Y., Hagiwara, N., Shinohara, S., Nakamura, M., Mitsuyoshi, S., Tokuno, S.: Development of Mind Monitoring System using Call Voice. In Neuroscience 2016, 97.02, San Diego (2016).
10. Nakamura, M., Shinohara, S., Omiya, Y., Hagiwara, N., Higuchi, M., Mitsuyoshi, S., Danno, H., Tanaka, S., Tokuno, S.: Relation between Severity of Sleep Apnea Syndrome and Mental Healthiness Evaluated from Voice. In 39th Annual International Conference of the IEEE Engineering in Medicine and Biology Society, FrDT10-01.2, Jeju (2017).

Finite Element Mapping for Efficient Image Reconstruction in Rotational Electrical Impedance Tomography

Olli Koskela, Mari Lehti-Polojärvi, Aku Seppänen, Edite Figueiras, and Jari Hyttinen

Abstract

Electrical impedance tomography (EIT) is a label free harmless imaging method capable of imaging differences in electrical conductivity of a sample. In EIT, a low frequency current is injected into the sample, voltage differences on sample surface are measured, and from these measurements, interior conductivity distribution is reconstructed. To increase the accuracy of reconstruction, rotational EIT (rEIT) has been proposed where independent measurements are taken from multiple rotational positions around the sample. However, the benefit of conventional electrode configurations are limited to small number of rotational positions. We have presented an approach called Limited Angle Full Revolution rEIT (LAFR-rEIT) that uses a small number of electrodes and large number of rotational measurement position measurements over 360°. The results are comparable to previous rotational EIT implementations, and furthermore, the limited EIT boundary access provides space for simultaneous attachment of other measurement modalities. On the other hand, the increased number of measurement positions cause an increase in computational complexity, and optimization is required until 3D applications are feasible. This work presents modifications into finite element mesh presentation of the imaging domain and outlines an optimization, that enables sufficiently light rotation for 3D LAFR-rEIT computations.

1 Introduction

Electrical impedance tomography (EIT) is a non-destructive electrical imaging modality used both in industrial and medical applications. In EIT, a current is injected into the sample of interest and potential differences are measured on the sample domain [1]. From these measurements, the electrical conductivity distribution is reconstructed. This reconstruction problem is severely ill-posed inverse boundary value problem where the accuracy of the solution benefits from additional independent data. Hence, adding measurement positions through rotating the sample (rotational EIT, rEIT) [2–4] and joint reconstruction of EIT in conjunction with an additional modality have been proposed including ultrasonic imaging and magnetic resonance imaging [5–7].

In our previous work [8], we presented a rEIT design principle in 2D using only a limited section of the sample surface for electrode positioning. The motivation for developing such an approach was to enable both of the mentioned modifications into EIT system: rEIT and simultaneous multimodal imaging. The approach we call Limited Angle Full Revolution rEIT (LAFR-rEIT) benefits from a large number of rotational measurement positions, but consequently, there is an increase of the computational complexity due to the increase of the number of measurements.

Previously rEIT has been modeled either by including modeling electrodes to account for all rotational positions, or by computing position nodes for electrodes in each rotational position. An in-detail comparison of reconstruction approaches used for modeling rotation in EIT is presented in [4]. However, for increased number of rotational positions, these approaches are not feasible: the modeling electrodes

O. Koskela (✉) · M. Lehti-Polojärvi · J. Hyttinen
BioMediTech Institute and Faculty of Biomedical Sciences and Engineering, Tampere University of Technology, Tampere, Finland
e-mail: olli.koskela@tut.fi

A. Seppänen
Department of Applied Physics, University of Eastern Finland, Kuopio, Finland

E. Figueiras
Ultrafast Bio- and Nanophotonics Group, INL - International Iberian Nanotechnology, Braga, Portugal

might overlap or the node structure on the boundary may become overly complex. To overcome these issues, we implemented weight-based mapping to model rotation [8], where mesh structure is created for initial position and element values are rotated inside this fixed mesh. The advantage of the weight-based mapping is that mesh rotation is independent from its construction. On the downside, the need of optimization persists as the mapping is computationally time and memory inefficient. Additionally, the weight-mapping produces local deformations of object during the rotation, because element boundaries vary in each rotational position.

For more efficient implementation of rEIT reconstructions, this paper proposes a novel approach for creating 2D finite element meshes for rEIT image reconstruction. The proposed mesh construction is composed of an inner boundary within computational domain, and rotational mapping is performed using this inner boundary instead of rotating whole domain with respect to electrodes. The implementation of the rotation inside this mesh is matrix free and, therefore, expected to perform computationally efficiently. We evaluate the computational speed of the proposed method against the weighted method in simulations. The efficacy of the method is verified using experimental LAFR-rEIT data.

2 Methods

The finite element mesh for efficient rotational computations was formed for circular 2D computational domain using triangular elements; an example is shown in Fig. 1. The mesh was composed of rotational boundary nodes at given distance from domain boundary, electrode nodes, and nodes out- and inside of rotational boundary. The basis of the proposed construction is that rotational boundary is rotation invariant for angles that are multiples of the intended angular step $360°/N$, where N is the total number of rotational
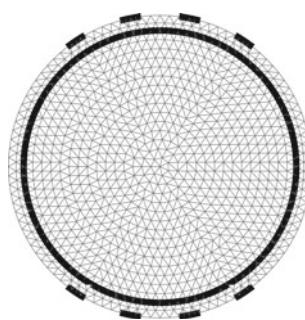
Fig. 1 Rotational boundary, marked with darker, thicker, circular line, is inside the computational domain. Only nodes on and inside the boundary are rotated. Electrodes are marked with darker, thicker short lines

measurement positions. Hence, there are no deformations in the mesh structure during rotation of the inside nodes. The rotation procedure itself can be considered as "clicking" the nodes on the boundary: The xy-coordinates of the rotational boundary and inside nodes are rotated with desired multiple of the step and, since the rotational boundary is invariant to these rotations, each rotated node on the boundary can be paired with a node on same coordinates in initial position. According to these pairs, the elements on the rotational boundary are the remapped to static outer elements.

For the rotational EIT problem, solved in the complete computational domain, we use the stacked forward model [8]

$$V_r = \begin{bmatrix} V_1 \\ V_2 \\ \vdots \\ V_m \end{bmatrix} = \begin{bmatrix} U(M_1\sigma) \\ U(M_2\sigma) \\ \vdots \\ U(M_m\sigma) \end{bmatrix} + n = U_r(\sigma) + n, \quad (1)$$

where U is the forward operator with complete electrode model [9], M_i is the mapping operator for each rotational position, V_i is the measurement data corresponding to conductivity distribution σ inside the sample and n is additive noise term. Inverse problem is solved using Taylor approximation

$$U_r(\sigma) = U_r(\sigma_0) + J_r(\sigma - \sigma_0), \quad (2)$$

where Jacobian is a stack of blocks: $J_r = (JM_i)_j$.

In difference mode EIT, the observation model $\Delta V_r = J_r\Delta\sigma + \Delta n_r$ is the difference between two measurement sets $V_r^{(1)}$ and $V_r^{(2)}$. Reconstruction of the change in conductivity distribution $\Delta\sigma$ inside the sample between first and second measurement is computed from boundary measurements as Tikhonov regularized solution to minimization problem

$$\hat{\Delta}\sigma = arg\,\min_{\Delta\sigma}\left\{\|\Delta V_r - J_r\Delta\sigma\|^2 + \alpha\|L\Delta\sigma\|^2\right\}, \quad (3)$$

where α is the weight given for regularization and L is smoothness promoting regularization matrix [8, 10].

For the weighted method, mapping matrix $M = (M_i)$ is a linear mapping that produces conductivity distribution in rotated coordinates $M_i\sigma$ through matrix multiplication. Elements of $M_i = (j, k)_i$ are the areas of intersection of elementes e_j and e_k, where j-coordinate is in the rotated while k-coordinate is in the original position [8].

We evaluated the speed of weighted and proposed rotations through simulation of rotational acquisitions having 8, 16, 32, 64, 128 or 256 measurement positions. The qualitative accuracy of the reconstructions were assessed using experimental data of a manually rotated gelatin phantom (250 mm in total diameter) in saline bath tank (280 mm in diameter). First measurement for difference EIT reconstruction was

homogeneous gelatin and for the second measurement, resisting inclusion of 29 mm in diameter was included. Measurement was conducted with eight electrodes in use on KIT4 EIT-device [11] and data was acquired from 64 equidistant rotational measurement positions. Experimental protocol is described in detail in our previous work [8].

The speed comparison was performed using EIDORS [12] v3.9 compatible MATLAB R2017a (The MathWorks, Inc.) implementation in Lenovo P51 laptop with Intel i7-7820HQ CPU, 32 GB of RAM and 64-bit Windows 10 operating system. We used complete electrode model with electrode impedance value of $z = 0.01$, and a Laplacian prior with hyperparameter value of 0.06 was chosen for the regularization.

3 Results

Regarding computation times in weighted mapping, most costly process is the formation of weighted mapping $M = (M_i)$. In forward solution, each M_i is implemented as matrix free rotation operation, and for inverse solution, complete M is computed at once and then used for the Jacobian $J_r = (JM_i)$, where J is the Jacobian in initial measurement position, i.e., no rotation. For proposed rotation method, computation of M is not required; however,

each rotational Jacobian block JM_i is computed separately as a single unit from "click" rotated mesh which constitutes for the most time in the inversion procedure.

A comparison of computation times for weighted and proposed methods is shown in Table 1. The advantage of proposed method is imminent in the computing times of the forward problem: proposed method uses only about 3% of the computing time compared to the weighted method. For inversion problem, the computation of Jacobian J_r and inversion itself are about the same order, but with the proposed method, time for creating M is saved.

The meshes used in the computations were composed of from 7290 to 7418 elements for the forward solution and from 1840 to 2160 elements for the inverse solution depending on the number of rotational measurement positions. The sizes of full weighted mapping matrices M are shown in Table 1 as it corresponds to the size of the Jacobian in both methods. The sparsity of M is of order 0.15%.

In Fig. 2, reconstructions from the data of experimental measurements agree qualitatively very well, but are not exactly matching. Using the weighted method, reconstruction in Fig. 2b shows slightly more variation even though smoothness promoting Laplacian prior was used. This is an indication of the local deformations caused by the weighted mapping. On the contrary, the proposed method is smoother

Table 1 Comparison of computation times between weighted and proposed rotation

Rotational measurement positions	8	16	32	64	128	256
Forward weighted (2x)[a]	4 min	9 min	18 min	39 min	75 min	149 min
Forward proposed (2x)[a]	7 sec	16 sec	35 sec	67 sec	2 min	4 min
Weighted inversion: computation of M	16 sec	32 sec	66 sec	136 sec	4 min	11 min
Weighted inversion (including Jacobian)	6 sec	12 sec	23 sec	45 sec	71 sec	128 sec
Proposed inversion (including Jacobian)	6 sec	12 sec	23 sec	47 sec	96 sec	218 sec
Size of full M in memory	0.2 GB	0.4 GB	0.9 GB	1.6 GB	2.8 GB	9.6 GB

[a]Solved for homogenous and non-homogenous samples
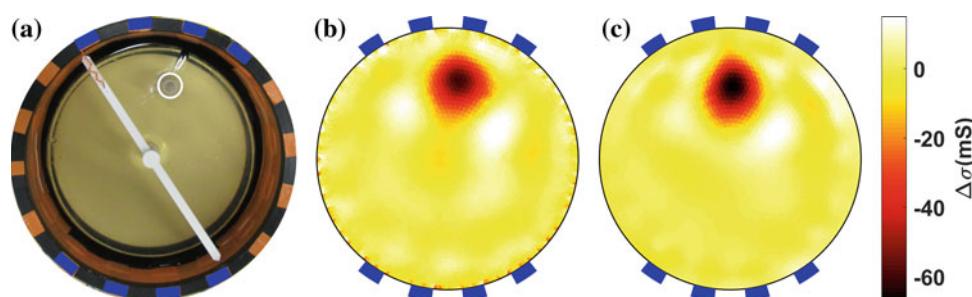
Fig. 2 **a** Photo of the gelatin sample and measurement tank, **b** reconstruction using the weighted method and **c** reconstruction using the proposed method

with the same hyperparameter value, indicating robustness against noise.

4 Conclusions

In this work, we have presented a rotational mesh construction that removes the dependency between electrode positions and rotational measurement positions in rEIT. Further, we have significantly decreased the computation time when compared to our previous rotational algorithm. Presented rotation procedure is applicable to any computational domain, where rotated object is bounded during rotation to a radius that is less than distance from center-of-rotation to closest electrode. Proposed method is efficiently extensible into 3D. Further optimization may be achieved by keeping the rotational mapping M and/or Jacobian matrix J_r in memory for consecutive uses, or through matrix-free implementation exploiting the block-structure of J_r.

Conflicts of Interest The authors declare that there are no conflicts of interests.

References

1. Holder, D.S.: Electrical impedance tomography: methods, history and applications. CRC Press (2004)

2. Huang, C.N., Yu, F.M., Chung, H.Y.: The scanning data collection strategy for enhancing the quality of electrical impedance tomography. IEEE Transactions on Instrumentation and Measurement **57** (6), 1193–1198 (2008)

3. Zhang, X., Chatwin, C., Barber, D.: A feasibility study of a rotary planar electrode array for electrical impedance mammography using a digital breast phantom. Physiological measurement **36**(6), 1311 (2015)

4. Murphy, E.K., Mahara, A., Halter, R.J.: Absolute reconstructions using rotational electrical impedance tomography for breast cancer imaging. IEEE Transactions on Medical Imaging **36**(4), 892–903 (2017). https://doi.org/10.1109/tmi.2016.2640944

5. Soleimani, M.: Electrical impedance tomography imaging using a priori ultrasound data. Biomedical engineering online **5**(1), 8 (2006)

6. Borsic, A., Syed, H., Halter, R., Hartov, A.: Using Ultrasound Information in EIT Reconstruction of the Electrical Properties of the Prostate. In: Conf EIT (2011)

7. Crabb, M.G., Davidson, J.L., Little, R., Wright, P., Morgan, A.R., Miller, C.A., Naish, J.H., Parker, G.J.M., Kikinis, R., McCann, H., Lionheart, W.R.B.: Mutual information as a measure of image quality for 3D dynamic lung imaging with EIT. Physiological Measurement **35**(5), 863 (2014)

8. Lehti-Polojärvi, M., Koskela, O., Seppänen, A., Figueiras, E., Hyttinen, J.: Rotational electrical impedance tomography using electrodes with limited surface coverage provides window for multimodal sensing. Measurement Science and Technology (2017)

9. Somersalo, E., Cheney, M., Isaacson, D.: Existence and uniqueness for electrode models for electric current computed tomography. SIAM Journal on Applied Mathematics **52**(4), 1023–1040 (1992)

10. Vauhkonen, M.: Electrical Impedance Tomography and Prior Information. Ph.D. thesis, University of Kuopio (1997)

11. Kourunen, J.: Imaging of mixing in selected industrial processes using electrical resistance tomography. Ph.D. thesis, University of Eastern Finland (2014)

12. Adler, A., Lionheart, W.R.: Uses and abuses of EIDORS: an extensible software base for EIT. Physiological measurement **27**(5), S25 (2006)

Multifunctional Photoplethysmography Sensor Design for Respiratory and Cardiovascular Diagnosis

Durmus Umutcan Uguz, Boudewijn Venema, Steffen Leonhardt, and Daniel Teichmann

Abstract

Photoplethysmography (PPG) is a transcutaneous optical signal acquisition method to monitor blood volume variations to assess cardiovascular health. Using a light source and a photodetector, PPG signals can be acquired and used in a vast application area. For the estimation of vital parameters like respiratory and heart rate, different properties of this pulsatile wave need to be further analyzed. This demands the utilization of different sensor techniques to be used like motion sensors, skin temperature monitoring and different wavelengths of light sources. This paper represents the proposed multipurpose PPG sensor design, called SmartPPG, which is able to measure multi-wavelength PPG from different skin penetration depths as well as skin temperature while providing motion tracking via an accelerometer. The manufactured prototype was tested for different PPG techniques to evaluate its applicability for arterial, venous and respiratory diagnosis.

Keywords

Photoplethysmography • Pulse oximetry • Respiratory rate Cardiovascular diagnostic • Venous muscle pump test

1 Introduction

Thanks to the improvements in the modern medicine, life expectancy has been increasing enormously. In addition to aging society, changes in lifestyle and habits of people made cardiovascular disease (CVD) prevalent, which accounts for the 40% of all deaths at ages younger than 75 in Europe [1]. This trend is also seen in the increasing number of diabetes mellitus patients. 75% of deaths in diabetics are due to coronary artery disease [2].

These statistics underline the importance of continuous and noninvasive monitoring of cardiovascular health to improve the quality of healthcare systems through preventive medicine. PPG offers noninvasive, cost-efficient solutions to everyday applications using sensors which do not cause a disturbance to the patients. Wide area of PPG applications makes it susceptible to motion artifacts as the measurements are not taken in a steady and standardized position. This creates the necessity of artifact reduction in PPG signals.

PPG has found itself several applications also in clinical diagnosis to assess the cardiovascular health. An example of this is the venous muscle pump test in which venous refilling time is measured to diagnose chronic venous insufficiency [3]. These examples can be extended to the arterial oxygen saturation measurement, assessment of arterial compliance [4], heart rate variability and respiratory rate [5].

Patent applications for multimodal PPG techniques aiming to differentiate skin layers for the monitoring of hemodynamics [6, 7] have been influential in this sensor design. The proposed design aims to provide end-users with a PPG sensor providing adequate signal quality in different PPG applications. As it claims multifunctionality, it was aimed to test the applicability of the design to these applications. Measurements were conducted on a small number of participants. The preliminary results of this study was presented at 21th International Student Conference on Electrical Engineering, POSTER 2017 Prague.

D. U. Uguz (✉) · S. Leonhardt · D. Teichmann
Chair for Medical Information Technology, RWTH Aachen University, Pauwelsstr. 20, 52074 Aachen, Germany
e-mail: uguz@hia.rwth-aachen.de
URL: https://www.medit.hia.rwth-aachen.de/en/

B. Venema
Department of Optical Sensors, Huf Huelsbeck & Fuerst GmbH & Co. KG, Steeger Str. 17, 42551 Velbert, Germany

2 Design of the Multifunctional Sensor

2.1 Photoplethysmography

PPG has two main modes: transmission and reflection modes. Transmission mode is limited to thin body parts such as finger and earlobe, whereas, a light source illuminates the skin at the same side with the light detector in reflection PPG, which offers wider range of measuring sites on the body. In a reflection-PPG sensor, there are two main optimization parameters: wavelength of the light and the distance between light source and the photodetector.

Extinction coefficient of hemoglobin is wavelength-dependent, which is utilized in pulse oximeters where at least two different wavelengths of light are used. In single wavelength PPG, mostly near-infrared light sources are used, whereas, different wavelengths could be more reliable for the measurements in which temperature changes take place in the environment [8].

The distance between the light source and the photodetector has a dramatic effect on the tissue penetration depth. By increasing the distance between LED and photodiode, deeper layers of the skin can be illuminated and monitored [9].

2.2 Auxiliary Measurement Techniques

PPG signals are heavily distorted with motion artifacts as these artifacts mostly lay in the same frequency band with the signal [10]. Solutions against this problem might be independent component analysis (ICA) [11] and using adaptive filters [12]. SmartPPG can measure more than one wavelength simultaneously, which allows ICA to be employed. Moreover, the accelerometer on the board allows noise cancellation techniques using motion tracking.

Skin temperature, affected by sympathetic and parasympathetic nervous systems, is an auxiliary tool to evaluate PPG signals. Peripheral vascular system is strongly coupled with body temperature regulation due its role in it. Monitoring of skin temperature on different locations can be used to detect sepsis or to evaluate acute stress [13].

2.3 Design on PCB

Considering these factors, the proposed design was produced as a circular two-sided PCB with a diameter of 21 mm. The final design without housing can be seen in Fig. 1. Optoelectronic components lay on the front side. Two photodiodes lay on the central vertical axis, whereas, to the right and to the left there are two infrared LEDs which are in-series connected. These two serve to illuminate a larger
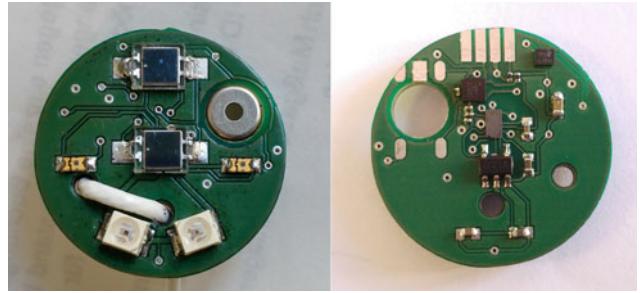
Fig. 1 Front (on the left) and back (on the right) sides of SmartPPG before housing is mounted. Diameter of PCB is 21 mm and it reaches total thickness of 4.8 mm after the housing is mounted

measurement region to reduce the susceptibility to contact imperfections. At the bottom, there are one infrared and one red LEDs. These can be operated time-multiplexed as in pulse oximetry. Two photodiodes provide different paths for photons traveling through the tissue, which allows users to change the effective skin penetration depth depending on the application.

On the back (right hand side) side of the PCB in Fig. 1, peripheral ICs can be seen. ADPD105 is an optical front end with a 14-Bit analog-to-digital converter. It offers operation of 2 optical sensing units and 3 LEDs with ambient light rejection, flexible sampling rate and LED current [14]. On this prototype, LIS2HH12TR is used as accelerometer offering three-axis linear 16-bit measurements [15]. M24C16 is a 16-KB EEPROM and can be read and written [16]. It serves to store important parameters on the sensor to be used during initialization or calibration. MLX90615 is a high accuracy infrared thermometer which can deliver measurements with a measurement resolution of 0.02 K [17]. All peripheral ICs are controlled using I^2C communication protocol, using microcontroller MSP432 during the tests.

The prototype is enclosed in a housing from material LUXACRYL-IR (TTV GmbH, Germany). The housing has only openings for the thermometer, photodiodes, and LEDs at the bottom, whereas, the in-series connected IR-LEDs are enclosed with this material which is transparent to IR light. Each optoelectronic component has a carved light barrier around its face to block interaction through direct light paths.

3 Results

3.1 Arterial Diagnostic

PPG signals can be used to calculate pulse rate (PR) and pulse rate variability (PRV). The former is a good estimator of HR, whereas, PRV may differ from heart rate variability (HRV) due to pre-ejection period and pulse transit time variability [18]. HR measurements were conducted on 4
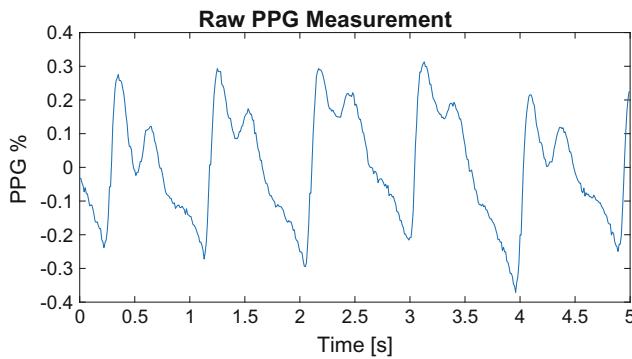
Fig. 2 Raw PPG signal without any filter

participants (male, ages 25–30, healthy) for 1-minute-long recordings. PR measurements were compared to HR measurements from a bedside patient monitor (Philips IntelliVue MX700) ECG measurements. Corresponding Bland-Altman plot, after eliminating from measurements distorted with motions artifacts, can be seen in Fig. 3.

Not only beat-to-beat interval but also the morphology of the PPG signal contains several information. The shape of the signal can be used to derive a stress index [19] and the second derivative of the signal can be used to assess cardiovascular health [20]. In the proposed design, photocurrents are digitized in few millimeters away from photodiodes enclosed by an optical housing, which improves signal quality. A sample of PPG signal without any filter operation can be seen in Fig. 2.

For the measurement of arterial oxygen saturation (S_pO_2), the model between ratio-of-ratios (RoR) and S_pO_2 needs to be derived experimentally in a clinical trial as Beer-Lambert Law does not consider the scattering effect of the tissue [21]. In this study, without any clinical trial, only RoR values were calculated. No significant variation was observed as all the

participants remained in a physiological state in which S_pO_2 is not expected to change.

3.2 Venous Diagnostic

Venous muscle pump test (VMPT), in which the patient executes calf extension while sitting, measures the venous refilling time (VRT), after the venous blood filling is decreased through muscle compression. An example measurement made on the leg of a participant can be seen in Fig. 4. This refilling time is much shorter in case of unhealthy venous valves due to pathologic reflux [3]. Individuals with VRT longer than 20 s are interpreted to have healthy venous valves [22]. Using SmartPPG's accelerometer, this test can also be automated. Moreover, different skin depth property of the design combined with different wavelengths may help to differentiate between microcirculation and larger veins.

3.3 Respiratory Assessments

Respiratory and cardiovascular systems are strongly coupled. For example, sinus rhythm of heart shows variations with respiration, which is called respiratory sinus arrhythmia (RSA) [23]. PPG signals can be used to estimate the respiratory rate (RR) most prominently in three ways: variation of HR as an autonomic response to respiration called respiratory-induced frequency variation (RIFV), variation in the perfusion baseline due to the intrathoracic pressure variation called respiratory-induced intensity variation (RIIV) and variation in the peripheral pulse strength due to changing ventricular filling called respiratory-induced amplitude variation (RIAV) [24]. These three variation sources can be seen in Fig. 5.
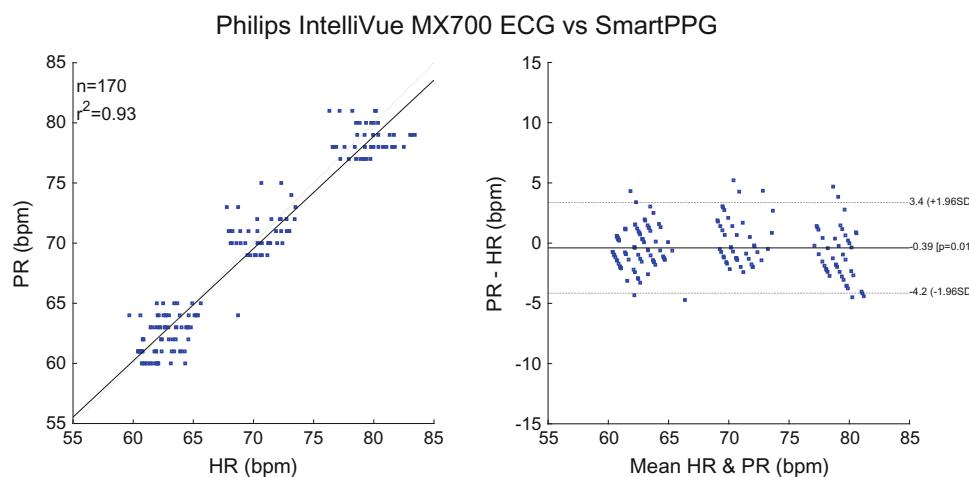
Fig. 3 Bland-Altman plot of PR measurements from SmartPPG comparing to HR values derived from ECG
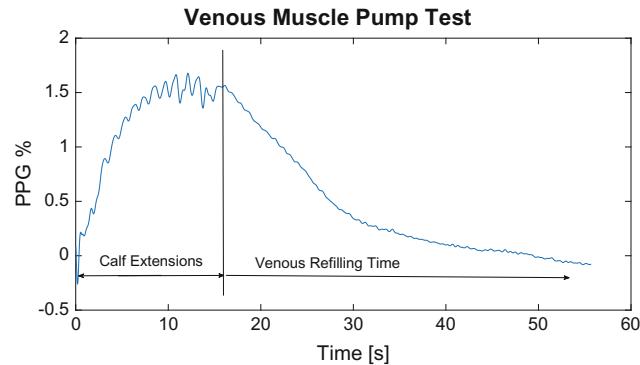
Fig. 4 VMPT showing VRT is around 30 s for a health participant
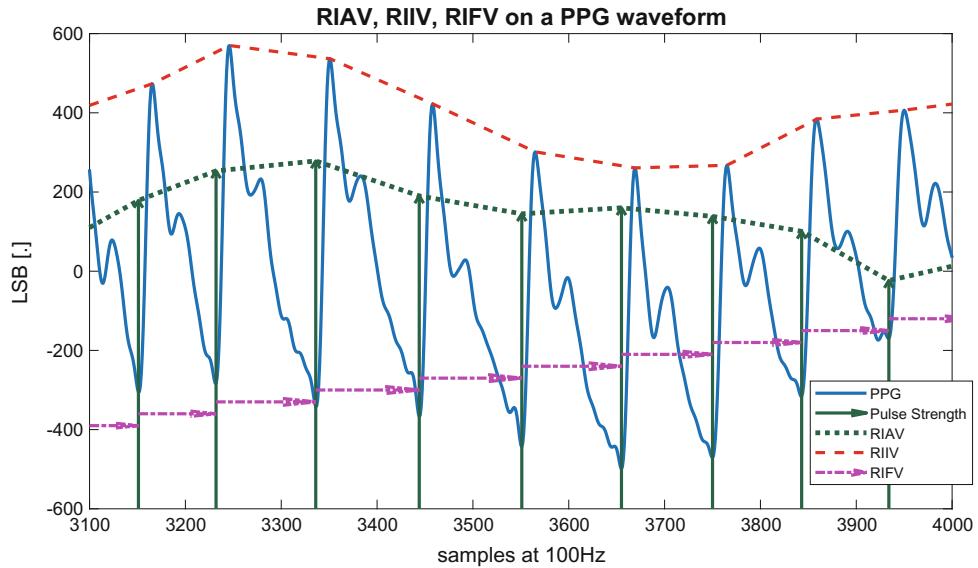
Fig. 5 Respiratory-induced variations in a PPG signal. The effects of respiration on a PPG signal can be seen in 3 different ways: RIAV, RIIV, RIFV

In this figure, the length of the pink arrows corresponds to each heart beat. Thus, the length variation (inverse of heart rate) of these arrows can be observed as RIFV. Green arrows for the pulse strength have been drawn with the same baseline level of −600 for demonstrative purposes. Using their length, RIAV can be followed. Whereas RIAV depends on the amplitude of the pulse, RIIV includes also the information of main baseline of PPG signal. This can be seen in the dashed red line. For test purposes, the result of these three estimations were combined in a fusion algorithm as following:

$$RR = \begin{cases} Average(RIFV, RIAV, RIIV) & \text{if } \sigma \leq 1 \\ Median(RIFV, RIAV, RIIV) & \text{if } 1 < \sigma \leq 4 \\ RIFV & \text{if } \sigma > 4 \end{cases}$$

This algorithm observes the standard deviation (σ) of three estimations: RIFV, RIAV, RIIV. A small σ indicates consistent estimations, whereas, a larger σ suggests an

erroneous estimation for at least one of these three methods. For the worst case scenario, RIFV is chosen since RSA is more reliable phenomenon and is calculated by each heart beat length which is less susceptible to noise in amplitude. The result of an experiment for RR estimation on a participant (male, 25, healthy) can be seen in the Fig. 6. The participant regulated his RR using a metronome for 5 discrete values.

4 Conclusions

Photoplethysmography has found several applications both in clinic and research, which requires multipurpose sensor designs that are able to meet various task-specific requirements. The proposed design provides time-multiplexed measurements of 4 channel PPG recordings from the combination of 2 photodiodes (different skin layers) and 2
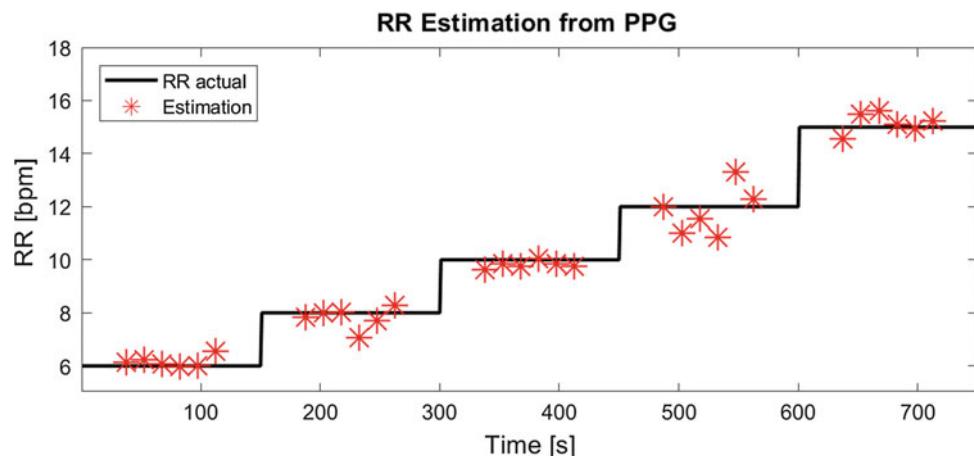
Fig. 6 RR estimations using suggested algorithm. During 6 min long measurement session, the algorithm was tested with 5 different respiratory rates

different wavelength (red and near infrared), with a flexible sampling up to 3 kHz.

Ethics Statement and Conflict of Interest The Institution's Ethical Review Board approved all experimental procedures involving human subjects under the reference code EK 024/18. The authors declare that they have no conflict of interest.

References

1. J. Perk, G. De Backer, H. Gohlke, I. Graham, Ž. Reiner, W.M. Verschuren, C. Albus, P. Benlian, G. Boysen, R. Cifkova, et al., Atherosclerosis **223**(1), 1 (2012)
2. P.T. O'gara, F.G. Kushner, D.D. Ascheim, D.E. Casey, M.K. Chung, J.A. De Lemos, S.M. Ettinger, J.C. Fang, F.M. Fesmire, B.A. Franklin, et al., Circulation **127**(4), 529 (2013)
3. U. Schultz-Ehrenburg, V. Blazek, Skin Pharmacology and Physiology **14**(5), 316 (2001)
4. Q. Yousef, M. Reaz, M.A.M. Ali, Measurement Science Review **12**(6), 266 (2012)
5. N. Blanik, A.K. Abbas, B. Venema, V. Blazek, S. Leonhardt, Journal of biomedical optics **19**(1), 016012 (2014)
6. V. Blazek. Vorrichtung und verfahren zur optoelektonischen, bewegungsartefakte-kompensierten erfassung und hauttiefenselektiver analyse der beinvenenhämodynamik (2010). Dt. Patentanmeldeschrift 10 2010 056 503.2
7. C. Blazek, V. Blazek. Bewegungskorreliertes verfahren und optoelektronische vorrichtung zur nichtinvasiven bestimmung der dermalvenösen sauerstoffversorgung peripherer beingebiete (2011). Dt. Patentanmeldschrift 10 2011 122 700.1
8. Y. Maeda, M. Sekine, T. Tamura, Journal of medical systems **35**(5), 829 (2011)
9. Y. Mendelson, B.D. Ochs, IEEE Transactions on Biomedical Engineering **35**(10), 798 (1988)
10. M.J. Hayes, P.R. Smith, IEEE Transactions on Biomedical Engineering **48**(4), 452 (2001)
11. B.S. Kim, S.K. Yoo, IEEE transactions on biomedical engineering **53**(3), 566 (2006)
12. H. Han, M.J. Kim, J. Kim, in *Engineering in Medicine and Biology Society, 2007. EMBS 2007. 29th Annual International Conference of the IEEE* (IEEE, 2007), pp. 1538–1541
13. K.A. Herborn, J.L. Graves, P. Jerem, N.P. Evans, R. Nager, D.J. McCafferty, D.E. McKeegan, Physiology & behavior **152**, 225 (2015)
14. Analog Devices, *ADPD105 Photometric Front End with I²C* (2016). Rev. 0
15. STMicroelectronics, *LIS2HH12 MEMS digital output motion sensor: ultra-low power high performance 3-axes pico-accelerometer* (2015). Rev. 5
16. STMicroelectronics, *M24C16 16-Kbit serial I²C bus EEPROM* (2016). Rev. 8
17. Melexis Microelectronic Integrated Systems, *MLX9061 Infrared Thermometer* (2008). Rev. 8
18. A. Schäfer, J. Vagedes, International journal of cardiology **166**(1), 15 (2013)
19. V. Blazek, N. Blanik, C.R. Blazek, M. Paul, C. Pereira, M. Koeny, B. Venema, S. Leonhardt, Anesthesia & Analgesia **124**(1), 104 (2017)
20. K. Takazawa, N. Tanaka, M. Fujita, O. Matsuoka, T. Saiki, M. Aikawa, S. Tamura, C. Ibukiyama, Hypertension **32**(2), 365 (1998)
21. J.G. Webster, *Design of pulse oximeters* (CRC Press, 1997)
22. A. Fronek, Dermatologic surgery **21**(1), 64 (1995)
23. P. Grossman, E.W. Taylor, Biological psychology **74**(2), 263 (2007)
24. W. Karlen, S. Raman, J.M. Ansermino, G.A. Dumont, IEEE Transactions on Biomedical Engineering **60**(7), 1946 (2013)

Microwave and Impedance Spectroscopy as a Useful Tool for Testing Dielectric Properties of Glucose Solutions

Izabela Osiecka and Tadeusz Pałko

Abstract

Diabetes is one of the most common social disease in the world. Due to the patient discomfort associated with sample collection using a commercially available devices, there is a great need to design a more favorable and precise sensor of blood glucose level. Promising techniques are based on the correlation between glucose-induced variations and blood dielectric properties. This report presents two possible methods showing the variations of impedance modulus and relative permittivity values in glucose-sodium chloride (0.9%) and glucose-bovine plasma solutions at different concentrations, ranging from 50 to 500 mg/dl, occurring in human blood. It is worth noticing, that in each sample the dielectric properties depend on the glucose concentration of the sample over the whole studied range, that is 1 kHz–2 MHz for impedance measurements and 100 MHz–5.5 GHz for microwave spectroscopy. The experimental results as well as discussion of the results, are presented in this paper.

Keywords

Permittivity • Glucose • Microwaves • Impedance spectroscopy

1 Introduction

As statistics show, diabetes is one of the most common social disease in the world. Currently, it is calculated, that 1 in 11 adults have diabetes, which means over 425 mln cases, including 212 mln who are undiagnosed. If this rise is not halted, there will be 629 million people by 2045 living with the disease [1]. Therefore, it is very important for diabetes to be diagnosed as early as possible, because it will get progressively worse if left untreated. Nowadays, measuring glucose level and regular monitoring of insulin is the only way to keep the patient safe. Conventional techniques, based on finger pricking and electrochemical or optical detection are unpleasant in terms of multiple punctures per day. Studies carry out by scientists around the world are going to make this process less painful as well as inexpensive and one the feasible options is to use spectroscopic technique. Many reports presented in literature confirmed the fact, that changes in blood glucose concentration levels, even in the physiological range (from 70 to 100 mg/dl) influence the dielectric properties of a tissue. Those dielectric properties are understood as features of the conduction of electrical current through the tissue without triggering effect of stimulation [2, 3]. In this article, the dependence of dielectric properties of the studied solution on glucose concentration is presented.

2 Materials and Methods

The normal level of blood glucose concentration is in the range from 70 to 100 mg/dl. Soon after every meal it may raise to a maximum of 140 mg/dl. High blood glucose concentration is called hyperglycaemia (>200 mg/dl) and low levels are referred to as hypoglycaemia (<70 mg/dl). For the preparation of the first set of samples we use 0.9% sodium chloride and glucose. First, we prepared our stock solution by diluting 500 mg of glucose in 100 ml of 0.9% sodium chloride. Then, we used diluting method to obtain the solution with the following concentrations: 50, 85, 150 and 500 mg/dl. The next set with the same concentrations and method was prepared by diluting glucose in bovine calf plasma (Sigma-Aldrich; stored in refrigerator in 4 °C).

Measurements on test samples were made within 24 hours from preparation. The dielectric properties in the

I. Osiecka · T. Pałko (✉)
Institute of Metrology and Biomedical Engineering, Warsaw University of Technology, Warsaw, Poland
e-mail: t.palko@mchtr.pw.edu.pl

I. Osiecka
e-mail: i.osiecka@mchtr.pw.edu.pl
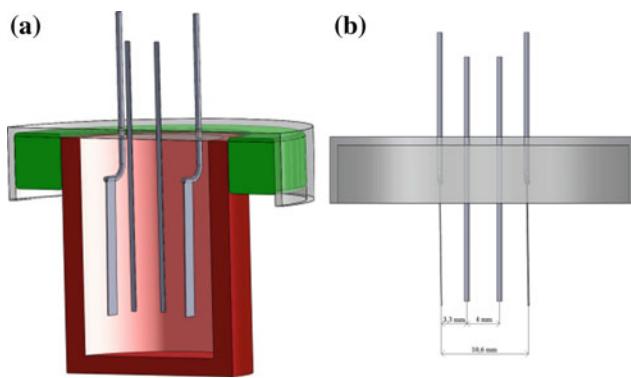
Fig. 1 **a** Visualization of glucose sensor model based on impedance spectroscopy, **b** spacing of platinum electrodes

prepared solutions were measured by two separate systems: a self-made impedance modulus sensor and an open-ended coaxial for measurement electrical permittivity.

The impedance of the sample was measured by tetrapolar current method using sinusoidal current. The system applied for impedance measurement is shown in Fig. 1. The range of frequency changes of the applied current was from 5 kHz to 1 MHz. The advantage of focusing on frequency values below 1 MHz for possible clinical applications may consist in lower sensitivity to the electromagnetic noise in the environment. As a result we observed that the increasing glucose concentration entails the increase in impedance modulus [4].

The second concept of measuring the permittivity ε of the tested solutions assumed the use of a measurement system with the Hewlett Packard HP vector network analyzer (VNA) in the frequency range from 100 MHz to 5.5 GHz in accordance with the following Fig. 2.

The applied microwave technique based on measuring the coaxial open line to half-space partially filled with the test solution allowed to determine the real and imaginary component of the relative permittivity of the sample [5]. According to the theory, the electric field of the propagated coaxial wave penetrates into the thin layer of the tested

material. Its permittivity affects the value of the complex reflection coefficient of the formed end of the line.

3   Results and Discussion

The relative permittivity ε is defined in accordance with the following relationship:
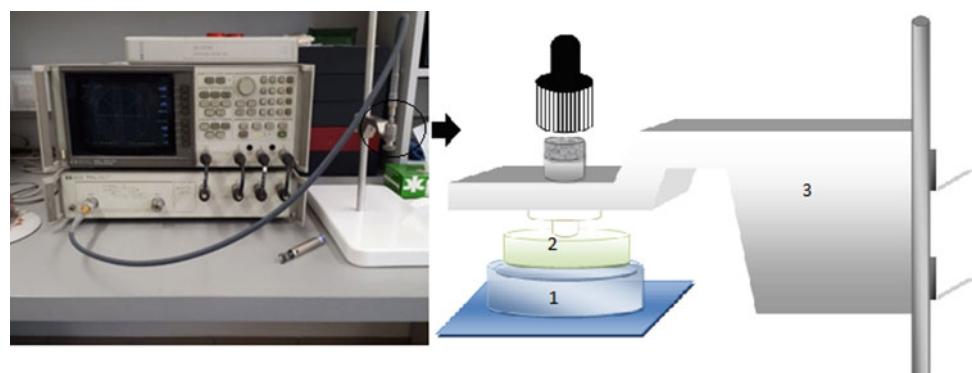
$$\varepsilon_r = \frac{\varepsilon}{\varepsilon_0} = \varepsilon'_r - j\varepsilon''_r \tag{1}$$

During the measurement, the real component ε'_r and the imaginary component ε''_r of the relative permittivity were determined. The results obtained for individual samples are presented in the following Figs. 3, 4, 5, 6, 7 and 8.

According to the literature reports, the dissolving glucose molecules are combined with polar water molecules, which react to the appearance of an external electric field by changing their position. The more such connections are observed, the lower the response speed is, and thus the frequency of relaxation and the value of effective electrical permittivity decrease [6, 7]—which means-that as the concentration of glucose in aqueous solutions increases, the permittivity decreases.

The measurements were repeated for a series of samples with distilled water, 0.9% sodium chloride and bovine calf. Figure 3 shows the results of measurements of permittivity component for water solutions which are confirmed by literature data [8]. However, contrary to water, 0.9% sodium chloride measurements show an increase in dielectric permeability compared to the increase in glucose concentration in the samples (see Figs. 4 and 5). Similarly, the results are shaped by the data obtained during the measurement series with the use of calf plasma solutions (see Figs. 6 and 7). Moreover, the decrease in the value of the imaginary component of the permittivity ε″ observed at the lowest frequency values was probably caused by ionic loss of conductivity. In addition, as can be seen in the Figs. 3, 4, 5, 6 and 7, there is a differentiation between each of the

Fig. 2 Hewlett Packard HP 8753C vector network analyzer (VNA) (1—measurement head, 2—measuring element, 3—tripod and a suitable gripper)
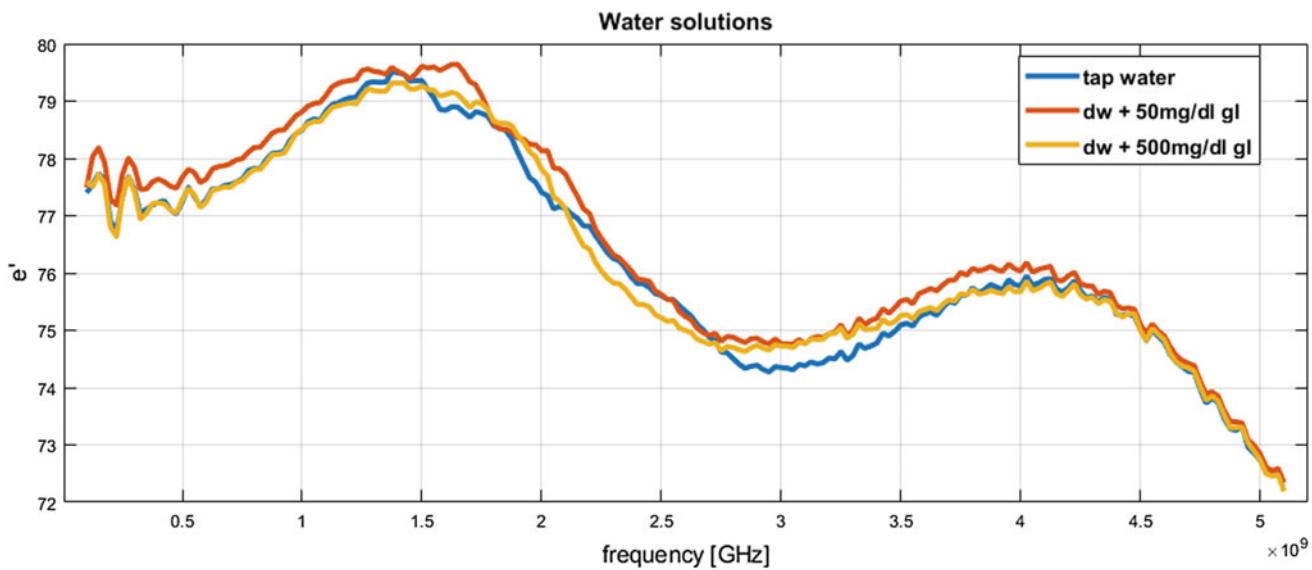
Fig. 3 Characteristics of dependence of real component of permittivity on the frequency in water solutions (orange-distilled water with gl. conc. 50 mg/dl, yellow-dist. water with gl. conc. 500 mg/dl) (Color figure online)
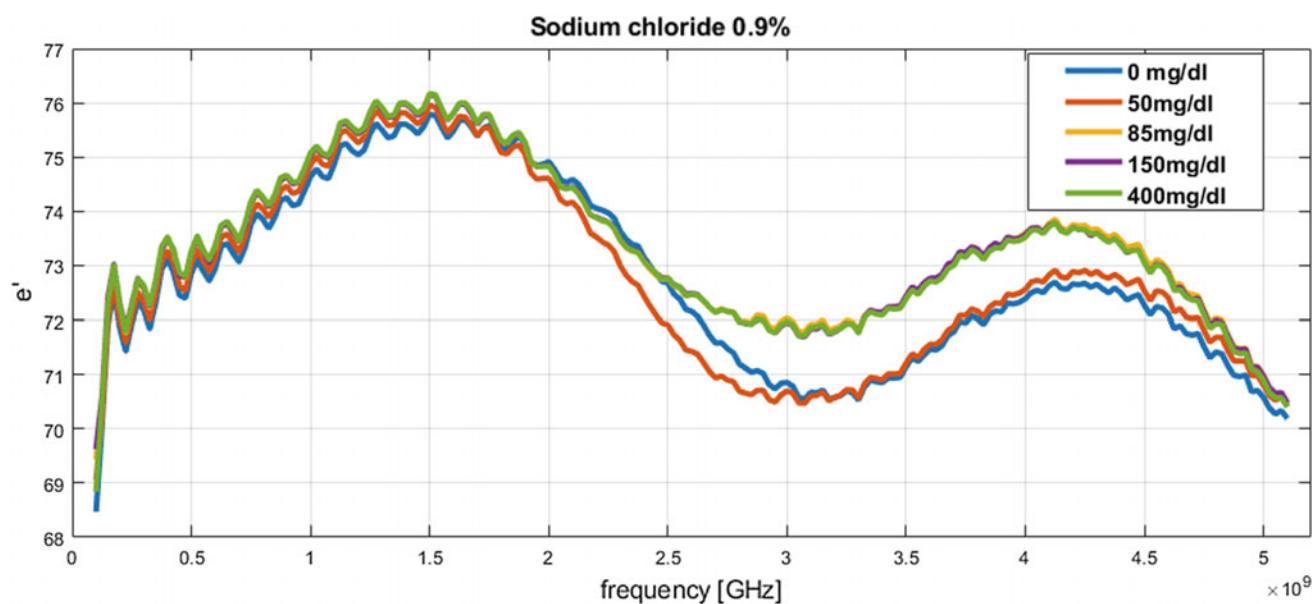
Fig. 4 Characteristics of the dependence of real component of permittivity on the frequency of saline solutions (glucose concentration range from 50 to 500 mg/dl)
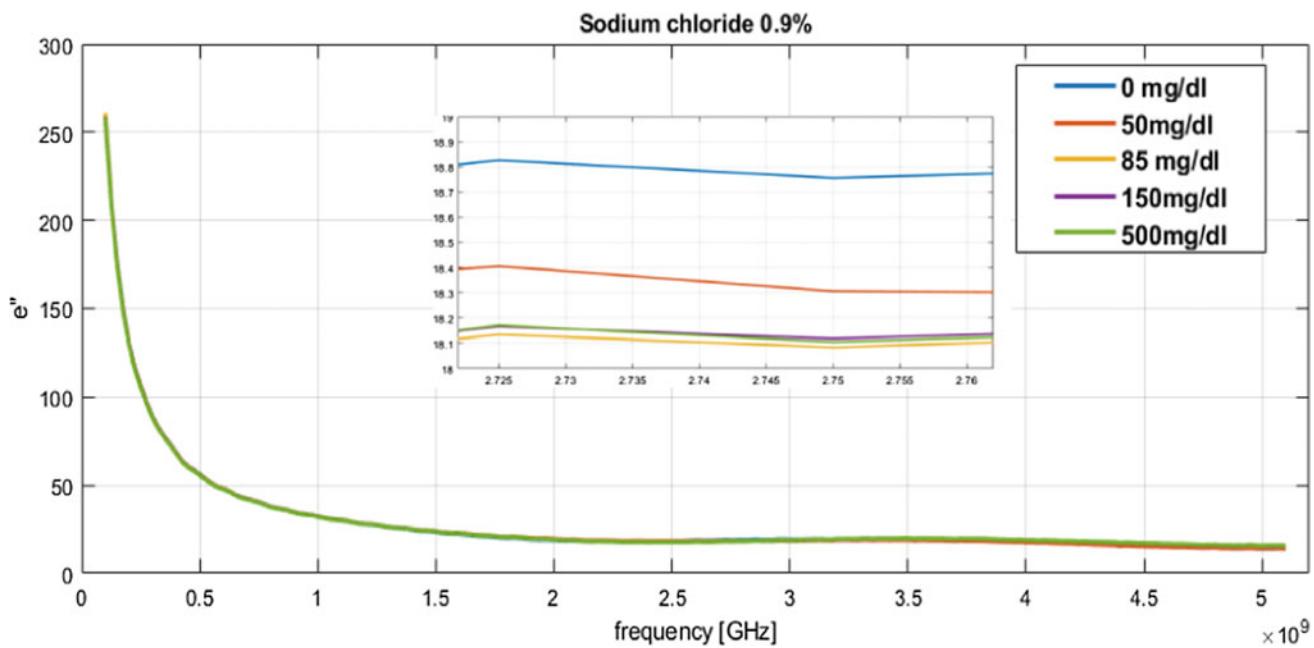
Fig. 5 Characteristics of dependence of the imaginary component of permittivity as a function of frequency (glucose concentration range from 50 to 500 mg/dl)
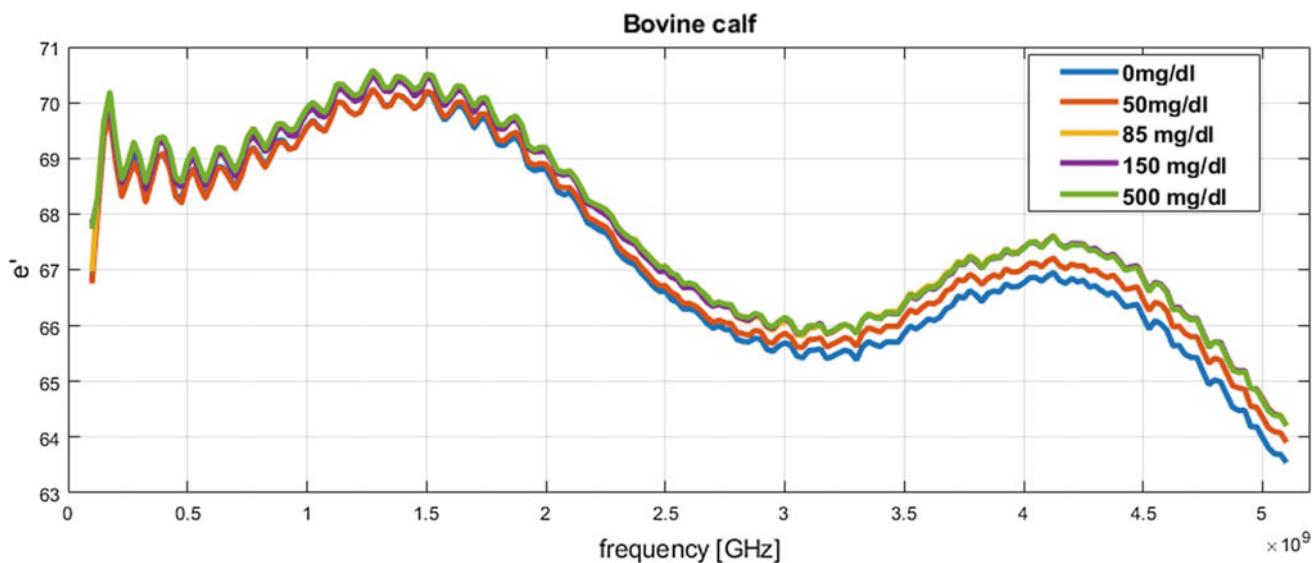
Fig. 6 Characteristics of the dependence of real component of permittivity on the frequency of solutions with calf plasma (glucose concentration range from 50 to 500 mg/dl)
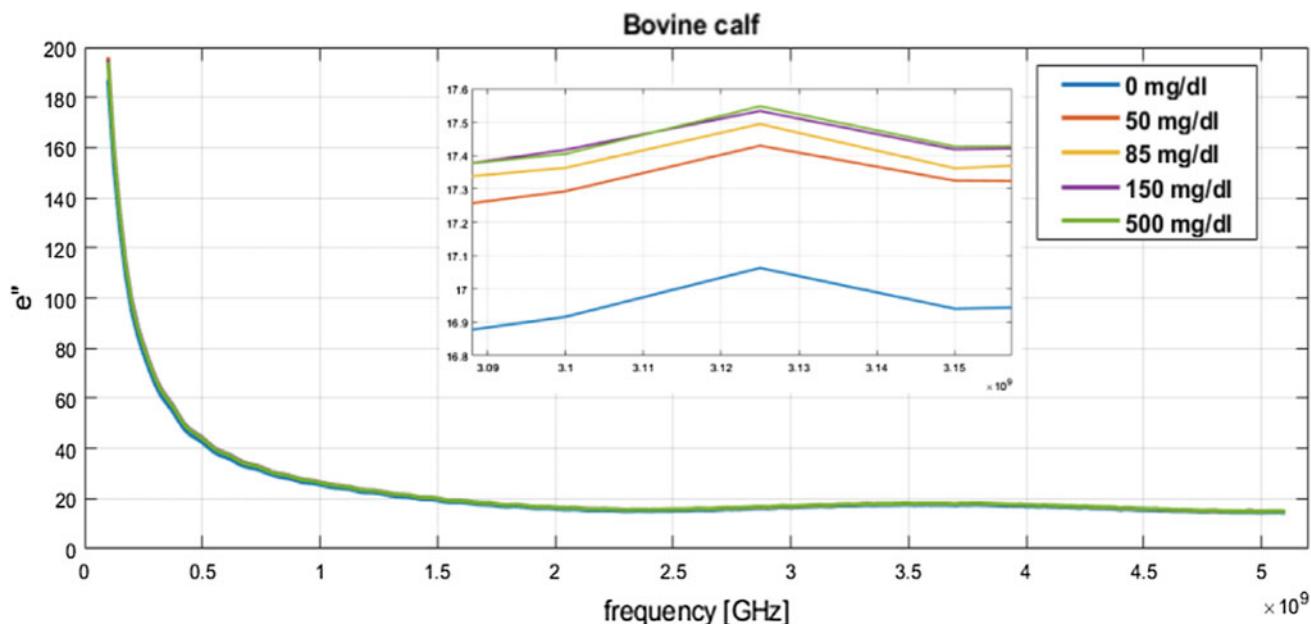
Fig. 7 Characteristics of dependence of the imaginary component of permittivity as a function of frequency (glucose concentration range from 50 to 500 mg/dl)

concentrations used and the appropriate up sequence is maintained. These surprising results can be caused by ineffective mixing of the tested aqueous solutions of glucose. The problem requires further investigation, which may explain the reported issue.

4 Summary and Conclusions

The easy and inexpensive method for measurement of glucose concentration in human blood is a very important and difficult question. Many scientists are struggling with this problem using different techniques. The paper presents two promising spectroscopic (microwave and impedance) methods, which may lead to the development of a multi-sensor for detecting glucose concentration. However, it requires further investigations in the near future.

Conflict of Interest The authors declare that they have no conflict of interest.

References

1. IDF Diabetes Atlas 2017, http://www.diabetesatlas.org/ IDF Diabetes Atlas, Eighth Edition, last accessed 23/01/2018
2. Pawlicki, G., Pałko, T., Golnik, N., et al.: Fizyka Medyczna, Akademicka Oficyna Wydawnicza, Warszawa (2002)
3. Palko T, Galwas, B.: Electrical and dielectric properties of biological tissue, Proc. Of 11th Intern. Microwave Conf. MIKON'96, Workshop Biomedical Applications of Microwaves, Warszawa (1996)
4. Osiecka, I., Pałko, T., et al.: Impedance spectroscopy as a method for the measurement of calibrated glucose solutions with concentration occuring in human blood. In: Recent Global Research and Education: Technological Challenges/ Jabłoński R., Szewczyk R. (red.), Advances in Intelligent Systems and Computing, 519, 211–216, Springer International Publishing (2017)
5. IT studies, http://wazniak.mimuw.edu.pl/index.php?title=TTS_Modu%C5%82_3, last accessed 24/01/2018
6. Saito, A., et al.: Dielectric relaxation of aqueous solutions with low-molecular weight nonelectronlytes and its relationship with solution structure. Bioscience, Biotechnology and Biochemistry 61 (11), 1831–1835 (1997)
7. Meriakri, V.V., et al.: Dielectric properties of glucose solutions in the millimeter-wave range and control of glucose content in blood. Measurements Science and Technology 18(4), 1–6 (2007)
8. Karacolak, T., et al.: Cole-cole model for glucose-dependent dielectric properties of blood plasma for continuous glucose monitoring. Microwave and Optical Technology Letters, 55(5), 1160–1164, (2013)

Changes of Body Composition and Bioimpedance During Pregnancy—Pilot Study in Czech Republic

J. Hlubik, K. Radocha, L. Lhotska, and L. Hruban

Abstract

Monitoring of specific physiological values during gestation process is a very important process. Body composition values and directly measured bioimpedance values however are currently not included into this monitoring although these values can help to track healthy process of gestation. In this work we are presenting new possible measurements of progress of body composition and electrical values during whole gestation process in Czech population. Bioelectrical resistance, reactance and body composition values were measured by BIA device Tanita MC 180 MA on 5, 50, 250 and 500 kHz. BIA measurements from 10 women were evaluated during second and third trimester of pregnancy. We discovered changes in directly measured electrical values and calculated values during a gestation period. Statistically significant increase was discovered in calculated body composition values: Weight (kg) (P = 0.005), Fat mass (kg) (P = 0.01), TBW (kg) (P = 0.005). Statistical significant (P = 0.05) decrease on all used frequencies was discovered in resistance and reactance values. Average decrease of resistance across all frequencies was 73.17 ± 7.62 Ω which presented $11.92 \pm 0.07\%$. Results suggest that body composition values and especially directly measured values that are not equation dependent can give precise description for gestation process and can be used as one of the markers of healthy gestation process in future. Hence this measuring and evaluating of directly measured electrical values and body composition values can give us more information about gestation process.

1 Introduction

Bioimpedance and BIA (bioimpedance analysis) becomes a non-invasive medical diagnosing technique in the past decades [1].

Currently multi frequency bioelectrical impedance analysis (MF-BIA) is often used as a method for assessment of body composition values such as TBW (total body water), FFM (fat free mass), Fat mass, ECW, etc. [2].

There were only few research studies published in the field of body composition and bioimpedance evaluation during pregnancy on European women. These studies are describing and setting reference ranges in Italian women gestation period in terms of body composition [3, 4]. The studies and guidelines that are observing the pregnancy are mainly focused on weight gain IOM [5] and BMI of a pregnant woman.

However, it also has to be considered that measurements of body composition are race specific and this can cause different outcome for different populations.

2 Patients Characteristics

Each patient previously attended medical consultation at University Hospital in Brno at the Clinic of Obstetrics and Gynecology. Before the beginning of measurements each woman was medically examined by an obstetrician and

J. Hlubik (✉) · L. Lhotska
Czech Institute of Informatics, Robotics and Cybernetics, Czech Technical University in Prague, Prague, Czech Republic
e-mail: Hlubikjan@post.cz

K. Radocha
Faculty of Science, University of Hradec Kralove, Hradec Kralove, Czech Republic

L. Hruban
Department of Gynecology and Obstetrics, Teaching Hospital of Masaryk University in Brno, Brno, Czech Republic

specialist to be included into the study. Also informed consent had to be signed to participate in the study.

Initially 49 women were included in our study. Nevertheless, thirty women were excluded from final evaluation because of only one measurement during the whole gestation. Other nine women were excluded because of no regular measurements.

From the final number ten women were measured in second and third trimester. Average age of our measured women was 33.6 ± 3.69 and BMI 28.71 ± 8.21 kg/m2.

Data were recorded directly from a device Tanita MC 180 MA (Tanita Co., Ltd, Japan) by an enclosed program (Tanita Health monitor v. 2.7.0) and exported in RAW format. Electrodes that are part of the device were cleaned by alcohol towel after every measurement to overcome possibility of measurement error. Measurements were done at the hospital's office by an educated nurse. All the measurements were done at the time of subject's normal examination visit during pregnancy period.

Measurement was taken in standing position with hand near body holding electrodes and patient`s hands were treated by alcohol towel as recommended in NIHT guidelines [6]. All measurements were taken twice to overcome measurement bias. Measurements were done over the whole frequency spectrum (5, 50, 250 and 500 kHz). Differences were evaluated on statistical level P = 0.05 and increase or decrease was reported. For statistical evaluation Wilcoxon and t tests were used.

3 Results and Discussion of Body Composition Changes During Pregnancy

Results are describing values measured in the second and third trimesters. Following calculated/obtained values were monitored: Weight, Body fat.%, Fat mass (kg), Fat free mass (kg), Muscle mass (kg), TBW (kg), TBW%, Intracellular water (kg), Extracellular water (kg), ECW% with an aim to get whole description of body composition. These values were obtained at frequency of 50 kHz.

Following directly measured (without calculation) electrical values were monitored: reactance and resistance (frequency 5, 50, 250 and 500 kHz). All the obtained values are considered for the whole body (right leg–right hand) observation.

After final evaluation the differences were found nearly in all monitored calculated/obtained parameters. Statistically significant increase differences were discovered in: Weight (kg) (P = 0.005), Fat mass (kg) (P = 0.01), TBW (kg) (P = 0.005). There was no statistical significance in values recorded in percentage: body fat.%, TBW%, and ECW%. Differences between trimesters (see Fig. 1).

We observed changes that were in all values that reported statistically significant increase bigger than 10% which means body composition values increased dramatically.

Increase in TBW kg was expected because of amniotic fluid. Hence the woman body is preparing for breastfeeding of an infant [7]. Overall increase in body fat (kg) was 3.16 kg which corresponds with other study [8].

There was also reported an increase in body weight parameter. The average increase in weight was 8.42 kg which was for selected group of women with average BMI 28.71 ± 8.21 (overweight in terms of BMI evaluation) in the middle of recommended weight gain. Recommended weight gain is for this group 7–11.5 kg [5] during pregnancy, although in some studies these was observed increase of 15 kg [9].

In the second part of observation setup directly measured values were observed. Also in this setup for resistance and reactance values statistical significant (P = 0.05) decrease on all used frequencies was discovered. Average decrease of resistance across all frequencies was 73.17 ± 7.62 Ω which presented 11.92 ± 0.07% decrease from the second trimester to the third trimester. Nevertheless, smaller decrease was

Fig. 1 Differences of selected calculated/obtained values between second and third trimester
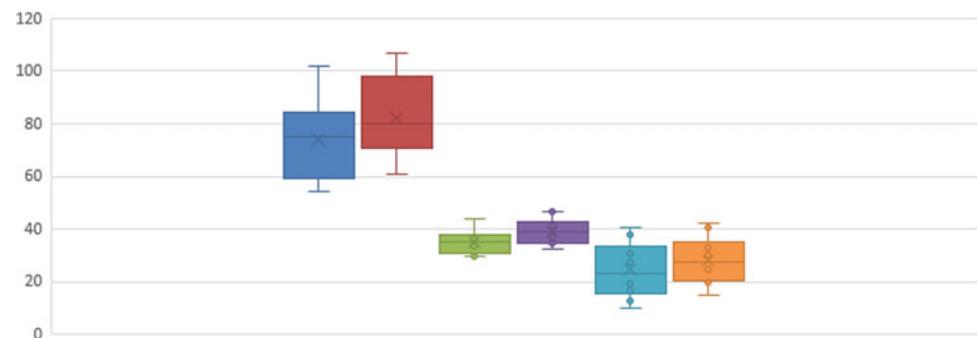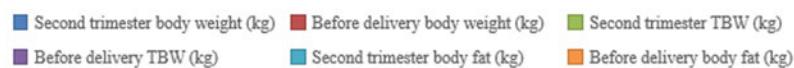
Table 1 The directly measured values in the second trimester

Second trimester (kHz)	Average	Standard dev.
Resistance 5	702.06	101.14
Resistance 50	632.50	95.79
Resistance 250	568.70	89.73
Resistance 500	553.82	88.35

Table 2 The directly measured values in the third trimester

Third trimester (kHz)	Average	Standard dev.
Resistance 5	619.09	87.91
Resistance 50	557.17	82.15
Resistance 250	500.53	74.65
Resistance 500	487.60	72.71

expected due to growth of the fetus. That should represent new cell mass with specific electrical values. Resistance values are shown in Tables 1 and 2.

During our measurements it was found out that parameters measured and recorded in percentage such as body fat.% and ICW% were not statistically different.

This was because of overall increase in body weight of measured patients. Hence values recorded in percentage wasn't statistically changed. Percentage of calculated/obtained values stays nearly the same during the whole gestation.

Displayed courses of resistance and calculated/obtained body composition also show that the biggest changes are between the second and third trimester. This corresponds with previously mentioned findings. All these outcomes result in important finding that the most important period for measurements and evaluation is between 25th and 30th week of pregnancy.

4 Discussion

During the last decade there were only few research studies published in a field of body composition and bioimpedance evaluation during pregnancy on European women [3, 4] and USA women [10]. The studies and guidelines that are observing the pregnancy are mainly focused on weight gain IOM [5]. However, no evidence based research on Czech population in this field was done before.

In pregnancy, increase in vascular bed is reported, this occurs because of blood volume increases. Hence increase in cardiac output of pregnant women is needed [11]. Observation of pregnancy progress in this paper shows that most important (from body composition view) are changes between the second and third trimester. The overall decrease between all trimesters was statistically significant (P = 0.05) for all electrical values of body composition and increase for

all calculated/obtained values (excluding values recorded in percentage). Nevertheless, in some cases even percentage values differed dramatically.

The decrease in directly measured parameters was bigger than increase in calculated/obtained parameters. This leads to conclusion that directly measured electrical parameters have better descriptive capabilities than calculated/obtained. Directly measured electrical values also do not introduce an error of other parameters in equations that are used for calculation of calculated/obtained.

The overall decrease of both reactance and resistance values were probably because of increase of whole body conductivity during gestation. This is because of majority of mass gain is amniotic water and also fetus that is composed mainly from water [7]. Although it was expected that decrease of reactance would be smaller than decrease of resistance because reactance stands for cell membranes whereas resistance stands for a pure resistive property of a tissue.

When resistance and reactance (frequency 50 kHz) that were obtained in the second and third trimesters were compared to reference ranges that were reported in previous study [3] it was discovered that these ranges did not apply to our measured values. This can conclude that reference ranges as reported by Ghezzi et al. need to be revised for specific population.

This leads to conclusion that not only equations that are used for calculation of body composition parameters are race specific but also a reactance and resistance of pregnant women can be race specific.

In all calculated/obtained measurements increases that are typical for gestation were reported. Weight and body fat kg, TBW kg values were for measured obese (in terms of BMI evaluation) group of women within range reported by IOM [5]. Measurements also showed good agreement that have reached BIA method in comparison with classical anthropometrical measurements reported by A. Paxton et al. [8].

TBW kg, evaluated by multi-frequency bioimpedance, increased significantly during the second trimester in the control group. The same results were reported in some previous studies although they were using different frequencies [12]. This also confirms importance of TBW kg and other body composition parameters observation.

Nevertheless, calculated/obtained values are showing problematic representation in some devices.

5 Conclusion

This paper discusses ranges of resistance in specific trimesters and concludes that measurements should be taken in all trimesters although first trimester is used only as a starting value in progress observation. Most important measurements

should be done in the second trimester to obtain information whether gestation process is physiological.

Gestation is a specific period in women's live. During this period physical and psychical change, levels of glycaemia, hormones are observed. Body composition is dramatically changing during all three trimester of gestation, increase of body weight, waist circumference is observed.

In this period all changes should be physiological. However, there is a risk of pathological situation that is even more dangerous than in non-gestation state of women.

In some cases there are risks of hypertension (caused by increase in TBW), polyhydramnion (caused by increase of amniotic water), post-gestation obesity (caused by increase of body fat during pregnancy), changes of newborn`s body weight.

Hence pregnant women are very closely observed to prevent pathological event and fatal result of gestation.

Measuring of all body composition parameters by bioimpedance method can give the examiner precise information about the process of gestation. This can help to identify some of mentioned pathologies early.

Bioimpedance proved to be important tool in gestation process evaluation. Hence this method is fast and repeatable and is reporting very good information about gestation process. This method is also very suitable for pregnant women because there is no need for specific preparation of a woman. Nevertheless, new approaches should be considered in a case of pregnancy.

Conflict of Interest The author declares that she has no conflict of interest.

Statement of Informed Consent Informed consent was obtained from all individual participants included in the study.

Protection of Human Subjects and Animals in Research All procedures performed in studies involving human participants were in accordance with the ethical standards of the institutional and/or national research committee and with the 1964 Helsinki declaration and its later amendments or comparable ethical standards.

References

1. Sverre Grimnes, Ørjan Grøttem Martinsen Bioimpedance and Bioelectricity Basics, 3rd Edition Academic Press 2014, ISBN: 9780124114708
2. Lukaski, H.C. Evaluation of body composition: why and how? 2009. Mediterr J Nutr Metab 2:1–10
3. Ghezzi F, Franchi M, Balestreri D, Lischetti B, Mele MC, Alberico S, Bolis P Bioelectrical impedance analysis during pregnancy and neonatal birth weight. Eur J Obstet Gynecol Reprod Biol. 2001
4. Larciprete G, Valensise H, Vasapollo B, Altomare F, Sorge R, Casalino B, De Lorenzo A, Arduini D., Body composition during normal pregnancy: reference ranges. Acta Diabetol. 2003 Oct;40 Suppl 1:S225–32
5. Kath Janssen n M Rasmussen and Ann L Yaktine, Weight Gain During Pregnancy Reexamining the Guidelines Washington (DC): National Academies Press (US); 2009, ISBN-13: 978-0-309-13113-1
6. NIHT Bioelectrical impedance analysis in body composition measurement: National Institutes of Health Technology Assessment Conference Statement. Am J Clin Nutr 1996;64(3 Suppl): S524–S532
7. Hartnoll G, Bétrémieux P, Modi N. Randomized controlled trial of postnatal sodium supplementation on body composition in 25 to 30 week gestational age infants. Arch Dis Child Fetal Neonatal Ed. 2000 Jan;82(1):F24–8
8. A Paxton, Sally A Lederman, Steven B Heymsfield, J Wang, J C Thornton, and R N Pierson Jr, Anthropometric equations for studying body fat in pregnant Women, Am J Clin Nutr 1998;67:104–10
9. Nohr, E Is intervening in pregnancy even too late? Obesity reviews (Suppl. 2), 206–248, March 2014
10. Van Loan, L E Kopp, J C King, W W Wong, P L Mayclin Fluid changes during pregnancy: use of bioimpedance spectroscopy. Journal of Applied Physiology 04/1995; 78(3):1037–42
11. M.H. Beall, J.P.H.M. van den Wijngaard, M.J.C. van Gemert, M. G. Ross Amniotic Fluid Water Dynamics Placenta - August 2007 (Vol. 28, Issue 8, Pages 816–823, https://doi.org/10.1016/j.placenta.2006.11.009)
12. Valensise H, Andreoli A, Lello S, Magnani F, Romanini C, De Lorenzo A. Multifrequency bioelectrical impedance analysis in women with a normal and hypertensive pregnancy. Am J Clin Nutr. 2000 Sep;72(3):780–3

On the Monitoring of Breathing Volume, Using Textile Strain Gauges

Artyom Rozevika, Alexei Katashev, Alexander Okss, Janne Mantyla, and Rene Coffeng

Abstract

Necessity to attach measurement device to the patient mouth makes use of spirometry difficult for continuous breathing volume monitoring in non-hospital applications. There were number of attempts to replace spirometry with measurements of the trunk volume. One of the potential solutions is evaluation of the breathing volume using set of respiratory belts, placed around the chest to measure changes in trunk circumference. Such belts could be made of the highly strain—sensitive knitted resistive fabric, integrated into tight underwear, like T-shirt or compressive body. The objective of the present research was to check usability of the garment—integrated knitted strain gauges for evaluation of the breathing volume. The breathing monitoring garment have been made in a form of T-shirt with seven knitted resistive stretch sensing ribbons, sewn around the T-shirt trunk and calibrated to measure circumference. Circumferences were used to estimate trunk volume of four healthy volunteers (2 male 2 female). Alongside, volunteers breathing volume was measured using commercial spirometer. The results demonstrated that T-shirt, being calibrated irrespectively to measured individual, could evaluates breathing volume with the uncertainty of 0.6 l, given all 7 ribbons are used for calculation of volume. The individual calibration of the T-shirt for particular individual could reduce uncertainty up to 0.3 l.

1 Introduction

Spirometry, being the golden standard method in respiratory monitoring, require measurement device to be attached to the patient mouth. This is inconvenient for patient and hospital staff and make use of spirometry inconvenient for continuous breathing volume monitoring in non-hospital applications. There were number of attempt to replace spirometry with measurements of the chest/trunk volume, using various methods, such as optical plethysmography [1], electric impedance tomography [2] etc. One of the potential solutions is evaluation of the chest volume using set of respiratory belts, placed around the chest at the various levels. Such belts could be manufactured of the highly strain—sensitive knitted resistive fabric, integrated in the tight underwear to measure changes in trunk circumference [3]. One of weak points of known knitted sensors is their comparatively low sensitivity [4].

Recently, smart textile solution, based on high strain—sensitive knitted fabric for mask-free breathing volume monitoring was developed and tested against commercially available resistive transducers [5]. Developed solution, that included four textile ribbons, calibrated to measure trunk circumference, was capable to measure breathing volume with the accuracy 0.5–0.8l. The goal of the present paper is to evaluate, in what extent one could reduce breathing volume estimation inaccuracy by increasing the number of sensing ribbons, integrated in the breathing monitoring garment.

A. Rozevika · A. Katashev (✉)
Institute of Biomedical Engineering and Nanotechnologies, Riga Technical University, Kalku 1, Riga, LV1658, Latvia
e-mail: katashev@latnet.lv

A. Okss
Institute of Design Technologies, Riga Technical University, Kalku 1, Riga, LV1658, Latvia

J. Mantyla · R. Coffeng
GE Healthcare, Kuortaneenkatu 2, 00510 Helsinki, Finland

2   Materials and Methods

2.1   Textile Strain Gauge Garment

The textile strain gauge were made of conductive fabric, kitted using conductive yarn in combination with cotton and elastane [6] and—cut in 3 cm wide ribbons. The ribbons demonstrated alteration of the electric resistance up to saturation at 15–17% strain. The ribbons were glued to the commercial compressive T-shirt with elastic textile adhesive (Fig. 1). The ribbons formed six circumferential rows #1–#6, numbered further from top to bottom, and one semi-circumferential row #7 on the frontal side of the T-shirt. The top, 7th row was placed just below armpits, and the distance between ribbons centers was 5 cm.

Upon deformation, the resistance of the ribbons varied over the range of 1 kΩ–1.5 MΩ. Each ribbon was connected in series to the load resistance 1 MΩ to form voltage divider, powered by stabilized 1.5 V DC voltage. Voltage drop over the ribbons' resistances was measured over time using BioRadio® data logger [7].

2.2   Acquisition of Strain Gauge and Spirometry Data

The study involved four healthy volunteers of age 24: female (168 cm, 54 kg), male (175 cm, 60 kg), male (181 cm, 65 kg), female (171 cm, 70 kg), referred further as #1–#4. Each volunteers performed set of 3–4 normal breaths, followed by three deep breaths, attempting to model either expressed chest breathing or abdominal breathing. Each set was repeated three times to collect 24 datasets. In parallel, breathing volume was measured using commercial spirometer SpiroUSB™ under control of Spida 5™ software [8]. The spirometer was capable of measuring breathing volume with uncertainty ±3% (following ATS standard, 1994). Typical set of T-shirt ad spirometer data are presented at Fig. 2.
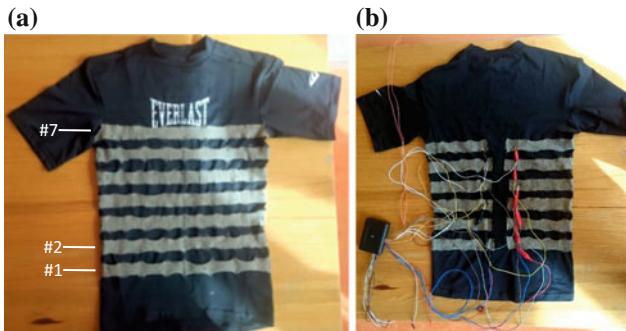
Fig. 1 Experimental garment with integrated textile strain gauges: front view (**a**) and rear view with attached measurement device (**b**)

2.3   T-Shirt Calibration and Calculation of Chest Volumes

The T-shirt strain gauge ribbons were calibrated individually to measure circumferences. For this, volunteer #3 performed a set of various depth inspirations and breathing-hold maneuvers, while his chest/waist circumferences were measured at the levels of sensor ribbons with the tailor's tape (accuracy ±2 mm). This calibration was used further for calculation of other individuals' volumes, too. The calibration lines and corresponding polynomials were constructed for each sensor (Fig. 3a), allowing measurement of circumference from the strain sensors data to be made with the accuracy of ∼0.7 mm. Calibration lines of different ribbons demonstrated good agreement. For the ribbon #7, the calibration was made against the length of the ribbon that was equal to ½ of the circumference.

The breathing volumes were calculated on the base of simple geometry model (Fig. 3b). The body was represented as a set of cylindrical slabs, having the same circumference, as have been measured by the strain gauge. The instant volume, measured in liters, was, therefore:

$$V = \sum_i V_i = \frac{1000}{4\pi} \sum_i h_i L_i^2, \qquad (1)$$

where i numbers slabs, used for calculations, V_i is a volume of ith slab, L_i—circumference of ith slab, but h_i is the thickness of the slab, being measured as a distance between middle lines of the ribbons, used for calculations. Both circumferences and heights are measured in centimeters. For the slab #7, the circumference was calculated as length of the ribbon, multiplied by 2. The calculation provided estimation of the chest volume as function on time. The breathing volumes were calculated from both T-shirt and spirometry data, by taking difference between local maximum volume and previous local minimum volume, i.e. breathing volumes were calculated using rising slopes of the breathing curves.

To analyze how the number of ribbons used affects the accuracy if the breathing volume estimation, the volumes were calculated, using 3 ribbons (ribbons #2, #4, #6), 4 ribbons (#1, #3, #5, #7), 5 ribbons (#1, #2, #4, #6, #7) and all 7 ribbons.

Correlation between volumes, measured using T-shirts and spirometry, was estimated using both scatter diagrams and Pearson's correlation coefficients. For Pearson's correlation coefficients, 95% confidence intervals were calculated using Fisher transformation method. The error of breathing volume estimation, using T-shirt was evaluated, using spirometry data as a golden standard, as

$$\delta V = \sqrt{\langle \Delta V^2 \rangle + S(\Delta V)^2}, \qquad (2)$$

Fig. 2 Typical output voltages of T-shirt sensors (**a**) and spirometry recording (**b**). Voltage curves are artificially shifted to order plots from ribbon #1 (lowest) to ribbon #7 (highest)
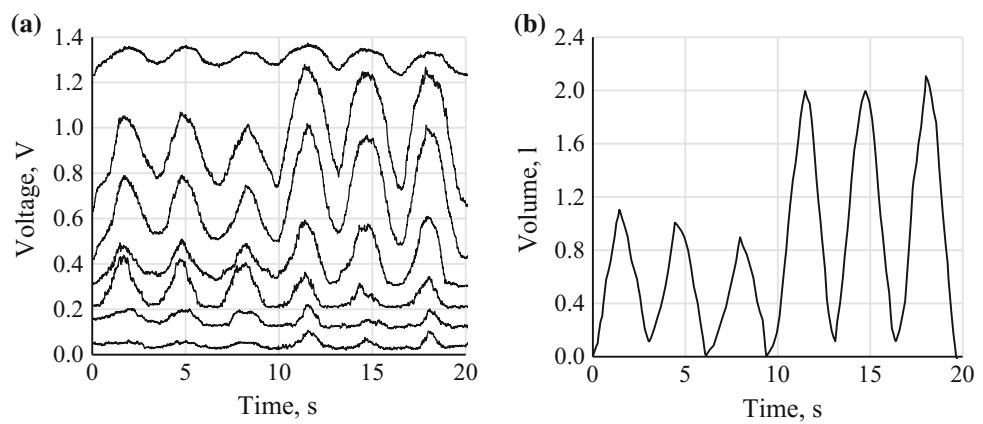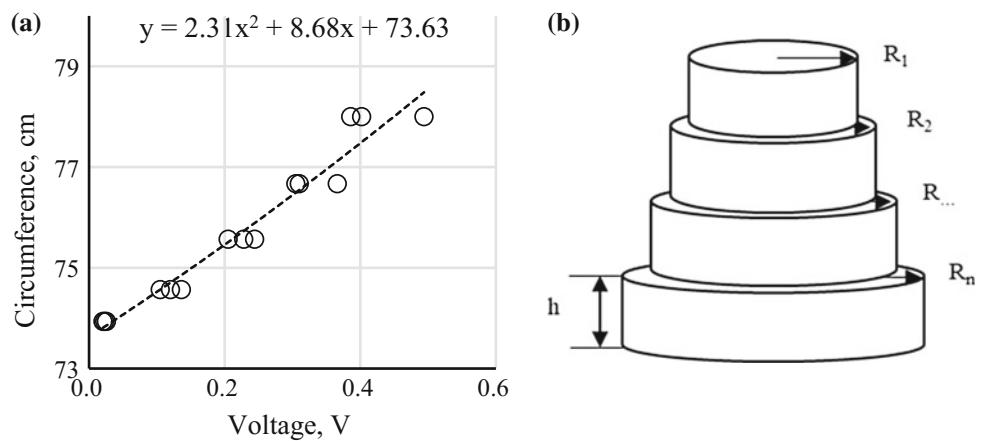
Fig. 3 Typical calibration curve of the textile ribbon (**a**); trunk model for the volume calculation (**b**)

$$y = 2.31x^2 + 8.68x + 73.63$$

where $\langle \Delta V \rangle$ is the average of the differences ΔV_i between T-shirt estimated volumes and spirometry measured volumes, but $S(\Delta V)$—standard deviation of these differences.

3 Results and Discussion

The scattering diagrams at Fig. 3a demonstrate correlation between breathing volumes, estimated by means of spirometry and T-shirt measurements for all volunteers. With exception of some outliers, there is reasonably good correlation, especially for chest breathing. The abdominal breathing data demonstrate more scattering. Figure 3b demonstrates extraction of data for the volunteer #3, for whom calibration of the T-shirt was performed. Although abdominal breathing data are less scattered, there is no noticeable difference principal are better alignment of abdominal breathing data, this scattering diagram does not differs much form the Fig. 3a.

In accordance with Fig. 3, for the chest breathing, the correlation coefficients between spirometry and T-shirt data, calculated for all individuals, do not differ from ones

calculated using T-shirt, individually calibrated for volunteer #3 (Table 1). Nevertheless, for abdominal breathing, correlations, calculated using individually calibrated data are generally higher, although this difference could not be treated as significant, because corresponding confidence intervals overlap (Fig. 4).
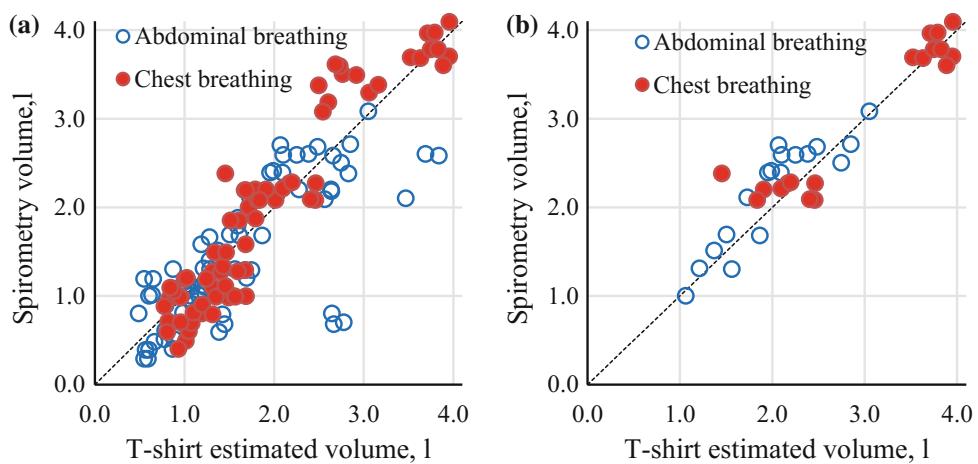
Although the correlation coefficients does not depend on the number of textile ribbon, the error of the breathing volume estimation tends to be smaller when greater number of ribbons is used. The inaccuracy of estimation is smaller for chest breathing (~ 0.4 l) and higher for abdominal breathing (~ 0.6 l). Such values are close to the tidal volume.

This fact makes use of the T-shirt for the tidal volume monitoring doubtful. For individually calibrated T-shirt, the inaccuracy for chest breathing was reduced by 25%—up to 0.3 l, but for abdominal breathing—by 50%, up to ~ 0.3l, too. Such inaccuracy is too high for tidal breathing measurements. Still, it could be tolerated for evaluation of deep breathing, for example, during exercises. For more accurate estimate, one would involve more volunteers and analyze data for males and females separately.

Table 1 Correlation coefficients between spirometry volumes and T-shirt estimated volumes and volume estimation errors for different numbers of used textile ribbons gauges

Nr. of ribbons	Correlation coefficient		Volume estimation error (l)	
	All individuals	Individual calibration	All individuals	Individual calibration
Chest breathing				
3	0.87 ± 0.09	0.87 ± 0.09	0.49	0.53
4	0.91 ± 0.07	0.91 ± 0.07	0.48	0.61
5	0.88 ± 0.09	0.89 ± 0.08	0.47	0.34
7	0.91 ± 0.06	0.91 ± 0.07	0.39	0.31
Abdominal breathing				
3	0.69 ± 0.22	0.90 ± 0.07	0.50	0.47
4	0.68 ± 0.23	0.82 ± 0.13	0.82	0.44
5	0.68 ± 0.26	0.82 ± 0.13	0.60	0.42
7	0.67 ± 0.23	0.85 ± 0.11	0.58	0.31

Fig. 4 Correlation between T-shirt estimated volumes and spirometry volumes. T-shirt estimated volumes calculated using 7 textile ribbons. **a** Data from all individuals, **b** data for individual for whom calibration was performed

4   Conclusion

The accuracy of the textile sensor based breathing evaluation garment depends on the number of garment—integrated ribbons: inaccuracy of measurements decreases by 20% when number of ribbons increased from 3 to 7. Individual calibration of the garment for each particular user could further reduce inaccuracy by 50%, yielding volume estimation error of ∼0.3 l. Such an error is not suitable for tidal volume measurements, but could be used for deep breathing monitoring.

Conflict of Interest Hereby authors declare, on the best of their knowledge, absence of any conflicts of interest related to the topic of the present paper.

References

1. Cala, S. J., Kenyon, C. M., Ferrigno, G., Carnevali, P., Aliverti, A., Pedotti, A., Rochester, D. F. Chest wall and lung volume estimation by optical reflectance motion analysis. Journal of Applied Physiology, 81(6), 2680–2689 (1996).
2. Lundin, S., Stenqvist, O. Electrical impedance tomography: Potentials and pitfalls. Current Opinion in Critical Care, 18(1), 35–41 (2012).
3. Hoffmann T., Eilebrecht B., Leonhardt S. Respiratory monitoring system on the basis of capacitive textile force sensors. IEEE Sens. J., 11, – P. 1112–1119 (2011).
4. Atalay O., Kennon W., Husain M. Textile-Based Weft Knitted Strain Sensors: Effect of Fabric Parameters on Sensor Properties. Sensors, 13, – P. 11114–11127 (2013).
5. Okss, A., Katashev, A., Mantyla, J., Coffeng, R. Smart Textile Garment for Breathing Volume Monitoring. In: Proc. of

International Conference "Biomedical Engineering 2016", Lithuania, Kaunas, 24–25 November, 2016. Kaunas: Technologija, pp. 167–170 (2016).

6. Okss A., Katashev A., Litvak J. Knitted Resistive Fabric: Properties and Applications. Material Science. Textile and Clothing Technology, Vol.9, pp 28–33 (2014).

7. Great Lake Neurotechnolohies homepage, https://glneurotech.com/bioradio/bioradio-150/, last accessed 2018/02/03.

8. MD Spiro homepage, https://mdspiro.com/spiroUSB-spirometer, last accessed 2018/02/03.

Application of Garment—Embedded Textile Electrodes for EIT Based Respiratory Monitoring

Alexei Katashev, Alexander Okss, Sabine Krüger-Ziolek, Benjamin Schullcke, and Knut Möller

Abstract

Electrical Impedance Tomography (EIT) is a technology capable of supplementing spirometry in a number of applications due to the ability to evaluate regional changes in lung volume. EIT measurements require an array of conventional bio-potential electrodes attached to the patient's chest. Replacement of conventional electrodes with knitted conductive textile electrodes integrated in a patient's undershirt could increase the area of EIT applications such as daily respiratory monitoring in hospitals, at home, during physical activity, etc. The goal of the present paper was to demonstrate the usability of textile electrodes for EIT measurements. The conductive textile was integrated in the chest of a long sleeves thermal undershirt to form three rows of 16 circumferential electrodes that can be connected to a commercially available EIT monitoring system. Two healthy male volunteers aged 45–50 performed tidal breathing, deep breathing, and FRC maneuvers. The breathing volumes and FRC were measured using a body plethysmograph. The course of measurements demonstrated that contact between skin and textile electrodes are not tight enough to operate with the EIT device. Applying additional pressure to the electrodes and the use of electrolyte spray reduced the impedance of the textile electrodes to adequate values. Under such conditions, there were no differences in correlation coefficients between spirometry volumes and EIT volumes obtained using either conventional or textile electrodes.

A. Katashev (✉)
Institute of Biomedical Engineering and Nanotechnologies, Riga Technical University, Kalku 1, Riga, LV1658, Latvia
e-mail: katashev@latnet.lv

A. Okss
Institute of Design Technologies, Riga Technical University, Kalku 1, Riga, LV1658, Latvia

S. Krüger-Ziolek · B. Schullcke · K. Möller
Institute of Technical Medicine, Furtwangen University, Jakob-Kienzle Strasse 17, 78054 Villingen-Schwenningen, Germany

1 Introduction

Electrical Impedance Tomography (EIT) is one of the alternative techniques capable to supplement spirometry both in medicine and non-medical fields—sport, fitness, singer training, etc. [1]. The advantage of EIT, compared to other methods like spirometry, is the ability to evaluate regional changes in lung volume [2]. EIT measurements require an array of conventional bio-potential electrodes attached to the patient's chest. The electrode arrays usually either are bulky belts or require a time—consuming procedure for the attachment. The potential solution is to replace conventional electrodes with ones made of conductive knitted textile. Knitted electrodes were successfully applied for registration of electrical biosignals, such as ECG [3] or EMG [4] as well as for bioelectrical stimulation [5]. Besides, there is a lack of information on the application of knitted conductive textile electrodes for EIT measurements. From the practical point of view, as wearables, textile electrodes integrated in a patient's undershirt could simplify permanent EIT respiratory monitoring in hospitals, at home, during physical activity, etc.

The goal of the present paper was to demonstrate the usability of textile electrodes for EIT measurements using commercially available EIT equipment.

2 Materials and Methods

2.1 Textile Electrodes Garment

The textile electrodes were made of terry fabric kitted from conductive yarn Shildex™ 110 × 2 ply. Terry fabric was thought to have tight contact with the skin owing to a great

Fig. 1 Experimental garment with integrated textile electrodes: external (**a**) and internal (**b**) view

number of individual loops. The fabric was cut in pieces sized 2×4 cm, forming separate electrodes. The electrodes were sewn with the same conductive yarn in the inner surface of the commercial long sleeves thermal undershirt of size M (Fig. 1). The electrodes formed three rows, each containing 16 circumstantially and equidistantly placed electrodes. The upper row was placed with the centers of the electrodes to be placed approximately at the level of the intercostal space (ICS) 4 or 5 of a 180 cm tall man, ~ 20 cm down form acromion. Subsequent rows had been shifted caudally by 10 cm each. Standard ECG electrodes snaps had been sewn to the outer side of the garment through pre-drilled 1 mm holes using conductive yarn providing electrical contact between snaps and textile electrodes. Standard ECG electrodes snaps made the garment suitable for the use with a commercially available EIT measurement system (PulmoVista® 500, Dräger, Germany).

2.2　Acquisition of EIT and Spirometry Data

Two healthy male volunteers (volunteer A: age 59, height 180 cm, weight 79 kg; volunteer B: age 45, height 182 cm, weight 83 kg) were involved in the study. Volunteers performed two sets of breathing maneuvers. The first includes tidal breathing and FRC maneuvers, while the second included tidal breathing with inclusion of deep breathing (about 5–6 deep breaths) and shallow breathing (about 10 shallow breaths) patterns. The breathing volumes and FRC were recorded using a spirometer integrated into a body plethysmograph (PowerCube® Body+, Ganshorn Medizin Electronic, Germany). Simultaneously, EIT measurements were performed using either conventional or textile electrodes. Both commercial and textile electrodes were connected to the EIT device, operating at a frequency of 130 kHz. Measurements were performed at the level of either first row, or second row. The third row of electrodes

was not in use. Hereby, for each volunteer, four measurements have been recorded: with conventional EIT electrodes, placed 22 cm down form acromion (top line); with conventional EIT electrodes, placed 32 cm form acromion (bottom line); with textile electrodes, placed 22 cm down to acromion, and with textile electrodes, placed 32 cm down to acromion.

The course of measurements demonstrated that textile electrodes had too loose contact with the skin for proper EIT measurements. Application of additional pressure to the electrodes by the use of rubber band warped around the volunteer's chest and the use of electrolyte spray (Signa-Spray™ by Parker Labs) reduced the impedance of the textile electrodes to acceptable value and allows the performance of EIT measurements.

2.3　Data Processing

The breathing volumes were calculated from both spirometry and EIT data. For this, local maxima and minima of the breathing waveform were identified. The breathing volume for the particular breathing cycle was calculated as the difference between maximum and precede minimum: i.e. using the inspiration part of the breathing cycle. The volumes from different measurement sets performed with specific electrode setups (i.e. combination of electrodes type and position) formed single series of data pairs "spirometry volume—EIT volume".

The volume scales of spirometry volumes and EIT volumes in each series were normalized to the unit range:

$$V_{norm} = (V - V_{min})/(V_{max} - V_{min}), \tag{1}$$

where V_{norm} is the normalized value, V_{min} and V_{max}—minimal and maximal volume in a series.

Correlation between normalized spirometry volumes and normalized EIT volumes were estimated using both scatter

diagrams and Pearson's correlation coefficients. For Pearson's correlation coefficients, 95% confidence intervals were estimated using Fisher transformation method.

3   Results and Discussion

Data acquired in a single measurement set consisted of the recording form the spirometer representing breathing volumes (measured in liters) and EIT data representing relative impedance changes resulting from changes in lung volumes (stated as arbitrary units) (Fig. 2).

There were no differences in the EIT—estimated breathing patterns, obtained either by the use of standard electrodes or by textile ones. Observed differences in signal levels and shape were related to the volunteer's ability to perform two maneuvers as similar as possible. Since there was no possibility to perform measurements with conventional and textile electrodes simultaneously, the maneuvers were performed sequentially.

The scattering diagram at Fig. 3 demonstrates the correlation between normalized volumes estimated by means of spirometry and EIT for both volunteers. The correlation is high (>0.98) for data measured with electrodes placed at the top line—at the level of ICS 4, 22 cm down to acromion.

Fig. 3 Correlation between normalized spirometry volumes and EIT estimated volumes. "T-shirt" data were obtained by means of textile electrodes

For the measurements with electrodes placed 10 cm below, there is still similar coincidence with spirometry data for higher breathing volumes. Besides, for the lower breathing volumes, EIT underestimates breathing volumes. There is no difference in the performance of conventional and textile electrodes: scattering diagrams for both type of measurements are similar.

Table 1 summarizes the evaluation of the correlations between spirometry data and EIT data for different types of electrodes. For the top electrodes position, the values of

Fig. 2 Typical spirometry and EIT estimated volume data for one volunteer. The first set (**a**) included prolonged tidal breathing and FRC maneuvers. The second set (**b**) included prolonged tidal breathing, 5–6 deep breathes, 5–6 tidal breathes, about 10 shallow breathes, 3–5 tidal breathes
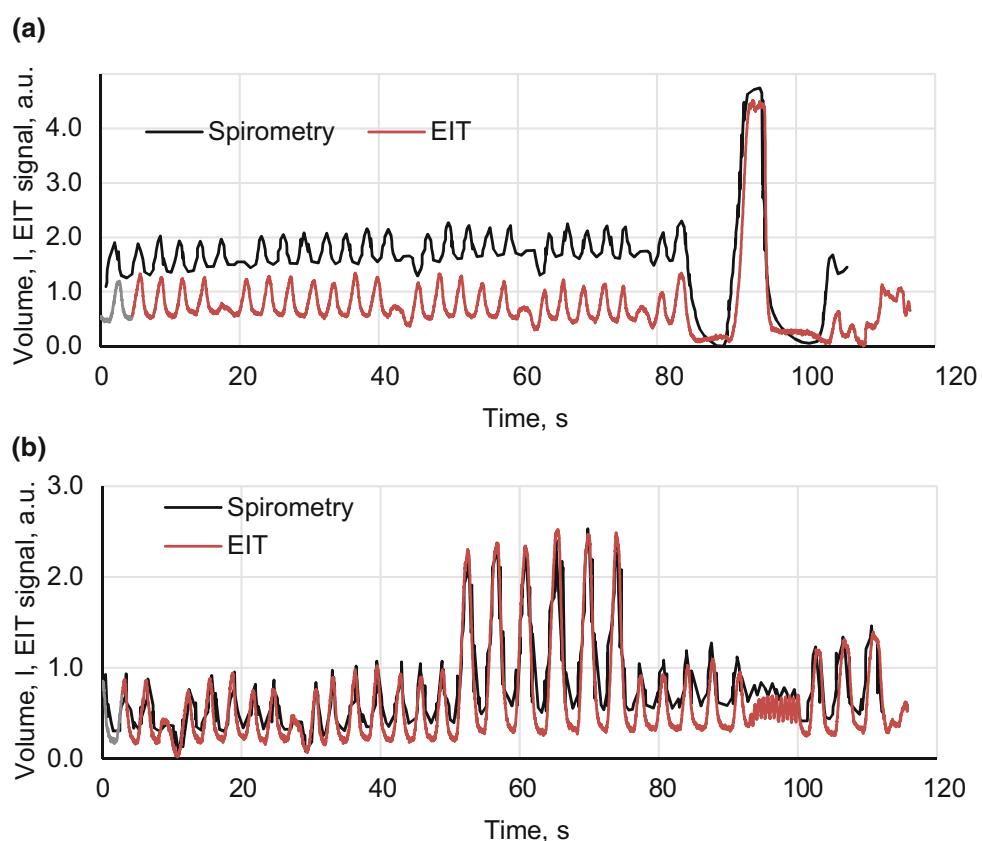
Table 1 Correlation coefficients between normalized spirometry volumes and EIT volumes

Person	Electrodes position	Conventional electrodes	Textile electrodes
Volunteer A	Top	0.9994 ± 0.0004	0.997 ± 0.002
	Bottom	0.976 ± 0.015	0.986 ± 0.009
Volunteer B	Top	0.978 ± 0.015	0.989 ± 0.007
	Bottom	0.929 ± 0.051	0.969 ± 0.020
Both	Top	0.983 ± 0.008	0.993 ± 0.003
	Bottom	0.927 ± 0.037	0.980 ± 0.010

correlation coefficients are slightly higher, if compared to the lower position. Moreover, for this position the differences in correlation coefficients between conventional and textile electrodes are not significant as corresponding confidence intervals overlap. For the bottom position, textile electrodes demonstrate a slightly higher correlation compared to the conventional electrodes. These findings support the conclusion already inferred from the analysis of Fig. 3.

4 Conclusion

Textile electrodes might be suitable for EIT measurements, providing a good skin contact will be established. With electrodes firmly pressed to the chest and wetted by electrolytic spray, textile electrodes performed as good as conventional electrodes. There were no discrepancies observed in the EIT signal due to switching to textile electrodes.

However, firm pressure should be applied to the electrodes either by the use of compressive fabric or by embedding elastic elements, like rubber bands, in the garment.

Conflicts of Interest Hereby authors declare, on the best of their knowledge, absence of any conflicts of interest related to the topic of the present paper.

References

1. Lundin, S., Stenqvist, O. Electrical impedance tomography: Potentials and pitfalls. Current Opinion in Critical Care, 18(1), 35–41 (2012).
2. Schullcke B, Gong B, Krueger-Ziolek S, Moller K. Reconstruction of conductivity change in lung lobes utilizing electrical impedance tomography Current Directions in Biomedical Engineering, 3(2), 513–516 (2017).
3. Bystřický, T., Moravcova, D., Kaspar, P., Soukup, R., Hamacek, A. A comparison of embroidered and woven textile electrodes for continuous measurement of ECG. In Proceedings of the International Spring Seminar on Electronics Technology, Vol. 2016–September, pp. 7–11, (2016).
4. Paiva, A., Carvalho, H., Catarino, A., Postolache, O., & Postolache, G. Development of dry textile electrodes for electromiography a comparison between knitted structures and conductive yarns. In Proceedings of the International Conference on Sensing Technology, ICST, Vol. 2016–March, pp. 447–451 (2016).
5. Poboroniuc, M.-S., Irimia, D.-C., Curteza, A., Cretu, V., & Macovei, L. Improved neuroprostheses by means of knitted textiles electrodes used for functional electrical stimulation. In Proceedings of the 2016 International Conference and Exposition on Electrical and Power Engineering, EPE 2016 pp. 320–325 (2016).

Estimation of Emptying Urinary Bladder in Paraplegic and Elderly People Based on Bioimpedance, Hypogastric Region Temperature and Neural Network

Michael Rodas, Layla Amoroso, and Mónica Huerta

Abstract

As is known, bioimpedance is a measurement method that can be used in medicine to know the volume of a person's urinary bladder. However, this method is not entirely reliable due to the multiple factors that influence its measurement, such as the weight of the person, body fat and even the different skin type of each person. Therefore, this paper proposes a method that combines bioimpedance, hypogastric region temperature and an artificial feed-forward neural network, sufficiently capable of determining when to empty the bladder, so that this muscle is not affected by the time exceeded of urine continence, this work is aimed to people who have suffered injuries to their spine, who do not have the ability of feeling when their bladder needs to be emptied. It is also aimed to older adults who begin to have problems with their bladder control, allowing them to improve their quality of life.

Keywords

Bioimpedance • Hypogastric region temperature
Neural network

1 Introduction

The loss of control of sphincters in people with spinal cord injury and incontinence in older adults are problems of big importance, that are present in the society, and need to be treated. In spinal cord injuries, patients lose sensitivity and the ability to send signals, from below the level where the injury occurred to the brain [1], resulting in pathologies such as atonic bladder, automatic bladder and neurogenic bladder [2], which hinder the voluntary emptying of the bladder. In the case of older adults, something different happens, they lose the awareness of urination, increasing the prevalence of UI urinary incontinence due to age [3], which weakens as the muscle walls of the bladder become older [4]. According to international studies, the prevalence of urinary incontinence in older adults is 29.4% (from 26.7 to 36.3% in women and from 6.4 to 17% in men) [5–7]. In the case of paraplegics, there are several methods of urinary drainage, intermittent catheterization, for example, it is a common method, which is invasive and is implemented during the first months of the injury, this method is annoying for the patient, and besides, may cause infections and complications to the health of patient [8]. With bioimpedance investigations, it has been possible to determine some physiological variables, such as dengue, basal cell carcinoma, estimation of the urinary bladder, among others [9, 10]. Bioimpedance is a non-invasive, safe, and economical method that allows constant monitoring of bladder volume [11]. However, factors as height, weight, body fat, and even the surface area of the electrode can cause variations on the measurements [12, 13].

Therefore, in this paper, a novel noninvasive method of measuring and monitoring bladder urinary volume based on bioimpedance, hypogastric region temperature and feed forward neural network is proposed. This method, uses a four-electrode structure with a 1mApp 50 kHz sine current excitation source, that measures the bioimpedance [14] and a chip MAX30205 that measures temperature of bladder region in real time, after this, the data is fed in a feed forward neural network of 3 layers, which identifies patrons and determines when the person should empty his/her bladder. It was demonstrated that, hypogastric region temperature, is highly correlated to bladder urinary volume.

M. Rodas (✉) · M. Huerta
Universidad Politécnica Salesiana, Cuenca, Ecuador
e-mail: mrodasa1@est.ups.edu.ec

M. Huerta
e-mail: mhuerta@ups.edu.ec

L. Amoroso
Universidad de Cuenca, Cuenca, Ecuador
e-mail: layla.amoroso@ucuenca.ec

2 Methodology

2.1 Structure System

Figure 1, shows the procedure of the proposed method. A voltage source of 1 Vpp at 50 kHz is configured by a function generator, then it is converted to a sine current excitation source of 1mApp, through a circuit called voltage controlled current source (VCCS), after this, the current excitation electrodes are placed on the right and left iliac region close to navel, and the voltage electrodes are placed on hypogastrium area. Once, we have the measurement of voltage, this data is introduced into a IIR Filter and subjected to a digital processing to reshape the sine wave and mitigate some defects that present the signal due to the noise and interferences present in the environment. With all the data processed, we apply the law of Ohm, where we obtain the bioimpedance of each patient. Chip of temperature is placed on hypogastrium region. Temperature and bioimpedance measurements, are inserted into the trained feed forward neural network, which determine if a patient should empty his/her bladder or not. This is visualized on a computer.

As shows Fig. 2, the neural network used, has the following characteristics:

- 3 layers, input, hidden, and output layer.
- 4 neurons in the input layer that, involves (age, height, weight, bioimpedance change, and hypogastric region temperature change), 10 neurons in the hidden layer, and 1 neuron in the output layer, which can be 1 or 0, as mentioned above.

2.2 Feed Forward Neural Network

For the selection of neurons in the hidden layer we performed several tests, with different numbers of neurons, observing with 10 neurons, the mean square error is low.

For training the data, we used the data we obtained of the 18 patients and 10 patients more, who were with the bladder just emptied. We used a Feed Forward Neural Network with the BFGS Quasi-Newton algorithm, since this model of network has had good result in tasks of recognition and classification of patterns, based on bioimpedance [6, 15, 16]. The network was programed in the software MATLAB.

2.3 Samples Collection

Eighteen patients, voluntarily performed bio impedance and hypogastric temperature measurement tests, where 11 patients are sane, 5 patients are elderly people, three of them have incontinence and 4 patients are people with spinal cord injuries.

Table 1 shows the patients. Informed consent was obtained from all individual participants included in the study.
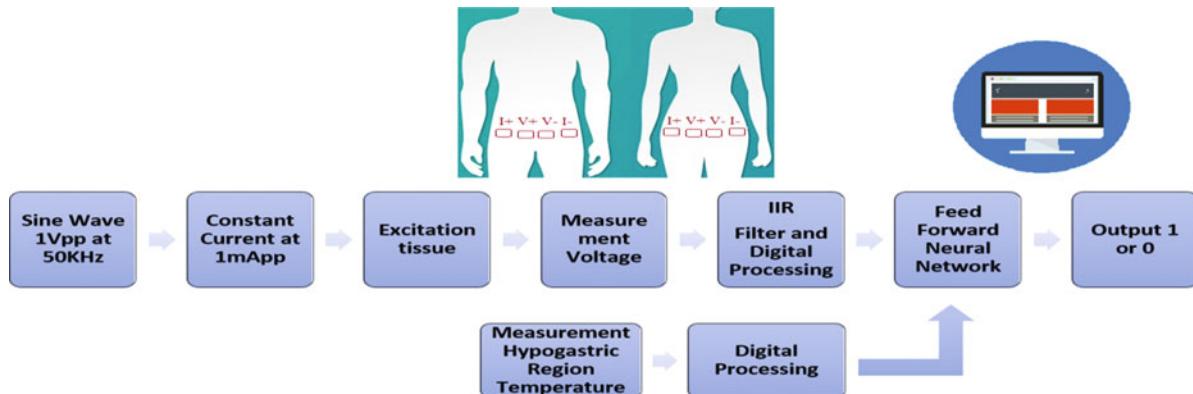
Fig. 1 Structure system of measurement, acquisition and processing data
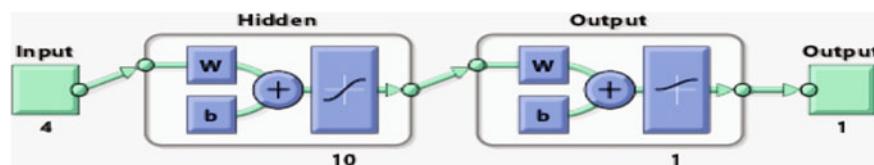
Fig. 2 Architecture of the neural network used

Table 1 Characteristics of the patients evaluated and tested

	Sex	Age	Height (cm)	Weight (lbs.)	Paraplegia	Incontinence urinary
Patient 1	M	14	146	90	No	No
Patient 2	M	17	178	120	No	No
Patient 3	F	19	157	114.4	No	No
Patient 4	F	19	158	115	No	No
Patient 5	F	20	155	91.02	No	No
Patient 6	M	21	180	132	No	No
Patient 7	M	21	182	127	Yes	No
Patient 8	F	22	165	154	Yes	No
Patient 9	M	23	184	129.8	No	No
Patient 10	M	24	179	140	No	No
Patient 11	M	26	180	140	No	No
Patient 12	M	31	160	110	Yes	No
Patient 13	M	34	172	134	No	No
Patient 14	F	58	158	130	No	No
Patient 15	M	65	165	140	No	No
Patient 16	M	65	168	120	No	Yes
Patient 17	F	81	165	150	No	Yes
Patient 18	M	84	178	125	No	Yes

The measurement of bioimpedance is taken for one minute before the patient develops an urge to urinate; after the patient empties his/her bladder another measurement of one minute is taken, registered and compared with the last measurement.

On the other hand, measurement of hypogastric temperature is taken for two minutes before the patient urinates; and after the patient empties his/her bladder another measurement is taken for two minutes in the same area.

Once, we have done the measurements, the data is inserted on the trained feed forward neural network, which was previously explained. This neural network has as output 1 or 0, which represent need to urinate or not, respectively.

3 Analysis and Results

Table 2 shows, there are cases where the value of bioimpedance, instead of raising, the impedance decreased, another study had the same issue as mentioned before [12], where the values fluctuate, and it is because the method of four electrodes, that it is not totally reliable.

Variation of temperature in most of the cases, have positive values, it means that when the bladder was almost full or completely full, it showed a greater temperature than when the organ was emptied; negative variations can be caused for the environmental factors or errors from the chip used.
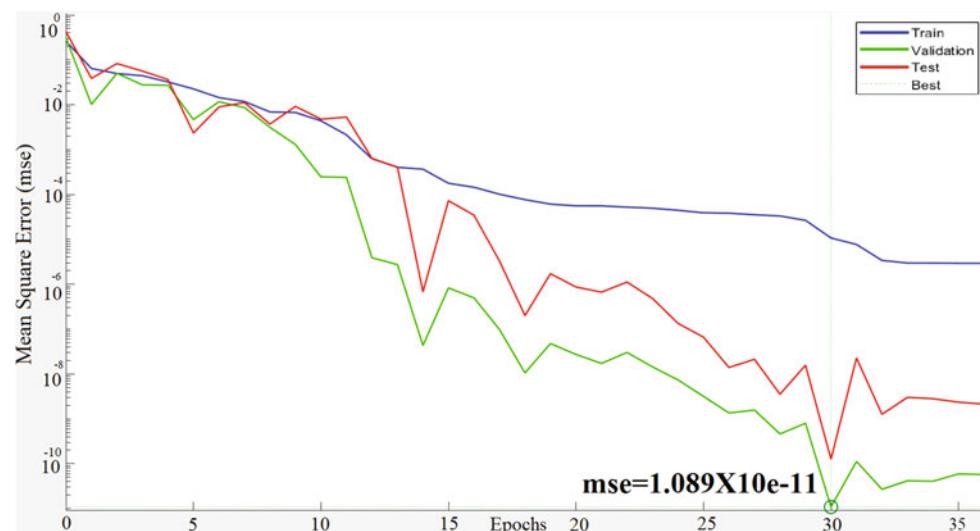
There was no difference on the trend of variating bioimpedance on sane or paraplegic people, that is why, we considered just to take 3 measurements of people with spinal cord injury. When testing with these patients, it is just necessary a better digital processing of the signal, because of the ground of the person respects to circuit is not coupled, since the person sits on the chair and has no contact with ground.

Figure 3 shows that, neural network has a very low mean square error of 1.08e−12, which means the neural network is high accuracy. Even though the proposed neural network does not have a lot training data, it works well determining when the patients should empty their bladder urinary.

We tested the network, with data totally different, obtaining an accuracy of 99.80%.

Table 2 Variation of bioimpedance and temperature, before and after emptying bladder

	Bioimpedance before emptying (Ohms)	Bioimpedance after emptying (Ohms)	Variation bioimpedance (Ohms)	Temperature before emptying (°C)	Temperature after emptying (°C)	Variation temperature (°C)
Patient 1	96.0200	106.100	10.08	33.150	32.140	1.010
Patient 2	110.416	125.694	15.27	32.100	32.010	0.090
Patient 3	147.569	166.666	19.09	33.640	32.872	0.767
Patient 4	147.300	166.333	19.03	31.910	31.490	0.420
Patient 5	98.0200	109.060	11.04	32.000	31.850	0.150
Patient 6	121.180	128.819	7.638	33.100	32.980	0.120
Patient 7	389.900	413.200	23.30	34.030	33.640	0.390
Patient 8	153.300	182.200	28.90	31.420	31.220	0.200
Patient 9	127.770	148.300	20.52	33.490	32.630	0.860
Patient 10	138.300	152.900	14.60	33.370	32.568	0.802
Patient 11	150.868	130.243	−20.62	33.105	33.015	0.090
Patient 12	186.001	148.000	−38.01	35.210	34.570	0.640
Patient 13	187.111	195.111	16.01	33.747	32.730	1.017
Patient 14	193.200	232.260	39.06	31.366	31.654	−0.288
Patient 15	171.800	135.800	−36.01	33.406	32.389	1.017
Patient 16	143.333	179.400	36.06	33.640	32.900	0.740
Patient 17	280.040	210.010	−70.03	34.751	34.512	0.239
Patient 18	156.100	190.200	34.10	35.200	34.963	0.236

Fig. 3 Mean square error of the neural network used

It was demonstrated, there is a high correlation among the hypogastric region temperature and bioimpedance with the act of emptying the bladder urinary. It means, when the bladder urinary is full, bioimpedance is lower, and temperature is higher, and when the organ is emptied, bioimpedance is higher, and temperature is lower.

4 Conclusions

It was concluded, measurement of hypogastric region temperature, represent a great parameter to estimate changes of bladder urinary volume.

Neural Network employed on this method is very accurate, since its mean square error is so low.

We realized that age, weight, bioimpedance and hypogastric region temperature are highly correlated, because when we trained the neural network, the height didn't have too much impact on the results, which is correct, because the bioimpedance depends directly of the body fat, the conditions of the skin, which in turn depends on the age.

As future works, we pretend to develop a feasible and ergonomic device that can be used all the time, and therefore help to elderly and paraplegic people to let them know, when to empty their bladder urinary.

Conflict of Interest The authors declare that they have no conflict of interest.

References

1. A. Wein, L. Kavoussi, A. Partin and C. Peters, Campbell-Walsh Urology. Saint Louis, MO: Elsevier Health Sciences, 2015.
2. Guyton and J. Hall, Guyton & Hall, Textbook of Medical Physiology, 13th Edition, Barcelona: Elsevier España, 2016.
3. J. Wu, C. Matthews, C. Vaughan and A. Markland, "Urinary, Fecal, and Dual Incontinence in Older U.S. Adults", Journal of the American Geriatrics Society, vol. 63, no. 5, pp. 947–953, 2015.
4. Alan J. Wein & Louis R. Kavoussi & Alan W. Partin & Craig A. Peters, Campbell-Walsh Urology, 11th Edition, Elsevier, 2016.
5. J. Junqueira and V. Santos, "Urinary incontinence in hospital patients: prevalence and associated factors", *Revista Latino-Americana de Enfermagem*, vol. 25, no. 0, 2018.
6. A. Zumrutbas, A. Bozkurt, E. Tas, C. Acar, O. Alkis, K. Coban, B. Cetinel and Z. Aybek, "Prevalence of lower urinary tract symptoms, overactive bladder and urinary incontinence in western Turkey: Results of a population-based survey", International Journal of Urology, vol. 21, no. 10, pp. 1027–1033, 2014.
7. L. Marques, I. Schneider, M. Giehl, D. Antes and E. d'Orsi, "Demographic, health conditions, and lifestyle factors associated with urinary incontinence in elderly from Florianópolis, Santa Catarina, Brazil", Revista Brasileira de Epidemiologia, vol. 18, no. 3, pp. 595–606, 2015.
8. Wyndaele, J. J. (2002). Complications of intermittent catheterization: Their prevention and treatment. Spinal Cord, 40, 536–541.
9. F. Ibrahim, T. Faisal, M. Mohamad Salim and M. Taib, "Non-invasive diagnosis of risk in dengue patients using bioelectrical impedance analysis and artificial neural network", Medical & Biological Engineering & Computing, vol. 48, no. 11, pp. 1141–1148, 2010.
10. R. Dua, D. Beetner, W. Stocker and D. Wunsch, "Detection of Basal Cell Carcinoma Using Electrical Impedance and Neural Networks", IEEE Transactions on Biomedical Engineering, vol. 51, no. 1, pp. 66–71, 2004.
11. H. Lukaski, "Evolution of bioimpedance: a circuitous journey from estimation of physiological function to assessment of body composition and a return to clinical research", European Journal of Clinical Nutrition, vol. 67, no. 1, pp. S2–S9, 2013.
12. R. Li, J. Gao, Y. Li, J. Wu, Z. Zhao and Y. Liu, "Preliminary Study of Assessing Bladder Urinary Volume Using Electrical Impedance Tomography", 2015.
13. L. Wen-Chien, J. Fu-Shan, Noninvasive electrical impedance analysis to measure human urinary bladder volume, 2011.
14. Rihui Li, Jinwu Gao, Hongbin Wang, Qing Jiang, "Design of a Noninvasive Bladder Urinary Volume Monitoring System Based on Bio-Impedance", 2013.
15. Aleksandar Kupusinac, Edita Stokić, Rade Doroslovački, "Predicting body fat percentage based on gender, age and BMI by using artificial neural networks, Computer Methods and Programs in Biomedicine", Volume 113, Issue 2, 2014.
16. J. Shell and W. D. Gregory, "A cancer detection device utilizing multi-tiered neural networks for improved classification," 2016 IEEE Healthcare Innovation Point-Of-Care Technologies Conference (HI-POCT), Cancun, 2016.

Research of Impedance Characteristics with a Negative Pressure Breathing Using Rheocardiographic and Rheoencephalographic Signals

P. V. Luzhnov, A. I. Dyachenko, and Yu. S. Semenov

Abstract

Negative pressure breathing is a spontaneous breathing with negative (relative to external, atmospheric) pressure in airways and lungs during the complete respiratory cycle or at certain phase. Our study was aimed at evaluation changes in cardiovascular system caused by applying negative pressure during inspiration (NPBin). Negative pressure was produced by enhanced inspiratory valve in standard valve box connected to mouthpiece. Seven healthy normal male volunteers participated in the study. An age of the volunteers was from 19–34 years, the mean $\pm$ SD was 25.7 ± 6.3. The study included five series conducted on the same protocol with each volunteer. Value of applied negative pressure was the only difference between series (0, −10, −15, −20, −25 cm water). Each series was divided into three stages: 15 min before applying NPBin, 25 min of NPBin, 15 min after NPBin. Rheocardiographic and rheoencephalographic signals were recorded continuously during all three stages. A study of an impedance changes was conducted with a negative pressure breathing using rheocardiographic and rheoencephalographic signals. Our study is shown that adaptation period duration to influence of different magnitude at volunteers is not equal. It depends on NPBin level and increases with rising of pressure magnitude.

Keywords

Impedance characteristics • Rheocardiography Rheoencephalography • Breathing

P. V. Luzhnov (✉)
Bauman Moscow State Technical University, 2-nd Baumanskaya 5, 105005 Moscow, Russia
e-mail: peterl@hotmail.ru

A. I. Dyachenko · Yu. S. Semenov
State Scientific Center—Institute of Biomedical Problems, Russian Academy of Sciences, Horoshevskoe 76A, 123007 Moscow, Russia

1 Introduction

The analysis of hemodynamic parameters is an important problem of medical and biological researches. It is necessary at diagnostics and monitoring of a condition of the person blood vascular system, at forecasting of disease development, for a choice of treatment procedure. Hemodynamic research impedance methods allow to simplify diagnostic procedures, and also to reduce cost of the necessary diagnostic equipment.

Being introduced into medical practice, new diagnostic equipment and algorithms able to determine any required number of parameters of the patient's body and organs increases the volume of information available to the doctor, but does not always facilitates the diagnosis. The difficulties encountered in the analysis of information flow by traditional techniques encourage the search for new methods of diagnostic in medicine and biological researches.

Negative pressure breathing (NPB) is a spontaneous breathing with negative (relative to external, atmospheric) pressure in airways and lungs during the complete respiratory cycle or at certain phase [1]. Our study was aimed at evaluation changes in cardiovascular system caused by applying negative pressure during inspiration (NPBin) [2–4]. Negative pressure was produced by enhanced inspiratory valve in standard valve box connected to mouthpiece [5, 6].

This paper presents the method of quantitative comparison of signals based on the rheocardiographic (RCG) signal parameters and rheoencephalographic (REG) signal parameters. RCG is a noninvasive method for the measurement of cardiac output, cardiac index, systolic time intervals, and other hemodynamic parameters [7]. RCG is a method for monitoring the relative changes in hemodynamics in many clinical situations and in physiological studies of cardiac activity [7–9]. REG is electrical impedance measurements of the brain blood flow [10]. Medical applications of REG are used for neuro-critical care and for primary prevention of stroke and cardiovascular diseases. REG technology is a

noninvasive, continuous and inexpensive method for many diagnostic applications [11, 12].

2 Materials and Methods

In our research mouth pressure (MP) was measured by Honeywell differential pressure transducer connected to mouthpiece. The enhanced inspiratory valve could be set up at a predetermined level of mouth negative pressure in the range from −10 to −25 cm water [6]. Value of applied negative pressure was the only difference between series (0, −10, −15, −20, −25 cm water). The study included five series. Each series was divided into three stages: 15 min before applying NPBin (later referred as stage "BEFORE"), 25 min of NPBin (later referred as stage "DURING") and 15 min after NPBin (later referred as stage "AFTER"). The following physiological signals were recorded continuously during all three stages: RCG, REG and MP.

Our RCG and REG devices utilize 100 kHz probing current, with amplitude $I_{RCG} = I_{REG} = 3$ mA (see Fig. 1). A measurement of biological tissues full impedance (base impedance, BI) and its change at pulse blood filling (rheographic index, RI) lies in basis of rheographic methods. BI was obtained as following: RCG and REG signals were low-pass filtered with cut-off frequency 0.1 Hz. For RI the RCG and REG signals were band-pass filtered from 0.1 to 100 Hz (see Fig. 2).

Description of an impedance cardiac system is presented in the papers [7, 8]. We used a tetrapolar system of electrodes. It means that four electrodes are positioned on a body surface, the pair of measuring electrodes is between pair of current electrodes. The scheme of the RCG electrodes location is presented in Fig. 1.

REG method characterizes the blood flow parameters estimation of the three main paired brain arteries: internal
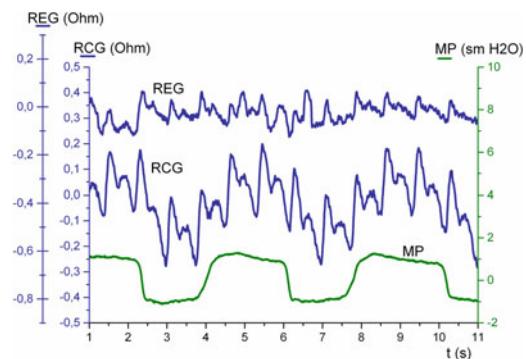
Fig. 2 The representative signals RI RCG, RI REG and MP

and external carotid arteries and vertebral artery. Usually four symmetric electrodes systems are used in clinical practice for REG signals registration: fronto-mastoidal electrodes system (F-M) and occipito-mastoidal electrodes system (O-M) [13]. In this case, one can diagnose internal carotid arteries and vertebral arteries in the both cerebral hemispheres. In our work we used REG signals registration in F-M electrodes system. The scheme of the REG electrodes location is presented in Fig. 1.

The study was performed in 2014 in the Institute of BioMedical Problems of the Russian Academy of Sciences. Seven healthy male volunteers participated in the study as test subjects. None of the subjects took medication and did not suffer from chronic or acute diseases. An age of the volunteers was from 19 to 34 years, the mean ±SD was 25.7 ± 6.3. The group is in detail presented in the Table 1.

All measurements were made with a subject in supine position. The study included five series conducted on the same protocol with each volunteer (see Fig. 3).

Series were conducted in random sequence. Each volunteer participated only in one series per day.

3 Compliance with Ethical Requirements

This study was performed in accordance with the Declaration of Helsinki. Informed consent from test subjects was received prior to study. The experiment was adopted by the Bioethics Committee of the Institute of BioMedical Problems of the Russian Academy of Sciences.

4 Results

The analysis of parameters BI and RI change at NPB has been carried out. At the analysis of BI change it has been established that its changes are not significant in a registration record (see Fig. 4). Therefore further we accepted that

Fig. 1 The scheme of simultaneous signals registration with electrodes location

Table 1 The group of healthy male volunteers
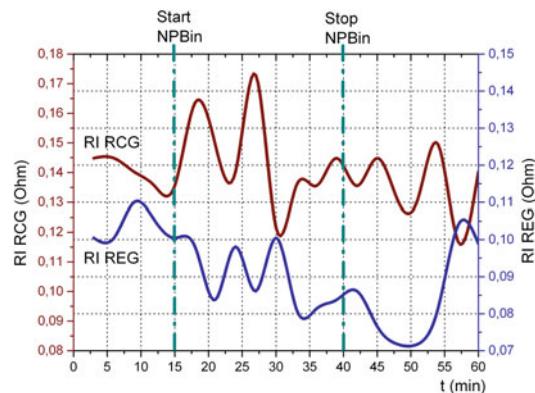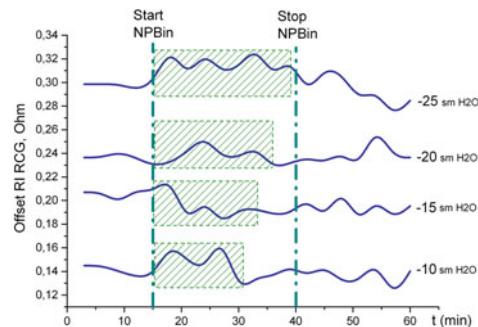
Volunteer	Age	Body height (m)	Weight (kg)	Body build
1	29	1.80	71	norm.
2	21	1.76	52	hyposthenia
3	24	1.81	74	norm.
4	33	1.80	82	norm.
5	34	1.85	78	norm.
6	19	1.76	65	norm.
7	20	1.77	68	norm.

Fig. 3 The volunteer №3 series of mouth pressure records

Fig. 4 BI RCG and BI REG changing during NPBin

BI does not change value during all record and remains constant.

At first we analysed tidal variations of RI of RCG and REG signals. To obtain the tidal variations, we averaged RI during each respiratory cycle, starting 1 s from the start of each inspiration until about 8 s passed from the beginning of inspiration. Actually this averaging procedure is meaningful until the beginning of the next inspiration. The time to beginning of the next inspiration depends upon breathing frequency. In practical terms this averaging is reasonable for time span about 4 s for stages BEFORE and AFTER and about 9 s for stage DURING.

At the analysis of RI change, it has been established that duration of reaction to affecting for is the different. The time

Fig. 5 RI RCG and RI REG changing during NPBin

Fig. 6 The adaptation period of cardiovascular system at different NPBin

of cardiovascular system reaction on affecting can be observed in RCG signal. At the same time in REG signal processes of cardiovascular system adaptation to NBPin influence are observed throughout all period of signals registration. The instance of RI change for one record is presented in Fig. 5.

For a records series at various types of NPBin it is possible to define the time of cardiovascular system adaptation at RCG signal. Therefore, for four records at different NPBin the signals of one volunteer have been analysed. Our results are presented in Fig. 6.

It is shown (see Fig. 6) that adaptation period duration to influence of different magnitude at this volunteer is not equal. It depends on NPBin level and increases with rising of pressure magnitude. In Fig. 6 the adaptation period of cardiovascular system is conditionally shown by the cross-hatched sections and it was defined by a maximum level of signal amplitude.

So the presented data on one of tests subjects demonstrate that there are tidal variations of rheographic parameters. An analysis and a discussion of the group statistical characteristics of the variations as well as discussion of physiological nature of the rheographic parameters will the matter of the further works.

5   Conclusions

Researches of a basic impedance changes are conducted with a negative pressure breathing using rheocardiographic and rheoencephalographic signals.

It is established that for calculations of cardiac output volumes it is possible to use BI value, registered in the research beginning.

It is shown that for an estimation of adaptation period duration to NPBin it is expedient to use RI RCG value.

Further it makes sense to use the signals presented in given paper together with breath phases for research of adaptation mechanisms to NPBin.

Conflict of Interest   The authors declare that they have no conflict of interest.

References

1. Donina, Z.A., Lavrova, I.N., Tikhonov, M.A., Kotov, A.N., Kolesnikov, V.I., Baranov, V.M. Influence of changes in intrathoracic and central venous pressure on cardiac filling dynamics. Bulletin of Experimental Biology and Medicine, 136(6), 540–542 (2003). https://doi.org/10.1023/b:bebm.0000020197.36386.f7.

2. Convertino, V.A., Ryan, K.L., Rickards, C.A., Glorsky, S.L., Idris, A.H., Yannopoulos, D., Lurie, K.G. Optimizing the Respiratory Pump: Harnessing Inspiratory Resistance to Treat Systemic Hypotension. Respiratory Care 56(6), 846–857 (2011). https://doi.org/10.4187/respcare.01018.

3. Convertino, V.A., Cooke, W.H., Lurie, K.G. (2005). Restoration of Central Blood Volume: Application of a Simple Concept and Simple Device To Counteract Cardiovascular Instability in Syncope and Hemorrhage. Journal of Gravitational Physiology 12, 55–60 (2005).

4. Ryan, K.L., Cooke, W.H., Rickards, C. Lurie, K.G., Convertino, V. Breathing through an inspiratory threshold device improves stroke volume during central hypovolemia in humans. Journal of Applied Physiology 104(5), 1402–1409 (2008). https://doi.org/10.1152/japplphysiol.00439.2007.

5. Semenov, Y.S., Popova, Y.A., Diachenko, A.I., Reushkina, G.D., Kolesnikov, V.I., Suvorov, A.V. Characteristics of negative pressure inspiration effect on the cardiorespiratory system of humans in the conditions of 5-day dry immersion. Aviakosmicheskaya I Ekologicheskaya Meditsina 45(6), 37–40 (2011).

6. Semenov, Yu.S., Dyachenko, A.I., Popova, Yu.A. Reaction of the human cardiovascular system to respiration with additional negative pressure at breath during 15-hour head-down hypokinesia. Aviakosmicheskaya i Ekologicheskaya Meditsina 51(3), 22–30 (2017). https://doi.org/10.21687/0233-528x-2017-51-3-22-30.

7. Kubicek, W.G., Karnegis, J.N., Patterson, R.P. Development and evaluation of an impedance cardiac output system. Aerospace medicine 37(12), 1208–1212 (1966).

8. Cybulski, G. Ambulatory Impedance Cardiography. The systems and their applications. Springer-Verlag (2011).

9. Vasilyeva, R.M. Rheocardiography, an advanced noninvasive circulatory system test in children and adults: Progress and prospects. Human Physiology 43(2), 229–239 (2017). https://doi.org/10.1134/s0362119717020165.

10. Seipel, J.H. The biophysical basis and clinical applications of rheoencephalography. Neurology 17, 443–451 (1967).

11. Yarullin, K.K., Krupina, T.N., Alekseev, D.A. Rheo- and encephalographic criteria for diagnosing latent cerebral circulation insufficiency in patients with cervical osteochondrosis. Sovetskaya Meditsina 43(3), 9–15 (1980).

12. Bodo, M. Studies in Rheoencephalography. Journal of Electrical Bioimpedance 1, 18–40 (2010).

13. Sokolova, I.V., Yarullin, K.K., Maksimenko, I.M., Ronkin, M.A. Analysis of the structure of rheoencephalogram as a pulse filling of blood. Journal of Nevropathol 77, 1314–1321 (1977).

Comparison of Home Blood Pressure Measurement Devices on Artificial Signals

Jan Havlík and Markéta Sušánková

Abstract

Cardiovascular diseases are well known as one of the leading causes of death in developed countries. The hypertension is a significant danger and should be monitor carefully. In recent decades, auscultatory and oscillometric methods become as widely used for blood pressure measurement. In clinical practice, blood pressure measuring devices are evaluated according to validating protocols. Despite these protocols, a market with the automatic devices for home self-measurement of the blood pressure is flooded by a lot of cheap devices with doubtful accuracy. The aim of this study is to compare selected devices for the self-measurement in the home conditions. The devices were evaluated using the blood pressure simulators. For each device and each type of blood pressure signal, the absolute and the relative errors of the diastolic and the systolic pressures were evaluated. The obtained results show that the measurement error of these devices could be frequently higher than 5 mmHg and it is necessary to concern with the accuracy of the devices.

Keywords

Blood pressure • Tonometers • Self-measurement Device comparison

1 Introduction

Cardiovascular diseases are well known as one of the leading causes of death in developed countries. Risk of coronary, cerebral or peripheral artery diseases closely relates to creeping changes in the cardiovascular system such as atherosclerosis or hypertension [1]. At the same time, the prevalence of arterial hypertension is about 44% in European countries and about 30% in the United States [2], respectively 24% in men and 20.5% in women [3]. Together with the ageing of the population in developed countries, which is well-documented [4], the hypertension is a significant danger and should be monitor carefully. Furthermore, many of the hypertension patients are not aware of their disease [5], and the numbers could be higher in fact. In all cases, the therapy of hypertension requires an accurate and reliable measurement of blood pressure.

Many studies in recent years show that a proper technique for the blood pressure monitoring is a self-measurement in home conditions [6, 7]. One significant advantage of the self-measurement of the blood pressure is a possibility to average a great number of measurements realized over a long period and to obtain a better projection of the real blood pressure. The other advantage of the self-measurement in comparison with a measurement provided by clinicians is an elimination of white coat effect which is conceived as an increase of blood pressure during a visit in a clinic followed with a decrease of the blood pressure to the normal level after the visit [8].

In 1987, a protocol for evaluating the accuracy of devices for the blood pressure measurement was published by the American Association for the Advancement of Medical Instrumentation [9]. Consequently, a protocol for validating the blood pressure monitors was also published by the British Hypertension Society in 1990 [10]. A blood pressure monitor could be recommended for clinical use if the AAMI criteria both for systolic and diastolic pressures are fulfils (the difference between the device and the mercury standard is lower than 5 mmHg) and if the device received a grade of A or B based on the BHS protocol. This procedure is relatively easily applicable for the blood pressure monitors used in the clinical practice, but unfortunately, it is very difficult

J. Havlík (✉) · M. Sušánková
Faculty of Electrical Engineering, Czech Technical University in Prague, Technická 2, CZ–16627 Prague 6, Czech Republic
e-mail: xhavlikj@fel.cvut.cz
URL: http://bmeg.fel.cvut.cz

to apply these criteria to the devices for self-measurement in home conditions. A market with the automatic devices for home self-measurement of the blood pressure is flooded by a lot of cheap devices with doubtful accuracy. Many of them have not passed any validation or have passed the validation with week results. Nevertheless, these devices are interesting for the costumers due to their low price, and in consequence of it, the devices are frequently used in home self-measurement of the blood pressure.

2 Methods

The aim of this study is to compare selected devices for the self-measurement of the blood pressure in the home conditions and to show the difference between the values obtained by these devices in the same conditions. The devices available in the global market with the different methods of the measurement have been selected one electronic tonometer which uses oscillometric method during the deflation of the cuff (Hartmann Digital HG160) and another one with oscillometric method during the inflation of the cuff (HuBDIC HPB-1520). The vital signs monitor Advisor BCI-9200 has been used as a clinically validated reference device. All devices were evaluated using the blood pressure simulators (Fluke BP Pump 2 and Fluke ProSim 8).

2.1 Evaluated Devices

Advisor BCI-9200 The device is a vital signs monitor intended for clinical use, which allows standard non-invasive blood pressure (NIBP) measurement during the deflation of the cuff. The device measures the blood pressure in the range of 20–250 mmHg for adults and in range of 20–130 mmHg for neonates. The manufacturer declares the accuracy as a greater value of ±3 mmHg and ±2% of obtained value. The safety and effectiveness evaluation of the device was passed before the measurement.

Hartmann Digital HG 160 Comfort The device is an automatic tonometer intended for self-measurement in home conditions. The device uses the oscillometric method during the deflation of the cuff for measurement of blood pressure in the range of 30–280 mmHg with a declared accuracy of ±3 mmHg.

HuBDIC HPB-1520 The device is an automatic tonometer for measurement of NIBP during inflation of the cuff. The manufacturer declares that the device measures in the range of 40–230 mmHg with the accuracy of ±3 mmHg.

2.2 Blood Pressure Simulators

FLUKE BP Pump 2 The device is a blood pressure simulator intended for testing of adult and neonatal blood pressure monitors. The simulator allows to simulate the systolic blood pressure (SBP) in range of 20–250 mmHg, diastolic blood pressure (DBP) in range of 10–200 mmHg, heart rate in the range of 30–250 bps and pulse volume in the range of 0.1–2.4 ml. The volume of the inner adult cuff is 310 and 20 ml of the neonatal cuff. The accuracy of pressure measurement is ±0.5% of measured value ±1 mmHg for pressure lower than 300 mmHg and ±2% for pressure up to 400 mmHg. The simulator provides 22 different presets for simulating blood pressure such as a heathy patient, geriatric patient, obese patient, a patient with tachycardia, bradycardia or atrial fibrillation etc. These presets have been used for tonometers evaluation.

FLUKE ProSim 8 The device is a vital signs simulator which can also simulate the oscillometric pulsations for testing of NIBP measurement devices. The device can generate the pressure in the range of 20–400 mmHg; the maximal pulse volume is 1.25 ml. The accuracy of pressure measurement is ±5% of measured value ±0.5 mmHg. Similarly, as BP Pump 2 the simulator provides different presets. For the tonometers comparison, the same presets have been used for both simulators.

2.3 Evaluation of the Device Accuracy

All devices have been evaluated using 22 simulated signals, generated both by FLUKE BP Pump 2 and Prosim 8 simulators. For each tonometer, the number N of successfully measurements have been obtained. Each measurement which was finished with SBP and DBP values on display is included in N.

The accuracy of the tonometers has been evaluated for all simulated signals. For each measurement, the absolute difference between obtained pressure and reference value

$$\Delta = NIBP - NIBP_{REF} \tag{1}$$

has been determined, where $NIBP$ is an obtained value of SBP or DBP respectively and $NIBP_{REF}$ is a simulated blood pressure (SBP or DBP respectively).

Consequently, from absolute values of obtained Δ the averaged value Δ_{AV} has been calculated.

$$\Delta_{AV} = \frac{1}{N} \sum_{n=1}^{N} |\Delta_n| \tag{2}$$

Table 1 Results for advisor BCI-9200, values obtained for both simulators

| | FLUKE BP Pump 2 | | FLUKE ProSim 8 | |
	SBP (mmHg)	DBP (mmHg)	SBP (mmHg)	DBP (mmHg)
N	21	21	20	20
Δ_{AV}	9.4	7.9	5.7	10.5
Δ for healthy patient	−9	3	−5	8
N with $\Delta_{SBP} < 12$ mmHg/$\Delta_{DBP} < 8$ mmHg	17	13	20	7
N with Δ higher than specified	18	14	16	18

Table 2 Results for hartmann digital HG 160 comfort, values obtained for both simulators

| | FLUKE BP Pump 2 | | FLUKE ProSim 8 | |
	SBP (mmHg)	DBP (mmHg)	SBP (mmHg)	DBP (mmHg)
N	22	22	21	21
Δ_{AV}	6.4	7.3	9.0	9.5
Δ for healthy patient	3	5	9	10
N with $\Delta_{SBP} < 12$ mmHg/$\Delta_{DBP} < 8$ mmHg	18	16	14	4
N with Δ higher than specified	7	18	18	19

Besides the Δ_{AV}, the Δ for the simulation of the healthy patient is presented with the results. As the number of accurately determined blood pressures is important, the number of measurements with $|\Delta_{SBP}| < 12$ mmHg and $|\Delta_{DBP}| < 8$ mmHg respectively has been determined, and also the number of measurements with Δ higher than the accuracy specified by the manufacturer for each blood pressure measuring device.

3 Results

For each device (three tonometers) and each type of blood pressure signal (22 different simulated signals), the absolute errors of the diastolic and the systolic pressures were evaluated.

Advisor BCI-9200 The results for Advisor BCI-9200 are shown in Table 1. The device did not determine the blood pressure for tachycardia for both simulators and the blood pressure for strenuous exercise simulated by FLUKE ProSim 8. The highest obtained Δ_{SBP} was-25 mmHg for simulation of controlled ventilation. Typically, the Advisor BCI-9200 undervalues SBP and overvalues DBP in comparison with the reference.

Hartmann Digital HG 160 comfort The results for Hartmann Digital HG 160 comfort are shown in Table 2. The device determined all the blood pressures with exception of simulation labelled Nr. 3 (patient with hypertension, parameters $SBP = 200$ mmHg, $DBP = 150$ mmHg, $HR = 80$ bps, $PV = 0.6$ ml; FLUKE ProSim 8). The highest obtained Δ_{SBP} was 52 mmHg for simulation of strenuous

Table 3 Results for HuBDIC HPB-1520, values obtained for both simulators

| | FLUKE BP Pump 2 | | FLUKE ProSim 8 | |
	SBP (mmHg)	DBP (mmHg)	SBP (mmHg)	DBP (mmHg)
N	22	22	22	22
Δ_{AV}	3.9	3.0	12.4	9.1
Δ for healthy patient	−1	1	7	8
N with $\Delta_{SBP} < 12$ mmHg/$\Delta_{DBP} < 8$ mmHg	21	21	13	10
N with Δ higher than specified	10	8	20	21

exercise. Typically, the Hartmann Digital HG 160 comfort overvalues both SBP and DBP in comparison with the reference.

HuBDIC HPB-1520 The results for HuBDIC HPB-1520 are shown in Table 3. The device determined all the blood pressures from both simulators. The highest obtained Δ_{SBP} was 27 mmHg for simulation of strenuous exercise and controlled ventilation respectively. Typically, the HuBDIC HPB-1520 overvalues both SBP and DBP in comparison with the reference.

4　Discussion

A self-measurement of NIBP in home conditions is recognized as one of the significant ways for early diagnosis of serious cardiovascular diseases and as a prevention of heart failure and/or brain stroke. However, it is clear that the proper measurement requires a proper measuring device. Unfortunately, the blood pressure measuring devices for home use have not to meet any requirements in fact and the obtained results could be highly different from the real values. While for the clinical devices the standards require certain accuracy (typically ± 5 mmHg for more than 60% of measurements for grade A), the accuracy of self-measurement in home conditions is uncertain.

The main aim of the study was to demonstrate how big could be the difference between obtained values and reference values. Even though the devices were evaluated in optimal conditions using the artificial signals, the results show that the measurement error of these devices could be very high. The difference higher than 5 mmHg was obtained frequently with all the evaluated devices, the differences in tens of mmHg were not been exceptional.

5　Conclusion

The paper presents the comparative study of selected devices for the self-measurement of blood pressure in the home conditions. The devices were evaluated using the blood pressure simulators. For each device and each type of blood pressure signal, the absolute errors of the diastolic and the systolic pressures were evaluated. The obtained results show that the measurement error of these devices could be frequently higher than 5 mmHg and it is necessary to concern with the accuracy of the devices in wide context.

References

1. van Popele, N.M., Bos, W.J.W., de Beer, N.A.M., van der Kuip, D.A.M., Hofman, A., Grobbee, D.E., Witteman, J.C.M.: Arterial stiffness as underlying mechanism of disagreement between an oscillometric blood pressure monitor and a sphygmomanometer. Hypertension 36(4), 484–488 (Oct 1, 2000)
2. Wolf-Maier, K., Rodrguez-Artalejo, F., Stegmayr, B., Thamm, M., Tuomilehto, J., Vanuzzo, D., Vescio, F., Cooper, R.S., Banegas, J. R., Giampaoli, S., Hense, H.W., Joffres, M., Kastarinen, M., Poulter, N., Primatesta, P.: Hypertension prevalence and blood pressure levels in 6 european countries, canada, and the united states. Journal of the American Medical Association 289(18), 2363–2369 (2003)
3. World Health Organization: World Health Statistics 2015. World Health Organization, Geneva (2015)
4. Ferrucci, L., Giallauria, F., Guralnik, J.M.: Epidemiology of aging. Radiologic clinics of North America 46(4), 643–652 (2008)
5. World Health Organization: A global brief on hypertension: silent killer, global public health crisis: World health day 2013 (2013), http://www.who.int/iris/handle/10665/79059
6. Tsuji, I., Imai, Y., Nagai, K., Ohkubo, T., Watanabe, N., Minami, N., Itoh, O., Bando, T., Sakuma, M., Fukao, A., Satoh, H., Hisamichi, S., Abe, K.: Proposal of reference values for home blood pressure measurement: prognostic criteria based on a prospective observation of the general population in ohasama, japan. American journal of hypertension 10(4 Pt 1), 409–418 (Apr 1997)
7. Asmar, R., Zanchetti, A.: Guidelines for the use of self-blood pressure monitoring: a summary report of the first international consensus conference. Journal of Hypertension 18(5), 493–508 (2000)
8. Ogedegbe, G., Pickering, T.: Principles and techniques of blood pressure measurement. Cardiology clinics 28(4), 571–586 (2010)
9. Electronic or automated sphygmomanometers (1987)
10. O'Brien, E., Petrie, J., Littler, W., de Swiet, M., Padfield, P.L., O'Malley, K., Jamieson, M., Altman, D., Bland, M., Atkins, N.: The british hypertension society protocol for the evaluation of automated and semi-automated blood pressure measuring devices with special reference to ambulatory systems. Journal of hypertension 8(7), 607–619 (Jul 1990)

Pulsed Transmission Waveform to Mitigate Tissue Thermal Effects in Transcutaneous Wireless Energy Supply Systems for High-Power Rated Medical Implants

Omar Escalona, Niall Waterman, James McLaughlin, and David McEneaney

Abstract

Therapeutic options in end stage heart failure include cardiac transplantation or mechanical circulatory support: Left Ventricular Assist Device (LVAD) or Total Artificial Heart (TAH). These devices have relatively high power requirements (5–80 W). Existing power supplies to LVAD and TAH are via percutaneous drivelines with a high frequency of complications including infection. We have developed a wireless Transcutaneous Energy Transmission (TET) waveform protocol and system technology which address the major clinical drawbacks of existing systems: skin tissue thermal effect and system durability. Conventional single-channel TET solutions have significant limitations, including inefficient energy transfer characteristics and high energy density levels producing tissue thermal effects. A reduced lifetime of the internal rechargeable battery is an additional drawback. In the proposed novel system, a multi-channel, time-space multiplexed and pulsed RF transmission waveform transcutaneous power delivery approach, is presented for sustained internal energy supply to high-power rated implantable devices. The bench system prototype performance evaluation results, revealed excellent high-energy transfer efficiency and safer management of lower energy density levels. In conclusion, the proposed pulsed transmission waveform protocol and multi-channel concepts can be configured for individual high-power rated LVAD devices to effectively mitigate tissue thermal effects and to prolong backup battery lifetime.

1 Introduction

Heart failure (HF) remains a significant and growing public health problem despite advances in drug therapy and implanted device technology. While the options for patients with advanced heart failure refractory to standard therapy are limited, heart transplantation remains an option. Limitation of donor availability restricts the number of heart transplants carried out worldwide to approximately 4000/year. Left ventricular assist devices (LVAD) are increasingly used as a bridge to transplantation or destination therapy. LVADs significantly improve survival and quality of life for patients with advanced heart failure [1, 2].

The current solution uses a percutaneous driveline carrying an electric cable through the skin. However, a high incidence (20%) of infection [2] with percutaneous drivelines has prompted the development of Transcutaneous Energy Transfer (TET) systems [3]. While none are presently licensed for clinical use, the available TET prototypes for LVADs and total artificial hearts (TAH) use a single bulky subcutaneous receiving coil channel in continuous transmission mode. They have a number of significant limitations which have restricted their application in the high power rated device (5–80 W) sector [4, 5]. They are currently under consideration for micro-LVADs (<4 W); if used in LVAD applications exceeding 5 W the heating effect of the subcutaneous receiver coil would reach clinically

O. Escalona (✉) · N. Waterman · J. McLaughlin
Engineering Research Institute, Ulster University, Newtownabbey, UK
e-mail: oj.escalona@ulster.ac.uk

D. McEneaney
Cardiovascular Research Unit, Craigavon Area Hospital, Portadown, UK

unacceptable levels exceeding 2 °C above body core temperature, as very well reported on this main blocking issue with conventional TET systems [3]. The work of Budgett et al. [6, 7], is a milestone reference addressing the main limitations of current mono-channel, continuous transmission TET systems. Over a 12-year period our research team developed the transcutaneously energised Passive Implantable Atrial Defibrillator (PIAD) technology [8, 9], as the precursor technology; also called the RF defibrillator in the clinical trials [10]. The PIAD technology enabled the efficient transmission of up to 20 J RF-energy packets in 15 ms DC defibrillation shock pulse duration, through a dual tuned RF coil system [11]. Thus by storing the shock energy in an implanted super-capacitor unit, using the PIAD defibrillation waveform, instead of the classic continuous RF power transmission, it would enable incorporating a variable cooling period, of 8–40 s, allowing dermal blood perfusion [12], during 10–50 heart beats, to the tissue area around the pair of radiofrequency (RF) energy transfer coils.

2 Methods and Materials

2.1 Pulsed Transmission Waveform Protocol

In order to address the above indicated dermal overheating effects, a novel pulsed transmission waveform protocol (15–320 ms pulse width) is proposed. It operates at ultra-low duty cycles (up to 0.1%, depending on the power drive), enabling considerable dermal tissue cooling time (40 s) during the idle waveform period (see Fig. 1), and with a multichannel system approach for Transcutaneous Wireless Energy Supply for Medical Implants (TWESMI) by periodic transmission of energy packs of 20–640 J (depending on the number of channels), through multiple flexible and thin (flexi-thin coils, see photo in Fig. 2) implanted coil channels (up to 4-channel system); enabling the use of disposable garments for TET systems, as illustrated in Fig. 2, and thus presenting an effective time-space multiplexing waveform
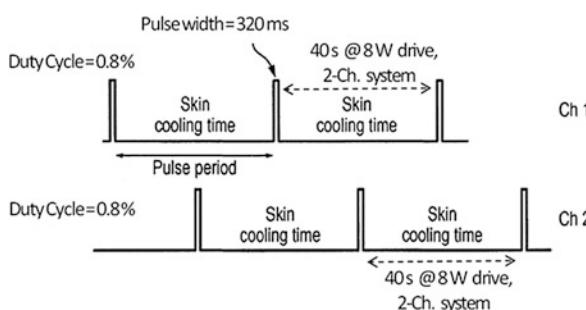
Fig. 1 Illustration of the pulsed transmission waveform of RF energy packs (e.g., 320 J packs every 40 s, in a 2-channel system), which could drive an 8 W LVAD continuously

concept; thus, the TWESMI system would be enhanced by a reduction on the energy density requirement through each coil pair, by increasing the number of channels (multichannel) of TET coil pairs. The selected operating RF transmission frequency was set to 200 kHz.

2.2 The Capacitive Load Drive Assessment Method

The transmission of energy packets to the implanted receiver coil would require an implanted storage capacitor, C_L, which could be provided by a compact non-electrolytic supercapacitor. However, there are various technological challenges for efficiently driving a secondary capacitive load during the relatively short pulse width of the energy pack (E_{PACK}) transmission. The latter is characterized by a capacitor charge up cycle rather than driving the resistive LVAD (R_L), see Fig. 3.

We thus evaluated the transmission efficiency for various capacitive load conditions and the inter-coil axial separation distance to determine the operating parameters for maximum efficiency. Here, the DC to DC efficiency definition was adopted [7]. For this, a capacitor energy supply, C_E, pre-charged at a certain initial level in the primary side RF transmitter, is measured by its voltage change during a single energy pack pulse transmission, and the energy received in the secondary side measured by voltage and current measurement using a digital storage oscilloscope (Fig. 3).

2.3 Inter-coil Axial Air Gap Distance Assessment Method

There is an important variable to be assessed when driving a capacitive load is the operating voltage level of the capacitor C_L, i.e., the instantaneous pre-charge voltage level at capacitor C_L at the moment when the RF transmission pulse is received. This operating voltage value needs to be controlled if the TET system efficiency is to be optimized. For this the C_L pre-charge voltage value is changed by two actions:

(a) by changing the transmitter voltage supply at C_E and
(b) by changing the inter-coil air gap distance; measured in mm steps (12–34 mm).

These two variables were varied and the efficiency parameters were measured, and the efficiencies calculated for every case of values used for the parameters (a) and (b).

2.4 Implemented System Block Diagram

Figure 4 shows a block diagram of the implemented multichannel pulsed transmission waveform protocol for
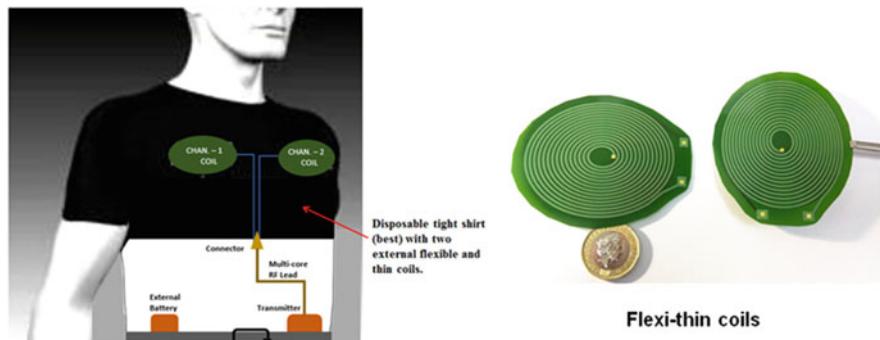
Fig. 2 Illustration of a 2-channel disposable garment for the TWESMI system enabled by the flexi-thin coils concept
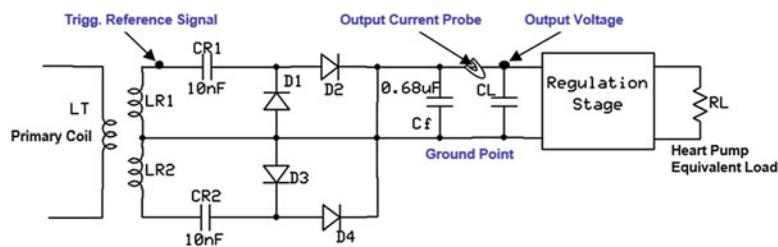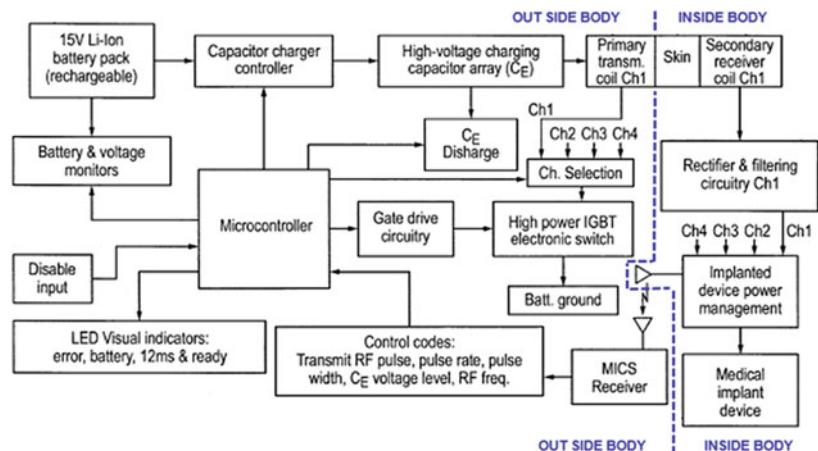
Fig. 3 Secondary side receiver circuit, which presents a capacitive load during the RF-pulse transmitted energy pack

Fig. 4 System block diagram of the multichannel pulsed transmission waveform protocol for addressing skin tissue thermal stability

addressing tissue thermal stability; which incorporates a cooling time for blood circulating in the tissue around the implanted secondary coil. The coils may be constructed to be flexible and thin by copper printing spiral on a flexible substrate: this flexi-thin coil approach will be presented in a subsequent article.

3 Results

Tissue cooling time performance of a dual channel portable TWESMI system prototype, designed to deliver at the secondary load an average of 514 W during transmission pulse width, which was varied from 20 to 320 ms, under three different LVAD power ratings (8, 15 and 40 W), is presented in Fig. 5. The measurements enabled the calculation of the energy pack (E_{PACK}) arriving at the capacitor C_L (in Fig. 3) for every case of transmission pulse width, and also the calculation of the efficiency as a function of the pre-charge level conditions of C_L modulated by the axial separation distance between the coils (skin thickness), and the results presented in Fig. 6.

The TWESMI system efficiency results in Fig. 6 reveal it's strong dependence on the operating level of pre-charge voltage at the output capacitor C_L, which in this empirical assessment was influenced by the above listed two factors:
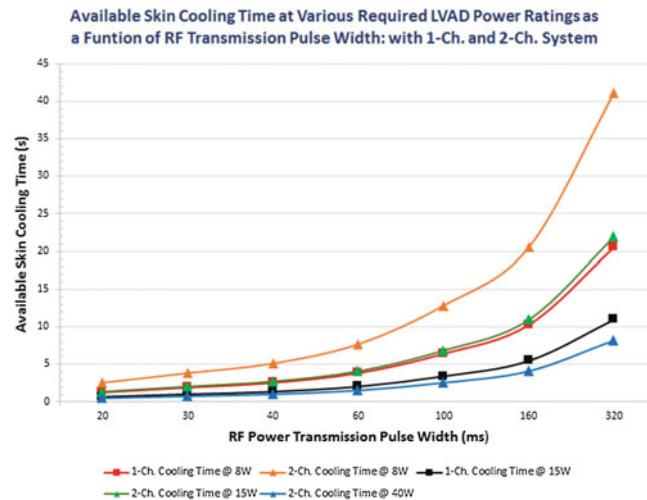
Fig. 5 Available time in seconds for heat absorption by dermal capillary blood perfusion, as a function of TWESMI RF power transmission pulse width in milliseconds, for various conditions of LVAD power rating (8, 15 and 40 W) and for 1-Ch. and 2-Ch. TWESMI system
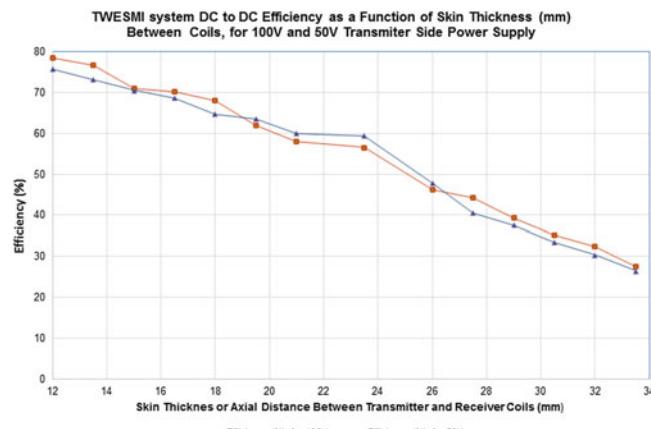
Fig. 6 DC to DC efficiency [7] of the TWESMI transcutaneous energy transfer at increasing axial inter-coil spacing due to several skin thickness values (mm), for 100 and 50 V operating supply voltages on the transmitter side

Fig. 7 Multichannel TWESMI enabling tissue cooling time as percentage of the transmission cycle period, for various power requirement conditions, with 1–4 channels system
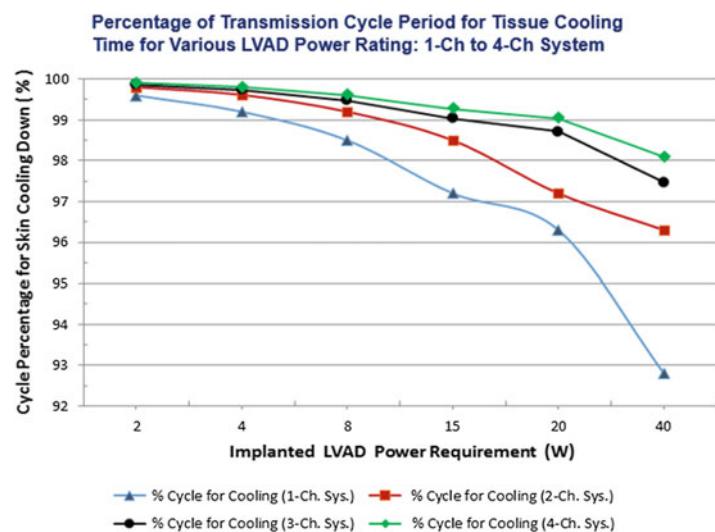
Table 1 Comparative advantages of our TWESMI system dedicated to LVADs

Concerning issue	Percutaneous drive line	Continuous transmission [13]	TWESMI energy delivery system
Infection	Is a major problem [4]	N/A	N/A
Profile	N/A	Rigid and bulky	Flexible and thin
Skin overheating	N/A	Significant [6, 7]	Can be minimised
Supercapacitor usability	**N/A**	Very poor (always use battery)	Excellent use (rarely uses battery)
Internal rechargeable battery lifetime	N/A	Short life [4] (constant use; 1–2 yrs)	Idle most of time, extended life
Power limitation	None	<15 W	25 W or more
Movement/ decoupling	Limited line durability	Problematic (moves) [7]	Light Coil → Minimal
Power control	No issues	By RF Change → Detuning → Heating [6, 7]	RF at Resonance → Maximum Efficiency → Less Heat
DC to DC efficiency [7]	N/A	>25% [7]	>45%

(a) and (b) in Sect. 2.3. A maximum efficiency of about 78%, was for the smallest gap (12 mm).

Multichannel TWESMI system power delivery performance as a function of pulsed transmission waveform configuration, indicated by the pulsed waveform cycle percentage available for skin tissue cooling down, was analysed for delivery power levels from 2 to 40 W, for systems of 1-Ch to 4-Ch, and results presented in Fig. 7.

4 Discussion and Conclusion

The competitive advantage of the proposed concept of pulsed transmission waveform for TETs, is revealed by the results presented in Figs. 5, 6 and 7, which enable considerable skin tissue cooling time (e.g., ∼40 s, with <1% duty cycle at 15 W drive; with a 4-Ch. system), in order to exploit factors of thermal diffusion by blood perfusion action; which is a process that requires some considerable time (40–80 heart beats). The TWESMI transmission waveform concept addresses the skin thermal issue that conventional TET systems have not overcome at power delivery rates above 5 W; this is not sufficient for a relatively large HF population with advanced HF. The TWESMI waveform and system technique are meant to unfold the envisaged immense potential benefits of LVAD or TAH treatment of chronic HF patients.

Table 1 presents a summary of the main advantages of the proposed multichannel pulsed transmission TWESMI system and waveform over conventional TET systems [6, 7].

However, a robust pre-clinical trial ready system needs to be configured.

References

1. Benjamin et al., Heart Disease and Stroke Statistics—2017 Update: A Report from the American Heart Association (7/Mar/2017), Circulation, 135:00–00, e390, (2017). https://doi.org/10.1161/cir.0000000000000485.
2. Holman WL: INTERMACS (Interagency Registry for Mechanically Assisted Circulatory Support), Circulation, 126, 1401–1406 (2012).
3. Dissanayake TD, Hu AP, Malpas S, Bennet L, Taberner A, Booth L and Budgett D. Experimental study of a TET system for Implantable biomedical devices. IEEE Transactions on Biomedical Circuits and Systems, 3 (6): 370–378 (2009).
4. Slaughter M, et al.: TET for Circulatory Support: History, Current Status and Future Prospects. J Card. Surg., 25:484–489 (2010).
5. Knecht, O., Bosshard, R., Kolar, J.W: High-Efficiency Transcutaneous Energy Transfer for Implantable Mechanical Heart Support Systems, IEEE Trans. Power Electron, 30, 6221–236 (2015).
6. Leung H., Budgett D., Hu A.P.: Minimizing Power Loss in Air-Cored Coils for TET Heart Pump Systems. IEEE J Emerging Sel. Topics Circ. Sys., 1(3) (2011).
7. Wang B, Hu A and Budgett D: Maintaining middle zero voltage switching operation of parallel-parallel tuned wireless power transfer system under bifurcation, IET Power Electronics; 7 (1), 78–84 (2014).
8. Walsh P.R., Rodrigues P.A., Velasquez J.J., Waterman N., Escalona O.J: Impedance compensated passive implantable atrial defibrillator. Electronics Letters, 50 (17), 1192–1193 (2014).
9. Walsh P., Kodoth V., McEneaney D., Rodrigues P., Velasquez J., Waterman N., Escalona O.J.: Towards low energy atrial defibrillation. Sensors (Switzerland), 15 (9), 22378–22400 (2015).

10. Kodoth, V., Castro, N.C., Glover, B.M., Anderson, J.M.C.C., Escalona, O.J., Lau, E. and Manoharan, G.: Waveform optimisation for internal cardioversion of atrial fibrillation. Journal of Electrocardiology, 44 (6), 689–693 (2011).

11. Escalona, O.J., Velasquez, J.J., Waterman, N., Chirwa, L. and Anderson, J.MC.C. Transcutaneous Dual Tuned RF Coil System Voltage Gain and Efficiency Evaluation for a Passive Implantable Atrial Defibrillator. In: Computing in Cardiology, 37, 741–744 (2010).

12. Matsuki H. and Matsuzaki T. Simulations of Temperature Rise on Transcutaneous Energy Transmission by Non-contact Energy Transmitting Coils. IEEE Transactions on Magnetics, vol. 29, pp. 3334–3336, (1993).

13. Budgett, D.: TET concept US-patent: http://www.google.com/patents/US9125242; in Dec (2017).

Author Index